

Reproduced by
**NATIONAL TECHNICAL
INFORMATION SERVICE**
U S Department of Commerce
Springfield VA 22151

AD-748232

TECHNICAL REPORT NO. 72-3

FINAL REPORT PROJECT VT/8706

DEVELOPMENT OF LP WAVE DISCRIMINATION
CAPABILITY USING LP STRAIN INSTRUMENTS

by

James E. Fix
and
John R. Sherwin

Sponsored by

Advanced Research Projects Agency
Nuclear Test Detection Office
ARPA Order No. 624

Acknowledgement

This research was supported by the Advanced Research Projects Agency, Nuclear Test Detection Office, under Project VELA-UNIFORM, and accomplished under the technical direction of the Air Force Technical Applications Center under Contract No. F33657-69-C-0121.

Approved for Public Release; Distribution Unlimited

TELEDYNE GEOTECH
3401 Shiloh Road
Garland, Texas

15 June 1972

ic

IDENTIFICATION

AFTAC Project No.	VELA T/8706
Project Title	Development of LP Wave Discrimination Capability Using LP Strain Instruments
ARPA Order No.	624
ARPA Program Code No.	8F10
Name of Contractor	Teledyne Industries, Inc. Geotech Division F33657-69-C-0121
Contract No.	1 July 1968
Effective Date of Contract	\$661,880
Amount of Contract	30 June 1972
Contract Expiration Date	James E. Fix
Project Manager	271-2561, A/C 214

The views and conclusions contained in this document are those of the authors and should not be interpreted as necessarily representing the official policies, either express or implied, of the Advanced Research Projects Agency, the Air Force Technical Applications Center, or the US Government.

UNCLASSIFIED

Security Classification

DOCUMENT CONTROL DATA - R & D

(Security classification of title, body of abstract and indexing annotation must be entered when the overall report is classified)

1. ORIGINATING ACTIVITY (Corporate author) Teledyne Industries, Inc., Geotech Division 3401 Shiloh Road - Garland, Texas 75040		2a. REPORT SECURITY CLASSIFICATION Unclassified
		2b. GROUP
3. REPORT TITLE Final Report, Project VT/8706 Development of LP Wave Discrimination Capability Using LP Strain Instruments		
4. DESCRIPTIVE NOTES (Type of report and inclusive dates) Final Report 1 July 1968 to 1 June 1972		
5. AUTHOR(S) (First name, middle initial, last name) Fix, James E. and Sherwin, John R.		
6. REPORT DATE 15 June 1972	7a. TOTAL NO. OF PAGES 597	7b. NO. OF REFS 183
8a. CONTRACT OR GRANT NO. F33657-69-C-0121	9a. ORIGINATOR'S REPORT NUMBER(S) TR 72-3	
b. PROJECT NO. VELA T/8706		
c.	9b. OTHER REF. ORT NO(S) (Any other numbers that may be assigned this report)	
d.		
10. DISTRIBUTION STATEMENT Approved for Public Release; Distribution Unlimited		
11. SUPPLEMENTARY NOTES	12. SPONSORING MILITARY ACTIVITY Advanced Research Projects Agency Nuclear Monitoring Research Office 1400 Wilson Blvd., Arlington, Va., 22209	
13. ABSTRACT This final report describes the development, construction, operation, data collection and data processing associated with the strain/inertial seismograph at Queen Creek, Arizona (QC-AZ), from 1 July 1968 to 1 June 1972. Strain seismographs were matched in sensitivity, amplitude, and phase to long-period (LP) inertial seismographs at 100K magnifications. Strain sensitivities of 2.5×10^{-13} at 30 sec were achieved. Operating magnifications were limited by ambient unrest of the ground which even for this quiet site was 6 dB or more above instrument noise at all periods from 0.1 to 2560 sec. The strain and inertial seismographs were combined to form an on-line directional array to enhance and to separate seismic waves, especially Rayleigh and Love waves and S_H and S_V waves. For example, a Rayleigh wave from an M_b 4.2 earthquake at 100 deg had a 17 dB signal-to-noise (S/N) ratio. The capability of the strain/inertial seismographs is demonstrated in the time domain with a variety of enhanced seismograms and in the frequency domain with many strain and inertial seismogram spectra having equivalent amplitudes, coherence of one, and correct phase angles. The concept of a single high-sensitivity station with combined strain/inertial seismographs offers LP detection and identification thresholds, S/N improvement, and beam forming capability equivalent to the 21-element Tonto Forest Observatory and 63-element Large Aperture Seismic Array spatial LP arrays. A comparison of QC-AZ LP detections and the PDE list of world-wide earthquakes was made for an 80-day interval. During this time, there were 887 earthquakes on the PDE list. The QC-AZ LP detections included 362 of these events with a 50 percent LP detection level of M_b 4.35. An additional 276 events were detected at QC-AZ that were not on the PDE list. Rayleigh waves of 45 to 60 sec are attenuated in the Basin and Range Province and the M_{S40} discriminant is materially affected. During the free oscillations after large earthquakes, the strain seismographs return to a normal detection level much earlier than inertial seismographs. Steps-of-strain (exponential strain pulses) are associated with conditions in the vicinity of the station and are not useful for source mechanism studies. The strain field at the tidal periods is the result of interaction among gravitational forces from the moon and the sun, air pressure fluctuations, and air temperature fluctuations. The strain seismographs detected repeatable acoustic signals which were separated into five acoustic wave modes.		

DD FORM 1 NOV 68 1473

Unclassified

Security Classification

UNCLASSIFIED

Security Classification

14.

KEY WORDS

Long-period strain seismograph
Seismology
Strain instruments
Wave discrimination

LINK A

LINK B

LINK C

ROLE

WT

ROLE

WT

ROLE

WT

18

UNCLASSIFIED

Security Classification

CONTENTS

	<u>Page</u>
ABSTRACT	
1. INTRODUCTION	1
1.1 Purpose	1
1.2 Organization	1
1.3 Previous reports	1
1.4 Topical summary	2
2. DESIGN GOALS	4
2.1 Strain seismograph sensitivity	4
2.2 Instrument considerations	7
2.3 Environmental considerations	8
3. THE MOST EFFECTIVE TECHNIQUE	14
3.1 Techniques considered	14
3.1.1 Laser-interferometer	14
3.1.2 RF-Variable capacitance transducer	16
3.1.3 Direct current-variable capacitance transducer	16
3.1.4 Optical displacement transducer	21
3.2 Techniques used	27
3.2.1 Moving-coil transducer	27
3.2.2 Solid-state amplifier	32
3.2.3 Strain seismometer design	35
3.2.4 Variable capacitance displacement transducer	42
4. SYSTEM DESIGN	51
4.1 Primary data system	51
4.1.1 Advanced long-period system (ALPS) - inertial	51
4.1.2 Short-period inertial system	52
4.1.3 The strain system	52
4.1.4 Meteorology system	62
4.2 Directional array seismic system (secondary)	63
4.3 Recording system	63
4.4 Other systems	63
4.5 Special equipment designed	63
4.5.1 Strain Filter Unit, Model 33350	68
4.5.2 The X10 mechanical amplifier	68
5. INSTALLATION	73
5.1 Site selection	73
5.1.1 Mine selection criteria	73
5.1.2 Areas investigated	74
5.1.3 The Queen Creek, Arizona, site (QC-AZ)	75
5.2 Site preparation	75
5.2.1 Excavation of the 55 deg azimuth drift	75
5.2.2 Excavation of the 325 deg azimuth drift	79
5.2.3 Excavation of the winze	79
5.2.4 Other site preparation work	80

CONTENTS, Continued

	<u>Page</u>
5.3 Instrument acquisition and fabrication	80
5.3.1 Government furnished equipment	80
5.3.2 Fabricated instrumentation	80
5.3.3 Purchased equipment	80
5.4 Instrument installation	81
5.4.1 Installation work during August and September 1969	81
5.4.2 Installation work during October through December 1969	81
5.4.3 Installation work during January through March 1970	84
5.4.4 Later installation work	91
6. OPERATION	92
6.1 Routine operations	92
6.1.1 Data recordings	92
6.1.2 Routine calibrations	92
6.1.3 Amplitude and phase responses	94
6.1.4 Determination of amplitude and phase responses by computer processing	96
6.1.5 Changes in system responses	98
6.2 Operating history	102
6.3 Operational problems	102
6.3.1 Elimination of power line pickup	102
6.3.2 Strain preamplifier saturation	104
6.3.3 Inertial seismograph response	105
6.3.4 Lightning protection	105
6.3.5 Noise on the S325 seismometer	106
7. NOISE AND STABILITY	109
7.1 Spectral analysis	109
7.2 Microseismic background	110
7.2.1 Absolute amplitude	110
7.2.2 Variation with time	116
7.3 Inertial seismograph theoretical and observed noise	128
7.4 Strain seismograph observed noise	138
7.4.1 Electronic noise	138
7.4.2 Other strain seismograph noise	138
7.4.3 Variation of strain background with time	142
7.5 Small earth motions	145
7.5.1 Amplitude of motions	145
7.5.2 Traveling dislocations	146
7.5.3 Other small motions	148
7.6 Seismic noise resulting from atmospheric pressure variations	149
7.6.1 Previous observations of wind-related long-period noise	150
7.6.2 Long-period earth strains and atmospheric pressure variation	153
7.6.3 Observed strains and pressure variations	156
7.7 Tilt noise on long-period inertial seismographs	190
7.7.1 Tilt theory for ALPS response horizontal seismographs	203

CONTENTS, Continued

	<u>Page</u>
7.7.2 Seismic spectral changes with pressure activity changes	206
7.7.3 Nonlinear tilting	206
7.8 Secular strains	209
7.9 Resistance of strain seismometers to acoustic vibrations	213
8. GENERAL PERFORMANCE OF INSTRUMENTS	218
8.1 Signals recorded on parallel strain seismographs	218
8.1.1 Earthquake signals	218
8.1.2 High wind signals	227
8.2 In-situ measurement of elastic parameters	232
8.2.2 Poisson ratio	235
8.2.3 Slope of stress-strain curve	237
8.2.4 Apparent local Q	241
8.3 Volumetric strain recorded on microbarograph and vertical strain seismograph	241
9. ENHANCEMENT OF SEISMIC WAVES WITH STRAIN AND INERTIAL SEISMOGRAPHS	247
9.1 Theory	248
9.1.1 Strain tensor	248
9.1.2 Rotation of the strain tensor	249
9.1.3 Enhancement of Rayleigh waves	251
9.1.4 Enhancement of Love waves	252
9.1.5 Relation between vertical strain and horizontal strain	253
9.1.6 Dilatation or volumetric strain	254
9.2 Combinations of strain and inertial seismographs	255
9.3 Enhancement of seismic waves	260
9.3.1 Long-period seismic waves enhanced by "on-line" recorders	263
9.3.2 Long-period seismic waves enhanced from magnetic tape recordings	276
9.3.3 Enhancement of ultra-long-period seismic waves	311
9.3.4 Enhancement of short-period waves	312
10. DETECTION THRESHOLD	324
10.1 Comparison with PDE events	324
10.2 Earthquake signal-to-ambient background signal ratio	329
10.3 The M_S/m_b discriminant	338
10.4 Effect of the Basin and Range Province upper mantle on Rayleigh wave signals at QC-AZ	344
10.5 Advantage of strain over inertial seismographs after large events	361
11. STEPS-OF-STRAIN	363
11.1 Review of the literature	363
11.2 Strain steps observed on QC-AZ strain seismographs	365
11.3 Interpretation of steps-of-strain	373

CONTENTS, Continued

	<u>Page</u>
12. SPECTRAL COMPARISONS, DISPLACEMENT, AND STRAIN	374
12.1 Theoretical relationship	374
12.2 Observed relationships	377
12.3 Summary of results of spectral comparisons	426
13. EARTH TIDES	442
13.1 Theory	442
13.2 Previous investigations of earth tides	447
13.3 Comparison of observed and predicted strains	449
13.3.1 Preparation of data	449
13.3.2 Secular strains	451
13.3.3 Time domain comparison	451
13.3.4 Frequency domain comparison	452
13.4 Pressure and temperature induced strains	483
13.5 Comments	498
14. ACOUSTIC SIGNALS ENHANCED BY STRAIN SEISMOGRAPHS	500
14.1 Review of theory and literature	500
14.2 Acoustic signals	503
15. CONCLUSIONS	522
16. ADMINISTRATION	524
17. REFERENCES	525
APPENDIX 1 - Bibliography of reports submitted on Project VT/8706	
APPENDIX 2 - Sensitivity required for long-period strain to be equivalent to advanced long-period inertial system	
APPENDIX 3 - Instrument nomenclature, recorder channel allocation, and polarity	
APPENDIX 4 - Routine operating instructions for QC-AZ	
APPENDIX 5 - Operating history of QC-AZ	
APPENDIX 6 - Selected bibliography of dislocation theory and observations of residual strains	

ILLUSTRATIONS

<u>Figure</u>		<u>Page</u>
1	Advanced LP system typical amplitude frequency response	5
2	Rayleigh wave horizontal strain per unit of displacement	9
3	The minimum strain to be sensed and/or the equivalent maximum allowable noise level for the horizontal strain seismograph	10
4	Basic concept of laser-interferometer technique	15
5	Dc-variable capacitance technique schematic	17
6	Simplified schematic of laboratory model direct current-variable capacitance transducer	19
7	Laboratory model of the variable capacitor for the direct current-variable capacitance transducer	20
8	Optical Displacement Transducer, Model 32770	22
9	Electrical schematic of Optical Displacement Transducer, Model 32770	24
10	Top view optical schematic of the Optical Displacement Transducer, Model 32770	25
11	Moving-coil technique magnet assembly	29
12	Data coil for moving-coil transducer	31
13	Ithaco, Inc., Long-Period Seismic Amplifier, Model 6089-34	33
14	Amplifier noise voltage power spectral density 164,000 Ω source resistance	36
15	Amplifier noise voltage power spectral density 54,000 Ω source resistance	37
16	Equivalent narrow-band rms voltages at input to pre-amplifier	39
17	Strain rod suspension frames	41
18	Electromagnetic calibrator for strain seismometer. The rf variable-capacitance transducer was temporarily mounted above the calibrator for calibration constant checks	43

ILLUSTRATIONS, Continued

<u>Figure</u>		<u>Page</u>
19	Strain rod anchor	44
20	Schematic of the detector for the variable capacitance transducer	46
21	Broad-band displacement transducer installed on 325 deg azimuth strain seismometer	47
22	Reproduction of a portion of a chart recording of the variable capacitance transducer showing the electronic noise level with fixed capacitors substituted for the active capacitors	49
23	Primary data system block diagram	53/54
24	Theoretical amplitude response of the advanced long-period system with two band-pass filters	55
25	Theoretical amplitude response of the extended range long-period inertial system with a Model 6824-14 band-pass filter	56
26	Theoretical amplitude response of the short-period system	57
27	Functional block diagram of a typical strain seismograph channel	58
28	Amplitude responses of typical strain seismographs at QC-AZ to traveling waves with constant phase velocity of 4.0 km/sec	59
29	Functional diagram of the directional array seismic system	64
30	Recording system	65
31	Timing and calibration subsystems	66
32	Power subsystem	67
33	Strain Filter Unit, Model 33350	69
34	Block diagram of a typical channel of the Strain Filter Unit, Model 33350	70
35	Vertical strain moving coil transducer with X10 mechanical amplifier	71
36	Location of Queen Creek seismological station (QC-AZ)	76

ILLUSTRATIONS, Continued

<u>Figure</u>		<u>Page</u>
37	Plan view of QC-AZ mine	77
38	Photographs taken during early part of site preparation task	78
39	View from tailing pile showing cable line from the mine, recording vans, power line, and access road	82
40	Phototube amplifiers and inertial LP seismometer controls in the instrument room in the mine	83
41	Long-period inertial seismometer tank vaults	85
42	Southwest end of 55 degree horizontal strain seismometer	86
43	Velocity transducer and preamplifier	87
44	Strain rod anchor	88
45	Side-by-side 325 degree azimuth strain seismometers. Permanent seismometer on left has been partially insulated. Vertical strain seismometer was located at gallows frame on left of figure	89
46	Ship's door installation	90
47	Maximum calibration amplitudes for QC-AZ strain systems	93
48	Phase response of strain and inertial seismograph in mid-October 1970, showing amount of phase mismatch	95
49	Pulses resulting from a step current into the calibration coil of P55L	97
50	Amplitude response of P55L calculated from the pulse in figure 49	99
51	P55L experimental amplitude response and amplitude response from smoothing and numerical differentiation of pulse from a step of acceleration	100
52	Phase response of P55L theoretical and calculated from the pulse in figure 49	101
53	Amplitude response to ground displacement of ALPS strain and inertial seismographs with 6-second notch filter and 40-second high-pass filters. Applicable to QC-AZ instruments in May and June 1971	103

ILLUSTRATIONS, Continued

<u>Figure</u>		<u>Page</u>
54	Schematic of modified lightning protection circuit for strain amplifiers at QC-AZ	107
55	Vertical earth motion amplitude spectral density	111
56	Horizontal (55 deg azimuth) earth motion spectral density	112
57	PZL microseismic background and instrument noise spectra, 1 to 256 sec	117
58	PZL microseismic background and instrument noise spectra, 30 to 2560 sec	118
59	P55L microseismic background and instrument noise spectra, 1 to 256 sec	119
60	P55L microseismic background and instrument noise spectra, 30 to 2560 sec	120
61	Power spectral density of microseismic background recorded on PZL and SZL seismographs on 29 August 1970	122
62	Power spectral density of microseismic background recorded on P325L and S325L seismographs on 29 August 1970	123
63	Power spectral density of microseismic background recorded on P55L and S55L seismographs on 29 August 1970	124
64	Power spectral density of microseismic background recorded on PZL and SZL seismographs on 31 October 1970	125
65	Power spectral density of microseismic background recorded on P325L and S325L seismographs on 31 October 1970	126
66	Power spectral density of microseismic background recorded on P55L and S55L seismographs on 31 October 1970	127
67	Power spectral density of microseismic background recorded on PZL and SZL seismographs on 1 December 1970	129
68	Power spectral density of microseismic background recorded on P325L and S325L seismographs on 1 December 1970	130
69	Power spectral density of microseismic background recorded on P55L and S55L seismographs on 1 December 1970	131
70	Vertical earth motion, 3 to 256 sec	134
71	Vertical earth motion, 30 to 2560 sec	135

ILLUSTRATIONS, Continued

<u>Figure</u>		<u>Page</u>
72	Horizontal Earth motion, 3 to 256 sec	136
73	Horizontal Earth motion, 30 to 2560 sec	137
74	S55L microseismic background and instrument noise spectra, 1 to 256 sec	139
75	Power spectral density and cross power spectral density of microseismic background recorded on parallel seismographs S325L1 and S325L2 on 11 June 1970	141
76	Possible travelling dislocation recorded on S325L1 and S325L2	147
77	Relationship between equivalent ground displacement and wind velocity at WMO	152
78	Reproduction of a 16 mm film recording of ground strains and tilts from microbarometric pressure loads on the surface of the ground	157
79	Power spectral density, coherence, and relative phase angle of perpendicular horizontal strain seismographs S325L1 and S55L during high wind conditions	161
80	Power spectral density, coherence, and relative phase angle of perpendicular horizontal strain seismographs S325U1 and S55U during high wind conditions	162
81	Power spectral density, coherence, and relative phase angle of parallel horizontal seismographs, S55L strain and P55L inertial, during high wind conditions	163
82	Power spectral density, coherence, and relative phase angle between horizontal strain seismograph S325L1 and microbarograph ML2	164
83	Power spectral density, coherence, and relative phase angle between horizontal strain seismograph S325U1 and microbarograph ML2	165
84	Power spectral density, coherence, and relative phase angle between horizontal strain seismograph S55L and microbarograph ML2	166
85	Power spectral density, coherence, and relative phase angle between horizontal strain seismograph S55U and microbarograph ML2	167

ILLUSTRATIONS, Continued

<u>Figure</u>		<u>Page</u>
86	Power spectral density, coherence, and relative phase angle between horizontal inertial seismograph P55L and microbarograph ML2	168
87	Power spectral density of pressure induced seismic noise recorded on PZL and SZL seismographs on 26 November 1970	169
88	Power spectral density of pressure induced seismic noise recorded on P325L and S325L seismographs on 26 November 1970	170
89	Power spectral density of pressure induced seismic noise recorded on P55L and S55L seismographs on 26 November 1970	171
90	Vertical earth motion, 20 to 2560 sec, high wind sample	174
91	Horizontal earth motion in 325 degree azimuth, 20 to 2560 sec, high wind sample	175
92	Horizontal earth motion in 55 degree azimuth, 20 to 2560 sec, high wind sample	176
93	Vertical earth strain, 20 to 2560 sec, high wind sample	177
94	Horizontal earth strain in 325 degree azimuth, 20 to 2560 sec, high wind sample	178
95	Horizontal earth strain in 55 degree azimuth, 20 to 2560 sec, high wind sample	179
96	Atmospheric pressure 1 to 256 sec	180
97	Atmospheric pressure 20 to 2560 sec	181
98	Atmospheric pressure, 20 to 2560 sec, high wind sample	182
99	Wind velocity, 20 to 2560 sec, high wind sample	184
100	Estimate of pressure to strain transfer function from S325L1	185
101	Estimate of pressure to strain transfer function from S325U1	186
102	Estimate of pressure to strain transfer function from S55L	187
103	Estimate of pressure to strain transfer function from S55U	188
104	Estimate of pressure to equivalent displacement for tilt transfer function from P55L	189
105	Estimate of pressure to vertical strain transfer function	191

ILLUSTRATIONS, Continued

<u>Figure</u>		<u>Page</u>
106	Estimate of pressure to horizontal strain transfer function from S325L	192
107	Estimate of pressure to horizontal strain transfer function from S55L	193
108	Estimate of pressure to vertical displacement transfer function	194
109	Estimate of pressure to horizontal displacement transfer function from P325L	195
110	Estimate of pressure to horizontal displacement transfer function from P55L	196
111	Estimate of wind velocity to vertical strain transfer function	197
112	Estimate of wind velocity to horizontal strain transfer function from S325L	198
113	Estimate of wind velocity to horizontal strain transfer function from S55L	199
114	Estimate of wind velocity to vertical displacement transfer function	200
115	Estimate of wind velocity to horizontal displacement transfer function from P325L	201
116	Estimate of wind velocity to horizontal displacement transfer function from P55L	202
117	Horizontal inertial ALPS seismograph response to displacement, tilt, and Rayleigh waves	204
118	Comparison of power spectral density between low and high wind conditions	207
119	Power spectral density, coherence, and relative phase angle of parallel horizontal seismographs, S325L1 strain and P325L inertial, during high wind conditions	208
120	Power spectral density, coherence, and relative phase angle with 128 lags for parallel horizontal seismographs, S325L1 strain and P325L inertial, during the LRI Rayleigh wave of and aftershock of the Peru earthquake	210
121	Secular strain 1 October 1970 to 28 March 1971	211

ILLUSTRATIONS, Continued

<u>Figure</u>		<u>Page</u>
122	Acoustic resonance of sealed seismometer chamber starting with second half-cycle of Pg from NTS explosion TIJERAS. NOS PDE data: 0 = 1430:00.0, 37.1 N, 116.0 W, h = 0 km, m_b = 5.5. Δ = 5.3 deg, azimuth = 318.7 deg	214
123	Acoustic resonance of sealed seismometer chamber starting with second half-cycle of Pg from NTS explosion TIJERAS	215
124	Acoustic resonance of sealed seismometer chamber generated by seismic signals from a Gulf of California earthquake. NOS PDE data: 0 = 2005:34.5, 30.1 N, 113.4 W, h = 33 km, m_b = 5.2. Δ = 3.4 deg, azimuth = 206.6 deg	217
125	Power spectral density, coherence, and relative phase angle of parallel strain seismographs S325LL1 and S325LL2 during the LR1 Rayleigh wave coda of the Peru earthquake	219
126	Reproduction of 16 mm film recording of part of the LQ3 Love wave, the LR2, and the LR3 Rayleigh wave from the Peru earthquake. NOS epicenter data: 0 = 2023:27.3, 9.2S, 78.8W, h = 43 km, near coast of northern Peru, m_b = 6.6 M_S = 7.8, Δ = 52.5 deg, azimuth = 137.5 deg	221
127	Power spectral density, coherence, and relative phase angle of parallel horizontal strain seismographs S325LL1 and S325LL2 during the LQ3 Love wave and the LR2 and the LR3 Rayleigh waves of the Peru earthquake	222
128	Power spectral density, coherence, and relative phase angle of perpendicular horizontal strain seismographs S325LL1 and S55LL during the LQ3 Love wave and the LR2 and the LR3 Rayleigh waves of the Peru earthquake	223
129	Reproduction of 16 mm film recording of LR1 Rayleigh wave from an aftershock of the Peru earthquake. NOS epicenter data: 0 = 0136:10.2, 9.3S, 79.0W, h = 48, off coast northern Peru, m_b = 6.0, M_S = 5.5, Δ = 52.5 deg, azimuth = 137.5 deg	224
130	Power spectral density coherence, and relative phase angle with 256 lags for parallel horizontal strain seismographs S325L1 and S325L2 during the LR1 Rayleigh wave of an after-shock of the Peru earthquake	225
131	Power spectral density, coherence, and relative phase angle with 128 lags for parallel horizontal strain seismographs S325L1 and S325L2 during the LR1 Rayleigh wave of an after-shock of the Peru earthquake	226
132	Reproduction of 16 mm film recording of a portion of the high wind sample	228

ILLUSTRATIONS, Continued

<u>Figure</u>		<u>Page</u>
133	Power spectral density, coherence, and relative phase angle of parallel horizontal strain seismographs S325L1 and S325L2 during high wind conditions, 1 to 256 sec range	229
134	Power spectral density, coherence, and relative phase angle of parallel horizontal strain seismographs S325L1 and S325L2 during high wind conditions, 20 to 2560 sec range	230
135	Power spectral density, coherence, and relative phase angle of parallel horizontal strain seismographs S325U1 and S325U2 during high wind conditions	231
136	Power spectral density, coherence, and relative phase angle of perpendicular horizontal strain seismographs S325L1 and S55L during high wind conditions	233
137	Power spectral density, coherence, and relative phase angle of perpendicular horizontal strain seismographs S325U1 and S55U during high wind conditions	234
138	Magnetic-tape playback showing the similarity between the sum of horizontal strain and vertical strain outputs	236
139	Force-strain curve in 325 deg azimuth	238
140	Force-strain curve in 55 deg azimuth	239
141	Short-period inertial seismograph recordings of ground motion following a blast in the small mine above the seismometer chamber	242
142	Vertical strain seismograph (SZB) and microbarograph (ML1 and ML1F) recording of volumetric strain from the San Fernando Earthquake, 9 February 1971. Microbarograph traces: ML1 as recorded, ML1F low-pass filtered 0.5 Hz, 24 dB/octave, polarity inverted	245
143	Azimuthal response to the horizontal components of Rayleigh, P, and S _y waves for (a) ground velocity, (b) ground strain, and (c) equalized ground velocity plus ground strain	257
144	Azimuthal response to horizontal transverse waves, Love, G, and S _H for (a) ground velocity, (b) ground strain, and (c) equalized ground velocity plus ground strain	259
145	Four beam azimuthal array at QC-AZ. Solid lines are response to Rayleigh and horizontal component of P and S _y waves; dashed lines are response to Love, G, and S _H waves	261

ILLUSTRATIONS, Continued

<u>Figure</u>		<u>Page</u>
146	Directional response toward 235 deg azimuth of TFO 7-element array	262
147	Reproduction of a QC-AZ 16 mm film record showing arrival of P, PP, and PPP from an earthquake in the D'Entrecasteaux Islands region	265
148	Reproduction of a QC-AZ 16 mm film record showing arrival of SKS, S (SH), PL, and PPS (SV) from an earthquake in the D'Entrecasteaux Islands region	266
149	Reproduction of a QC-AZ 16 mm film record showing arrival of SSP (SV) and SSS (SH) from an earthquake in the D'Entrecasteaux Islands region	267
150	Reproduction of a QC-AZ 16 mm film record showing LR1 Rayleigh wave enhancement on the difference trace and attenuation on the sum trace from an earthquake in the D'Entrecasteaux Islands region	268
151	Reproduction of a QC-AZ 16 mm film record showing LR2 Rayleigh wave enhancement on the sum trace and cancellation on the difference trace from an earthquake in the D'Entrecasteaux Islands region	269
152	Enhancement of 15 sec microseisms traveling toward an azimuth of 235 deg	270
153	Power spectral density of S+P55L and S-P55L on 31 October 1970	272
154	Enhancement of SSS, separation of SH and SV or S coupled PL, and enhancement of LR1 from an earthquake on the West Chile Rise. NOS PDE: 0 = 1101:28.4, 36.5 S, 97.2 W, h = 33 km, m_b = 5.5. Δ = 70.6 deg, azimuth = 167.7 deg	273
155	Enhancement of LR1 from an earthquake in the Iran-Iraq border region. NOS FDE: 0 = 1122:18.2, 36.8 N, 45.1 E, h = 33 km, m_b = 5.0. Δ = 107.1 deg, azimuth = 19.4 deg	274
156	Enhancement of LR1 from an earthquake south of Panama. NOS PDE: 0 = 1310:13.2, 6.7 N, 82.5 W, h = 33 km, m_b = 4.8. Δ = 37.7 deg, azimuth = 127.8 deg	275
157	Reproduction of 16 mm film recording of LR1 Rayleigh wave. NOS preliminary epicenter data: 0 = 0517:14.0, 39.2N, 29.5E, Turkey, h = 27 km, m_b = 4.2, Δ = 99.5 deg., azimuth = 29.6 deg	277

ILLUSTRATIONS, Continued

<u>Figure</u>		<u>Page</u>
158	Reproduction of 16 mm film recording showing enhancement of LR1 Rayleigh wave on S325L-P325L and S55L-P55L difference traces. NOS preliminary epicenter data: 0 = 0517:14.0, 39.2N, 29.5E, Turkey, h = 27 km, m_b = 4.2, Δ = 99.5 deg, azimuth = 29.6 deg	278
159	Reproduction of a 16 mm film recording of a Rayleigh wave train from an earthquake in the Tonga Island Region. 0 = 0621:16.3, 19.3S, 173.6W, h = 33, m_b = 5.3, Δ = 78.9 deg, azimuth = 238 deg	279
160	Enhancement of seismic waves from an earthquake in the Kermadec Islands region. NOS PDE data: 0 = 2159:42.9, 31.9S, 177.9W, h = N, m_b = 5.9, M_S = 6.2, Δ = 90.0 deg, azimuth = 231.1 deg, (a) individual channels, (b) directional array	281/282
161	Directional array enhancement of seismic waves from three earthquakes in the Kermadec Islands region. NOS PDE data: (a) 0 = 2159:42.9, 31.9S, 177.9W, h = N, m_b = 5.9, M_S = 6.2, Δ = 90.0 deg, azimuth = 231.1 deg, (b) 0 = 0316:49.6, 31.8S, 178.1W, h = N, m_b = 5.6, M_S = 6.3, Δ = 90.9 deg, azimuth = 231.2 deg, (c) LR2 from earthquake of (b) and 0 = 0538:06.0, 32.1S, 177.8W, h = 32 km, m_b = 5.6, M_S = 6.1, Δ = 90.0 deg, azimuth = 230.9 deg	283/284
162	Enhancement of seismic waves from two low-level earthquakes in the Solomon Islands region. NOS PDE data: (a) 0 = 1256:34.9, 2 Oct 1970, 6.9S, 155.0E, h = 36 km, m_b = 4.2, Δ = 96.5 deg, azimuth = 266.1 deg, (b) 0 = 1930:50.5, 30 Oct 1970, 6.8S, 154.8E, h = 34 km, m_b = 4.2, Δ = 96.7 deg, azimuth = 266.2 deg	285/286
163a	Enhancement of seismic waves from several earthquakes in the New Hebrides Islands. NOS PDE data: (1) 0 = 0932:23.0, 16.9S, 167.8E, h = 44 km, m_b = 5.5, M_S = 5.9, Δ = 91.5 deg, azimuth = 250.9 deg, (2) 0 = 0948:02.9, 17.0S, 167.8E, h = 34 km, m_b = 4.8, Δ = 91.5 deg, azimuth = 250.8 deg, (3) 0 = 0959:04.1, 17.0S, 167.9E, h = 33 km, no m_b given, Δ = 91.5 deg, azimuth = 250.7 deg, (4) 0 = 1034:23.0, 17.0S, 167.8E, h = 40 km, m_b = 4.7, Δ = 91.5 deg, azimuth = 250.8 deg, (5) 0 = 1210:23.4, 17.1S, 167.7E, h = 21 km, m_b = 4.5, Δ = 91.7 deg, azimuth = 250.8 deg	289/290

ILLUSTRATIONS, Continued

Figure

Page

- | | | |
|------|---|---------|
| 163b | Enhancement of seismic waves from several earthquakes in the New Hebrides Islands. NOS PDE data: (1) 0 = 0932:23.0, 16.9S, 167.8E, h = 44 km, m_b = 5.5, M_S = 5.9, Δ = 91.5 deg, azimuth = 250.9 deg, (2) 0 = 0948:02.9, 17.0S, 167.8E, h = 34 km, m_b = 4.8, Δ = 91.5 deg, azimuth = 250.8 deg, (3) 0 = 0959:04.1, 17.0S, 167.9E, h = 33 km, no m_b given, Δ = 91.5 deg, azimuth = 250.7 deg, (4) 0 = 1034:23.0, 17.0S, 167.8E, h = 40 km, m_b = 4.7, Δ = 91.5 deg, azimuth = 250.8 deg, (5) 0 = 1210:23.4, 17.1S, 167.7E, h = 21 km, m_b = 4.5, Δ = 91.7 deg, azimuth = 250.8 deg | 291/292 |
| 164 | Enhancement of waves from an earthquake in the Molucca Sea. NOS PDE data: 0 = 0702:46.6, 1.1S, 126.8E, h = 26 km, m_b = 5.8, M_S = 5.5, Δ = 116.7 deg, azimuth = 287.5 deg | 293/294 |
| 165 | Enhancement of seismic waves from two earthquakes in opposite azimuths. NOS PDE data: (a) off the coast of Kamchatka, 0 = 0016:25.9, 55.2N, 163.2E, h = 31 km, m_b = 5.2, Δ = 60.9 deg, azimuth = 319.2 deg, (b) near west coast of Colombia, 0 = 1416:55.3, 6.4N, 77.5W, h = 25 km, m_b = 5.2, M_S = 5.1, Δ = 41.4 deg, azimuth = 122.5 deg | 297/298 |
| 166 | Enhancement of seismic waves from an earthquake in Northern Colombia. NOS PDE data: 0 = 0459:53.4, 7.4N, 76.1W, h = 38 km, m_b = 5.7, M_S = 5.5, Δ = 41.7 deg, azimuth = 120.0 deg | 299/300 |
| 167 | Enhancement of seismic waves from an earthquake in the Greenland Sea. NOS PDE data: 0 = 2053:32.4, 79.8N, 2.7E, h = 32 km, m_b = 5.6, M_S = 5.7, Δ = 61.7deg, azimuth = 10.6 deg, (a) individual seismograms, (b) directional array, (c) combined strain seismographs to separate LQ and LR | 301/302 |
| 168 | Enhancement of seismic waves from an earthquake on the Central Mid-Atlantic Ridge. NOS PDE data: 0 = 1550:05.5, 7.7N, 37.6W, h = N, m_b = 5.3, M_S = 5.5, Δ = 72.5 deg, azimuth = 92.2 deg | 303/304 |
| 169 | Great circle paths from two earthquakes to QC-AZ | 305 |
| 170 | Magnetic tape playback of arrivals from interfering events. Event 1: 0 = 2003:42.2, south Sandwich Island region, h = 70 km, m_b = 6.0, Δ = 113.5 deg, azimuth = 142.5 deg; event 2: 0 = 2030:54.7, Andreanoff Island, h = 48, m_b = 5.7, Δ = 50.6 deg, azimuth = 312.0 deg | 306 |

ILLUSTRATIONS, Continued

<u>Figure</u>		<u>Page</u>
171	Enhancement of seismic waves from several earthquakes in the Gulf of California. NOS PDE data and Pg arrival times of unlisted events: (1) 0 = 0637:31.3, 30.8N, 113.7W, h = N, m _b = 4.0, Δ = 3.0 deg, azimuth = 217.0 deg, (2) Pg at 0707:12 not listed on PDE, (3) 0 = 0721:18.4, 30.0N, 113.9W, h = N, m _b = 4.0, Δ = 3.7 deg, azimuth = 211.9 deg, (4) Pg at 1659:25 not listed on PDE, (5) Pg at 1713:39 not listed on PDE, (6) 0 = 1739:45.5, 30.6N, 113.6W, h = N, m _b = 5.0, Δ = 3.1 deg, azimuth = 213.5 deg	309/310
172	Reproduction at X1.5 of 35 mm. film recording on the S325U seismograph of multiple revolution G and R phases	313/314
173	Three-component strain recordings of G1 and other waves from an earthquake near the north coast of New Guinea. NOS PDE: 0 = 1753:9.3, 4.9S, 145.5E, h = 42 km, m _b = 6.0, Δ = 103.4 deg, azimuth = 272.9 deg	315
174	Three-component strain recordings of G2 and other waves from an earthquake near the north coast of New Guinea. NOS PDE: 0 = 1753:9.3, 4.9S, 145.5E, h = 42 km, m _b = 6.0, Δ = 103.4 deg, azimuth = 272.9 deg	316
175	G1 and G2 waves recorded on S55U strain seismograph from an earthquake near the north coast of New Guinea. NOS PDE: 0 = 1753:9.3, 4.9S, 145.5E, h = 42 km, m _b = 6.0, Δ = 103.4 deg, azimuth = 272.9 deg	317
176	Enhancement of short-period arrivals from an explosion	319/320
177	Enhancement of short-period arrivals from an earthquake during the coda of an earlier event	321/322
178	Events listed on PDE cards with a stated magnitude for 80 days in March, April, and May, 1971. Dots are events detected at QC-AZ. Triangles are events not detected at QC-AZ	326
179	Events detected by QC-AZ and NOS in May, 1971	327
180	Events detected by NOS but not QC-AZ in May, 1971	328
181	Number of phases detected at QC-AZ for 80 days in March, April, and May 1971. m _b from NOS. m _b = NL means not listed on PDE list	330
182	PZL power spectral density m _b = 4.2, Δ = 96.7 deg earthquake and background noise signals	331

ILLUSTRATIONS, Continued

<u>Figure</u>		<u>Page</u>
183	P325L power spectral density $m_b = 4.2$, $\Delta = 96.7$ deg earthquake and background noise signals	333
184	P55L power spectral density $m_b = 4.2$, $\Delta = 96.7$ deg earthquake and background noise signals	334
185	SZL power spectral density $m_b = 4.2$, $\Delta = 96.7$ deg earthquake and background noise signals	335
186	S325L power spectral density $m_b = 4.2$, $\Delta = 96.7$ deg earthquake and background noise signals	336
187	S55L power spectral density $m_b = 4.2$, $\Delta = 96.7$ deg earthquake and background noise signals	337
188	M_S (QC-AZ) versus m_b (NOS) for July and August 1970 earthquakes	340
189	M_S (QC-AZ) versus m_b (NOS) for NTS announced explosions and presumed explosions at teleseismic distance	342
190	Cumulative number of events per month versus m_b , M_{S20} , M_{S40}	343
191	Seismograph amplitude responses normalized to 100,000 at calibration frequencies	346
192	Seismic waves recorded at GA-TX and QC-AZ from an $m_b = 4.8$ earthquake in the Greenland Sea on 19 May 1970 (day 139)	347/348
193	Seismic waves recorded at GA-TX and QC-AZ from an $m_b = 5.5$ earthquake on the North Atlantic Ridge on 19 June 1970 (day 170)	349/350
194	Seismic waves recorded at GA-TX and QC-AZ from an $m_b = 5.2$ earthquake on the South Atlantic Ridge on 21 June 1970 (day 172)	351/352
195	Seismic waves recorded at GA-TX and QC-AZ from an $m_b = 5.4$ earthquake north of Ascension Island on 26 June 1970 (day 177)	353/354
196	Seismic waves recorded at GA-TX and QC-AZ from an $m_b = 4.3$ earthquake in the Iceland region on 30 June 1970 (day 181)	355/356
197	Seismic waves recorded at GA-TX and QC-AZ from an $m_b = 4.3$ earthquake south of the Fiji Islands on 19 May 70 (day 139)	359/360
198	Earthquake duration on strain and inertial seismographs as function of m_b for (a) hypocenter depths > 60 km and (b) hypocenter depths < 60 km	362

CONTENTS, Continued

<u>Figure</u>		<u>Page</u>
199	Seismic waves recorded on the broad-band strain seismographs. NOS PDE epicenter data: (a) 0 = 0434:38.8, 10 Dec 70 (344), 4.0S, 80.7W, h = 25 km, Peru-Ecuador border region, m_b = 6.3, M_s = 7.6, Δ = 47.2 deg, azimuth = 135.6 deg, (b) 0 = 1605:00.2, 17 Dec 70 (351), 37.1N, 116.1W, h = 0 km, southern Nevada, NTS, CARPETBAG, m_b = 5.7, Δ = 5.4 deg, azimuth = 318.1 deg, (c) 0 = 0316:53.6, 19 Jan 71 (019), 23.8N, 108.6W, h = N, Gulf of California, m_b = 5.5, M_s = 5.9, Δ = 9.7 deg, azimuth = 163.3 deg, (d) 0 = 1400:41.6, 9 Feb 71 (040), 34.4N, 118.4W, h = 13 km, San Fernando, California, m_b = 6.2, M_s = 6.5, Δ = 5.8 deg, azimuth = 284 deg, (e) 0 = 1138:42.1, 14 Apr 71 (104), 27.7N, 112.4W, h = N, Baja California, m_b = 5.4, M_s = 5.2, Δ = 5.5 deg, azimuth = 187.1 deg	367/368
200	Seismic waves recorded on (a) the broad-band strain seismographs and (b) the ultra-long-period strain seismographs from an earthquake on West New Guinea, NOS PDE data: 0 = 0717:03.7, 10 Jan 71, 3.1S, 139.7E, h = N, m_b = 7.3, M_s = 8.1, Δ = 107.4 deg, azimuth = 278.0 deg	369/370
201	Power spectral density, coherence, and relative phase angle of P55LL and S55LL seismographs during signals from Kermadec Islands earthquake, 2233/2305, 10 October 1970	379
202	Power spectral density, coherence, and relative phase angle of P55LL and S55LL seismographs during the LR_1 Rayleigh wave from Kermadec Islands earthquake, 0400/0432, 11 October 1970	381
203	Power spectral density, coherence, and relative phase angle of P55LL and S55LL seismographs during the LR_1 Rayleigh wave from Kermadec Islands earthquake, 0621/0653, 11 October 1970	382
204	Amplitude spectral density of ground displacement and ground strain during signals from Kermadec Islands earthquake, 2233/2305, 10 October 1970	384
205	Amplitude spectral density of ground displacement and ground strain during the LR_1 Rayleigh wave from Kermadec Islands earthquake, 0400/0432, 11 October 1970	385
206	Amplitude spectral density of ground displacement and ground strain during the LR_1 Rayleigh wave from Kermadec Islands earthquake, 0621/0653, 11 October 1970	386
207	Fourier transform amplitude spectra, P55LL seismograph, during LR_1 Rayleigh wave from Kermadec Islands earthquake, 2159, 10 October 1970	388

ILLUSTRATIONS, Continued

<u>Figure</u>		<u>Page</u>
208	Fourier transform amplitude spectra, S55LL seismograph, during LR ₁ Rayleigh wave from Kermadec Islands earthquake, 2159, 10 October 1970	389
209	Fourier transform amplitude spectra, P55LL seismograph, during LR ₁ Rayleigh wave from Kermadec Islands earthquake, 0316, 11 October 1970	390
210	Fourier transform amplitude spectra, S55LL seismograph, during LR ₁ Rayleigh wave from Kermadec Islands earthquake, 0316, 11 October 1970	391
211	Fourier transform amplitude spectra, P55LL seismograph, during LR ₁ Rayleigh wave from Kermadec Islands earthquake, 0538, 11 October 1970	392
212	Fourier transform amplitude spectra, S55LL seismograph, during LR ₁ Rayleigh wave from Kermadec Islands earthquake, 0538, 11 October 1970	393
213	Rayleigh wave phase velocity in 55 deg azimuth calculated from signals from Kermadec Islands earthquakes	395
214	Inertial seismograms of 2159Z, 10 October 1970, Kermadec Islands earthquake illustrating possible higher mode surface waves	400
215	Instantaneous vector wave number Kermadec Islands earthquake, 2159Z, 10 October 1970	401/402
216	Instantaneous vector wave number Greenland Sea earthquake, 2053Z, 26 October 1970	405/406
217	Power spectral density, coherence, and relative phase angle with 790 time samples of PZLL and SZLL seismograms during LR ₁ Rayleigh wave of New Hebrides m _b = 5.5 earthquake	408/409
218	Power spectral density, coherence, and relative phase angle with 3841 time samples of PZLL and SZLL seismograms during LR ₁ Rayleigh wave of New Hebrides m _b = 5.5 earthquake	410/411
219	Power spectral density, coherence, and relative phase angle of P325LL and S325LL seismograms during LR ₁ Rayleigh wave of New Hebrides m _b = 5.5 earthquake	412/413
220	Power spectral density, coherence, and relative phase angle of P55LL and S55LL seismograms during LR ₁ Rayleigh wave of New Hebrides m _b = 5.5 earthquake	414/415

ILLUSTRATIONS, Continued

<u>Figure</u>		<u>Page</u>
221	Power spectral density, coherence, and relative phase angle of PZL and SZL seismograms during LR ₂ Rayleigh wave of New Hebrides m _b = 5.5 earthquake	416/417
222	Power spectral density of P325L seismogram during LR ₂ Rayleigh wave of New Hebrides m _b = 5.5 earthquake	418
223	Power spectral density, coherence, and relative phase angle of P55L and S55L seismograms during LR ₂ Rayleigh wave of New Hebrides m _b = 5.5 earthquake	420/421
224	Power spectral density of PZL seismogram during LR ₃ Rayleigh wave of New Hebrides m _b = 5.5 earthquake	422
225	Power spectral density of P325L seismogram during LR ₃ Rayleigh wave of New Hebrides m _b = 5.5 earthquake	423
226	Power spectral density, coherence, and relative phase angle of P55L and S55L seismograms during LR ₃ Rayleigh wave of New Hebrides m _b = 5.5 earthquake	424/425
227	Power spectral density, coherence, and relative phase angle of PZL and SZL seismographs during Rayleigh wave of an m _b = 5.2 earthquake off the east coast of Kamchatka	427
228	Power spectral density, coherence, and relative phase angle of P325L and S325L seismographs during Rayleigh wave of an m _b = 5.2 earthquake off the east coast of Kamchatka	428
229	Power spectral density, coherence, and relative phase angle of P55L and S55L seismographs during Love wave of an m _b = 5.2 earthquake off the east coast of Kamchatka	429
230	Power spectral density, coherence, and relative phase angle of PZL and SZLL seismographs during Rayleigh wave of an m _b = 5.0 earthquake in the Gulf of Alaska	430
231	Power spectral density, coherence, and relative phase angle of P325L and S325L seismographs during Rayleigh wave of an m _b = 5.0 earthquake in the Gulf of Alaska	431
232	Power spectral density, coherence, and relative phase angle of P55L and S55L seismographs during Love wave of an m _b = 5.0 earthquake in the Gulf of Alaska	432
233	Power spectral density, coherence, and relative phase angle of PZLL and SZLL seismographs during Rayleigh wave of an m _b = 5.9 earthquake on Honshu, Japan	433

ILLUSTRATIONS, Continued

<u>Figure</u>		<u>Page</u>
234	Power spectral density, coherence, and relative phase angle of P325LL and S325LL seismographs during Rayleigh wave of an $m_b = 5.9$ earthquake on Honshu, Japan	434
235	Power spectral density, coherence, and relative phase angle of P55LL and S55LL seismographs during Love wave of an $m_b = 5.9$ earthquake on Honshu, Japan	435
236	Power spectral density of PZL and SZL seismographs during Rayleigh wave of an $m_b = 4.2$ Solomon Islands earthquake, 2 October 1970	437
237	Power spectral density of P55L and S55L seismographs during Rayleigh wave of an $m_b = 4.2$ Solomon Islands earthquake, 2 October 1970	438
238	Power spectral density of PZL and SZL seismographs during Rayleigh wave of an $m_b = 4.2$ Solomon Islands earthquake, 3 October 1970	439
239	Power spectral density of P55L and S55L seismographs during Rayleigh wave of an $m_b = 4.2$ Solomon Islands earthquake, 3 October 1970	440
240	Three types of tides from W_2 gravity potential	444
241	Vertical earth tide strains 7 April to 18 May 1971	453/454
242	325 deg azimuth earth tide strains 7 April to 18 May 1971	455/456
243	55 deg azimuth earth tide strains 7 April to 18 May 1971	457/458
244	Observed (dark line) and predicted (light line) earth tide strain in 325 deg azimuth 7 April to 18 May 1971	459/460
245	Observed (dark line) and predicted (light line) earth tide strain in 55 deg azimuth 7 April to 18 May 1971	461/462
246	Observed vertical strain (dark line) and inverted predicted areal strain (light line) for earth tides 7 April to 18 May 1971	463/464
247	Observed (dark line) and predicted (light line) earth tide areal strain (reversed polarity) 7 April to 18 May 1971	465/466
248	Fourier transform amplitude of observed and predicted earth tide strains in the 325 deg azimuth 7 April to 18 May 1971	467

ILLUSTRATIONS, Continued

<u>Figure</u>		<u>Page</u>
249	Fourier transform amplitude of observed and predicted earth tide strains in the 325 deg azimuth 7 April to 18 May 1971, expanded scale	468
250	Gravity tide periods and amplitudes relative to M ₂	469
251	Fourier transform amplitude of observed and predicted earth tide strains in the 55 deg azimuth 7 April to 18 May 1971	471
252	Fourier transform amplitude of observed and predicted earth tide strains in the 55 deg azimuth, 7 April to 18 May 1971, expanded scale	472
253	Fourier transform amplitude of observed vertical and predicted areal earth tide strains 7 April to 18 May 1971	473
254	Fourier transform amplitude of observed and predicted areal earth tide strains 7 April to 18 May 1971	474
255	Fourier transform amplitude of observed vertical and observed areal earth tide strains and predicted areal earth tide strains 7 April to 18 May 1971, expanded scale	475
256	Power spectral density, coherence, and relative phase angle of observed and predicted earth tide strains in the 325 deg azimuth	477
257	Power spectral density, coherence, and relative phase angle of observed and predicted earth tide strains in the 55 deg azimuth	478
258	Power spectral density, coherence, and relative phase angle of observed vertical and predicted areal earth tide strains	479
259	Power spectral density, coherence, and relative phase angle of observed vertical and observed areal earth tide strains	480
260	Power spectral density, coherence, and relative phase angle of observed and predicted areal earth tide strains	481
261	Air pressure fluctuations 7 April to 20 May 1971	485/486
262	Air temperature fluctuations 7 April to 20 May 1971	487/488
263	Fourier transform amplitude of observed air pressure 7 April to 19 May 1971	489
264	Power spectral density of observed air pressure 7 April to 19 May 1971	490

ILLUSTRATIONS, Continued

<u>Figure</u>		<u>Page</u>
265	Fourier transform amplitude of observed air temperature 7 April to 19 May 1971	491
266	Power spectral density of observed air temperature 7 April to 19 May 1971	492
267	Coherence between air pressure and each strain component 7 April to 18 May 1971	493
268	Phase angle that each strain component leads air pressure 7 April to 18 May 1971	494
269	Coherence between air temperature and each strain component 7 April to 18 May 1971	495
270	Phase angle that each strain component leads air temperature 7 April to 18 May 1971	496
271a	Recordings of ground strain, ground tilt, ground vertical displacement, and air pressure variations from a presumed acoustic source in the Tuomotu Archipelago region, 3 July 1970	505/506
271b		507/508
272	Theoretical group velocity dispersion curves for a model atmosphere with a half-space beginning at an altitude of 300 km (replotted from Pfeffer and Zarichny (1963))	511/512
273	Group velocity dispersion curves calculated from S55L strain seismogram for 5 modes of acoustic-gravity waves that travelled the short-arc path from the presumed source on 3 July 1970	513/514
274	Group velocity dispersion curve calculated from S325L strain seismogram for 5 modes of acoustic-gravity waves that travelled the long-arc path from the presumed source on 3 July 1970	515/516
275	Group velocity dispersion curve calculated from S55L strain seismogram for 5 modes of acoustic-gravity waves that travelled the short-arc path from the presumed source on 30 May 1970	517/518
276	Group velocity dispersion curve calculated from ML2 microbarogram for 5 modes of acoustic-gravity waves that travelled the short-arc path from the presumed source on 30 May 1970	519/520

TABLES

<u>Table</u>		<u>Page</u>
1	Differential displacements	8
2	Specifications of the moving-coil transducer	28
3	Parameters for calculation of power spectral density of Ithaco amplifier noise	35
4	Comparison of manufacturer's specifications to measured values for the Ithaco Long-Period Seismic Amplifier, Model 6089-34	38
5	Measured specifications of the variable capacitance transducer	50
6	Comparison of close coupled and loosely coupled seismograph systems with matched responses	60
7	Microseismic background spectra parameters	113
8	Ground motion amplitude spectra	114
9	Total mean square and total root-mean-square equivalent displacement in the passband 1 to 256 sec observed on inertial seismographs during quiet background samples. Seismographs are calibrated at 25 sec, but are uncorrected for system response	132
10	Total mean square and total root-mean-square equivalent strain in the passband 1 to 256 sec observed on strain seismographs during quiet background samples. Seismographs are calibrated at 25 sec, but are uncorrected for system response	144
11	Equivalent mean-square values during high wind sample 0046Z to 0730Z, 31 May 1970	159
12	Total mean-square and total root-mean-square displacement and strain in the passband 1 to 256 sec during an interval of large pressure variations. Seismographs are calibrated at 25 sec, but are uncorrected for system response	172
13	Tilt response of horizontal inertial seismometers to Rayleigh waves	205
14	Comparison of NOS and QC-AZ detections	325
15	Epicenter data for recordings in figures 192 through 197	357

TABLES, Continued

<u>Table</u>		<u>Page</u>
16	Epicenter data for recordings in figures 199 and 200	371
17	Epicenter data for recordings in figures 227 through 235	436
18	Principal tidal waves	445
19	Component M_2 obtained from the results of Japanese extensometers (from Melchior, 1966, after Ozawa, 1961)	448
20	Apparent site coupling factors (column C) computed from the ratio of observed strain (column B) to the calculated earth tide (column A) for the S_2 , M_2 , S_1 and O_1 components of the earth tide corresponding to tidal periods of 12.0, 12.42, 24.0, and 25.8 hours, respectively (from Shopland, 1971)	450
21	Observed amplitude, amplitude ratio (theo/obs), and phase angle of observed relative to theoretical for earth tide strain components from the Fourier transform analysis	476
22	Amplitude ratio (theo/obs), coherence, and phase angle of observed relative to theoretical for earth tide strain components from power spectral density analysis	482
23	Comparison of horizontal Earth tide strains from power spectral density analysis	483
24	Amplitude ratio, coherence, and phase angle of observed strain to pressure or temperature from power spectral density analysis	497
25	Epicenter data	504

ABSTRACT

This final report describes the development, construction, operation, data collection, and data processing associated with the strain/inertial seismograph at Queen Creek, Arizona (QC-AZ), from 1 July 1968 to 1 June 1972. Strain seismographs were matched in sensitivity, amplitude, and phase to long-period (LP) inertial seismographs at 100K magnifications. Strain sensitivities of 2.5×10^{-13} at 30 sec were achieved. Operating magnifications were limited by ambient unrest of the ground which even for this quiet site was 6 dB or more above instrument noise at all periods from 0.1 to 2560 sec. The strain and inertial seismographs were combined to form an on-line directional array to enhance and to separate seismic waves, especially Rayleigh and Love waves and S_H and S_V waves. For example, a Rayleigh wave from an m_b 4.2 earthquake at 100 deg had a 17 dB signal-to-noise (S/N) ratio. The capability of the strain/inertial seismographs is demonstrated in the time domain with a variety of enhanced seismograms and in the frequency domain with many strain and inertial seismogram spectra having equivalent amplitudes, coherence of one, and correct phase angles. The concept of a single high-sensitivity station with combined strain/inertial seismographs offers LP detection and identification thresholds, S/N improvement, and beam forming capability equivalent to the 21-element Tonto Forest Observatory and 63-element Large Aperture Seismic Array spatial LP arrays. A comparison of QC-AZ LP detections and the PDE list of worldwide earthquakes was made for an 80-day interval. During this time, there were 887 earthquakes on the PDE List. The QC-AZ LP detections included 362 of these events with a 50 percent LP detection level of m_b 4.35. An additional 276 events were detected at QC-AZ that were not on the PDE list. Rayleigh waves of 45 to 60 sec are attenuated in the Basin and Range Province and the M_{S40} discriminant is materially affected. During the free oscillations after large earthquakes, the strain seismographs return to a normal detection level much earlier than inertial seismographs. Steps-of-strain (exponential strain pulses) are associated with conditions in the vicinity of the station and are not useful for source mechanism studies. The strain field at the tidal periods is the result of interaction among gravitational forces from the moon and the sun, air pressure fluctuations, and air temperature fluctuations. The strain seismographs detected repeatable acoustic signals which were separated into five acoustic wave modes.

XXVII

FINAL REPORT PROJECT VT/8706

DEVELOPMENT OF LP WAVE DISCRIMINATION CAPABILITY USING LP STRAIN INSTRUMENTS

1. INTRODUCTION

1.1 PURPOSE

This report is the final technical report on Project VT/8706, Development of LP Wave Discrimination Capability Using LP Strain Instruments. It is submitted in compliance with Sequence No. A005 of the Contract Data Requirements List, Contract F33657-69-C-0121. Form DD-250 is being submitted along with this report in accordance with contract requirements.

1.2 ORGANIZATION

This report summarizes the work accomplished during the entire contract interval from 1 July 1968 to 1 June 1972. The report is organized by subject matter. Sections 2, 3, and 4, respectively, treat the design goals, the selection of the most effective sensing technique to meet these goals, and the design of the instrument system. Sections 5 and 6 describe the installation of the instruments, including site selection and site preparation, and the operation of the system. The remaining sections describe the wave discrimination capability of the strain/inertial instrumentation complex. Section 7 discusses the background noise field and the stability of the seismographs. The general performance of the instruments is presented in section 8. The enhancement of signals with various combinations of strain and inertial seismographs is demonstrated in section 9. This enhancement of long-period (LP) seismic waves is the most important result of the project. Section 9 presents illustrations demonstrating that a single high-sensitivity strain/inertial seismograph station can provide as much signal-to-noise enhancement as the spatial arrays of 21 elements at the Tonto Forest Observatory (TFO) and of 63 elements at the Large Aperture Seismic Array (LASA). Section 10 discusses an investigation of the detection threshold of a single high-sensitivity station. Steps-of-strain are interpreted in section 11. The spectral comparisons between ground displacement and ground strain are presented in section 12. The coupling of the station to the earth is studied using the earth tide signals in section 13. The ability of a strain seismograph to enhance signal-to-noise ratio of acoustic signals is demonstrated in section 14 with the detection of three acoustic signals and with the identification of several distinct modes in each. Section 15 presents conclusions.

1.3 PREVIOUS REPORTS

Eleven quarterly reports and two special reports have been submitted on Project VELA T/8706. A bibliography of these reports is given in appendix 1.

1.4 TOPICAL SUMMARY

This report on the accomplishments during the 4 years of the Project covering the development, construction, operation, data collection, and data processing is voluminous. This section provides a topical summary of the major results. The reader is referred to the table of contents to determine the sections of the report where the details on these results are given.

A satisfactory method for the design, construction, and installation of a three-component strain seismograph system was developed. The strain seismographs were constructed with amplitude and phase responses that matched short-period (SP) inertial seismographs and that matched long-period (LP) inertial seismographs. The match of the frequency responses allowed stable, continuous, on-line, real-time enhancement of earthquake signals. The sensitivity of the strain seismographs equalled the sensitivity of the inertial seismographs. The sensitivities achieved were 2-1/2 to 3 orders of magnitude greater than previously attained with strain seismographs. The LP response has a sensitivity of about 2.5×10^{-13} strain at 30 sec and the broad-band response has a sensitivity of about 1×10^{-10} strain from dc to 7.5 Hz. At the Queen Creek (Arizona) Seismological Station (QC-AZ), the ambient unrest of the ground is as small as observed at any point on the earth over the period range of 0.1 to 2560 sec. Even at this quiet site, the operating magnifications were limited by the motion of the ground and not by instrument noise. The minimum background signal-to-instrument noise ratio is about 6 dB in the period range from 60 to 200 sec for both the inertial and strain seismographs.

The strain seismographs and the inertial seismographs can be used separately and in various combinations (sums and differences) to enhance earthquake signals and to separate and to identify wave types. The enhancement is especially good for both Rayleigh and Love surface waves, including higher modes, and for body waves arriving as S phases. The multiple bounce body waves, such as PS, SS, SSS, etc., are enhanced more than direct body waves. The ability to enhance earthquake signals and to separate wave types is demonstrated both in the time domain and in the frequency domain. A suite of seismograms are illustrated to demonstrate the capabilities of the instrumentation complex with a variety of signals. Some of the illustrations are reproductions of real-time recordings and others are of recordings played back from magnetic tape. Among both types of seismograms are illustrations of enhancement of Rayleigh waves from earthquakes with m_b of 4.2 and from epicentral distances of about 100 km. The time domain and the frequency domain analyses both demonstrate the faithfulness in recording and enhancing signals. This system stability is demonstrated with three similar signals from the same epicenter and with multiple passes of the Rayleigh wave (LR_1 , LR_2 , and LR_3) from an $m_b = 5.5$ earthquake. Both Fourier transform analysis and power spectral density analysis were used to make the frequency domain comparisons of signals on the strain and inertial seismographs. At the peak of the earthquake signal spectra, the spectra of the two types of seismographs have identical shape; the coherence is one; and the relative phase angle is as predicted by theory. Spectral comparisons between a Rayleigh wave from an $m_b = 4.2$ earthquake and a microseismic background sample indicate 17 dB signal-to-noise ratio. Capon et al. (1969) have reported an 11 dB noise reduction in the octave between 20 and 40 sec for the 63-element LP array at LASA. The LASA microseismic background at 40 sec and longer periods is larger than the QC-AZ strain microseismic background at these periods. The favorable signal enhancement

comparison of the single station strain/inertial combination at QC-AZ with the TFO and LASA long-period spatial arrays establishes the concept of the strain/inertial complex as one of the solutions to the detection and identification problem.

An 80-day QC-AZ station bulletin was compared to the National Ocean Survey (NOS) Preliminary Determination of Epicenters (PDE) list for world-wide epicenters. The QC-AZ detections were made from the long-period data with many events being detected from the directional array of combined strain/inertial seismographs. The QC-AZ bulletin listed 40.8 percent of the events on the PDE list and had almost as many events (78 percent) that were not on the PDE list. Based on the 40.8 percent events on both the NOS and QC-AZ lists, the 50 percent probability level of an LP detection from world-wide epicenters is an m_b of 4.35. Many of the large-to-great earthquakes excite free oscillations of the earth that continue for hours after the origin time. Since most of these continuing free oscillations have high phase velocities, the strain seismographs return to a normal background and normal detection threshold much quicker than the inertial seismographs.

Rayleigh waves traveling through the Basin and Range Province have significant attenuation of 45 to 60 sec energy. This energy dissipation greatly affects the M_{S40} earthquake/explosion discriminant.

Steps-of-strain have been reported in the literature by Press (1965), Wideman and Major (1967), and others as being related to permanent dislocations at the focus of an epicenter. The QC-AZ data indicate that while many strain disturbances begin during the Rayleigh wave train of an earthquake, these disturbances reflect conditions in the vicinity of the strainmeter rather than at the earthquake focus.

The strain field at the earth tide periods is the result of several interacting phenomena. The gravitational force from the moon and from the sun each contribute to the strain field. Air pressure loads introduce a strain field that varies with the gravitational attraction forces and with temperature changes from the radiant energy from the sun. The thermal strain field varies with the radiant energy from the sun and with pressure changes from the gravitational forces on the atmosphere. The temperature and pressure changes affect the strains associated with the S_1 tide (24.00 hr period) and P_1 tide (24.07 hr period) (unseparated in this analysis) more than the strains associated with the O_1 tide (25.82 hr period). Similarly, the strains at the periods of the S_2 (12.00 hr) and K_2 (11.97 hr) tides (unseparated in this analysis) are affected more than at the period of the M_2 (12.42 hr) tide. Because of the interaction among gravitational forces, pressure, temperature, and strain, coupling factors determined for the coupling of the strainmeters to the earth as a whole do not reflect the pure strain output resulting from the gravitational force input.

A buried strainmeter will respond to the ground strain from air pressure waves in a manner that attenuates exponentially with depth and wave number. Small wave number acoustic waves are enhanced relative to large wave number wind related pressure variations. Recordings on the QC-AZ strain seismographs are used to detect and to identify five distinct modes from two acoustic waves which travelled the short arc and one acoustic wave which travelled the long arc from two presumed acoustic sources in the South Pacific Ocean.

2. DESIGN GOALS

The first task of the project was to "Develop design specifications for vertical and horizontal long-period (LP) strain seismometers, which will be capable of gain and response characteristics equivalent to those of the 'advanced' LP inertial seismometers such as Geotech Models 7505A and 8700C." This task was interpreted as referring to the entire seismograph and as including all devices that sense, amplify, filter, and transmit the signal from the earth motion to the recorder. This section of the report defines the goals which were adopted and the design problems to be overcome in reaching these goals. The strain seismograph sensitivity and amplitude and phase response requirements are defined in section 2.1. Considerations that were applied to the instrument selection and design are presented in section 2.2. Considerations that were applied to the control of the environment in the vicinity of the seismometers are discussed in section 2.3.

2.1 STRAIN SEISMOGRAPH SENSITIVITY AND RESPONSE

Many of the applications of strain seismographs involve comparisons between the phase and amplitude responses of strain and inertial seismograph systems. This necessity for comparisons places two requirements on the phase and amplitude responses of the strain and inertial systems.

The first requirement relates to the limited dynamic range of the recorder (normally about 40 dB). Earthquake and seismic noise signals are of wide frequency content and reflect a large dynamic range of amplitudes. In inertial seismographs, the wide frequency content and some of the amplitude range is modified by filters before recording. For instance, in the Advanced Long-Period System (ALPS), the period of the inertial seismometer and the period of the galvanometer were selected to enhance seismic signals in the 10 to 100 sec period range and to attenuate seismic noise outside this passband. However, the amplitude of the microseismic noise in the 5 to 8 sec period range is often very large. Therefore, it was necessary to use a 6 sec notch filter in the ALPS high gain channel to notch out these microseismic signals to allow recording of smaller earthquakes. Typical ALPS high gain and low gain amplitude frequency response curves are given in figure 1. The effect of the 6 sec notch filter can readily be seen. Also, from figure 1, note the period ranges of the high gain and low gain channels.

<u>dB down from peak</u>	<u>Period range (sec)</u>	
	<u>high gain</u>	<u>low gain</u>
20	11-100	6.5-100
40	7.8-220	3-230
60	2.5(or 6)-500	1.5-500

Similar considerations for recording wide dynamic range signals on a limited dynamic range analog recorder apply to the strain system. One of the important objectives was to establish limits on the filtering necessary to allow

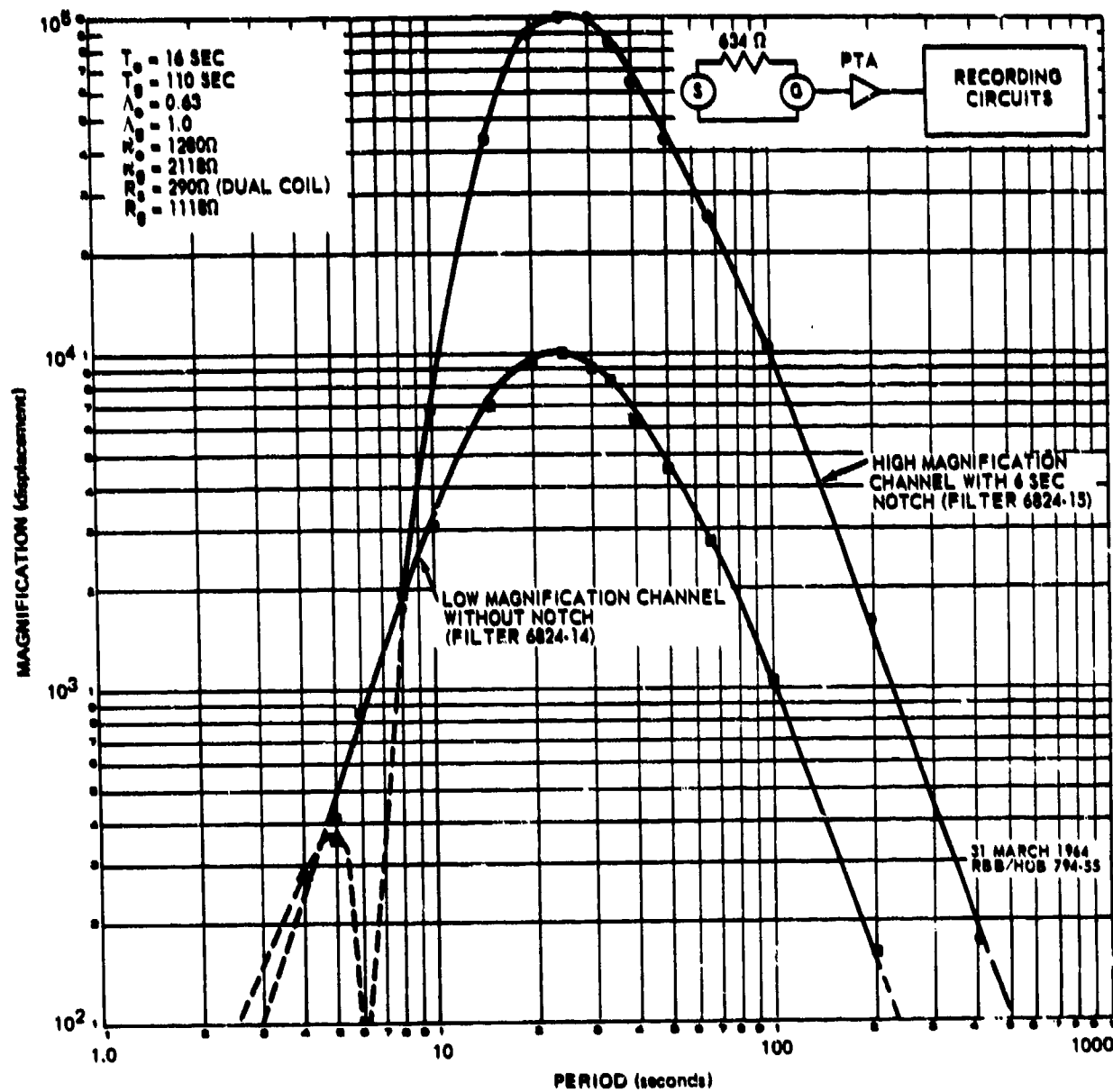


Figure 1. Advanced LP system typical amplitude frequency response.

recording of signals over a suitable frequency and amplitude range. Some of the factors that affected this specification were:

- a. Minimum amplitude signal to be recorded;
- b. Maximum amplitude signal to be recorded;
- c. Frequency content of the signals to be recorded;
- d. Dynamic range of recorders that could be used with both the inertial and strain systems;
- e. Response to earth strain of the particular sensing technique selected;
- f. Amplitude and frequency content of the noise; and
- g. Suitability of the signal format for subsequent processing.

The second requirement for comparing strain and inertial seismographs relates to the match between their respective phase and amplitude responses. For some of the applications of the strain/inertial seismograph combinations, the match between the two systems for apparent longitudinal waves must be extremely good. Since the initial objective of this program was of a research category, there was no specific requirement for on-line processing. Consequently, the final and accurate matching of the two system responses could have been done in a digital computer during final data processing. However, for visual analysis in the laboratory, and for visual verification of proper operation of both strain and inertial systems in the field, a matched response was specified. If differences in amplitude and phase responses were not corrected so that waves appeared the same on both the strain and inertial systems, much time would have been lost in the testing program. If the responses were not the same, it would have been difficult to compare signal recordings from the different systems and especially to identify and correct instrumental and environmental problems that might not have been apparent if the systems were not matched.

The previous discussion in this section primarily relates to seismic signals in the period range of sensitivity of the ALPS from 10 to 100 sec. Strain seismographs are inherently capable of recording longer period signals than inertial seismographs. Earthquake signals of periods longer than 100 sec have been observed and could possibly lead to valuable detection and identification criteria. Therefore, the long-period strain seismograph was designed to include an ultra-long-period output. There was no extended effort to enhance the sensitivity at the longer periods. But, provisions were made for a band-pass filter to shape the response and for recording any signals within the sensitivity range of the ultra-long-period channel. A response flat to equivalent ground displacement from 60 to 200 sec was specified to record these longer period signals.

2.2 INSTRUMENT CONSIDERATIONS

The objective of this program was to develop a strain seismograph having gain and response characteristics equivalent to those of the ALPS. In accomplishing this objective, three types of earth motion were considered: First, there is a motion from seismic signals and seismic noise in the period range of interest. Second, there are tides of the solid earth caused by the gravitational attraction among the moon, the sun, and the earth. Third, there are the secular motions which are here defined to include all longer term disturbances. Some of these disturbances are ground expansion and contraction from seasonal temperature changes, regional tectonic strain, unusual local loads such as lakes and reservoirs filling and draining, pier movement from resettling after instrument installation, dimensional changes of the mined-out cavity containing the instrumentation, and other unexplainable long-term disturbances. Typical values of horizontal long-period strain for these three types of ground motion are:

1. Seismic strain (smallest strain to be measured): 5.24×10^{-13} m/m strain at 30 sec period;
2. Earth tide strain: about 2×10^{-8} m/m strain at 4.5×10^4 sec (12-1/2 hr) period;
3. Secular strain: mine - 3.0×10^{-6} m/m at 1 yr period
trench - 1.0×10^{-5} m/m at 1 yr period.

The secular strain data for the mine are from Benioff's (1959) data on the Dalton Canyon installation, and for the trench are from observations at the strain installation at the Wichita Mountains Observatory (WMO). Note that the earth tide strains are about five orders of magnitude, and the secular strains are about 7 or 8 orders of magnitude, larger than the seismic signal to be recorded. The strain transducer must be able to accommodate the 92 dB range of the diurnal tides and still maintain 40 to 60 dB earthquake signal recording range. This 150 dB dynamic range is a minimum when the strain seismograph is used with analog and frequency-modulated, magnetic-tape recorders. If digital recorders are used, another 50 to 60 dB dynamic range could be available for earthquake recording, making 200 dB the minimum dynamic range required for the strain transducer. If the transducer is to operate without seasonal adjustment for secular strain, it will require an additional 40 dB or up to 240 dB of dynamic range. This large dynamic range capability of the transducer was one of the major design problems. Table 1 converts the above values of strain (a change of length divided by a length) to sets of differential displacements for four different spacings between piers.

The differential displacement, which is the actual motion to be sensed by the transducer, is seen to be on the order of 0.1 Å from seismic signals at 30 sec. Since the output is linearly related to the distance between the piers, a larger distance can provide additional signal for the transducer and reduce its sensitivity requirements.

Another major design problem was the extreme sensitivity required for the strain transducer as compared to the transducer on an inertial seismometer. Figure 2 shows the horizontal strain per unit of displacement as a function of period for a Rayleigh wave. The vertical strain signal is only about one-third

Table 1. Differential displacements

Signal source	Distance between piers (m)			
	20 m	40 m	60 m	80 m
Seismic	1.05×10^{-11}	2.1×10^{-11}	3.15×10^{-11}	4.2×10^{-11}
Earth tide	4×10^{-7}	8×10^{-7}	1.2×10^{-6}	1.6×10^{-6}
Secular				
Mine	6×10^{-5}	1.2×10^{-4}	1.8×10^{-4}	2.4×10^{-4}
Trench	2×10^{-4}	4×10^{-4}	6×10^{-4}	8×10^{-4}

the amplitude of the horizontal strain signal. Notice that at 100 sec period, the horizontal strain is only about 1×10^{-5} m/m for each meter of displacement. Thus, at 100 sec, the strain transducer of a 20 m long strain seismometer must be 3,333 times as sensitive as an inertial transducer.

The design objective for the strain seismograph for the maximum allowable noise level and the minimum signal to be sensed was calculated by the following method. The design objective was defined as the strain equivalent to 1×10^{-3} m peak-to-peak recorded on film at X10 view on the inertial ALPS at the magnification shown in figure 1. The minimum signal to be sensed was taken as the maximum allowable noise level. The ground displacement equivalent to 1×10^{-3} m peak-to-peak on the ALPS was determined using the amplitude response of the high-gain channel from figure 1. Then the strain and differential displacement corresponding to this ground displacement were calculated. Appendix 2 gives the details of the calculations. Figure 3, which reflects the design objective, is a plot of horizontal strain versus period for the maximum allowable noise level and/or minimum signal to be sensed. Also shown on figure 3 is the average strain resulting from the surface wave of an earthquake of magnitude $M_S = 4$ at epicentral distance (Δ) of 30 deg and 60 deg.

In summary, the strain transducer must be able to sense 0.1 \AA in the presence of the semidiurnal tides which are 4×10^4 times larger and annual strains which could be 10^7 times larger.

2.3 ENVIRONMENTAL CONSIDERATIONS

The usable sensitivity of any strain system will be limited by the amount of environmental stability that can be obtained. In the long-period range of interest, environmental instability can be divided into six categories as follows:

1. True unrest of the ground from microseismic motion;
2. Effects of temperature change on the ground;
3. Effects of air pressure cells and wind gusts on the ground;
4. Effects of temperature change on the instruments and their installation;

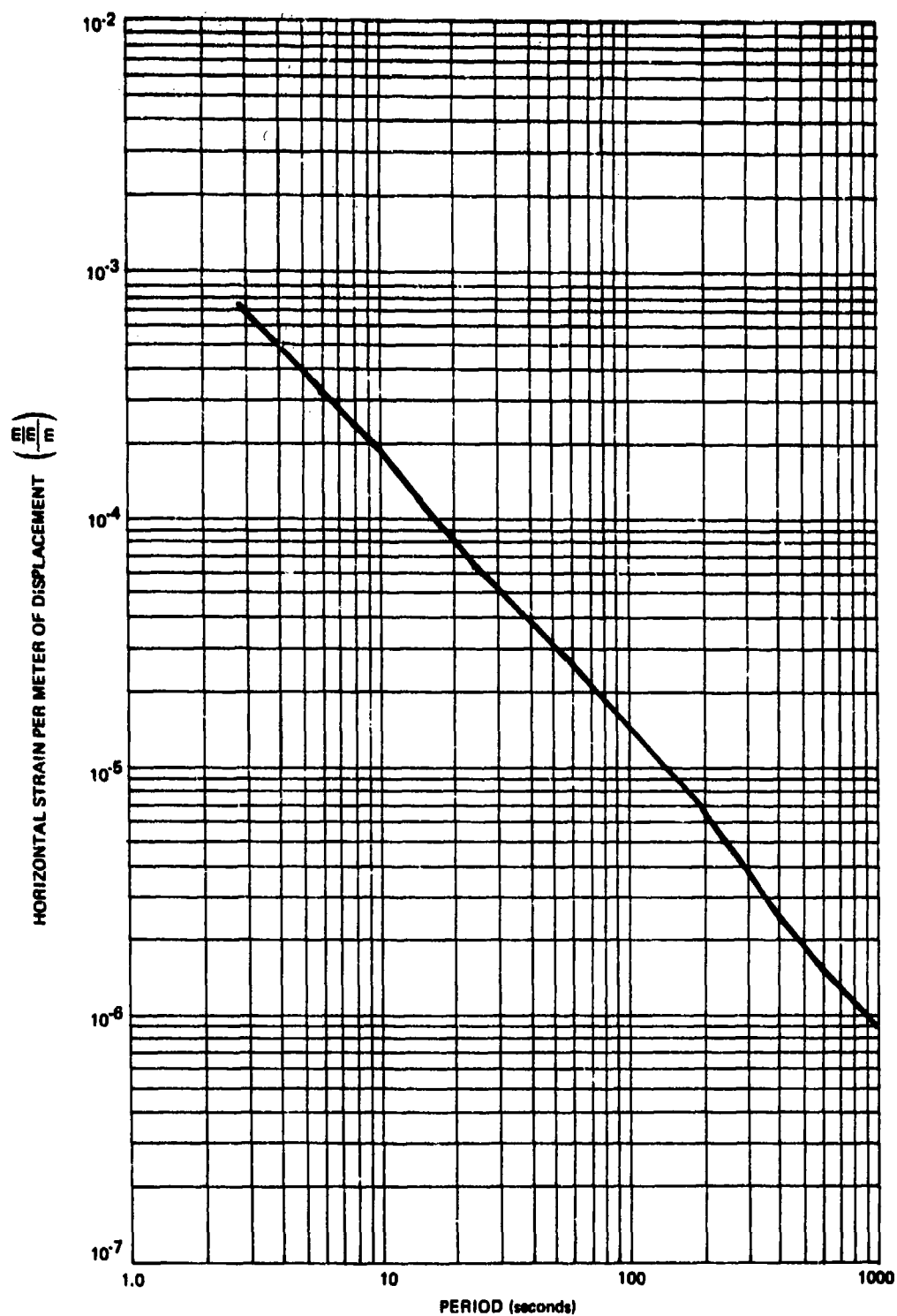


Figure 2. Rayleigh wave horizontal strain per unit of displacement.

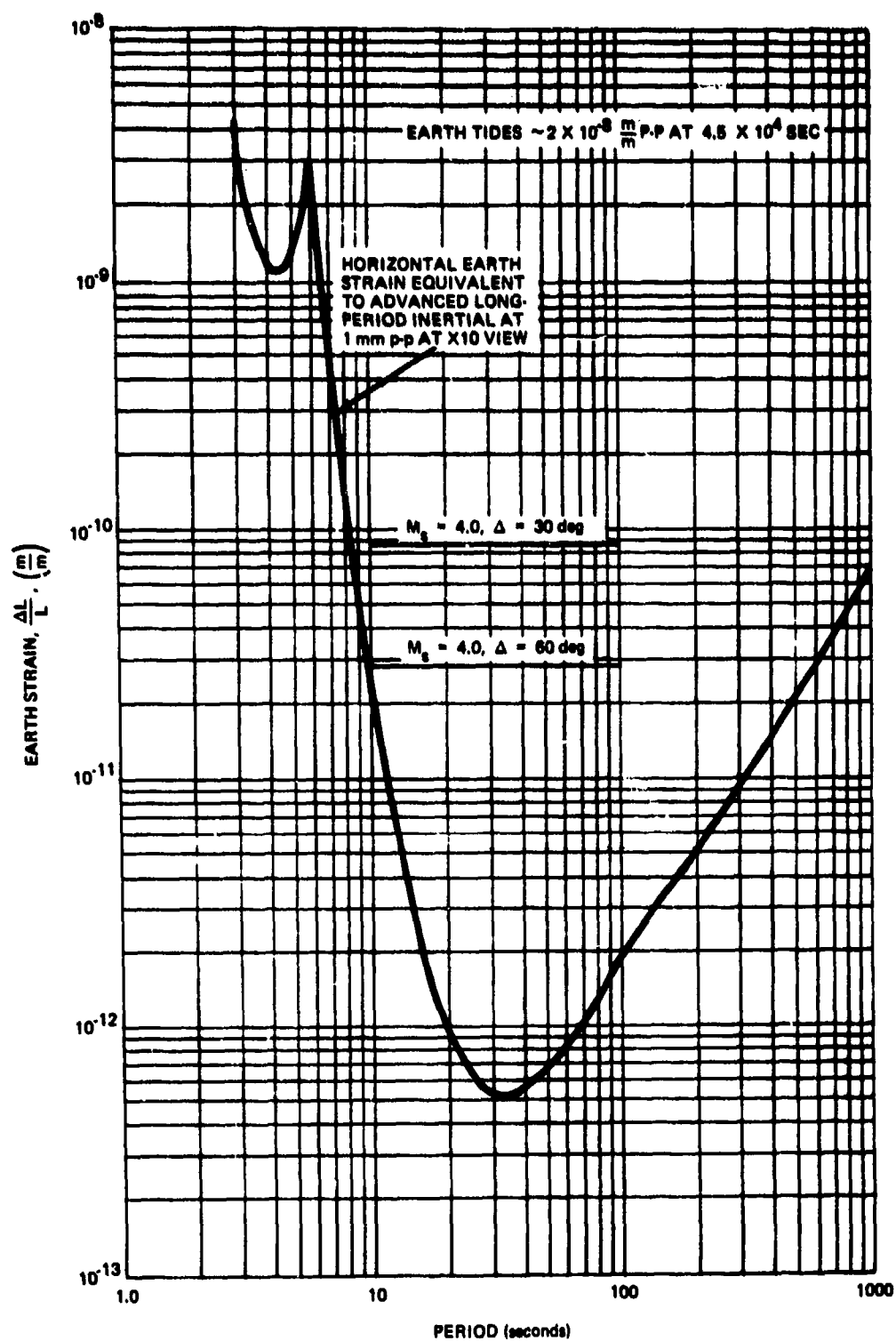


Figure 3. The minimum strain to be sensed and/or the equivalent maximum allowable noise level for the horizontal strain seismograph

G 6618

5. Effects of air pressure cells and wind gusts on the instruments and their installation; and

6. Effects of mine strain and regional tectonic strain.

The true unrest of the ground from microseismic motion varies from region to region by factors as large as 10. However, in the area of the central United States at such sites as TFO, Payson, Arizona, and the Long-Range Seismic Measurement Program (LRSM) site in a mine at Las Cruces, New Mexico (LC-NM), the ground unrest has been of a sufficiently low nature as to allow operation of the vertical and horizontal inertial ALPS at their maximum magnification of 100,000. In very carefully controlled experiments at the Las Cruces mine, Trott (1965) found the broadband instrument noise level of the ALPS to be equivalent to 1 mm on a X10 magnification film viewer at 130,000 magnification at the peak of the response curve (see figure 1). He also found that the signal-to-noise ratio of the ALPS at this quiet site was about 10:1 from 4 sec down to about 30 sec period decreasing to about 3:1 at about 100 sec period. It was anticipated that the LP strain system to be designed under this project would be installed in a mine where the microseismic ground unrest is sufficiently low so as to allow the inertial ALPS to be operated at its maximum magnification of 100,000. Thus, the design criteria of the strain system noise equalling the ALPS at 100,000 magnification provided a signal-to-noise ratio approximately equal to that of the ALPS.

The effect of temperature variation on the ground unrest can be minimized by installing a seismograph system in an existing mine. At reasonable depths of only a few feet, the temperature variation is small and occurs on an annual basis. However, vaults or mines that contain instruments must have entrances. Temperature disturbances occur whenever the instrument areas are entered for maintenance or work on the systems. The strain system at WMO was installed in a trench that was backfilled so that the instruments were underground at depths ranging from 12 to 15 ft. This depth is probably marginally sufficient for isolation from temperature changes in the immediate vicinity of the instruments. (The depth at WMO is not sufficient for isolation from air pressure cells discussed later.) This depth may not be sufficient to remove the instruments from the highly localized earth strains that occur near the surface where the temperature varies daily or at shorter periods, such as on partly cloudy days when the ground is shielded from the radiation from the sun as clouds blow over. The most effective way to minimize the effect of temperature-caused strain is to select an existing mine with sufficient depth from the surface of the ground to minimize these disturbances.

At the beginning of the project, the effects of air pressure cells and wind gusts on the ground was one of the biggest unknowns in the environmental considerations. The exact mechanism of the disturbance was not entirely known. Part of the disturbance was considered to be an atmospheric loading of the ground which produces small vertical displacements and horizontal tilts. Haubrich and MacKenzie (1965) hypothesize disturbances from pressure circles with radii of 0.7 km and 1.5 km for periods of 100 sec and 400 sec, respectively. Yet, in ALPS tests at WMO, Burden (1964) found pressure effects from the wind apparently associated with the construction of a walk-in type vault. When air pressure inside the vault was increased, the horizontal seismometers

tilted toward the center of the vault. Later installation of a ship's door to make the vault airtight did not appreciably improve the performance in this vault (Milam, 1965). Much of this horizontal noise was localized and apparently associated with this particular vault. Milam found that a horizontal inertial seismometer in a good tank installation 183 m (600 ft) away could consistently operate at 10 times the magnification as a similar instrument in the walk-in vault. Milam also found in tests of the ALPS at the Las Cruces mine that air pressure variations had unpredictable effects on the instrumentation, causing noise on the seismographs. Noise was found to be generated by such things as plastic bags filled with insulation, the vermiculite insulation itself, buoyancy of the steel tanks containing the seismometer in the concrete piers, and suspected instantaneous differential temperature changes between the concrete and steel tanks resulting from adiabatic temperature and pressure changes. Fortunately, most of the instrumental air pressure effects at Las Cruces were eliminated by sealing off the mine chamber with a ship's door. When the wind velocity would reach 30 mph, the instruments would indicate some disturbance attributed to a localized tilting because the horizontal instruments would react and the vertical instruments would not. In the discussion of air pressure noise so far in this paragraph only inertial instruments have been considered. It was expected that disturbances that tilt the surface of the earth would create a proportionate localized strain. Thus, the horizontal strain seismographs probably would be subjected to the same noise outputs as the inertial seismographs. In preliminary long-period strain tests made at WMO, this phenomenon had been observed on a qualitative basis. Thus, it is apparent that the specific location for a long-period system - even within a small area - is important and that the type of installation is important. Proper installation of long-period inertial seismographs has, in many locations, resulted in reduction of environmental noise, allowing operation at 10 times more magnification. A similar relationship was expected for the strain seismograph with proper installation.

The effect of temperature variations on the strain instruments and their installation can be as critical as it is with the inertial systems. In developing high magnification, inertial long-period system, Teledyne Geotech (Geotech) has discovered the importance of thermal stability. (See Hamilton, 1964, for a summary.) Exact temperature control is not necessary, but a temperature stable to better than 0.001°C must be maintained. This type of stability is obtained by following these rules:

1. Obtain an inherent temperature stability by installing underground;
2. Install instruments in sealed vaults and/or sealed tank vaults in sealed walk-in rooms;
3. Surround the instrument with ample insulation so there will be no temperature differences between metal parts;
4. Prevent convection currents by baffles or insulation; and
5. Where necessary, apply heat at the top of the enclosure to insure stratification of the air.

The effects of the air pressure cells and wind gusts on the instruments can be minimized by sealing the instruments in an enclosure such as a mine chamber. While the exact mechanism of disturbance would have been different for the various strain sensing techniques considered, it was expected that all techniques would be subjected to air pressure variation disturbances. The disturbances from a separation of the piers resulting from a balloon effect of pressure change in the chamber should be alleviated by sealing the installation. However, for an installation in a side room in a large mine, the effect of pressure changes in the rest of the mine is unknown. If the mine is sufficiently large, and the airflow is not gusty in the mine, the disturbances might be outside the period range of interest.

Because of the unknowns that could possibly severely degrade performance in a large mine, considerations were given in the design to comparing problems in mines of various sizes. Consideration was also given to various methods of sealing chambers in the types of mines considered.

The strain in mines resulting from plastic flow of the surrounding rock into the mined-out cavity is another factor to be considered in designing a long-period strain installation. The senior author (see Geotech, 1960) has made measurements in the Carey Salt Company mine in Hutchinson, Kansas. The excavations are at a depth of 664 ft in a layer of rock salt with interlayering of shale and salt. The area monitored had about 60 percent of the salt removed in a room-and-pillar mining method. At the center of a 50 ft wide room about 15 ft from the perpendicular hallway, the 12 ft 9-1/2 in. distance between the ceiling and floor was decreasing at the rate of 0.0128 in. per month. At a height of 7 ft above the floor, the walls across the 50 ft width were moving together at the rate of about 0.0100 in. per month, which was about 2.7 times the creep rate at the floor. In a 3-month interval, the cumulative strain was 250×10^{-6} m/m vertically and 50×10^{-6} m/m horizontally. Creep in rock salt is greater than in granitic rocks so these strain values are larger than should be experienced in a hard rock mine. Because of the convenient large mined-out areas at horizontal right angles, the Carey Salt mine, in Hutchinson, Kansas, and the Morton Salt mine in Grand Saline, Texas, were considered as possible sites for the installation of the prototype system.

Regional tectonic strain can also be a factor affecting a strain installation. Bolt, McEvilly, and Filson (1968) have reported a strain accumulation of about 1×10^{-6} m/m in a year's time along the San Andreas Fault. Since this amount of strain along the largest known fault in the United States is the same order of magnitude as the secular strain, tectonic strains at any location should not present any unexpected strains or demands on a strain system.

The design of the field-test installation considered the effect of environmental disturbances. The magnitude and period range of the noises to be expected were estimated. The design included proper installation techniques, equipment, and procedures.

3. THE MOST EFFECTIVE TECHNIQUE

Among the early major tasks under this program was the selection of a technique to measure the very small strain displacements expected (about 2×10^{-11} m). In studying the various options available at the time, consideration was given to such factors as sensitivity, stability, reliability, ease of installation, maintenance, and cost. Several types of systems were considered which showed promise of meeting these requirements.

3.1 TECHNIQUES CONSIDERED

3.1.1 Laser-Interferometer

A relatively low sensitivity strain seismometer using the laser interferometer had been used previously with some success by Vali et al. (1965). Therefore, this technique was carefully studied early in the program to determine the feasibility of increasing its sensitivity. The laser technique offers an advantage over the other techniques in that it only requires a line of sight between piers. All other techniques require a mechanical rod contact between the two piers and mechanical support along the rod. Also, different separations between piers do not present any of the problems resulting from fixed length rods. Another advantage is that there is little difference between horizontal and vertical versions, making hardware requirements simpler.

Figure 4 shows the basic concept of the laser interferometer technique. An interference pattern is formed by combining the light from a strain measuring path with the light from a reference path. The interference pattern is reflected from a galvanometer mirror onto a photocell bridge. The bridge output is then fed back to the galvanometer, causing it to rotate and keeping the fringe pattern stable on the photocells. The electrical output for recording is taken from the servo feedback loop.

This technique has two major disadvantages. First, the transducer detects displacements and, therefore, it will detect the large, out-of-passband displacements caused by earth tides that are about 10^4 times larger than the minimum signal to be detected. In addition, strain instruments are subject to secular disturbances caused by the local environment which can be 10^6 times larger than the minimum signal, depending on the installation. The second major disadvantage is that the best commercial laser available at the time had a long-term frequency stability of about 1 part in 10^8 . Calculations showed that this stability would have to be improved by about 10^4 if this technique was used.

Methods to compensate for these two problems were designed, which resulted in a considerably more complex version than that shown in figure 4. However, development of these compensators was not done since other transducer techniques showed more promise of producing a workable system at lower cost and in less time. It should be pointed out that with future improvements in laser technology, the inherent advantage of using a light beam rather than a mechanical rod can make the laser an excellent instrument for measuring strains.

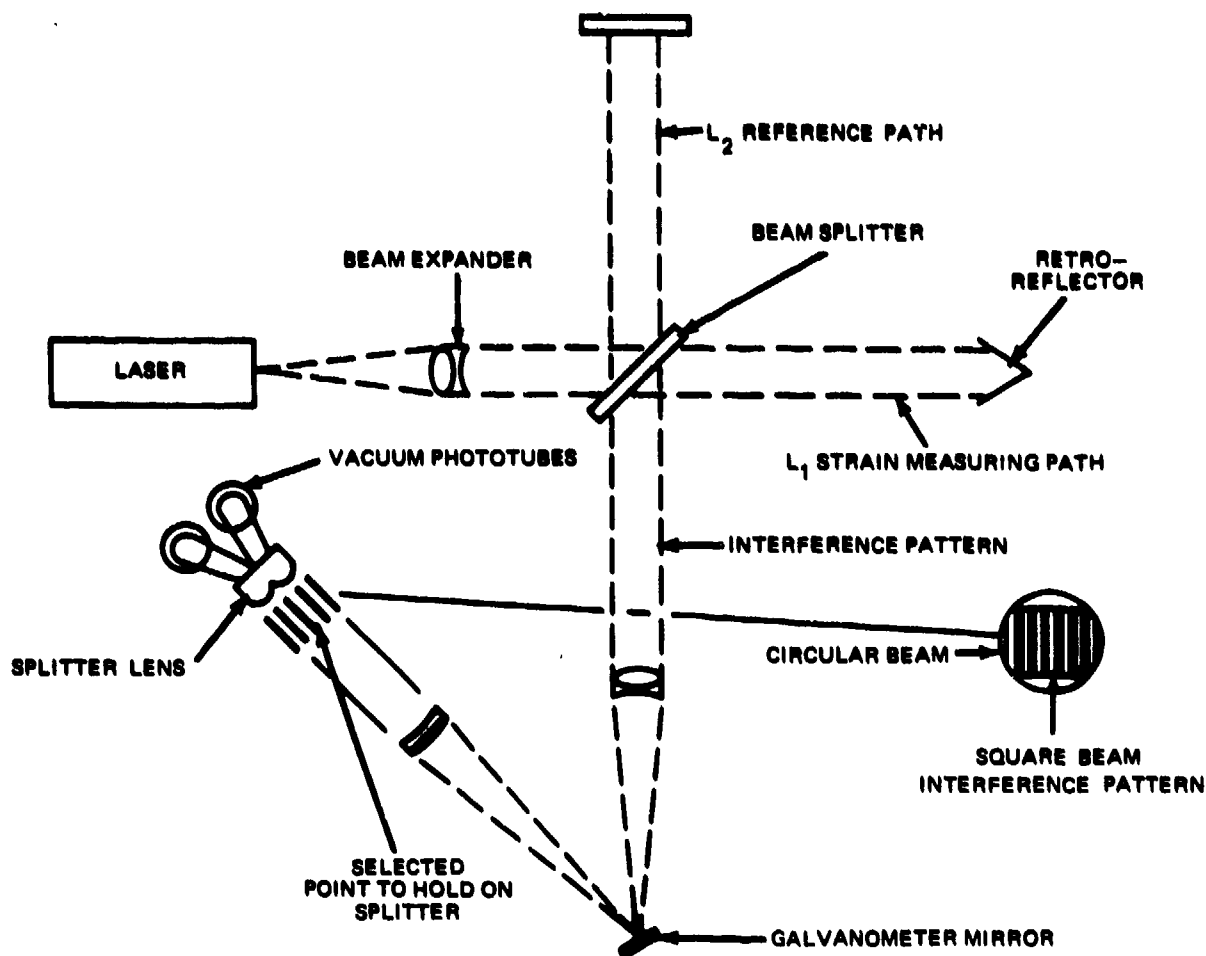


Figure 4. Basic concept of laser-interferometer technique

3.1.2 RF-Variable Capacitance Transducer

The RF-variable capacitance transducer (RF-VC) was also considered for this application. This unit was originally designed by Benioff (1955, 1959) and an improved version was used by Geotech on an earlier strain program described by Shopland (1966). Transducers of this type are also used in strain installations at various universities.

Like the laser interferometer, this transducer required a significant improvement in sensitivity (10^3) and some method of compensating for the earth tides and other large local phenomena. Since the RF-VC also required a strain rod in addition to these improvements, development of an improved unit was not pursued.

3.1.3 Direct Current-Variable Capacitance Transducer

The direct current-variable capacitance transducer (DC-VC) was thoroughly investigated for use as the primary transducer for the strain system. Work on this unit progressed through the laboratory model stage before the final selection of the moving coil transducer. The following paragraphs discuss the principles of operation of the DC-VC and the findings made during the development work.

3.1.3.1 Principles of Operation

The DC-VC is inherently a displacement transducer with a 6 dB/octave high pass characteristic produced by the variable capacitor and its leakage resistance. The DC-VC operates on the principle of the "charge" amplifier shown in the simplified schematic of figure 5. This technique has been used for many years in audio microphones. The DC-VC functions by virtue of the fact that if the charge on a capacitor is held constant as the capacitance is varied, the voltage across the capacitor will also vary. To vary the capacitance, one may vary effective plate area, plate separation, or the material between the plate. For this application, variable plate separation was chosen because it was easier to achieve and it provided the greatest sensitivity for a given transducer size. The mathematical derivation of circuit operation given in Quarterly Report No. 1 (Grissom, Erwin, Shopland, 1968) shows that for small displacements,

$$\frac{\Delta V}{V} = \frac{\Delta d}{d} \quad (1)$$

where V is the capacitor voltage and d is the plate separation. This equation shows that the transducer is linear for very small changes in d and that the sensitivity is independent of the total capacitance. Sufficient capacitance is required only to achieve the desired frequency response.

In the circuit shown in figure 5, the operational amplifier not only provides gain, but it also transforms the very high impedance of the transducer to a low impedance suitable for further amplification and filtering.

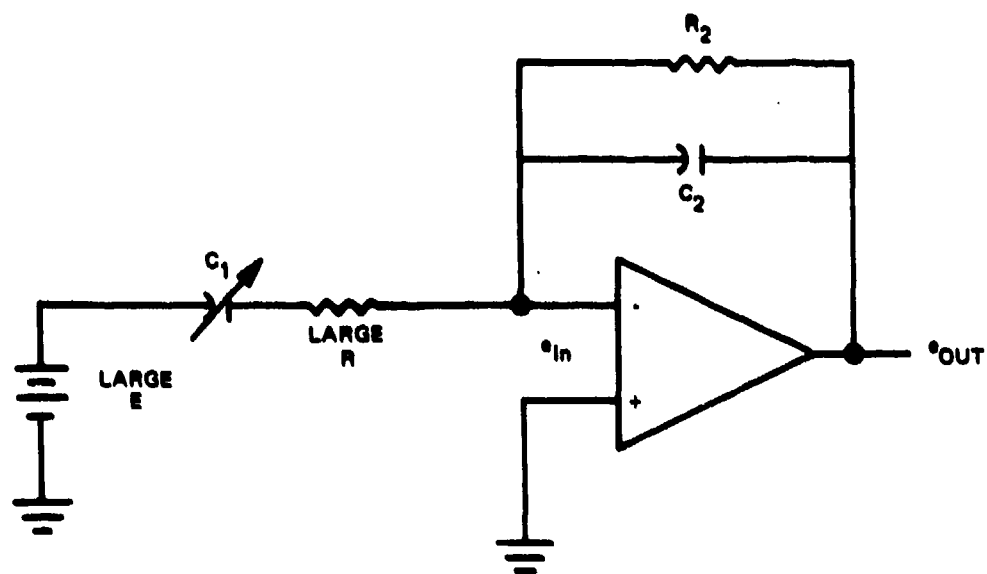


Figure 5. Dc-variable capacitance technique schematic

3.1.3.2 Laboratory Model DC-VC

Based on the successful completion of feasibility tests, a laboratory model DC-VC, complete with the necessary electronic circuitry, was designed and built for further testing.

Figure 6 is the schematic for the transducer. Overvoltage protection circuits and a follower amplifier-filter have been omitted from the figure for clarity. This circuit incorporates two significant changes that were found necessary during feasibility tests.

First, notice that the variable capacitor has been changed to a differential capacitor where one section increases capacitance while the other decreases for input displacements. The signals from the two sections have the same polarity because the battery polarities are opposite. The differential configuration was necessary to maintain transducer linearity in the presence of relatively large displacements caused by tidal and secular strains.

Then, a second high pass filter stage was added at the amplifier input (R_2 and C_2). This stage allows a significant reduction in the values of the input and feedback resistances, reducing noise and increasing circuit stability. The 12 dB/octave filter thus provided offers an equally important advantage of increasing the rejection of earth tides.

The variable capacitor shown in figure 6 has a nominal sensitivity of 3×10^6 V/m with the 1000 V batteries and a plate spacing of 3.3×10^{-4} m. Resistors R_3 and R_4 set the gain of the operational amplifier at 10. The low frequency cutoff is 1000 sec at a 12 dB/octave rate. A 10 Hz, 12 dB/octave high cutoff is provided by an additional amplifier-filter, which is not shown.

Figure 7 is a photograph of the laboratory model variable capacitor unit. In each of the 10 groups of 3 plates, the inner plate is attached to a movable center rod that is supported by four taut wire suspensions at each end. The center plates are maintained at ground potential. The outer plates are insulated and are supported by rods rigidly attached to the case. The cables leading from the transducer are connected to the two sets of outside plates and lead to the high voltage batteries, as shown in figure 6. The plastic case, which was later replaced by an aluminum case, seals the transducer to contain the dielectric liquid and to prevent dust contamination. Each section of the capacitor has a total area of 0.3 m^2 , spacing of 3.3×10^{-4} m, and a nominal capacitance of $0.008 \text{ }\mu\text{F}$ with air as the dielectric.

3.1.3.3 Problems Encountered

Two major problems were encountered in development of the DC-VC which ultimately led to the cancellation of further work.

First, a suitable dielectric liquid with a relatively high dielectric constant (k) and very high volume resistivity could not be found. Such a liquid would have increased the capacitance of the transducer and thereby decreased the value of the resistors needed to obtain the proper low frequency response. Of the liquids tested, only mineral oil ($k = 2.05$) and transformer oil ($k = 2.60$) had sufficient volume resistivity. Use of these liquids would offer other advantages over air, but would not significantly reduce the impedances required.

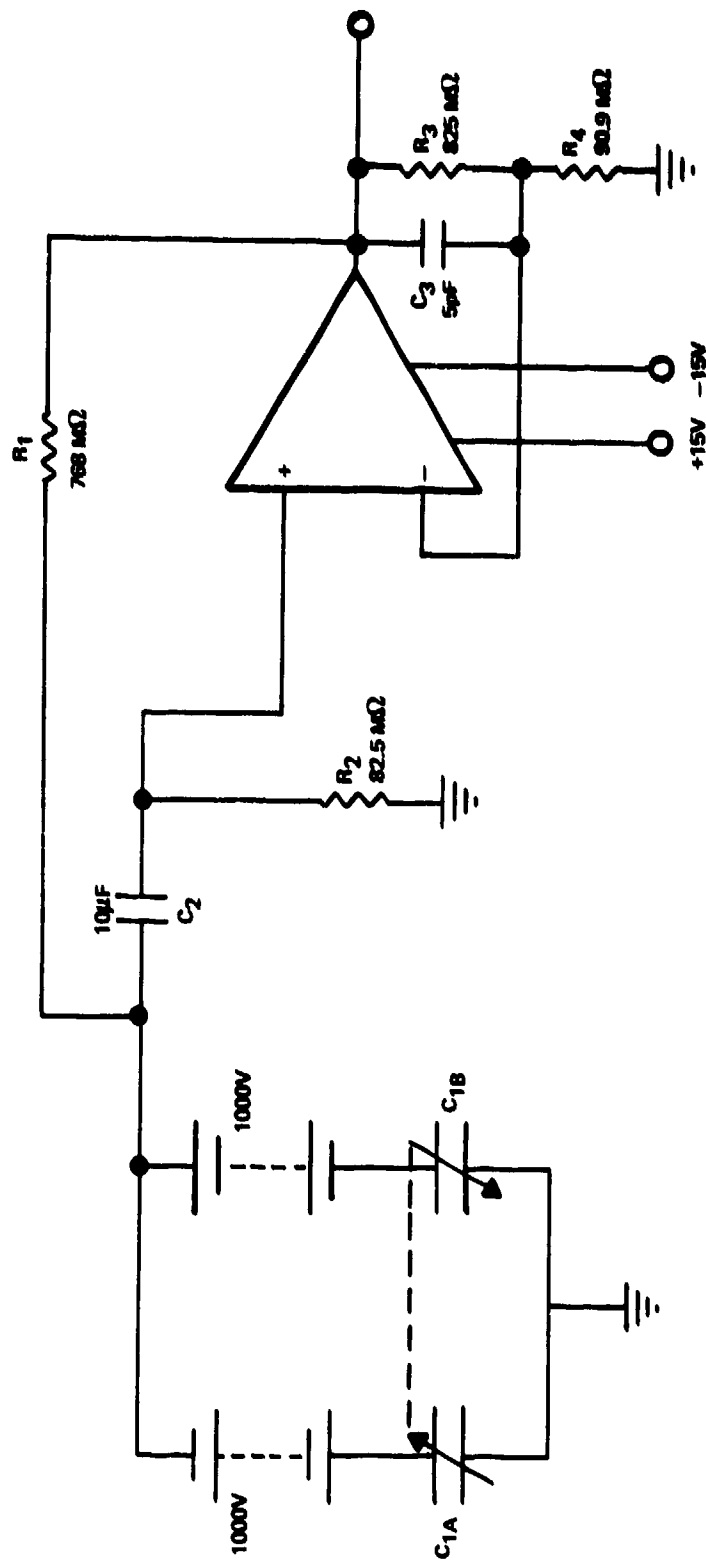


Figure 6. Simplified schematic of laboratory model direct current -variable capacitance transducer

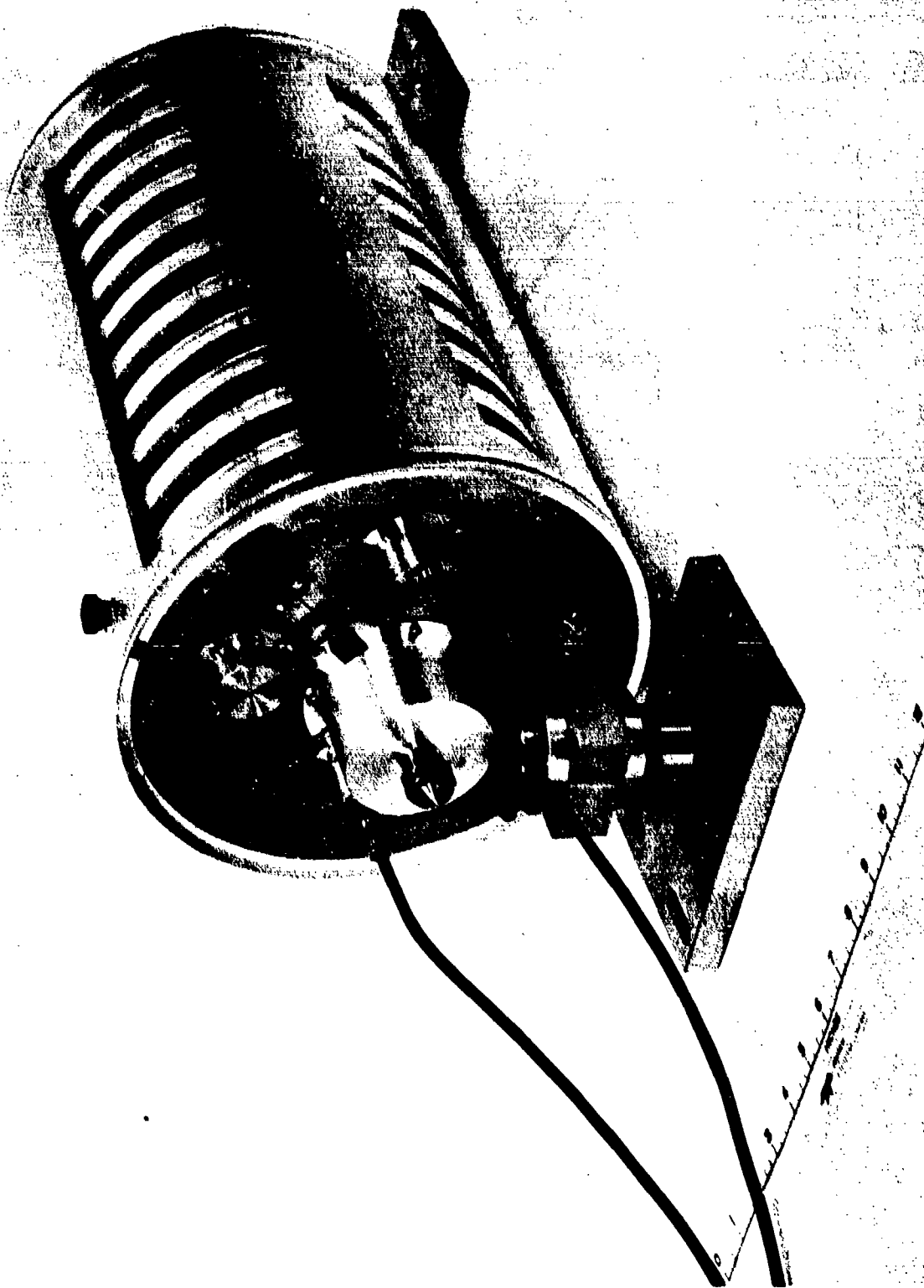


Figure 7. Laboratory model of the variable capacitor for the direct current-variable capacitance transducer

00022

The most serious problem was the high noise level discovered when tests were run on the completed transducer. With no voltage applied to the variable capacitor, the electronic noise level was low. The noise level was measured at 9, 90, and 500 V applied to the capacitor and was found to increase exponentially as the voltage increased. Circuit theory indicated that the noise should increase linearly if it was caused by small displacements in the capacitor. The exponential change in noise suggested that there may have been some dimensional instability in the aluminum and other components of the variable capacitor. Since the force between the plates due to electrostatic attraction is proportional to the square of the applied voltage (12 N per section at 1000 V), this force could cause changes in capacitor plate spacing due to stress relaxation. Since no simple solution to this problem was apparent and time did not allow the continuation of further testing, work on the DC-VC was stopped.

3.1.4 Optical Displacement Transducer

Early in the development of the strain system, the need was seen for a relatively low sensitivity, broad-band (dc to 10 Hz) transducer. This unit would serve three important functions. First, it could be calibrated using a precision micrometer and could therefore be used to determine calibration constants of the strain calibrators. Secondly, the outputs caused by earth tides and instrument settling could be recorded to verify proper operation of the strain rod and its attachment to the rock. Finally, the output of the transducer could be recorded to detect residual strains from large earthquakes.

Preliminary design specifications developed for the transducer were as follows:

Response:	dc to 10 Hz, flat to ground strain
Noise level:	Equivalent to 3×10^{-9} m displacement (7.5×10^{-11} m/m strain based on 40 m strain rod)
Dynamic range:	60 dB, minimum

The noise level and dynamic range values were chosen to allow detection of the 6 to 8 sec microseisms (about 7×10^{-9} m) and high level surface waves in the presence of the maximum earth tide signal (estimated at 4×10^{-7} m p-p relative displacement).

The first technique considered for this transducer was an optical-phototube bridge system, similar to that used in Geotech's phototube amplifier (PTA). In an earlier laboratory test, the feasibility of the technique had been demonstrated. Test data showed that a reduction in the noise level was the only improvement necessary to meet the requirements. Therefore, development on this transducer was started and a laboratory model unit was built and tested. Figure 8 shows the completed unit mounted on an Invar test fixture.

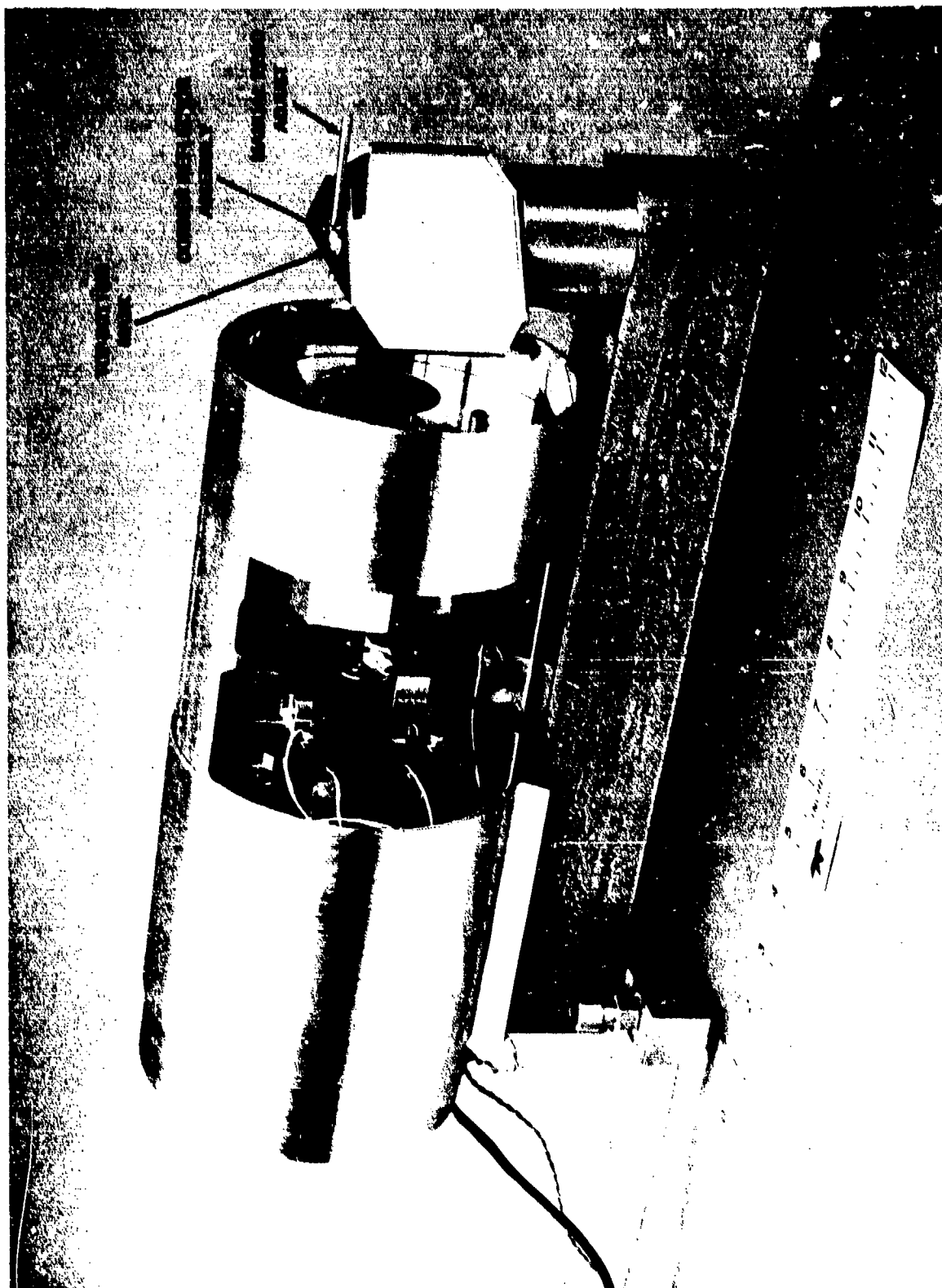


Figure 8. Optical Displacement Transducer, Model 32770.

0 5400

3.1.4.1 Description

Figure 9 is the electrical schematic of the transducer. Vacuum phototubes were selected for the bridge circuit because of their better linearity and longer term stability than similar gas-filled phototubes. The batteries used for the photocell supply voltages have very small current drains, which assured long life. The operational amplifier is used as a current amplifier to sense the very small imbalances in current caused by unequal illumination of the phototube cathodes. Exciter lamp power is furnished by a well regulated, dc power supply. Lamp voltage is maintained well below the rated level to increase lamp life and to reduce power dissipation.

Figure 10 is a top view optical schematic of the transducer. Light from the incandescent lamp is collimated by the condensing lens assembly and passes through the first cylindrical lens. This lens forms the beam into a narrow bar of light and focuses it on a vertical slit mask. The mask eliminates scattered light and sharply defines the sides of the beam. The image of this mask is focused by the cylindrical lens relay assembly onto another mask situated in the middle of the corner reflector assembly. This mask defines the top and bottom of the beam, forming a sharp, bright rectangle of light. This rectangle of light is then focused by the objective lens assembly onto the beam splitter mirror. The beam is divided into two equal parts that fall on the cathodes of two phototubes.

3.1.4.2 Principles of Operation

In operation, the lamp, lens, and electronic assembly are mounted on the rock while the corner reflector assembly is mounted on the strain seismometer rod. If the corner reflector is displaced in a direction perpendicular to the major axis of the transducer, as shown in figure 10, it can be seen that the beam entering the objective lens assembly is displaced twice that amount. The resulting unequal illumination of the photo-cathodes causes an unbalanced bridge output, which is amplified and made available at the transducer output.

In theory, transducer sensitivity is directly proportional to the exciter lamp power and inversely proportional to the width of the first slit mask. The design is a compromise between these factors because increased lamp power increases undesirable heat dissipation, and slit masks narrower than one or two millimeters require expensive, high-quality optics. On the other hand, instrument noise is determined primarily by the dark noise current of the phototubes and the Johnson noise of the photocell load resistance - in this case, the selected operational amplifier feedback resistor. In this circuit, the theoretical optimal noise level is achieved when the load resistance is between 10^9 and 10^{10} ohms.

3.1.4.3 Remotely Operated Calibrator

The remote calibrator is an optical device used periodically to check the transducer sensitivity. It consists of a thin, flat piece of glass mounted at the pivot point of a relay-type actuator. The glass plate is placed in the optical path between the objective lens and the beam splitter mirror. When the glass is pivoted, the emerging light beam is laterally displaced a small amount because of the refraction of the glass. The amount of calibration displacement can be determined by measuring the angle of rotation or by

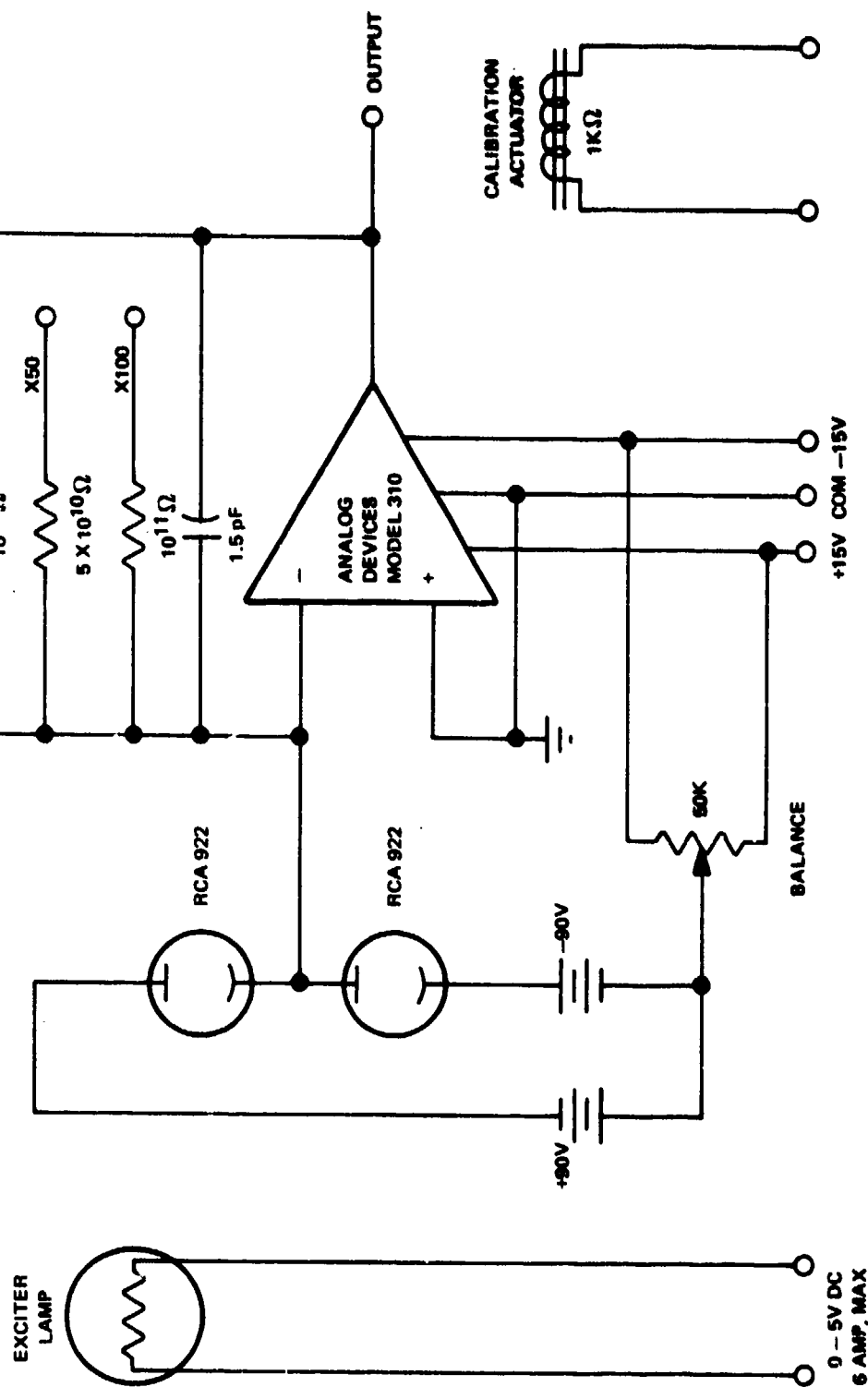


Figure 9. Electrical schematic of Optical Displacement Transducer, Model 32770.

G 5405

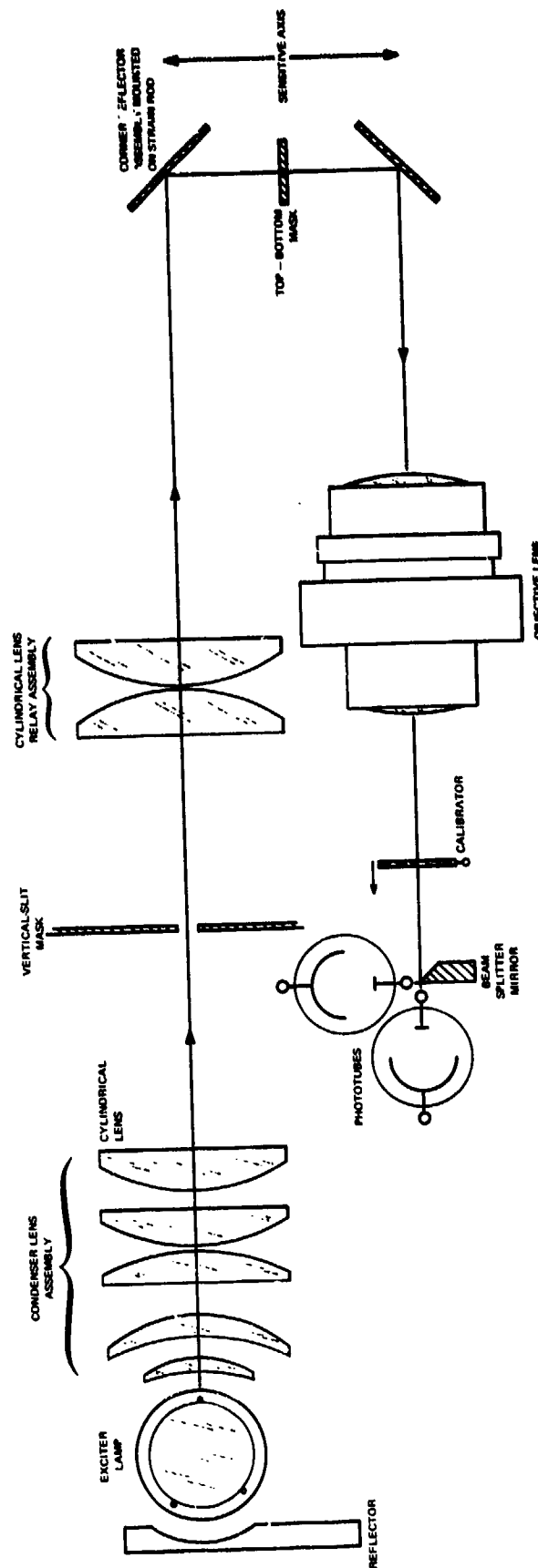


Figure 10. Top view optical schematic of the Optical Displacement Transducer, Model 32770

6 0023

comparing the calibration output to that produced by a known displacement of the corner reflector.

3.1.4.4 Test Results

Bench tests of the transducer began soon after the assembly was completed. It was immediately apparent that large noise voltages were produced by convection currents that changed the index of refraction of the air in the optical path. Therefore, all holes in the instrument case were covered and future tests were run using an insulated box to cover the instrument.

With the insulated cover in place and the lamp operated at half power of 16 W, instrument temperature rose to about 55°C (120°F). Although the electronic components are rated at temperatures well above that level, methods of reducing the heat dissipation were sought, primarily to reduce heating of the surroundings that could cause noise in other instruments. Semiconductor light-emitting diodes (LEDs) operating at high peak currents and relatively high frequencies were tested. The LEDs were found capable of producing sufficient light at peak currents, but the short duty cycle necessary to prevent overheating required somewhat complicated sample and hold circuits in the transducer. When tests indicated that the transducer would operate satisfactorily with the incandescent lamp power below 10 W, it was decided to delay further tests on this problem until the effects of such heat loads in the mine at Queen Creek, Arizona (QC-AZ), were determined.

Initial noise tests indicated that lamp voltage fluctuations produced as much as one hundred times greater output voltage fluctuations than expected. Since power supplies capable of the required regulation (noise less than 1 mV) were expensive and impractical, other methods of reducing the noise were used. First, the sensitivity of the phototubes was matched as closely as possible - a task that proved somewhat difficult because of large variations between off-the-shelf phototubes. Secondly, the spectra of light reaching the two phototubes was balanced by improving the quality of the beam splitter mirror. These improvements greatly reduced short-term effects, but some longer term noise was still evident. This longer term noise was traced to expansion and contraction of the filament supports in the original exciter lamp, which was mounted horizontally. Incorporation of a lamp with vertical filament supports greatly reduced these longer term effects of lamp voltage fluctuation.

Final testing of the completed transducer was done in the stable mine environment at QC-AZ. These tests were directed mainly toward a determination of the sources of a serious long-term drift in the transducer. This long-term drift, which has been observed during tests at Garland, was not improved by operation of the unit in the thermally stable mine environment. With all optical elements mounted on the test fixture, the drift continued consistently in the same direction and usually exceeded the dynamic range of the instrument within 24 hours. The problem was further aggravated because the necessary frequent adjustments disturbed the thermal equilibrium of the instrument and started the drift cycle all over again. Although the drift was obviously an effect of temperature change, field tests were unsuccessful in pinpointing the source. Therefore, further development of the optical transducer was abandoned.

3.2 TECHNIQUES USED

The moving-coil, permanent-magnet transducer was selected as the primary transducer for this project. An equally important part of the primary system is the solid-state preamplifier, which was carefully selected after extensive noise tests of amplifiers from several manufacturers. In the following paragraphs, the design and/or selection of these components for the strain system will be discussed. Also, the design of the strain rod and its suspension and the secondary displacement transducer will be discussed.

3.2.1 Moving-Coil Transducer

The moving-coil transducer has been found to be simple and reliable over many years of use. It was therefore chosen as one of the most promising techniques for detailed study early in the program. The velocity-sensitive, moving-coil technique offered an advantage over displacement techniques by eliminating the problems created by the very long period, high amplitude earth tides and secular strains. The major disadvantage of this transducer is the high weight of the magnet structure required which made handling difficult.

3.2.1.1 Magnet and Coil Design

The design of the magnet for this project was primarily an updating of the existing unit then in use at the strain facility at WMO. The original magnet structure design was modified to take advantage of the magnet manufacturer's capability of fabricating larger magnets. These larger magnets resulted in a 20 percent increase in flux density in an air gap of the same dimensions as the original design.

The coil assembly was completely redesigned. The existing transducer required a low impedance coil to provide maximum power transfer between the coil and the galvanometer in a standard long-period PTA. Since a high input impedance, solid-state amplifier was to be used, a high impedance coil was required for this application. In addition, a new coil form was designed using a more dimensionally stable material than the original unit. Finally, the coil width was increased so that it was longer than the 1 in. magnet gap to improve linearity and to take advantage of an increase in the generator constant afforded by utilizing stray flux outside the gap. The specifications for the transducer are given in table 2.

3.2.1.2 Magnet Assembly

Fabrication of the soft steel components of the magnet structure was done at Geotech's Garland plant. When the uncharged magnet segments were received from Indiana General Corporation, the magnet manufacturer, the magnets were assembled. Figure 11a shows the 8-segment Alnico V magnet in place. Figure 11b shows the complete magnet structure just prior to final assembly. (The scale in the figure is 15 in. long.) To charge the first magnet, Indiana General requested that a large coil of No. 6 AWG wire be wound between the magnet and the outer cylinder. The coil was manufactured and installed and the complete assembly was returned to Indiana General for charging.

Charging of the magnet proved to be more difficult than expected. The No. 6 wire coil did not function as expected and it was necessary for the vendor to

Table 2. Specifications of the moving-coil transducer

Magnet assembly

Flux density in gap	1.2 Tesla (T) (12,000 gauss)
Magnet gap dimensions	12.000 in. o.d., 11.400 in. i.d. (0.300 in. gap) 1.000 in. long
Magnet: material	Alnico V
shape	8 pie-shaped segments
weight	250 lb total
Dimensions	20 in. diameter x 12 in. long
Weight of complete assembly	700 lbs

Coil assembly

Wire size	No. 42 AWG
Number of turns	31,000 approx
Total wire length	29,000 m, approx
Resistance	165,000 ohm, nominal

Transducer generator constant

Calculated, Minimum	29,000 V/m/sec
Typical	32,000 V/m/sec

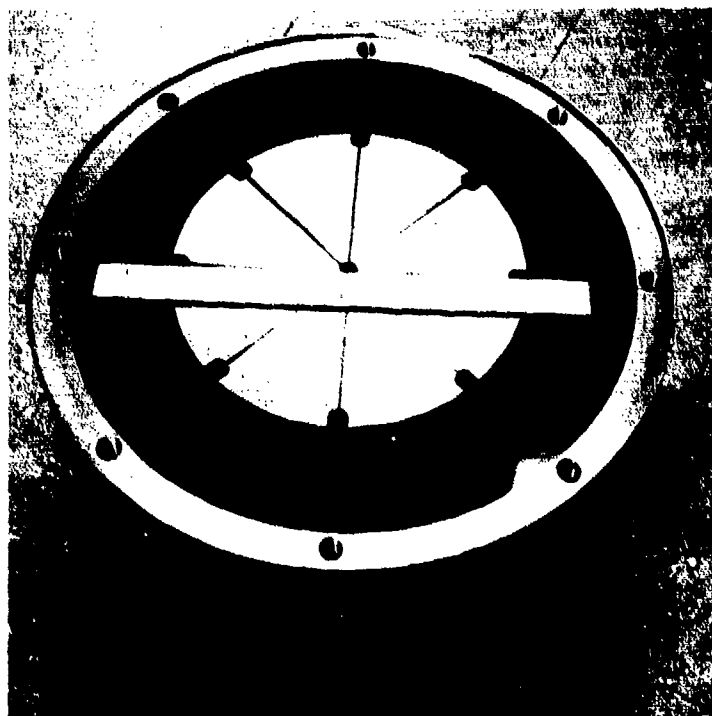


Figure 11a. Eight magnet segments and outer pole pieces

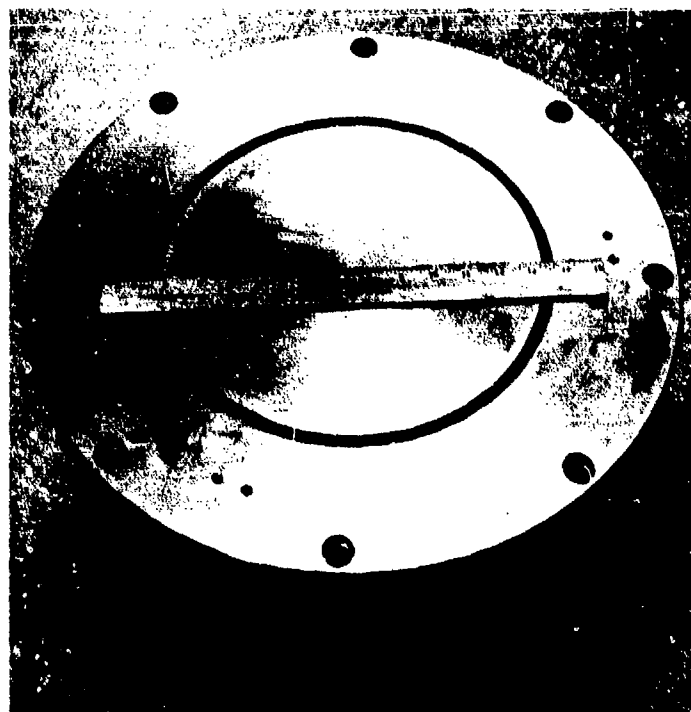


Figure 11b. Magnet assembly

Figure 11. Moving coil technique magnet assembly

G 4553

use a large capacitor-discharge type magnet charger in conjunction with a large electromagnetic charger to obtain the maximum flux density possible in the assembly. Indiana General was able to charge the assembly to 1.25T (12,500 gauss) at saturation. This saturation flux provided 1.2T in the stabilized condition rather than the 1.3T level that was originally expected.

The manufacturer made several suggestions to improve the assembly design, including elimination of the charging coil and increasing the thickness of the soft iron magnet components. These suggestions were incorporated in the drawings and the second and third magnet assemblies built later. The original magnet assembly was not modified.

3.2.1.3 Coil Assembly

Figure 12 is a photograph of the coil assembly designed for the project. The coil assembly involves the random winding, in epoxy, of a coil of copper wire on a fiberglass-epoxy laminated coil form. A prototype coil was wound with No. 39 AWG wire in order to meet the manufacturer's suggested maximum input impedance specification of the solid-state amplifier. This coil had an impedance of 54 k Ω and yielded a calculated generator constant of 17,300 V/m/sec. Later tests of the amplifier (see paragraph 3.2.2.1) indicated that the impedance and generator constant could be increased without significantly increasing the noise level. Therefore, the wire size was changed to No. 42 AWG, yielding a 164 k Ω coil and a calculated generator constant of 29,000 V/m/sec.

3.2.1.4 Transducer Tests

The first test of the moving-coil transducer was a determination of the generator constant (G) using the two coils. The coil was mounted on a 2 m long steel tube, which was suspended by two prototype taut wire suspensions. The coil and tube thus effectively became the mass of a horizontal inertial seismometer with a natural frequency of about 1.5 Hz. This assembly was placed in the underground walk-in vault at the Garland laboratory. The G of the transducer was then determined by measuring the deflection produced by a known force from a weight lift and then measuring a current applied to the data coil to produce an identical deflection. Assuming equal deflections, the G can be determined by

$$G = \frac{W}{i} g \quad (2)$$

where

G is the motor constant in V/m/sec or N/A,

w is the effective mass of the weight lifted, in kilograms,

i is the current through the coil in amperes, and

g is the acceleration of gravity (9.8 m/sec²)

Two methods were used to measure the deflection. In the first, the laboratory model electromagnetic calibrator was mounted on the rod and was used with an

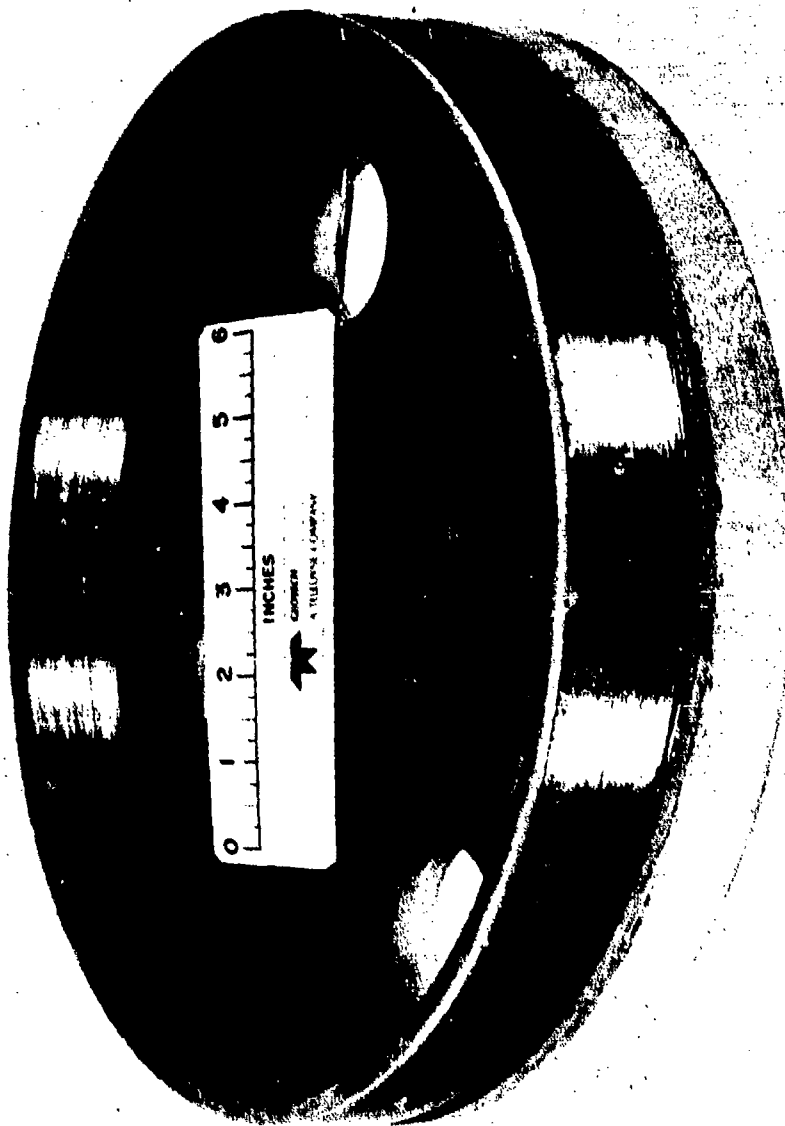


Figure 12. Data coil for moving-coil transducer

6 0024

amplifier as a velocity transducer. The voltage pulses produced by several weight lifts were amplified and averaged. Then, a series of dc pulses was applied to the data coil and the current was adjusted to produce an identical output of the amplifier. In the second method, a high-power microscope was used to measure the static deflection of the inertial mass caused by the application of a constant force from the weight. With the force still applied, current through the data coil was adjusted to return the inertial mass to its original rest position. Both methods produced similar results, but the microscope method is considered to be the most accurate.

The G of the coil with No. 39 AWG wire was determined to be 18,580 V/m/sec. Weight lift tests were repeated for the coil with No. 42 AWG wire and the G was determined to be 31,600 V/m/sec. The generator constants were about 10 percent higher than the theoretical minimum value. This higher G results from the coil being physically longer (1.20 in.) than the magnet gap (1.00 in.) which allows utilization of the stray magnetic flux outside the gap. Also, these data show that use of the higher impedance coil results in a 4.5 dB improvement in the signal-to-noise ratio of the seismometer.

Other tests were conducted to determine whether the inherent inductance and capacitance of the data coil and its associated circuitry would produce undesirable phase shifts in any passband of interest. The resonant frequency of the LRC circuit was determined for several values of external capacitance. The resonant frequencies with the maximum expected capacitance were higher than 30 Hz, which was sufficiently high to eliminate any phase shift problems.

3.2.2 Solid-State Amplifier

The amplifier selected for use on this project was the Ithaco, Inc., Long-Period Seismic Amplifier, Model 6089-34, and is shown in figure 13. As seen in the figure, the amplifier is enclosed in an insulated metal box which provides magnetic and electromagnetic shielding as well as isolation from temperature effects. The decision to use this amplifier was based on the requirements of the project. Noise tests performed previously by Geotech, and further noise tests on a Philbrick Operational Amplifier, Model SP2A/X, and an Ithaco, Model 154, contributed to the decision. All parameters of the amplifier were checked to determine if it conformed to the manufacturer's specifications. Primary attention was given to the noise level.

3.2.2.1 Amplifier Noise Tests

When the low-noise amplifier was received from Ithaco, Inc., tests were run to determine whether the unit met the manufacturer's noise specification. These tests were carefully conducted because amplifier noise level was the parameter of greatest concern to the project.

In the first test, the amplifier input was terminated with a 54 k Ω carbon film resistor in accordance with the manufacturer's specifications. A long term, calibrated noise sample (about 20 hours) was recorded on an analog magnetic-tape recorder and a 6.7 hour sample was selected for analysis. A visual analysis of an analog playout of the sample showed that the maximum peak-to-peak excursion (referred to the input) was 0.64 μ V in the passband of 0.6 to 333 sec (1.7 to 0.003 Hz). If it is assumed that this noise is all the result

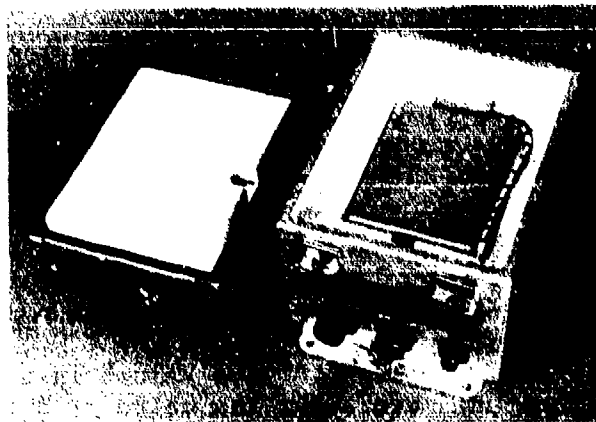
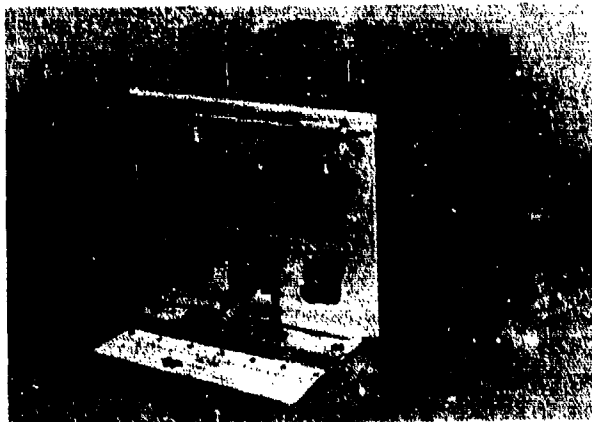


Figure 13. Ithaco, Inc., Long-Period Seismic Amplifier, Model 6089-34

G 6625

of thermal agitation in the input resistor, then the maximum peak-to-peak noise in the passband from 30 to 333 sec (0.033 to 0.003 Hz) can be estimated by multiplying 0.64 μ V by the square root of the ratio of the passbands. This gives a calculated noise level of 0.091 μ V peak-to-peak. The specified maximum noise level for the amplifier is 0.025 μ V rms in the 30 to 333 sec passband. Using a factor of 6 to convert the rms rating to a gaussian, 99 percent occurrence peak-to-peak level yields 0.150 μ V peak-to-peak. This analysis showed, then, that the amplifier was well within specifications for noise level.

In addition to the visual analysis, the selected sample was digitized for calculation of the power spectral density (PSD) of the amplifier noise. The resulting spectra showed that the noise consisted of two separate components. One component was from the thermal agitation in the input resistor and was characterized by a horizontal (white) spectra from about 15 sec toward the shorter periods. The other component was from the 1/f flicker noise in the components of the amplifier and was characterized by a rise of about 3 dB/octave from 15 sec toward the longer periods. This two-component characteristic of the spectra indicated that a data coil with a greater wire length could increase the generator constant and signal voltage more than the amplifier noise voltage was increased as a result of the increased coil resistance. The shape of the noise spectra in the ALPS passband indicated that the ALPS instrument noise would be dominated by the 1/f noise which is (to the first order) independent of source resistance. Therefore, an increase in the wire length would increase the generator constant and signal-to-noise ratio in the ALPS passband, while the resulting increase in amplifier noise would be outside the passband. Calculations were made which indicated that a coil could be wound using No. 42 AWG wire instead of the No. 39 AWG wire in the first coil. The new coil had a resistance of 164 k Ω as compared to the 54 k Ω of the original coil.

To test this hypothesis, calibrated long-term noise samples were again recorded on magnetic tape for the two values of input resistance. For both cases, calibration signals and typical samples of the noise data were digitized for calculation of the PSD of the noise. Three period ranges were of interest so the data were digitized at three different sampling rates with noise samples starting at the same time. After digitizing, the data were digitally filtered to improve the antialiasing and then decimated to provide a longer time interval of data. A calibration factor determined from the calibration signal was used. Then a Parzen smoothing window was applied. The power spectral densities were calculated in frequency bands of width $\frac{1}{5.12}$ Hz, 1/128 Hz, and 1/2560 Hz and divided by the bandwidth to give values in units of V^2/Hz . Table 3 shows the pertinent parameters for the calculation.

Figures 14 and 15 are the composite power spectral densities in the three calculated passbands for the 164 k Ω and 54 k Ω input resistance cases, respectively. The PSDs of the amplifiers in the three passbands overlap each other well within the statistical confidence limits. The last two points in the middle passband contain portions of the power from an infinite period up to 128 sec period and thus lie above the spectra from the longer period analysis.

The two different components of amplifier noise can be seen clearly in both figures. The "white" resistor noise component intersects the 1/f component at about 20 sec for the high input resistance case (figure 14), and at about 15 sec for the other (figure 15). As predicted by Johnson noise theory, the

Table 3. Parameters for calculation of power spectral density of Ithaco amplifier noise

Passband No.	1	2	3
Digitizing rate, samples/sec	50	4	1
Analog antialias low-pass filters:			
Corner, Hz	10	0.5	0.1
Cutoff rate, dB/octave	24	24	24
Digital antialias low-pass filter:			
Corner, Hz	None	0.5	0.04
>60 dB down, at, Hz	None	2.0	0.0085
Digitizing rate after decimate			
Samples/sec	50	2	0.1
Samples used in PSD, No.	3,969	3,969	2,410
Length of time in sample for PSD			
Sec	79.38	1984.5	24100
h	0.022	0.55	6.7
Lags used in PSD, No.	127	127	127
Confidence limit, dB			
96%	±2.3	±2.3	±2.8
90%	±1.8	±1.8	±2.3
Period range of PSD	1/25-5.12	2-128	20-2560

white noise component increases by the square root of the ratio of resistances, from about $2.5 \times 10^{-15} \text{ V}^2/\text{Hz}$ for the 54 k Ω source resistance to about $5 \times 10^{-15} \text{ V}^2/\text{Hz}$ for the 164 k Ω source resistance. The 1/f flicker noise component rises at about 3 dB/octave toward longer periods and can be seen to be independent of source resistance by comparing figures 14 and 15.

3.2.2.2 Other Amplifier Tests

In addition to the noise tests, the amplifier was thoroughly tested to determine whether it met all other specifications. The results of these other tests are shown in table 4, which indicates that the amplifier essentially conforms to published specifications.

3.2.3 Strain Seismometer Design

After selection of the moving-coil transducer and the Ithaco amplifier as the best technique, there remained the task of designing the strain seismometer. The design included a determination of the minimum required length, development of a method of suspension, selection of the material to be used, and design of the necessary calibrators.

3.2.3.1 Strain Seismometer Length

To achieve the goal of a low-noise strain system comparable to inertial systems, an estimate of the expected signal-to-system-noise ratio was required. From this information, the total length of the strain rod could be determined.

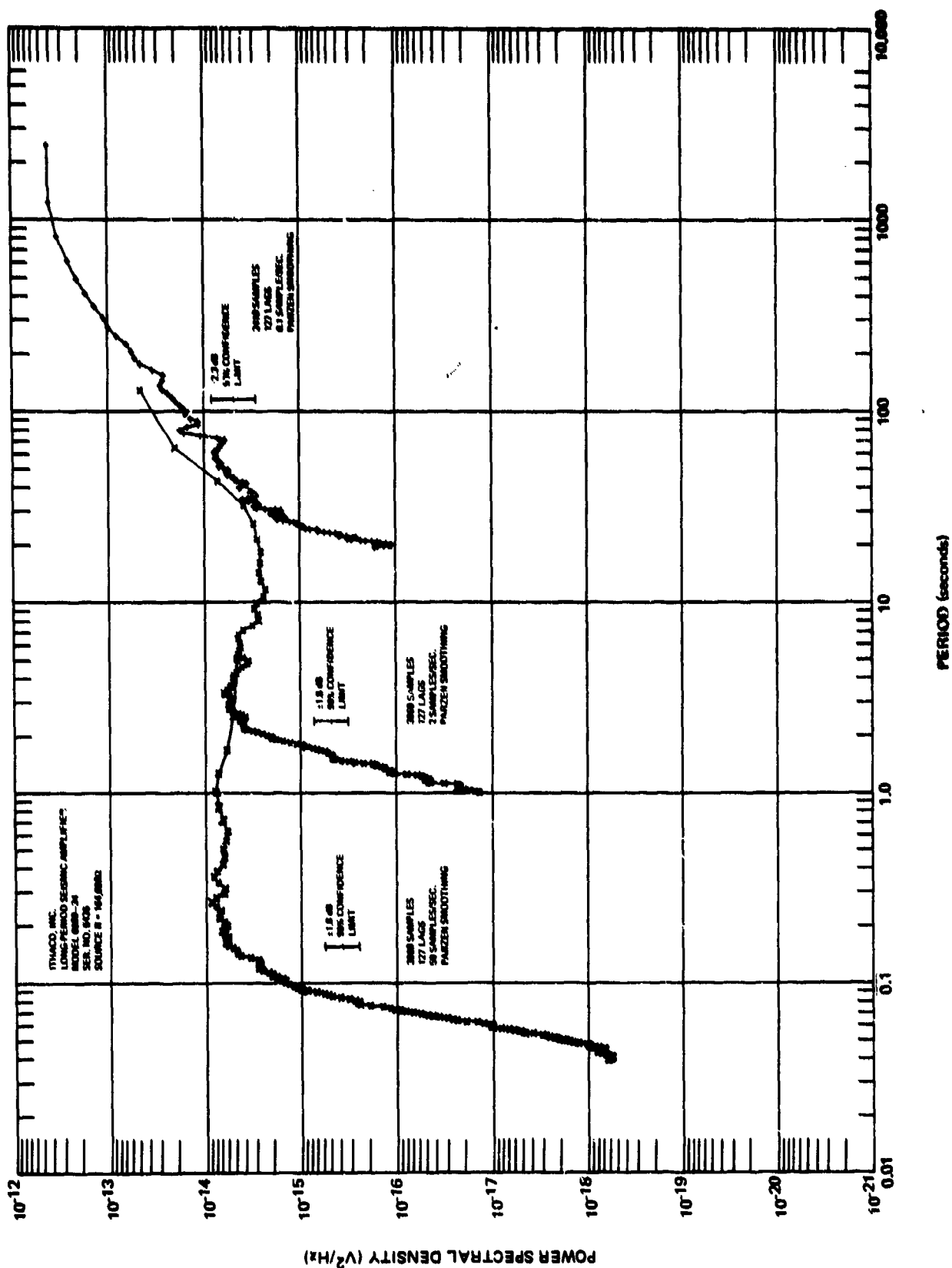


Figure 14. Amplifier noise voltage power spectral density 164,000 Ω source resistance

G 6006

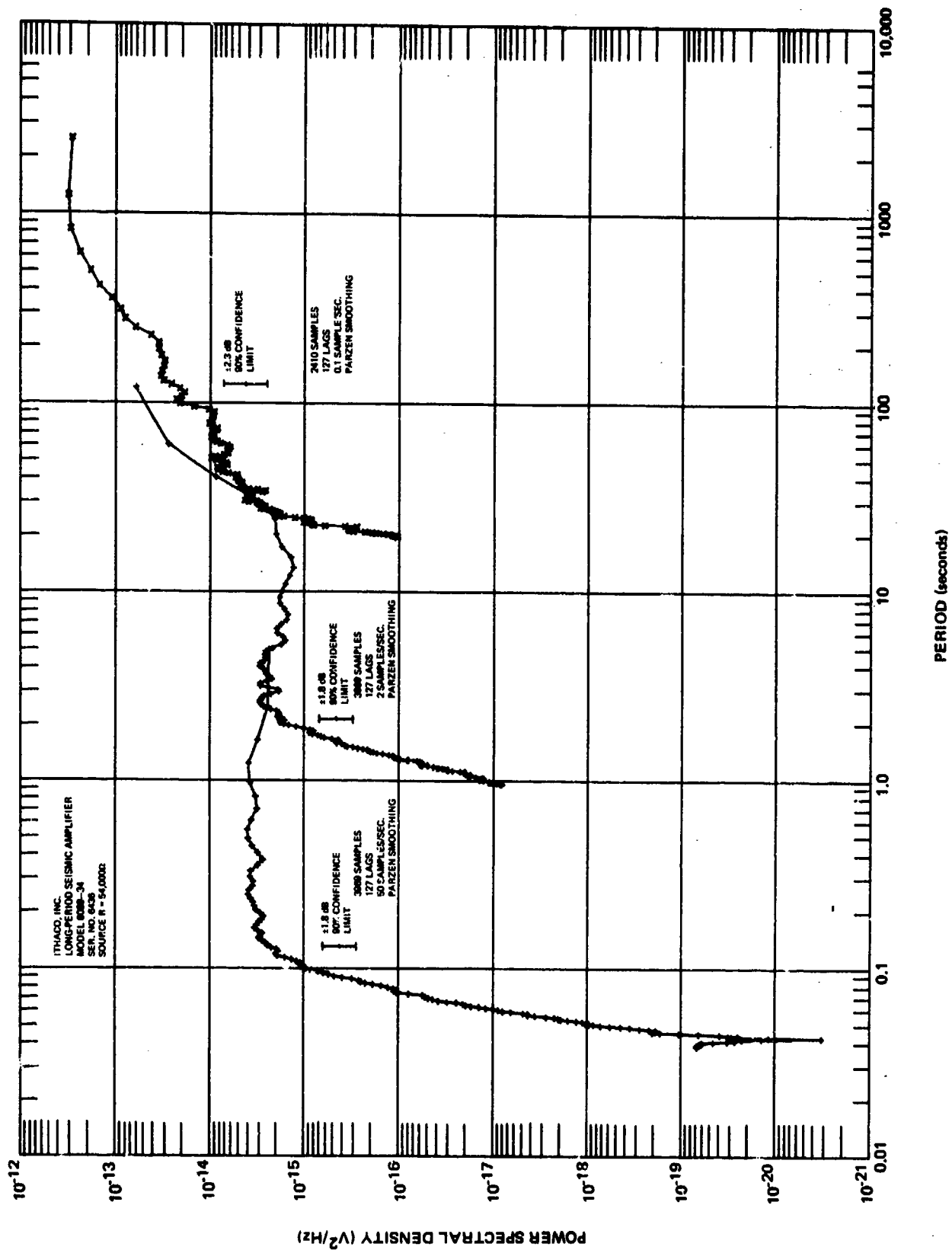


Figure 15. Amplifier noise voltage power spectral density 54,000 Ω source resistance G 6627

Table 4. Comparison of manufacturer's specifications to measured values for the Ithaco Long-Period Seismic Amplifier, Model 6089-34

<u>Parameter</u>	<u>Specification</u>	<u>Measured Value</u>
Gain	80 dB	80 dB
Change in gain with power supply variation	+0.2 dB (+2%)	+0.2% to -0.8%
Clipping voltages (p-p)	60 V	74 V
Common mode rejection		
Periods >0.3 sec	60 dB	60 to 110 dB
Periods <0.3 sec	60 dB	54 to 60 dB
Response to power supply variation	(No specification)	0.0002 to 2.3 V/V
Response to capacitive load	(No specification)	Satisfactory
Response to magnetic field	(No specification)	Satisfactory

The estimate of expected background signal level was based on data taken at Las Cruces, New Mexico (LC-NM), as reported by Trott (1965). This site was chosen as the basis of comparison, first, because of its very quiet background level and secondly, because calibrated spectra of the background from carefully conducted tests were available. The spectrum of the LC-NM microseismic noise level (vertical component) expressed as root-mean-square (rms) millimicrons of ground displacement per milliHertz bandwidth was converted to strain as a function of period. The voltage generated by a 40 m horizontal strain seismometer with a generator constant of 31,600 V/m/sec was calculated for these displacements assuming the noise is fundamental Rayleigh waves and that the horizontal motion is equal to vertical motion.

The estimate of strain system noise was based on two assumptions. First, it was assumed that the noise of the Ithaco amplifier would be the predominant component of system noise and the electronic amplifiers and filters following it would not add appreciable noise to the system. Secondly, it was not possible to estimate the noise contribution of the seismometer itself, and thus it was assumed that its noise would be lower than electronic noise. Therefore, the PSD of the Ithaco amplifier shown in figure 14 was normalized to a mHz bandwidth, the square root was taken, and the results smoothed, yielding a spectrum in rms volts per mHz.

The microseismic and amplifier noise spectra are compared in figure 16. From the figure it can be seen that the background signal-to-strain-system noise level varies from almost 60 dB at 6 sec to just over 0 dB for periods longer than 40 sec. This signal-to-noise ratio was considered sufficient for the purposes of the program and the strain rod length was therefore set at 40 m.

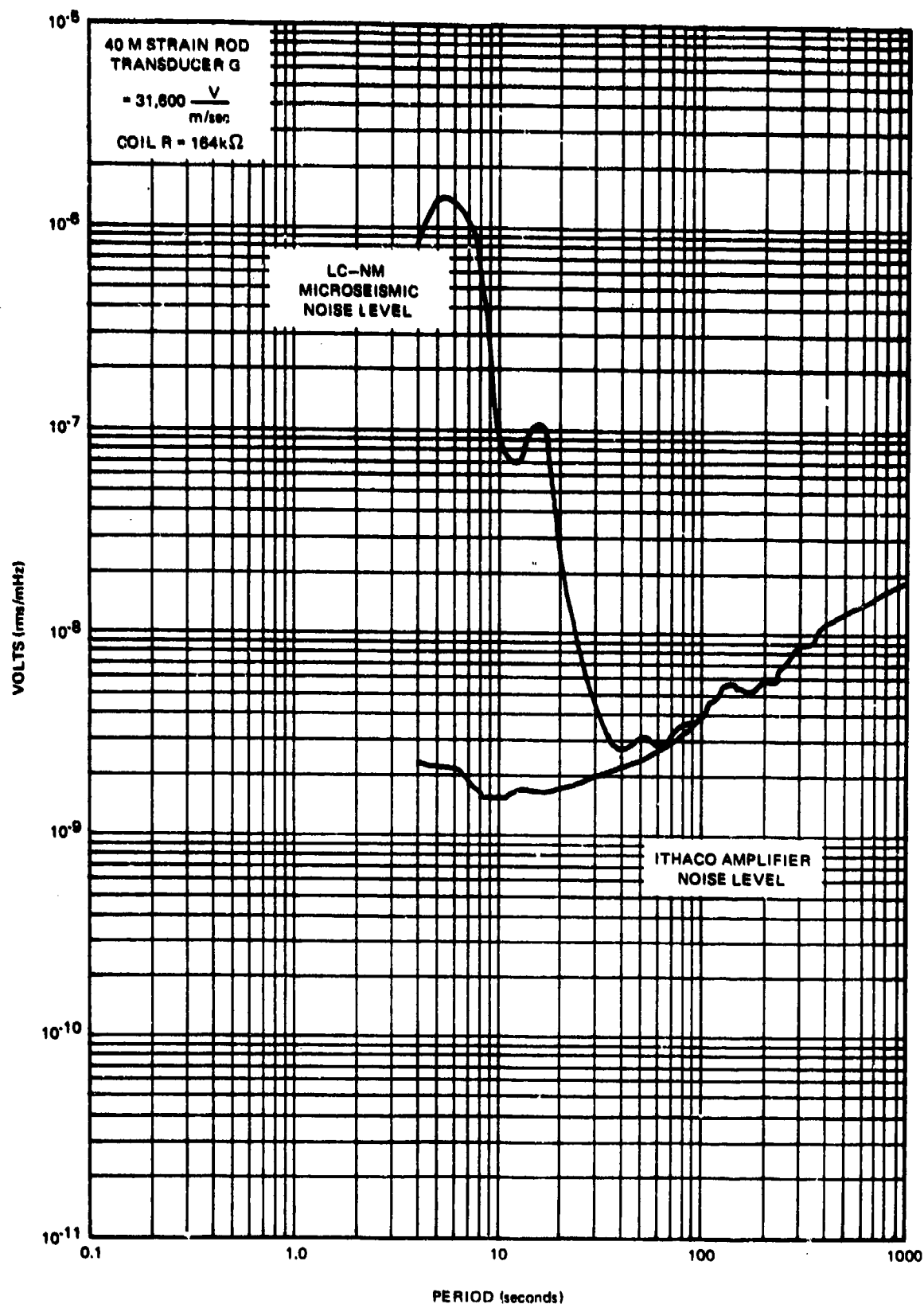


Figure 16. Equivalent narrow-band rms voltages at input to preamplifier

G 6628

3.2.3.2 Materials and Construction

In deciding on the materials to be used for the strain seismometers, careful consideration was given to the effects of temperature changes that could cause noise in the passband of interest. The strain rod itself, of course, was given the greatest consideration. Four materials were considered for the rod: fused quartz, Invar, steel, and CER-VIT, an extremely low expansion ($1.5 \times 10^{-7}/^{\circ}\text{C}$) ceramic material manufactured by Owen-Illinois, Inc. CER-VIT was eliminated because of its high cost. Steel tubing was also rejected because the disadvantage of a relatively high coefficient of expansion was not offset by a material cost reduction as compared to Invar. Invar was available and offered several advantages over quartz tubing then being used. First, it was not subject to breakage and would not require as much care in installation and maintenance. Secondly, it could be easily joined by external clamp-type couplers because of its uniform size. Finally, fixtures could be rigidly clamped to the tube, allowing support configurations different from the then existing sling arrangement. Although Invar's expansion coefficient ($9 \times 10^{-7}/^{\circ}\text{C}$) is about twice that of fused quartz, heat flow calculations showed that 4 in. of insulation were more than sufficient to eliminate the effects of temperature changes as great as 5°C peak-to-peak at 30 sec. Design calculations showed that a tube with an outside diameter of 2 in. (51 mm) and a wall thickness of 1/16 in. (1.6 mm) was acceptable.

Invar was also selected for other machined parts of the seismometer, such as the support frames, their baseplates, and the rod anchor assemblies. All hardware, including the rock anchors, was either stainless or cadmium-plated steel.

It should be noted that the strain seismometer was assembled using bolts, nuts, and screws exclusively; welded construction was avoided to prevent possible noise caused by stress relief in welded joints.

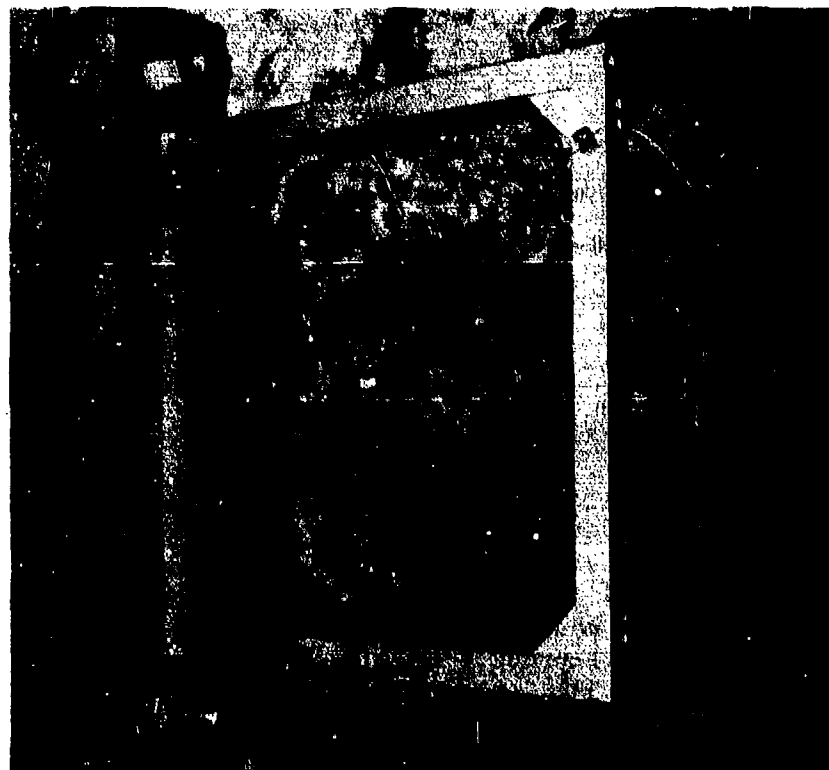
3.2.3.3 Strain Rod Suspension

The design of the strain rod suspension was carefully done because of its importance. The purpose of the suspension assemblies is to restrain the rod from transverse vibrations without materially restraining axial motion along the rod. In addition, the suspension should not contribute noise to the system. Most existing suspension methods use slings to support the rod. For this program, it was desired to more completely constrain the rod in all directions perpendicular to the rod axis and to make the assembly vertically symmetrical to minimize the effects of temperature. Therefore, a three-point suspension was designed and prototypes using two methods were fabricated for testing.

In the first method, the rod was supported by three stiff spokes attached to auxiliary leaf springs at the corners of a triangular frame. This method provided a relatively linear and soft axial spring rate, but was rejected because it allowed too much transverse vibration. In the second method, the rod was supported by three taut wires strung from clamps on the rod to clamps on the supporting frame. Figure 17 shows the two types of suspension frames used in the program. Figure 17a shows the triangle frame support used on the vertical (shown) and floor-mounted horizontal instruments. Figure 17b shows the square frame support used on the wall-mounted horizontal strainmeter. Both of these supports are symmetrical about the vertical axis so that temperature



a. Triangular frame support for vertical and floor-mounted horizontal strainmeter



b. Square frame support for wall-mounted horizontal strainmeter

Figure 17. Strain rod suspension frames

G 6629

changes in vertically stratified air produce symmetrical expansion. The suspension wire is Hamilton Metals' Elinvar Extra, a constant modulus of elasticity alloy made especially for precision springs.

The taut-wire suspensions are very stiff to transverse vibration and moderately stiff for axial motion. Calculations were made to determine whether suspension stiffness would cause appreciable loss of signal by compressing the strain rod. Since it was desirable to limit losses to less than 1 percent, the combined axial stiffness of all the suspension assemblies had to be less than 1 percent of the axial stiffness of the strain rod. The worst case calculations showed that with upper wire tension of about 10 lb and misalignment of every suspension by 1 deg (approx. 0.1 in.), losses would be less than 1 percent for any expected level of secular strain.

3.2.3.4 Calibrator and Strain Rod Anchor

The calibrator designed for the strain seismometers used an electromagnetic transducer to apply an axial force to the strain rod, producing a small displacement at the free end. Figure 18 shows one of these calibrators. Mounted above it is the RF-VC transducer that was used for initial calibration constant checks. The calibrator consists of a single magnet and a coil mounted concentrically on the strain rod so that no twisting motion is imparted to the rod. The coil is attached to the rod and the magnet is attached to the rock. Two calibrators were mounted on each 40 m horizontal instrument: one about 4 m and the other about 36 m from the fixed end. The 4 m calibrator was the primary unit used for most high gain calibrations. The 36 m unit was used for high level calibrations for the broadband transducers and also served as a backup in case of problems with the other unit.

The only remaining major component of the seismometer is the strain rod anchor. Figure 19 is a photograph of one of the anchors as installed on the wall in the 55 deg azimuth tunnel. As can be seen, the anchor is very rigid and construction is relatively simple. It is constructed of Invar to minimize disturbances from temperature fluctuations.

3.2.4 Variable Capacitance Displacement Transducer

Development of a variable capacitance displacement transducer (VCT) for use on a strainmeter was begun under the LRSM program, Project VT/8703, at about the same time that work was started on the optical transducer on Project VT/8706. The VCT, described by Shopland (1970), was successfully operated as part of a strainmeter in a special test under Project VT/8703 during 1970. When field tests on the optical transducer produced unfavorable results, it was decided to adapt the VCT for use at QC-AZ. Since the original transducer was designed for unattended operation in shallow trench installations that would be subject to large strain noise rates, it was possible to simplify the new design to take advantage of better operating conditions in the QC-AZ mine. In particular, the following design modifications were made:

1. Only one variable capacitance detector was used for the transducer;
2. Power supply circuits were modified to be compatible with the existing QC-AZ power subsystem;

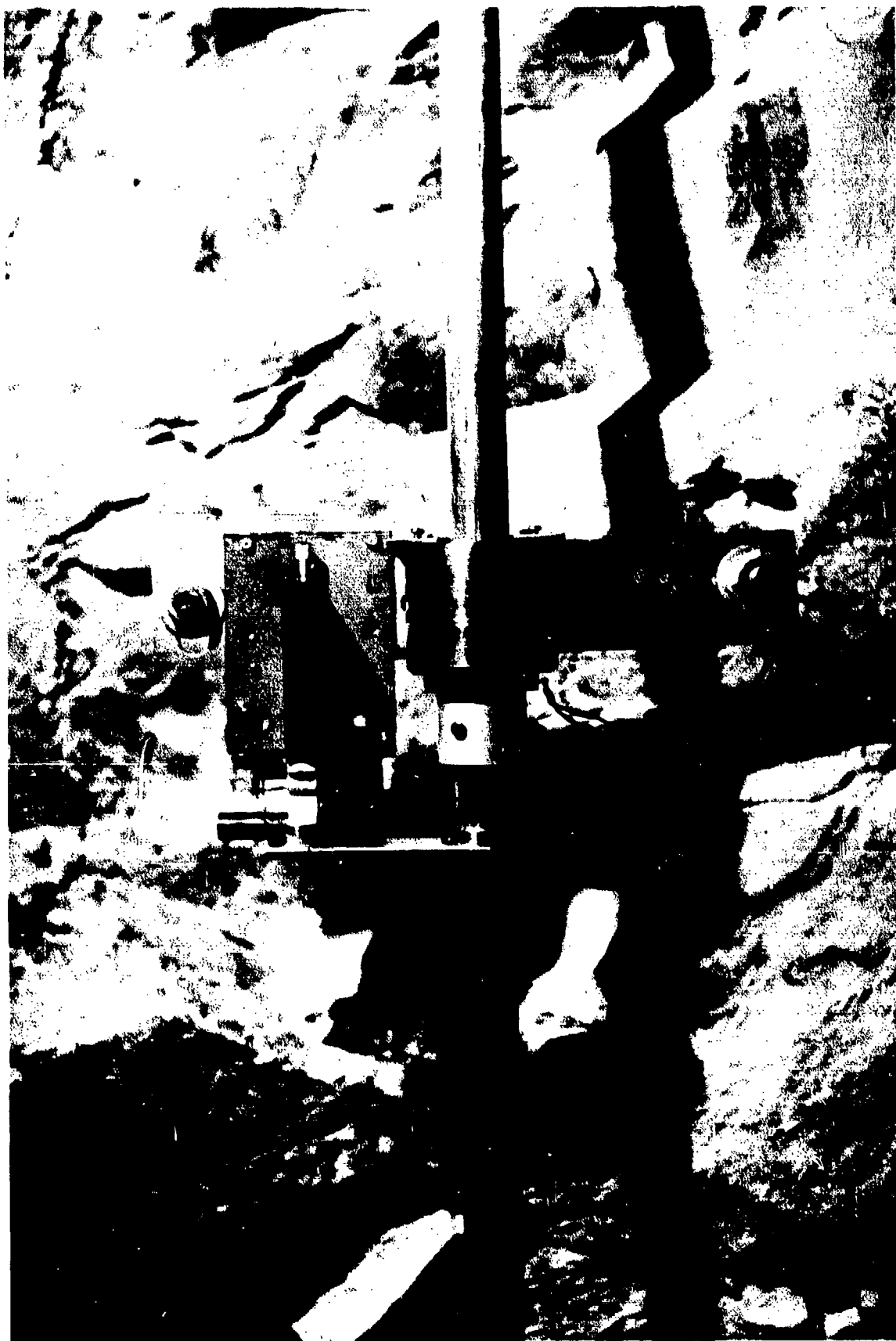


Figure 18. Electromagnetic calibrator for strain seismometer. The rf variable-capacitance transducer was temporarily mounted above the calibrator for calibration constant checks

G 6030

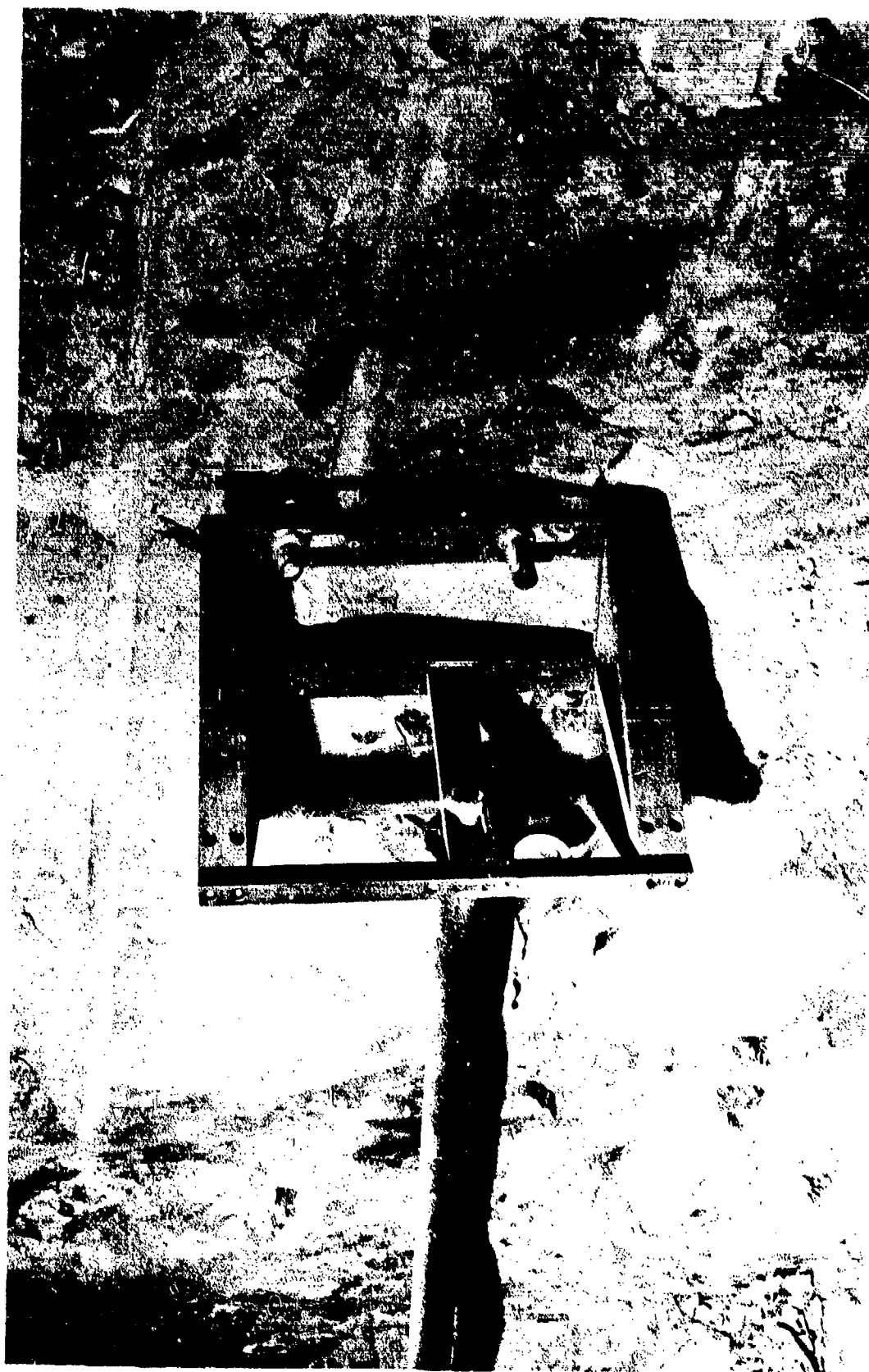


Figure 19. Strain rod anchor

00001

3. Remotely operated coarse and fine adjusting assemblies were omitted;

4. A 10:1 parallelogram lever-type motion reducer, driven by a 2 μm per division micrometer, was substituted for the 100:1 reducer driven by a 10 $\mu\text{m}/\text{div}$ micrometer.

The resulting design, although lacking some of the features of the original design, was built quicker and at a considerably lower cost.

3.2.4.1 Principles of Operation

The transducer consists of a dual, differential capacitor connected to a detector circuit as shown schematically in figure 20. The center capacitor plate is attached to the strain rod and is maintained at ground potential. It moves between two fixed, active capacitor plates. With the center plate midway between the other plates, capacitance of both capacitors is nominally 100 pF. In the detector, Z1 and Z2 are integrated circuit operational amplifiers connected as a free-running multivibrator. At balance, the complementary outputs of Z1 and Z2 are symmetrical square waves which contain no dc component. If the center plate is displaced, the capacitance of one side of the dual capacitor goes down while the other capacitance goes up in proportion to the displacement. Proportional changes are produced in the time constant circuits used to control multivibrator symmetry. The multivibrator output is then a nonsymmetrical square wave at approximately the same frequency as that at balance. These nonsymmetrical outputs are then filtered and the resulting dc components are applied to the positive and negative inputs of amplifier Z3. The output of Z3 is a dc voltage proportional to displacement. A following low noise amplifying stage and power regulating circuits, not shown on the schematic, complete the transducer.

3.2.4.2 Construction

Figure 21 shows the complete VCT installed on the 325 deg strain seismometer (S325). The center capacitor plate attached to the strain rod is at ground potential and moves between the two fixed, active plates. The plate spacing of each capacitor section is nominally 200 μm (0.008 in.). The VCT electronics and the first amplifier stage are housed in the metal enclosure. Nominal sensitivity prior to amplification is 40 mV/ μm . Calibration of the VCT is accomplished by displacing the fixed plates a known amount using the micrometer and the parallelogram 10:1 motion reducer. Bendix cross-flexures are used at all pivot points for low-noise, elastic, friction-free operation. In general, the installation of the unit was straightforward and no problems were encountered.

3.2.4.3 Operation and Tests

The three VCTs were placed into operation soon after installation. The only major problem encountered was excessive hum pickup on the single-ended output line leading from the mine to the recording van. Therefore, an integrated-circuit operational amplifier, connected as a unity gain inverter, was installed in the VCT electronics enclosure. This provided a balanced output that greatly reduced the hum pickup and also increased the overall gain of the amplifier stage from 10 to 20.

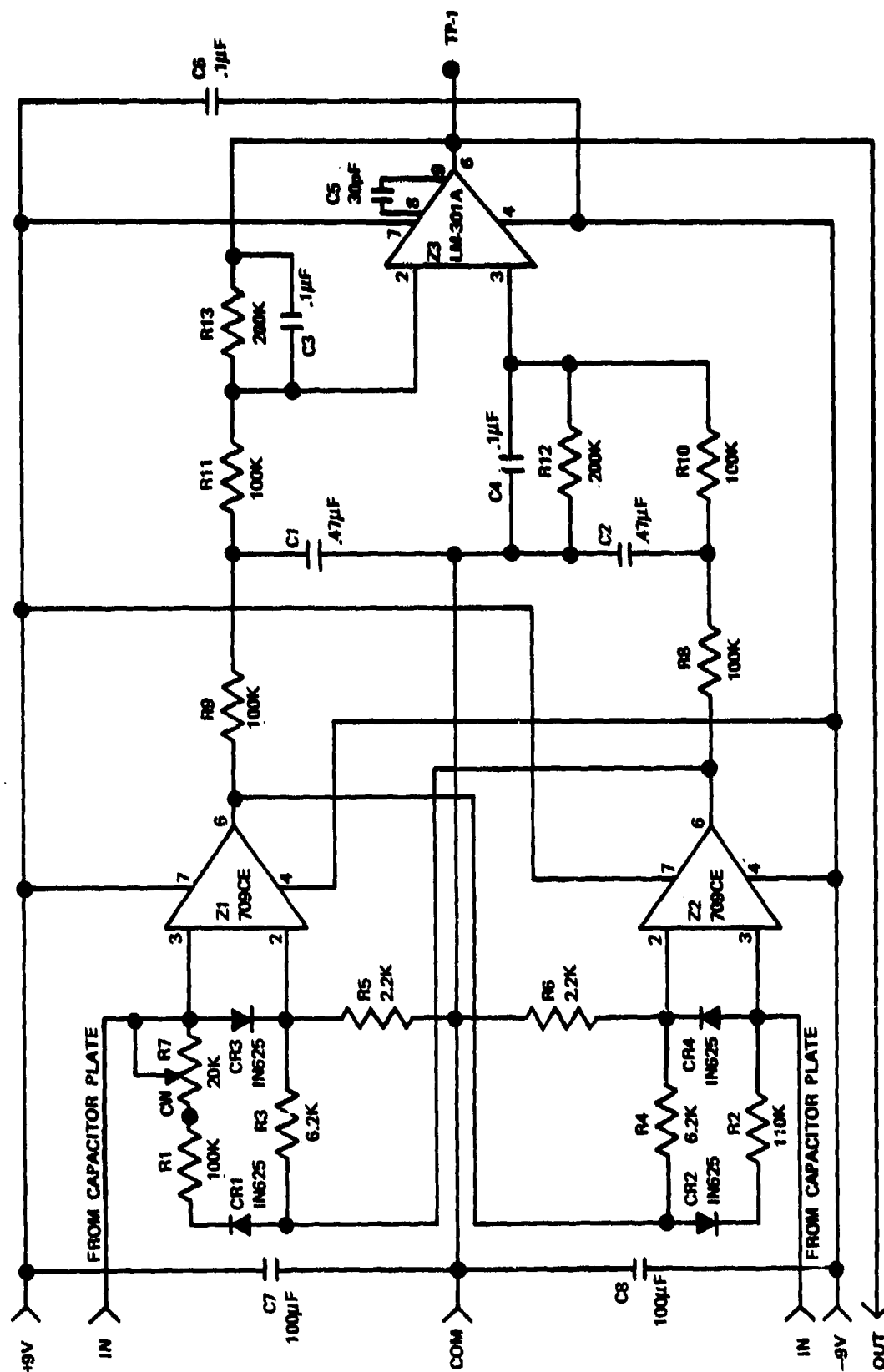


Figure 20. Schematic of the detector for the variable capacitance transducer

G 5888

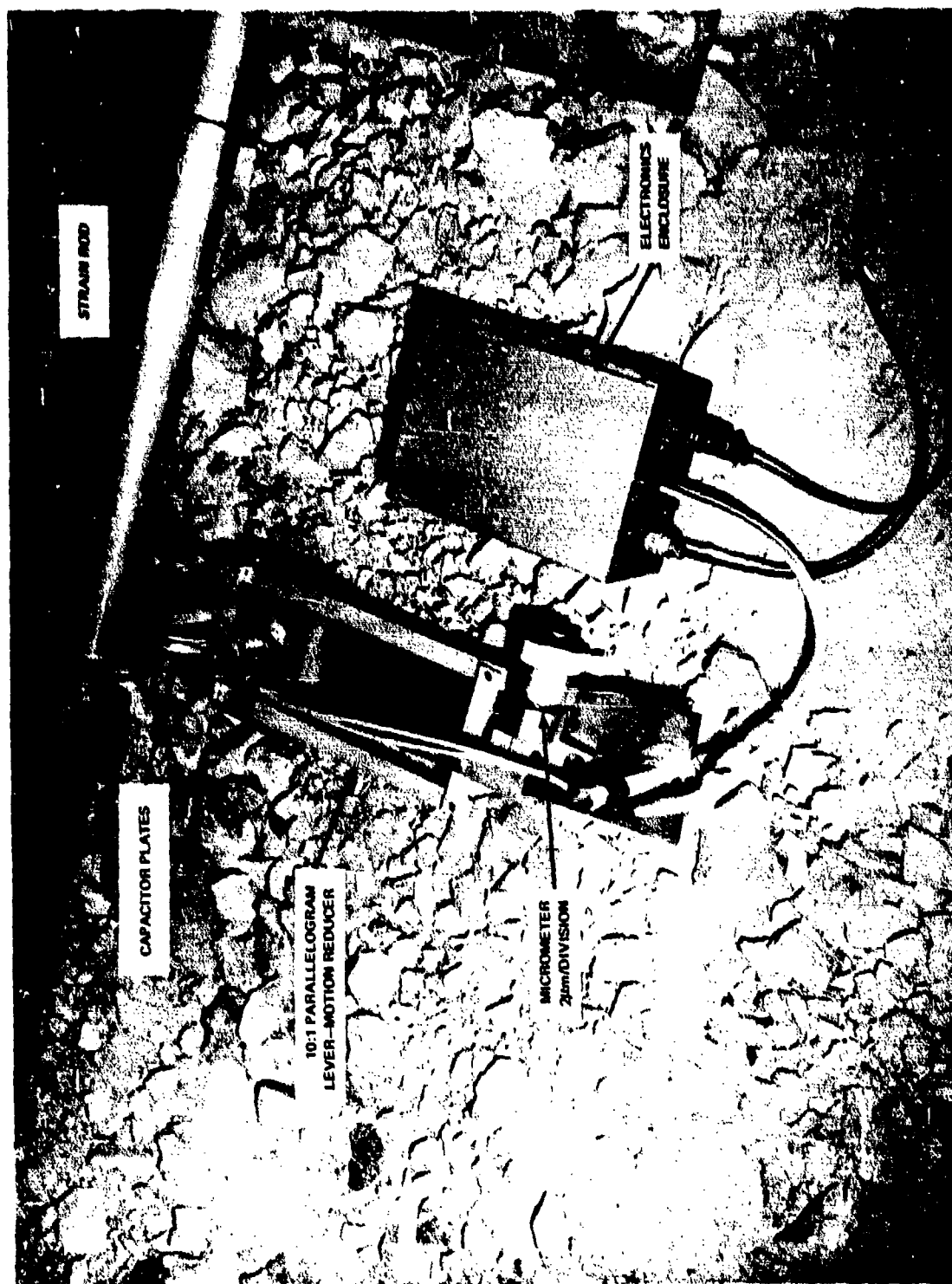


Figure 21. Broad-band displacement transducer installed on 325 deg azimuth strain seismometer

C 0032

The electronic noise level and drift were determined by substituting fixed capacitors in place of the active capacitors. A long-term noise sample was recorded at high gain on magnetic tape and on the chart recorder for several days. A 12-hour segment of this sample was selected and a calibrated playout from magnetic tape was made for visual analysis. Figure 22 is the lower gain chart record covering the same time period. The maximum peak-to-peak excursion during this sample was equivalent to 6×10^{-10} m/m in the passband from dc to 1 sec. Using the factor of 1/6 (see paragraph 3.2.2.1 above), this yields a noise level of 1×10^{-10} m/m rms, for the VCT. The electronic drift data were taken from a 36-hour uninterrupted segment of the chart record. The maximum drift was equivalent to 7×10^{-10} strain.

Several tests were run to determine other operating characteristics of the VCT. The transducer specifications are summarized in table 5.

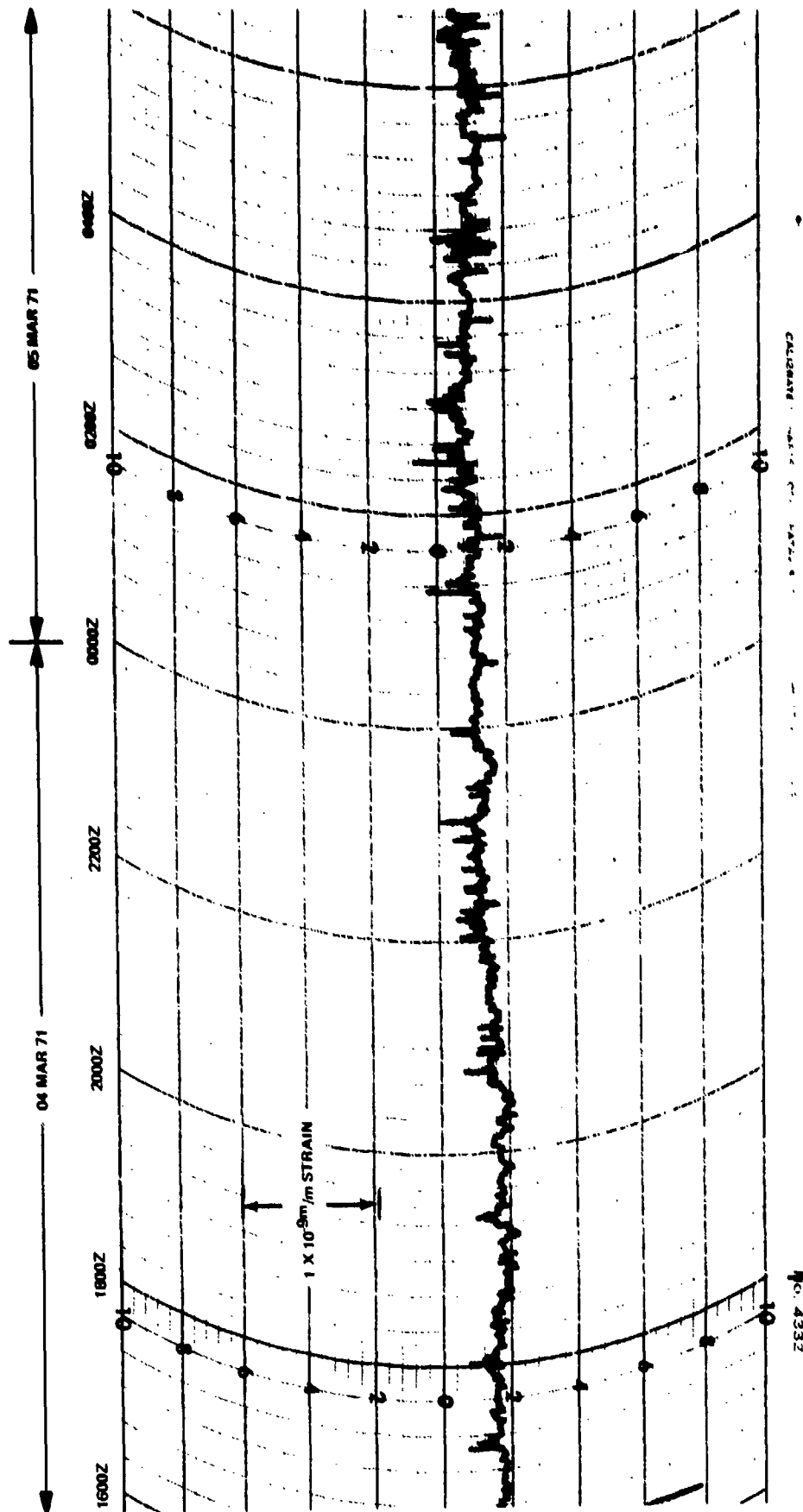


Figure 22. Reproduction of a portion of a chart recording of the variable capacitance transducer showing the electronic noise level with fixed capacitors substituted for the active capacitors

G 0033

Table 5. Measured specifications of the variable capacitance transducer

Sensitivity (detector)	40 mV per μm displacement, max
Noise level (detector)	100 μV rms, in the period range of 1 to 43,000 sec
Dynamic range (detector)	80 dB, typical
Long-term drift	150 $\mu\text{V}/^\circ\text{C}$
Linear range of operation	$\pm 25 \mu\text{m}$ for $\pm 2\%$ linearity at full sensitivity
Frequency response	Flat from dc; 6 dB down at 7.5 Hz
Cutoff rate	12 dB/octave
Minimum detectable strain	1×10^{-10} m/m, dc to 5 Hz (40 m rod length)
Power: voltage	+19 to +23 Vdc, -19 to -23 Vdc, center common
current	50 mA, max

4. SYSTEM DESIGN

After completion of the design of the strain seismometer, the next major task was the design of the complete data collection system. The completed system ultimately included 21 separate seismic data channels and 5 environmental data channels, which were recorded on two 16 mm film recorders, one 35 mm film recorder, three 14-channel FM magnetic-tape recorders, and three chart recorders. All seismometers and primary amplifiers were installed in the mine for thermal stability. All other equipment necessary for operation, plus support equipment, was installed in two 26 ft long recording vans. With the exception of the special strain components, the complete system was designed to use available Government equipment. In the following paragraphs, the various subsystems will be discussed.

Refer to appendix 3 for a listing of instrument nomenclature, recorder channel allocation, and instrument polarity used in the following discussion.

4.1 PRIMARY DATA SYSTEM

The primary data system includes the three strain and the six inertial seismometers, their primary amplifiers, associated filters, secondary amplifiers, and data control circuits. Also included is the major environmental equipment. Figure 23 is a block diagram of this primary data system.

4.1.1 Advanced Long-Period System (ALPS) - Inertial

The Advanced Long-Period System (ALPS) - Inertial - was developed several years ago and was found to be a reliable system during operation at several observatories. Since strain instruments appropriately combined with inertial instruments showed promise of improved seismic wave discrimination, it was desirable for this program to utilize an inertial system which was widely used and well understood. The ALPS inertial was therefore used for this program without modification.

The block diagram (figure 23) shows the major components of the ALPS inertial system. Components for mass position monitoring and motors for remote mass centering and free period adjustment are not shown. The three-component LP system has Geotech seismometers with 10 kg masses and natural periods set at 17.25 sec close coupled to Harris galvanometers with natural periods of 110 sec. The galvanometers are in phototube amplifiers (PTAs) that have dual outputs, each of which can be shaped separately by plug-in band-pass filters. Two PTA filters are used in the ALPS system - one has a 6 sec notch and the other does not. Figure 24 shows the response of the ALPS with these two filters. In the original ALPS inertial system, the notched response data were recorded at high gain and the unnotched data were simultaneously recorded at low gain (usually 1/10) for study of larger signals. For this system, it was decided that high and low gain data channels should have identical responses to simplify analysis; it was also desirable to use the notch filter only when the level of the 6 sec microseisms made it necessary.

During the completion of the system design, considerable interest was generated in the study of long-period waves at periods around 40 sec. In most cases, LP system responses were extended to peak near 40 sec by increasing the seismometer free period from 17 to 30 sec. At the direction of the Project Office, design work was done to include this extended range LP operation in the total strain/inertial system. Since it was not possible to change the inertial instrument free period because of response matching requirements with the strain system, the longer period response was generated using filters. The second output of the long-period PTAs was used for this extended range system so that response changes could be easily made using different plug-in filters without disturbing the primary ALPS response outputs. The amplifier output was fed into a special two pole, low pass, active filter to simulate a longer period instrument. The resulting amplitude response of the system is shown in figure 25. This response is essentially identical to that used by Pomeroy et al. (1969).

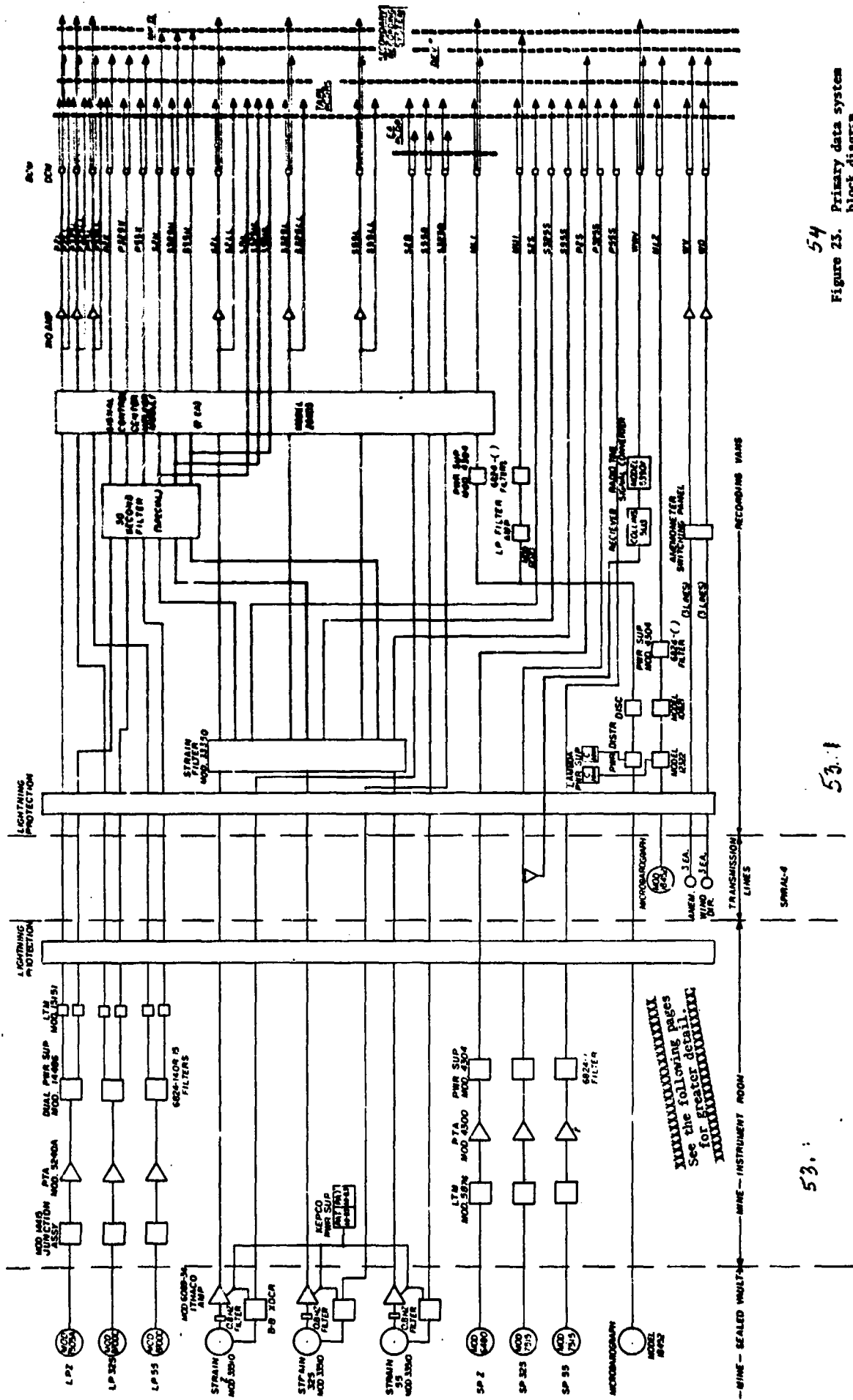
4.1.2 Short-Period Inertial System

The short-period (SP) inertial system used for this program has, like the ALPS inertial system, operated reliably for several years. This three-component system has Johnson-Matheson seismometers with 18 kg masses and natural periods set at 1.25 sec. The seismometers are connected through normal line trim and damping circuits to short-period PTAs that have 3 Hz galvanometers. In the initial design, system parameters were identical with those of the system used at the SP strain installation at WMO. After the first few months of operation, changes in the SP response of the strain instruments were made to prevent saturation of the solid-state amplifiers (see section 6.3.2). This required that the SP inertial seismometer damping be changed from 0.69 to 1.0 critical to preserve the response match between strains and inertials. Figure 26 shows the theoretical amplitude response of this modified system.

4.1.3 The Strain System

The design of the strain system was, of course, the major task of this program. The ALPS response was of primary interest, but it was decided early in the program to take advantage of the unique capabilities of sensitive strain seismometers by including other responses. These responses could be used, first, to evaluate the overall operation of the strain instruments and, second, to provide new methods of detecting and identifying seismic waves. Figure 27 is a functional block diagram of a typical strain seismograph channel. Note that the seismic outputs associated with the moving-coil transducer are all appropriately shaped by filters specially designed for this program. The flag output is a unique feature of the system that has not been used in any previous seismographs. Its operation is described in paragraph 4.5.1 below. The operation of the seismic outputs is described in the following paragraphs. Figure 28 shows the amplitude response and relative operating level of these outputs.

A comment about matching responses of strain and inertial systems should be made here. Since strain and inertial instruments respond differently to the various types of seismic waves, the two systems cannot be truly matched for all wave types. In fact, it is these differences in response to the various wave types which make combinations of strain and inertial seismographs useful. In section 12.1 it will be shown that for a travelling wave, ground strain is



54
Figure 23. Primary data system block diagram

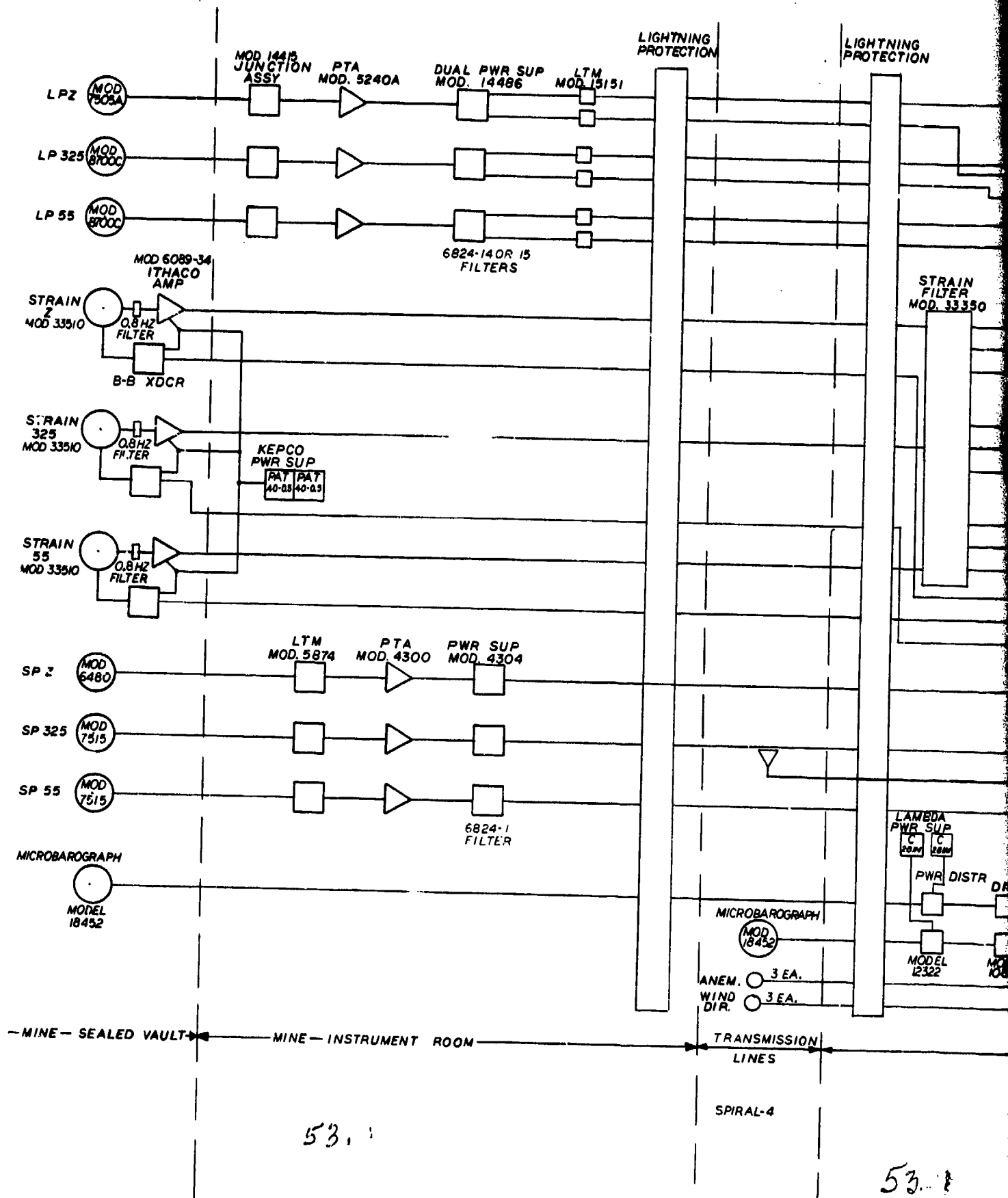
-53/54-

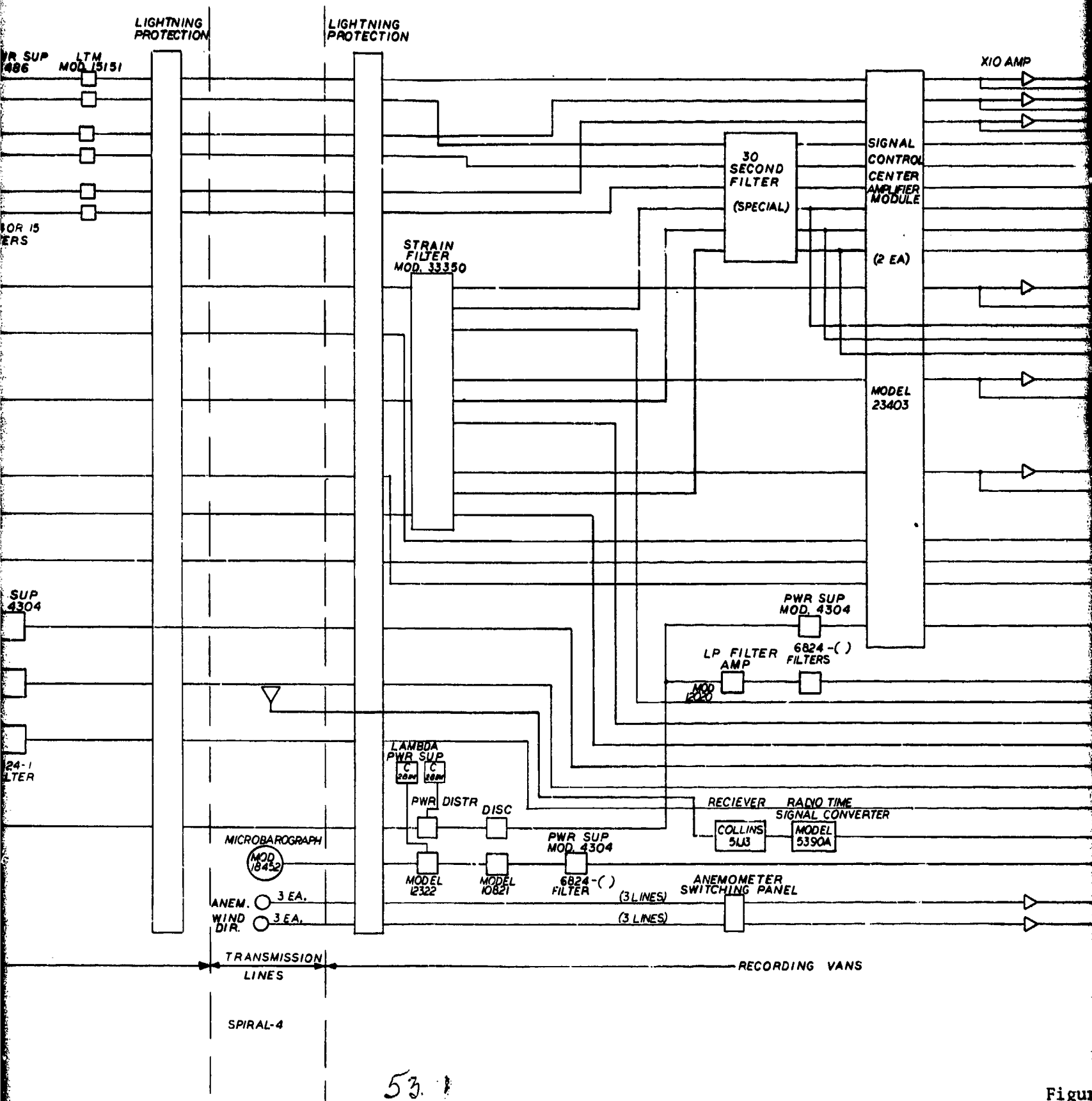
TR 72-3

53.1

53.1

XXXXXXXXXXXXXXXXXXXX
See the following pages
for greater detail.
XXXXXXXXXXXXXXXXXXXX





Figure

NG
TION

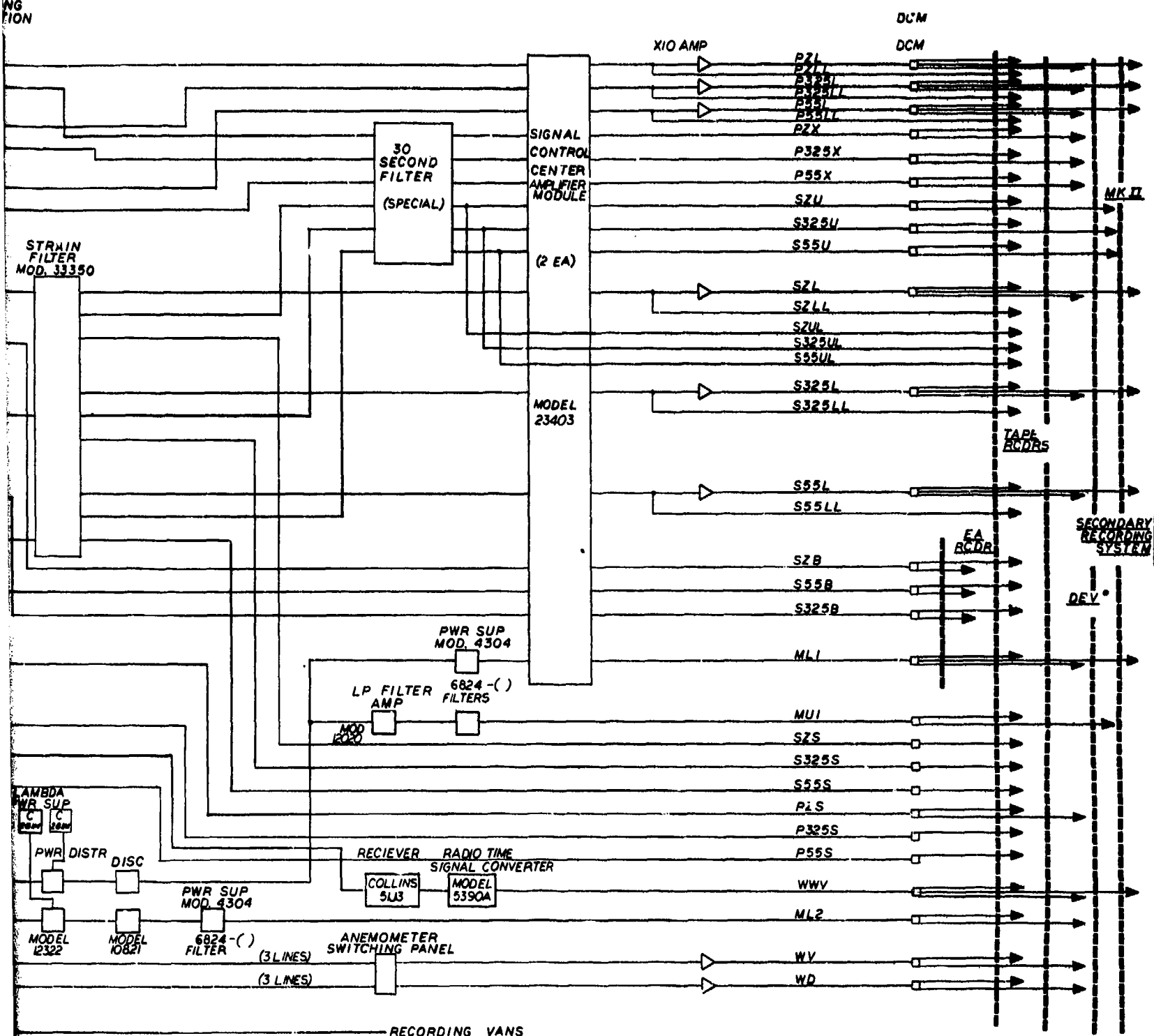


Figure 23. Primary data system block diagram

G 6534

-53/54-

TR 72-3

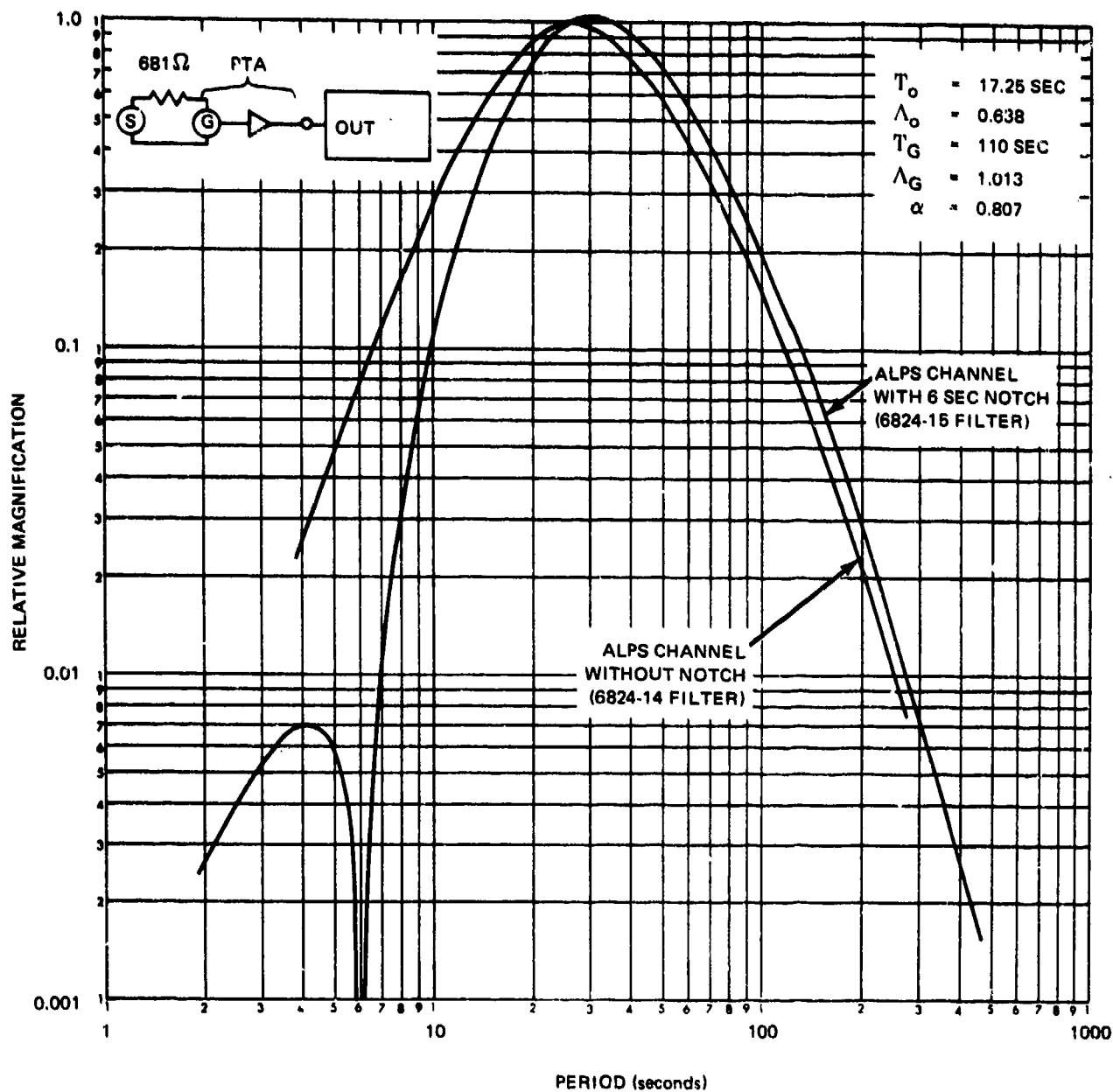


Figure 24. Theoretical amplitude response of the advanced long-period system with two band-pass filters

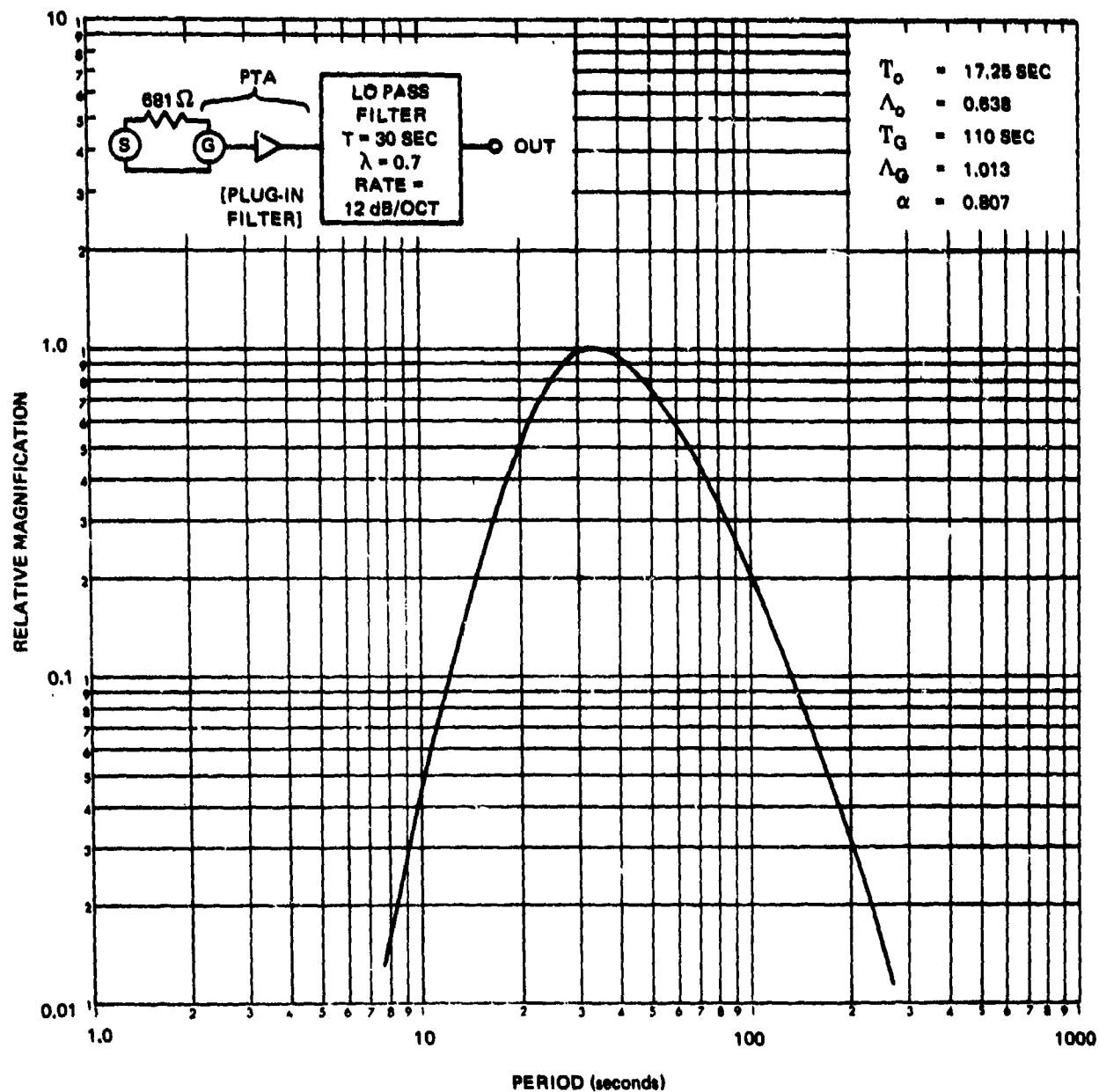


Figure 25. Theoretical amplitude response of the extended range long-period inertial system with a Model 6824-14 bandpass filter

G 6636

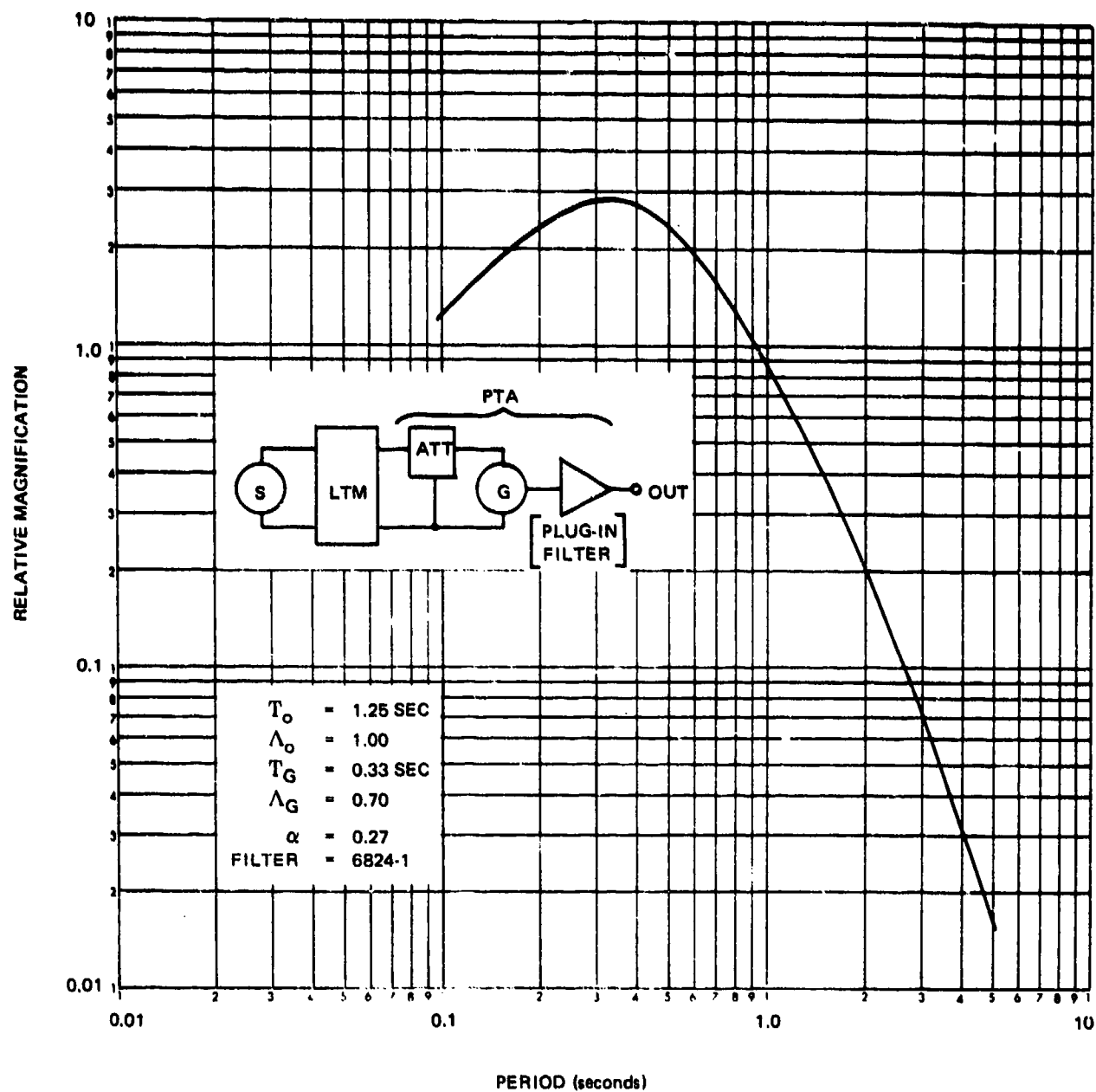


Figure 26. Theoretical amplitude response of the short-period system

G 6637

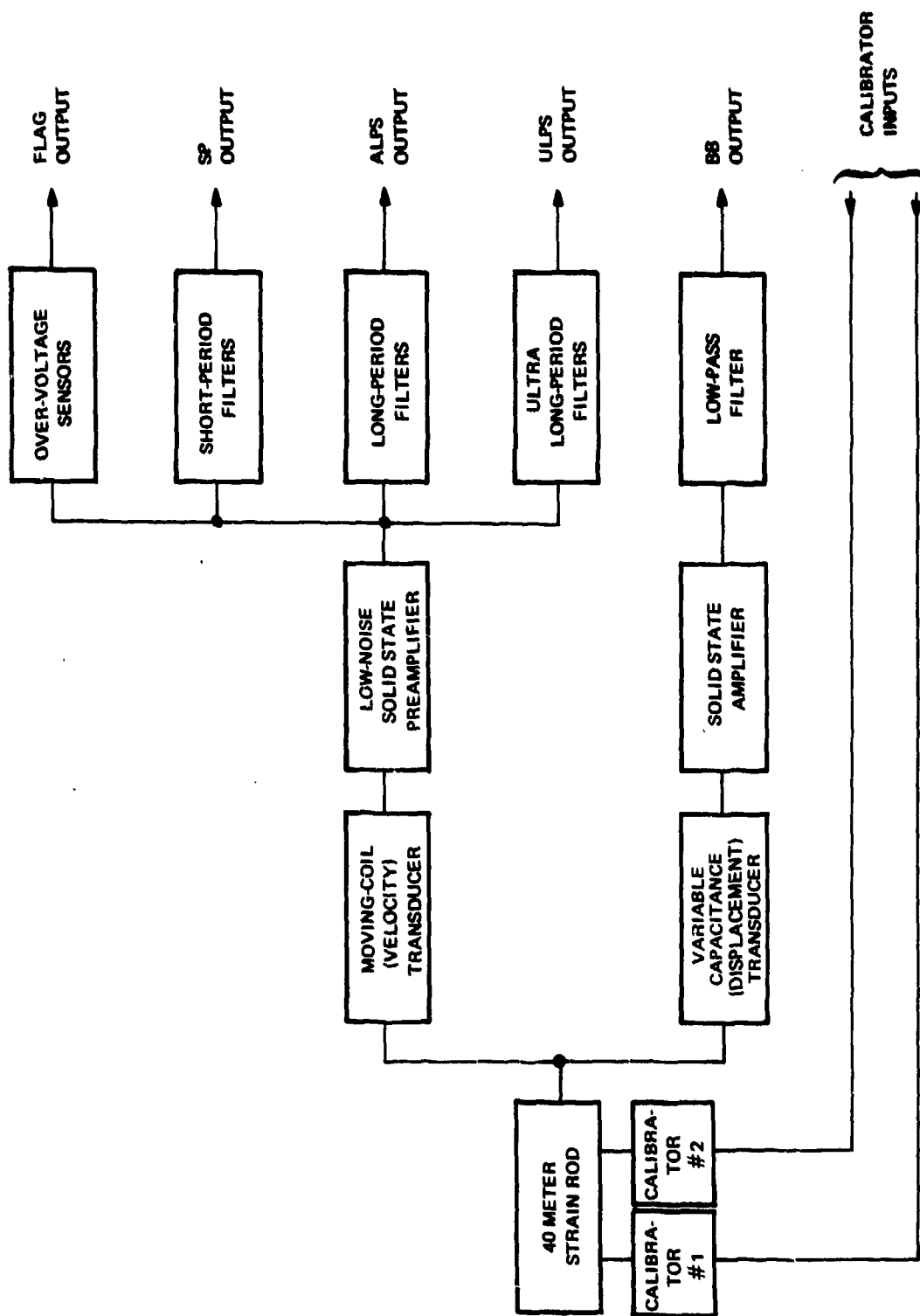


Figure 27. Functional block diagram of a typical strain seismograph channel.

G 5467

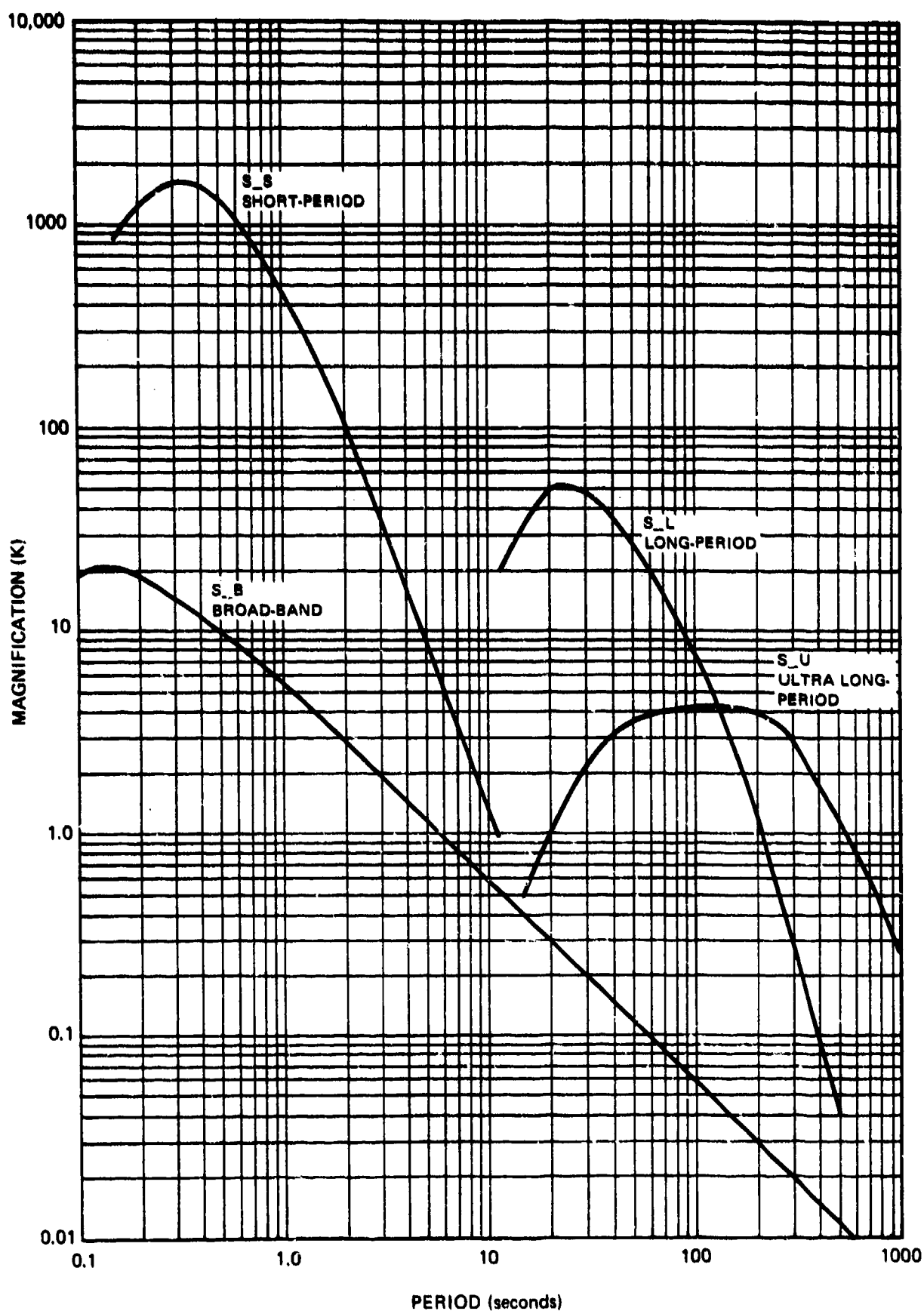


Figure 28. Amplitude responses of typical strain seismographs at QC-AZ to traveling waves with constant phase velocity of 4.0 km/sec

G 6290

equal to the ground velocity divided by the phase velocity of the wave. Ground velocity leads ground displacement by 90 deg and the amplitude of the velocity is equal to $(2\pi/T)$ times the amplitude of the displacement, where T is the period of the wave in seconds. The $(1/T)$ factor introduces a 6 dB/octave decrease in strain signal toward longer periods. This 6 dB/octave amplitude difference and the 90 deg phase difference between ground strain and ground displacement is introduced by the earth. In matching the output of the strain seismograph to ground strain and the output of the inertial seismograph to ground displacement, this 6 dB/octave amplitude response and 90 deg phase response is considered an integral part of the strain seismograph response to equivalent ground displacement. In matching the two types of seismographs, the phase velocity is assumed to be constant within the passband of the seismograph. This assumption is not correct, but is sufficiently close to allow on-line combinations of strain and inertial seismographs without correction for variation of phase velocity with period. Apparent surface phase velocity varies with wave type as well as with period. In operation, equalizations of magnification between strain and inertial seismographs were made for 25 sec Rayleigh waves propagating in the direction of the instruments.

4.1.3.1 ALPS Strain

The primary signal output of the LP strain seismographs was designed to match the amplitude response, phase response, and equivalent sensitivity of the inertial ALPS. It was therefore necessary to make the ALPS strain response identical with the ALPS inertial response shown in figure 24.

The ALPS inertial system is a close-coupled system with a mean coupling coefficient, α , of 0.81. The interchange of energy between the seismometer and the galvanometer with close coupling produces an amplitude and phase response different from a loosely coupled system with equal parameters. To provide an equivalent strain system, the parameters for a loosely coupled inertial system with the same amplitude and phase response was theoretically determined. Table 6 compares the parameters of the two systems.

Table 6. Comparison of close coupled and loosely coupled seismograph systems with matched responses

	<u>Close coupled</u>	<u>Loosely coupled</u>
Seismometer free period	17.25 sec	23.5 sec
Seismometer damping	0.64	0.725
Galvanometer free period	110 sec	80 sec
Galvanometer damping	1.013	1.25

Since the strain transducer-solid state amplifier combination is essentially broad-banded, the parameters of the equivalent loosely coupled system were duplicated using active filters. The resulting theoretical mismatch between the two systems was determined to be ± 1 percent for amplitude and ± 1 deg for phase.

In designing this system, careful consideration was given to system dynamic range and to noise levels - both for individual stages and for the total system. The expected background and earthquake signal voltages were calculated. The various filter stages were then strategically positioned within the total seismograph system to take advantage of their individual parameters. This assured that clipping in the initial filter stages (which could be masked by following filters) would not occur. The system dynamic range was therefore limited by the recorders alone.

4.1.3.2 Ultra-Long-Period Strain

The ultra-long-period strain (ULPS) output utilizes the inherent ability of the strain seismograph to remain stable at very long periods. This output was included in the total system; first, to provide data for evaluation of the strain seismometer operation, and secondly, to provide data for studies of seismic energy at periods longer than those detected by normal LP systems.

Since the ULPS output was for research in a new passband, no specific sensitivity requirements were set. The spectra of the Ithaco amplifier noise showed that the sensitivity of this output would be limited by the $1/f$ flicker noise in the amplifier. However, the output would have enough sensitivity to detect ultra-long-period waves from moderate to small magnitude earthquakes. In the initial design, the amplitude response was flat from 30 to 1000 sec with high and low cutoff rates of 18 dB/octave. When stable operation was achieved, it became evident that the ULPS output was being dominated by ambient earth noise with periods approaching 1000 sec. Therefore, a 1000 sec, 12 dB/octave low-pass filter in the circuit was replaced by a similar filter with a corner of 283 sec. This produced the response shown in figure 28 and greatly enhanced the usefulness of the data.

4.1.3.3 Short-Period Strain

The SP output was provided in the design to obtain data in the normal SP passband. The design of this output did not require appreciable time since most of the filtering techniques used had been developed previously for the SP strain installation at WMO. Amplifier noise data in this passband showed that this output would have sufficient sensitivity to be limited by ground unrest rather than by system noise. Although the ALPS passband was given primary consideration, data from this SP output would be useful for instrument evaluation and for study of relatively close earthquakes. Short-period strain data were recorded on magnetic tape only.

4.1.3.4 Broad-Band Strain

The broad-band (BB) strain output uses the variable capacitance displacement transducer described in paragraph 3.2.4 above. The amplitude response of this seismograph to ground strain is flat from dc to 7.5 Hz. The amplitude

response of this seismograph to ground displacements is determined primarily by the approximate 6 dB/octave response of the strain rod itself. The transducer electronics limit the high frequency response at frequencies above 7.5 Hz. The BB output had three objectives, all of which were important, especially during initial stages of operation. The first objective was to provide a sensitive electrical output for calibration purposes. After calibration of the BB output using a precision micrometer, the transducer could be used to calibrate the electromagnetic calibrators at a wide range of frequencies. The second objective was to record earth tides and pier and anchor settling noises during the early months of field operation. The earth tides could provide large natural quasi-calibration signals to verify proper operation of the strain rods and their anchors to the ground. The third objective of the BB output was to record the residual strains from large earthquakes which had been reported by Wideman and Major (1967) and others.

Completion of the design of the BB seismograph was relatively simple since the variable capacitance transducer, which is the only major component, was complete. The only additional circuitry necessary was a remote dc offset compensator, which was incorporated in the recording van in the post-amplifier circuits for each BB output. This circuit allowed for secular strain offsets of up to $\pm 35 \mu\text{m}$ so that relatively high gain operation (up to $\pm 1 \mu\text{m}$, full scale) could be made without frequently disturbing the instruments for mechanical adjustments. The BB outputs were recorded on magnetic tape and on slow-speed (0.75 in./hr) chart recorders.

4.1.4 Meteorology System

The meteorology system is an important part of the primary data system. This system was included primarily to define as fully as practical the environmental factors that affect all of the seismic sensors. The meteorological equipment was especially important in this program because the design of the strain system was being evaluated for the first time. Figure 23 shows the major components, which are discussed below.

The meteorology system includes two microbarographs. The first was installed inside the seismometer chamber and was used to determine the effectiveness of the sealed doors. With the mine doors opened, data from this channel were also used to determine the effects of direct pressure changes on the seismic instruments. The second microbarograph was installed outside the mine in various locations to determine the external pressure field acting on the mountain. Data from this channel were ultimately used for several noise studies that are discussed later in this report.

Figure 23 also shows the three anemometer-wind direction units. The three units were placed on top, on the north side, and on the south side of the mountain at QC-AZ. Three units were required for simultaneous collection of wind data to determine which location produced data that best indicated the forces of wind on the mountain.

Other components of the meteorology system, which are not shown on the block diagram, include a recording thermometer and a recording barometer. Both of these units produced 7-day chart records which were useful during various data analysis tasks.

4.2 DIRECTIONAL ARRAY SEISMIC SYSTEM (SECONDARY)

The directional array seismic system provided the capability of on-line algebraic summations of LP strain and inertial seismographs. This system accepts seismograph inputs from the primary system; buffers, amplifies, controls magnifications, and sums appropriate seismographs in an Analog Computer, Electronics Associates, Inc., Model TR-10; and provides data control circuits for recording both summed and individual outputs. Figure 29 is a functional diagram of this system.

This on-line system was included in the total system design for two reasons. First, the various combinations of strain and inertial instruments could be used to demonstrate the on-line capability of the strain/inertial complex to enhance surface waves, to provide for rapid determination of azimuth of arriving earthquake signals, and to aid in wave discrimination and wave type identification. The second reason was that the system was a valuable diagnostic tool for the station operators in determining whether the instruments were operating properly.

4.3 RECORDING SYSTEM

The recording system includes the recorders plus the calibration and control equipment shown in figure 30. The three magnetic-tape systems are 14-channel, FM recorders with a tape speed of 0.3 ips. These units were originally used in the LRSM program and required daily tape changes. The 35 mm Film Recorder, Model 1301A, was also originally used in the LRSM program and was specially modified for a drum rotation rate of one revolution per day. This recorder provided for records of up to 5 days' length and was used for recording the ULP strain channels. The two Develocorders are standard LP units - one 20 channel and one 16 channel. These recorders use 16 mm film at a film speed of 3 mm per minute and require film change once per week. Both film recorders were modified to include the light-slash time mark unit for ease of analysis. The three-channel Helicorder with associated amplifiers was used as a station monitor for calibrations, maintenance, etc. Finally, the three Esterline-Angus chart recorders were used to record the broad-band strain data consisting of secular strains, earth tides, and signals from large earthquakes. These pen-and-ink recorders were operated at a chart speed of 0.75 in./hr.

4.4 OTHER SYSTEMS

The timing, calibration, and power subsystems for this program were relatively complete in the vans when they were transferred from the LRSM program. Only minor modifications were necessary to adapt the existing systems for operation of the strain/inertial complex. Block diagrams of these subsystems are shown in figures 31 and 32.

4.5 SPECIAL EQUIPMENT DESIGNED

Two major items of special equipment were designed for this project and are discussed in the following paragraphs.

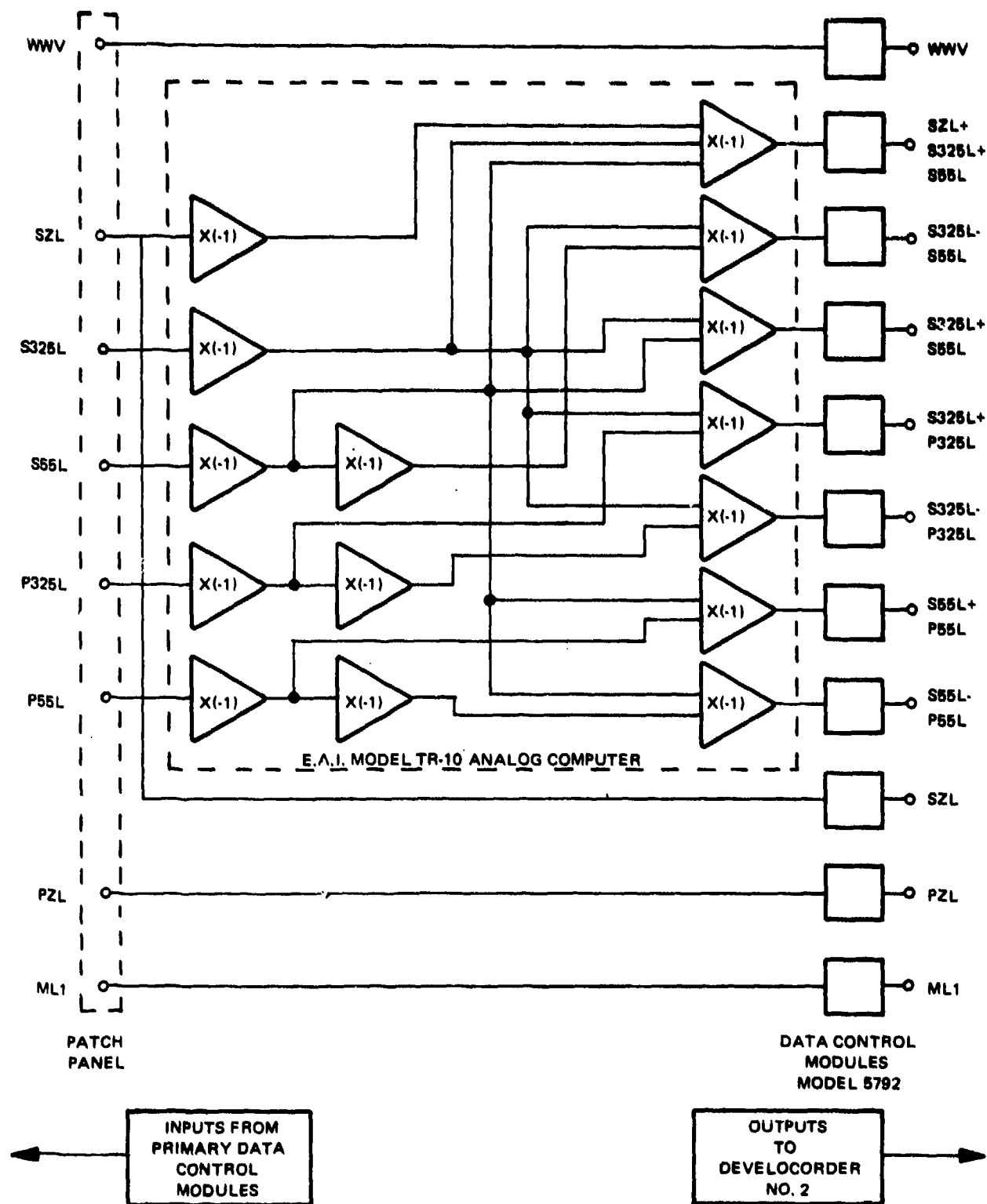


Figure 29. Functional diagram of the directional array seismic system

G 6638

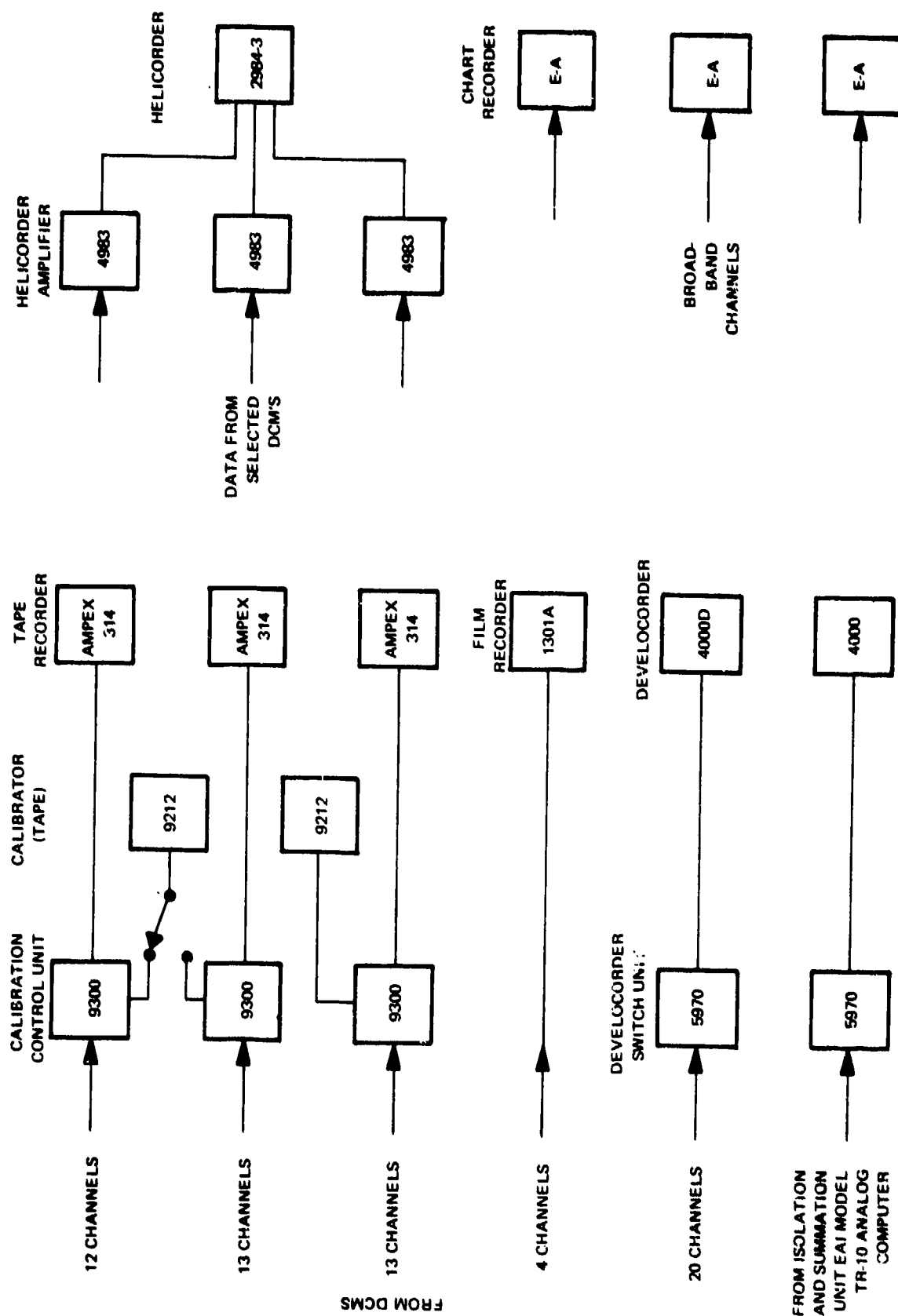


Figure 30. Recording system

G 6639

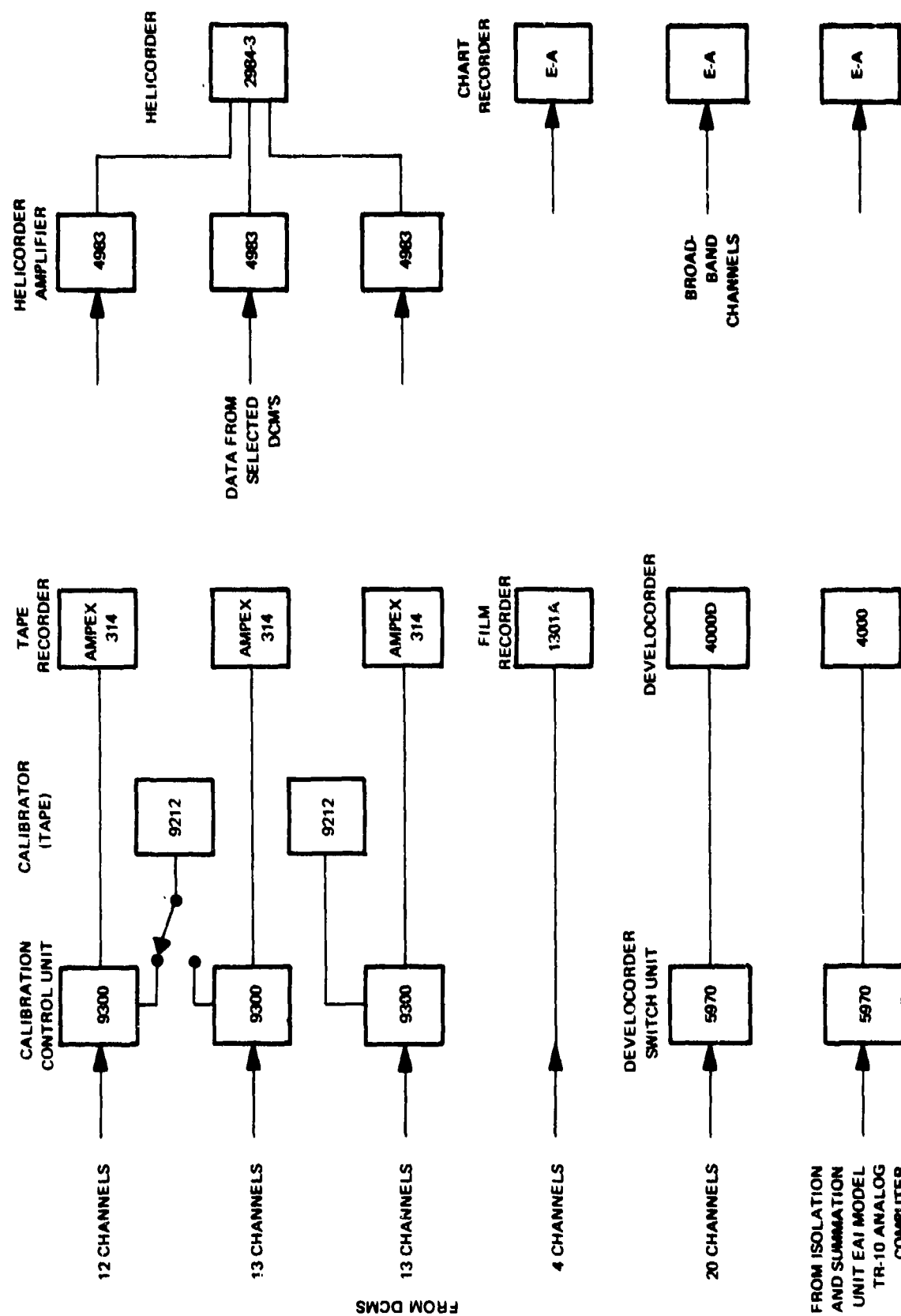


Figure 30. Recording system

G 6639

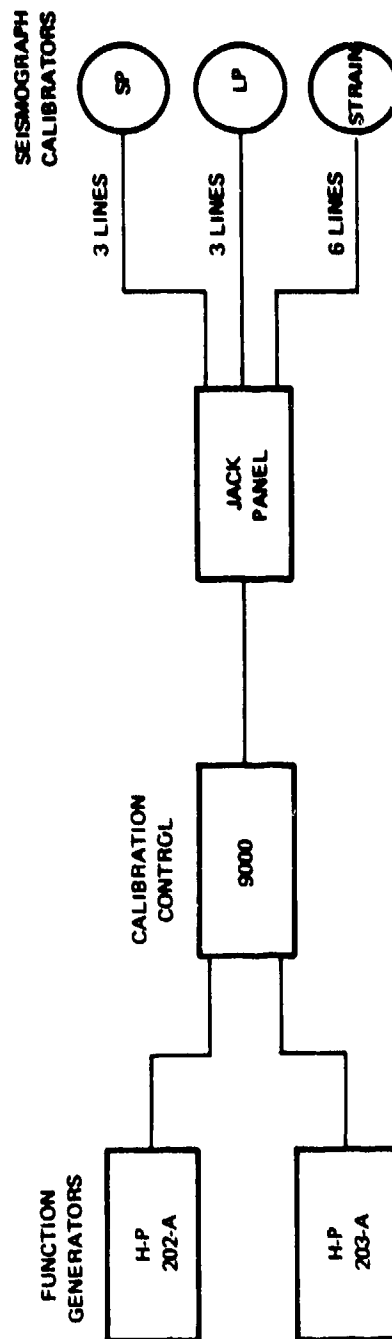
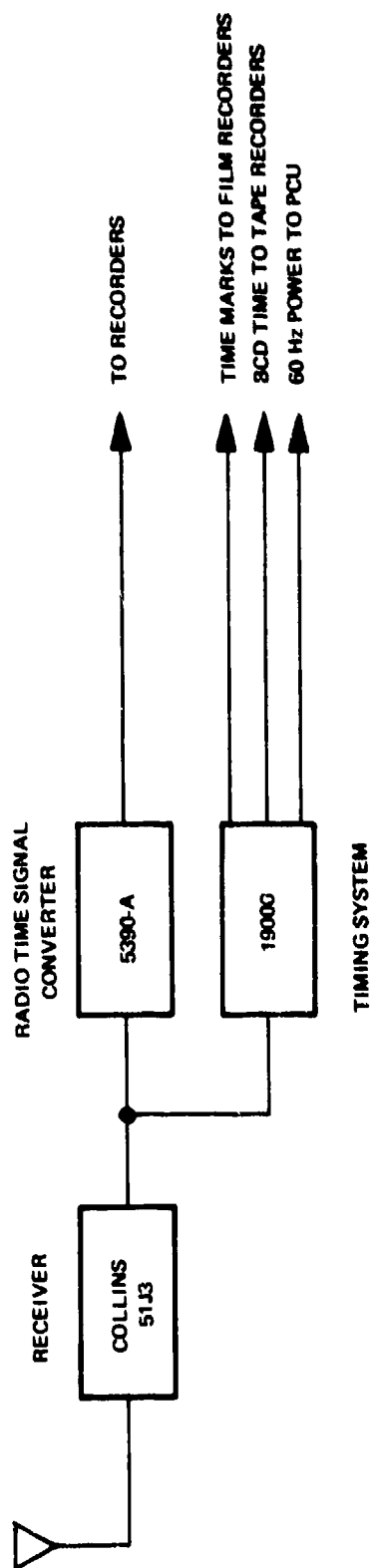


Figure 31. Timing and calibration subsystems

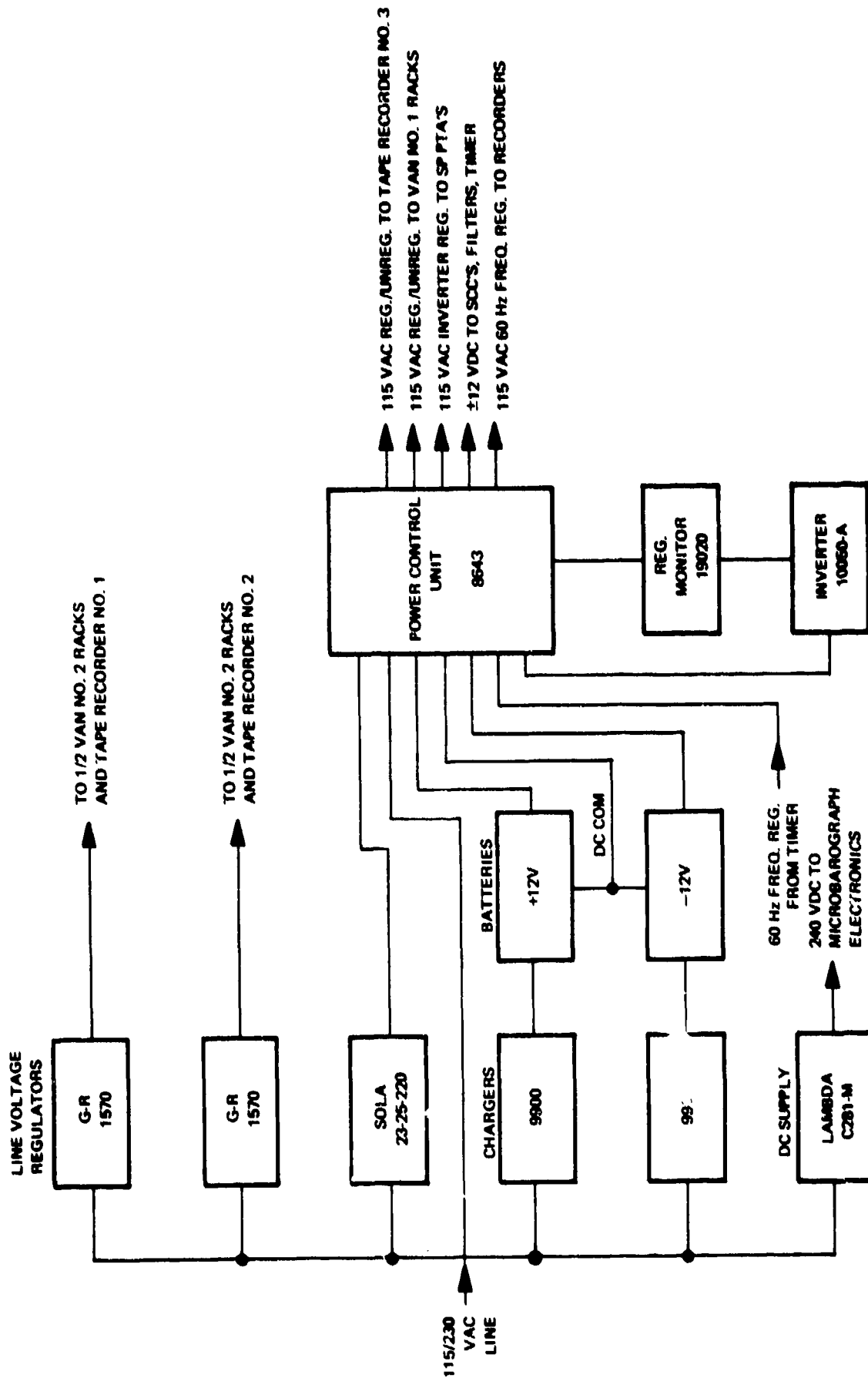


Figure 32. Power subsystem

G 0041

4.5.1 Strain Filter Unit, Model 33350

Since the strain seismographs required a series of active electronic filters to provide the proper frequency response, the Strain Filter Unit, Model 33350, was designed. A photograph of the unit is shown in figure 33, and figure 34 is a block diagram of a typical channel. The unit has three seismic outputs for each of the three inputs from the strain preamplifiers. The data circuits are balanced-to-ground throughout the unit for improved noise rejection. Most of the active filter circuits use the FET input Operational Amplifier, Geotech Model 24146-07. Components for the various filters are mounted on plug-in printed circuit cards for ease of maintenance. The unit also includes power regulation circuits to provide stable operation from an unregulated plus and minus 12 Vdc (nominal) power supply.

The flag circuit is a unique feature not included in any previous seismographs. With the heavy, narrow-band filtering of the output of the preamplifier, the preamplifier could be clipped by a large out-of-passband signal and the actual recorded signals would not necessarily give a clue to the clipped state of the amplifier. The flag output gives an indication that the maximum linear range of the preamplifier output has been reached. By a 1, 2, 4 coding, a single trace on the film recorder indicates which, if any, of the three preamplifiers has reached saturation.

The filter circuits designed use ± 1 percent tolerance metal film resistors and ± 5 percent tolerance metalized-Mylar capacitors. After final assembly, the phase and amplitude response of each filter was measured and all filters were found to match their theoretical curves with ± 1 percent for amplitude and ± 1 deg for phase. Tests were run with the inputs shorted to determine the noise level of the filters. In all cases, the noise level was found to be below the output noise level of the primary preamplifier.

4.5.2 The X10 Mechanical Amplifier

During March 1970, when it became evident that the winze for the vertical strain seismometer SZ would not be completed to the full 40 m depth, a mechanical amplifier was designed. An amplification factor of 10 was chosen: (1) to compensate for the reduction of rod length by a factor of 3.5, and (2) to compensate for the approximate factor of 3 lower signal levels of the vertical strain compared to the horizontal strain at the surface of the earth. It should be noted that strain magnification calculations are not affected by the amplifier because both calibrations and earth motions are acted on equally. The mechanical amplifier simply acts like any other amplifier in the system, and its sole purpose is to assure that signal voltages at the input of the preamplifier are high enough to provide an adequate signal-to-amplifier noise ratio. Figure 35 is a photograph of the primary SZ transducer showing the X10 mechanical amplifier.

One of the first tests run was the determination of the amplification factor. By applying equal calibrations to the SZ and one of the horizontal strain seismometers, the ratio of the voltages produced at the preamplifier outputs is the approximate amplification factor of the unit. This test assumes that the generator constants of the two velocity transducers and the gain of the preamplifiers are equal. This assumption is probably correct within 5 or 10 percent. Output voltages at equal calibration inputs were compared at periods of 25, 10,

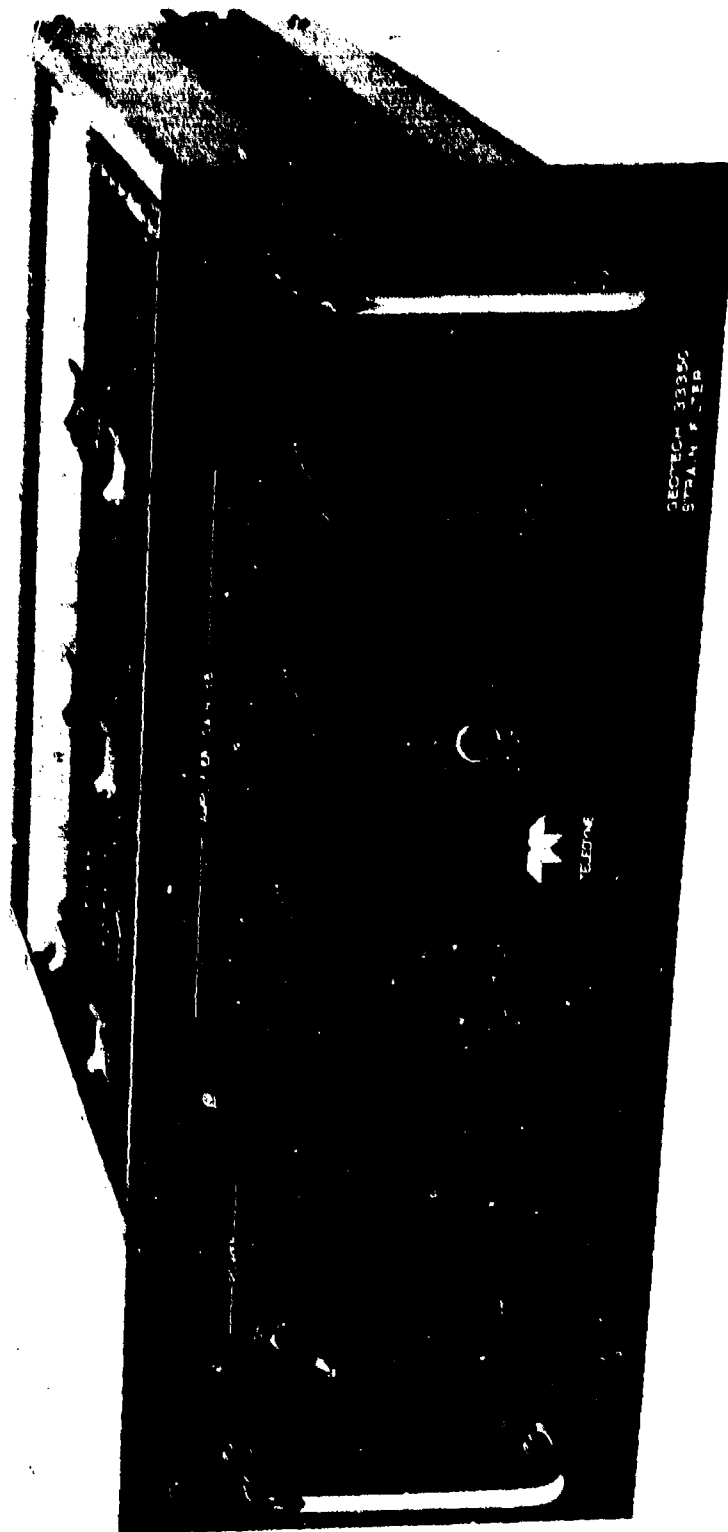


Figure 33. Strain Filter Unit, Model 33350

G 0042



Figure 35. Vertical strain moving coil transducer with X10 mechanical amplifier

G 6100

and 1 sec, yielding mechanical amplification factors of 10, 10, and 4.5, respectively. This indicated that the amplifier was operating properly in the LP and ultra-long-period passbands, but losses were occurring in the short-period range. An explanation for these losses is some nonlinear spring-mass action at higher frequencies caused by coil inertia and column loading of the flat flexures in the amplifier.

In general, the X10 mechanical amplifier apparently operates properly at frequencies below about 0.3 Hz and compensated for the relative shortness of the SZ strain rod. Disadvantages include extreme sensitivity to mechanical damping in the coil-magnet assembly and the changes in the SZS response. In addition, there is some evidence that the stiffness in the amplifier may cause some linear attenuation of both calibrations and signals, resulting in an overall operational amplification of the system of 5 to 7 rather than 10.

The X10 mechanical amplifier amplifies the relative pier motion for the moving-coil transducer, but did not amplify the motion for the SZB broad-band transducer.

5. INSTALLATION

The installation phase of this program included site selection and site preparation as well as the actual installation of the instruments.

In general, these installation tasks were performed concurrently with the design and development phases of the total system.

5.1 SITE SELECTION

The ability to adapt a site to protect the sensitive instruments from environmental noises is critical to the successful operation of a seismograph station. The rock to which a seismometer is attached is an integral part of any seismograph installation - especially a strain seismograph. Therefore, great care was used in selecting the best possible site for this installation. The task of site selection was started very early in the program because of the possibility (which later proved to be a fact) that required excavation in an existing mine would be extensive and time consuming.

5.1.1 Mine Selection Criteria

Criteria for selection of a mine suitable for installation of the long-period strain seismograph system were established as follows:

- a. Commercial power will be available to the site.
- b. The site must be accessible to heavy equipment during the initial phase of the installation and accessible to light vehicles after the system is operational.
- c. Mine requirements are as follows:
 - (1) One vertical shaft and two horizontal tunnels, all of which are perpendicular to each other;
 - (2) The shaft and two tunnels must be within a reasonable distance of each other.
 - (3) The shaft and two tunnels must be at least 45 m (150 ft) in length.
 - (4) The shaft and tunnels must be dry or nearly so.
 - (5) The shaft and tunnels must be safe to enter or in such a condition that a safe condition could be attained at a reasonable cost.
 - (6) The shaft and tunnel must be capable of being sealed to reduce wind currents and to stabilize the temperature.
- d. Geological requirements are as follows:
 - (1) Bedrock should be as competent and homogeneous as possible.

(2) Igneous bedrock is preferable to sedimentary or metamorphic bedrock.

(3) All three instruments should be emplaced in the same lithologic type of bedrock if at all possible.

(4) Geology of the area should be as simple as possible.

(5) Faults between the two ends of any of the instruments will be avoided.

e. The noise requirements for a typical LRSM seismic station apply to a strain seismometer installation. Some of the minimum distances from a noise source to produce a negligible effect are given below.

(1) Frequently used logging or mining roads - 1 mile;

(2) Farm roads or infrequently used logging and mining roads - 1/4 mile;

(3) Oil-well activities, drilling, or pumping - 2 miles;

(4) Railroads - 2 miles;

(5) Large rivers, lakes, bays, and oceans should be avoided;

(6) Active volcanic and active tectonic regions should be avoided;

(7) Hydroelectric generators should be avoided;

(8) Large mining operations - 10 miles;

(9) Small mining operations - 5 miles.

These distances are not fixed because their effect upon an installation will vary greatly from one area to another. The effect a given noise source will have on the installation will be left to the judgment of the site selector.

5.1.2 Areas Investigated

Two primary areas of investigation were selected in locating a suitable mine. The first was the mining areas within a 200 mile radius of TFO, near Payson, Arizona, and the second was the area near the LRSM site at Las Cruces, New Mexico. These areas were selected based on their characteristic low level of seismic background. The Morton Salt Company Kleeer Mine at Grand Saline, Texas, was also considered, but was rejected because it is an active mine and pressure sealing of the instruments would have been a problem.

In the investigation of an area, a map study was made first. Then, persons familiar with a particular mining area were contacted and those mines thought to be suitable were visited by an experienced geologist. About 40 mines were visited and all but 9 were immediately eliminated because of failure to meet the basic criteria. Most of these mines were rejected because of extensive faulting or jointing in the rock; a few were unsuitable due to water and

inaccessibility. The remaining mines were then visited by the program manager and the geologist for final selection. In December 1968, a recommendation was made to and accepted by the Project Office to select and prepare a mine in central Arizona.

5.1.3 The Queen Creek, Arizona Site (QC-AZ)

The selected site is in Goldmine Mountain, Section 9, Township 3S, Range 7E, Gila and Salt River Meridian, Pinal County, Arizona. QC-AZ is approximately 30 miles southeast of Phoenix and is about 125 km (77 miles) from TFO. The site is located on the map in figure 36. The coordinates of the mine are: 33°11'03" north latitude and 111°38'02" west longitude. The elevation at the site is 610 m (2000 ft) above sea level.

The mine met most of the selection criteria. The rock is a very competent quartz diorite with only minor jointing and faulting. The mine was dry and no work was required to make it safe. Commercial power and phone lines were only 1-1/2 miles away. Although there was no vertical shaft, there were indications that the full 40 m long perpendicular horizontal drifts could be obtained with a minimum of excavation. In addition, the back of the mine was 350 ft under the peak of the mountain and 430 ft from the mine adit. This depth would provide adequate isolation from environmental effects.

After selection of the mine for the strain installation, permits were obtained for its use. A Special Use Permit was obtained from the Bureau of Land Management, which controls the surface land. Permits were also obtained from the mine claim holder and from one land owner for an access road.

5.2 SITE PREPARATION

The major task in preparing the site was the modification of the mine. Figure 37 is a plan view of the mine. The dotted lines indicate the original walls of the mine and the solid lines show the walls after modification.

During early 1969, specifications were written for the necessary modifications to the mine and competitive bids were solicited. Representatives from the three companies responding to the bids were interviewed at the mine. The requirements of the instrument installations were discussed and the need to preserve the integrity of the rock on which the instruments would be mounted was emphasized. A contract was placed on 18 March 1969 to the Asbestos Manufacturing Company, Globe, Arizona. This company was the low bidder and had men and equipment available to begin work immediately. A Geotech employee was assigned as resident supervisor to oversee the excavation, to perform all necessary surveying, and to locate mounting holes for the instruments.

Considerable road work was necessary before actual mining work began as shown by the photographs in figure 38.

5.2.1 Excavation of the 55 deg Azimuth Drift

After moving in the necessary equipment and laying track for the mine car, air lines, and water line work was started on the back (55 deg) drift on

TO PAYSON
28 MI.

G 6844

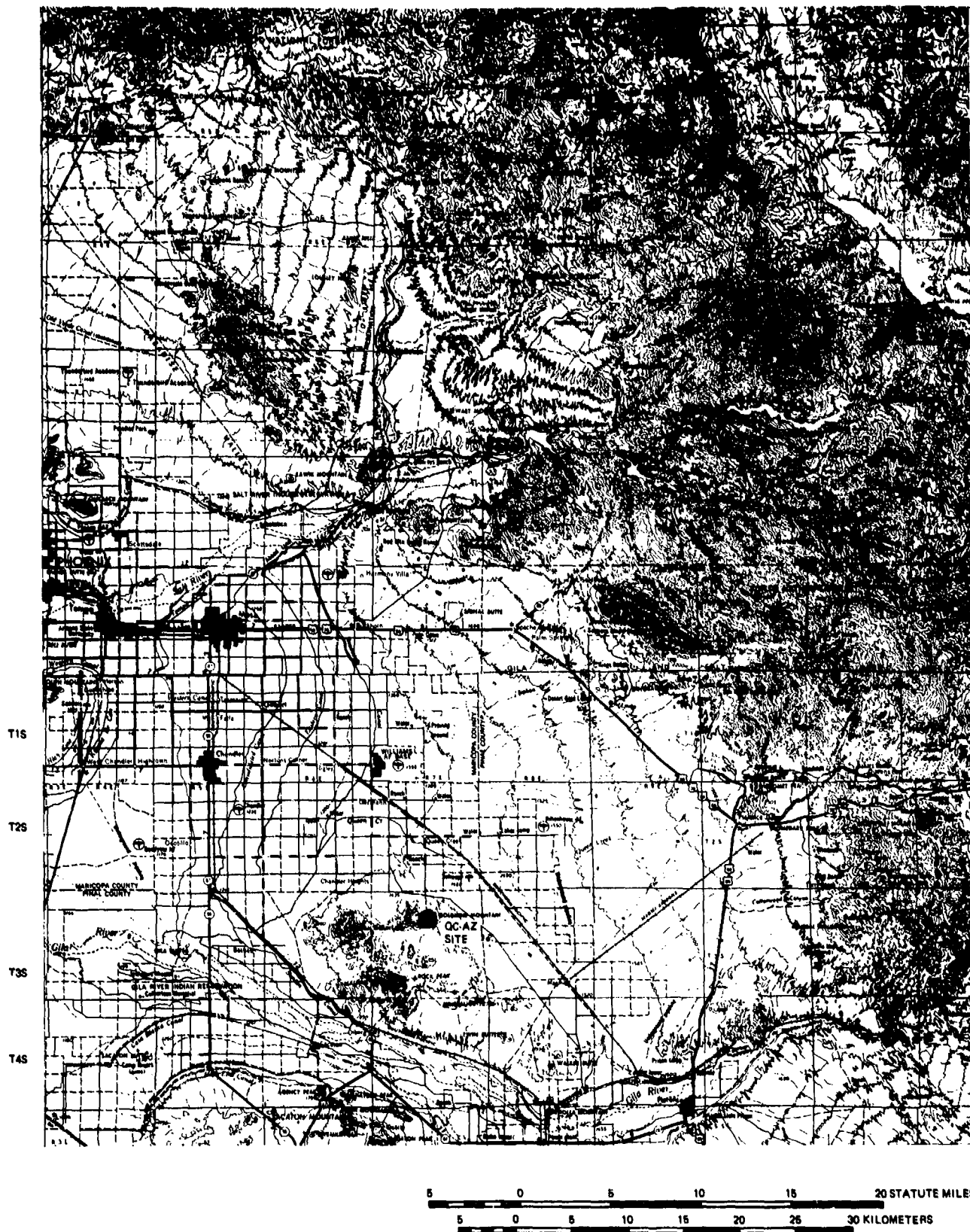


Figure 36. Location of Queen Creek seismological station (QC-AZ)

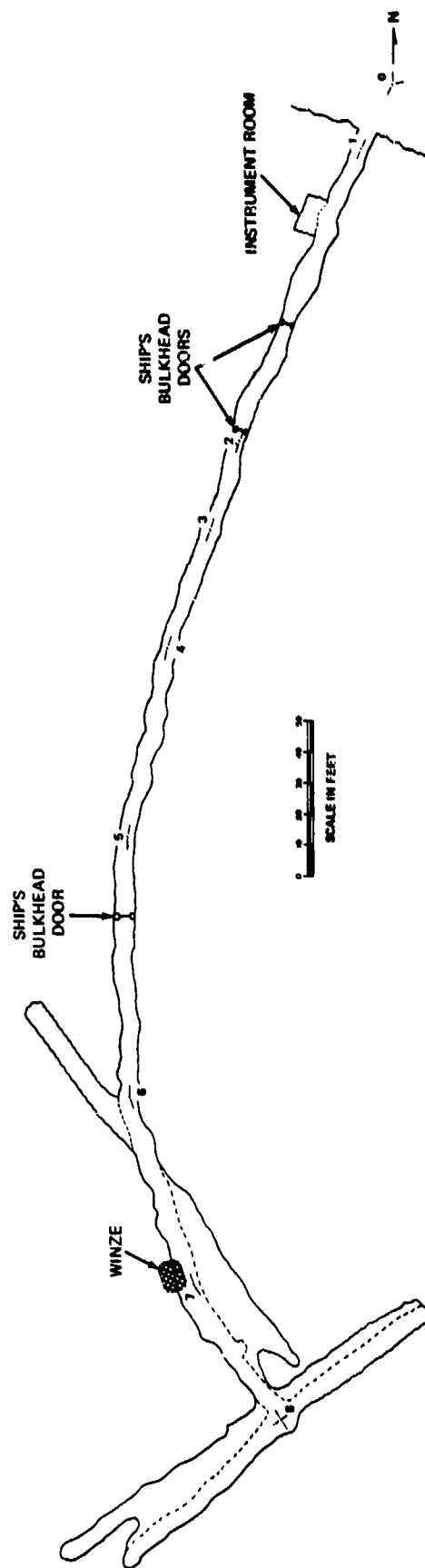


Figure 37. Plan view of QC-AZ mine

G 6645



a. Section of new access road up to site



b. Access roads for moving equipment to mine adit



c. Miners' camp and parking area



d. Tracks with air and water supply lines installed

Figure 38. Photographs taken during early part of site preparation task

G 6646

about 12 April 1969. Figure 37 shows that this drift required much more excavation than originally anticipated. As the contractor began smoothing the wall of the original drift, considerable fractured material was encountered. To provide rock with good integrity, the azimuth of the tunnel was rotated about 5 deg clockwise. This change required the removal of about 200 tons more rock and the digging of about 20 ft more drift than planned. To prevent excessive fracturing on the wall where the instrument was to be mounted, a special controlled blasting technique was used to slab off rock during the final smoothing process. This technique required more drilled holes and lighter explosive charges and consequently further slowed progress. As a result of these delays and equipment failures, final work on this drift was not completed until September 1969.

5.2.2 Excavation of the 325 deg Azimuth Drift

Rough excavation on the 325 deg drift was started soon after beginning on the 55 deg drift. However, final excavation and smoothing of the floor for mounting the instrument could not be completed until a final azimuth was established on the 55 deg drift. This drift was considerably wider than standard mining practice to accommodate the two horizontal strain seismometers for the planned side-by-side evaluation. Another problem was discovered in preparing this drift for floor mounting of the strain seismometer supports. When the drift was completed to its full length, holes were drilled in the floor to about 1-1/2 ft depth for the expansion bolt anchors for the instruments. However, as these holes were drilled, it was found that the floor was fractured more than anticipated, and the expansion bolts bought for anchoring would not hold. Consequently, it was necessary to drill larger holes to a depth of at least 3 ft in order to use an expanding shell mine roof anchor. The fracturing on the floor was apparently the result of two factors: (1) the floor surface contains fractured rock held together loosely yet strongly enough to resist being scooped up by the "slusher" (air-operated dragline) that removed the blasted rock; and (2) even though the floor was finished with a light blast, more dynamite was necessary to lift the rock from the floor than is required to slab off a wall. Further delays caused by equipment failures delayed completion of the major excavation of this drift until November 1969. Mounting holes could not be completed until equipment used for digging the vertical shaft (winze) was removed.

5.2.3 Excavation of the Winze

With the completion of excavation in the 55 deg drift and moving of the slusher and track, work on the winze was begun along with excavation of the 325 deg drift in late August 1969. Upward excavation of about 16 ft was required for assembly of the "gallows" frame - the heavy timbering used for the hoisting equipment. Downward digging on the winze started in early October. Because of the equipment failures mentioned, and more importantly, because of the mining contractor's personnel problems, the winze had been excavated only to a depth of about 24 ft by January 1970. The contractor was repeatedly unable to keep an adequate labor force on site to expedite completion of the full 40 m deep winze. Therefore, a termination agreement was made in mid-January. A total depth of 39-1/2 ft was available for the vertical seismometer - 16 ft up and 23-1/2 ft down. The contractor completed the removal of all loose rock and drilling the mounting holes for the vertical and the 325 deg horizontal. All contractor equipment was removed from the mine by early February.

5.2.4 Other Site Preparation Work

Other work done by the mining contractor during site preparation included excavation of a small instrument room near the mine entrance and the leveling of a large parking area for the recording vans. The 1-1/2 mile long power line from the main highway to the van site was installed by the power company.

5.3 INSTRUMENT ACQUISITION AND FABRICATION

Effective on 1 May 1969, the original contract was amended to include a task for acquisition of the existing Government equipment and fabrication of new equipment required to install the designed system. Also included in the amendment were tasks for system tests and preliminary operation. The gathering of Government furnished property and fabrication of new equipment was begun soon after approval was received.

5.3.1 Government Furnished Equipment

As stated previously, the complete system was designed to use as much available Government furnished equipment (GFE) as practical. This included the SP and LP inertial seismometers and amplifiers, the recording system, the calibration system, and the majority of required support equipment. All GFE was thoroughly checked and modified where necessary for proper operation in the designed strain/inertial system. The layout of the rack-mounted equipment was planned for ease of operation in the two 26 ft long recording vans. Equipment wiring and provisions for van interconnections were completed and tested before transporting the vans to the field. Installation and checkout of this equipment was completed by mid-July 1969.

5.3.2 Fabricated Instrumentation

The major components of the strain systems - rods and supports, moving-coil transducers, calibrators, and the Strain Filter Unit, Model 33350 - were fabricated in the Garland plant. All raw materials were ordered during mid-May 1969 and, with the exception of the Invar material for the seismometers, vendor delivery schedules were satisfactory. The Invar material proved to be somewhat more difficult to locate than anticipated, in the quantities required for this project. With few exceptions, most of the material had to be manufactured by the mills. Also, since this alloy requires a high percentage of nickel (36 percent) which was then difficult to get, delivery was further delayed. Fortunately, the longest delivery schedule was for the 2 in. o.d. tubing which required little shop work. Although long delivery did delay manufacturing operations, delays in completion of the mine modifications (para. 5.2) caused more serious problems.

Actual fabrication of the equipment proceeded without serious problems. The strain filter unit was completed during August and the machined components were completed by late October 1969.

5.3.3 Purchased Equipment

Equipment purchased for this project included two additional Ithaco amplifiers, power supplies for the strain amplifiers, and environmental monitoring equipment. There were no particular problems in obtaining this equipment.

5.4 INSTRUMENT INSTALLATION

Because of delays in completing mine modifications and delays in receiving Invar from suppliers, the installation phase at QC-AZ began in August 1969 with transporting of the two vans to the site. It was completed in March 1970, when the installation of the three strain instruments was completed. The installation phase was begun well before the expected completion of the mine work in order to finish as much of the installation of peripheral instrumentation as possible before actual seismometer installation. Since plans called for many tests to check for the proper operation of the newly developed strain system, it was important that all other components of the system be as trouble-free as possible. The following paragraphs describe the various stages in chronological order.

5.4.1 Installation Work During August and September 1969

The two recording vans and the support vehicles left Garland on 18 August 1969. The vans were set up on the van pad below the mine on 21 August. During the remainder of this period, only two men from the three man operating team were on site, together with the Geotech mining supervisor. Since mining operations were in progress, work on the system was limited to work outside the mine in the 120°F desert sun. By the time the power line installation was completed on 10 September, the vans had been unpacked and work had begun on final equipment wiring in the vans.

The three wind direction and anemometer units were emplaced on the top, north, and south sides of the mountain as planned and wired using Spiral-4 cable. The first microbarograph was installed above the mine adit. A power line and 52 Spiral-4 cables were strung between the vans and the mine. The Spiral-4 cables were stripped and prepared for installation in the lightning protectors at both ends. Figure 39 is a photograph taken during this period.

Efforts were made to do some minor installation work in the mine between dynamite blasts. However, work was severely hampered here because of the desire not to interfere with the miners. An equally serious problem was a lack of adequate ventilation in the 55 deg drift where work could have been done. Without ventilation, the gases from the nitroglycerine would accumulate in the drift and caused severe headaches which persisted for hours.

5.4.2 Installation Work During October through December 1969

During October, downward excavation was begun on the winze and ventilation tubing could be installed without suffering damage from flying rock. Also during this time, the mining contractor's progress was very slow. During this quarter, considerable progress was made on installation of equipment inside the mine. Temporary electric lighting circuits were run into the mine for this phase.

The instrument room near the adit (see figure 37) had been previously completed by the mining contractor. A concrete pad was poured and a shelf was installed for the phototube amplifiers for the SP and LP seismographs (figure 40). The mass position monitors and controls for the LP seismometers were installed in a rack seen in the left of the figure.



Figure 39. View from tailing pile showing cable line from the mine, recording vans, power line, and access road.

G 5467



Figure 40. Phototube amplifiers and inertial LP seismometer controls in the instrument room in the mine.

The three tank vaults were installed near the intersection of the 55 deg and 325 deg drifts and are shown in figure 41. A groove was cut in the rock and the bottomless tanks were set in each groove. Before the tanks were cemented in place, the loose rock inside each vault was removed. Three holes were drilled, expansion bolts were installed in the holes, and heavy steel plates were screwed onto the expansion bolts for the feet of the seismometers. Then the three vaults were cemented into the grooves, but cement was not poured in the bottom of the vault as is usually done. This was done to avoid concrete curing noise on the LP seismographs. When the cement cured, the interior porous areas were painted with several coats of epoxy paint to seal the vault.

The three-component inertial SP seismometers were installed in the 55 deg drift. No special treatment was given to their installation. The three-component LP instruments were installed in the three tank vaults. Temporary cabling between the seismometers and the amplifiers was strung and the systems were placed in operation, recording on film for a preliminary look at the background level at the site. Routine operation with normal background at magnifications of 500K on the SP and up to 100K on the LP seismographs (without sealing) confirmed that the site was very quiet, as hoped.

Also during this time, the 55 deg azimuth strain seismometer (S55) was assembled. Figure 42 shows about one-third of the total rod, with the moving-coil transducer in the background. Figure 43 is a close-up view of the transducer. The Ithaco amplifier was temporarily placed on the magnet mount for preliminary recording. Figure 44 shows the fixed end anchor for the strain rod.

5.4.3 Installation Work During January through March 1970

When the mining contractor had cleared his equipment from the mine in early February, work could be done more efficiently and the installation of the instruments was considered completed by the end of March. The S55 strain instrument was completely enclosed with 4-in. thick polyurethane foam insulation. Two full-length strain seismometers were assembled side-by-side in the 325 deg drift. The second unit used components built for the vertical instrument. These two identical instruments proved to be very useful in evaluating the operation of the strain instruments. Figure 45 is a photograph taken from near the fixed anchors looking toward the transducers. The figure shows the insulating cover almost completed on the permanent (S325-1) seismometer. The triangle support frames seen on the temporary unit (S325-2) are typical of both units. The S325-2 instrument was operated during the nighttime hours for about 2 weeks without insulation. Comparison of the data from the two instruments clearly demonstrated the necessity of the insulation. Therefore, this instrument was similarly insulated during late March. (The timbering in the left of figure 45 is the "gallows" frame over the winze.)

The ship's doors were installed to provide an air seal. A 1/4-in. thick steel flange was cut to fit the opening in the drift and was welded to the commercial door frame. After moving loose rock, the assembly was then wedged in position and the bottom was cemented as shown in figure 46a. Then, both the inside and the outside of the frame were bricked to provide structural support and to complete the air seal. Figure 46b shows the completed installation of one of the doors, along with about 40 Spiral-4 cables that were strung from the mine adit to the seismometer chamber. In the upper left of figure 46b is the power cable sealed inside a 1-1/2 in. pipe. The power circuits were also



Figure 41. Long-period inertial seismometer tank vaults

G 5471

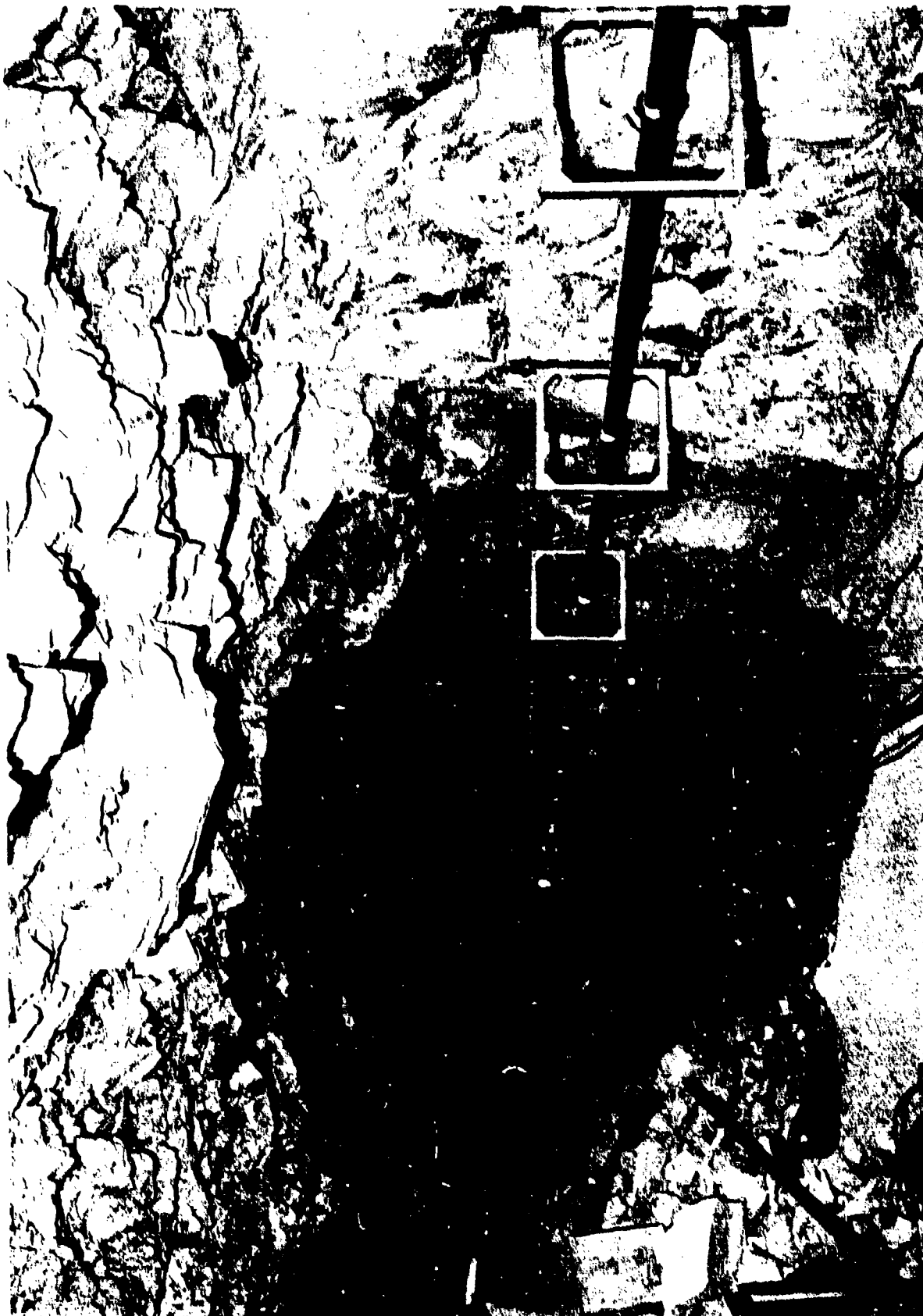


Figure 42. Southwest end of 55 degree horizontal strain seismometer.

0540



Figure 43. Velocity transducer and preamplifier.

G 5460



Figure 44. Strain rod anchor.

G 5468



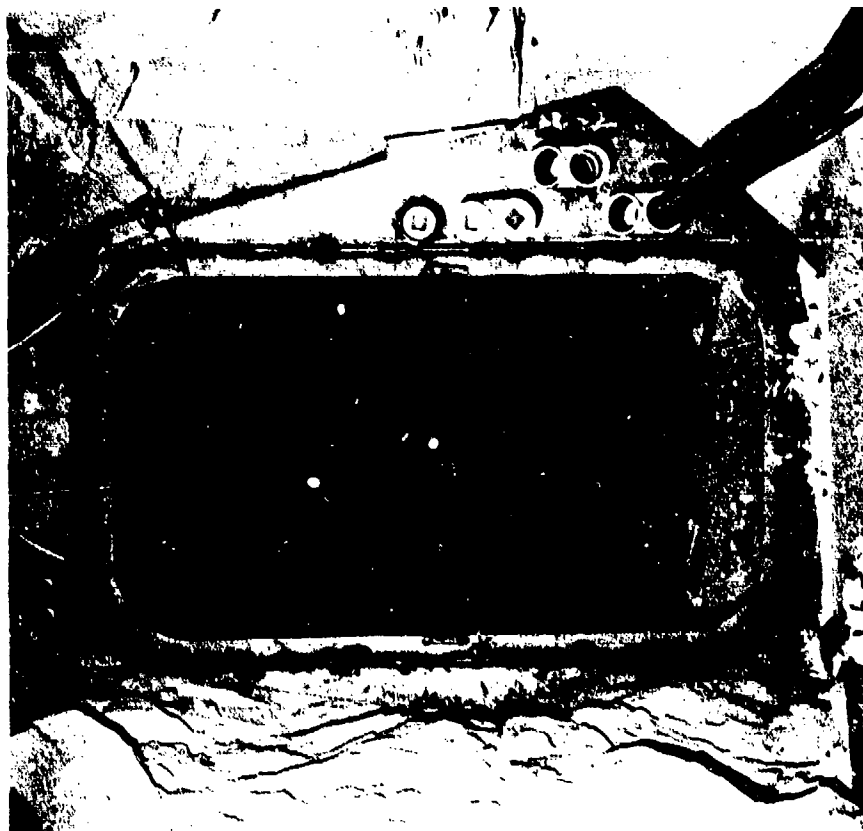
Figure 44. Strain rod anchor.

G 8408

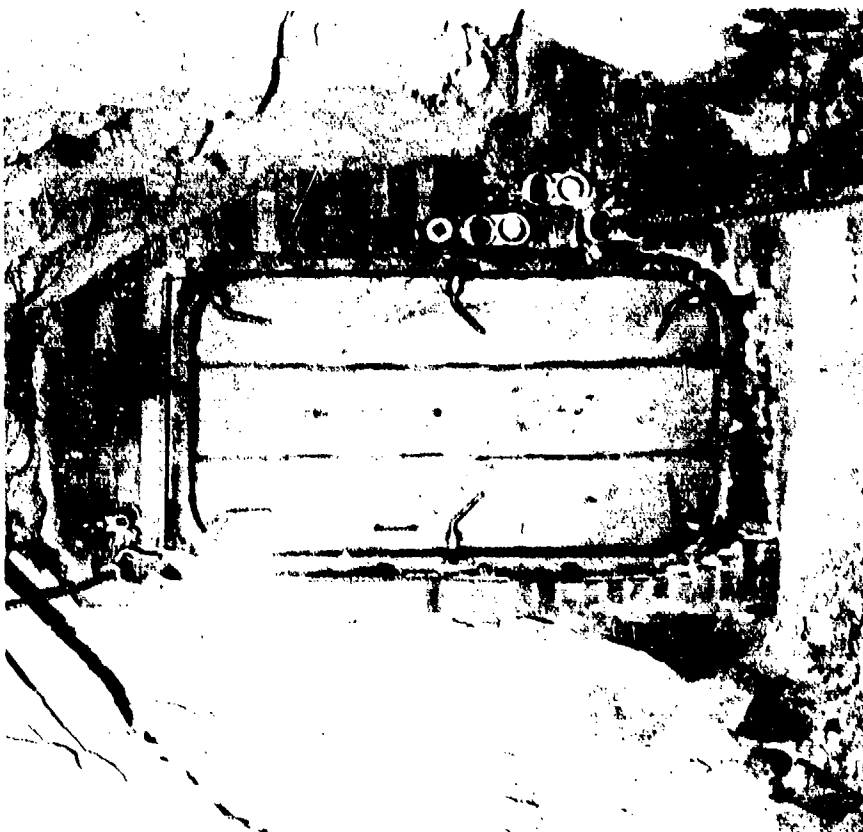


Figure 45. Side-by-side 325 degree azimuth strain seismometers. Permanent seismometer on left has been partially insulated. Vertical strain seismometer was located at gallows frame on left of figure.

G 55051



a. Door frame wedged into opening and cemented into the floor.



b. Final installation

Figure 46. Ship's door installation

G 5552

completed during this period, with several outlets placed in convenient locations in the rear chamber. The valve shown was used for pressure tests and to equalize pressure on both sides of the door before opening.

Finally, cabling to the LP inertial instruments was permanently installed and the tank vaults were thoroughly insulated inside and out with fiberglass insulation. All instruments were turned on and the installation phase was considered complete by late March.

5.4.4 Later Installation Work

Although the QC-AZ station had been declared operational, considerable further installation work was done through August 1970. This was especially true in the case of additional instrumentation, which became useful as more was learned about the capabilities and limitations of the strain instruments.

A second microbarograph system to monitor outside air pressure changes was installed in early April. Comparison of the simultaneous data from this and the instrument inside the sealed mine showed that the seal provided more than 40 dB attenuation of outside pressure changes. Also, this outside unit was ultimately installed on top of the mountain to more accurately describe the pressure forces acting on the mountain.

Another major addition was the installation in mid-May of the Directional Array Subsystem, as described in paragraph 4.2 above. Recordings of the various on-line sums and differences of the LP strain and inertial seismographs provided four beams steered toward azimuths of 325, 55, 145, and 235 degrees. Data from this system were very useful for the various analysis tasks and as a diagnostic tool for determining proper system operation.

When side-by-side comparison tests were completed, the S325-2 instrument was disassembled and installed as the vertical strain seismometer (SZ) in early July. The X10 Mechanical Amplifier, discussed in paragraph 4.5.2 above, was installed on the transducer at the bottom of the winze. After completing the assembly of the SZ, the unit was completely insulated with the same rigid polyurethane used on the other seismometers. The gallows frame was floored at intervals of 6 to 8 ft to minimize vertical convection currents and to support the insulation. This installation was completed on 17 July 1970.

Finally, the three variable capacitance transducers, described in paragraph 3.2.4 above, were installed to provide broad-band strain outputs. Fabrication and installation of these transducers was delayed longer than originally intended because of more pressing operational problems. Installation of these units, along with their chart recorders, was uncomplicated and was completed by mid-August.

6. OPERATION

Routine operation - in the sense of operating an established system - is seldom obtained as soon as hoped by the designers of state-of-the-art systems, and the QC-AZ strain/inertial complex was certainly no exception to this rule. Although installation tasks continued, tests to evaluate the strain instruments were conducted, and many hours were spent trying to locate mysterious "glitches," nevertheless the QC-AZ system was declared in "routine" operation on 1 August 1970.

6.1 ROUTINE OPERATIONS

Routine operation at QC-AZ officially began on 1 August 1970 and continued until the station was closed on 1 June 1971. Appendix 4 contains the Routine Operating Instructions that were used. Field personnel followed these instructions insofar as it was practical in the light of continuing special tests and problems. Since it was not always possible to follow a routine schedule, considerable latitude was allowed the three-man field team in the operation of QC-AZ.

6.1.1 Data Recordings

Data were recorded on three magnetic-tape recorders, two 16 mm film recorders, one 35 mm film recorder and three chart recorders. Tape systems required tape changes once per day. The two 16 mm film recorders were changed weekly, the 35 mm recorder was changed every 5 days, and chart records were cut every week. A daily log was made for each recorder, giving channel assignments, magnifications, and other pertinent information. Also, a master log was made each day giving times for all work concerning the system, such as calibrations, special tests, problems, etc. All data, with logs, were shipped weekly to the Garland office where they were catalogued, critiqued, and stored for later analysis.

6.1.2 Routine Calibrations

With few exceptions, all SP and LP data channels were calibrated daily. These daily magnification checks were especially important for the ALPS strain and inertial systems because optimum operation of the directional array required closely matched gains. The ULPS and broad-band records were calibrated every five days.

For all strain calibrations, it was necessary to be aware that the calibrators had the capability of overdriving the various elements in the filter system. This was especially important for attenuated special data runs and for frequency responses when input attenuation between the seismometer and the amplifiers was not used. An analysis was made of the expected voltage levels in the system for calibrations at various frequencies. In all cases, the first active filter stage (3 Hz filter in SP system, 80 sec filter in ALPS system, and 30 sec filter in the ULPS system) would be the first to clip. Subsequent filtering could mask this clipping so maximum calibration levels were established as shown in figure 47. Note that the input filters clip in overlapping frequency ranges, but at least one unit clips anytime the preamplifier output exceeds 20 V p-p. The ALPS amplifier in the Strain Filter Unit clips at a

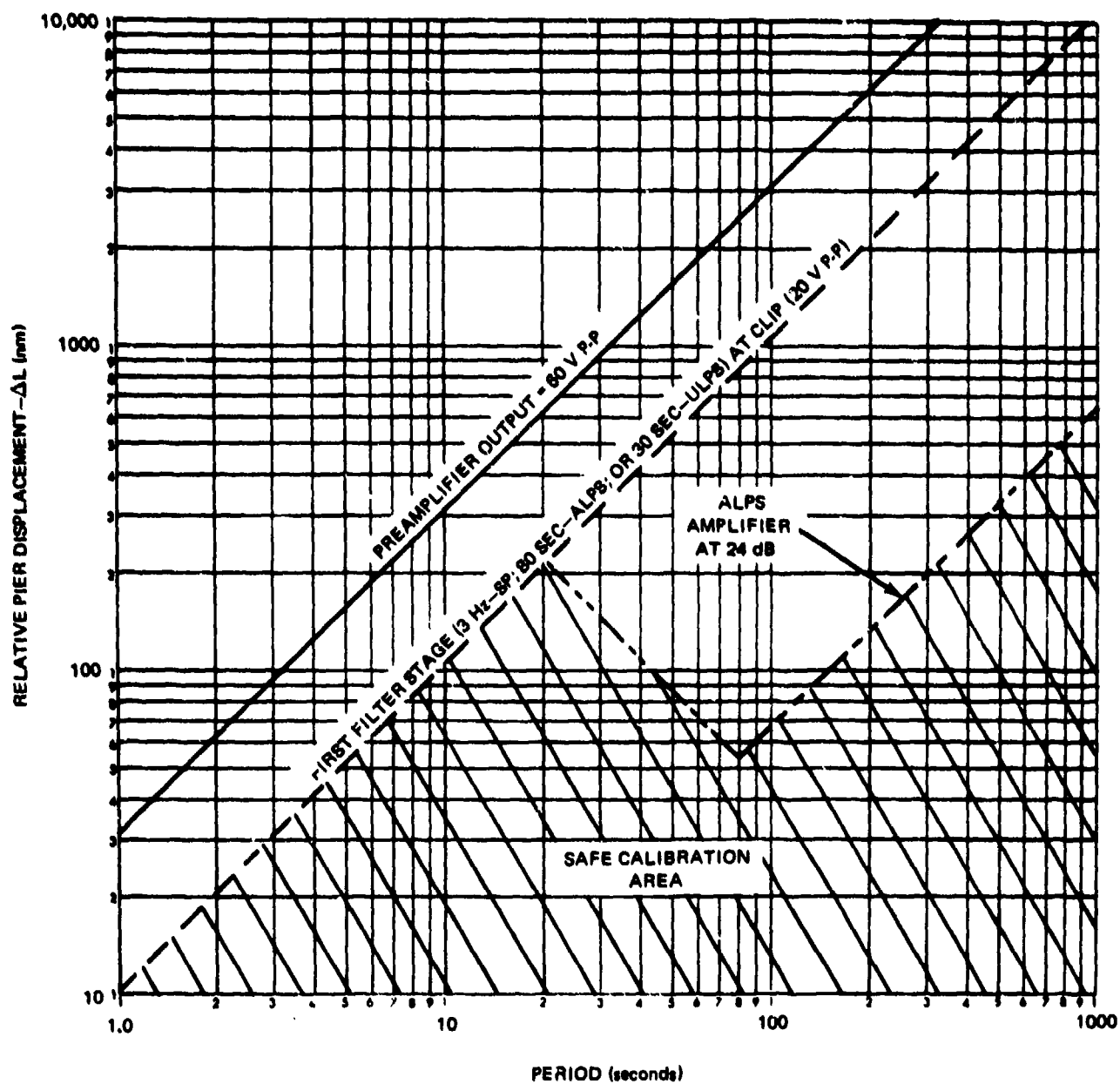


Figure 47. Maximum calibration amplitudes for QC-AZ strain systems

G 6647

different calibration level for each of its gain settings. The figure shows the worst-case condition (24 dB gain) for this circuit which improves as the gain approaches 0 dB, where the input filter again becomes the limiting factor.

6.1.3 Amplitude and Phase Responses

Amplitude and phase responses were run several times during the operational period at QC-AZ, especially after changes were made to the system. In all cases, the greatest emphasis was placed on the ALPS strain and inertial channels. As was originally expected, the three inertial seismographs exhibited the greatest amount of variation from response to response. The strain seismograph responses were reasonably consistent since response shaping was done almost entirely by stable electronic filters.

In October 1970, after the problem with the inertial seismometers had been solved, amplitude and phase responses were determined for all three components of the following seismographs: P_S, P_L, P_X, S_S, S_L, and S_U. (Throughout the report, the dash in the seismograph nomenclature will designate any of all of the three components Z, 325, and 55.) Among the three components of the six types of seismographs, the phase and amplitude responses were exceptionally consistent. The amplitude responses for similar types of seismographs matched one another within a few percent (± 3 percent for ALPS response strain (S_L) and ± 5 percent for ALPS response inertial (P_L), for example). The phase response of a seismograph is more sensitive to variations in parameters than the amplitude response and is therefore a better basis of comparison between strain and inertial channels. The phase spread between similar instruments gives an indication of the stability of the particular type. The maximum spread between the three short-period inertial (P_S) channels was 4 deg, 5 deg for the P_L's, and 3 deg for the S_L's. This set of responses is typical of others run during the operations at QC-AZ, in that the P_L seismographs showed the most instability in both amplitude and phase. In the strain seismographs, where the responses are formed by electronic filters, the stability was very good. The match between strain and inertial channels is an indication of how successfully these channels can be combined for wave discrimination studies. The P_S seismographs and the horizontal strain seismographs, S325S and S55S, had a maximum mismatch of 8 deg from 1 to 10 sec period and within 20 deg for 1 to 5 Hz frequency. The short-period vertical strain seismograph (SZS) was affected by an additional high-frequency cutoff at about 3 Hz due to the response of the mechanical amplifier. The SZS phase was within 10 deg of the S325S and S55S from 10 to 2 sec and is 60 deg different at 5 Hz. Figure 48 shows the phase responses of the ALPS response inertial (P_L) and the ALPS response strain (S_L) seismographs and the phase difference between them. Note that the maximum mismatch is 12 deg at 10 sec and is within ± 9 deg for other periods up to 100 sec. Despite these slight mismatches, the directional array, formed by sums and differences, operated very well in enhancing all types of seismic waves. The inertial extended-long-period (P_X) seismographs and the strain ultra-long-period (S_U) seismographs were not matched to each other because the strain seismograph response could be extended to periods much longer than the inertial seismograph response without increasing system noise.

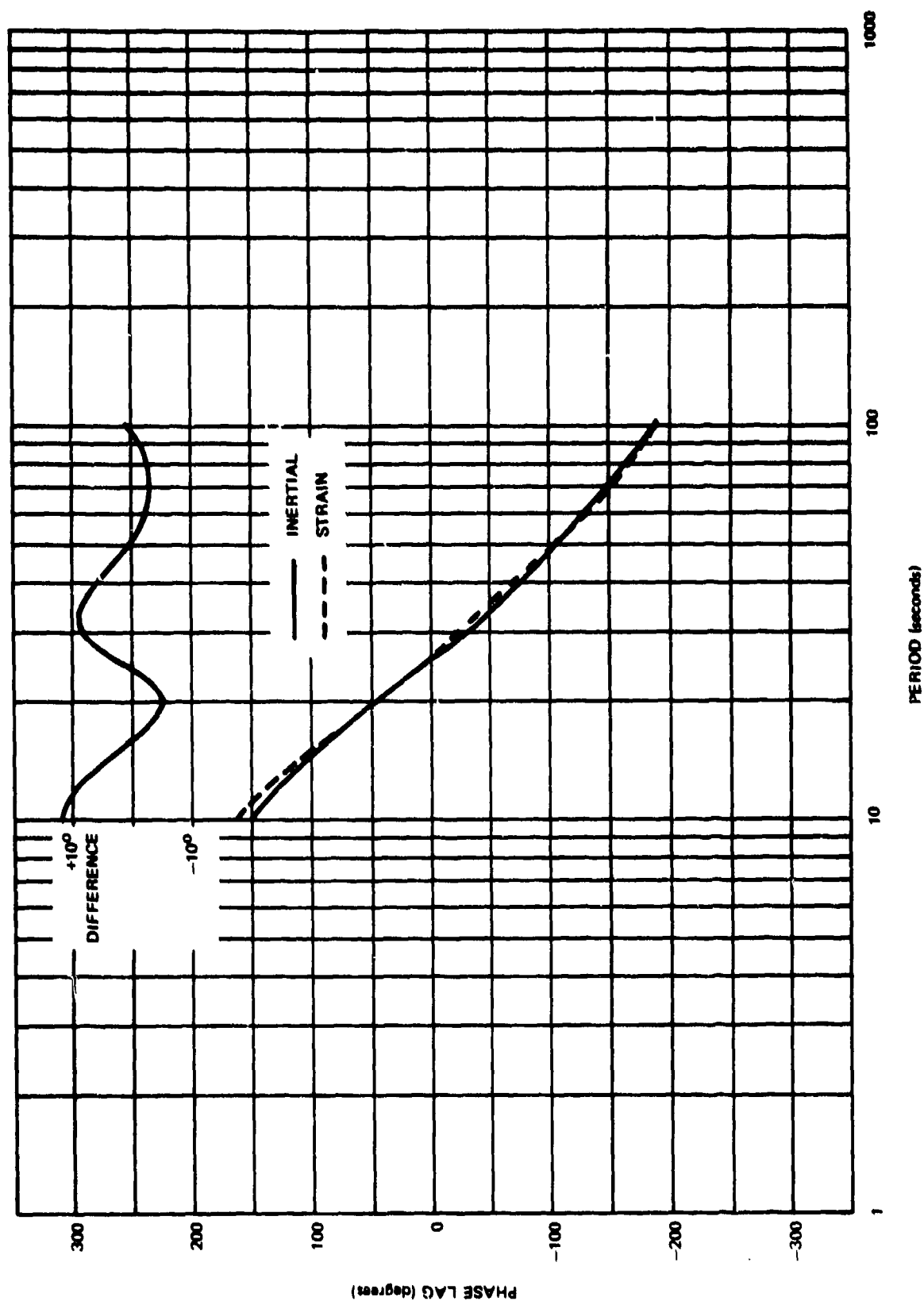


Figure 48. Phase response of strain and inertial seismograph in mid-October 1970, showing amount of phase mismatch

G 6848

6.1.4 Determination of Amplitude and Phase Responses by Computer Processing

The determination of the amplitude and phase responses of all the seismographs is essential to evaluate the precision of match between the strain and inertial seismographs. Considerable time is required to obtain amplitude and phase responses of long-period systems. Several cycles of each frequency with good signal-to-noise ratio are required. Amplitude responses are recorded on the film recorders and can be measured and plotted at a later time. Phase responses are obtained by adjusting phase of a calibration signal on a variable-phase function generator until the Lissajous figure on an oscilloscope indicates zero phase between the function generator reference output and the seismograph output. After numerous cycles are observed, phase adjusted, and reobserved, the phase difference is read from the dial and written down.

Three methods of obtaining the system transfer function by analytical processing of special test data were considered: (1) random noise input; (2) numerical differentiation of the response to a step of current into the calibration coil; and (3) a least square fit between a theoretical pulse from a seismograph with known parameters and an actual pulse resulting from a step of current into the calibration coil. The second method was found to be the most practical because it required less lost data than the first method and because it produced a more satisfactory solution than the third method.

To obtain the seismograph transfer function from a random noise input, a sufficiently long data sample must be obtained to provide the desired statistical stability of the cross power spectral density between the input and the output. A data sample at least 32 min duration would be necessary for periods up to 100 sec and at least 6.7 hr duration would be necessary for periods up to 2000 sec. An attempt was made to use the white noise from a resistor on the input of a broad-band dc amplifier driving the calibration coil of an inertial LP seismometer. With the broad-band system, 60 Hz noise dominated the calibration coil input. When it became evident that extreme grounding precautions would be necessary, the experiment was deferred to the other two methods and to other more pressing installation problems.

The three inertial P(Z, 325, 55)L seismographs were attenuated to improve the signal-to-noise ratio and several steps of current were applied to each of the three calibration coils separately. Figure 49 is a recording made from the magnetic tape. It shows the reduction in microseismic background by the attenuation and the first current-on and current-off and second current-on pulses on the P55L seismograph. These pulses were digitized and were used for evaluation of both methods two and three. Both methods use the fast Fourier transform algorithm of Cooley and Tukey to perform the required calculations rapidly.

The second method is straightforward, but contains the problems associated with numerical differentiation. The seismogram pulses are equivalent to the output of the seismograph for a step of acceleration input. (A step of current into the calibration coil produces a step of force F on the inertial mass M which is accelerated at the rate of F/M .) The desired amplitude and phase response is for an input of an impulse of displacement. To obtain the desired transfer function three derivatives are taken. Because of the excellent signal-to-noise ratio, the first attempt was to take the Fourier transform into the frequency domain and take a triple derivative by multiplying by $(i\omega)^3$. The first

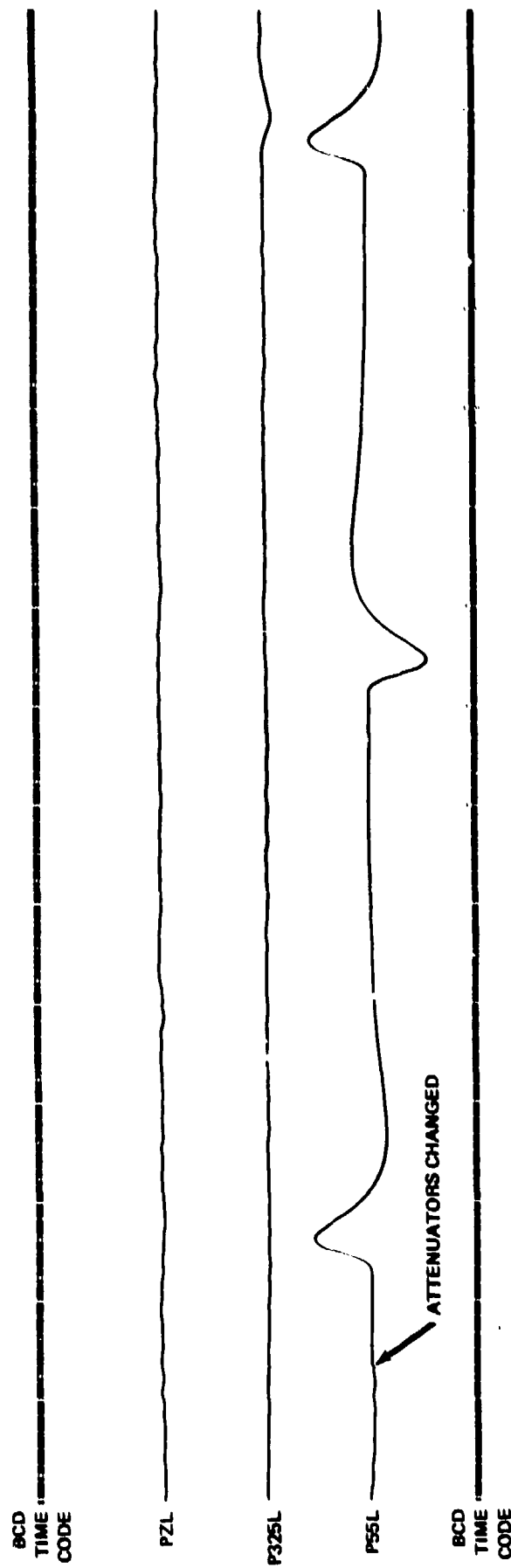


Figure 49. Pulses resulting from a step current into the calibration coil of P55L

QC-AZ
PLAYOUT FROM
TAPE RECORDER 1
RUN 139
19 MAY 1970

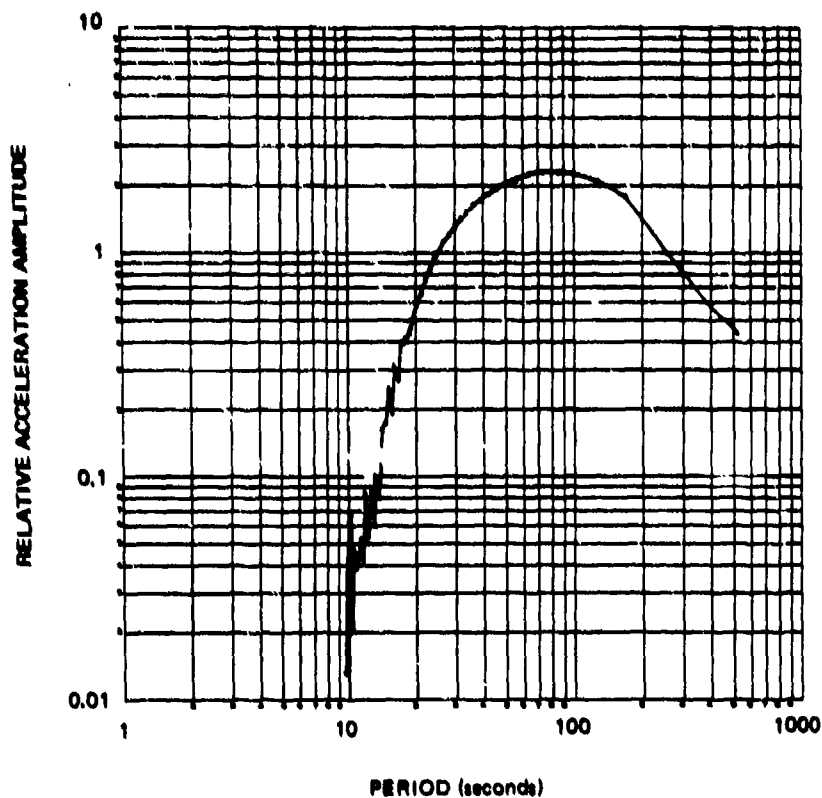
G 6005

derivative (figure 50) appeared smooth at all frequencies, and the desired third derivative (figure 50) was relatively smooth at periods from 512 down to 20 sec. Below 20 sec the noise caused erratic results. A seven-point, parabolic, least-squares smoothing (Lanczos, 1956) was then accomplished before each derivative was taken. The smoothed amplitude response is plotted down to 10 sec in figure 51 along with the experimentally measured amplitude curve. At 18 sec and 12 sec microseisms are seen to contribute noise to the result; however, when matched with the experimental curve, the results are very good when the microseismic energy is allowed for. The phase response curve is plotted in figure 52 along with the theoretical curve. A five-point, parabolic, least-squares smoothing was also tried, but the true data are sufficiently smooth that the seven-point smoothing produced better results for very little additional computation time.

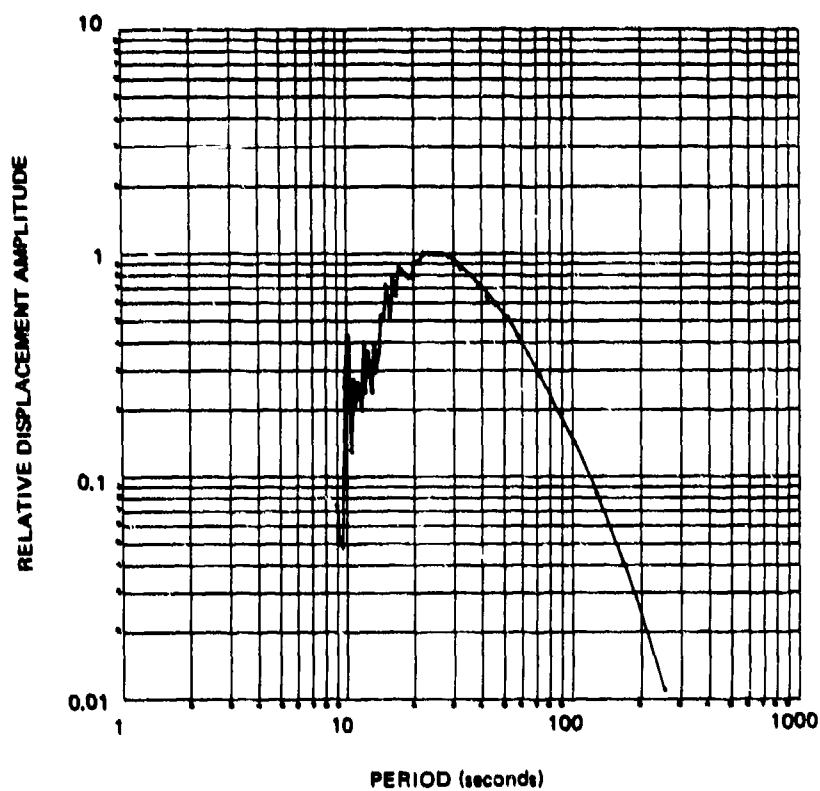
The third method used to obtain the seismograph transfer function was considered unsuccessful. The method was developed by Mitchell and Landisman (1969) for the World-Wide Standard Seismograph Network (WWSSN) recordings. A set of seismograph parameters are input to the program. A theoretical time domain response to an input step of acceleration is calculated using numerical integration, which is inherently more stable than numerical differentiation. A set of partial derivatives of the time domain pulse to changes in seismometer and galvanometer free period and damping is calculated. A least-squares adjustment increment in these four parameters is calculated. The parameters are adjusted and the program iterates until the residual sum of squares between the theoretical and the actual time series is below a predetermined acceptable level. The WWSSN LP seismograph has a seismometer, an attenuation circuit, a galvanometer, and a photographic recorder with a light beam reflected off the mirror in the galvanometer. The QC-AZ seismographs contain electronic filters that do not have a counterpart in the WWSSN. It was necessary to add the transfer function of these filters to the program so that the proper theoretical response could be calculated. The filters are PTA plug-in filters, Model 6824-14, without a 6 sec notch, and Model 6824-15, with the notch. The parameters of the actual filters vary slightly from one to another, and the use of slightly incorrect corner frequencies may have affected the results somewhat, but more serious problems were encountered. Since Mitchell and Landisman had such good success, the program was first used with real data. After completely unacceptable results were obtained, the measured system parameters were input to the program and the theoretical time domain pulse was output to use an artificial signal for a test case. With this artificial signal, and parameters within 5 percent of the true parameters input to the program, it did not arrive at a correct solution after 25 iterations, although it was slowly incrementing in the right direction. Because the program did not converge rapidly, because it was very sensitive to the pulse start time and thus signal-to-noise ratio, and because of the longer computation time, this method was abandoned in favor of the second more straightforward method.

6.1.5 Changes in System Responses

During the course of operation at QC-AZ, changes were made in the response of the various systems as specific needs arose. The primary ALPS systems (strain and inertial) were maintained in their original design configuration for all but the last two months of operation. The only changes made until that time were the substitution of the 6 sec notched filters (6824-15) for the unnotched



a. P55L response to impulse of acceleration (one derivative, no smoothing)



b. P55L response to impulse of displacement (three derivatives, no smoothing)

Figure 50. Amplitude response of P55L calculated from the pulse in figure 49

G 6006

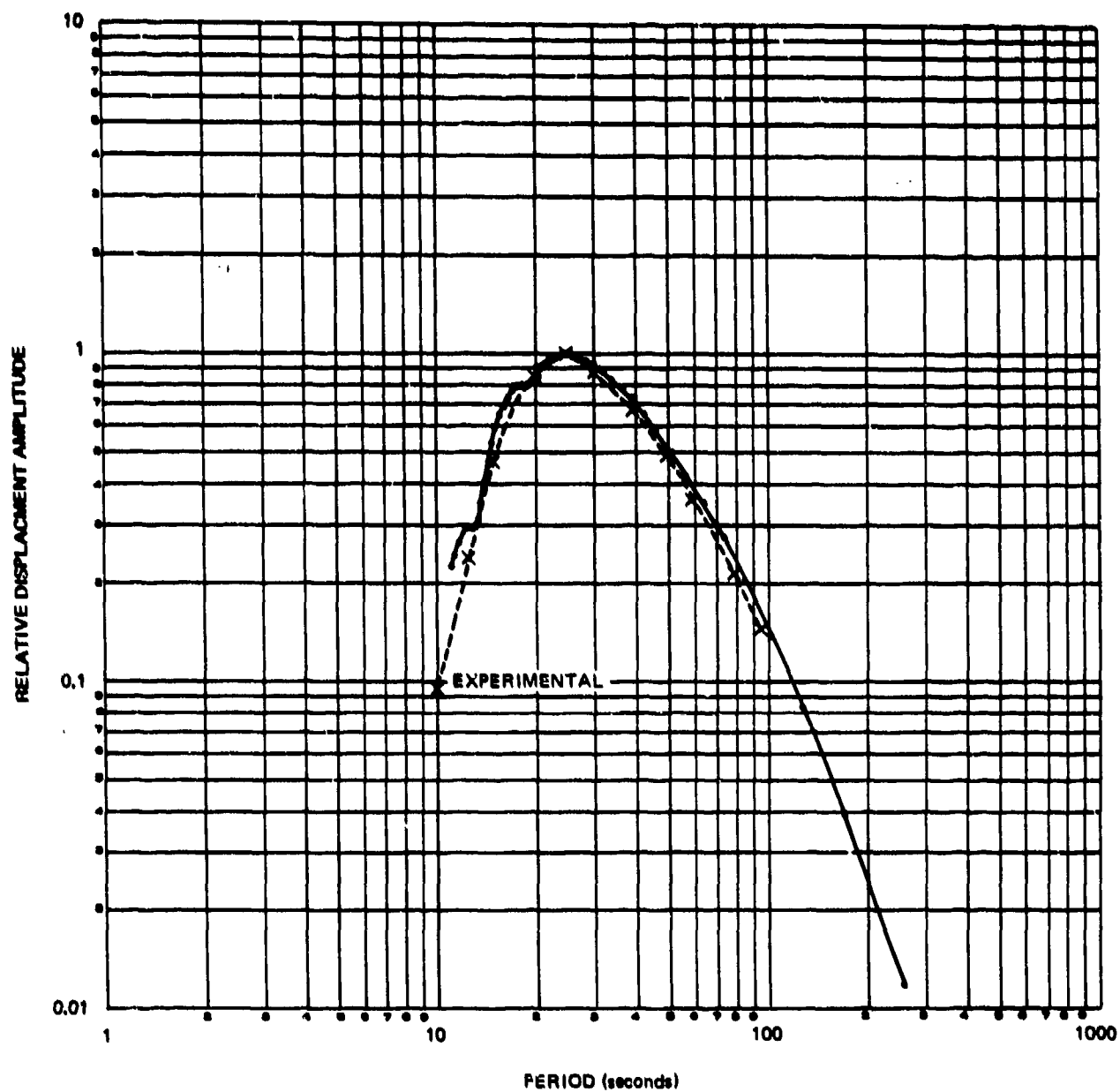


Figure 51. P55L experimental amplitude response and amplitude response from smoothing and numerical differentiation of pulse from a step of acceleration

G 6007

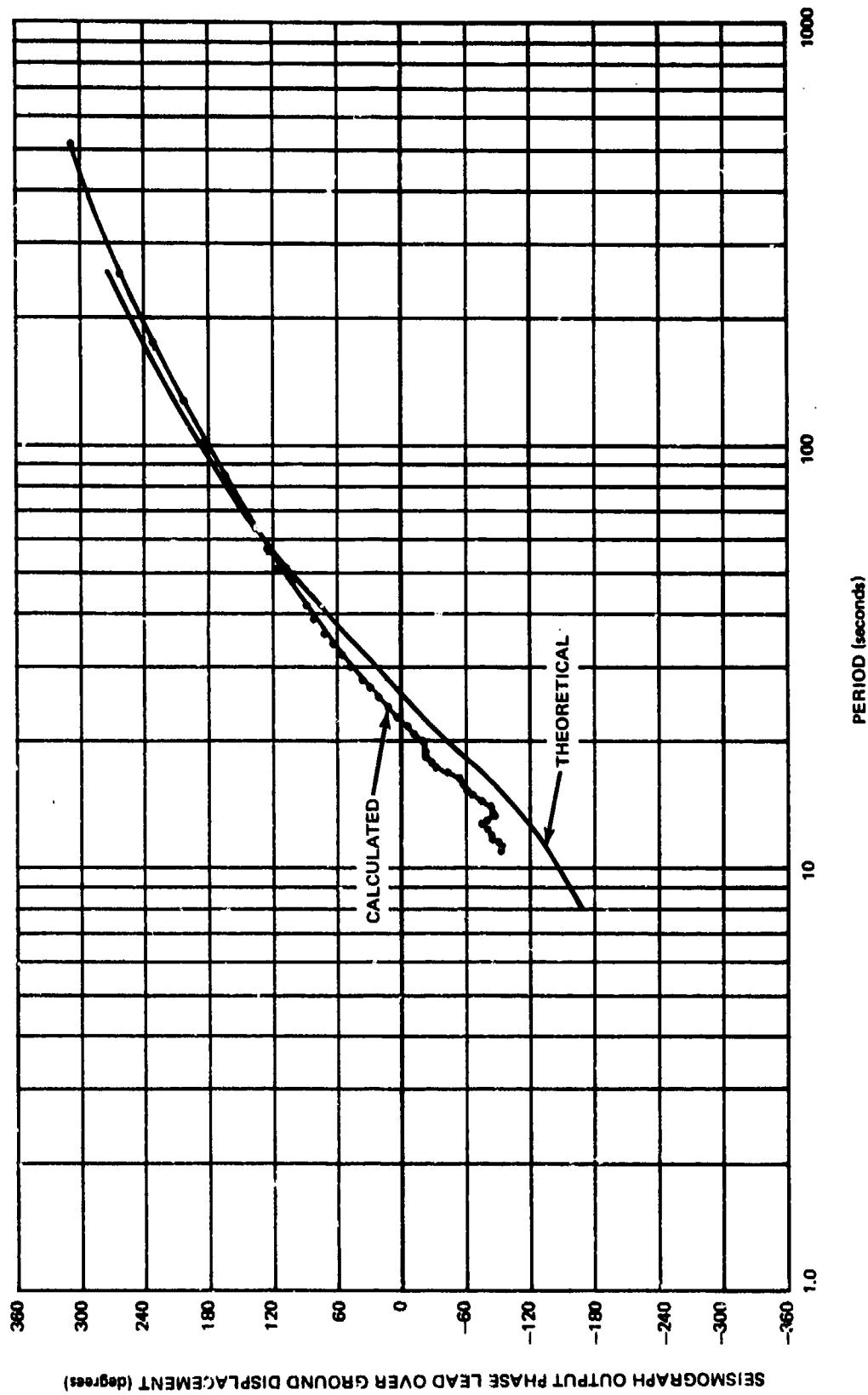


Figure 52. Phase response of PSSL theoretical and calculated from the pulse in figure 49

G 6649

band-pass filters (6824-14) when local microseismic activity became troublesome. These filter changes did not materially affect the response of the P X channels. During May and June of 1971, high-pass filters with corners at 40 sec and cut-off rates of 12 dB/octave were placed in all six ALPS seismographs to reduce the longer period noise, especially on the strain channels. Well-matched filters were put in all channels to preserve the overall phase match between the strain and inertial channels. Figure 53 shows this modified response.

In addition, a significant change was made in the short-period channels when 0.8 Hz, 6 dB/octave, low-pass filters were installed at the input of the strain preamplifiers. At this time, the SP inertial seismometer damping was changed from 0.7 to 1.0 and the SP strain filters were also modified to preserve the match. The actual change in amplitude response was small with the curve being somewhat more sharply peaked with a slight reduction in relative gain near 1.0 Hz.

In another modification, the responses of the ultra-long-period (ULP) strain seismographs were changed in April 1970 to reduce the signal level at the recorders for periods longer than about 300 sec. The original ULP2 response, which was flat to ground displacements from traveling waves at periods from 30 to 1000 sec, allowed recording of high level, very long period noise which limited the usefulness of the ULP recordings. The new response, designated ULP3, was achieved by substituting 283 sec low-pass filter cards for the 1000 sec filter cards, and was flat to ground displacements from traveling waves at periods from 30 to 283 sec.

6.2 OPERATING HISTORY

Appendix 5 gives a chronological operating history of QC-AZ. This history gives the date of significant tests, changes, etc., and will be helpful to those who may desire to use the QC-AZ data.

6.3 OPERATIONAL PROBLEMS

There were several problems that occurred during the operations at QC-AZ which required considerable time to correct. The problems that proved to be the most serious and required the most manpower are discussed in the following paragraphs.

6.3.1 Elimination of Power Line Pickup

Despite careful design and attention to detail, pickup of the 60 Hz noise from the power lines was a problem several times during routine operation. Fortunately, all the long field data circuits between the mine and the vans were operated in the balanced mode and the resulting common mode rejection capability of the van filters and the amplifiers was a great asset. The primary problem at QC-AZ is one typical of very dry desert locations in that there was as much as a 15 V p-p difference in 60 Hz ground voltage between the vans and the instruments in the mine. To reduce pickup from this, it was necessary to solidly reference all circuits to one common ground point. At QC-AZ, the power line ground at the van power pole was selected as the best point. A heavy ground line was run from this point to the instrument room at the mine adit

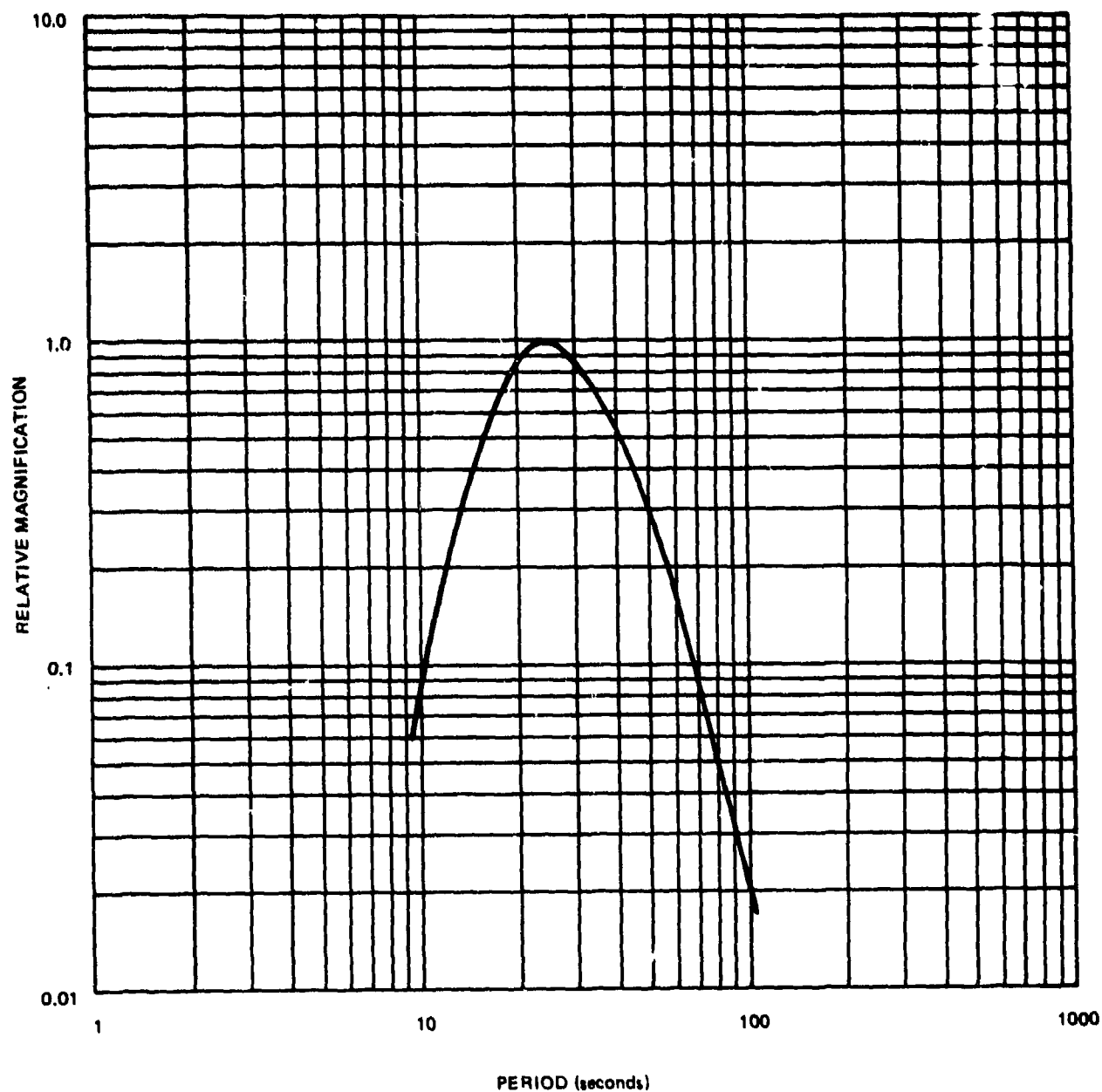


Figure 53. Amplitude response to ground displacement of ALPS strain and inertial seismographs with 6-second notch filter and 40-second high-pass filters. Applicable to QC-AZ instruments in May and June 1971

G 6650

and from there to the electronic instruments in the back of the mine. The ground leads of the six inertial PTAs were isolated from the mine ground and connected to the common bus. The dc common of the power supplies for the strain preamplifiers and the broad-band transducers was also connected. In the instrument area, the Ithaco preamplifiers were isolated from the local ground and connected to the van ground. With this configuration, hum pickup and noise spikes were excessive on the strain channels. This was traced to 60 Hz coupling between the magnet (at mine ground) and the data coil (referenced to van ground). The resulting voltage exceeded the common mode specification of the preamplifier by a large margin. When the strain magnets were grounded, the noise was eliminated.

Another serious noise problem, also traced to 60 Hz pickup, required almost 2 months to completely correct. This occurred on the LP inertial system, especially on the P55L and X channels. The noise was characterized by large spikes that coincided with the cycling of the van air conditioners. The data coils and lines were all checked for leakage to ground and slight leakage was noted in the P55 seismometer. The instrument was removed from the vault and all potential leakage points were carefully cleaned with solvent. The instrument was reinstalled and no leakage could be detected. However, several days of operation showed no improvement in the noise level. The data coils were replaced in the seismometer, again without significant improvement. Finally, the solid-copper, twisted-pair data lines were dummy loaded at the seismometers. Despite the fact that no leakage was detectable, the noise was still seen on the dummy loaded traces. When the twisted-pair lines were replaced with shielded Spiral-4, the noise was almost completely eliminated.

The last serious 60 Hz problem illustrates the need for balanced circuits in field work. The broad-band transducers were originally designed with single-ended outputs. The 60 Hz pickup was so serious that the tape recordings of BB outputs were virtually useless. To solve this problem, integrated circuit operational amplifiers were installed in the broad-band electronics packages in the mine. These units were connected as unity gain inverters and provided a "pseudo-balanced mode" output. The van amplifiers were then able to reject the 60 Hz to a reasonable level.

6.3.2 Strain Preamplifier Saturation

When using broad-band, solid-state amplifiers with velocity transducers, high frequency signals outside the normal passband can very easily saturate the amplifiers. In the strain system, this problem was anticipated and the flag output was incorporated in the strain filter unit to sense this excess voltage.

After a spare 20-channel galvanometer bank became available to replace the galvanometer bank in Develocorder No. 1, recording of the flag trace as a 20th channel was begun on 27 April 1970. It was immediately obvious that many of the large spikes recorded on LP strain channels were the result of Ithaco amplifier clipping associated with high-amplitude, short-period signals. To minimize this preamplifier clipping problem, capacitors were put across the transducer coil output leads on 11 May. The capacitors and coil resistances form single-pole, low-pass filters with a cutoff corner at 0.8 Hz. These filters reduce 10 Hz signals by about 20 dB, but do not affect periods long compared to 1.25 sec (0.8 Hz). These filters were very effective in reducing

the frequency of occurrence of saturation. The only flag indications noted after the modification were the result of very large earthquake signals that drove the high gain data recordings out of range. These capacitors made necessary the changes in the SP seismograph responses, which were discussed earlier.

6.3.3 Inertial Seismograph Response

In early April 1970, the amplitude responses of the LP inertial seismographs indicated a serious variation from the theoretical curve. Since the strain seismographs were built to match the theoretical ALPS response, the different inertial response resulted in a degradation of on-line sums and differences between strain and inertial seismographs. The problem was traced to the seismometers, which were equipped with more efficient transducers than the standard design. These prototype transducers were installed in another program prior to the transfer of the seismometers to Project VT/8706. The higher magnet charge and greater length of wire in the coils resulted in a seismometer with a much higher critical damping resistance (CDR) than normal. For example, the two horizontal seismometers had a CDR of about 2500 Ω as compared to the standard value of 1510 Ω . This high CDR resulted in overdamped seismometers when other system parameters were set to nominal values. In the ALPS system where the seismometer and galvanometer are direct coupled, seismometer and galvanometer damping plus the coupling coefficient are interrelated so that one parameter cannot be changed without affecting the others. It was therefore necessary to modify the transducers to obtain standard values of coil wire length, coil resistance, and magnet flux density.

New coils with less wire were wound and installed on the seismometers beginning in late May. These new coils incorporated a recent improvement in LP seismometer coils developed especially for high-gain operation. This improvement balances the diamagnetic and paramagnetic properties of the coil/coil-form assembly so that nonlinearities in restoring force are minimized. In addition to the installation of new coils, magnet charge was adjusted on the seismometers. The vertical seismometer presented more of a problem than the horizontals. Since the vertical instrument requires a higher flux density than the horizontals (0.195T and 0.175T, respectively) and the prototype magnets could not be charged to a 0.195T flux density, standard magnets were used as replacements. The modifications to the vertical seismometer were completed on 18 June.

6.3.4 Lightning Protection

When the strain system was designed, considerable thought was given to the adequate protection of the strain system preamplifiers against lightning damage. Solid-state circuitry is considerably more sensitive than tube-type PTAs to the high amplitude, short duration pulses that can occur on data lines as a result of lightning pulses many miles distant. It was therefore disturbing when two Ithaco amplifiers were found to have been damaged by lightning on 27 April and on 24 June 1970. In both cases, shorted transistors in the amplifier output stage indicated that overvoltage had occurred on the field lines between the mine and the vans. The lightning protection circuits consisted of gas-discharge diodes and high surge semiconductor diodes across the line and large inductors in series with the line. The circuits were identical with circuits being successfully used on other programs, but no reasons could be found

for their failure to adequately protect the QC-AZ circuits. The circuits were carefully checked and the ground points were improved.

Then, on 7 July and 19 July 1970, lightning again damaged all three preamplifiers. Before putting the twice-repaired units in operation on 22 July, the protection circuits were moved from near the mine adit to within a few feet of the preamplifiers. In addition, the circuits were modified by adding resistance to the output data lines to absorb overvoltages. A schematic of a typical modified circuit is shown in figure 54. Heavy thunderstorms during the remainder of this period caused no damage to any equipment. The improved operation of the protection circuits indicates that overvoltages on the protected lines were the result of differences in earth potential and/or pickup from other less heavily protected lines between the instruments and the mine adit. All future lightning protection circuits should be installed as close as possible to the devices to be protected.

6.3.5 Noise on the S325 Seismometer

Probably the most perplexing problem encountered during operations at QC-AZ was the high noise level of the S325 seismometer. This problem became evident when the two side-by-side S325 instruments were first put in operation and was no closer to a solution when operations were terminated. Between these times, many manhours were spent in efforts to locate some source of the noise. Rod alignment was checked and adjusted several times, insulation was removed and checked for rubbing on the rod, suspensions were adjusted, bolts were tightened, the data coil was replaced several times and the Ithaco amplifier was exchanged with one from other channels.

On two occasions during alignment checks with a surveyor's transit, the rod anchor was found to be displaced. As a further check of anchor instability, a dc current near normal calibration levels was applied to the calibrator of the seismometer. The resulting force applied to the rod and the rod anchor caused a marked increase in noise level on the S325L channel. Therefore, in mid-July, 1970, about 1/3 cu. yd of concrete was poured around the base of the rod anchor, completely filling the almost 8 in. gap between the fractured rock base on the floor and the bottom of the anchor. Later operation indicated that the noise decreased somewhat after the concrete cured.

From February to April 1971, another test series was run in connection with the S325 noise. In late January, the mine was visited by the State mine inspector. He recommended that some very large rocks in the ceiling near the winze should be timbered and that the ceiling in part of the 55 deg drift should be "barred down." When the mining contractor started doing the suggested work, the main blower was turned on and the mine was ventilated for the first time in several months. Surprisingly, the noise on the S325L seismograph dropped to a level comparable to the S55L. After a few days' operation, the noise level began to rise again. It was thought that the noise might be related to the high humidity in the mine air or trapped water in the fractured rock on the floor. The humidity was caused by the great amounts of water used during the mine modifications. A dehumidifier was installed and operated intermittently until mid-April. A total of about 20 gallons of water was removed, but the relative humidity showed no appreciable drop. It was concluded that the mine would have to be ventilated for several months to determine whether drying the mine truly had any effect on the noise in the S325.

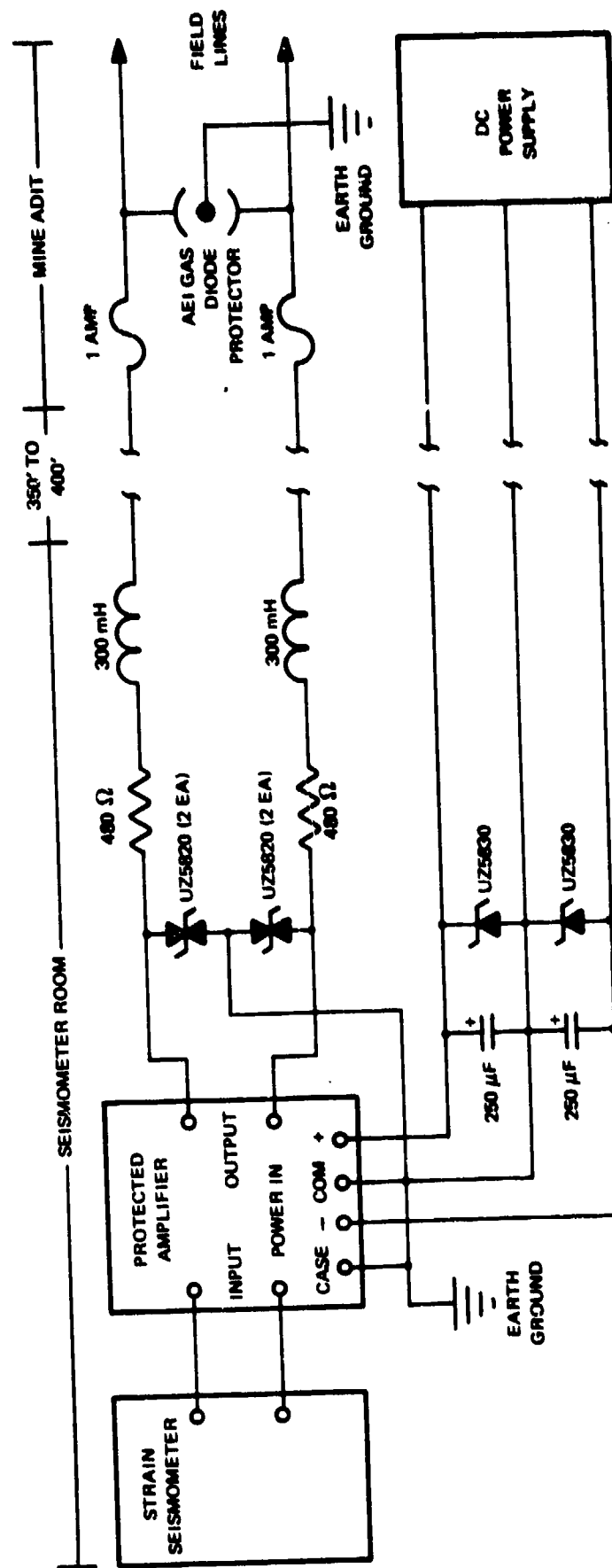


Figure 54. Schematic of modified lightning protection circuit for strain amplifiers at QC-AZ.

The overall conclusion concerning this noise was that it was caused by local movement in the fractured rock on the floor where the anchors were placed. The 325 deg azimuth is almost perpendicular to the axis of the mountain and is subparallel to the local joint pattern. The structure of the mountain is much weaker in this direction, allowing greater extraneous displacements and strains than in the 55 deg azimuth parallel to the axis of the mountain. Barjansky (1944) determined the tangential stress and the hoop stress around a circular hole in a semi-infinite elastic solid directly under the point source load of a Boussinesq field. He found that at depths of 10 or more hole radii, the ceiling and floor were subjected to a tensile stress concentration factor of -1 and the wall was subjected to a compressive stress concentration factor of +2. The stress concentration factors are relative to the stress at the depth of the center of the hole if the hole did not exist. The tensile hoop stress on the floor will act in a sense of opening the joints, of loosening the rock, and of creating noise on the S325 strain seismometer. Conversely, the compressive hoop stress on the wall will act in a sense of closing the joints, of tightening the rock, and of reducing the noise on the S55 strain seismometer. The fluctuations of the air pressure create repetitive loads that continually work toward the loosening of the rocks on the ceiling and the floor of a mine. The obvious conclusion then, is that all strainmeters should be attached to the wall rather than the floor for optimum performance.

7. NOISE AND STABILITY

The QC-AZ seismograph station has a microseismic background that is as quiet as any of the better sites anywhere on earth. This low background noise has provided a good test base for instrument evaluation. This section discusses the earth noise field, its stability, the instrument noise of the inertial and strain seismographs, atmospheric disturbances, and small ground motions that result in undesired noise on the strain seismographs. General details of the time series analyses used in many parts of this report are described in section 7.1. Section 7.2 gives quantitative values of earth motion from 10 Hz to 2560 sec. Instrument noise and microseismic background signals for the inertial system are presented in section 7.3 and for the strain system in section 7.4. Small earth motions that contribute to the noise on the strain seismographs are discussed in section 7.5. The noise field generated by variations in atmospheric pressure is discussed in section 7.6. Tilt response of inertial LP seismographs is discussed in section 7.7. Secular strains are presented in section 7.8. The resistance of the strain seismometers to spurious resonances induced by acoustic vibrations is discussed in section 7.9.

Any consideration of data system performance should not only consider the system noise level and maximum sensitivities, but should also consider signal-to-noise ratios. Section 7 treats the subject of noise only. Section 8.2 discusses earthquake signal-to-background noise ratios.

7.1 SPECTRAL ANALYSIS

Many of the time series analysis plots in this report are similar. Part a of the figures is the power spectral density of one or more seismographs or the cross power spectral density between them. Part b of the figures is the coherence and part c is the relative phase angle. Where a plot of coherence is shown, note that it is coherence and not coherence squared. Long time series and a small number of lags were used for good statistical stability. Time samples of 33.1 min (with 128 lags) or 32.0 min (with 256 lags) were used for spectra between 1 and 256 sec periods and generally time samples of 6.7 hr (with 128 lags) were used for spectra between 20 and 2560 sec periods. In general, the shorter period spectra were calculated with 256 lags, but in a few cases, they were also calculated with 128 lags for greater smoothing and a smaller confidence limit.

Unless stated otherwise, the spectra are uncorrected for system responses and are calibrated relative to earth strain or earth displacement at 25 sec for the ALPS response and at 100 sec for the ULP response. Thus, if the reader wishes to estimate the power spectral density of ground strain or ground displacement at another period, the values in the figures should be divided by the square of the ratio of the response of the system at the desired period to the response of the system at the calibration period of 25 or 100 sec. In several of the figures in which strain is compared to displacement, the strain has been normalized to displacement based on a 25 sec Rayleigh wave phase velocity of 4.00 km/sec and the resulting power ratio of $(6.28 \times 10^{-5})^2$ strain²/m². Cross power spectral density between strain and displacement is normalized based on a power ratio of 6.28×10^{-5} strain -m/m². The normalization constants are given in the figures. The spectra are presented as a

power spectral density normalized to a 1 Hz passband. The passband used in the actual calculations was either $1/128 = 7.81 \times 10^{-3}$ Hz, $1/256 = 3.91 \times 10^{-3}$ Hz, or $1/2560 = 3.91 \times 10^{-4}$ Hz. If the reader wishes to normalize to a passband of 1 mHz = $1/1000$ Hz for comparison with several published microseismic spectra, the plotted values can be divided by 1000.

Many of the spectra show 1 or 2 peaks at 1.7 and 3.2 sec. These peaks are the residual power noise in the playback and digitization electronics. Actual playback was at 100 times the field recording speed, so a true 60 Hz noise at playback relates to an equivalent 0.6 Hz or 1.7 sec noise in the time scale of the field recorder.

Computational noise was also observed in the course of the calculations but is well below any meaningful data. The spectra are calculated using the fast Fourier transform (FFT) algorithm of Cooley and Tukey. A single FFT on the Geotech CDC 3100 computer has a noise about 10^{12} to 10^{13} below the largest number in the calculations. This error results in part from the fact that the FFT algorithm takes differences from almost equal numbers. The spectral program used employs three FFT, and erratic results occur about 10^5 or 10^6 below the largest spectral number. These erratic results are interpreted as computational noise. When two time series are analyzed together with the cross spectral program using the FFT, they must be scaled so that their spectra are within the 10^5 to 10^6 range of no computational noise. The first cross spectrum calculated comparing the inertial seismograph and the strain seismograph showed this noise since the strain power values are 39.5×10^{-10} smaller than the displacement values. In subsequent calculations, the strain values were scaled to alleviate this numerical problem.

7.2 MICROSEISMIC BACKGROUND

7.2.1 Absolute Amplitude

The ambient ground unrest or microseismic background at QCAZ is as low as reported for any seismograph station in the world. Figure 55 is the amplitude spectra and power spectral densities of vertical earth motion in the passband from 10 Hz to 2560 sec. The horizontal amplitudes shown in figure 56 for the 55 deg azimuth are about equal to the vertical amplitudes. These two figures are composites of spectra calculated in four overlapping period ranges. Recordings from the SP inertial seismographs were used for two of the ranges and recordings from the LF inertial seismographs were used for the other two ranges. Calibration of the two seismographs was of such an accuracy that all spectra overlaid and no artificial smoothing between the different frequency intervals was necessary. Parameters of the spectral analyses are given in table 7. The power spectral density was calculated; it was normalized to a mHz bandwidth and was corrected for the instrument response. Then the square root was taken. Figures 55 and 56 are plotted as rms meters in a milliHertz bandwidth and as mean-square meters in a 1 Hz bandwidth. The Queen Creek data plotted in figures 55 and 56 are given in table 8 at representative periods.

Previous investigators have reported quantitative data on the microseismic background in several formats over various portions of the range of periods covered here. The summary made by Brune and Oliver (1959) of the maximum

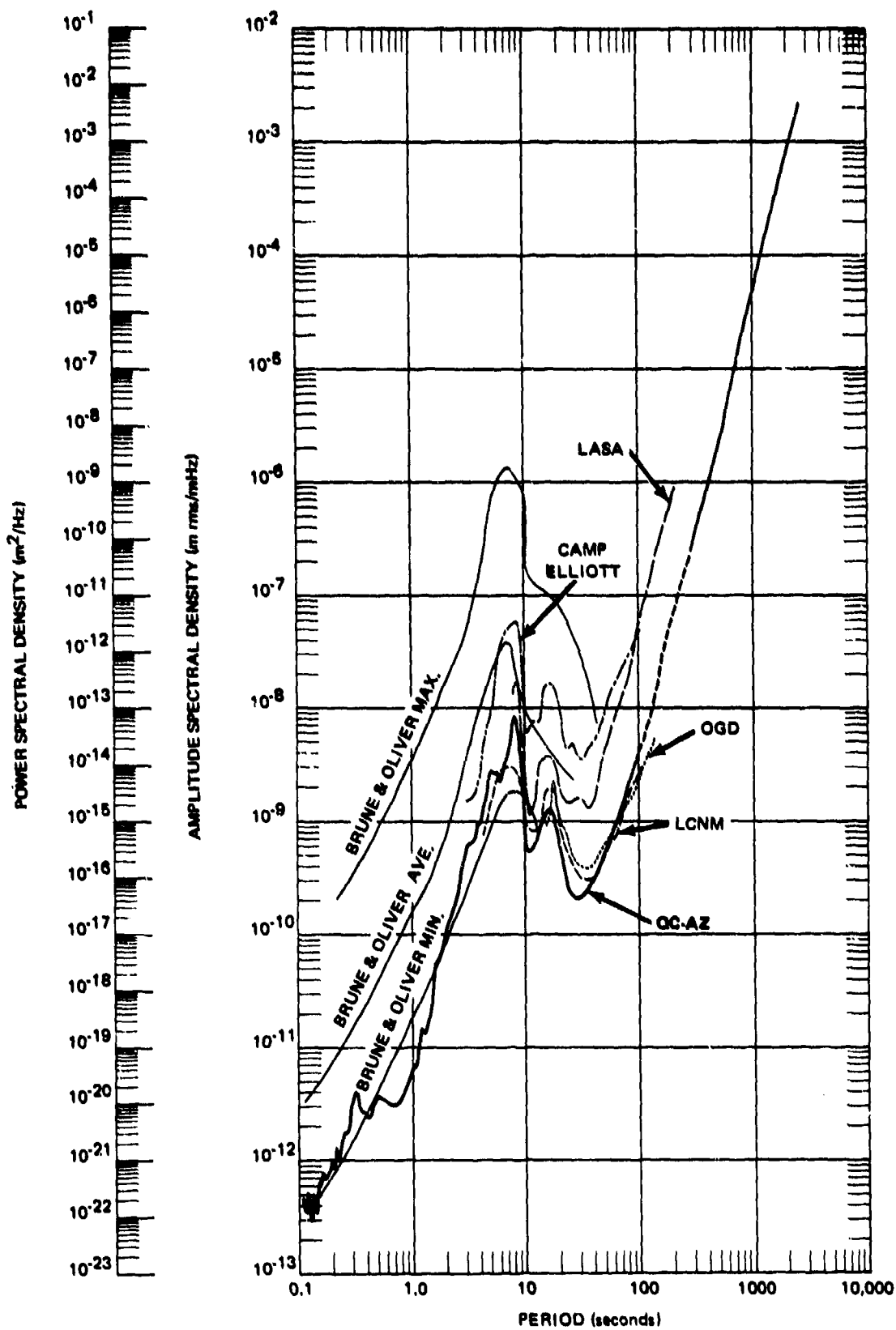


Figure 55. Vertical earth motion amplitude spectral density

G 6651

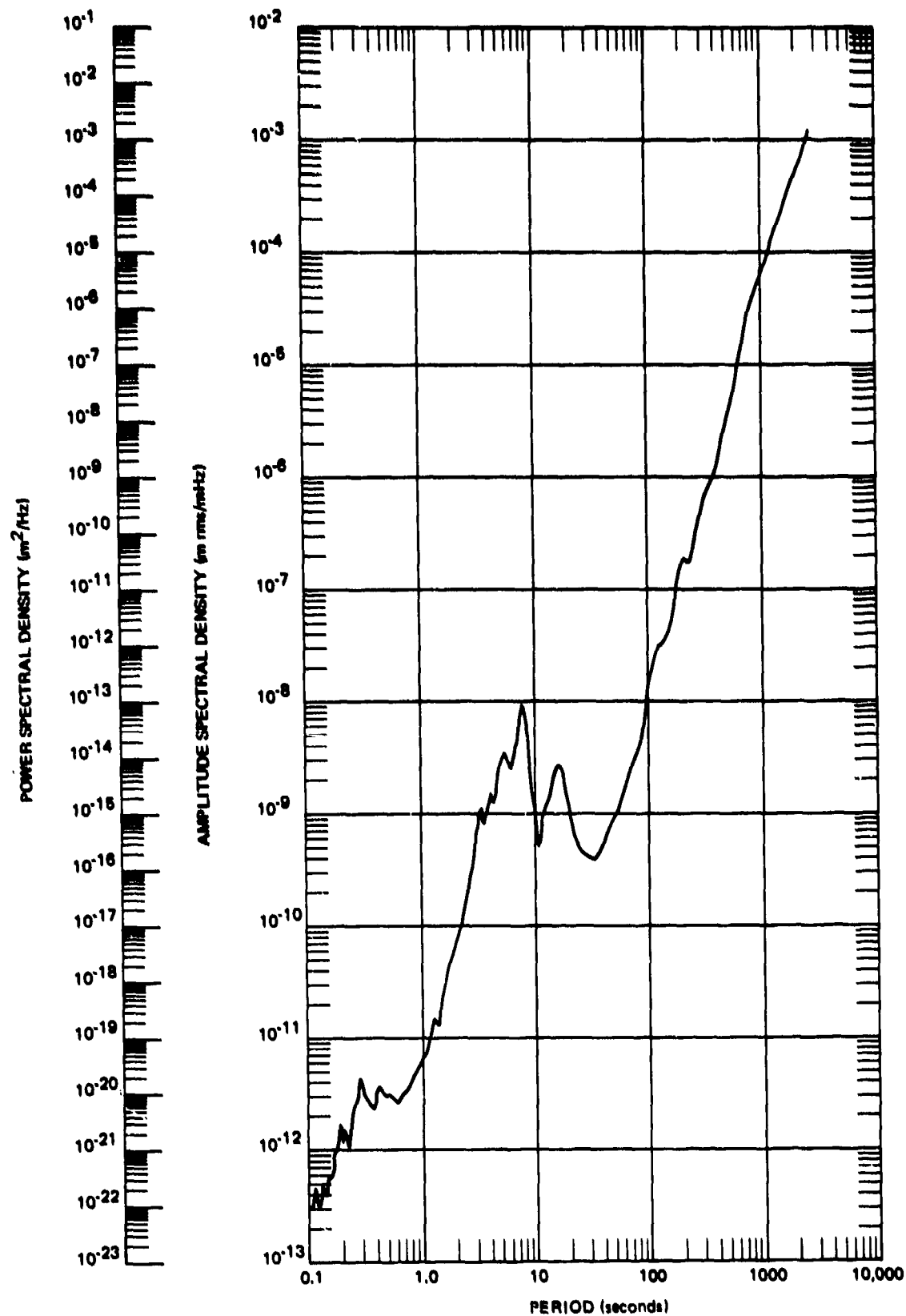


Figure 56. Horizontal (55 deg azimuth) earth motion spectral density

G 6682

Table 7. Microseismic background spectra parameters

<u>Seismograph</u>	<u>Period range</u>	<u>Sample time duration</u>	<u>Sample rate</u>	<u>No. of samples</u>	<u>No. of lags</u>	<u>90% Confidence limits</u>
	<u>sec</u>		<u>s/sec</u>			<u>dB</u>
SP	0.04-10.24	76.8 sec	50	3841	256	± 1.96
SP	0.16-40.96	307.3 sec	12.5	3841	256	± 1.96
LP	1-256	32.0 min	2	3841	256	± 1.96
LP	10-2560	6.7 hr	0.1	2410	128	± 1.74

and minimum of published vertical amplitude versus period values has been used most commonly as a reference in the period range from 0.01 to 20 sec. Their data were derived primarily by the various authors from visual analysis in which peak-to-peak amplitude and period were measured from a seismogram. In general, the measured values represented the authors' best estimate of the average values of the microseismic background. In 1959, very little data were available at the longer periods. Frantti et al. (1962) measured short-period seismic noise spectra at 16 sites in the frequency range of 31.5 to 0.5 Hz. Their frequency analysis was made by analog playback of magnetic tape through 1/3 octave filters. Their data substantially fit between the maximum and minimum curves of Brune and Oliver (1959) at frequencies between 31.5 and 1 Hz and rose above the minimum curve at 2 sec by a factor of 5 at one site and a factor of 10 or more at the other sites. Haubrich (1965) and Haubrich and MacKenzie (1965) reported power spectral densities of ground velocities, sea wave amplitudes, and atmospheric pressure near La Jolla, California. Their data covered the period range from 2 to 200 sec (500 to 5 mHz) and were taken near the coast to study sources of the microseisms. As such, their spectra represent the ambient ground unrest that can be expected at a coastal location during the arrival of storm-generated microseisms. The senior author (JEF) and Milam (1965) established the techniques of achieving high sensitivity (100+K magnification) in the three-component, long-period seismographs at Las Cruces, New Mexico. The seismometers were installed in insulated, sealed tanks within airtight chambers in mines. Trott (1965) and the senior author used this installation to investigate the noise of LP seismographs and to obtain the amplitude spectra of ground motion in the period range from 4 to 100 sec. Pomeroy et al. (1969) used similar techniques at a mine in Ogdensburg, New Jersey. Savino and Hade (1970), Savino in Ward and Hade (1970), Savino (1970), and Savino et al. (1972) have reported amplitude spectra from this observatory. Capon et al. (1967, 1969) and Haubrich and McCamy (1969) report power spectral densities of ground amplitudes uncorrected for seismograph response from the Large Aperture Seismic Array in Montana.

Vertical amplitude spectra derived from these previous authors have also been plotted in figure 55. These other spectra were read from figures, corrected for instrument response if necessary, converted to amplitude spectra if necessary, and the calculated values plotted. The maximum, average, and minimum curves from Brune and Oliver (1959) were calculated in the following manner. Since the data from the 16 sites of Frantti et al. (1962) all fell within the

Table 8. Ground motion amplitude spectra

<u>Period Sec</u>	<u>Frequency Hz</u>	<u>Vertical Amplitude mrms/mliz</u>	<u>Horizontal Amplitude mrms/mliz</u>
2560.000	3.91E-04	2.11E-03	1.62E-03
1280.000	7.81E-04	1.40E-04	1.11E-04
853.333	1.17E-03	2.76E-05	2.66E-05
640.000	1.56E-03	7.71E-06	9.44E-06
512.000	1.95E-03	2.69E-06	3.53E-06
426.667	2.34E-03	1.27E-06	1.35E-06
365.714	2.73E-03	7.37E-07	8.60E-07
320.000	3.13E-03	4.37E-07	6.74E-07
284.444	3.52E-03	2.65E-07	4.28E-07
256.000	3.91E-03	1.79E-07	2.28E-07
232.727	4.30E-03	1.36E-07	1.69E-07
213.333	4.69E-03	1.04E-07	1.76E-07
196.923	5.08E-03	7.62E-08	1.53E-07
182.857	5.47E-03	5.64E-08	1.02E-07
170.667	5.86E-03	4.44E-08	6.09E-08
160.000	6.25E-03	3.43E-08	4.55E-08
150.588	6.64E-03	2.67E-08	3.86E-08
128.000	7.81E-03	1.11E-08	1.51E-08
85.333	1.17E-02	2.72E-09	4.68E-09
64.000	1.56E-02	1.17E-09	2.02E-09
51.200	1.95E-02	6.37E-10	1.04E-09
42.667	2.34E-02	4.19E-10	6.31E-10
36.571	2.73E-02	2.96E-10	4.43E-10
32.000	3.13E-02	2.38E-10	3.82E-10
28.444	3.52E-02	2.16E-10	4.11E-10
25.600	3.91E-02	2.13E-10	4.48E-10
23.273	4.30E-02	2.61E-10	4.81E-10
21.333	4.69E-02	3.85E-10	5.99E-10
19.692	5.08E-02	5.57E-10	9.23E-10
18.286	5.47E-02	8.07E-10	1.52E-09
17.067	5.86E-02	1.11E-09	2.22E-09
16.000	6.25E-02	1.30E-09	2.59E-09
15.059	6.64E-02	1.28E-09	2.46E-09
13.474	7.42E-02	1.00E-09	1.39E-09
12.190	8.20E-02	6.90E-10	1.03E-09
10.667	9.38E-02	5.55E-10	5.05E-10
9.846	1.02E-01	7.02E-10	6.75E-10
9.143	1.09E-01	1.82E-09	1.56E-09
8.533	1.17E-01	5.12E-09	4.00E-09
8.000	1.25E-01	8.43E-09	7.82E-09
7.758	1.29E-01	7.81E-09	8.57E-09
7.529	1.33E-01	6.51E-09	8.21E-09
7.111	1.41E-01	4.75E-09	5.27E-09
6.400	1.56E-01	2.99E-09	3.10E-09

Table 8 (Continued)

<u>Period Sec</u>	<u>Frequency Hz</u>	<u>Vertical Amplitude mrms/mHz</u>	<u>Horizontal Amplitude mrms/mHz</u>
5.565	1.80E-01	2.78E-09	2.93E-09
5.120	1.95E-01	2.70E-09	2.85E-09
4.571	2.19E-01	2.31E-09	1.91E-09
4.000	2.50E-01	1.14E-09	1.39E-09
3.507	2.85E-01	7.19E-10	8.13E-10
3.012	3.32E-01	6.28E-10	5.82E-10
2.560	3.91E-01	3.09E-10	2.48E-10
2.048	4.88E-01	1.35E-10	8.59E-11
1.517	6.59E-01	5.22E-11	2.82E-11
1.241	8.06E-01	1.41E-11	1.48E-11
1.024	9.76E-01	7.36E-12	5.68E-12
.890	1.12E-00	4.37E-12	4.84E-12
.788	1.27E-00	4.10E-12	4.10E-12
.683	1.46E-00	3.27E-12	3.22E-12
.602	1.66E-00	3.19E-12	2.83E-12
.512	1.95E-00	3.66E-12	3.04E-12
.465	2.15E-00	3.89E-12	3.05E-12
.410	2.44E-00	2.64E-12	3.51E-12
.353	2.83E-00	2.82E-12	2.31E-12
.301	3.32E-00	4.13E-12	2.69E-12
.256	3.91E-00	1.99E-12	2.66E-12
.228	4.39E-00	1.59E-12	1.45E-12
.201	4.98E-00	1.34E-12	1.54E-12
.176	5.66E-00	8.44E-13	9.35E-13
.148	6.74E-00	7.85E-13	5.70E-13
.126	7.91E-00	5.18E-13	4.70E-13
.103	9.67E-00	3.96E-13	3.05E-13

Brune and Oliver maximum and minimum curves, it was assumed that the Brune and Oliver data could be taken as an average peak-to-peak amplitude spectra over 1/3 octave passbands, the same as used in the analog spectra of Frantti et al. Stated another way, this assumption is that a seismologist reading wiggly line records will integrate energy over 1/3 octave passbands when reading average microseismic background signals. With this assumption, the Brune and Oliver curves were read from their figure 1; squared; multiplied by 3 to get mean square amplitude per octave; divided by $0.67/T$, where T is period in seconds, to get mean square amplitude per Hz; divided by 1000 to convert to a mHz passband, the square root was taken; divided by 2.828 to convert from an average peak-to-peak to rms; then the result was plotted. The data from Haubrich and MacKenzie (1965) were read from their figure 5 for 6 March 1964. Their spectra were converted from velocity squared per mHz to amplitude spectra per mHz and plotted. The data from Las Cruces, New Mexico, are direct from figure 28 in Trott (1965). The LASA data are from figure 4 of Capon et al. (1969). Their values were read from the figure, converted to amplitude squared per Hz, corrected for instrument response, converted to m rms per mHz passband and plotted. The Ogdensburg, New Jersey, data are direct from Savino's figure 3 in Ward and Hade (1970).

The essential equality of the spectra from Queen Creek, Las Cruces, and Ogdensburg, all of which are high-sensitivity, long-period seismograph stations, confirms the long-period values presented in figures 55 and 56 as being representative of the quietest sites. In the shorter period range from 0.1 to 10 sec, the Brune and Oliver (1959) minimum curve data essentially coincides with the QC-AZ data. Therefore, the QC-AZ amplitude spectra represent a typical minimum that can be expected anywhere on the earth.

These spectra can be useful as design criteria for a minimum ground motion input signal into a seismograph. For instance, these amplitude spectra can be multiplied by the frequency domain transfer function of a seismometer and of the coupling network from the seismometer to an amplifier to determine the voltage spectra at the input of the amplifier. The microseismic background voltage spectra can then be compared to the noise voltage spectra of the amplifier and an estimate can be made of the expected minimum signal-to-amplifier noise ratio.

7.2.2 Variation with Time

The variation of microseismic background with time is also of interest in evaluating the performance of QC-AZ and the background that might be expected at other quiet sites. The following group of figures present power spectral densities of background noise from a selected group of days with low wind velocity and during intervals of low earthquake activity. Finding samples with low earthquake activity is a problem on these high sensitivity seismographs, and some of the samples may include signals with a 1:1 or 1.5:1 signal-to-noise ratio. These spectra are calibrated relative to 25 sec. They are uncorrected for instrument response. As such, they represent the signals as presented to the recorder; after having passed from the ground motion through the system transfer functions. The long-period vertical data of 6 July 1970 from figure 55, uncorrected for instrument response, are shown in figures 57 and 58. The uncorrected long-period horizontal data of 6 July 1970 from figure 56 are shown in figures 59 and 60. These four figures also contain instrument noise spectra,

NOISE

3841 SAMPLES, 256 LAGS, 2.0 SPS, PARZEN SMOOTHING

GC-AZ

29 OCTOBER 1970

+ PZL-E

* PZL-M

1.0000E+00

1.0000E+00

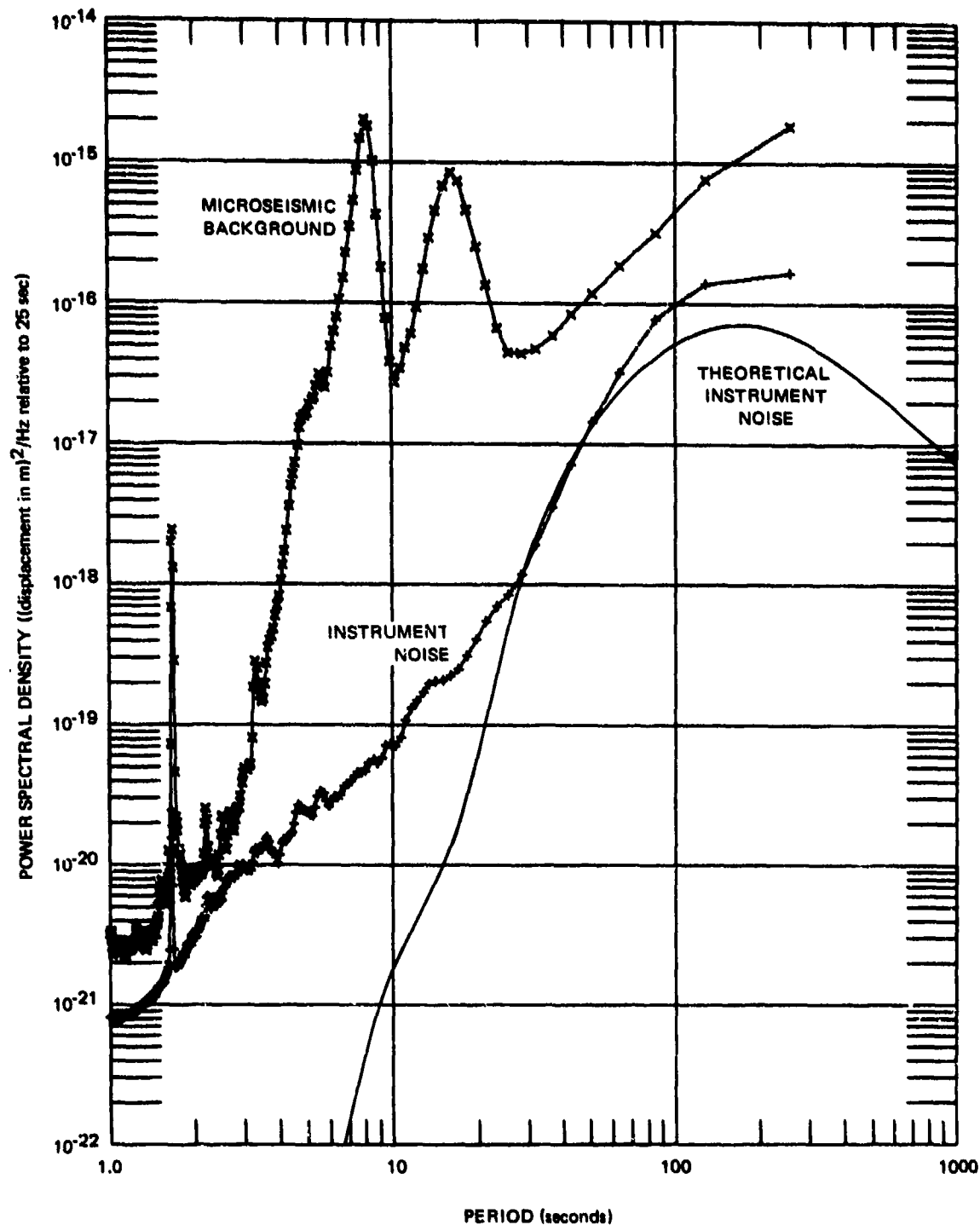


Figure 57. PZL microseismic background and instrument noise spectra, 1 to 256 sec

G 6653

NOISE

2410 SAMPLES, 128 LAGS, 0.1 SPS, PARZEN SMOOTHING

GC-A2

6 JULY 1970

* PZL-E

* PZL-M

1.0000E+00

1.0000E+00

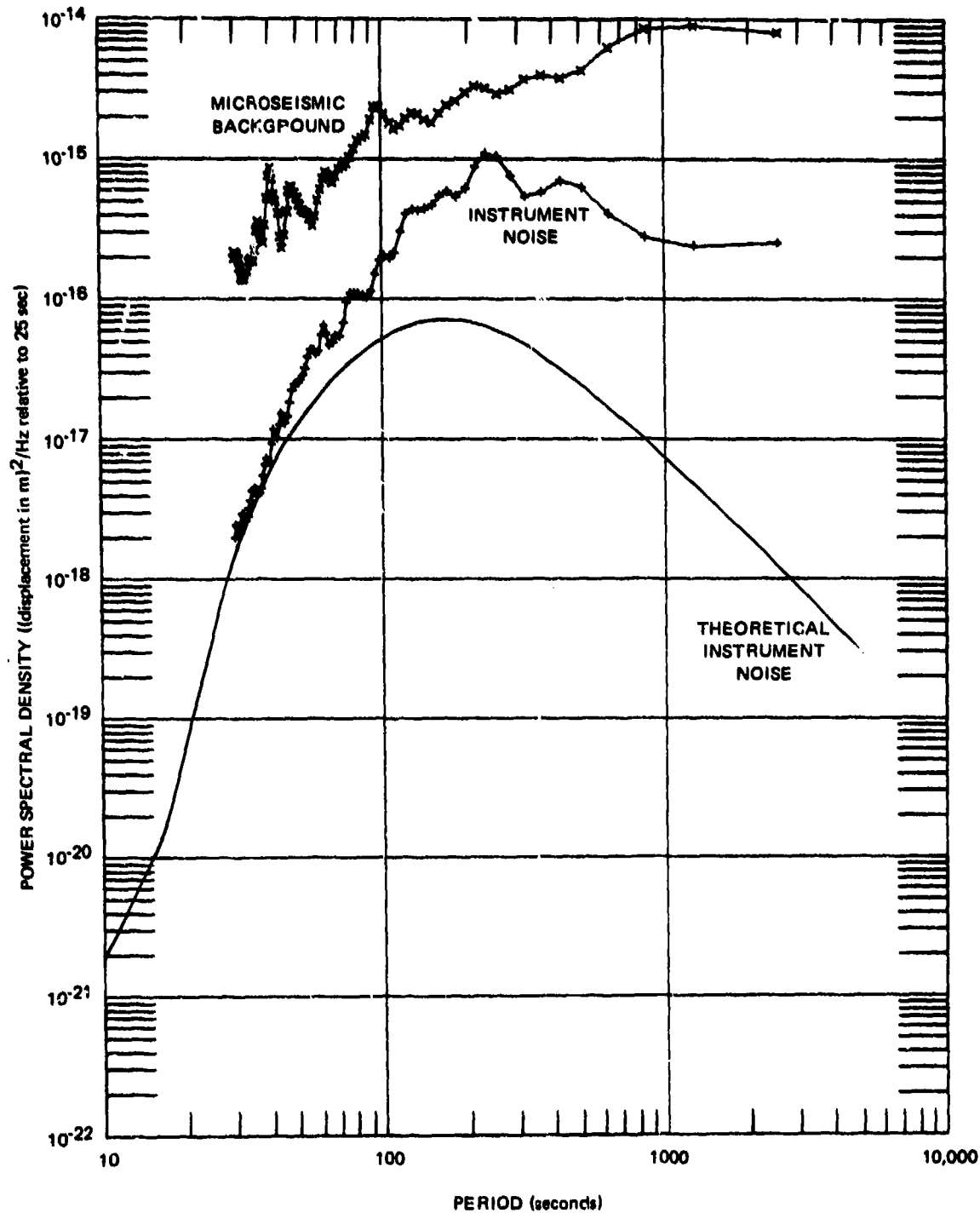


Figure 58. PZL microseismic background and instrument noise spectra, 30 to 2560 sec

G 6654

NOISE

3841 SAMPLES, 256 LAGS, 2.0 SPS, PARZEN SMOOTHING

DC-AZ

6 JULY 1970

♦ P55L-E

* P55L-M

1.0000E+00

1.0000E+00

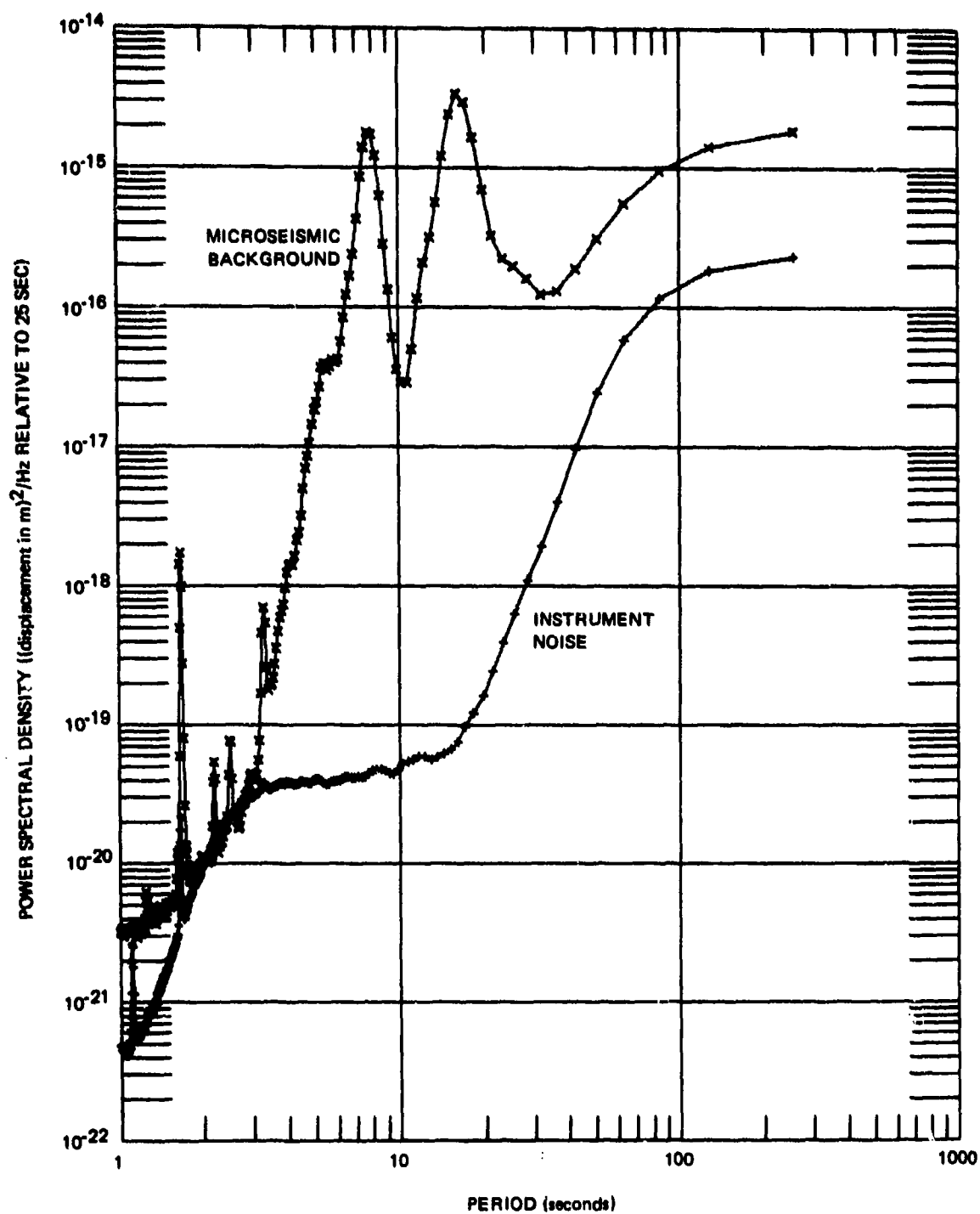


Figure 59. P55L microseismic background and instrument noise spectra, 1 to 256 sec

G 6293

NOISE

1937 SAMPLES, 128 LAGS, 0.1 SPS, PARZEN SMOOTHING

QC-AZ

6 JULY 1970

+ P55L-E

* P55L-M

1.0000E+00

1.0000E+00

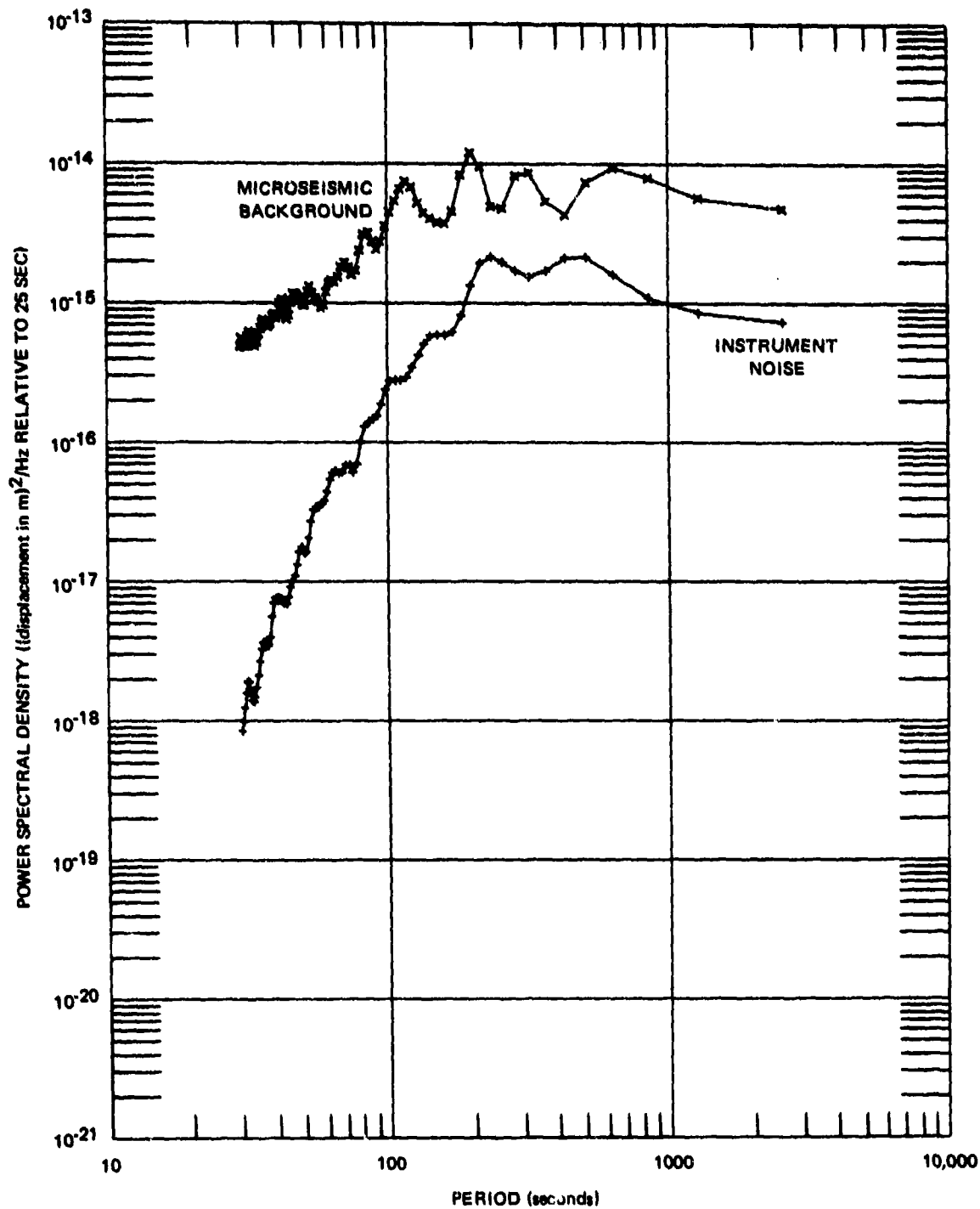


Figure 60. P55L microseismic background and instrument noise spectra, 30 to 2560 sec

G 6294

which will be discussed in the next section. The following figures also contain the background strain signals. The strain power spectral densities have been normalized to the displacement power spectral densities in accord with an empirical normalization to equalize Rayleigh wave signals. The normalizations, shown on each figure, are as follows:

<u>Component</u>	<u>Strain squared per Hz relative to 25 sec</u>	<u>Displacement (m) squared per Hz relative to 25 sec</u>
Vertical	5.44×10^{-24}	1.0×10^{-14}
325 azimuth	6.74×10^{-24}	1.0×10^{-14}
55 azimuth	9.88×10^{-24}	1.0×10^{-14}

The significance of these normalizations will be discussed in sections 9.3 and 12.2. The strain noise will be discussed in section 7.4. This section is concerned with the displacement microseismic background as observed on the inertial seismographs.

Certain parts of the last four and the following figures will be of interest to the reader:

- a. The value of the spectra at the 8 sec microseismic peak;
- b. The relative value of the 8 sec and 16 sec spectral peaks;
- c. The value of the spectra at the 20 to 40 sec minimum;
- d. The value of the spectra at periods greater than 80 sec; and
- e. The relative values of all the above between the vertical and the two horizontal components.

Figures 61, 62, and 63 are from 29 August 1970 during a quiet background sample. The 8 sec microseisms are larger than on 6 July, the 16 sec microseisms are larger than the 8 sec, the noise minimum has a larger value, and there is more energy at the longer periods. The shape of the spectra at the longer periods suggests the possibility of atmospheric pressure generated noise (see section 7.6) that is independent of surface wind velocity. The strain spectra reinforce this interpretation.

Figures 64, 65, and 66 are from 31 October 1970. In comparison with the spectra from 29 August, the 8 sec microseisms have increased by a factor of 10 in power. The 16 sec microseisms are about the same value. The spectral minimum is lower on the vertical and about the same on the horizontals, and there is less energy at the longer periods on both the inertial and strain seismographs.

MICROSEISMIC BACKGROUND

3841 SAMPLES, 256 LAGS, 2.0 SPS, PARZEN SMOOTHING

QC-AZ
29 AUGUST 1970
0438/0510

+ SZL
* PZL

5.4400E-24
1.0000E-14

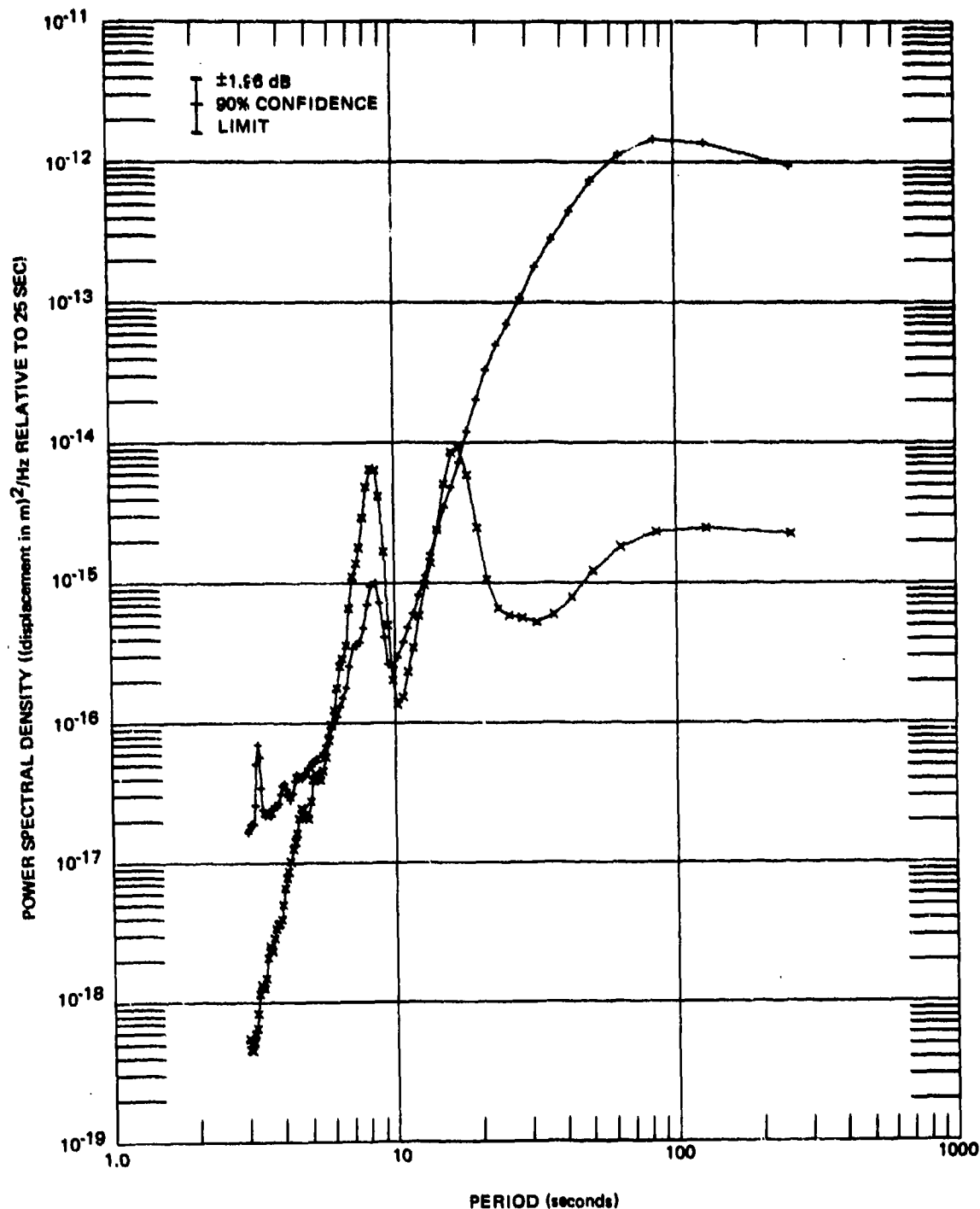


Figure 61. Power spectral density of microseismic background recorded on PZL and SZL seismographs on 29 August 1970.

G 6348

MICROSEISMIC BACKGROUND

3841 SAMPLES, 256 LAGS, 2.0 SPS, PARZEN SMOOTHING

QC-A2

29 AUGUST 1970

0438/0510

+ S325L

* P325L

6.7400E-24

1.0000E-14

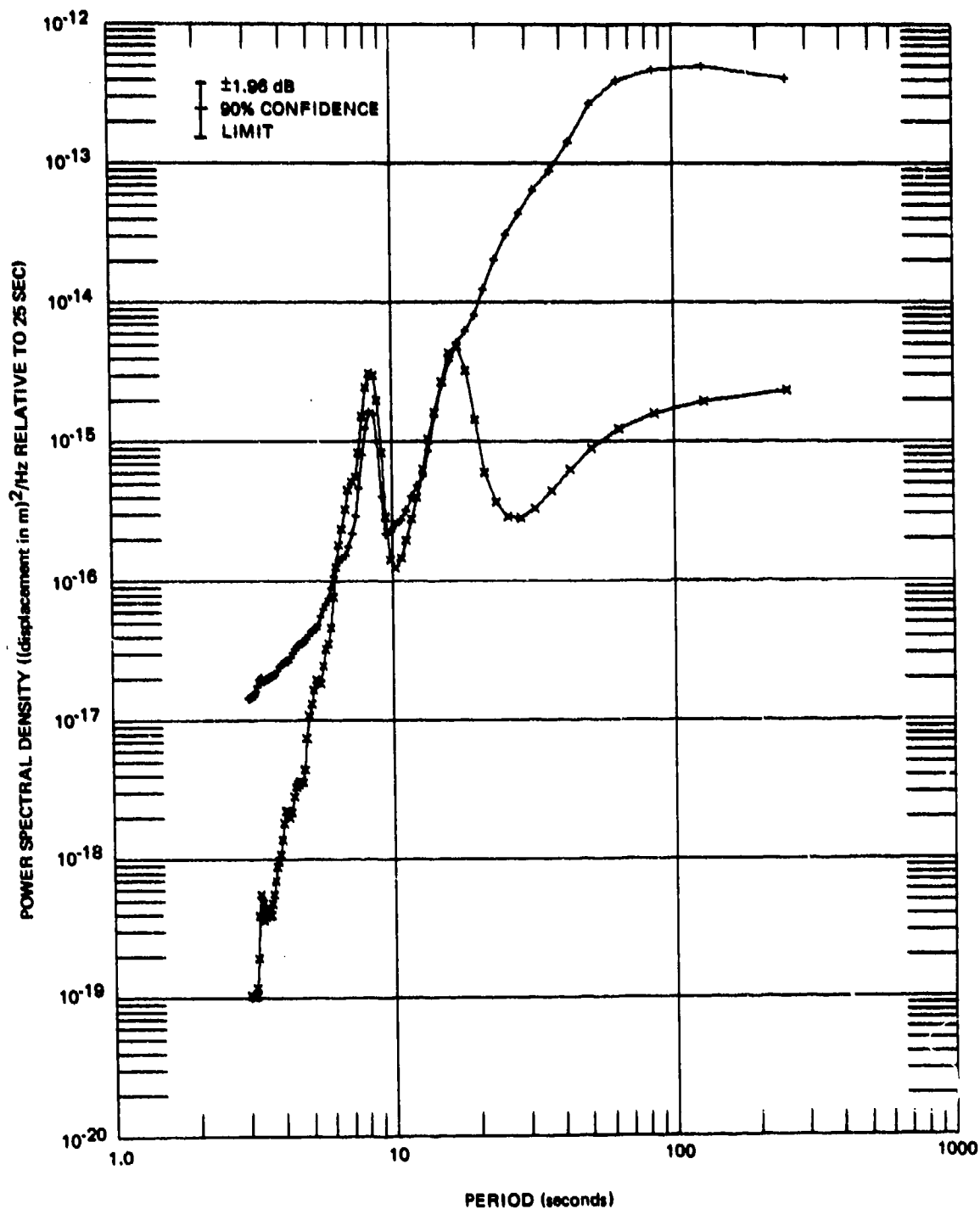


Figure 62. Power spectral density of microseismic background recorded on P325L and S325L seismographs on 29 August 1970.

G 6349

MICROSEISMIC BACKGROUND

3841 SAMPLES, 256 LAGS, 2.0 SPS, PARZEN SMOOTHING

QC-AZ
29 AUGUST 1970
0438/0510

+ S55L
* P55L

9.8800E-24
1.0000E-14

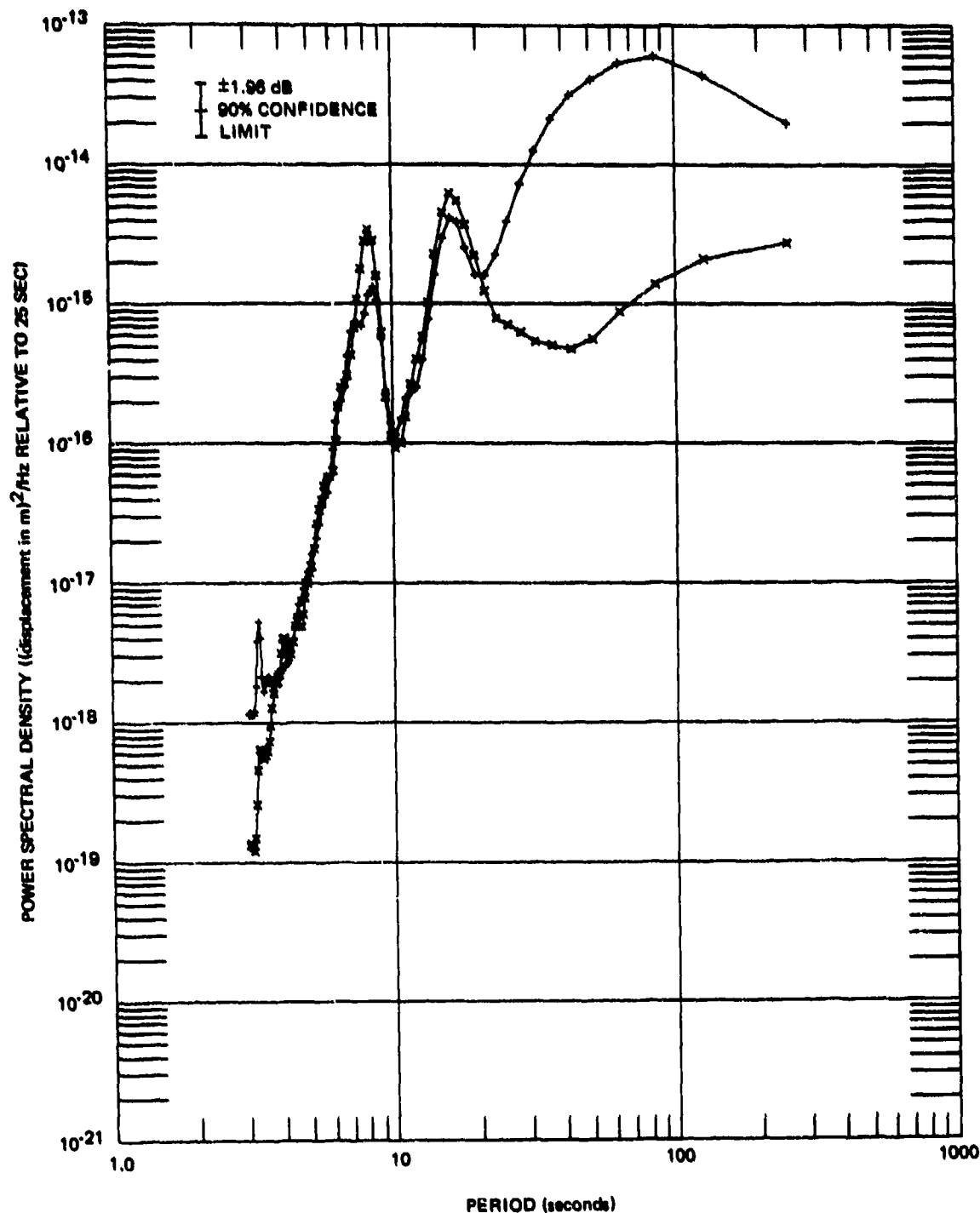


Figure 63. Power spectral density of microseismic background recorded on P55L and S55L seismographs on 29 August 1970.

G 6350

MICROSEISMIC BACKGROUND

3841 SAMPLES, 256 LAGS, 2.0 SPS, PARZEN SMOOTHING

GC-A2
31 OCTOBER 1970
0737/0809

+ SZL
x PZL

5.4400E-24
1.0000E-14

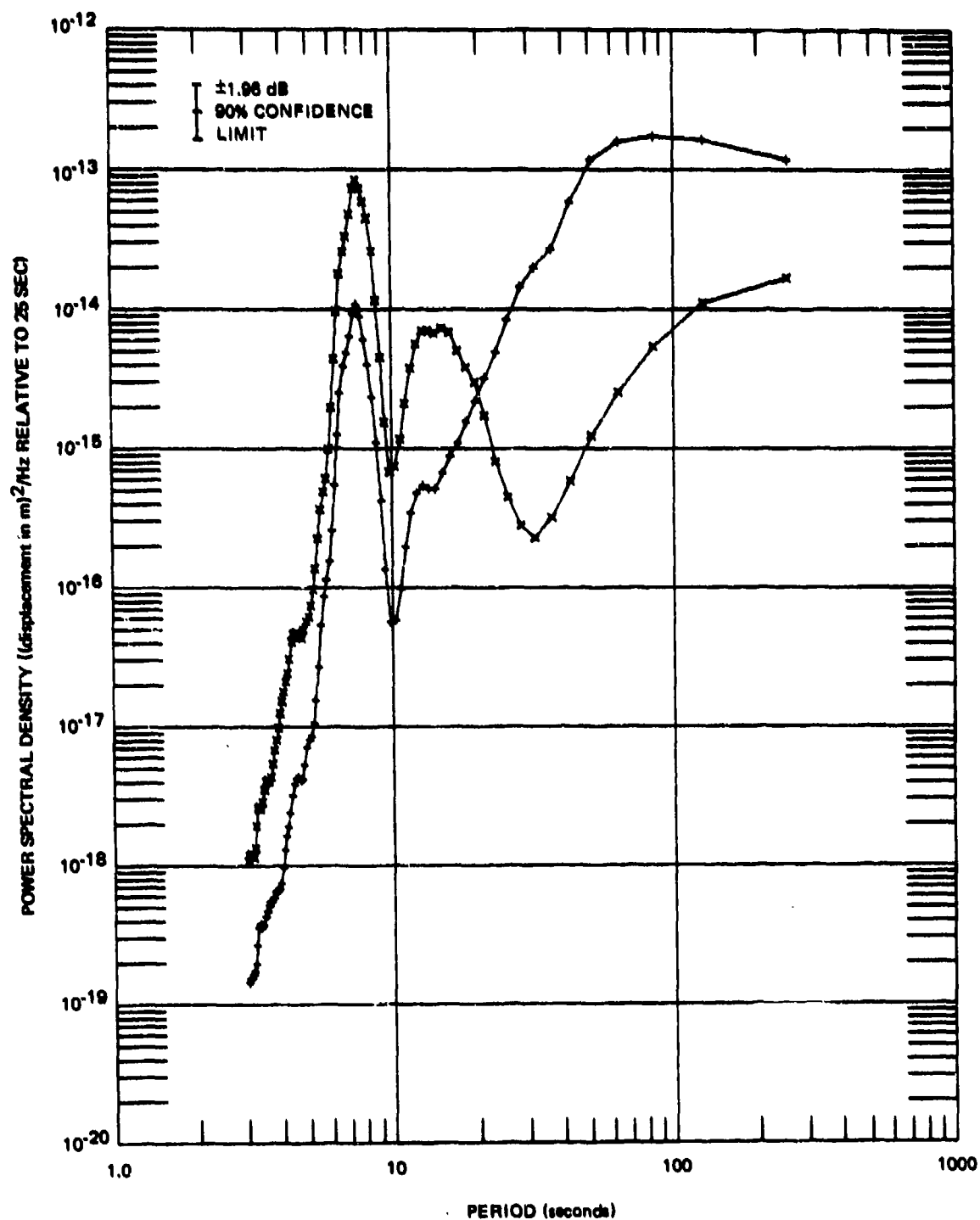


Figure 64. Power spectral density of microseismic background recorded on PZL and SZL seismographs on 31 October 1970.

G 4351

MICROSEISMIC BACKGROUND

3841 SAMPLES, 256 LAGS, 2.0 SPS, PARZEN SMOOTHING

QC-AZ
31 OCTOBER 1970
07370809

* S325L
* P325L

6.7400E-24
1.0000E-14

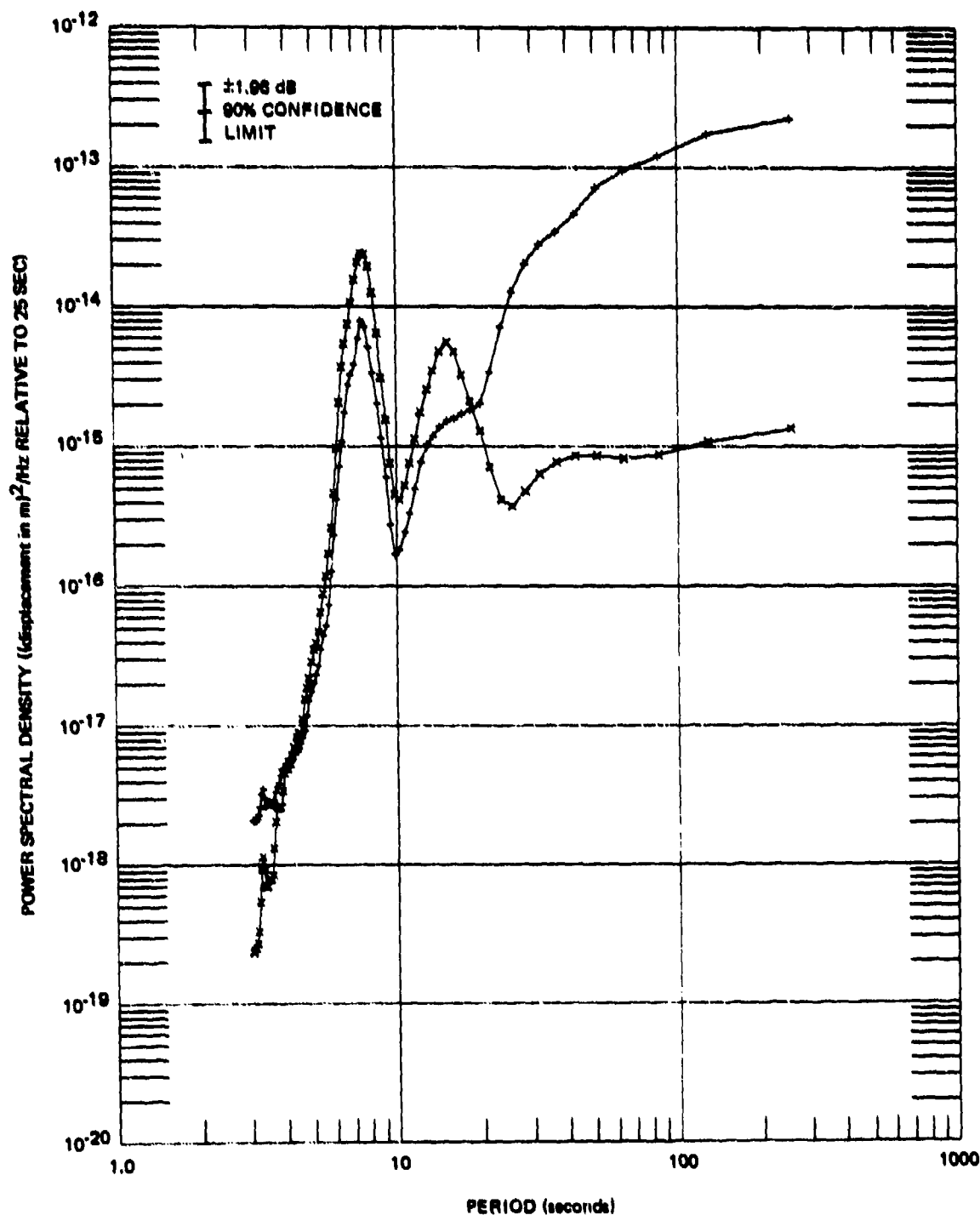


Figure 65. Power spectral density of microseismic background recorded on P325L and S325L seismographs on 31 October 1970.

0 0352

MICROSEISMIC BACKGROUND

3841 SAMPLES, 256 LAGS, 2.0 SPS, PARZEN SMOOTHING

QC-AZ
31 OCTOBER 1970
0737/0809

+ S55L
* P55L

9.8800E-24
1.0000E-14

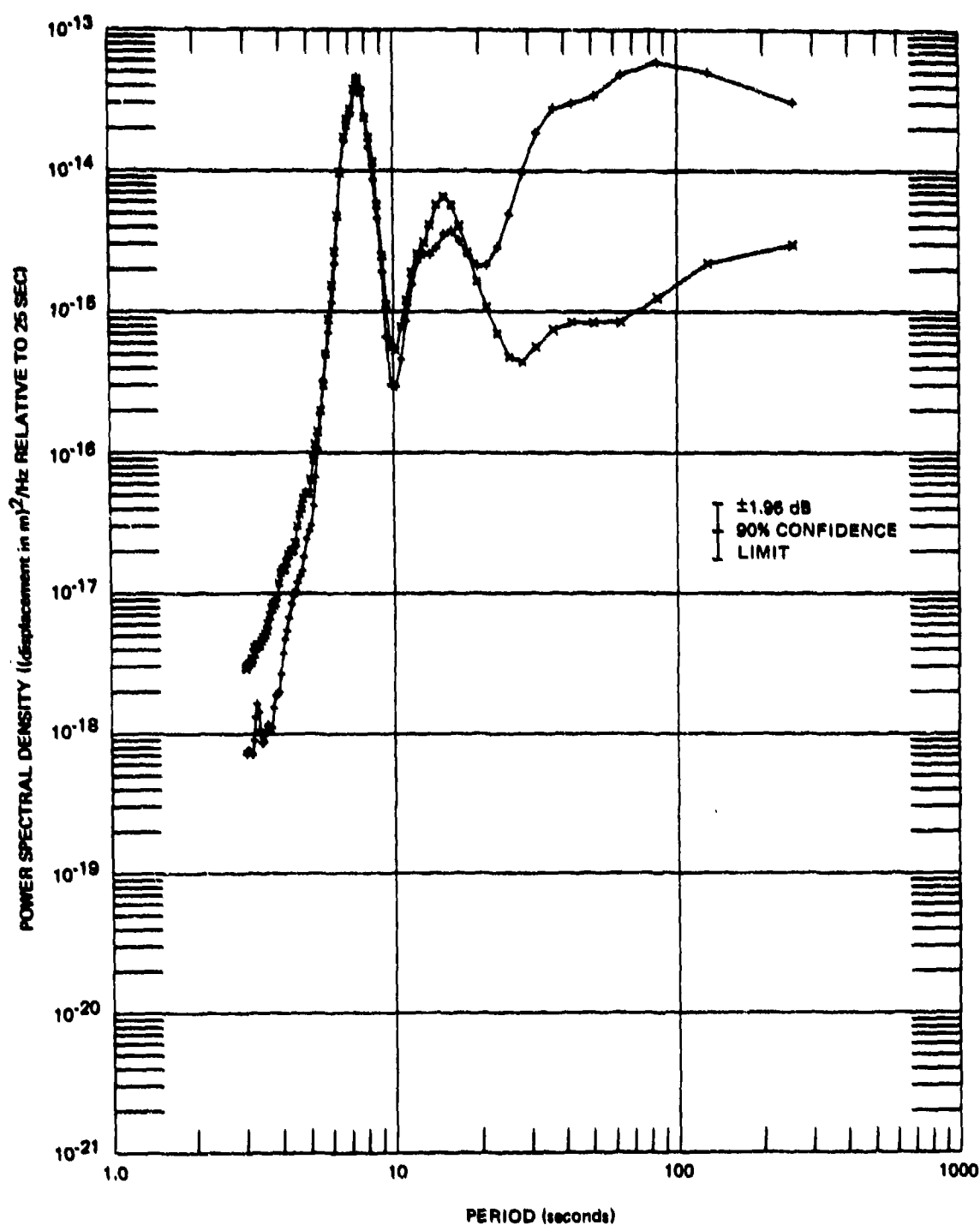


Figure 66. Power spectral density of microseismic background recorded on P55L and S55L seismographs on 31 October 1970.

G 6353

The spectra of data from 1 month later, on 1 December 1970 (figures 67, 68, and 69), are very similar to the spectra of 29 August except the 8 sec peak is higher.

The variation of the microseismic background with time can also be evaluated by comparing the total mean square signal presented to the recorders. The total mean square displacement and the total root mean square displacement in the 1 to 256 sec passband of the seismographs for the displacement spectra plotted in figures 57 through 69 are given in table 9. The displacements are given relative to a 25 sec period, because the spectra are calibrated at this period, but they are uncorrected for instrument response. The effect of the build-up of the 8 sec microseisms from summer to winter is clearly evident in the table and the suite of figures. The 8 sec microseisms increased about 17 dB from 6 July to 1 December but the 16 sec microseisms remained the same during this interval. The lack of change in the 16 sec microseisms suggests they are caused by a different mechanism than the 8 sec microseisms. The PZL vertical seismograph has a larger total displacement than either horizontal component for the 29 August, 31 October, and 1 December samples. This larger total amplitude is the result of larger amplitudes at 8 sec and at periods longer than 64 sec. The vertical component of a Rayleigh wave in an infinite half-space is 1.5 times larger than the horizontal component. The 8 sec microseisms are generally thought to be fundamental Rayleigh waves and a larger vertical amplitude is expected. Not much is known about the background noise energy at the longer periods, but it is thought to be the result of high altitude, high velocity acoustic waves. However, the relative amplitude between the vertical and horizontal inertial components does not rule out the possibility of residual spherical mode free oscillations of the earth excited by earthquakes that occurred well before the time interval analyzed.

7.3 INERTIAL SEISMOGRAPH THEORETICAL AND OBSERVED NOISE

Minimum seismograph signal-to-instrument noise (S/N) ratio is of interest in evaluating seismograph capabilities. This section presents spectra of microseismic background signal during a quiet time, of observed seismograph noise, and of theoretical seismograph noise. The spectra are presented both as they exist at the recorders and as equivalent ground displacement.

A quiet microseismic sample was taken on 6 July 1970. Three data sample lengths were used to get good spectral stability in the complete range of interest. These time samples were 32.0 min duration for all the spectra plotted from 1 to 1000 sec, 5.38 hr (5 hr 22 min 50 sec) duration for the microseismic background plotted from 10 to 10,000 sec, and 6.69 hr (6 hr 41 min 40 sec) duration for the electronic noise plotted from 10 to 10,000 sec. The microseismic background samples were selected during an interval of normal July microseismic activity. No earthquake activity was visible on the time traces during the 32.0 min sample, which was within the 5.38 hr sample. The 5.38 hr sample started in the tail end of a teleseismic Rayleigh wave and stopped at the P-wave arrival from another teleseism. One or two possible small (S/N ratio about 1.5) Rayleigh waves of short duration were also observed during this interval.

System noise data were obtained by replacing the inertial or strain seismometers with fixed resistors of the same value as the transducer coil resistance.

MICROSEISMIC BACKGROUND

3841 SAMPLES, 256 LAGS, 2.0 SPS, PARZEN SMOOTHING

QC-A2
1 DECEMBER 1970
0955/1027

+ SZL
* PZL

5.4400E-24
1.0000E-14

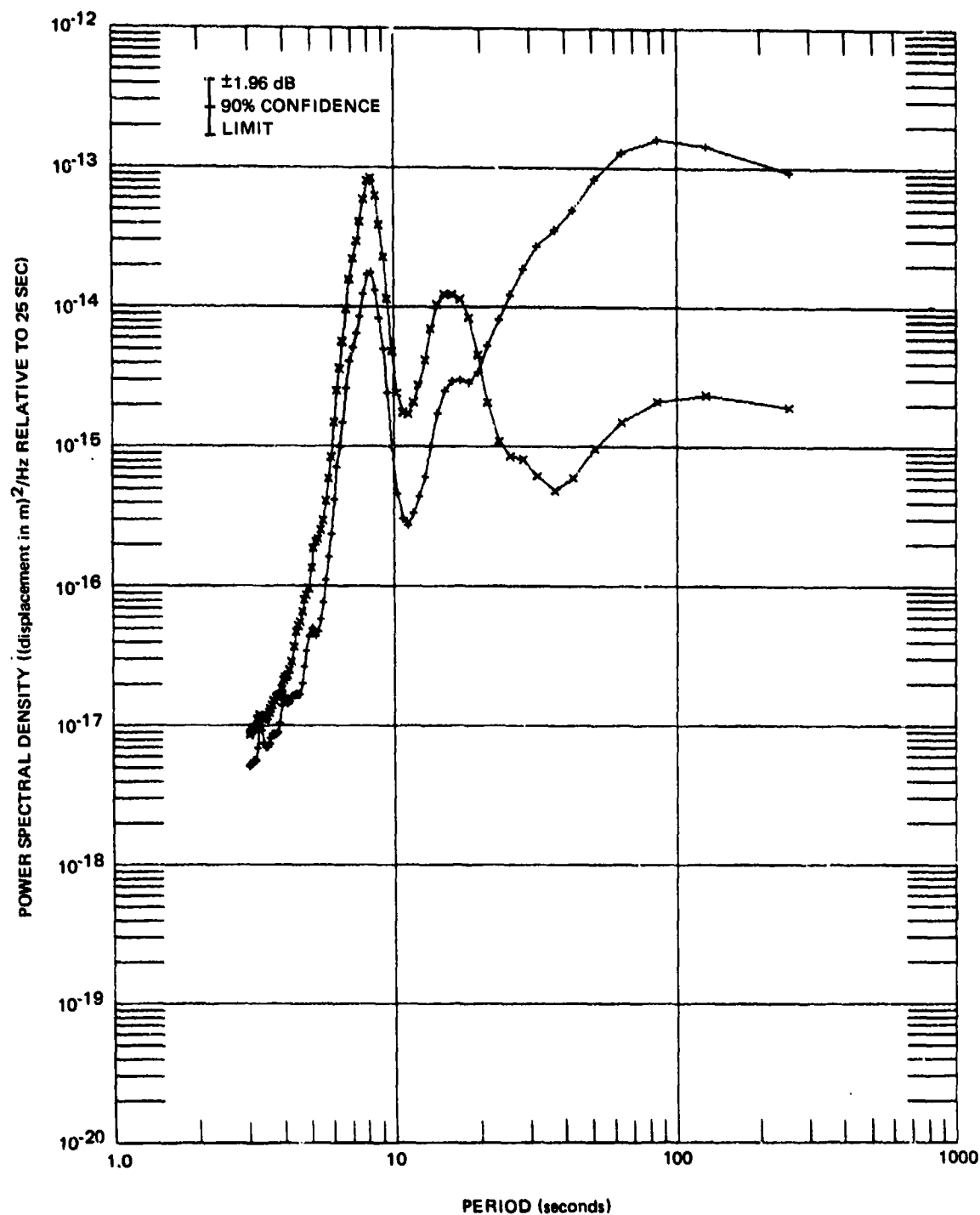


Figure 67. Power spectral density of microseismic background recorded on PZL and SZL seismographs on 1 December 1970.

G 6357

MICROSEISMIC BACKGROUND

3841 SAMPLES, 256 LAGS, 2.0 SPS, PARZEN SMOOTHING

QC-AZ

1 DECEMBER 1970

0955/1027

* S325L

* P325L

6.7400E-24

1.0000E-14

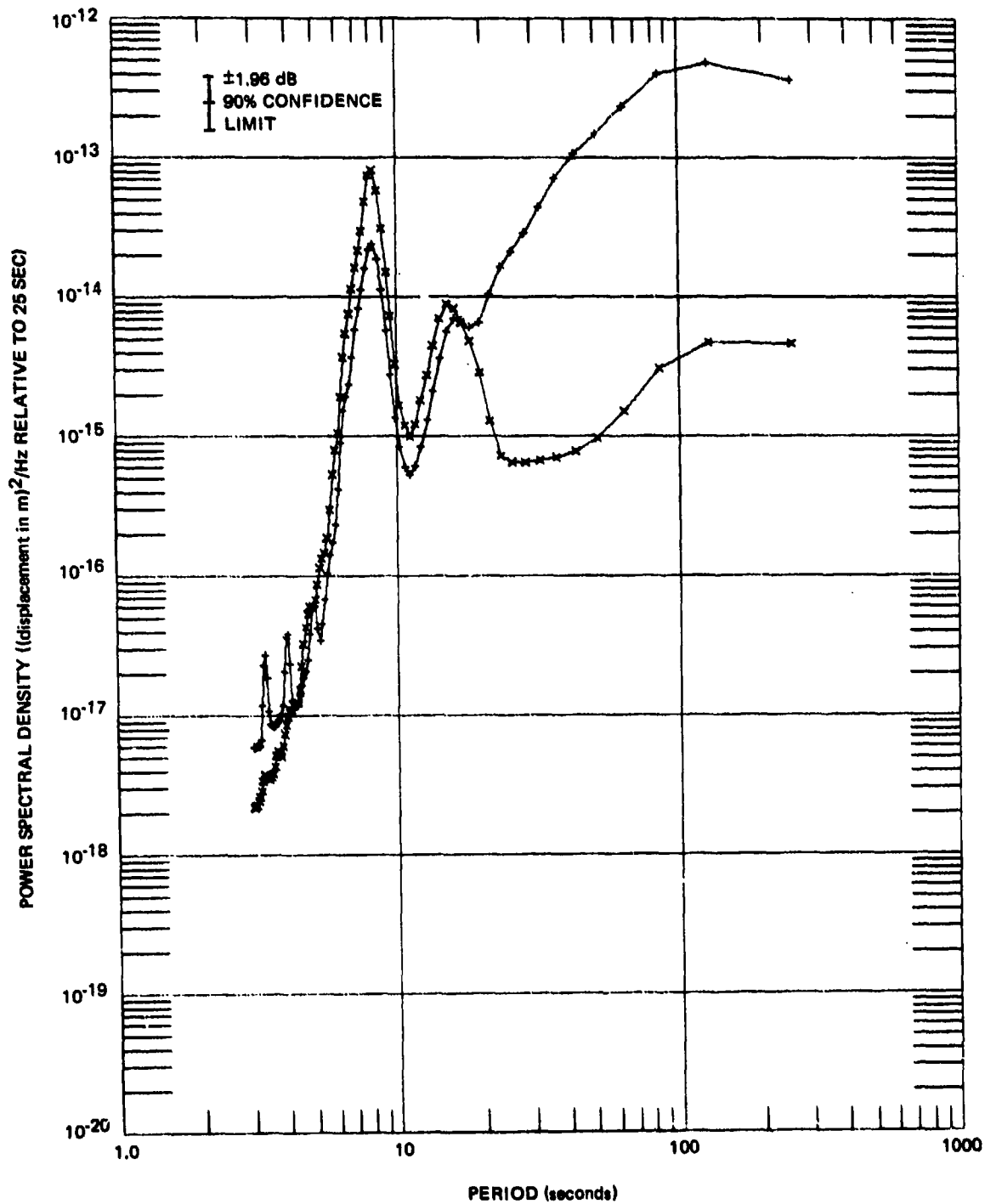


Figure 68. Power spectral density of microseismic background recorded on P325L and S325L seismographs on 1 December 1970.

G 6358

MICROSEISMIC BACKGROUND

3841 SAMPLES, 256 LAGS, 2.0 SPS, PARZEN SMOOTHING

QC-AZ
1 DECEMBER 1970
0955/1027

+ S55L
* P55L

9.8800E-24
1.0000E-14

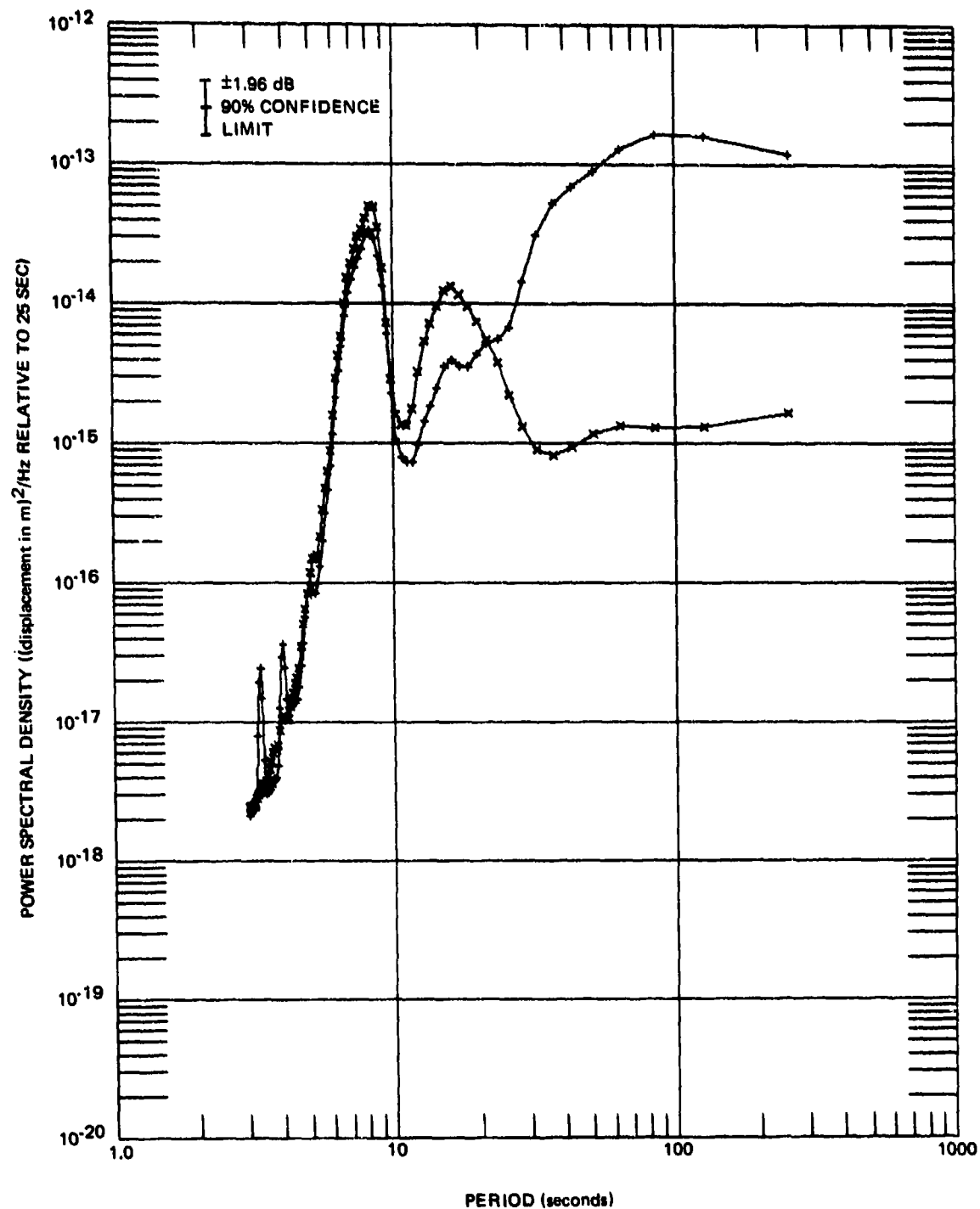


Figure 69. Power spectral density of microseismic background recorded on P55L and S55L seismographs on 1 December 1970.

G 6359

Table 9. Total mean square and total root-mean-square equivalent displacement in the passband 1 to 256 sec observed on inertial seismographs during quiet background samples. Seismographs are calibrated at 25 sec, but are uncorrected for system response.

<u>Date</u>	<u>Day</u>	<u>Seismograph</u>	Total mean square displacement 1 to 256 sec (m^2 relative to 25)	Total rms displacement 1 to 256 sec (m relative to 25 sec)	Spectra plotted in figure
6 July 1970	187	PZL P55L	7.45×10^{-17} 1.21×10^{-16}	8.63×10^{-9} 1.10×10^{-8}	57 59
29 August 1970	241	PZL P325L P55L	3.42×10^{-16} 1.97×10^{-16} 2.30×10^{-16}	1.85×10^{-8} 1.40×10^{-8} 1.52×10^{-8}	61 62 63
31 October 1970	304	PZL P325L P55L	3.50×10^{-15} 7.95×10^{-16} 9.15×10^{-16}	5.92×10^{-8} 2.82×10^{-8} 3.02×10^{-8}	64 65 66
1 December 1970	335	PZL P325L P55L	2.34×10^{-15} 1.94×10^{-15} 1.81×10^{-15}	4.84×10^{-8} 4.40×10^{-8} 4.25×10^{-8}	67 68 69

With single instruments, this technique is the simplest method of obtaining an estimate of the system noise spectra. Trott (1965), working with the present senior author, demonstrated that the same results could be obtained with the inertial LP seismographs by (1) bucking two identical seismographs, (2) very carefully blocking the moving mass of the seismometer, (3) replacing the seismometer with a coil wedged in a magnet oriented vertically, (4) replacing the seismometer with a coil wedged in a magnet oriented north-south, and (5) replacing the seismometer with a resistor. Since replacing the seismometer with a resistor is the easiest method, it is the preferred method and was used in this experiment. The theory as confirmed by the 1965 tests indicates that there is no significant contribution to the ALPS inertial noise spectra from the mechanical noise of the seismometer. The same conclusion may not be correct for the strain seismometer, its attachment to the rock, and the rock itself.

The spectra plotted in figures 57, 58, 59, and 60 have not been corrected for instrument response so that the actual minimum signal-to-instrument noise ratio can be observed. The spectra have been calibrated relative to ground displacement or ground strain at a 25 sec period. The spectra are presented for the vertical inertial LP seismograph PZL and the horizontal inertial LP seismograph P55L (oriented in a 55 deg azimuth). The P55L inertial seismograph is generally typical of the 325 deg azimuth instrument.

The spectra in figures 57 and 58 indicate that the S/N ratio on the PZL vertical inertial seismograph for this quiet microseismic background sample is a minimum of about 6 dB near 90 sec and near 300 sec and is 10 dB or better at all other periods from 3 to 2560 sec.

The spectra in figures 59 and 60 indicate that the S/N ratio on the P55L horizontal inertial seismograph is about the same as on the PZL. This ratio is about 6 dB from 250 to 500 sec and is 10 dB or better at all other periods. The instrument noise in figure 59 at periods shorter than 15 sec is dominated by magnetic-tape recorder noise and the antialias filter.

The theoretical noise spectra in figures 57 and 58 were calculated from a theory developed by Matheson and Gilbert of the National Bureau of Standards. This theory has only been published as an appendix to another related report (Trott, 1966). The derived equations were programmed by the present senior author, and the theoretical noise spectra were calculated using the parameters of the QC-AZ ALPS seismographs. The observed instrument noise presented here matches the theoretical noise almost perfectly for periods between 30 and 100 sec and is a good fit out to 2560 sec. At periods shorter than 30 sec, the recorder noise is beginning to contribute to the observed noise spectra. The fit between the theoretical and observed data is better than found by Trott (1965) in the Las Cruces experiment. The better fit is the result of using more accurate physical parameters for the theoretical calculations.

Another way of looking at the same S/N ratio is in terms of ground displacement. The spectra of figures 57, 58, 59, and 60 were interpreted as ground displacement as described in section 7.2. The vertical earth motion is plotted in figures 70 and 71, and the horizontal earth motion is plotted in figures 72 and 73. The Las Cruces, New Mexico, vertical data and the Ogdensburg, New Jersey, vertical and horizontal data were discussed in section 7.2 and are included in these figures for reference.

EARTH MOTION

3841 SAMPLES, 256 LAGS, 2.0 SPS, PARZEN SMOOTHING
 QC-AZ 6 JULY 1970 * P2L-M
 * P2L-E

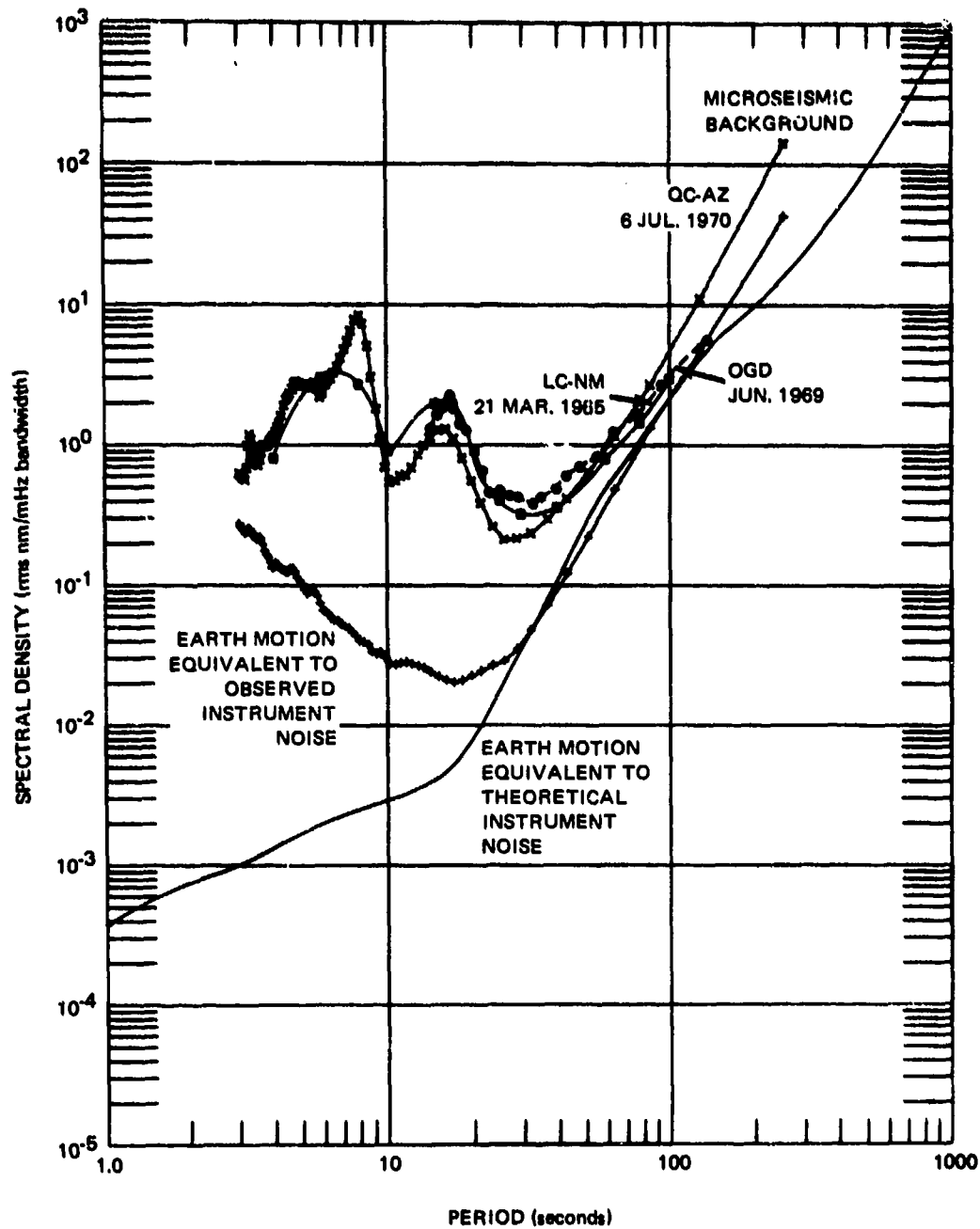


Figure 70. Vertical earth motion, 3 to 256 sec

G 6655

EARTH MOTION
 1937/2410 SAMPLES, 128 LAGS, 0.1 SPS, PARZEN SMOOTHING
 QC-A2
 6 JULY 1970

• P2L-M
 • P2L-E

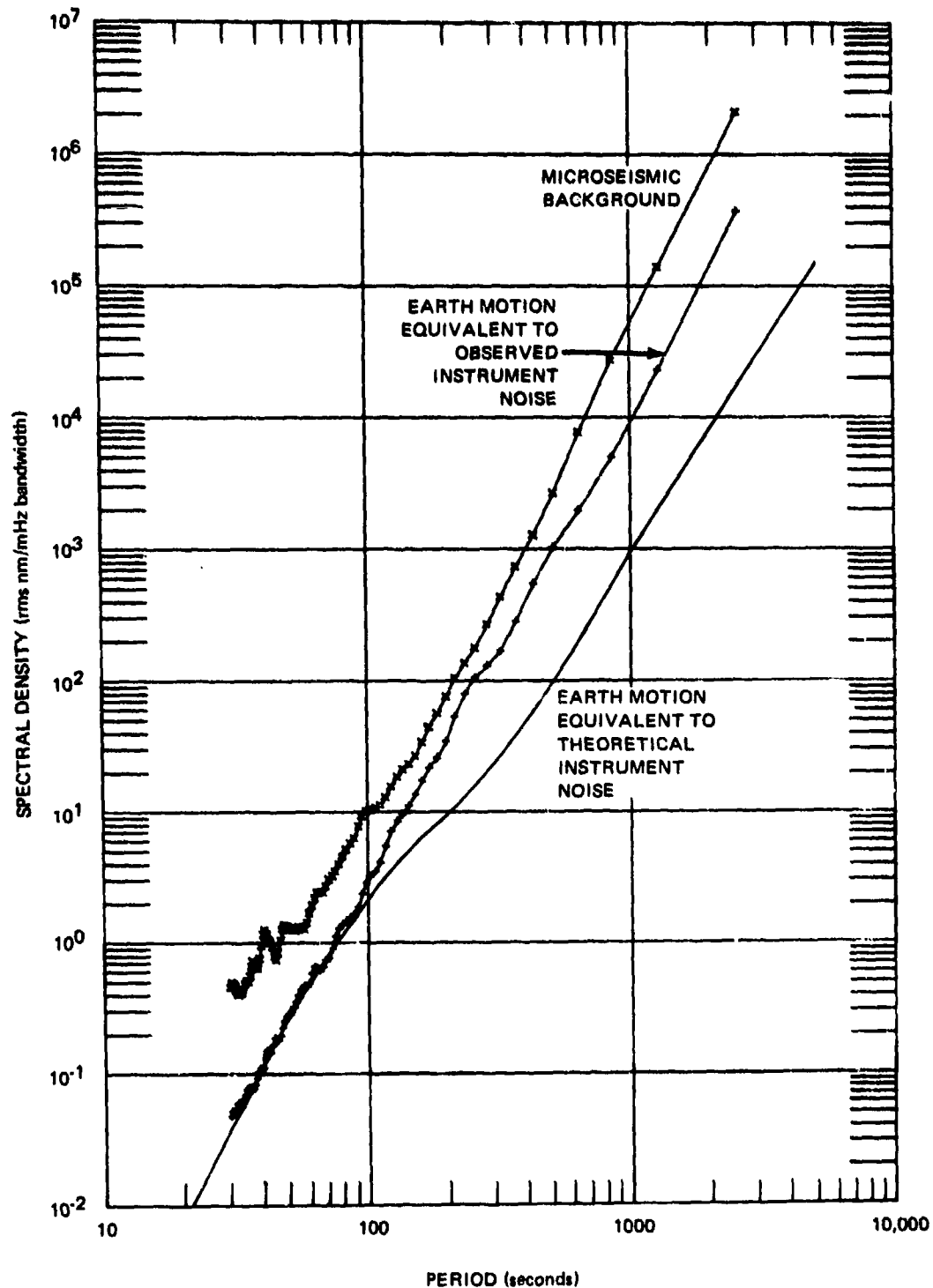


Figure 71. Vertical earth motion, 30 to 2560 sec

G 6656

EARTH MOTION

3841 SAMPLES, 256 LAGS, 2.0 SPS, PARZEN SMOOTHING

QC-AZ
6 JULY 1970

+ P55L-E
* P55L-M

1.0000E+00
1.0000E+00

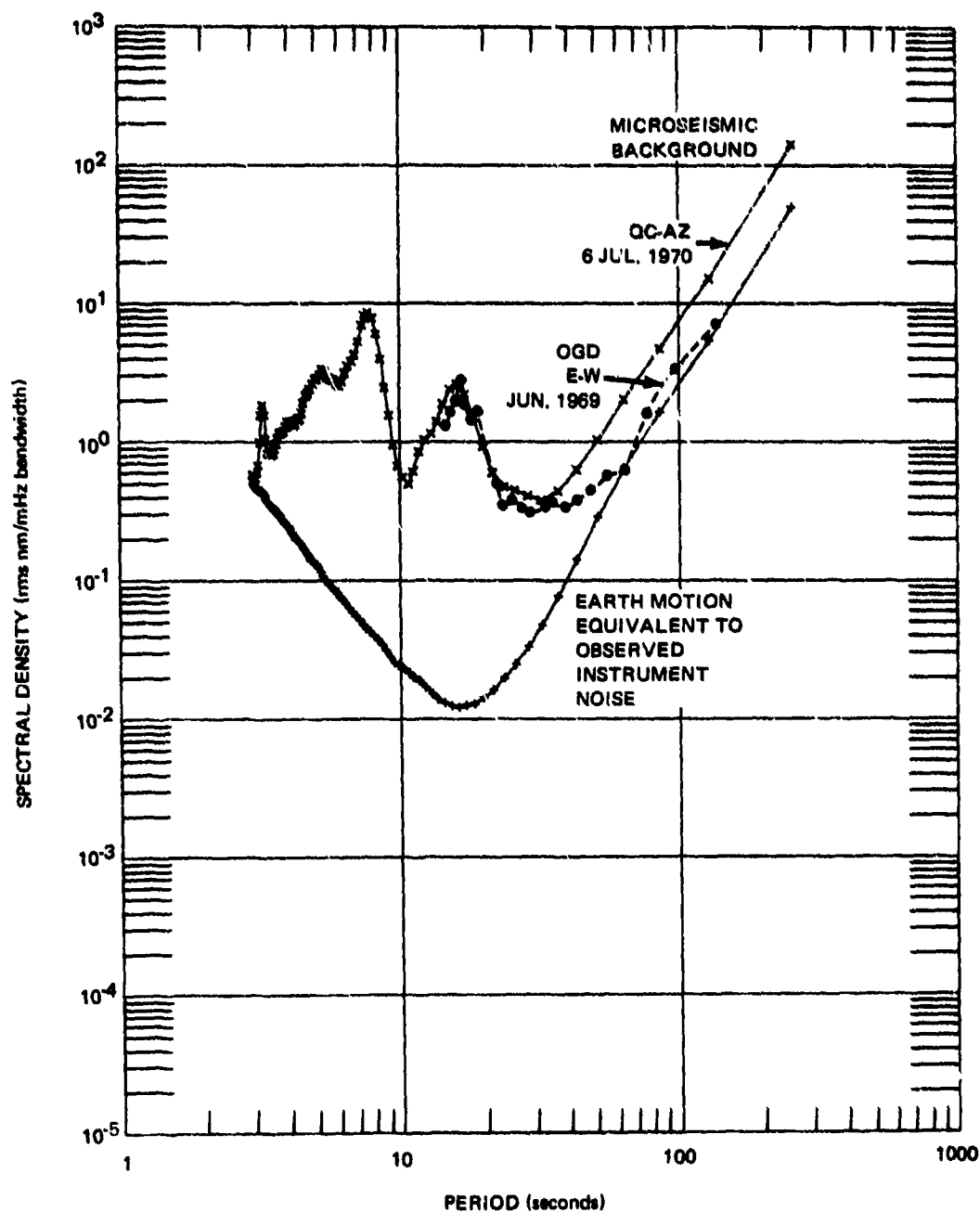


Figure 72. Horizontal Earth motion, 3 to 256 sec

G 6299

EARTH MOTION

1937 SAMPLES, 128 LAGS, 0.1 SPS, PARZEN SMOOTHING

DC-AZ
6 JULY 1970

* P55L-E
* P55L-M

1.0000E+00
1.0000E+00

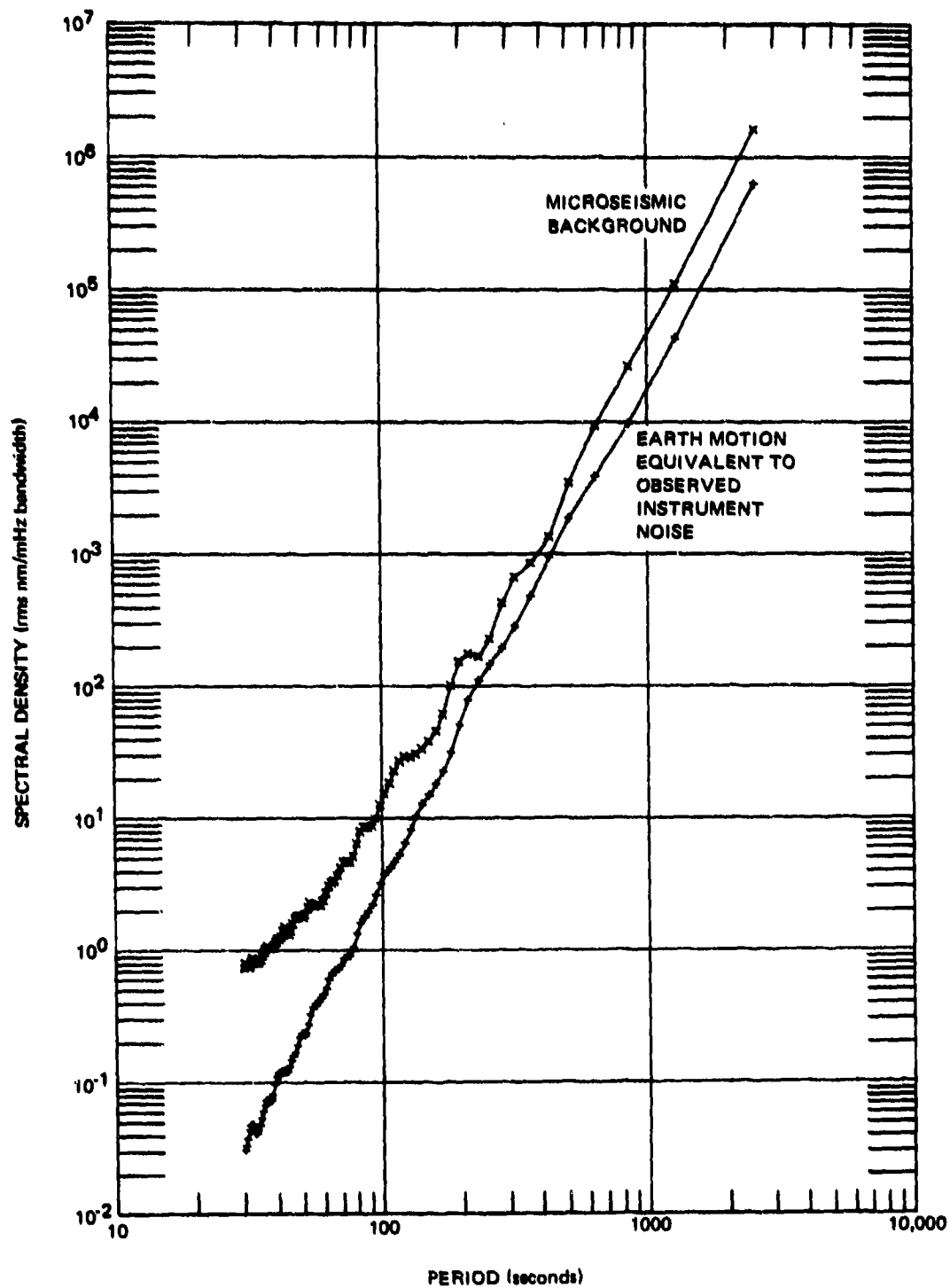


Figure 73. Horizontal Earth motion, 30 to 2560 sec

G 6300

In figures 70 through 73, the ground motion is seen to be sufficiently above instrument noise so as to confirm the existence of significant earth motion out to periods as long as 2560 sec (42.67 min). Because the signal-to-noise ratio is limited, the present analysis is not sufficient to describe the type of motion or to hypothesize on its source or character. However, the agreement between the LC-NM, the OGD, and the QC-AZ data indicates that this noise is probably always present.

7.4 STRAIN SEISMOGRAPH OBSERVED NOISE

Noise in the strain seismographs is more difficult to evaluate than in the inertial seismographs. Part of the noise can be attributed to the electronic components and part of the noise possibly can be attributed to the Brownian motion of the mechanical parts of the seismometer, to the mechanical suspension of the strain seismometers, to the mounting of the strain seismometers in the rock, to the small motions in the rock (and/or on the rock joints) in the very immediate vicinity of the mounting bolts, or to the general ambient strain background of the earth. The electronic noise can be easily evaluated by replacing the seismometer coil with a fixed resistor. Results of this test are discussed in section 7.4.1. Detectable small earth strains input to the seismographs and other system noise sources are discussed in section 7.4.2 and in section 7.5. The variation of the strain background noise with time is discussed in section 7.4.3.

7.4.1 Electronic Noise

The electronic noise contribution to the total strain seismograph noise was determined by replacing the seismometer coil with a fixed resistor. The power spectral density of this electronic noise is plotted in figure 74 as instrument noise. The power spectral density of the S55L strain seismograph for the 6 July 1970 quiet background sample is also plotted in figure 74. This quiet background sample is from the same time window as used for the inertial seismometers in figures 57 through 60 and 70 through 73. The electronic noise spectra of all three strain seismographs is similar to the S55L instrument noise spectra in figure 74. The quiet background signal-to-electronic noise ratio is about 6 dB at periods greater than 20 sec.

7.4.2 Other Strain Seismograph Noise

In addition to the electronic noise, there are other mechanisms that can create noise in the strain seismographs. Among these mechanisms are:

- (1) The Brownian motion of the rock in the vicinity of the seismometer piers,
- (2) The Brownian motion of the mechanical parts of the seismometer suspension,
- (3) The mechanical stability of the magnetic domains in the transducer,
- (4) The mechanical suspension of the strain seismometers,

NOISE

3841 SAMPLES, 256 LAGS, 2.0 SPS, PARZEN SMOOTHING

GC-AZ

6 JULY 1970

+ S55L-E
* S55L-M

1.0000E+00
1.0000E+00

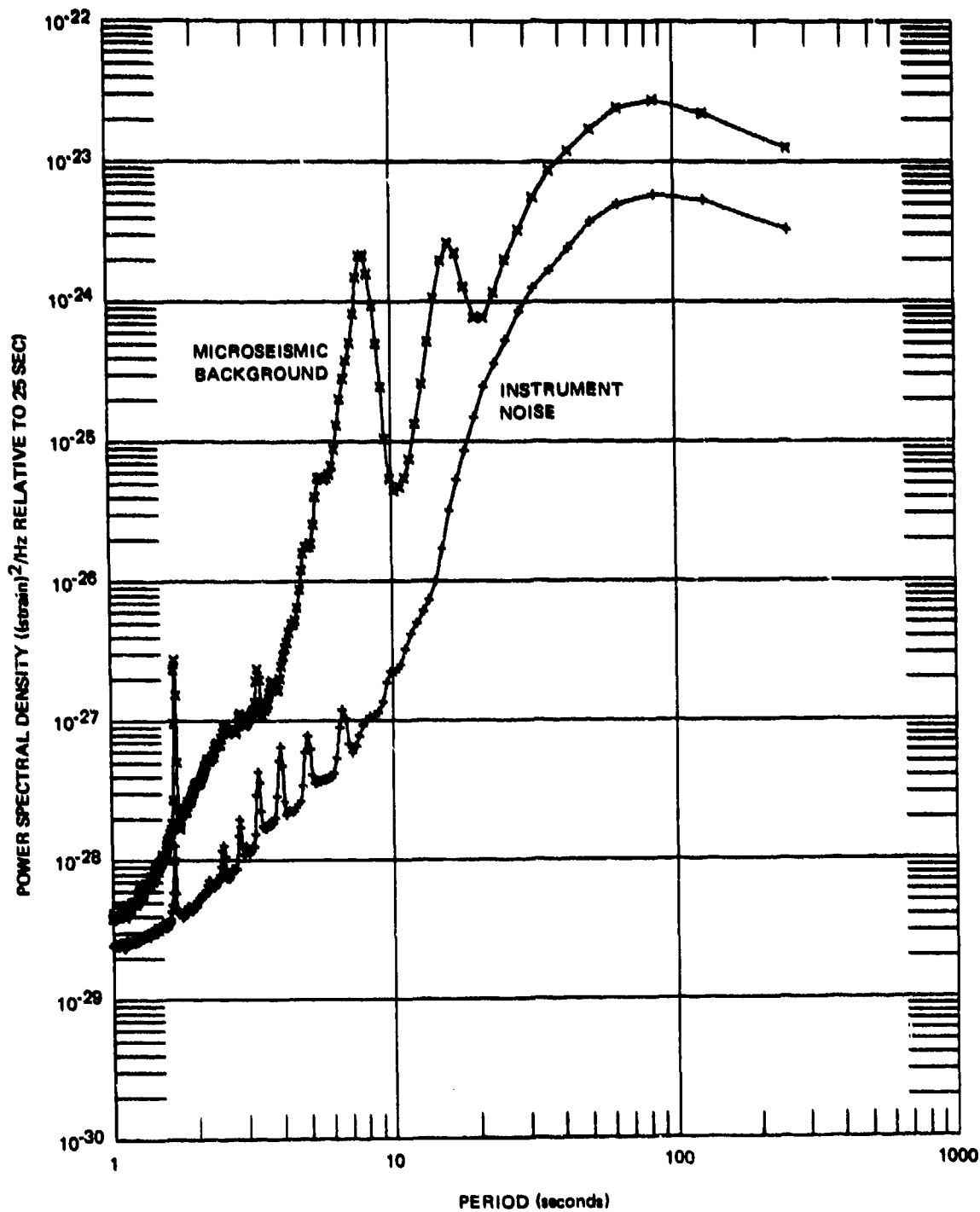


Figure 74. S55L microseismic background and instrument noise spectra, 1 to 256 sec

G 6295

(5) Small motions in the rock or on the rock joints in the immediate vicinity of the seismometer piers,

(6) Dislocations propagating through the rock or along joints in the rock,

(7) Natural electromagnetic variations whose flux density variation is superimposed on the 1.2T of the permanent magnet,

(8) Temperature fluctuations of the strain rods and of the rock in the seismometer chamber, and

(9) Air currents acting directly on the strain rods.

Most of these sources of noise cannot be evaluated individually and can only be considered collectively. From March through most of June 1970, two strain seismographs S325L1 and S325L2 were operated next to each other in the 325 deg azimuth tunnel. (See figure 45.) The centerline separation was about 0.7 m (28 in.). The two auto-power spectral densities (PSD) and cross power spectral density (XPSD) of the S325L1 and S325L2 seismographs are plotted in figure 75 for a quiet background sample. The two PSD are identical at the 8 sec microseismic peak and they differ somewhat at the longer periods. The cross power spectral density can be considered as the true seismic strain signal coming out of the ground. At 20 sec and longer periods, the XPSD in figure 75 is a factor of about 16 in power (4 in amplitude) above the electronic instrument noise PSD, as plotted in figure 74. The 12 dB S/N ratio further confirms that the XPSD is coherent strain coming from the ground.

This coherent strain signal will include the ambient strain unrest of earth plus some rock strain noises that are coherent in the 1 m x 40 m dimensions of the mounting of the two strain seismometers. These noises could be the coherent part of the Brownian motion of the rock, (1) above; small motions in the rock, (5) above; natural electromagnetic variations, (7) above; and possibly temperature fluctuations of the strain rods or the rock.

Because of the temperature stability of the seismometer chamber and because the strain rods are well insulated to reduce temperature fluctuations within the passband of the seismographs, it is unlikely that temperature effects are significant in the coherent power of the XPSD.

Geomagnetic fluctuations are a possible source of extraneous noise on the strain seismographs. The geomagnetic field will add vectorially to the static magnetic field in the strain transducer. As the geomagnetic field varies, the lines of flux cut the wire in transducer coils. Since the transducer coils have about 31,000 turns of wire, and since the preamplifiers have a low noise threshold, the sensitivity to the rate-of-change of geomagnetic fluctuation is about 0.06 gamma/sec in an octave centered at 100 sec and about 0.2 gamma/sec in an octave centered at 20 sec. While these flux change rates are within the values expected for geomagnetic fluctuations of this period range (Maple, 1959a, b; Benioff, 1960; Fernando and Kannangara, 1966; Stening and Gupta, 1971; Gupta et al. 1971; Sen, 1971; and others) no positive correlation could be established. Benioff (1960) and Fernando and Kannangara (1966) used horizontal coils to sense the geomagnetic fluctuations. Maximum signal was

MICROSEISMIC BACKGROUND

2841 SAMPLES, 256 LAGS, 2.0 SP5, PARZEN SMOOTHING

GC-AZ
11 JUNE 1970
1309/1341

* S325L1
x S325L2
v S325L1 X S325L2

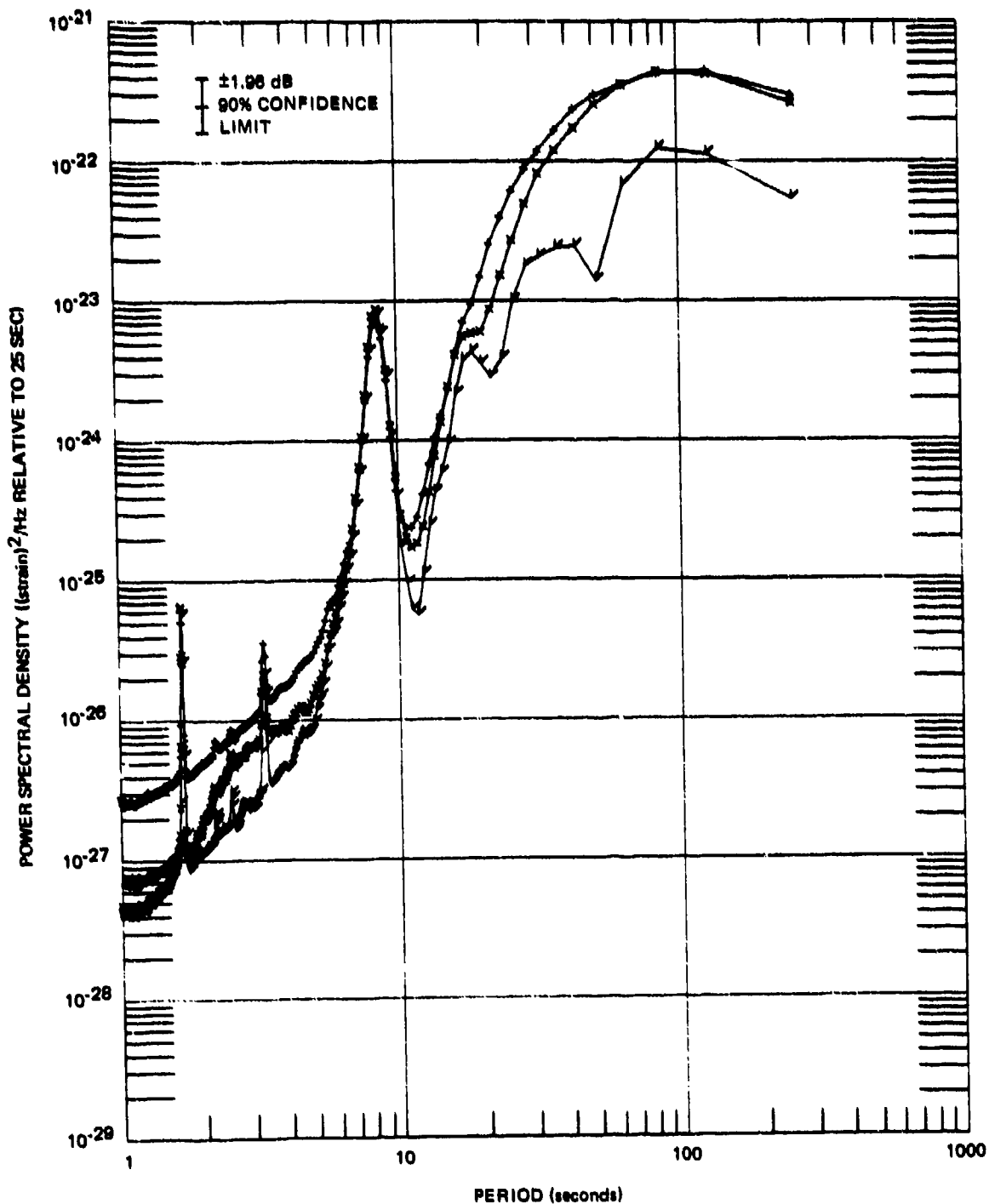


Figure 75. Power spectral density and cross power spectral density of microseismic background recorded on parallel seismographs S325L1 and S325L2 on 11 June 1970.

© 6360

obtained with the axis of the coil parallel to the local magnetic meridian. At QC-AZ the magnetic meridian is 14 deg east of north. This gives angles of 49 deg to the 325 deg azimuth and 41 deg to the 55 deg azimuth. The geomagnetic latitude of QC-AZ is between 40 and 45 deg. Therefore, all three strain transducers are at an angle of about 45 deg from the geomagnetic vector. Any magnetic variations that are aligned with the total field should be of about equal amplitude on all components. No visual correlation of unexplained noise was ever observed on all three strain seismographs simultaneously. During several nights in April and May 1971, large sinusoidal oscillations were observed on the S325L strain seismograph. These oscillations were generally 20 to 30 sec in period. On one occasion, the oscillations started with an 18 sec period and over about an hour interval increased to 180 sec period. Records from the National Ocean Survey (NOS) Tuscon magnetic observatory were obtained for this time, but no unusual activity could be noted on their records. (The time base of their recordings will not allow resolution of 180 sec waves.) During the S325L oscillations, the overall geomagnetic activity was low. It must then be assumed that in the absence of signal on the other two QC-AZ components and in the absence of magnetic disturbance at Tuscon, that the S325L oscillations were caused by some source other than magnetic fluctuations. To investigate the geomagnetic sensitivity further, the coils were disconnected from the strain rods for a few days. These tests were inconclusive because of the manner in which the coils were restrained from mechanical movement. The conclusion concerning strain seismograph noise caused by geomagnetic fluctuations is: The systems have sufficient sensitivity to sense the larger Pc3, Pc4, and Pi2 fluctuations, but no geomagnetic signals were identified in any of the recordings.

If we assume that neither temperature variations nor geomagnetic fluctuations contribute to the coherent XPSD in figure 75, then this motion must be true relative motion between the seismometer piers. This relative motion will include the ambient strain unrest of the earth plus random motion of the rock that is coherent in the dimension of the seismometer chamber.

During the course of the recordings from March 1970 through May 1971, the noise on the S55L seismograph remained relatively constant. On many occasions, the noise on the S325L seismograph would increase to a significantly greater value than on the S55L. When this noise would increase, considerable effort was expended verifying proper performance of the mechanical and electronic parts of the seismograph. The ultimate conclusion was that the noise was originating in random movements within the rock mass. These movements took place along the joints in the rock which were subparallel to the 325 deg azimuth and almost perpendicular to the 55 deg azimuth. Consequently, the 325 deg azimuth strainmeter was experiencing more noise from these motions. Small earth motions are discussed further in section 7.5.

7.4.3 Variation of Strain Background with Time

The variation with time of the ambient strain unrest of the earth is of interest in planning future high-sensitivity strain installations. Spectra for several days, taken from the three-components during quiet times, are plotted with the inertial seismograph spectra in figures 61 through 69. The strain spectra have been normalized to the displacement spectra as described in section 7.2 using the relative values given in the figures. These spectra are uncorrected for

system response but are calibrated at 25 sec. The total mean square strain and root mean square strain in the 1 to 256 sec passband of the seismographs for the strain spectra in figures 61 through 69 and 74 are given in table 10. The strains are given relative to a 25 sec period because the spectra are calibrated at this period, but they are uncorrected for instrument response. Comments regarding the displacement spectra were given in section 7.2. Additional comments on the strain spectra follow.

The strain spectra in figures 61 through 69 and in figure 74 are considered typical of quiet background strains. The strain spectra on 29 August 1970 are larger than during the other samples. The increased amplitude at periods longer than 20 sec is attributed to long-period acoustic waves that were loading the earth and creating strains that were detected on the strain seismographs. Air pressure loading is discussed in section 7.6. Even if the normalizations between displacement spectra and strain spectra are correct, the spectra will not necessarily overlay because of the difference in azimuthal response of the two classes of seismographs. (See section 9.) The 55 deg azimuth spectra in figures 66 and 69 indicate that a major portion of the 8 sec microseisms are traveling either in the 55 deg or 235 deg azimuths. Notice that relative to the displacement power the 16 sec microseismic peaks contain less strain power than the 8 sec peaks. This could mean that the direction of travel is different or that the phase velocity of the 16 sec microseisms is not equal to the phase velocity of the 8 sec microseisms. Since the strain amplitudes are lower at 16 sec, the phase velocity would have to be higher.

The strain spectra generally cross the displacement spectra at 20 to 30 sec and are larger at the longer periods. This is attributed to the true relative ground motion between the piers discussed in section 7.4.2 above. Referring to figure 66, for the purposes of discussion, it can be seen that the minimum in the microseismic background spectra between 20 and 70 sec is visible on the P55L displacement spectra. However, the strain spectra cross the displacement spectra and the minimum in the background is filled with strain power.

If the relative strain and displacement noise spectra are interpreted in terms of signals, it can be said that:

- (1) The two types of seismographs have the same noise field for enhancing long-period body waves, which generally have periods between 10 and 25 sec.

- (2) They have essentially the same noise field for the 20 to 30 sec Rayleigh wave Airy phase.

- (3) At periods longer than 30 sec, the detection capability of the strain seismographs is about 10 dB less than the inertial seismographs and the signal-to-noise ratio on the directional array formed by the sum and difference of the strain and inertial seismographs will be about 4 dB less than the individual inertial channel. (10 dB more noise - 6 dB more signal = 4 dB less S/N).

Even though the strain seismographs have more noise than the inertial seismographs at periods longer than 30 sec, their noise level is about 10 dB lower than the vertical noise background at the LASA based on the amplitude spectra calculated from Capon et al. (1969). The LASA spectra are plotted in figure 55 along with the amplitude spectra from QC-AZ. The following discussion compares the S/N ratios at QC-AZ and LASA where the LASA vertical microseismic background is taken from the spectra of Capon et al. This single set of LASA spectra is interpreted

Table 10. Total mean square and total root mean square equivalent strain in the passband 1 to 256 sec observed on strain seismographs during quiet background samples. Seismographs are calibrated at 25 sec, but are uncorrected for system response.

<u>Date</u>	<u>Day</u>	<u>Seismograph</u>	<u>Total mean square strain 1 to 256 sec (strain² relative to 25 sec)</u>	<u>Total rms strain 1 to 256 sec (strain relative to 25 sec)</u>	<u>Spectra plotted in figure no.</u>
29 Aug 1970	241	SZL	1.55×10^{-23}	3.90×10^{-12}	61
		S325L	7.05×10^{-24}	2.66×10^{-12}	62
		S55L	1.30×10^{-24}	1.14×10^{-12}	63
31 Oct 1970	304	SZL	2.09×10^{-24}	1.45×10^{-12}	64
		S325L	2.69×10^{-24}	1.64×10^{-12}	65
		S55L	2.38×10^{-24}	1.54×10^{-12}	66
1 Dec 1970	335	SZL	1.98×10^{-24}	1.41×10^{-12}	67
		S325L	5.94×10^{-24}	2.44×10^{-12}	68
		S55L	4.56×10^{-24}	2.14×10^{-12}	69
6 July 1970	187	S55L	6.40×10^{-25}	8.00×10^{-13}	74

by the present author as being typical for the LASA seismographs used in the S/N ratio studies of Capon et al. As such, it is indicative of typical conditions during that time interval and may or may not be typical of conditions at other times. At periods longer than 20 sec, the LASA amplitudes are about 20 dB larger than the QC-AZ amplitudes. By comparison, the S/N ratio of the QC-AZ directional array is at the worst only about 4 dB above the individual QC-AZ inertial seismograph. But, the LASA individual inertial seismograph is 20 dB above the QC-AZ individual inertial seismograph. The beam-formed LASA array provides an average 11 dB S/N ratio improvement (Capon et al., 1969). In the period range from 17 to 33 sec, the S/N ratio improvement is 15 to 20 dB; between 33 and 50 sec the improvement decreases to 0 dB and at 100 sec is -4 dB. The LASA beam width is not the same for longer period Rayleigh waves as it is for 6 to 8 sec microseisms. But, if it is assumed that the 11 dB S/N ratio improvement holds for all periods, then the detection threshold of the beam-formed LASA is about equal to or 5 dB less than an individual QC-AZ inertial seismograph at periods of 17 to 33 sec, 20 dB less at 50 sec, and 24 dB less at 100 sec. The detection threshold of the beam-formed LASA is 6 to 11 dB less than the QC-AZ directional array at periods of 17 to 33 sec, 26 dB less at 50 sec, and 30 dB less at 100 sec. Thus, the basic concept of beam forming at a single station has achieved better success than the 63 seismometer long-period LASA array.

7.5 SMALL EARTH MOTIONS

The high sensitivity of the QC-AZ instruments has permitted observation of motions of the earth that are smaller than previously detected at any other seismograph station. At times, these small motions have manifested themselves as noise on the seismographs, especially the strain seismographs. This section describes some of the observations and suggests several possible phenomena, all of which could be mechanisms that are contributing to the observed noise. It is felt by the authors that these motions are taking place along the joints and cracks in the rock.

7.5.1 Amplitude of Motions

During the early part of the recording interval, two strain seismographs were operated next to each other in the 325 deg azimuth tunnel (see figure 45). These two seismographs recorded signals identically, as will be shown in section 8.1. However, only part of the ambient background signal was identical.

To establish an order of magnitude of these small earth motions, consider the coherent energy on the two parallel seismographs. Figure 75 in section 7.4.2 shows the power spectral density of the individual S325L1 and S325L2 seismographs and of the cross power spectral density between them. At 100 sec, the coherent strain, as determined from the cross power spectral density, is 10^{-22} strain²/Hz. In an octave centered at 100 sec, the power is 6.7×10^{-25} strain²/octave at 100 sec. In this octave, the rms strain is about 8×10^{-12} . If we assume that all of this strain is generated by the random displacement of one pier while the second pier remains fixed, then this random pier displacement is about 3.2×10^{-10} m rms in the octave. This 3.2 Å displacement is of the order of the dimension of the molecules of the minerals in the rock. This motion applies to the coherent or identical part of the signal on both seismographs, which were separated by about 0.7 m. Very possibly, the additional energy seen in figure 75 to have a similarly shaped spectra on each of the individual seismographs could be random motion of the individual piers that was not coherent over the 0.7 m dimension. Displacements of 3.2 Å are below

the detection threshold of the inertial seismographs. Therefore, motions of this amplitude cannot be identified on the most sensitive inertial seismographs.

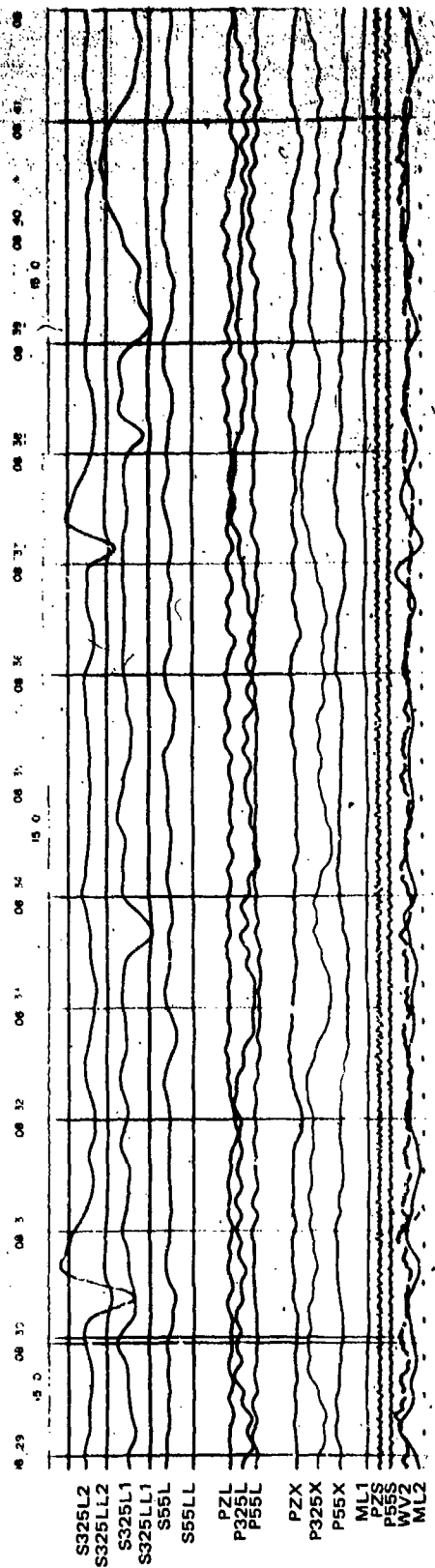
When motions are of the order of the dimension of an atom, many of the usual assumptions used in deriving equations for elastic wave propagation do not apply. In this dimensional scale, elasticity is dependent upon the elastic response of a group of crystals. An individual crystal is not homogeneous and isotropic in its elastic parameters, but a large group of crystals average out to be generally homogeneous, isotropic, and the elastic parameter tensor reduces to the two parameters λ and μ of Lamé. The 3.2 Å deflections of the strain seismometer pier mounts in the local rock are probably somewhere in between contact with a single crystal and contact with a large number of crystals. The exact response of the strain seismometer mounting response to earth strain inputs could only be tested by the parallel mounting of seismometers as described above.

The shape of the individual S325L1 and S325L2 power spectral density curves in figure 75 at periods longer than 25 sec is essentially the response of the strain seismographs. This output power then leads to the assumption that the input approximates a white random input having the same input power at all periods within the range of the analysis. It was shown in section 7.4 that this input is well above electronic noise and definitely an input from the ground. The white, random character of this input suggests it is related to atomic motions, possibly of a thermal agitation nature.

7.5.2 Traveling Dislocations

Some of the small motions appear to be traveling dislocations. Pulses of strain were often observed on one of the parallel strain seismographs followed after a period of time by pulses on the second parallel strain seismograph. An illustration of this effect is shown in figure 76.

The nomenclature "steps-of-strain" has been applied to similar phenomena in the literature. Observations of "steps-of-strain" at QC-AZ relative to signals are discussed in section 11. This section considers disturbances of this character in the concept of recurring noise of a much lower threshold than considered in section 11 and much smaller than detectable by previous investigators. The QC-AZ strain sensitivity of 2.5×10^{-13} is 1-1/2 to 2 orders of magnitude more sensitive than other strain seismographs on which steps have been observed (Wideman and Major, 1967; Press, 1965; and others). As a result, a clearer picture of the physical phenomena has been available. The pulses of strain observed have been compared to the theoretical response of the strain seismographs to various inputs. The conclusion of the senior author from this comparison is that the input is not a step of strain, but that it is a permanent strain offset whose time function is an exponential. The time constant of the exponential varies with each strain offset. The shape of the pulse as measured by the amplitude of the peaks and the time of the zero crossings varies from one pulse to another. The zero crossings are much later than obtained from the theoretical impulse or step input. Ramp time functions increasing linearly from zero to one in 10, 100, and 1000 sec were convolved with the impulse response of the strain seismograph and did not compare with the observations either. The ramp functions had a positive pulse at the beginning of the ramp and a negative pulse at the end of the ramp. Very few



QC-AZ
RUN 150
28 MAY 1970

Figure 76. Possible travelling dislocation recorded on S325L1 and S325L2

G 6657

sets of pulses were observed with different polarity on the same seismograph that would indicate a ramp function input. The only time function that approaches the observations is an exponential.

The time interval for apparent migration from one seismograph to the other varied from a few seconds to about 300 sec, with approximately 100 sec common. Dividing the 0.71 m seismometer spacing by 100 sec gives an apparent migration rate of 55 km/yr. This migration rate is comparable to the 80 km/yr obtained by Mogi (1968a) for earthquake migrations along the Anatolian Fault. It is also comparable to the 60 km/yr earthquake migration rate along the transform faults that bound the west coast of North America reported by Savage (1971). A 6.2 sec time interval gives a migration rate of 10 km/day. This rate, which is among the smallest observed at QC-AZ, is the rate observed by Nason (1969) for the propagation of an identifiable creep episode from one creep station to another along the San Andreas Fault. Mogi (1968a, 1968b) has reported migration rates for large earthquakes of 12 km/yr in Japan and 150 to 270 km/yr in the circumPacific belt. Major et al. (1971) have observed large strain-rate episodes in the Central Aleutian Islands. These typical strain rates are sustained for intervals of 15 to 30 hours, are observed at stations 330 km apart, and do not correlate with meteorologic phenomena. These significant deformations could be explained as migrating creep along a fault.

The concept of a dislocation flow or creep waves has only developed within the last few years. Only a few observations have been reported by Mogi (1968a, 1968b, 1968c, 1969a, 1969b, 1969c), Nason (1969), Savage (1971), Major et al. (1971), and in this report. Teisseyre (1966, 1967, 1970) and McGarr (1971a, 1971b) have treated crack formation and dislocation flow theoretically.

7.5.3 Other Small Motions

Variations in the ambient background strain field were observed from time to time during the recording interval. The S325 strain seismograph, which is subparallel to the joint structure of the rock, was the most sensitive to these variations; and when the ambient noise increased, it was the first to get noisy and it was disturbed the most.

Ambient noise was reduced by barring down the mine and ventilating for three days. At the recommendation of the Arizona State Mine Inspector, the mine was thoroughly barred down (all loose rocks were pried out and knocked down) and additional shoring was added under one large boulder near the winze. During the three days, between 15 and 17 February 1970, required for this work, the mine was ventilated. After completion of this mine sealing and ventilating, the background noise on all six LP seismographs returned to a normal state after a long interval of ever increasing noise. Apparently, the small motions along the cracks in the rocks had worked several rocks loose from the ceiling and walls so that their movements were more frequent and of a larger amplitude. During the barring down, the loose rocks were eliminated, and the small movements were greatly reduced in number and in amplitude.

The stagnation of water-saturated air within the mine appeared to increase the noise. When first located, the mine was completely dry. During the mine preparation phase, water was brought into the mine to use as a lubricant in drilling and to settle the dust in the air. Some of this water flowed into

the cracks and joints and they did not dry out before the mine was sealed. After the mine was sealed, the water vapor would saturate the air to 100 percent relative humidity. It was observed that for several days after the mine was ventilated and the saturated air was replaced with dry desert air, that the noise lessened. Originally, bags of desiccant were used to remove the water from the air. (About 8 kg of water is all that could be held in the saturated air at the mine temperature.) Drying the bags became a problem and an electrical dehumidifier was obtained and was operated intermittently. The use of the dehumidifier helped reduce the noise, but did not eliminate it. One hypothesis that can be applied to these observations is that part of the noise could be associated with crystal growth in the local rock joints. When the water vapor becomes stagnant, conditions are such that crystals can grow in the joints, creating small motions on the order of atom diameters as the atoms precipitate from solution and attach themselves to the crystal. When the air is dehumidified, the water molecules are removed from the air. The water molecules in the cracks then migrate toward and into the air. The motion of the water molecules in the cracks then disturbs the precipitation of atoms into the forming crystals and the atomic scaled motion sensed by the strain seismographs is reduced. Martin (1972) in laboratory tests on the static fatigue and creep behavior in quartzite found that the time to failure increased significantly as the partial pressure of water was decreased. A decrease of 10^{-2} mbar of partial pressure of water increased the time to failure by at least 100 sec. Martin's laboratory tests suggest that the increased strain noise at QC-AZ is the result of increased creep in the rock joints as the partial pressure of water in the rock increased with the stagnation of the water molecules in the 100 percent humidity air.

Other observations of small motions were made on the SP seismographs when the wind blew. As wind velocity increased, the general background level of the SP inertial seismographs increased, especially at frequencies of 4 Hz and higher. It is speculated that these high frequency motions were the result of the blocks of rock grinding on each other along the local joint set as a result of the load and forces of the wind.

7.6 SEISMIC NOISE RESULTING FROM ATMOSPHERIC PRESSURE VARIATIONS

The fact that long-period seismographs become noisy when the wind blows has been known for several years. Recently, Sorrells and Der (1970) have shown that for simple models the vertical displacements resulting from forces created by variations in the atmospheric pressure field can be predicted with good success. This section of the report reviews some of the past observations of pressure induced noise; extends the recently developed theory to predict ground displacements to include ground strain and tilt; and presents a spectral comparison between the strain seismographs and the microbarograph. Section 7.7 extends the noise considerations to include linear and nonlinear tilt noise on horizontal inertial seismographs.

Some of the motions referred to in these two sections are on the order 1 to 0.1 Angstroms. While these small motions have undoubtedly contributed to seismograph noises at other locations, only the high sensitivity available at QC-AZ and the comparison between strain and inertial seismographs have enabled the investigators to begin to detect phenomena that are contributing to seismograph noise.

The understanding of the relationship between the air pressure input and the seismic output is basic to the operation of high-sensitivity, long-period seismographs. The present complex of high-sensitivity seismographs used at QC-AZ and in use by others have demonstrated the engineering ability to build seismographs with sufficiently high outputs and sufficiently low electronic noise that the most quiet ambient motions of the earth can be faithfully recorded. The installation methods minimize the effects of temperature variations, air convection cells, and air pressure acting directly on the transducer by putting the seismometers well underground, covering them with insulation, and in sealing the vaults and chambers in which the seismometers are installed. Even with all of these developments, when the wind blows, the air pressure fluctuates, and seismographs become noisy. If the cause and effect can be mathematically related by a simple theory as preliminary observational data seem to indicate, then the theory can be used (1) for deciding an optimum depth at which new installations should be made with a tradeoff of cost versus performance and/or (2) for removing wind-induced noise from the seismographs during signals of special interest recorded during times of unusually high winds.

7.6.1 Previous Observations of Wind-Related Long-Period Noise

Khorosheva (1958) investigated the effect of atmospheric pressure on the tilting of the earth's surface. He concluded that the tilts were not large enough to be observed on the tiltmeters in use at that time. Effects of pressure loadings on the ground began to be quantitatively observed in 1963 and 1964 after instrument stability and installation problems were solved for the Advanced Long-Period System, which was operated as a three-component long-period seismograph at 100K magnifications at WMO. The history of the improvement of the instruments and the techniques of instrument installation to increase their stability will not be discussed here. Instrumentation noise is discussed by Whalen (1963) and a summary of long-period seismograph development was given by Hamilton (1964).

One of the present authors (JEF) working with Burden (1964) established that noise on horizontal pendulum seismographs was positively correlated with wind action. It was also observed that seismometers installed in a walk-in vault within a small hill were significantly more susceptible to wind noise than a seismometer installed in a tank vault about 1 m below the surface but only 60 m away from the hillock. The wind-related (pressure-induced) noise was deemed to be a localized tilt having a dimension of about 50 m. The dimension of the tilting region was deduced from the relationship between the horizontal and the vertical displacements. The geomorphology of WMO encompasses layers of rhyolite, which are broken up into large blocks by joints easily visible at the surface by local vegetation changes. The dimensions of the tilting surfaces deduced from the seismograms agree with the dimensions of the physical block structure in the vicinity.

Under the same author's (JEF) supervision, Milam (1965) continued the development of improved installation techniques to minimize all noise in the ALPS system. Pressure-induced tilt was reduced by a further significant amount on a horizontal seismometer installed in an 8 m deep vault about 100 m from the walk-in vault and the 1 m deep tank vault. A second seismograph installation was made about 100 m from the surface in the Stevenson-Bennett Mine near Las

Cruces, New Mexico (LC-NM). (A Long-Range Seismic Measurements (LRSN) program team co-occupied the mine during these experiments but operated independently.) The Las Cruces installation verified the capability of the full three-component seismograph to operate at magnifications of 100K (at X10 view) for extended periods of time. During this experiment, the need to use tank vaults inside a sealed seismometer chamber well within a mine was conclusively established. After all pressure and temperature effects acting directly on the seismometers were eliminated, noise was observed on the horizontal seismometers when the wind velocity exceeded about 30 mph. The existence of a wind-related noise threshold at both WMO and LC-NM confirms that the elastic loading is proportional to the pressure-induced force at the surface. Since the wind velocity related to the noise threshold at a 100 m depth at LC-NM was greater than the wind velocity related to the noise threshold in the 1 m deep or the 8 m deep tank vaults at WMO, the observations confirmed that the amplitude of the displacements was related to the wind velocity.

A similar attenuation of pressure-induced noise was observed at the WMO short-period strain installation in 1967. (See Shopland, 1968.) The original trench depths were 2.8 to 3.7 m on the east strain seismometer and 3.6 to 3.7 m on the north strain seismometer. An additional 1.3 m of overburden was added. The wind velocity related to the noise threshold increased from about 7 km/hr on the east seismograph and about 20 km/hr on the north seismograph to about 35 km/hr on both seismographs. A spectral comparison of the east seismograph during 15 to 20 mph winds before and after the additional overburden was added showed a 5 to 10 dB power reduction at frequencies above 0.8 Hz and not much change in power at longer periods. Figure 77 shows a replot of the data points in figure 51 from Shopland (1968) on a log-log scale. Straight lines have been visually fit to these data points. The equations for the lines are:

strain east before

$$u = 0.1625 C^{1.495} \quad (3a)$$

strain north before

$$u = 0.000324 C^{2.91} \quad (3b)$$

strain north after

$$u = 0.000563 C^{2.20} \quad (3c)$$

where

u = Equivalent ground motion in millimicrons
peak-to-peak calculated from the strain
seismograms

C = wind velocity in km/hr

The improvement of the operation of a long-period seismograph by burial in a culturally noisy location was also demonstrated by Rector (1965). Three seismometers in a 15.25 m deep cased hole, in a surface tank vault inside a

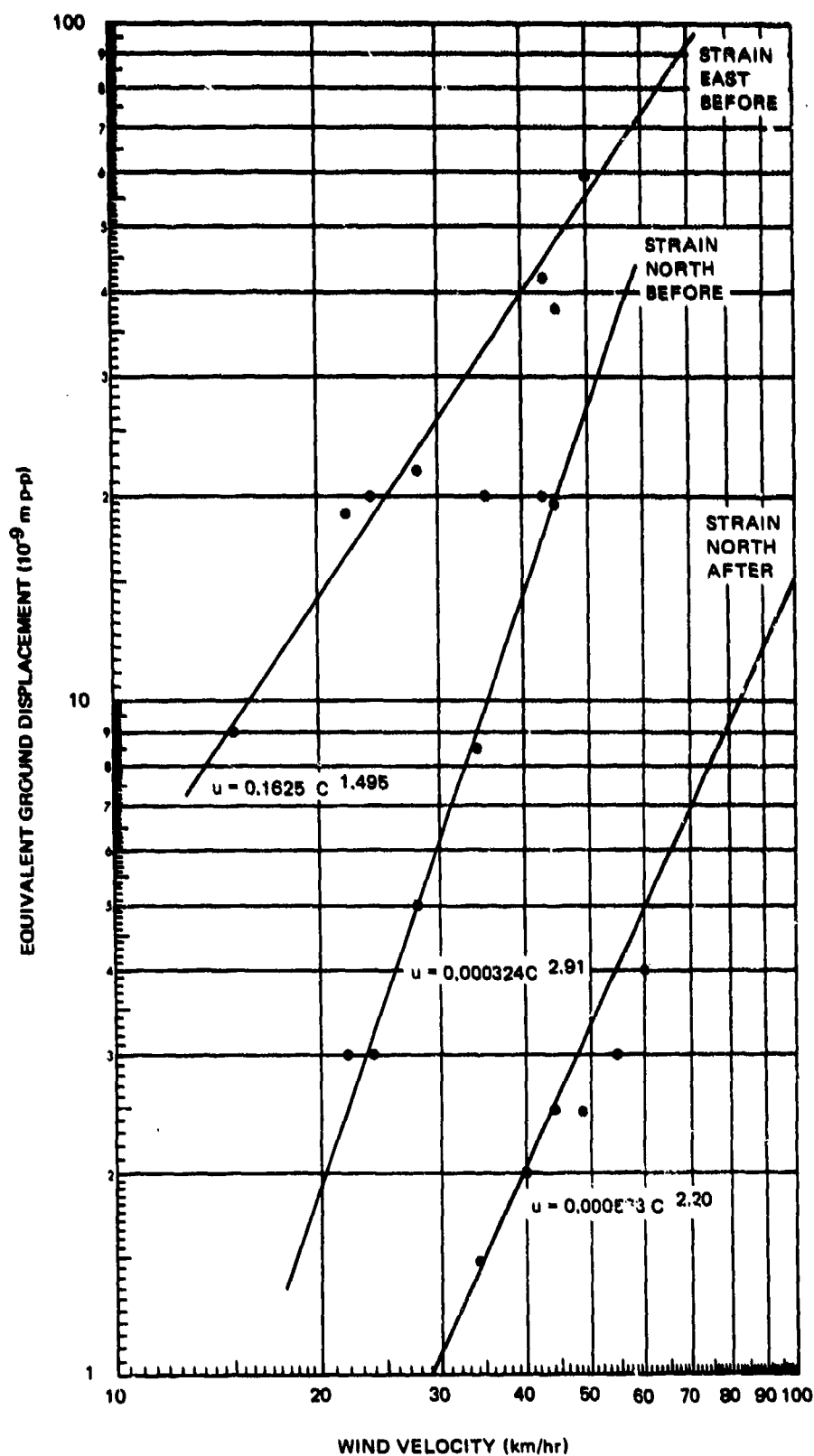


Figure 77. Relationship between equivalent ground displacement and wind velocity at WMO

G 6029

building, and on a concrete pier in a building were used for the tests at the Geotech Garland facility. After properly pressure sealing and insulating the buried seismometer, operating magnifications of 10 to 20K were possible. During the same time intervals, the two surface seismometers could only operate at 0.5 to 2K. The burial sufficiently attenuated most cultural vibrational and pressure-induced noises; however, all seismometers responded to large tilts resulting from surface loading by trains and vehicles. No quantitative tilt comparisons could be made because of the relative locations and depths of the various piers.

Other cases of improved long-period seismograph operation were reported in the LRSM program. Warren (1966) excavated a 9.1 m deep vault at La Paz, Bolivia. In conjunction with improvements made in the thermal and pressure stability, the depth of the installation attenuated wind-related disturbances and resulted in an improvement of operating magnifications from the 10 to 20K range to the 100 to 200K range. Simons (1968) reported on an experiment that compared the operation of long-period seismographs in surface tanks and at the bottom of 162 ft deep missile silos at two different locations, both of which were in sediments. He concluded that there was noise on the horizontal seismometers that positively correlated with wind gusts (more than a steady wind). However, no quantitative relationship could be established between tilt at the surface and at depth. In fact, at times the surface horizontal seismometers would tilt first and at other times the silo seismometers would tilt first. The relative amplitudes of the tilts also varied with either the surface or the silo seismometers having the largest amplitude.

The Uinta Basin Observatory (UBO), Vernal, Utah, operated three sets of three-component long-period seismographs simultaneously (Teledyne Industries, 1966). The approximate depths to the three piers were 0.6 m, 2 m, and 15 m. By visual comparison of recordings made, the deeper vaults during windy conditions were about 6 dB and about 18 dB quieter, respectively, than the shallowest vault. A detailed quantitative study of the relationship between the wind velocity, pressure, and seismic noise versus depth was not made.

During testing of the triaxial long-period seismometer in a 60 m (200 ft) deep hole at UBO, the coordinate transformed horizontal outputs of the triaxial system were compared to the three-component system at the 15 m depth. The triaxial system output from a depth of 53 m (175 ft) was found to be about 12 dB quieter than the output of the shallower system (Kirkpatrick, 1968).

7.6.2 Long-Period Earth Strains and Atmospheric Pressure Variation

To explain the many observations of (1) wind-related noise on long-period seismographs and (2) attenuation of this noise with depth, Sorrells (1969), Der (1969), and Sorrells and Der (1970) developed a theory for the displacements associated with the passage of a plane wave of air pressure over an infinite, isotropic, homogeneous, half-space and over a layered half-space. Sorrells and Goforth (1972) have extended the theory to include two dimensional pressure loads over a layered half-space. However, since the geologic structure at QC-AZ involves a hard rock mountain projecting 260 m above and an unknown distance below a soft alluvial valley, neither model exactly applies for the 100 to 400 m wave-lengths involved. Therefore, the simplest model of a plane wave passing over a half-space will be used to investigate the general relationships between the atmospheric pressure input and the strain and tilt output.

Consider a system of axes in which the 1 axis is in the direction of wave propagation and the 3 axis is vertical down. The displacements derived by Sorrells (Sorrells and Der, 1970) with a slight change in nomenclature are

$$u_1(x_1, x_3, t) = \frac{ic_0 P}{2\mu|\omega_0|} \left(\frac{\mu}{\lambda+\mu} - \frac{|\omega_0|x_3}{c_0} \right) e^{-\frac{|\omega_0|x_3}{c_0}} e^{i\omega_0 \left(t - \frac{x_1}{c_0} \right)} \quad (4)$$

and

$$u_3(x_1, x_3, t) = \frac{-c_0 P}{2\mu|\omega_0|} \left(\frac{\lambda+2\mu}{\lambda+\mu} + \frac{|\omega_0|x_3}{c_0} \right) e^{-\frac{|\omega_0|x_3}{c_0}} e^{i\omega_0 \left(t - \frac{x_1}{c_0} \right)} \quad (5)$$

By taking the appropriate derivatives, the linear strain in the direction of propagation, the vertical linear strain, the shear strain in the 1-3 plane, and the tilt in the 1 direction are found to be:

$$e_{11} = \frac{du_1}{dx_1} = \frac{P}{2\mu} \left(\frac{\mu}{\lambda+\mu} - \frac{|\omega_0|x_3}{c_0} \right) e^{-\frac{|\omega_0|x_3}{c_0}} e^{i\omega_0 \left(t - \frac{x_1}{c_0} \right)} \quad (6)$$

$$e_{33} = \frac{du_3}{dx_3} = \frac{P}{2\mu} \left(\frac{\lambda+2\mu}{\lambda+\mu} + \frac{|\omega_0|x_3}{c_0} - 1 \right) e^{-\frac{|\omega_0|x_3}{c_0}} e^{i\omega_0 \left(t - \frac{x_1}{c_0} \right)} \quad (7)$$

$$e_{13} = \frac{1}{2} \left(\frac{\partial u_1}{\partial x_3} + \frac{\partial u_3}{\partial x_1} \right)$$

$$e_{13} = \frac{iP}{2\mu} \frac{|\omega_0| x_3}{c_0} e^{-\frac{|\omega_0| x_3}{c_0}} e^{i\omega_0 \left(t - \frac{x_1}{c_0}\right)} \quad (8)$$

$$\text{tilt} = \frac{du_3}{dx_1} = \frac{iP}{2\mu} \left(\frac{\lambda+2\mu}{\lambda+\mu} + \frac{|\omega_0| x_3}{c_0} \right) e^{-\frac{|\omega_0| x_3}{c_0}} e^{i\omega_0 \left(t - \frac{x_1}{c_0}\right)} \quad (9)$$

$$u_2 = e_{22} = e_{12} = 0, \quad i = 1, 2, 3 \quad (10)$$

where:

1,2,3 = axes designators

X_1 = coordinate in i^{th} axis

x_1 = independent variable in i^{th} axis

u_1 = displacement in i^{th} direction

e_{ij} = component of strain tensor acting across plane perpendicular to i axis in direction of j axis

P = amplitude of pressure wave

λ, μ = Lamé elastic constants

ω_0 = angular frequency of pressure wave

c_0 = velocity of pressure wave in the X_1 direction, assumed to be much smaller than the shear wave velocity

t = time

Several observations can be made about equations (6) through (9) and their relationships to equations (4) and (5).

a. The linear strains and the tilt do not have the $1/k_0 = c_0/|\omega_0|$ in their amplitude coefficients (where k is wave number). This result is to be expected because for a plane wave

$$u_m = e^{-ik \left(x_m - \frac{t}{c} \right)} \quad (11)$$

$$e_{mn} = \frac{\partial u_m}{\partial x_n} = -ik e^{-ik \left(x_m - \frac{t}{c} \right)} ; \quad m = n. \quad (12)$$

Since the velocity of the pressure wave is much less than the velocity of seismic surface waves, k is much larger for the pressure wave. Consequently, the ratio of pressure-induced noise to surface wave signal on the strain seismograph is proportionally greater than the ratio of noise to signal on the inertial seismographs.

b. The linear strains are either in-phase or 180 deg out-of-phase with each other, depending on the sign of the terms in the parentheses.

c. For each wave number, there is one depth where the horizontal strain e_{11} is zero.

d. For a given depth, for the same phase velocity, and at the longer periods, the term containing x_3 in the parentheses becomes negligible.

e. The linear strains e_{11} and e_{33} are ± 90 deg out-of-phase with the u_1 displacement, the shear strain e_{13} , and the tilt.

f. The tilt is ± 90 deg out-of-phase with the vertical displacement u_3 and in-phase or 180 deg out-of-phase with the horizontal displacement.

g. The factor controlling the attenuation with depth of all displacements, strains, and tilt is the exponential term $\exp(-k_0 x_3)$.

The amplitude of the pressure-induced noise on strain and inertial instruments decays much more rapidly with depth than the amplitude of surface waves decays with depth. Therefore, by increasing the depth of an installation, the pressure-induced noise can be reduced for better performance. This improvement in signal-to-noise ratio is one of the main reasons why a mine was selected for the installation site on this project.

7.6.3 Observed Strains and Pressure Variations

All three strain seismographs respond to ground strain induced by loading of the surface by forces resulting from air-pressure cells. Figure 78 illustrates an example of this response. The air-pressure pulse at about 2207Z on ML2 is 49 μ bar. The strain introduced in the ground in the 325 deg azimuth is 1.71×10^{-10} , in the 55 deg azimuth is 1.78×10^{-11} , and in the vertical direction is estimated at 1.2×10^{-10} . The extended-long-period horizontal inertial seismographs P325X and P55X tilt in response to the pressure loading, and some vertical displacement is indicated on the PZX vertical inertial seismograph.

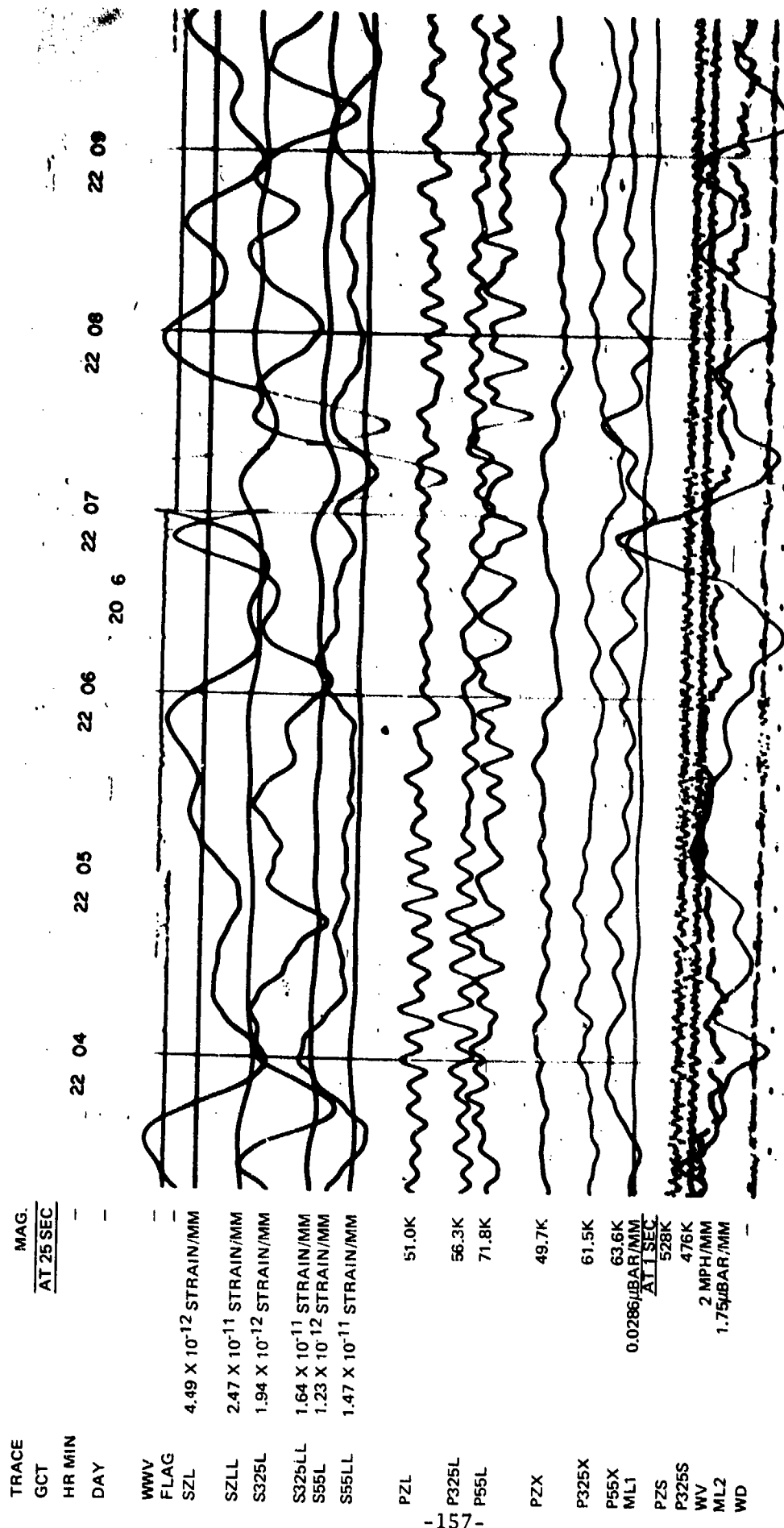


Figure 78. Reproduction of a 16 mm film recording of ground strains and tilts from microbarometric pressure loads on the surface of the ground

QC-AZ
CAMERA 1
RUN 206
25 JULY 1970

The ALPS response seismographs do not respond to the 90 sec pressure disturbance as noticeably as the extended-long-period response seismographs. Note, however, that the possible low-level surface wave signal between 2206Z and 2208Z is much clearer on the P55X than on the P55L.

7.6.3.1 Spectral Comparison Among Strain and Inertial Seismographs and the Microbarograph

This section presents a comparison of the power spectral density among the various strain and inertial seismographs and the microbarograph. Two time intervals are used; one on 31 May 1970 and the other on 26 November 1970. These spectra provide an evaluation of the non-earthquake signals that occur during times of high winds. The reader will find it instructive to compare the spectra in this section with the spectra of the microseismic background during quiet times as presented in sections 7.2, 7.3, and 7.4. It can be seen that as the pressure activity increases, the overall spectra begins to rise. First, the notch in the background spectra between 20 and 50 sec is filled. Then, as the pressure activity continues to increase, the whole spectrum is masked with even the microseismic peak blending into the pressure generated noise under the severest conditions.

The spectra from 31 May 1970 are uncorrected for system responses and are calibrated relative to earth strain or earth displacement at 25 sec for the ALPS response and at 100 sec for the ULP response. The microbarograph is calibrated relative to air pressure at 116 sec. Thus, if the reader wishes to estimate the power spectral density of ground strain, ground displacement, or air pressure at another period, the calibration values in the figures should be divided by the square of the ratio of the response of the system at the desired period to the response of the system at the calibration period of 25, 100, 116 sec. In the figures in which strain is compared to displacement, the strain has been normalized to displacement based on a 25 sec Rayleigh wave phase velocity of 4.00 km/sec and the resulting power ratio of $(6.28 \times 10^{-5})^2$ strain²/m². Cross power spectral density between strain and displacement is normalized based on a power ratio of 6.28×10^{-5} strain-m/m². In the figures in which strain and displacement are related to air pressure, the power spectral densities and cross power spectral densities are plotted with an arbitrary normalization of 1 μ bar equivalent to 10^{-13} strain and 10^{-10} m displacement.

The amplitude spectra from 26 November 1970 have been corrected for system responses and are estimates of ground displacement, ground strain, atmospheric pressure, and wind velocity.

The spectra are presented as a power spectral density normalized to a 1 Hz passband. The passband used in the actual calculations was either $1/256 = 3.91 \times 10^{-3}$ Hz or $1/2560 = 3.91 \times 10^{-4}$ Hz. If the reader wishes to normalize to a passband of 1 mHz = 1/1000 Hz for comparison with several published microseismic spectra, the plotted values can be divided by 1000.

The first three figures are plots of the spectra from the various seismographs. The total equivalent mean square energy of the various instruments during this high wind sample is given in table 11. The table gives the period of the calibration to which the mean squares are referred, the equivalent mean square in the passband of the channel, and the equivalent root-mean-square (rms). These

Table 11. Equivalent mean-square values during high wind sample
0046Z to 0730Z, 31 May 1970

<u>Instrument</u>	<u>Period of calibration (sec)</u>	<u>Total mean-square in passband</u>	<u>Total rms in passband</u>	<u>Figure no.</u>
S325L1	25	$2.28 \times 10^{-23} \text{ strain}^2$	$4.77 \times 10^{-12} \text{ strain}$	79, 82
S55L	25	$2.62 \times 10^{-23} \text{ strain}^2$	$5.12 \times 10^{-12} \text{ strain}$	79, 81, 84
S325U1	100	$1.30 \times 10^{-21} \text{ strain}^2$	$3.61 \times 10^{-11} \text{ strain}$	80, 83
S55U	100	$2.71 \times 10^{-22} \text{ strain}^2$	$1.65 \times 10^{-12} \text{ strain}$	80, 85
P55L	25	$9.07 \times 10^{-18} \text{ m}^2$	$3.01 \times 10^{-9} \text{ m}$	81, 86
ML2	116	$4.75 \times 10^2 \text{ } \mu\text{bar}^2$	21.8 μbar	82, 83, 84, 85, 86

values are described as equivalent, because the seismograms were not corrected for the instrument response. They are good values for the total mean-square signal at the recorders. The table also gives the figure numbers in which the spectral data appear. Figure 79 is a plot of the spectra from 20 to 2560 sec of the S325L1 and S55L ALPS response seismographs. The spectra are almost identical in magnitude and shape. The coherence is generally between 0.25 and 0.5. For the peaks in the coherence, the phase angle is close to 135 deg. The wind was from the south for the entire 6.7 hr interval. There were small changes in azimuth, but not over ± 20 deg. The strain seismometers then have about a 35 deg and a 55 deg angle between their azimuth and that of the wind. Figure 80 is a plot of the spectra from the S325U1 and S55U. The ULP response seismographs are recorded with less strain sensitivity than the ALPS response and therefore have less signal-to-noise ratio. This decrease is evident in the coherence plots. The S325U1 spectra at periods longer than 200 sec appears to contain instrument noise. Figure 81 is a plot of the spectra from the S55L strain and the P55L inertial seismographs. The cross spectra has the shape of the strain spectra, indicating that the horizontal pendulum is probably responding to tilts at the longer periods in a nonlinear manner. The coherence is above 0.25 from 30 to 300 sec and 600 to 2560 sec. The phase angle is about 90 deg from 30 to 450 sec. At periods longer than 600 sec, the electronic noise is probably entering both spectra. Similar spectra are not presented for the P325L inertial seismograph because the seismometer had been worked on a few days prior to this sample and the data are not considered reliable.

Figures 82, 83, 84, 85, and 86 contain the spectra of the five seismographs and the ML2 microbarograph outside the mine.

The microbarograph response is closer to the ALPS response than the ULP response. Therefore, the uncorrected spectra of the S325L1 and S55L have a shape more similar to the ML2 than do the S325U1 and S55U. Even though the spectra are very similar in shape, the coherence values indicate that the linear relation between the air pressure and the ground strain only accounts for one-fourth to one-half of the strain and inertial seismographs. At the time of this experiment, the ML2 microbarograph was in the unsealed adit of the mine. Turbulence within the adit could possibly have reduced the correlation. Another factor that must be considered is the flexure of the mountain as a beam from the force of the wind. This experiment was repeated with the 26 November 1970 data with the microbarograph above the seismometer chamber and with the vertical strain seismograph operational.

The power spectral density of the six LP seismographs during the 26 November 1970 sample are shown in figures 87, 88, and 89 for the period range between 3 and 256 sec. The 8 sec microseismic peak is visible on all six spectra. But, at periods longer than 10 sec, the strain seismograph spectra are dominated by the air pressure loading and the 16 sec microseismic peak is masked. The inertial seismograph spectra show the 16 sec microseismic peak, but the notch in the noise is substantially reduced by the ground motion generated by the air pressure loading. The smoothing out of the notch can be seen by comparing figures 87, 88, and 89 with the similar spectra in figures 61 through 69 taken during intervals of low wind velocities. The total mean square and total rms displacements and strains in the passband from 1 to 256 sec are given in table 12 for the time intervals of the spectra in figures 87, 88, and 89. These displacements and strains are given relative to the 25 sec period of the calibrations because the spectra are not corrected for instrument responses. The

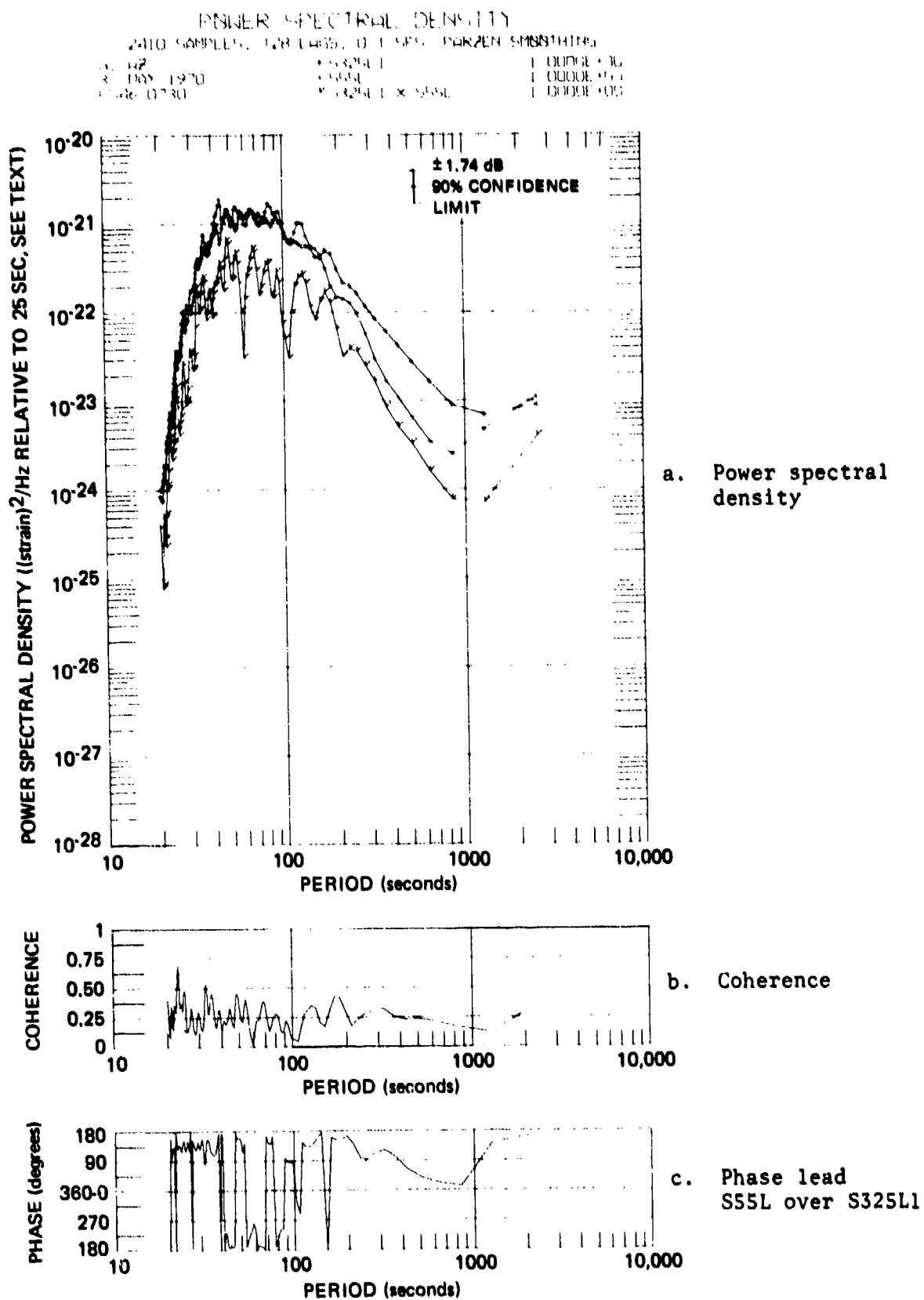
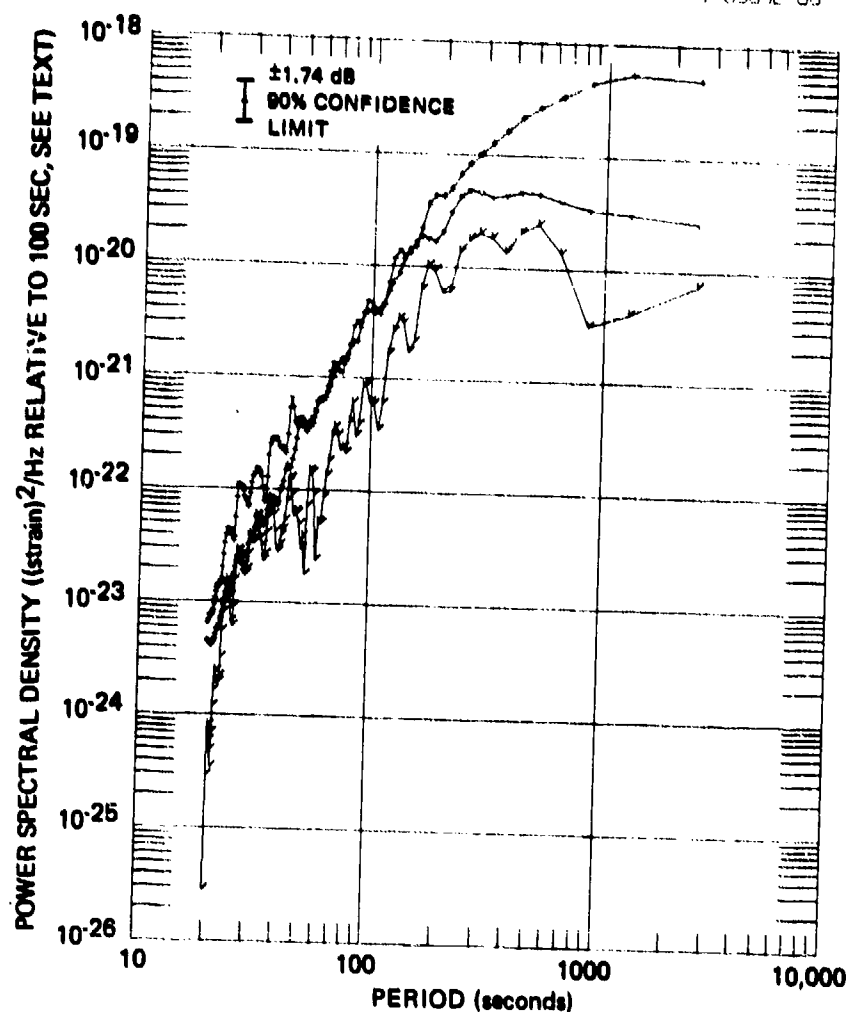


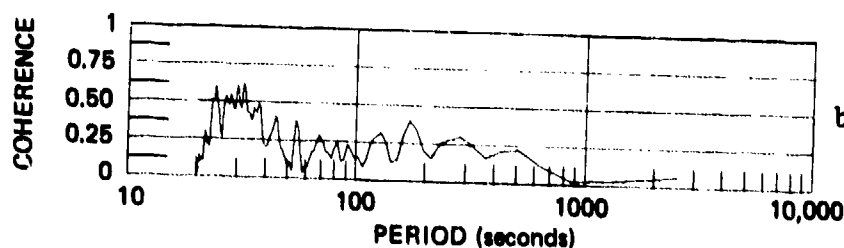
Figure 79. Power spectral density, coherence, and relative phase angle of perpendicular horizontal strain seismographs S325L1 and S55L during high wind conditions

G 6177

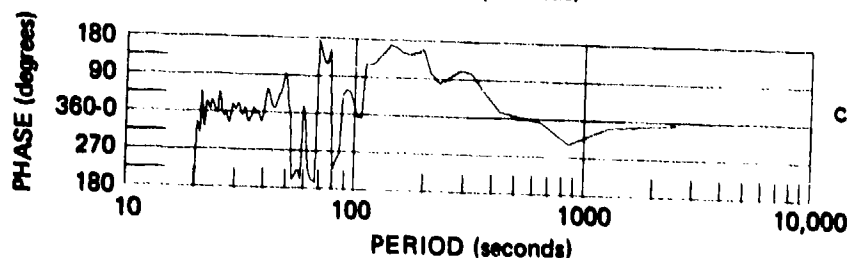
POWER SPECTRAL DENSITY (STRAIN $\times 2/HZ$)
 2410 SAMPLES, 128 LAGS, 0.1 SPS, PARZEN SMOOTHING
 06-07
 31 MAY 1970
 054640130
 S325U1
 S55U
 S325U1 \times S55U
 1.000E+00
 1.000E+00
 1.000E+00



a. Power spectral density



b. Coherence



c. Phase lead
S55U over S325U1

Figure 80. Power spectral density, coherence, and relative phase angle of perpendicular horizontal strain seismographs S325U1 and S55U during high wind conditions

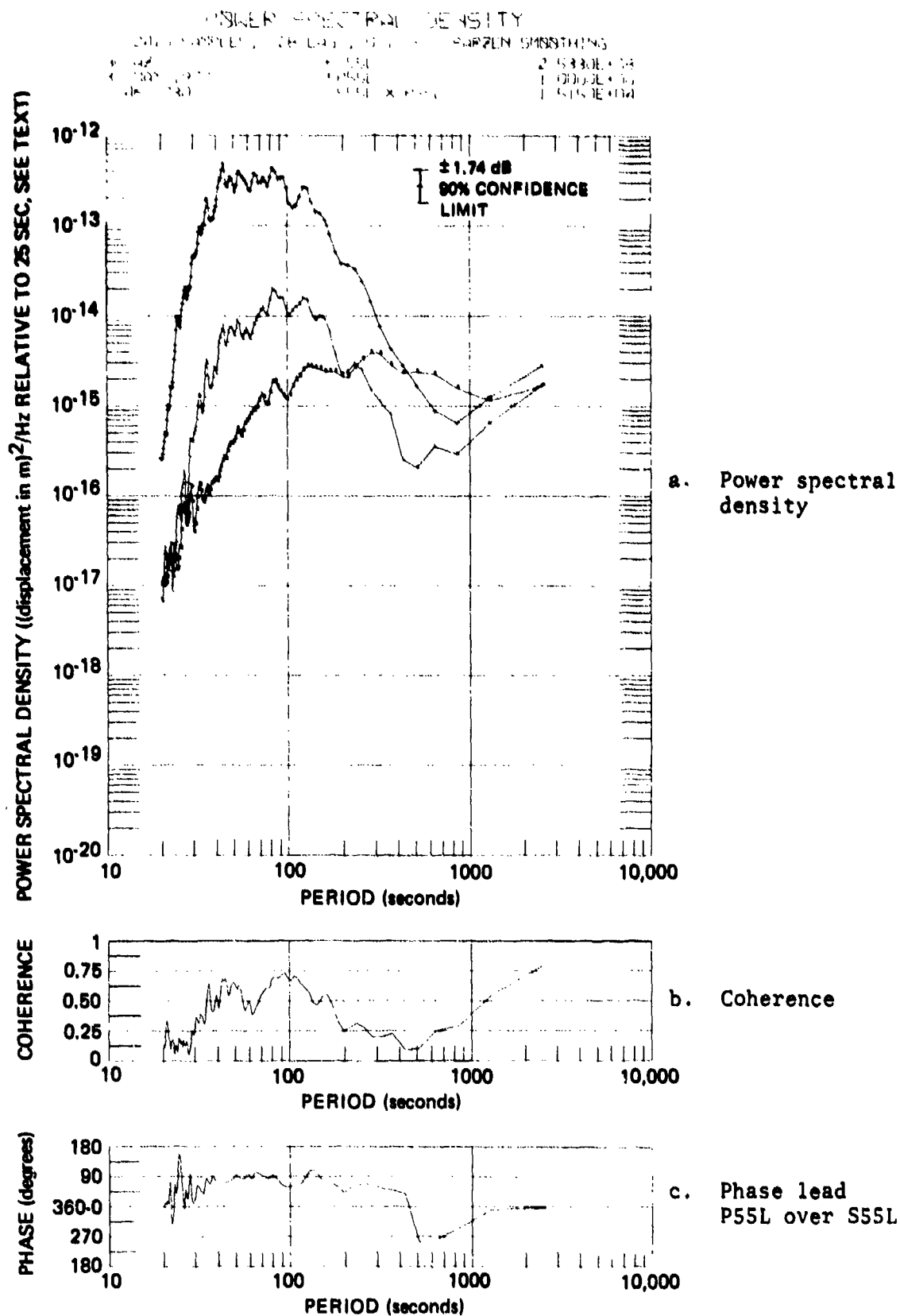


Figure 81. Power spectral density, coherence, and relative phase angle of parallel horizontal seismographs, S55L strain and P55L inertial, during high wind conditions

G 6179

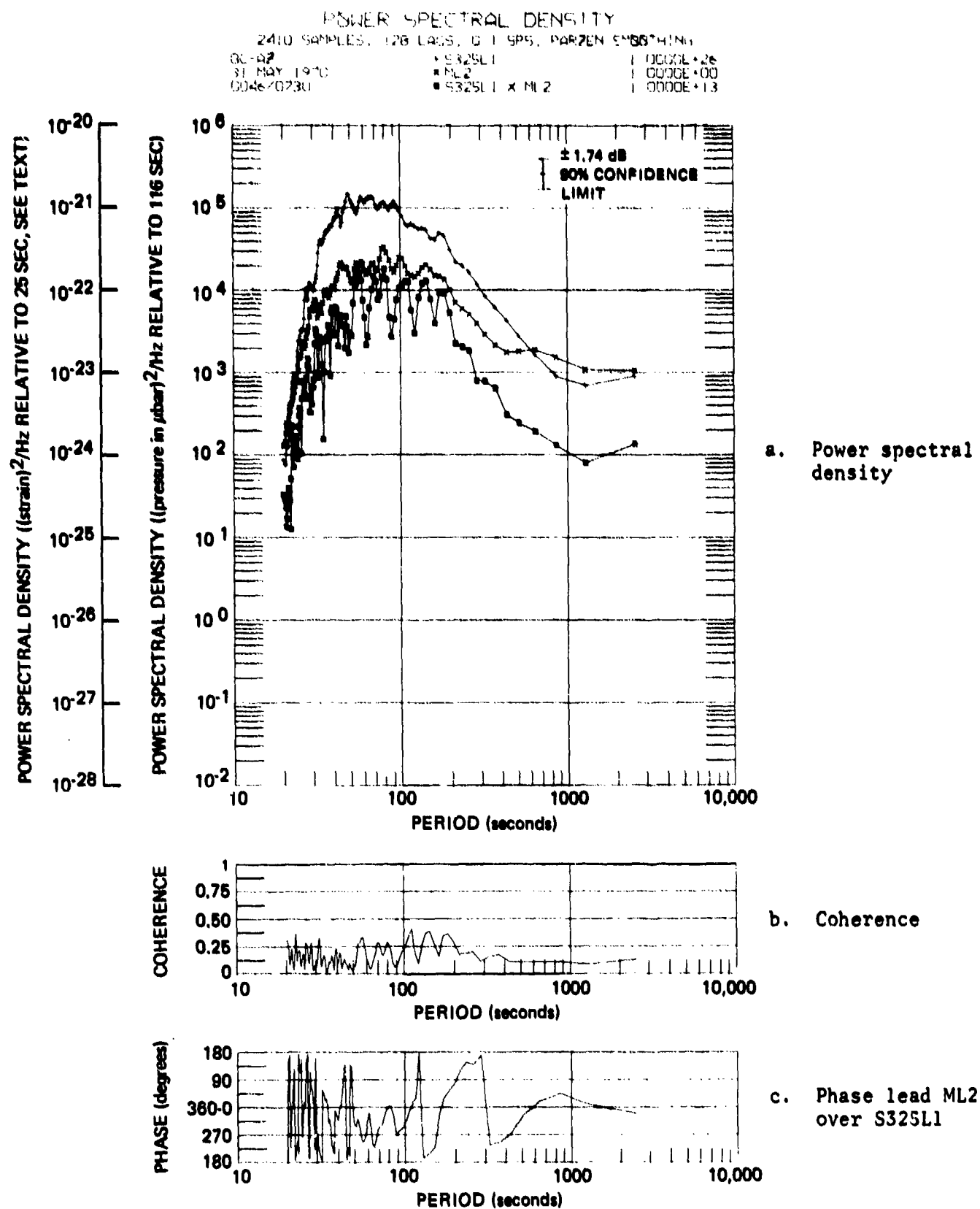


Figure 82. Power spectral density, coherence, and relative phase angle between horizontal strain seismograph S325L1 and microbarograph ML2

Q 6180

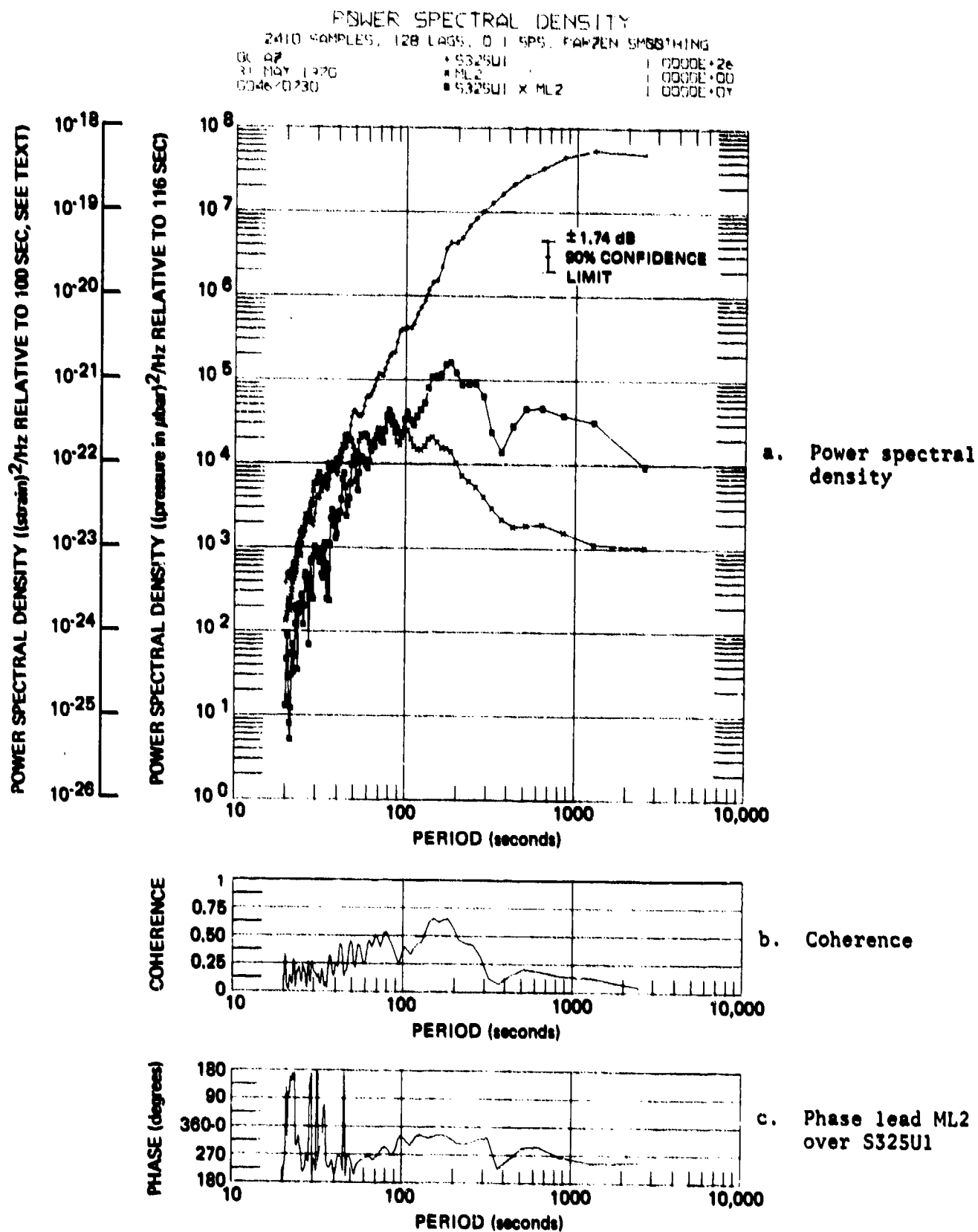


Figure 83. Power spectral density, coherence, and relative phase angle between horizontal strain seismograph S325U1 and microbarograph ML2

06181

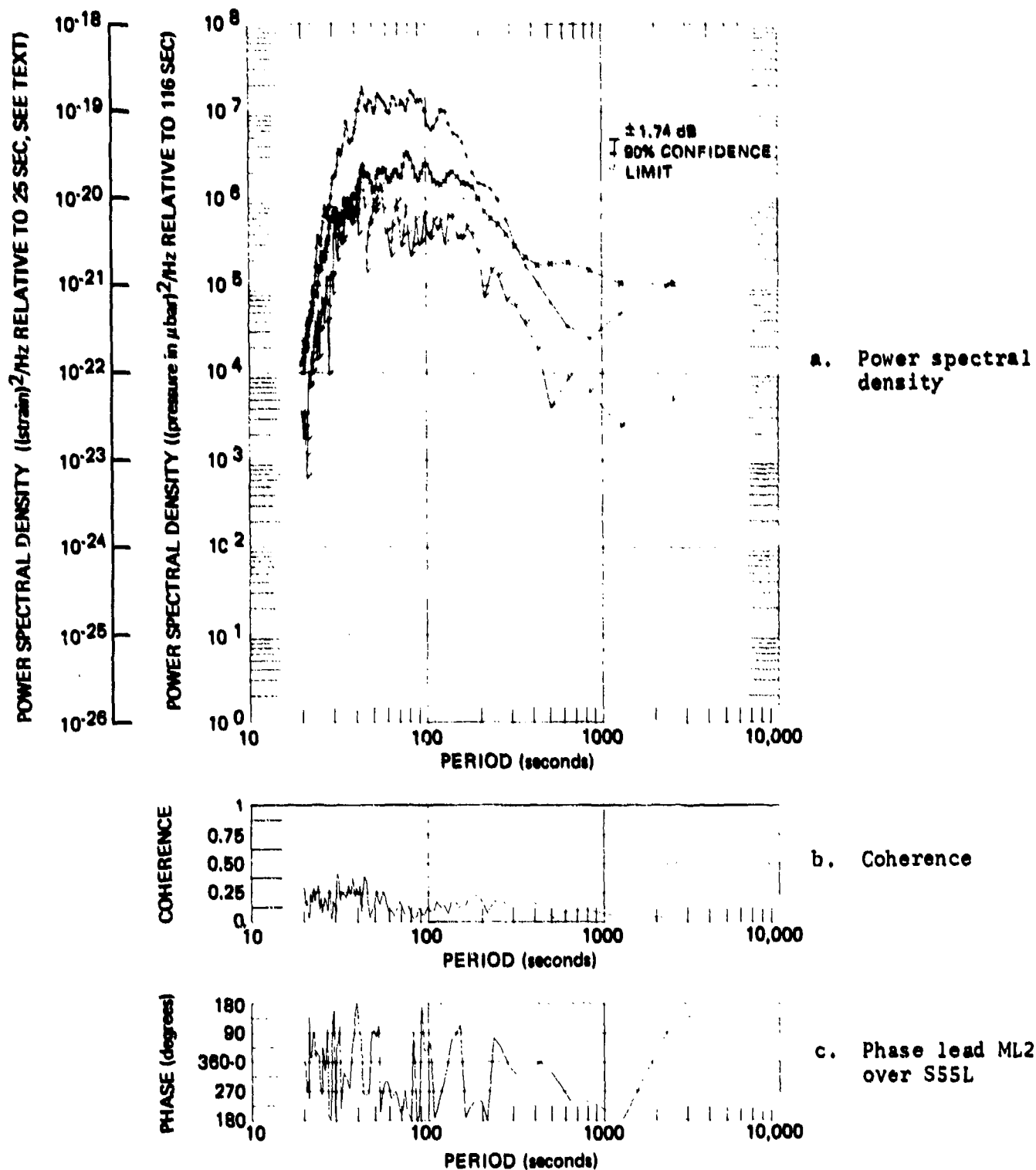


Figure 84. Power spectral density, coherence, and relative phase angle between horizontal strain seismograph S55L and microbarograph ML2

06182

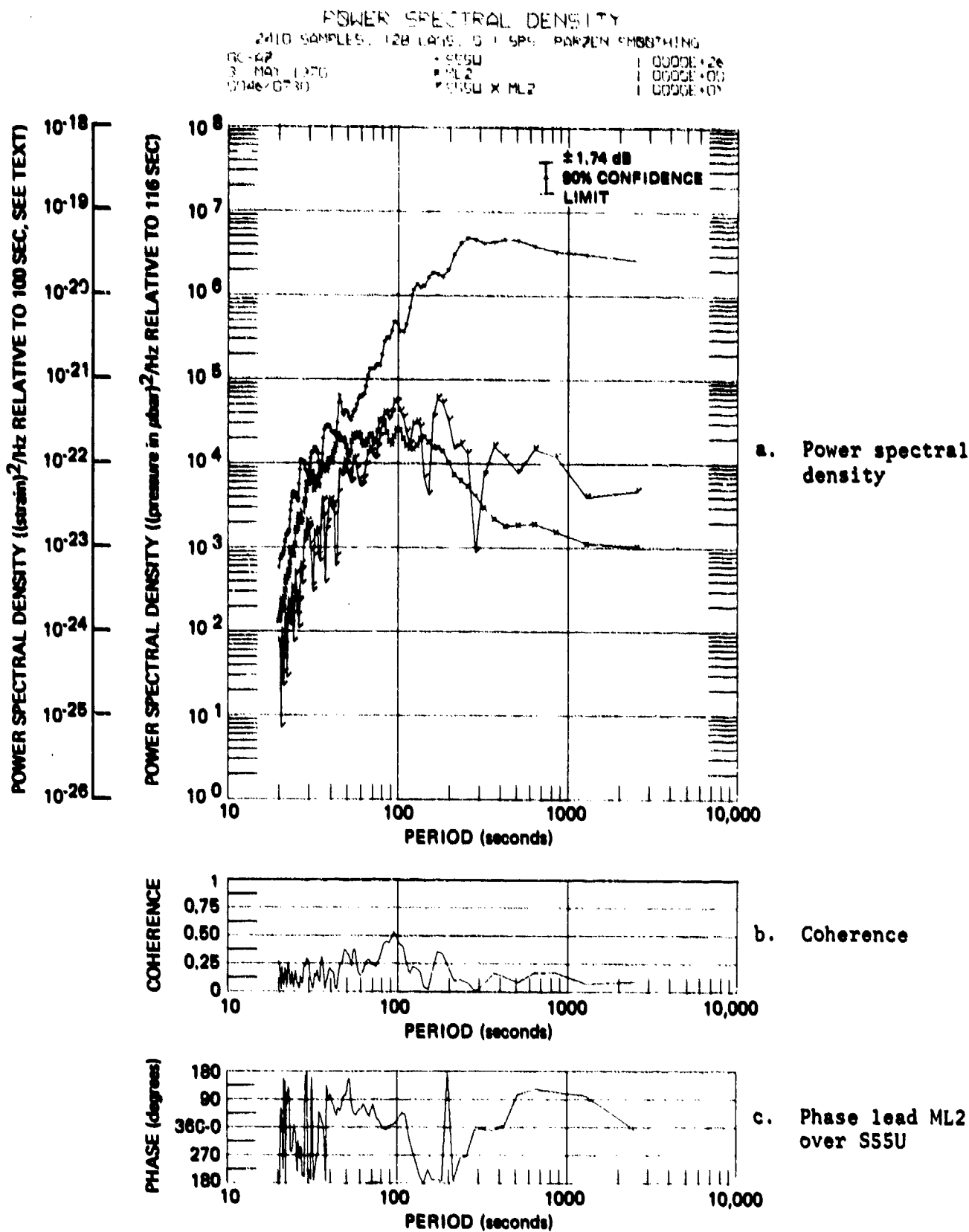
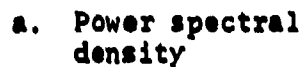


Figure 85. Power spectral density, coherence, and relative phase angle between horizontal strain seismograph S55U and microbarograph ML2

G 6183



G 6184

ATMOSPHERIC NOISE

3841 SAMPLES, 256 LAGS, 2.0 SPS, PARZEN SMOOTHING

QC-AZ

26 NOVEMBER 1970

0920/0952

* SZL

* PZL

5.4400E-24

1.0000E-14

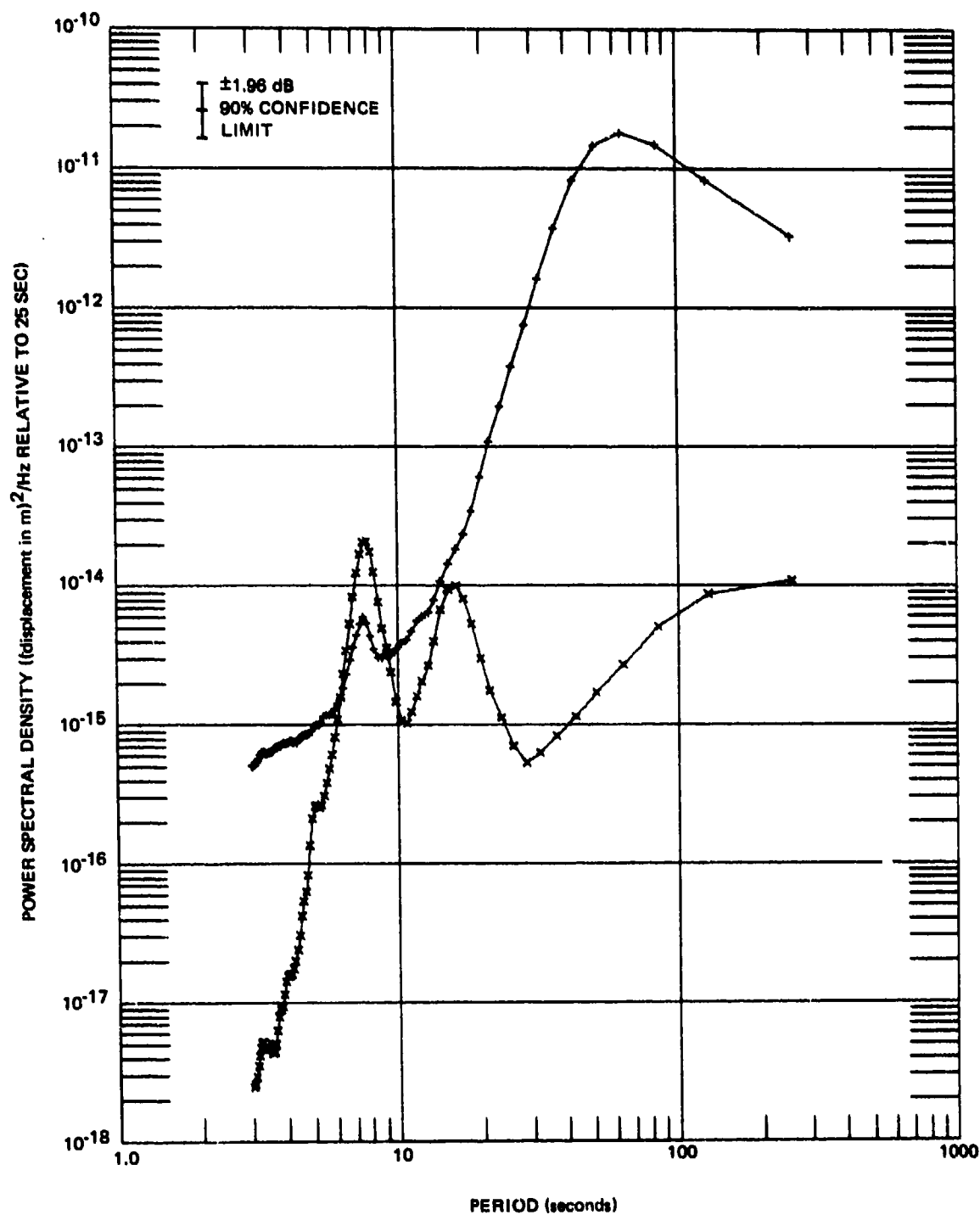


Figure 87. Power spectral density of pressure induced seismic noise recorded on PZL and SZL seismographs on 26 November 1970.

G 6354

ATMOSPHERIC NOISE

3841 SAMPLES, 256 LAGS, 2.0 SPS, PARZEN SMOOTHING

QC-AZ
26 NOVEMBER 1970
0920/0952

+ S325L
* P325L

6.7400E-24
1.0000E-14

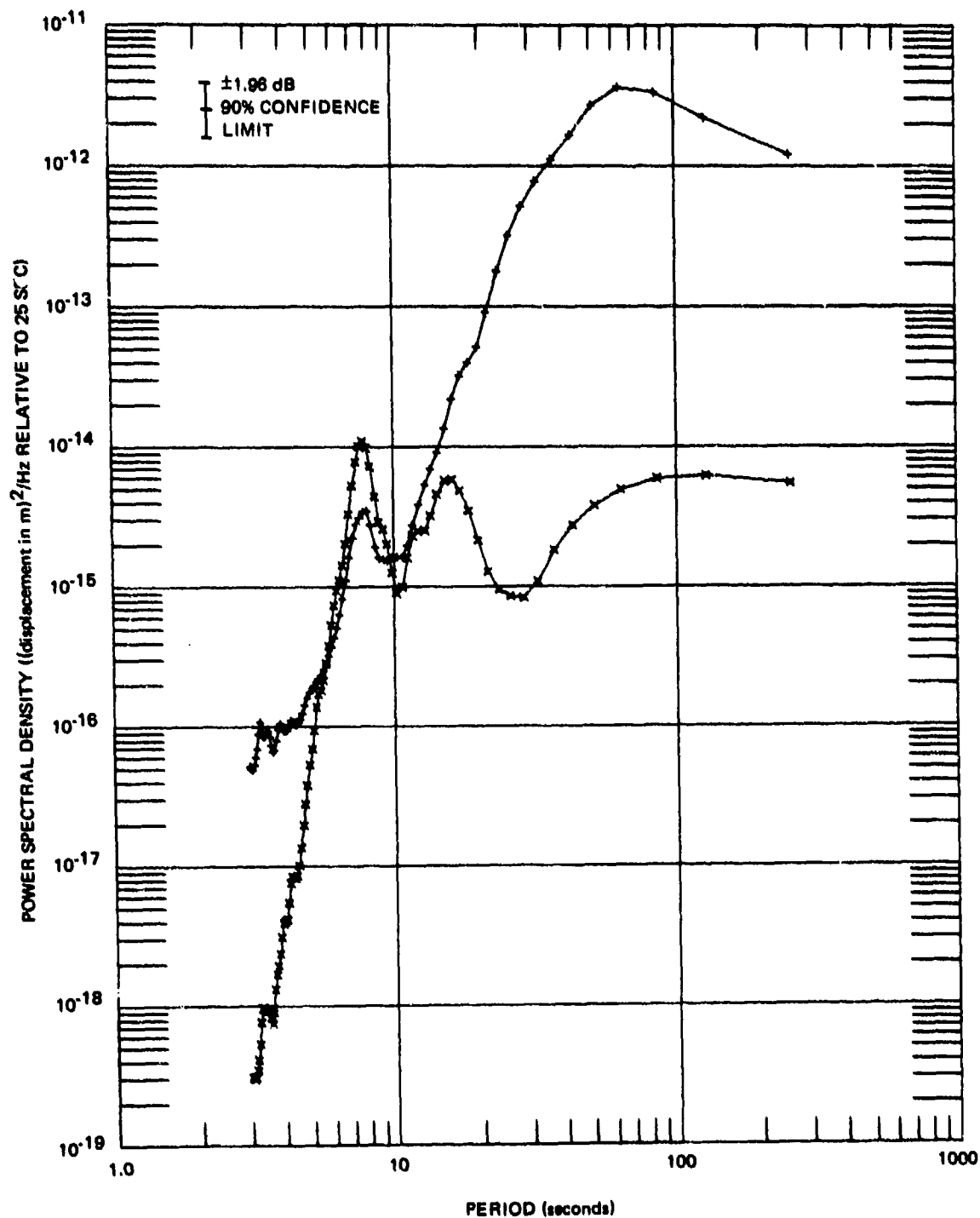


Figure 88. Power spectral density of pressure induced seismic noise recorded on P325L and S325L seismographs on 26 November 1970.

G 6355

ATMOSPHERIC NOISE

3841 SAMPLES, 256 LAGS, 2.0 SPS, PARZEN SMOOTHING

QC-AZ
26 NOVEMBER 1970
0920/0952

+ S55L
* P55L

9.8800E-24
1.0000E-14

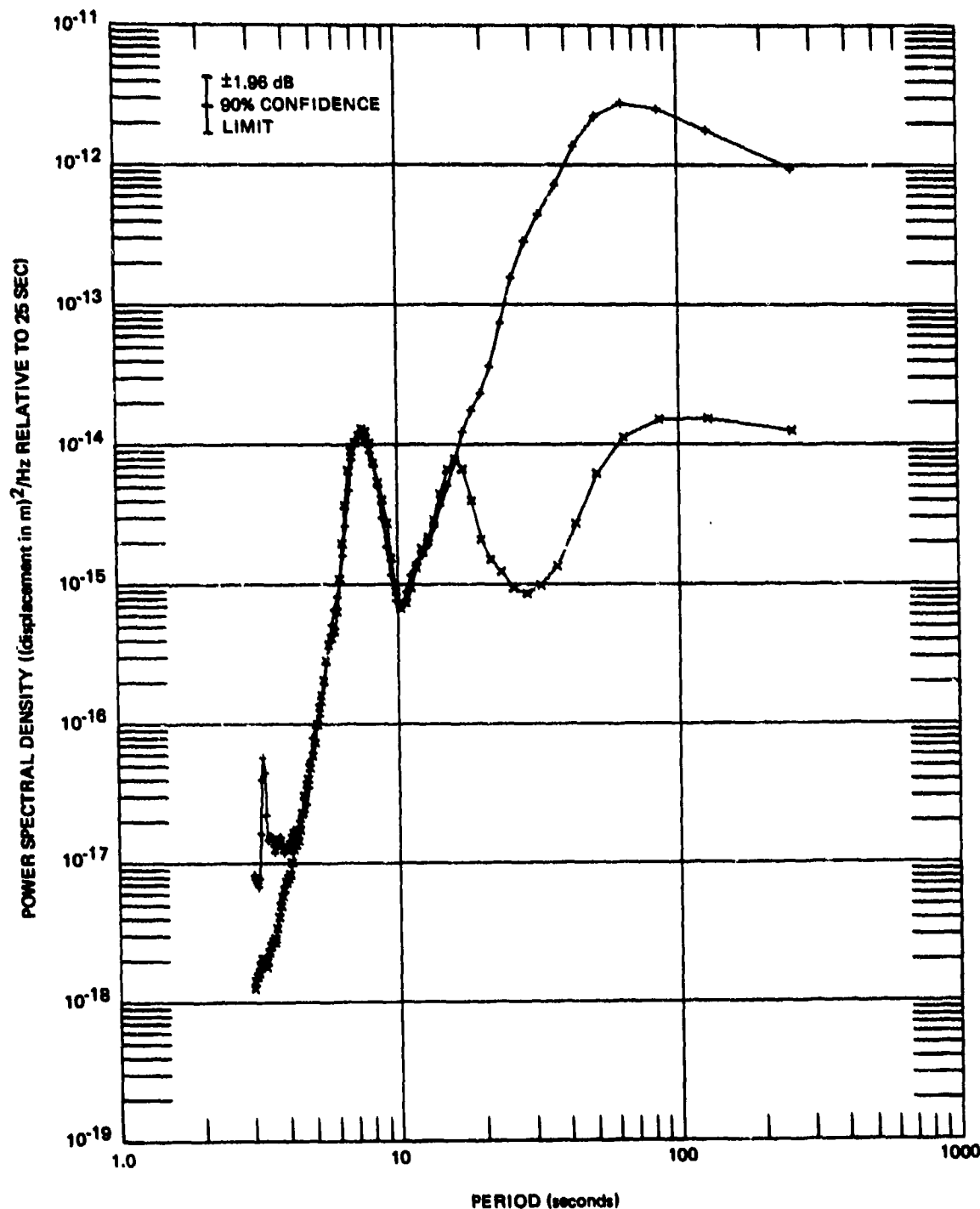


Figure 89. Power spectral density of pressure induced seismic noise recorded on P55L and S55L seismographs on 26 November 1970.

G 6366

Table 12. Total mean square and total root-mean-square displacement and strain in the passband 1 to 256 sec during an interval of large pressure variations. Seismographs are calibrated at 25 sec, but are uncorrected for system response.

Date	Day	Seismograph	Displacement		Total rms value relative to 25 sec in 1 to 256 sec passband	Spectra plotted in figure no.
			m ²	m		
26 Nov 70	330	PZL	9.57 x 10 ⁻¹⁶		3.09 x 10 ⁻⁸	87
		P325L	6.07 x 10 ⁻¹⁶		2.46 x 10 ⁻⁸	88
		P55L	8.72 x 10 ⁻¹⁶		2.95 x 10 ⁻⁸	89
			Strain			
			strain ²		Strain	
		SZL	1.60 x 10 ⁻²²		1.26 x 10 ⁻¹¹	87
		S325L	4.85 x 10 ⁻²³		6.96 x 10 ⁻¹²	88
		S55L	5.37 x 10 ⁻²³		7.33 x 10 ⁻¹²	89

displacements and strains in table 12 from a period of large air pressure fluctuations can be compared to the displacements and strains from intervals of small pressure fluctuations given in tables 9 and 10, respectively.

The amplitude spectra from 26 November are presented in the next group of figures. These spectra have been corrected for instrument response and are an estimate of the input ground motion signals.

Figures 90, 91, and 92 are from the three inertial seismographs. By comparing the PZL amplitude spectra in figure 90 and in figure 71 and the P55L amplitude spectra in figure 92 and in figure 73 the increase in ground motion as a result of the pressure activity can be seen as a smooth variation with increases at all periods within the range of the analysis.

The strain amplitude spectra are plotted in figures 93, 94, and 95. The three displacement spectra are almost identical in amplitude, with the P55L being slightly larger. The SZL and S325L spectra are almost identical, but the S55L spectra are larger than the other two at periods longer than 80 sec.

By comparing the vertical seismographs with the horizontal seismographs, it is concluded that the energy transfer between the air and the ground was more than a simple load that can be modeled by a pressure wave above a half-space. In this model the horizontal inertial seismometers respond to the deformation as tilt meters and have larger outputs than the vertical. The vertical strain seismograph will respond in this model with a larger output than the horizontal strain seismographs because it has a finite length and the upper and lower anchors will be subjected to different vertical displacements which will produce a larger differential pier motion than the true strain at either anchor would require. Since the horizontal strain seismographs are at one depth, they are indicating the true strain.

With the vertical inertial seismograph having more signal than expected by the simple model, and with the vertical strain seismograph having less signal than expected by the simple model, it is hypothesized that the mountain was subjected to bending by the force of the wind on the face of the mountain as well as being subjected to the vertical pressure forces.

The amplitude spectra of the ML1 and ML2 microbarographs for 31 May 1970 are plotted in figures 96 and 97 for the short and long samples, respectively. The units of the spectra in these two figures are rms μ bars in a 1 Hz passband. The ML2 spectra are about a factor of 2 high in the short sample compared to the longer sample. However, the spectra from the ML1 microbarograph inside the sealed seismometer chamber are identical. The equality of the two ML1 spectra probably indicates that the pressure variations within the mine are so small that only electronic noise is being recorded. The shape of the ML2 curve indicates that the spectra of the rms air pressure variations are flat from 1 sec to about 25 sec and then rise at about 6 dB/octave toward longer periods.

The amplitude spectra of the ML2 microbarograph for the 26 November 1970 sample are plotted in figure 98. The units of this spectra are rms μ bar in a mHz passband. Thus, the spectra in figure 98 have numerical values 31.62 (the square root of 1000) less than the spectra in figure 97. If the ML2 curve in figure 97 is shifted by this amount, the two curves overlay each other.

EARTH MOTION

2498 SAMPLES, 128 LAGS, 0.1 SPS, PARZEN SMOOTHING

QC-AZ

+ PZL

26 NOVEMBER 1970

0800/1456

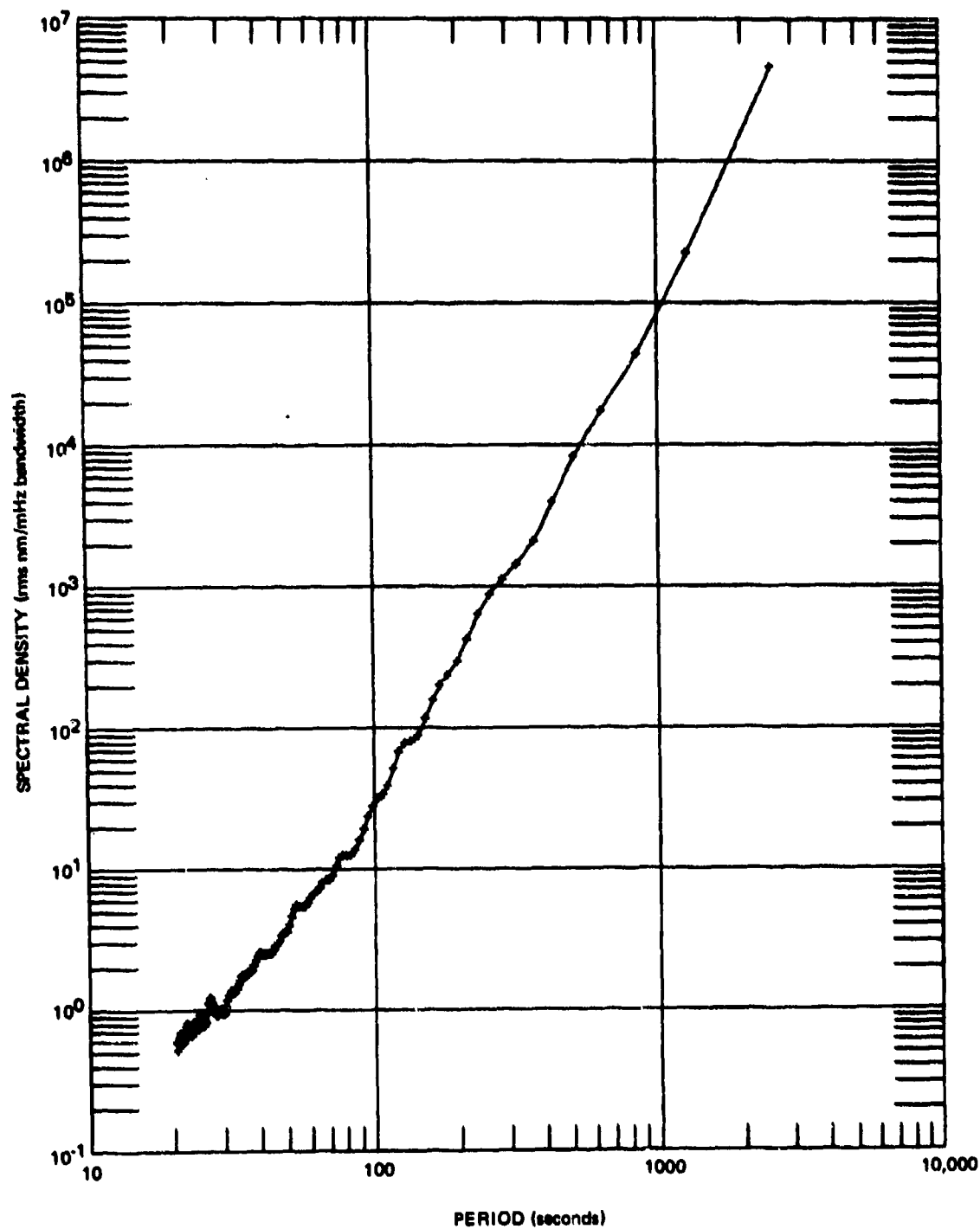


Figure 90. Vertical earth motion, 20 to 2560 sec, high wind sample

G 6659

EARTH MOTION

2498 SAMPLES, 128 LAGS, 0.1 SP5, PARZEN SMOOTHING

QC-AZ

26 NOVEMBER 1970

0800/1456

+ P325L

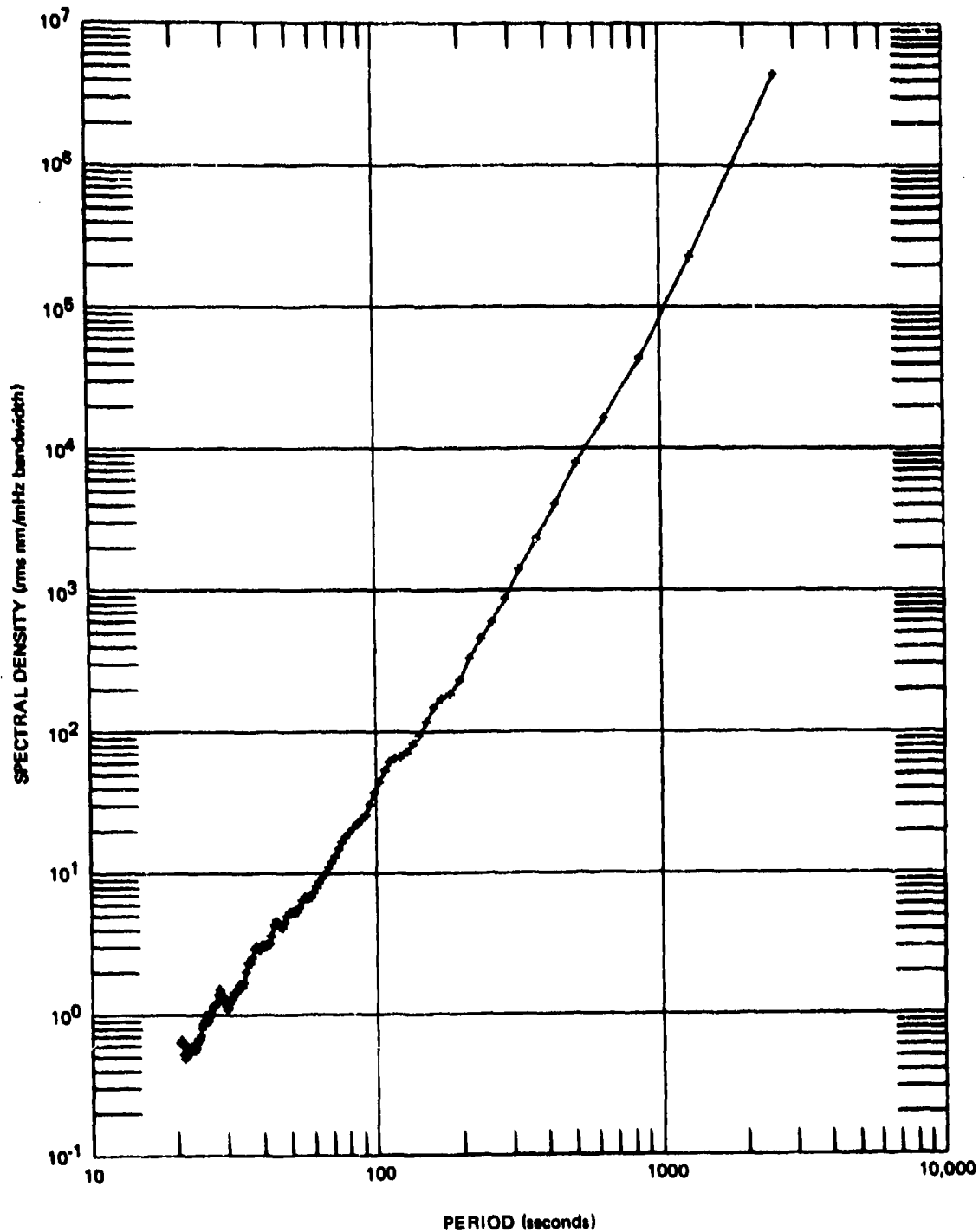


Figure 91. Horizontal earth motion in 325 degree azimuth, 20 to 2560 sec, high wind sample

G 6660

EARTH MOTION

2498 SAMPLES, 128 LAGS, 0.1 SPS, PARZEN SMOOTHING

QC-AZ

• P55L

26 NOVEMBER 1970

0800/1456

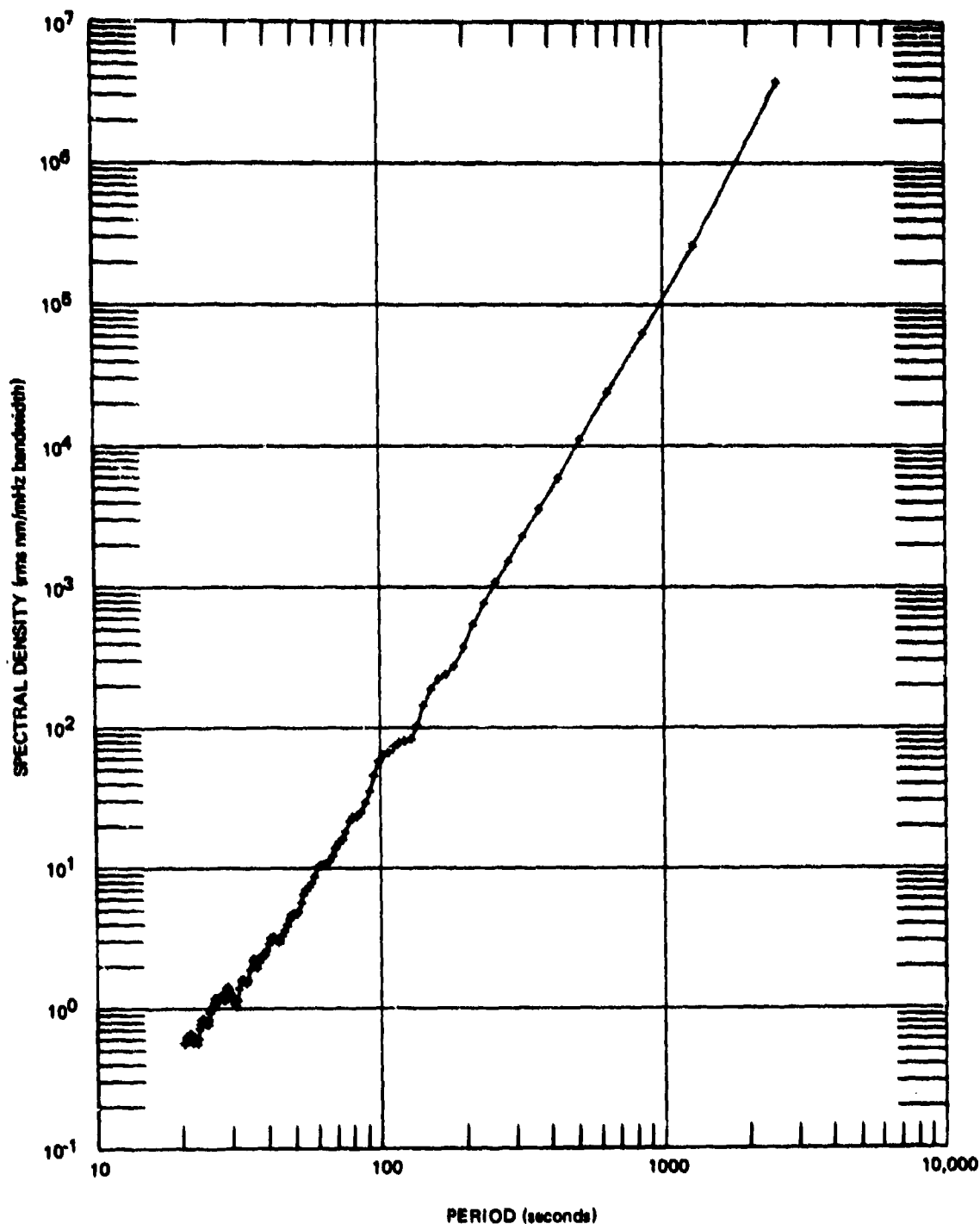


Figure 92. Horizontal earth motion in 55 degree azimuth, 20 to 2560 sec, high wind sample

G 6661

EARTH STRAIN

2498 SAMPLES, 128 LAGS, 0.1 SPS, PARZEN SMOOTHING

QC#A2

26 NOVEMBER 1970

0600/1456

* 52L

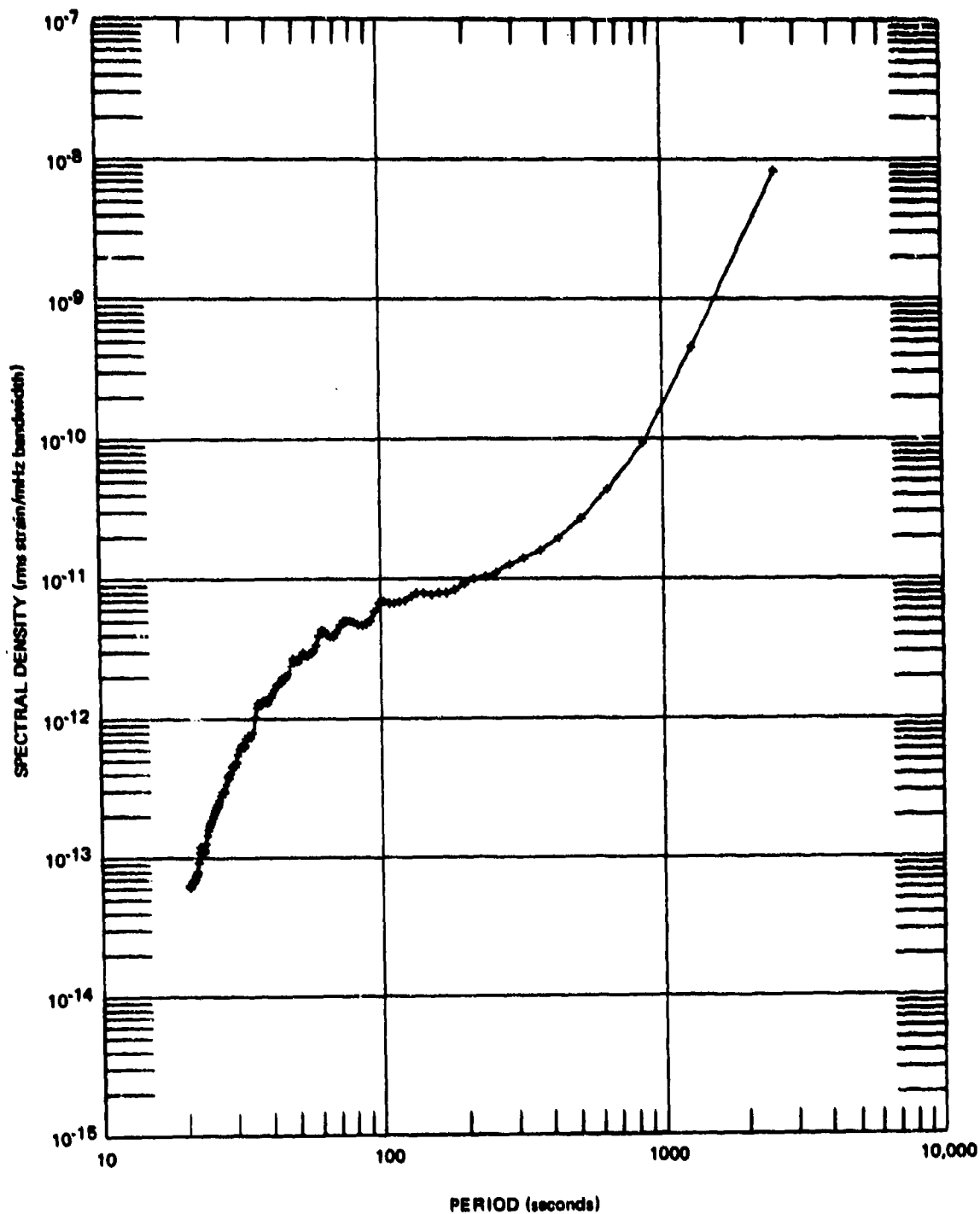
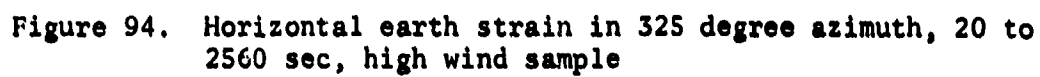


Figure 93. Vertical earth strain, 20 to 2560 sec, high wind sample G 6662

2498 SAMPLES, 128 LAGS, 0.1 SPS, PARZEN SMOOTHING
DC-AZ * S325L
26 NOVEMBER 1970
0800/1456

800/1456

◆ S325L



G 6663

EARTH STRAIN

2498 SAMPLES, 128 LAGS, 0.1 SP5, PARZEN SMOOTHING

QC-AZ

+ S55L

26 NOVEMBER 1970

0800/1456

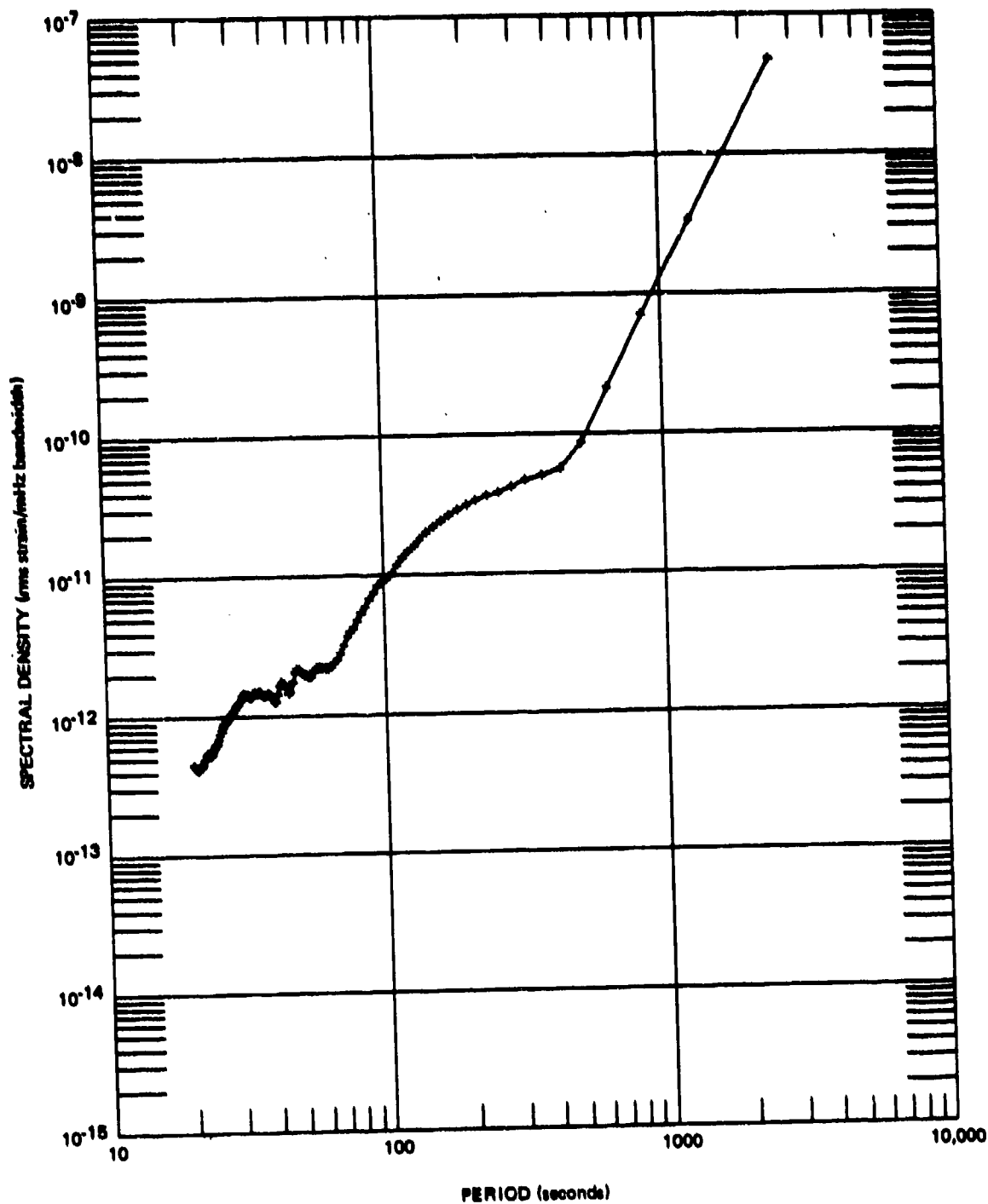


Figure 95. Horizontal earth strain in 55 degree azimuth, 20 to 2560 sec, high wind sample

G 6664

ATMOSPHERIC PRESSURE

3841 SAMPLES, 256 LAGS, 2.0 SPS, PARZEN SMOOTHING

GC-A2

31 MAY 1970

0438/0510

* ML1

* ML2

1.0000E+00

1.0000E+00

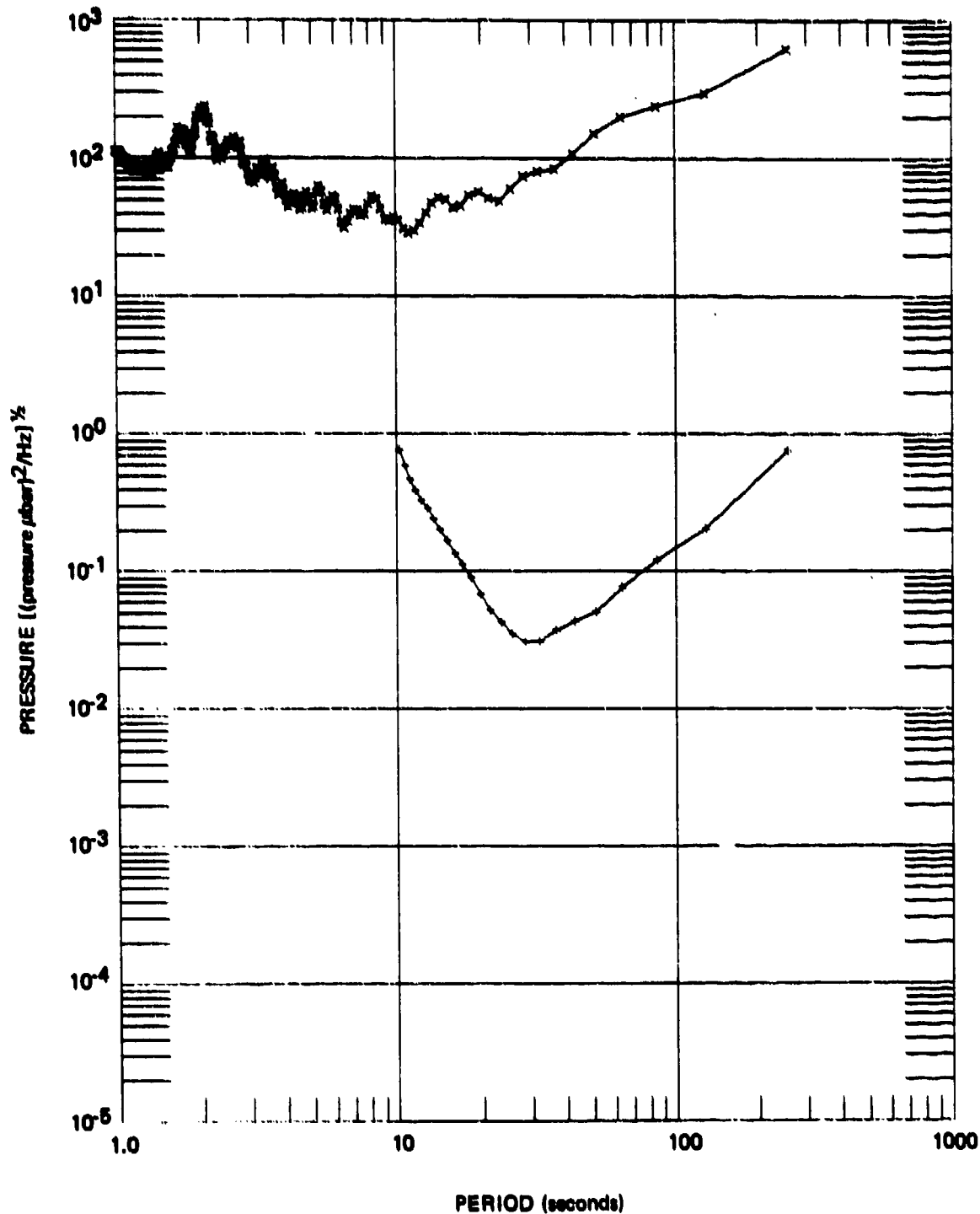


Figure 96. Atmospheric pressure 1 to 256 sec

G 6190

ATMOSPHERIC PRESSURE

2410 SAMPLES, 128 LAGS, 0.1 SPS, PARZEN SMOOTHING

QC-A7
31 MAY 1970
0046/0730

* ML1
* ML2

1.0000E+00
1.0000E+00

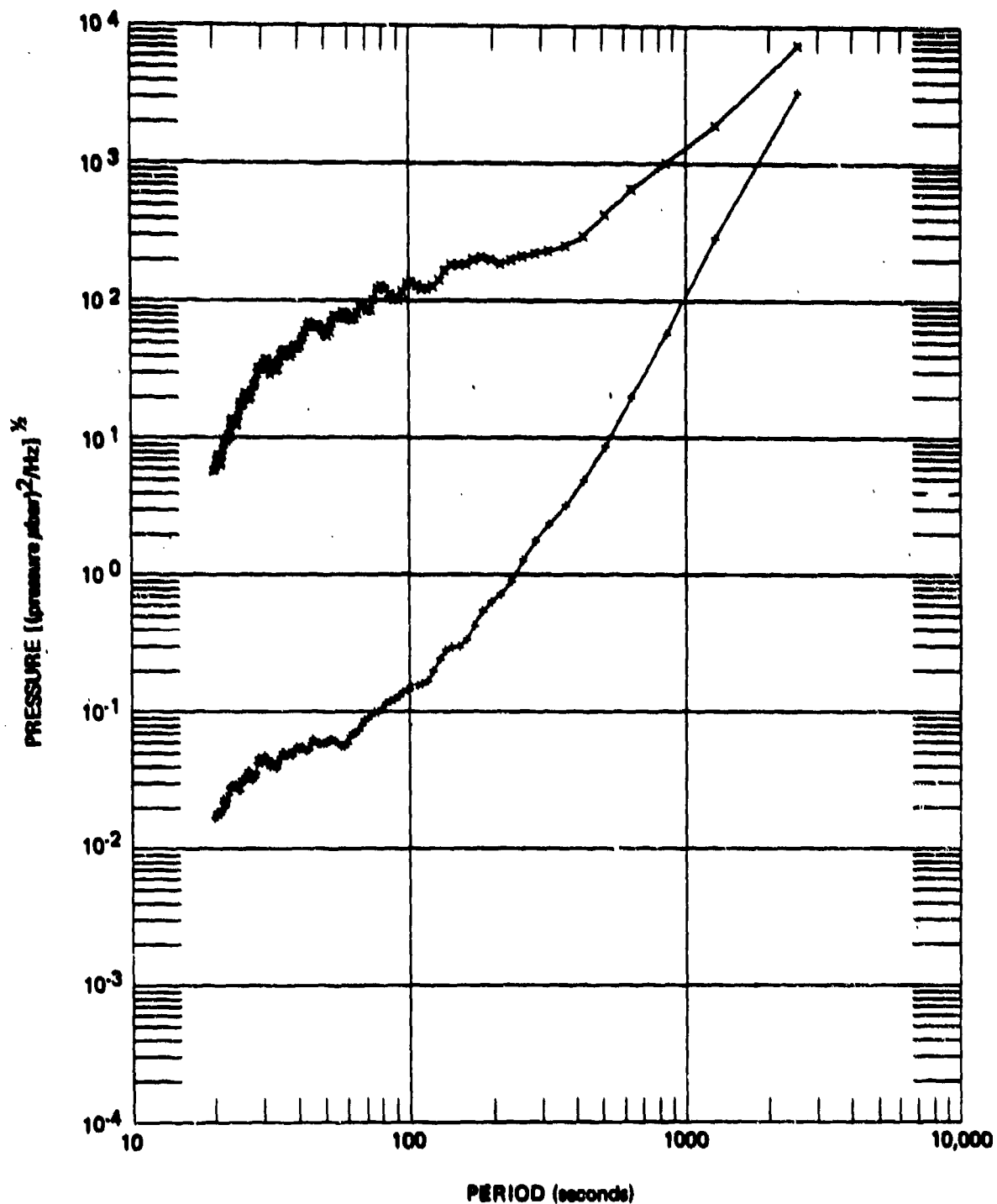


Figure 97. Atmospheric pressure 20 to 2560 sec

06191

ATMOSPHERIC PRESSURE

2498 SAMPLES, 128 LAGS, 0.1 SPS, PARZEN SMOOTHING

QC#A2

* ML2

26 NOVEMBER 1970

0800/1456

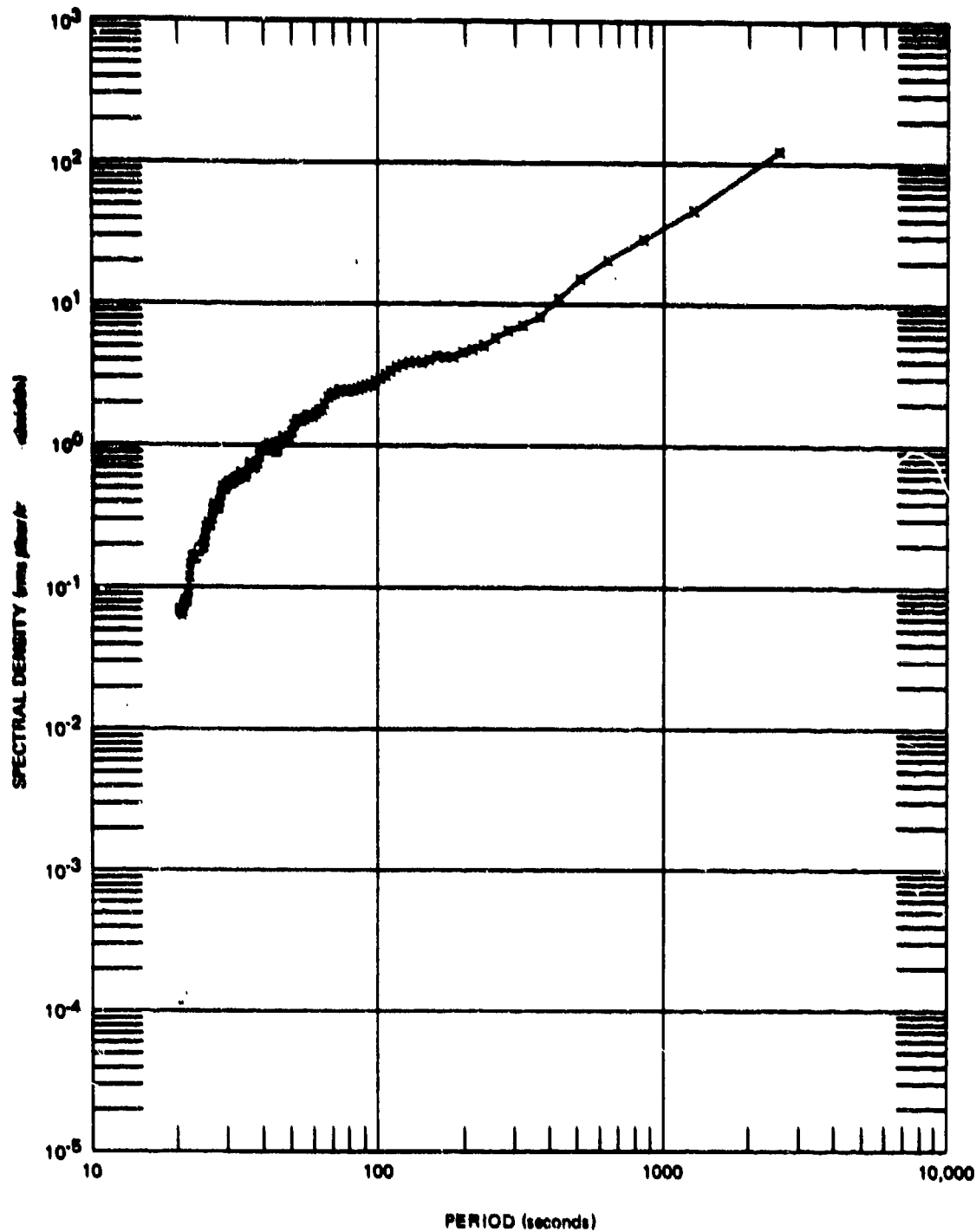


Figure 98. Atmospheric pressure, 20 to 2560 sec, high wind sample

G 6668

The amplitude spectra of the WV2 wind velocity is plotted in figure 99.

7.6.3.2 Transfer Functions from Air Pressure to Ground Strain and Displacement

This section presents estimates of the transfer function from air pressure fluctuations to ground strain and apparent displacement and of the transfer function from wind velocity to ground strain and displacement. The transfer function is estimated in the following manner. The cross spectra between the microbarograph and the seismograph represents the linearly related energy recorded by both instruments. This linearly related energy spectra is then divided by the microbarograph spectra. The quotient is then corrected for the response of both instrument systems, and the result is an estimate of the transfer function from the air pressure to ground strain or displacement. The units cancel as follows:

$$\frac{\text{cross spectra (strain x } \mu\text{bar)}/\text{Hz}}{\text{ML2 spectra } (\mu\text{bar})^2/\text{Hz}} = \frac{\text{strain}}{\mu\text{bar}} \quad (13)$$

Figures 100, 101, 102, and 103 are the transfer function for ground strain as estimated from the 30 May sample for the S325L1, S325U1, S55L, and S55U seismographs, respectively. The estimates between 20 and 1000 sec are from the spectra in figures 82 through 85. The estimates between 1 and 256 sec are from similar spectra calculated from the 33.0 min sample from 0438Z to 0510Z within the longer sample from 0046Z to 0730Z. The shorter sample was during the interval of maximum pressure activity. The estimates are considered satisfactory for the period range from 10 to 1000 sec. (See the coherence in figures 82 through 86.) The smooth fit of the longer periods in the short sample along the middle of the curve of the longer sample indicates that all the estimates can be improved by additional smoothing. The divergence at periods shorter than 10 sec of the estimates of the transfer functions between the S_L and S_U data results from the original recordings being in the magnetic tape recorder noise. The tape recorder noise is essentially flat, so that when these data are corrected for the two different system responses, two different values are obtained.

Figure 104 is the transfer function for displacement equivalent to the effect of ground tilt on the seismogram. The following discussion is based on the equations in section 7.7.1. If the recorded signal is taken as the sum of the outputs from a displacement input and a tilt input, and if typical values are substituted for elastic parameters of the rock, the air pressure wave velocity, and the wave frequency, then the contribution to the total seismogram of displacement is seen to be -1 while the contribution of tilt is +500. Therefore, the P55L seismogram which is calibrated in displacement must be considered as the apparent displacement equivalent to the tilt of the ground.

The relationship between the strain and the equivalent displacement transfer functions is that which is expected from the equation in section. 7.6.2. The

WIND VELOCITY
 2498 SAMPLES, 128 LAGS, 0.1 SPS, PARZEN SMOOTHING
 QC-AZ * WU2
 26 NOVEMBER 1970
 0800/1456

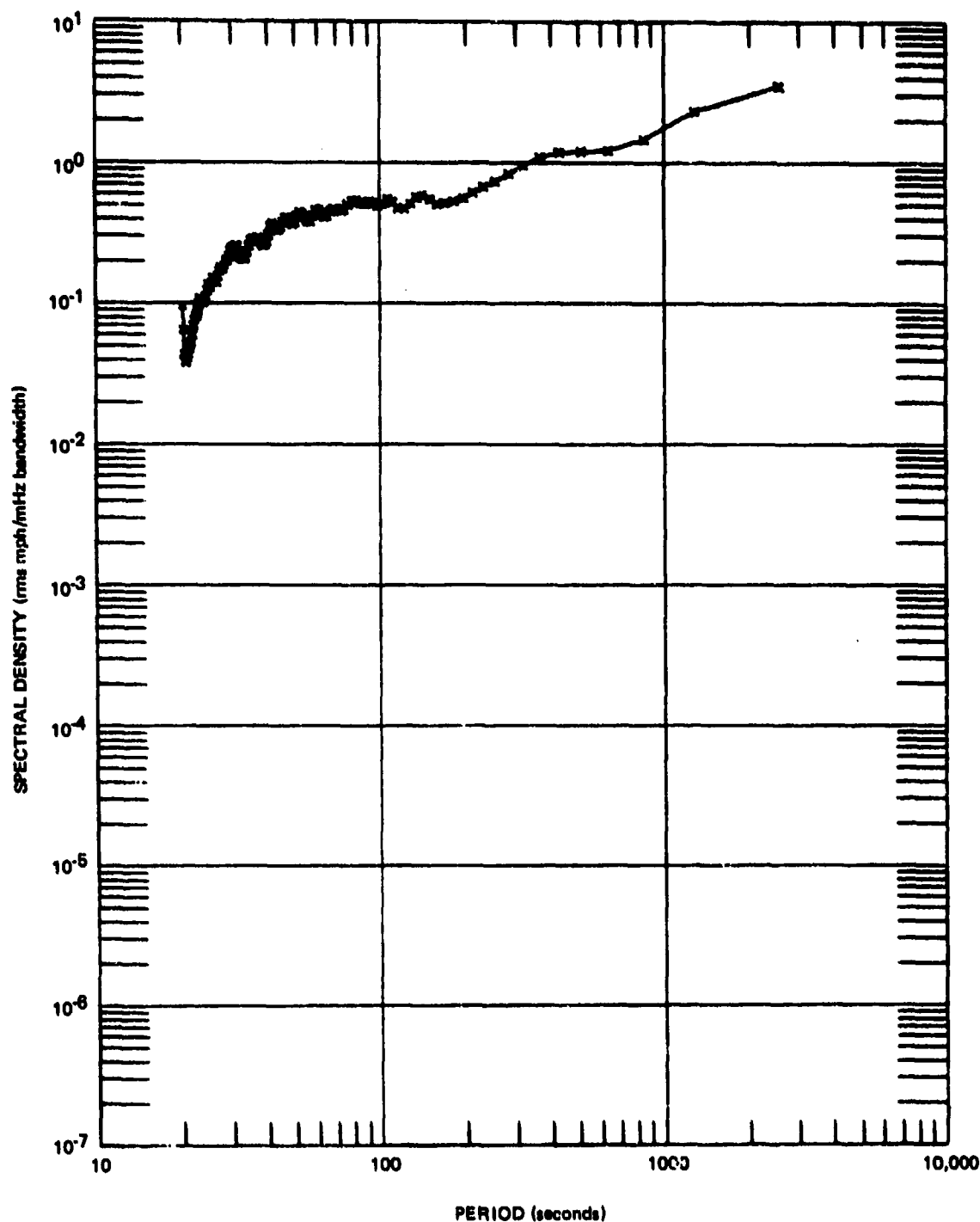


Figure 99. Wind velocity, 20 to 2560 sec, high wind sample

G 6666

STRAIN/MICROBAR

3841/2410 SAMPLES, 256/128 LAGS, 2.0/0.1 SPS, PARZEN
 DC-A2 + S325L1XML2/ML2A 1.0000E+00
 31 MAY 1970 * S325L1XML2/ML2B 1.0000E+00
 0046/0730

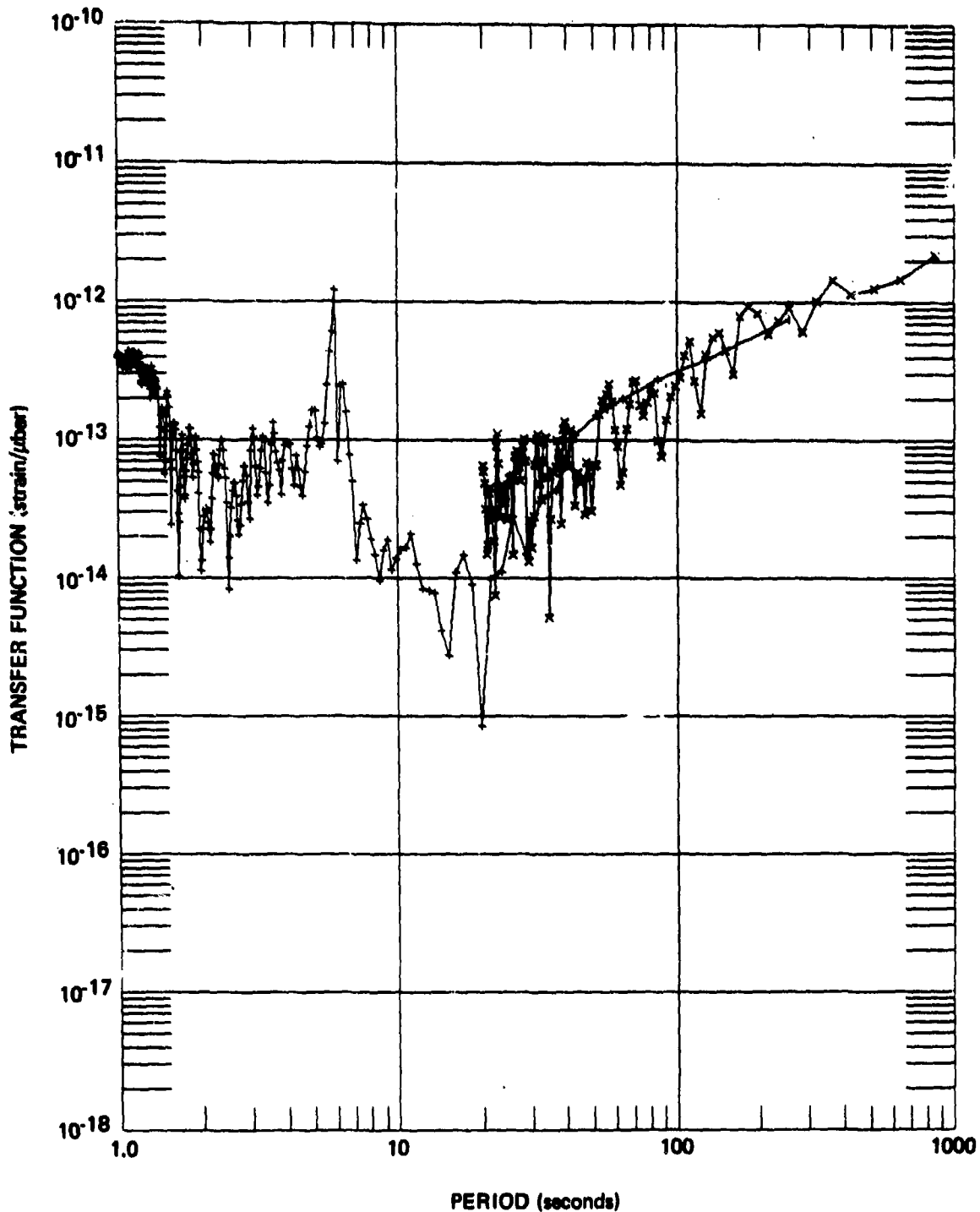


Figure 100. Estimate of pressure to strain transfer function from S325L1

G 6185

STRAIN/MICROBAR

3841/2410 SAMPLES, 256/128 LAGS, 2.0/D.O. 1 SP5, PARZEN
 GC-A7
 31 MAY 1970
 0046/0730
 * S325U1 XML2/ML2A
 * S325U1 XML2/ML2B
 1.0000E+00
 1.0000E+00

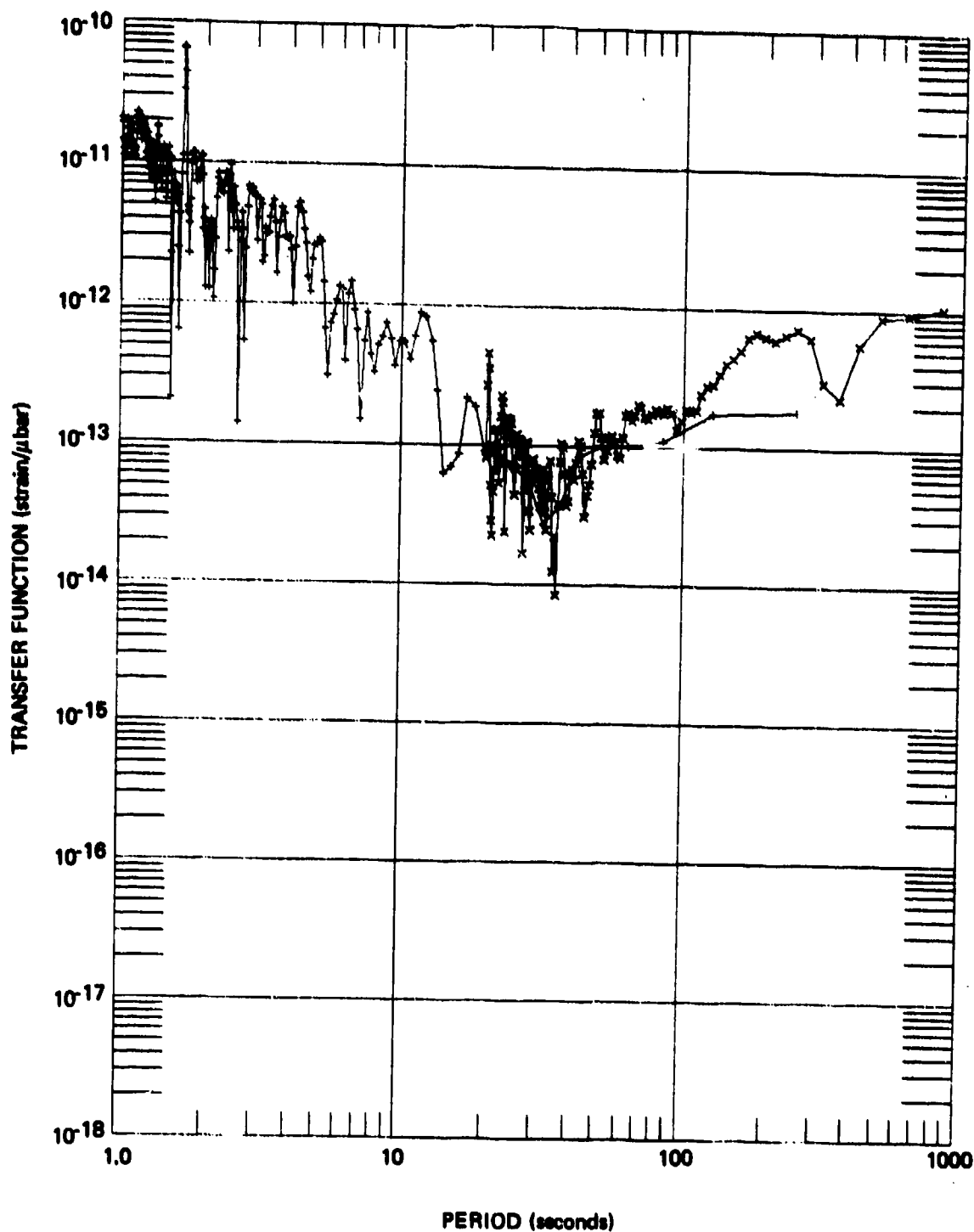


Figure 101. Estimate of pressure to strain transfer function from S325U1

Q 8188

STRAIN/MICROBAR

38-11-21.0 SAMPLES, 256 LAGS, 2.040 1 SPS, PARZEN
 30-APR
 31 MAY 1968
 0146 0730
 * S55LXML2/ML2A 1.0000E+00
 * S55LXML2/ML2B 1.0000E+00

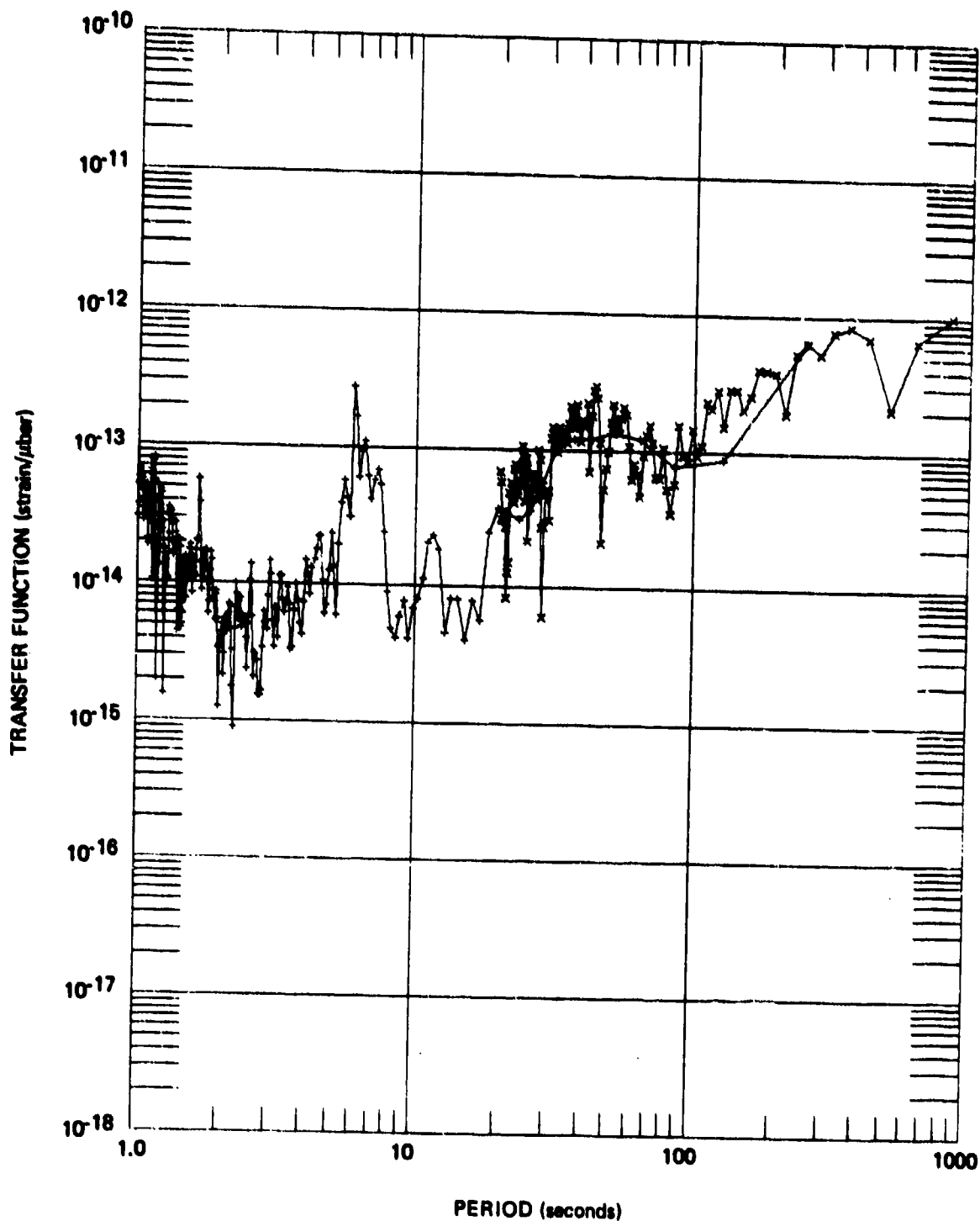


Figure 102. Estimate of pressure to strain transfer function from S55L

G 6187

STRAIN/MICROBAR

3841/2410 SAMPLES, 256/128 LAGS, 2.0/0.1 SPS, PARZEN

GC-A7

31 MAY 1970

0046/0730

* S55UXML2/ML2A

1.0000E+00

* S55UXML2/ML2B

1.0000E+00

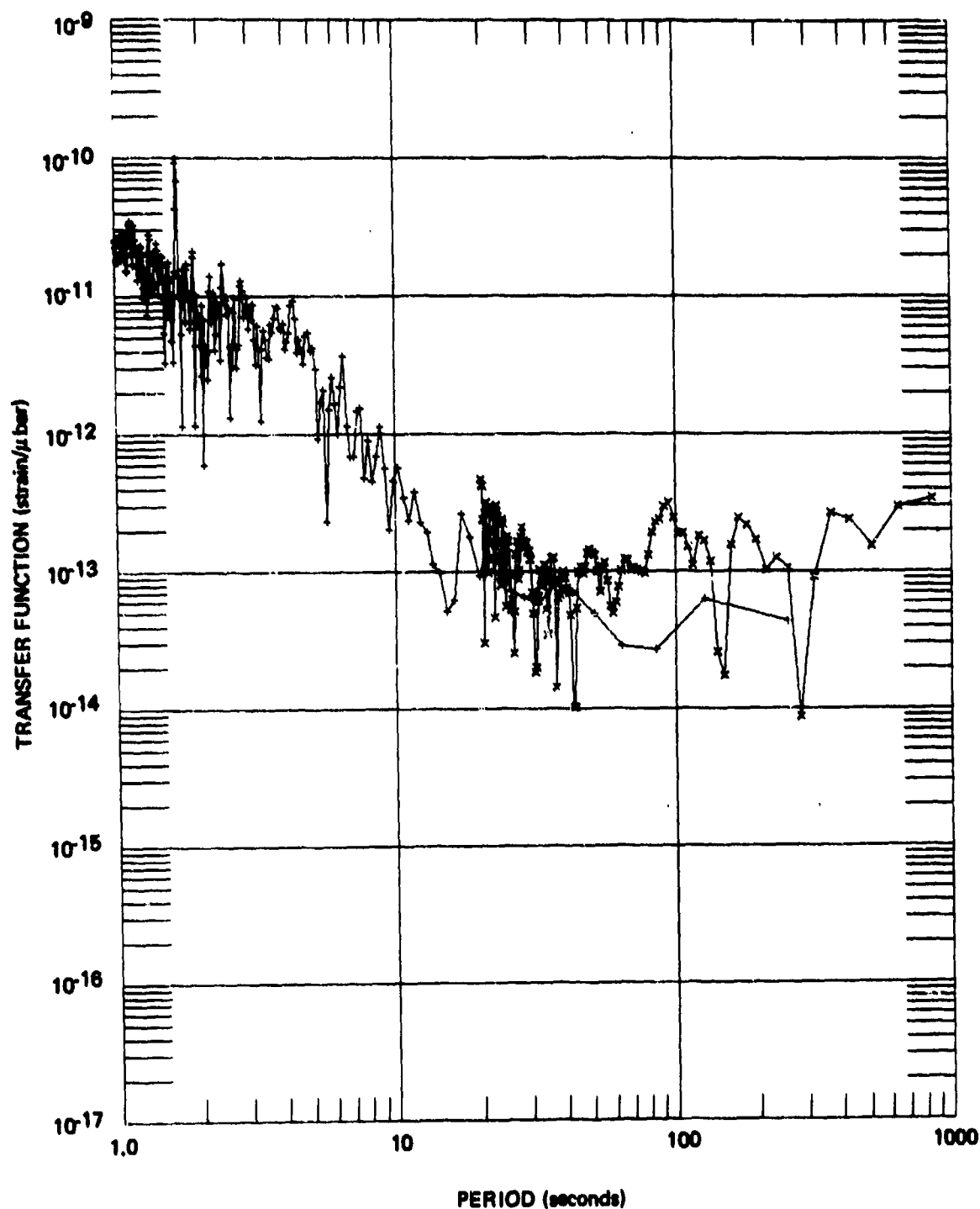


Figure 103. Estimate of pressure to strain transfer function from S55U

G 6188

DISPLACEMENT/MICROBAR

3841/2410 SAMPLES, 256/128 LAGS, 2.0'D 1 SPS, PARZEN

GC-AZ
31 MAY 1970
0046/0730

* P55LXML2/ML2A
* P55LXML2/ML2B

1.0000E+00
1.0000E+00

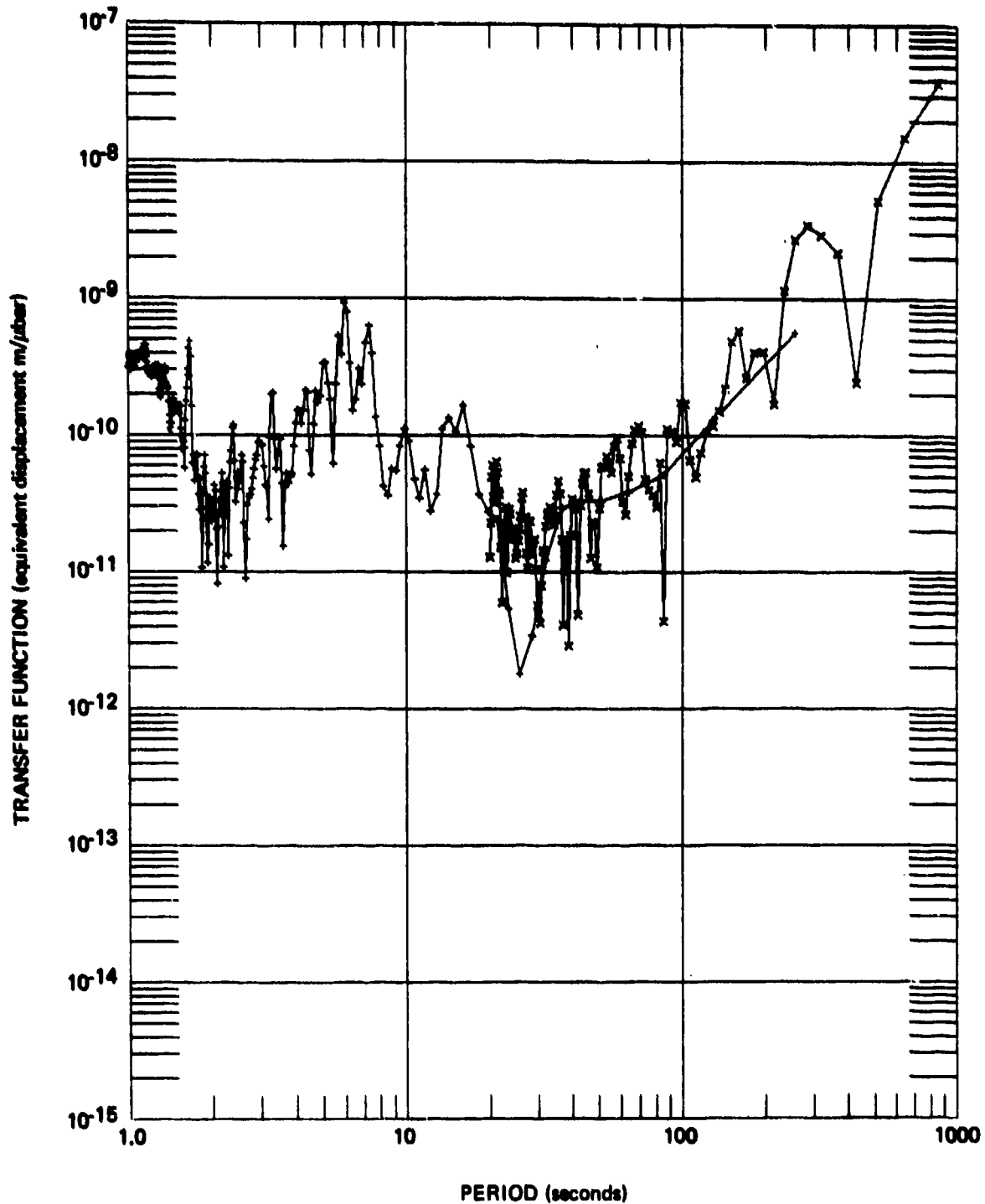


Figure 104. Estimate of pressure to equivalent displacement for tilt transfer function from P55L.

G 6189

strain transfer function in all four figures rises toward long periods at about 6 dB/octave. The equivalent displacement response rises at about 12 dB/octave.

Transfer functions from the 26 November sample are plotted in the following figures. The strain output per microbar input transfer functions for the SZL, S325L, and S55L seismographs are plotted in figures 105, 106, and 107, respectively. The displacement output per microbar input transfer functions for the PZL, P325L, and P55L seismographs are plotted in figures 108, 109, and 110, respectively.

The shapes of the transfer functions from both samples are similar. All the strain transfer functions rise at approximately 6 dB/octave toward longer periods as predicted by the equations in section 7.6.2. The 26 November sample of the S55L is an exception. It rises at about 12 dB/octave at periods longer than 420 sec. This change of slope suggests a second mechanism from pure vertical loading at the surface. Numerical values for the transfer functions from the two time samples differ by a factor of about 10. The reason for this difference is not known. The difference is not thought to be the result of an error in the calibration because the two microbarograph samples overlay, and each set of transfer functions are consistent among the sets.

The strain output per mile-per-hour of wind velocity transfer functions for the SZL, S325L, and S55L seismographs are plotted in figures 111, 112, and 113, respectively. The displacement per mile-per-hour of wind velocity for the PZL, P325L, and P55L seismographs are plotted in figures 114, 115, and 116, respectively. No theory has been developed to relate displacements and strains to wind-generated forces on mountain sides, so these results cannot be compared to theoretical expectations. The strain transfer functions rise toward longer periods. Between 20 sec and about 400 sec, the slope is about 6 dB/octave; at the longer periods, the slope is about 18 dB/octave.

The displacement transfer functions rise toward longer periods at about 18 dB/octave at periods longer than 50 sec.

The similarity of the transfer functions of all three components of the two types of seismographs lends confidence to the hypothesis that the mountain is being deformed by forces created by the wind load on the face of the mountain. The fact that the coherent part of the energy in all three components of the two types of seismographs relates to the wind velocity in an identical manner certainly identifies some mechanism of input load-output signal.

Wind velocity was used in the above calculations. If the mechanism acting is a deflection of the mountain from a wind-created force, then better results should have been obtained with wind velocity squared since the force is proportional to the kinetic energy of the air flow. The calculations have not been repeated with wind velocity squared.

7.7 TILT NOISE ON LONG-PERIOD INERTIAL SEISMOGRAPHS

The ground tilts with the passage of Rayleigh waves and with the application of localized forces. Seismographs respond to these tilts with varying degrees

STRAIN/MICROBAR
 2498 SAMPLES, 128 LAGS, 0.1 SPS, PARZEN SMOOTHING
 QC#AZ
 26 NOVEMBER 1970
 0800/1456
 + S2L X ML2/ML2

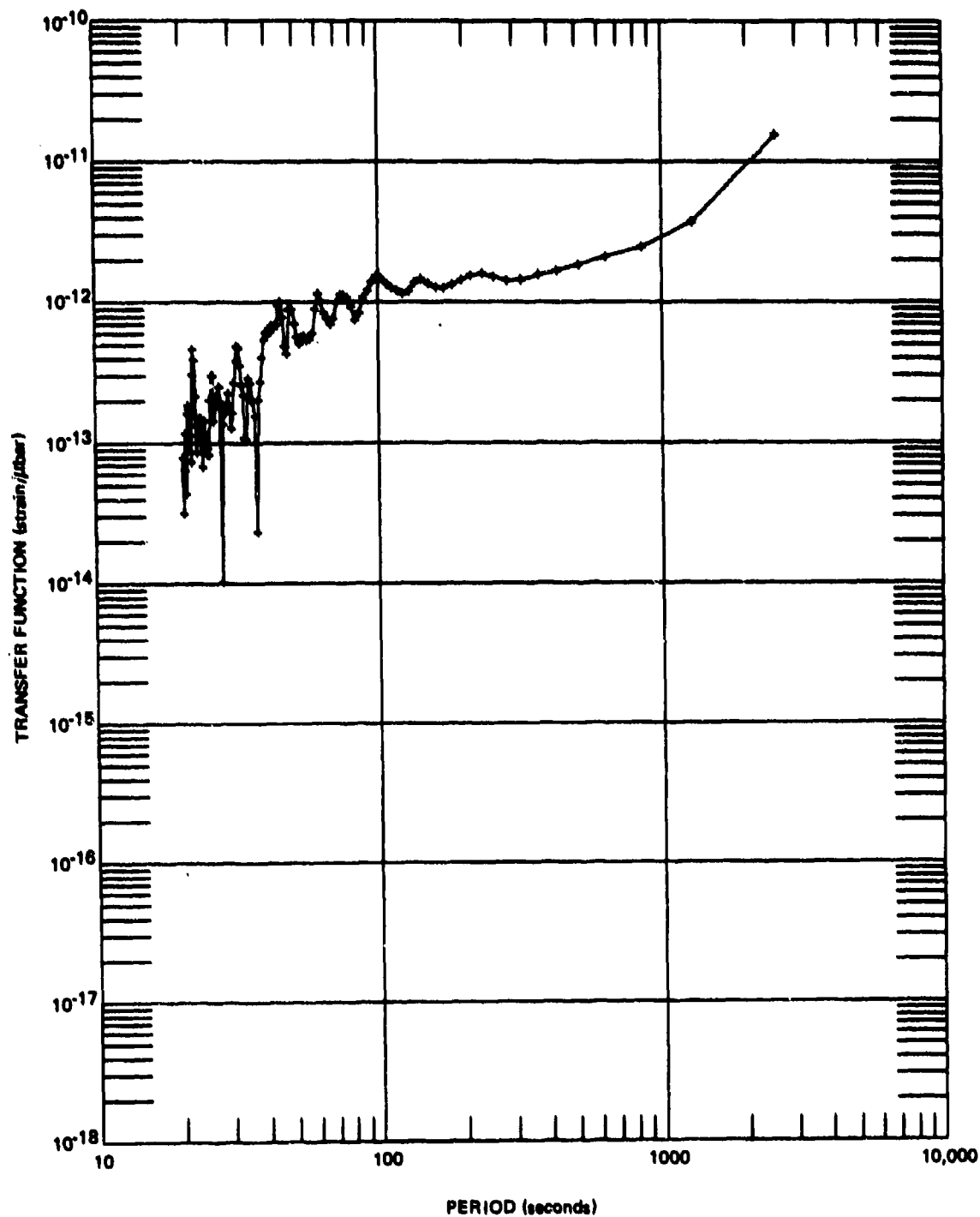


Figure 105. Estimate of pressure to vertical strain transfer function

G 6667

STRAIN/MICROBAR

2498 SAMPLES, 128 LAGS, 0.1 SPS, PARZEN SMOOTHING

QC#A2

+ S325L X ML2/ML2

26 NOVEMBER 1970

0800/1456

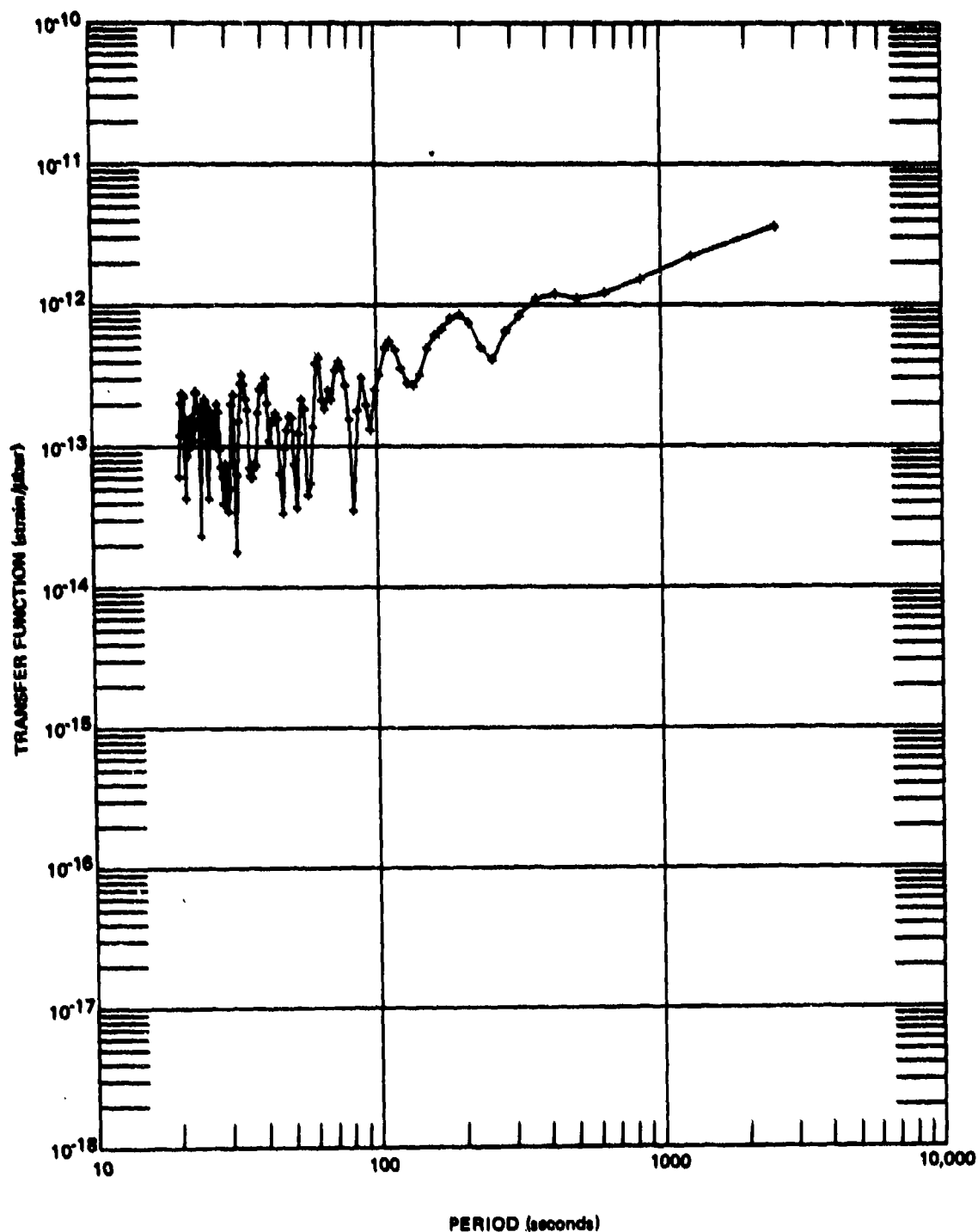


Figure 106. Estimate of pressure to horizontal strain transfer function from S325L

G 6668

STRAIN/MICROBAR

2498 SAMPLES, 128 LAGS, 0.1 SPS, PARZEN SMOOTHING
 GC=A2 + S5SL X ML2/ML2
 26 NOVEMBER 1970
 0800/1456

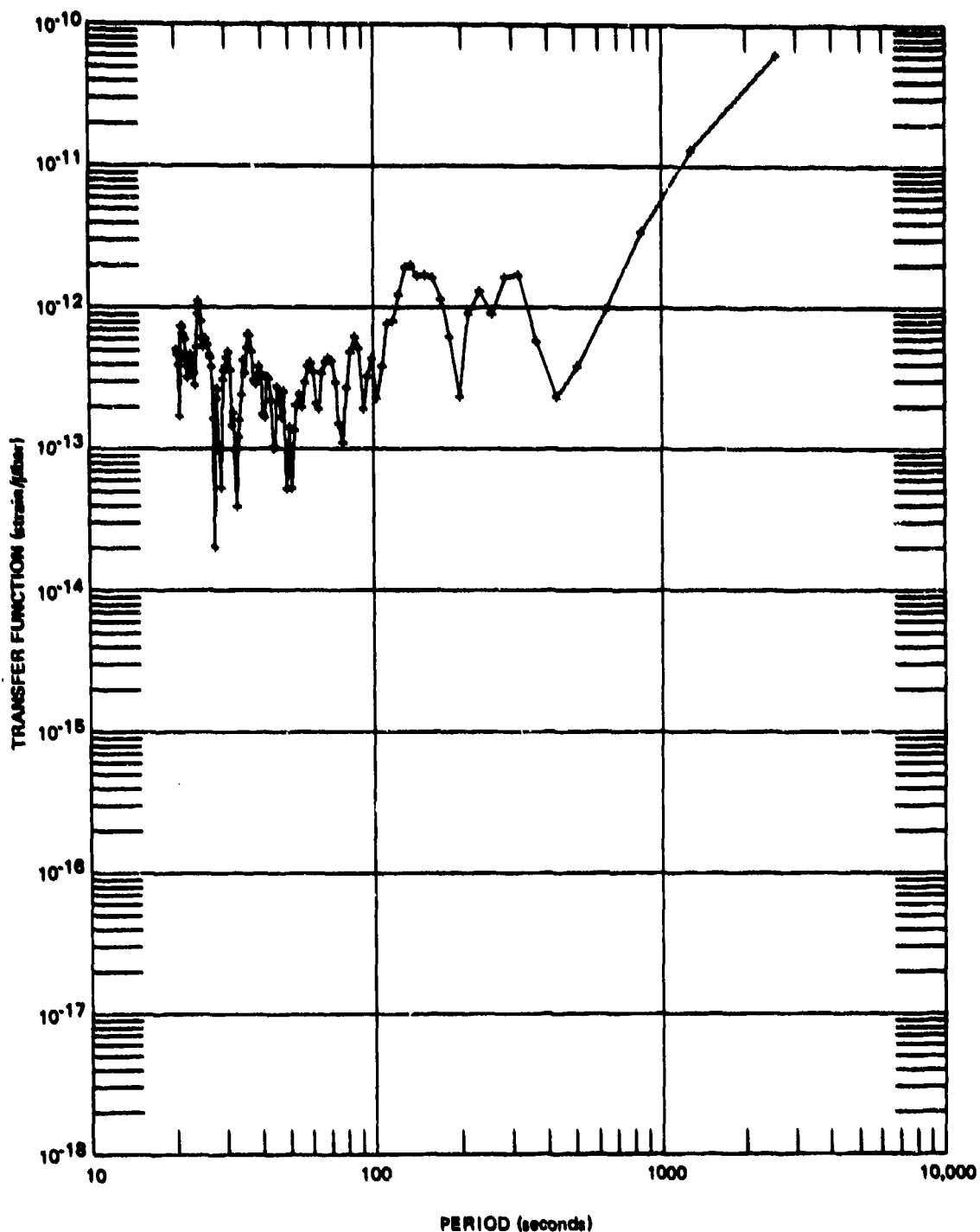


Figure 107. Estimate of pressure to horizontal strain transfer function from S5SL

Q 6669

DISPLACEMENT/MICROBAR

2498 SAMPLES, 128 LAGS, C.1 SPS, PARZEN SMOOTHING

GC-AZ

26 NOVEMBER 1970

0800/1456

+ P2L X ML2/ML2

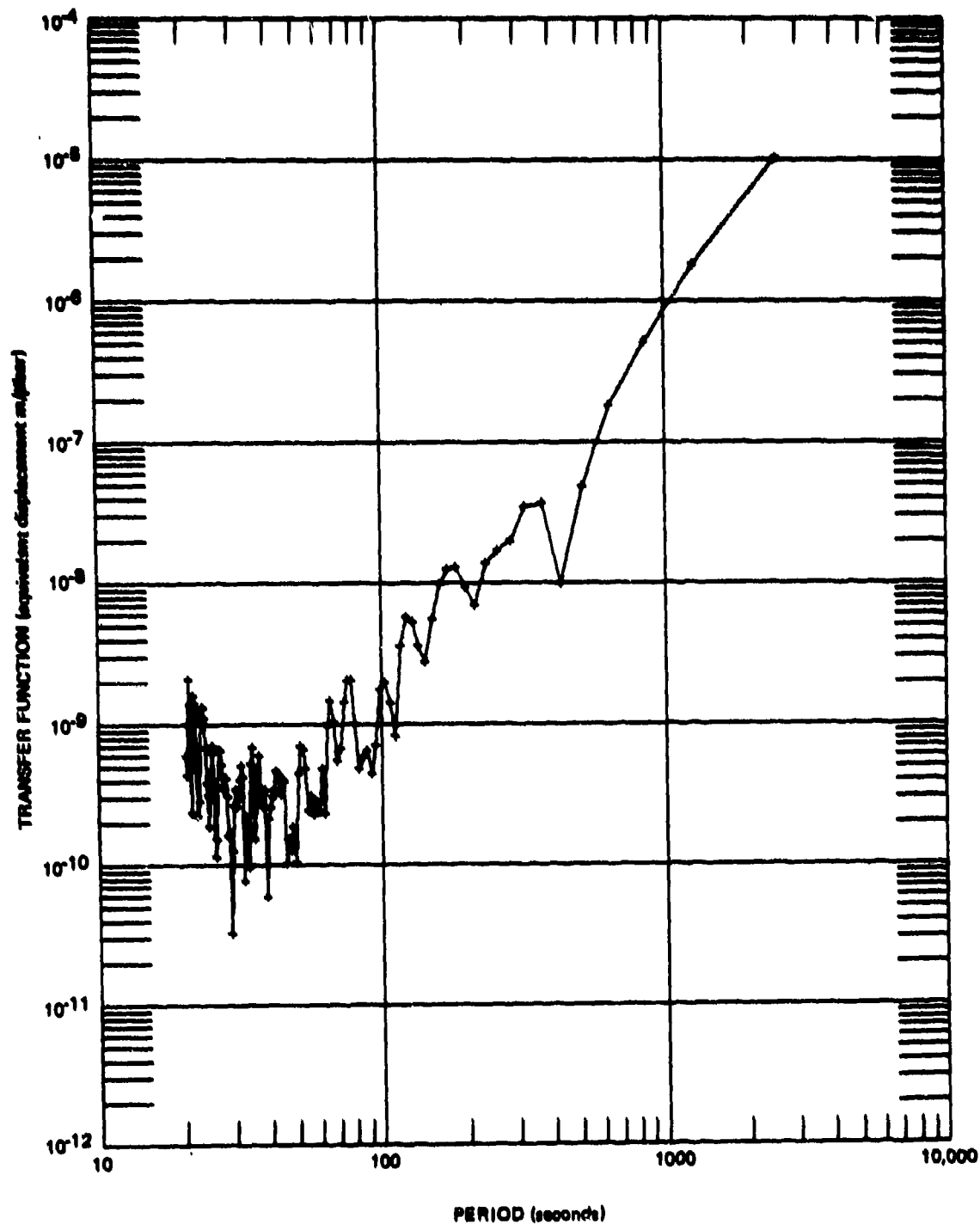


Figure 108. Estimate of pressure to vertical displacement transfer function

Q 6670

DISPLACEMENT/MICROBAR

2498 SAMPLES, 128 LAGS, 0.1 SPS, PARZEN SMOOTHING

QC#A2

26 NOVEMBER 1970

0800/1456

+ P325L X ML2/ML2

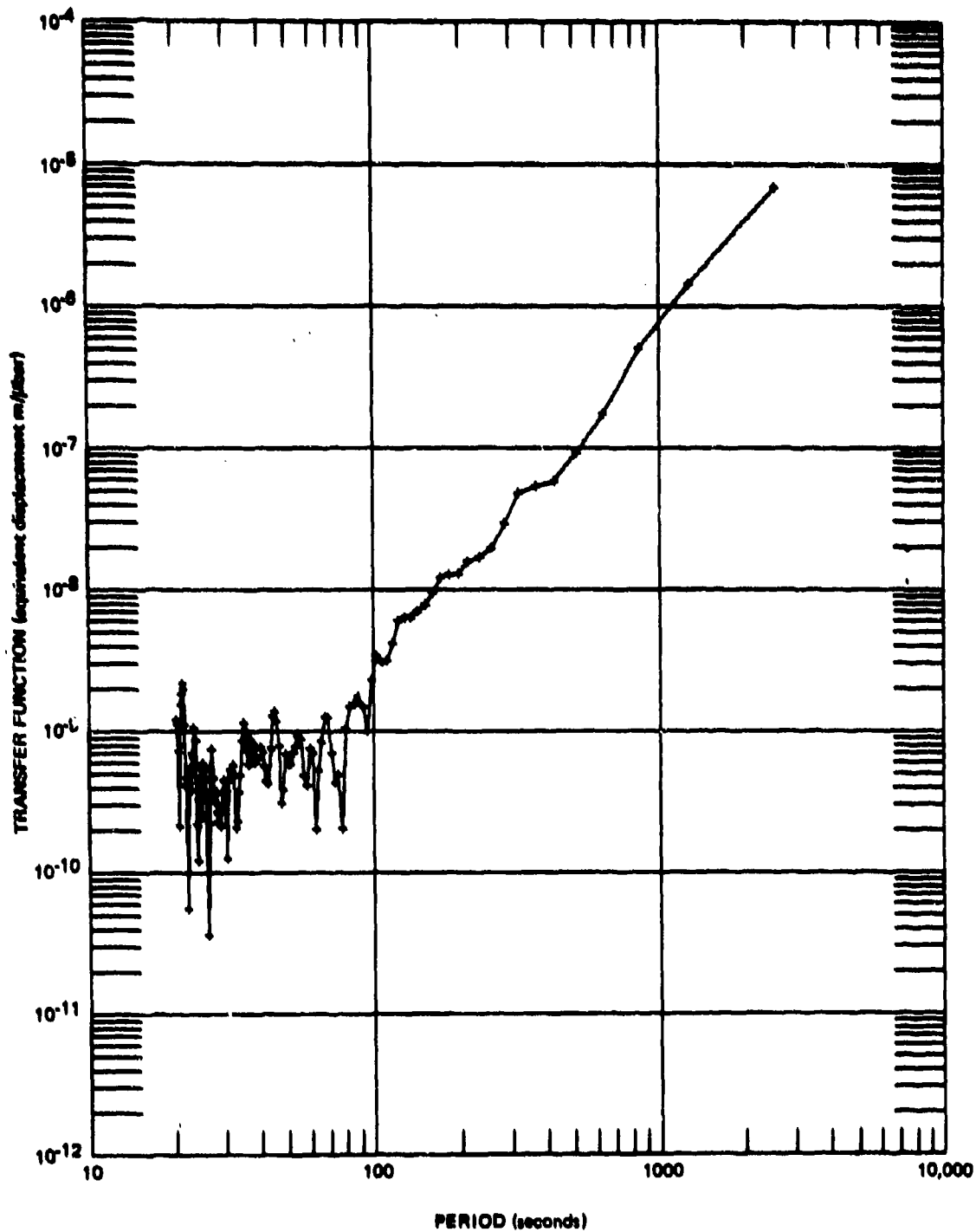


Figure 109. Estimate of pressure to horizontal displacement transfer function from P325L

G 6671

DISPLACEMENT/MICROBAR
 2498 SAMPLES, 128 LAGS, 0.1 SPS, PARZEN SMOOTHING
 QC#A2
 26 NOVEMBER 1970
 0800/1456
 + P55L X ML2/ML2

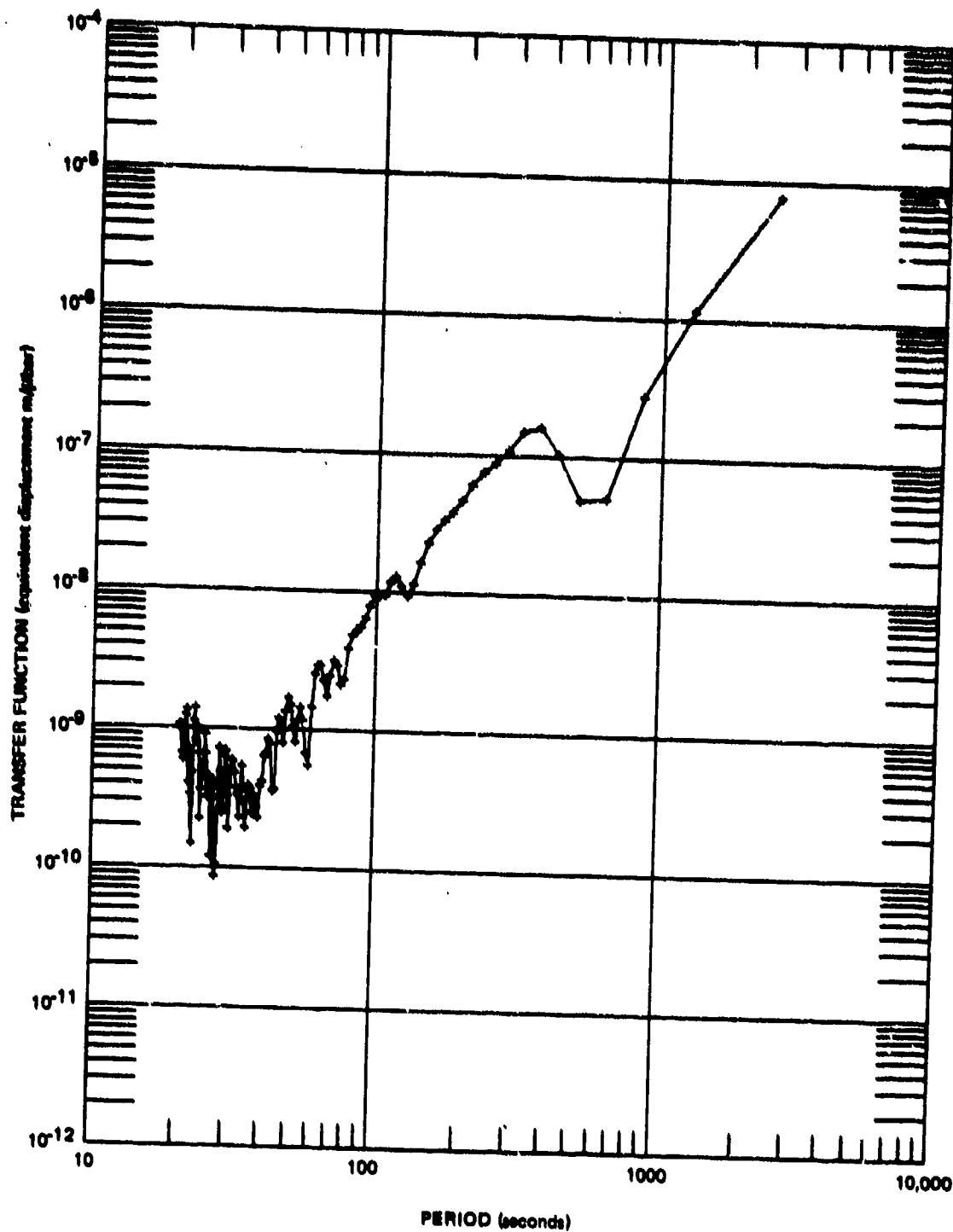


Figure 110. Estimate of pressure to horizontal displacement transfer function from P55L

3 6672

STRAIN/MPH

2498 SAMPLES, 128 LAGS, 0.1 SP5, PARZEN SMOOTHING

QC#A2

26 NOVEMBER 1970

0800/1456

+ SZL X WUZ/WUZ

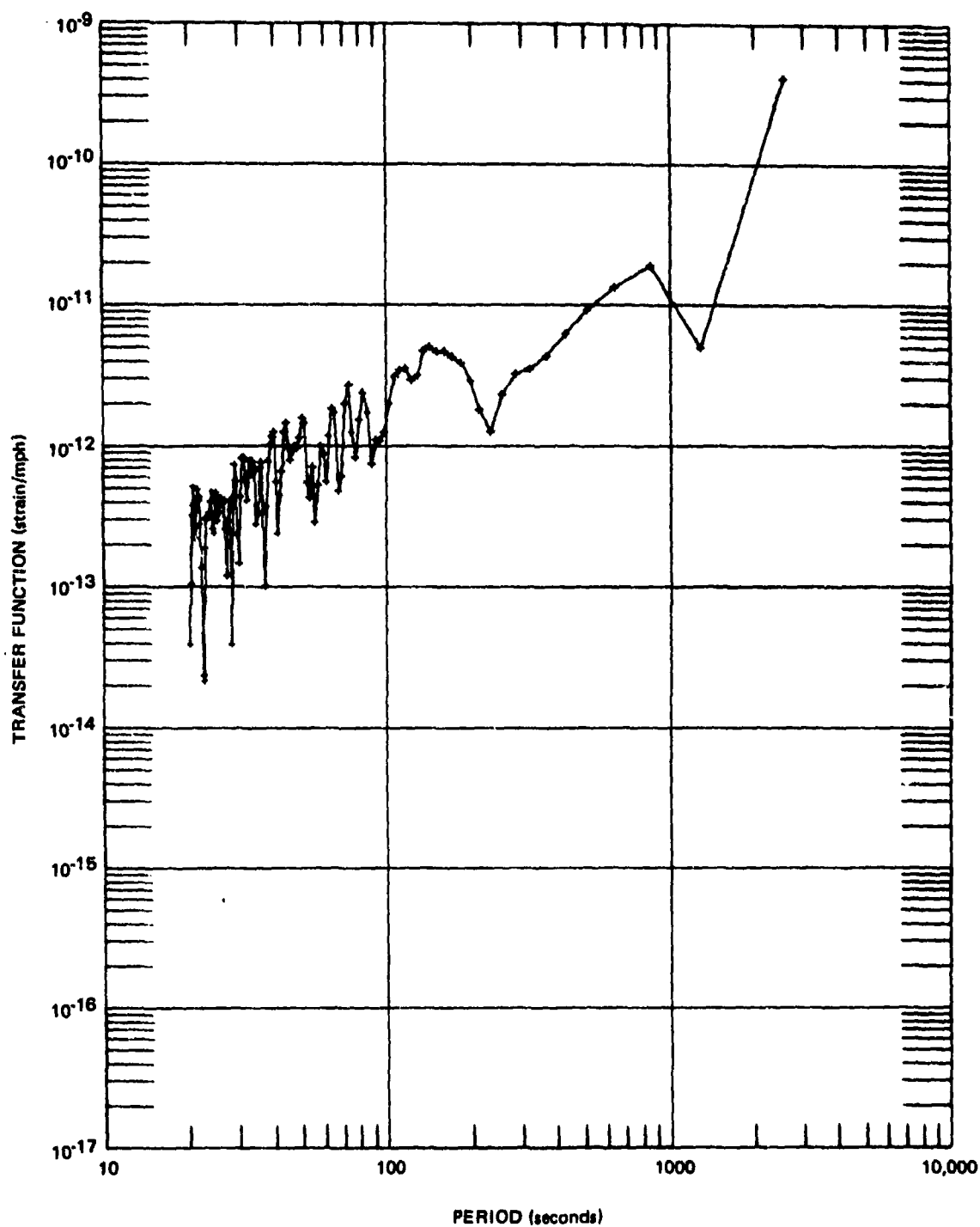


Figure 111. Estimate of wind velocity to vertical strain transfer function

G 6673

STRAIN/MPH

2498 SAMPLES, 128 LAGS, 0.1 SPS, PARZEN SMOOTHING

QC#A2

+ S325L X WU2/WU2

26 NOVEMBER 1970

0800/1456

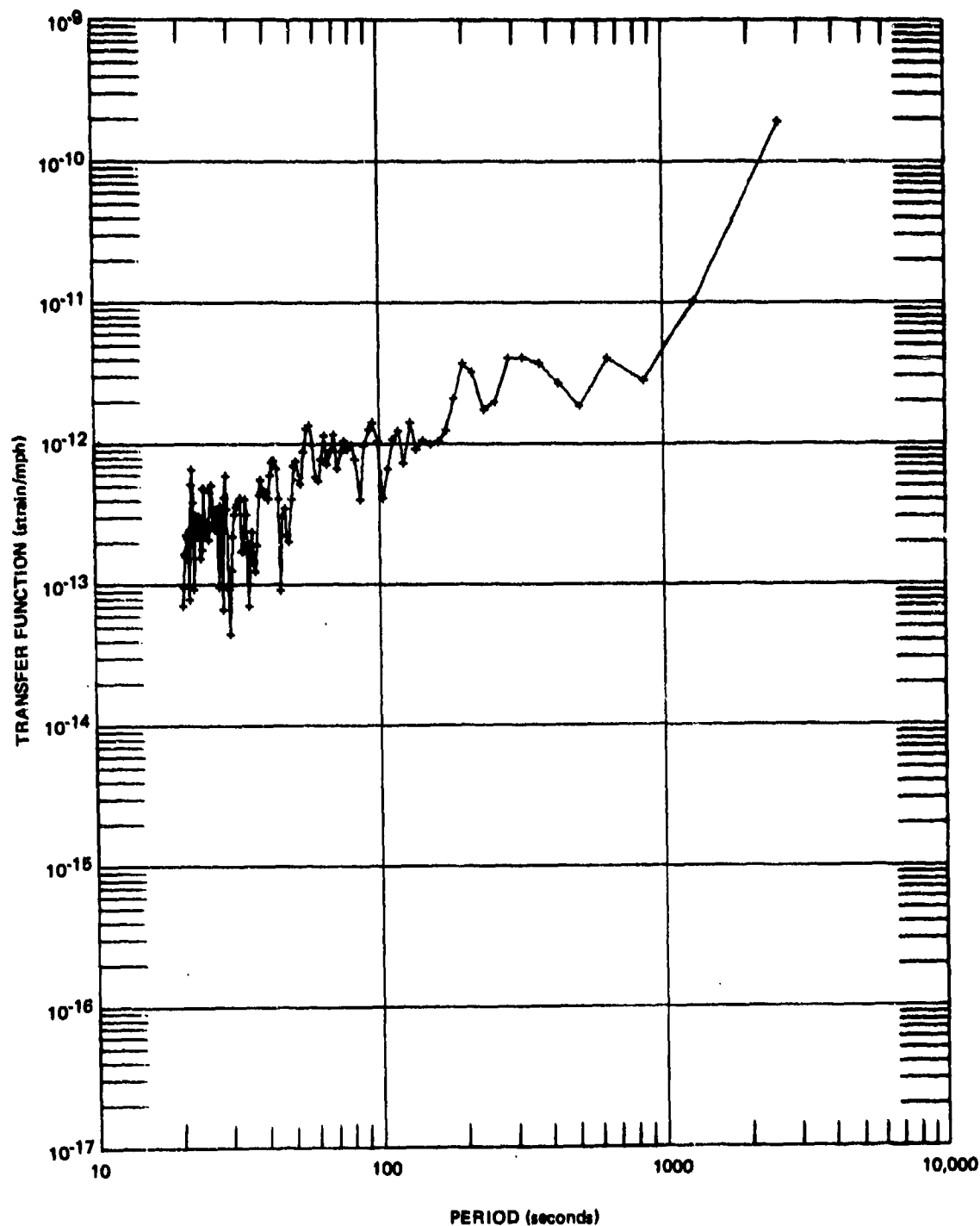


Figure 112. Estimate of wind velocity to horizontal strain transfer function from S325L

G 6674

STRAIN/MPH

2498 SAMPLES, 128 LAGS, 0.1 SPS, PARZEN SMOOTHING
 GC-AZ + S55L X WU2/WU2
 26 NOVEMBER 1970
 0800/1456

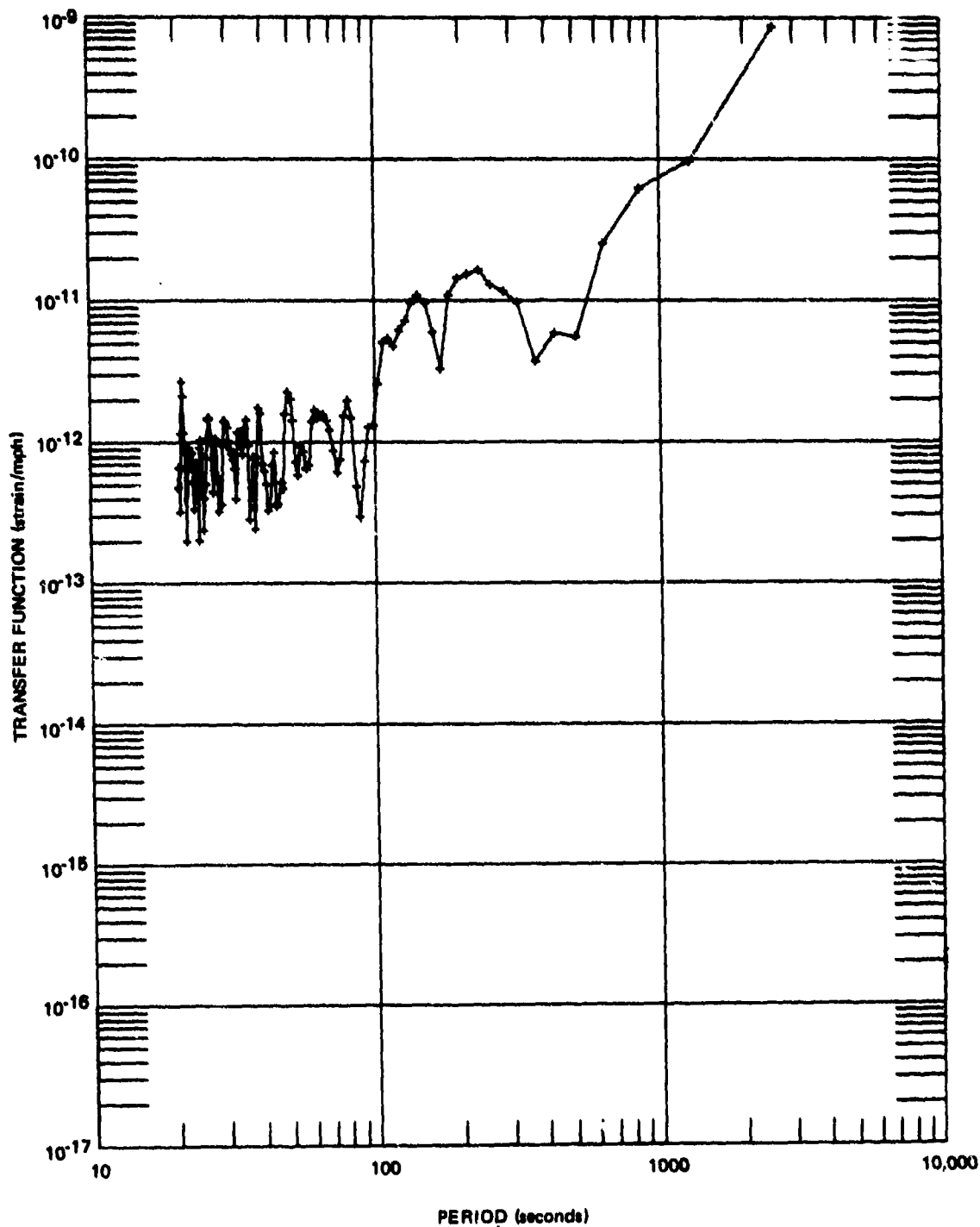


Figure 113. Estimate of wind velocity to horizontal strain transfer function from S55L

G 8875

DISPLACEMENT/MPH

2498 SAMPLES, 128 LAGS, 0.1 SP5, PARZEN SMOOTHING

QC-AZ

+ PZL X WU2/WU2

26 NOVEMBER 1970

0800/1456

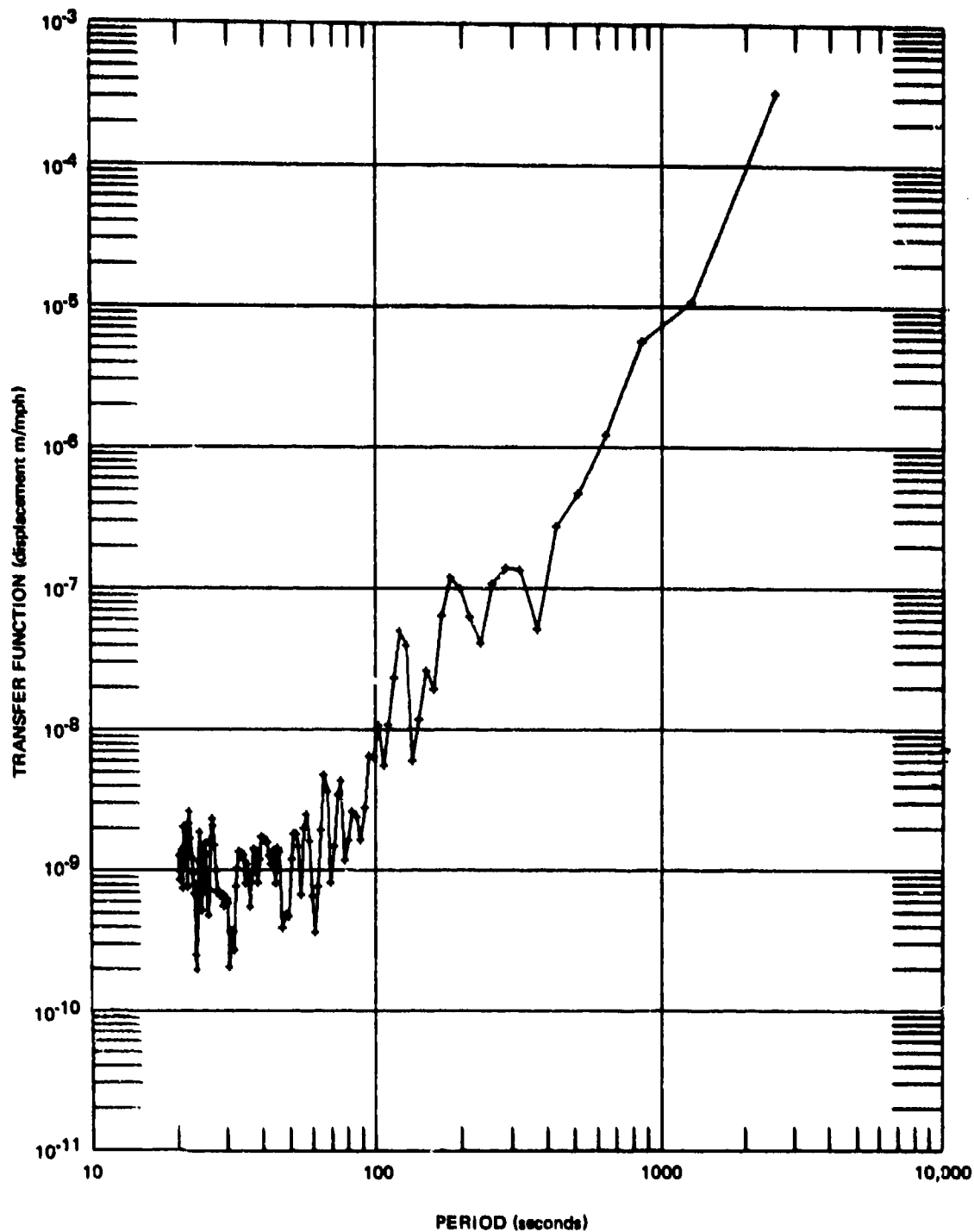


Figure 114. Estimate of wind velocity to vertical displacement transfer function

G 6676

DISPLACEMENT/MPH

2498 SAMPLES. 128 LAGS, 0.1 SPS, PARZEN SMOOTHING

QC-AZ

+ P325L X WU2/WU2

26 NOVEMBER 1970

0800/1456

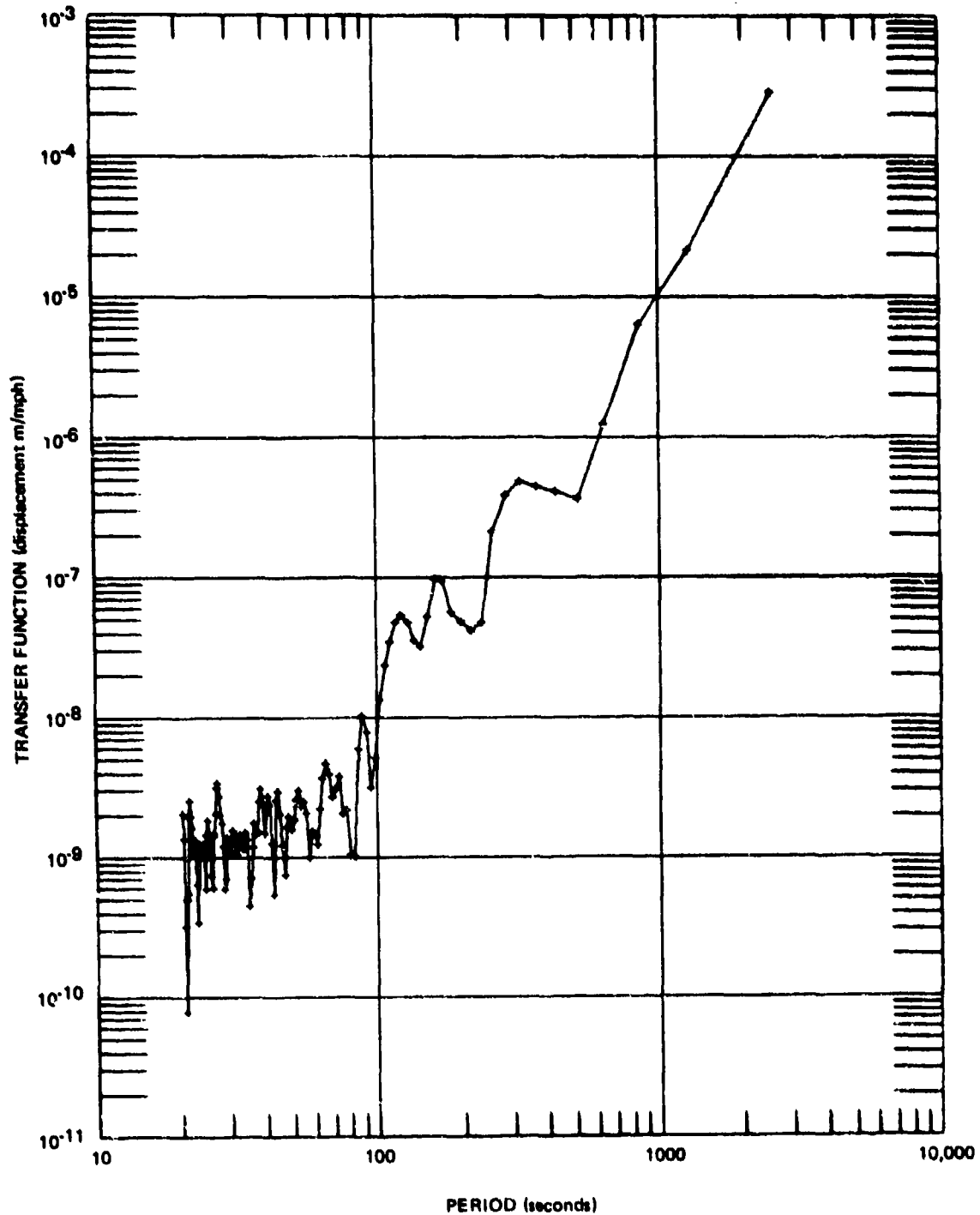


Figure 115. Estimate of wind velocity to horizontal displacement transfer function from P325L

G 6677

DISPLACEMENT/MPH

2498 SAMPLES, 128 LAGS, 0.1 SPS, PARZEN SMOOTHING

DC=A2

26 NOVEMBER 1970

0800/1456

*P55L X WU2/WU2

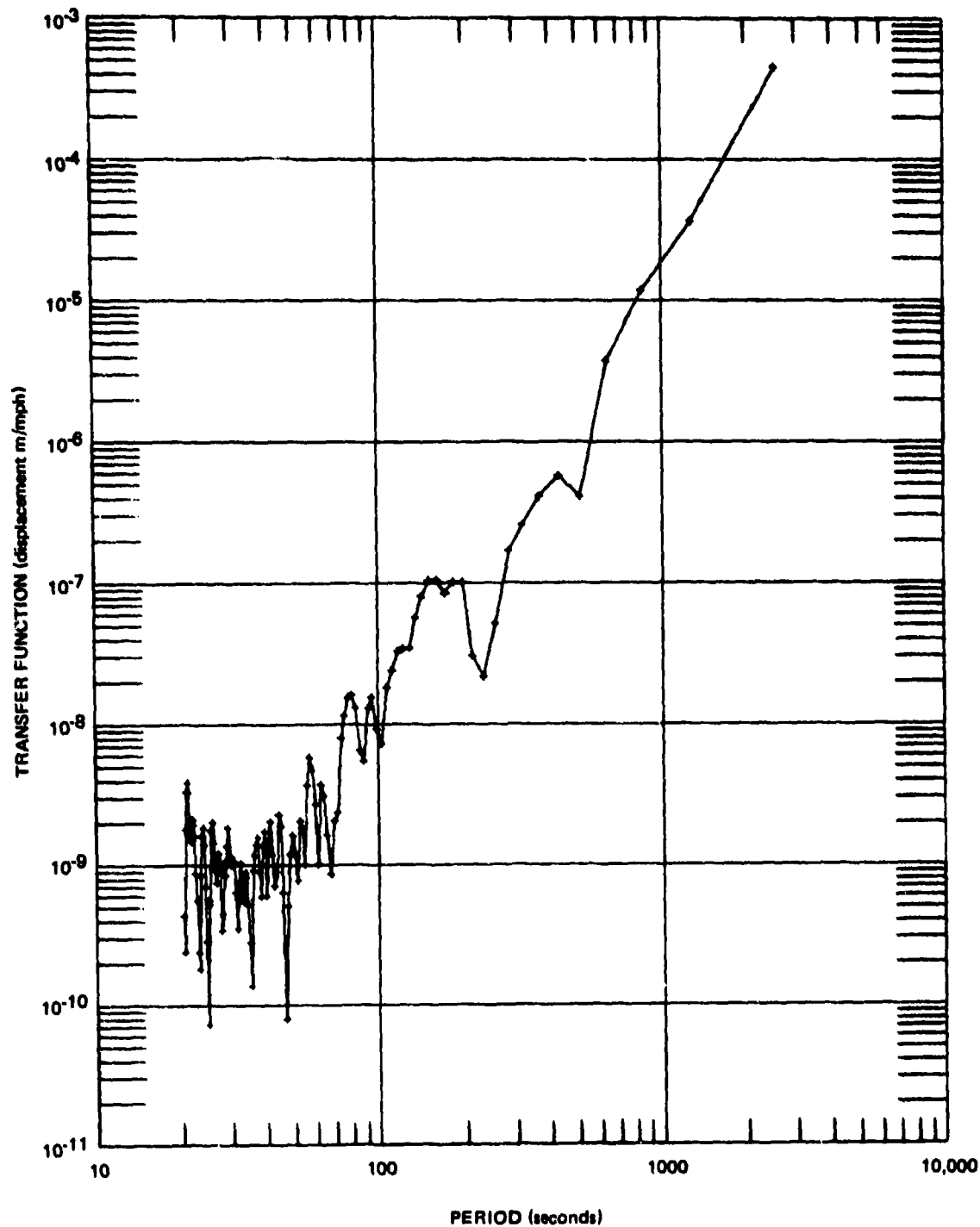


Figure 116. Estimate of wind velocity to horizontal displacement transfer function from P55L

G 6678

of sensitivity. Linear strain seismographs respond to differential motion along their sensitive axis and are insensitive to motions orthogonal to this axis. Therefore, a linear strain seismograph constructed to measure the strain component e_{11} will be insensitive to the other eight strain components e_{ij} , $i = 1,2,3, j = 1,2,3$, except $i = j = 1$. The vertical-inertial seismograph will respond to the vertical displacement component of the tilt. Generally, for pressure-induced noise, the output of a vertical-inertial seismograph is about 1/10 the output of the horizontal-inertial seismograph. The horizontal seismograph must respond to a true horizontal acceleration in the same manner as it does to the component along the sensitive axis of the instrument of the gravitational acceleration created by a tilt of the base on which the seismometer rests.

This part of the report will (1) adapt a general theory for non-sensitive axis disturbances to horizontal-pendulum seismometers developed by Rodgers (1968) to the specific parameters of the ALPS response for tilt resulting from Rayleigh waves and pressure loading; (2) present some data on the nature of the change of the seismic spectrum with increasing wind velocity and pressure variations; and (3) present data that indicate much of the tilting observed in horizontal-inertial seismographs is the result of rigid block nonlinear tilting and amplification of the tilts significantly above predicted values.

7.7.1 Tilt Theory for ALPS Response Horizontal Seismographs

Rodgers (1968) very thoroughly treats the response of the horizontal-pendulum seismometer to Rayleigh and Love waves, tilts, and free oscillations. The most significant spurious response is to tilt and to the tilt associated with Rayleigh waves. These two spurious responses will be considered in this paragraph. As mentioned above, the horizontal-pendulum responds to the component of the gravity acceleration created by the tilt of the base. Thus, the seismometer responds to tilt as an accelerometer. If $A_D(\omega)$ is the displacement amplitude frequency response and $A_T(\omega)$ is the tilt amplitude frequency, with g the gravitational acceleration, Rodgers (1968, equation (72)) has shown that

$$A_T(\omega) = \frac{g}{\omega^2} A_D(\omega) . \quad (14)$$

The ALPS displacement amplitude response is plotted in figure 117, equalized to a magnification of 100,000 (meter record amplitude per meter ground motion) at 25 sec period. The equivalent tilt response is plotted in the figure to the same scale and is seen to reach a maximum of about 30,000,000 (meter record amplitude per radian ground tilt) for a rather broad peak of frequencies. Rodgers also gives an equation for the output of a seismograph for a retrograde Rayleigh wave as

$$\phi = \phi_i \left(1 + \frac{g/c}{2\pi\beta} \tau \right) \quad (15)$$

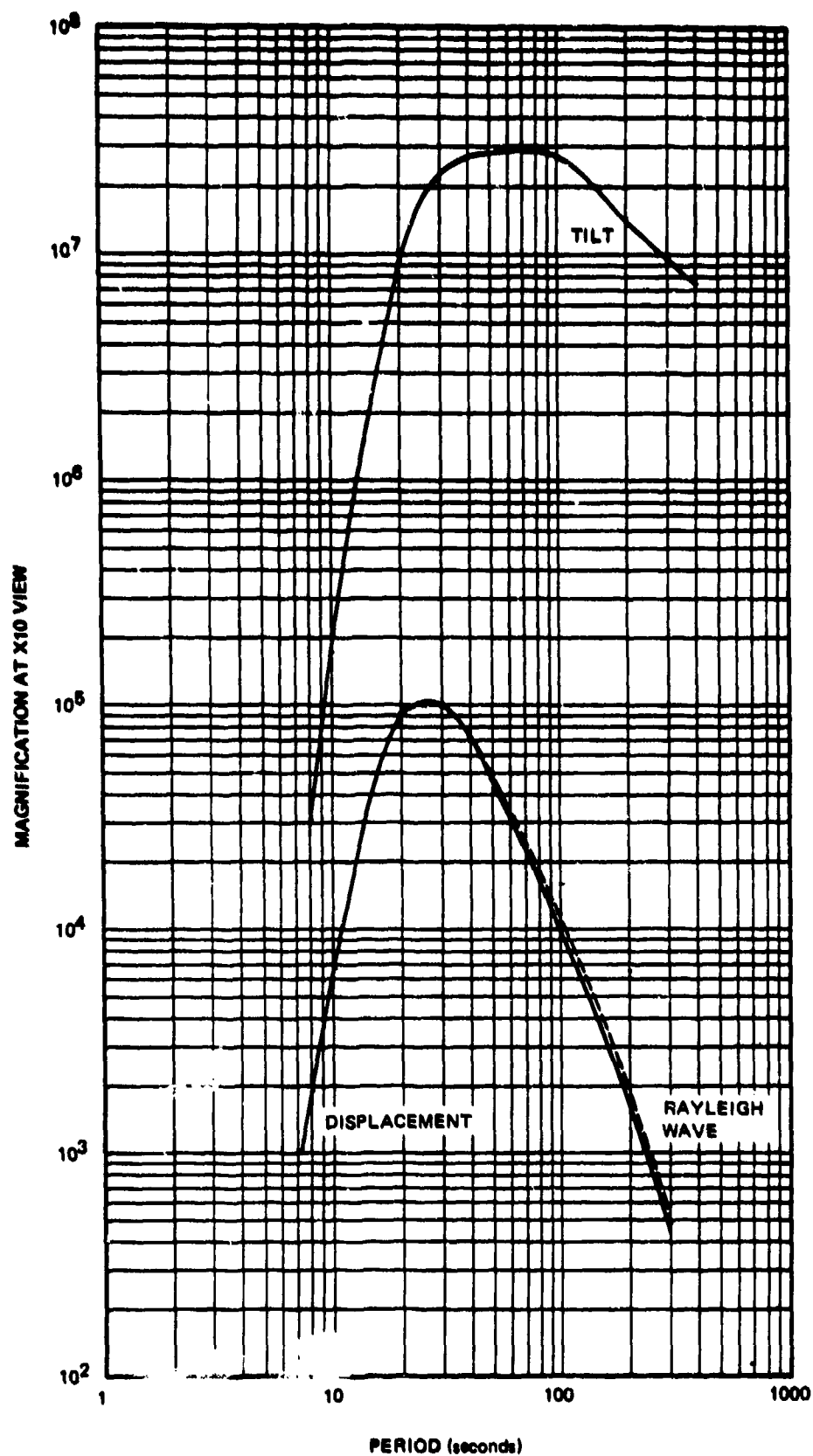


Figure 117. Horizontal inertial AL eismograph response to displacement, tilt, and Rayleigh waves

G 6032

where

- ϕ = actual seismogram
- ϕ_1 = ideal seismogram
- g = gravity acceleration
- c = wave phase velocity
- β = particle motion ellipticity parameter, ratio of horizontal semiaxis to vertical semiaxis
- τ = period of wave

The second term in the parentheses in equation 15 is the tilt term. The first term in the parentheses (one) is the displacement term. Values for the tilt term have been calculated with typical values for Rayleigh wave phase velocity, and using $\beta = 2/3$, which would apply for an infinite half-space. These calculated values are listed in table 13. The Rayleigh wave response

Table 13. Tilt response of horizontal inertial seismometers to Rayleigh waves

Period sec	Phase velocity km/sec	$\frac{g/c}{2\pi\beta} \tau$
10	3.0	0.008
15	3.0	0.012
20	3.36	0.014
24	3.50	0.016
26	3.56	0.017
30	3.65	0.019
34	3.78	0.021
40	3.90	0.024
45	3.93	0.027
50	3.97	0.029
55	3.98	0.032
60	3.99	0.035
70	4.00	0.041
80	4.03	0.046
90	4.07	0.052
100	4.11	0.057
150	4.28	0.082
200	4.57	0.102
250	4.90	0.119
300	5.28	0.133

$(1 + \frac{g/c}{2\pi B} \tau) [A_D(\omega)]$, is plotted in figure 117. From this figure, it can be seen that the addition of the tilt response to the displacement response for a Rayleigh wave is very small compared to the potential response that a horizontal seismometer could have to an extraneous tilt at the same periods. The difference between the Rayleigh wave response and the tilt response will be referred to later.

7.7.2 Seismic Spectral Changes with Pressure Activity Changes

Now let's consider the spectral content of the pressure-induced noise, then the effect on the horizontal pendulum of pressure-induced tilts and of Rayleigh wave induced tilts will be discussed. Figure 118 shows a plot of the S325L1 spectra under low and high wind conditions and the P325L spectra under high wind conditions. As the wind-associated, pressure-induced noise increases, it increases over the whole spectra. The microseismic peaks visible on the S325L1 strain during the low wind conditions are completely swamped with the strains from the high wind pressure changes. The same raising and lowering of the entire spectrum was observed by Herrin (1963, personal communication) during an experiment in south Texas using a vertical seismograph flat to ground velocity from 1.25 sec to 110 sec. At low wind conditions microseismic peaks were clearly visible at 2 Hz and 6 sec. As the wind velocity increased, valleys in the spectra were filled in until finally the 2 Hz then the 6 sec peaks disappeared into the pressure-induced spectra. Thus, the pressure-induced noise to a first order approximation can be considered to be a white noise source. The output of any system to a white noise source is the system response. Therefore, the shape of the spectral output of a seismograph can give strong indications as to the input character.

7.7.3 Nonlinear Tilting

Several sets of data demonstrating the tilt response have already been presented; two will be discussed here. The spectra of the inertial P325L during high wind conditions are compared to the spectra of the S325L1 strain in figures 118 and 119. At periods longer than 64 sec, the S325L1 spectra decreases, but the P325L spectra continues to increase. This divergence in the spectra implies a nonlinear relationship, which is confirmed in the coherence plotted in figure 119. It is hypothesized that the additional output on the inertial system is a symptom of rigid body tilting with possibly relative movement on the local joint and fault pattern. Movement on local joints and faults in the immediate vicinity of instrument systems has been observed by Harrison (1968, 1969) in the Poorman Fault near Boulder, Colorado. Stewart Smith (1970, personal communication) has hypothesized that the residual strains observed in the near field of large explosions (and possibly in the far field of earthquakes) are actually the readjustment of the strain field in the vicinity (10's m to 10's km) of the seismometers.

For teleseismic earthquakes, this readjustment is triggered by the passage of the Rayleigh wave, which is generally the largest amplitude elastic wave. Both Harrison's and Smith's observations apply to a step readjustment. The hypothesis presented here is that the readjustments along local joints and faults is a dynamic phenomenon occurring all the time in much smaller amplitudes (on the order of 0.1 Angstrom) than have previously been resolved. It is thought that

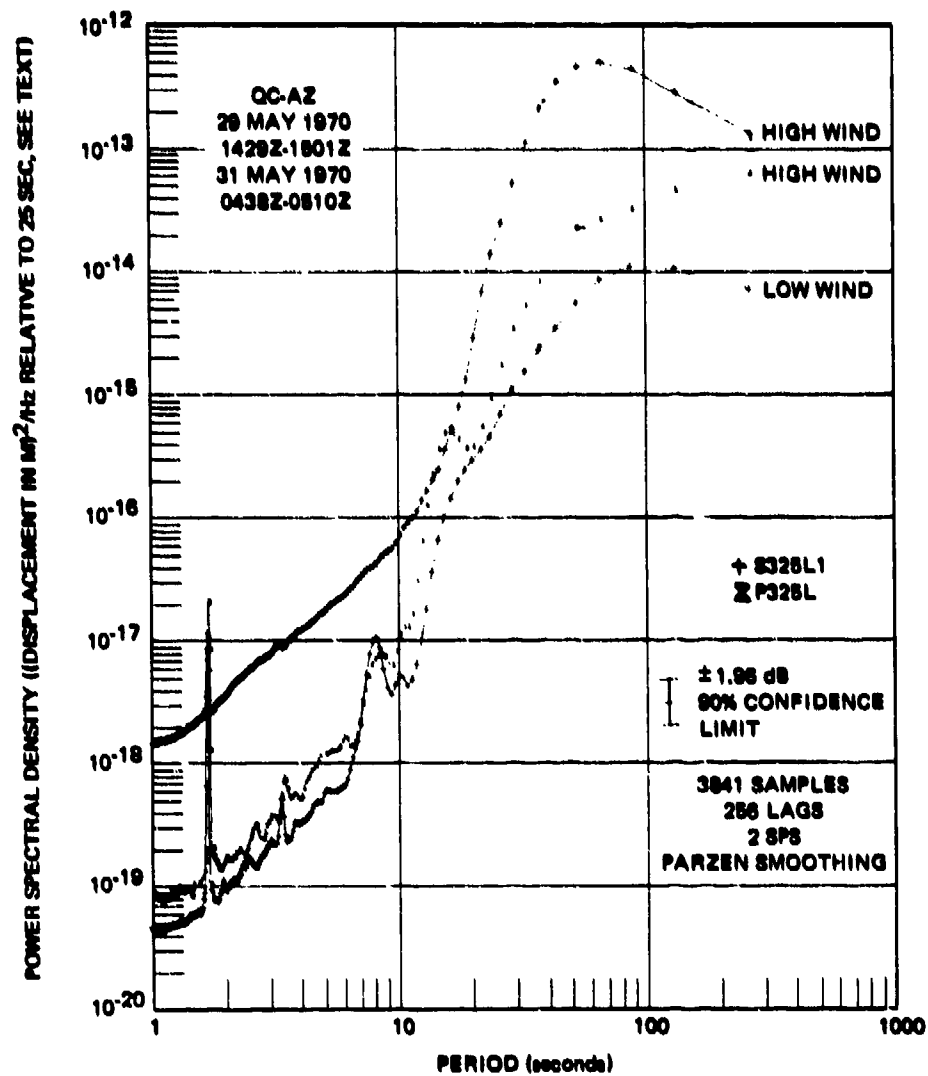


Figure 118. Comparison of power spectral density between low and high wind conditions

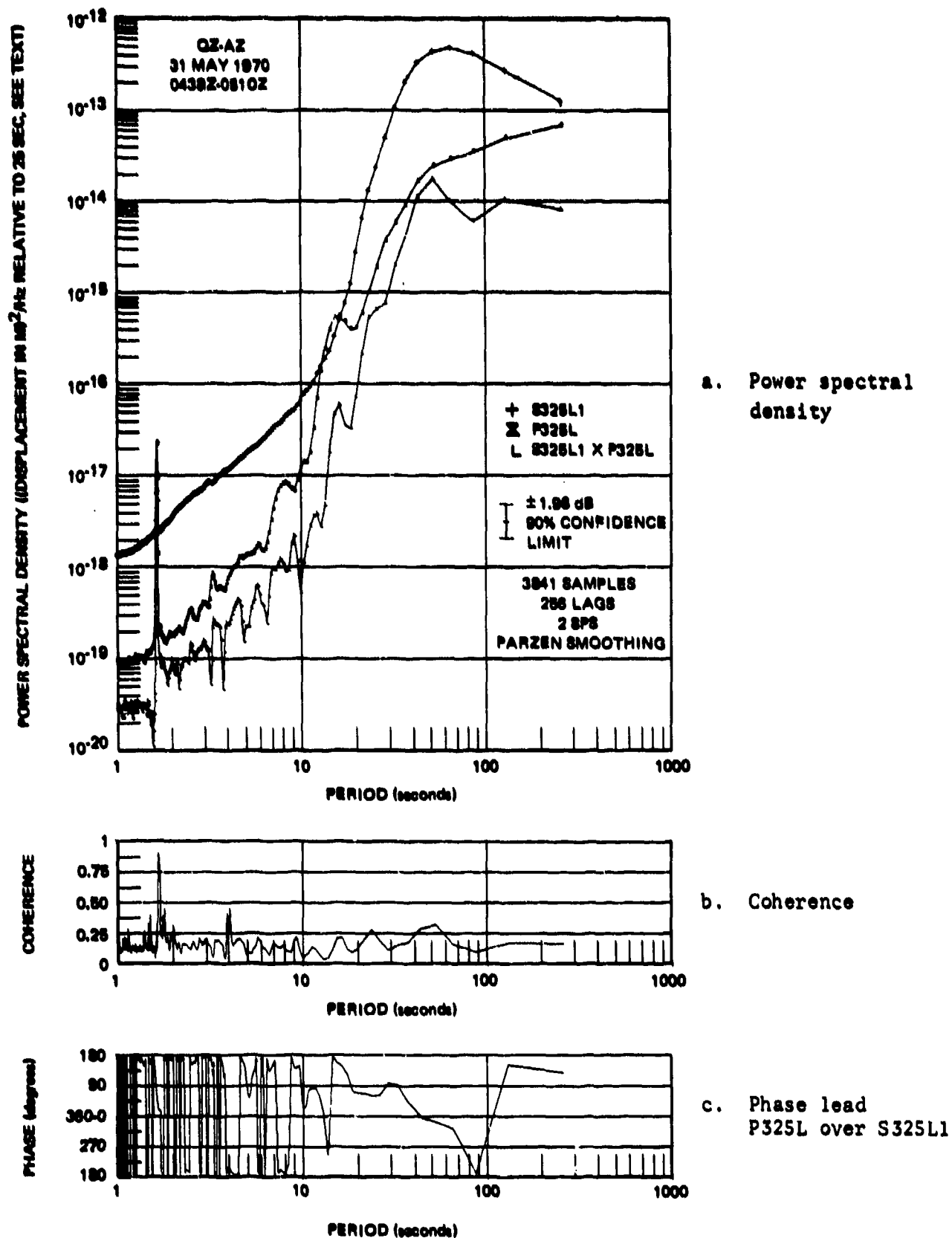


Figure 119. Power spectral density, coherence, and relative phase angle of parallel horizontal seismographs, S325L1 strain and P325L inertial, during high wind conditions

G 6020

this phenomenon is not unique to QC-AZ, but that it can be observed at any high-sensitivity seismic observatory.

The LR1 Rayleigh wave spectra in figure 120 also substantiates the excess tilt response of the horizontal inertial P325L over the response of the strain S325L1. If the S325L1 spectra is taken as representative of the true Rayleigh wave motion, then table 13 and figure 117 indicate that at 100 sec there should only be about 5.7 percent greater amplitude on the pendulum from the Rayleigh wave tilt. The assumption that the S325L1 spectra represents the true Rayleigh wave motion is supported by the cross spectra in figure 120 which is almost identical to the S325L1 spectra. The observed output in power spectral density at 100 sec of the P325L is a factor of about 30 larger than the power of the S325L1. The ratio of the observed 30:1 difference is so much greater than the 1.057:1 difference predicted by the theory, that it has to be related to a phenomenon other than an elastic response to the traveling wave. Even if the S325L1 spectra is normalized upward by the empirical 3.5 power ratio, the tilt output is still in excess over the Rayleigh wave tilt.

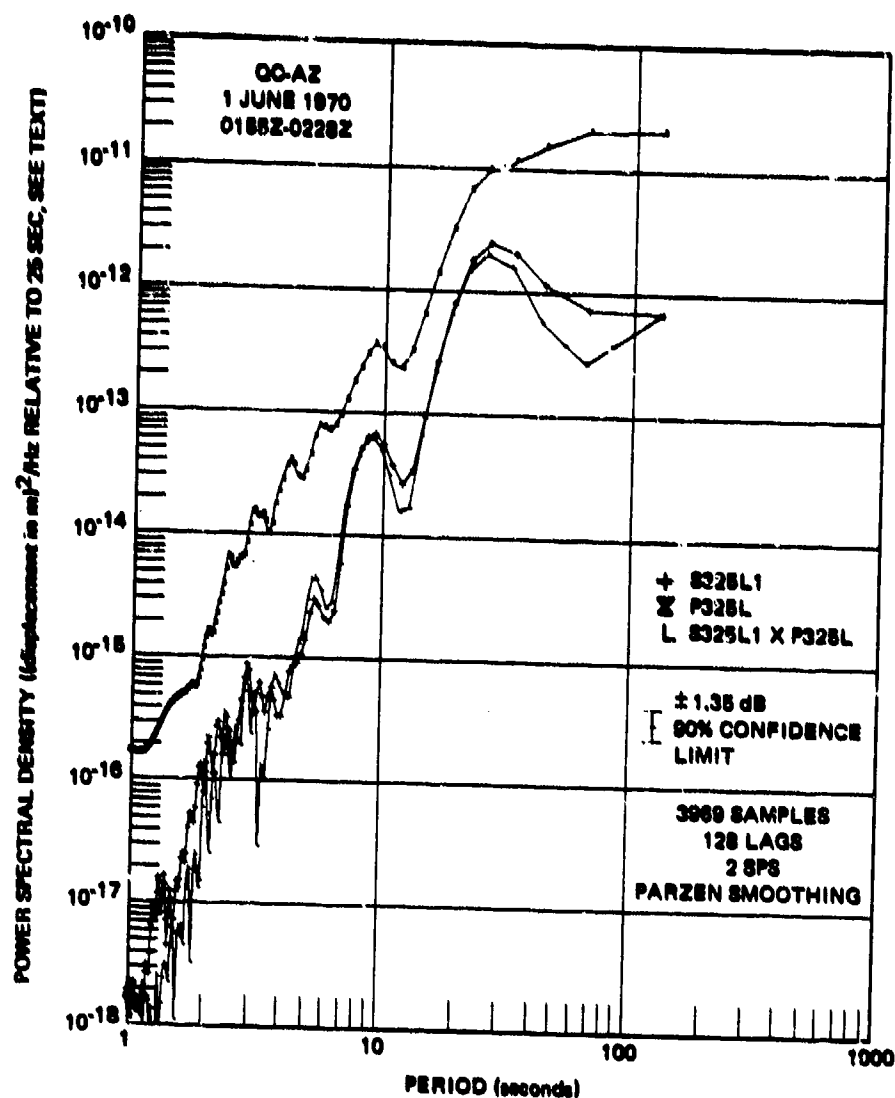
Non-elastic tilts also have been observed by Tomascheck (1937, 1953). Tomascheck (1937) deduced from observations with gravimeters that the loading effect of tidal water masses and of atmospheric air masses seemed to cause non-elastic movement of individual tectonic blocks of a diameter on the order of 1000 km. Tomascheck (1953), using records of tilt measurements performed with horizontal pendulums in England in a mine at a depth of 145 m below the surface, observed load tilts that correlated with barometric pressure distributions and that were not due to elastic deformations of the earth's crust. He concluded that the tilts could be ascribed to movements of tectonic blocks of large extension.

In summary, the senior author's contention is that this unusually large tilt is caused by a rigid block motion on the order of 0.1 Å in amplitude on the local joint pattern. It is expected that this same action will be observed at any high-sensitivity seismic observatory.

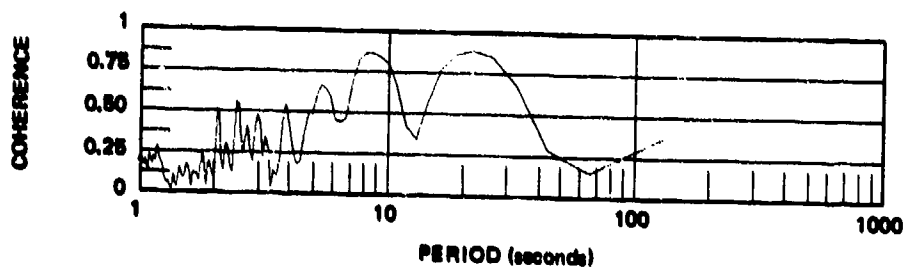
7.8 SECULAR STRAINS

Secular strain, as used in this section, is defined as the long-term strain that is observed on a seismograph. The secular strain consists of strain created by seasonal temperature changes, regional tectonic strain, and strain from unknown sources.

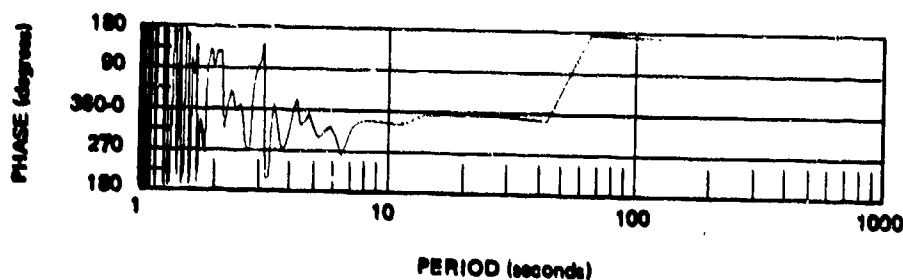
The change in the secular strain observed at QC-AZ between 1 October 1970 and 28 March 1971 is plotted in figure 121. The zero at the 1 October starting point is arbitrary. The secular strain was observed on the broad-band strain seismographs S2B, S325B, and S55B. The observations plotted were taken from the balance adjustments made on the seismographs. As the secular strain offset approached the maximum voltage of the recorders, an electrical centering was accomplished in the seismograph circuits. After seven to nine electrical re-centering adjustments, the capacitor plate would be recentered with the micrometer on the transducer. (Refer to section 3.2.4 and figure 21.) The data points plotted in figure 121 are thus discrete adjustments and actually represent the time integral of the secular strain from the previous adjustment. Over a long interval of time, a smoothed line through the points will give a good history of the secular strain rates.



a. Power spectral density



b. Coherence



c. Phase lead
P325L over S325L1

Figure 120. Power spectral density, coherence, and relative phase angle with 128 lags for parallel horizontal seismographs, S325L1 strain and P325L inertial, during the LRI Rayleigh wave of an aftershock of the Peru earthquake.

G 6028

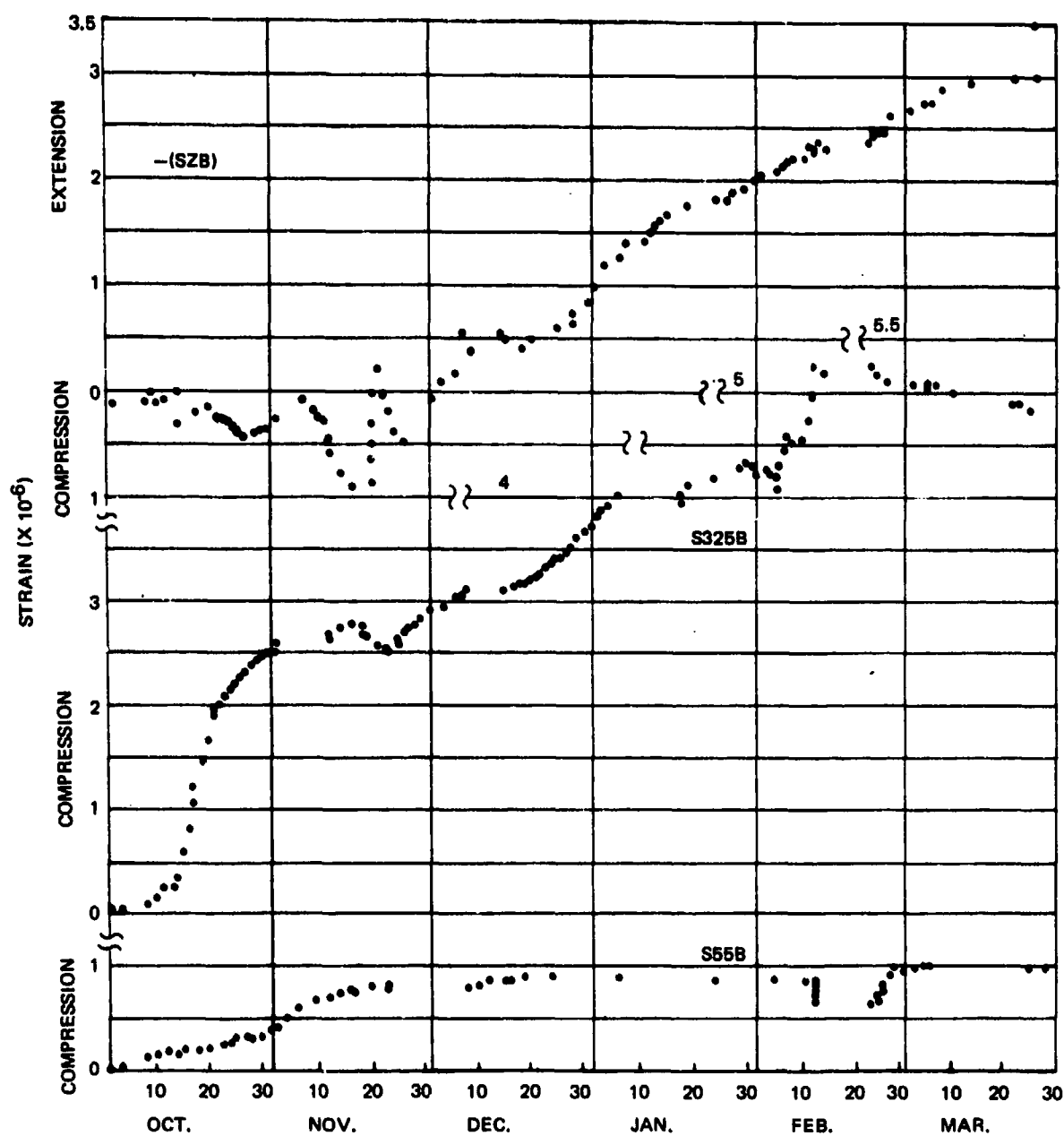


Figure 121. Secular strain 1 October 1970 to 28 March 1971

G 6679

Several observations can be made from figure 121. The SZB vertical strain is plotted upside down to facilitate comparison with the S325B and S55B horizontal strains. The SZB vertical strain recorded a compressive strain from 1 October to 1 December and then reversed direction, continuing an increasing extension until the end of the plotted period. The slope was relatively stable at about 10^{-6} extension strain per month. There is a decrease in slope during March. The sign of the SZB strain was the same as the two horizontal strains from 1 October to 1 December, but was opposite after 1 December. The large extension step on 20 November may have been an instrumental artifact.

The S325B secular strain was more erratic than the other two. This strain seismometer is sub-parallel to the joint pattern of the local geologic structure and was subjected to more extraneous movements. The secular strain is another example of the greater susceptibility of this direction to small motions. The S325B secular strain was all in compression during the period covered. However, there were two intervals - around 20 November and from 10 February on - when the slope of the curve was extensional in nature. From 1 December to 10 February, the average slope was about 10^{-6} compressive strain per month. The high strain rate (large slope) between 12 and 20 October 1970 is not thought to be instrumental, but is taken as actual ground strain. The large increases in secular strain on 11, 12, and 13 February are shortly after the San Fernando, California, earthquake of 9 February. Association of these strains with this earthquake would be highly speculative. However, if they were associated, the strain migration rate would have been about 13 km/hr, which is very close to the 10 km/hr observed by Nason (1969) along the San Andreas Fault. The gap in the data between 15 and 22 February was the time during which the mine was barred down and ventilated.

The S55B secular strain was the smallest of the three confirming the greater stability in this azimuth. Between 1 October and 1 December, the secular strain rate was about 0.4×10^{-6} compressive strain per month. After 1 December, the S55B secular strain was almost zero, except for 12 February and 22 to 26 February.

Comparisons among the three seismographs can be made. Prior to 1 December, the strain rates were more irregular. After 1 December, the S55B stayed almost constant, and the S325B and SZB were almost equal and opposite. The S325B was in compression and the SZB was in extension. The net dilatation (i.e., SZB + S325B + S55B) is about 0.7×10^{-6} extension strain from 1 December to 10 February and about 1.1×10^{-6} extension strain from 1 December to 28 March. These net dilatations give rates of -0.3×10^{-6} strain/mo and -0.275×10^{-6} strain/mo, respectively. The uniformity of these rates suggests that the deviation from the normal rates on 11, 12, and 13 February were corrected by 28 March. Indeed, figure 121 suggests that most of the correction occurred by 27 February. The opposite signs on the two horizontal strains and the lack of vertical strain during the February deviation indicates a shear type of strain. The vanishing of the vertical stress P_{zz} at a free surface gives a constant proportionality between vertical strain and areal strain (the sum of two perpendicular horizontal strain components). Using the net strains from 1 December to 10 February, the constant of proportionality is -1.50 and from 1 December to 28 March it is -1.44. For a Poisson solid with $\lambda = \mu$, the constant of proportionality is -0.333. The proportionality between vertical and areal strain is discussed also in sections 8.3 and 9.1.5.

Secular strain rates calculated by a least squares fit to the 43 days' data used in the earth tide analysis are given in section 13.3.2.

7.9 RESISTANCE OF STRAIN SEISMOMETERS TO ACOUSTIC VIBRATIONS

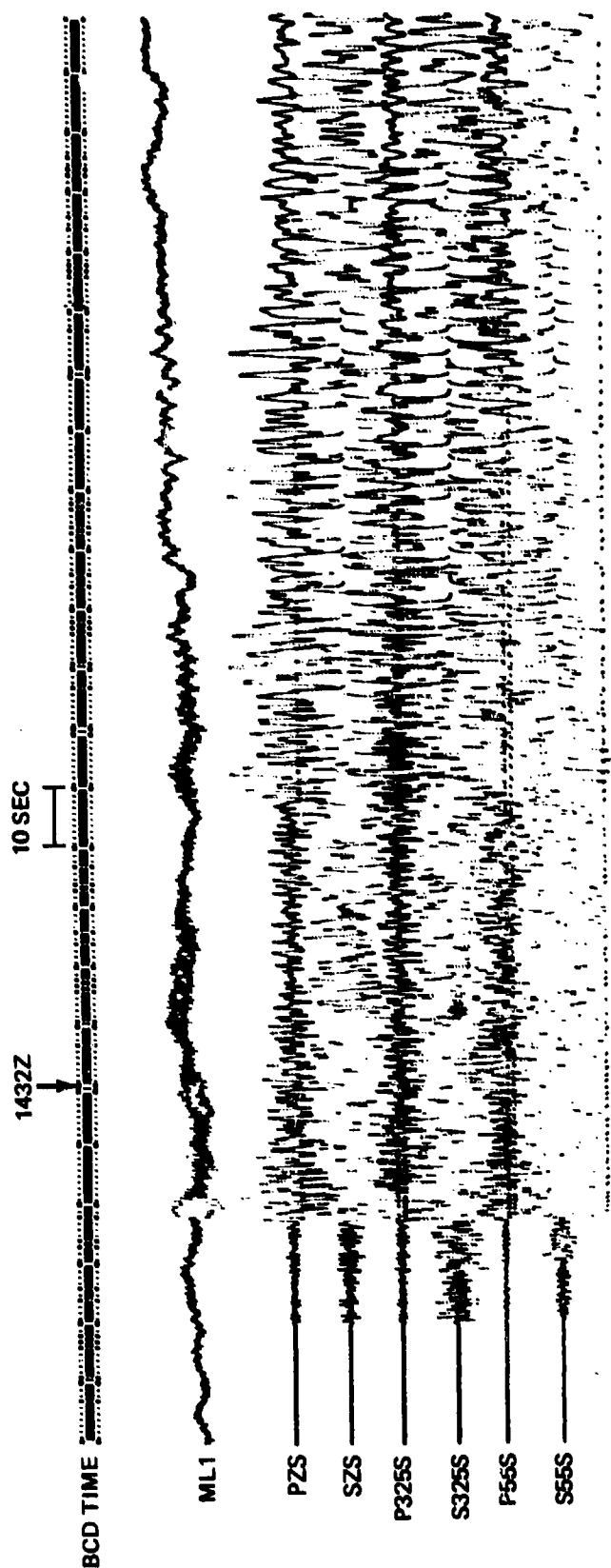
The design of the suspension of the strain seismometers was intended to provide sufficient rigidity to move the first spurious resonance of the strain rod outside the passband of interest. This design was successful. The first spurious mode is about 13 Hz, as determined by exciting the seismometer calibration coil and observing the output signal. Several natural signals also provided a demonstration that the rigidity of the suspension was sufficient to prevent acoustic vibrations from exciting the rod into sympathetic vibration.

Several examples of coupling from seismic energy to acoustic energy were observed for medium-size, near-regional and regional events. The acoustic energy appears as a resonance of the sealed seismometer chamber. Figure 122 is a composite made from playbacks of two magnetic tapes showing the acoustic energy recorded on the ML1 microbarograph inside the sealed mine. The seismic signal is from the Nevada Test Site (NTS) explosion TIJERAS. The National Ocean Survey (NOS) (formerly the U.S. Coast and Geodetic Survey - USC&GS) Preliminary Determination of Epicenter (PDE) data are: origin = 1430:00.0, 37.1N, 116.0W, h = 0 km, m_b = 5.5. This epicenter is at an epicentral distance of 5.3 deg and at an azimuth of 318.7 deg. The acoustic resonance started about a half-cycle after the seismic P_g wave arrived, as can be seen in the expanded time base in figure 123.

The maximum pressure was about 0.075 μ bar peak-to-peak at 2.07 Hz. This resonance frequency was different from the frequency content of all the seismographs - strain and inertial. The difference in frequency is significant from two aspects. First, it demonstrates that the strain rod supports are sufficiently rigid that acoustic signals are not exciting the three strain seismographs into spurious oscillations. Secondly, the difference in frequency permits the identification of the type of disturbance as acoustic resonance of the chamber.

The 2.07 Hz resonant frequency of the roughly 42 m long chamber driven by the seismic energy as a quarter-wave-length resonance tube gives a calculated velocity of sound of 348 m/sec. This velocity is fortuitously close to the 346 m/sec expected velocity with the unknowns of the dimensions of the actual resonating cavity in the irregularly shaped chamber.

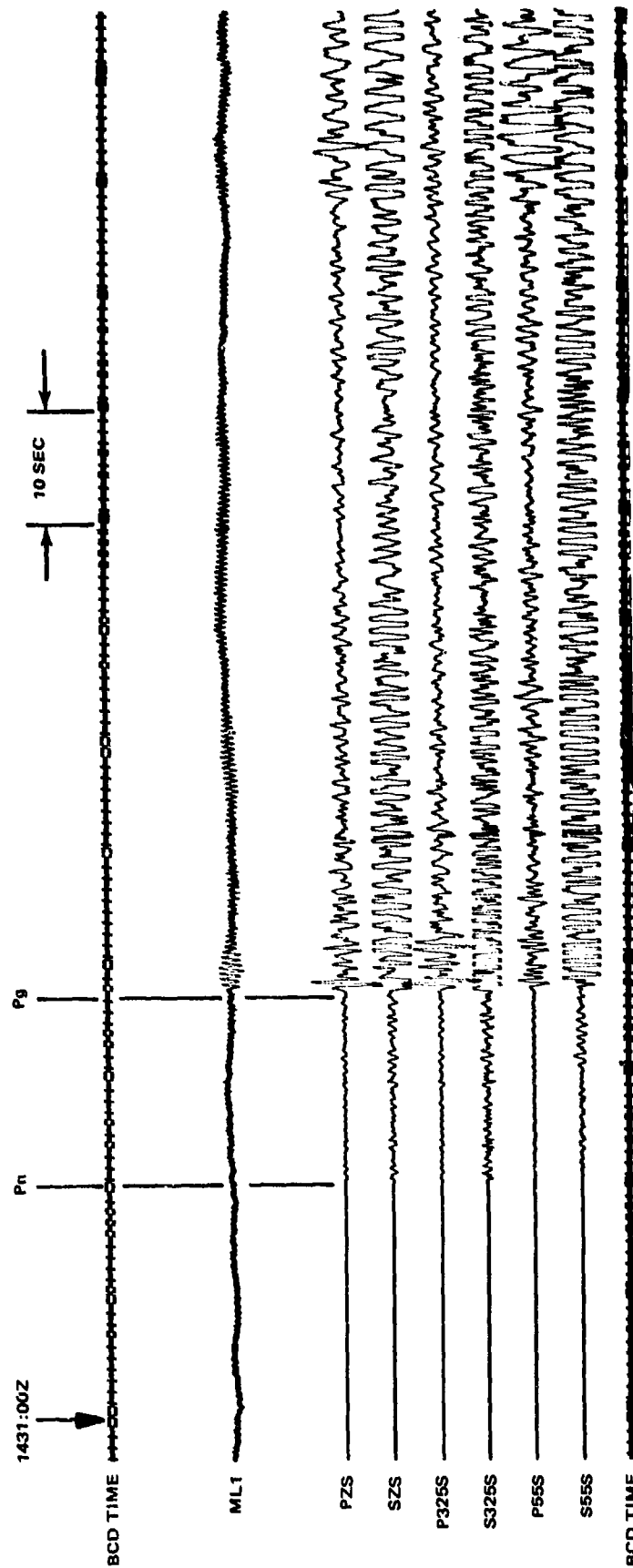
The 2.07 Hz resonance is not a volumetric strain recorded on the microbarograph. Using the method described in Fix (1972) and in section 8.3 to determine volumetric strain from a microbarograph in a sealed chamber and from a vertical-linear strain seismograph, the volumetric strain determined from the microbarograph would have to be 5.4×10^{-8} strain. Extrapolating the clipped peaks of the first pulse of the P_g arrival on the vertical-linear strain seismograph SZS, an estimate of the volumetric strain of 1.5×10^{-9} (at the 1 sec period of the signal) is obtained. The volumetric strain is then a factor of 36 (or about 32 dB) below the observation on microbarograph ML1 and is well into the noise of the microbarograph. The microbarograph noise is rated at 0.03 μ bar by the manufacturer. The difference between the character of the waveforms on the ML1 microbarograph and all six of the seismic traces also confirms that this is a recording of a different signal input.



QC-AZ
 RUN 287
 14 OCT 1970

Figure 122. Acoustic resonance of sealed seismometer chamber starting with second half-cycle of Pg from NTS explosion TIJERAS. NOS PDE data:
 0 = 1430:00.0, 37.1 N, 116.0 W, h = 0 km, $m_b = 5.5$, $\Delta = 5.3$ deg,
 azimuth = 318.7 deg

G 6308



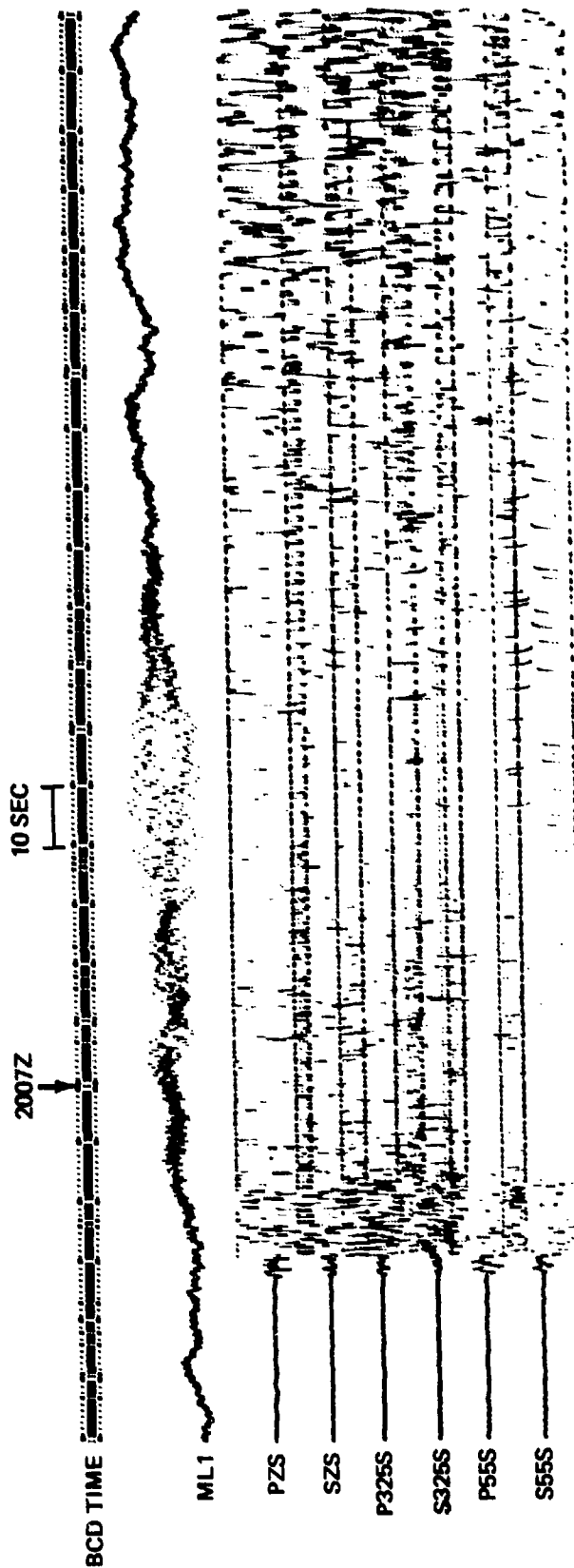
QC-AZ
 RUN 287
 14 OCT 1970

Figure 123. Acoustic resonance of sealed seismometer chamber starting with second half-cycle of Pg from NTS explosion TIJERAS

6 0930

The approximately 4 sec oscillations seen on the ML1 trace in figure 122, beginning at about 1433Z, are a recording of a volumetric strain of 1.7×10^{-8} strain. The strain signal is saturating two or more amplifier stages of the strain seismographs and meaningful amplitude data are unobtainable. At a 4 sec period, the strain seismograph magnifications are down by a factor of 28 from the magnifications at 1 sec (the period of the Pg first arrival). For a 4 sec volumetric strain of 1.7×10^{-8} , the amplitude on the S2S vertical strain seismograph would be about 50 percent larger than the clipped amplitude recorded. This amplitude is certainly a possibility in the poor recording. The 4 sec period energy is masked in the seismograms by the 2 sec energy, which is recorded on all six seismograms at six times the magnification of 4 sec energy.

An example of a similar signal observed from a near-regional earthquake in the Gulf of California at an epicentral distance of 3.4 deg and an azimuth of 206.6 deg, is given in figure 124. The NOS PDE data are: origin = 2005:34.5, 30.1N, 113.4W, $h = 33$ km, $m_b = 5.2$. The same frequency of chamber resonance is seen on the ML1, with the largest amplitudes during the Lg time interval. The beginning of the resonance is more of a buildup rather than the impulsive start seen in figures 122 and 123. The difference in the beginning is the consequence of the mine configuration and the direction of the wave travel. The direction of travel of the signal from the NTS explosion is almost perpendicular to the 55 deg azimuth tunnel at the back of the cavern. The acoustic resonance probably began with the second half of the seismic signal as the back wall of the cavern recovered from the initial compressive wave and moved toward the 319 deg azimuth, which is toward the center of the chamber.



QC-AZ
 RUN 285
 12 OCT 1970

Figure 124. Acoustic resonance of sealed seismometer chamber generated by seismic signals from a Gulf of California earthquake. NOS PDE data:
 $0 = 2005:34.5$, 30.1 N, 113.4 W, $h = 33$ km, $m_b = 5.2$. $\Delta = 3.4$ deg,
 azimuth = 206.6 deg

G 6308

8. GENERAL PERFORMANCE OF INSTRUMENTS

The general performance of the entire complex of strain seismographs and of inertial seismographs met the expected performance. Sensitivities were achieved on the twelve strain seismographs 1-1/2 to 2 orders of magnitude smaller than attained by previous investigators. At periods shorter than 25 sec, operating magnifications of the strain seismographs were limited only by the ambient earth strains. Sensitivities were achieved on the six inertial seismographs that were equal to those attained on the most sensitive seismographs available anywhere in the world. At all periods, operating magnifications of the inertial seismograph were limited only by the ambient earth motion.

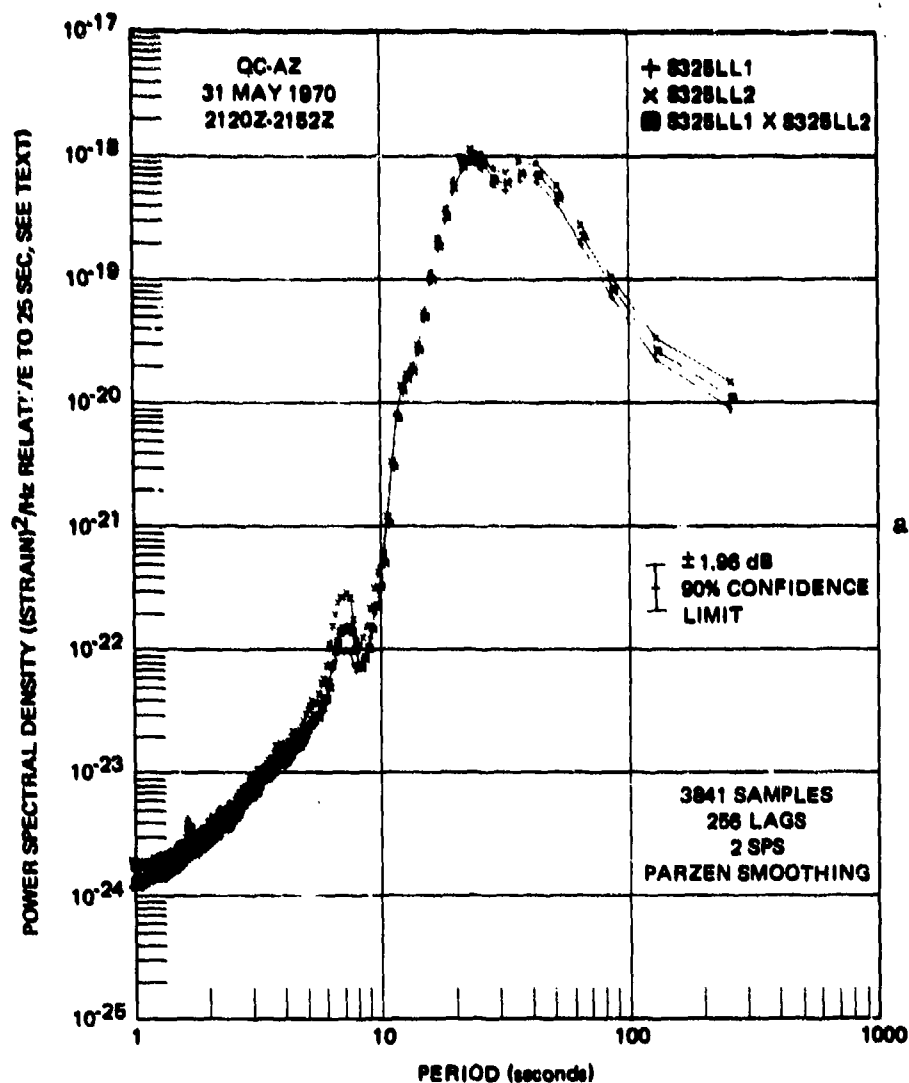
This section presents data on the general performance of the instruments, with emphasis on the strain seismographs. Section 8.1 illustrates the ability of the strain seismographs to faithfully reproduce signals recorded on the two parallel strain seismographs. The in-situ measurement of elastic parameters is possible with the QC-AZ strain system. Examples are given in section 8.2. Section 8.3 illustrates the recording of volumetric strain with a microbarograph and with a vertical strain seismograph.

8.1 SIGNALS RECORDED ON PARALLEL STRAIN SEISMOGRAPHS

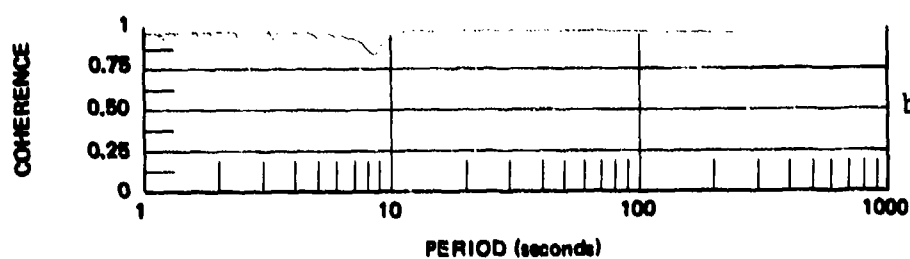
8.1.1 Earthquake Signals

Three earthquake signals are used to demonstrate that the parallel horizontal strain seismographs produced the same outputs for travelling waves. All three signals are associated with the large Peru earthquake of 31 May 1970. The NOS PDE data on this earthquake are: $0 = 2023:27.3$, $9.2S$, $78.8W$, $h = 43$ km, near coast of northern Peru, $m_b = 6.6$, $M_S = 7.8$. This epicenter is at a distance of 52.5 deg and at an azimuth of 137.4 deg from QC-AZ. The first signal used from this earthquake was from the coda of the LR1 Rayleigh wave during a time window equivalent to group velocities of 1.72 to 1.10 km/sec. The second sample is a combined signal from the LR2 Rayleigh wave, with a group velocity window of 2.52 to 2.20 km/sec, and from the LQ3 Love wave and the LR3 Rayleigh wave, with a group velocity window of 3.37 to 2.95 km/sec. During both of these time samples all high gain channels were driven off the film and were clipping the magnetic-tape recorders. Therefore, the low gain strain seismograph channels were used for the comparisons. The third earthquake signal is a major portion of the LR1 Rayleigh wave from an aftershock. The high gain seismographs were used for the analysis of the third sample. The time window corresponds to group velocities between 5.43 and 2.01 km/sec. The NOS PDE card data for the aftershock are: $0 = 0136:10.2$, $9.3S$, $79.0W$, $h = 49$ km, off the coast of northern Peru, $m_b = 6.0$, $M_S = 5.5$. This epicenter is at a distance of 55.2 deg and at an azimuth of 138 deg from QC-AZ.

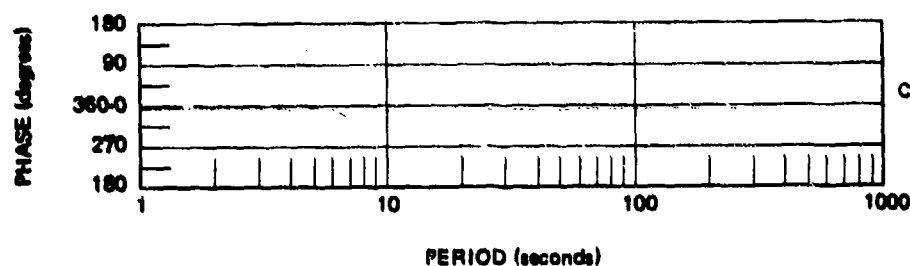
The spectra for the first sample are plotted in figure 125. This sample was taken at the earliest window that could be selected after the low gain tape channels stopped clipping. Thus, this sample represents the maximum signal that can be recorded without distortion on the ALPS response channels, which are recorded at two signal levels. The spectra are seen to be almost identical with either a little less power on the S325LL1 at 7 sec and at periods longer



a. Power spectral density



b. Coherence



c. Phase lead
S325LL2 over S325LL1

Figure 125. Power spectral density, coherence, and relative phase angle of parallel strain seismographs S325LL1 and S325LL2 during the LRI Rayleigh wave coda of the Peru earthquake

G 6023

than 20 sec or a slight calibration error. The coherence is one and the relative phase angle is zero at all periods. During this sample, the rms strain (referred to 25 sec) in the whole passband was 1.71×10^{-10} strain on the S325LL1 and 1.91×10^{-10} strain on the S325LL2.

The two parallel strain seismographs are seen to track each other identically during the portion of the second sample shown in figure 126. The spectra, figure 127, show the same results for the S325LL1 and S325LL2. Again, the S325LL1 has either slightly less power or a small calibration error. The coherence is one at all periods except 10 sec, which is in the noise, and the relative phase angle is zero. The spectra of the tape recorder-reproducer noise is evident as the approximately white noise between 3 and 10 sec. The analog antialias filter acting upon the tape noise is clear between 1 and 3 sec. The same antialias filter was used in digitizing all the data for which spectra were calculated in the 1 to 256 sec passband. The action of the filter is not seen in any of the other figures because the spectra between 1 and 3 sec in all the other figures is well below the computational noise level. The peak of the spectra at about 10^{-18} strain²/Hz in figure 125 and the tape noise at about 10^{-24} strain²/Hz in figure 127 indicate a potential 60 dB dynamic range with narrow band-pass spectral analysis. The same dB value applies to both power and amplitude.

The strain spectra from the perpendicular S325LL1 and S55LL are plotted in figure 128. The spectra are similarly shaped, but the S325LL1 has only about two-thirds the magnitude of the power on the S55LL. This difference is attributed to a possible cancellation of LR2 and LR3 Rayleigh motion on the almost radial 325 deg azimuth instruments. The coherence is good and the relative phase angle is 180 deg. The rms strain (referred to 25 sec) in the whole passband for this sample was: S325LL1 1.500×10^{-11} strain, S325LL2 1.704×10^{-11} strain, and S55LL 1.983×10^{-11} strain.

The third earthquake signal further confirms that the two parallel strain seismographs give the same output. The analog signals on the low gain channels are seen to track identically in figure 129. The spectra essentially overlay in figure 130. The data below 7 sec are into the noise. The peaks at the shorter periods are the result of using clipped data for about 5 percent of the sample. The peaks of the recordings on the high gain S325L1 and S325L2 strain seismographs were clipped between 0203Z and 0206Z and the P325L was clipped between 0203Z and 0207Z. The two strain seismographs have identical spectra even with the clipping. The coherence is one and the relative phase angle is zero at all periods. Because of the clipped data, the spectra were also calculated with 128 lags for better statistical stability. The results plotted in figure 131 are the same as in figure 130 except that the noise only affects periods shorter than 4 sec. The coherence is one at all periods, indicating a more reliable statistical estimate.

Figure 120, section 7.7.3, contains the spectra of the S325L1 and the P325L seismographs. There are two significant differences. First, at 25 sec, the S325L1 is a factor of 3.5 lower in (equivalent) power or 1.9 lower in amplitude than the P325L. Secondly, the cross spectra very closely follows the S325L1 in shape and power. There are two interpretations that can be taken from these data. First, the similarity of the strain spectra and the cross spectra suggests that the strain seismograph, S325L1, represents the linear portion of true ground motion; and the additional power on the inertial seismograph, P325L, represents a nonlinear output generated by localized tilting of the nearby rock. The concept of nonlinear tilt response of the rock is discussed in section 7.7.3.

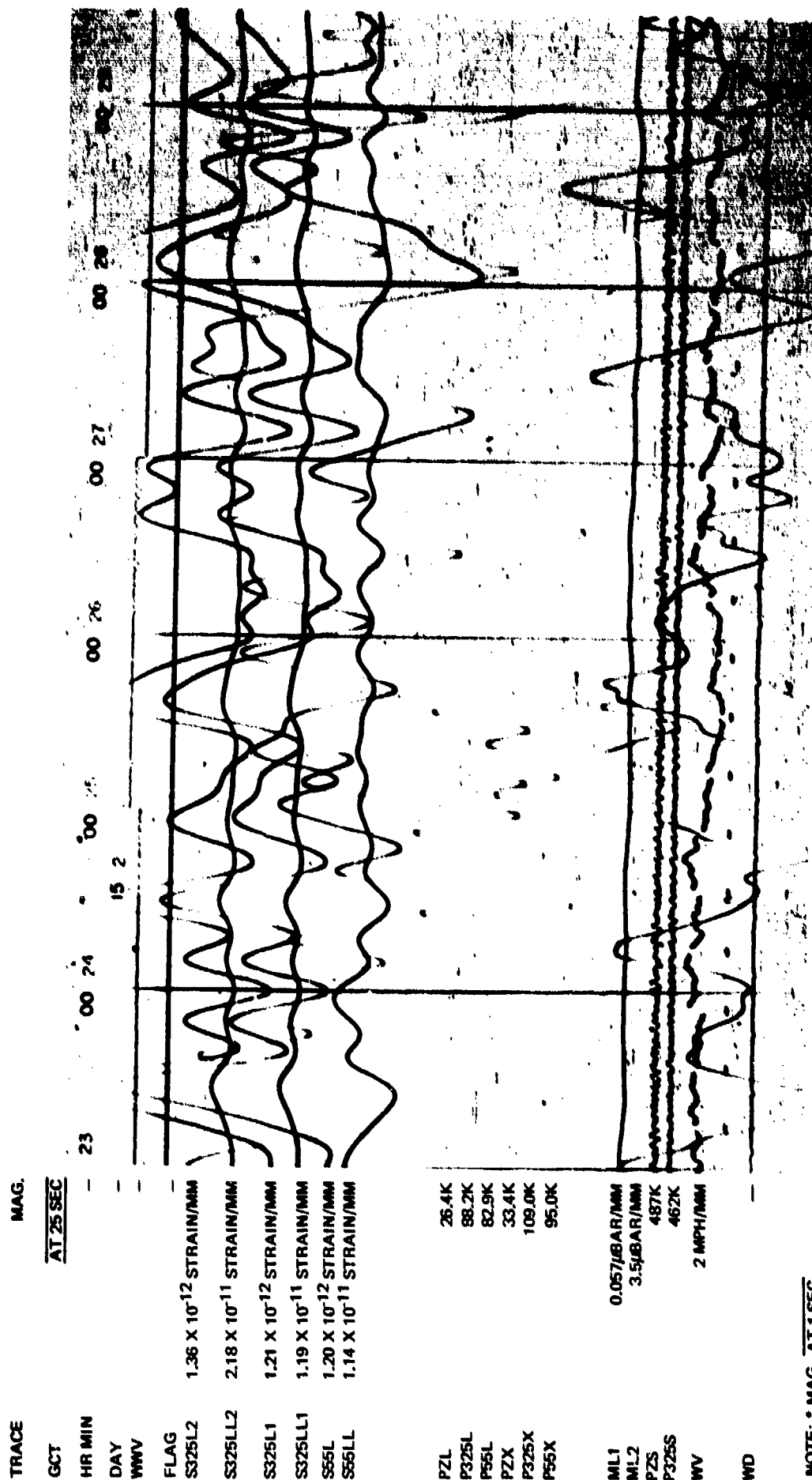
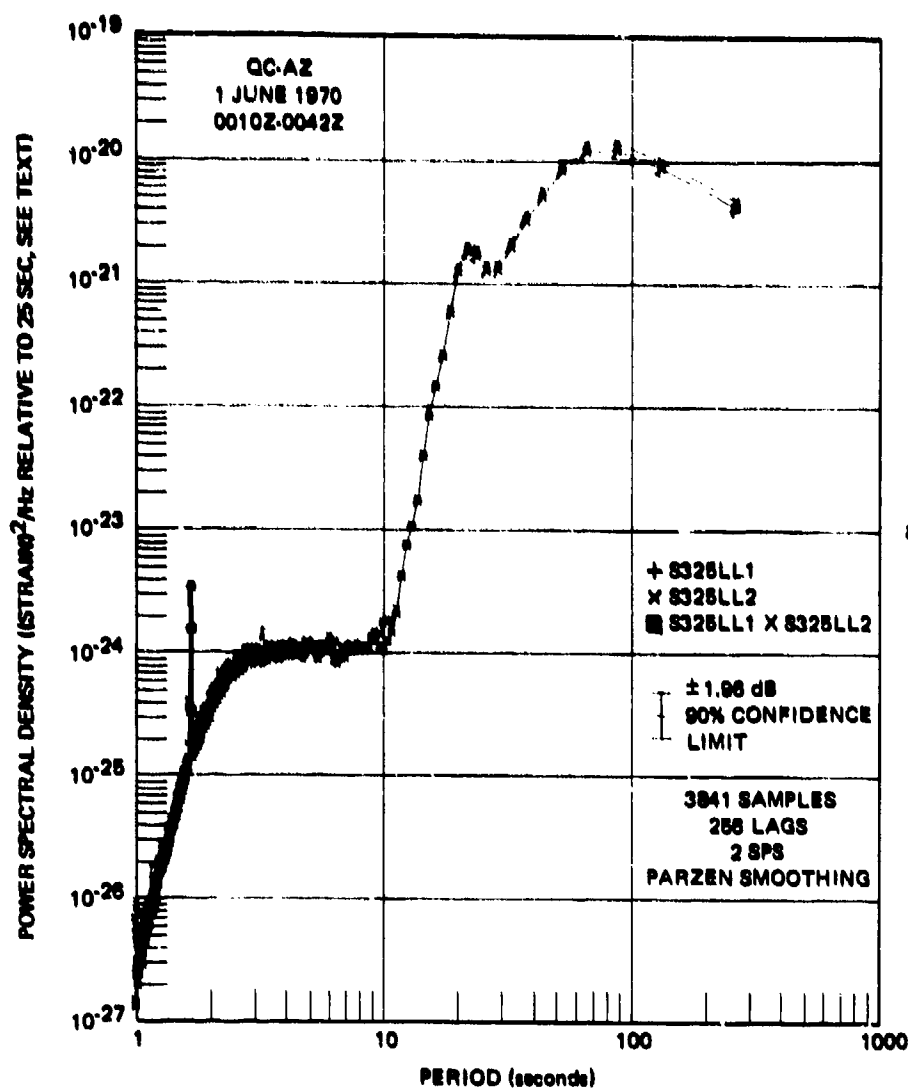


Figure 126. Reproduction of 16 mm film recording of part of the LQ3 Love wave, the LR2, and the LR3 Rayleigh wave from the Peru earthquake. NOS epicenter data: $\phi = 2023:27.3$, $9.2S$, $78.8W$, $h = 43$ km, near coast of northern Peru, $M_b = 6.6$, $M_S = 7.8$, $\Delta = 52.5$ deg, azimuth = 137.5 deg

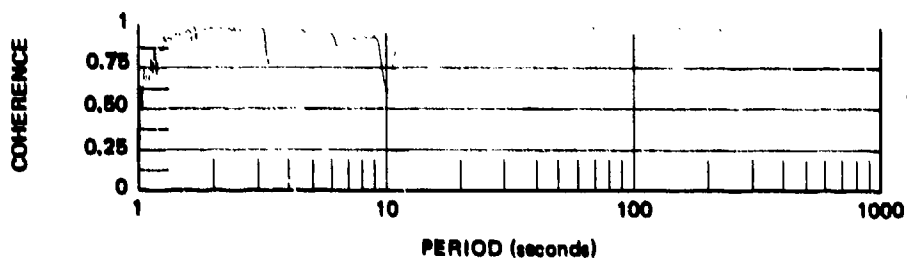
G 0001

QC-AZ
CAMERA 1
RUN 152
1 JUNE 1970

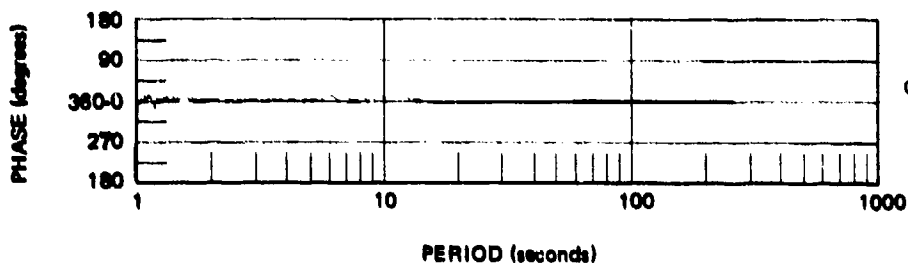
TR 72-3



a. Power spectral density



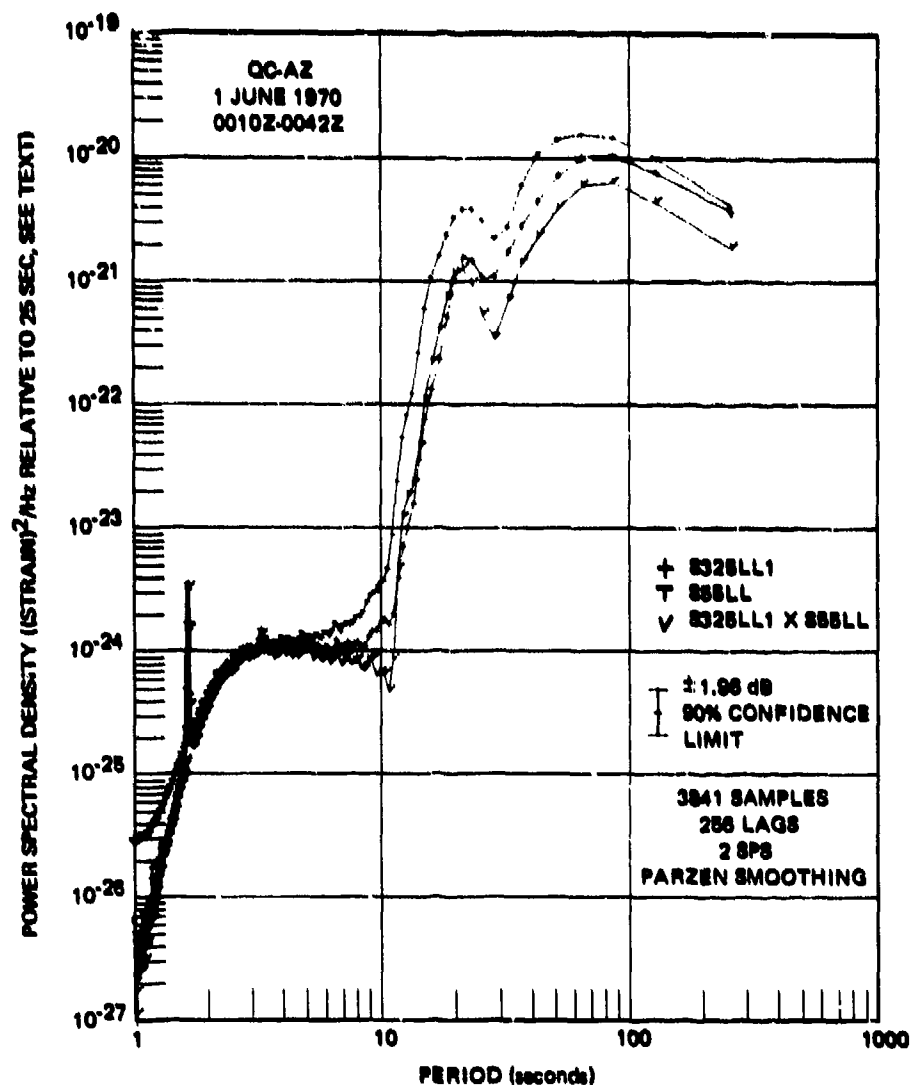
b. Coherence



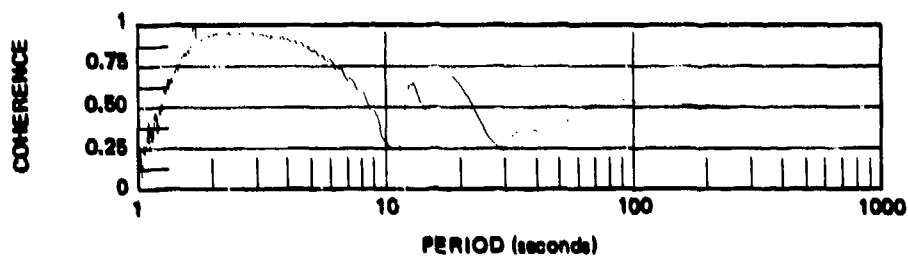
c. Phase lead
S325LL2 over S325LL1

Figure 127. Power spectral density, coherence, and relative phase angle of parallel horizontal strain seismographs S325LL1 and S325LL2 during the LQ3 Love wave and the LR2 and the LR3 Rayleigh waves of the Peru earthquake

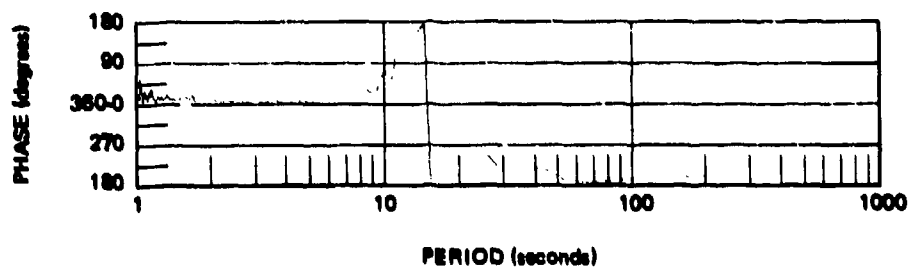
G 6024



a. Power spectral density



b. Coherence



c. Phase lead
S55LL over S325LL1

Figure 128. Power spectral density, coherence, and relative phase angle of perpendicular horizontal strain seismographs S325LL1 and S55LL during the LQ3 Love wave and the LR2 and the LR3 Rayleigh waves of the Peru earthquake

G 6028

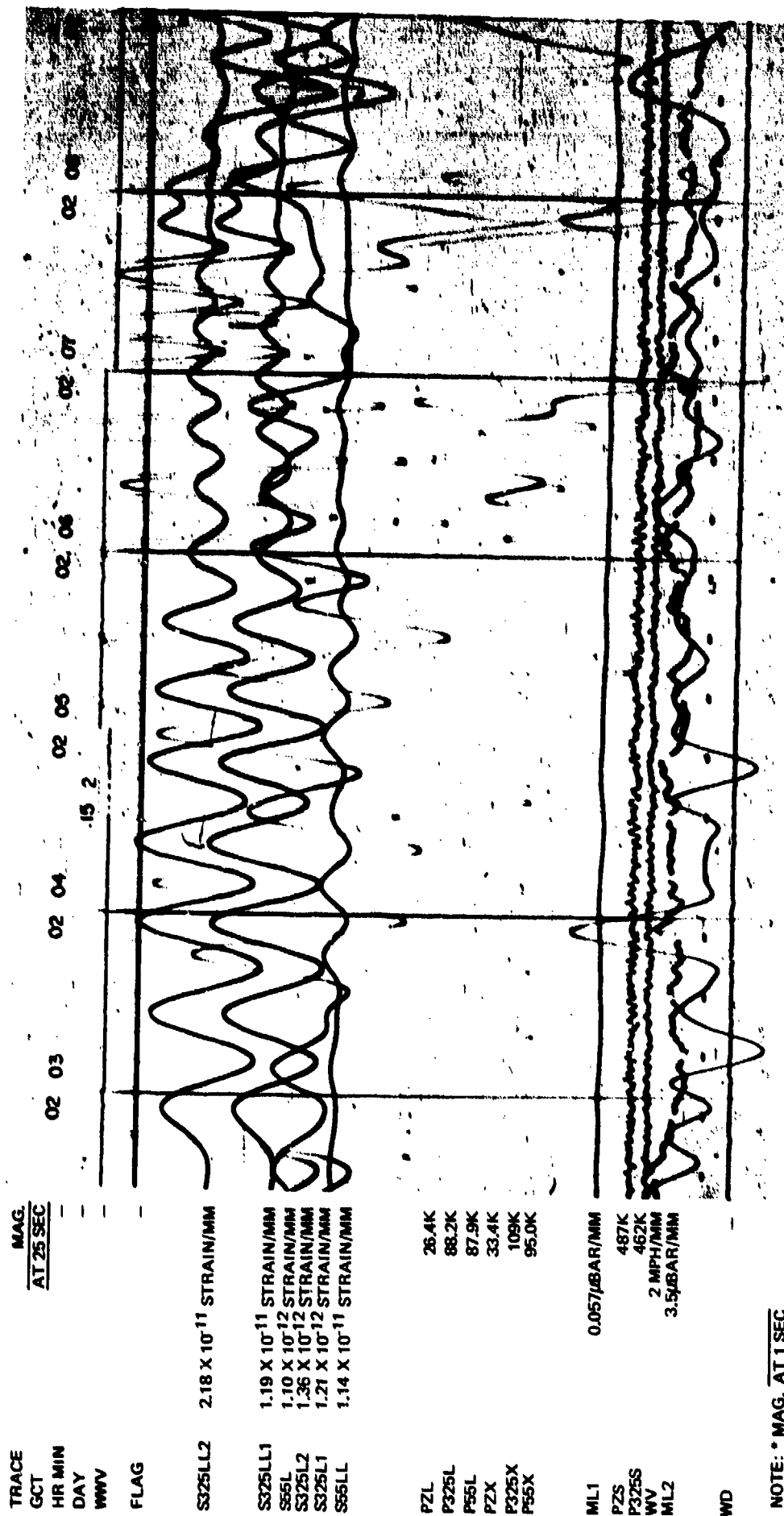
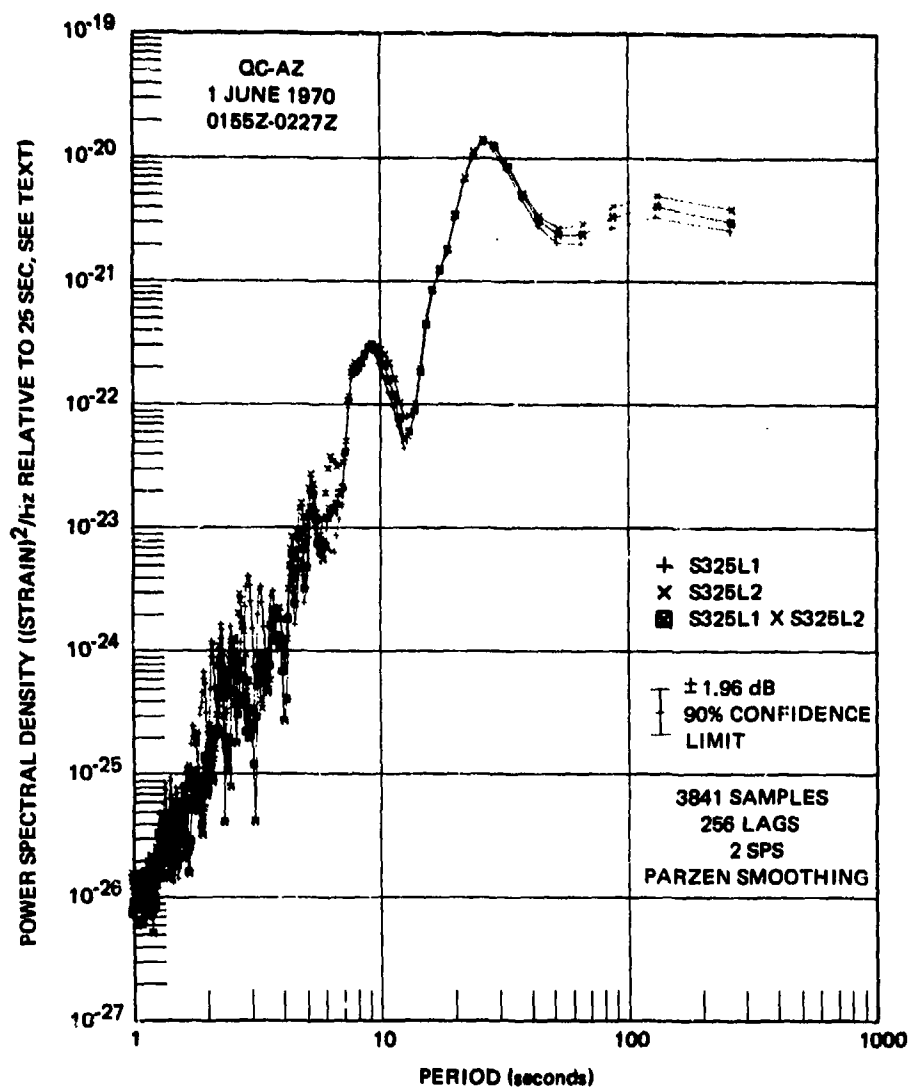


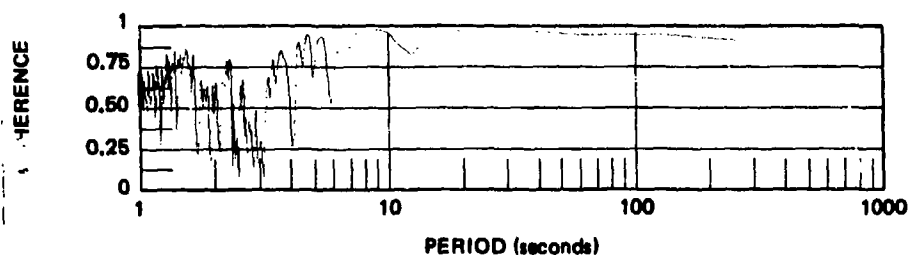
Figure 129. Reproduction of 16 mm film recording of LR1 Rayleigh wave from an aftershock of the Peru earthquake. NOS epicenter data: $0 = 0136$, 10.2 , $9.3S$, $79.0W$, $h = 48$, off coast northern Peru, $m_b = 6.0$, $M_S = 5.5$, $\Delta = 52.5$ deg, azimuth = 137.5 deg

G 0002

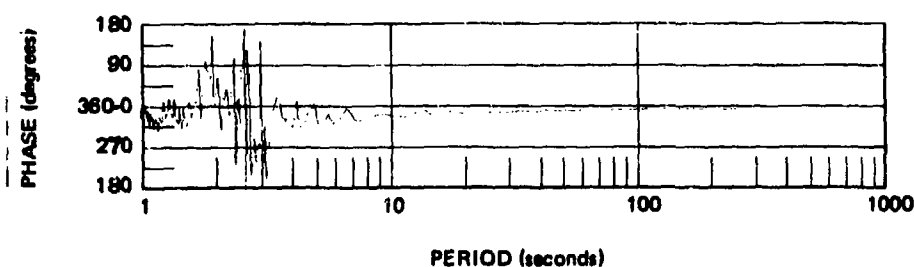
OC-AZ
CAMERA 1
RUN 152
1 JUNE 1970



a. Power spectral density



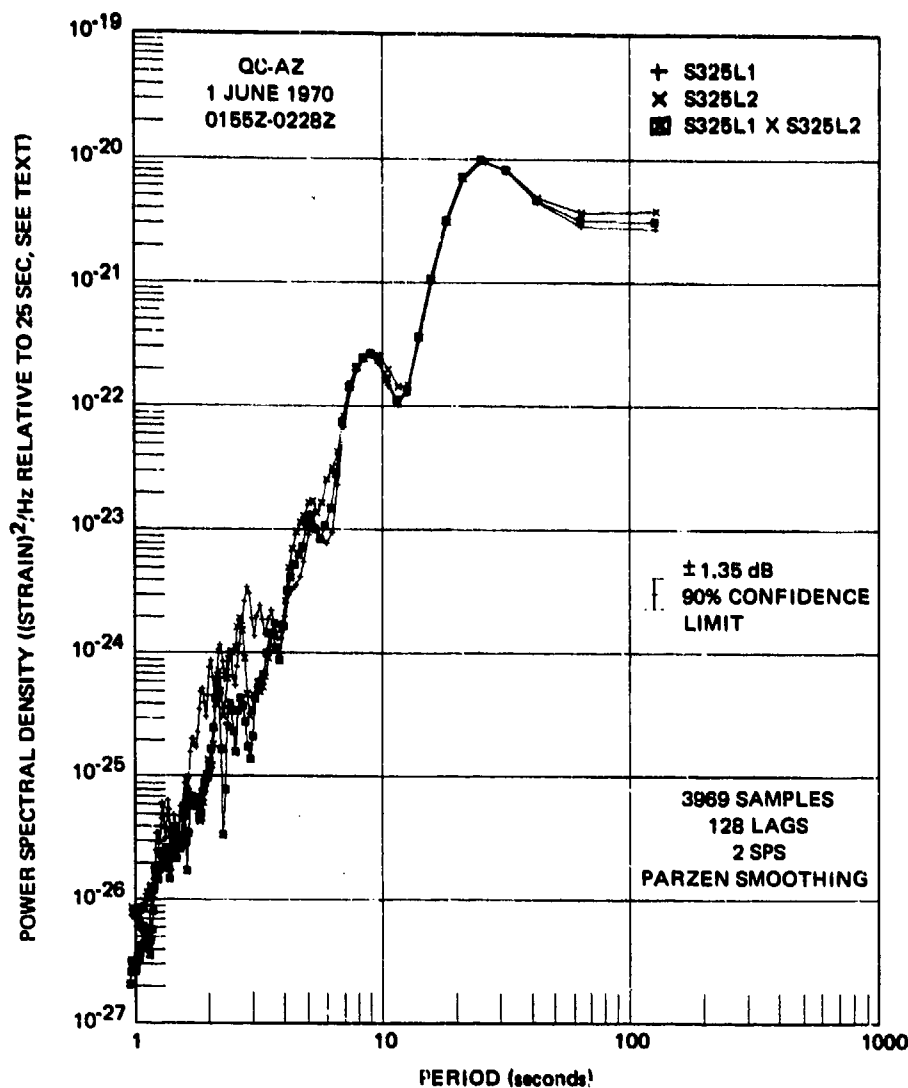
b. Coherence



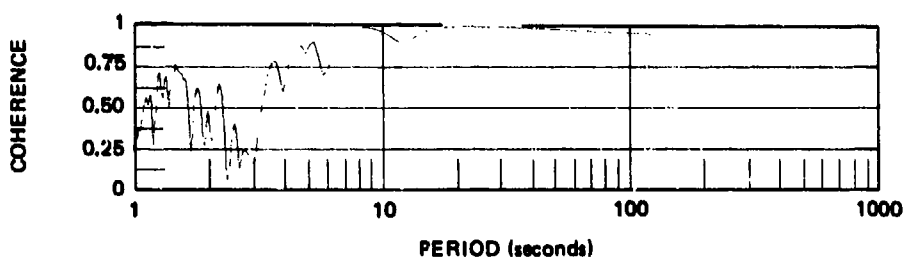
c. Phase lead
S325L2 over S325L1

Figure 130. Power spectral density coherence, and relative phase angle with 256 lags for parallel horizontal strain seismographs S325L1 and S325L2 during the LR1 Rayleigh wave of an aftershock of the Peru earthquake

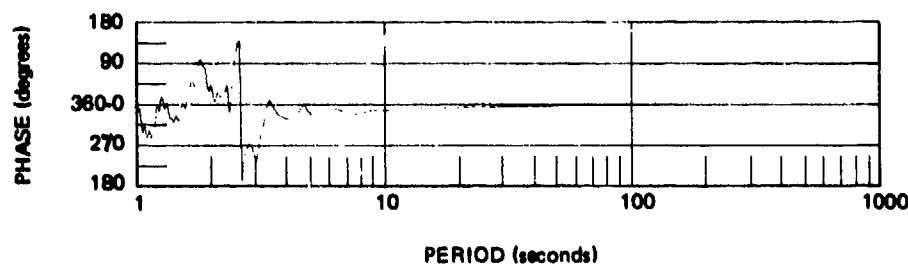
G 6026



a. Power spectral density



b. Coherence



c. Phase lead
S325L2 over S325L1

Figure 131. Power spectral density, coherence, and relative phase angle with 128 lags for parallel horizontal strain seismographs S325L1 and S325L2 during the LR1 Rayleigh wave of an aftershock of the Peru earthquake

G 6027

The second interpretation is that the 325 deg azimuth component of the vector wave number in the vicinity of the instruments has been altered from the expected wave number component. Therefore, a better comparison could be made by empirically adjusting the strain seismograph output by the 3.5 power ratio. Even when this adjustment is made, the inertial seismograph has a significantly greater power than the strain seismograph at periods longer than 25 sec.

A nonlinear response to tilting could smooth out the spectral peaks on the inertial seismogram also. This lowering of the Q could result from a mechanical friction between blocks along the local fault and joint pattern. The 9 sec peak in figure 120 is not as high a Q on the P325L as it is on the S325L1.

In figure 120, the coherence is about 0.9 near 8 sec and 25 sec. The relative phase angle is zero except at periods of 64 and 128 sec where it is 180 deg. During the third earthquake signal analyzed, the rms motion (relative to 25 sec) in the whole passband was: S325L1 1.82×10^{-11} strain; S325L2 1.95×10^{-11} strain; and P325L 9.05×10^{-7} m.

8.1.2 High Wind Signals

During episodes of high wind, there are variations in the pressure field that create displacements, tilts, and strains within the ground. These disturbances were discussed in detail in section 7.6. The two parallel horizontal strain seismographs, S325L1 and S325L2, respond identically to these ground strains. Figure 132 is a portion of the time sample that was analyzed for a comparison during windy conditions. The wind was blowing about 20 mph and gusting to 35 mph. The ML2 microbarograph outside the mine was responding to large pressure fluctuations. In the figure, equal and opposite strain is visible at several points, with an especially large, yet typical, pulse at about 0503Z. The S325L1 and S325L2 seismographs track each other identically in the time domain in figure 132, and the spectra almost overlay in the frequency domain in figure 133. During this sample, the total mean square strain (referenced to 25 sec) in the passband was 4.198×10^{-23} strain² for the S325L1, and 5.458×10^{-23} strain² for the S325L2; and the rms values were 6.479×10^{-12} strain and 7.388×10^{-12} strain, respectively. In figure 133, the spectra are seen to be almost identical except for a slight increase in value for the S325L2 at increasing period. The coherence is one and there is no relative phase shift between the seismographs. The seismographs are recording identically. The time sample was extended to 6.7 hr and analyzed for the comparison for periods between 20 and 2560 sec seen in figure 134. The results are the same as at the shorter periods except between 300 and 1280 sec where the S325L1 has more power than the S325L2. The coherence is almost one except in the anomalous period range, and the relative phase angle remains at essentially zero for all periods. A comparison between the ULP response seismographs S325U1 and S325U2 is illustrated in figure 135. The rms strains (referred to 25 sec) during the 6.7 hr period in the total passband of these seismographs were 3.61×10^{-11} strain and 2.08×10^{-11} strain, respectively. The two are seen to be essentially the same at periods out to 234 sec, and then the S325U1 exhibits considerably more power than the S325U2.

During the pressure-induced disturbances, the horizontal-inertial seismometers are subjected to considerable tilting, as can be seen in the seismogram in figure 132, on the inertial ALPS response channels (P_L). The tilts are more evident on the inertial extended-long-period response (P_X), which has a higher magnification at the longer periods than the ALPS response. The inertial P325L

TRACE	MAG.
GCT	AT 25 SEC
HR MIN	-
DAY	-
WVV	-
FLAG	-
S325L2	1.36 X 10 ⁻¹² STRAIN/MM
S325LL2	2.18 X 10 ⁻¹¹ STRAIN/MM
S325L1	1.21 X 10 ⁻¹² STRAIN/MM
S325LL1	1.19 X 10 ⁻¹¹ STRAIN/MM
S55L	1.20 X 10 ⁻¹² STRAIN/MM
S55LL	1.14 X 10 ⁻¹¹ STRAIN/MM
P2L	26.4K
P55L	88.2K
P325L	82.9K
PZX	33.4K
P55X	109K
P325X	95.0K
ML1	0.057/μBAR/MM
WV	2 MPH/MM
*PZS	487K
*P325S	462K
ML2	3.5/μBAR/MM
WD	-

NOTE: * MAG. AT 1 SEC

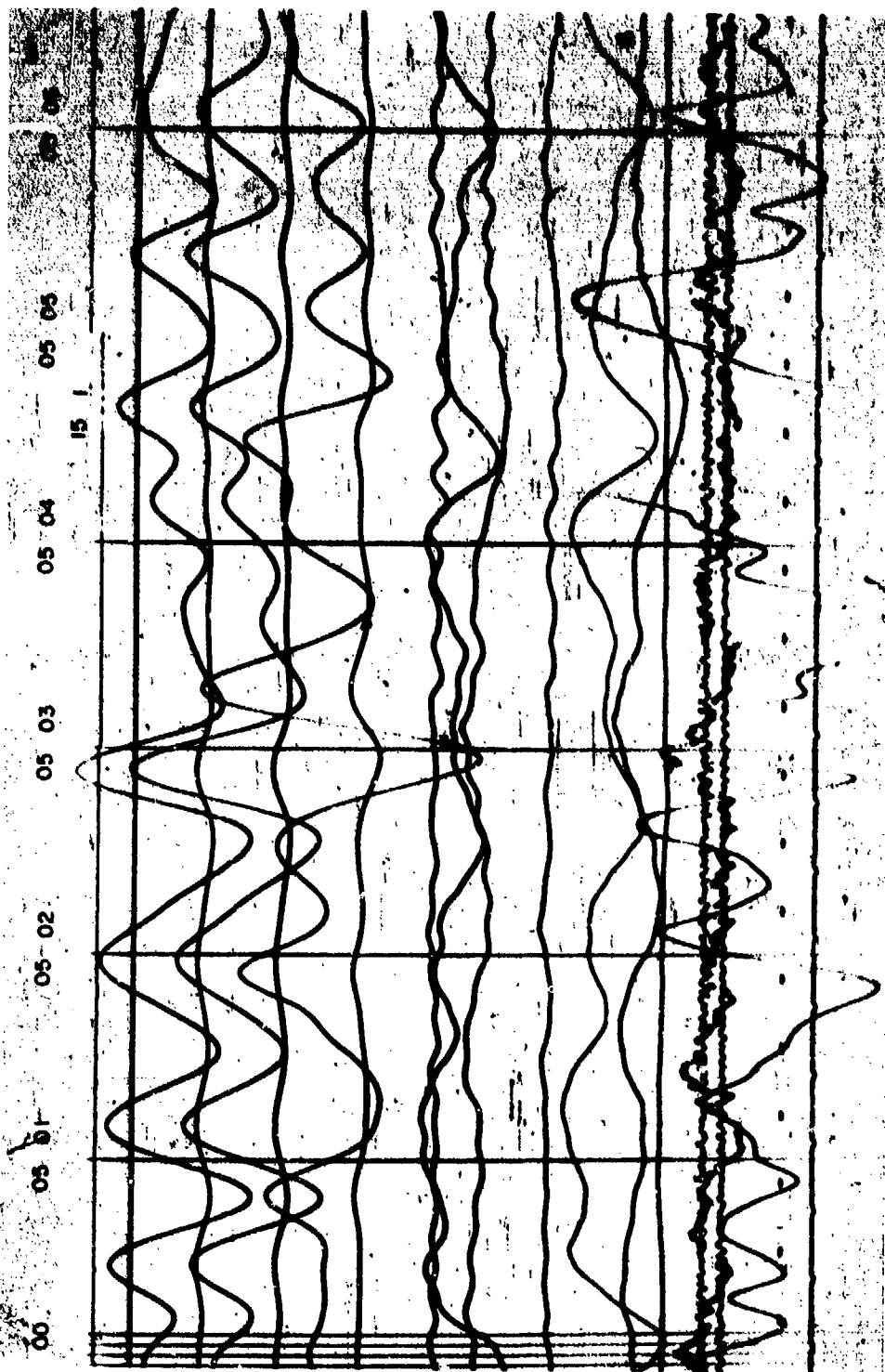
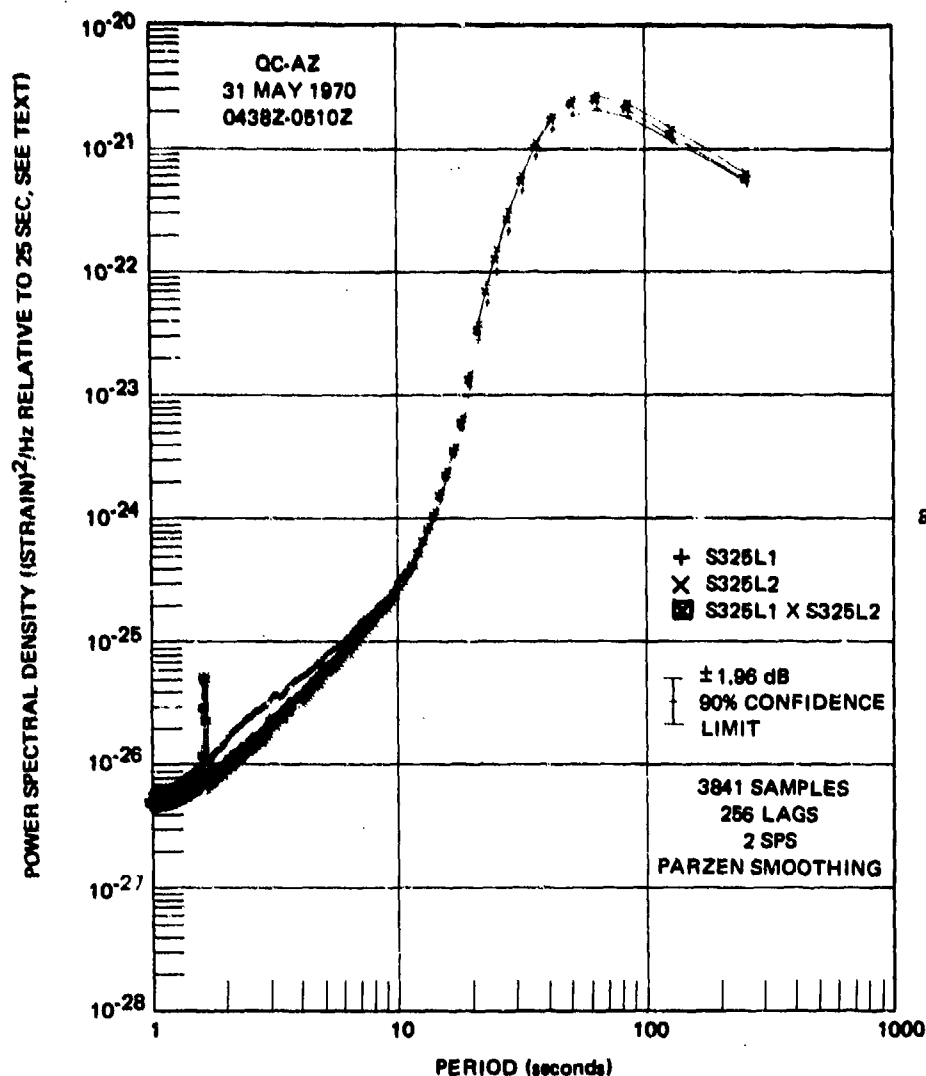


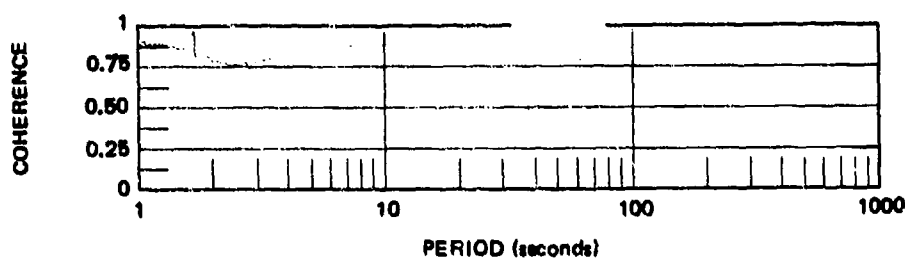
Figure 132. Reproduction of 16 mm film recording of a portion of the high wind sample

G 6083

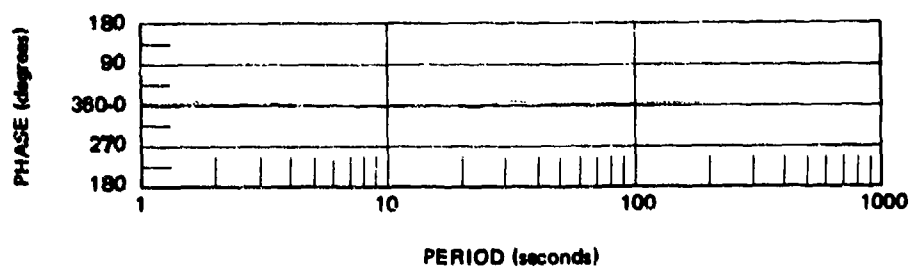
OC-AZ
CAMERA 1
RUN 151
31 MAY 1970



a. Power spectral density



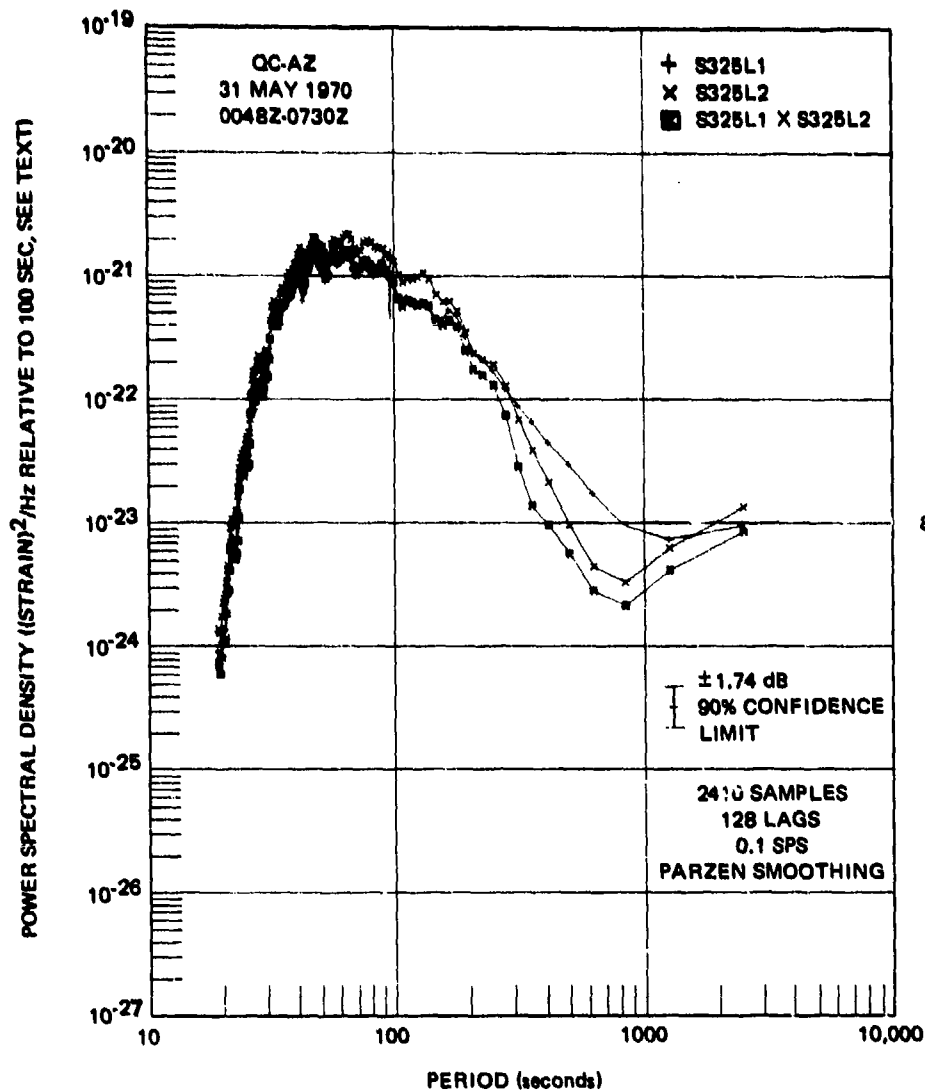
b. Coherence



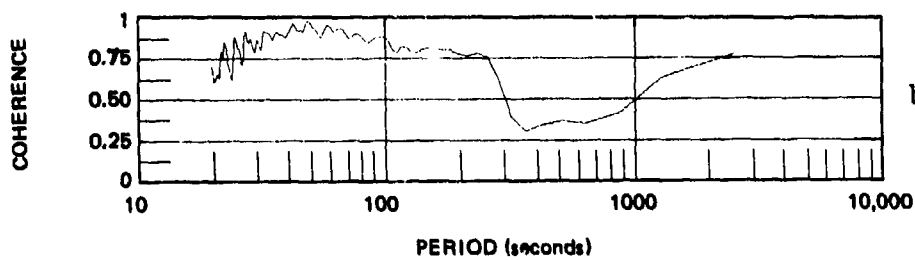
c. Phase lead
S325L2 over S325L1

Figure 133. Power spectral density, coherence, and relative phase angle of parallel horizontal strain seismographs S325L1 and S325L2 during high wind conditions, 1 to 256 sec range

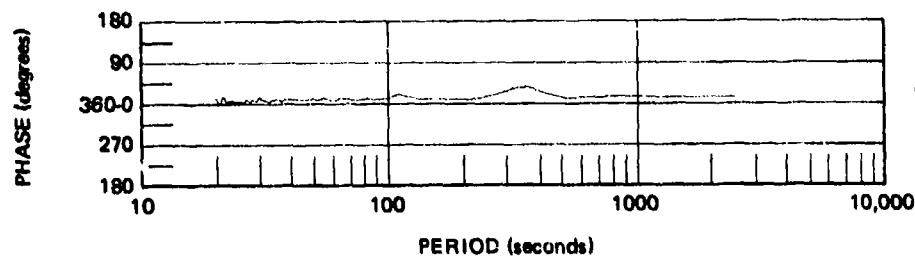
G 6017



a. Power spectral density



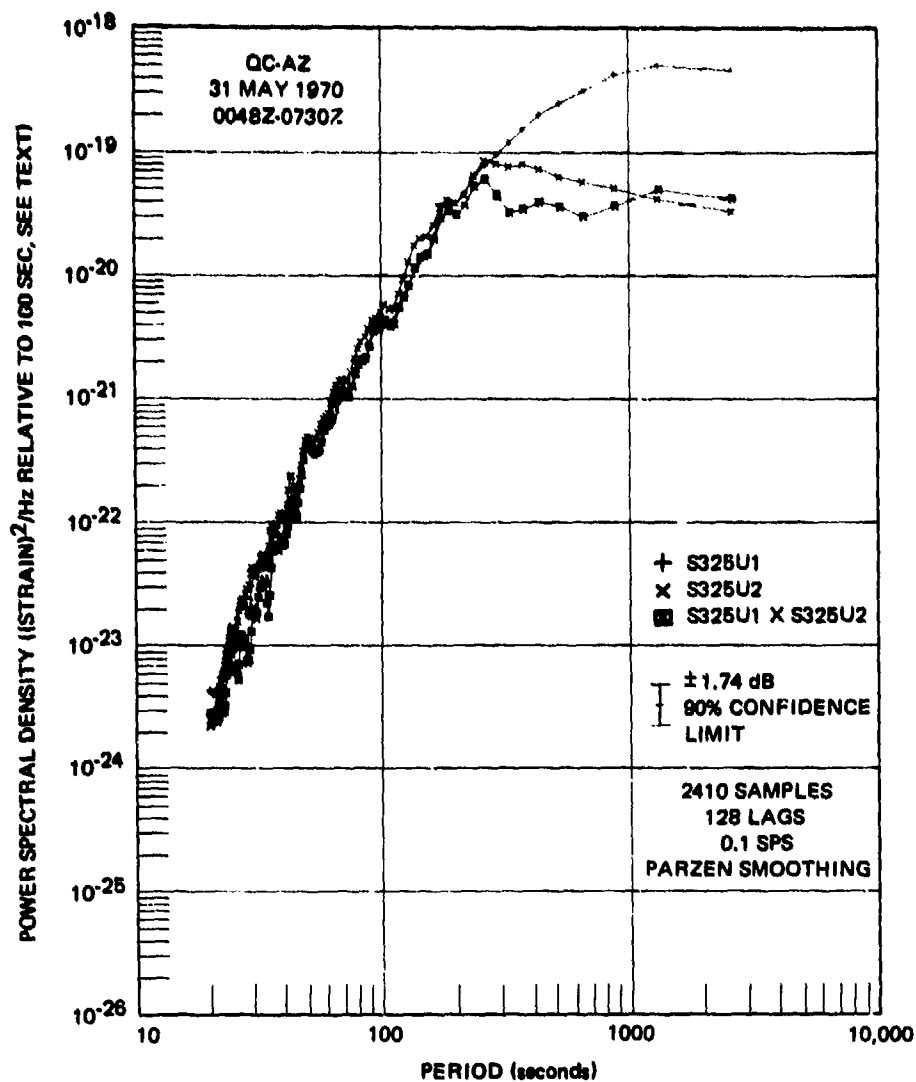
b. Coherence



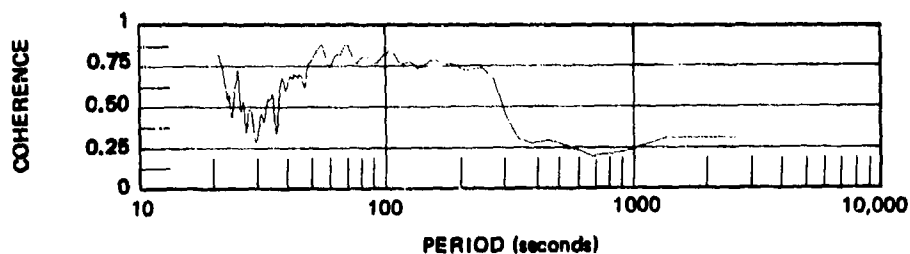
c. Phase lead
S325L2 over S325L1

Figure 134. Power spectral density, coherence, and relative phase angle of parallel horizontal strain seismographs S325L1 and S325L2 during high wind conditions, 20 to 2560 sec range

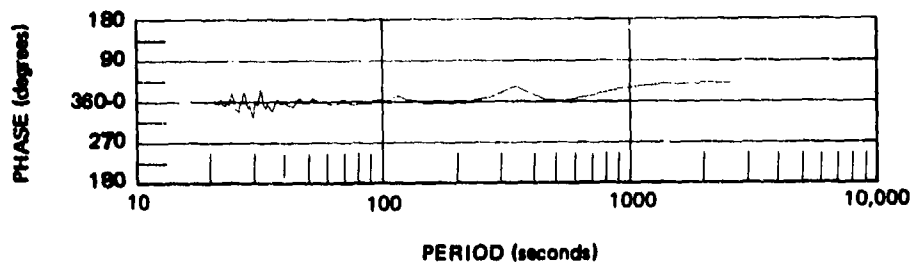
G 6018



a. Power spectral density



b. Coherence



c. Phase lead
S325U2 over S325U1

Figure 135. Power spectral density, coherence, and relative phase angle of parallel horizontal strain seismographs S325U1 and S325U2 during high wind conditions

G 6019

is compared with the strain S325L1 in figure 119. The rms ground displacement (referred to 25 sec) during this 32.0 min sample was 33.0 μ . In the P325L spectra in figure 119, the general background spectrum has risen until the microseismic peaks at 8.4 and 16.2 sec are almost swamped by the general rise in the spectrum. The coherence is relatively low, indicating that the tilt response of the horizontal-inertial seismometer is only partially linearly related to the ground strain. The ground strain has increased so that the entire spectra is above the strain of the microseismic peaks, which are not visible either in the analog trace or as a spectral peak.

The perpendicular-horizontal strain seismographs are very comparable in spectra. During the high wind sample analyzed, the rms strain (referenced to 25 sec) for the S55L seismograph was 6.500×10^{-12} strain. This value is within 0.32 percent of the 6.479×10^{-12} rms strain on the S325L1. The fact that the rms values are this close is fortuitous considering the errors in calibration and analysis, but it does substantiate that calibrations are very close and are well within acceptable operational tolerances. The spectral comparison is plotted in figure 136. The spectra at periods shorter than about 10 sec are in the computational noise and are not meaningful. The spectra are seen to be very smooth and devoid of any peaks. The cross spectra does show a minor peak at the microseismic period of 16 sec. This small amount of microseismic strain apparently mixes with the pressure-induced strain in a nonlinear manner, resulting in the dip in the coherence at 20 sec. The coherence holds to reasonable values except for a minimum at 20 sec and at periods longer than 100 sec. The phase angle is almost 180 deg at all periods. The comparison to longer periods is extended in figure 137 with the ULP response seismographs S325U1 and S55U. About the same picture is seen as before. The spectra are similar in appearance out to periods near 250 sec. A comparison of figures 135 and 137 shows that at the longer periods, the S55U resembles the S325U2 more than the S325U1. The cross spectra have many sharp high Q peaks. With the frequency resolution and statistical stability of the analysis, these peaks are considered as being real and are definitely not an artifact of the data analysis. Also, since these peaks appear in the cross spectra of the perpendicular strains, but not in the cross spectra of the parallel strains, they must be associated with shear strain phenomena.

The coherence between the perpendicular-strain seismographs shows the coherence of the peaks in the cross spectra at between about 0.25 and 0.4. The relative phase angle tends toward 180 deg at periods between 50 and 210 sec and tends toward 0 deg at other periods.

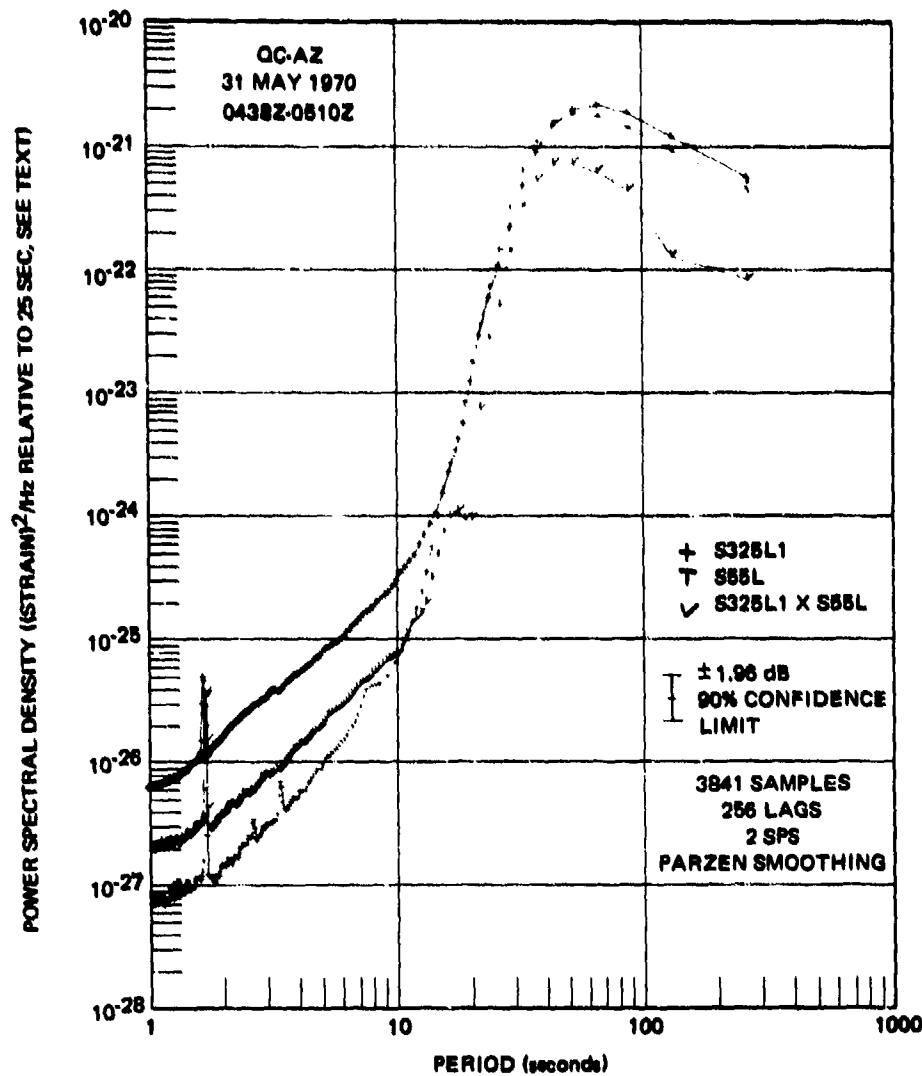
8.2 IN-SITU MEASUREMENT OF ELASTIC PARAMETERS

The QC-AZ instrumentation complex has been used to measure several elastic parameters in-situ.

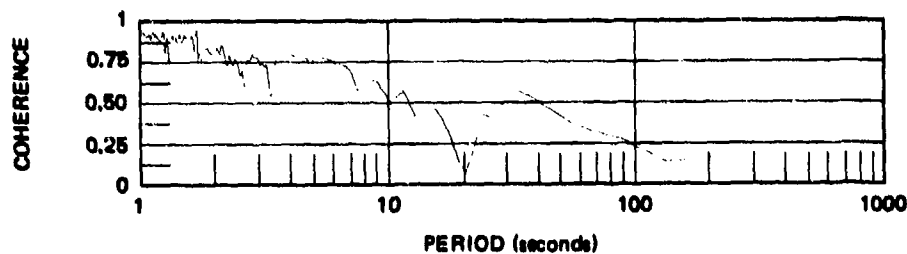
8.2.1 The ratio, $\lambda/(2\mu + \lambda)$

It will be shown in section 9.1.4 that

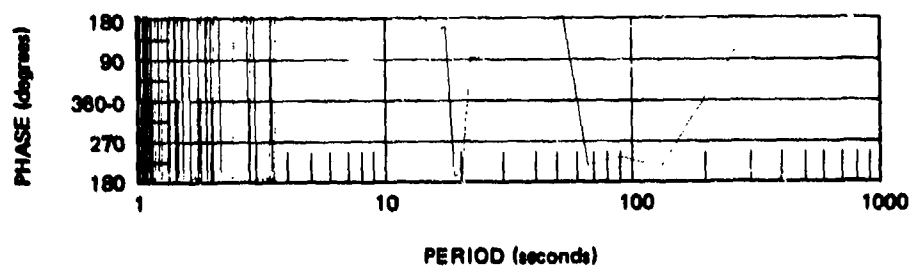
$$\frac{\lambda}{2\mu + \lambda} = \frac{(\text{vertical strain})}{(\text{sum of perpendicular horizontal strains})}$$



a. Power spectral density



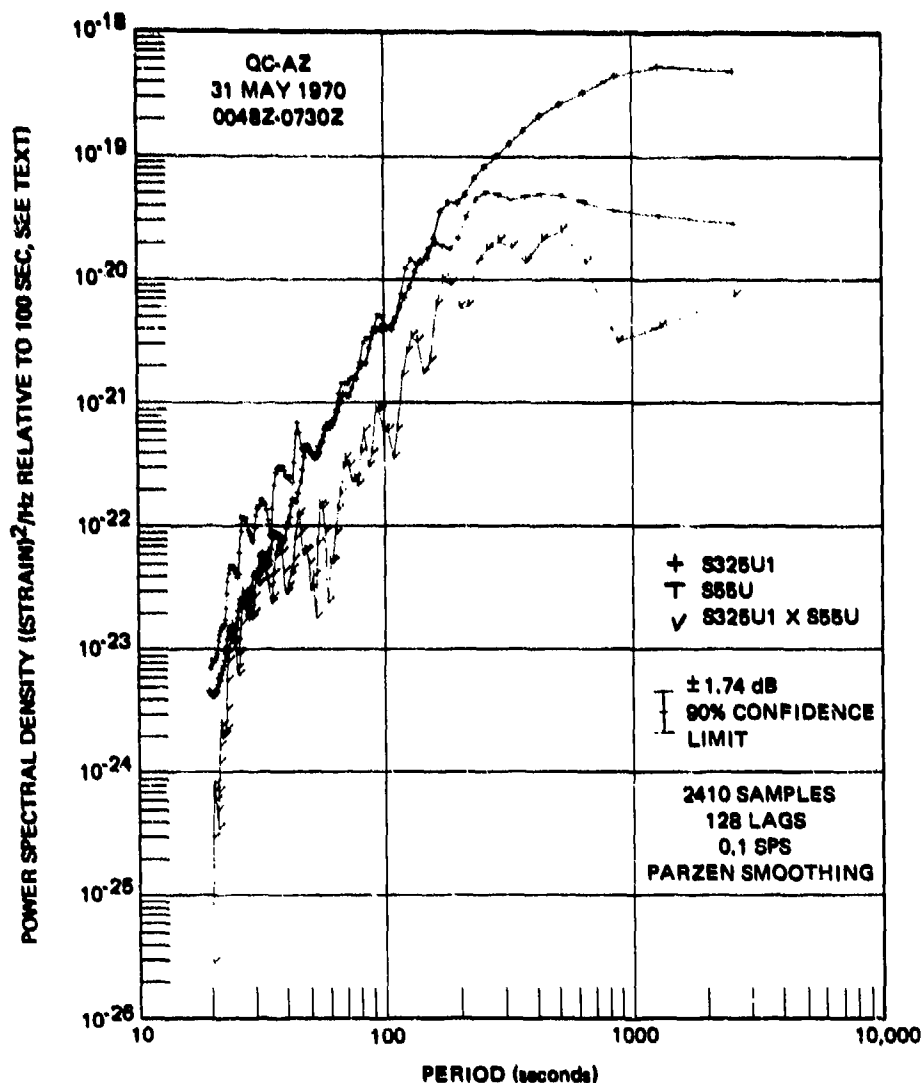
b. Coherence



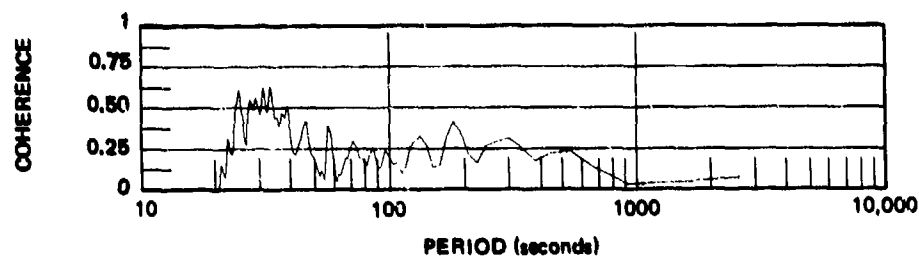
c. Phase lead
S55L over S325L1

Figure 136. Power spectral density, coherence, and relative phase angle of perpendicular horizontal strain seismographs S325L1 and S55L during high wind conditions

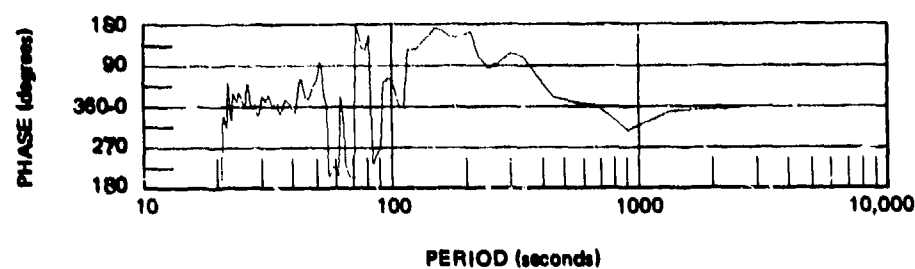
G 6021



a. Power spectral density



b. Coherence



c. Phase lead
S55U over S325U1

Figure 137. Power spectral density, coherence, and relative phase angle of perpendicular horizontal strain seismographs S325U1 and S55U during high wind conditions

G 6022

To determine this ratio, an off-line recording was made from magnetic tape. In figure 138, the first trace is the sum of S325L and S55L, with strain magnifications adjusted for approximately equal contribution from both. The SZL channel (trace 2) was algebraically added to the horizontal sum and SZL magnification was adjusted to achieve maximum cancellation for earthquakes and microseisms, as shown on the third trace. Note that the small event, which occurs during a calibration of one of the horizontal instruments, is quite effectively cancelled on the third trace, as are the microseisms preceding the event. The residual background on the composite trace is a result of random noise in all three seismographs, but primarily the S55L, which was noisy following previous maintenance and possibly from air pressure disturbances.

By using instrument calibrations, the ratio of vertical strain to the sum of the horizontal strains was found to be 0.46. The reciprocal of 0.46 is 2.17.

8.2.2 Poisson Ratio

The Poisson ratio σ can be calculated in the following manner. From the experimental results in the previous paragraph:

$$\frac{\lambda}{2\mu + \lambda} = 0.46 \quad (16)$$

$$\lambda = 1.73\mu. \quad (17)$$

The Poisson ratio is related to the elastic constants by

$$\sigma = \frac{\lambda}{2(\lambda + \mu)} \quad (18)$$

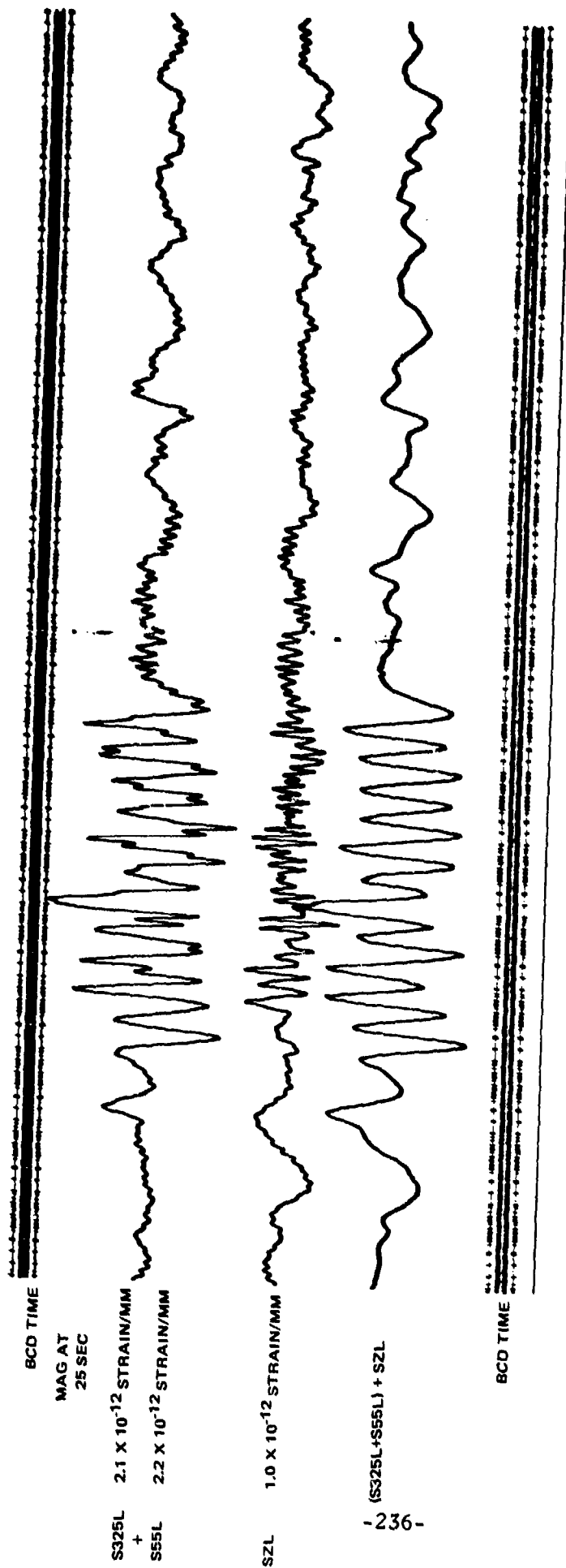
substituting

$$\sigma = \frac{1.73\mu}{2(2.73\mu)} \quad (19)$$

thus

$$\sigma = 0.32. \quad (20)$$

The authors have noticed a phenomenon that they have called the "Poisson ratio effect." When the direction of travel of a Rayleigh wave is generally lined up with either one of the horizontal strain seismometers, the perpendicular strain seismograph has a signal that is about -1/3 of the in-line signal. Figure 129 in section 8.1.1 is an illustration of the "Poisson ratio effect." The Rayleigh wave is travelling from an epicenter at an azimuth of 137.5 deg, or 7.5 deg off the back azimuth of the 325 deg azimuth instruments. The low gain S325LL1 and S325LL2 seismographs have identical signals. One peak was measured at 20.25×10^{-11} strain. The corresponding peak on the S55LL seismograph is 5.7×10^{-11} strain of the opposite polarity. The ratio of these strains is -0.29, which is within 10 percent of the above 0.32 value. In a homogeneous, isotropic, layered half-space, there is no displacement in a direction perpendicular to the direction of travel of a Rayleigh wave. If there is no displacement, there will be no strain. The senior author's conclusion is that either (1) the anisotropic nature of the jointed rock, as demonstrated in section 8.2.3, or (2) the existence of



-236-

QC-AZ
MAGNETIC
TAPE PLAYOUT
RUN 270
27 SEPT. 1970

Figure 138. Magnetic-tape playback showing the similarity between the sum of horizontal strain and vertical strain outputs

G 0004

a free surface in the horizontal direction is causing the ground to respond in a manner significantly different from the theoretical layered half-space. The existence of a free surface in the horizontal direction is very possible in the block structure of the Basin and Range Province. The Bouguer gravity map of this part of Arizona (Peterson, 1968) indicates a major fault trending northwest by west and lying at depth under the town of Queen Creek 7.25 km to the north of the station. Since the Basin and Range Province does consist of large uplifted blocks of rock, separated by alluvial valleys with several thousand feet of sedimentary deposits, the phenomena observed at QC-AZ are probably common to all seismograph stations in the Basin and Range Province, but cannot be detected with only inertial seismographs. It is very possible that other geologic provinces throughout the world similar to the Basin and Range may also respond as anisotropic material or as rigid blocks of rock surrounded by weaker material.

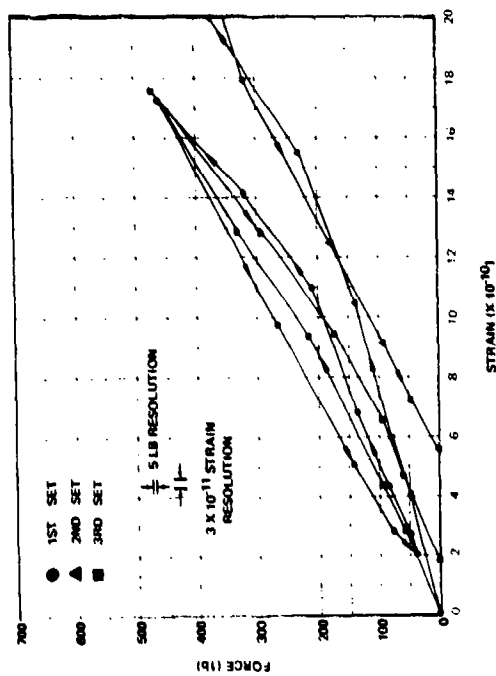
8.2.3 Slope of Stress-Strain Curve

The slope of the stress-strain curve for the local rock was measured in-situ by applying a known force to the rock and reading the strain on the broad-band strain seismograph. The strains were on the order of the 1 to 10×10^{-10} strain or about 1 to 10 percent of the diurnal earth tide.

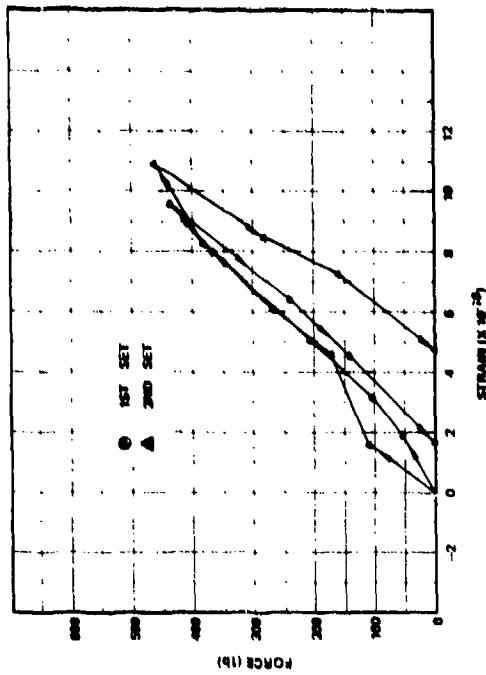
The load was applied in steps by a "come-along" puller tensioning a steel wire rope between bolts anchored next to the strain seismometers. The bolts were in the floor of the 325 deg azimuth tunnel and on the wall of the 55 deg azimuth tunnel. A load cell was in series with the wire rope. The output voltage of the load cell was amplified by 100. This voltage was monitored on an oscilloscope and recorded on magnetic tape. After playback of the magnetic tape, the minimum resolution of the load cell data was about 5 lb, which is 1 percent of the rated full-scale 500 lb load. The wire rope was attached to the bolts as close to the surface of the rock as possible. Since the bolts were cantilevered from the rock, a small torsion moment was introduced into the rock in the vicinity of the bolt as well as the net compressional load. Different loads were attainable in repetitive tests by adjusting the total length of the wire rope assembly with a turnbuckle.

The broad-band strain output was recorded on the normal channel on the magnetic tape recorder. After playback of the magnetic tape, the minimum strain resolution of the broad-band seismographs for these tests was 1.07×10^{-11} strain on the S55B and 3.14×10^{-11} strain on the S325B. The strain resolution was about 1 percent of the maximum strain observed.

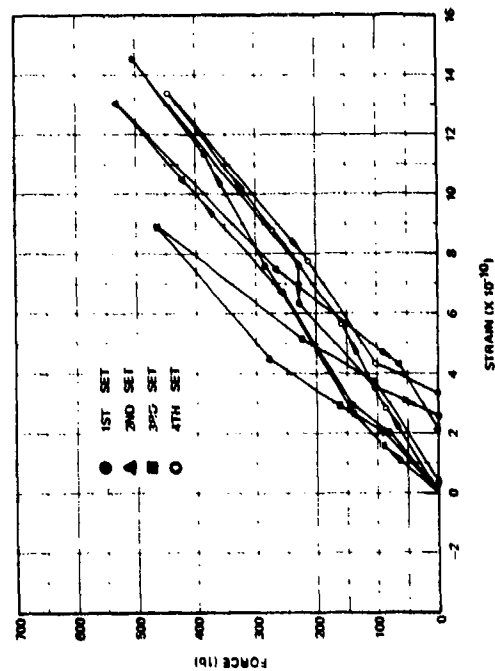
The results of the tests in the 325 deg azimuth tunnel are plotted in figure 139, and the results of the tests in the 55 deg azimuth tunnel are plotted in figure 140. The load bolts were mounted at 10m increments along the strain rods. The (a) part of the two figures is for the load applied to bolts separated the full 40m length of the tunnels. The (b), (c), and (d) parts of the figures are plots of data from tests with the main seismometer transducer end of the wire rope fixed and the other end of the rope attached at lengths of 30m, 20m, and 10m, respectively. The load and strain resolutions are indicated in the figures. The arrowheads indicate the direction of load application and removal.



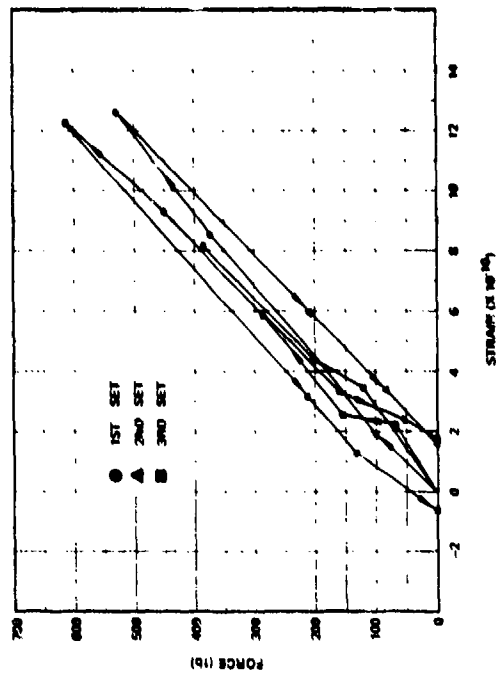
a. Load points separated by 40 m



b. Load points separated by 30 m



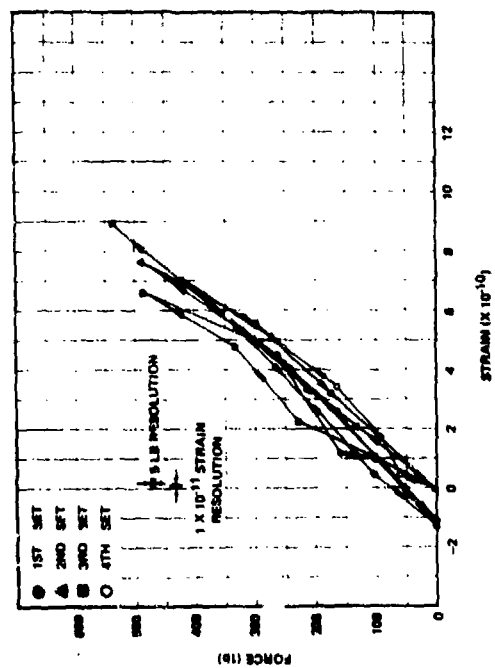
c. Load points separated by 20 m



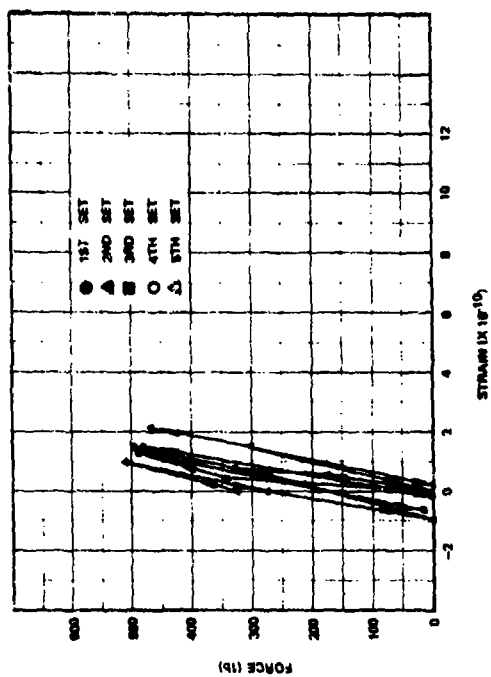
d. Load points separated by 10 m

Figure 139. Force-strain curve in 325 deg azimuth

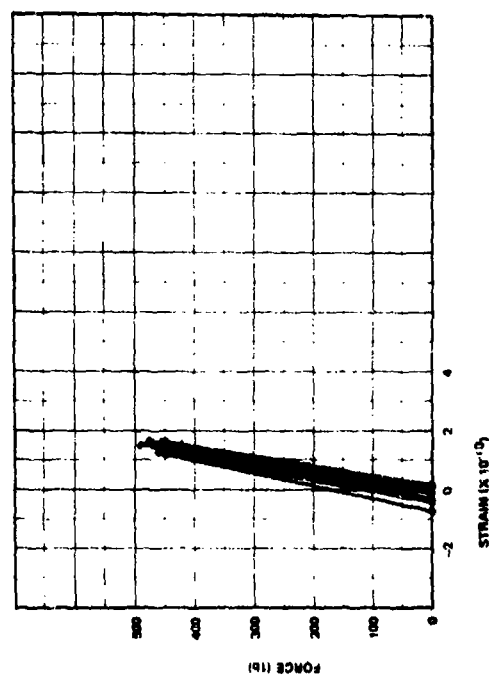
G 6685



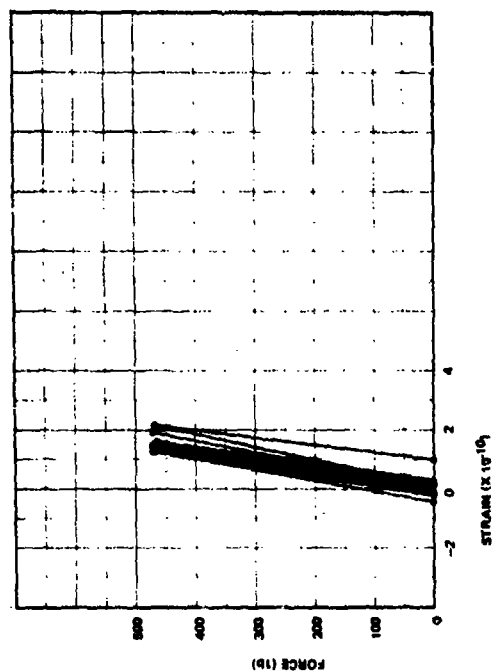
a. Load points separated by 40 m



b. Load points separated by 30 m



c. Load points separated by 20 m



d. Load points separated by 10 m

Figure 140. Force-strain curve in 55 deg azimuth

G 6686

Three primary observations can be made from these figures:

(a) There is a change in slope at about the middle of the curves.

(b) There is a significant difference (greater than the resolution) in the curves for repetitive load applications, with the results in the 325 azimuth showing normal hysteresis and in the 55 azimuth showing negative hysteresis.

(c) There is a significant difference between the average slope of the curves in the two directions. The ratio of the slope of the 325 deg curve to the 55 deg curve is about 1.25. This ratio will be referred to later in section 12 as it relates to the relative transfer function of ground displacement to strain in the two directions.

The change in slope and the hysteresis effects are both the result of the joints in the rock. Probably, in some joints, calcium carbonate remineralized zones, visible in thin sections of the rock, have a lower Young's Modulus than the native quartz diorite. In other joints there are probably microfractures that close and open with varying degrees of stick-slip motion as the rock is compressed and then released. After the microfractures are closed, the load acts directly on the rock and the slope of the load-strain curve increases. The calcium carbonate remineralization will tend to modify the action of the microfractures.

These effects are much larger in the 325 deg azimuth because of the orientation of the local rock joint structure. The smaller slope of the load-strain curve for the 325 deg tunnel is also a consequence of this joint pattern. The joint structure results in an anisotropic rock that is 1.25 times weaker in the 325 deg azimuth than in the 55 deg azimuth. The joint structure in the immediate vicinity of the mine is parallel to the major geological structure in the central portion of Arizona as shown on the state geologic map (Wilson et al., 1969). It is not merely a localized condition. The physiography of the basins and ranges strikes in the same direction. Gravity anomalies in the immediate vicinity of the mine (Peterson, 1968) and in central Arizona (West and Sumner, 1972) substantiate that the northwest trend of the geologic structure is a major feature of the region.

The slope of the load-strain curves are equal to Young's Modulus E multiplied by the area A being stressed. The definition of Young's Modulus in the linear range is

$$\begin{aligned} E &= \frac{\text{stress}}{\text{strain}} \\ &= \frac{\frac{\text{force}}{\text{area}}}{\text{strain}} \\ &= \frac{\frac{F}{A}}{e_{ij}} \end{aligned} \quad (21)$$

$$EA = \frac{F}{e_{ij}} \quad (22)$$

The slope of the curves is the right-hand side of equation (22). The statements above that the rock is 1.25 times weaker in the 325 azimuth tacitly assume that the area affected by the load is identical in both tunnels. This assumption is a good approximation. If we assume that the area being stressed is constant for the range of loads used in the experiment, then the area A can be estimated using a typical value of E. Clark (1966) gives values of E for diorite and for granite between 0.52 and 0.87 Mbar. Assuming E is 0.5 Mbar and calculating the stressed area in the 55 deg tunnel from equation (22) gives an estimate of 580 ft². This estimate seems reasonable for the area loaded by a bolt in the wall or floor of a tunnel of about 80 ft² in cross-section.

8.2.4 Apparent Local Q

An apparent local Q was obtained from the recording of a damped oscillation following a blast of 12 lb of dynamite in the small mine directly above the seismometer chamber. The adit of this mine is visible in figure 38b.

The short-period inertial seismograms are shown in figure 141. The 1 sec damped oscillation is clearly visible on the PZS vertical seismogram. The first large negative peak is 152×10^{-9} m of ground motion.

If the vertical motion in figure 141 is taken as the vertical damped oscillation of a block of rock, the apparent damping and Q can be calculated using the log decrement of the motion. This calculation gives a damping ratio of 0.069 and a Q of 7.2.

Boucher (1972) calculated spectra of P and S waves from microearthquakes in west-central Nevada and from the Faultless explosion. His calculations indicated a best fit of the data was obtained with a Q of 10 to 15. The value above of 7.2 is in general agreement with his results.

8.3 VOLUMETRIC STRAIN RECORDED ON MICROBAROGRAPH AND VERTICAL STRAIN SEISMOGRAPH

Volumetric strain, or dilatation, from the San Fernando earthquake of 9 February 1971 was recorded with identical waveform on the linear strain, vertical, broad-band seismograph (SZB) and on the microbarograph (ML1) inside the sealed seismometer chamber.

Volumetric strain is dilatation and can be written as

$$\begin{aligned} \theta &= e_{ii} \quad , \quad i = 1, 2, 3 \\ &= e_{11} + e_{22} + e_{33}, \end{aligned} \quad (23)$$

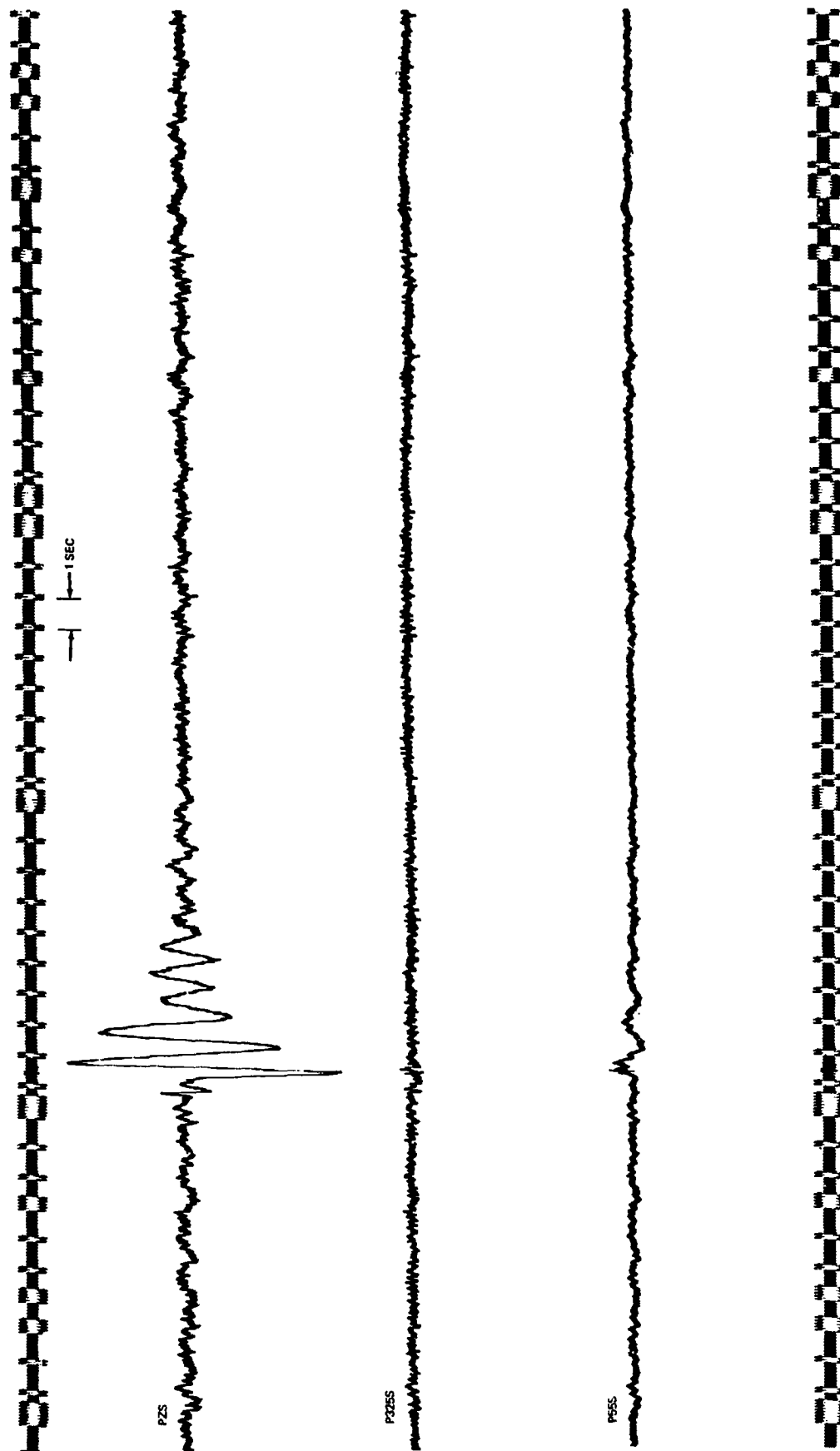


Figure 141. Short-period inertial seismograph recordings of ground motion following a blast in the small mine above the seismometer chamber

G 6687

where θ is dilatation and e_{ij} is a strain tensor component acting across the i face in the j direction. Dilatation is an invariant of the strain tensor and can be measured on any three mutually orthogonal axes. Let the vertical linear strain

$$e_{zz} = e_{33} \quad (24)$$

The vertical stress component at a free surface must vanish. Stress tensor components are related to strain tensor components by (e.g., Bullen, 1963)

$$P_{ij} = \lambda \theta \delta_{ij} + 2\mu e_{ij} \quad , \quad i = 1, 2, 3 \quad (25)$$

$$j = 1, 2, 3$$

where P_{ij} is the component of the stress tensor acting across the i face in the j direction, λ and μ are the Lamé elastic constants, and δ_{ij} is the Kronecker delta. The vertical stress component P_{zz} at a free surface must vanish. Therefore,

$$\begin{aligned} P_{zz} &= P_{33} \\ &= \lambda \theta + 2\mu e_{33} \\ &= \lambda(e_{11} + e_{22} + e_{33}) + 2\mu e_{33} \\ &= 0 \end{aligned}$$

which can be written

$$e_{11} + e_{22} = - \frac{\lambda + 2\mu}{\lambda} e_{33} \quad (26)$$

Substituting equation (26) into equation (23)

$$\begin{aligned} \theta &= \left(1 - \frac{\lambda + 2\mu}{\lambda}\right) e_{33} \\ &= A e_{33} \\ &= A e_{zz} \end{aligned} \quad (27)$$

Thus, dilatation is equal to the vertical linear strain times a factor related to the elastic parameters.

For an adiabatic process in air

$$P_1 V_1^{1.4} = P_2 V_2^{1.4} \quad (28)$$

where P is pressure, V is volume, subscript 1 indicates initial conditions, and

subscript 2 indicates final conditions. For small changes in pressure and volume

$$P_1 V_1^{1.4} = (P_1 + \Delta P) (V_1 + \Delta V)^{1.4}$$

$$\frac{1}{1 + \frac{\Delta P}{P_1}} = \left(1 + \frac{\Delta V}{V_1}\right)^{1.4}$$

Expanding in a Maclaurin series and neglecting second order and higher terms

$$1 - \frac{\Delta P}{P_1} = 1 + 1.4 \frac{\Delta V}{V_1}$$

$$\frac{\Delta V}{V_1} = \frac{1}{1.4} \frac{\Delta P}{P_1} \quad (29)$$

Volumetric strain

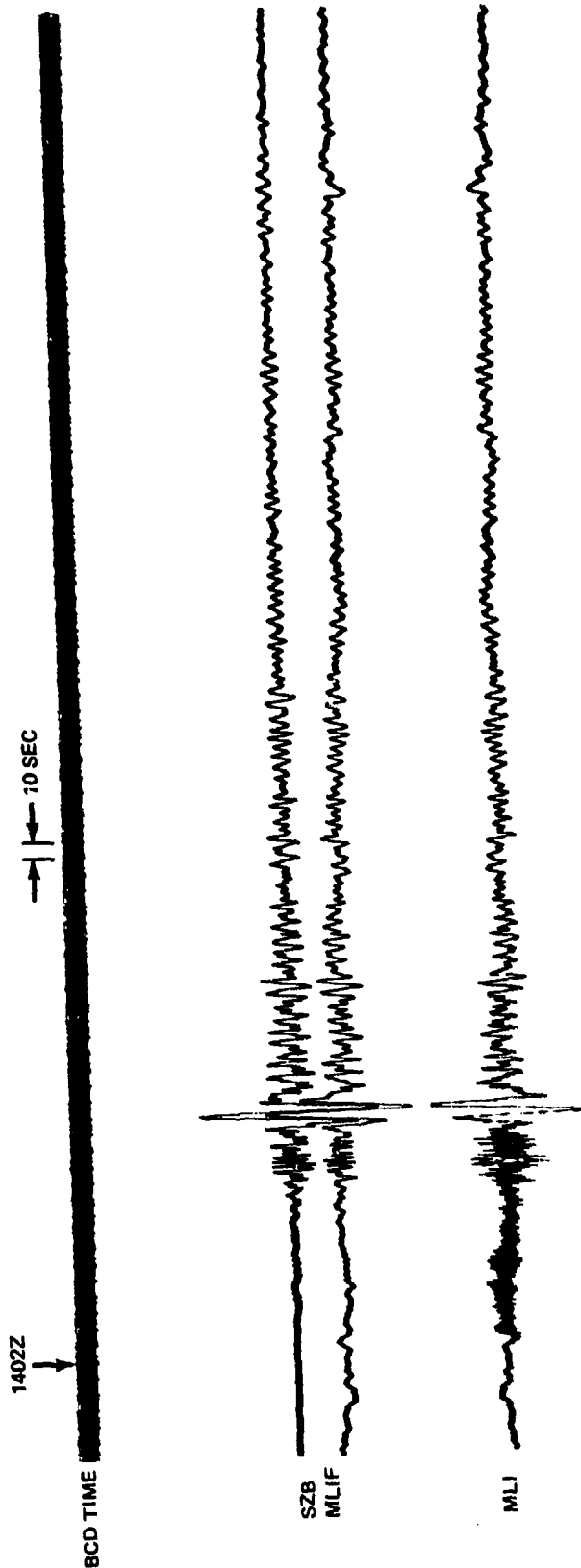
$$\theta = \frac{\Delta V}{V_1}$$

$$= - \frac{1}{1.4} \frac{\Delta P}{P_1} \quad (30)$$

A microbarograph in a sealed chamber senses ΔP and by equation (30) is directly proportional to volumetric strain.

The SZB seismograph has a variable capacitance displacement transducer and has a response that is flat to strain from dc to 7.5 Hz. The ML1 microbarograph has a response that is flat to pressure fluctuations with frequencies (or period) from 20 Hz to 68 sec and falls off at 6 dB/octave from 68 sec to 1000 sec. Thus, in the frequency range (2+ Hz to about 0.1 Hz or 10 sec) of the recordings from this near-regional earthquake, the responses of the two instruments are essentially flat to volumetric strain.

The NOS PDE data for the San Fernando earthquake of 9 February 1971 are: origin = 1400:41.6Z, hypocenter at 34.4N, 118.4W, $h = 13$ km, $m_b = 6.2$, $M_s = 6.5$. This hypocenter is at an epicentral distance of 5.8 deg and at an azimuth of 284.0 deg from QC-AZ. The vertical strain seismograph and microbarograph recordings of volumetric strain are illustrated in figure 142. The top trace in figure 142 is the vertical strain seismograph SZB as recorded. The second trace is the microbarograph ML1F filtered by a 0.5 Hz, 24 dB/octave, low-pass filter and inverted to match polarity with the vertical strain seismograph. The third trace is the microbarograph ML1 as recorded. It contains a 2.07 Hz signal from the acoustic resonance of the sealed seismometer chamber. This resonance is excited by the coupling of seismic energy to acoustic energy inside the sealed chamber (see section 7.9). The vertical strain and microbarograph traces are playbacks from two magnetic tape recordings. The two tape recorders had slightly different



QC-AZ
RUN 040
9 FEB 71

Figure 142. Vertical strain seismograph (SZB) and microbarograph (ML1 and ML1F) recording of volcanic strain from the San Fernando Earthquake, 9 February 1971. Microbarograph traces: ML1 as recorded, ML1F low-pass filtered 0.5 Hz, 24 dB/octave, polarity inverted

G 6588

speeds and the time alignment becomes degraded in the right-hand portion of the figure. However, the waveforms are seen to be identical on both types of volumetric strain seismographs.

The amplitude of the maximum excursion of the main Rayleigh wave pulse between 1404:30Z and 1404:40Z was 3.72×10^{-7} bar on the microbarograph and 1.54×10^{-7} strain on the vertical strainmeter. The calibrations are thought to be known to about 20 percent on the microbarograph and to about 10 percent on the strainmeter. The ambient pressure at the time of the signal was 1.02 bar; therefore, the volumetric strain from the ML1 microbarograph and equation 30 is 2.61×10^{-7} . The ratio of the elastic parameters in equation (26) at QC-AZ has been empirically found to be 2.46 (+ about 10 percent). Using this value, A in equation (27) is -1.46. Volumetric strain from the SZB seismograph and equation (27) is 2.25×10^{-7} . The difference between the amplitudes measured on the two different types of instruments is within the expected unknowns of the parameters involved.

9. ENHANCEMENT OF SEISMIC WAVES WITH STRAIN AND INERTIAL SEISMOGRAPHS

Combinations of linear strain seismographs and combinations of linear strain and inertial seismographs can be used to enhance Rayleigh waves, to enhance and to separate Love waves from Rayleigh waves, to enhance S_H and S_V waves, and to separate S_H waves from S_V waves. Benioff (1935) developed the first practical horizontal, linear strain seismographs. He derived, from the basic solution to the wave equation, the azimuthal response of horizontal, linear, strain seismographs to apparent horizontal waves of longitudinal polarization and of transverse polarization. Benioff and Gutenberg (1952) extended Benioff's earlier work and described the response of strain and pendulum seismographs to surface waves and illustrated Love (G) and Rayleigh wave identification by visual comparison of strain and inertial seismograms. Benioff (1962) summarized previous results and heuristically presented azimuthal responses of combined strain and inertial seismographs. Major et al. (1964), using the notation of Love (1927), gave expressions for the transformation of the horizontal components of strain for longitudinally polarized waves and for horizontally polarized shear waves. These expressions were used in the visual interpretation of seismograms recorded on two non-orthogonal, horizontal, linear, strain seismographs and on a vertical, linear strain seismograph. Romney (1964) described a method of increasing the detectability of P waves by combining either a vertical strain seismograph, or a sum of orthogonal horizontal strain seismographs, and a vertical inertial seismograph. Shopland and Kirklin (1969, 1970) demonstrated that the technique for P wave enhancement proposed by Romney (1964) provides significant signal-to-noise improvement at sites where the predominant microseisms are essentially single-mode Rayleigh waves, but this technique is not so fruitful when the microseismic noise is more complex. Smith and Kasahara (1969) presented methods of wave and mode separation based on three horizontal, linear, strain seismographs - two orthogonal and the third at 45 deg. They derived expressions for the amplitude coefficients of spheroidal free oscillations and of toroidal free oscillations in terms of the three strain seismographs and the geometry of the source-station model. They also derived expressions for the amplitude coefficients of mixed S_H waves and P or S_V wave horizontal components. Even though their observational data contained noise, they were able to obtain some separation of spectra of spheroidal and toroidal oscillations excited by the Alaskan earthquake of 1964, and they were able to separate S_V and S_H motion from a near-regional earthquake.

Section 9.1 presents the derivation of the response of a strain seismograph to the various wave types, individually and as combinations of strain seismographs. The strain seismograph response is then combined with the response of an inertial seismograph to obtain the azimuthal response of a summed strain and inertial seismograph in section 9.2. Seismograms demonstrating the enhancement and separation of LP seismic waves in accord with these equations are illustrated in section 9.3.

The relative spectral content of strain and inertial seismographs has direct bearing on the ability to enhance earthquake waves by combining the two types of seismograms. Section 9 treats the subject of enhancement of seismic waves from the viewpoint of the analog seismogram, using recordings made on-line

and simulating on-line conditions with playback of magnetic tapes. The consideration of the potential capability of enhancement of seismic waves from the spectral viewpoint is delayed until section 12 where spectral comparisons are made between displacement and strain seismograms.

9.1 THEORY

9.1.1 Strain Tensor

Before proceeding to the derivation of the response of a linear strain seismograph to the several earthquake wave types, a summary of strain tensor notation is beneficial. The general application of the tensor rotation equation and its relation to the strain seismometer will be investigated. An important assumption in the derivation of the seismometer response will be pointed out. This assumption is implied by Benioff (1935) and Major et al. (1964), but neither paper stated the assumption or its implication. For a complete discussion of the strain tensor, the reader should see a recent text on elasticity such as Bullen (1963) or Shames (1964).

Strain is a second rank symmetrical tensor that has nine components. The strain tensor can be represented mathematically as a matrix

$$\begin{array}{ccc} e_{11} & e_{12} & e_{13} \\ e_{21} & e_{22} & e_{23} \\ e_{31} & e_{32} & e_{33} \end{array} \quad (31)$$

or in Einstein's abbreviated form

$$e_{ij}, \quad \begin{array}{l} i = 1, 2, 3 \\ j = 1, 2, 3 \end{array} \quad (32)$$

where X_1, X_2, X_3 represent a system of three cartesian coordinates. (Often X_1, X_2, X_3 are written as x, y, z .) Each of the nine components is related to the spatial partial derivatives of the displacement vector \vec{u} by

$$e_{ij} = \frac{1}{2} \left(\frac{\partial u_j}{\partial x_i} + \frac{\partial u_i}{\partial x_j} \right) \quad \begin{cases} i=1,2,3 \\ j=1,2,3 \end{cases} \quad (33)$$

where u_j and u_i are components of the displacement vector in the j and the i direction, respectively. It can be seen from (33) that strain is a symmetrical tensor and

$$e_{ij} = e_{ji} \quad \left\{ \begin{array}{l} i=1,2,3 \\ j=1,2,3 \end{array} \right. \quad (34)$$

Because of symmetry, the nine components reduce to six independent components.

A difference exists between the expression for a shear strain ($i \neq j$) in tensor notation in equation (33) and the expression given by Love (1927) who did not use the coefficient of $1/2$.

9.1.2 Rotation of the Strain Tensor

In this section, the three independent horizontal strain components are determined for a general strain field having one principal axis in the vertical direction.

The strain tensor can be transformed from one cartesian coordinate system (X_1', X_2', X_3') to another cartesian coordinate system (X_1, X_2, X_3) by

$$e_{km} = a_{i'k} \quad a_{j'm} \quad e_{i'j'} \quad \left\{ \begin{array}{l} i' = 1', 2', 3' \\ j' = 1', 2', 3' \\ k = 1, 2, 3 \\ m = 1, 2, 3 \end{array} \right. \quad (35)$$

where k and m denote axes in the new system (some of which could be the same as in the old system if desired), i' and j' denote axes in the old system, and $a_{i'k}$ and $a_{j'm}$ are direction cosines between the respective axes. In equation (35), the summation convention applies. The strain component measured in a plane perpendicular to the X_1 axis and in the X_2 direction is e_{12} . From equation (35)

$$\begin{aligned} e_{12} = & a_{1'1} a_{1'2} e_{1'1'} + a_{1'1} a_{2'2} e_{1'2'} + a_{1'1} a_{3'2} e_{1'3'} \\ & + a_{2'1} a_{1'2} e_{2'1'} + a_{2'1} a_{2'2} e_{2'2'} + a_{2'1} a_{3'2} e_{2'3'} \\ & + a_{3'1} a_{1'2} e_{3'1'} + a_{3'1} a_{2'2} e_{3'2'} + a_{3'1} a_{3'2} e_{3'3'} \end{aligned} \quad (36)$$

If we assume that X_1 and X_2 lie in the X_1' and X_2' plane, then X_3 must coincide with X_3' and the strain ellipsoid has two of the three principal axes in the X_1, X_2 plane. (For instance, if X_1, X_2, X_1' , and X_2' are all in the horizontal plane, then X_3 and X_3' are vertical.) With X_3' perpendicular to the X_1, X_2 plane, all direction cosines involving the $3'$ index in equation (36) are zero.

Equation (36) becomes

$$\begin{aligned}
 e_{12} &= a_{1'1} a_{1'2} e_{1'1'} + a_{1'1} a_{2'2} e_{1'2'} + 0 \\
 &\quad + a_{2'1} a_{1'2} e_{2'1'} + a_{2'1} a_{2'2} e_{2'2'} + 0 \\
 &\quad + 0 \qquad \qquad \qquad + 0 \qquad \qquad \qquad + 0 \qquad \qquad \qquad (37) \\
 &= a_{1'1} a_{1'2} e_{1'1'} + a_{2'1} a_{2'2} e_{2'2'} \\
 &\quad + (a_{1'1} a_{2'2} + a_{2'1} a_{1'2}) e_{1'2'}
 \end{aligned}$$

$$\text{Let } a_{1'1} = \cos \alpha \qquad (38)$$

$$\text{Then } a_{1'1} = a_{2'2} = \cos \alpha \qquad (39)$$

$$\text{and } a_{1'2} = a_{2'1} = \sin \alpha \qquad (40)$$

Substituting in (37) and using the symmetry properties of the strain tensor

$$e_{12} = \cos \alpha \sin \alpha (e_{1'1'} + e_{2'2'}) + e_{1'2'} \qquad (41)$$

Similarly, it can be shown that

$$e_{11} = e_{1'1'} \cos^2 \alpha + e_{2'2'} \sin^2 \alpha + 2e_{1'2'} \cos \alpha \sin \alpha \qquad (42)$$

and

$$e_{22} = e_{1'1'} \sin^2 \alpha + e_{2'2'} \cos^2 \alpha + 2e_{1'2'} \cos \alpha \sin \alpha \qquad (43)$$

Note that equations (41), (42), and (43) for the three independent horizontal strain components apply if, and only if, principal axis X_3' is perpendicular to axes X_1 and X_2 . Also note that in these equations if X_1' and X_2' are principal axes, $e_{1'2'}$ is zero. These three equations are similar to those derived by Benioff (1935) and Major et al. (1964). These authors assumed horizontal wave motion, but neither paper stated the fact that the effect of five of the nine tensor components became zero (see equation (37) above) with this assumption. In a semi-infinite, layered model, this assumption is valid for Love and Rayleigh waves. In a real geologic structure, this

assumption is adequate, although at times some signals are observed that could be explained by local variations of the X_3 axis from the vertical.

9.1.3 Enhancement of Rayleigh Waves

Rayleigh waves for a homogeneous half-space can be derived from a coupled longitudinal wave potential and vertically polarized shear wave potential (e.g., Bullen, 1963). Consider a horizontal component of angular frequency ω traveling in a direction X_1 , which is at an angle α measured clockwise from the 0 deg azimuth. Then, the only horizontal strain component of the signal is

$$e_{11}(\omega) \equiv e_{11}$$

and

$$e_{ij} = 0 \quad \begin{matrix} i = 1, 2 \\ j = 2 \end{matrix}$$

(44)

The derivations given here are general and apply either to a harmonic component of the wave of angular frequency ω or to the Fourier integral of all harmonic components over the passband of interest. For simplicity of notation, the dependence of all variables upon frequency is not given in the equations but is implied.

From (42), on a linear strain seismograph oriented in a 0 deg azimuth (designated by strain component e_{NN}), the response to the horizontal Rayleigh wave strain component e_{11} is

$$\begin{aligned} e_{NN} &= e_{11} a_{1N}^2 \\ &= e_{11} \cos^2 \alpha \end{aligned}$$

(45)

and on a linear strain seismograph oriented in a 90 deg azimuth

$$\begin{aligned} e_{EE} &= e_{11} a_{1E}^2 \\ &= e_{11} \cos^2 (90 - \alpha) \\ &= e_{11} \sin^2 \alpha \end{aligned}$$

(46)

Adding the outputs of the orthogonal, horizontal, strain seismographs

$$\begin{aligned} e_{NN} + e_{EE} &= e_{11} \cos^2 \alpha + e_{11} \sin^2 \alpha \\ &= e_{11} \end{aligned}$$

(47)

Thus, the sum of two orthogonal strain seismographs enhances Rayleigh waves with no azimuthal dependence.

If there is a mixture of Rayleigh and Love waves traveling in the X_1 direction, let the Rayleigh wave horizontal strain component be e_{11} and the Love wave strain component be e_{12} . Then, the horizontal strain components of the signal are

$$\begin{aligned} e_{11} &= e_{11} \\ e_{21} &= e_{12} = e_{12} \\ e_{22} &= 0 \end{aligned} \quad (48)$$

From equations (42) and (43)

$$e_{NN} = e_{11} a_{1N}^2 + 2e_{12} a_{1N} a_{2N} \quad (49)$$

$$\begin{aligned} e_{EE} &= e_{11} a_{1E}^2 + 2e_{12} a_{1E} a_{2E} \\ &= e_{11} a_{2N}^2 - 2e_{12} a_{1N} a_{2N} \end{aligned} \quad (50)$$

and

$$\begin{aligned} e_{NN} + e_{EE} &= e_{11} (a_{1N}^2 + a_{2N}^2) + 2e_{12} (a_{1N} a_{2N} - a_{1N} a_{2N}) \\ &= e_{11} \end{aligned} \quad (51)$$

Thus, the presence of Love waves does not affect the enhancement of a Rayleigh wave.

9.1.4 Enhancement of Love Waves

Love waves are horizontally polarized shear waves. If a Love wave is traveling in the X_1 direction

$$\begin{aligned} e_{ij} &= 0, \quad i=j=1, 2, 3 \\ e_{21} &= e_{12} = e_{12} \\ e_{31} &= e_{13} = 0 \\ e_{ij} &= 0 \quad \left\{ \begin{array}{l} i=2, 3 \\ j=2, 3 \end{array} \right. \end{aligned} \quad (52)$$

From (42) and (43) or (49) and (50)

$$\begin{aligned} e_{NN} &= 2e_{12} a_{1N} a_{2N} \\ e_{EE} &= 2e_{12} a_{1E} a_{2E} \\ &= -2e_{12} a_{1N} a_{2N} \end{aligned} \quad (53)$$

Therefore

$$\begin{aligned} e_{NN} - e_{EE} &= 4e_{12} a_{1N} a_{2N} \\ &= 4e_{12} \cos \alpha \sin \alpha \end{aligned} \quad (54)$$

Thus, subtracting two orthogonal, horizontal, linear strain seismographs enhances Love waves by a factor of two, but does not remove the azimuthal dependence.

If there is a mixture of Rayleigh and Love waves, from (49) and (50)

$$\begin{aligned} e_{NN} - e_{EE} &= e_{11} (a_{1N}^2 - a_{2N}^2) + 4e_{12} a_{1N} a_{2N} \\ &= e_{11} [\cos^2 \alpha - (1 - \cos^2 \alpha)] + 4e_{12} \cos \alpha \sin \alpha \\ &= e_{11} [2\cos^2 \alpha - 1] + 4e_{12} \cos \alpha \sin \alpha \\ &= Ae_{11} + 4e_{12} \cos \alpha \sin \alpha. \end{aligned} \quad (55)$$

If α is known, A can be calculated. From (51) and (55)

$$\begin{aligned} (e_{NN} - e_{EE}) - A (e_{NN} + e_{EE}) &= Ae_{11} + 4e_{12} \cos \alpha \sin \alpha - Ae_{11} \\ &= 4e_{12} \cos \alpha \sin \alpha \end{aligned} \quad (56)$$

Thus, if the direction of the wave travel is known, it may be possible to eliminate the effect of a Rayleigh wave and to enhance a Love wave.

9.1.5 Relation Between Vertical Strain and Horizontal Strain

Romney (1964) has shown that for a homogeneous, isotropic medium that obeys Hooke's Law, the vanishing of the stress component P_{ZZ} at the free surface can be written (with a change of notation)

$$P_{ZZ} = \lambda (e_{11} + e_{22} + e_{33}) + 2 \mu e_{33} = 0 \quad (57)$$

where λ and μ are Lamé's elastic constants. Collecting terms

$$(e_{11} + e_{22}) = - \frac{2\mu + \lambda}{\lambda} e_{33}. \quad (58)$$

The vertical strain seismograph measures e_{ZZ} , which is equal to e_{33} . In the presence of a single, horizontal, longitudinal component e_{11} , substituting equation (47) in equation (58) gives

$$e_{NN} + e_{EE} = - \frac{2\mu + \lambda}{\lambda} e_{ZZ} \quad (59a)$$

$$= -B e_{ZZ}. \quad (59b)$$

Implicit in equations (57), (58), and (59) is the assumption of an isotropic medium. This assumption allows reduction of the 81 component (36 independent) elastic constant tensor relating stress and strain by a generalized Hooke's Law to only the two independent constants λ and μ .

9.1.6 Dilatation or Volumetric Strain

Another property of the strain tensor is that the sum of three strain components, e_{ij} , $i = j = 1, 2, 3$, is a constant regardless of the relative orientation of the three axes 1, 2, 3 and the strain tensor. Mathematically

$$e_{ii} = C, \quad i = 1, 2, 3$$

$$e_{k'k'} = C, \quad k' = 1', 2', 3'$$

$$\text{or} \quad e_{ii} = e_{11} + e_{22} + e_{33} \quad (60)$$

$$e_{k'k'} = e_{1'1'} + e_{2'2'} + e_{3'3'}$$

$$e_{ii} = e_{k'k'}$$

The quantity e_{ii} is called the dilatation. It is the solution of the wave equation for longitudinal (P) waves transmitted in isotropic elastic bodies. The reader should note that the measurement of the strain tensor or the dilatation is not dependent upon the properties of the material; but, that when the material transmits a wave, force, or motion, then assumptions regarding the behavior of the medium must be made to relate the strain observed to the source disturbance.

A vertical, linear strain seismograph near the free surface can be used as a volumetric strain or dilatation seismograph.

Let

$$e_{33} = e_{zz} \quad (61)$$

substituting (59b) and (61) in (60)

$$\begin{aligned} e_{ii} &= -B e_{zz} + e_{zz} \\ &= (1-B) e_{zz}. \end{aligned} \quad (62)$$

9.2 COMBINATIONS OF STRAIN AND INERTIAL SEISMOGRAPHS

Inertial seismographs can be added to and subtracted from linear strain seismographs to enhance seismic waves coming from certain azimuths and to diminish seismic waves or noise traveling from other azimuths.

The horizontal component of displacement for a Rayleigh wave, a P wave, and an S_y wave traveling in the x_1 direction can be expressed as

$$u_1 = D \sin (kx_1 - \omega t) \quad (63)$$

where u_1 is the displacement vector component in the x_1 direction, D is an amplitude coefficient, k is the vector wave number component in the x_1 direction, $\omega = 2\pi f$ is the angular frequency of the wave, and t is time. The velocity of a particle of ground is

$$\frac{du_1}{dt} = -\omega D \cos (kx_1 - \omega t). \quad (64)$$

The only non-zero horizontal strain component is the linear strain component

$$\begin{aligned} e_{11} &= \frac{du_1}{dx_1} \\ &= kD \cos (kx_1 - \omega t). \end{aligned} \quad (65)$$

If a strain seismograph is constructed so that it will have the same transfer function as ground velocity, then from equations (64) and (65), we see that

$$\begin{aligned} \frac{du_1}{dt} &= -\frac{1}{c} e_{11} \\ &= M e_{11} \end{aligned} \quad (66)$$

where $k = \omega/c$ and c is the phase velocity component in the direction of the instruments for the wave being recorded. Most seismographs - short period and long period - have very narrow passbands and $\frac{1}{\omega}$ is effectively constant within the narrow passband, allowing the generalization of equation (66) to all ω within the peak of the seismograph response.

In the N direction

$$\frac{du_N}{dt} = \frac{du_1}{dt} \cos \alpha \quad (67)$$

and

$$\begin{aligned} e_{NN} &= e_{11} \cos^2 \alpha + e_{33} \cos^2 \left(\frac{\pi}{2}\right) + 2 e_{13} \cos \alpha \cos \left(\frac{\pi}{2}\right) \\ &= e_{11} \cos^2 \alpha. \end{aligned} \quad (68)$$

If the magnifications of the ground velocity seismograph and the ground strain seismograph are equalized for the same absolute wave amplitude output, the sum of the two seismographs becomes

$$M_1 \frac{du_N}{dt} + M_2 e_{NN} = (\text{constant}) (\cos \alpha + \cos^2 \alpha) \quad (69)$$

The azimuthal response of a velocity seismograph, a strain seismograph, and the sum of equalized magnification velocity and strain seismographs from equation (69) is plotted in figure 143. These azimuthal responses are the properties of the rotation of vector and tensor components and are independent of frequency.

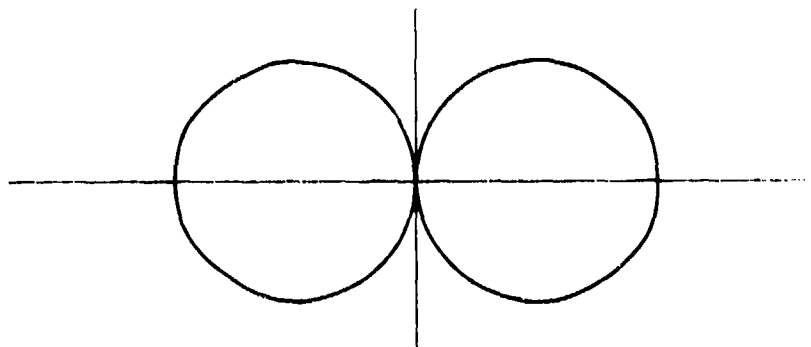
The horizontal component of displacement for a Love wave, a G wave, and an S_H wave traveling in the X_1 direction can be expressed as

$$u_2 = D \sin (kx_1 - \omega t). \quad (70)$$

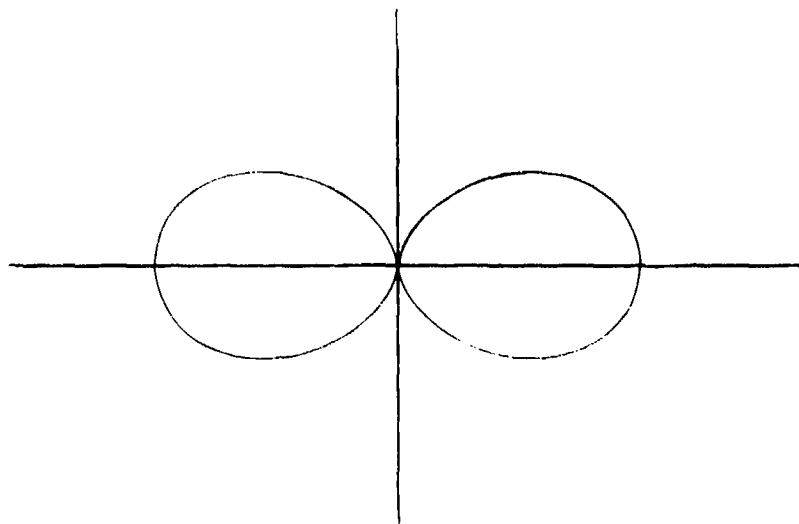
The velocity of a particle of ground is

$$\frac{du_2}{dt} = -\omega D \cos (kx_1 - \omega t). \quad (71)$$

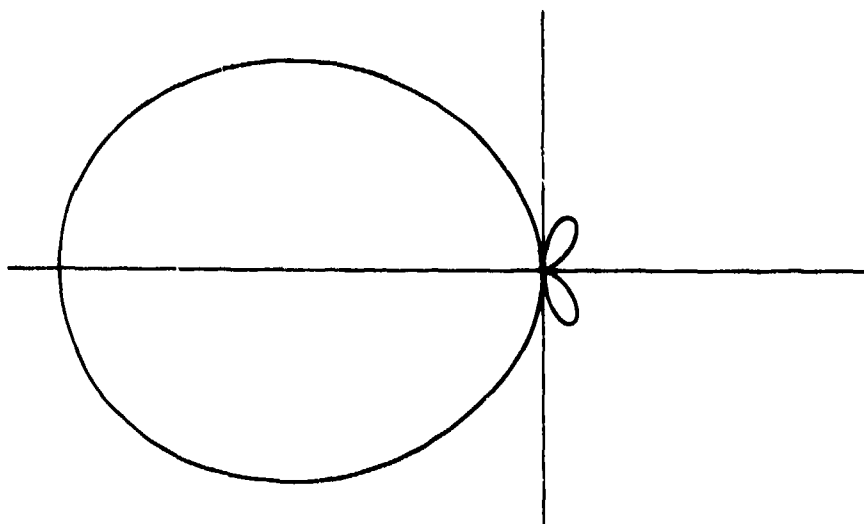
The only non-zero strain components are the equal shear components



a. $\cos \alpha$



b. $\cos^2 \alpha$



c. $\cos \alpha + \cos^2 \alpha$

Figure 143. Azimuthal response to the horizontal components of Rayleigh, P, and Sy waves for (a) ground velocity, (b) ground strain, and (c) equalized ground velocity plus ground strain

G 6000

$$\begin{aligned}
e_{12} &= e_{21} \\
&= \frac{du_2}{dx_1} \\
&= k D \cos (kx_1 - \omega t).
\end{aligned}
\tag{72}$$

In the N direction,

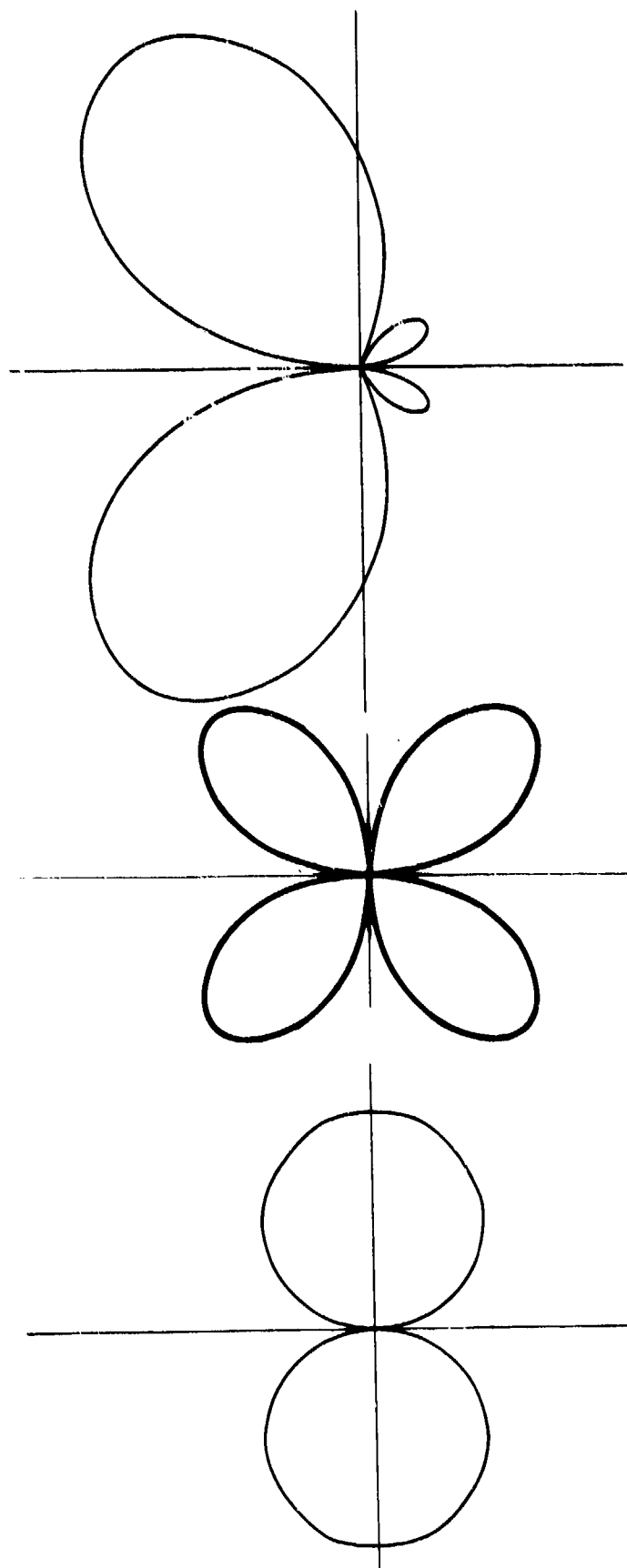
$$\frac{du_N}{dt} = \frac{du_2}{dt} \sin \alpha \tag{73}$$

$$e_{NN} = 2 e_{12} \cos \alpha \sin \alpha. \tag{74}$$

If the magnifications of the ground velocity seismograph and the ground strain seismograph are equalized for the same absolute wave amplitude output, the sum of the two seismographs becomes

$$M_3 \frac{du_N}{dt} + M_4 e_{NN} = (\text{constant}) (\sin \alpha + 2 \cos \alpha \sin \alpha). \tag{75}$$

Azimuthal responses of a velocity seismograph, a strain seismograph, and the sum of equalized magnification seismographs from equation (75) are plotted in figure 144. These azimuthal responses are also independent of frequency. The reader should note that the strain component in equations (74) and (75) contains a coefficient of 2 because there are two equal non-zero strain components. The azimuthal responses given by equations (74) and (75) differ by this coefficient from that given by Benioff and Gutenberg (1952), Benioff (1962), Major et al. (1964), and illustrated by Fix and Sherwin (1970). The previous investigators used Love's (1927) definition of a shear strain component that does not contain the 1/2 coefficient of equation (33), as pointed out previously. The linear strain seismograph responds to the two equal strain tensor components e_{12} and e_{21} in accord with equation (53), and the 2 coefficient belongs in the azimuthal response. This response also agrees with observations in that Love waves (from the proper azimuths) are recorded on strain seismographs with about the same amplitude as Rayleigh waves. Without the 2 coefficient, Major et al. (1964) concluded that Love waves would only be 0.5 the amplitude of Rayleigh waves. The main lobe in figure 144(c) is very similar to the shape and double the amplitude of the summed responses given by Benioff (1962). The main difference between the two shapes is the two small back lobes in figure 144(c).



c. $\sin \alpha + 2 \cos \alpha \sin \alpha$

b. $2 \cos \alpha \sin \alpha$

a. $\sin \alpha$

Figure 144. Azimuthal response to horizontal transverse waves, Love, G, and S_H for (a) ground velocity, (b) ground strain, and (c) equalized ground velocity plus ground strain

G 6600

9.3 ENHANCEMENT OF SEISMIC WAVES

The parallel strain/inertial horizontal components at QC-AZ are oriented toward azimuths of 325 and 55 deg. The combined strain/inertial seismograph azimuthal responses of figures 143 and 144 have been oriented in figure 145 in the azimuths of the QC-AZ instruments. The response of the strain plus inertial seismographs (denoted S+P325L and S+P55L) is for waves traveling toward the 325 deg or 55 deg azimuth, respectively. (The nomenclature used is as follows: S+P for pendulum seismograph added to normalized strain seismograph, and S-P for pendulum seismograph subtracted from normalized strain seismograph.) The response of the strain minus inertial seismographs (S-P325L and S-P55L) is for waves traveling toward the 145 deg and 235 deg azimuths. In figure 145, the solid lines are the azimuthal response to Rayleigh waves and the horizontal component of P and S_V waves. The dashed lines are the azimuthal response to Love, G, and S_H waves.

By way of comparison, the TFO seven-element, 45 km aperture, LP spatial array response to Rayleigh waves arriving from the 235 deg azimuth is shown in figure 146. At 10 sec, the TFO array main lobe is sharper than the strain/inertial combination main lobe, but the array has some serious side lobes. At 25 sec, the main lobe is similar to the strain/inertial combination response, but the side lobes are still large; and at 40 sec, the TFO array has lost most of its directional sensitivity and capability of enhancement, while the strain/inertial combination has the same azimuthal response at all periods.

This section illustrates the enhancement of seismic waves and the improved discrimination capability possible with high-sensitivity strain seismographs, inertial seismographs, and combined strain/inertial seismographs. The illustrations in this section are all in the time domain (analog) from the "on-line" film recorders or from playbacks of magnetic tape recordings simulating the possibilities of the "on-line" recordings. Frequency domain comparisons among the seismographs are deferred until section 12 where power spectral densities and amplitude spectra are presented for many of the earthquakes illustrated in this section.

Section 9.3 is organized so that the LP seismic waves enhanced by "on-line" recorders are illustrated in section 9.3.1. The LP waves enhanced from playback of magnetic tape recordings are illustrated in section 9.3.2. The enhancement of ultra-long-period waves is discussed in section 9.3.3, and enhancement of SP waves is mentioned in section 9.3.4.

In presenting seismograms of earthquakes, the authors have elected to illustrate as much of the signal from the selected events as practical rather than to illustrate only that portion of the event that relates to the enhancement of a particular earthquake phase. Therefore, in the following subsections the arrangement of the illustrations is arbitrary, with the first preference to azimuth of approach and the second preference to variety of earthquake phase. Illustrating the complete signal from an earthquake allows the reader to evaluate the performance of the strain/inertial instrumentation complex in terms of a variety of actual signals in the normal recording sequence rather than in terms of only isolated phases selected to illustrate the enhancement of a particular wave type.

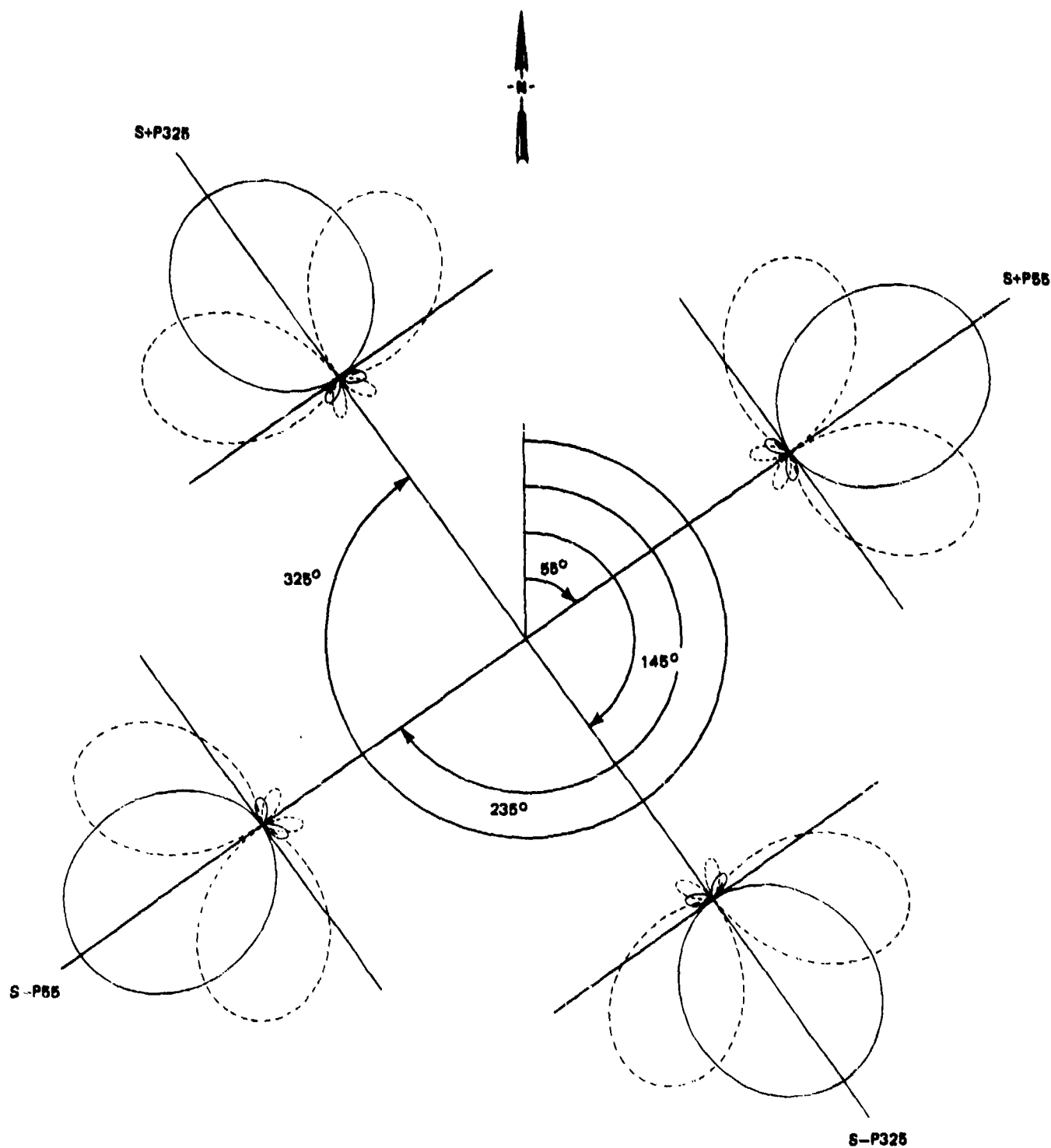


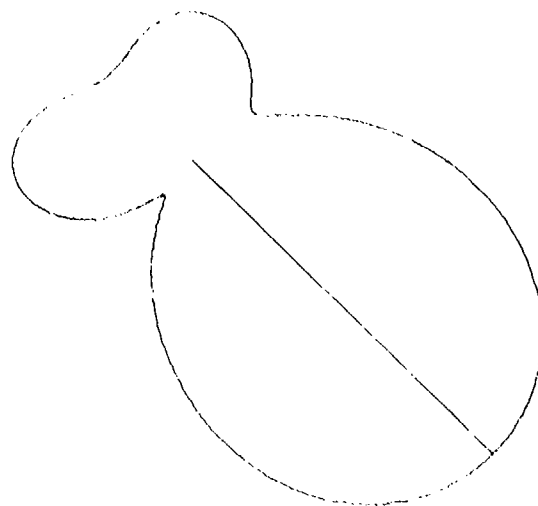
Figure 145. Four beam azimuthal array at QC-AZ. Solid lines are response to Rayleigh and horizontal component of P and S_y waves; dashed lines are response to Love, G, and S_H waves

G 6691

10 SEC
RAYLEIGH WAVE



25 SEC
RAYLEIGH WAVE



40 SEC
RAYLEIGH WAVE

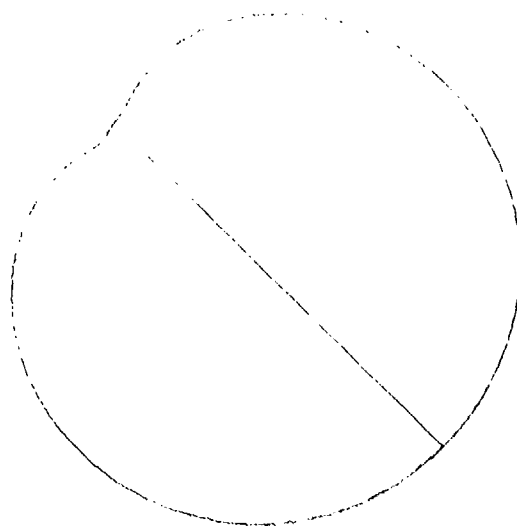


Figure 146. Directional response toward 235 deg azimuth of TF0 7-element LP array.

G 5474

In the following sections, the reader will observe that the strain/inertial directional array will provide better enhancement for Rayleigh waves, Love waves, and body waves arriving at the station as an S phase. The response of a horizontal strain seismograph is inversely proportional to the apparent horizontal phase velocity of the wave. Since the apparent horizontal phase velocity increases with decreasing angle of emergence, the more steeply arriving waves will produce less signal on the strain seismographs. Therefore, waves arriving at the station as a P phase will have less strain signal than waves arriving as an S phase. Waves that have traveled shallower paths with multiple bounces from the surface of the earth will arrive at smaller angles of emergence than the direct waves and the multiple bounces will have more strain signal. Thus, if source, transmission path, and attenuation differences are neglected, SSS will have more strain signal than SS; SS and PS more than SP; multiple phases more than S or P; and S more than P. The relative response of a parallel strain and inertial seismograph can be used visually to compare apparent phase velocities between different earthquake arrivals and can aid in identifying wave types in a very simple manner.

9.3.1 Long-Period Seismic Waves Enhanced by "On-Line" Recorders

This section presents illustrations of enhancement of seismic waves and discrimination of earthquake wave types from the recordings made "on-line" in real time on the two 16 mm film recorders. Camera 1 (see section 4.3 and appendix 3) recorded the individual seismograms and camera 2 recorded the directional array and other selected data channels including combinations of strain seismographs. The original objective of the film recorders was merely to monitor the data that was being recorded on the magnetic tapes. Consequently, all available data traces were utilized - 19 on camera 1 and 15 on camera 2 - resulting in a somewhat crowded data presentation. Even with the full cameras, the nine individual high-gain, long-period seismographs on camera 1 were operated at a nominal 50K magnification at 25 sec and at X10 view. The directional array on camera 2 was operated at a nominal 25K magnification. Because of the full data and the overlining of traces during signals, the illustrations in this section are generally shorter than in the next section where a better separation of traces could be made and gains could be set for the maximum signal level on playback from the magnetic tape recordings.

The relative contributions to the directional array of the strain seismographs and of the inertial seismographs were adjusted empirically to obtain maximum cancellation of Rayleigh waves on the back azimuth trace. The magnification ratio between the displacement gain of the inertial seismograph (M_1 in equation (69) and the strain gain of the strain seismograph (M_2 in equation (69) were originally set assuming a phase velocity of 4.00 km/sec at a 25 sec period. After nature provided an earthquake whose Rayleigh wave traveled along the sensitive axes of the instruments, the relative magnifications were adjusted to improve cancellation on the back azimuth trace which is more sensitive to this adjustment. This procedure was repeated until optimum performance was achieved. The strain seismograph magnifications were increased over the original settings by a factor of 2.0 in the 55 deg azimuth and by 2.4 in the 325 deg azimuth. Thus, the apparent 25 sec Rayleigh wave phase velocity is 8.0 km/sec in the 55 deg azimuth and 9.6 km/sec in the 325 deg azimuth. The ratio between the apparent phase velocities in the two directions is 1.2.

An early recording of a South Pacific earthquake illustrates some of the capabilities of the system. An increasing strain signal is observed for a decreasing angle of emergence; S_H motion is separated from S_V motion by the direction response of the sum and difference traces; the LR1 Rayleigh wave is enhanced on the difference trace and attenuated on the sum trace; and the LR2 Rayleigh wave is enhanced on the sum trace and attenuated on the difference trace. At the time of this recording, the mine was not sealed, only the 55 deg azimuth strain seismometer was installed, and none of the instruments were insulated. The S55L strain and P145L (the polarity on this instrument was later reversed and it became P325L) inertial seismographs had 30 to 70 sec noise that correlated with the microbarograph. The trace identifications used in the illustrations are as follows: prefix S for strain, P for pendulum; numbers indicate azimuth for up motion on trace; suffix L for ALPS response where (LOW) has no notch filter and (HI) has a 6 sec notch filter, and S for SP response. Strain polarity is up for compression. Time lines are at 1 min intervals as printed on the film. The earthquake occurred on 6 January 1970. The NOS PDE data are: D'Entrecasteaux Islands region, 0 = 0535:51.8, 9.6S, 151.5E, $h = 8$ km, $m_b = 5.7$, $M_s = 6.2$. This epicenter is at a distance of 100.9 deg and at an azimuth of 265.6 deg from QC-AZ.

Figure 147 shows the P, PP, and PPP arrivals on the vertical inertial seismographs, with no significant motion recorded on the horizontal strain because of the large angle of emergence. Two distinct arrivals are recorded on the vertical, inertial seismograph PZL(HI) 23 sec and 43 sec after the initial arrival. Since both of these arrivals have the same polarity as the initial arrival, they are not likely to be pP and sP. At the 100.9 deg epicentral distance, they may be waves diffracted around or refracted through the core. In figure 148, the SKS wave arrived at 0600:28 and the S wave at 0601:06.5 with slightly enhanced S_H arrivals on the sum trace and some cancellation on the difference trace. The S wave is followed by shear-coupled PL to about 0604. At 0603:00 the PPS phase arrives as S_V motion as seen on the difference trace. In figure 149, SSP arrives at 0608:32 as an S_V wave on the difference trace and SSS arrives at 0612:18 as an S_H wave on the sum trace. In figure 150, the LR1 Rayleigh wave has driven all LP traces off the film except the sum trace, which shows cancellation compared to the S55L, P55L, and the difference trace. The LR2 Rayleigh wave from the major arc arriving from the opposite azimuth is enhanced on the sum trace and is cancelled on the difference trace in figure 151.

The directional array regularly gives earthquake signal-to-microseismic background noise improvements in excess of 10 dB. This factor of 3+ improvement in S/N ratio is the improvement that would be expected for about a 10 element spatial array of inertial seismographs. In addition to an improved S/N ratio, the directional array provides much clearer time breaks and often (depending upon azimuth of approach) clearly separates multiply-reflected P arrivals from multiply-reflected S arrivals and S_H arrivals from S_V arrivals. Several examples of the signal improvement are given in this section. The figures are all X10 reproductions of the 16 mm film recordings made on-line on camera No. 2. The normal equivalent displacement operating magnifications at 25 sec are as follows: PZL, 25K; S+P325L and S-P325L, 12.5K; S+P55L and S-P55L, 25K.

The enhancement of 15 sec microseisms traveling toward an azimuth of 235 deg is illustrated on the S-P55L trace in figure 152. These waves are completely

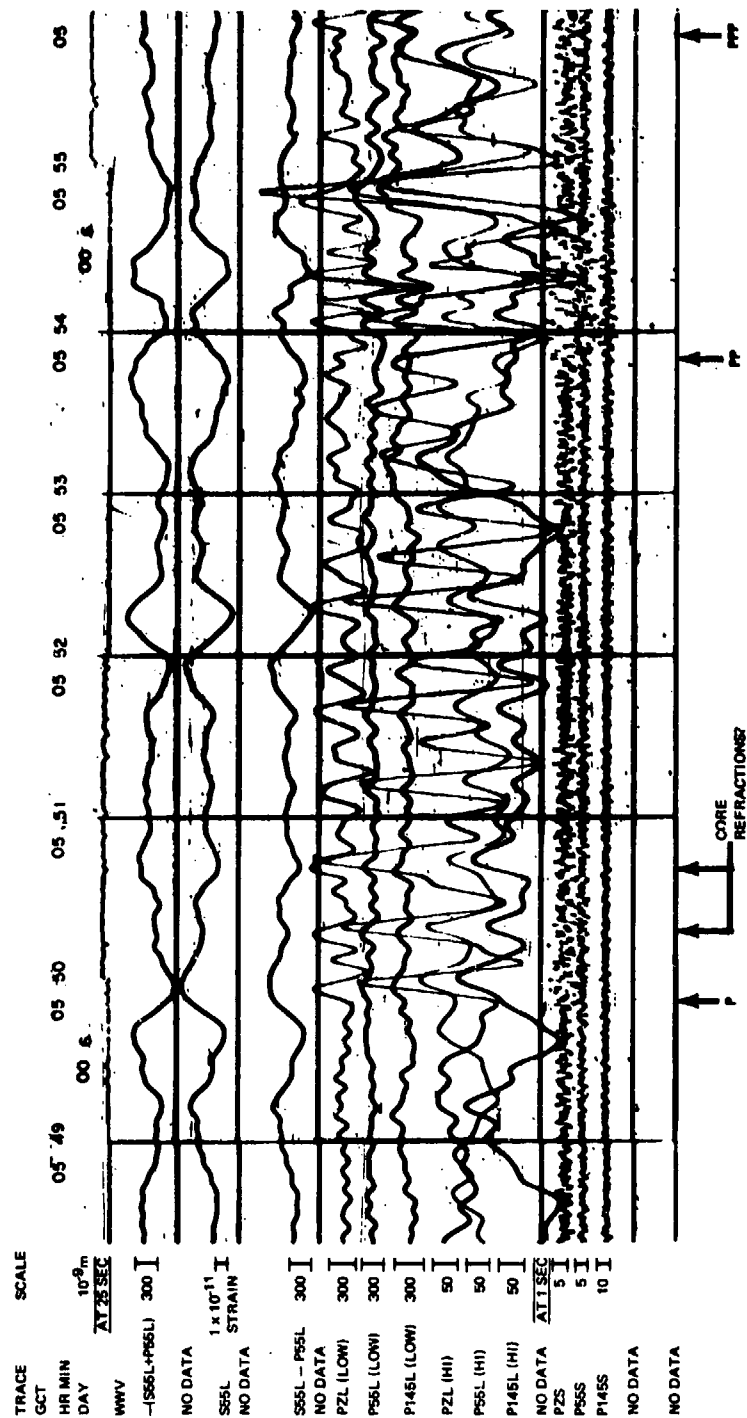


Figure 147. Reproduction of a QC-AZ 16-mm film record showing arrival of P, PP, and PPP from an earthquake in the D'Entrecasteaux Islands region



G 5693

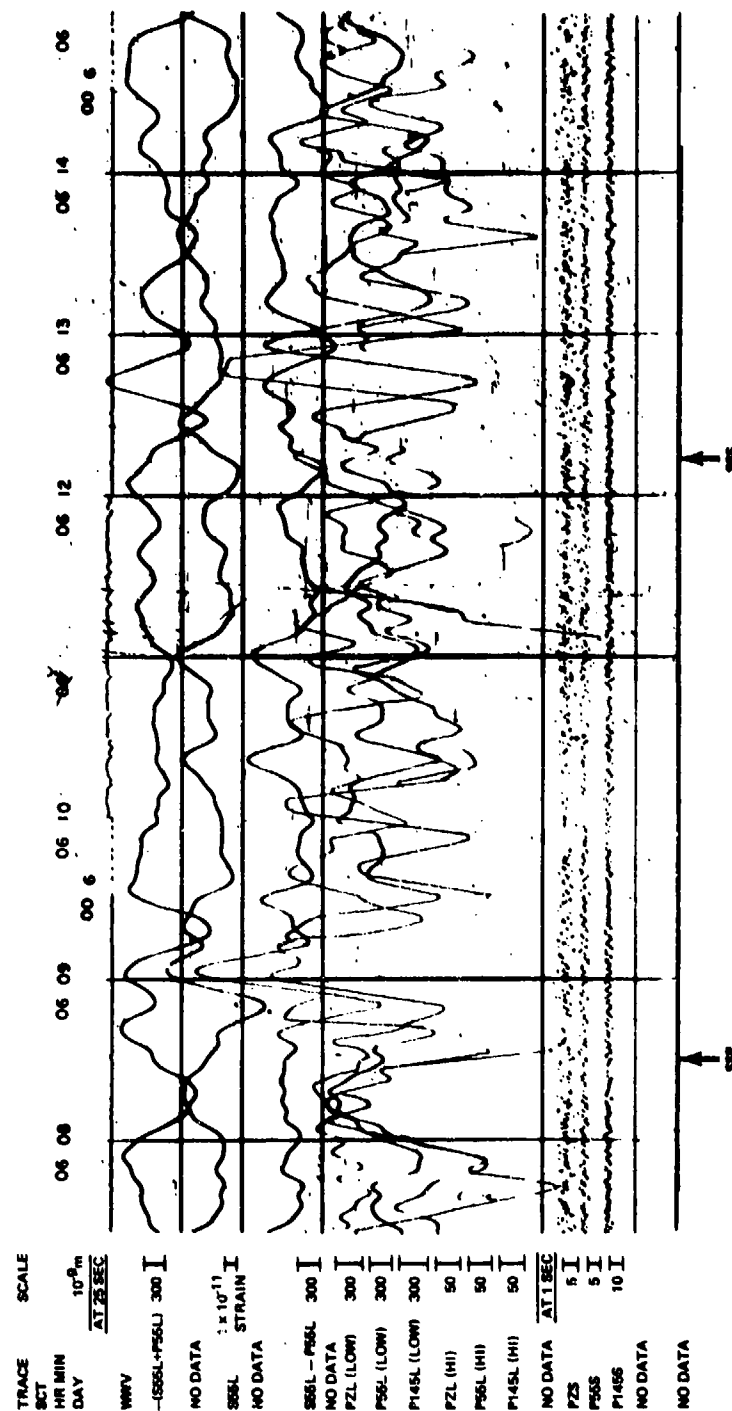


Figure 149. Reproduction of a QC-AZ 16-mm film record showing arrival of SSP (SV) and SSS (SH) from an earthquake in the D'Entrecasteaux Islands region

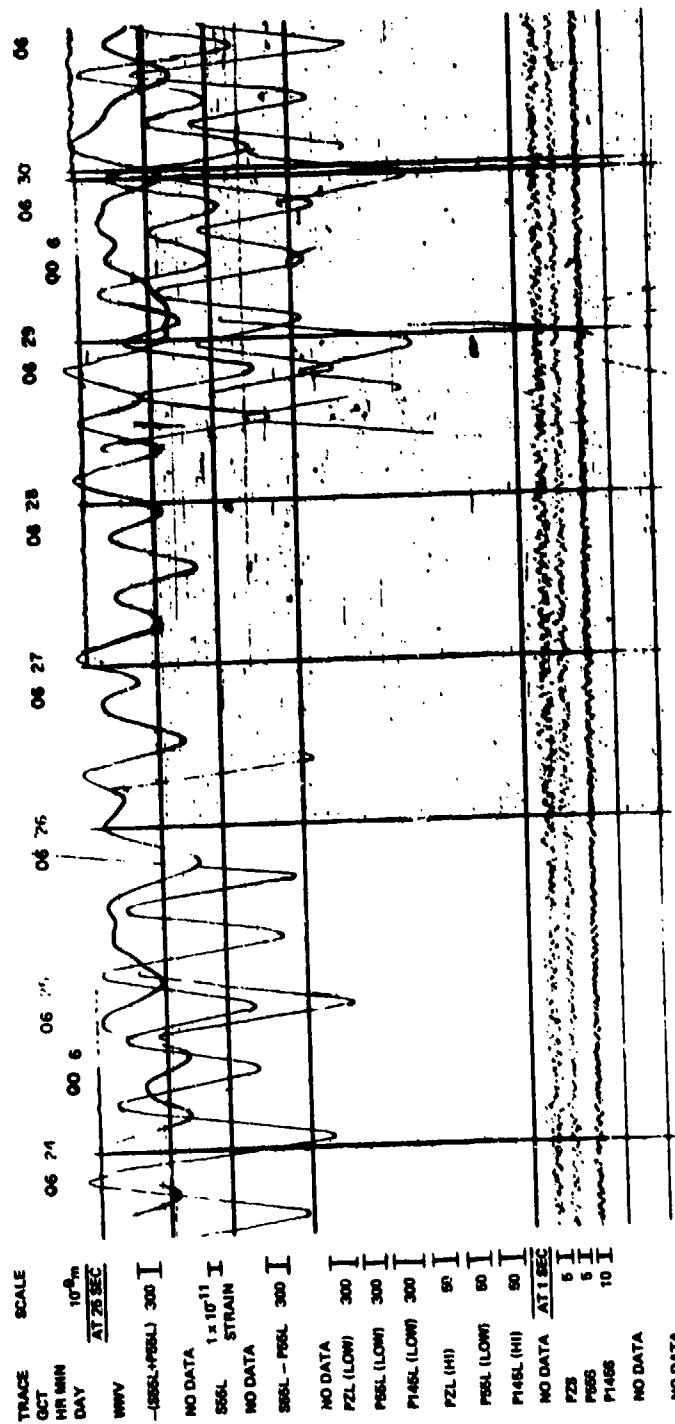


Figure 150. Reproduction of a QC-AZ 16-mm film record showing LR1 Rayleigh wave enhancement on the difference trace and attenuation on the sum trace from an earthquake in the D'Entrecasteaux Islands region

G 6695

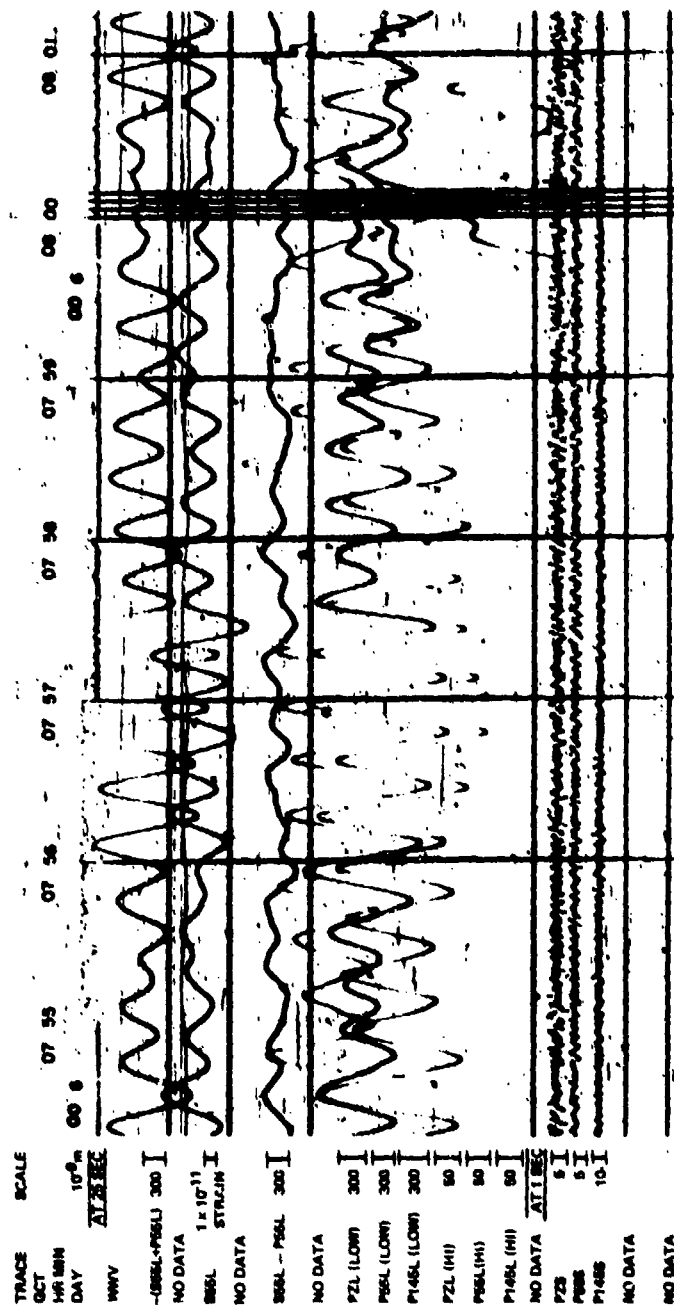


Figure 151. Reproduction of a QC-AZ 16-mm film record showing LR2 Rayleigh wave enhancement on the sum trace and cancellation on the difference trace from an earthquake in the D'Entrecasteaux Islands region

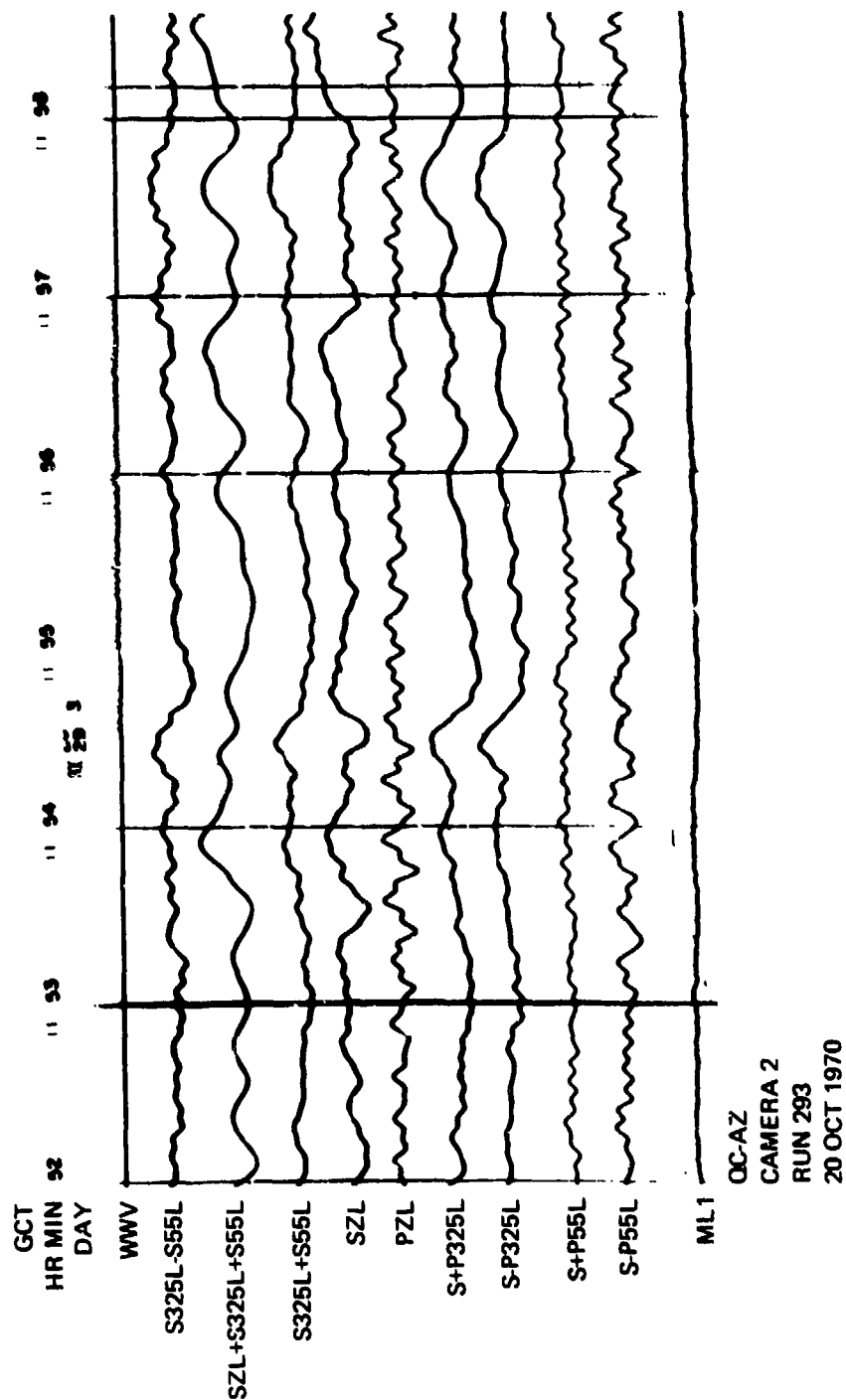


Figure 152. Enhancement of 15 sec microseisms traveling toward an azimuth of 235 deg

G 6301

cancelled on the S+P55L sum trace. Note the Rayleigh wave particle motion indicated by the PZL and S-P55L traces.

In the power spectral densities plotted in figure 153, a 12 dB difference can be seen in the power at 8 sec on the S+P55L and on the S-P55L. Therefore, during this 31 October 1970 quiet background sample used in sections 7.3 and 7.4, a 12 dB enhancement (or cancellation) of the 8 sec microseisms was possible similar to that seen for the 15 sec microseisms in figure 152.

Figure 154 illustrates the enhancement of SSS and its separation into S_H and S_V (or PL) components and the enhancement of the beginning of the Rayleigh wave. This figure is the recording of waves from an earthquake on the West Chile Rise. The NOS PDE data are: origin = 1101:28.4, 36.5S, 97.2W, $h = 33$ km, $m_b = 5.5$. This epicenter is at an azimuth of 167.7 deg and at an epicentral distance of 70.6 deg from QC-AZ. Of particular interest in the recording is the response of the various instrument combinations to the SSS arrival beginning just before 1132. The single cycle pulse on the S-P55L difference trace is interpreted as S_H motion. The 2-1/2 cycle pulse on the S325L-S55L, S+P325L, and S+P55L traces is interpreted as the initial S_H pulse followed by S_V or S coupled PL leaky mode motion. The factors leading to this interpretation are (1) the sharp stop of the single cycle on the S-P55L trace; (2) the complete absence of signal on the dilatation trace (SZL + S325L + S55L); (3) the complete absence of signal on the S-P325L trace; (4) the absence of motion on the vertical inertial PZL during the initial 1 cycle pulse on S-P55L, but the PZL response to motion during the following 1-1/2 cycles; and (5) similar response, but smaller, on vertical strain traces SZL and S325L + S55L. The Rayleigh wave begins about 1136 and is recorded on most traces with the greatest enhancement on the S+P55L trace.

The enhancement of a teleseismic Rayleigh wave and the cancellation of 8 sec microseisms is illustrated in figure 155. This earthquake occurred in the Iran-Iraq border region at an epicentral distance of 107.1 deg and at an azimuth of 19.4 deg. The NOS PDE data are: origin = 1122:18.2, 36.8N, 45.1E, $h = 33$ km, $m_b = 5.0$. Enhancement is seen on the S-P55L trace and the lower gain S-P325L trace. Good cancellation of the 8 sec microseisms occurs on the S-P55L since the 8 sec microseisms appear to be traveling toward the 55 deg azimuth. This Rayleigh wave is a good example of the signal-to-noise improvement achievable with the combined strain/inertial seismographs. The S/N ratio on the S-P55L trace is well above 10:1, while the S/N on the vertical inertial is only about 3:1.

An example of enhancement of a Rayleigh wave traveling toward the 325 deg azimuth is illustrated on the S+P325L trace in figure 156. The earthquake that generated this Rayleigh wave occurred south of Panama at an epicentral distance of 37.7 deg and at an azimuth of 127.8 deg. The NOS PDE data are: origin = 1310:13.2, 6.7N, 82.5W, $h = 33$ km, $m_b = 4.8$. The Rayleigh wave is significantly enhanced on the S+P325L trace and is almost cancelled on the S-P325L trace. The vertical inertial PZL confirms the Rayleigh wave particle motion. The SZL vertical strain trace is seen to be opposite in sign and proportional to the S325L + S55L sum of horizontal strain trace, as predicted by theory.

STRAIN/PENDULUM COMBINATIONS

3841 SAMPLES, 256 LAGS, 2.0 SPS, PARZEN SMOOTHING

QC-AZ

31 OCTOBER 1970

0737/0809

+ S55L + P55L

* S55L - P55L

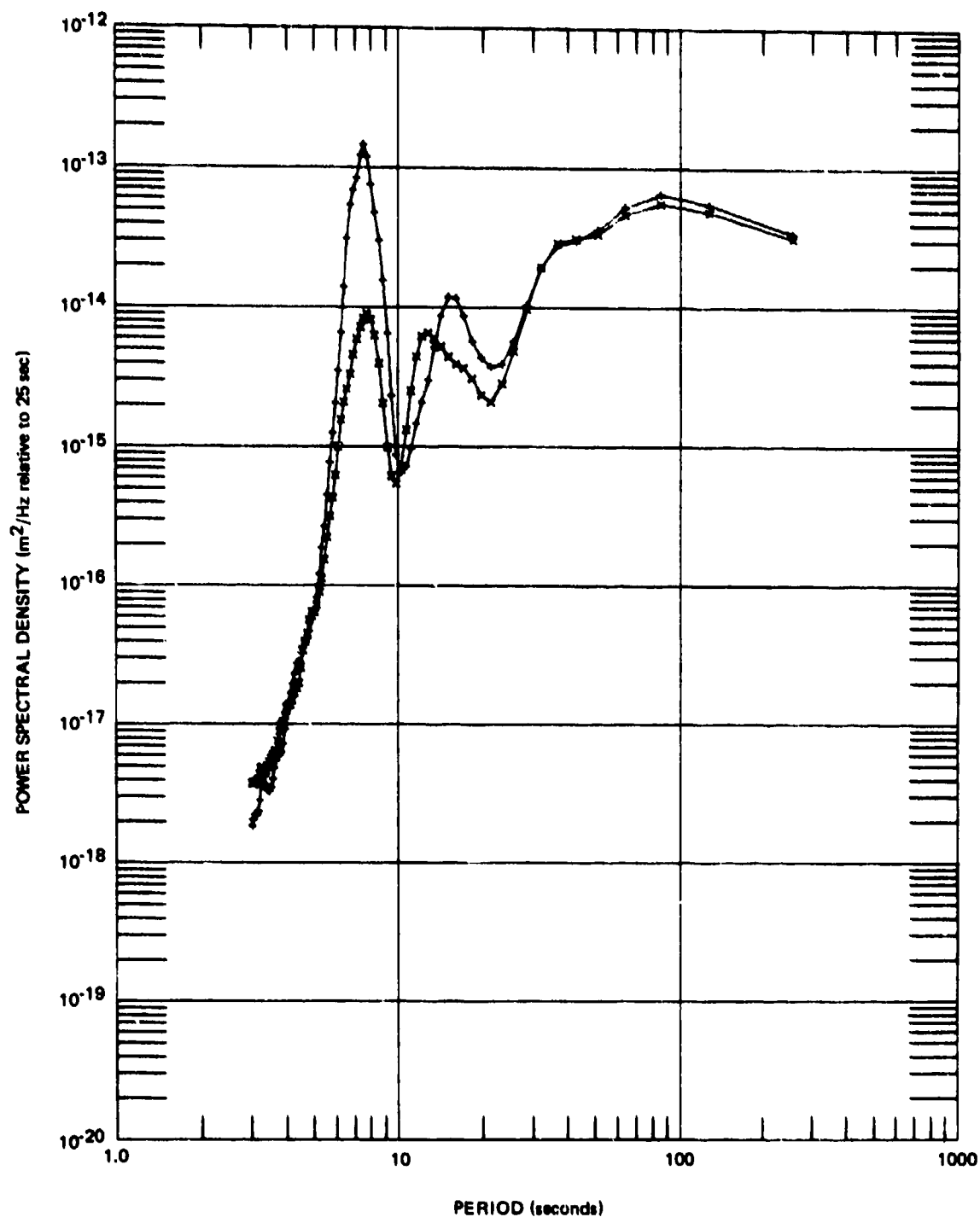


Figure 153. Power spectral density of S+P55L and S-P55L on 31 October 1970

G 6697

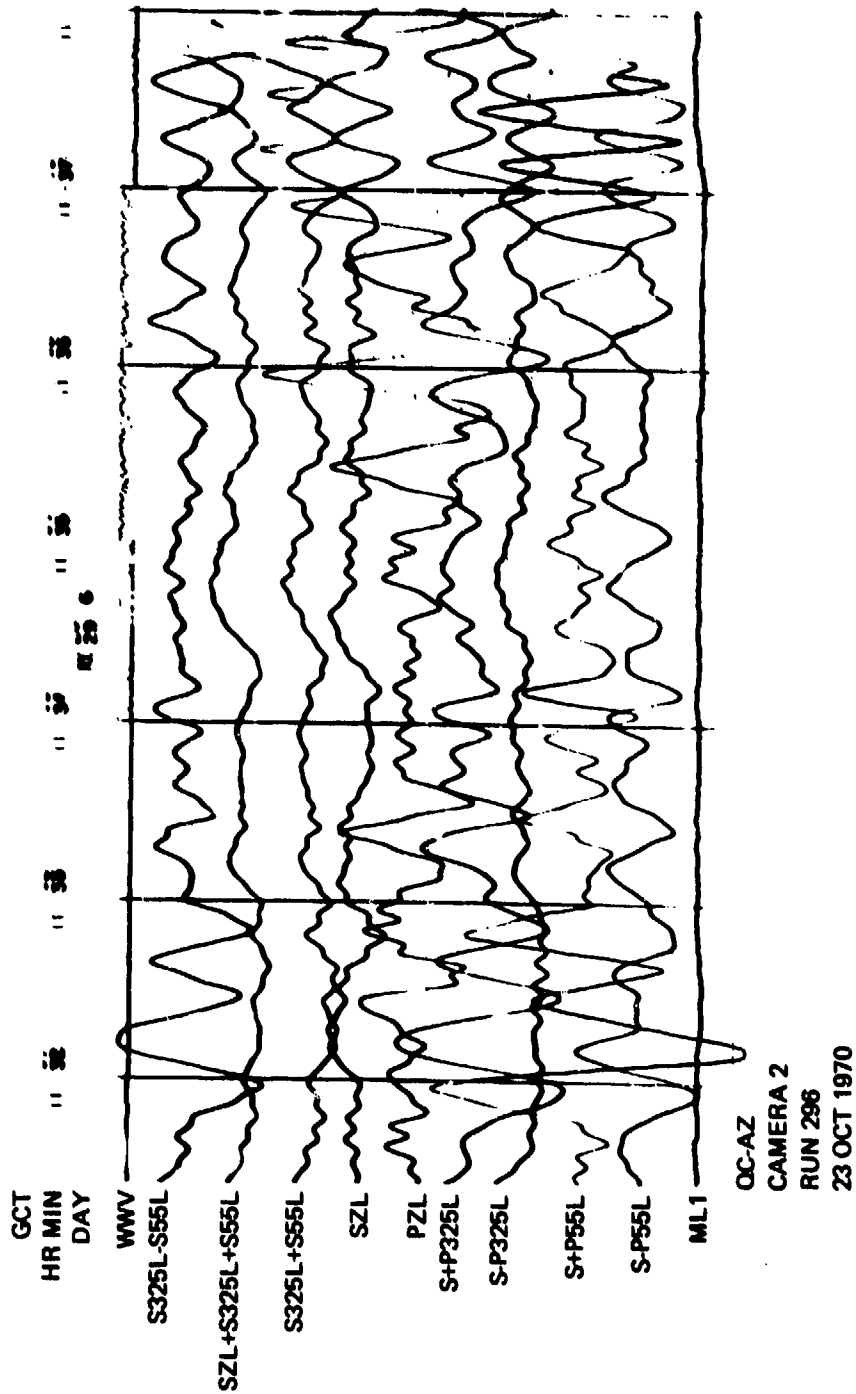


Figure 154. Enhancement of SSS, separation of SH and SV or S coupled PL, and enhancement of LRI from an earthquake on the West Chile Rise. NOS PDE: 0 = 1101:28.4, 36.5 S, 97.2 W, $h = 33$ km, $m_0 = 5.5$. $\Delta = 70.6$ deg, azimuth = 167.7 deg

G 6302

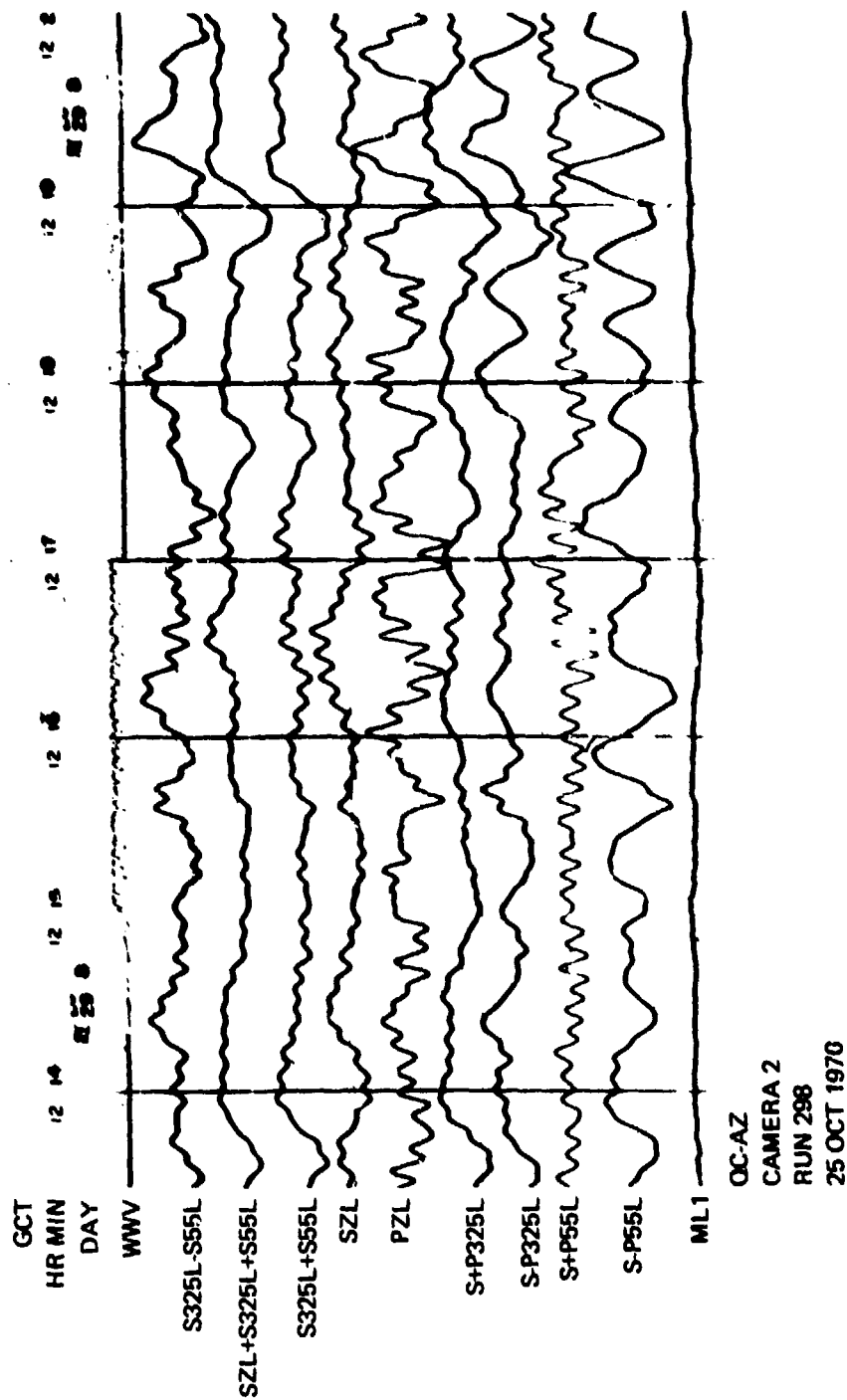


Figure 155. Enhancement of LRI from an earthquake in the Iran-Iraq border region. MOS
 PDE: $\theta = 1122:18.2$, 36.8 N, 45.1 E, $h = 33$ km, $m_b = 5.0$. $\Delta = 107.1$ deg,
 azimuth = 19.4 deg

G 6303

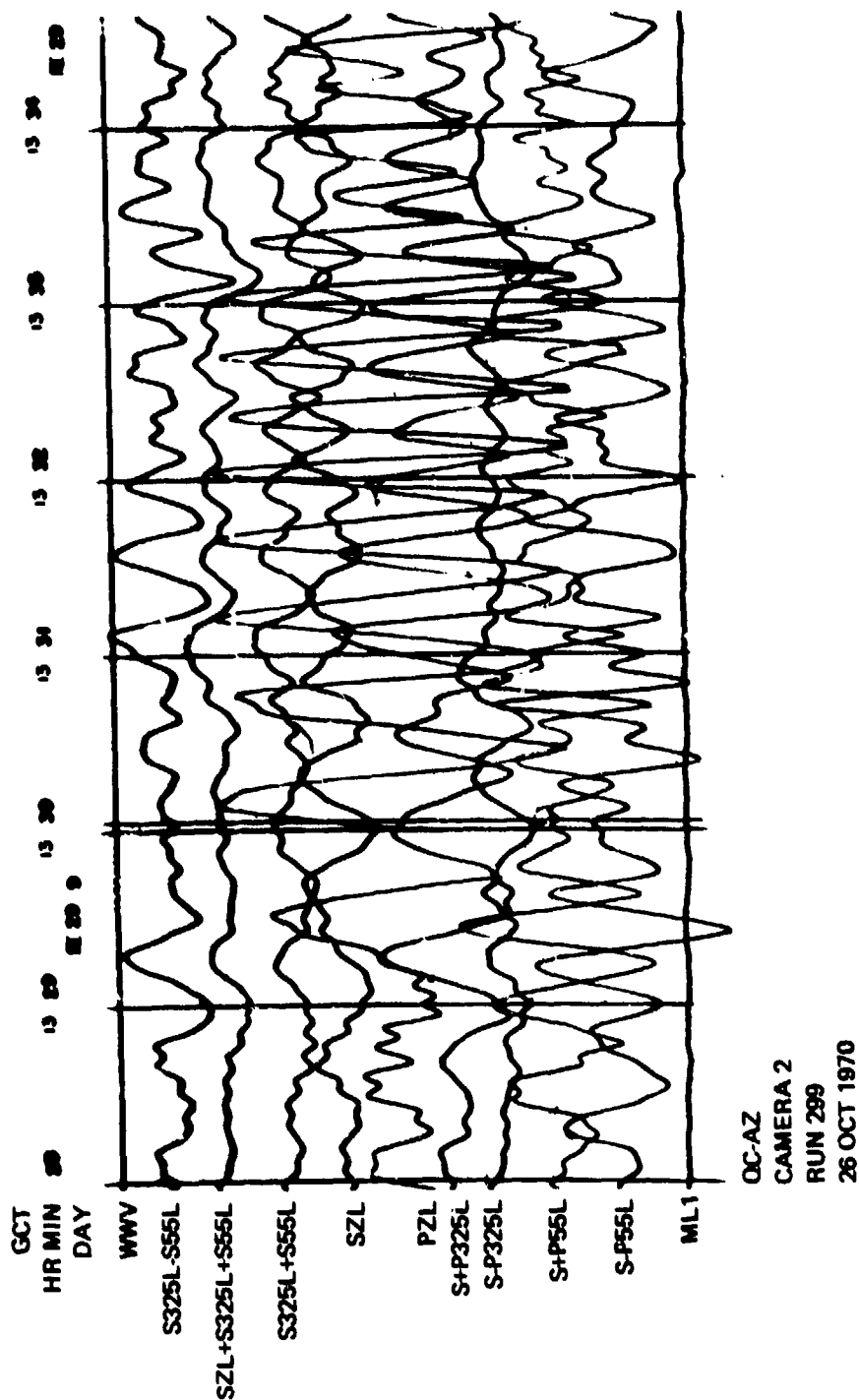


Figure 156. Enhancement of LR1 from an earthquake south of Panama. NOS PDE:
 $0 = 1310:13.2, 6.7 \text{ N}, 82.5 \text{ W}, h = 33 \text{ km}, m_b = 4.8, \Delta = 37.7 \text{ deg},$
 azimuth = 127.8 deg

G 6304

Figures 157 and 158 are reproductions of recordings from cameras 1 and 2, respectively, of a magnitude 4.2 earthquake in Turkey at an epicentral distance of 99.5 deg and an azimuth of 29.6 deg. In figure 157, the event would possibly not be detected if only the ALPS response inertial seismographs were present. However, the 30 sec signals are seen more clearly on the extended-long-period (XLP) response because the large microseisms present at this time have been eliminated by the XLP response. Even so, the detection of this event would still be questionable except for the clear enhancement in figure 158 on the S325L1-P325L and on the S55L-P55L difference traces and the clear cancellation on the two sum traces. Note also that the 8 sec microseisms are enhanced on the S55L+P55L sum and are generally cancelled on the difference trace. (The camera drive was erratic between 0610 and 0611.)

Figure 159 is a copy of a magnetic tape payout from a recording of the Rayleigh wave from a magnitude 5.3 earthquake in the Tonga Island Region at an epicentral distance of 78.9 deg and an azimuth of 238 deg. This figure illustrates the 90 deg phase difference, in accord with theory, between the vertical inertial seismograph PZL and the sum of the two orthogonal strain seismographs S325L1+S55L.

9.3.2 Long-Period Seismic Waves Enhanced from Magnetic Tape Recordings

This section presents results of enhancement of seismic waves and discrimination of wave types using recordings played back from magnetic tape. The majority of the illustrations are from combinations of strain and inertial seismograms and of strain and strain seismograms using an analog computer. The relative magnifications of the strain and inertial seismograms in each of the two azimuths were determined once and all of the illustrations were made with the same relative contributions from both types of seismographs. Therefore, the enhanced seismograms represent typical results that can be achieved by "on-line" recording. These results are similar to those achieved on camera 2 except that magnification and trace separation were optimized for the best presentation.

The first two figures are from recordings of three earthquakes at almost the same epicenter in the Kermadec Islands region. The great circle paths from QC-AZ to these epicenters are at azimuths of 231.1 deg, 231.2 deg, and 230.9 deg - only 3.9, 3.8, and 4.1 deg, respectively, off the back azimuth of the 55 deg instruments. Figure 160 is the recording of the first of these events. The NOS PDE data are: 0 = 2159:42.9, 10 October 1970, 31.9S, 177.9W, h = N, $m_0 = 5.9$, $M_S = 6.2$. This epicenter is at an epicentral distance of 90.0 deg and at an azimuth of 231.1 deg. The (a) part of the figure contains the three P_L inertial seismograms and the three S_L strain seismograms. The (b) part contains the PZL vertical-inertial seismogram and the four-azimuth directional array formed by the sum and difference of the strain and inertial seismograms in the two directions.

The easily identifiable earthquake phases are marked in the (b) part of the figure. The performance according to many parts of the theory can be seen in the figure. The radial strain seismograph, S55L, records the Rayleigh wave with almost equal amplitude with the P55L. The S+P55L enhances the Rayleigh wave by a factor of 2, while the S-P55L cancels the Rayleigh wave to about 0.3 of the original value. If the ratio of the sum to the difference is taken as

TRACE	MAG.
GCT	AT 25 SEC
HR MIN	-
DAY	-
WVV	-
FLAG	-
S325L2	1.11 X 10 ⁻¹² STRAIN/MM
S325LL2	1.19 X 10 ⁻¹¹ STRAIN/MM
S325L1	1.05 X 10 ⁻¹² STRAIN/MM
S325LL1	1.09 X 10 ⁻¹¹ STRAIN/MM
S55L	1.25 X 10 ⁻¹² STRAIN/MM
S55LL	1.19 X 10 ⁻¹¹ STRAIN/MM
P2L	51.2K
P32EL	50.0K
P55L	43.0K
PZX	45.8K
P325X	48.6K
P55X	42.0K
ML1	0.057/ubar/MM
•PZS	487K
•P325S	462K
WV	2 MPH/MM
WD	-
ML2	3.5/ubar/MM

NOTE: * MAG. AT 1 SEC

QC-AZ
CAMERA 1
RUN 161
10 JUNE 1970

Figure 157. Reproduction of 16 mm film recording of LRI Rayleigh wave. NOS preliminary epicenter data: 0 = 0517:14.0, 39.2N, 29.5E, Turkey, h = 27 km, $m_b = 4.2$, $\Delta = 99.5$ deg., azimuth = 29.6 deg.

G 6000

TRACE	..
GCT	<u>AT 25 SEC</u>
HR MIN	-
DAY	-
WWV	-
{S325L1-S325L2}	~500K
S325L1-S55L	51.3K
S325L2+S55L	57K
S325L2	-
PZL	19.7K
S325L1+P325L	63.0K
S325L1	32.9K
P325L	31.3K
S325L1-P325L	61.3K
S55L+P55L	53.5K
S55L	31.1K
P55L	26.2K
S35L-P55L	54.1K
ML1	0.0904BAR/MM

****EQUIV.
INERTIAL
MAG.
RAYLEIGH
WAVE**

QC-AZ
CAMERA 2
RUN 161
10 JUNE 1970

Figure 158. Reproduction of 16 mm film recording showing enhancement of LRI Rayleigh wave on S325L-P325L and S55L-P55L difference traces. NOS preliminary epicenter data: $0 = 0517:14.0$, $39.2N$, $29.5E$, Turkey, $h = 27$ km, $m_0 = 4.2$, $\Delta = 99.5$ deg, azimuth = 29.6 deg

SECRET

EQUIV.
INERTIAL
MAG.
RAYLEIGH
WAVE

TRACE
REF. NO. AT 25 SEC

DAY

BCD
TIME

S325L1

18.2K

S55L

18.6K

S325L1+ S55L

36.8K

S325L1- S55L

36.8K

PZL

17.6K

BCD
TIME

QC-AZ
MAGNETIC TAPE
PLAYOUT
RUN 101
11 APR. L 1970

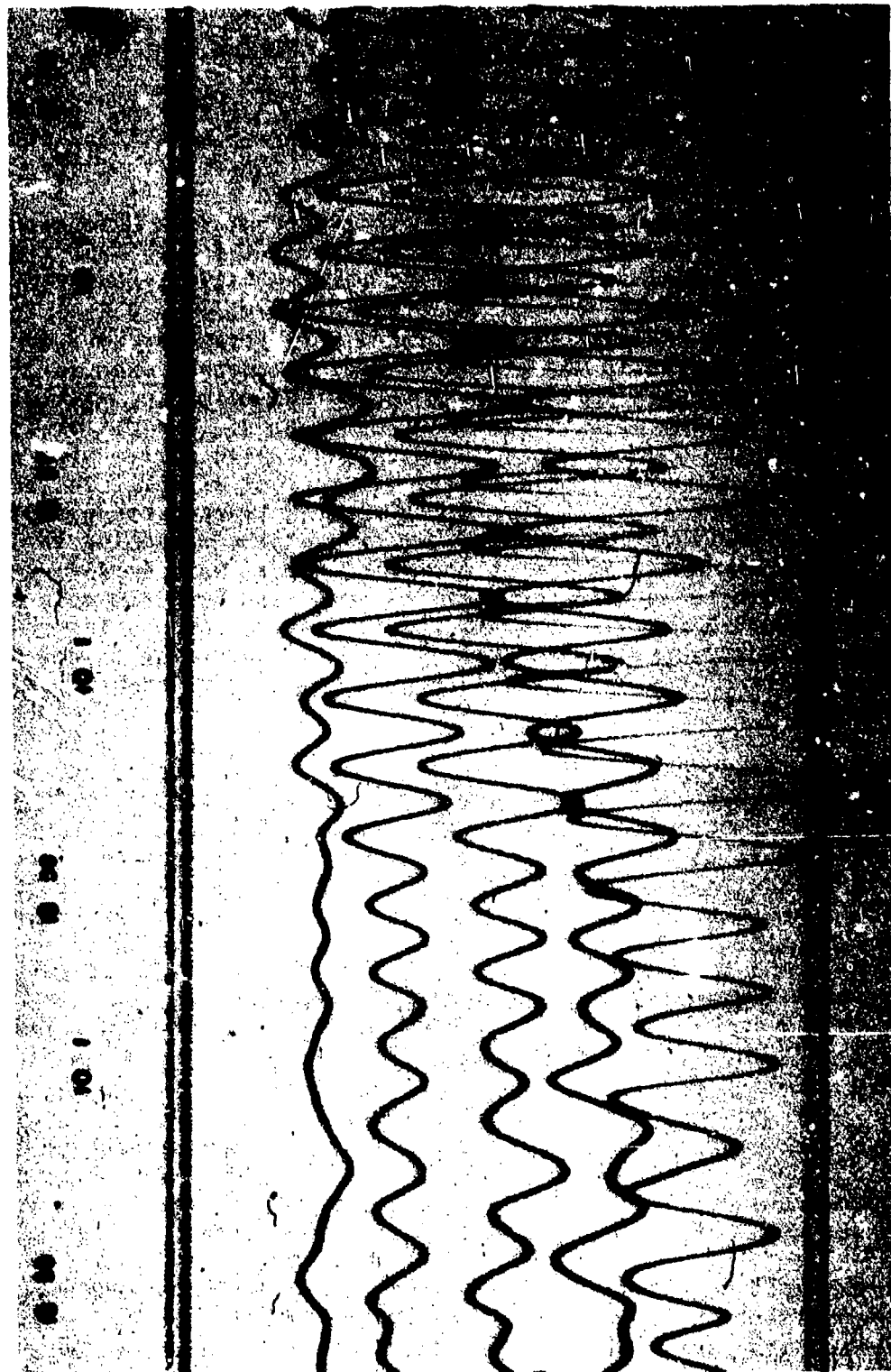


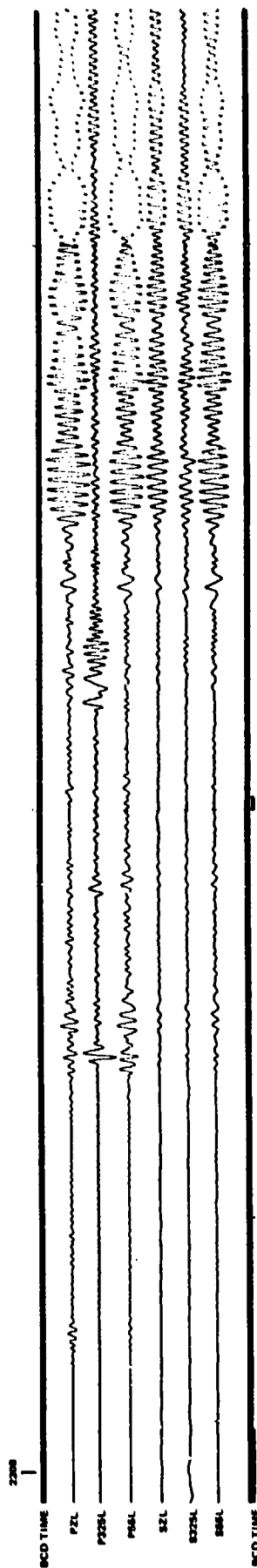
Figure 159. Reproduction of a 16 mm film recording of a Rayleigh wave train from an earthquake in the Tonga Island Region. $\Delta = 0621:16.3$, $19.3S$, $173.6W$, $h = 33$, $m_b = 5.3$, $\Delta \pm 78.9$ deg, azimuth $= 238$ deg.

G 6700

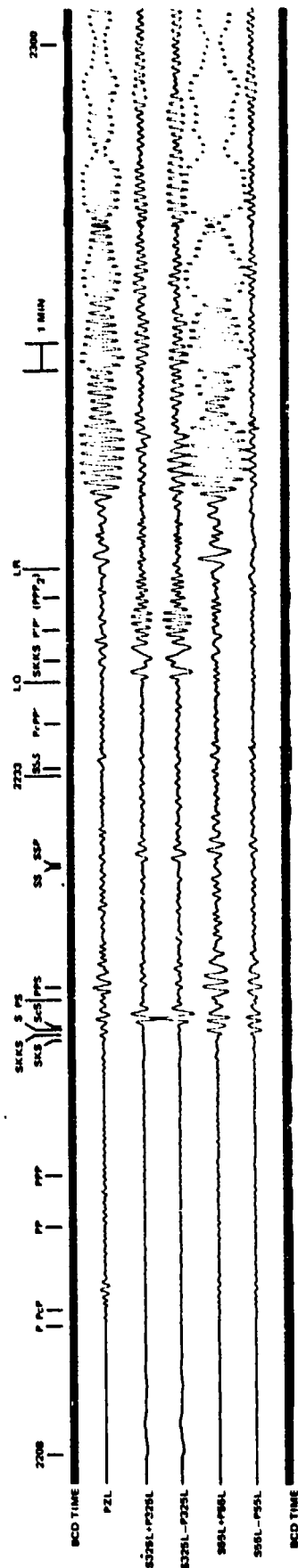
the S/N ratio improvement we get 16.4 dB enhancement. Notice that the S325L transverse strain seismograph recorded the Rayleigh wave at about $-1/3$ the value of the S55L seismograph. This is not in accord with theory and has been discussed in section 8.2.2 as the "Poisson ratio effect." Some lateral refraction can be seen in the coda of the Rayleigh wave. The effect of the lateral refraction can be observed in the S-P55L, and both the S+P325L and S-P325L traces. Since the great circle path to this epicenter is essentially radial with one strain seismograph, both are on nulls for the Love wave (LQ). The absence of Love wave signal is obvious on all but the P325L transverse inertial seismograph. The absence of strain LQ signal is also evident in the directional array where the S+P325L trace and the S-P325L trace are mirror images. The S wave on the S+P325L and S-P325L traces is another example of the transverse strain being on a null of the S_H azimuthal response. The all inertial response confirms the discrimination of S_H from S_V . The mirror image in the directional array is also common for body waves, which arrive with a high phase velocity and primarily have inertial seismograph signal. The SKKS, S, PS, and PPS, all arriving as S_V on the 55 deg azimuth traces, are examples of approximate mirror images for body waves. Using the same reasoning in reverse, the single 30 sec pulse at the beginning of the LR wave is definitely part of the Rayleigh wave train even though it is separated from the main part of the LR signal by about 2 min. Also according to theory, the phases with smaller angles of emergence have larger strain signals. Referring to the S55L, the reader can note that PP has more signal than P, S much more than P, and PS more than S.

The repeatability of the strain seismographs and the strain/inertial combinations can be seen in figure 161. This figure is a computer plot of the individual P55L and S55L seismograms and of the combined S+P55L and S-P55L seismograms. This figure contains seismograms from the three Kermadec Islands region earthquakes. The (a) part is the same signal as in figure 160. Better, but very similar, results can be seen with the digital computer enhancement (S+P55L) and cancellation (S-P55L) of the signal as were obtained with the analog enhancement. The NOS PDE data are: part (b) 0 = 0316:49.6, 11 October 1970, 318S, 178.1W, $h = N$, $m_b = 5.6$, $M_S = 6.3$; and part (c) 0 = 0538:06.0, 11 October 1970, 32.1S, 177.8W, $h = 32$ km, $m_b = 5.6$, $M_S = 6.1$. These epicenters are at distances of 90.0 and 90.0 deg and at azimuths of 231.2 and 230.9 deg, respectively. All three signals are almost identical, including the separated 30 sec pulse at the beginning of the Rayleigh wave. The LR₂ long-arc path Rayleigh wave from the second event is clear at the beginning of the (c) part of the figure. The LR₂ on the S-P55L trace is clearly separated from the S group of body wave arrivals on the S+P55L trace. This signal separation explicitly demonstrates the potential of the directional array.

The enhancement of small amplitude Rayleigh waves on the directional array is one of the major applications of the high-sensitivity strain/inertial seismograph complex. Rayleigh waves from two $m_b = 4.2$ (NOS) earthquakes at an epicentral distance of 96.7 deg are shown enhanced on the directional array in figure 162. The NOS PDE data for these events are: part (a) 0 = 1256:34.9, 2 October 1970, 6.9S, 155.0E, $h = 36$ km, $m_b = 4.2$; and part (b) 0 = 1930:50.5, 3 October 1970, 6.8S, 154.8E, $h = 34$ km, $m_b = 4.2$. These epicenters are at epicentral distances of 96.5 and 96.7 deg and at azimuths of 266.1 and 266.2 deg, respectively, from QC-AZ. The two parts of the figure are time aligned at a group velocity (U) of 3.25 km/sec. (The photographic reduction was slightly different in the two parts of the figure.) Although the NOS assigned



(a) Individual seismograms



(b) Directional array

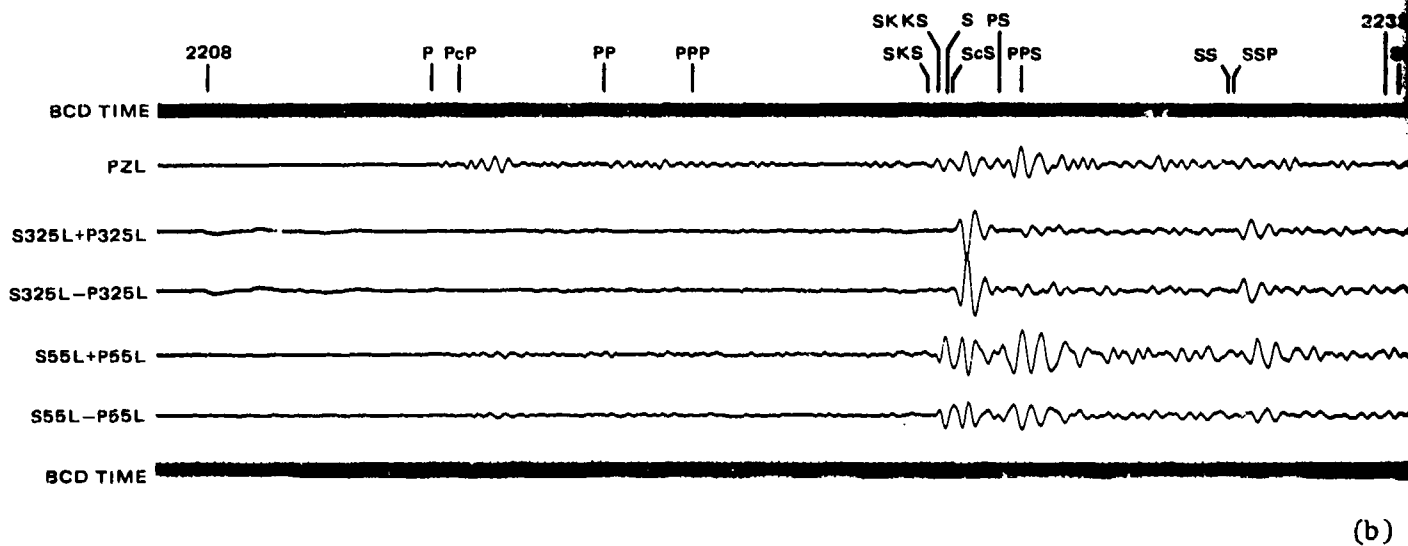
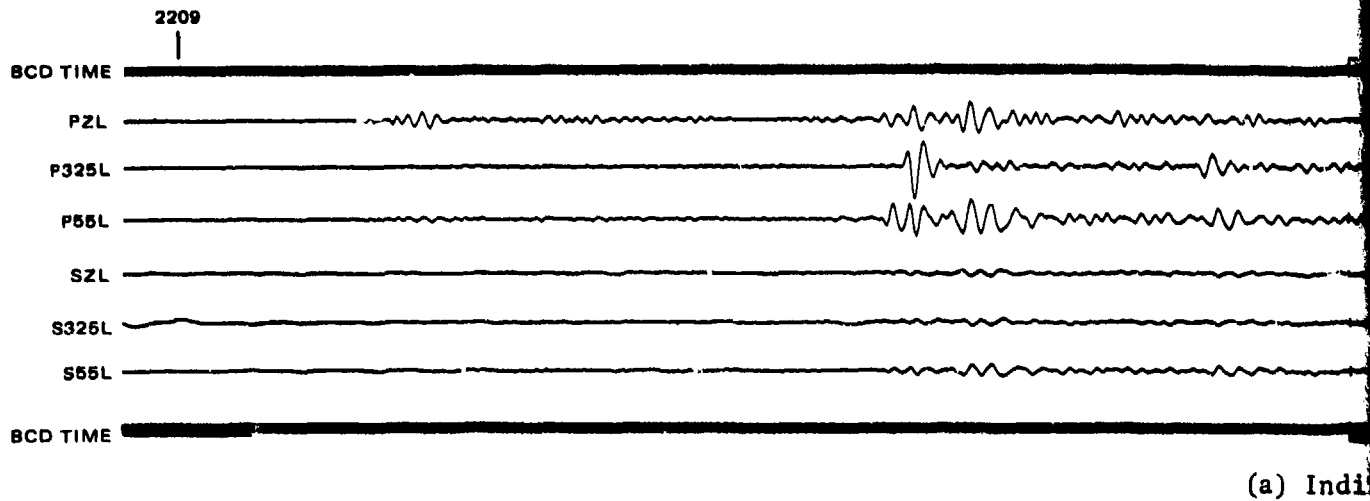
GC AZ
RUN 285
10 OCT 1970

REPRODUCED FROM
ORIGINAL RECORDING
SEE THE FOLLOWING PAGE

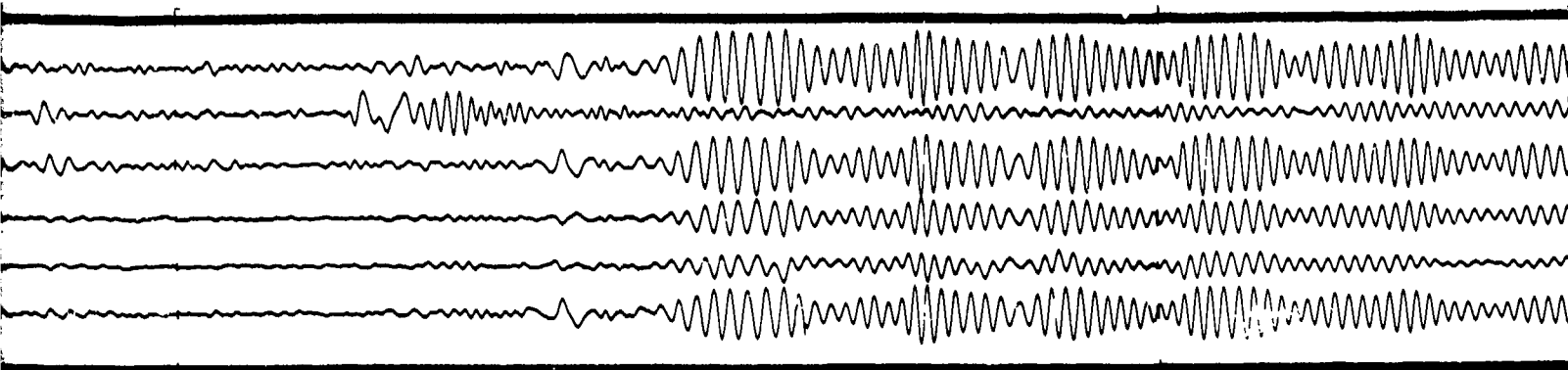
Figure 160. Enhancement of seismic waves from an earthquake in the Kermadec Islands region. NOS PDE data: 0=2159:42.9, 31.95, 177.9M, h=N, $m_0=5.9$, $M_s=6.2$, $\Delta=90.0$ deg, azimuth=231.1 deg, (a) individual channels, (b) directional array

285 -281/282-

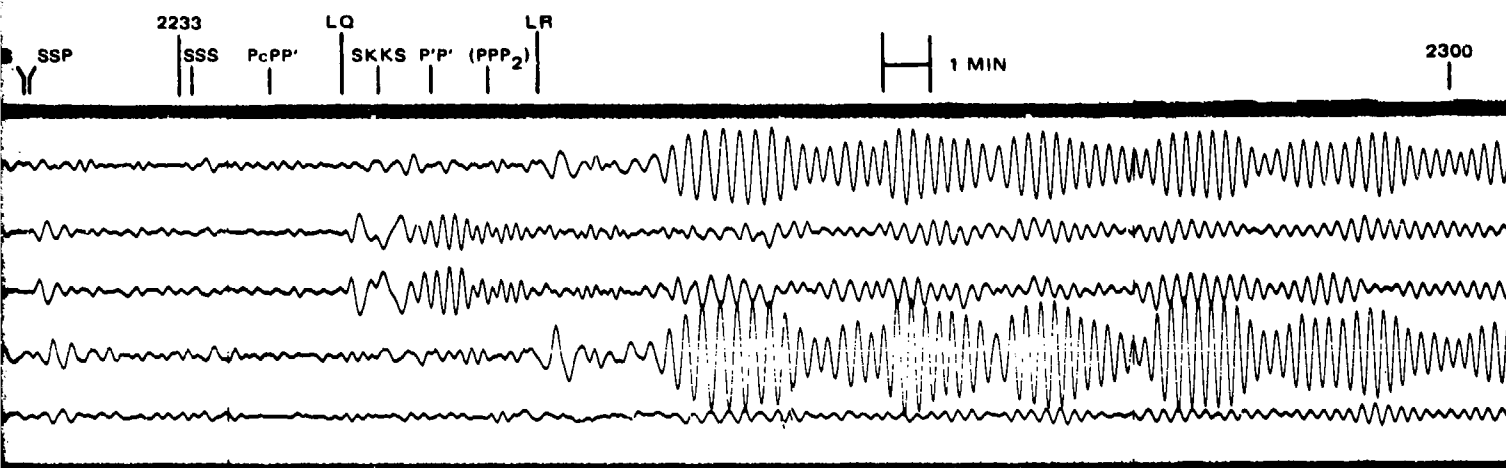
TR 72-3



QC-AZ
 RUN 283
 10 OCT 1970



(a) Individual seismograms



(b) Directional array

Figure 160. Enhancement of seismic waves from an earthquake in the Kermadec Islands region. NOS PDE data: $\theta=2159:42.9$, $31.9S$, $177.9W$, $h=N$, $m_b=5.9$, $M_s=6.2$, $\Delta=90.0$ deg, azimuth= 231.1 deg, (a) individual channels, (b) directional array

G 6701

282

-281/282-

2233

1

PSGL

SSGL+PSGL

SSGL-PSGL

SSGL

(a) 2159:42.9, 10 Oct 1970

PSGL

SSGL+PSGL

SSGL-PSGL

SSGL

(b) 0316:49.6, 11 Oct 1970

PSGL

SSGL+PSGL

SSGL-PSGL

SSGL

(c) LR_2 from (b) and 0538:06.0, 11 Oct 1970

QC-AZ
RUN 283 AND 284
10 AND 11 OCT 1970

283

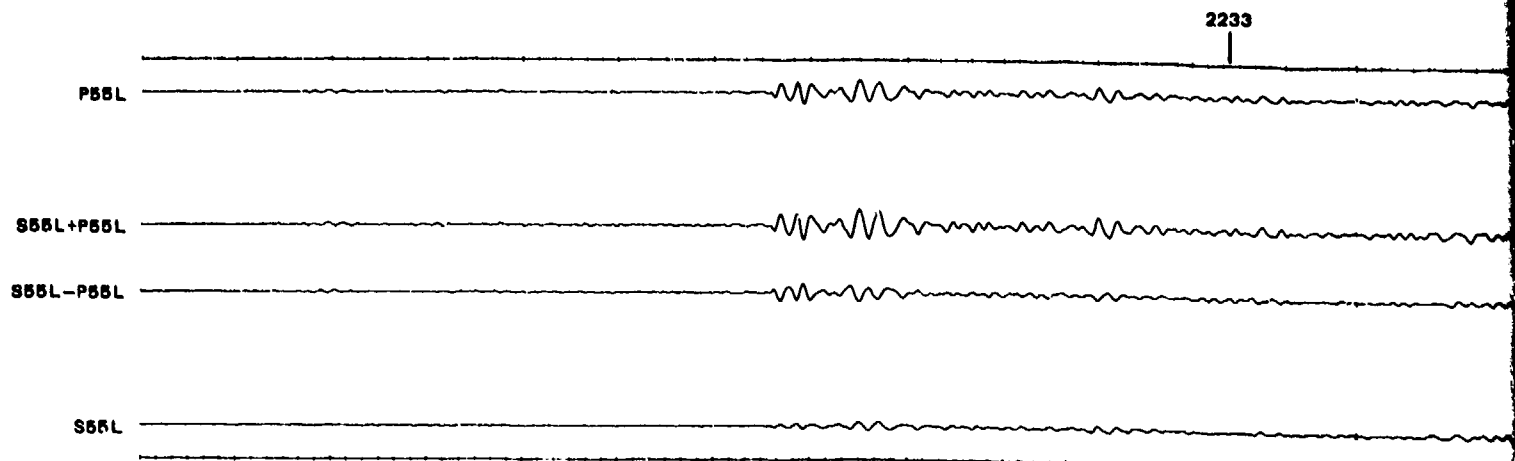
XXXXXXXXXXXXXXXXXXXX
See the following pages
for greater detail.
XXXXXXXXXXXXXXXXXXXX

Figure .61. Directional array enhanced
0-2159:42.9, 31.9S, 177.8W, $M_0=5.9$, $M_2=6.2$, $\Delta=90.0$ deg, azimuth=231.1 deg, (b) 0-
0316:49.6, 31.8S, 178.1W, $M_0=5.6$, $M_2=6.3$, $\Delta=90.9$ deg, azimuth=231.2 deg, (c) LR_2 from
earthquake of (b) and 0-0538:06.0, 32.1S, 177.8W, $M_0=5.6$, $M_2=6.1$, $\Delta=90.0$ deg,
azimuth=230.9 deg.

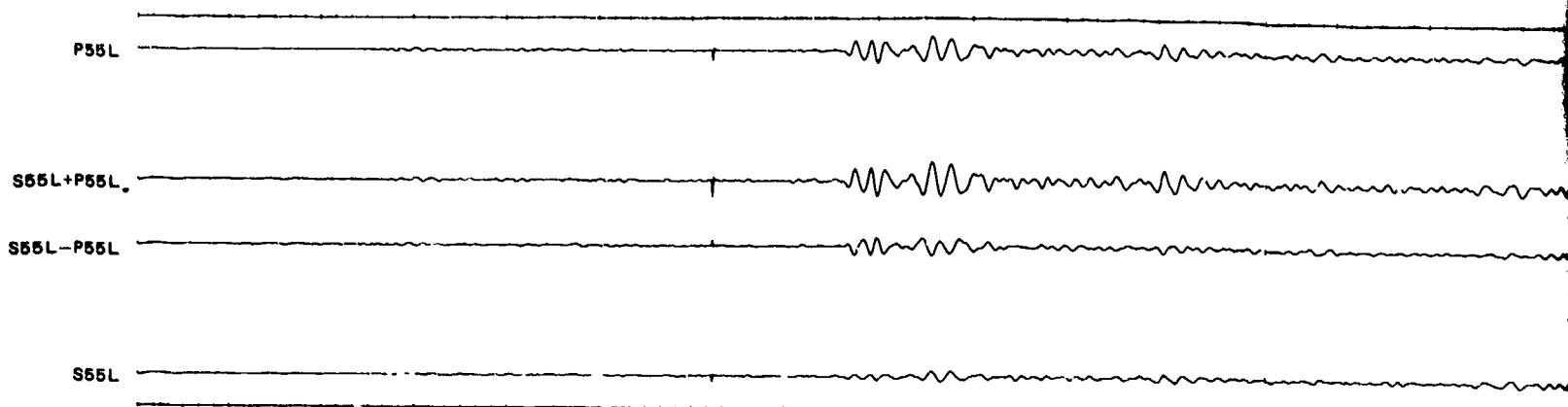
283

284 -283/284-

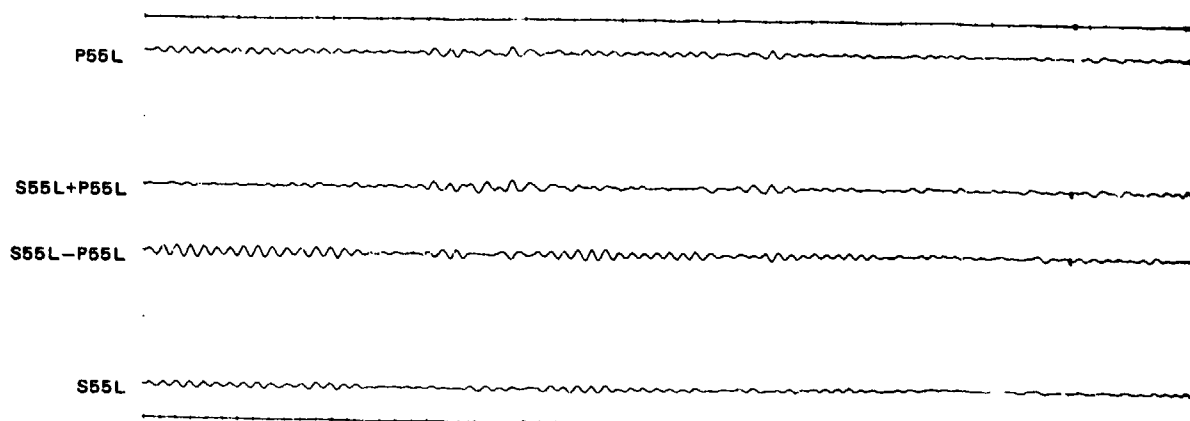
TR 7



(a) 2159:42.9, 10 Oct 1970



(b) 0316:49.6, 11 Oct 1970



(c) LR₂ from (b) and 0538:06.0, 11 Oct 1970

QC-AZ
RUN 283 AND 284
10 AND 11 OCT 1970

283.

of seismic
0=2159:42.9
0316:49.6,
earthquake
azimuth=230

283

2233

1 MIN

2159:42.9, 10 Oct 1970

0400

9.6, 1 1970

0621

1970

Figure 161. Directional array enhancement of seismic waves from three earthquakes in the Kermadec Islands region. NOS PDE data: (a) 0=2159:42.9, 31.9S, 177.9W, h=N, $m_b=5.9$, $M_s=6.2$, $\Delta=90.0$ deg, azimuth=231.1 deg, (b) 0=0316:49.6, 31.8S, 178.1W, h=N, $m_b=5.6$, $M_s=6.3$, $\Delta=90.9$ deg, azimuth=231.2 deg, (c) LR2 from earthquake of (b) and 0=0538:06.0, 32.1S, 177.8W, h=32 km, $m_b=5.6$, $M_s=6.1$, $\Delta=90.0$ deg, azimuth=230.9 deg

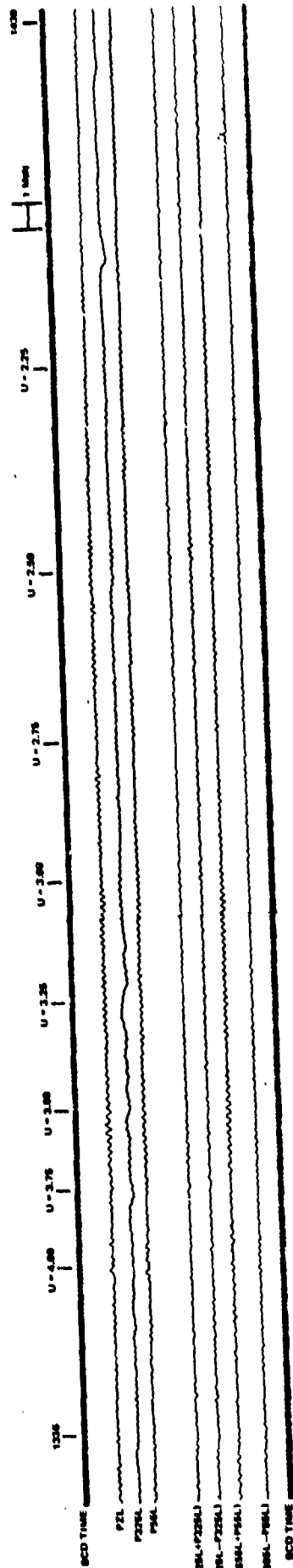
2831

284

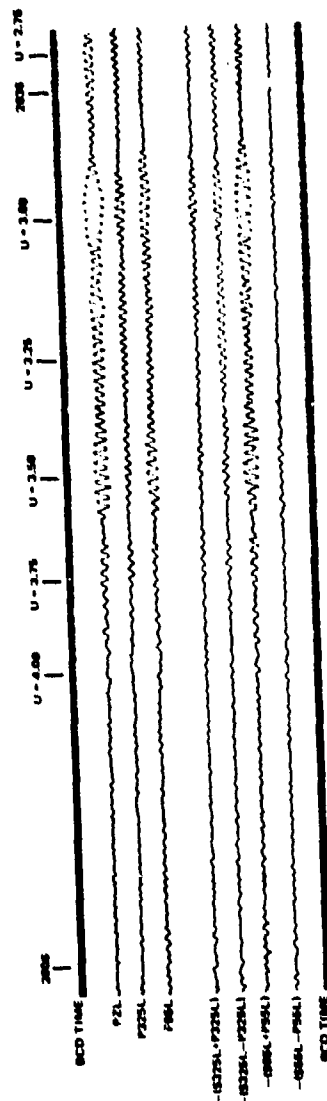
-283/284-

G 6702

TR 72-3



(a) 2 Oct. 70 (275)



(b) 3 Oct. 70 (276)

XXXXXXXXXXXXXXXXXXXX
See the following pages
for further details
XXXXXXXXXXXXXXXXXXXX

Figure 162. Enhancement of seismic waves from two low-level earthquakes in the Solomon Islands region. NOS PDE data: (a) 0-1256:34.9, 2 Oct 1970, 6.95, 155.07, 36 km, $m_0 = 4.2$, $\Delta = 96.5$ deg, azimuth = 214 deg, (b) 0-1930:50.5, 30 Oct 1970, 6.8, 154.85, 34 km, $m_0 = 4.2$, $\Delta = 96.7$ deg, azimuth = 266.2 deg.

6.8

-285/286-

286

285.1

285.

TR 7.

1335 U = 4.00 U = 3.75 U = 3.50 U = 3.25 U = 3.00
BCD TIME

PZL

P325L

P55L

-(S325L+P325L)

-(S325L-P325L)

-(S55L+P55L)

-(S55L-P55L)

BCD TIME

(a)

2006 U = 4.00 U = 3.75 U = 3.50 U = 3.25 U = 3.00
BCD TIME

PZL

P325L

P55L

-(S325L+P325L)

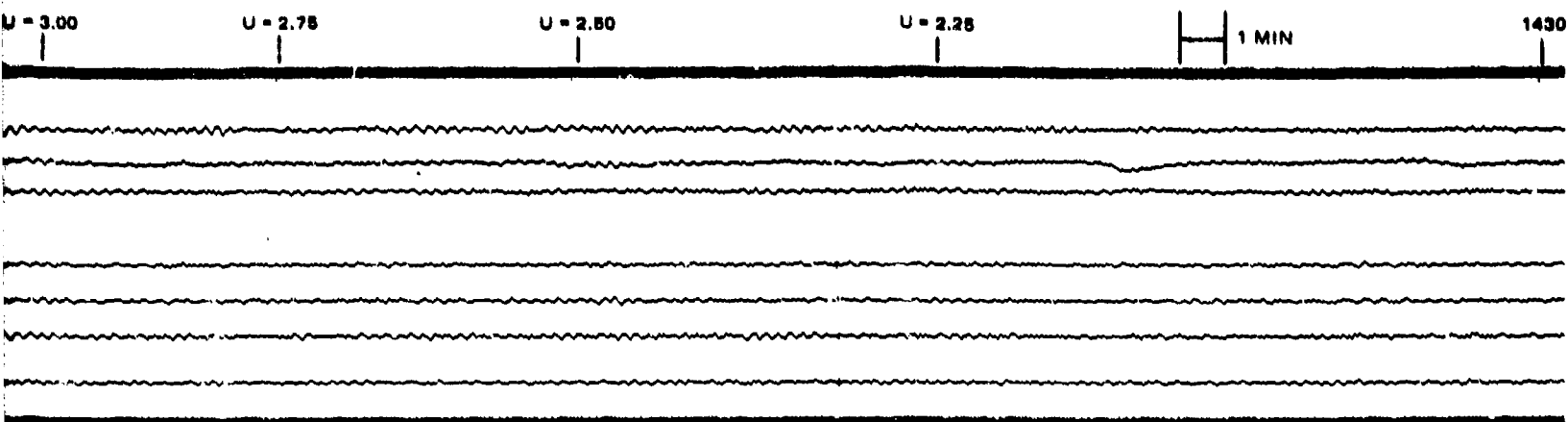
-(S325L-P325L)

-(S55L+P55L)

-(S55L-P55L)

BCD TIME

(b) 3 Oct. 70 (276)



(a) 2 Oct. 70 (275)

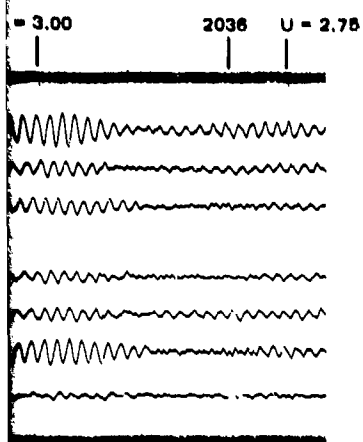


Figure 162. Enhancement of seismic waves from two low-level earthquakes in the Solomon Islands region. NOS PDE data: (a) 0=1256:34.9, 2 Oct 1970, 6.9S, 155.0E, h=36 km, $m_b = 4.2$, $\Delta=96.5$ deg, azimuth=266.1 deg, (b) 0=1930:50.5, 30 Oct 1970, 6.8S, 154.8E, h=34 km, $m_b=4.2$, $\Delta=96.7$ deg, azimuth=266.2 deg

G 6703

285.1

286

-285/286-

the same 4.2 magnitude to both events, the 3 October 1970 Rayleigh wave has a larger amplitude than the 2 October 1970 Rayleigh wave. The (a) part of figure 162 and figure 158 (also from an $m_b = 4.2$ earthquake) are good examples of the ability of the directional array to detect and identify a traveling wave. By comparing the S+P55L trace and S-P55L trace in figure 162 (a), the distinct difference allows the analyst to affirm the presence of a Rayleigh wave signal that is traveling toward the 55 deg azimuth.

Note: In figure 162, and in many of the following figures, the directional array traces are illustrated with inverse polarity. The inverse polarity resulted from the inverting amplifiers in the analog computer in which the sums and differences were formed. This inverse polarity is indicated by the minus sign preceding the trace identification; for example, $-(S325L + P325L)$. In the text, no further reference will be made to the inverse polarity. The traces will be referred to merely as S+P325L.

In a similar manner, the comparison in figure 158 of the S+P325L and S-P325L and of the S+P55L and S-P55L allows the analyst to detect and to affirm the presence of a Rayleigh wave signal that is traveling toward an azimuth between 235 and 145 deg, but closer to the 235 deg direction. The great circle path is toward a 209.6 deg azimuth. A secondary application of the directional array is the identification of lateral refraction in the coda of the Rayleigh wave. By comparing in figure 162 (b) the S+P55L, the S-P325L, and the S+P325L, it can be determined that the beginning of the Rayleigh wave from about $U = 4.00$ to about $U = 3.3$, the wave train is traveling toward the 55 deg azimuth almost exclusively. Starting at about $U = 3.3$, the direction of travel swings slightly toward the 145 deg azimuth. At about $U = 3.0$, the S+P55L continues to indicate the major energy is traveling toward the 55 deg azimuth; however, the almost equal and opposite S+P325L and S-P325L traces are an indication of a low S325L strain signal. The Rayleigh wave from the 3 October 1970 earthquake is used in section 10.2 to establish the ratio of a small earthquake signal to the ambient ground unrest during a quiet time.

Figure 163 (a) and (b) is a four strip continuous segment illustrating enhancement of waves from a series of earthquakes in the New Hebrides Islands. The first event was the largest and only the earthquake phases from it are marked in the illustration. The phases and times of the phases indicated in figure 163 and most of the other figures in this section are calculated arrival times based upon the NOS origin time and a polynomial fit to standard travel time tables.

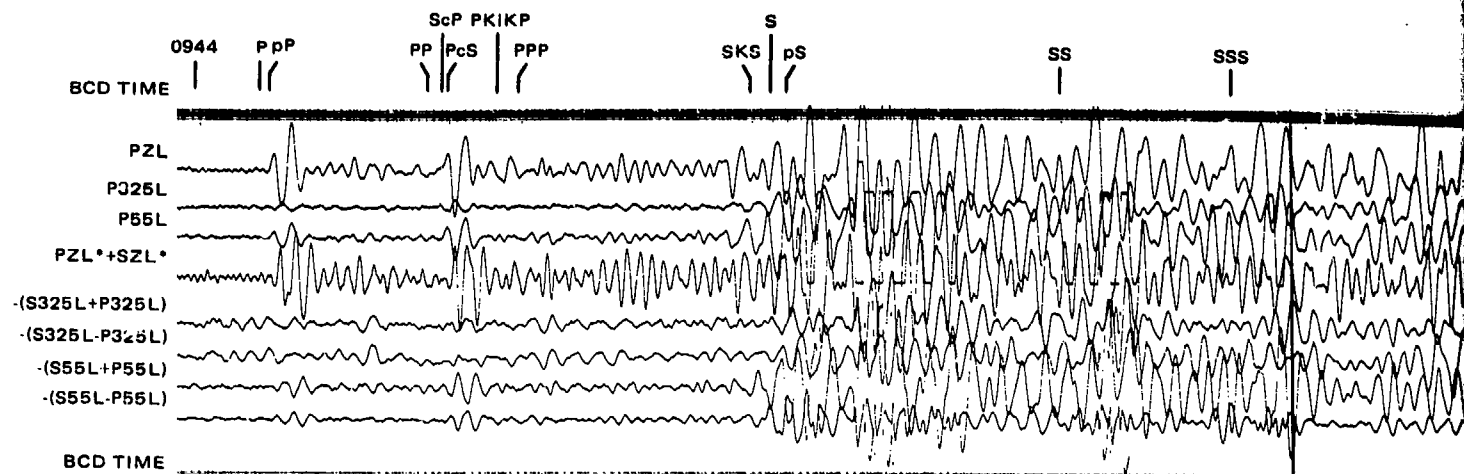
A seismograph trace is illustrated in figure 163 that has not appeared in any previous illustrations up to this point, but will be in several of the following figures. It is the PZL*+SZL* seismogram. This seismogram is formed by phase shifting the PZL inertial seismogram and SZL strain seismogram to correct for the 90 deg phase difference between the two seismograms that exist for Rayleigh waves. In the illustrations in this report, this trace was amplified from the sensitivity of the PZL seismogram by a factor of about 4. The phase shift and summation amplifier used in these presentations is assigned to another project but was available for the magnetic tape playbacks. The unit was used as a SP phase compensator, but was suitable for use with the LP recordings with a times ten speed-up of the magnetic tape on playback. The output had a relative phase shift of 90 ± 4 deg from 5 to 50 sec. At 25 sec, the total phase shift of the

PZL seismogram was 192 deg and of the SZL seismogram was 103 deg. The polarity was inverted to be the same as the PZL seismogram. Thus, the PZL*+SZL* trace has a net time delay over the PZL trace. This time delay is evident in the figures.

The NOS PDE data on the 3 September 1970 earthquakes whose signals are recorded in figure 163 are (1) 0 = 0932:23.0, 16.9S, 167.8E, h = 44 km, m_b = 5.5, M_S = 5.9; (2) 0 = 0948:02.9, 17.0S, 167.8E, h = 34 km, m_b = 4.8; (3) 0 = 0959:04.1, 17.0S, 167.9E, h = 33 km, no m_b given; (4) 0 = 1034:23.0, 17.0S, 167.8E, h = 40 km, m_b = 4.7; and (5) 0 = 1210:23.4, 17.1S, 167.7E, h = 21 km, m_b = 4.5. These epicenters are at epicentral distances of (1) 91.5 deg, (2) 91.5 deg, (3) 91.5 deg, (4) 91.5 deg, and (5) 91.7 deg, and at azimuths of (1) 250.9 deg, (2) 250.8 deg, (3) 250.7 deg, (4) 250.8 deg, and (5) 250.8 deg from QC-AZ.

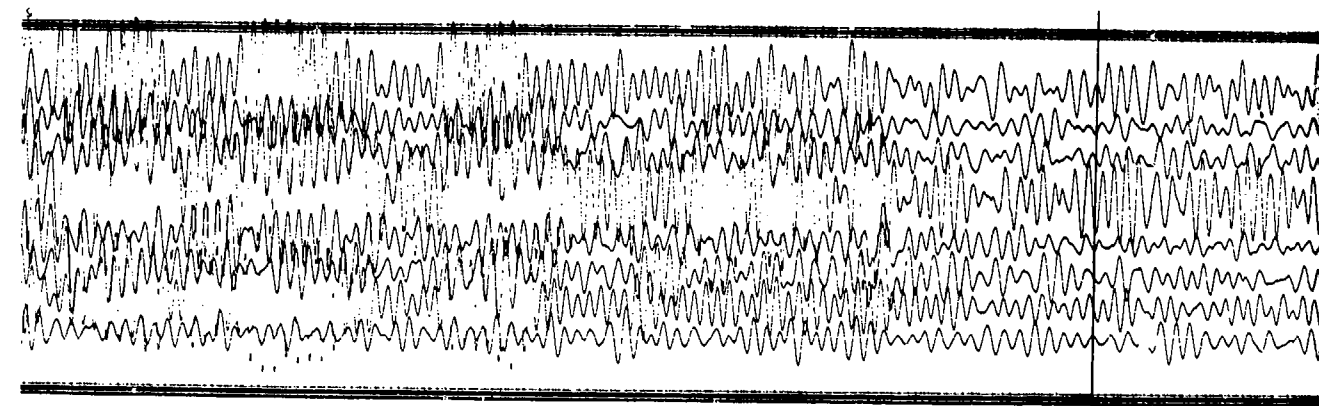
In figure 163 (a), the PZL*+SZL* trace has clearly separated P and pP, PP and the combined ScP, PcS group and S and pS. These three sets of second arrivals cannot be distinguished on the individual inertial or the directional array traces. As a matter of fact, their existence in the data cannot even be detected and the time differences from the first arrivals cannot be estimated. The detection and identification of pP and pS are valuable to the determination of the depth of the hypocenter. The phase shifted trace also enhances the time break on PPP. The PKiKP arrival is clearly recorded on the PZL and PZL*+SZL* traces. Travel times for this phase are from Engdahl et al. (1970) and Bolt and O'Neill (1956). As illustrated previously, the body waves in the P and PP groups appear with almost equal amplitudes on the S+P55L and S-P55L traces, indicating mostly P55L inertial seismograph signal. The S55L strain seismograph has increasing signal on the PP and S arrivals as indicated by the larger ratio of the sum to the difference trace. The large arrival preceding SKS on the PZL, P55L, and PZL*+SZL* traces is unidentified. Most of the P55L seismograph signal was degraded in the directional array starting with the S arrival group, because the P55L and S55L seismographs saturated (clipped) the magnetic-tape recorders. All channels were saturating the recorders for the first 13 to 15 min of the LR₁ Rayleigh wave signal. The majority of the energy in the S wave group and in SSS was S_y motion, while SS contained a significant amount of S_H motion. This separation of S_y and S_H polarizations is possible with the use of the S+P55L and S-P325L traces. Several other body phase arrivals are present in the seismogram between S and LR₁, but they have not been indicated for clarity. The LR₁ short-arc Rayleigh wave is recorded with a beginning group velocity of about 4.15 km/sec. The enhanced signal is so large on the S+P55L sum trace that it has disappeared from the illustration until about 1043. The LR₂ long-arc Rayleigh wave begins at about 1138 and is enhanced on the S-P55L difference trace. The cancellation of this wave is almost complete on the S+P55L trace. Starting at about 1252, the LR₃ short-arc plus one revolution Rayleigh wave is enhanced on the S+P55L sum trace and is cancelled on the difference trace. The fact that the successive passes of the Rayleigh waves (LR₁, LR₂, LR₃) are enhanced first on either the sum or the difference trace of a pair of traces in the directional array and the next pass is on the opposite trace facilitates the identification of the direction of travel and the association of the Rayleigh wave with the earlier event rather than from a new event.

The enhancement of the Rayleigh waves from an earthquake in the Molucca Sea is illustrated in figure 164. The NOS PDE data are: 0 = 0702:46.6, 3 December 1970, 1.1S, 126.8E, h = 26 km, m_b = 5.8, M_S = 5.5. This epicenter is



*PHASE SHIFTED

1043



CC-AZ
RUN 246
3 SEPT 1970

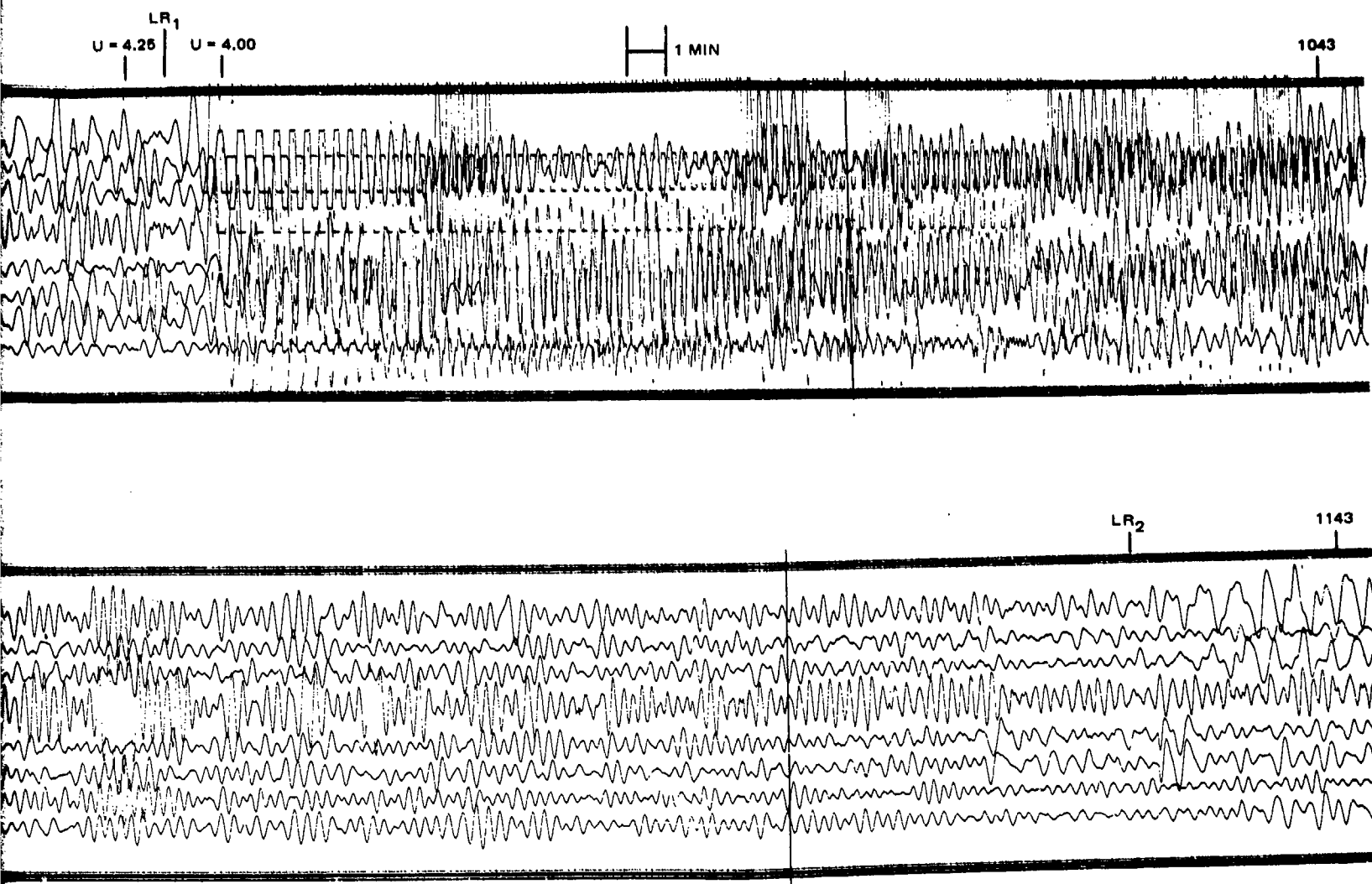


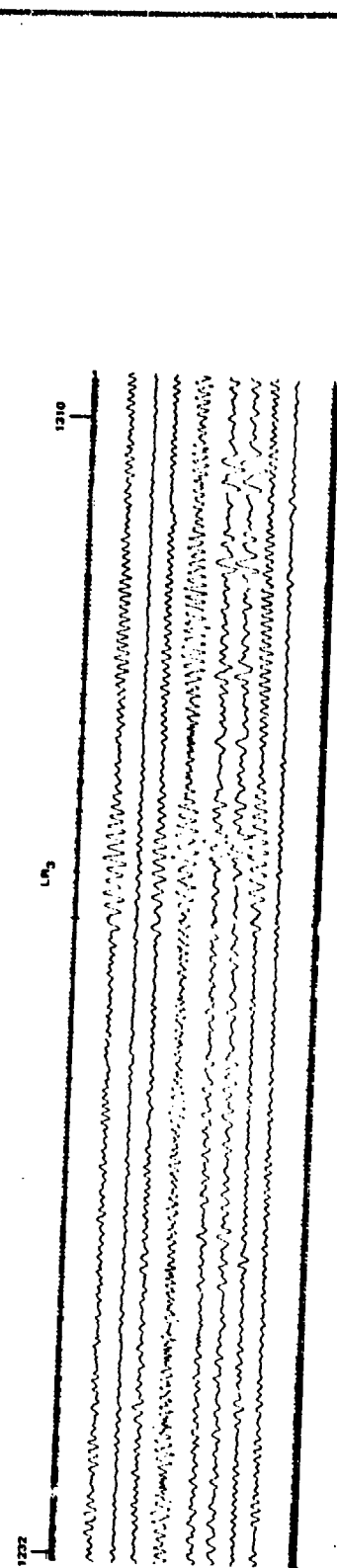
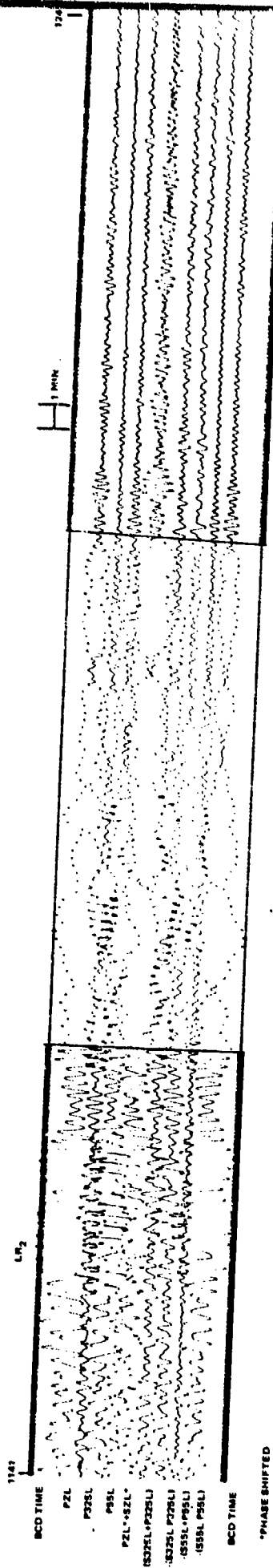
Figure 163a. Enhancement of seismic waves from several earthquakes in the New Hebrides Islands. NOS PDE data: (1) 0=0932:23.0, 16.9S, 167.8E, h=44 km, $m_b=5.5$, $M_s=5.9$, $\Delta=91.5$ deg, azimuth=250.9 deg, (2) 0=0948:02.9, 17.0S, 167.8E, h=34 km, $m_b=4.8$, $\Delta=91.5$ deg, azimuth=250.8 deg, (3) 0=0959:04.1, 17.0S, 167.9E, h=33 km, no m_b given, $\Delta=91.5$ deg, azimuth=250.7 deg, (4) 0=1034:23.0, 17.0S, 167.8E, h=40 km, $m_b=4.7$, $\Delta=91.5$ deg, azimuth=250.8 deg, (5) 0=1210:23.4, 17.1S, 167.7E, h=21 km, $m_b=4.5$, $\Delta=91.7$ deg, azimuth=250.8 deg

G 6704

2 89.1

290

-289/290-



CC-AZ
RUN 246
3 SEPT 1970

XXXXXXXXXXXXXXXXXXXX
XXXXXXXXXXXXXXXXXXXX
See the following pages
for further details
XXXXXXXXXXXXXXXXXXXX

Fig re 163b. Enhancement of seismic waves from several earthquakes in the New Hebrides Islands. NOS PDE data: (1) 0-0932:23.0, 16.9S, 167.8E, h=44 km, $m_b=5.5$, $M_s=5.9$, $\Delta=91.5$ deg, azimuth=250.9 deg, (2) 0-0948:02.9, 17.0S, 167.8E, h=34 km, $m_b=4.8$, $\Delta=91.5$ deg, azimuth=250.8 deg, (3) 0-0959:04.1, 17.0S, 167.9E, h=33 km, no m_b given, $\Delta=91.5$ deg, azimuth=250.7 deg, (4) 0-1034:23.0, 17.0S, 167.8E, h=40 km, $m_b=4.7$, $\Delta=91.5$ deg, azimuth=250.8 deg, (5) 0-1210:23.4, 17.1S, 167.7E, h=21 km, $m_b=4.5$, $\Delta=91.7$ deg, azimuth=250.8 deg

291.

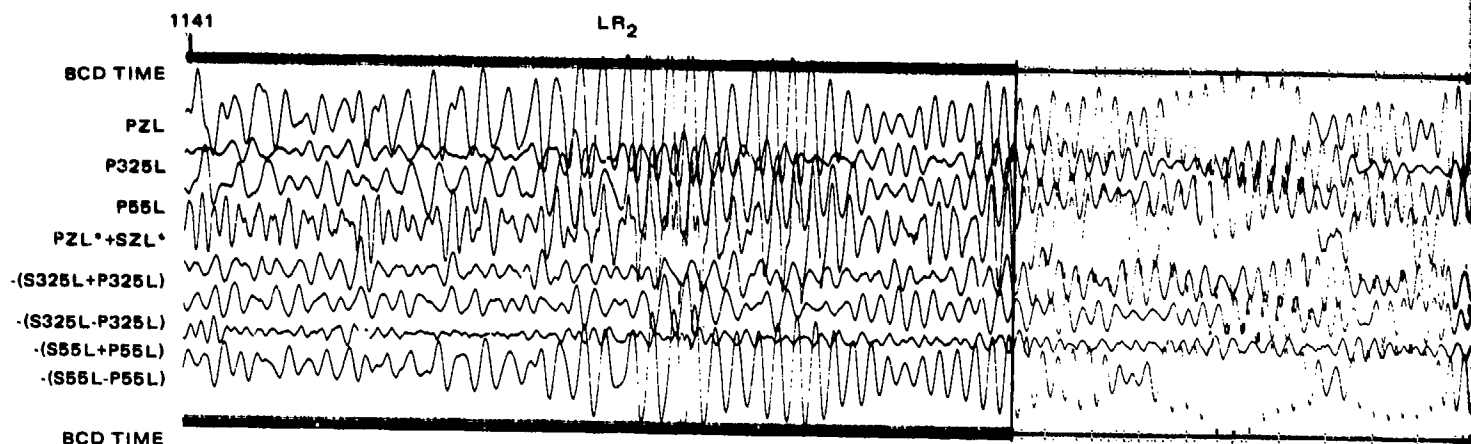
291.1

291

-291/292-

CC-AZ

TR 72-3



*PHASE SHIFTED

1232

QC-AZ
RUN 246
3 SEPT 1970

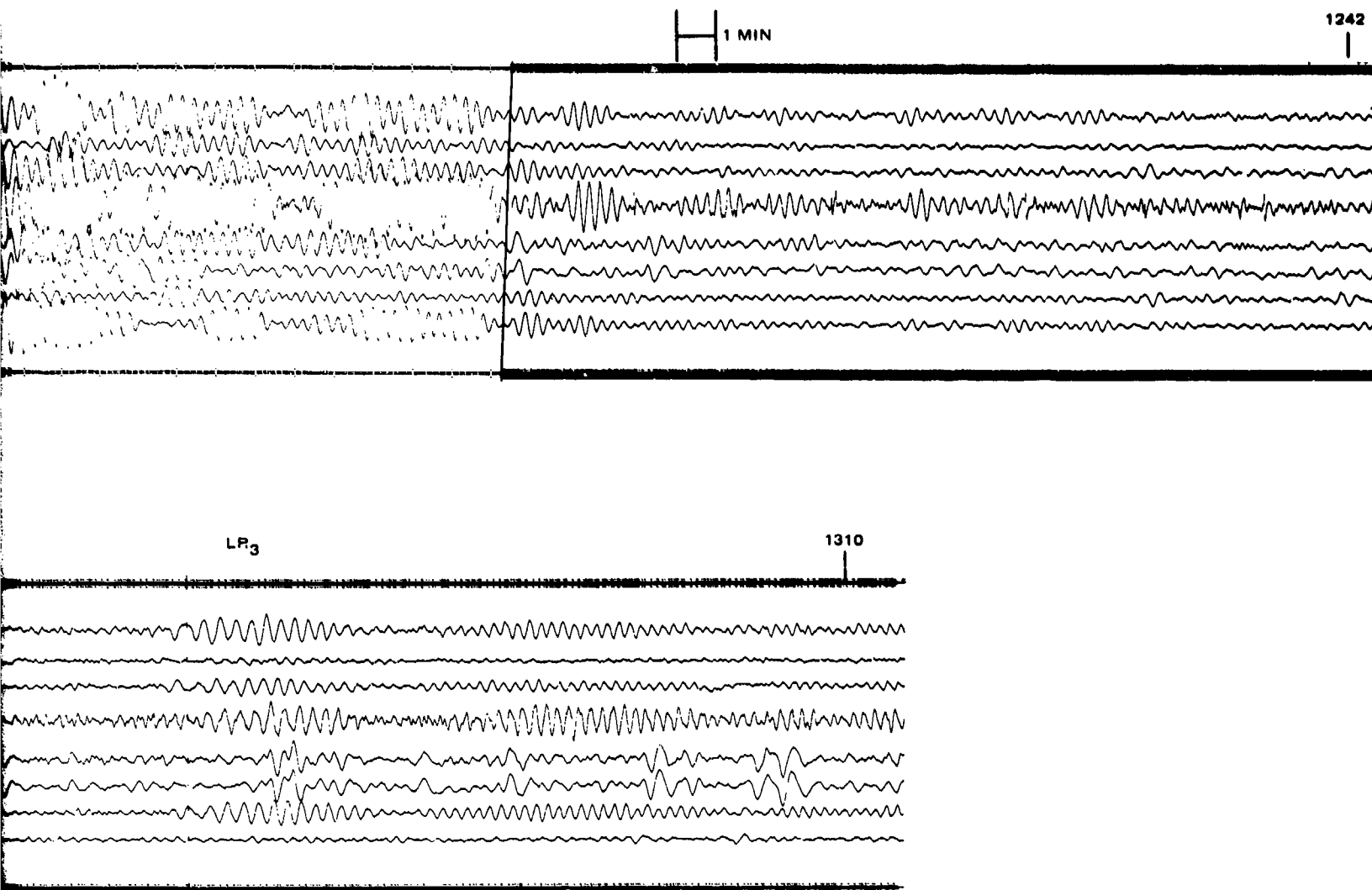


Figure 163b. Enhancement of seismic waves from several earthquakes in the New Hebrides Islands. NOS PDE data: (1) 0=0932:23.0, 16.9S, 167.8E, $h=44$ km, $m_b=5.5$, $M_s=5.9$, $\Delta=91.5$ deg, azimuth=250.9 deg, (2) 0=0948:02.9, 17.0S, 167.8E, $h=34$ km, $m_b=4.8$, $\Delta=91.5$ deg, azimuth=250.8 deg, (3) 0=0959:04.1, 17.0S, 167.9E, $h=33$ km, no m_b given, $\Delta=91.5$ deg, azimuth=250.7 deg, (4) 0=1034:23.0, 17.0S, 167.8E, $h=40$ km, $m_b=4.7$, $\Delta=91.5$ deg, azimuth=250.8 deg, (5) 0=1210:23.4, 17.1S, 167.7E, $h=21$ km, $m_b=4.5$, $\Delta=91.7$ deg, azimuth=250.8 deg

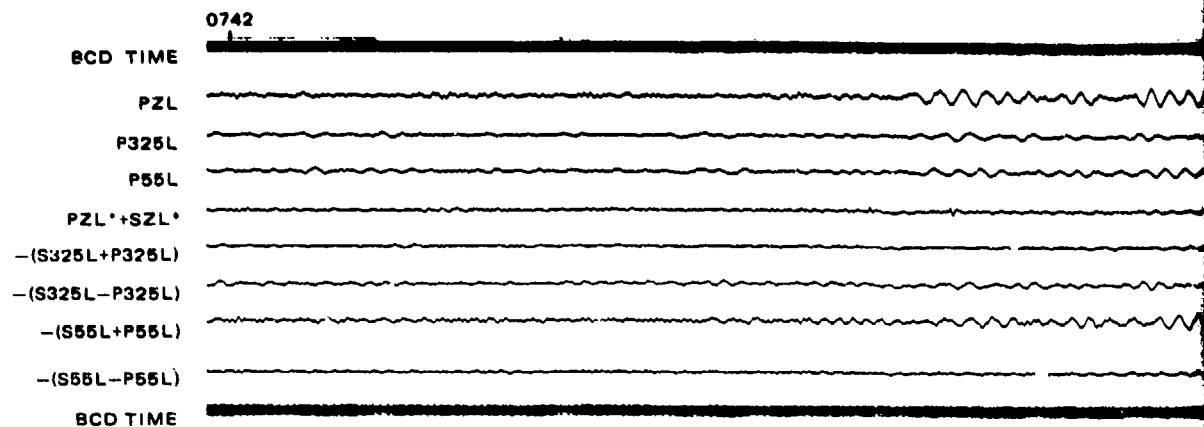
291.1

292

-291/292-

G 6705

TR 72-3



*PHASE SHIFTED

QC-AZ
RUN 337
3 DEC 1970

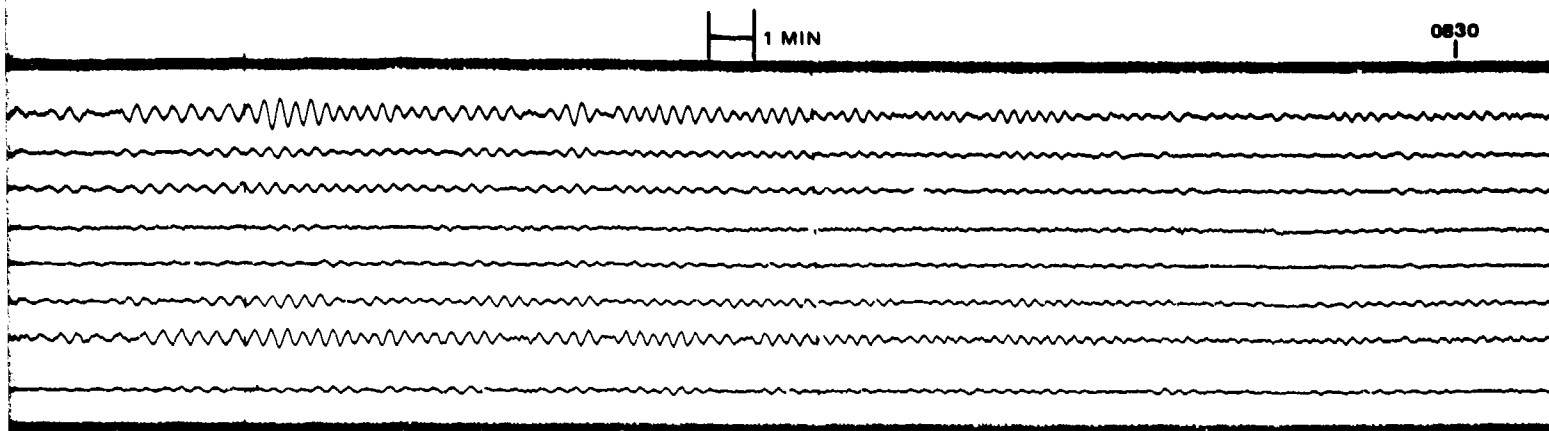


Figure 164. Enhancement of waves from an earthquake in the Molucca Sea. NOS PDE data: $\phi = 0702:46.6$, $1.1S$, $126.8E$, $h = 26$ km, $m_b = 5.8$, $M_S = 5.5$, $\Delta = 116.7$ deg, azimuth = 287.5 deg

G 6706

293.1

294

-293/294-

at an epicentral distance of 116.7 deg and at an azimuth of 287.5 deg from QC-AZ. The Rayleigh wave is enhanced on the S+P55L and the S-P325L traces. The recordings indicate the wave is traveling toward an azimuth between 55 deg and 145 deg, with the direction of travel 35 to 40 deg off the 55 deg component or toward an azimuth of 80 to 95 deg. The great circle azimuth would indicate a direction of travel of 107.5 deg, suggesting lateral refraction.

The enhancement of earthquake waves traveling in the opposite azimuths of 319.2 deg and 122.5 deg is illustrated in figure 165. The NOS PDE data on these two earthquakes are: part (a) off the coast of Kamchatka, 0 = 0016:25.9, 3 October 1970, 55.2N, 163.2E, h = 31 km, m_b = 5.2; part (b) near the west coast of Colombia, 0 = 1416:55.3, 3 October 1970, 6.4N, 77.5W, h = 25 km, m_b = 5.2, M_s = 5.1. These two epicenters are at epicentral distances of 60.9 deg and 41.4 deg and at azimuths of 319.2 deg and 122.5 deg, respectively, from QC-AZ. The earthquake waves recorded in the (a) part of figure 165 are expected to travel along the great circle path toward an azimuth of 139.2 deg. As expected, P, S_v , and Rayleigh waves are enhanced on the S-P325L trace; and S_H and Love waves are recorded on the P55L inertial seismogram with the S55L strain seismogram not recording much motion since this azimuth is close to a null for all wave types. (Compare the S+P55L and the S-P55L traces.) The PKiKP phase is enhanced on the PZL*+SZL* trace. The earthquake waves recorded in the (b) part of figure 165 are expected to travel in the opposite direction along the great circle path toward an azimuth of 302.5 deg. The P, S_v , and Rayleigh waves are enhanced on the S+P325L trace. Since these waves are traveling 21.5 deg off perfect alignment with the instruments, S_H and Love waves are enhanced on the S-P55L trace. From a comparison of the S+P325L and S-P55L traces, it is seen that for this earthquake the S wave is about 60 percent S_v and 40 percent S_H , the SS wave is absent, and the SSS wave is about 40 percent S_v and 60 percent S_H . The recordings in figure 165 illustrate that the theory concerning the strain seismographs and the combined strain/inertial seismographs can be applied at QC-AZ in all azimuths.

A recording of enhanced waves from an earthquake in Northern Colombia is shown in figure 166. The NOS PDE data are: 0 = 0459:53.4, 3 December 1970, 7.4N, 76.1W, h = 38 km, m_b = 5.7, M_s = 5.5. This epicenter is at an epicentral distance of 41.7 deg and at an azimuth of 120.0 deg from QC-AZ. The enhancement of waves in the figure is similar to that illustrated in other figures. Note that the motion recorded on the PZL*+SZL* trace following P, PPP, and S is attenuated from the signals recorded on the PZL inertial seismogram.

Seismic waves from an earthquake in the Greenland Sea are enhanced in figure 167. This figure illustrates the enhancement of Love waves and the separation of Love and Rayleigh waves by the sum and difference of two orthogonal strain seismographs. The individual seismograms are shown in the (a) part of the figure. The directional array is shown in the (b) part. The (c) part has the sum and difference of the two strain seismographs. The NOS PDE data on the earthquake are: 0 = 2053:32.4, 26 October 1970, 79.8N, 2.7E, h = 32 km, m_b = 5.6, M_s = 5.7. This epicenter is at a distance of 61.7 deg and at an azimuth of 10.6 deg from QC-AZ. This great circle azimuth is 44.4 deg off the direction of the 55 deg instruments and 45.6 deg off the direction of the 325 deg instruments. The reader can notice that the largest peaks of the Love wave (LQ) on the inertial seismograms are clipped at group velocities near 3.5 km/sec. These clipped peaks have introduced distortion into the corresponding portion of the directional array. The directional array traces S-P325L and S-P55L in

figure 167 part (b) are seen to produce almost equal enhancement of the Love wave and the Rayleigh wave with no separation of the two wave types. In accord with the theory in section 9.1.4, the difference between the two orthogonal strain seismographs enhances the Love wave and at this azimuth (45 deg difference) cancels the Rayleigh wave. The sum of the two orthogonal strain seismographs cancels the Love wave and enhances the Rayleigh wave at any azimuth, as derived in section 9.1.5. The enhancement and separation of the two wave types is illustrated in figure 167 (c). A complete dispersed wave train from 60 sec down to 20 sec is seen for the Love wave. This is in contrast to the almost complete lack of 45 to 60 sec Rayleigh waves, as discussed later in section 10.4.

The enhancement of seismic waves from an earthquake on the Central Mid-Atlantic Ridge is illustrated in figure 168. This earthquake was at an epicentral distance of 72.5 deg and at an azimuth of 92.2 deg from QC-AZ. This azimuth is to the southeast, making a 40 and 50 deg angle with the instrument directions. Thus, this earthquake will be recorded similar to the Greenland Sea event recordings in figure 167 except that the signal will be on different channels of the directional array. The seismograms in figure 168 confirm this similarity with the Love and Rayleigh waves enhanced but not separated on the S+P325L and S-P55L traces. The NOS PDE data for this earthquake are: $O = 1550:05.5$, $7.7N$, $37.6W$, $h = N$, $m_b = 5.3$, $M_s = 5.5$.

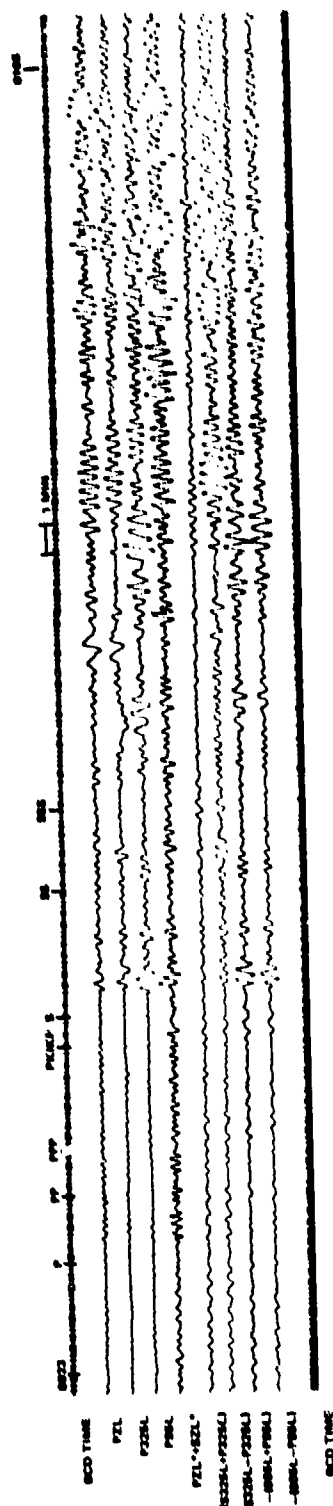
On 20 May 1970, two earthquakes occurred in opposite azimuths from QC-AZ. The arrival times of many of the elastic waves overlapped. The NOS PDE data on the two events are:

Event 1: $O = 2003:42.2$, $15.9S$, $28.3W$, South Sandwich Island region,
 $h = 70$ km, $m_b = 5.0$.

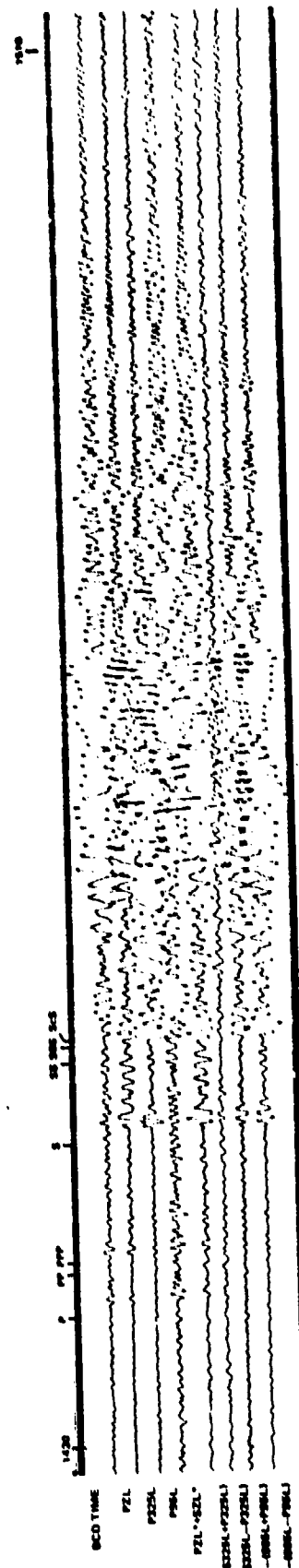
Event 2: $O = 2030:54.7$, $51.5N$, $178.5W$, Andreanof Islands, Aleutian Is.,
 $h = 48$ km, $m_b = 5.7$.

These epicenters are at an epicentral distance of 113.5 deg and 50.6 deg and at an azimuth of 142.5 deg and 312.0 deg, respectively, from QC-AZ. Figure 169 shows the great circle paths from the two epicenters to QC-AZ. Note that the path from event 2 is tangent to the Aleutian Island Arc at the beginning of its path. This passage through the anomalous island arc structure undoubtedly affected the amplitude and direction of travel of the seismic waves received at QC-AZ.

The enhancement of seismic waves from these events is shown in figure 170. Five minute time marks are identified above the traces. There is some overlap between lines in the figure. The first four seismic traces are related to the 325 deg azimuth, with the sum of the strain and pendulum seismographs on top, then the strain, the pendulum, and the difference seismographs. The next four seismic traces are a similar arrangement for the 55 deg azimuth. The last three seismic traces are the vertical pendulum, the sum of the two orthogonal horizontal strain, and the difference between the orthogonal horizontal strain seismographs. The arrival times of many earthquake phases are enhanced considerably, with wave identification clarified, and in many cases the time break are sharpened for accurate timing. Earthquake phases are identified in the figure with the phases from event 1 on the upper line and from event 2 on the lower line.



a. Azimuth 319.2



b. Azimuth 122.5

XXXXXXXXXXXXXXXXXXXX
See the following page
for continuation

Figure 165. Enhancement of seismic wave from two earthquakes in opposite azimuth from PNE data: (a) off the coast of Lima, 0 = 0016:25.9, 55.2N, 163.2E, h = 31 km, $M_0 = 5.2$, $\Delta = 60.9$ deg, azimuth = 319.2 deg, (b) near west coast of Colombia, 0 = 1416:55.3, 6.4N, 77.5W, h = 25 km, $M_0 = 5.1$, $\Delta = 41.4$ deg, azimuth = 122.5

297.

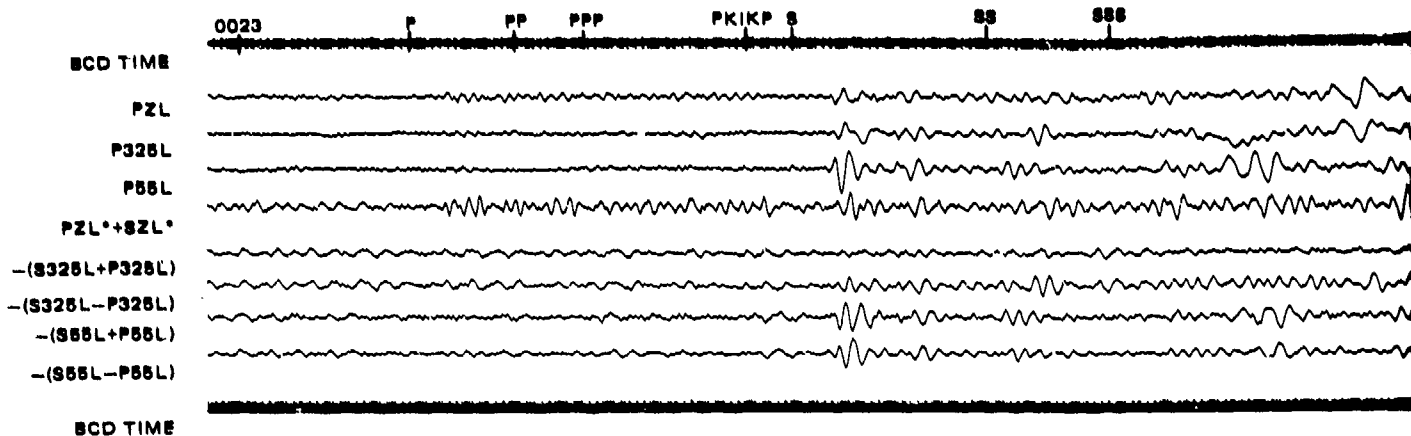
297.1

297.2

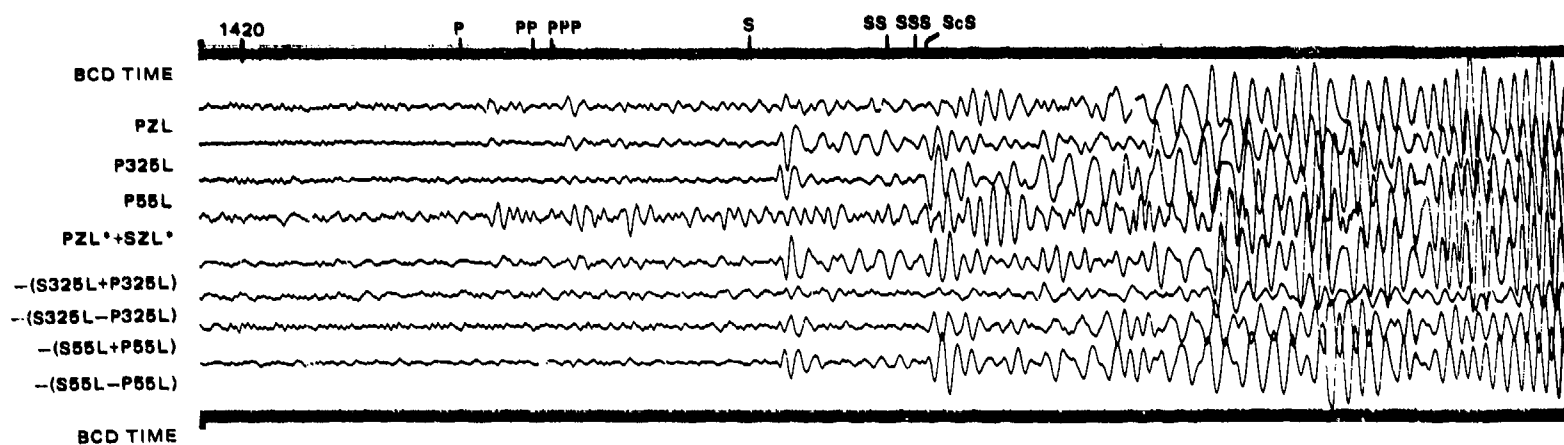
TR

*PHASE SHIFTED

QC-AZ
RUN 276
3 OCT 1979



a. Azimuth 319.2



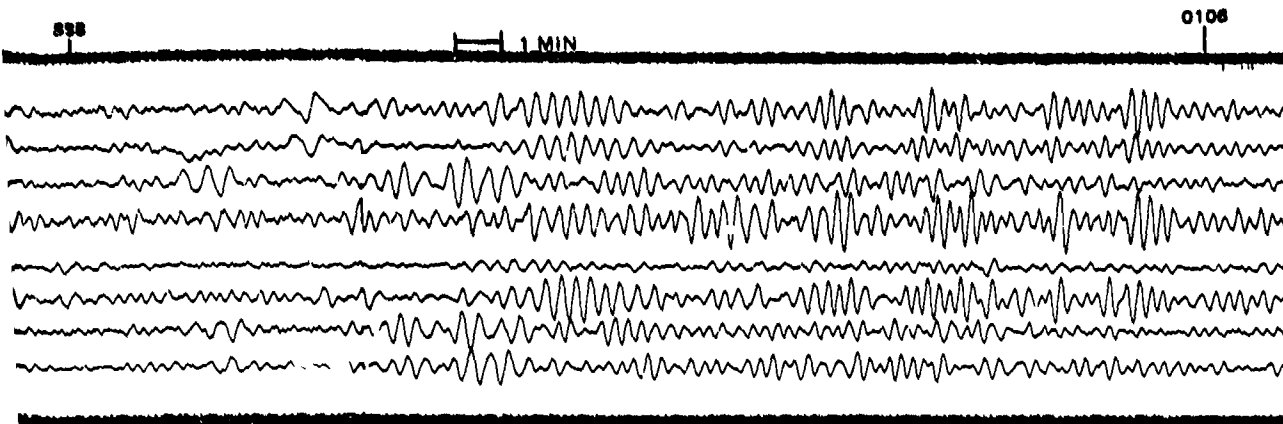
*PHASE SHIFTED

b. Azimuth 122.5

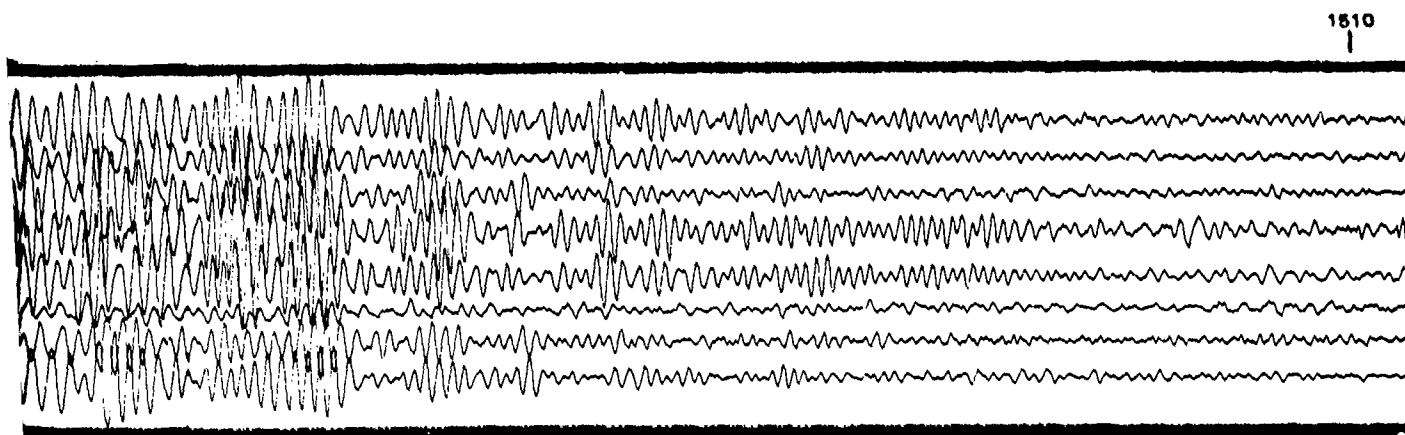
QC-AZ
RUN 276
3 OCT 1970

297.

297.1



Azimuth 319.2



Azimuth 122.5

Figure 165. Enhancement of seismic waves from two earthquakes in opposite azimuths. NOS PDE data: (a) off the coast of Kamchatka, $O = 0016:25.9$, $55.2N$, $163.2E$, $h = 31$ km, $m_b = 5.2$, $\Delta = 60.9$ deg, azimuth = 319.2 deg, (b) near west coast of Colombia, $O = 1416:55.3$, $6.4N$, $77.5W$, $h = 25$ km, $m_b = 5.2$, $M_S = 5.1$, $\Delta = 41.4$ deg, azimuth = 122.5 deg

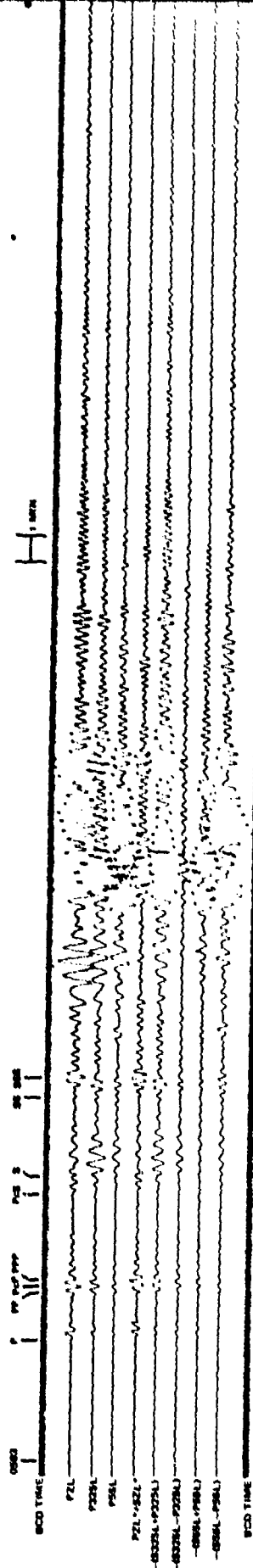
G 6707

278

-297/298-

TR 72-3

297.1



"PAUSE SHIFTED

OC/AZ
NUM 337
3 DEC 1978

XXXXXXXXXXXXXXXXXXXX
See the following pages
for greater detail.
XXXXXXXXXXXXXXXXXXXX

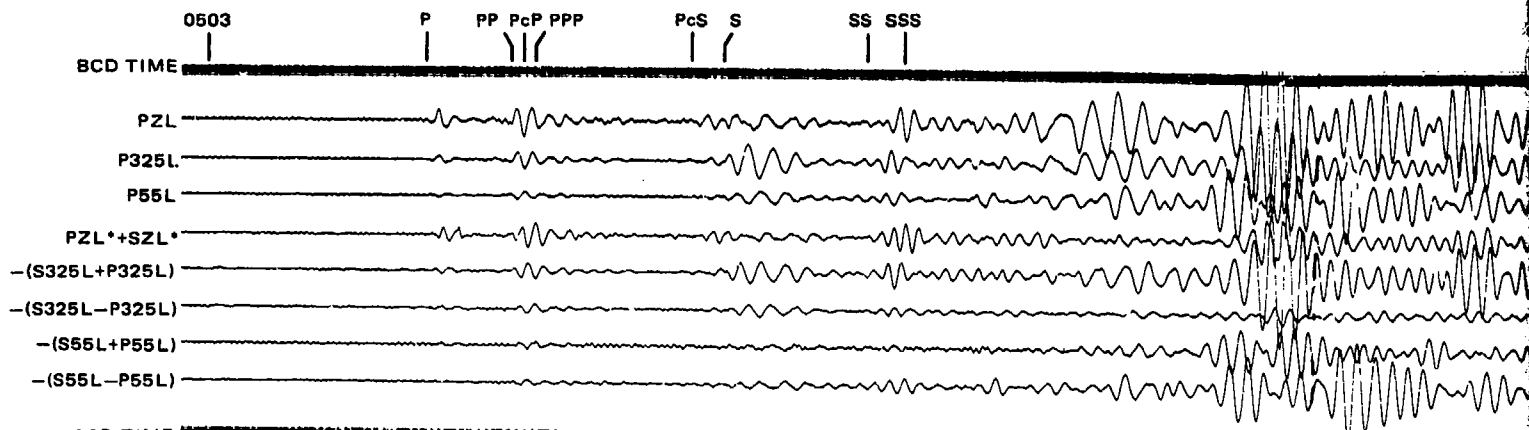
Figure 166. Enhancement of seismic waves from an earthquake in Northern Colombia. NOS PDE data: $\theta = 0459:53.4$, 7.45 , 76.11 , $h = 38$ km, $m_b = 5.7$, $M_s = 5.5$, $\delta = 41.7$ deg, azimuth = 120.0 deg

299.1

299.

-299/300-

TR 72



*PHASE SHIFTED

QC-AZ
 RUN 337
 3 DEC 1970

299.

299.1

H 1 MIN

0600

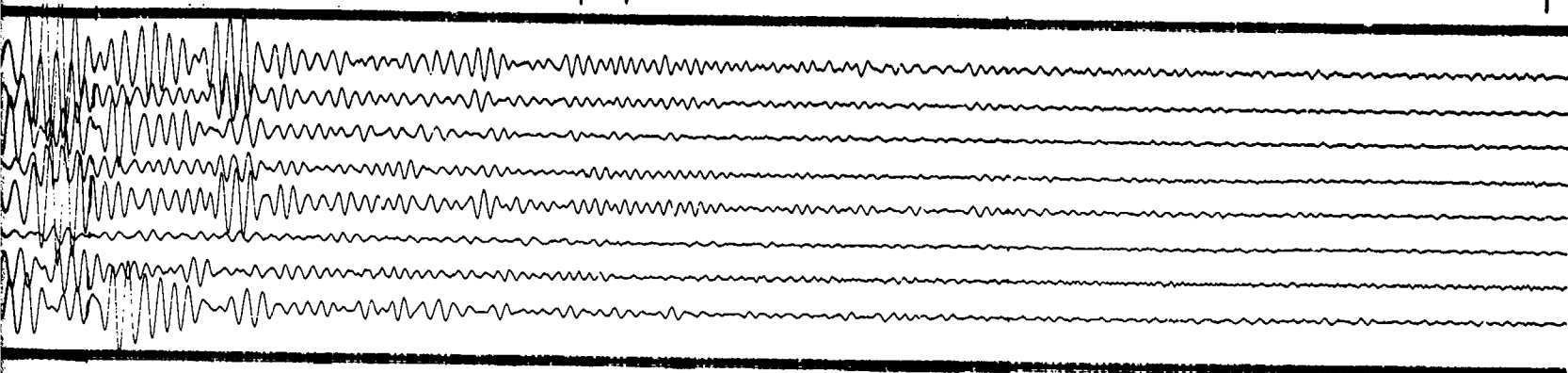


Figure 166. Enhancement of seismic waves from an earthquake in Northern Colombia.
NOS PDE data: 0 = 0459:53.4, 7.4N, 76.1W,
h = 38 km, $m_b = 5.7$, $M_s = 5.5$, $\Delta = 41.7$ deg,
azimuth = 120.0 deg

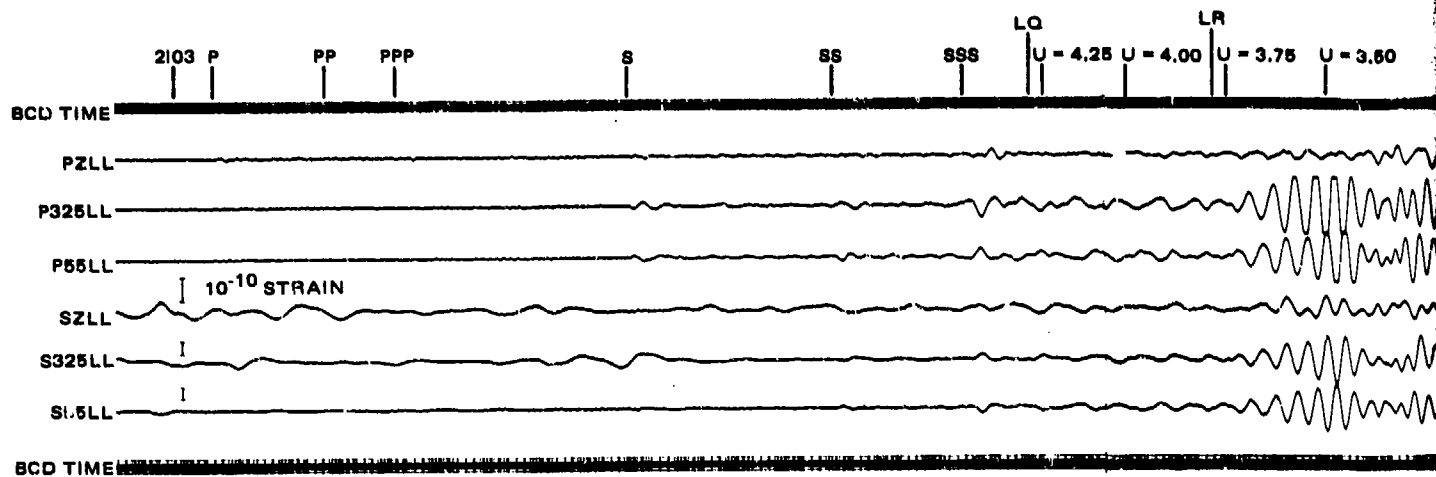
G 6708

299.1

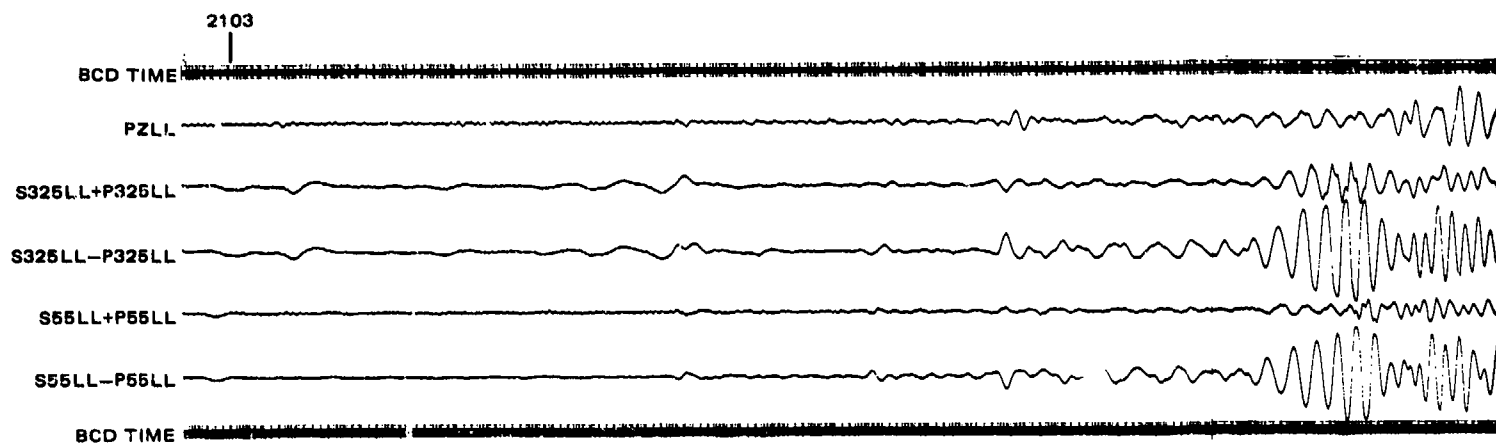
300

-299/300-

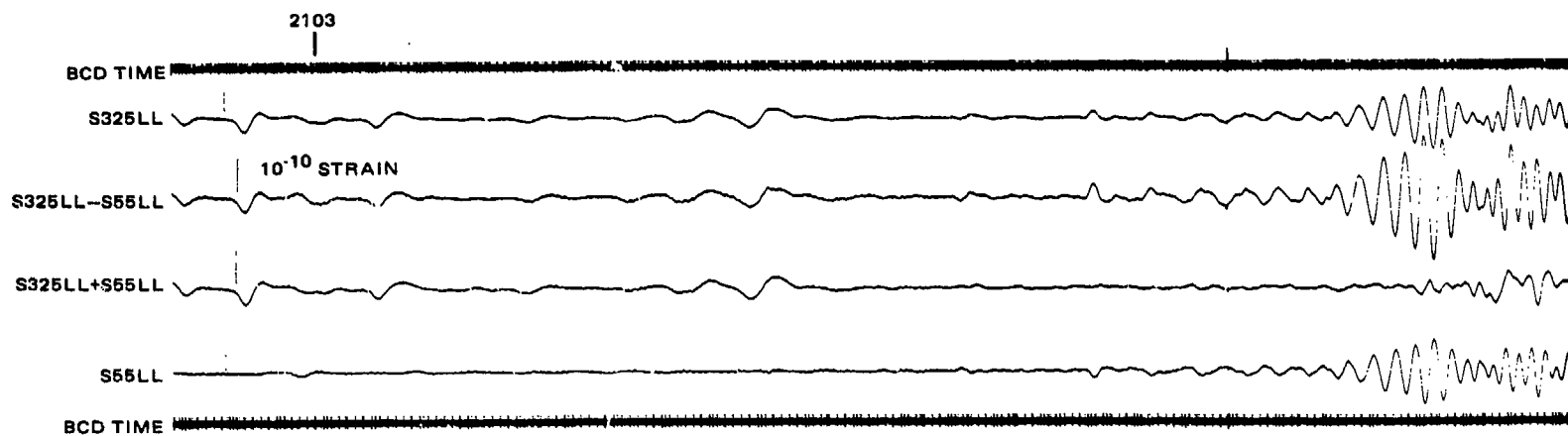
TR 72-3



a. Individual



b. Direction

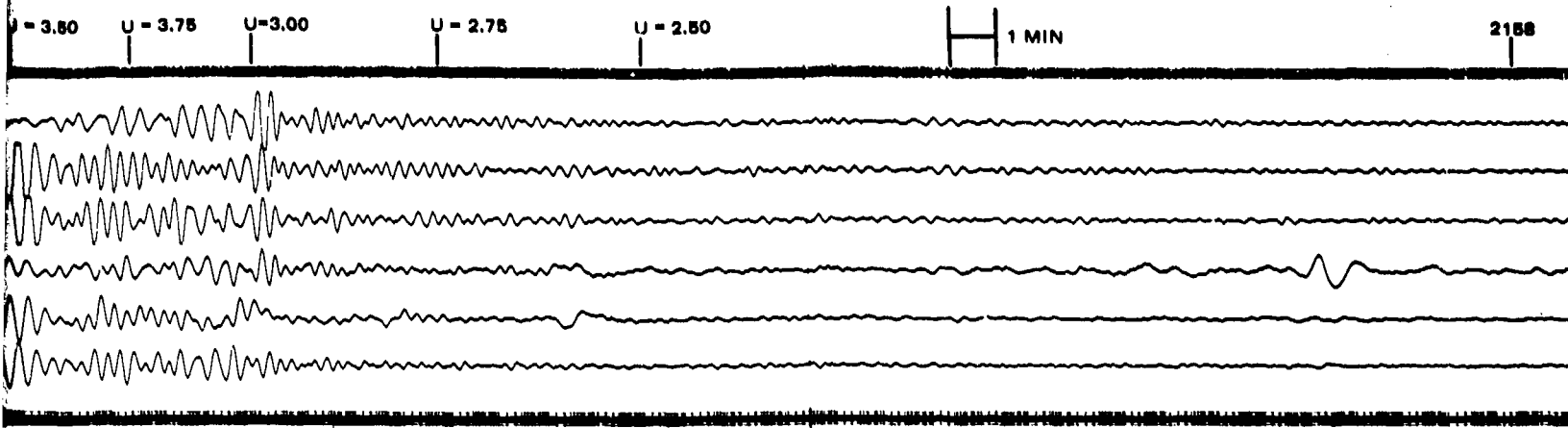


c. Combined strain

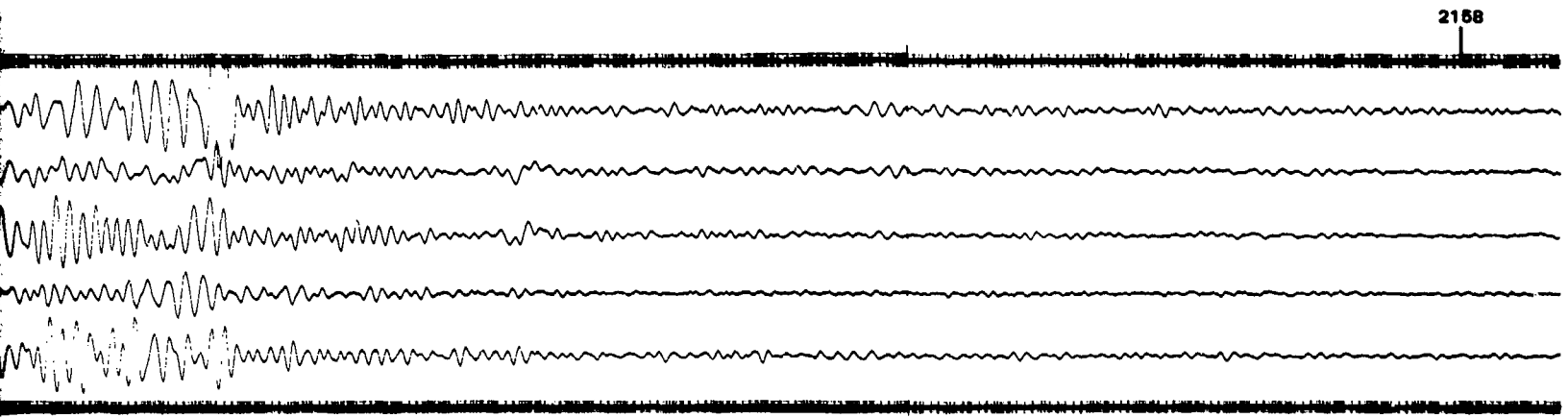
QC-AZ
RUN 299
26 OCT 1970

301.

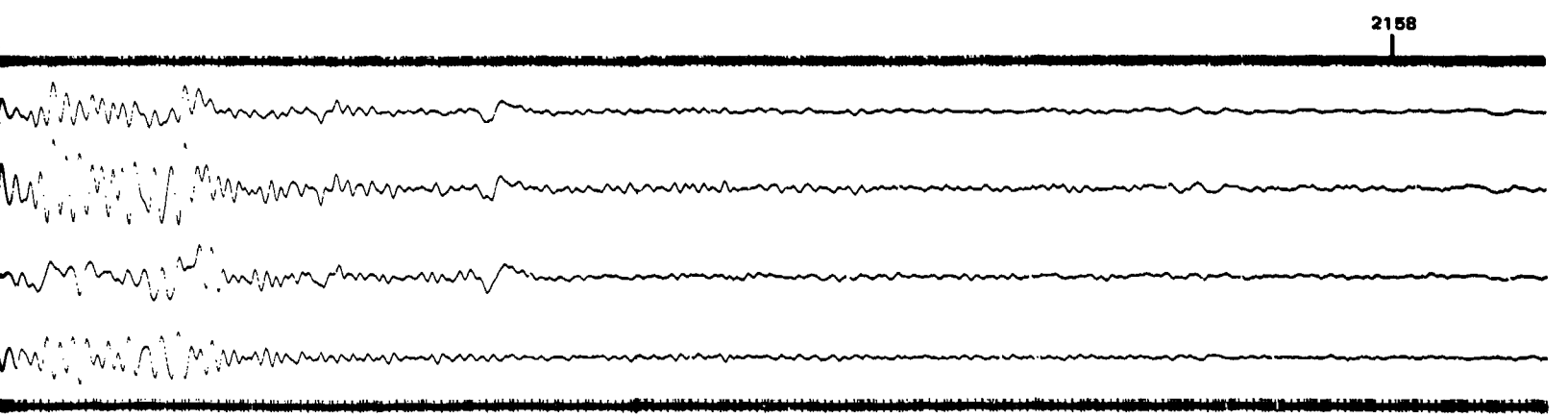
301.1



Individual seismograms



Directional array

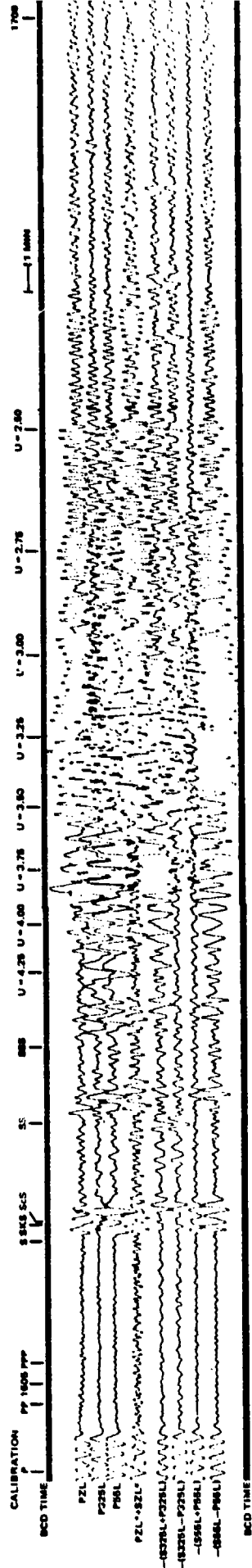


Combined strain seismograms

Figure 167. Enhancement of seismic waves from an earthquake in the Greenland Sea. NOS PDE data: O=2053:32.4, 79.8N, 2.7E, h=32 km, $m_b=5.6$, $M_s=5.7$, $\Delta=61.7$ deg, azimuth=10.6 deg, (a) individual seismograms, (b) directional array (c) combined strain seismographs to separate LQ and LR

301.1

G 6709



*PHASE SHIFTED

QC-AZ
RUN 284
21 OCT 1979

XXXXXXXXXXXXXXXXXXXX
See the following pages
for greater detail.
XXXXXXXXXXXXXXXXXXXX

Figure 168. Enhancement of seismic wave-
from an earthquake on the Central Mid-
Atlantic Ridge. MOS PVE data: 0 =
1550-05.5, 7.7M, 37.6M, h = N, mb = 5.3,
Ms = 5.5, Δ = 72.5 deg, azimuth = 92.2
deg

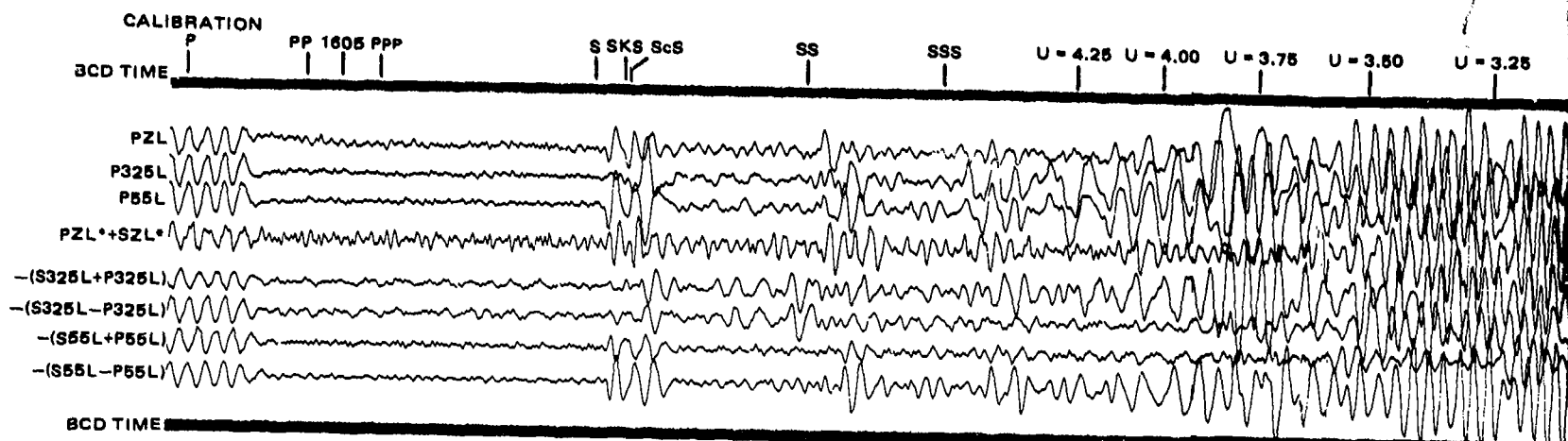
-303/304-

304

303.1

303.

TR 7.



*PHASE SHIFTED

QC-AZ
RUN 294
21 OCT 1970

303.

303.1

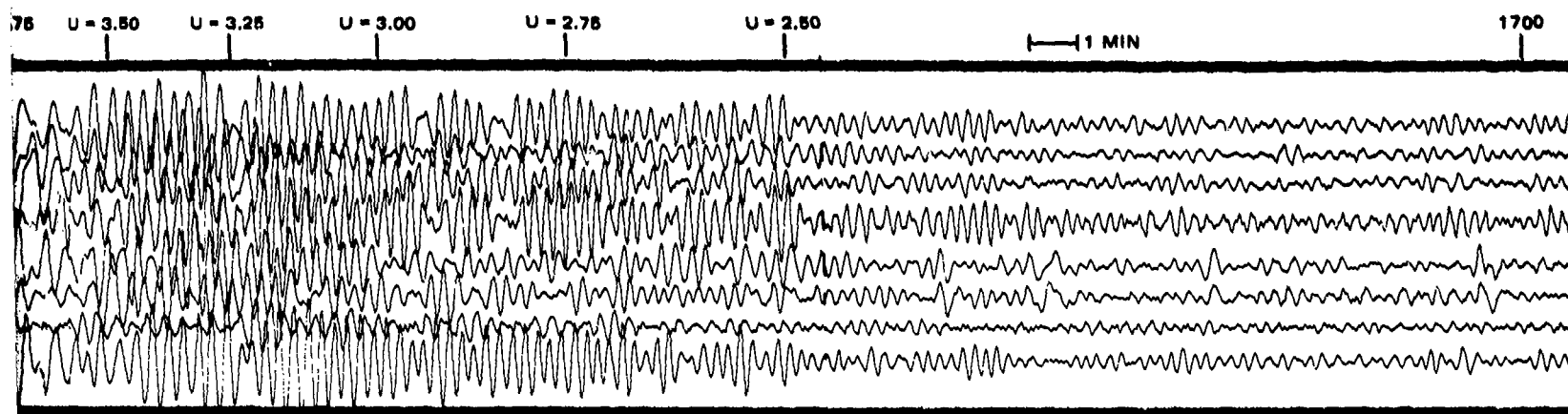


Figure 168. Enhancement of seismic waves from an earthquake on the Central Mid-Atlantic Ridge. NOS PDE data: 0 = 1550:05.5, 7.7N, 37.6W, h = N, $m_b = 5.3$, $M_S = 5.5$, $\Delta = 72.5$ deg, azimuth = 92.2 deg

G 6710

303.1

304

-303/304-

TR 72-3

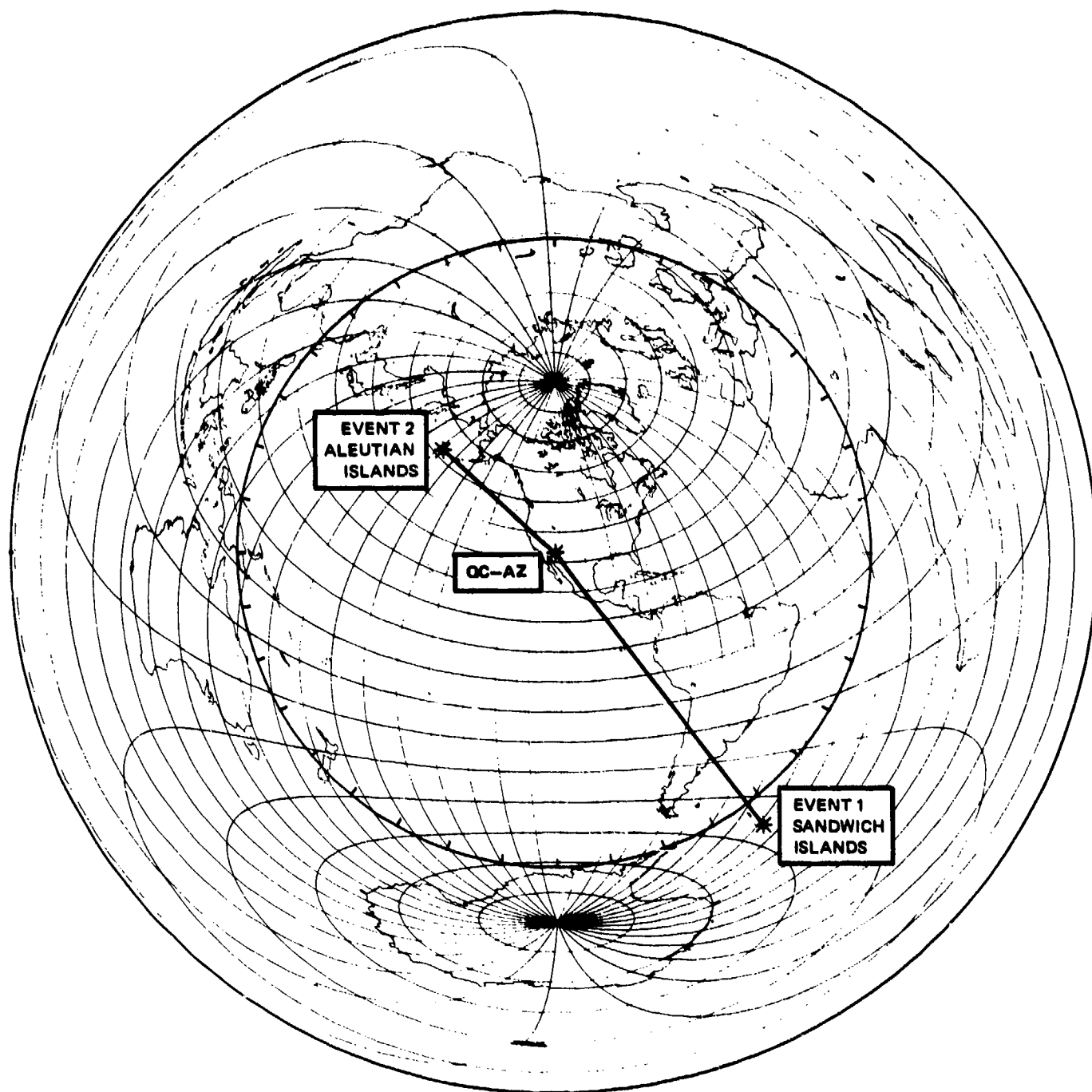


Figure 169. Great circle paths from two earthquakes to QC-AZ

G 6009

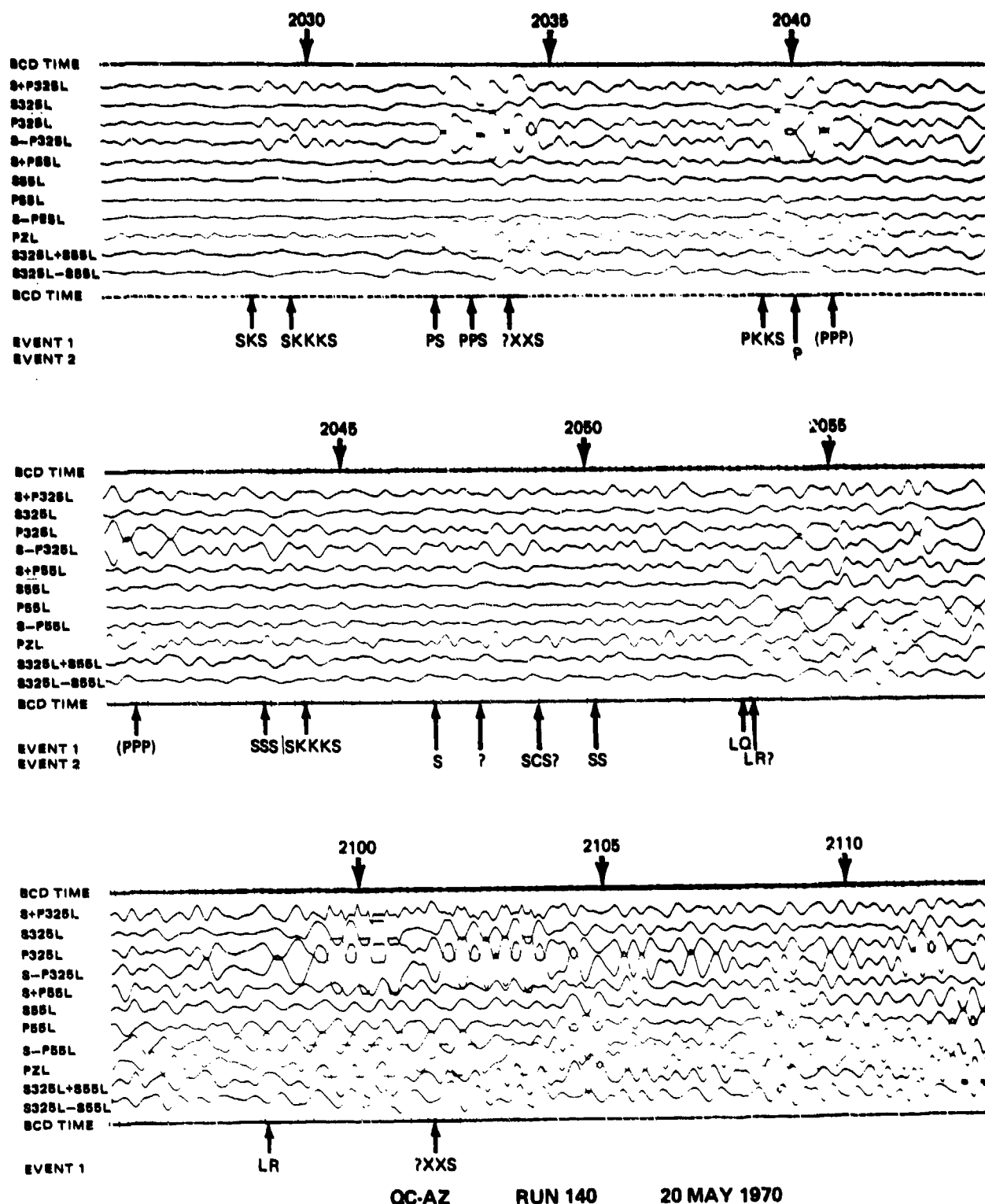


Figure 170. Magnetic tape playback of arrivals from interfering events. Event 1: $\Delta = 2003:42.2$, south Sandwich Island region, $h = 70$ km, $m_b = 6.0$, $\Delta = 113.5$ deg, azimuth = 142.5 deg; event 2: $\Delta = 2030:54.7$, Andreanoff Island, $h = 48$, $m_b = 5.7$, $\Delta = 50.6$ deg, azimuth = 312.0 deg

G 6011

All the arrivals from event 2 are smaller than those from event 1. Several arrivals are particularly interesting. The time break is sharpened for PS and PPS on S-P325L at 2032:37 and 2033:23. An unidentified phase arrival is detected on the PZL and S-P325L at 2034:08. The SSS and SKKKS arrivals are detected on S-P325L and can be timed at 2043:24 and 2044:18. The arrival of the LQ Love wave from event 1 is enhanced on the S-P55L at about 2053. The possible arrival of the LRI Rayleigh wave from event 2 at about 2053 is indicated by possible signals on S+P325L, S+P55L (?), PZL, and S325L+S55L. The LRI Rayleigh wave from event 1 at 2058 is enhanced on the S-P325L and is cancelled on the S+P325L, even with the magnetic tape recorder clipping. Many body phases are detected as arriving after the times for presently tabled phases. These phases are probably either (a) multiple core reflections, (b) second reflected phases arriving by the long arc, and/or (c) thrice reflected phases arriving by the short or long arc. Some of these body phase arrivals are:

<u>Suspected type of arrival</u>	<u>Nearest minute</u>	<u>Channel detecting phase</u>
P	2101	PZL, S325L, S-P325L?
S	2101	S325L-S55L, S-P325L?
P or S?	2103	PZL, S325L+S55L S325L-S55L, S-P325L
P	2104	S-P325L, S-P55L S325L+S55L, PZL
P or S?	2105	PZL, S-P325L, S+P55L S325L+S55L, S325L-S55L
P or S?	2108	S-P55L, S325L+S55L, PZL
P or S?	2109	PZL, S-P325L, S-P55L S325L-S55L

The last figure in this section presents some interesting observations of dispersed trapped S_V and S_H waves propagated in the crust and the lid of the upper mantle from the Gulf of California to QC-AZ. The recordings of seismic waves on 4 October 1970, from five foreshocks and an $m_b = 5.0$ earthquake, are illustrated in figure 171. Three of these events were on the NOS PDE list, and the epicenter data for them are (1) $0 = 0637:31.5$, $30.8N$, $113.7W$, $h = N$, $m_b = 4.0$; (3) $0 = 0721:18.4$, $30.0N$, $113.9W$, $h = N$, $m_b = 4.0$; and (6) $0 = 1739:45.4$, $30.6N$, $113.6W$, $h = N$, $m_b = 5.0$. These epicenters are at near-regional distances of 3.0 deg, 3.7 deg, and 3.1 deg, and at azimuths of 217.0 deg, 211.9 deg, and 213.5 deg, respectively, from QC-AZ. The other three earthquakes were not listed by NOS. The approximate Pg arrival times for these events were (2) 0707:12, (4) 1659:25, and (5) 1713:39. The seismic waves from all six earthquakes were very similar, as can be seen in figure 171. Prior to and during event 4, the SZL strain seismograph was being calibrated. During event 5 and

part of event 6, the S325L strain seismograph was being calibrated. The body waves show clearer on the largest event. The P_g arrival is clear on all events, with the best enhancement on the PZL^*+SZL^* and the $S+P55L$ traces. The core refracted phase $PKKP$ is possibly enhanced on the PZL^*+SZL^* trace about 18 sec after the predicted arrival time, and $PKKS$ is possibly enhanced on the same trace about 55 sec after the predicted arrival time. The phase shifted sum trace PZL^*+SZL^* produced an interesting, enhanced, dispersed wave train that matches the $P325L$ in character. (See event 2 for a clearer trace.) Comparison of the PZL trace with the PZL^*+SZL^* trace is surprising. The PZL seismogram appears unusually small in comparison with the other components. Apparently, the wave as recorded on the PZL has been subjected to some type of interference phenomenon. When the vertical inertial and strain seismograms are phase shifted and summed, the interference phenomenon is counteracted and a more normal appearing wave results. The great circle path from the first event is only 18 deg off the back azimuth of the 55 deg instruments. The enhancement of the main wavelet on the $S+P55L$ trace and cancellation on the $S-P55L$ indicates the wave type to be P , S_v , or Rayleigh. Close inspection of the PZL and $P55L$ individual seismograms for all the events reveals that the two are exactly 180 deg out of phase. Thus, the particle motion is rectilinear, not elliptical, and has a vector in the plane of propagation that has maxima in the directions of up-235 deg azimuth and of down-55 deg azimuth. The direction of travel, the enhancement on the $S+P55L$ trace, and the particle motion leads the senior author to conclude that this motion is S_v energy trapped in the crust and lid of the upper mantle, which extends to depths of about 80 km (Fix, 1969, Herrin, 1971). This wavelet is dispersed from a 16.5 sec period with a group velocity of 3.21 km/sec to a 5 sec period with a group velocity of 1.60 km/sec. The wavelet on the $P325L$ is mostly SH type motion. Since the 325 deg azimuth is almost transverse to the signal, little strain was recorded because 90 deg is a null direction for SH waves. The $S+P325L$ trace is a mirror image of the $S-P325L$ trace, confirming primarily inertial seismograph input and SH motion. This transverse wavelet is dispersed from a 25 sec period with a group velocity of 3.30 km/sec to an 8.5 sec period with a group velocity of 1.68 km/sec. Considering these wavelets in terms of mode theory, they would be considered higher mode Rayleigh waves ($S+P55L$, PZL) and Love waves ($P325L$). Note that if the recorded wavelets are higher mode surface waves, the fundamental surface waves are not apparent. Simon (1968) has also recognized higher mode surface waves from a Gulf of California earthquake. She comments, "Note: Many types of guided waves - several interpretations possible ... Remarkable Love wave dispersion for short distance."

In arriving at the conclusion that the radial and transverse wavelets in figure 171 are higher mode Rayleigh waves (trapped S_v) and Love waves (trapped SH), a very important consideration comes to light. Earthquake signals from the Gulf of California have been used by Savino et al. (1971), and possibly others, in studies of the M_s/m_b discriminant. The Gulf of California earthquakes logically were used because of their proximity to NTS and because of their similar azimuth from NTS and the Gulf of California to Ogdensburg. However, if all the surface waves from the Gulf of California earthquakes that propagate northwardly through the Basin and Range Province are similar to the six whose surface waves are illustrated in figure 171, then erroneous conclusions could be drawn about world-wide fundamental Rayleigh waves and the M_s/m_b discriminant. A similar suite of Gulf of California events at another time had similar signals. Savino et al. (1971) used other western United States

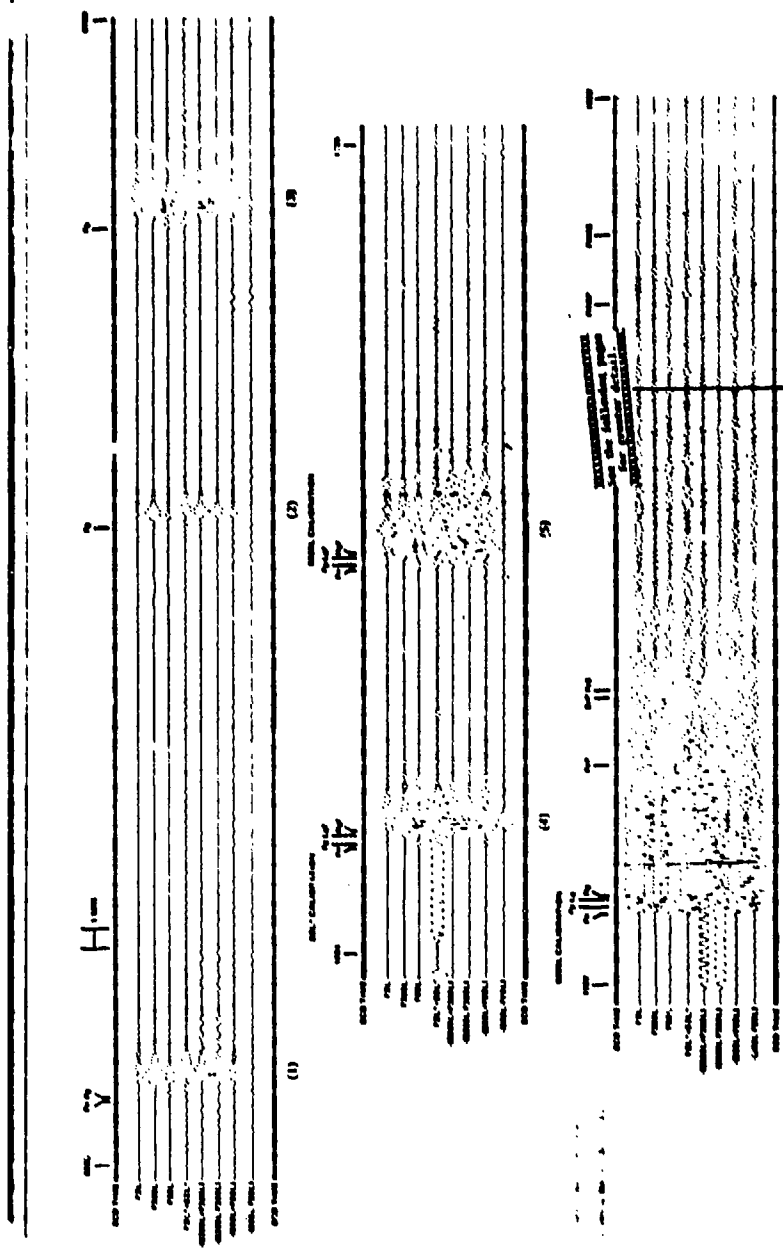
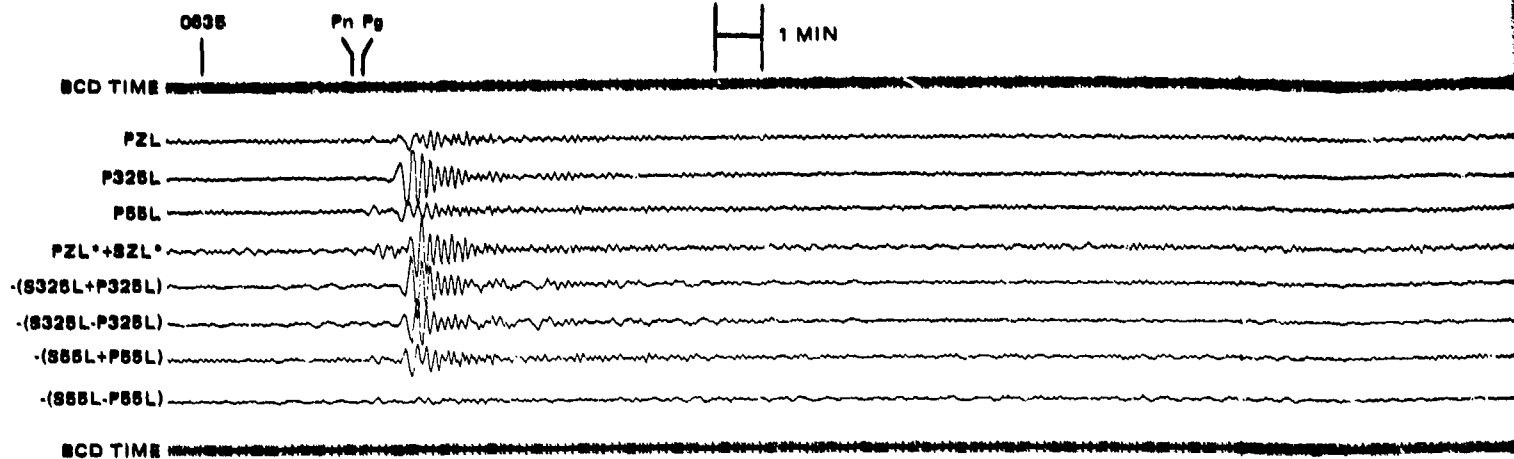
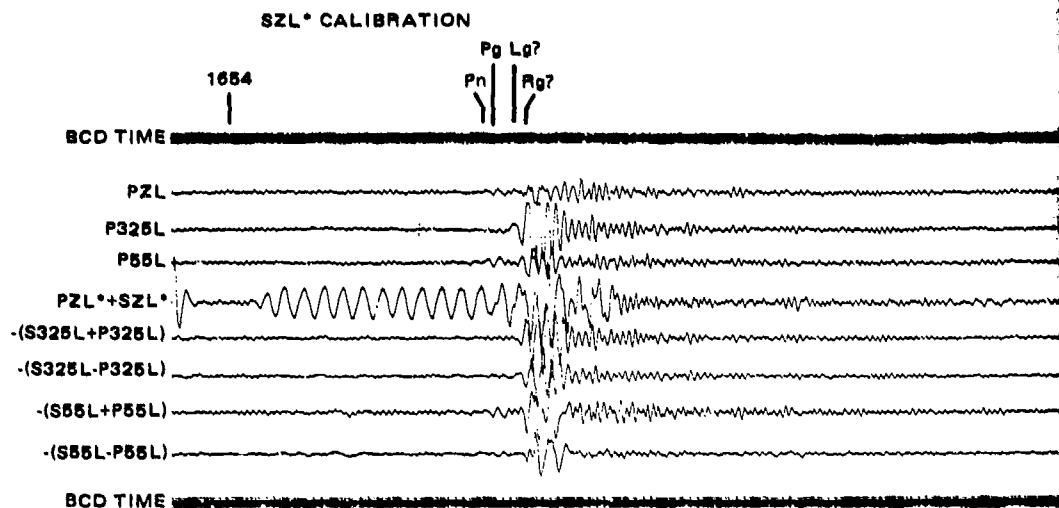


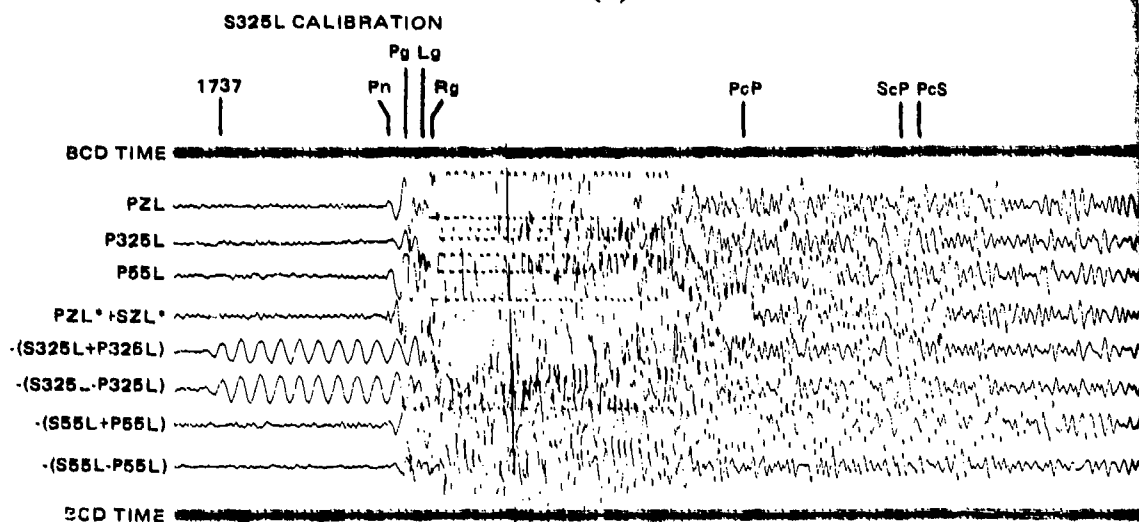
Figure 171. Submarine of atomic type.
 (1) Hull and internal compartments.
 (2) Hull and internal compartments with a different internal layout.
 (3) Hull and internal compartments with a different internal layout.
 (4) Hull and internal compartments with a different internal layout.



(1)



(4)



(6)

*PHASE SHIFTED

QC-AZ
RUN 277
4 OCT 1970

from
listed
(2) P
azimuth
(6) 0

309.

309.1

Pg

Pg

07

(2)

(3)

S325L CALIBRATION

Pg Lg?
Pn Rg?

1735

(5)

ScP PcS

PKKP

PKKS

1822

Figure 171. Enhancement of seismic waves from several earthquakes in the Gulf of California. NOS PDE data and Pg arrival times of unlisted events: (1) 0=0637:31.3, 30.8N, 113.7W, h=N, $m_b=4.0$, $\Delta=3.0$ deg, azimuth=217.0 deg, (2) Pg at 0707:12 not listed on PDE, (3) 0=0721:18.4, 30.0N, 113.9W, h=N, $m_b=4.0$, $\Delta=3.7$ deg, azimuth=211.9 deg, (4) Pg at 1659:25 not listed on PDE, (5) Pg at 1715:39 not listed on PDE, (6) 0=1739:45.4, 30.6N, 113.6W, h=N, $m_b=5.0$, $\Delta=3.1$ deg, azimuth=213.5 deg

G 6711

-309/310-

309.1

310

TR 72-3

earthquakes. These other events and all of their Gulf of California earthquakes separated from NTS explosions, so their conclusions are probably valid.

9.3.3 Enhancement of Ultra-Long-Period Seismic Waves

Ultra-long-period seismic waves (60 to 1000 sec) have previously only been recorded from great earthquakes. There is a practical long-period limit at which inertial seismometer-galvanometer seismographs can be constructed and operated with high sensitivity. The inertial seismographs are decreasing in sensitivity at the rate of 18 dB/octave or more at periods longer than the longest natural period of either the seismometer or the galvanometer. In the ALPS inertial system (the P_L response) and in the extended long-period (the P_X response) of Pomeroy et al. (1969), this period is 110 and 100 sec, respectively. At these periods, both of these inertial systems are already down about 12 dB from the peak of the response. Thus, for even these most sensitive systems, their ability to record 100 to 600 sec waves is severely limited. Also, previous university strain seismographs have been limited in sensitivity for recording earthquake waves in the 60 to 1000 sec range. Whereas, the QC-AZ ultra-long-period seismograph (ULPS) channels were capable of operating at the equivalent displacement magnification of 4000 from 50 sec to 250 sec and were only down 20 dB at 15 sec and 800 sec; as a result of these sensitivities many ultra-long-period earthquake waves were recorded.

The ultra-long-period strain seismograph data are recorded on a 35 mm film-strip drum recorder with one revolution of the drum (900 mm) per day with 5 days recorded on each film strip. A clear recording was made on 31 July 1970 (day 212) of G and R waves for several revolutions around the earth. Figure 172 is a X 1.5 reproduction of the 5-day recording from 1646Z on 29 July 1970 (day 210) to 1541Z on 3 August 1970 (day 215). (The continuous film strip has been divided into four segments in the figure.) The 100 sec period calibration at the beginning of the recording is a strain input of 1.09×10^{-10} m/m, which is a differential pier motion of 4.37×10^{-9} m. The 100 sec calibration can be used as a time scale for determining the period of the recorded oscillations. The P wave from the earthquake that generated the multiple revolution waves was recorded at 1716:08. The NOS PDE lists this earthquake as: 0 = 1708:05.4, 1.5S, 72.6W, Colombia, h = 651 km, $m_b = 7.1$. This location is at an epicentral distance of about 51.5 deg and the great circle azimuth from QC-AZ to the epicenter is 125 deg. The 325 deg azimuth instruments are within 20 deg from radial to the great circle path. The arrival times for G1 through G18 and R1 through R16 were calculated. A group velocity of 4.38 km/sec was used for the G waves (Benioff et al., 1955, and Satô, 1958) and a group velocity of 3.972 km/sec was used for the R waves (Jeffreys, 1962). These 34 calculated arrival times are shown in figure 172. Although all the marked times cannot be positively identified as phase arrivals, inspection of successive even or odd numbered phases (the same wave on sequential revolutions of the earth) reveals that R10, R13, G5, and G8 are positively recorded and there are very probable arrivals up to R14 and R16. The system electronic noise was recorded from 2341Z on day 210 to 1514Z on day 211 and is seen on the top line of the second, third, and fourth segments of figure 172. The signals recorded between about 0600 and 0900Z on day 214 and between about 0120 and 0330Z on day 215 are ground strains resulting from large air pressure fluctuations at the surface. From this figure, it can be seen that in the 10 to 1000 sec period range, the background microseismic signal level is substantially above the

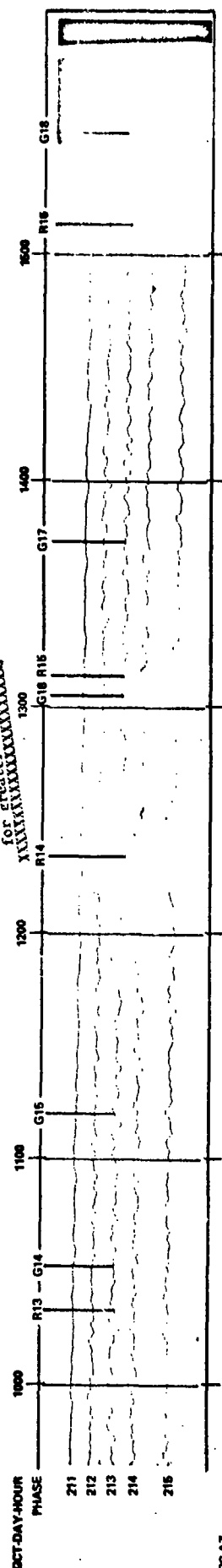
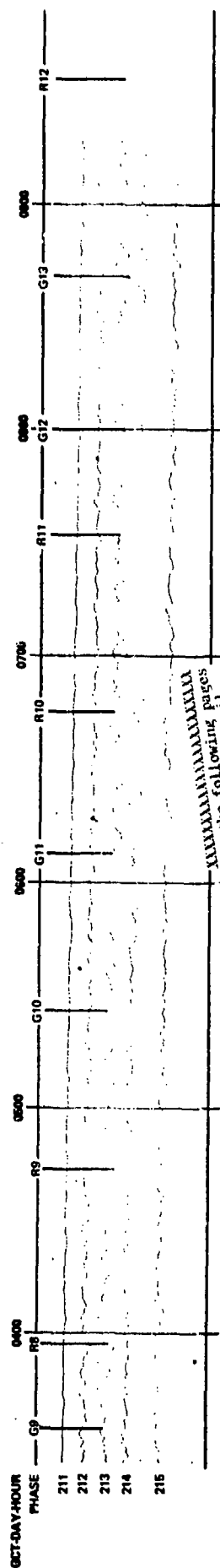
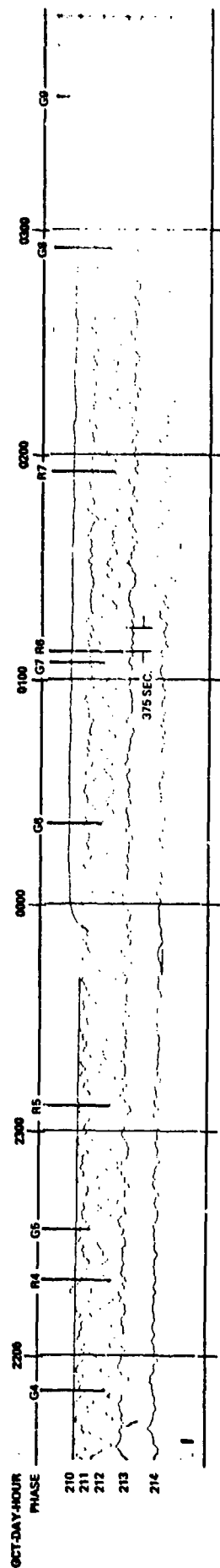
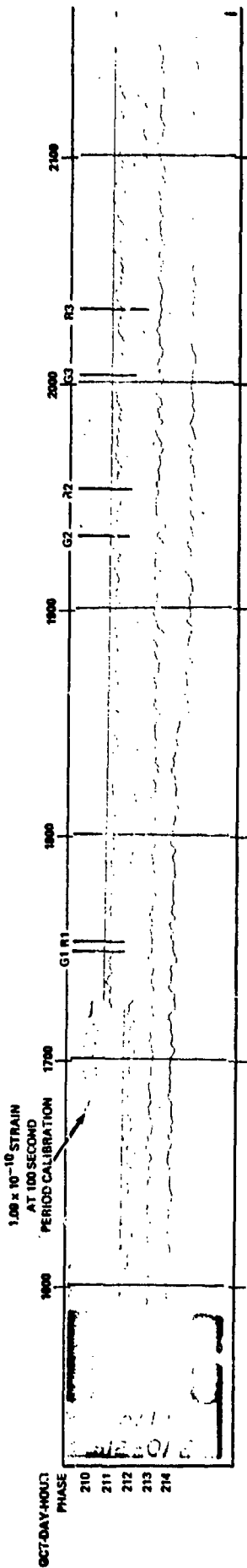
electronic instrument noise. It can be seen that the strain seismograph has sufficient sensitivity to record 30 to 500 sec period seismic waves from a large (but not great) earthquake after the waves have traveled more than seven revolutions around the earth. Also, it can be seen that large air pressure fluctuations create ground strains that increase the background motion. However, in this 5-day interval, only about 2 hours of data were degraded on two occasions or about 3 percent of the total recording time.

The recordings on the ultra-long-period strain seismograph S_U of the signals from an earthquake near the north coast of New Guinea are reproduced in figures 173, 174, and 175. The NOS PDE data are: origin = 1753:9.3, 4.9S, 145.5E, $h = 42$ km, $m_b = 6.0$. This origin is at an azimuth of 272.9 deg, at an epicentral distance of 103.4 deg. Figures 173 and 174 are three-component composites made from sections of the 35 mm film recordings. The large pulse-like signal in figure 173 is the G1 wave and in figure 174 is the G2 wave. The G3 wave was also clearly recorded. As predicted by theory, these S_H type waves are equal and opposite as recorded on perpendicular horizontal strain seismographs. The SZU vertical strain seismograph recorded a smaller pulse at the time of G1 and G2. Close inspection reveals this signal to have a different frequency content from the G waves. Another interesting observation from these recordings is the comparison of the G1 and G2 waves recorded on the S55U seismograph and reproduced in figure 175. These traces have been aligned by the peak and trough of the G waves. On the top trace (G1), about 10 min before the arrival of G1, there is a wave somewhat step-like in character at the time of arrival of SS. There is a similar wave about 5 min before G1 at the time of arrival of SSS. There appears to be two waves with slightly longer time intervals ahead of the G2. The waves with G2 cannot be body waves and their transmission mode is unknown.

Another illustration of enhancement of ultra-long-period earthquake waves is given in the second figure in section 11 where an S_U ULPS seismogram is compared to an S_B broad-band seismogram. In this figure, the vertical strain seismograph also has recorded a pulse at the same time as the G1 and G2 waves. In this figure, the SZUL signal has the same period as the G wave on the S325UL and S55UL. Three possible mechanisms have been considered for this wave: (1) it is a spheroidal mode-type wave trapped in the same wave guide and traveling at the same group velocity as the G wave; (2) it is the result of the anisotropy of the Basin and Range Province (the wave length is about 400 km); or, (3) it is the strain resulting from a horizontal free surface as well as a vertical free surface. The LR2 wave in the figure is a beautiful example of the inverse dispersion branch from 50 sec to 190 sec periods. The PS, SS, and SSS waves are also clearly recorded.

9.3.4 Enhancement of Short-Period Seismic Waves

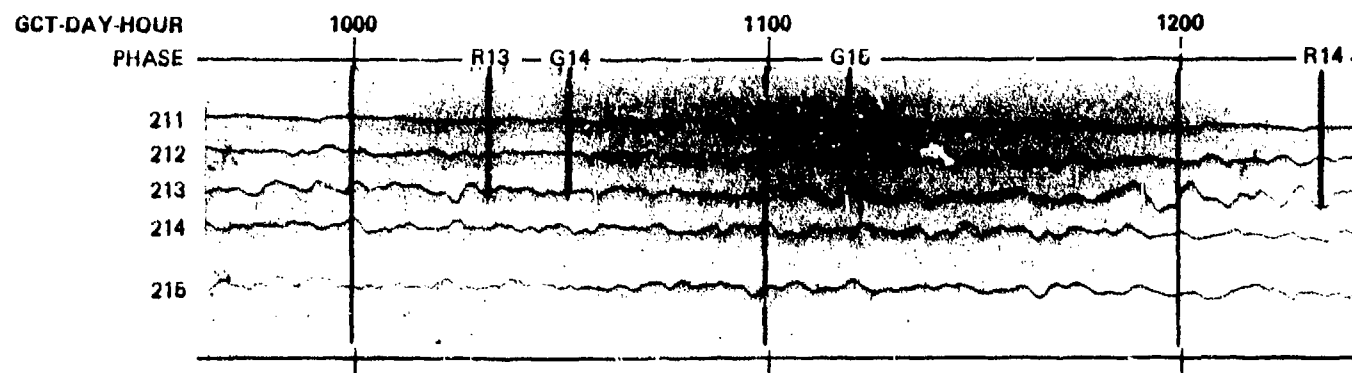
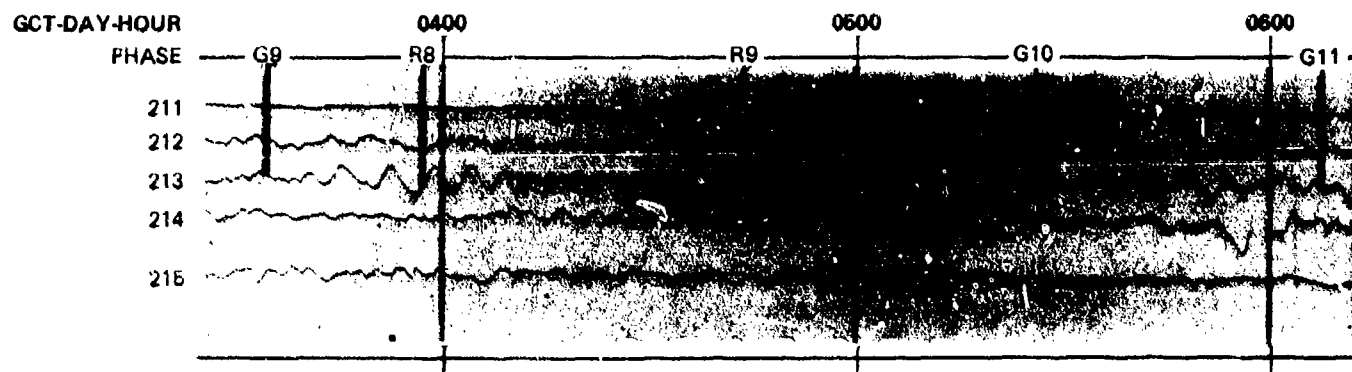
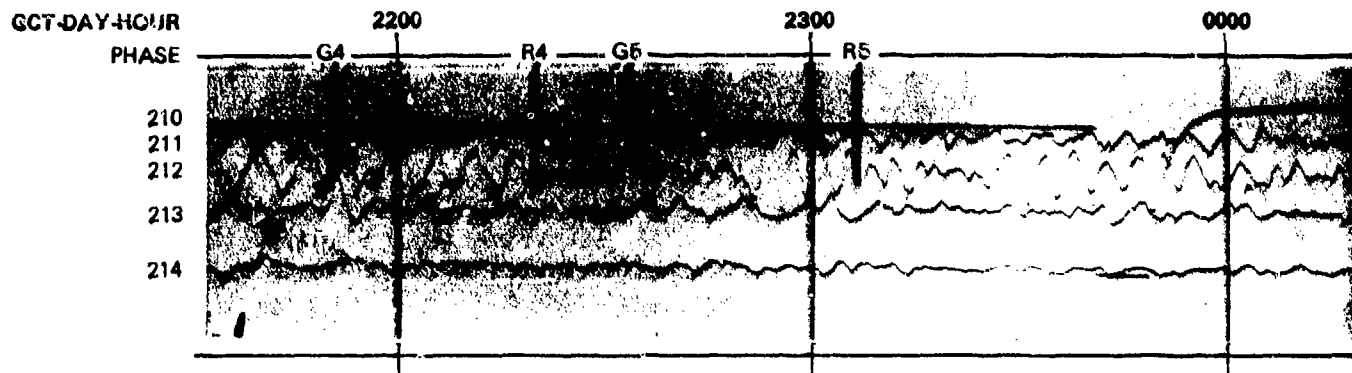
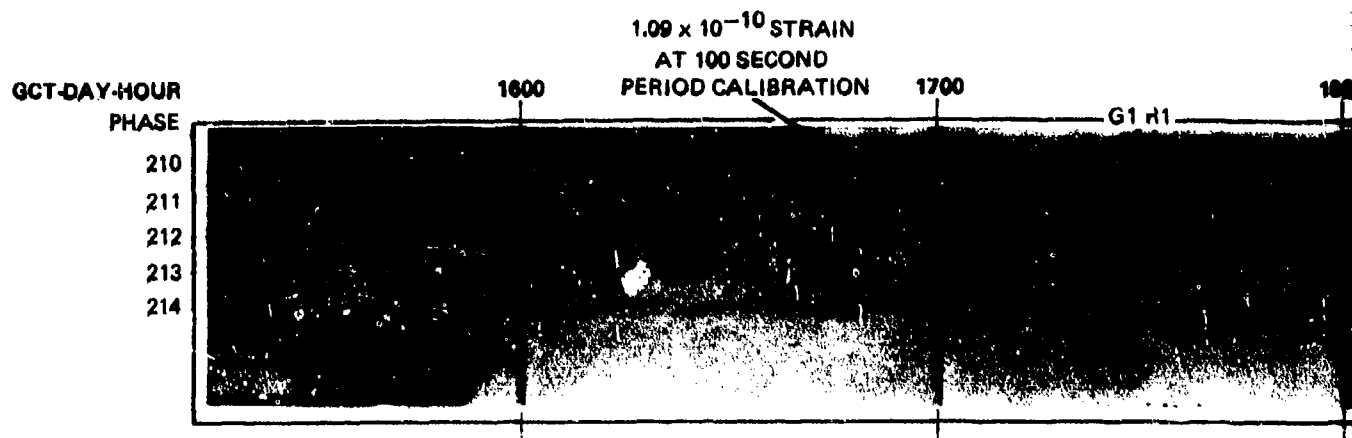
Although the primary objective of Project VT/8706 was to develop methods of long-period wave discrimination, magnetic tape recordings were made of short-period (SP) inertial and strain seismographs. The SP strain and inertial seismographs can be added and subtracted for the same azimuthal response, as shown in figure 145. Two examples of enhancement accomplished with the short-period systems are shown in figures 176 and 177. At the time of these recordings, the P55S inertial seismograph was inoperational. Magnifications for these recordings are not known; but based on the amplitude of the microseisms,



QC-AZ
CAMERA 3
RUN 210-215
20 JULY 1970
TO 3 AUGUST 1970

Figure 172. Reproduction at X1.5 of 35 mm film recording on the S325U seismograph of multiple revolution G and R phases

313
314
-313/314-
TR 72-3



QC-AZ
CAMERA 3
RUN 210-215
29 JULY 1970
TO 3 AUGUST 1970

313

313

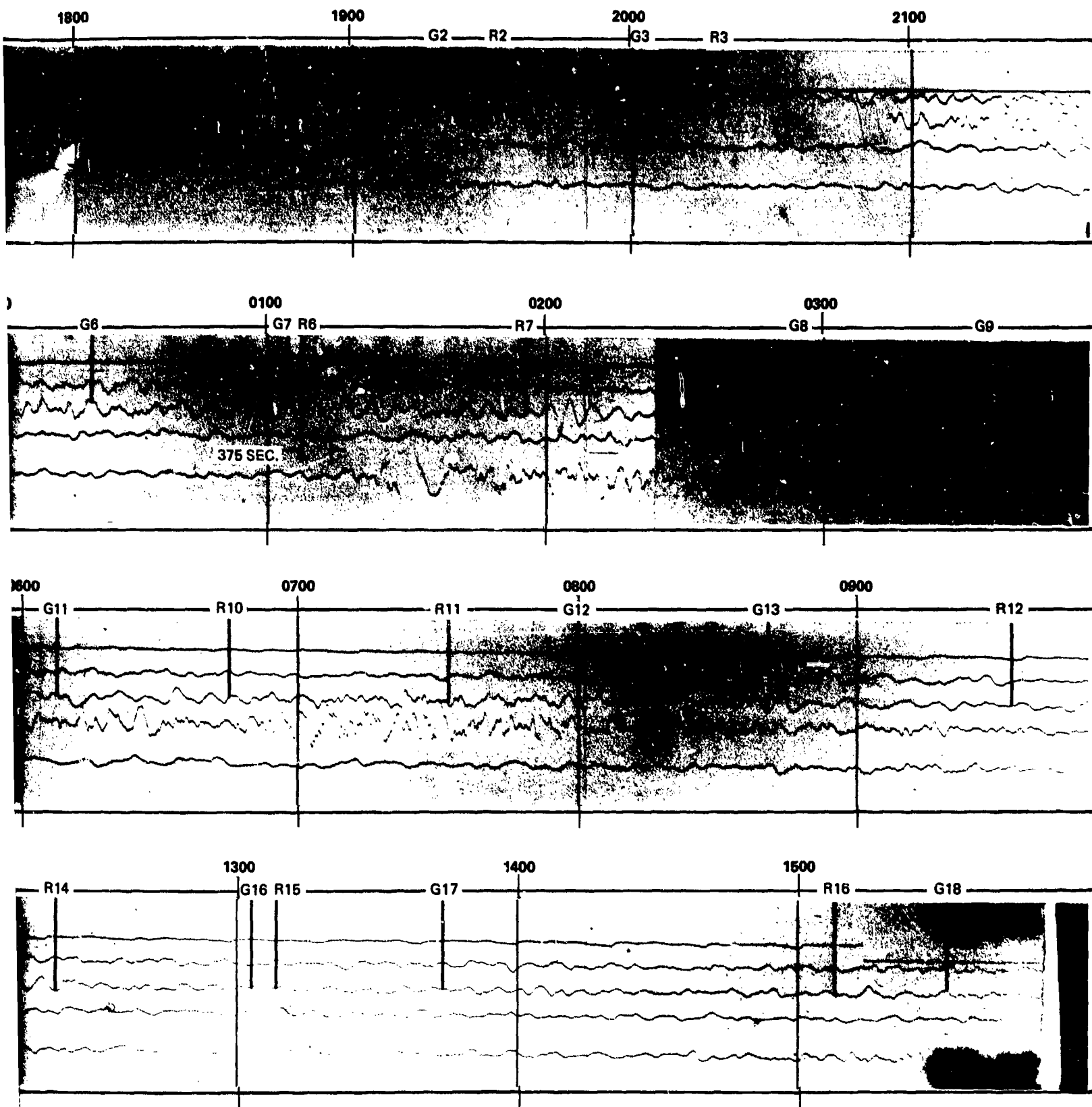


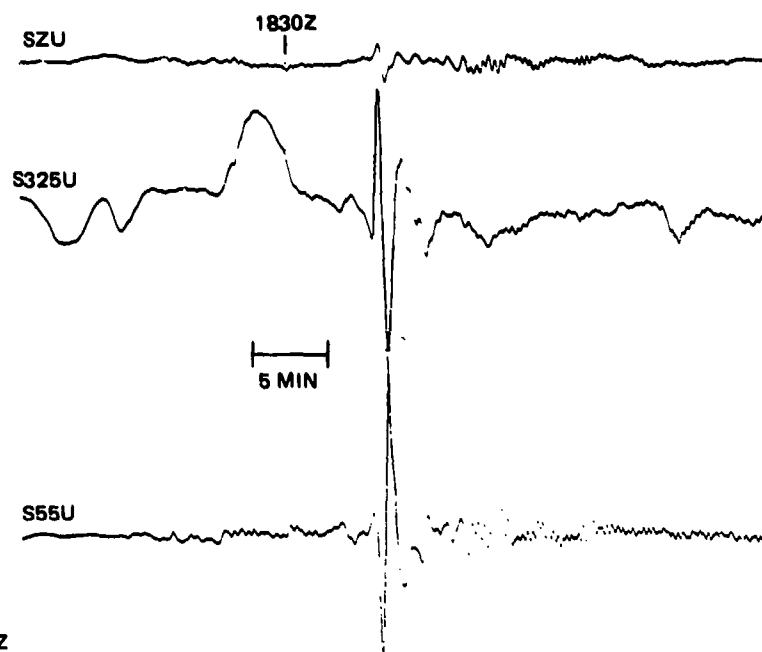
Figure 172. Reproduction at X1.5 of 35 mm film recording on the S325U seismograph of multiple revolution G and R phases

G 6712

313.1

314

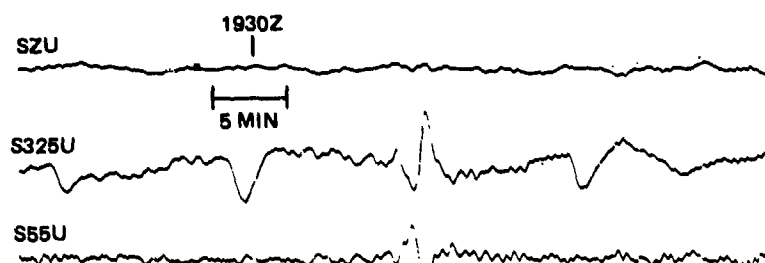
-313/314-



QC-AZ
CAMERA 3
RUN 304
31 OCT, 1970

Figure 173. Three-component strain recordings of G1 and other waves from an earthquake near the north coast of New Guinea.
NOS PDE: $\theta = 1753:9.3$, $4.9S$, $145.5E$, $h = 42$ km,
 $m_D = 6.0$, $\Delta = 103.4$ deg, azimuth = 272.9 deg

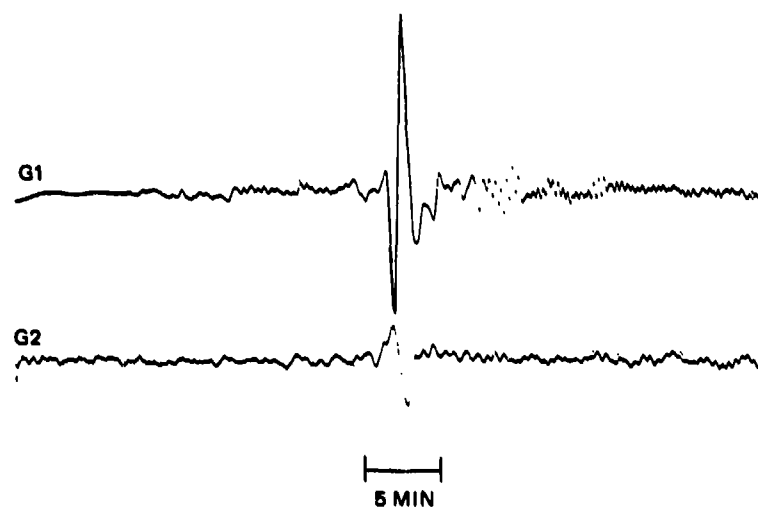
G 6305



QC-AZ
CAMERA 3
RUN 304
31 OCT. 1970

Figure 174. Three-component strain recordings of G2 and other waves from an earthquake near the north coast of New Guinea.
NOS PDE: $\theta = 1753:9.3$, $4.9S$, $145.5E$, $h = 42$ km,
 $m_b = 6.0$. $\Delta = 103.4$ deg, azimuth = 272.9 deg

G 6306



QC-AZ
CAMERA 3
RUN 304
31 OCT. 1970

Figure 175. G1 and G2 waves recorded on S55U strain seismograph from an earthquake near the north coast of New Guinea.
NOS PDE: $\theta = 1753:9.3$, $4.9S$, $145.5E$, $h = 42$ km,
 $m_b = 6.0$. $\Delta = 103.4$ deg, azimuth = 272.9 deg

G 6307

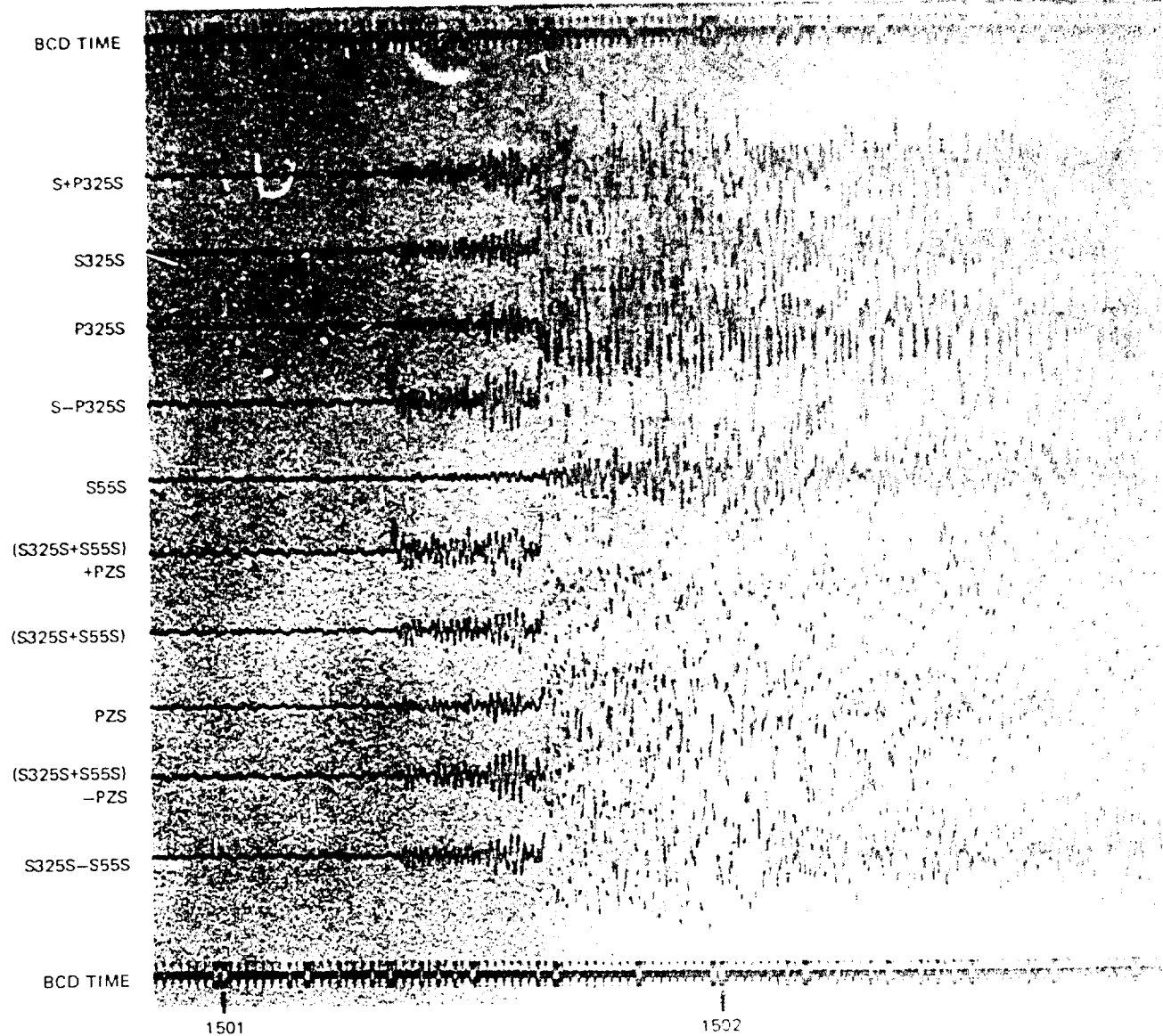
the magnifications are estimated to be about 200K in both figures. Figure 176 is a reproduction of the payout made from magnetic tape No. 2 for 21 April 1970. The NOS PDE card data for this event are:

0 = 1500:00.0, 37°06'50.0"N, 116°04'51.0"W, Nevada Test Site (NTS)
 event "CAN," h = 0, m_b = 4.8, Δ = 5.5 deg = 613 km, azimuth
 station-to-epicenter = 318.5 deg.

The vertical strain seismograph is formed by the sum of the perpendicular, horizontal strain seismographs. Very clear arrival times can be picked for the initial Pn arrival on the S-P325S and the (S325S+S55S) + PZS traces. These traces show much sharper first breaks than the P325S and PZS inertial traces. A second P arrival is clearly detected between the Pn and Pg. The arrival of the Sg-Lg phases at 1502:50 saturates the magnetic-tape recorder electronics. Several distinct P and several distinct S arrivals can be seen in the coda after the electronics stopped clipping. Times were picked from a high-speed payout and the travel time was divided by the distance to obtain an estimate of a minimum P or S velocity for various layers between NTS and QC-AZ for the following arrivals:

<u>Phase</u>	<u>Travel time/distance</u>
Pn ₁	7.534 km/sec
Pn ₂	7.474 km/sec
P ₁	6.662 km/sec
Pg	6.207 km/sec
Sn?	3.996 km/sec
Sg-Lg ₁	3.597 km/sec

During the Lg coda from the explosion, arrivals were recorded from an earthquake located by the United States Geological Survey (USGS) close-in network near Rangely, Colorado (see figure 177). The NOS PDE card data are: 0 = 1505:47.5, 40°05.39'N, 108°53.87'W, Rangely, Colorado, h = 4 km, m_b = 4.6, Δ = 7.2 deg = 804 km, azimuth = 16.9 deg. The Pn (or P₁) phase is recorded with an impulsive break on the S-P325S, S325S+S55S, and the (S325S+S55S) -PZS traces about 3 sec before the Pg phase. Several S and surface wave phases, including Sn, are clearly enhanced. The travel time divided by the distance is:



QC-AZ
MAGNETIC
TAPE PLAYOUT
RUN 111
21 APRIL 1970

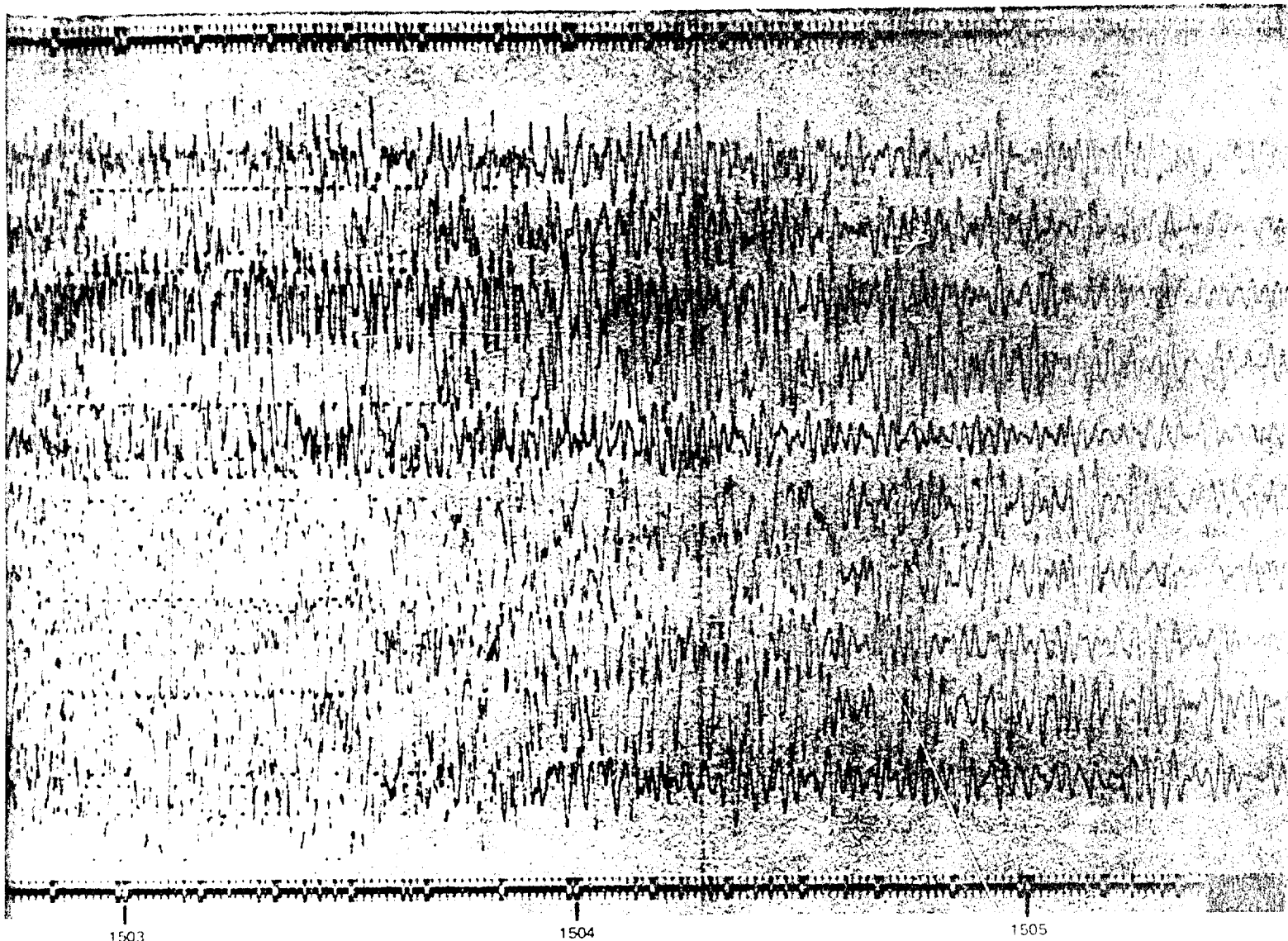


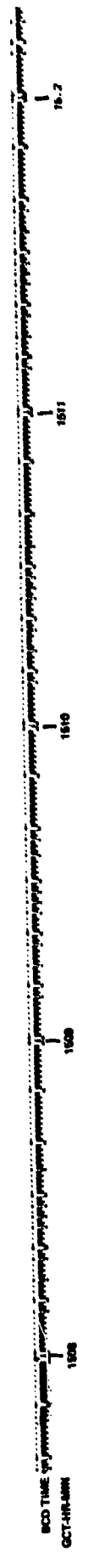
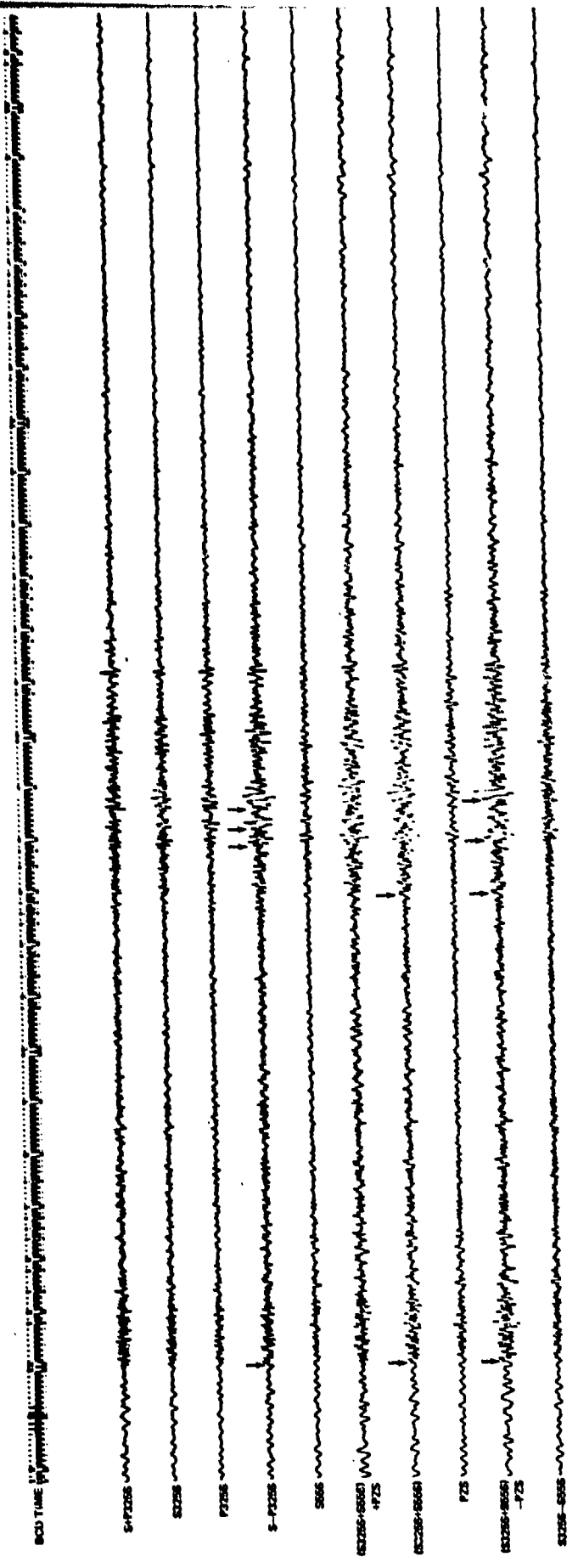
Figure 176. Enhancement of short-period arrivals from an explosion

G 67

-319/320-

320

TR 72-



11
 10
 9
 8
 7
 6
 5
 4
 3
 2
 1
 0
 -1
 -2
 -3
 -4
 -5
 -6
 -7
 -8
 -9
 -10
 -11
 -12
 -13
 -14
 -15
 -16
 -17
 -18
 -19
 -20
 -21
 -22
 -23
 -24
 -25
 -26
 -27
 -28
 -29
 -30
 -31
 -32
 -33
 -34
 -35
 -36
 -37
 -38
 -39
 -40
 -41
 -42
 -43
 -44
 -45
 -46
 -47
 -48
 -49
 -50
 -51
 -52
 -53
 -54
 -55
 -56
 -57
 -58
 -59
 -60
 -61
 -62
 -63
 -64
 -65
 -66
 -67
 -68
 -69
 -70
 -71
 -72
 -73
 -74
 -75
 -76
 -77
 -78
 -79
 -80
 -81
 -82
 -83
 -84
 -85
 -86
 -87
 -88
 -89
 -90
 -91
 -92
 -93
 -94
 -95
 -96
 -97
 -98
 -99
 -100

Figure 177. Enhancement of short-period arrivals from an earthquake during the coda of an earlier event

QC-AZ
 MAGNETIC
 TAPE PLAYOUT
 RUN 111
 21 APRIL 1970

-321/322-

TR 72-3

522

321.1

321.

BCD TIME

S+P325S

S325S

P325S

S-P325S

S55S

(S325S+S55S)
+PZS

(S325S+S55S)

PZS

(S325S+S55S)
-PZS

S325S-S55S

BCD TIME

GCT-HR-MIN

1508

1509

1510

QC-AZ
MAGNETIC
TAPE PLAYOUT
RUN 111
21 APRIL 1970

321.

321.1

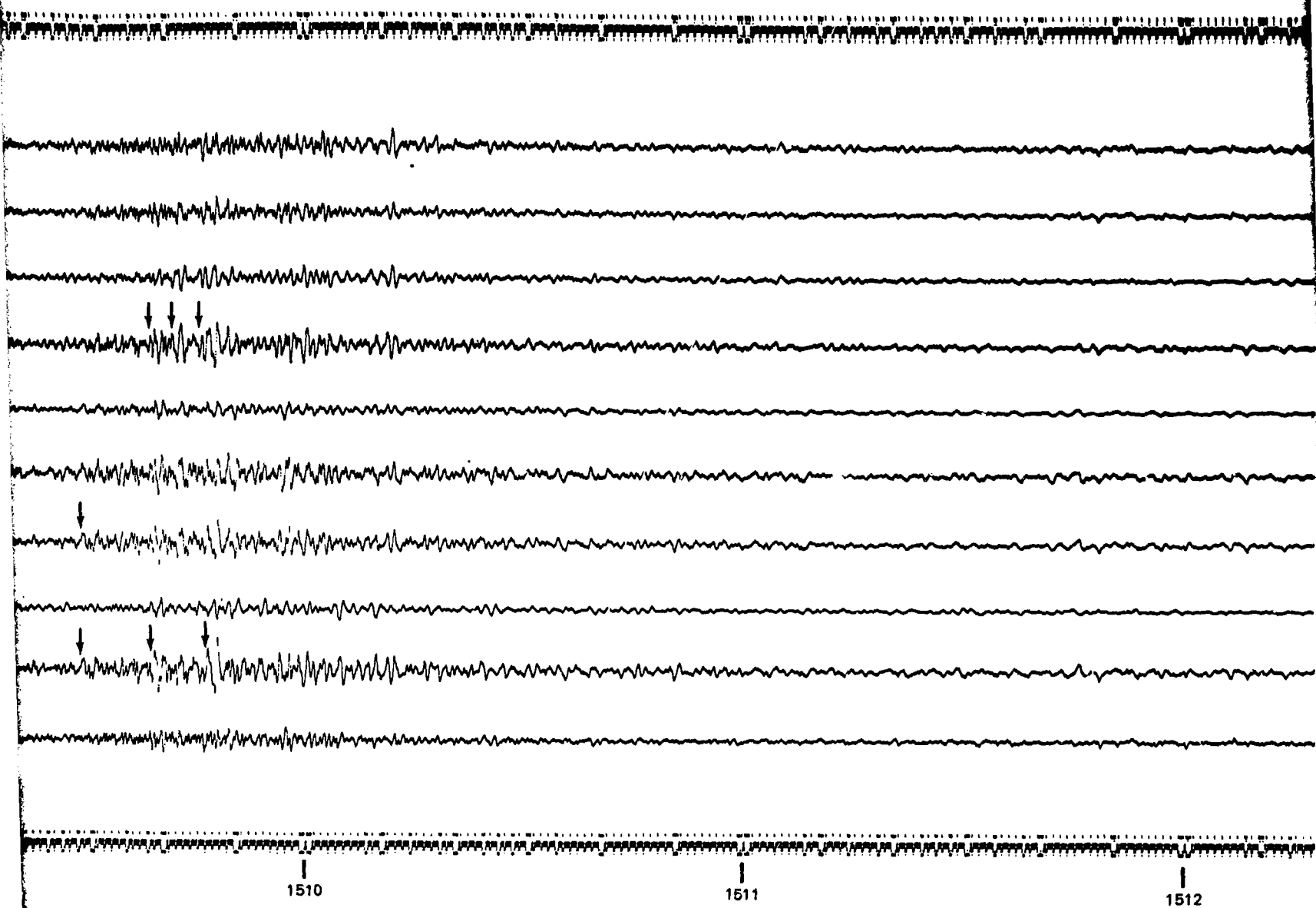


Figure 177. Enhancement of short-period arrivals from an earthquake during the coda of an earlier event

G 6714

321.1

522

-321/322-

TR 72-3

<u>Phase</u>	<u>Travel time/distance</u>
Pn(or P ₁)	6.101 km/sec
Pg	5.983 km/sec
Sn ₁	3.655 km/sec
Sn ₂	3.640 km/sec
Sn ₃	3.631 km/sec
Sg-Lg ₁	3.486 km/sec
Sg-Lg ₂	3.478 km/sec

The travel times and velocities between Rangely, Colorado, and QC-AZ are considerably slower than the travel times from NTS to QC-AZ. To the authors' knowledge, the above observations are the first reported Sn travel times in the Basin and Range Province.

10. DETECTION THRESHOLD

The apparent detection threshold of a high-sensitivity strain/inertial complex such as QC-AZ has been investigated by several methods. These methods were intended to reflect conditions that apply to the capabilities of a single high-sensitivity station with a large sample of data and not to just the smallest event ever detected. Since the detection capabilities described here are based solely on one station, the reader is cautioned to evaluate the methods employed carefully when making comparisons to other detection threshold studies. Section 10.1 compares events picked daily by an analyst at QC-AZ with events given weeks later on the NOS PDE lists. The ratio of earthquake signal-to-ambient background signal is discussed in section 10.2. Section 10.3 is a study of the M_S/m_b discriminant using m_b from NOS and M_S from the QC-AZ seismograms. Section 10.4 illustrates the effect of the Basin and Range Province upper mantle structure on Rayleigh wave signals recorded at QC-AZ. The advantage of strain seismographs over inertial seismographs in the time interval following large events is presented in section 10.5.

10.1 COMPARISON WITH PDE EVENTS

The seismograms recorded on cameras 1 and 2 (both long-period data) were reviewed daily by an analyst at QC-AZ and a station bulletin was prepared. When the NOS monthly PDE summaries were available, the QC-AZ station bulletin and the monthly summary were compared. The study covered 80 days in March, April, and May 1971. The results are given in table 14.

Since the analyst was working on his own without access to data from other stations, some events mixed in with larger signals were missed. No attempt was made to remove these events from the number of events in the PDE list tabulated in column 1.

The events listed on the PDE cards with a stated magnitude for the 80-day interval are plotted in figure 178 as a function of epicentral distance and m_b . The dots represent PDE events that were detected at QC-AZ and the X's represent events that were not detected. The detections were made on the long-period data channels, with the P arrivals being confirmed on the PZS short-period vertical seismogram. The PZS was recorded on the No. 1 camera for this purpose and proved to be very useful. The NOS PDE lists do not include many events with an $m_b < 4.0$ on a worldwide basis. Therefore, there is a definite bias toward larger events.

The May data are plotted in figures 179 and 180. The base maps are an equal-angle, equal-distance projection of the world about QC-AZ, and azimuth and distance can be scaled from the figures. The two circles are at distances of 105 and 180 deg. Figure 179 contains the PDE events detected by QC-AZ. Figure 180 contains the PDE events not detected by QC-AZ.

Table 14. Comparison of NOS and QC-AZ detections

<u>Month</u>	<u>Number of events in PDE list</u>	<u>Number of events in QC-AZ bulletin</u>	<u>Number of events on both lists</u>	<u>Number of events on only QC-AZ list</u>	<u>Number of events on only QC-AZ list with 2 or more phases</u>
March	237	151	92	59	8
April	289	213	110	103	23
May	361	274	160	114	30
Total	887	638	362	276	61
Percent of number of PDE events	100	72	40.8	31.2	6.9

Inspection of figures 178, 179, and 180 reveals that some events are detected and some events are not detected at all distances and at all azimuths. There are no obvious regions of no detections except for Montana. Earthquakes from this region at an epicentral distance of about 14 deg did not propagate across the Colorado Plateau to QC-AZ. The seismograms were rechecked for many of the Montana events, but no recognizable body waves or surface waves could be seen even for events with m_b of 4.5 to 4.9, which is well above the QC-AZ general detection threshold. Apparently, the attenuation in the upper mantle of the Colorado Plateau is significantly different from other regions to the extent that it will not efficiently transmit signals.

The data in table 14 indicate that while QC-AZ detected 72 percent as many events as listed on the PDE lists, only 40.8 percent of these detections were common. Three-fourths as many (31.2 percent as many as the PDE events) were detected by QC-AZ, but not by the NOS location system. Of these 276 events, 61, or 22.1 percent, involved detection of two or more phases. The remaining 215 events were primarily detected by the Rayleigh wave as identified by the strain/inertial directional array on camera No. 2. A Rayleigh wave can be clearly recognized as an identifiable long-period traveling wave by comparing the sum and difference traces of the directional array. Several examples of this enhancement are illustrated in the figures in section 9.

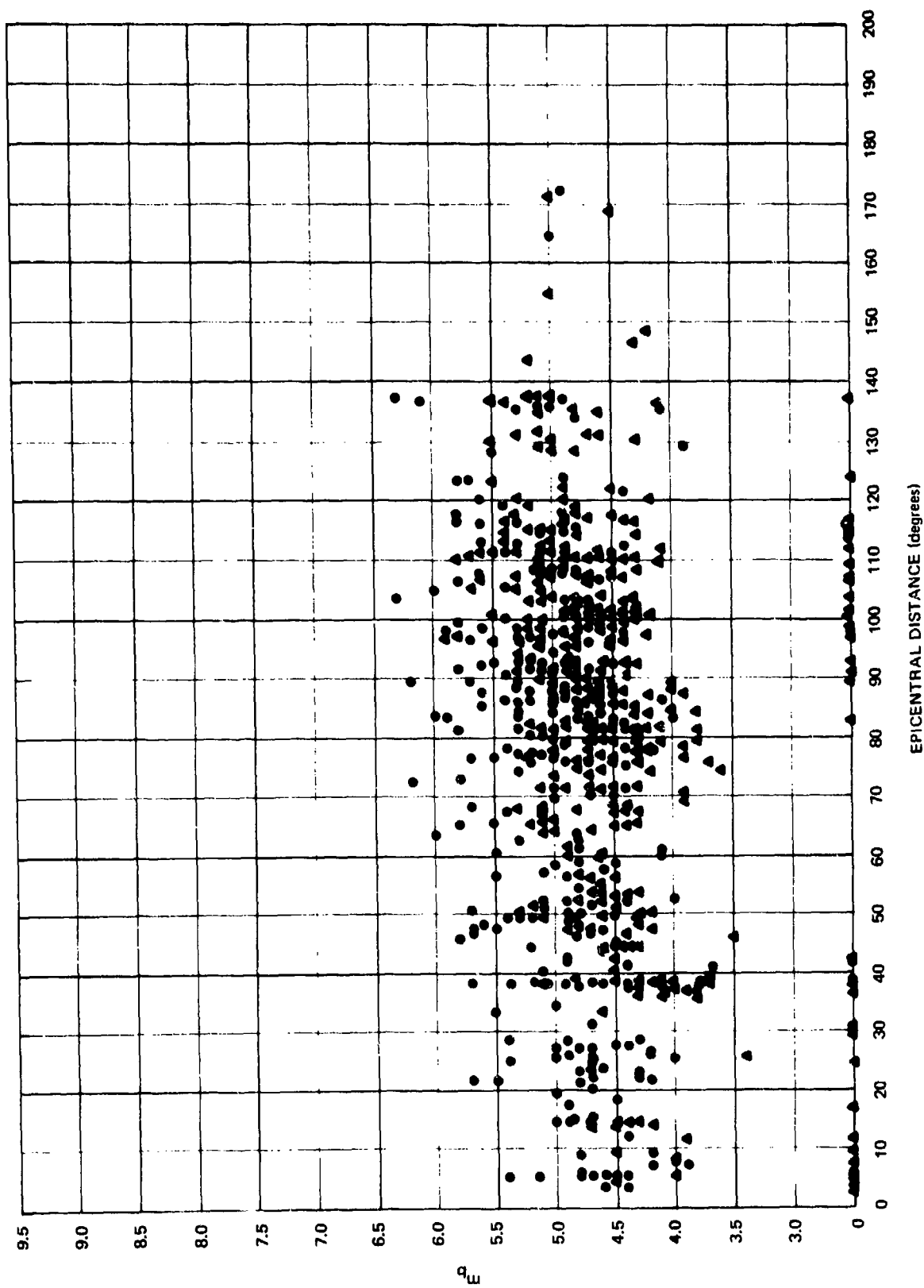


Figure 178. Events listed on PDE cards with a stated magnitude for 80 days in March, April, and May, 1971. Dots are events detected at QC-AZ. Triangles are events not detected at QC-AZ

G 6715

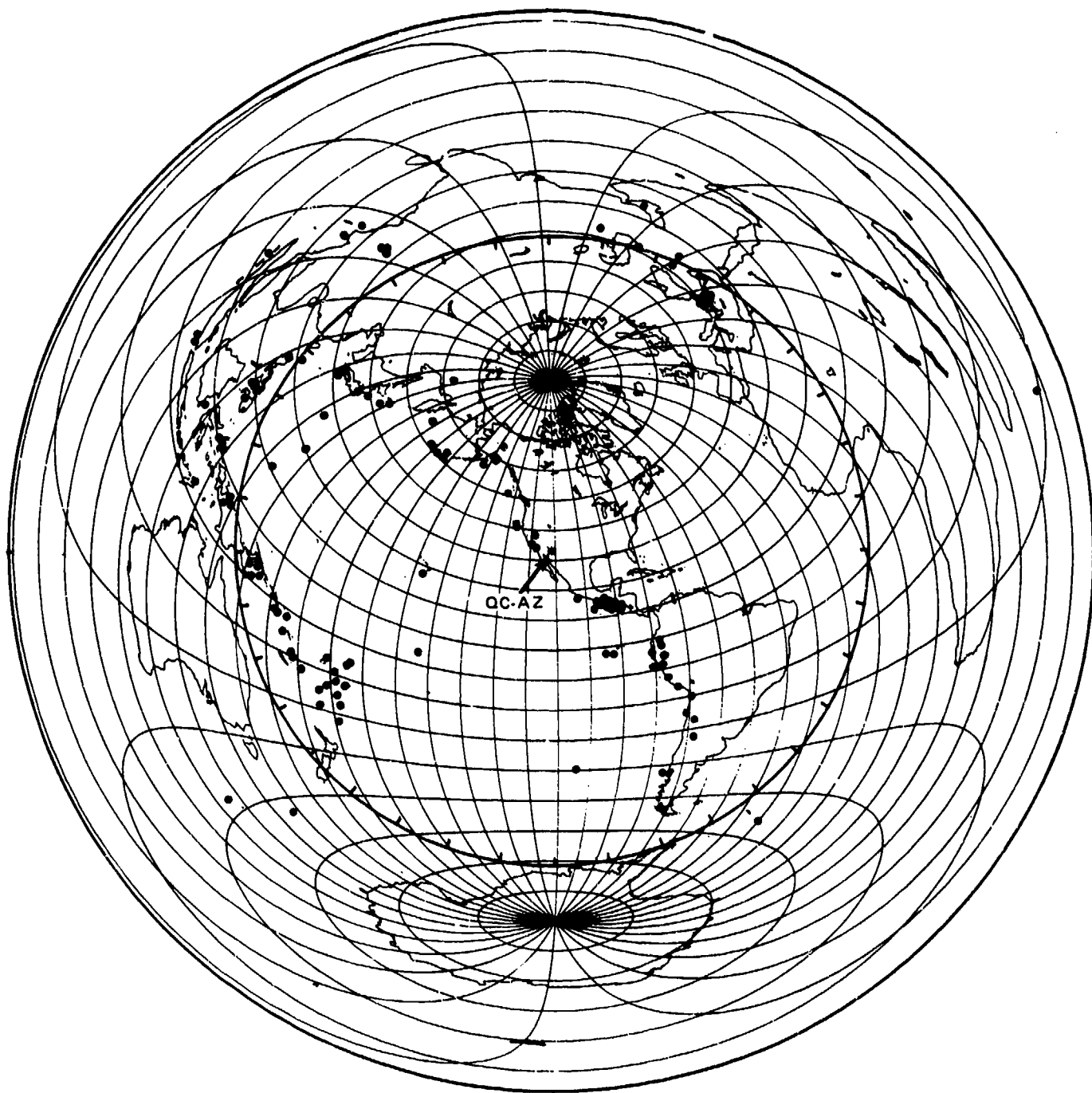


Figure 179. Events detected by QC-AZ and NOS in May, 1971

G 6716

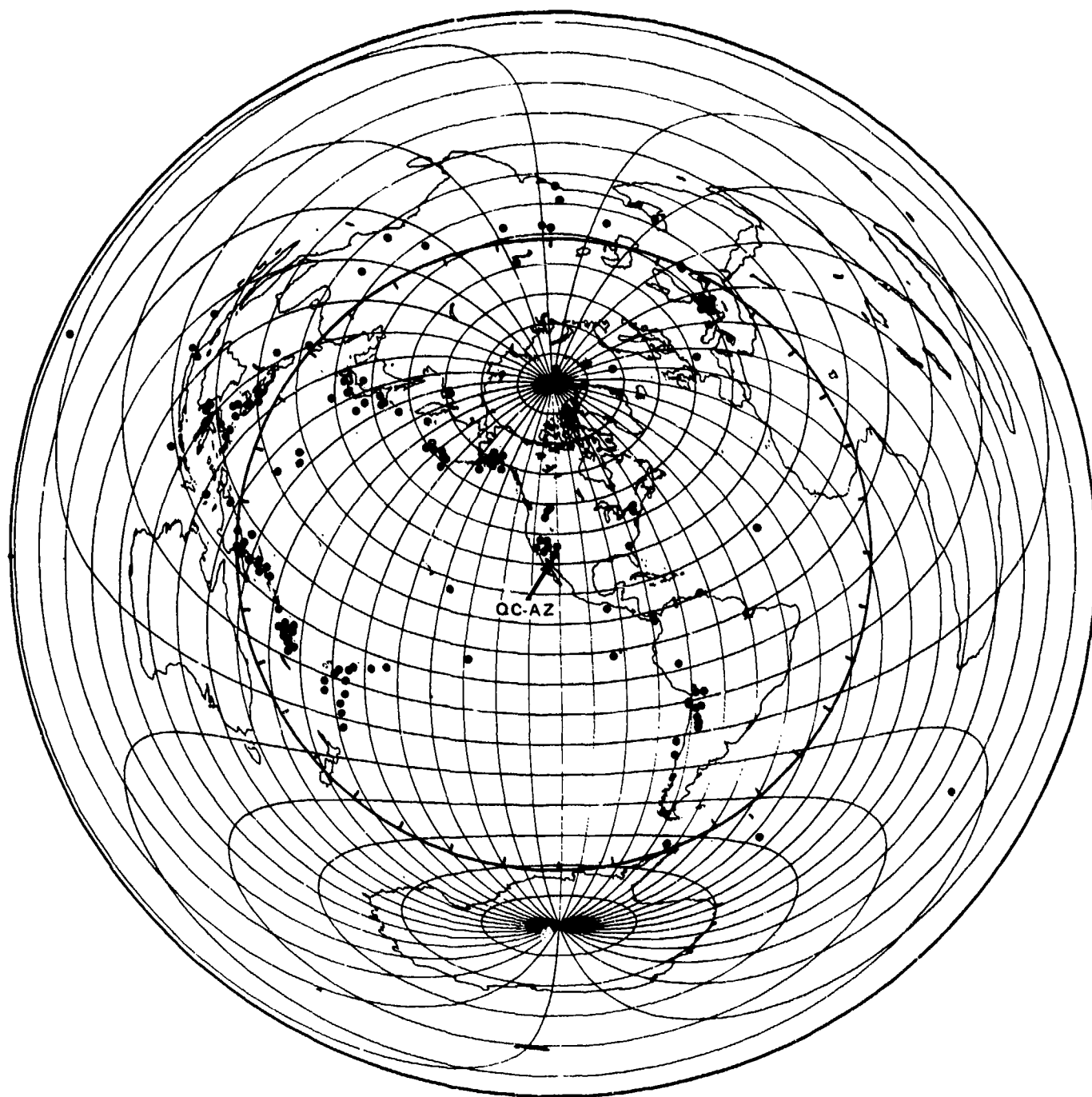


Figure 180. Events detected by NOS but not QC-AZ in May, 1971

G 6717

The primary purpose of this project is to enhance long-period wave discrimination capabilities using strain and inertial seismographs. One measure of this capability is the ability of an analyst to detect and identify the various earthquake phases in the seismograms. The number of phases for each event detected during the 80 days of the QC-AZ bulletin are plotted as a function of epicentral distance and m_b in figure 181. This plot contains all events that were jointly detected by both NOS and QC-AZ. If only one phase was detected, the event is plotted as a dot. NOS does not list m_b for some events. These events are plotted at m_b of zero. For the events not listed by NOS, epicentral distances were estimated for those events with two or more phases detected. These events are plotted on the line NL (not listed). From the figure, it can be seen that beyond an epicentral distance of 20 deg, 28 events were detected by QC-AZ with 2 to 7 phases identified. These earthquakes were presumably small and possibly with a magnitude of less than four since they were not listed by NOS. Figure 181 is a qualitative evaluation of the on-line identification capability of a high-sensitivity strain/inertial seismograph complex such as QC-AZ.

10.2 EARTHQUAKE SIGNAL-TO-AMBIENT BACKGROUND SIGNAL RATIO

One of the most effective methods of evaluating a seismograph's performance is to compare the signal-to-noise ratio between an earthquake signal and the ambient ground unrest signal. This section presents a comparison between the signal from an $m_b = 4.2$ earthquake at an epicentral distance of 96.7 deg and the signal from the ambient earth motion during a quiet time. In this section, the earthquake signal will be referred to as signal and the ambient earth motion signal will be referred to as noise (of the seismograph and ground). The reader can make additional comparisons between the various earthquake spectra in section 12.2 and the various noise spectra in sections 7.3 and 7.4. To approximate a detection threshold, the spectra from the earthquakes can be scaled down using the relationship of a factor of 10 in amplitude or a factor of 100 in power for each magnitude unit.

The NOS PDE data on the epicenter of the earthquake used as a signal are: 0 = 3 October 1970 (day 276), 1930:50.5, 6.85, 154.8E, $h = 34$ km, Solomon Islands, $m_b = 4.2$, 12 stations reporting to NOS detected event. This epicenter is at an epicentral distance of 96.7 deg and at an azimuth of 256.2 deg from QC-AZ. The seismogram is reproduced in figure 162(b). The ambient ground unrest sample chosen was from 31 October 1970 (day 304). This was one of the quiet background samples discussed in sections 7.3 (inertial) and 7.4 (strain). The power spectral densities for this sample of the strain and inertial seismograms are plotted in figures 64, 65, and 66 for the three seismograph orientations. All of these spectra are calibrated at 25 sec, but are uncorrected for instrument response.

The PZL vertical-inertial seismograph power spectral density is plotted in figure 182. The earthquake signal is plotted with a + and the background signal is plotted with an X. The 8 sec microseisms and energy at longer periods than 64 sec were higher on 31 October than on 3 October during the signal. This signal has a large spectral peak at about 18 sec. This peak

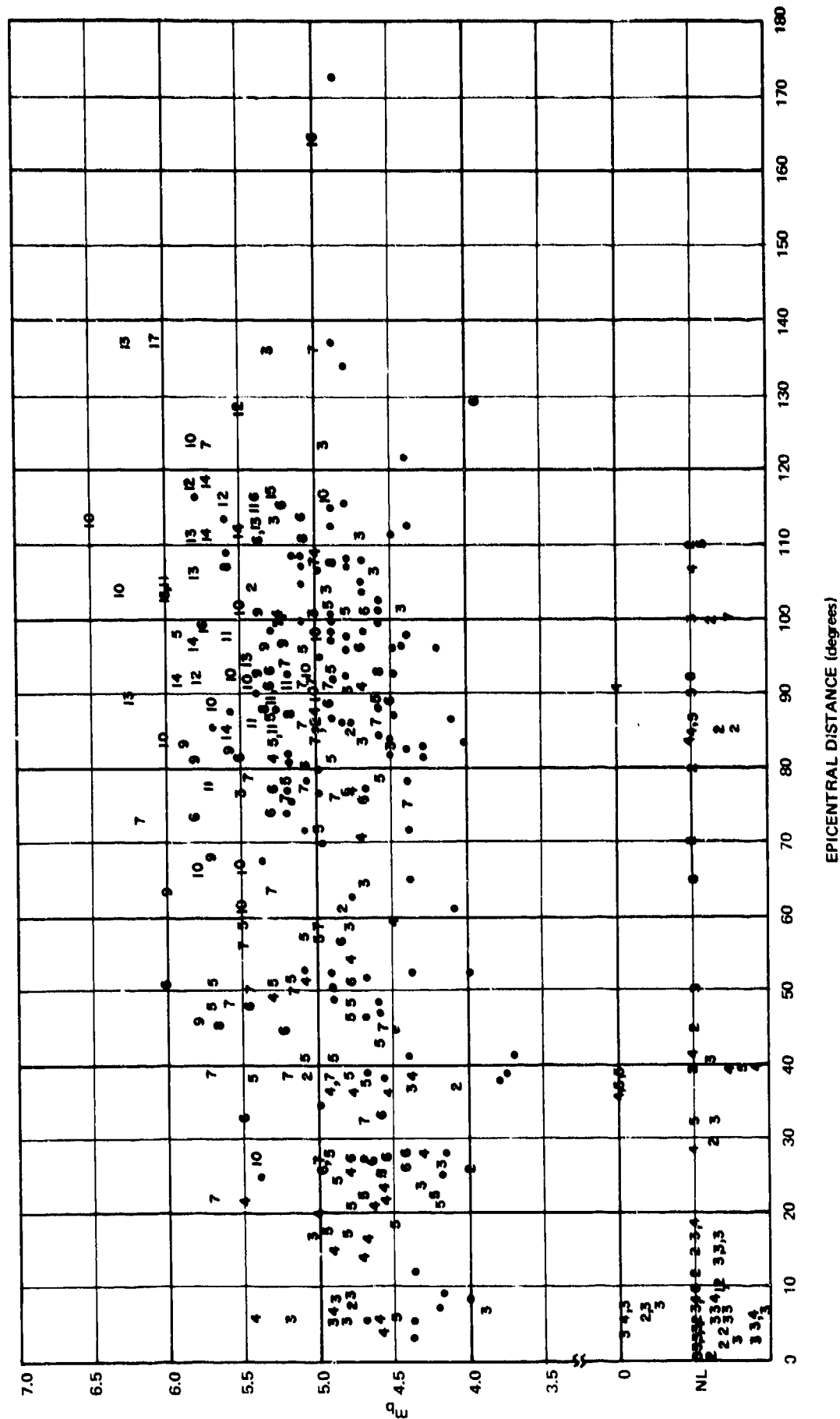


Figure 181. Number of phases detected at QC-AZ for 80 days in March, April, and May, 1971.
 m_b from NOS. m_b = NL means not listed on PDE list

G 6718

MB 4.2 SIGNAL / NOISE RATIO
 2640/3841 SAMPLES, 256 LAGS, 2.0 SPS, PARZEN SMOOTHING
 GC-AZ
 3 OCT 1970
 31 OCT 1970
 * PZL-276
 * PZL-304

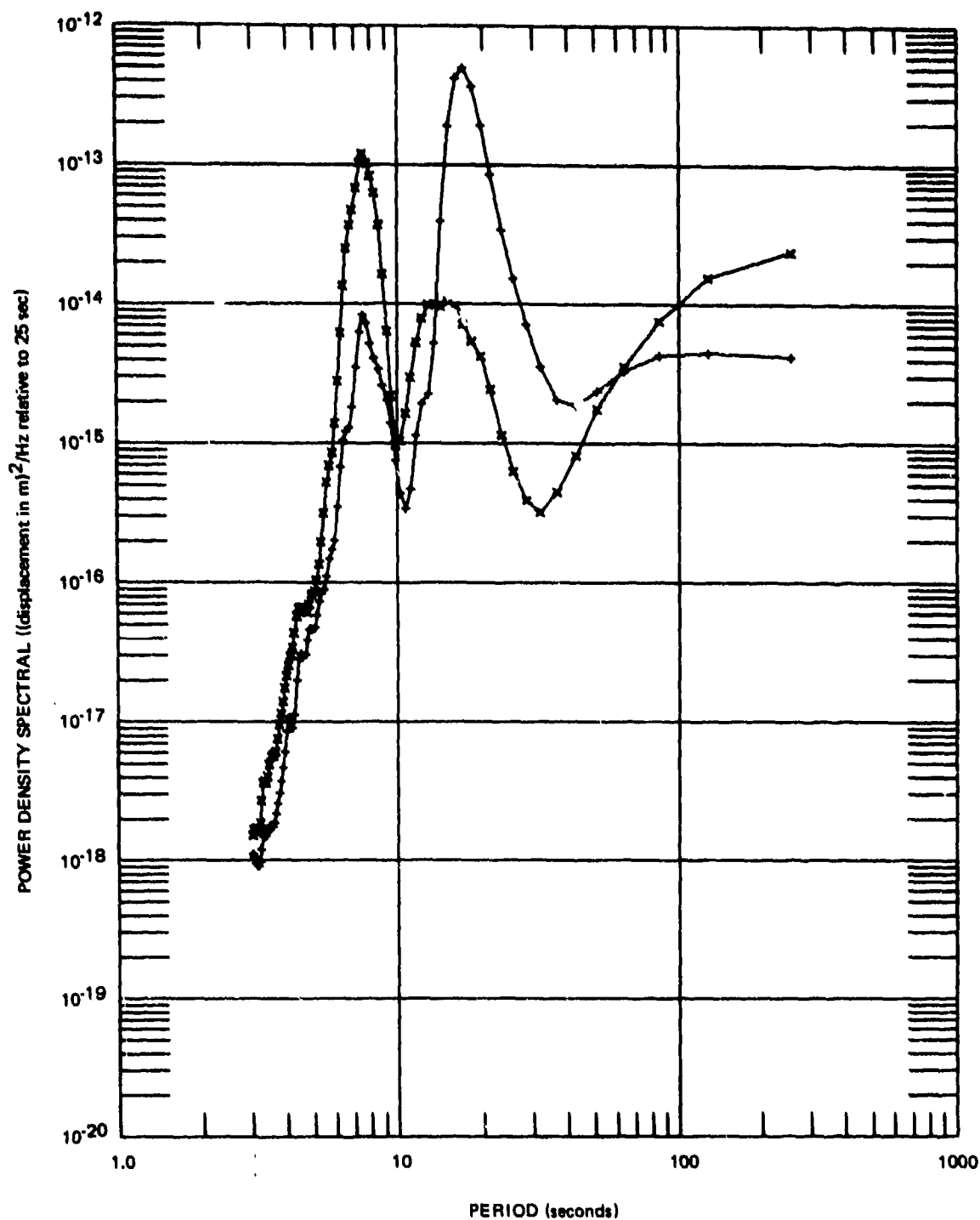


Figure 182. PZL power spectral density $m_b = 4.2$, $\Delta = 96.7$ deg. earthquake and background noise signals

G 6719

is 18 dB above the background sample at 18 sec. The spectra of the earthquake also fills in the notch in the background spectra such that the signal is 10 dB above the background at the 32 sec minimum. Filling the notch in the background spectra is typical of all signals.

The P325L horizontal inertial seismograph power spectral density is plotted in figure 183. This instrument is at a 58.8 deg angle with the great circle path from the epicenter. At the spectral peak there is a 15 dB signal-to-noise ratio. There is more energy at periods longer than 64 sec on the P325L seismograph than on the vertical seismograph.

The P55L horizontal inertial seismograph power spectral density is plotted in figure 184. This instrument is at a 31.2 deg angle with the great circle path. At the spectral peak there is a 17 dB signal-to-noise ratio. The energy at the longer periods is comparable to the energy on the P325L horizontal seismograph and greater than on the PZL vertical seismograph.

The SZL vertical strain power spectral density is plotted in figure 185. The S/N ratio at the 18 sec spectral peak is 15 dB, with the peak rising well above the noise. There was more energy at the longer periods during the earthquake sample than during the noise sample. From the shape of the spectra, it is difficult to identify the increased longer period energy as being associated with the earthquake. However, the vertical and more radial S55L strain seismographs have more longer period energy than the S325L strain seismograph. The relationship is what is expected for Rayleigh waves.

The S325L horizontal strain seismograph power spectral density is plotted in figure 186. This instrument is at a 58.8 deg angle with the great circle path from the epicenter. The S/N ratio at the spectral peak of 18 sec is about 10 dB. The energy between 23 and 32 sec during the two time samples is almost identical. The earthquake sample has more energy at the longer periods.

The S55L horizontal strain seismograph power spectral density is plotted in figure 187. This instrument is at a 31.2 deg angle with the great circle path from the epicenter. At the spectral peak, the signal-to-noise ratio is 17 dB. There is longer period energy associated with the earthquake. This longer period energy is slightly less than on the SZL vertical seismograph and slightly more than on the S325L horizontal seismograph.

The following observations can be made concerning comparisons among the figures in this section. The expected ratio between horizontal seismographs can be calculated from the ratio of the direction cosines between the instruments and the great circle path. The P55L/P325L power spectral density ratio should be

$$\left(\frac{\cos 31.2 \text{ deg}}{\cos 58.8 \text{ deg}} \right)^2 = 2.74.$$

MB 4.2 SIGNAL / NOISE RATIO
 2640/3841 SAMPLES, 256 LAGS, 2.0 SPS, PARZEN SMOOTHING
 QC-AZ + P325L-276
 3 OCT 1970 * P325L-304
 31 OCT 1970

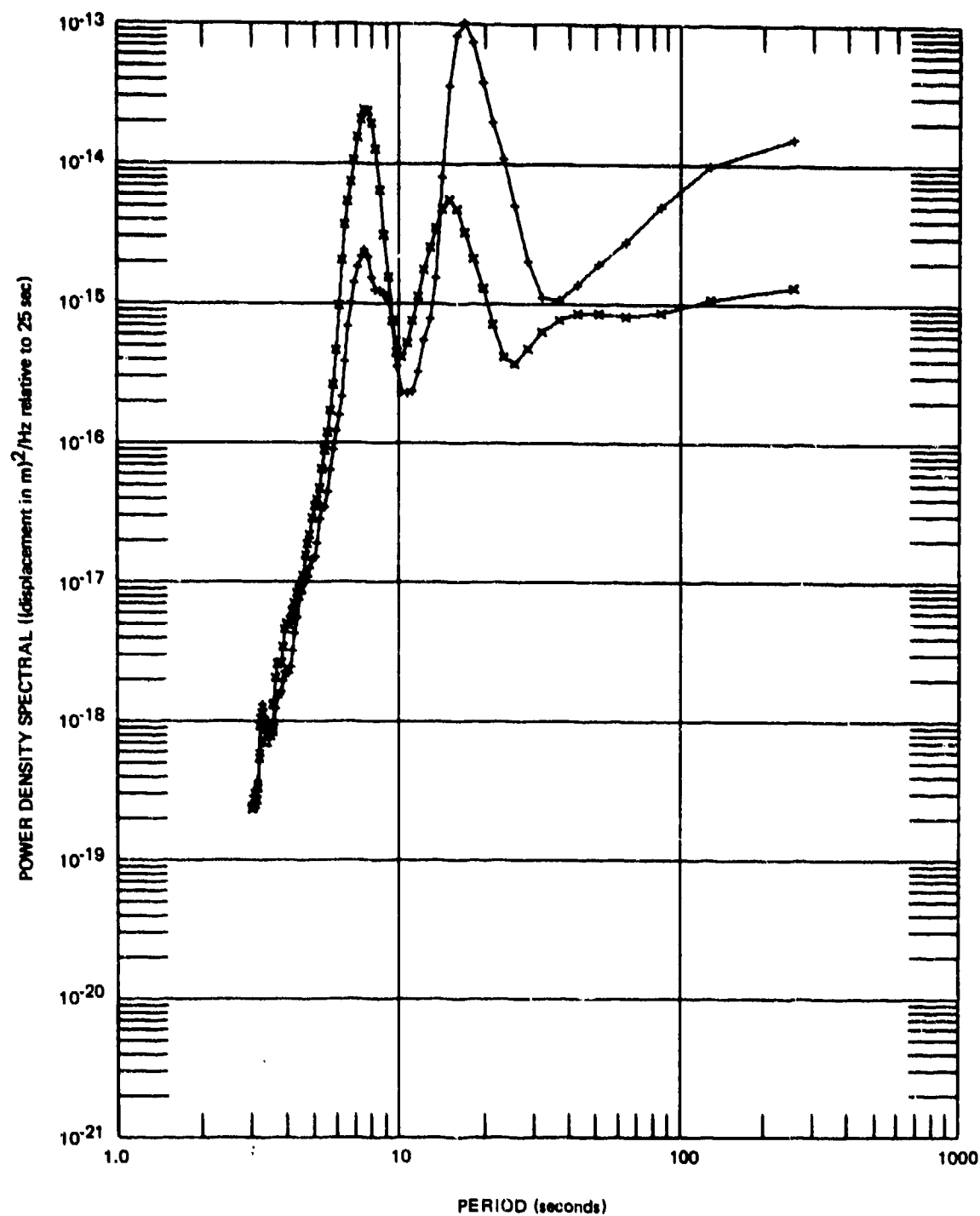


Figure 183. P325L power spectral density $m_b = 4.2$, $\Delta = 96.7$ deg. earthquake and background noise signals

G 6720

MB 4.2 SIGNAL / NOISE RATIO
 2640/3841 SAMPLES, 256 LAGS, 2.0 SP5, PARZEN SMOOTHING
 QC-AZ ♦ P55L-276
 3 OCT 1970 ✱ P55L-304
 31 OCT 1970

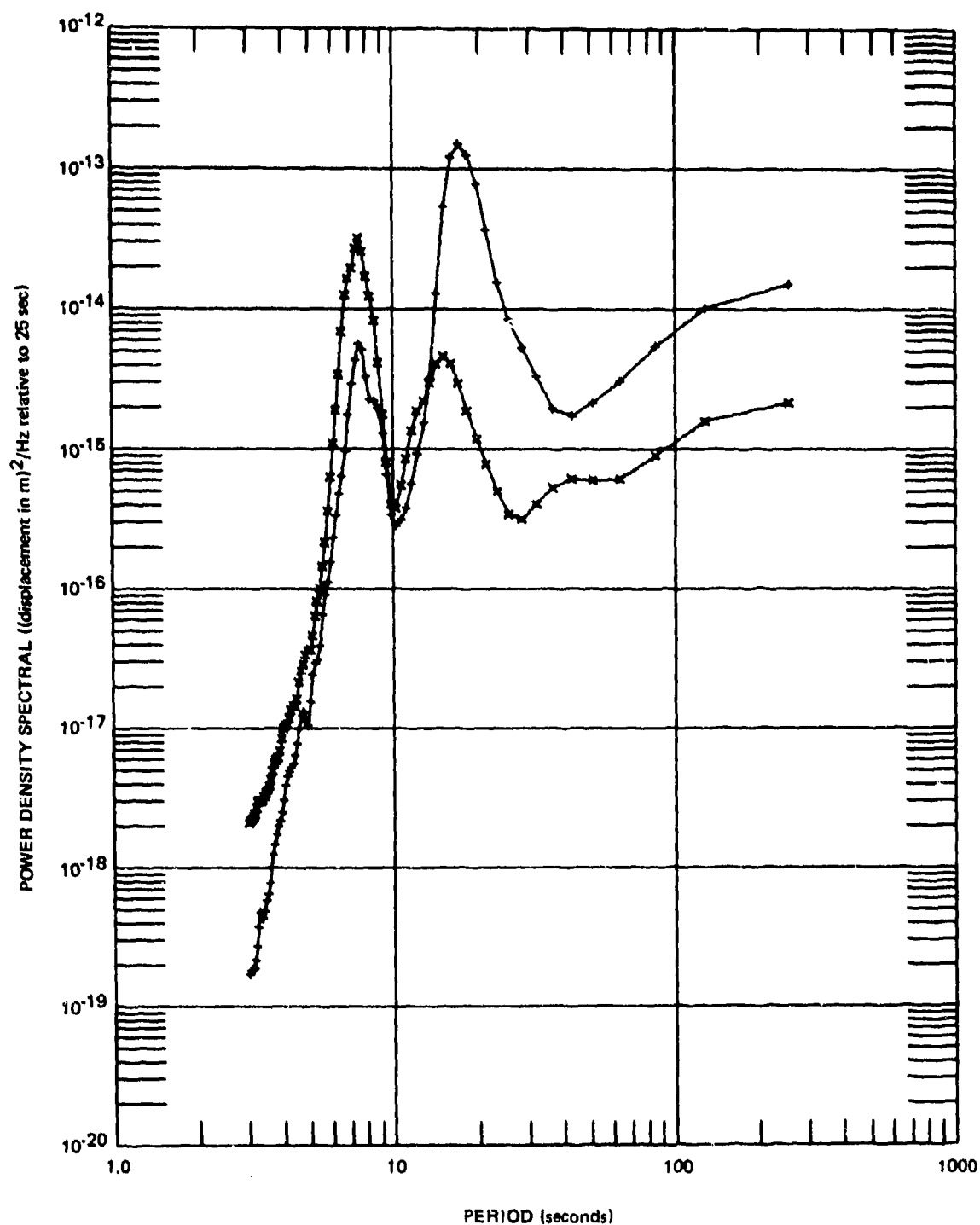
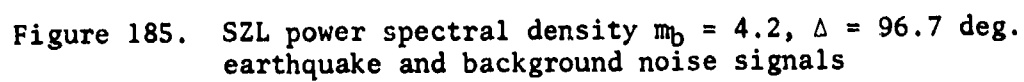


Figure 184. P55L power spectral density $m_b = 4.2$, $\Delta = 96.7$ deg.
 earthquake and background noise signals

G 6721

31 OCT 1970



MB 4.2 SIGNAL / NOISE RATIO
 2640/3841 SAMPLES, 256 LAGS, 2.0 SPS, PARZEN SMOOTHING
 DC-AZ + S325L-276
 3 OCT 1970 ■ S325L-304
 31 OCT 1970

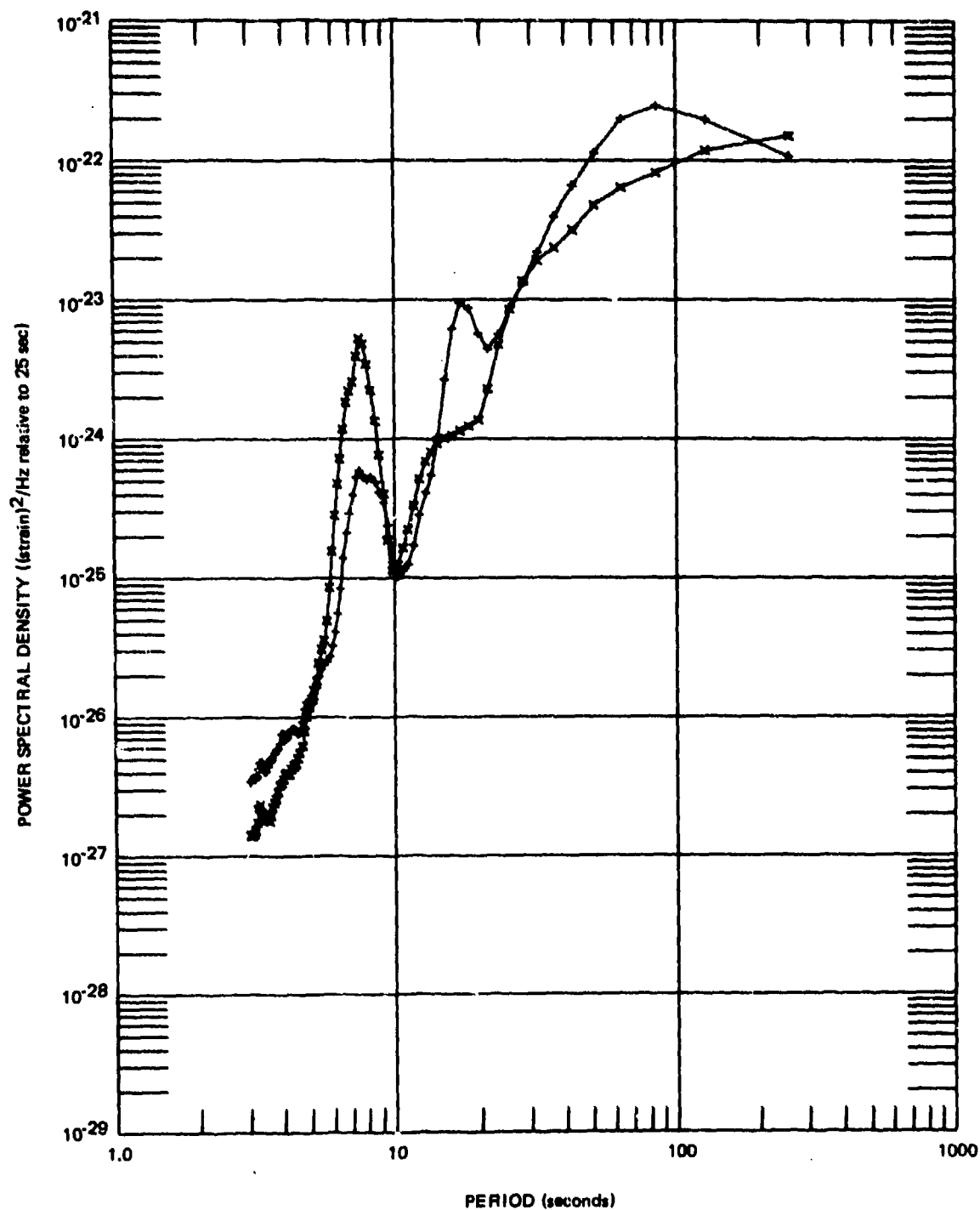


Figure 186. S325L power spectral density $m_b = 4.2$, $\Delta = 96.7$ deg. earthquake and background noise signals

G 6723

MB 4.2 SIGNAL / NOISE RATIO

2640/3841 SAMPLES, 256 LAGS, 2.0 SPS, PARZEN SMOOTHING

GC-AZ

3 OCT 1970

31 OCT 1970

• S55L-276

* S55L-304

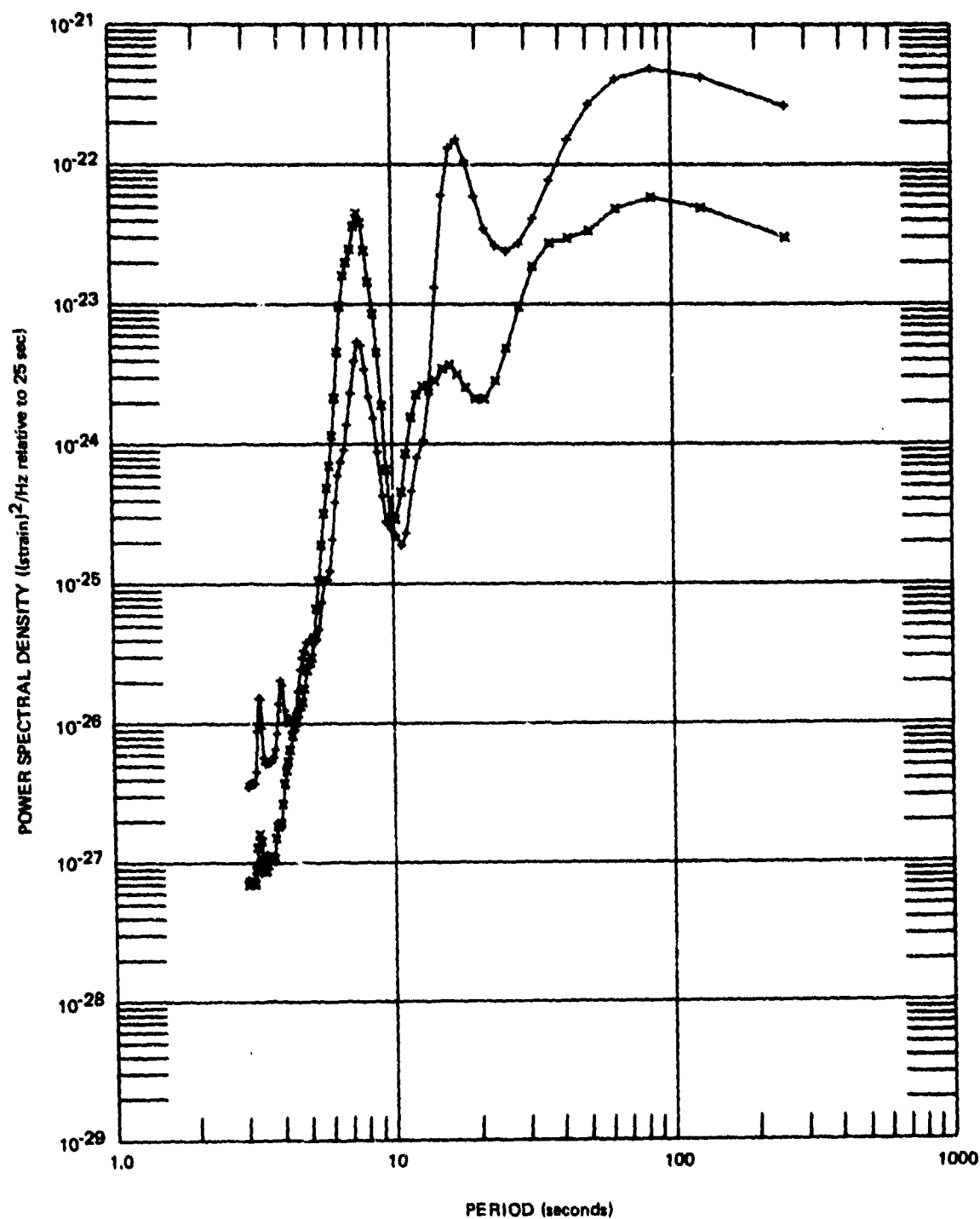


Figure 187. S55L power spectral density $m_b = 4.2$, $\Delta = 96.7$ deg. earthquake and background noise signals

G 6724

The S55L/S325L power spectral density ratio would be $(2.74)^2$, or 7.5. The observed ratios at the 18 sec peak are 1.5 and 16, respectively. The strain ratio and the directional array enhancement on the S+P55L trace seen in figure 162 indicate that the Rayleigh wave had been laterally refracted and was arriving at an azimuth closer to the 235 deg trace than the 266.2 deg great circle path azimuth. At the 83 sec peak, the observed ratios are 1.1 for the inertial seismographs and 2.0 for the strain seismographs.

In figures 182 through 187, the ability to detect an $m_b = 4.2$ earthquake at an epicentral distance of 96.7 deg with a 17 dB signal-to-noise ratio is clearly illustrated. While this signal from a small earthquake consisted of primarily 18 sec energy, similar signals are received from most small earthquakes. Most of the earthquake detections made by QC-AZ, but not listed by NOS (see section 10.1), were surface waves with periods of 18 to 25 sec. Even though the strain noise interpreted in terms of relative ground displacement exceeds the inertial seismograph noise at periods longer than 25 sec, the majority of the small surface wave signals are at periods shorter than 25 sec where the strain seismograph noise is equivalent to or less than the inertial seismograph noise, depending on the direction of travel of the noise waves. Thus, the strain/inertial directional array can provide high-sensitivity enhancement of low-level surface wave signals at teleseismic distances.

10.3 THE M_S/m_b DISCRIMINANT

The difference between the energy content of explosions and earthquakes in the long-period and short-period passbands is the basis for the more effective discrimination criteria (Evernden, 1969). The simplest method of comparing the energy in these two passbands is to compare body wave magnitude m_b and surface wave magnitude M_S . M_S was originally defined (Gutenberg, 1945) only for 20 sec waves, but has been generalized to other periods by dividing amplitude A by period T and adding a constant to the equation to compensate for the ratio of the observed period to 20 sec.

Recently, Molnar et al. (1969) have proposed using a surface wave magnitude calculated at about 40 sec. (This magnitude will be designated M_{S40} herein to distinguish it from the normal M_S or M_{S20} .) The M_{S40} was partly proposed to take advantage of the hole in the spectrum of the ambient ground unrest. (See section 7.2.) In addition to the proposal of using $M_{S40}-m_b$ comparisons, it has been proposed that the ratio of Rayleigh wave energy at 20 sec to the energy at 40 sec be used as a discriminant. The energy ratio is represented by the amplitude at 20 sec, A_{20} , divided by the amplitude at 40 sec, A_{40} (Molnar et al., 1969; Derr, 1970). These two $M_{S40}-m_b$ and A_{20}/A_{40} studies have been made with data recorded in the eastern United States (EUS) at Ogdensburg, New Jersey, and at Harvard, Massachusetts.

Many of the other $M_{S20}-m_b$ studies (Capon et al., 1967; Lieberman and Pomeroy, 1969; Basham, 1969; Basham et al., 1970; Evernden, 1969, 1971; and others) have been made largely from data recorded at the Large Aperture Seismic Array (LASA), at stations in the EUS, or at Canadian stations predominantly on the

Canadian Shield. Also, EUS stations have been used to obtain teleseismic data from NTS explosions. Thus, much of the existing $M_{S20}-m_b$ data are from stations in a tectonic setting generally represented by stations in the EUS and may contain bias from the path-station tectonic structures. Evernden (1971) used recordings made by Teledyne Geotech in the Long-Range Seismic Measurements (LRSM) program to plot M_S and m_b (Evernden, 1967) versus epicentral distance Δ for several western North America earthquakes and explosions, one Mississippi earthquake, and one Libya earthquake. Evernden concluded that M_S should be smaller for distances less than 25 deg. The data he presented were heavily biased from close-in stations ($\Delta < 25^\circ$) in tectonic settings more like QC-AZ than the EUS, and the phenomena that caused the differences in Rayleigh waves illustrated in section 10.4 may have contributed to his results as much as epicentral distance.

In preparing data for the evaluation of the M_S/m_b discriminant from QC-AZ recordings, a lack of 45 to 60 sec Rayleigh waves was discovered. Several earthquake signals recorded at both QC-AZ and the Grand Saline, Texas, salt mine station (GA-TX) were compared and were found to have significantly different character. Seismograms from some of these events are presented in section 10.4. The significance of this discovery is that seismograph stations located in tectonic structures under which there is significant partial melting in the upper mantle may be severely handicapped in the application of the M_{S40}/m_b and the A_{20}/A_{40} discriminants. A second consequence of this discovery is that epicenter-to-station path effects can be as important as source effects in determining the spectral content of a Rayleigh wave.

To evaluate the effectiveness of the M_S/m_b discriminant using the data from a single high-sensitivity station, a study of the July and August 1970 recordings was made. The QC-AZ records were read for amplitudes and periods at 20 ± 2 sec and at 35 to 40 sec where energy of this period range was present. M_{S20} and M_{S40} were calculated. The calculated QC-AZ values for M_S are plotted against the NOS PDE value for m_b in figure 188. No attempt was made to improve the m_b value for epicentral distances of less than 1800 km, as described by Evernden (1967), since the NOS values were taken as representative of values determined by a network of stations.

The Gutenberg and Richter (1956) relationship for earthquakes

$$M_S = 1.59 m_b - 3.97 \quad (76)$$

and the Thirlaway and Carpenter (1966) relationship for explosions

$$M_S = m_b - 1.8 \quad (77)$$

are plotted on the figure. The third line is derived from the QC-AZ data set

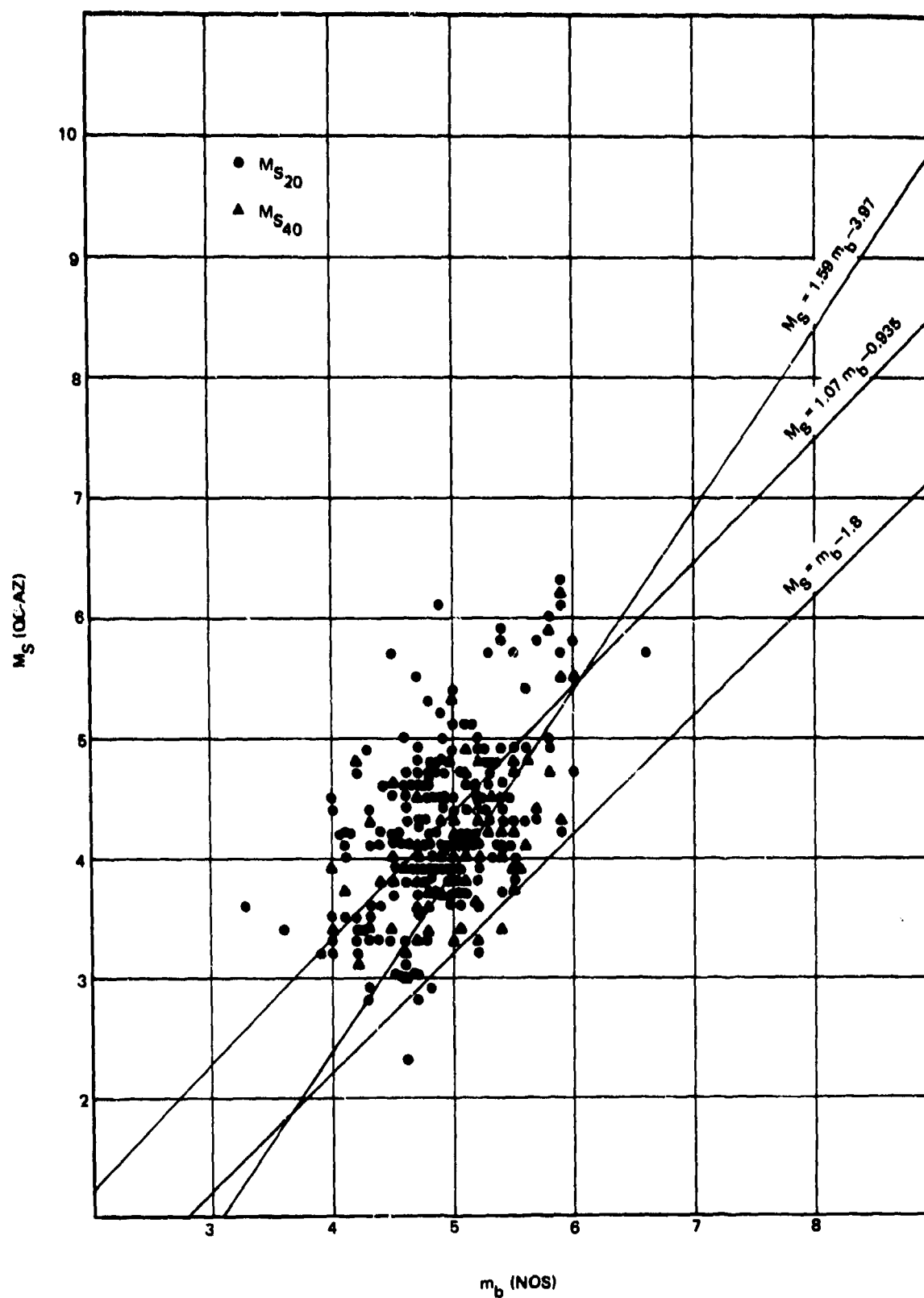


Figure 188. M_S (QC-AZ) versus m_b (NOS) for July and August 1970 earthquakes

G 6725

and will be discussed below. The M_{S20} data are plotted as dots, and the M_{S40} data are plotted as +. The entire data set lies significantly above the Gutenberg and Richter (1956) line. In almost every case where both M_S values were available, the M_{S40} value was closer to the Gutenberg and Richter line than the M_{S20} value.

Figure 189 is a plot of QC-AZ values for M_{S20} and NOS values for m_b for announced NTS explosions and presumed explosions at other worldwide sites. No 40 sec Rayleigh waves were recorded for these events. The presumed explosions were identified on the PDE list from press releases, epicenter locations, and a zero depth. The Gutenberg and Richter (1956) and Thirlaway and Carpenter (1966) lines are also drawn in figure 189. The NTS epicenters are at a nominal epicentral distance of 6 deg and the Gutenberg (1945) M_S equations (original and as modified) do not strictly apply. The reader should use the NTS values only as gross approximations. They are included because of the greater range of m_b values than available on the teleseismic events. The data of figure 189 fit both lines equally poor and do not separate into a distinct grouping either by M_{S20}/m_b or M_{S40}/m_b .

The M_{S20} and M_{S40} data from July and August 1970 are plotted in figure 190 as cumulative number of events per month versus the respective magnitude. Also, the data from the 80 day station bulletin (QC-AZ detection of PDE events) used in section 10.1 are plotted as cumulative number of events per month versus m_b . With the small data samples, there are irregularities in the curves that would probably not exist if larger data samples were available. All three curves are heavily biased by the capabilities of the NOS network. Since QC-AZ detected 76 percent as many events that were not on the PDE lists as it detected events that were on the list, the minimum detection threshold of QC-AZ will be over estimated from figure 190. Lines have been visually fit to the m_b and M_{S20} curves where the data appear more uniform. These lines can be expressed as

$$\log N = 6.32 - 0.903 m_b \quad (78)$$

and

$$\log N = 5.53 - 0.845 M_{S20} \quad (79)$$

where N is the average cumulative number of events per month.

Setting N in equation (78) equal to N in equation (79) and solving for M_{S20} in terms of m_b gives

$$M_{S20} = 1.07 m_b - 0.935 \quad (80)$$

This equation is plotted in figure 188 along with the observational data. Equation (80) gives a more realistic fit to the observational data than

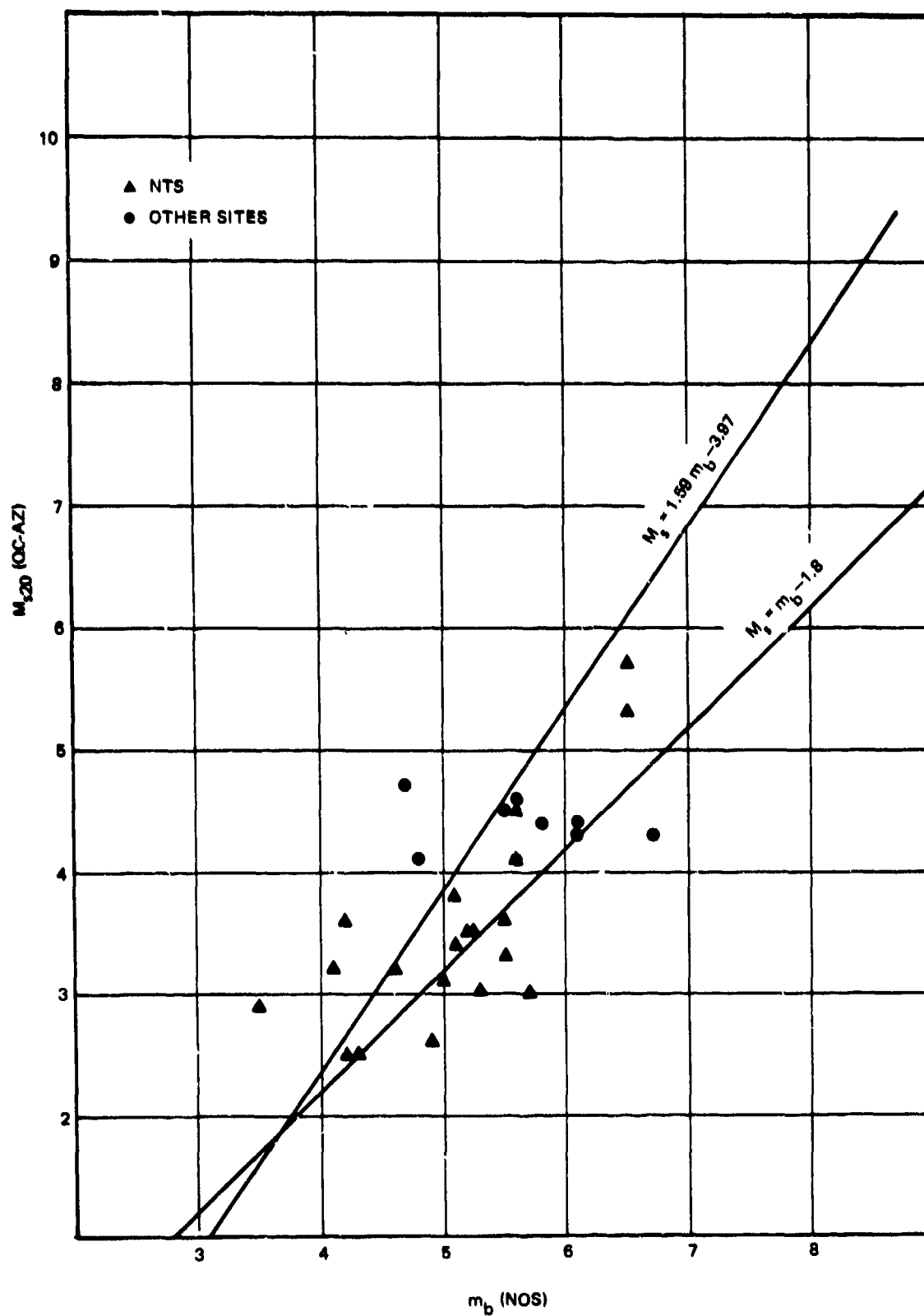


Figure 189. M_s (QC-AZ) versus m_b (NOS) for NTS announced explosions and presumed explosions at teleseismic distance

G 6726

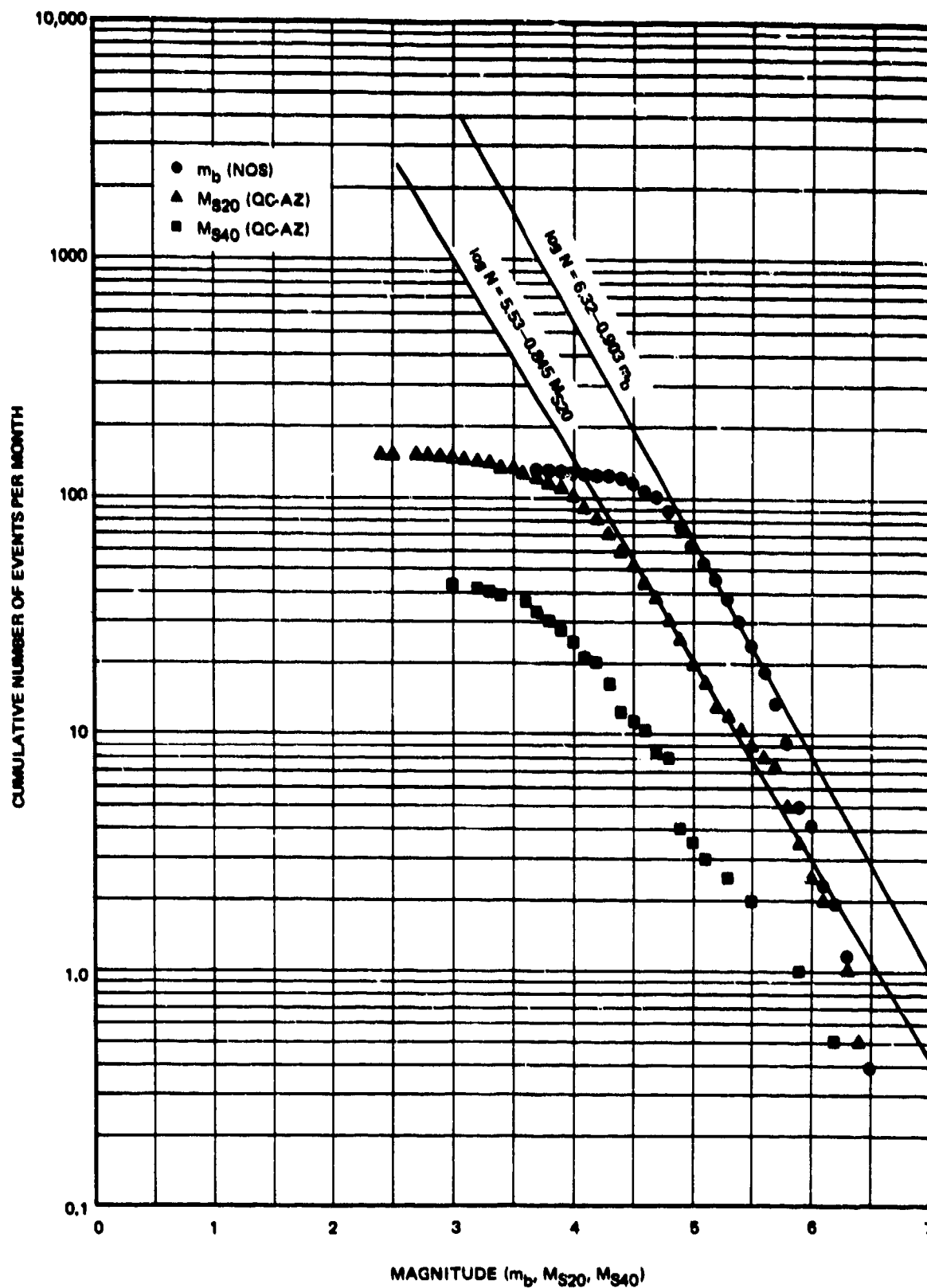


Figure 190. Cumulative number of events per month versus m_b , M_{S20} , M_{S40}

G 6727

fitting all the observations with a least squares line. The least squares fits to both M_{S20} and M_{S40} are dominated by the greater quantity of samples with m_b between 4.5 and 5.5 and give unrealistic small slopes.

Even though the m_b data in figure 190 do not include 43 percent of all QC-AZ detected events, the reader might note that an m_b of 4.35 is the 50 percent detection level for the worldwide events jointly detected by both NOS and QC-AZ. The actual 50 percent detection level is somewhat lower. This level demonstrates the usefulness of high-sensitivity seismograph stations.

10.4 EFFECT OF THE BASIN AND RANGE PROVINCE UPPER MANTLE ON RAYLEIGH WAVE SIGNALS AT QC-AZ

The partial melting in the upper mantle under the Basin and Range Province has significantly altered the 45 to 60 sec energy content of Rayleigh waves recorded at QC-AZ. In studying the QC-AZ recordings to establish the capabilities of the strain/inertial system to enhance LP waves, a general lack of 45 to 60 sec Rayleigh waves was discovered.

Another high-sensitivity inertial seismograph complex was installed at the Morton Salt Company mine in Grand Saline, Texas (GA-TX). It was operated during May, June, July, and part of August 1970, under a joint research effort of Teledyne Geotech and Southern Methodist University (SMU). Geotech's effort was performed under the LRSM program, VELA-Uniform Project VT/0703, Contract F33657-70-C-0646, with the support of the Advanced Research Projects Agency, Nuclear Test Detection Office, and was accomplished under the technical direction of the Air Force Technical Applications Center. SMU's effort was performed under Air Force Office of Scientific Research Grant Nos. AFOSR-414-67 MOD, 67-0414C, and Contract Nos. AFOSR-F-44620-68-C-0086 and AFOSR-F-44620-71-C-0073.

The GA-TX installation consisted of one 3-component long-period seismograph installed in the mine and another installed in tank vaults on the surface. There were five microbarographs, one in the mine and four in an array on the surface, and one anemometer. Recordings were made on a 16-channel digital recording system, described by Herrin et al. (1970).

A significant first-order distinction between seismic surface wave signals recorded at both QC-AZ and GA-TX was observed. Rayleigh wave trains from sources to the east that travelled the same great circle path to both stations were recorded with widely different character. At GA-TX the Rayleigh wave train begins with a pulse of 45 to 60 sec energy and at QC-AZ the same wave train has very small amplitudes at these periods. This surface wave character difference is also seen in most of the Rayleigh waves from sources to the east and is thought to be more of a path effect than a source effect. Even though the QC-AZ Rayleigh wave trains do not have much 45 to 60 sec energy, the Love waves often contain normal energy at these periods.

The following paragraphs discuss examples of seismograms illustrating the signal differences. A brief digression from these differences is necessary to present seismograph magnification curves and seismograph nomenclature. The two stations operated independent of each other and had different seismograph transfer functions and different operating procedures. The QC-AZ seismographs were calibrated at a period of 25 sec and the GA-TX seismographs were calibrated at 50 sec. The seismograph magnification curves that apply to the illustrations are given in figure 191 normalized to 100,000 at the calibration periods. The long-period vertical seismograph in the salt mine at GA-TX is designated LPZ. The LPZ amplitude response peaks at 55 sec. At QC-AZ, two long-period seismograph responses were used. The PZL, P325L, and P55L seismographs have the ALPS response, which peaks at a 25 sec period. The second QC-AZ seismograph response is designated PZX, P325X, and P55X. This response peaks at 40 sec and is designed to be similar to the response of the seismograph operated at Ogdensburg, New Jersey, (Pomeroy et al., 1969). It was recorded at only one level on magnetic tape. The P X seismograph magnifications at 50 sec are equal to the magnifications at 25 sec, as can be seen in figure 191. Thus, in the figures where the P X response is illustrated with the LPZ, the seismogram magnifications at the calibration periods can be compared directly by the lengths of the respective calibration bars in the figures.

Figures 192 through 196 illustrate typical differences in signals recorded at the two stations with sources from the east. The signals are presented in chronological order. Table 15 gives the epicentral data from the NOS PDE and the calculated epicentral distances Δ and azimuths from the epicenter to the station (E-S) and from the station to the epicenter (S-E). The seismograms are aligned at a group velocity U of 4.00 km/sec. The GA-TX seismograms in the top of the figures are reproductions of computer plots of the digital data. Only the vertical component has been used in studies to date since the horizontal components at GA-TX were often subjected to localized tilts by machinery in the working mine. The QC-AZ three-component seismograms in the bottom of the figures are reproductions of playbacks of the FM magnetic tapes. Throughout the operating period, the QC-AZ horizontal seismographs were operated at the same high sensitivity as the vertical seismograph and, therefore, contain much useful information.

The differences in the signals are considerable at the longer periods which propagate in the upper mantle, but the differences are small at the shorter periods which propagate in the crust and in the lid of the mantle. Thus, while the beginning of the Rayleigh wave trains have significantly different character at these two stations, the Airy phases with group velocities of 3 to almost 3-1/2 km/sec are very similar.

The recordings from the $m_b = 4.8$ Greenland Sea earthquake of 19 May 1970 (day 139) are illustrated in figure 192. The two stations are at about the same epicentral distance from the source and are on great circle paths separated by 15.2 deg at the epicenter. The recordings from the $m_b = 5.5$ North

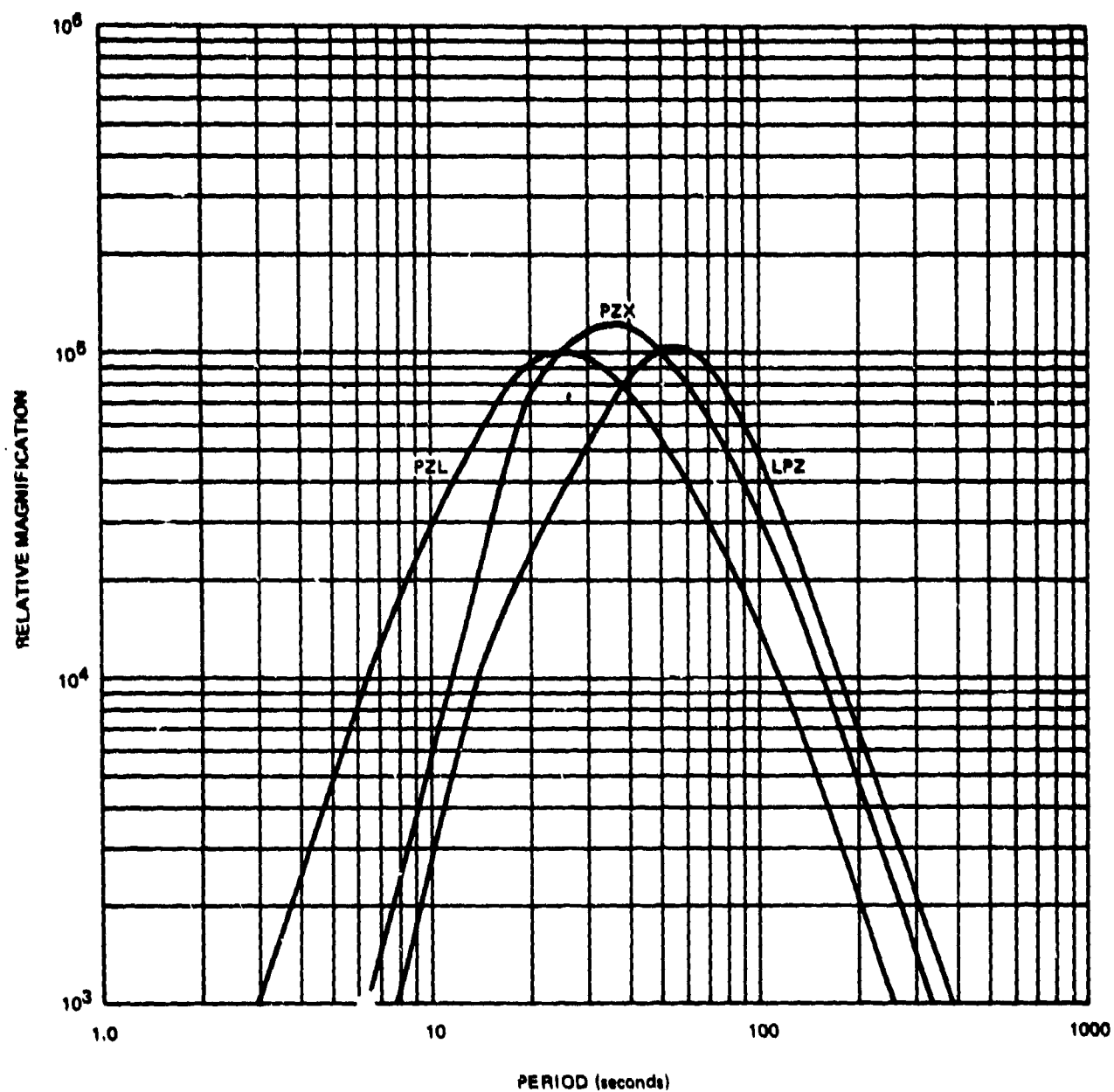


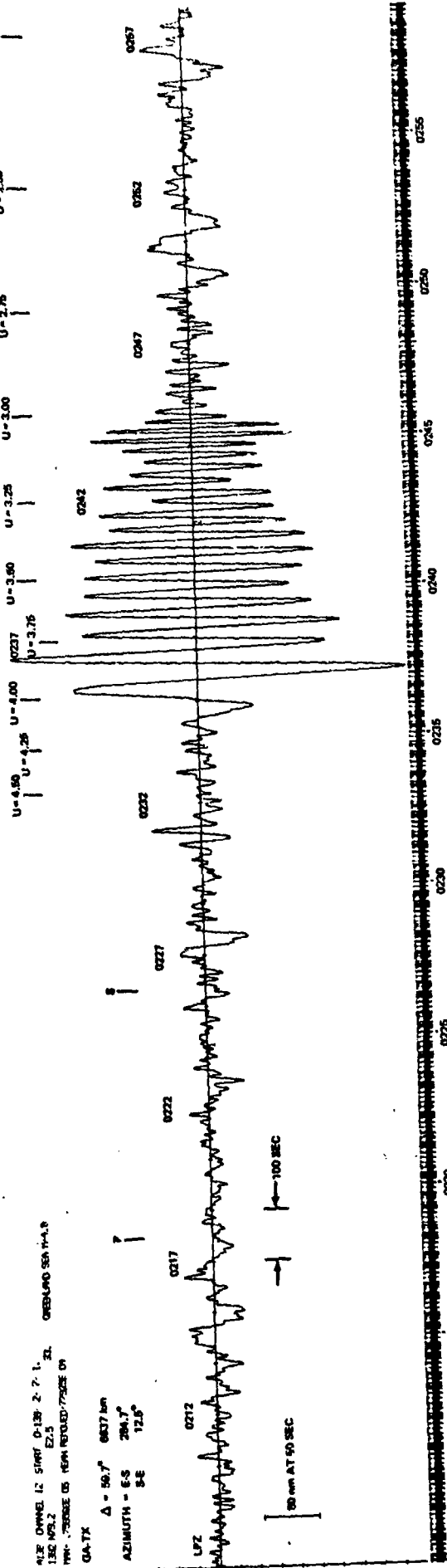
Figure 191. Seismograph amplitude responses normalized to 100,000 at calibration frequencies

G 6612

412 CHANNEL 12 START 0-139 2-7-1. 21. GREENLAND SEA 14-1.9
130.000.2 E2.5
TIME: 700000 IS NEW RETROD-700000 ON

QA-TX

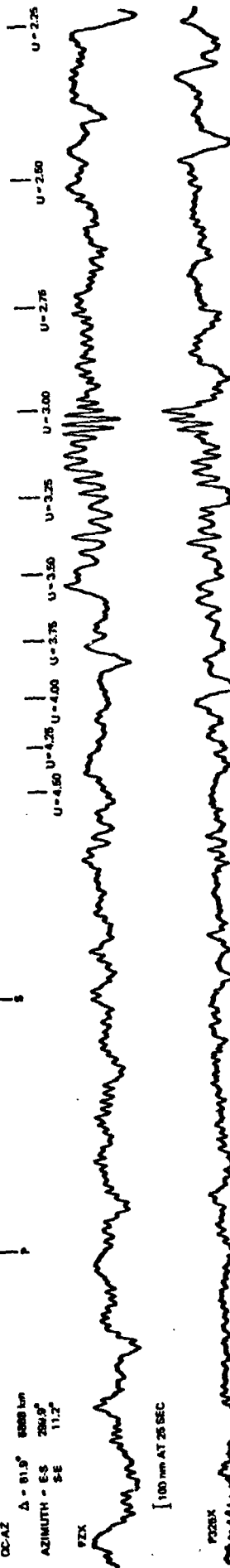
$\Delta = 50.7^\circ$ 6837 km
AZIMUTH - E-S 284.7°
S-E 12.5°



QC-AZ

$\Delta = 81.8^\circ$ 8388 km
AZIMUTH - E-S 284.9°
S-E 11.2°

PZ-X

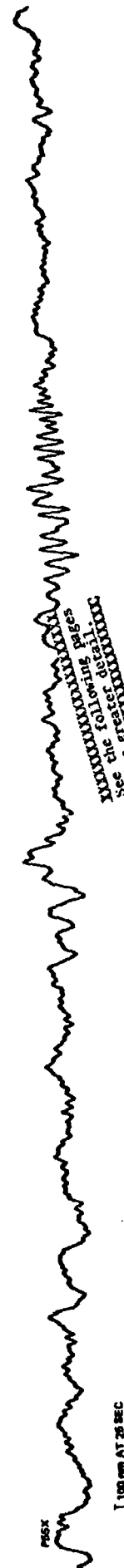


PZ-BX

[100 mm AT 25 SEC]

[100 mm AT 25 SEC]

PZ-SX



[100 mm AT 25 SEC]

XXXXXXXXXXXXXXXXXXXX
See the following pages
for greater detail.

Figure 192. Seismic waves recorded at QA-TX
and QC-AZ from an $M_b = 4.8$ earthquake in the
Greenland Sea on 19 May 1970 (day 139). 66013

347.

347.1

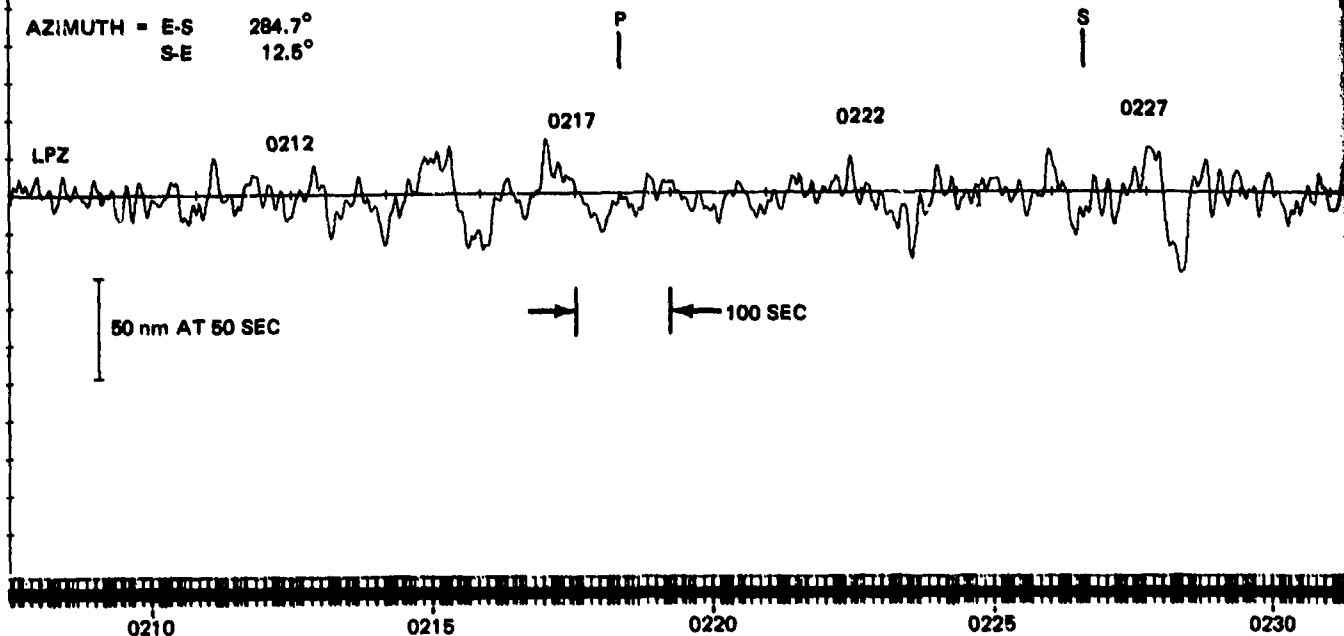
348 -347/348-

TR 72-3

AL38 CHANNEL 12 START 0-139-2-7-1.
1392 N79.2 E2.5 33. GREENLAND SEA M+4.0
MAX. 799566E 05 MEAN REMOVED 77925E 04

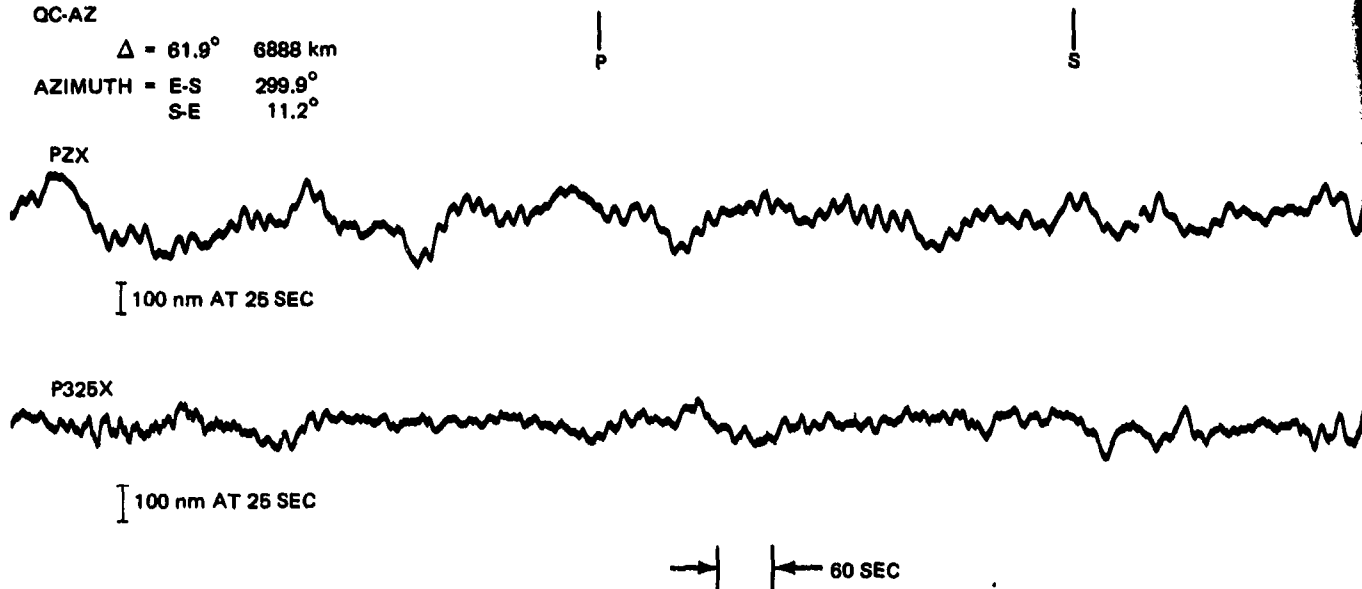
GA-TX

$\Delta = 59.7^\circ$ 6637 km
AZIMUTH = E-S 284.7°
S-E 12.5°



QC-AZ

$\Delta = 61.9^\circ$ 6888 km
AZIMUTH = E-S 299.9°
S-E 11.2°



P55X

100 nm AT 25 SEC

347.

347.1

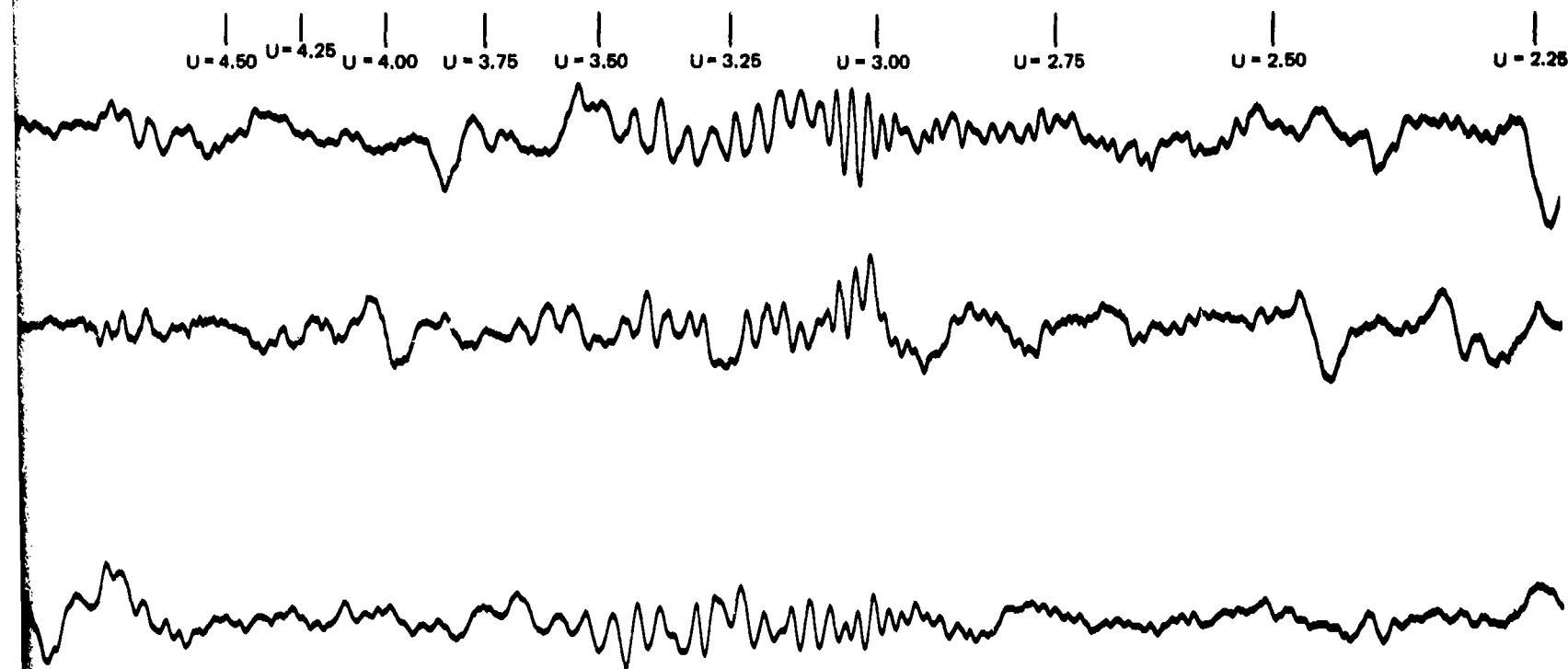
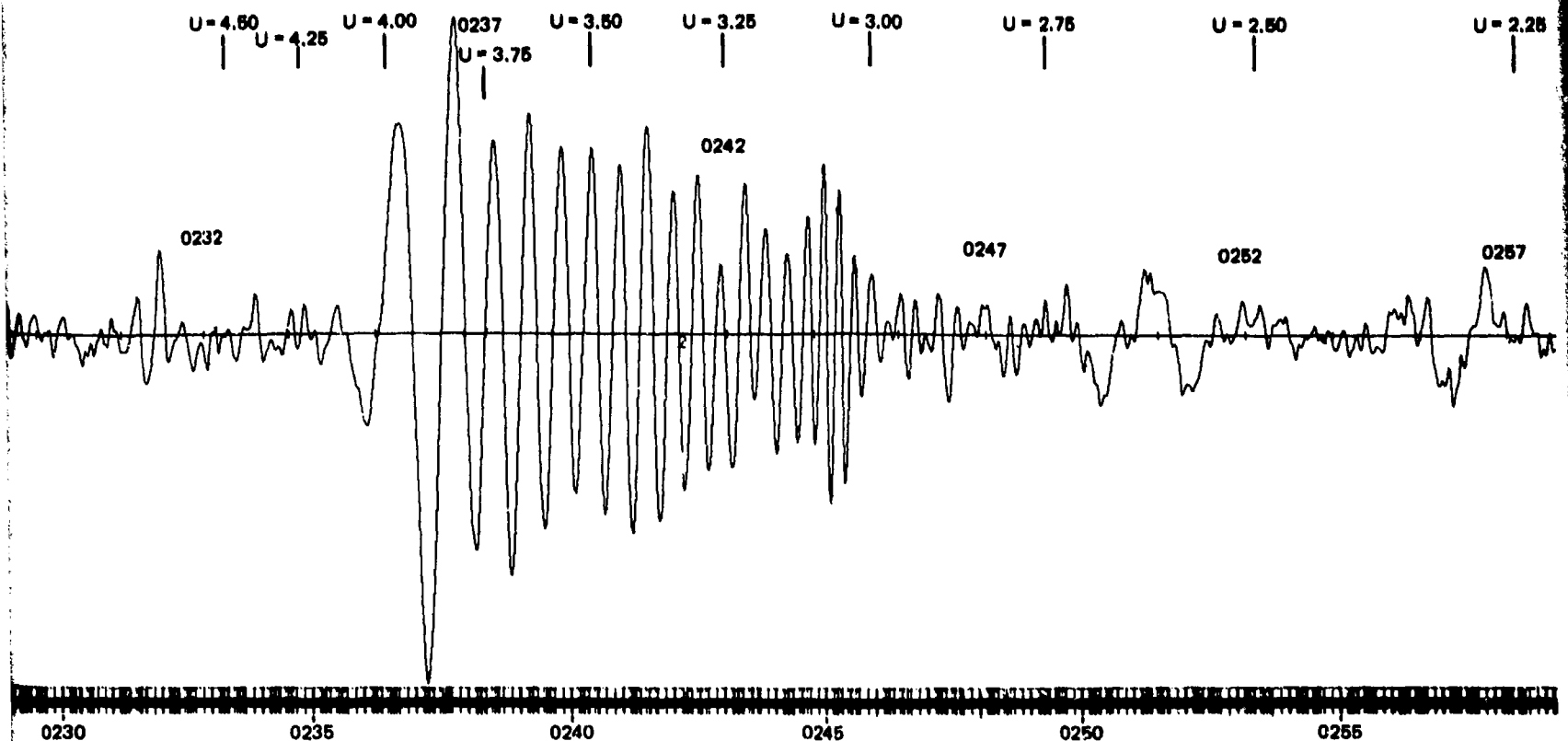


Figure 192. Seismic waves recorded at GA-TX and QC-AZ from an $m_b = 4.8$ earthquake in the Greenland Sea on 19 May 1970 (day 139).

G 6513

347.1

348.

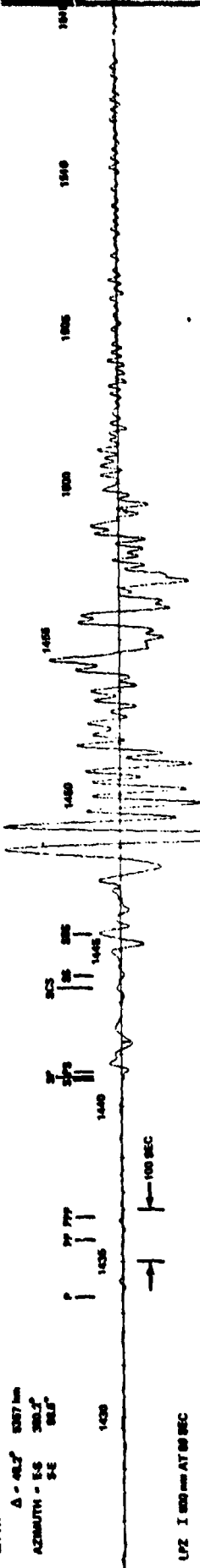
-347/348-

TR 72-3

170-10 QC-AZ 3170 14.25 1.
 170-10 QC-AZ 3170 14.25 1.
 170-10 QC-AZ 3170 14.25 1.

GA-7K
 Δ = 48.3°
 AZIMUTH = 55
 55 88.3°

U-4.5 U-4.00 U-3.75 U-3.50 U-3.25 U-3.00 U-2.75 U-2.50 U-2.25 U-2.00



100 mm AT 20 SEC

1435 1440 1445 1450 1455 1460 1465 1470 1475 1480 1485 1490 1495 1500 1505 1510 1515 1520

170-10 QC-AZ 3170 14.25 1.
 Δ = 48.3°
 AZIMUTH = 55
 55 88.3°

U-4.50



100 mm AT 20 SEC

XXXXXXXXXXXXXXXXXXXX
 See the following pages
 for greater detail.

PZLL

100 mm AT 20 SEC

Figure 193. Seismic waves recorded at GA-7K
 and QC-AZ from an $M_0 = 5.5$ earthquake on the
 North Atlantic Ridge on 19 June 1970 (day 1).

349.

3491

350

-349/350-

TR 72

349

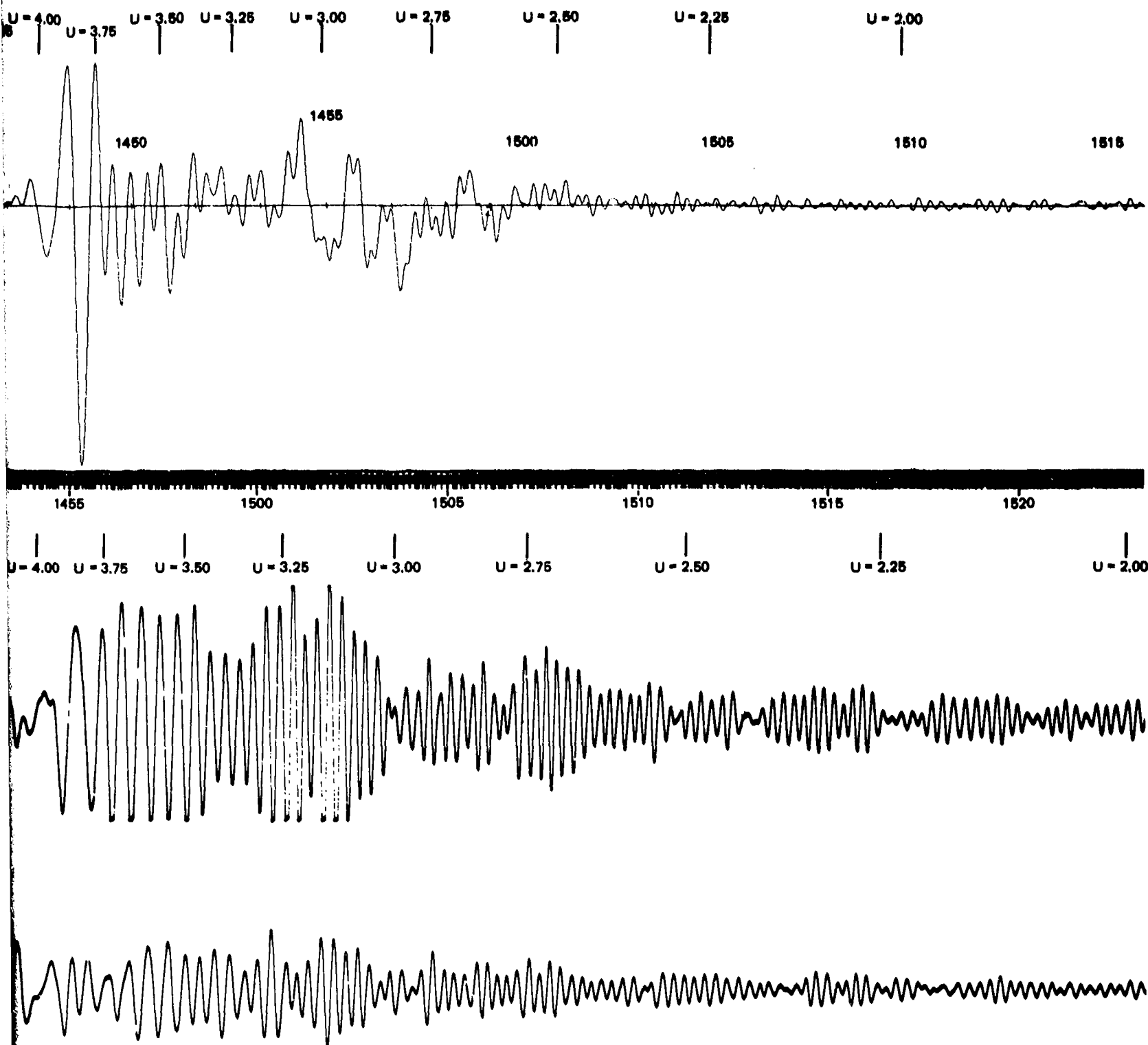


Figure 193. Seismic waves recorded at GA-TX and QC-AZ from an $m_b = 5.5$ earthquake on the North Atlantic Ridge on 19 June 1970 (day 170).

3491

350

-349/350-

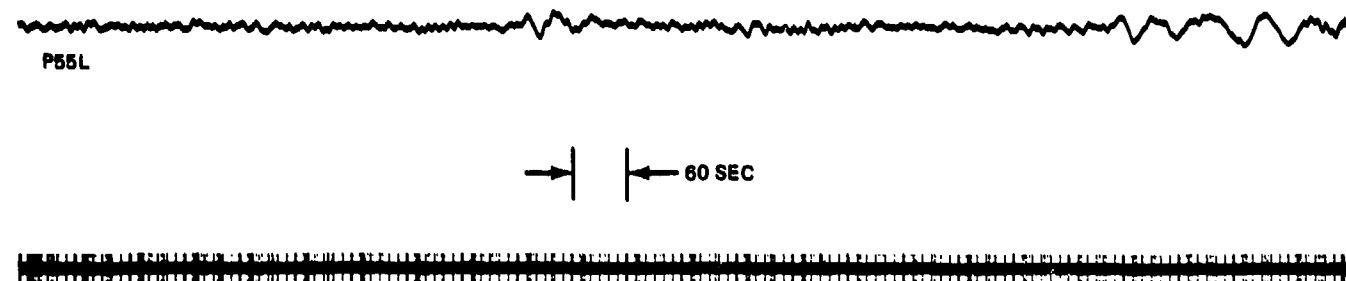
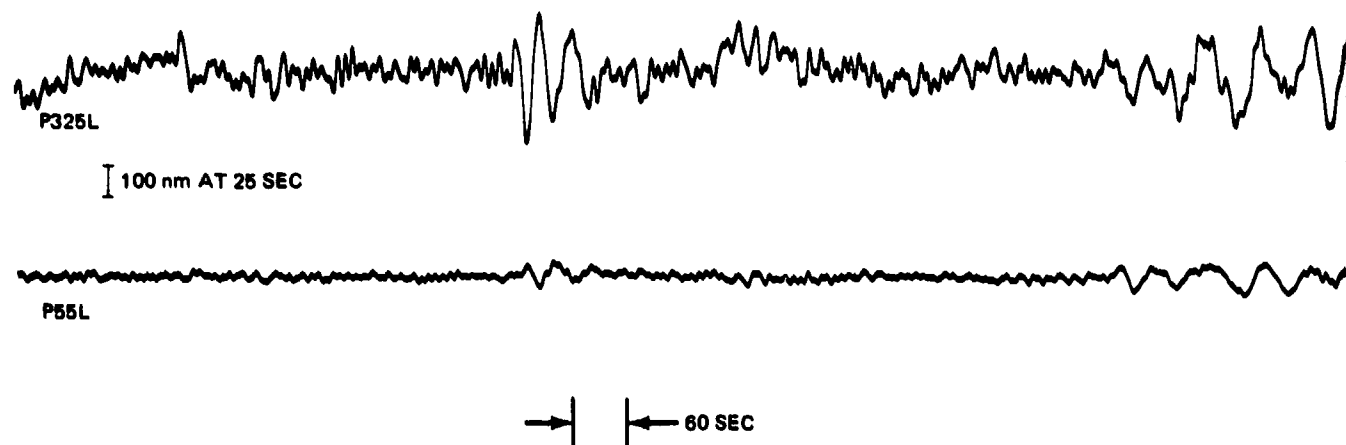
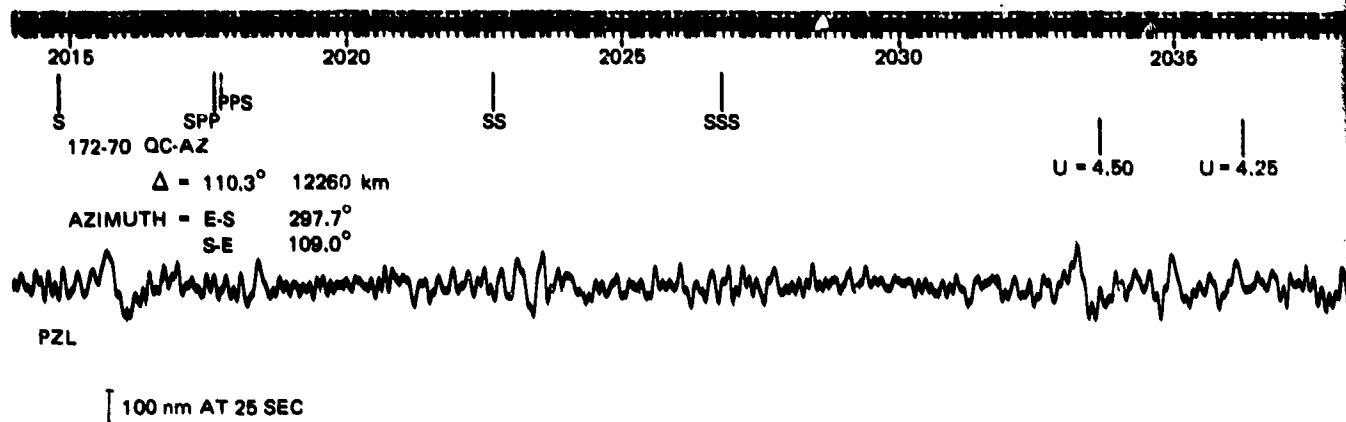
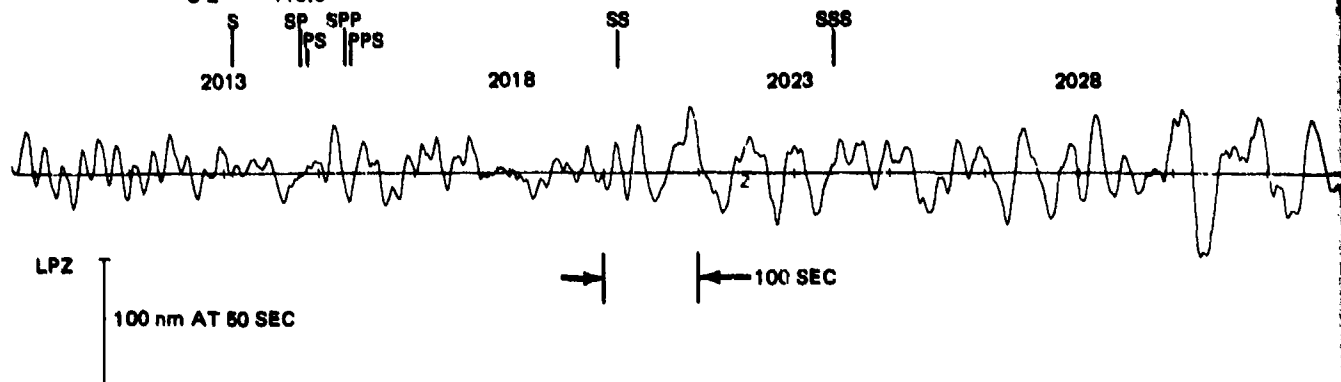
G 6814
TR 72-3

AL70 CHANNEL 12 START 0-172-19 48 1.
 1721 526.6 W13.7 33. SOUTH ATLANTIC RIDGE M-B.2
 MAX. 119324E 06 MEAN REMOVED 119324E 06

U = 4.5 U = 4.25

GA-TX

$\Delta = 97.7^\circ$ 10865 km
 AZIMUTH = E-S 302.5°
 S-E 116.6°



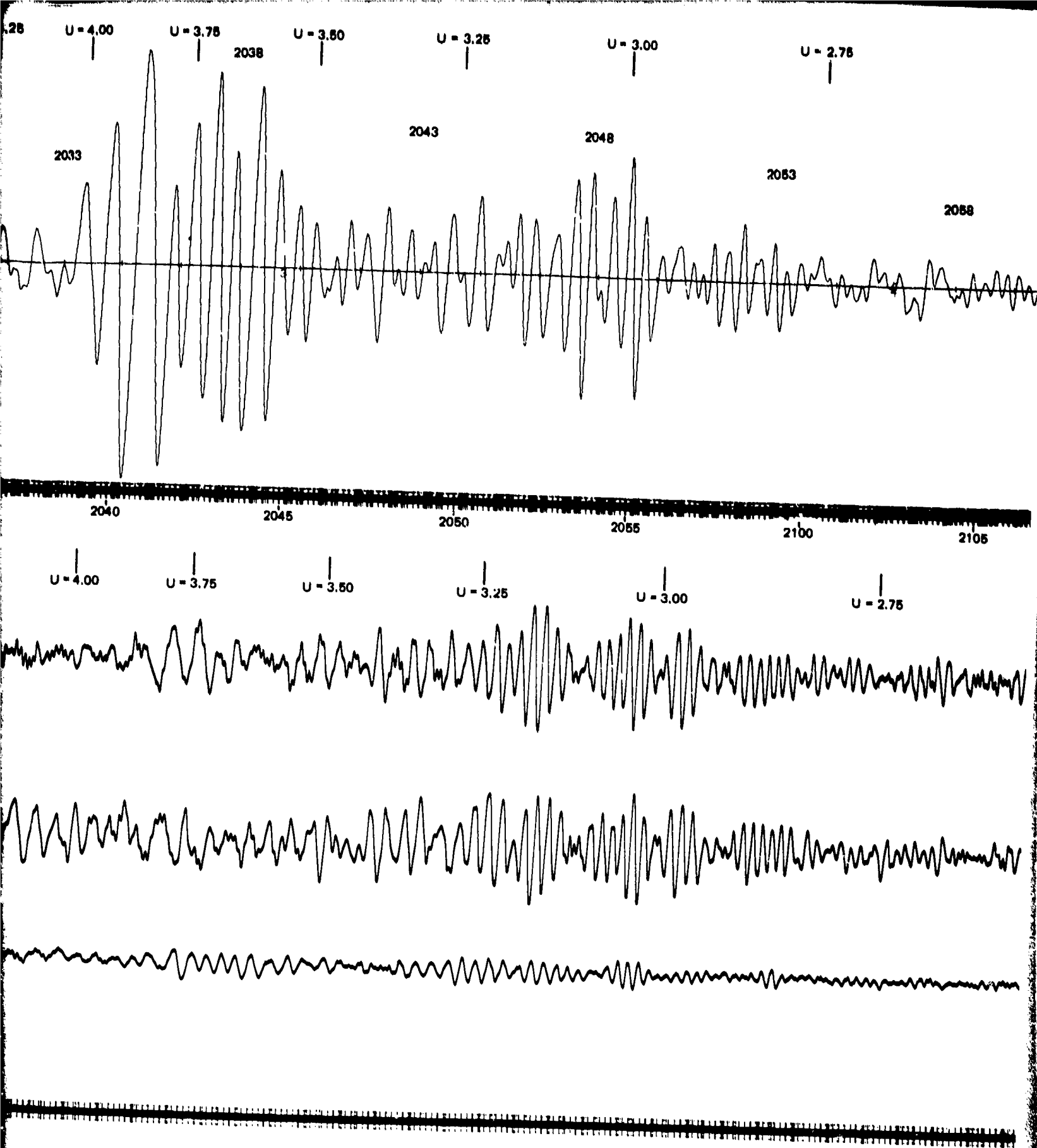


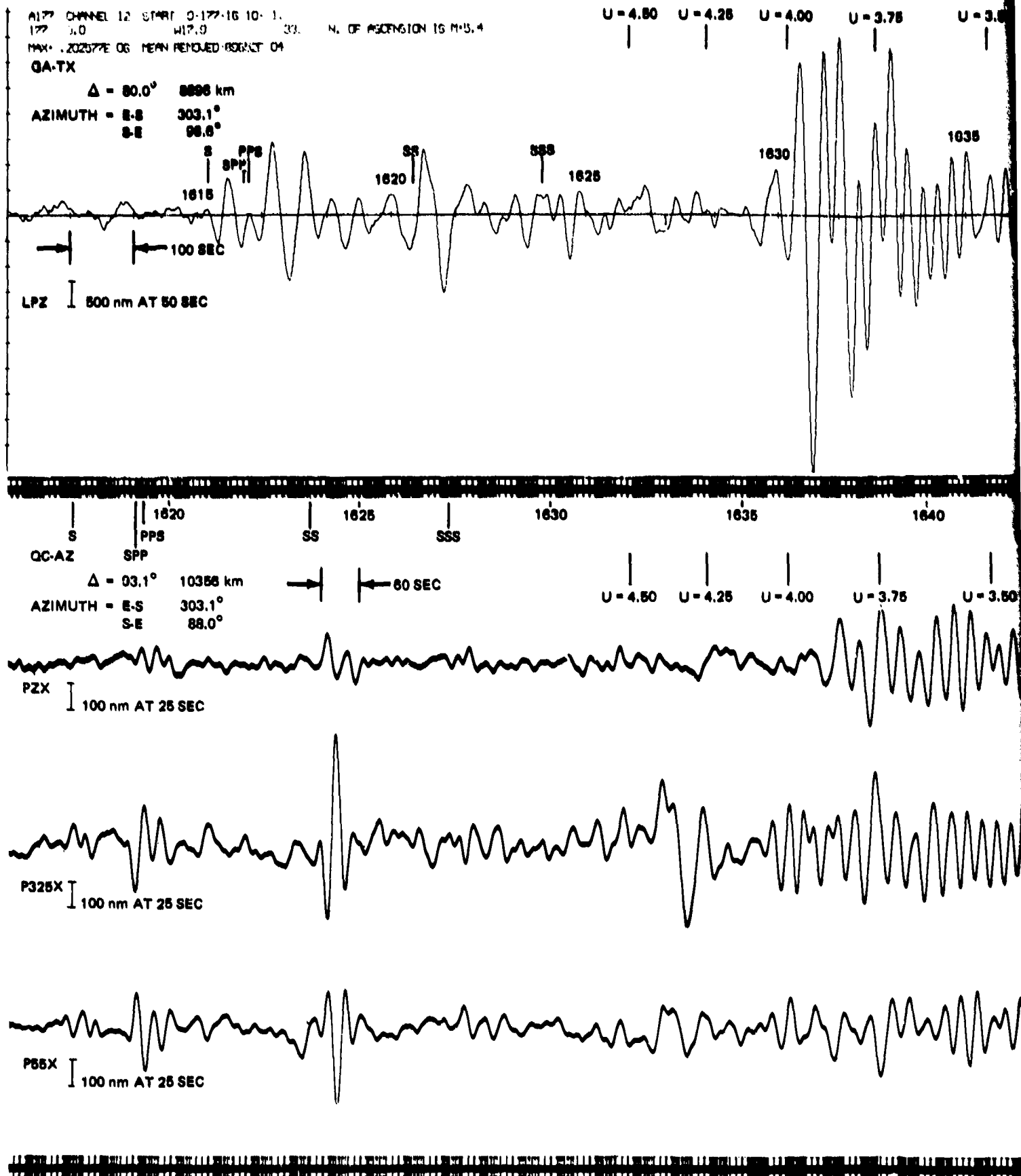
Figure 194. Seismic waves recorded at GA-TX and QC-AZ from an $m_b = 5.2$ earthquake on the South Atlantic Ridge on 21 June 1970 (day 172).

352

-351/352-

G 6515

TR 72-3



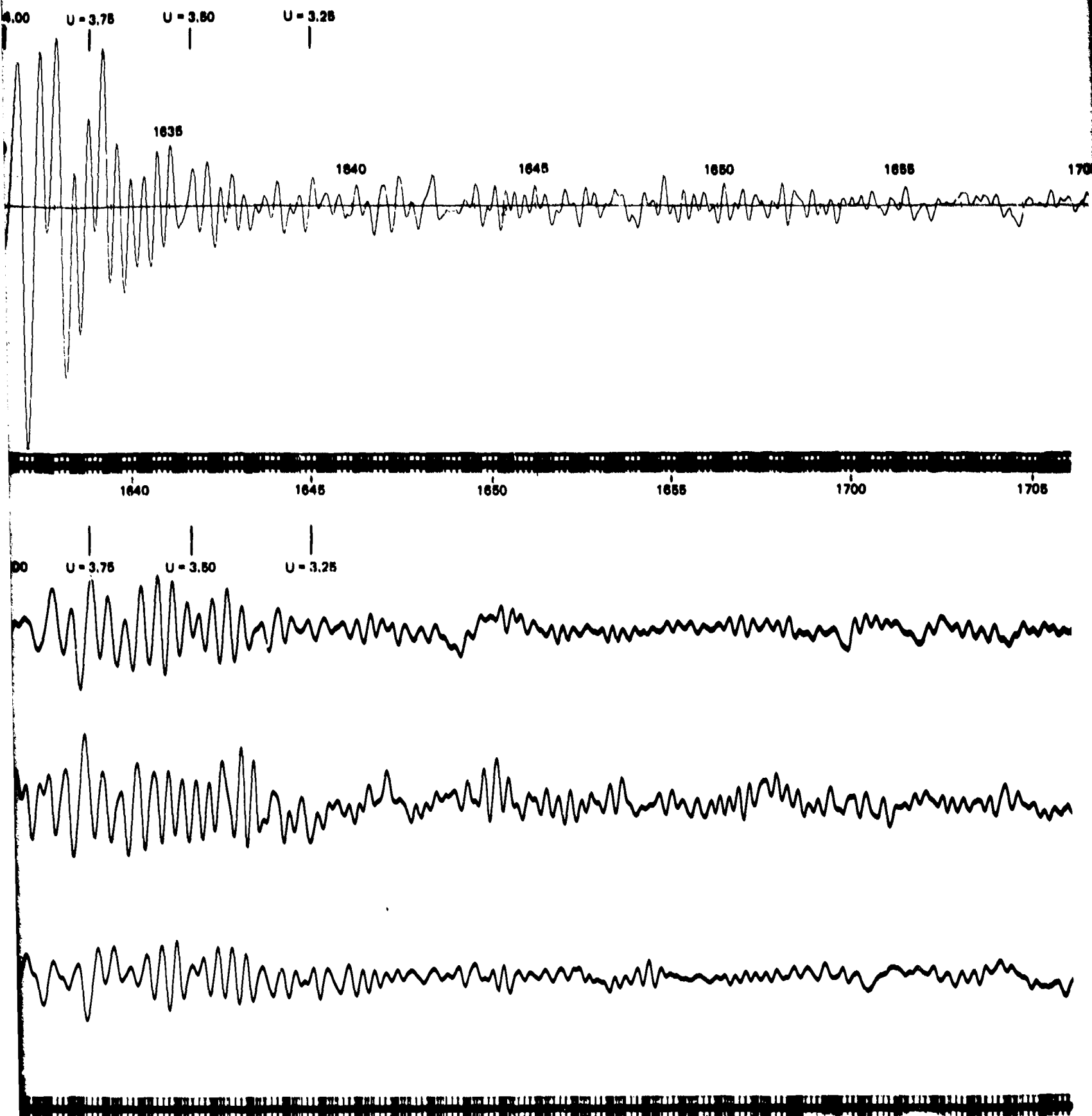


Figure 195. Seismic waves recorded at GA-TX and QC-AZ from an $m_b = 5.4$ earthquake north of Ascension Island on 26 June 1970 (day 177).

G 6816

-353/354-

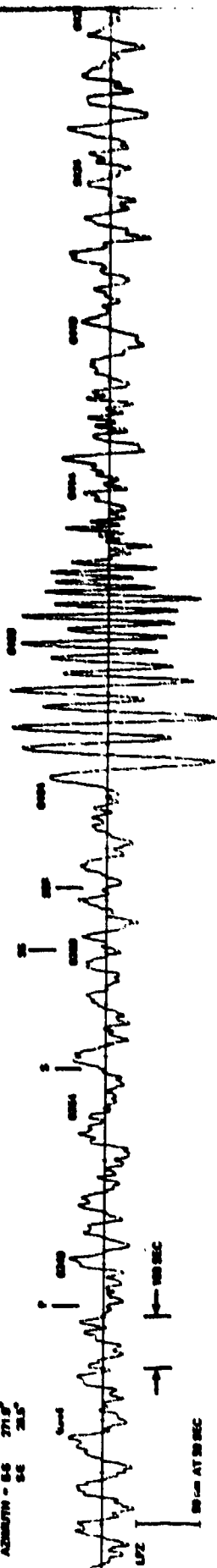
TR 72-3

353.1

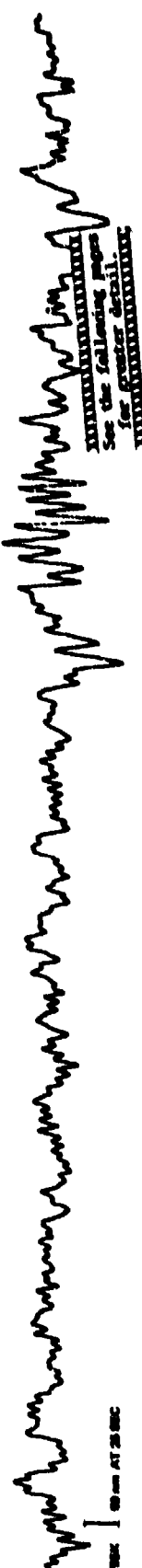
35.4

1250 0000 12 5400 2 20 3
 1250 0000 12 5400 2 20 3
 1250 0000 12 5400 2 20 3
 1250 0000 12 5400 2 20 3

A - 0.5
 AZIMUTH - 0.5
 0.5
 0.5



00-12
 A - 0.5
 AZIMUTH - 0.5
 0.5
 0.5



See the following pages
 for greater detail.

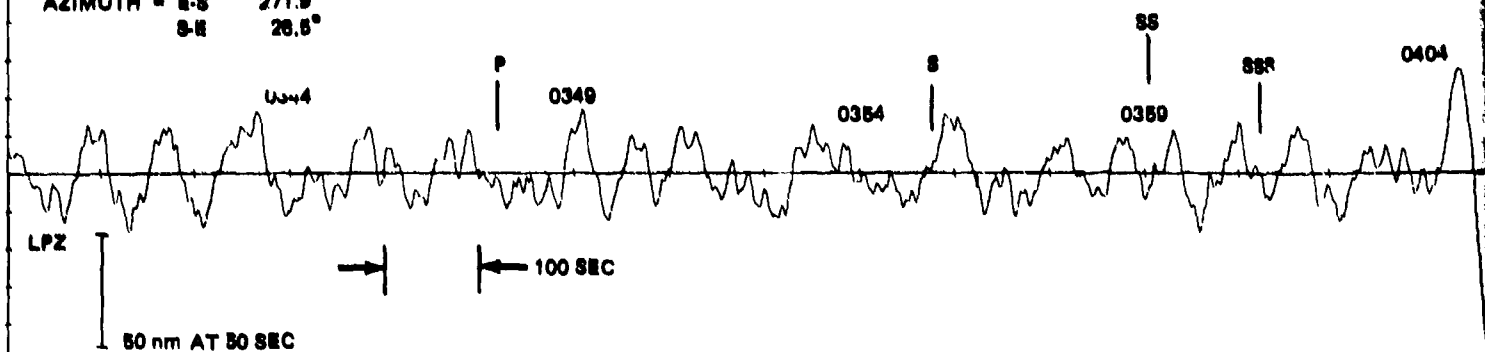
Figure 106. Seismic waves recorded at 00-12
 and 00-12 from an $M_0 = 4.5$ earthquake in the
 Iceland region on 20 June 1970 (day 120).

ATMO CHANNEL 12 START 0101-3.30-01
 1013 NDB.0 W10.7 35. ICELAND REGION H-4.3
 MAX. 0.002330E 03 MIN. 0.001200E 03

U = 4.80 U = 4.25 U = 4.00 U

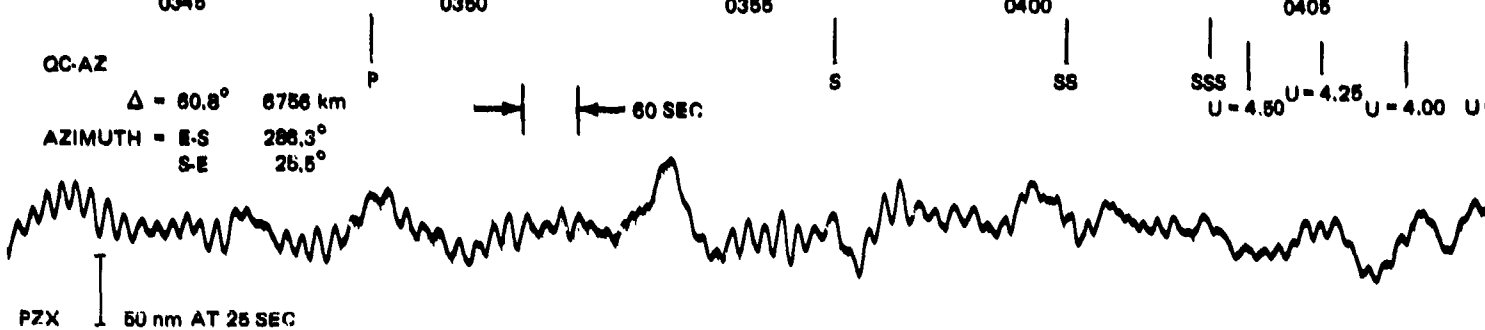
GA-TX

$\Delta = 86.3^\circ$ 6162 km
 AZIMUTH = E-S 271.9°
 S-E 26.6°



QC-AZ

$\Delta = 80.8^\circ$ 6756 km
 AZIMUTH = E-S 286.3°
 S-E 26.6°



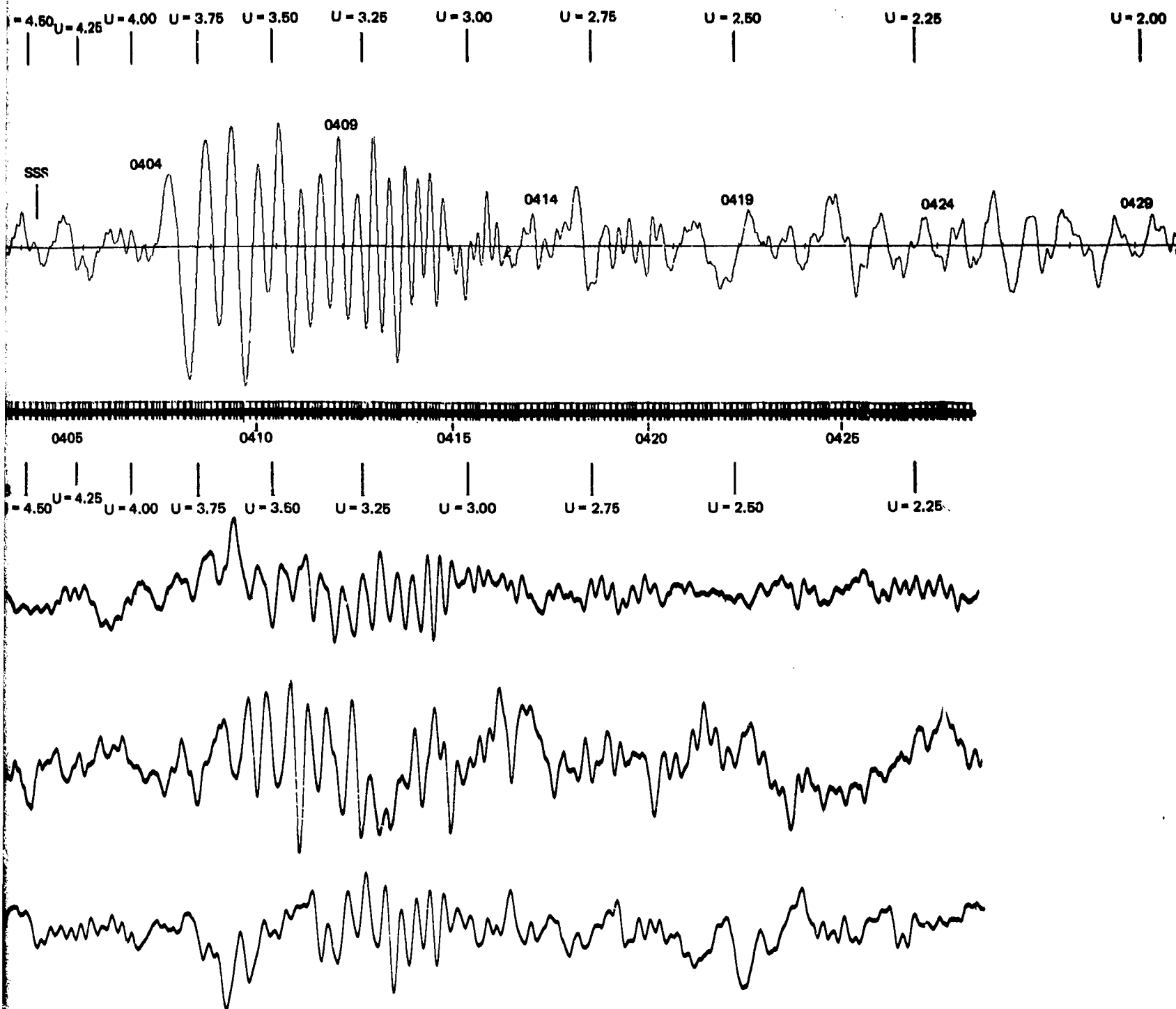


Figure 196. Seismic waves recorded at GA-TX and QC-AZ from an $m_b = 4.3$ earthquake in the Iceland region on 30 June 1970 (day 181).

35-51

Table 15. Epicenter data for recordings in figures 192 through 197

Figure No.	Date	Day	Origin time (GCT)	Lat. deg.	Long. deg.	Depth km	Location	Mb	Station	Azimuth, (deg)		
										Epi. dist. deg.	Epi. to sta.	Sta. to epi.
192	19 May 70	139	0207:41.5	79.2N	2.5E	33	Greenland Sea	4.8	GA-TX QC-AZ	59.7 61.9	284.7 299.9	12.5 11.2
193	19 Jun 70	170	1425:18.4	15.4N	45.9W	33	N. Atlantic Ridge	5.5	GA-TX QC-AZ	48.2 61.6	300.2 299.6	98.6 89.7
194	21 Jun 70	172	1948:14.3	26.6S	13.7W	33	S. Atlantic Ridge	5.2	GA-TX QC-AZ	97.7 110.3	302.5 297.7	116.5 109.0
195	26 Jun 70	177	1553:11.2	0.0S	17.9W	33	N. of Ascension Island	5.4	GA-TX QC-AZ	79.7 93.1	303.1 303.1	96.6 88.0
196	30 Jun 70	181	0338:9.5	68.0N	18.7W	33	Iceland region	4.3	GA-TX QC-AZ	55.3 60.8	271.9 286.3	26.5 25.5
197	19 May 70	139	0231:23.0	20.9N	176.8E	33	S. Fiji Is.	4.3	GA-TX QC-AZ	99.0 86.9	58.6 52.8	251.0 242.7

Data in columns 2 through 9, for figures 192-196 from National Ocean Survey Preliminary Determination of Epicenters, for figure 197 from LASA preliminary epicenter list.

Atlantic Ridge earthquake of 19 June 1970 (day 170) are illustrated in figure 193. The two stations are on great circle paths separated by only 0.6 deg at the epicenter and can be considered as being at the same azimuth of the radiation pattern for this event. The epicentral distance between the two stations is about 1500 km. About 1000 km is on the central North American plate and about 500 km is in the Basin and Range Province. The 500 km distance is about three wave-lengths for a 40 sec Rayleigh wave. Recordings from the $m_b = 5.2$ South Atlantic Ridge earthquake of 21 June 1970 (day 172) are illustrated in figure 194. The two stations are on great circle paths separated by only 4.8 deg at the epicenter and again can be considered as being at the same azimuth of the radiation pattern for this event. The Love wave at QC-AZ is seen to have 60 sec energy at 2035Z. The recordings from the $m_b = 5.4$ earthquake north of Ascension Island on 26 June 1970 (day 177) are illustrated in figure 195. Both stations are on identically the same great circle path at an azimuth of 303.1 deg from the epicenter. Rayleigh waves with periods longer than 100 sec from the long period, inverse dispersion branch can be seen at both stations. Signals from an $m_b = 4.3$ earthquake in the Iceland region on 30 June 1970 (day 181) are shown in figure 196. At GA-TX, the Rayleigh wave begins with 60 sec energy and disperses normally without a pulse. The Rayleigh wave at QC-AZ also starts with 60 sec energy and disperses normally. An interesting observation from this event is that the $m_b = 4.3$ earthquake contained energy at a period as long as 60 sec.

The epicenters of the earthquakes in figures 192 through 196 were all to the east of the two stations. Rayleigh waves from epicenters in the Pacific Ocean have similar character at both locations. Figure 197 contains the recordings from an event south of Fiji Island that was not listed on the NOS PDE cards, but was listed on the now discontinued LASA preliminary epicenter list. This event was assigned an m_b of 4.3. Data on the epicenter are given in table 15. The two wave trains both begin with a 41 sec period and trail off into the noise with 15 sec energy. The group velocities are significantly faster across the Pacific Ocean than from the combined Atlantic Ocean-Continental North America path of the other figures.

In summary, the Rayleigh waves from the east are recorded at GA-TX with a pulse of energy and generally contain longer periods than the Rayleigh waves recorded at QC-AZ. At QC-AZ, the Rayleigh waves do not have the 40 to 60 sec pulse and have less apparent energy in this period range than GA-TX.

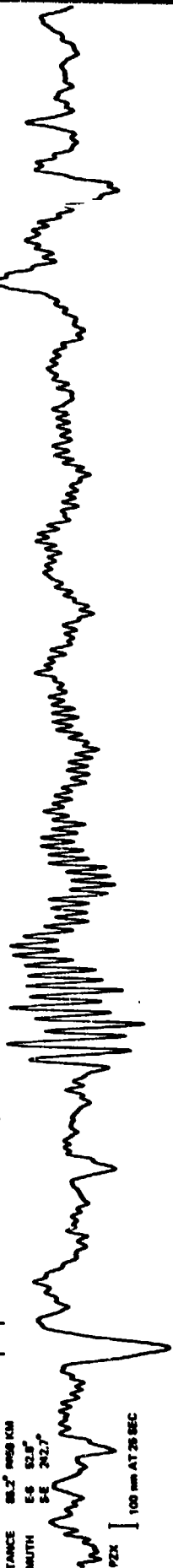
The differences in the Rayleigh waves at these two high quality stations are important to the explosion/earthquake discrimination problem. The two stations would give significantly different AR , M_{S40} , and A_{20}/A_{40} values. However, the M_{S20} values would be comparable. While there is a real and significant difference in the short-period/long-period energy of earthquakes and explosions, the Rayleigh waves illustrated indicate that the separation of these differences most assuredly must consider the tectonic setting of the source, of the source-to-station path, and of the station. Many of the best detection stations and the lowest seismic background stations have been

GA-7K
DISTANCE 88.8° 11008 KM
AZIMUTH 5.5 52.8°
5.6 281.8°



100 mm AT 80 SEC

QC-AZ
DISTANCE 88.8° 11008 KM
AZIMUTH 5.5 52.8°
5.6 281.8°

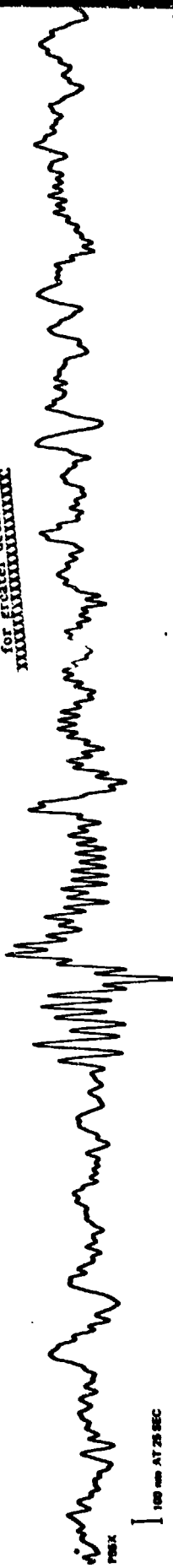


100 mm AT 25 SEC



100 mm AT 25 SEC

XXXXXXXXXXXXXXXXXXXX
See the following pages
for greater detail.
XXXXXXXXXXXXXXXXXXXX



100 mm AT 25 SEC

Figure 197. Seismic waves recorded at GA-7K and QC-AZ from an $M_b = 4.3$ earthquake south of the Fiji Islands on 19 May 1970 (day 132 of the year).

GA-TX

DISTANCE 98.0° 11008 KM

AZIMUTH E-S 58.6°
S-E 251.0°

U = 4.50

U = 4.25

U = 4.00

U = 3.75

U = 3.50

0257

0302

0307

0312

0317

0322

LPZ

50 nm AT 50 SEC

100 SEC

0255

0300

0305

0310

0315

QC-AZ

DISTANCE 86.2° 9659 KM

AZIMUTH E-S 52.8°
S-E 242.7°

U = 4.50

U = 4.25

U = 4.00

U = 3.75

U = 3.50

80 SEC

PZX

100 nm AT 25 SEC

P325X

100 nm AT 25 SEC

P65X

100 nm AT 25 SEC

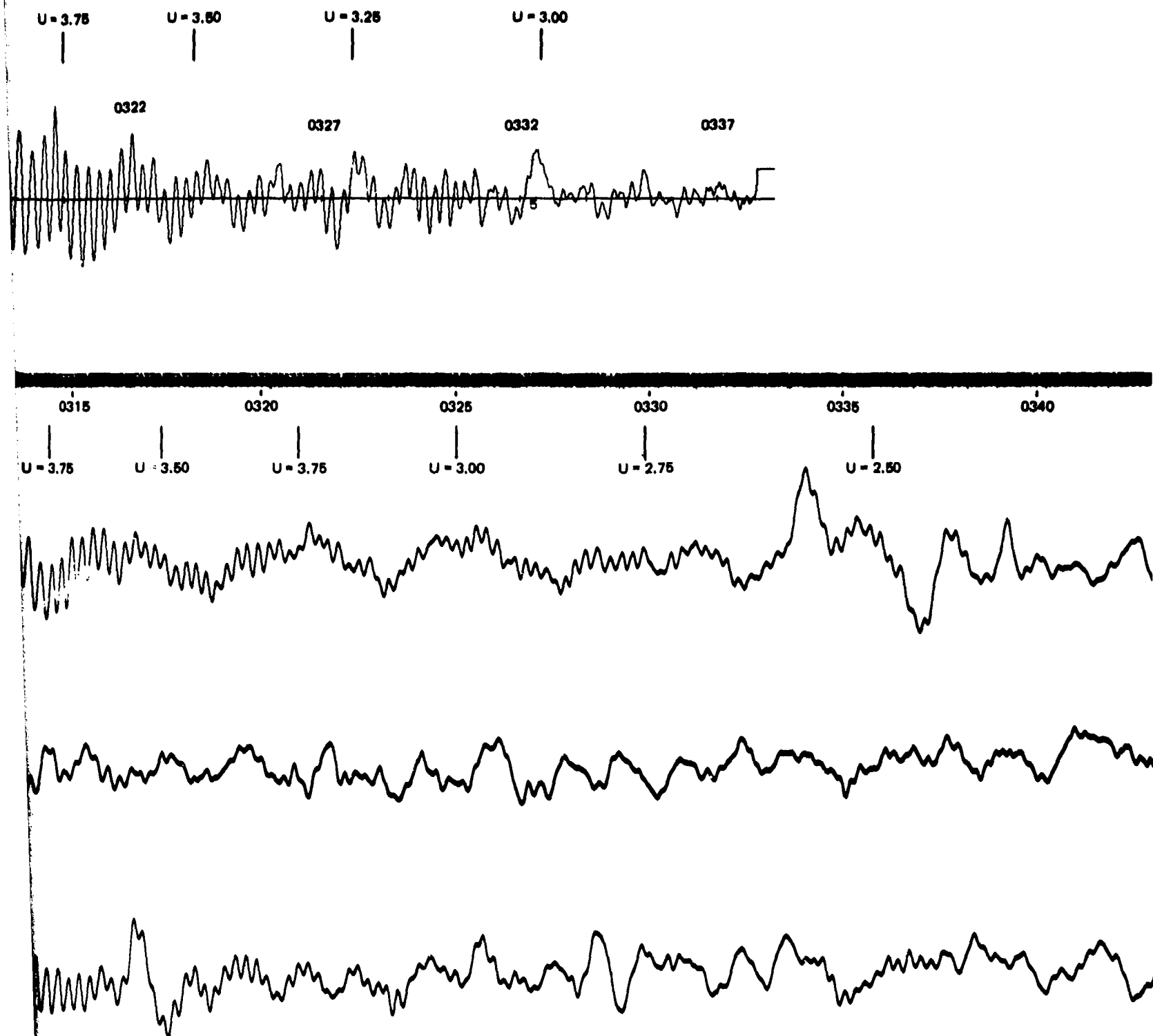


Figure 197. Seismic waves recorded at GA-TX and QC-AZ from an $m_b = 4.3$ earthquake south of the Fiji Islands on 19 May 1970 (day 139).

G 6518

7.1

360

-359/360-

TR 72-3

located in mountains or in regions of more recent tectonic movements. Among these better stations are the Tonto Forest Observatory (TFO), the better (higher magnification) LRSM stations including most of the mine sites, the Uinta Basin Observatory (UBO), and the Blue Mountains Observatory (BMO). Thus, much of the existing VELA-Uniform data base for extended long-period discrimination studies comes from stations in tectonic settings somewhat similar to QC-AZ. Data from these stations may have a previously unnoticed bias in the character of the Rayleigh wave because of reduced signals in the 40-60 sec period range.

10.5 ADVANTAGE OF STRAIN OVER INERTIAL SEISMOGRAPHS AFTER LARGE EVENTS

At any given time, the detection threshold of a high-sensitivity seismograph station, such as QC-AZ, can be reduced by the coda of signals following large ($m_b > 5.8$) earthquakes. For events deeper than 60 km, the higher modes of the free oscillations of the earth are excited, and with their higher Q , the earth rings for longer periods of time. The higher mode oscillations have a higher phase velocity than the fundamental and lower modes. It was shown in section 9.2, equation 66, that for the same ground velocity, the strain is inversely proportional to the phase velocity of the wave. Therefore, following a large earthquake, the strain seismograph output will return to the normal background quicker than an inertial seismograph will return to the normal background. The time difference between the return to normal of the two types of seismographs is significantly greater for deep earthquakes than for shallow earthquakes.

All QC-AZ records from March 1970 through May 1971 were reviewed for all earthquakes with m_b (NOS) or M_S (NOS) ≥ 5.8 . An analyst determined the noise level on both the inertial and strain seismographs before the P wave and the length of time after the P wave until the background on each type of seismograph returned to the same noise level as before the P wave. The measurements are somewhat subjective and could be in error by ± 15 min. Some events were not included because of maintenance on the systems and others because of interfering events or large aftershock sequences. The time durations are plotted against m_b (NOS) in figure 198. Time durations are plotted for events deeper than 60 km in figure 198a and for events shallower than 60 km in figure 198b. In the plot for events deeper than 60 km, the dashed line is a visual fit to the strain seismographs and the solid line is for the inertial seismographs. The solid line is from similar observations made at the Ogdensburg, New Jersey, mine (Savino et al., 1972). With the scatter of the QC-AZ data, the Ogdensburg curve is considered an acceptable fit. Savino et al. (1972) did not show data for shallow events, but their line is drawn in figure 198b for reference purposes. In all cases, for both shallow and deep events, the strain seismographs returned to normal before the inertial seismographs, thereby returning to service to detect additional events. For the deeper events, the time differences ranged up to 5-1/2 hr for an $m_b = 5.9$ event.

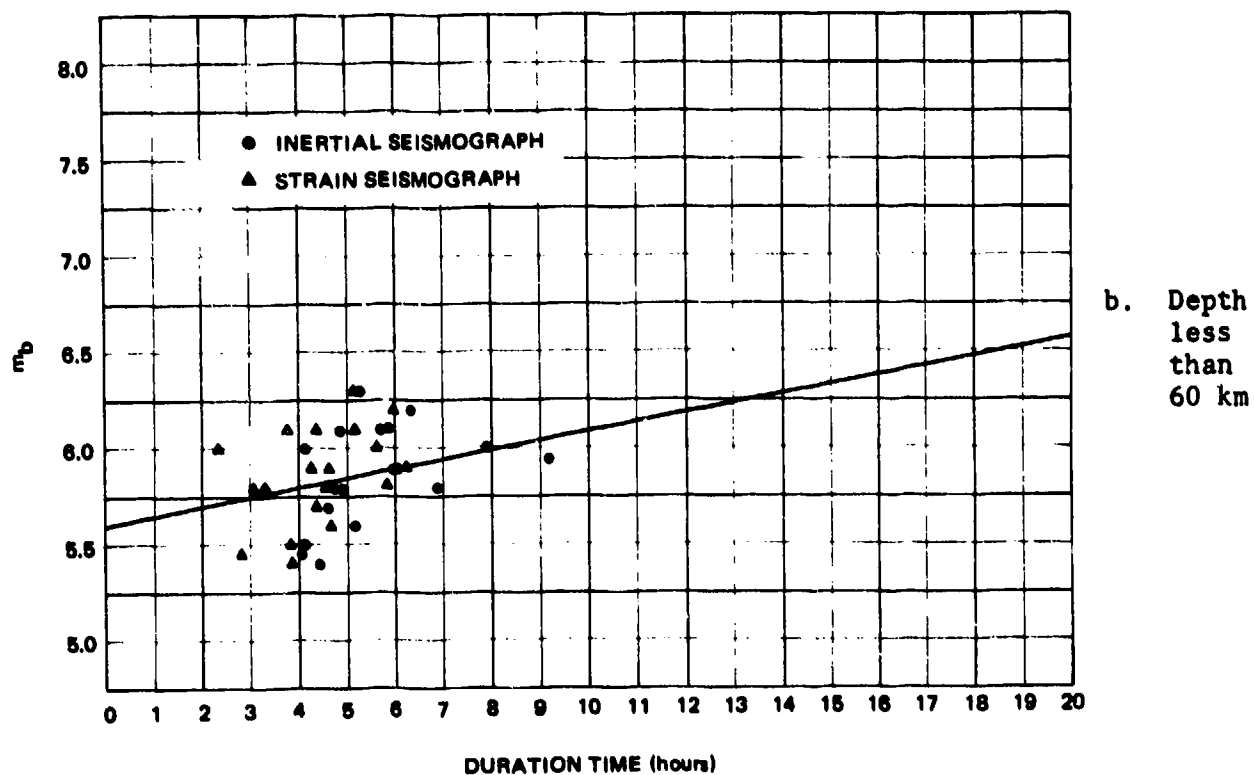
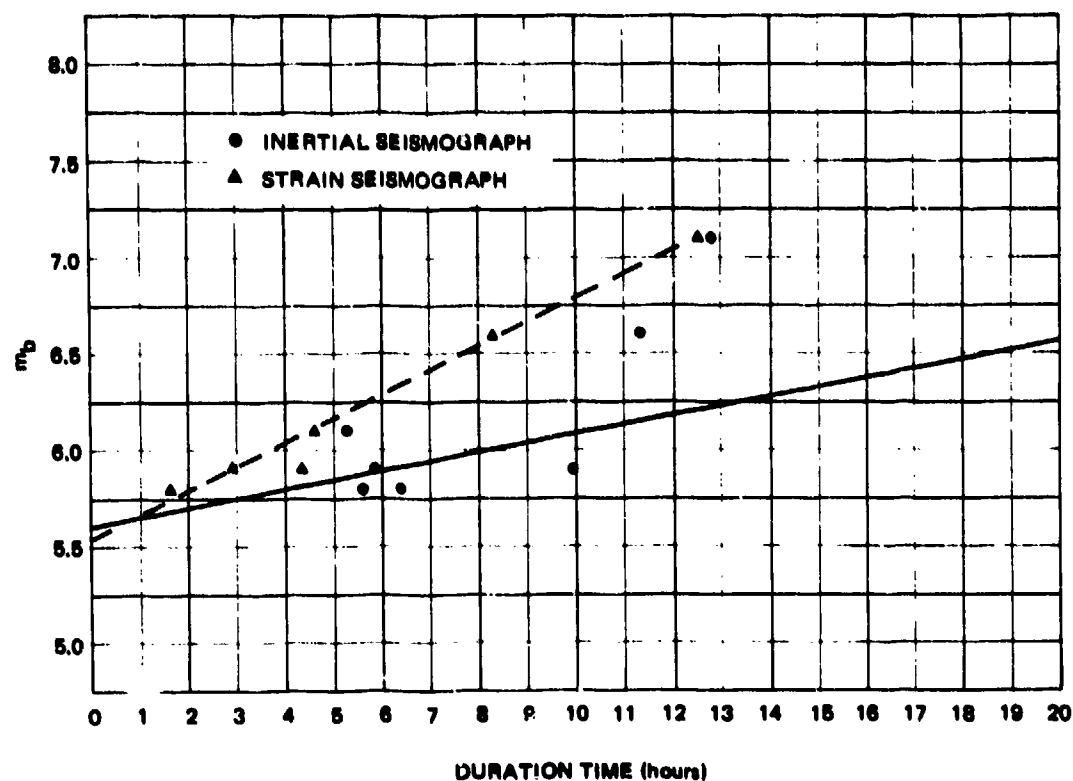


Figure 198. Earthquake duration on strain and inertial seismographs as function of m_b for (a) hypocenter depths > 60 km and (b) hypocenter depths < 60 km

G 6728

11. STEPS-OF-STRAIN

This section treats the subject of steps-of-strain propagated from earthquake foci to teleseismic distances. According to dislocation theory, the finite discontinuity in the displacement field along a fault which has ruptured results in residual displacements, strains, and tilts throughout the earth. Section 11.1 gives a descriptive (not mathematical) summary of the related work of other investigators in this field. A suite of recordings from the QC-AZ broad-band strain seismographs of signals from large earthquakes are illustrated in section 11.2. Other observations of steps-of-strain on the other QC-AZ strain seismographs are also discussed in section 11.2. The senior author's interpretation of these signals is given in section 11.3.

The nomenclature "step-of-strain" will be used in this report because it has been applied to the observed phenomenon by previous investigators. To date, the theory that has been used in the study of the permanent dislocations is a static theory. The physical, dynamic description of the process in the time domain has not been defined mathematically. Traveling dislocations were discussed in section 7.5.2 of this report. In this previous section, it was pointed out that the observed pulses actually had exponential time functions rather than step time functions. Even though the physical phenomena are pulses with exponential time functions, the nomenclature "step-of-strain" will be used as being descriptive of the static observation.

11.1 REVIEW OF THE LITERATURE

This section gives a descriptive overview of related references in the literature pertaining to steps-of-strain. The mathematics involved in the theoretical papers is cumbersome and lengthy, and no attempt will be made to summarize the results here. The interested reader is referred to the references cited in appendix 6 for further details of the theory and application of dislocation theory to earthquake disturbances.

The literature can be grouped into several categories. There is a group of papers that develop the dislocation theory for a flat earth model. Other papers have applied this theory to displacements and strains from large earthquakes. Recently, a theory has been developed for dislocations in a non-rotating, non-gravitating spherical earth. This theory has been applied to the earth as a whole and the resulting changes in moment-of-inertia of the earth to determine the effect large and great earthquakes have on changes in the pole of rotation of the earth and in the Chandler Wobble. Another group of papers, more germane to this report, are primarily papers describing observations of steps-of-strain in both the near field and the far field of explosions and of earthquakes.

Among the observational papers, those of Press (1965) and Wideman and Major (1967) were among the first and are the most quoted. Press (1965), using the fields from various nuclei of strain in a half-space developed by Mindlin and Cheng (1950), derived equations applying to a flat earth for displacements, strains in the horizontal plane, and tilts. He considered vertically-oriented faults with dip-slip and strike-slip motion. His theoretical results were presented as equations and as graphs of the resulting displacement, strain,

11. STEPS-OF-STRAIN

This section treats the subject of steps-of-strain propagated from earthquake foci to teleseismic distances. According to dislocation theory, the finite discontinuity in the displacement field along a fault which has ruptured results in residual displacements, strains, and tilts throughout the earth. Section 11.1 gives a descriptive (not mathematical) summary of the related work of other investigators in this field. A suite of recordings from the QC-AZ broad-band strain seismographs of signals from large earthquakes are illustrated in section 11.2. Other observations of steps-of-strain on the other QC-AZ strain seismographs are also discussed in section 11.2. The senior author's interpretation of these signals is given in section 11.3.

The nomenclature "step-of-strain" will be used in this report because it has been applied to the observed phenomenon by previous investigators. To date, the theory that has been used in the study of the permanent dislocations is a static theory. The physical, dynamic description of the process in the time domain has not been defined mathematically. Traveling dislocations were discussed in section 7.5.2 of this report. In this previous section, it was pointed out that the observed pulses actually had exponential time functions rather than step time functions. Even though the physical phenomena are pulses with exponential time functions, the nomenclature "step-of-strain" will be used as being descriptive of the static observation.

11.1 REVIEW OF THE LITERATURE

This section gives a descriptive overview of related references in the literature pertaining to steps-of-strain. The mathematics involved in the theoretical papers is cumbersome and lengthy, and no attempt will be made to summarize the results here. The interested reader is referred to the references cited in appendix 6 for further details of the theory and application of dislocation theory to earthquake disturbances.

The literature can be grouped into several categories. There is a group of papers that develop the dislocation theory for a flat earth model. Other papers have applied this theory to displacements and strains from large earthquakes. Recently, a theory has been developed for dislocations in a non-rotating, non-gravitating spherical earth. This theory has been applied to the earth as a whole and the resulting changes in moment-of-inertia of the earth to determine the effect large and great earthquakes have on changes in the pole of rotation of the earth and in the Chandler Wobble. Another group of papers, more germane to this report, are primarily papers describing observations of steps-of-strain in both the near field and the far field of explosions and of earthquakes.

Among the observational papers, those of Press (1965) and Wideman and Major (1967) were among the first and are the most quoted. Press (1965), using the fields from various nuclei of strain in a half-space developed by Mindlin and Cheng (1950), derived equations applying to a flat earth for displacements, strains in the horizontal plane, and tilts. He considered vertically-oriented faults with dip-slip and strike-slip motion. His theoretical results were presented as equations and as graphs of the resulting displacement, strain,

and tilt fields. In the same paper, Press illustrated strain steps at Kipapa, Oahu, Hawaii, for the great Alaskan earthquake of 27 March 1964, and for a local Hawaiian earthquake. Also shown was a strain step from a local earthquake near Nānā, Peru. Wideman and Major (1967) reported 22 strain steps from earthquakes with magnitudes of 3.0 to 8.5, at epicentral distances ranging from 47 km to 13,650 km. They observed a velocity of propagation of 3.0 ± 0.3 km/sec for continental paths and near 3.6 km/sec for oceanic paths. The strain step had an amplitude dependence upon distance R to the minus $3/2$ power, i.e., $R^{-3/2}$. Their observations were based upon the step response of two filtered strain seismographs designed for recording earthquakes. Thus, their observations were made in a manner similar to the observations on the QC-AZ ALPS response strain seismographs (S_L). Their minimum sensitivity was 10^{-10} strain, whereas, the QC-AZ strain seismographs have a minimum sensitivity of 2.5×10^{-13} strain. Romig et al. (1969) and Smith et al. (1969) monitored strains from the NTS underground nuclear test BENHAM. The most significant observation from the measurements from both sets of investigators was a step of strain followed by an exponential return to the initial strain state with a time constant of 13 minutes. The exponential decay of the strain was related to the time history of the pressure in the cavity as scaled to the estimated yield from the expressions of Olsen (1967) for an earlier explosion. Romig et al. (1969) had strainmeters at epicentral distances of 28 km and 71 km and confirmed the amplitude - distance dependence as $R^{-3/2}$. On the other hand, Smith et al. (1969) had strainmeters at 29 km and 250 km and were not able to confirm this distance dependence. Their data suggested R^{-3} was a better fit.

Dickey (1969) measured strain with geodetic quadrilaterals in the vicinity of the BENHAM explosion. He concluded that the maximum strain ϵ varied with distance as

$$\log \epsilon = -3.2823 - 0.1087R$$

At distances greater than 5 km, the strain changes were fault controlled. Dickey (1971) also measured strain before and after the JORUM explosion. In monitoring distance over a 2 km range following the explosion, he observed five steplike distance changes; one was associated with an identifiable seismic event and the other four were not. Dickey again came to the conclusion that the strains within 15 km from the epicenter were strongly controlled by the geological features of the area. As a result of this conclusion, he states that an ordinary strain-versus-distance curve for these data could be highly misleading.

Boucher et al. (1971) monitored strains 165 km from the JORUM explosion and 162 km from the HANDLEY explosion. They observed extensional strain offsets that did not decay within the first few hours after the explosion. These observations led them to conclude that the strain changes were tectonic in origin and that the explosions initiated the strain release. Olsen (1970) measured radial and transverse dynamic and quasi-static strain at 457, 914, and 1524 m from ground zero of the NTS nuclear explosion HUTCH ($m_b = 5.4$). His observations showed considerable complexity in the strain data at these short ranges. The geologic structure of the alluvium was the dominating factor in the data complexity. The observed strains seemed to be dependent upon the depth of the alluvium. The best fit of the peak of the dynamic strain to distance was proportional to R^{-3} . The static strain step showed no decay with time as was

observed after the JORUM event rather than the exponential decay as was observed after the BENHAM event.

Berg and Lutschak (1971) have recorded, in Alaska, tilts generated by magnitude 2 to 8 earthquakes at epicentral distances of 20 to 9000 km. They have observed propagation velocities of 2.7 km/sec in the near field and 3.1 km/sec at large distances. Strain steps have also been observed in Japan. Shichi et al. (1970) observed strain steps and a rapid increase in water flow following earthquakes of magnitude 6.6 at 48 km epicentral distance, and of magnitude 7.8 at 1200 km distance. The Japanese Network of Crustal Movement Observatories (1970) used strainmeter records from fifteen crustal movement stations to study the strain field associated with a magnitude 6.6 earthquake. They found the amplitude of the strain steps to be inversely proportional to the cube of the distance from the source. There was considerable scatter in the observations, but there was an "indistinct but systematic correlation" with the theoretical residual strain patterns of Press (1965). Takemoto (1970) observed strain steps at three Japanese observatories for earthquakes ranging in magnitude from 3.2 to 7.9. He found that the amplitude of the strain step depends on distance proportionately with $R^{-2.4}$. He obtains fair agreement with the residual strain patterns of Press (1965). McGinley (1968) made a detailed study of several clearly recorded steps-of-strain associated with earthquakes for which the focal mechanisms were well understood. Since the observed strains were much larger than theoretically predicted strains, he concluded that changes in the strain field near the seismograph station played an important part in the steps-of-strain that accompanied these earthquakes. Stacey and Rynn (1970) report the observation of permanent offsets on tiltmeters and on strainmeters in S. E. Queensland. Since the majority of the offsets normally occurred in the direction of any secular trend in the record, they concluded that the majority of the residual strains were local effects stimulated by the seismic waves.

11.2 STRAIN STEPS OBSERVED ON QC-AZ STRAIN SEISMOGRAPHS

The strain seismographs at QC-AZ were operated in four passbands at four sensitivities. (See figure 28 in section 4.1.3) The broad-band (BB) strain seismographs S B were intended to record ground strain over a passband that would not distort steps-of-strain. The passband selected was from dc to 7.5 Hz. The system was capable of sensing permanent offsets with sufficient high frequency response to determine the character of the time function of the steps. The BB strain seismographs had an operating minimum sensitivity of about 10^{-10} strain. This sensitivity was limited by the 10^{-8} strain earth tides and the 40 dB dynamic range of the recorders. With this sensitivity, the QC-AZ BB strain seismographs with the dc to 7.5 Hz had about the same routine operating sensitivity as the Wideman and Major (1967) filtered seismograph with a peaked response for recording earthquake waves. As pointed out previously in this report, the QC-AZ ALPS response strain seismographs had a minimum detectable strain of 2.5×10^{-13} strain.

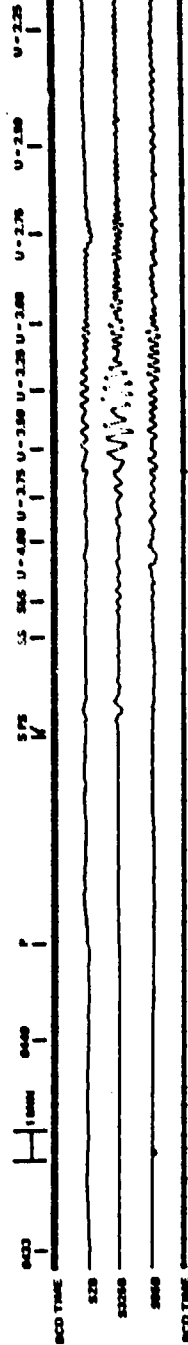
Recordings from several selected medium ($m_b = 5.4$) to large ($m_b = 7.3$) earthquakes, which were recorded on the broad-band strain seismographs, are illustrated in figures 199 and 200. Of these earthquakes, only one - the San Fernando, California, earthquake of 9 February 1971, shown in figure 199(d) - indicated a permanent strain offset. There were several other large earthquakes recorded on the broad-band seismographs, but the illustrated events have been selected as representative.

The NOS PDE data and the calculated epicentral distances and station-to-epicenter azimuths are given in table 16 for the earthquakes whose signals are illustrated. In this section, observations relative to steps-of-strain will be discussed first, then other observations will be made concerning the seismograms illustrated.

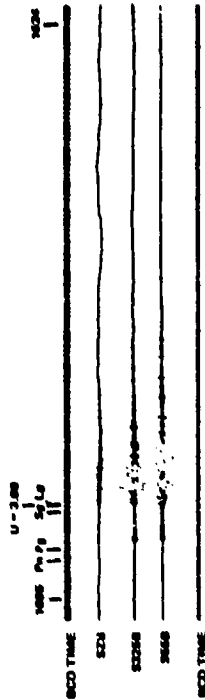
The San Fernando, California, earthquake of 9 February 1971 produced an apparent residual strain of 3.26×10^{-8} strain in the 325 deg azimuth, as recorded on the S325B seismograph and illustrated in figure 199(d). By inspection of this trace in the figure, it can be noted that the peaks of the waves appear normal, but the troughs of the oscillations are severely distorted. After recording this signal, the electronics in this channel were checked and a bad diode was found in the lightning protection circuit. This malfunctioning of the electronics clouds the positive identification of the residual strain detected. However, the senior author interprets this recording as being a distorted recording of a true residual strain of 3.26×10^{-8} strain. The reasons for this interpretation are (1) The residual strain was not a step but had an exponential time function of about a 2 min time constant. The distortion from the diode would have acted at a much higher frequency. (2) The offset was permanent, indicating a permanent change in the transducer output voltage which the diode could not have created. (3) Following this event, there were anomalies in the secular rate as discussed in section 7.8.

If the recorded residual strain is taken as a real ground phenomenon, two major observations are to be made. First, as stated previously in several places in this report, the 325 deg azimuth is weak structurally since it is sub-parallel to the local joint pattern. This direction was shown to be weaker than the 55 deg azimuth direction by the loading tests in section 8.2.3. This is the direction in which a permanent offset or slippage along the local joint pattern would be expected, if residual displacements and strains are phenomena of the geologic structure in the vicinity of the station rather than phenomena of the source mechanism of the earthquake. The second major observation is that only one component of the three orthogonal component set was subjected to the residual ground movement. There was no accompanying residual strain recorded on either the S55B horizontal seismograph or the SZB vertical seismograph. It is impossible for an elastic strain at a free surface to act in only one direction. Equation (59), developed in section 9.1.5 to relate vertical strain to the sum of orthogonal horizontal strains, was based solely on the boundary condition that the vertical stress P_{zz} at the ground-air interface must vanish. This boundary condition holds regardless of the source or type of the strain. Therefore, either the orthogonal, horizontal strain seismograph should have had an equal and opposite residual strain or the vertical strain seismograph should have had a residual strain. The obvious conclusion, then, is that if the apparent residual offset is real, it is the result of a non-elastic differential displacement between the piers of the strain seismometer and must therefore be strictly a phenomenon of the ground in the vicinity of the station and not of the source mechanism.

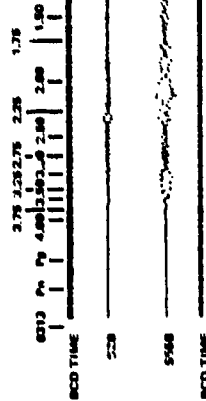
The observation that the step-of-strain (or pulse-of-strain) occurs on only one component applies directly to all the observed pulses recorded at QC-AZ at all levels of sensitivity. Another example of only one horizontal component recording pulses is illustrated in figure 76, in section 7.5.2, where travelling dislocations are discussed. After the parallel S325-2 horizontal seismometer was assembled as the vertical SZ seismometer, the fact that only one of the three strain components



(a) 10 Dec 1970 (344)



(b) 17 Dec 1970 (351)



(c) 19 Jan 1971 (019)



(d) 9 Feb 1971 (040)



(e) 14 Apr 1971 (104)

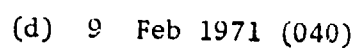
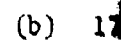
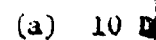
Figure 199. Seismic waves recorded on the broad-band strain seismographs. NOS PNE epicenter data: (a) 0-0434:38.8, 10 Dec 70 (344), 4.05, 80.7N, h=25 km, Peru-Ecuador border region, $m_b=6.5$, $M_s=7.6$, $L=47.2$ deg, azimuth=155.6 deg, (b) 0-1605:00.2, 17 Dec 70 (351), 37.1N, 116.1W, h=0 km, southern Nevada, NVN, CAMPIRAN $m_b=5.7$, $\Delta=5.4$ deg, azimuth=318.1 deg, (c) 0-0316:53.6, 19 Jan 71 (019), 23.8N, 104.6E, h=5 km, Gulf of California, $m_b=5.5$, $M_s=5.9$, $\Delta=9.7$ deg, azimuth=163.3 deg, (d) 0-1400:41.6, 9 Feb 71 (040), 34.4N, 118.4W, h=15 km, San Fernando, California, $m_b=6.2$, $M_s=6.5$, $L=5.8$ deg, azimuth=284 deg, (e) 0-1138:42.1, 14 Apr 71 (104), 27.7N, 112.4W, h=3 km, Baja California, $m_b=5.4$, $M_s=5.2$, $\Delta=5.5$ deg, azimuth=187.1 deg

-367/368-

348

349

See the following pages for greater detail.



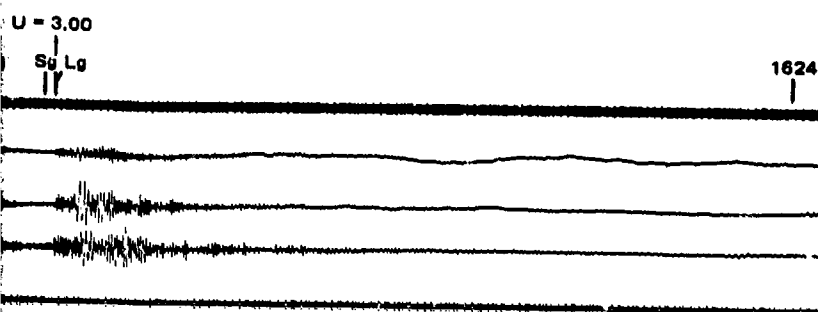
367

bro
4.0
deg
mb=
Gu1
(04
284
5.2

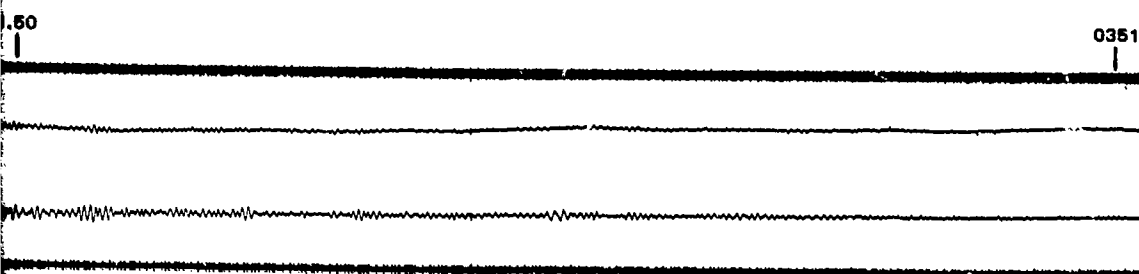
367. 1

U = 4.00 U = 3.75 U = 3.50 U = 3.25 U = 3.00 U = 2.75 U = 2.50 U = 2.25

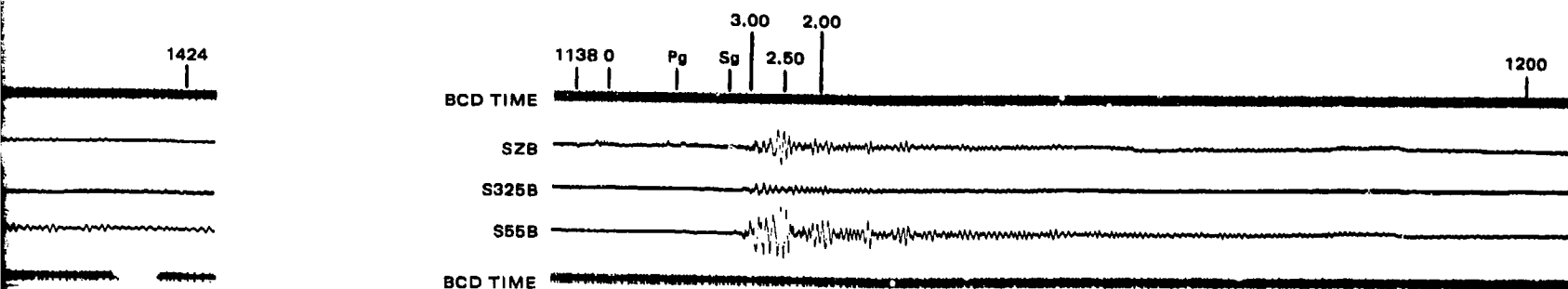
(a) 10 Dec 1970 (344)



(b) 17 Dec 1970 (351)



(c) 19 Jan 1971 (019)



(e) 14 Apr 1971 (104)

Figure 199. Seismic waves recorded on the broad-band strain seismographs. NOS PDE epicenter data: (a) 0=0434:38.8, 10 Dec 70 (344), 4.0S, 80.7W, h=25 km, Peru-Ecuador border region, $m_b=6.3$, $M_s=7.6$, $\Delta=47.2$ deg, azimuth=135.6 deg, (b) 0=1605:00.2, 17 Dec 70 (351), 37.1N, 116.1W, h=0 km, southern Nevada, NTS, CARPETBA $m_b=5.7$, $\Delta=5.4$ deg, azimuth=318.1 deg, (c) 0=0316:53.6, 19 Jan 71 (019), 23.8N, 108.6W, h=N, Gulf of California, $m_b=5.5$, $M_s=5.9$, $\Delta=9.7$ deg, azimuth=163.3 deg, (d) 0=1400:41.6, 9 Feb 71 (040), 34.4N, 118.4W, h=13 km, San Fernando, California, $m_b=6.2$, $M_s=6.5$, $\Delta=5.8$ deg, azimuth=284 deg, (e) 0=1138:42.1, 14 Apr 71 (104), 27.7N, 112.4W, h=N, Baja California, $m_b=5.4$, $M_s=5.2$, $\Delta=5.5$ deg, azimuth=187.1 deg

367.1

368

-367/368-

TR 7

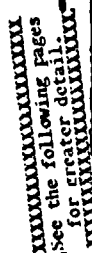


Figure 200. Seismic waves recorded on (a) ultra-broad-band strain seismographs and (b) the long-period strain seismographs from the earthquake on West New Guinea, SOS PRE Data 0 = 0717:03.7, 10 Jan 71, 3.15, 139.7E, $\delta = 278.0$ deg, $\Delta = 107.4$ deg, $M_0 = 7.3$, $M_S = 8.1$, $\Delta = 107.4$ deg, azimuth = 278.0 deg

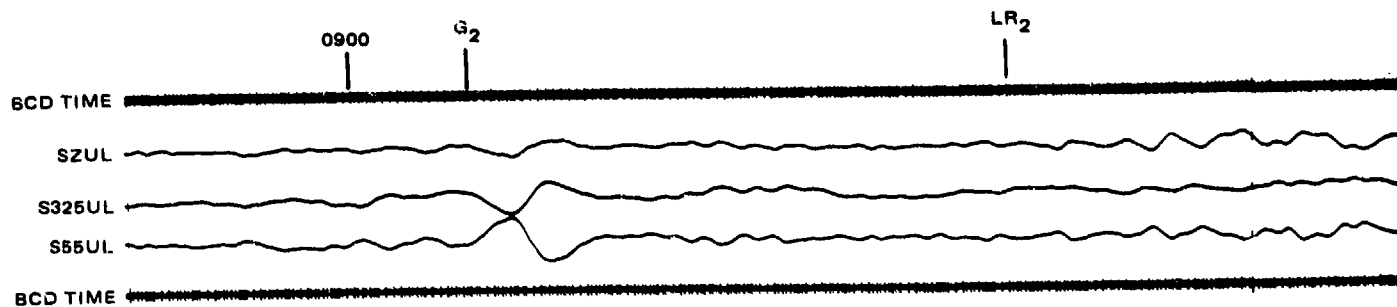
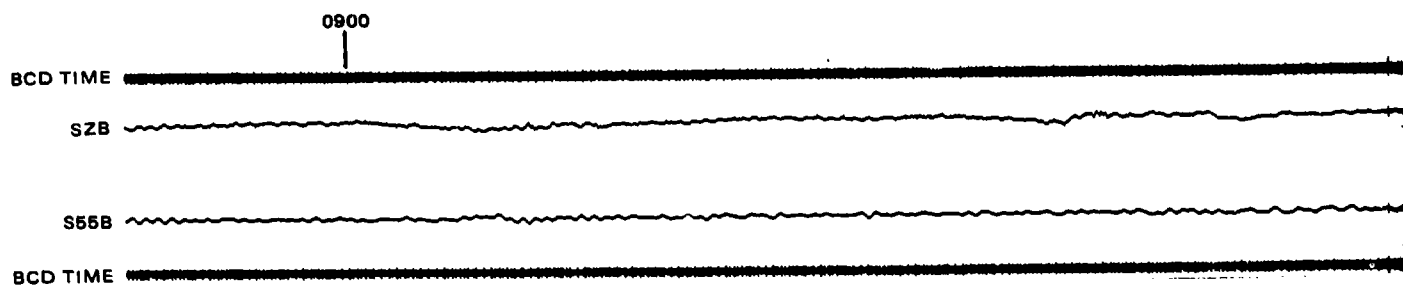
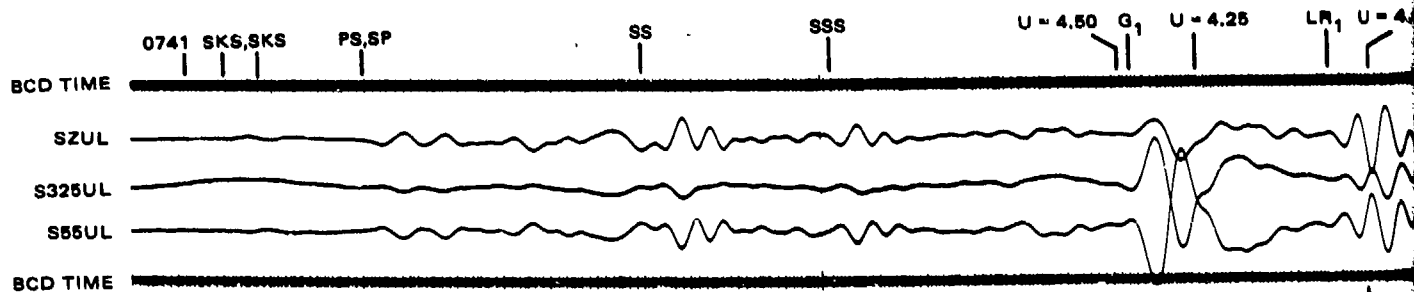
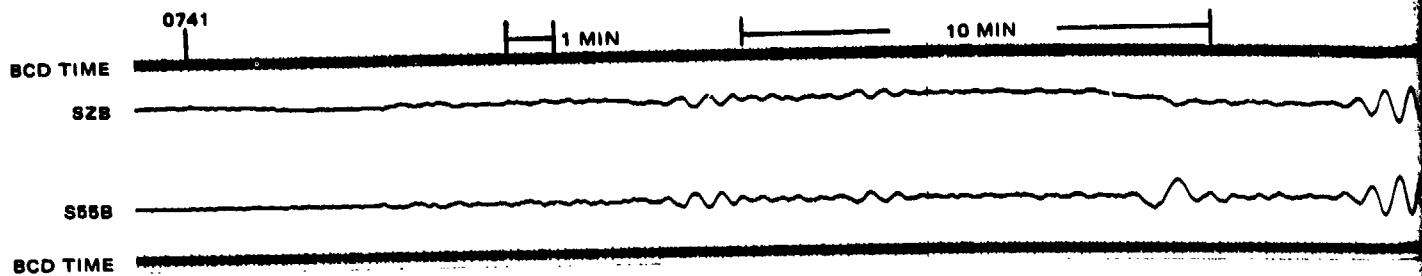
710

72

QC-AZ
RUN 010
10 JAN 1971

369.

369.1



QC-AZ
RUN 010
10 JAN 1971

369.

36

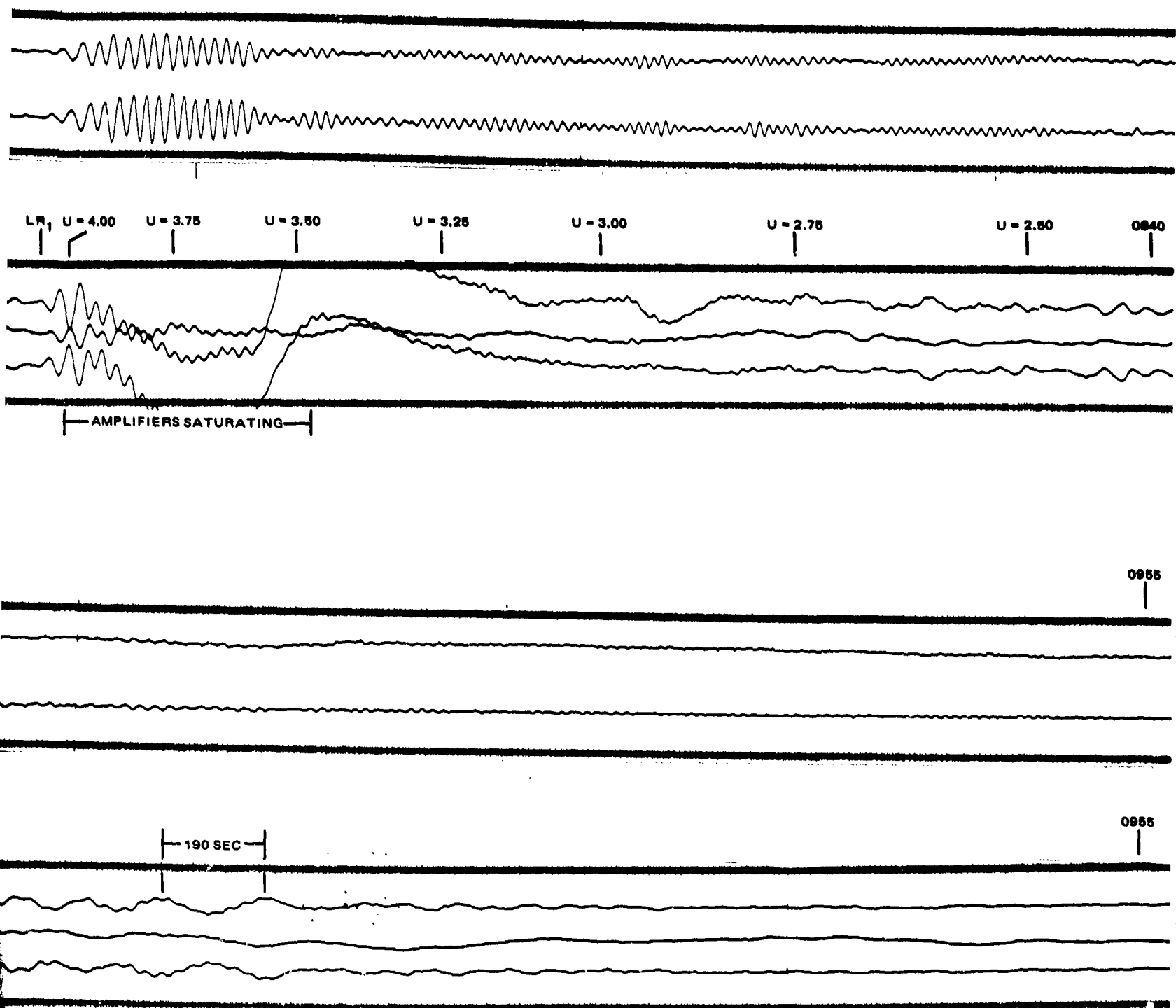


Figure 200. Seismic waves recorded on (a) the broad-band strain seismographs and (b) the ultra-long-period strain seismographs from an earthquake on West New Guinea, NOS PDE data: $0 = 0717:03.7$, 10 Jan 71, $3.1S$, $139.7E$, $h = N$, $m_b = 7.3$, $M_S = 8.1$, $\Delta = 107.4$ deg, azimuth = 278.0 deg

369.1

370 -

Table 16. Epicenter data for recordings in figures 199 and 200

Fig. No.	Origin		Lati- tude Deg	Longi- tude Deg	Depth km	Location	m_b	M_S	Δ	
	Date	Time							Deg	Azimuth Deg
199	10 Dec 70(344)	0434:38.8	4.0 S	80.7 W	25	Peru-Ecuador border region	6.3	7.6	47.2	135.6
199	17 Dec 70(351)	1605:00.2	37.1 N	116.1 W	0	NTS - CARPETBAG	5.7		5.4	318.1
199	19 Jan 71(019)	0316:53.6	23.8 N	108.6 S	N	Gulf of California	5.5	5.9	9.7	163.3
199	9 Feb 71(040)	1400:41.6	34.4 N	118.4 W	13	San Fernando, Calif.	6.2	6.5	5.8	284.0
199	14 Apr 71(104)	1138:42.1	27.7 N	112.4 W	N	Baja California	5.4	5.2	5.5	187.1
200	10 Jan 71(010)	0717:03.7	3.1 S	139.7 E	N	West New Guinea	7.3	8.1	107.4	278.0

would be pulsed became firmly established. The conclusion must then be generalized that steps-of-strain associated with earthquake signals and travelling dislocations are non-elastic phenomena that occur in the vicinity of the strain seismometer. Data that led to this conclusion have not been available to other investigators because all the other strain installations, except Ogdensburg, have had only horizontal strain seismometers. The recording of vertical strain data is a necessary requirement for the proper interpretation of travelling dislocations.

The dimensions implied in the phrase "in the vicinity of the strain seismometer" are not well known at this time. For the travelling dislocations discussed in section 7.5.2, and for the incoherent part of the ambient ground strain discussed in sections 7.4.2 and 7.5.1, the dimension is less than 0.7m. For residual strains associated with earthquakes (or explosions), the dimension may be on the order of tens of kilometers. A set of six single-component strain seismometer installations deployed at six sites in the NTS area produced residual strains that could be interpreted as being coherent on the dimensional scale of tens of kilometers (Shopland, 1971).

On the other broad-band seismograms in figures 199 and 200 there are no steps-of-strain for any of the other events. These events include some near-regional earthquakes and some teleseismic earthquakes. Wideman and Major (1967) reported propagation velocities of 3.0 ± 0.3 km/sec for continental paths and of about 3.6 km/sec for oceanic paths. A range of group velocities (U) are indicated in the figures for the reader's convenience in looking for possible steps.

In all the figures, the SZB seismograms have more system noise than the horizontal seismograms. The vertical broad-band transducer was attached to the strain rod ahead of the X10 mechanical amplifier that amplified the signal to the velocity transducer used for the other three strain responses. Therefore, the vertical seismograph had about 1/12 the signal that was available for the horizontal seismographs. (The strain rod was about 1/4 the length and the vertical signal is about 1/3 the horizontal signal.) In figure 199(a), the pulse on the SZB trace at a group velocity of about 2.75 km/sec is interpreted as system noise similar to the smaller pulses between 0440Z and the P wave arrival and before 0532Z.

During many Rayleigh wave signals, one of the three strain seismographs would be subjected to pulses and/or long period oscillations as observed on the ALPS response seismograms (S L). Usually, the disturbances were in the form of oscillations rather than pulses. The oscillations - which could be considered as being strain noise - might continue for a few minutes or for several hours. These oscillations might begin at any point in the Rayleigh wave train, but frequently were well after the largest amplitudes of the wave train and were at equivalent group velocities less than 2.5 km/sec.

Additional comments not concerned with steps-of-strain will now be made concerning the seismograms in figures 199 and 200. In comparing the seismograms on the BB seismographs to those on the ALPS response (S L) and ULPS response (S U) seismographs, the frequency response must be considered. (Frequency response curves are given in figure 28.) It will be noted that the BB seismograph is flat to strain, but its response to equivalent ground displacement decreases at 6 dB/octave toward longer periods.

The shorter period waves are then amplified relative to the longer period waves. The effect of the system response differences is more vivid in figure 200.

One of the additional purposes of the BB seismographs was to verify that the primary moving-coil transducers were faithfully reproducing seismic strain inputs. This verification is demonstrated in figures 199 and 200 where a variety of earthquake wave types are recorded in a similar manner from both classes of transducers.

The advantage of an important factor included in the QC-AZ instrumentation complex design is brought out in the SZUL and SSSUL seismograms in figure 200. For the time interval between group velocities of about 4.0 to about 3.5, the pre-amplifier and other amplifiers in the system were saturating from the large signals. This clipping was indicated by the flag trace on camera 1. As can be seen in figure 200, the 20 to 40 sec waves were smoothed out by the following system response filters and none of the individual peaks appears clipped, although they all were. The large disturbance apparent on the recordings is the result of the loading of some of the capacitors in the long period (283 sec and 1000 sec) filters. The flag trace indicates caution in use of the data, but as can be seen in the figure, much useful information (e.g., a dispersion curve) can still be obtained from the seismogram.

11.3 INTERPRETATION OF STEPS-OF-STRAIN

Based on observations in the previous section and based on the detailed study of all the QC-AZ recordings, it is the senior author's (JEF) conclusion that the steps-of-strain, pulses-of-strain, or large strain fluctuations are all symptomatic of physical processes taking place in the rock and the rock joints in the vicinity of the strain seismometers. The strain activity is often triggered by the repeated loading from earthquake waves, but it can also start spontaneously. Frequently, steps or pulses act in the sense of the current loading from combined earth tide and secular strain fields. The steps-of-strain are not symptomatic of the earthquake source mechanism, and future use of dc strain systems for source mechanism studies does not appear to be beneficial.

12. SPECTRAL COMPARISONS, DISPLACEMENT AND STRAIN

This section discusses the subject of the enhancement of signals and the discrimination of wave types from the viewpoint of the frequency domain. Section 9 dealt with the same subject from the viewpoint of the time domain. Comparing signals in both the time and frequency domains can provide better insight into the capabilities of the QC-AZ strain/inertial complex. In the following paragraphs, the theoretical relationships between ground displacement and ground strain will be derived in section 12.1. Signals from several earthquakes are used in section 12.2 to demonstrate the similarity of the spectra between the parallel strain and inertial seismographs. The results are summarized in section 12.3.

12.1 THEORETICAL RELATIONSHIP

This section will derive an expression for the transfer function from ground displacement to ground strain. It will then be shown that the local phase velocity at the station can be determined from the transfer function.

Assume that horizontal displacement is composed of harmonic components of plane waves travelling in the positive X_1 direction and that these components can be expressed as:

$$u_1(\omega) = A(\omega) \exp [-i(\omega t - k(\omega)x_1)] \quad (81)$$

where

$u_1(\omega)$ = a displacement of angular frequency ω

ω = $2\pi f$ = angular frequency, rad/sec

f = frequency, Hz

$A(\omega)$ = amplitude of displacement, 0-p, m

t = time, sec

$k(\omega)$ = wave number, 1/m

x_1 = independent distance variable.

In the X_2 direction perpendicular to X_1 , $u_2(\omega)$ is zero.

From equation (33)

$$e_{ij} = 1/2 \left(\frac{\partial u_i}{\partial x_j} + \frac{\partial u_j}{\partial x_i} \right) \quad (33)$$

where $i = j$

$$e_{ij} = \frac{\partial u_i}{\partial x_j}$$

Taking the derivative of (81)

$$e_{11}(\omega) = \frac{\partial u_1(\omega)}{\partial x_1}$$

$$e_{11}(\omega) = i k(\omega) A(\omega) \exp [-i(\omega t - k(\omega)x_1)] \quad (82a)$$

$$= i k(\omega) u_1(\omega) \quad (82b)$$

The transfer function is

$$H(\omega) = \frac{\text{strain (output)}}{\text{displacement (input)}}$$

$$= \frac{e_{11}(\omega)}{u_1(\omega)} \quad (83)$$

Substituting from equations (81) and (82) and cancelling terms

$$H(\omega) = i k(\omega) \quad (84)$$

The transfer function from displacement to strain is seen to be a leading phase lead of strain over displacement with an amplitude factor of the wave number.

The wave number is related to other properties of the wave.

$$k(\omega) = \frac{\omega}{c(\omega)} \quad (85)$$

where $c(\omega)$ = phase velocity, m/sec.

Writing

$$\omega = 2\pi f$$

$$= \frac{2\pi}{T} \quad (86)$$

where T = period of wave, sec.

and substituting in (85)

$$k(\omega) = \frac{2\pi}{c(\omega)T} \quad (87)$$

and

$$k(\omega) = \frac{2\pi}{\lambda(\omega)} \quad (88)$$

where $\lambda(\omega)$ = wave length, m.

The phase velocity at the station can be determined from equations (83) and (85)

$$\frac{e_{11}(\omega)}{u_1(\omega)} = i \frac{\omega}{c(\omega)}$$

or

$$c(\omega) = \frac{i\omega u_1(\omega)}{e_{11}(\omega)} \quad (89)$$

If the direction of wave travel X_1 makes an angle α with the direction of the seismometers X_s , then

$$e_{ss}(\omega) = e_{11}(\omega) \cos^2 \alpha$$

and

$$u_s(\omega) = u_1(\omega) \cos \alpha \quad (90)$$

Substituting $e_{11}(\omega)$ and $u_1(\omega)$ from (90) in (89) gives

$$c(\omega) = \frac{i\omega u_s(\omega) \cos \alpha}{e_{ss}(\omega)} \quad (91)$$

Two sets of digital computer programs were written to calculate phase velocity from the strain and inertial seismograms. One set of programs was based on using power spectral density to get a better statistical estimate of the transfer function. The other set of programs obtained an estimate of $u_s(\omega)$ and $e_{ss}(\omega)$ from the Fourier transform of the seismograms. The results of these calculations are given in the next section.

Equation (91) can be written

$$\frac{e_{ss}(\omega)}{i\omega} = \frac{u_s(\omega) \cos \alpha}{c(\omega)} \quad (92)$$

If the phase velocity is constant for all frequencies within the passband of the seismographs, the strain seismograph response can be built to have an output proportional to ground displacement. This proportionality is achieved by giving the electronics in the strain response 6 dB/octave more gain toward the longer periods than the inertial seismograph displacement response. With a constant phase velocity, the ground strain introduces the $(i\omega)$ in equation (92). The QC-AZ strain seismographs were matched to the inertial seismographs in just such a manner. Many of the spectra in the next section are plotted without correcting for instrument response. If the phase velocity is constant with period, the strain and inertial spectra should overlay. Phase velocity actually increases slightly toward longer periods (between 10 and 300 sec), so the strain spectra would be expected to rotate from the inertial spectra. The degree of match between the shape of the strain and inertial spectra is a frequency domain measure of the ability of the directional array to enhance the signal being studied. Notice that

$\cos \alpha$ does appear in equation (92) and does affect the relative amplitudes of the strain and inertial seismograms. In all cases considered in this report, α was taken as the angle to the great circle path and was considered a constant with period. Lateral refraction of Rayleigh waves can be significant (Evernden, 1953, 1954, and Capon, 1970, 1971), but was not considered in this analysis.

Another relationship between displacement and strain is helpful in understanding the physical phenomena that the seismometers are measuring. Equation (82) is the space derivative of the displacement in equation (81). Now let us take the time derivative

$$\frac{du_1(\omega)}{dt} = -i\omega A(\omega) \exp [-i(\omega t - k(\omega)x_1)] \quad (93)$$

Comparing equations (82) and (93)

$$\begin{aligned} \frac{du_1(\omega)}{dx_1} &= \frac{-k(\omega)}{\omega} \frac{du_1(\omega)}{dt} \\ \frac{du_1(\omega)}{dx_1} &= \frac{1}{c(\omega)} \frac{du_1(\omega)}{dt} \end{aligned} \quad (94)$$

In words, strain - the space derivative of displacement - is proportional to velocity - the time derivative of displacement. Equation (94) has been helpful to the authors in visualizing how the delay of movement between the strain rod piers is physically translated to strain seismograph output. A plane wave displacement travelling at 3 km/sec will take 13 msec to travel from one pier to the other pier 40 m away. The time rate-of-change of displacement divided by the phase velocity will be equal to the strain or the distance rate-of-change of displacement.

12.2 OBSERVED RELATIONSHIPS

This section presents the observed relationships between the strain seismograph and the inertial seismographs in several formats. Comparisons are made between recordings of earthquakes from the two types of seismographs with power spectral densities, coherence, and phase angle. Other comparisons are made with Fourier transforms. The transfer function expressed in the form of phase velocity provides still another comparison. Finally, oscilloscope patterns of instantaneous vector wave number give a presentation of the detailed interaction of ground displacement and ground strain.

The results are first presented in all forms for the three earthquakes in the Kermadec Islands region, as illustrated in section 9, figures 160 and 161. Then, results are presented for several other earthquakes.

The seismograms of the first studied earthquake in the Kermadec Islands region are shown in figure 160. The 2233Z starting time of the data used in the analysis is indicated in the figure. The individual seismograms are illustrated in part (a),

and the directional array is illustrated in part (b). The seismograms from the 55 deg azimuth - P55L, S55L, S+P55L, and S-P55L - for the three earthquakes are illustrated in figure 161. The 2233Z, 0400Z, and 0621Z starting times of the data used in the analysis are indicated in the figure. Epicenter data were given in section 9 and with the seismograms.

The power spectral densities (PSD) of the P55L low-gain inertial seismograph and of the S55LL low-gain strain seismograph, the coherence (square root of coherence squared), and the phase angle between the two seismographs are plotted in figure 201. The power spectral densities are not corrected for instrument response, but are calibrated at 25 sec. The strain PSD has been normalized to the inertial PSD by multiplying the spectra (squared domain) by the number indicated in the figure ($1.205 \times 10^{+09}$). The number chosen for most of the figures is the ratio of the two PSD at the peak of the power. The format of figure 201 will be used in many of the illustrations in this section, and the detailed description of the parts of the figure will not be repeated. The text will state where the instrument response has been removed from the data. Most of the PSD calculations were made with 3841 samples or about 32 min of data and 256 lags. With the Parzen smoothing window, these parameters give 27 degrees of freedom; and with the Hanning smoothing window, they give 20 degrees of freedom.

The reader should compare the spectra of the earthquake signals in this section to the spectra of the ambient ground displacement and strain during quiet times illustrated in sections 7.3 and 7.4. The minimum magnitude earthquakes detectable with similar spectra to the earthquakes analyzed can be estimated using the formula for m_b . By this method, the minimum magnitude can be estimated by dividing the earthquake PSD by 100 for each magnitude unit until the threshold of the background motion spectra at all frequencies equals the scaled earthquake motion spectra. As an example: The P55L microseismic background spectra of 31 October 1970 (figure 66) has an amplitude of about $3.5 \times 10^{-15} \text{ m}^2/\text{Hz}$ at 17 sec. The P55L spectra in figure 201 has an amplitude of $5.4 \times 10^{-8} \text{ m}^2/\text{Hz}$. The ratio between these spectra is 1.54×10^7 . This power ratio is equivalent to 3.6 magnitude units. This calculation gives an estimated minimum earthquake detectability of $m_b = 5.9 - 3.6 = 2.3$ for an earthquake from the Kermadec Islands region with the 31 October 1970 background motion sample.

The statistics of power spectral density analysis are based upon random, stationary, ergodic processes with spectra that are not rapidly varying with frequency (e.g., Bendat and Piersol, 1966, Blackman and Tukey, 1958, and others). From a theoretical standpoint, discrete signals do not satisfy the conditions on which the statistics of power spectral density analysis are based. However, it can be shown from Parseval's theorem that

$$\int_{-\infty}^{\infty} |F(\omega)|^2 d\omega = \int_{-\infty}^{\infty} G_{xx}(\omega) d\omega \quad (95)$$

where $\omega = 2\pi f = \text{angular frequency}$

$F(\omega) = \text{amplitude of the Fourier transform at frequency } \omega$

$G_{xx}(\omega) = \text{power spectral density at frequency } \omega.$

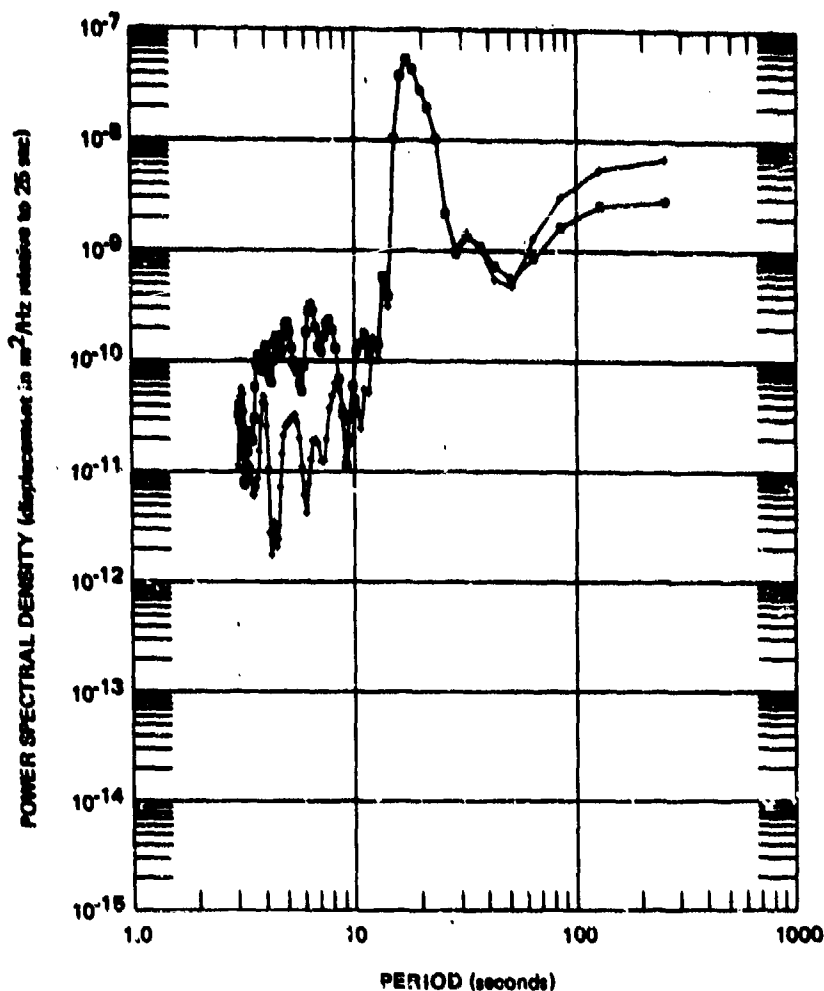
KERMADEC ISLANDS EARTHQUAKE $M_B=5.9$

3841 SAMPLES, 256 LAGS, 2 DBPS, HANNING SMOOTHING

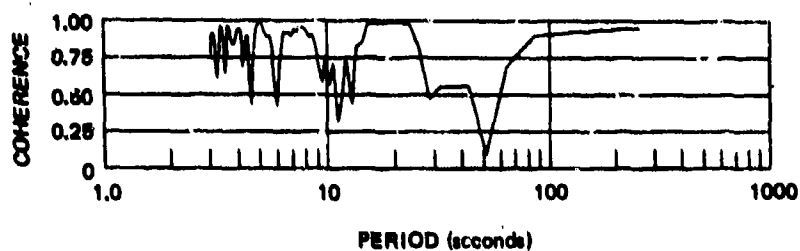
00-00
10 OCTOBER 1970
2233/2305

• P55LL
• S55LL

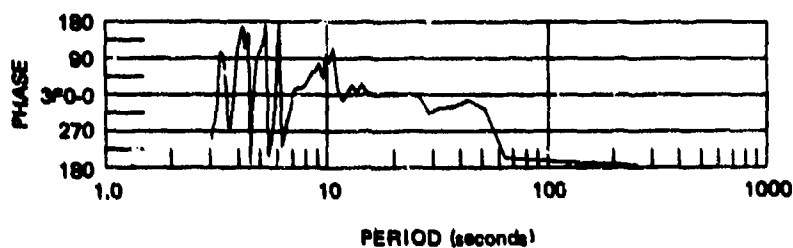
1.0
FORCE-09



a. Power spectral density



b. Coherence



c. Phase lead
S55LL over
P55LL

Figure 201. Power spectral density, coherence, and relative phase angle of P55LL and S55LL seismographs during signals from Kermadec Islands earthquake, 2233/2305, 10 October 1970

G 6731

From equation (95), it is seen that the square root of the power spectral density is a smoothed estimate of the Fourier transform of a discrete signal.

In figure 201, the PSD from the strain and inertial seismographs are seen to overlay from 14.2 to 51.2 sec and to diverge from 51.2 to 256 sec. The divergence is in the sense of increasing phase velocity toward the longer periods. At periods shorter than 10 sec there is no signal, only recorder noise. The coherence is above 0.976 for the peak of the curve above $10^{-8} \text{ m}^2/\text{Hz}$. It is above 0.900 at 85.3, 128, and 256 sec, and it is above 0.800 from 13.5 to 25.6 sec inclusive. The two seismographs in the coherent zones are in-phase at the short periods and are about 180 deg out-of-phase at the long periods.

The comparison between the P55LL and the S55LL for the second and third Kermadec Islands region earthquakes produced similar results in the 13.5 to 25.6 sec period range. The PSD, coherence, and relative phase angles are plotted in figures 202 and 203. The similarity of all three sets of spectra and the coherence of essentially 1.0 demonstrate that signals can be faithfully recorded with identical outputs on high-sensitivity strain seismographs and inertial seismographs. The repetition of identical spectra for these three earthquakes demonstrates that the strain seismographs are capable of reliable duplication of signals. The spectra of other earthquakes presented later in this report further demonstrate this capability.

To the scale used in figures 201, 202, and 203, the phase velocity for these Rayleigh waves is essentially constant in the period range from 13.5 to 25.6 sec. From the ratio of the strain to inertial PSD at the peak of the power, as shown in the figures, the phase velocities at 25 sec (the period at which the spectra are calibrated) calculate to be 8.72 km/sec, 8.34 km/sec, and 8.38 km/sec, respectively. These values for the Rayleigh wave phase velocity in the vicinity of the station are about twice the phase velocities found by other investigators for the Basin and Range Province and for world averages. The possible causes for these high values will be discussed later in this section when the phase velocity determinations are discussed. The cause of this apparently high phase velocity is the existence of less strain signal than would be expected for a phase velocity of 4.00 km/sec, the number used in the system design. The net effect of the strain signal being less than expected is merely the use of a larger voltage gain in the amplifiers and corresponding amplification of the system electronic noise. Since the phase velocity is essentially constant over the pass-band of interest, the ratio between the strain and inertial seismographs will remain constant.

The results differ at the longer periods. During the second event, the coherence dropped to 0.25 between 42.6 and 85.3 sec and the seismograms were incoherent at 128 and 256 sec. During the third earthquake, the seismograms were completely incoherent at 32.0 sec and longer periods. The time sample used in the analysis of the first earthquake started earlier in the signal and included the longer period Rayleigh waves. The spectra in figure 201 and the corresponding seismogram in figure 160 further illustrate the lack of 45 to 60 sec Rayleigh waves at QC-AZ, as discussed in section 10.4. Notice how the shape of this earthquake sample is similar to the shape of the ambient ground motion spectra with a notch between 30 and 60 sec. The time samples used in the analysis of the second and third earthquakes did not include the long period Rayleigh waves. As a result, the amplitude of both spectra in figure 202 and of the P55LL spectra in figure 203 is considerably smaller than in figure 201. During the third earthquake,

KERMADEC ISLANDS EARTHQUAKE MB=5.6

3841 SAMPLES, 756 LAGS, 2.0SPS, HANNING SMOOTHING

QC-A2

11 OCTOBER 1970

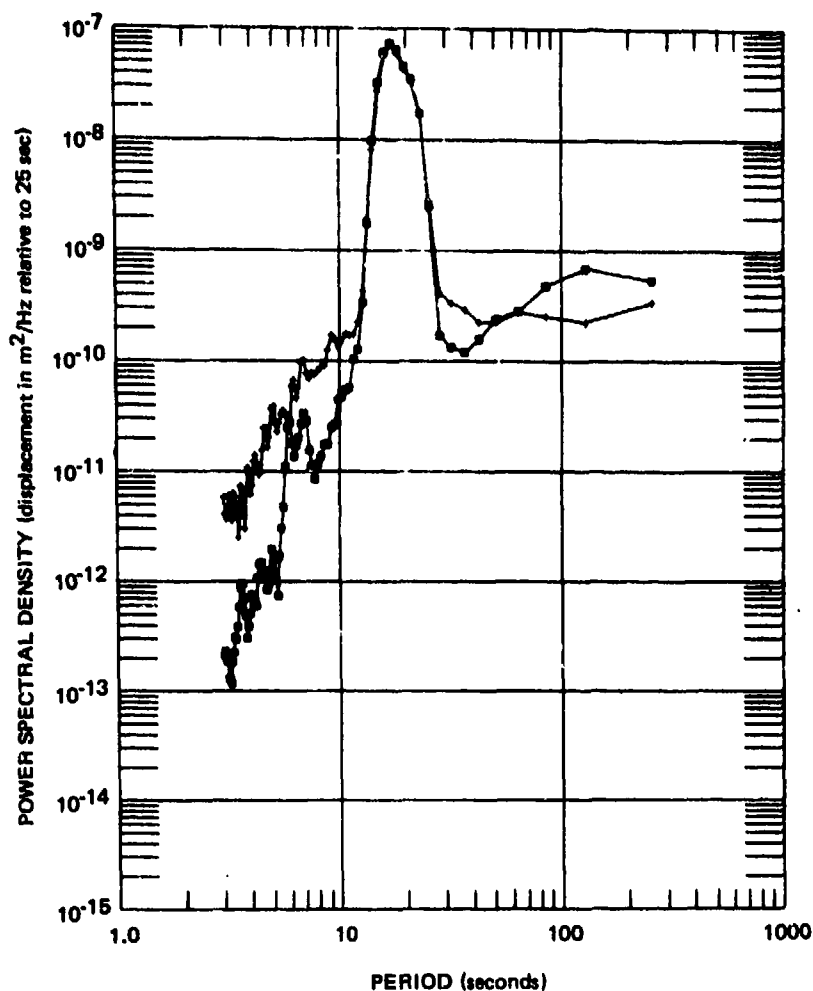
0400/0432

+P55LL

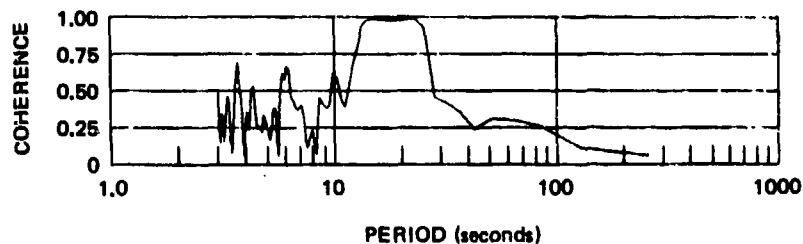
+S55LL

1.0

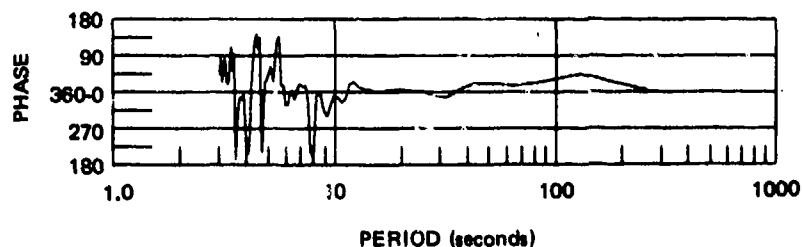
0990E+09



a. Power spectral density



b. Coherence

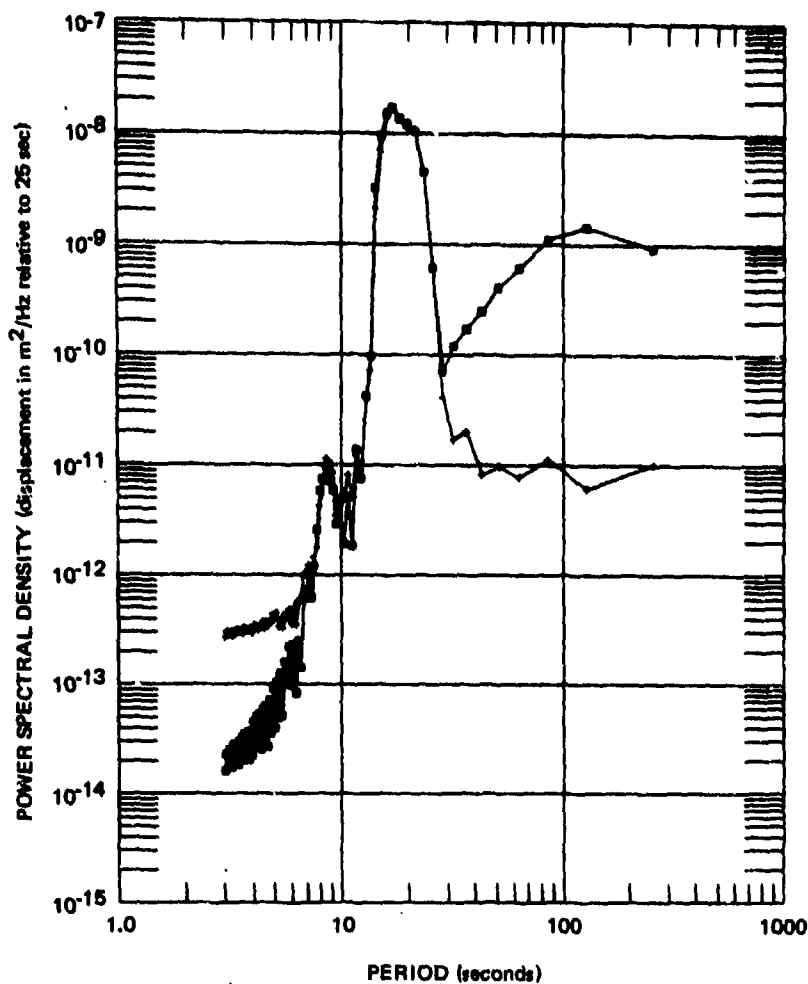


c. Phase lead
S55LL over
P55LL

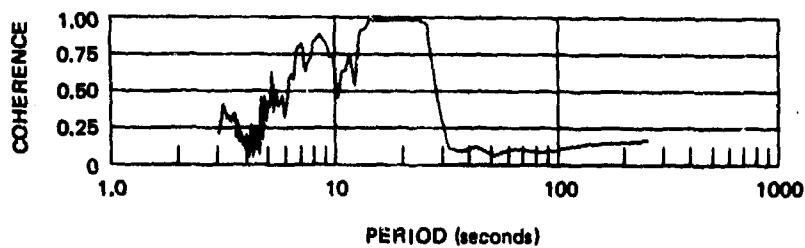
Figure 202. Power spectral density, coherence, and relative phase angle of P55LL and S55LL seismographs during the LR₁ Rayleigh wave from Kermadec Islands earthquake, 0400/0432, 11 October 1970

G 6732

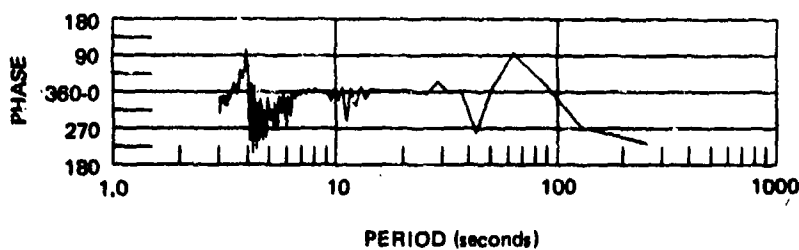
KERMADEC ISLANDS EARTHQUAKE MB=5.6
 3841 SAMPLES, 256 LAGS, 2.0SPS, HANNING SMOOTHING
 QC-A2 • P55LL 1.0
 11 OCTOBER 1970 • S55LL 1.1130E+09
 0621/0653



a. Power spectral density



b. Coherence



c. Phase lead
S55LL over
P55LL

Figure 203. Power spectral density, coherence, and relative phase angle of P55LL and S55LL seismographs during the LR_1 Rayleigh wave from Kermadec Islands earthquake, 0621/0653, 11 October 1970

G 6/33

the 55 deg azimuth strain seismograph began to oscillate with large amplitudes. The S55LL spectra at periods longer than 32.0 sec in figure 203 is the result of these oscillations. These oscillations are of the type described in section 11.2 in relation to steps-of-strain. As can be seen in figures 160 and 161, no steps-of-strain occurred during the time segments illustrated; yet, well after the large amplitudes from the third Rayleigh wave, these oscillations began. They continued for about two days.

The PSDs in figures 201, 202, and 203 were corrected for seismograph response, converted to a mHz bandwidth and the square root taken. The corresponding ground displacement amplitude spectral density and ground strain amplitude spectral density are plotted in figures 204, 205, and 206. (Note the change in symbols between the two sets of three figures.) These amplitude spectra are corrected for instrument response and are calibrated at all periods. They are an estimate of the amplitude of the Fourier transform. The strain amplitude spectra have been normalized to the displacement amplitude spectra at the 17.1 sec peak by multiplying the strain values by the constant given in the figures. From these constants, phase velocities at 17.1 sec of 8.74 km/sec, 8.38 km/sec, and 8.41 km/sec are calculated from the respective spectra. The amplitude spectra in these three figures at periods shorter than 10 sec are not valid because the original PSDs were only tape recorder noise at these periods. From 13.5 to 25.6 sec, the phase velocity is almost constant and the strain spectra overlay the displacement spectra in all three figures. At the longer periods, the three sets of spectra are different. In figure 204, at periods longer than 51.2 sec, the displacement rises at 18 dB/octave toward the longer periods and the strain rises at 12 dB/octave. These slopes indicate either a phase velocity increasing at 6 dB/octave or some other mechanism acting, such as air pressure loading, as discussed in section 7.6. In figure 205, the two spectra are parallel at the longer periods, with the displacement being about three times as large as the normalized strain. The long period amplitudes in figure 206 are almost equal, with both spectra rising at about 12 dB/octave. The strain spectra are the amplitude distribution of the large oscillations that began during the coda of the third earthquake.

The Fourier transform is preferred by some investigators to represent the spectra of discrete signals. The next set of six figures (207 through 212) shows the amplitude of the Fourier transform of the first part of the time sample used to calculate the power spectral density. Each figure applies either to the P55LL or the S55LL seismograph. The (a) part of each figure is the amplitude of the transform of the first 1024 samples. The (b) part of each figure is the amplitude of the transform of the first 512 samples and of the second 512 samples. (The fast Fourier transform (FFT) algorithm was used and data samples in powers of 2 are convenient with this algorithm.) For each of the three earthquakes, the P55LL spectra are on the left page and the S55LL spectra are on the right page. The spectra are all calibrated at 25 sec, but have not been corrected for instrument response.

Comparisons among these six spectra lead to the same conclusions as reached with the power spectral density analysis. The peak of the signal between 13.5 and 25.6 sec is directly proportional between the P55LL inertial seismograph and the S55LL strain seismograph. The seismographs are repeatable for similar earthquakes.

It is instructive to compare the smoothed estimate of the Fourier transform (corrected for instrument response) in figures 204, 205, and 206 with the discrete Fourier transform (uncorrected for instrument response) of different segments of

KERMADEC ISLANDS EARTHQUAKE MB=5.9

GROUND DISPLACEMENT AND STRAIN

DC-AZ
10 OCTOBER 1970
2233/2305

• SSLL
• PSSLL

2.3832E+04
1.0

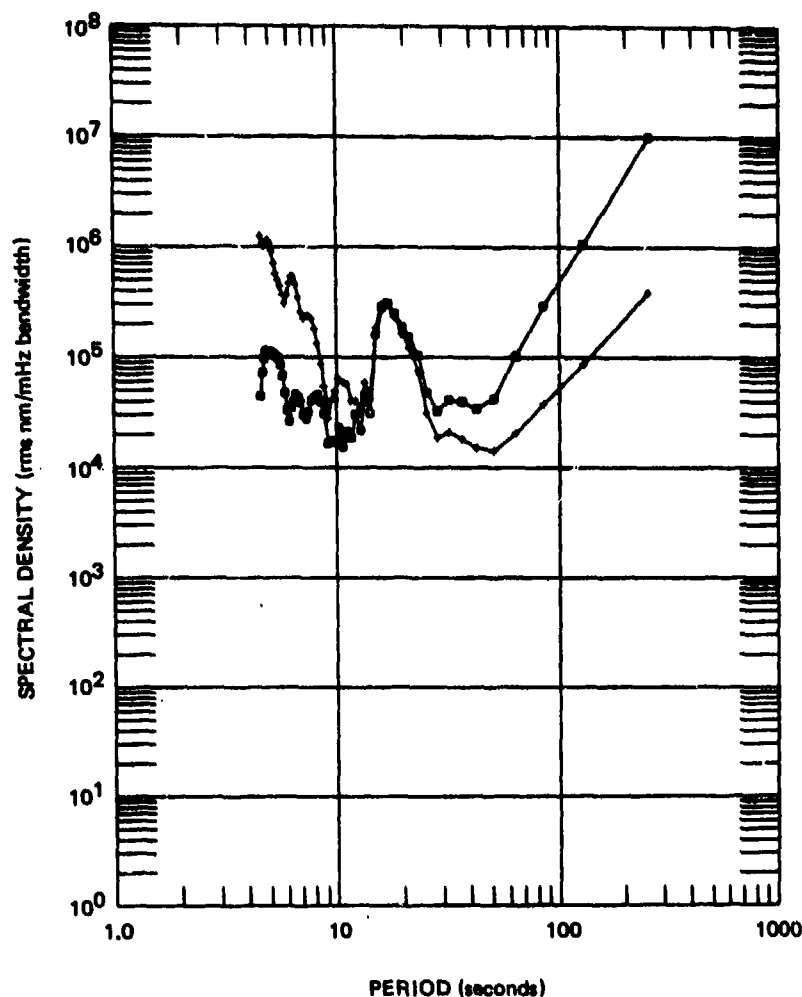


Figure 204. Amplitude spectral density of ground displacement and ground strain during signals from Kermadec Islands earthquake, 2233/2305, 10 October 1970

G 6734

KERMADEC ISLANDS EARTHQUAKE MB=5.6

GROUND DISPLACEMENT AND STRAIN

QC-AZ
11 OCTOBER 1970
0400/0432

• SSSL
• PSSLL

2.2761E+04
1.0

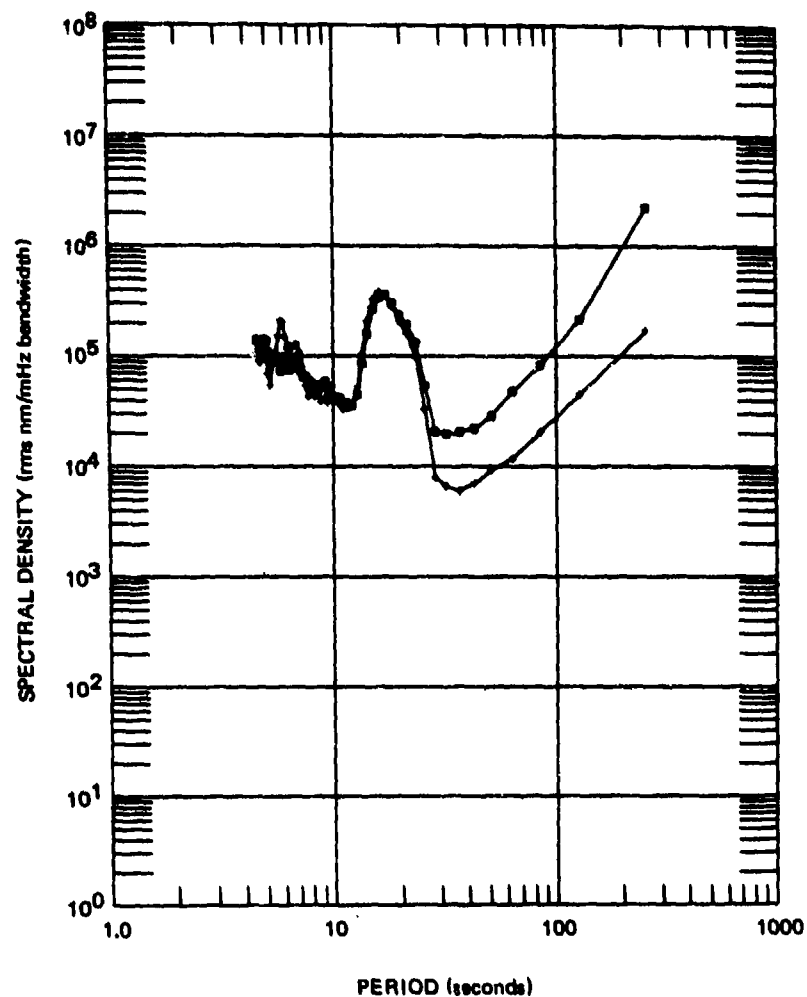


Figure 205. Amplitude spectral density of ground displacement and ground strain during the LR₁ Rayleigh wave from Kermadec Islands earthquake, 0400/0432, 11 October 1970

G 6735

KERMADEC ISLANDS EARTHQUAKE MB=5.6

GROUND DISPLACEMENT AND STRAIN

QC-AE
11 OCTOBER 1970
0621/0653

• SSLL
• PSLL

2.290E+04
1.0

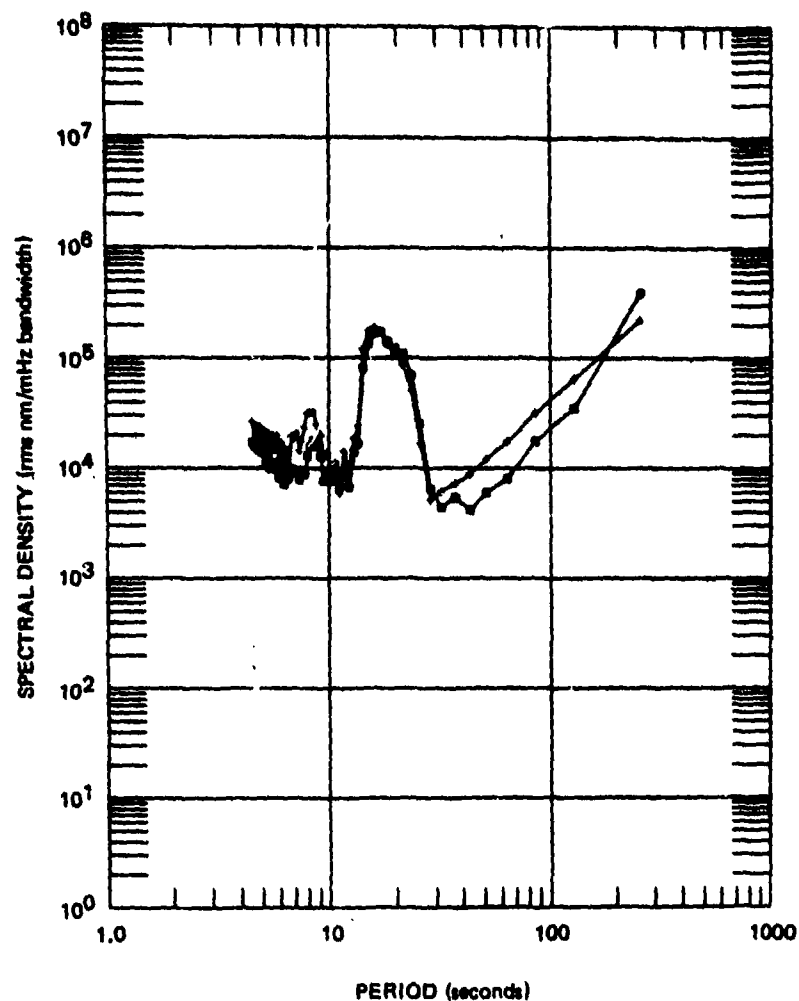
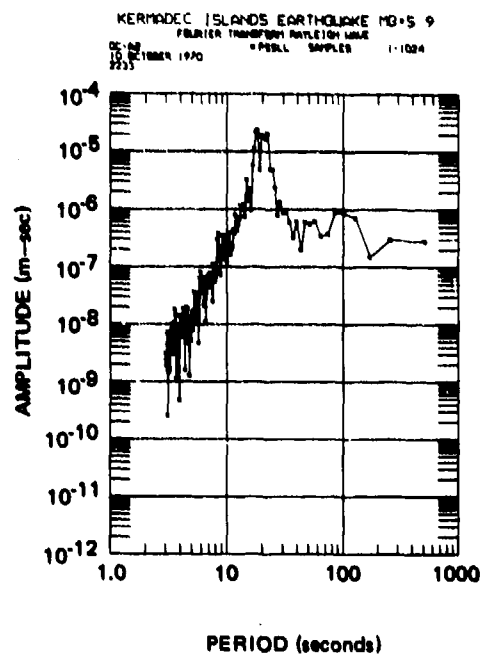


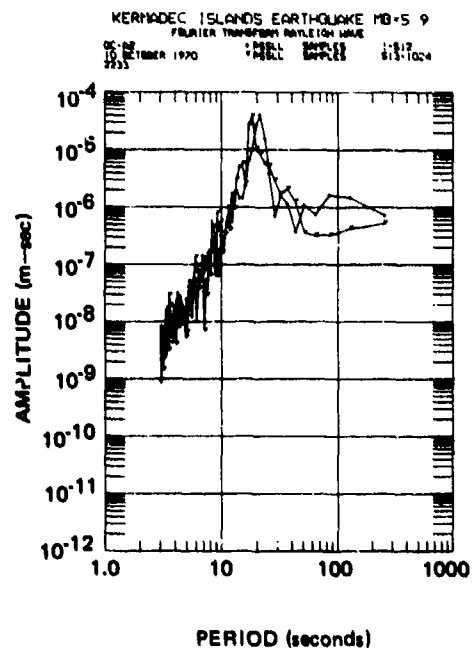
Figure 206. Amplitude spectral density of ground displacement and ground strain during the LR_1 Rayleigh wave from Kermadec Islands earthquake, 0621/0653, 11 October 1970

G 6736

This page intentionally left blank.

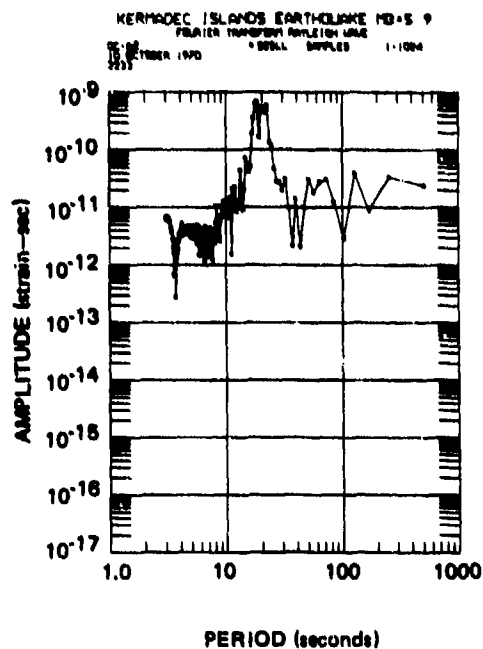


a. Samples no.
1-1024

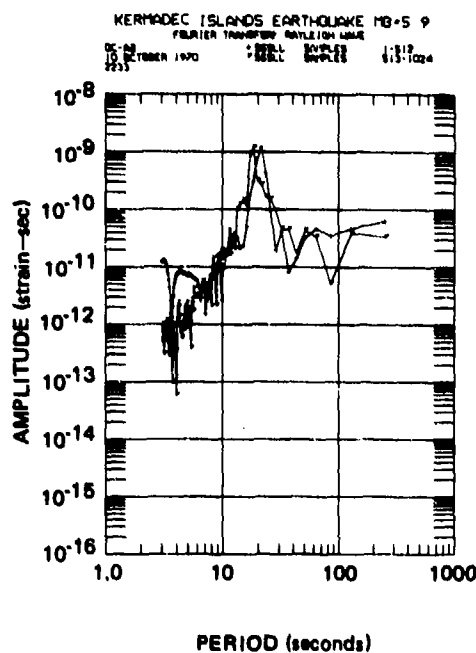


b. Samples no. 1-512
and 513-1024

Figure 207. Fourier transform amplitude spectra, P55LL seismograph, during LR₁ Rayleigh wave from Kermadec Islands earthquake, 2159, 10 October 1970



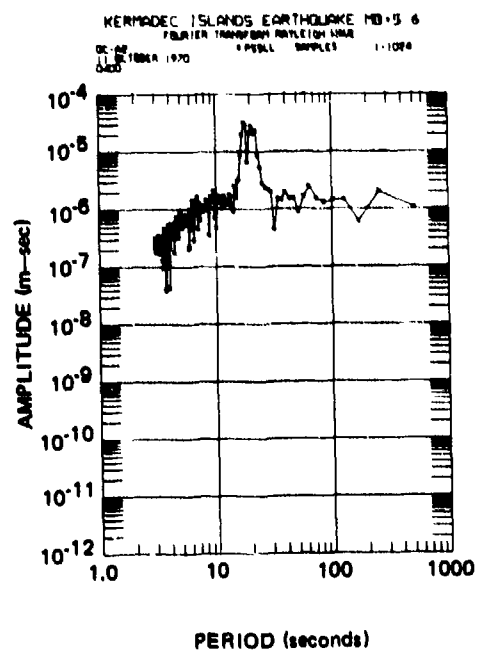
a. Samples no.
1-1024



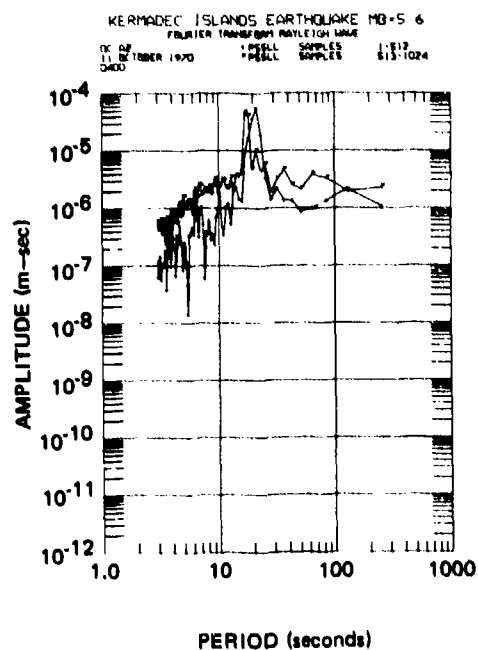
b. Samples no. 1-512
and 513-1024

Figure 208. Fourier transform amplitude spectra, S55LL seismograph, during LR₁ Rayleigh wave from Kermadec Islands earthquake, 2159, 10 October 1970

G 6738



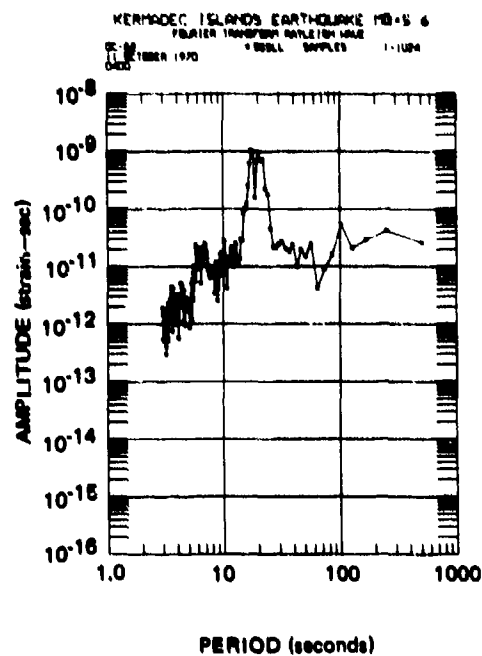
a. Samples no.
1-1024



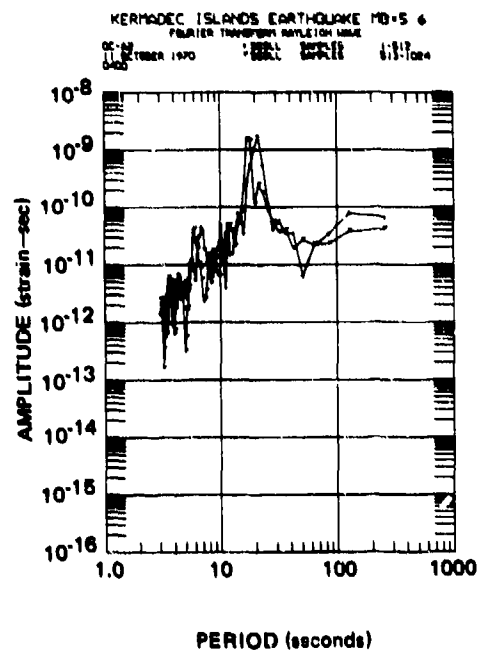
b. Samples no. 1-512
and 513-1024

Figure 209. Fourier transform amplitude spectra, P55LL seismograph, during LR₁ Rayleigh wave from Kermadec Islands earthquake, 0316, 11 October 1970

G 6739

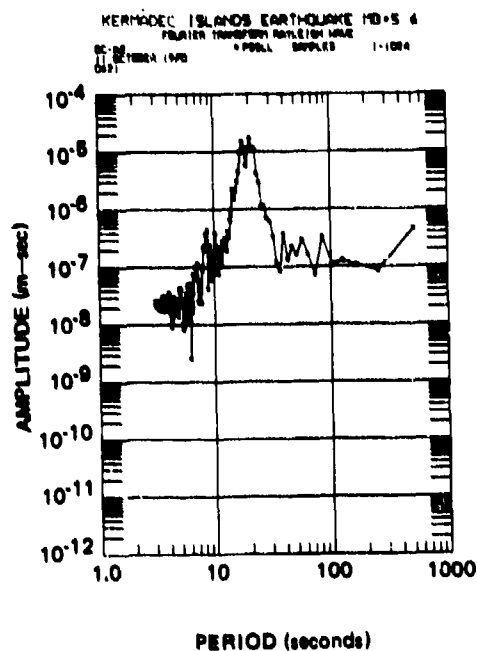


a. Samples no.
1-1024

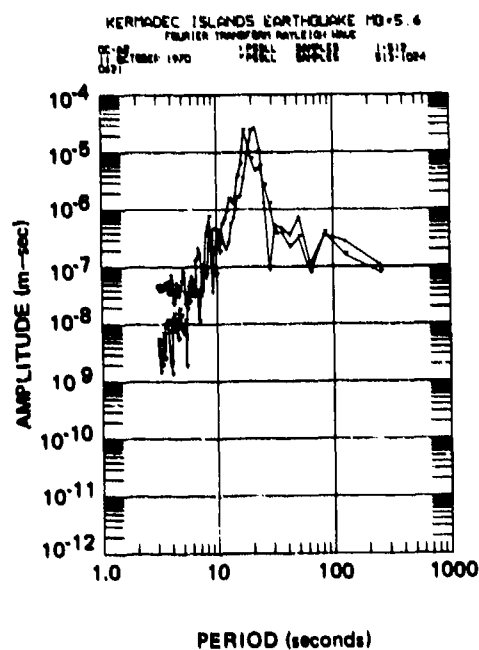


b. Samples no. 1-512
and 513-1024

Figure 210. Fourier transform amplitude spectra, S55LL seismograph, during LR₁ Rayleigh wave from Kermadec Islands earthquake, 0316, 11 October 1970



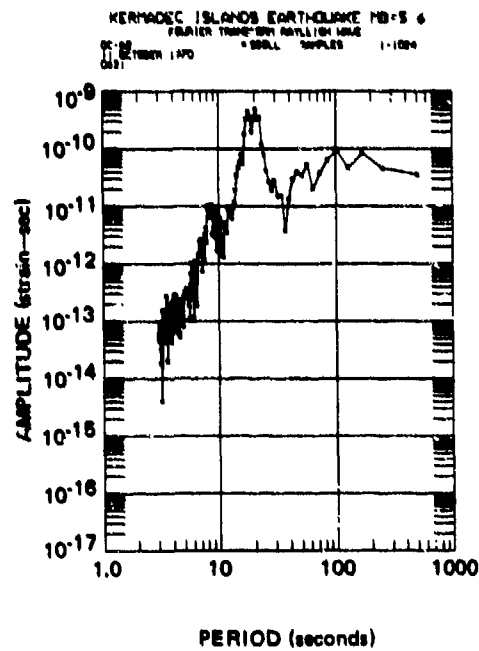
a. Samples no.
1-1024



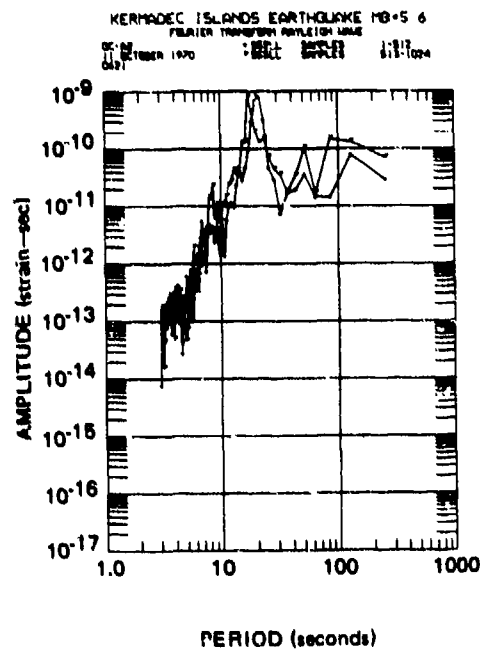
b. Samples no. 1-512
and 513-1024

Figure 211. Fourier transform amplitude spectra, P55LL seismograph, during LR₁ Rayleigh wave from Kermadec Islands earthquake, 0538, 11 October 1970

3 6741



a. Samples no.
1-1024



b. Samples no. 1-512
and 513-1024

Figure 212. Fourier transform amplitude spectra, S55LL seismograph, during LR₁ Rayleigh wave from Kermadec Islands earthquake, 0538, 11 October 1970

G 6742

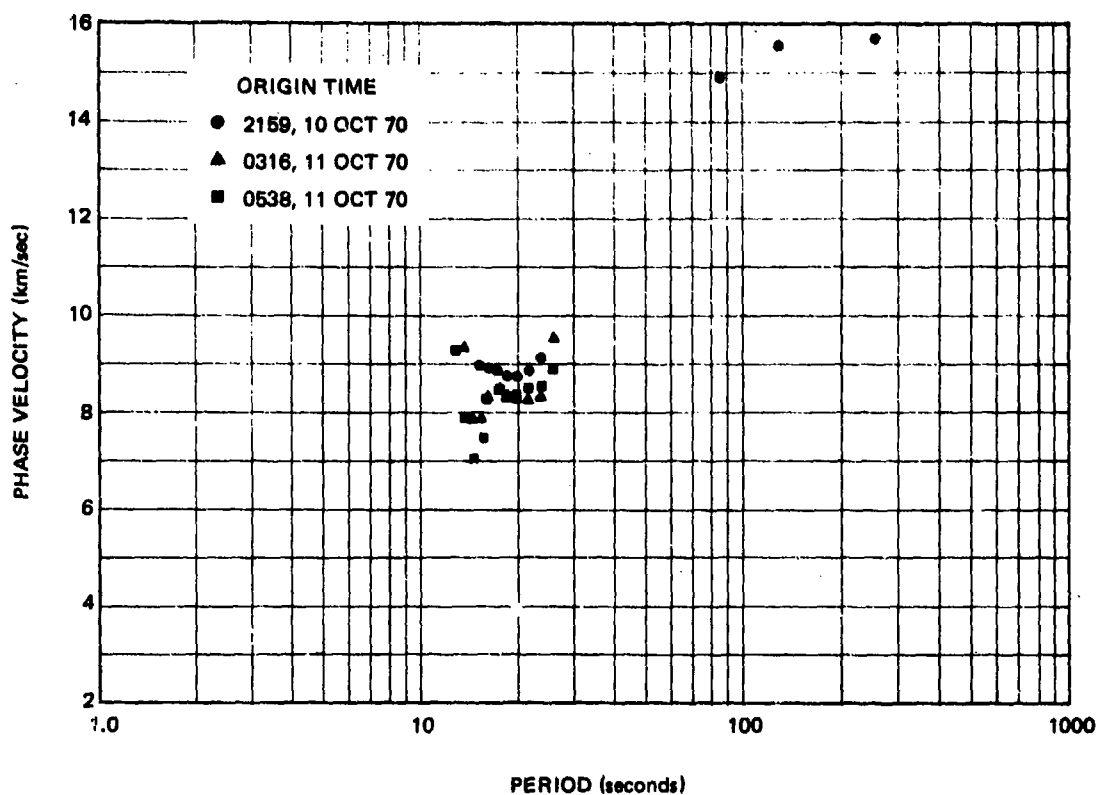
the same data in figures 207 through 212. The smoothed estimates all have one peak at 17.1 sec and a broader peak than the discrete transforms. The discrete transform of samples 1 to 512 has a sharp peak at 21.3 sec and the discrete transform of samples 513 to 1024 has a sharp peak at 17.1 sec. The discrete transform of samples 1 to 1024 has a sharp peak at 17.7 sec and a less sharp double peak at 20.5 and 22.3 sec, with a notch at 19.0 sec between the two peaks. Thus, it is seen that the PSD smoothed out the sharp peaks and completely eliminated the notch between them. The dispersion from 21.3 sec in the first part of the Rayleigh wave to the 17.1 sec in the second part is normal dispersion. However, the sharpness of the individual peaks and the notch - or missing energy - between them is a little surprising.

The phase velocity was calculated for the Rayleigh waves of several earthquakes. Equation (91) was used for the calculations with the amplitude spectra of displacement $u_s(\omega)$ and of strain $e_{ss}(\omega)$ estimated both from the discrete Fourier transform and from the power spectral densities. The computer program corrects both spectra for the frequency response of the seismographs. The results for the Kermadec Islands earthquakes are given in figure 213. The first calculations were made using the Fourier transform amplitude spectra. The scatter in the data shown in figure 213(b) suggested that a better statistical estimate of the amplitude spectra would be beneficial and the later calculations used the PSD. The estimate of the ratio of strain amplitude to displacement amplitude is made by dividing the cross power spectral density (XPSD) by the PSD of the inertial seismogram. This is the same type of calculation used in section 7.6.3.2 in calculating the transfer function from air pressure and wind velocity to displacement and strain. The values of phase velocity plotted in figure 213(a) are all from spectra with coherence of 0.9 or greater. For data with this high coherence and with spectra that overlay so well, the scatter in the data was disappointing. If the apparent phase velocity varies as much as is indicated in figure 213, this variation does not affect the real-time enhancement of signals, as demonstrated in section 9. The apparent variations from one signal to the next are probably inaccuracies in the calculations. Any difference in α the angle of approach of the wave because of lateral refraction from the great circle path would also cause a variation in the results.

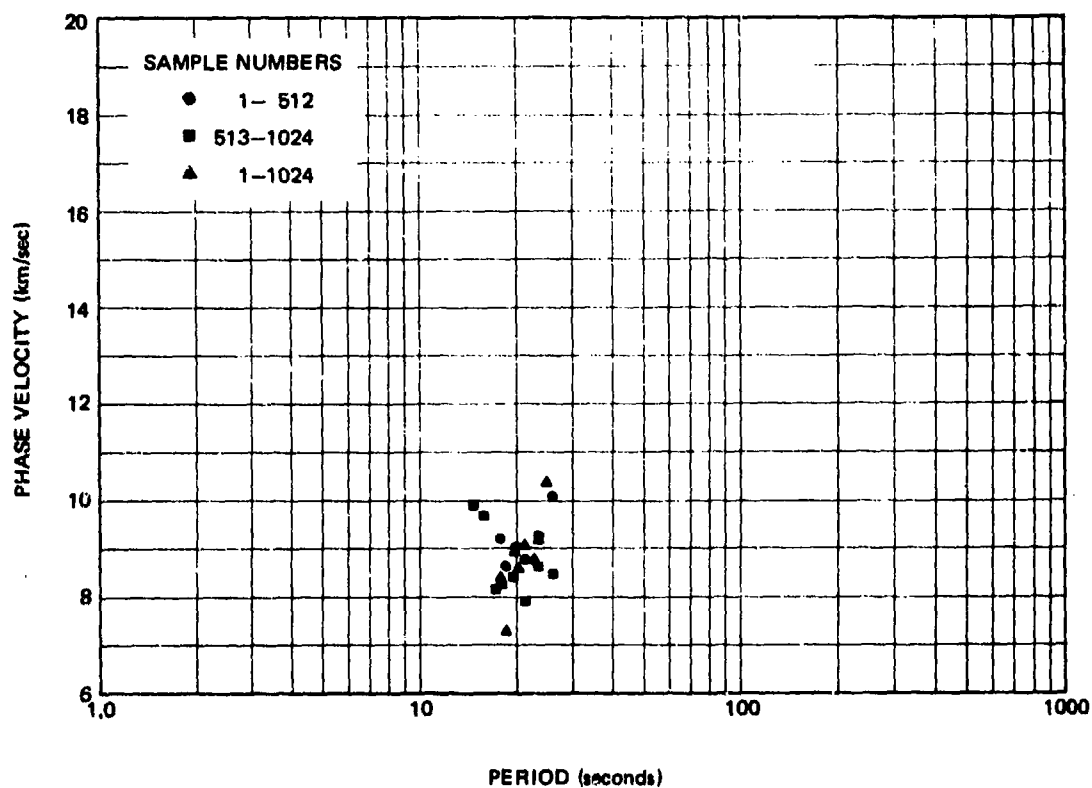
Similar calculations have been made in the 325 deg azimuth using Rayleigh waves from several earthquakes. The scatter of the data was worse in the 325 deg azimuth than in the 55 deg azimuth. Numerical values in the vicinity of 20 to 25 sec clustered around an apparent phase velocity of 10.0 to 10.7 km/sec.

If the high apparent phase velocities are interpreted as being caused by a loss of strain signal, then the ratio of the phase velocities will be a ratio of relative strain loss. The ratio of 10.3 km/sec in the 325 deg azimuth to 8.3 km/sec in the 55 deg azimuth is 1.24. This is the same as the ratio obtained for the slopes of the stress-strain curves in section 8.2.3.

The numerical values obtained from these calculations differ significantly from phase velocities given in the literature. Pilant (1967) has calculated phase velocities from Rayleigh waves crossing North America and recorded at World-Wide Standardized Seismic Network (WWSSN) stations. Interpolation of his figures gives the Rayleigh wave phase velocities at QC-AZ listed below. Dorman (1969) summarized phase velocities from all over the world. For the Rocky Mountain - Basin and Range data, his values, also listed below, generally agree with Pilant.



a. Calculated
from power
spectral density
3841 samples
256 lags



b. Calculated
from discrete
Fourier transform
origin time 2159,
10 Oct. 1970

Figure 213. Rayleigh wave phase velocity in 55 deg azimuth calculated from signals from Kermadec Islands earthquakes

G 6743

Period	Phase Velocity	
	Pilant (1967)	Dorman (1969)
20 sec	3.48 km/sec	3.30 - 3.44 km/sec
25 sec	3.55 km/sec	3.48 - 3.58 km/sec
30 sec	---	3.58 - 3.20 km/sec
40 sec	3.74 km/sec	---
51 sec	3.80 km/sec	---
100 sec	---	4.1 - 4.2 km/sec
256 sec	---	4.75 km/sec

Several hypotheses have been considered to explain the high apparent phase velocities and the difference in the apparent phase velocities in the two horizontal directions.

The high apparent phase velocities are the direct consequence of less strain signal than would be available if the phase velocity were equal to the published values for the Basin and Range Province. One of the strongest hypotheses as to the reason for the high apparent phase velocities - or low strain signals - is that an installation of strainmeters in a hole in the ground cannot be coupled to seismic waves travelling through the earth without experiencing some attenuation because of the attachment of the instrument at a void in the ground. No means of testing this hypothesis have been devised. The load tests to determine the slope of the stress-strain curve discussed in section 8.2.3 are the only tests that have ever been made to determine the output of a seismic strainmeter in response to a known input. The force applied to the rock next to the strainmeter approximates the measurement of strain at a point, but it does not approximate the strain field from a Rayleigh wave with a 70 km wave length.

No theory has yet been developed to study the variation of the strain at the surface of a mined-out cavity in a half-space as a seismic wave passes. We have tacitly assumed that the strain at the edge of the cavity is the same as if the strain were measured at that point without the existence of the cavity. This assumption obviously is not valid. Mindlin (1939) expanded a general study in elasticity in bipolar coordinates made by Jeffery (1921) to get a closed solution in terms of an infinite series for the normal stress and the hoop stress around a horizontal cylindrical hole in a semi-infinite elastic solid under the action of gravity. (Bipolar coordinates are described by Morse and Feshback (1953) and others.) Mindlin's paper (1939) on the stress distribution around a tunnel stimulated comments (Richmond and Feld, 1939, and Brahtz, 1940) and a reply (Mindlin, 1940). Barjansky (1944), also using bipolar coordinates, determined the distortion in a Boussinesq field caused by a circular hole. He considered only the tangential stress and the hoop stress with the point load directly over the cross section studied, and he did not investigate the stress variation along the tunnel as a function of distance from the load. Barjansky (1944) found that the hoop stress at the periphery of the hole was most significant. He defined

a stress factor as the ratio of the hoop stress to the stress at the depth of the center of the hole if the hole did not exist. For holes with a depth to radius ratio of ten or more, the stress factor has a value of 1 in tension at the top and bottom of the hole; it passes through zero at 30 and 150 deg, as measured from straight up; and it has a maximum value of 2 in compression at 90 deg. The 55 deg azimuth strainmeter is mounted on the wall or at 90 deg. The 325 deg azimuth strainmeter is mounted on the floor, or at 180 deg. Therefore, the hoop stress from a single concentrated load on the surface will be of opposite sign at the two strainmeters and twice as large on the 55 deg instrument as on the 325 deg instrument. The fact that the floor has a tensile hoop stress is significant. The tensile stress will tend to open the joints in the rock and is probably the explanation of why the 325 deg strainmeter was subjected to more noise than the 55 deg strainmeter.

The load at the surface from an air pressure wave approaches the two-dimensional Boussinesq problem in the limit as phase velocity approaches zero. If the longitudinal stress (or strain) along a tunnel has a stress concentration factor around the periphery of the hole of the same sign as the hoop stress concentration factor, then the two strainmeters would have opposite signs for air pressure loads. The opposite signs have been observed for air pressure fluctuation loads as illustrated in figure 78 in section 7.6.3, in figure 131 in section 8.1.2, and for presumed acoustic signals as will be illustrated in figure 271 in section 14.2.

If the variation of the longitudinal stress concentration factor around the periphery of a tunnel is similar to the variation of the hoop stress concentration factor, the strainmeters on the wall and on the floor would probably not have a loss of signal from this effect.

The calibration techniques used at QC-AZ assure an accurate measurement of differential pier motions. Resolution and repeatability of all QC-AZ seismographs are on the order of 0.1 percent and absolute accuracy is on the order of 5 percent. The illustrations of identical seismograms and identical spectra in section 8.1 demonstrate the accuracy of the calibrations. Instrument calibration is not the reason for the anomalous observed values.

In considering the calculated values of phase velocity, it is helpful to inspect the scale of volume of the earth involved in the physical phenomena being measured. The Rayleigh waves that are providing the signal have a wave length of

$$\lambda(\omega) = c(\omega)T. \quad (96)$$

Using values from Pilant above, the wave length at 20 sec is 70 km and at 25 sec is 89 km. However, the displacement is measured at one point and the strain is measured over a 40m interval, which is a close approximation to a point when compared to a 70 km wave. Since both displacement and strain are measured at a single point, they then respond to the apparent horizontal phase velocity in the direction of the orientation of the instruments in the immediate vicinity of this point. If the phase velocity vector has been deflected upward by the geologic structure in the vicinity of the instruments, then the apparent phase velocity in the horizontal direction will be larger than the phase velocity along the direction of wave travel. For the apparent horizontal phase velocity to be two times the phase velocity (55 deg azimuth), the direction of wave travel would have to be deflected up at a 60 deg angle. For it to be three times

(325 deg azimuth), the wave would have to be deflected up to a 70 deg angle. These deflection angles seem unreasonably steep even for a short wavelength entering a mountain sitting on top of a half-space.

The geologic structure in the crust and upper mantle has major discontinuities in the Basin and Range Province. Goldmine Mountain is on the edge of a Precambrian range that probably extends to considerable depth within the crust. The range is surrounded by an alluvial valley. This type of structure could provide a wedge or sloped hard rock channel that would deflect horizontal waves upward. Models of the upper mantle structure of the western U.S. have been constructed by Herrin (1971) based on seismic velocities and heat flow, and by Fix (1969) based on geologic structure, seismic refraction surveys, seismic reflection surveys, Pn velocity patterns, P wave delay times, S wave delay times, heat flow data, geomagnetic and magnetotelluric surveys, gravity measurements, radiogenic isotope ratios, and high-pressure high-temperature petrological studies. The Basin and Range model of both investigators has partial melting beginning at a depth of 80 km. In the Sierra Nevadas to the west and the Central Plains to the east there is no partial melting. The profile of the partial melting depth in the transition zone from the adjacent provinces to the Basin and Range Province very probably forms a sloped surface or wedge. The disappearance of 45 to 60 sec Rayleigh waves from Texas to Arizona, as illustrated in section 10.4, confirms a major first-order change that is probably associated with a wedge shape at depth. Boore (1970) used a finite difference approximation of the elastic equation of motion to study Love wave propagation across the ocean-continent sloped boundary. His calculations showed that waves propagating into a region of thinning have anomalously high phase velocities. Model studies on the effect of a sloping interface on Rayleigh waves by Kuo and Thompson (1963) indicated that in the region of a sloping interface, the phase velocity changes nonlinearly with distance. The photoelastic analysis of Rayleigh wave propagation in wedges made by Lewis and Dally (1970) indicated that the Rayleigh wave transmission and reflection coefficients are rapidly changing functions of the wedge angle. All of these studies lead to the conclusions that (1) there is very probably a wedge structure above the partial melt zone, and (2) this wedge structure could lead to high apparent phase velocities measured at a point along the wedge.

James (1971) has observed anomalously high Love wave phase velocities in the period range 60 to 110 sec between La Paz, Bolivia, and Arequipa, Peru. This path is perpendicular to the Benioff zone of downgoing mantle along the west coast of South America. This is certainly a significant wedge structure. James concluded that his results strongly suggested higher mode interference was responsible for the high phase velocities, but he may have overlooked the influence of the upper mantle geometry. Pilant and Knopoff (1964) considered the effects of multiple seismic events created either by the temporal or spatial distribution at the source or by multipath propagation. They found that each of these causal mechanisms influences the apparent phase velocities and amplitude ratios of the resulting wave trains. One of the authors (JEF) has observed recordings of many Rayleigh wave trains with multipath beats in the seismograms. Many times, these beats occur at different times on the parallel strain and inertial seismograms. The results of this effect are most pronounced on the off-azimuth traces of the directional array, which become larger when the on-axis trace becomes smaller during a beat. This effect can be seen to some extent in figure 161 of the Kermadec Islands earthquakes.

In addition to the problem with multipath effects, higher mode surface waves are often in a recording, but are not always obvious. Figure 214 shows the P55L seismogram from the first Kermadec Islands earthquake (0 = 2159Z, 10 October 1970), band-pass filtered from 8 to 14.3 sec and from 5 to 10 sec. Coincident with the beginning of the Love wave on the P325L seismogram, there is a small dispersed wave train on the P55L filtered traces that could be a higher mode Love or Rayleigh wave. Similarly, shortly after the first large Rayleigh wave pulse, there is another dispersed wave train on the filtered traces that could also be a higher mode.

If higher modes or if multipath wave trains are present, the strain seismograph will respond properly. However, the ratio of displacement to strain becomes meaningless without additional information. Assume we have two separate traveling waves of displacement u_1 and u_2 , both satisfying equation (81) and both having the same frequency. From equation (82), the two strains are

$$e_{11} = i k_1 u_1$$

$$e_{22} = i k_2 u_2$$

The total displacement vector is

$$u_3 = u_1 + u_2$$

and the total strain tensor component is

$$e_{33} = e_{11} + e_{22}$$

since the derivative operator is a linear operator. However, if u_3 and e_{33} are substituted in equation (91), we get

$$\text{LHS} = \frac{i \omega (u_1 + u_2) \cos \alpha}{(e_{11} + e_{22})}$$

The left hand side of this equation is not the phase velocity of either u_1 or u_2 . Therefore, if there are two waves present from either multipath transmission, two or more different wave types, or signals from different sources, equation (91) should not be applied until the two waves are separated. The phase velocity results plotted in figure 213 could have been improved by separating the modes by time varying filters before attempting to calculate phase velocity. Time was not available on Project VT/8706 to pursue this approach further.

Another method of looking at the transfer function from displacement to strain is to look at the instantaneous vector wave number in the direction of the instruments. The vector wave number was formed by a Lissajous pattern on an oscilloscope with the inertial seismograph on the horizontal axis and the strain seismograph on the vertical axis. A set of vector wave number plots are illustrated in figure 215 for the first Kermadec Islands earthquake (0 = 2159Z, 10 October 1970). The camera shutter was actuated manually, so the times indicated in the figure are approximate to about a second. The individual seismograms are repeated from figure 160 at the bottom of the figure. The several seismic wave types are identified in

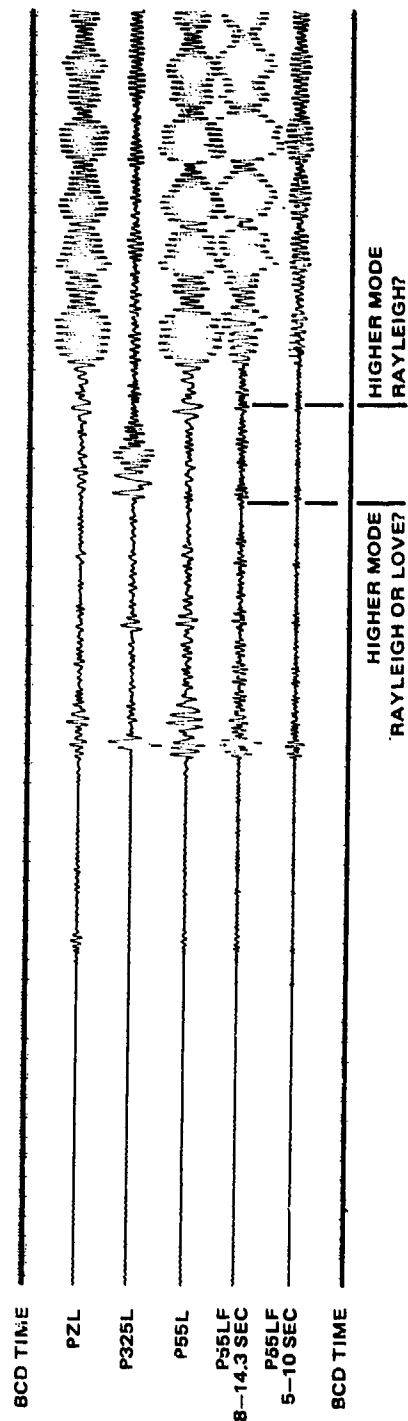


Figure 214. Inertial seismograms of 2159Z, 10 October 1970, Kermadec Islands earthquake illustrating possible higher mode surface waves

G 6744

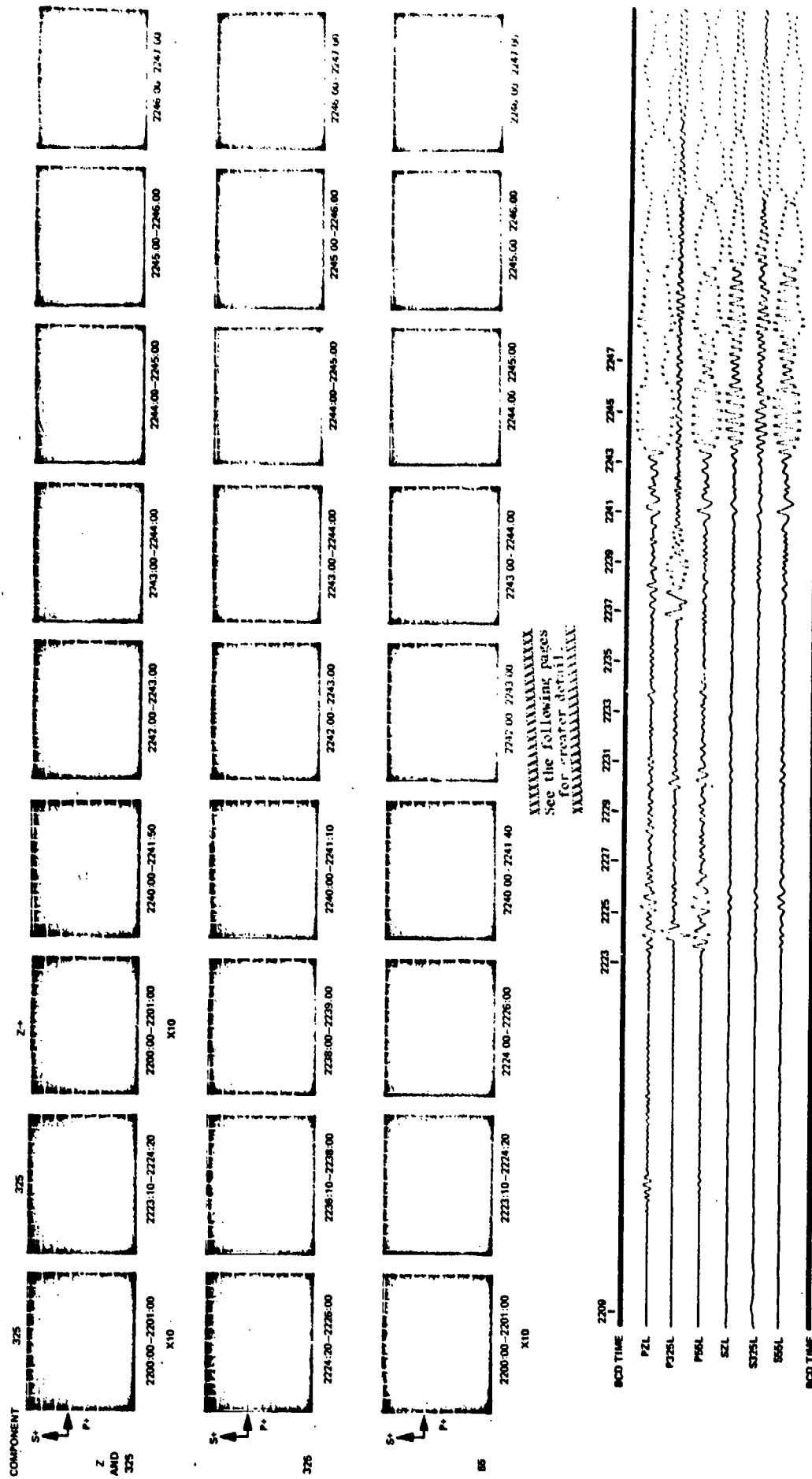


Figure 215. Instantaneous vector wave number Kermadec Islands earthquake, 2159Z, 10 October 1970

40108

-401/402-

0.0729

TR 72-3

COMPONENT

325

325

Z→

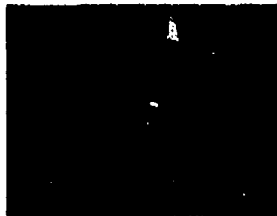
Z
AND
325

S+
P+



2200:00-2201:00

X10



2223:10-2224:20



2200:00-2201:00

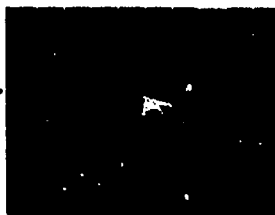
X10



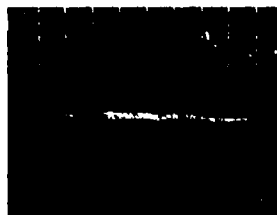
2240:00-2241:50

325

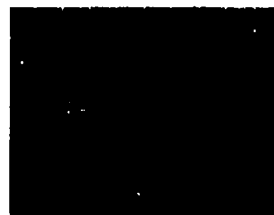
S+
P+



2224:20-2226:00



2238:10-2238:00



2238:00-2239:00



2240:00-2241:10

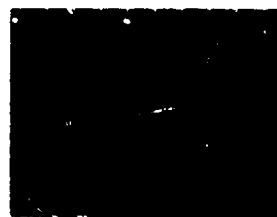
55

S+
P+



2200:00-2201:00

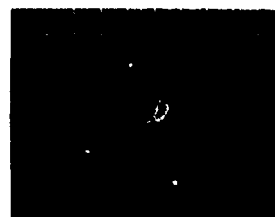
X10



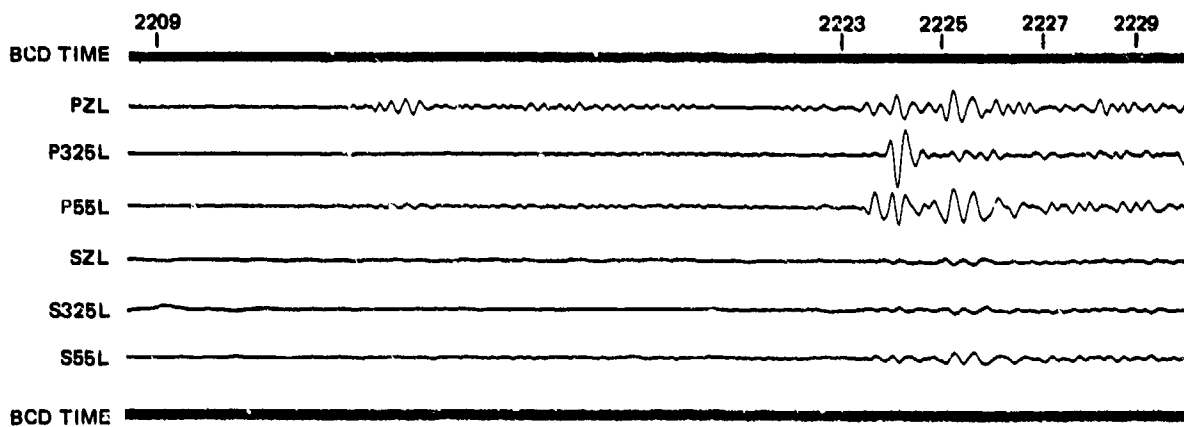
2223:10-2224:20



2224:00-2226:00



2240:00-2241:40



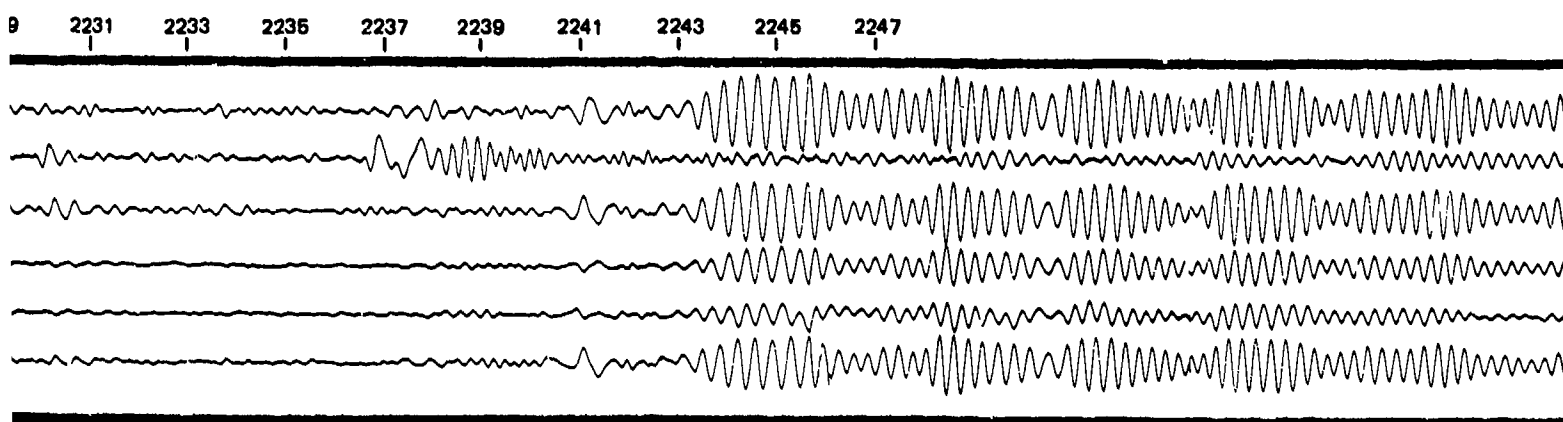
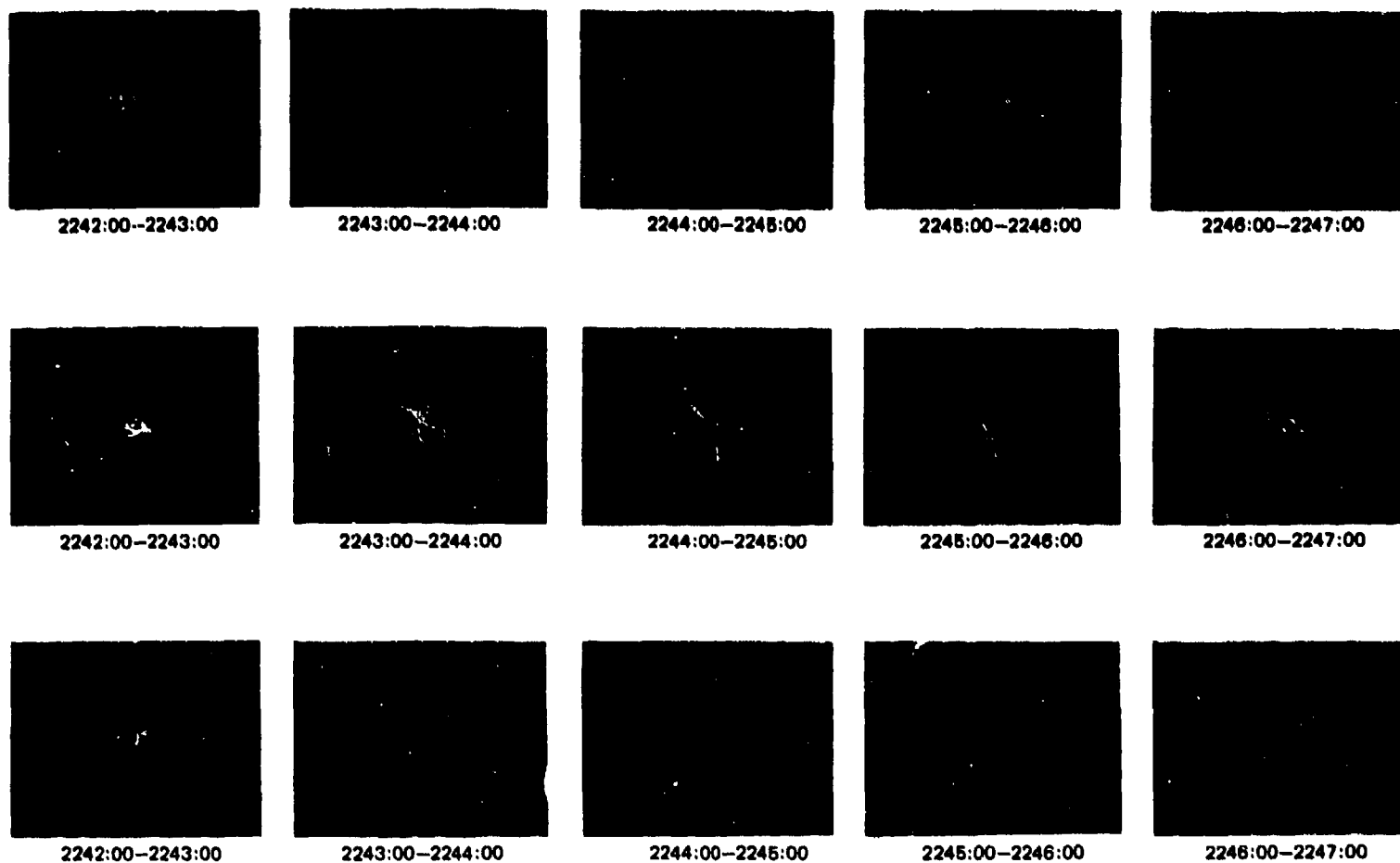


Figure 215. Instantaneous vector wave
number Kermadec Islands
earthquake, 2159Z, 10 Octo-
ber 1970

G 6745

-401/402-

TR 72-3

section 9, figure 160. In forming the Lissajous patterns, the amplifiers were set for approximately equal maximum deflections in both oscilloscope axes. An exact calibration is not known, although this type of presentation could be calibrated if desired.

The small spikes visible in most of the frames were caused by 60 Hz noise in the oscilloscope. For comparison purposes, the microseismic background between 2200:00 and 2100:00 was amplified by a factor of ten and is shown as the first frame for each component. For the two horizontal directions, the slope of the line at any point is proportional to the vector wave number component in that direction. The line is more horizontal for the higher phase velocities. In the vertical direction, for a body wave the slope of the line is proportional to the vector wave number, but for a Rayleigh wave, the two types of seismograms are 90 deg out-of-phase and the Lissajous pattern should be a circle.

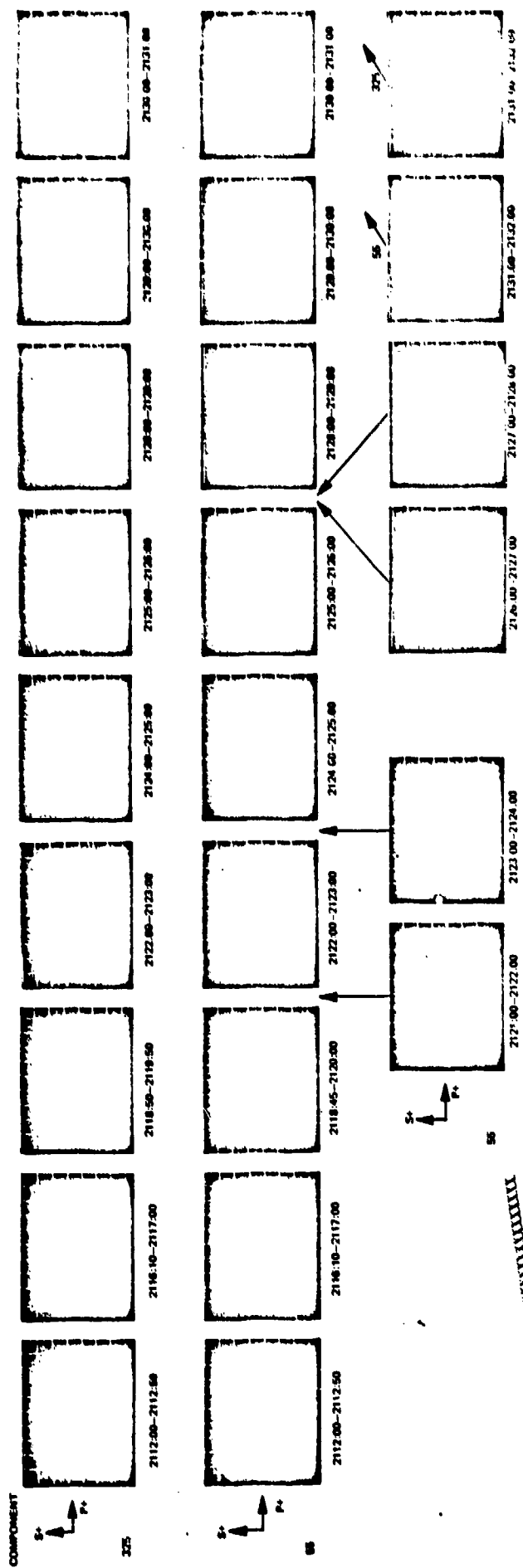
The second frame in figure 215 for the two horizontals is the S arrival group. In the 55 deg azimuth, this frame records the SKS, SKKS, S_V , and S_{CS_V} arrivals. In the 325 deg azimuth, S_H and S_{CS_H} are on the P325L but the S325L is on a null for S_H and Love particle motion from this event. The third frame for the two horizontals has the PS_V and PPS_V arrivals. The 55 deg azimuth third frame has a larger slope than the second frame, indicating a smaller apparent phase velocity because of the smaller angle of emergence of these later multiple bounce phases. This change of slope is useful in separating wave types. The same effect of more strain signal can also be seen in the seismogram. The fourth and fifth frames of the 325 deg set are from the Love wave, which has a very small strain signal. The strain signal gets larger toward the end of the fifth frame, probably as a result of lateral refraction of the shorter wavelength waves. Notice that the lines in the fifth frame are ellipses rather than straight lines. This shape could be the result of either hysteresis in the rock or of a mixture of fundamental and higher modes. The Rayleigh wave begins at about 2240:40 and continues through the other frames. The first two Rayleigh wave frames indicate a complex wave number, but the last four frames indicate motion similar to that expected on the vertical and 55 deg azimuth. The strain in the 325 deg azimuth is responding according to the Poisson ratio effect described in section 8.2.2. The S325L transverse seismograph is about -1/3 the S55L radial seismograph. The P325L seismograph is responding to the coda of the Love wave and to a small component of the Rayleigh wave. In the last four frames, the 55 deg azimuth figures are ellipses rather than lines, indicating possible hysteresis in the rock. (The S55L has a noise from a magnetic tape dropout in the eighth frame.) The center of the Lissajous pattern for the vertical seismogram is slightly displaced from the center of the reticle. The vertical figures are slight ellipses with the major axis in the sense of displacement down-strain compression and displacement up-strain extension.

The discussion in this section up to this point has centered around the three earthquakes from the Kermadec Islands region. Using data from these same earthquakes in the various methods of analysis, it has been shown that the two types of seismographs produce repeatable outputs in which strain is linearly related to displacement. These outputs are sufficiently similar to provide material signal-to-noise ratio improvement to lower detection thresholds and to identify wave types. In the following paragraphs, signals from other earthquakes are used to broaden the catalog of earthquake signals included in this report.

The instantaneous vector wave number from an off-axis signal is illustrated in figure 216. The great circle path to the epicenter in the Greenland Sea is at an azimuth of 10.6 deg. The seismograms from this earthquake are shown in figure 167 where the several earthquake phases are identified. The individual seismograms are repeated at the bottom of figure 216. The first three frames are the S, SS, and SSS waves, respectively. The decreasing phase velocity and wave type identification is easily seen with the increasing slope. The S325L seismograph was somewhat noisy during this signal. The frames from 2121 through 2124 are of long period Love waves. The apparent phase velocity is about the same as SSS and appears to be constant in the three frames. The shape of the curves is irregular. The frames from 2124 through 2127 are of the larger amplitude Love waves. Clipping and distortion of the tape recorder occurs on the peaks of the inertial channels from 2125 to 2127. The curves are open and are not straight lines, suggesting significant hysteresis. The hysteresis is worse in the 325 deg azimuth than in the 55 deg azimuth. Notice that it affects the inertial seismograms as well as the strain seismograms. Beginning at about 2126, the Rayleigh wave is becoming significant and the wave number becomes a complex mixture of the Love-wave and Rayleigh-wave wave numbers. The last four frames are a graphical explanation of why equation (91) should not be applied until some method of separating wave types is employed. The success of the separation of Love and Rayleigh waves in figure 167 can be appreciated more after seeing figure 216. The ability of the sum of the orthogonal strains to enhance the Rayleigh waves and the ability of the difference of the orthogonal strains to enhance Love waves is a robust process that provides significant enhancement in the presence of adverse conditions.

The next set of figures are presented as a suite of power spectral densities, coherences, and relative phase angles from the LR_1 , LR_2 , and LR_3 Rayleigh waves from an $m_b = 5.5$ earthquake in the New Hebrides Islands. The seismograms of this earthquake are shown in figure 163. Epicenter data are given in section 9. The great circle azimuth from QC-AZ to the epicenter is 250.9 deg, so the 55 deg azimuth instruments have larger Rayleigh wave signals than the 325 deg azimuth instruments.

Most of the figures in this suite are arranged with the PSD of the inertial seismogram and the relative phase angle on the left page and the accompanying PSD of the strain seismogram and the coherence on the right page. Some of the figures are only the PSD of the inertial seismograms. All the PSDs begin at a zero crossing at the beginning of the corresponding Rayleigh wave. The times indicated in the figures do not represent the time interval covered by the PSD. Figures 217 through 226 are the spectral analyses of the three Rayleigh waves. The first 790 samples of the vertical component seismograms were used for the analysis in figure 217 to illustrate that smaller segments of the data can produce higher coherence and more stable phase angles than longer segments of data, which often have degradation from multipath and other effects. The remaining analyses of the LR_1 and LR_2 Rayleigh waves utilized 32 min of data, or 3841 samples. The analyses of the LR_3 seismograms utilized 17 min of data or 2040 samples. The vertical component is repeated in figure 218 with 3841 time samples so that the reader can compare the results of the analyses with the two time segment lengths. The SZL seismogram lags the PZL seismogram by 90 deg (270 deg lead), in accord with theory, at all periods greater than 10 sec for LR_1 and between 12 and 64 sec for LR_2 . The S55L seismogram is in-phase with the P55L seismogram for LR_1 and LR_3 and 180 deg out-of-phase for LR_2 . The coherence



See the following pages
for greater detail.

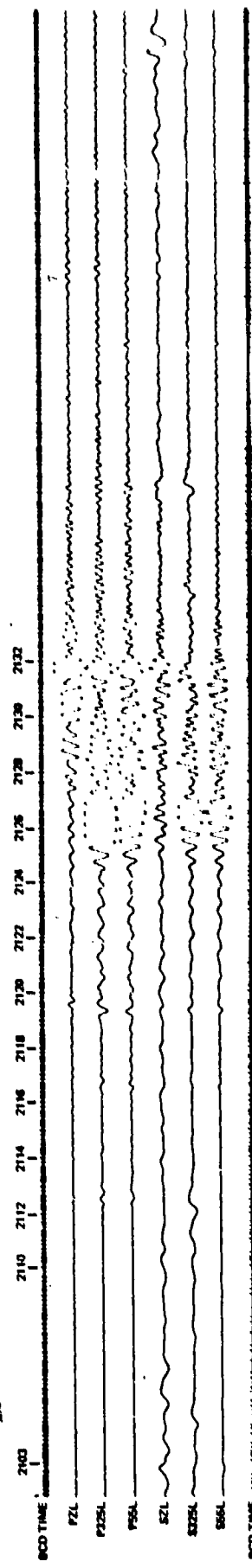


Figure 216. Instantaneous vector wave number Greenland Sea earthquake, 2053Z, 26 October 1970

COMPONENT



325



2112:00-2112:50



2116:10-2117:00



2118:50-2119:50



2122:00-2123:00



2124:00-2125:00



55



2112:00-2112:50



2116:10-2117:00



2118:45-2120:00



2122:00-2123:00



2124:00-2125:00



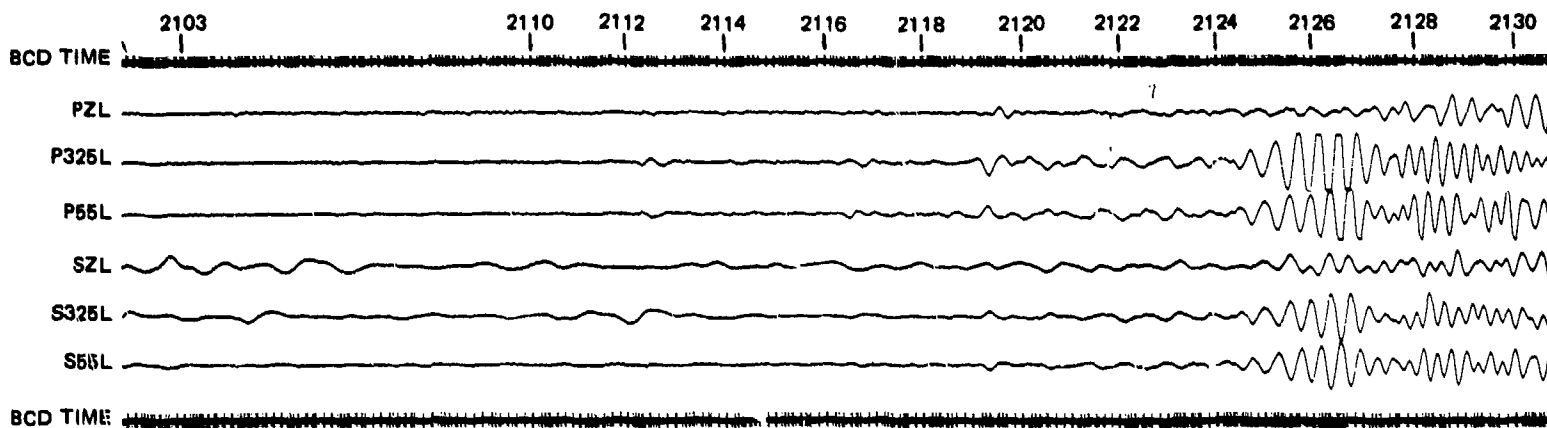
55



2121:00-2122:00



2123:00-2124:00



405

405.1

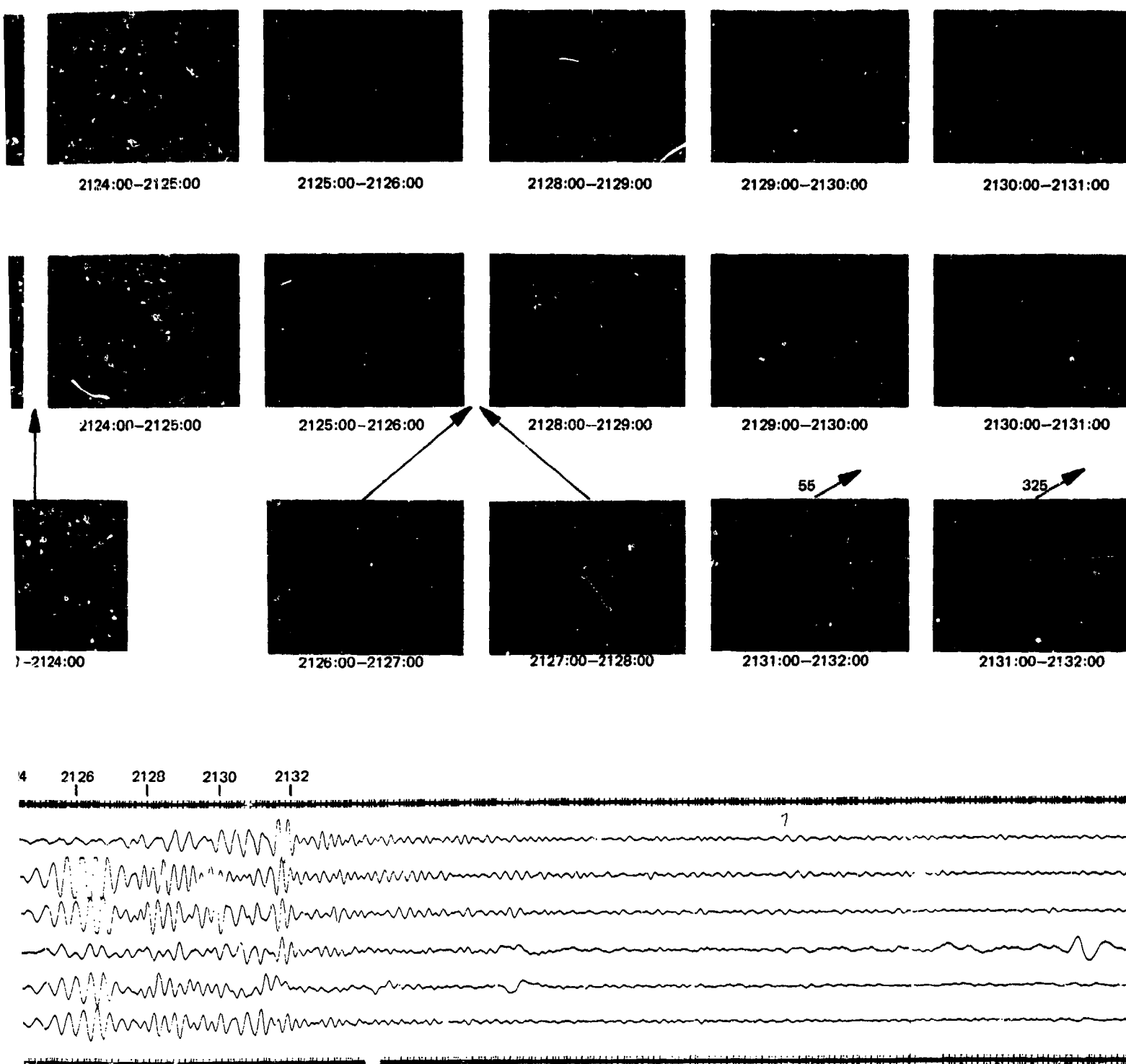


Figure 216. Instantaneous vector wave number Greenland Sea earthquake, 2053Z, 26 October 1970

G 6746

405.1

406

TR 72-3

This page intentionally left blank.

NEW HEBRIDES EARTHQUAKE $M_B=5.5$

790 SAMPLES, 256 LAGS, 2.0 SPS, PARZEN SMOOTHING

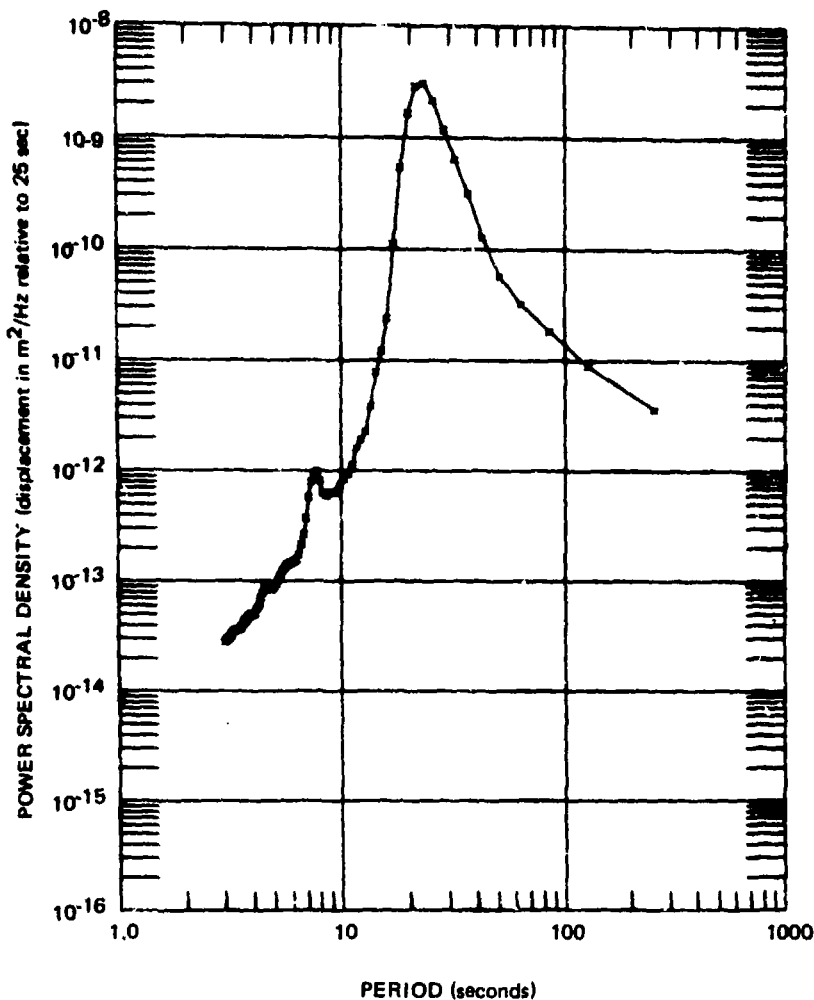
QC-A2

3 SEPTEMBER 1970

0940/1050

= PZLL

1.0



a. PZLL power spectral density

PHASE

790 SAMPLES, 256 LAGS, 2.0 SPS, PARZEN SMOOTHING

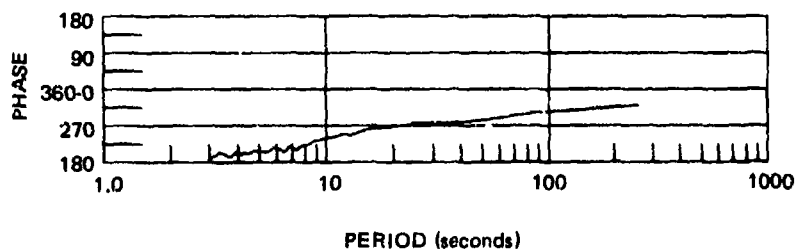
QC-A2

3 SEPTEMBER 1970

0940/1050

SZLL X PZLL

1.0

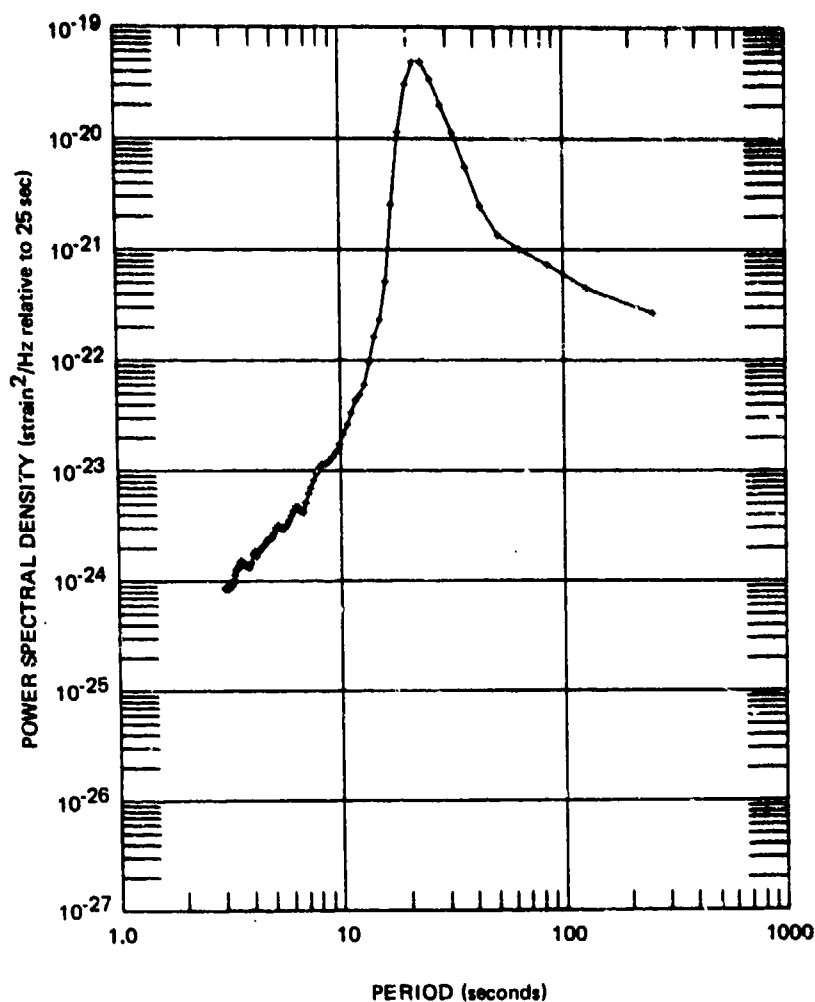


b. Phase lead SZLL over PZLL

Figure 217. Power spectral density, coherence, and relative phase angle with 790 time samples of PZLL and SZLL seismograms during LR_1 Rayleigh wave of New Hebrides $m_b = 5.5$ earthquake

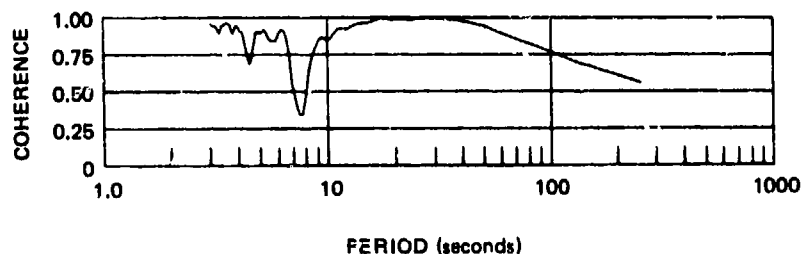
G 6747

NEW HEBRIDES EARTHQUAKE $M_b = 5.5$
 790 SAMPLES, 256 LAGS, 2.0 SPS, PARZEN SMOOTHING
 DC-A2 3 SEPTEMBER 1970 0940/1050
 + SZLL 1.0



c. SZLL power spectral density

COHERENCE
 790 SAMPLES, 256 LAGS, 2.0 SPS, PARZEN SMOOTHING
 DC-A2 3 SEPTEMBER 1970 0940/1050
 SZLL X PZLL 1.0

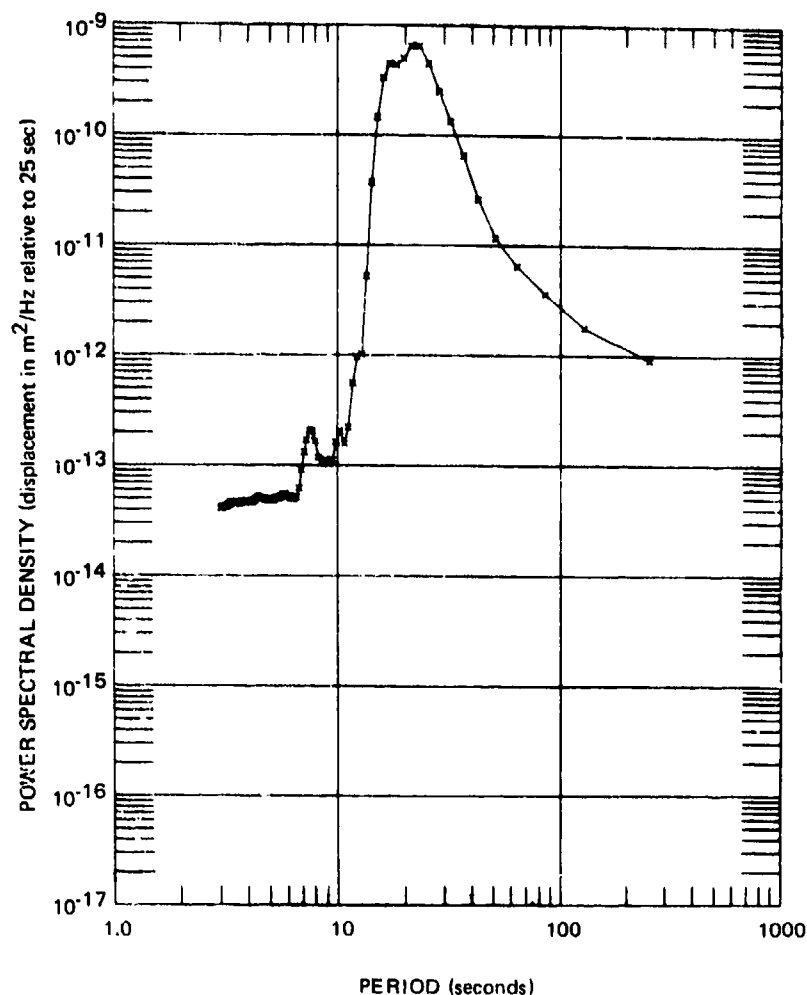


d. Coherence

Figure 217. Power spectral density, coherence, and relative phase angle with 790 time samples of PZLL and SZLL seismograms during LR_1 Rayleigh wave of New Hebrides $m_b = 5.5$ earthquake

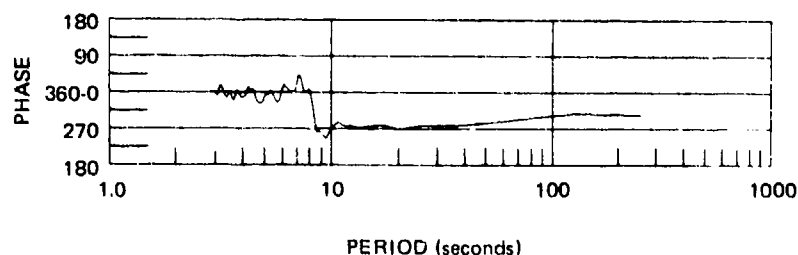
G 6748

NEW HEBRIDES EARTHQUAKE $M_B=5.5$
 3841 SAMPLES, 256 LAGS, 2.0 SPS, PARZEN SMOOTHING
 QC-A2 * PZLL 1.0
 3 SEPTEMBER 1970
 0940/1050



a. PZLL power spectral density

PHASE
 3841 SAMPLES, 256 LAGS, 2.0 SPS, PARZEN SMOOTHING
 QC-A2 SZLL X PZLL 1.0
 3 SEPTEMBER 1970
 0940/1050

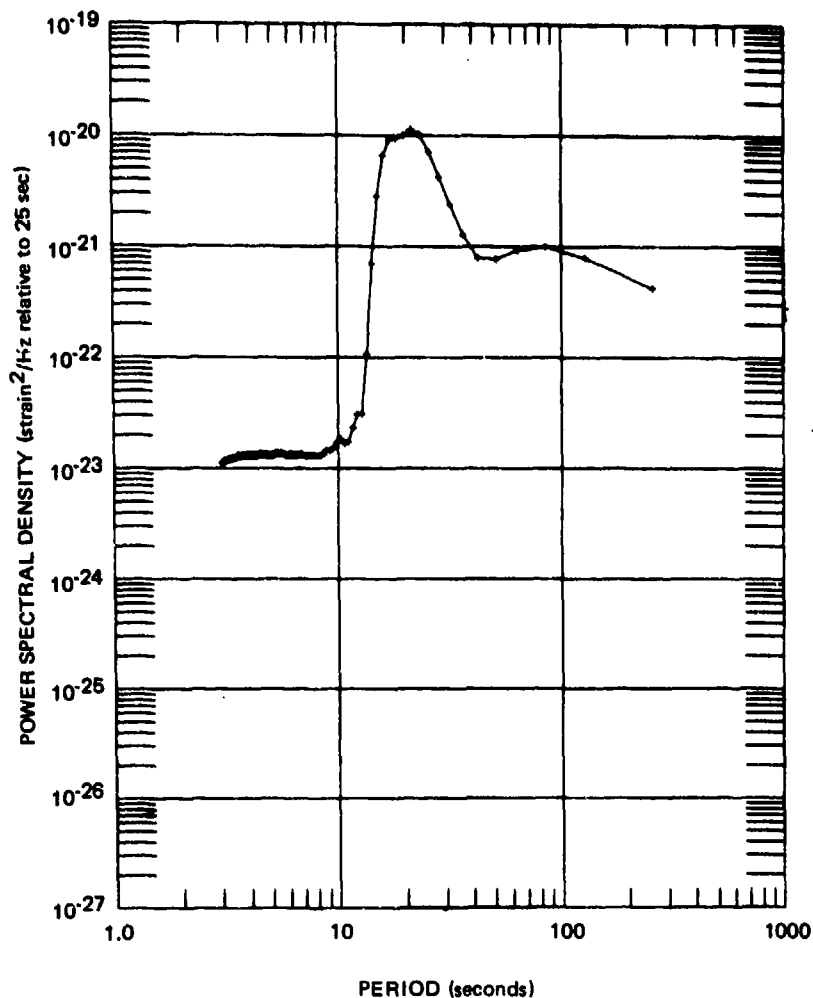


b. Phase lead SZLL over PZLL

Figure 218. Power spectral density, coherence, and relative phase angle with 3841 time samples of PZLL and SZLL seismograms during LR_1 Rayleigh wave of New Hebrides $m_b = 5.5$ earthquake

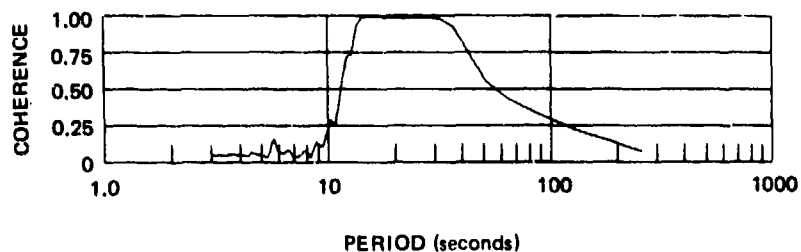
G 6749

NEW HEBRIDES EARTHQUAKE $M_b = 5.5$
 3841 SAMPLES, 256 LAGS, 2.0 SPS, PARZEN SMOOTHING
 UC-A2 3 SEPTEMBER 1970 0940/1050
 • SZLL 1.0



c. SZLL power spectral density

COHERENCE
 3841 SAMPLES, 256 LAGS, 2.0 SPS, PARZEN SMOOTHING
 UC-A2 3 SEPTEMBER 1970 0940/1050
 SZLL X PZLL 1.0

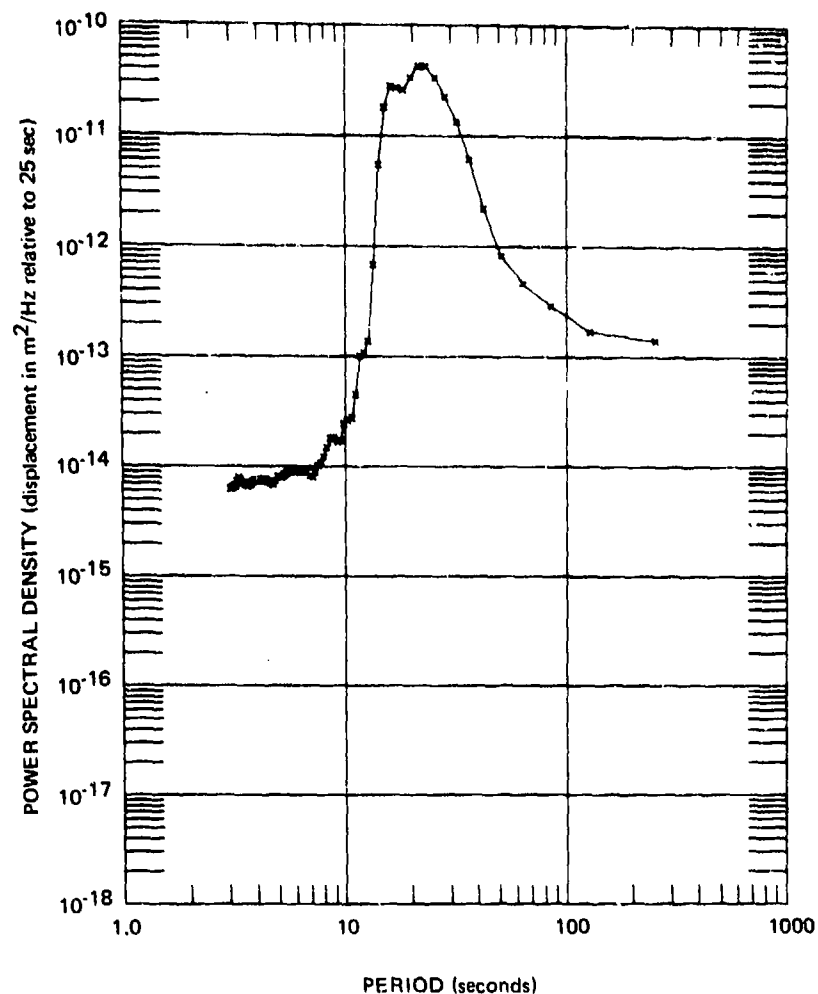


d. Coherence

Figure 218. Power spectral density, coherence, and relative phase angle with 3841 time samples of PZLL and SZLL seismograms during LR₁ Rayleigh wave of New Hebrides $m_b = 5.5$ earthquake

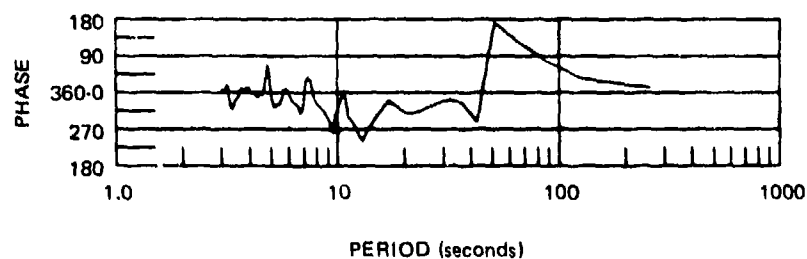
G 6750

NEW HEBRIDES EARTHQUAKE $M_b = 5.5$
 3841 SAMPLES, 256 LAGS, 2.0 SPS, PARZEN SMOOTHING
 QC-A2 * P325LL 1.0
 3 SEPTEMBER 1970
 0940/1050



a. P325LL power spectral density

PHASE
 3841 SAMPLES, 256 LAGS, 2.0 SPS, PARZEN SMOOTHING
 QC-A2 S325LL X P325LL
 3 SEPTEMBER 1970
 0940/1050

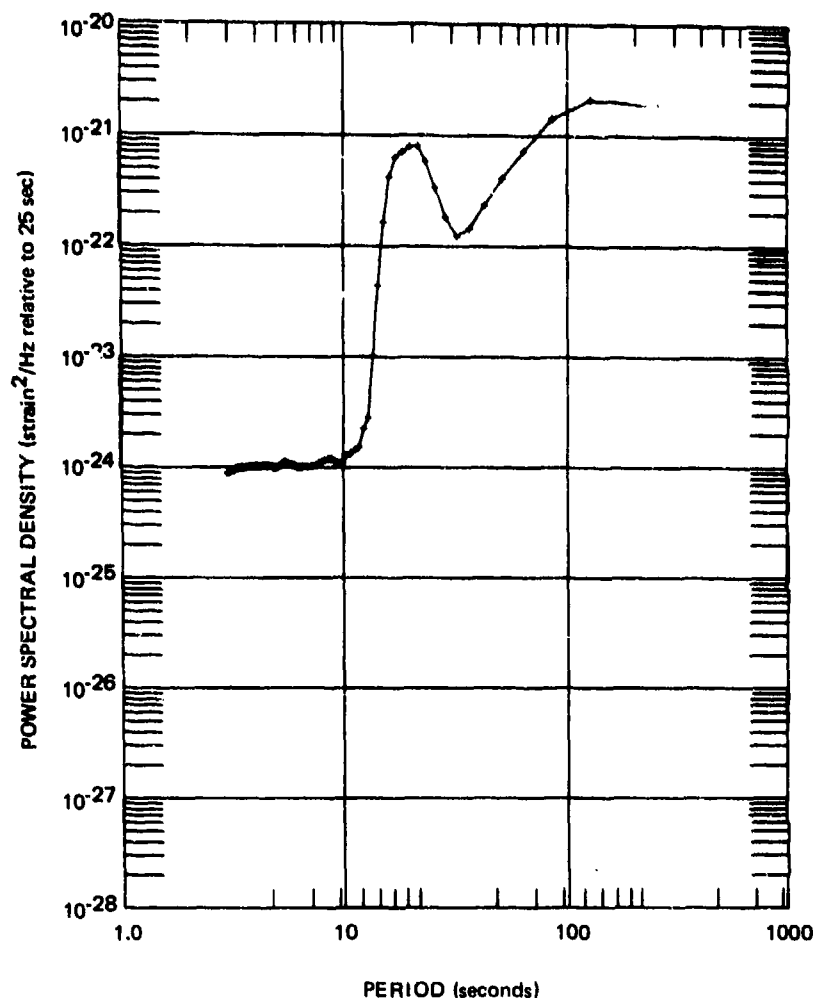


b. Phase lead P325LL over S325LL

Figure 219. Power spectral density, coherence, and relative phase angle of P325LL and S325LL seismograms during LR_1 Rayleigh wave of New Hebrides $m_b = 5.5$ earthquake

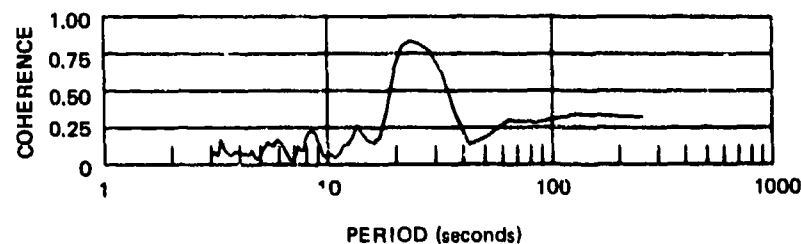
G 6751

NEW HEBRIDES EARTHQUAKE $M_b = 5.5$
 3841 SAMPLES, 256 LAGS, 2.0 SPS, PARZEN SMOOTHING
 GC-A2 3 SEPTEMBER 1970 0940/1050 * S325LL 1.0



c. S325LL power spectral density

COHERENCE
 3841 SAMPLES, 256 LAGS, 2.0 SPS, PARZEN SMOOTHING
 GC-A2 3 SEPTEMBER 1970 0940/1050 S325LL X P325LL

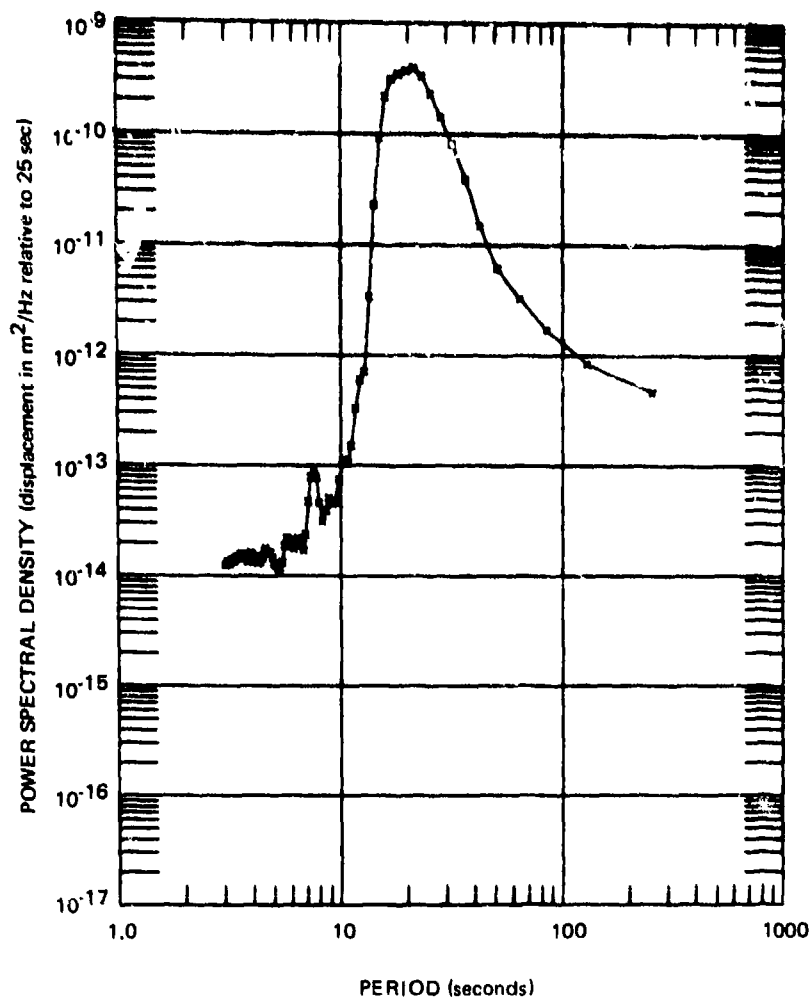


d. Coherence

Figure 219. Power spectral density, coherence, and relative phase angle of P325LL and S325LL seismograms during LR_1 Rayleigh wave of New Hebrides $m_b = 5.5$ earthquake

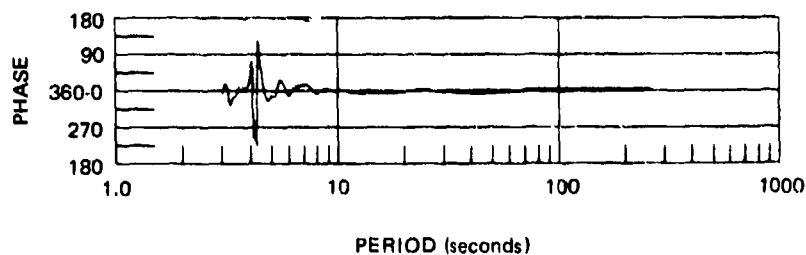
G 6752

NEW HEBRIDES EARTHQUAKE $M_B=5.5$
 3841 SAMPLES, 256 LAGS, 2.0 SPS, PARZEN SMOOTHING
 GC-A2 = P55LL 1.0
 3 SEPTEMBER 1970
 0940/1050



a. P55LL power spectral density

PHASE
 3841 SAMPLES, 256 LAGS, 2.0 SPS, PARZEN SMOOTHING
 GC-A2 S55LL X P55LL 1.0
 3 SEPTEMBER 1970
 0940/1050

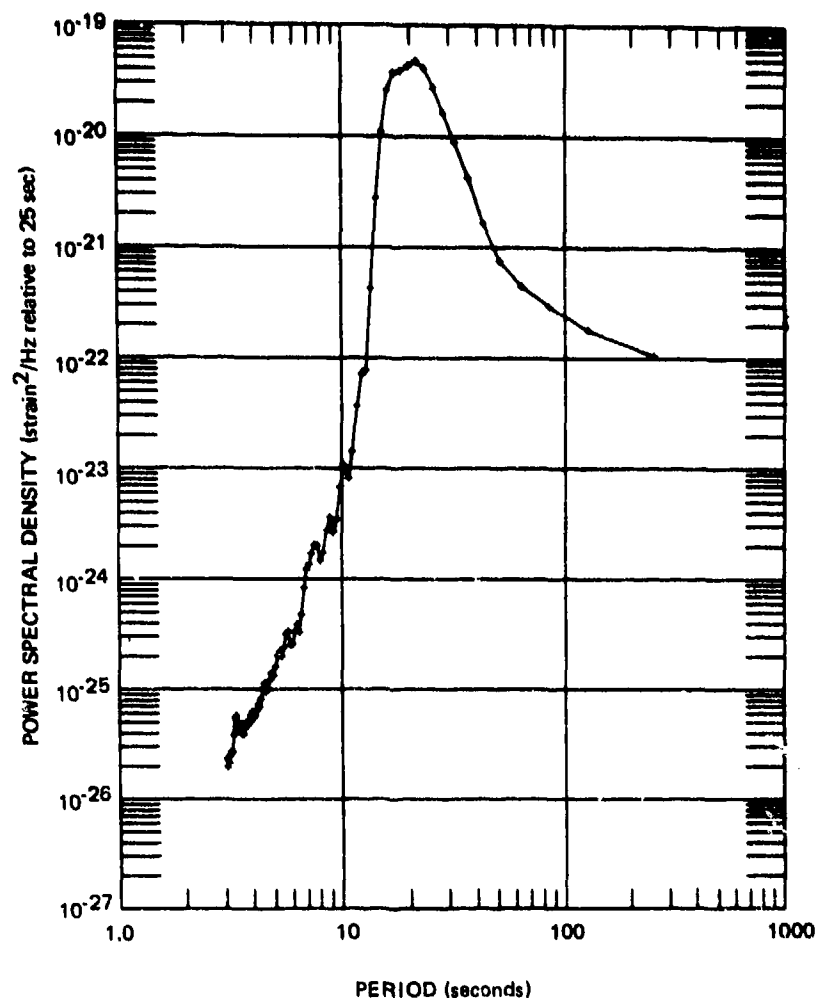


b. Phase lead S55LL over P55LL

Figure 220. Power spectral density, coherence, and relative phase angle of P55LL and S55LL seismograms during LR_1 Rayleigh wave of New Hebrides $m_b = 5.5$ earthquake

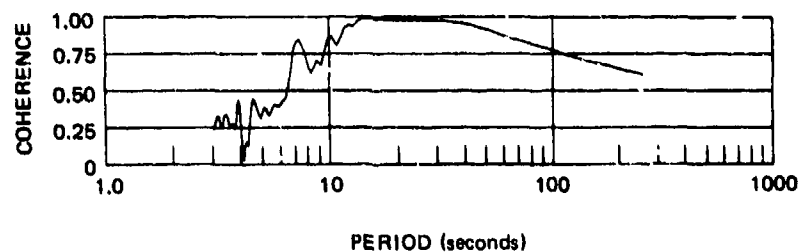
G 6753

NEW HEBRIDES EARTHQUAKE $M_b=5.5$
 3841 SAMPLES, 256 LAGS, 2.0 SPS, PARZEN SMOOTHING
 QC-A2 3 SEPTEMBER 1970 0940/1050 S55LL 1.0



c. S55LL power spectral density

COHERENCE
 3841 SAMPLES, 256 LAGS, 2.0 SPS, PARZEN SMOOTHING
 QC-A2 3 SEPTEMBER 1970 0940/1050 S55LL X P55LL 1.0

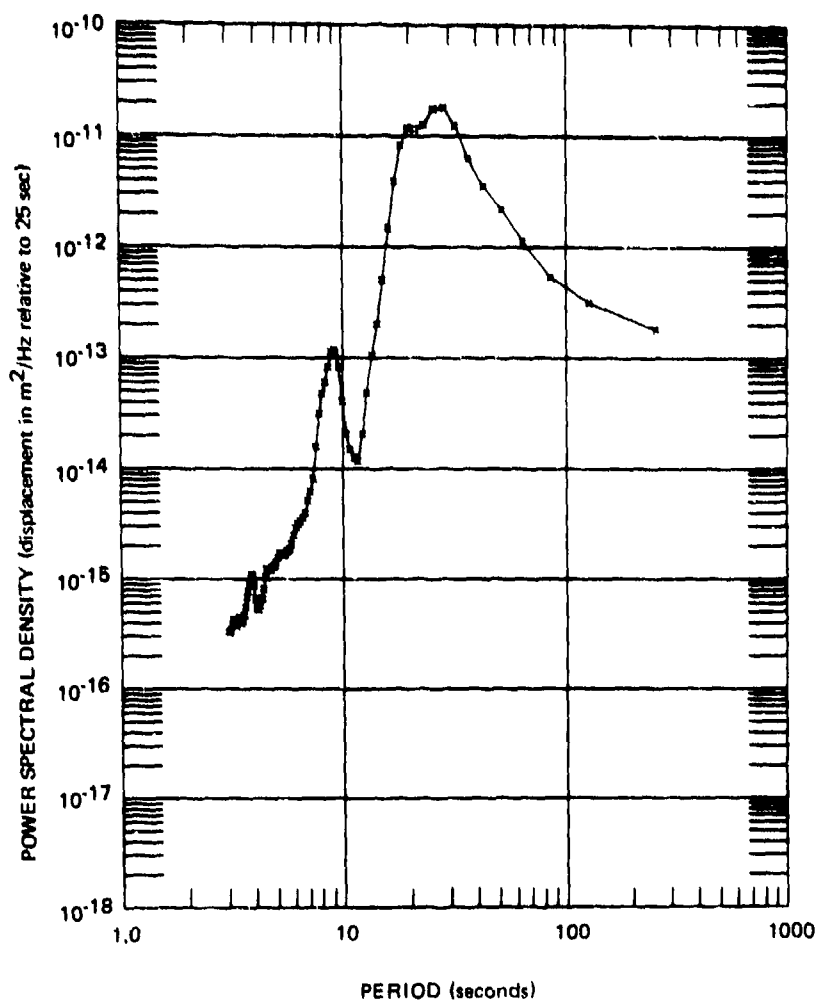


d. Coherence

Figure 220. Power spectral density, coherence, and relative phase angle of P55LL and S55LL seismograms during LR_1 Rayleigh wave of New Hebrides $m_b = 5.5$ earthquake

G 6754

NEW HEBRIDES EARTHQUAKE $M_b = 5.5$
 3841 SAMPLES, 256 LAGS, 2.0 SPS, PARZEN SMOOTHING
 QC-A2 *PZL 1.0
 3 SEPTEMBER 1970
 1130/1225



PHASE
 3841 SAMPLES, 256 LAGS, 2.0 SPS, PARZEN SMOOTHING
 QC-A2 SZL X PZL 1.0
 3 SEPTEMBER 1970
 1130/1225

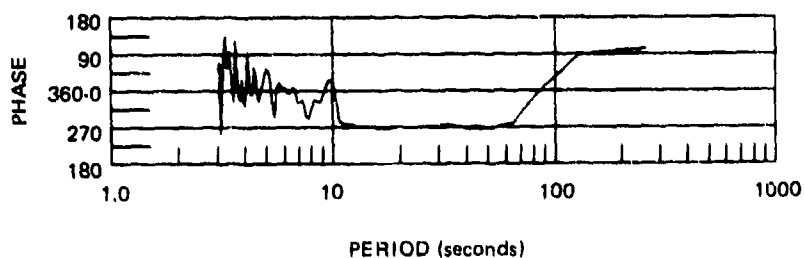
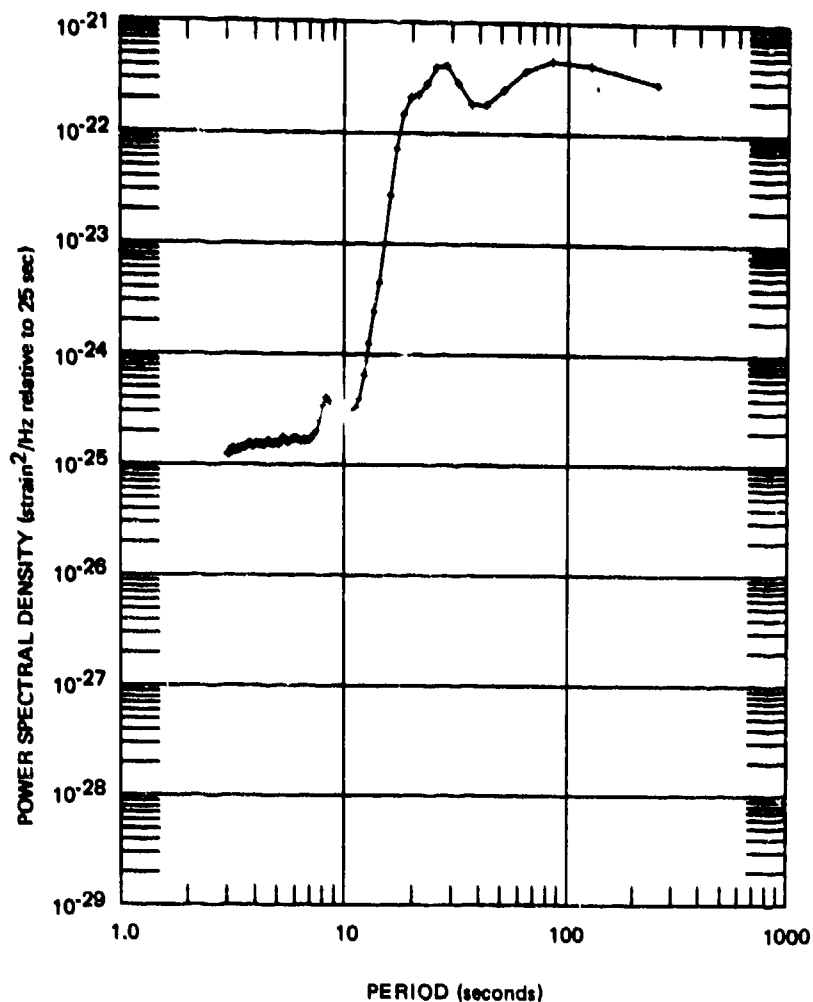


Figure 221. Power spectral density, coherence, and relative phase angle of PZL and SZL seismograms during LR_2 Rayleigh wave of New Hebrides $m_b = 5.5$ earthquake

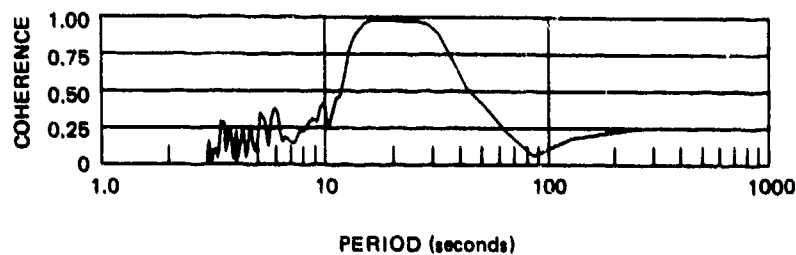
G 6755

NEW HEBRIDES EARTHQUAKE $M_B=5.5$
 3841 SAMPLES, 256 LAGS, 2.0 SPS, PARZEN SMOOTHING
 DC-A2 • SZL 1.0
 3 SEPTEMBER 1970
 1130/1225



c. SZL power spectral density

COHERENCE
 3841 SAMPLES, 256 LAGS, 2.0 SPS, PARZEN SMOOTHING
 DC-A2 SZL X PZL 1.0
 3 SEPTEMBER 1970
 1130/1225



d. Coherence

Figure 221. Power spectral density, coherence, and relative phase angle of PZL and SZL seismograms during LR_2 Rayleigh wave at New Hebrides $m_b = 5.5$ earthquake

G 6756

NEW HEBRIDES EARTHQUAKE $M_B=5.5$
 3841 SAMPLES, 256 LAGS, 2.0 SPS, PARZEN SMOOTHING
 DC-A2 * P3251 1.0
 7 SEPTEMBER 1970
 1130/1225

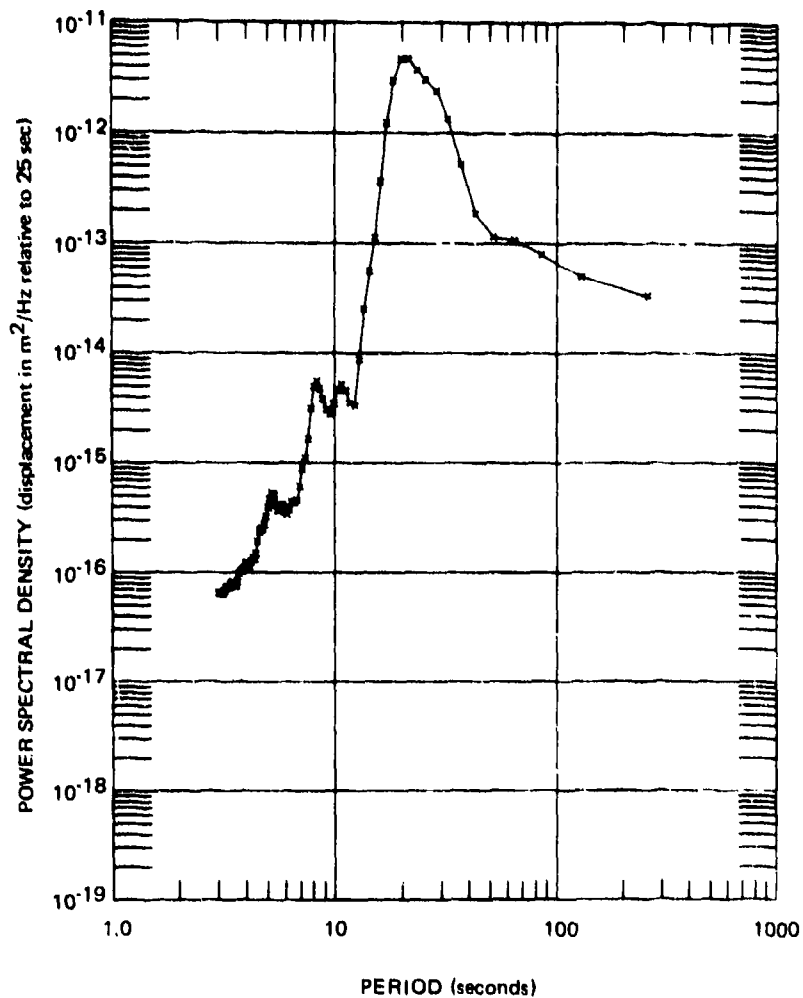
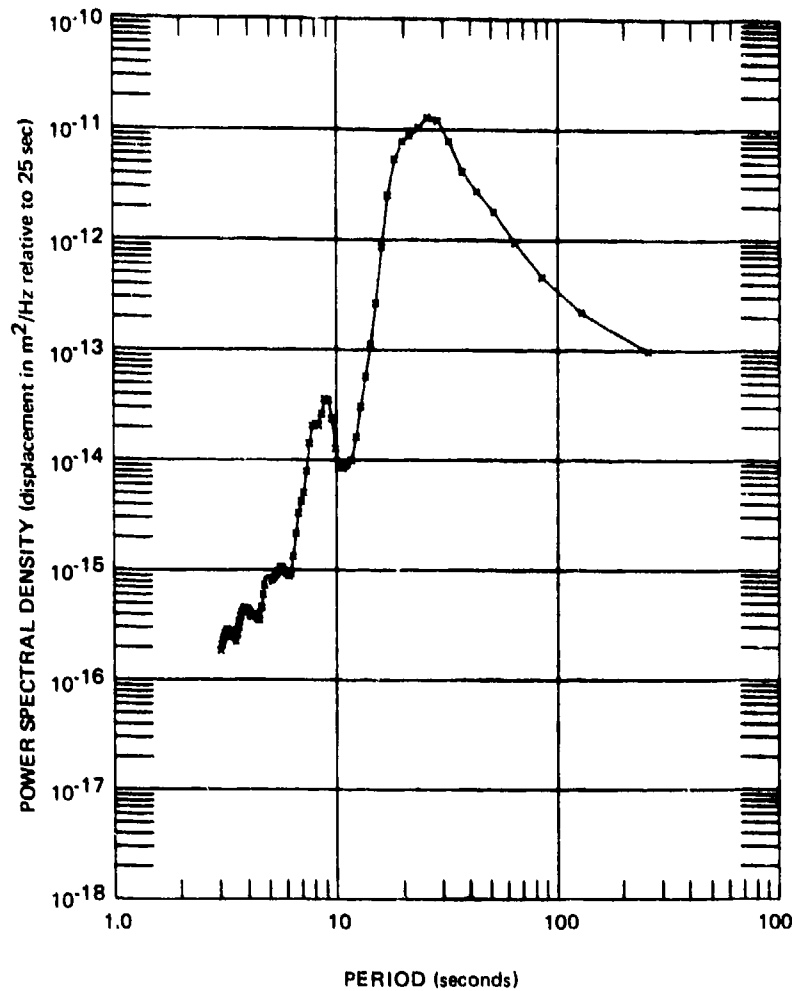


Figure 222. Power spectral density of P325L seismogram during LR_2 Rayleigh wave of New Hebrides $m_b = 5.5$ earthquake

G 6757

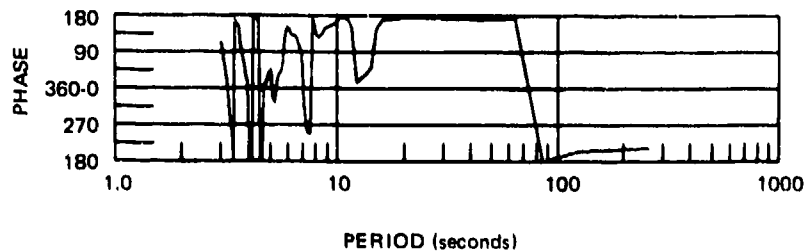
This page intentionally left blank.

NEW HEBRIDES EARTHQUAKE $M_b = 5.5$
 3841 SAMPLES, 256 LAGS, 2.0 SPS, PARZEN SMOOTHING
 QC-A2 * P55L 1.0
 3 SEPTEMBER 1970
 1130/1225



a. P55L power spectral density

PHASE
 3841 SAMPLES, 256 LAGS, 2.0 SPS, PARZEN SMOOTHING
 QC-A2 S55L X P55L 1.0
 3 SEPTEMBER 1970
 1130/1225

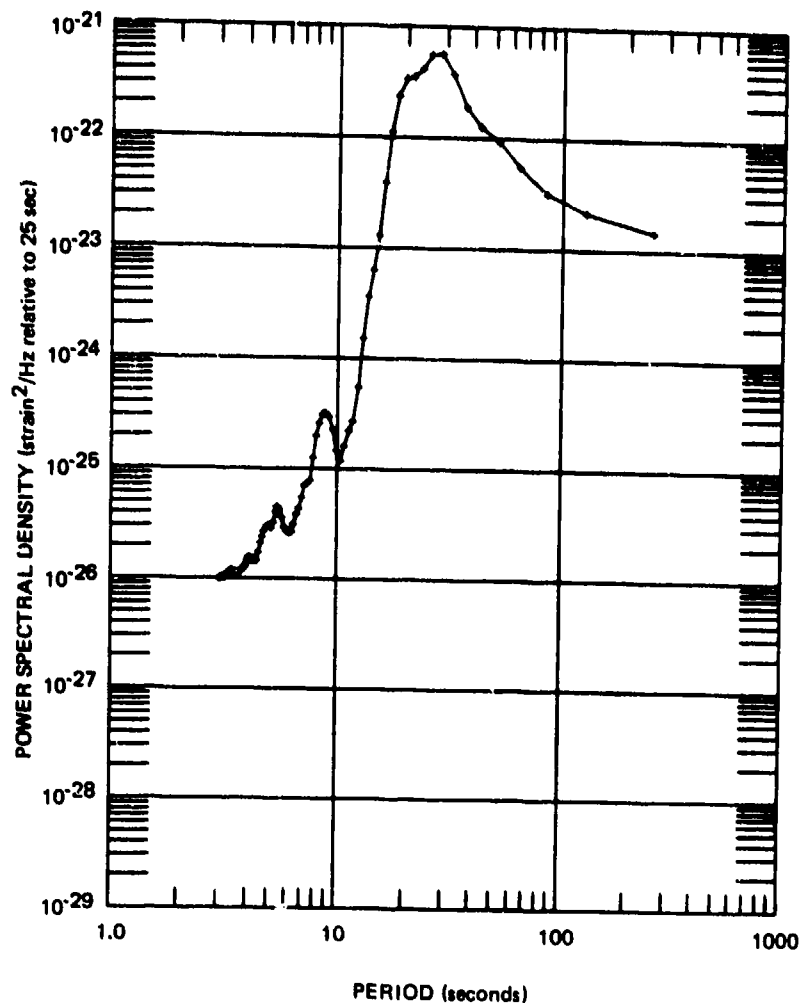


b. Phase lead S55L over P55L

Figure 223. Power spectral density, coherence, and relative phase angle of P55L and S55L seismograms during LR_2 Rayleigh wave of New Hebrides $m_b = 5.5$ earthquake

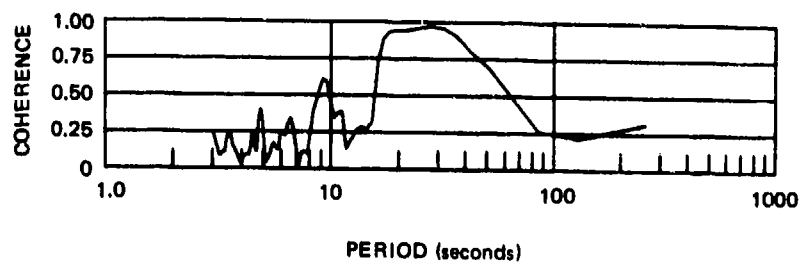
G 6758

NEW HEBRIDES EARTHQUAKE $M_B=5.5$
 3841 SAMPLES, 256 LAGS, 2.0 SPS, PARZEN SMOOTHING
 DC-A2 3 SEPTEMBER 1970 • S55L 1.0
 1130/1225



c. S55L power spectral density

COHERENCE
 3841 SAMPLES, 256 LAGS, 2.0 SPS, PARZEN SMOOTHING
 DC-A2 3 SEPTEMBER 1970 S55L X P55L 1.0
 1130/1225



d. Coherence

Figure 223. Power spectral density, coherence, and relative phase angle of P55L and S55L seismograms during LR₂ Rayleigh wave of New Hebrides $m_b = 5.5$ earthquake

G 6759

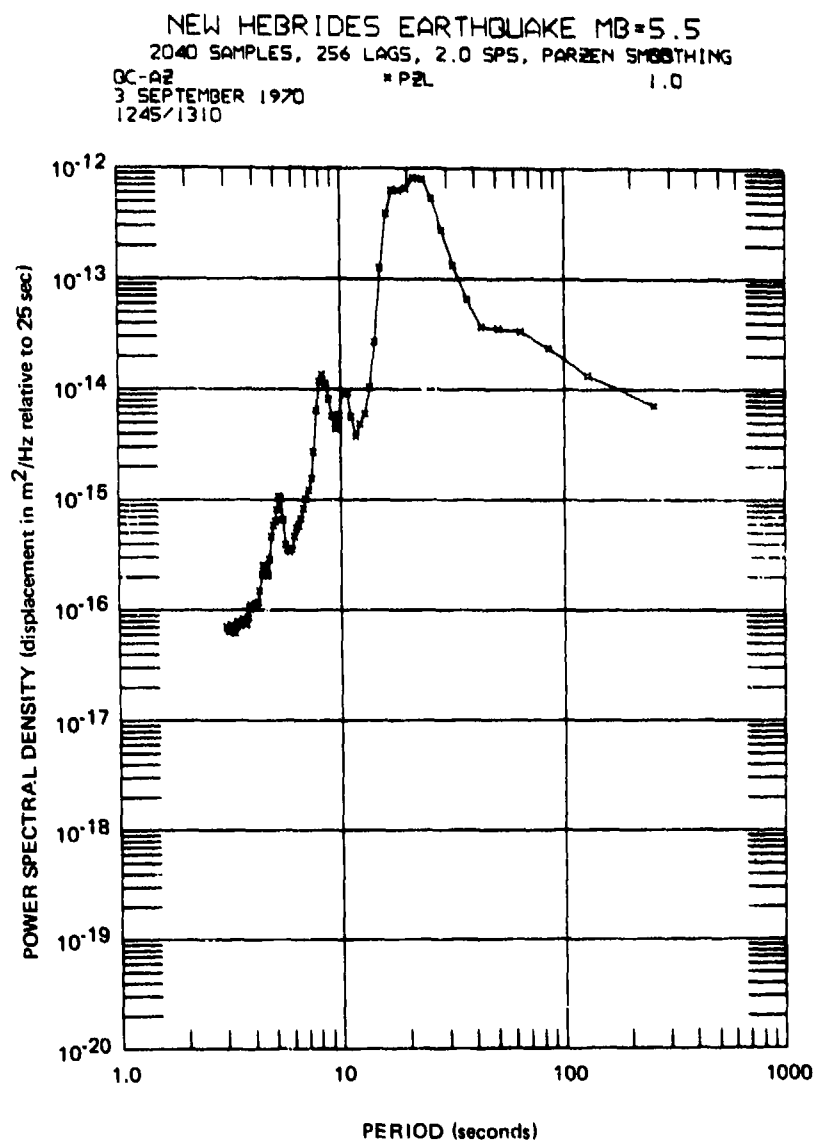


Figure 224. Power spectral density of PZL seismogram during LR₃ Rayleigh wave of New Hebrides $m_b = 5.5$ earthquake

G 6760

NEW HEBRIDES EARTHQUAKE $M_B=5.5$
 2040 SAMPLES, 256 LAGS, 2.0 SPS, PARZEN SMOOTHING
 QC-A2 * P325L 1.0
 3 SEPTEMBER 1970
 1245/1310

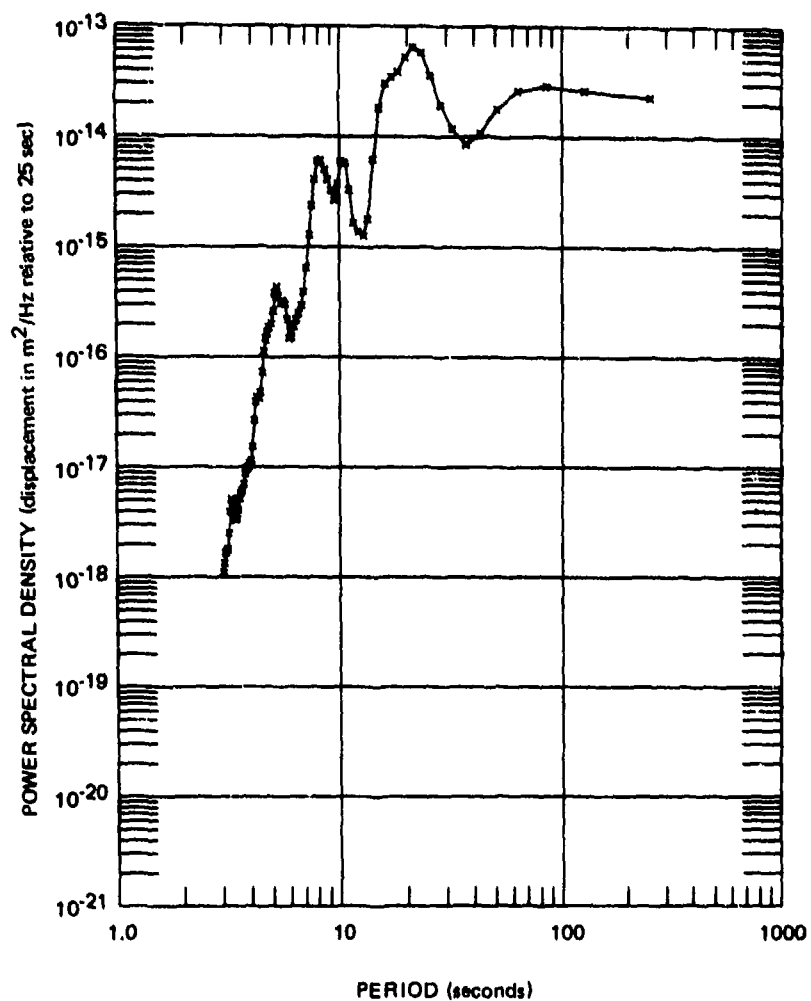
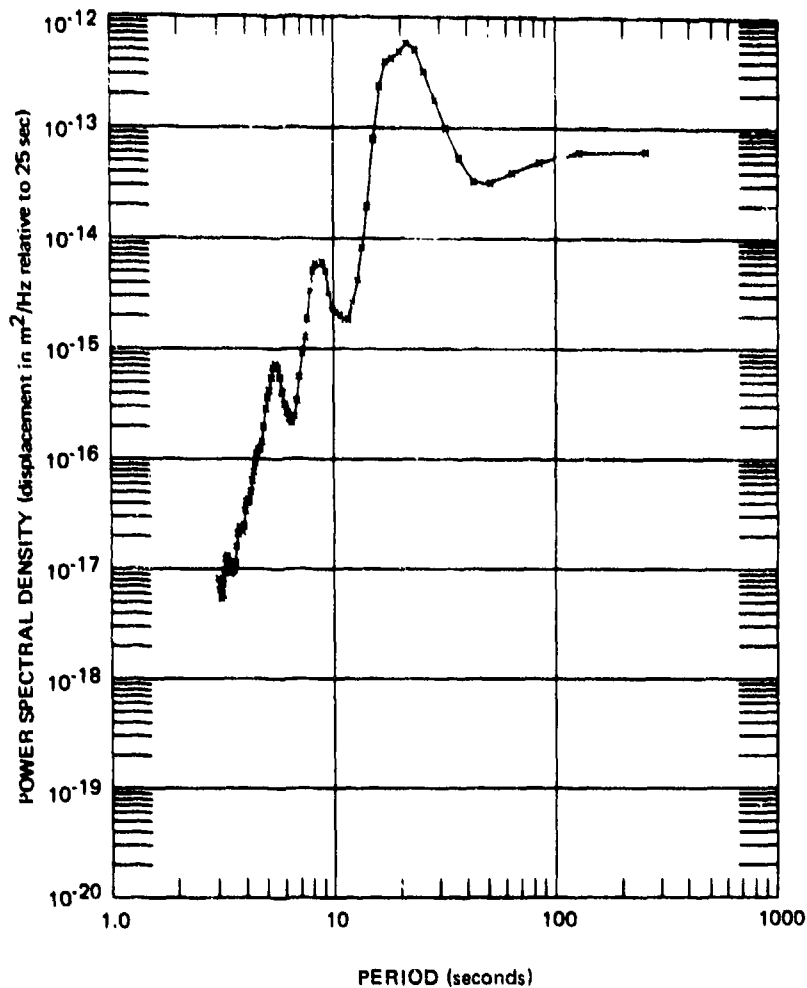


Figure 225. Power spectral density of P325L seismogram during LR₃ Rayleigh wave of New Hebrides $m_b = 5.5$ earthquake

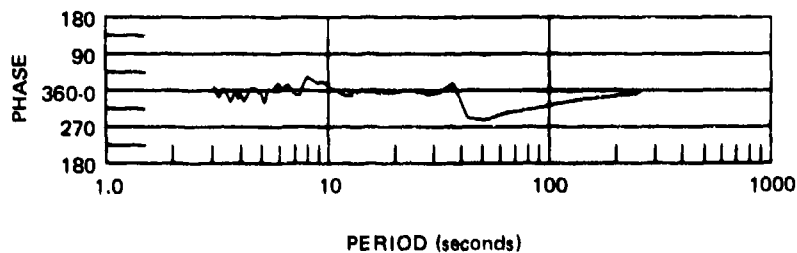
G 6761

NEW HEBRIDES EARTHQUAKE $M_b = 5.5$
 2040 SAMPLES, 256 LAGS, 2.0 SPS, PARZEN SMOOTHING
 GC-A2 * P55L 1.0
 3 SEPTEMBER 1970
 1245/1310



a. P55L power spectral density

PHASE
 2040 SAMPLES, 256 LAGS, 2.0 SPS, PARZEN SMOOTHING
 GC-A2 S55L X P55L 1.0
 3 SEPTEMBER 1970
 1245/1310

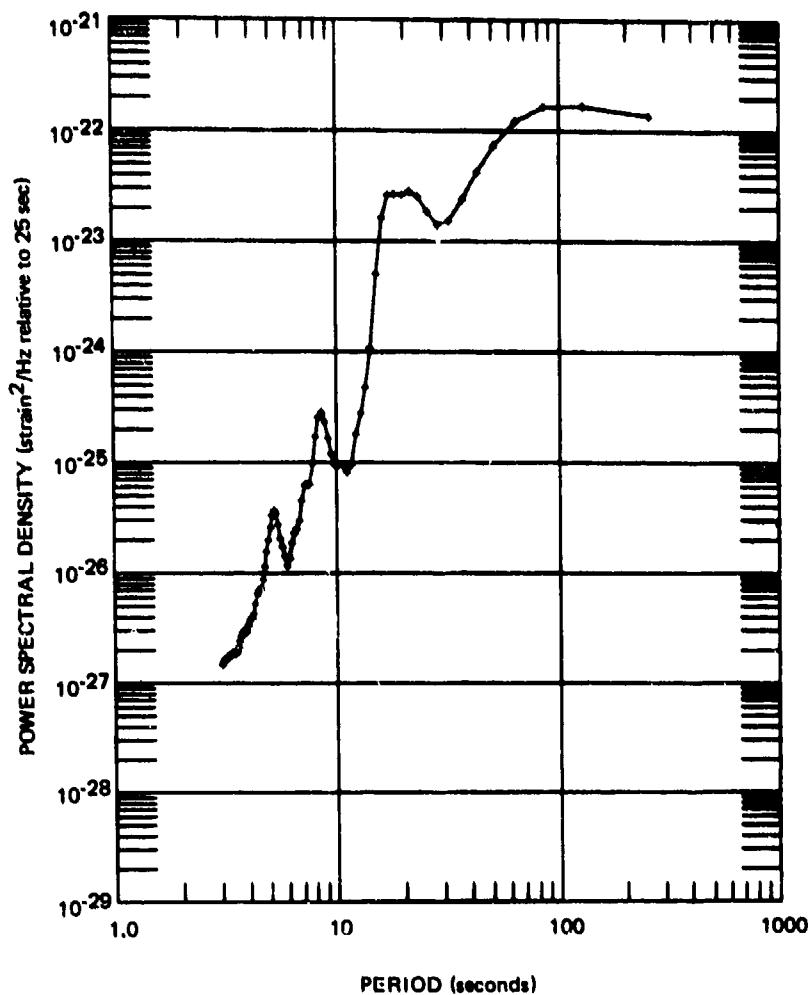


b. Phase lead S55L over P55L

Figure 226. Power spectral density, coherence, and relative phase angle of P55L and S55L seismograms during LR_3 Rayleigh wave of New Hebrides $m_b = 5.5$ earthquake

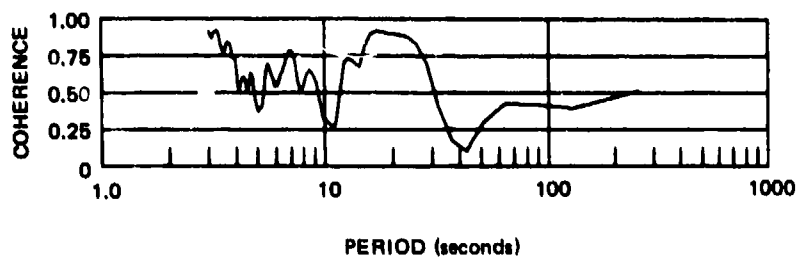
G 6762

NEW HEBRIDES EARTHQUAKE $M_b=5.5$
 2040 SAMPLES, 256 LAGS, 2.0 SPS, PARZEN SMOOTHING
 GC-A2 + S5SL 1.0
 3 SEPTEMBER 1970
 1245/1310



c. S5SL power spectral density

COHERENCE
 2040 SAMPLES, 256 LAGS, 2.0 SPS, PARZEN SMOOTHING
 GC-A2 S5SL X P5SL 1.0
 3 SEPTEMBER 1970
 1245/1310



d. Coherence

Figure 226. Power spectral density, coherence, and relative phase angle of P55L and S55L seismograms during LR₃ Rayleigh wave of New Hebrides $m_b = 5.5$ earthquake

G 6763

of all seismogram pairs is essentially 1.0 for the peak of the spectra and falls off on both sides of the peak. The repeatability of the spectra for all three Rayleigh waves again confirms the ability of the strain/inertial directional array to enhance signals. The relative values of the spectra for the 17 to 23 sec peak and for the longer period signals gives a qualitative evaluation of the greater ability of the directional array to enhance signals at periods shorter than 40 sec than at the longer periods. The coherence between the P55L and S55L seismograms for the LR_3 Rayleigh wave (figure 226) is between 0.25 and 0.50 at periods greater than 50 sec. This high coherence indicates that the two seismograms are linearly related and suggests that the spectra at these periods is from the LR_3 Rayleigh wave and not from random noise.

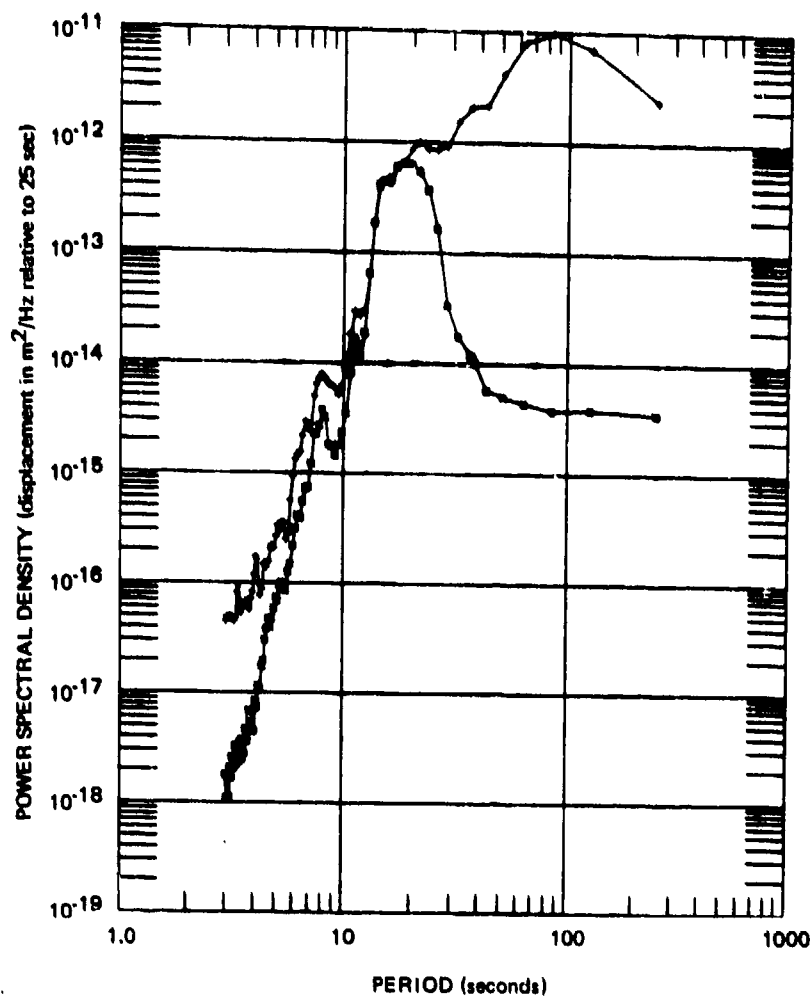
The next suite of nine figures (227 through 235) presents the power spectral densities, coherences, and relative phase angles for the three components for each of three earthquakes. The NOS PDE data and calculated distance and azimuth from QC-AZ to the epicenter are listed in table 17. The strain spectra have been equalized to the peak of the inertial spectra by multiplication with the numbers shown in the figures. These figures are presented to give spectral analysis examples of the relation between the strain and inertial seismographs for earthquakes with great circle paths at azimuths near 325 deg. All the figures show high coherence and the proper phase angles at the peak of the spectra. Results are similar to those in previous figures. The 55 deg azimuth strain seismographs are close to a null in the azimuthal response for S_H and Love waves. The low coherence in figures 229 and 232 is a result of small strain Love wave signal. The Honshu earthquake is farther off the null and the coherence in figure 235 is close to 1.0. During the time interval used in figure 230, the vertical strain seismograph was noisy and the low gain SZLL data were used. The peak of the Rayleigh wave spectra is well above the noise.

The power spectral density of the vertical components and of the radial 55 deg azimuth components for the two $m_b = 4.2$ Solomon Islands earthquakes are plotted in figures 236 through 239. The seismograms of these earthquakes are illustrated in figure 162 and the epicenter data are given in section 9. The SZL strain spectra have been normalized to the PZL displacement spectra such that at 25 sec, 5.44×10^{-24} strain²/Hz is equal to 1×10^{-14} m²/Hz. The S55L strain spectra have been normalized to the P55L displacement spectra such that at 25 sec, 9.88×10^{-24} strain²/Hz is equal to 1×10^{-14} m²/Hz. These normalizations are the same as were used in sections 7.3 and 7.4 for the microseismic background samples. The spectra from both earthquakes are similar. At periods shorter than 21 sec, the signal has sufficiently greater power than the noise that it can be easily detected and enhanced as illustrated in the directional array seismograms in figure 162.

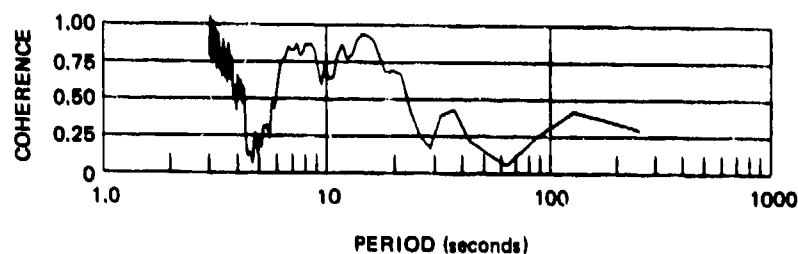
12.3 SUMMARY OF RESULTS OF SPECTRAL COMPARISONS

In section 12, it has been shown that when strain and inertial seismographs are compared in the frequency domain, they respond in a manner as predicted by theory. For large signals and for small signals, the spectra of the two types of seismographs are similar at the peak of the energy. This similarity holds for both Fourier transform amplitude spectra and for power spectral density spectra. At the peak of the signal energy, the coherence is essentially 1.0 and the relative phase angles are in accord with theory. The combination of strain and inertial seismographs to form a directional array is a robust process that performs well in the presence of mixed wave types and of noise in the seismographs. Spectra

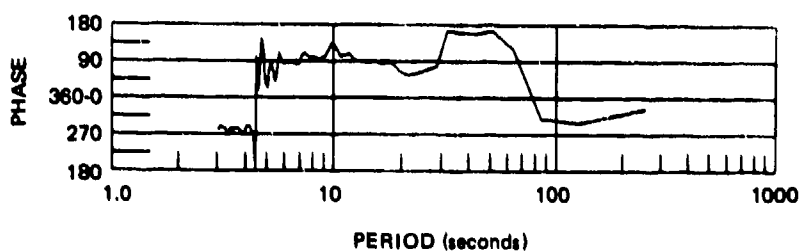
OFF C. KAMCHATKA EARTHQUAKE $M_b = 5.2$
 1793 SAMPLES, 256 LAGS, 2.0SP5, HANNING SMOOTHING
 QC-A2 03 OCTOBER 1970 • P&L 1.0
 0051/0105 • S&L 9.1950E+09



a. Power spectral density



b. Coherence

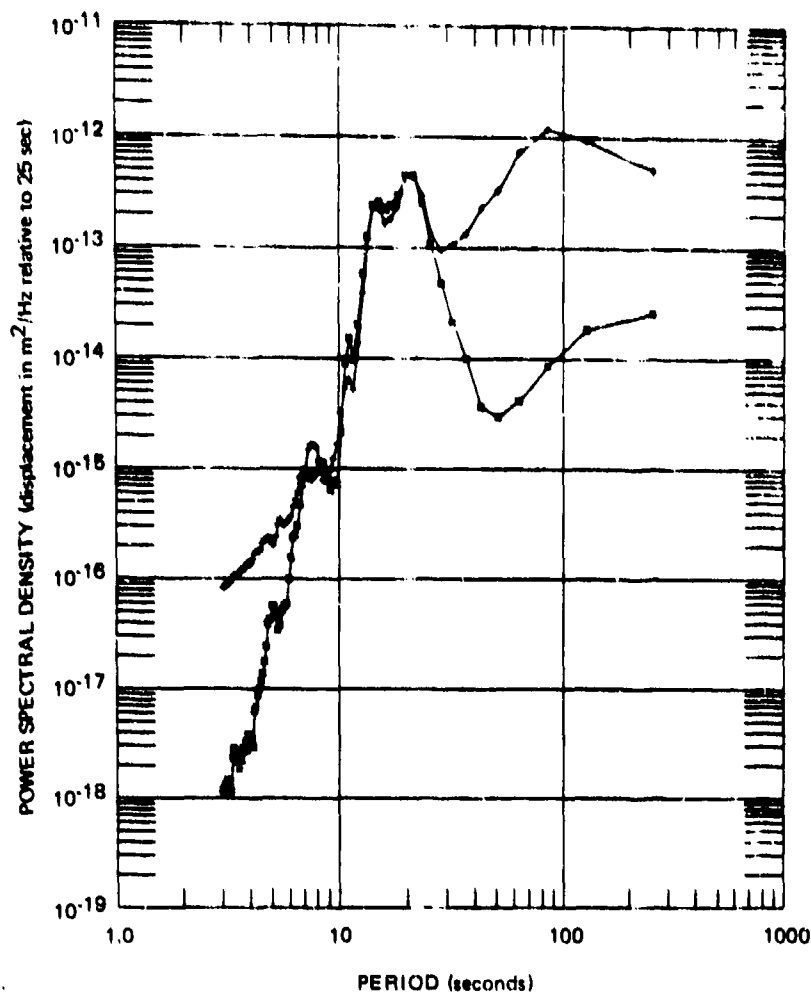


c. Phase lead SZL over PZL

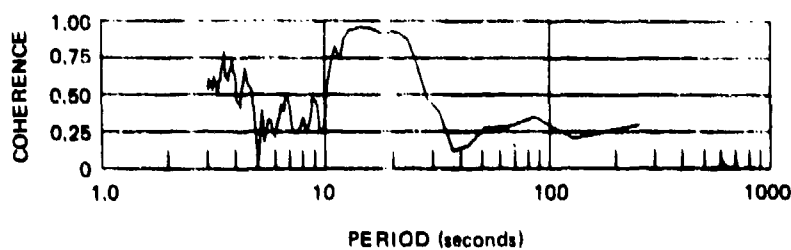
Figure 227. Power spectral density, coherence, and relative phase angle of PZL and SZL seismographs during Rayleigh wave of an $M_b = 5.2$ earthquake off the east coast of Kamchatka

G 6764

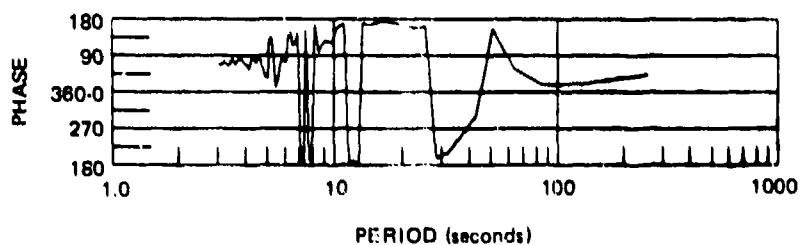
OFF C. KAMCHATKA EARTHQUAKE $M_b = 5.2$
 1793 SAMPLES, 256 LAG, 2 OPS, HANNING SMOOTHING
 OK AR
 03 OCTOBER 1971
 005170105
 3 05400-00
 1 0



a. Power spectral density



b. Coherence

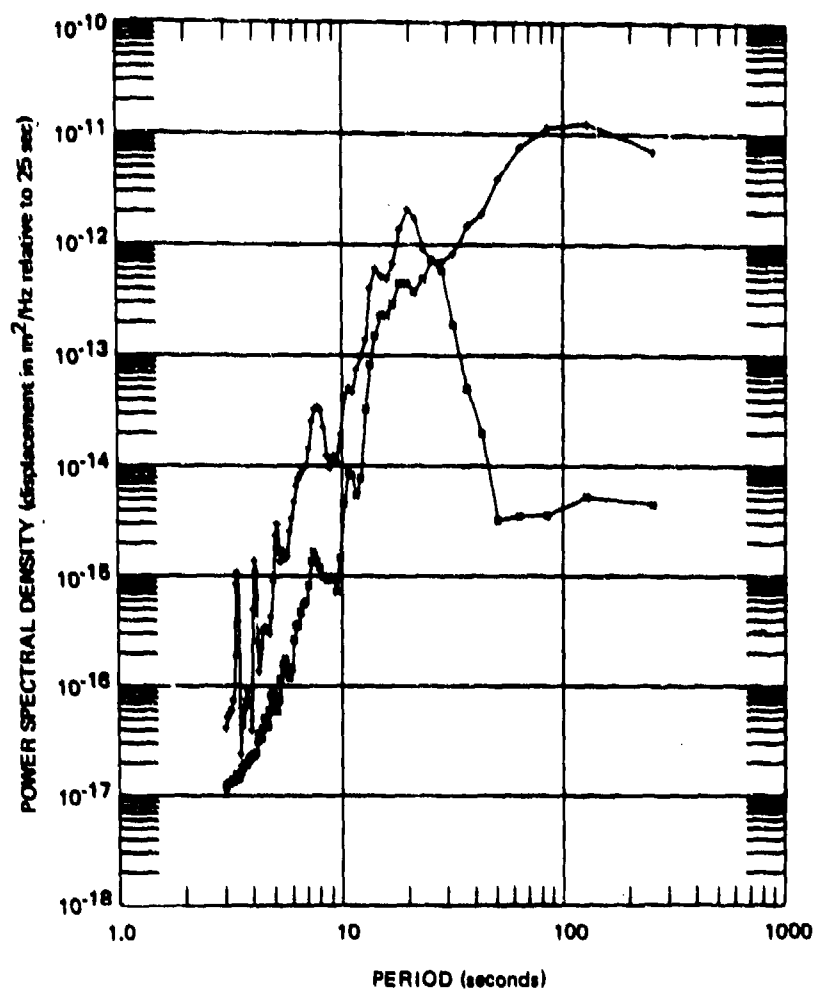


c. Phase lead
P325L over
S325L

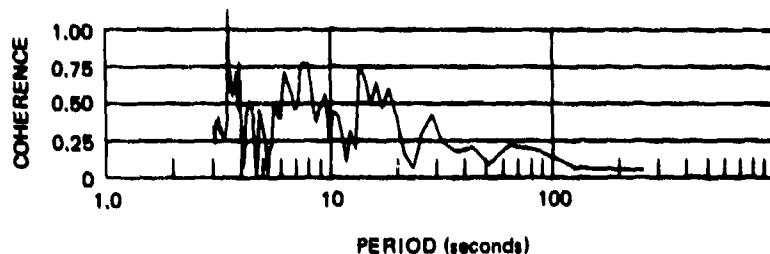
Figure 228. Power spectral density, coherence, and relative phase angle of P325L and S325L seismographs during Rayleigh wave of an $M_b = 5.2$ earthquake off the east coast of Kamchatka

G 6765

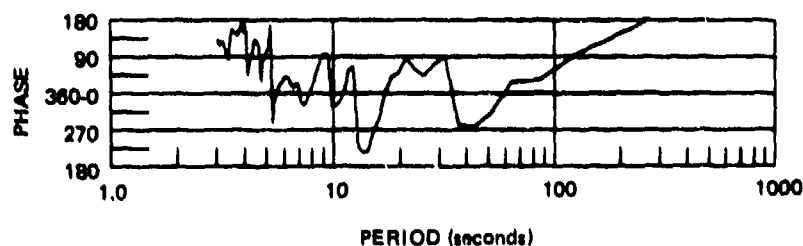
OFF C. KAMCHATKA EARTHQUAKE $M_b = 5.2$
 1793 SAMPLES, 256 LAGS, 2 DBPS, HANNING SMOOTHING
 DC-AR * P55L 1.0
 03 OCTOBER 1970 * S55L 2.1390E+10
 0047/0102



a. Power spectral density



b. Coherence

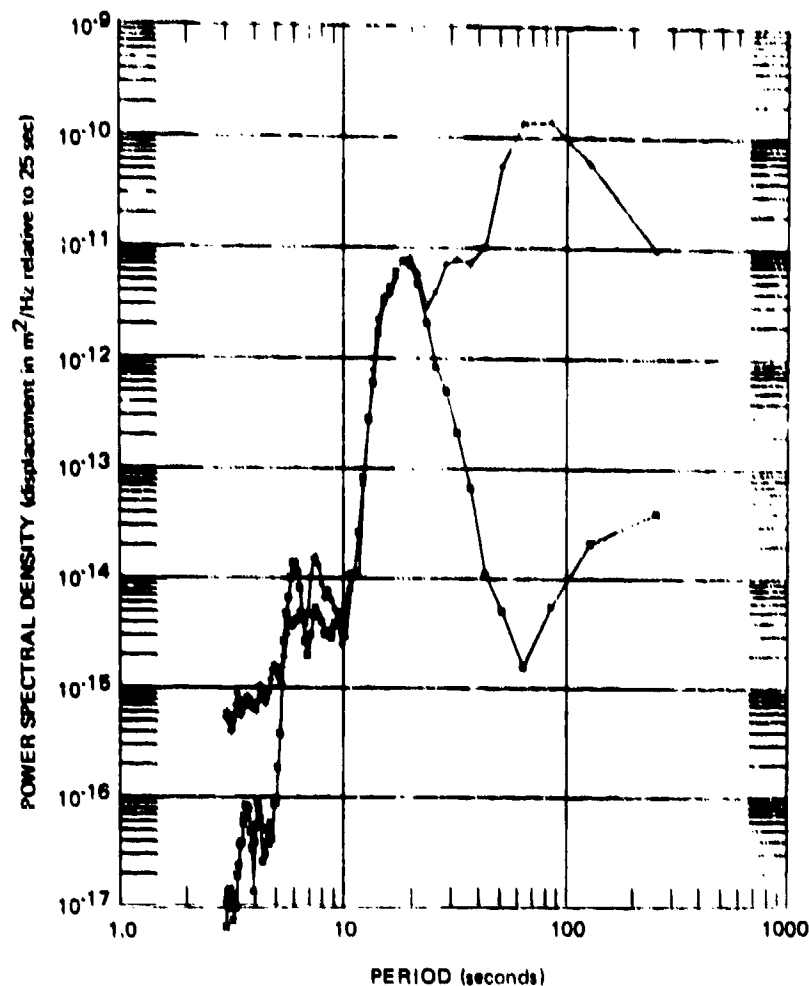


c. Phase lead S55L over P55L

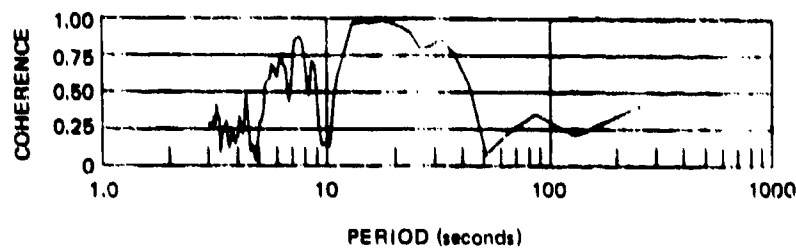
Figure 229. Power spectral density, coherence, and relative phase angle of P55L and S55L seismographs during Love wave of an $m_b = 5.2$ earthquake off the east coast of Kamchatka

G 6766

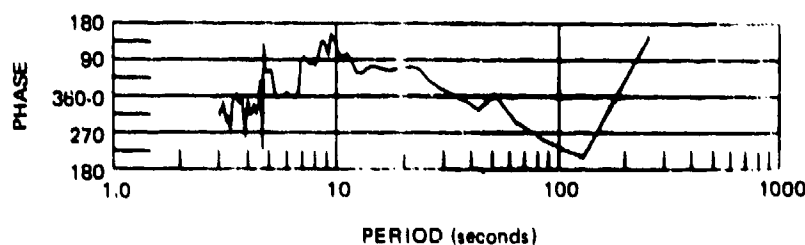
GULF OF ALASKA EARTHQUAKE $M_b = 5.0$
 249 SAMPLES, 256 LOGS, 100 SPS, HANNING SMOOTHING
 03 OCTOBER 1970
 0811/0818
 10
 00702.116



a. Power spectral density



b. Coherence



c. Phase lead SZLL over PZL

Figure 230. Power spectral density, coherence, and relative phase angle of PZL and SZLL seismographs during Rayleigh wave of an $m_b = 5.0$ earthquake in the Gulf of Alaska

G 6767

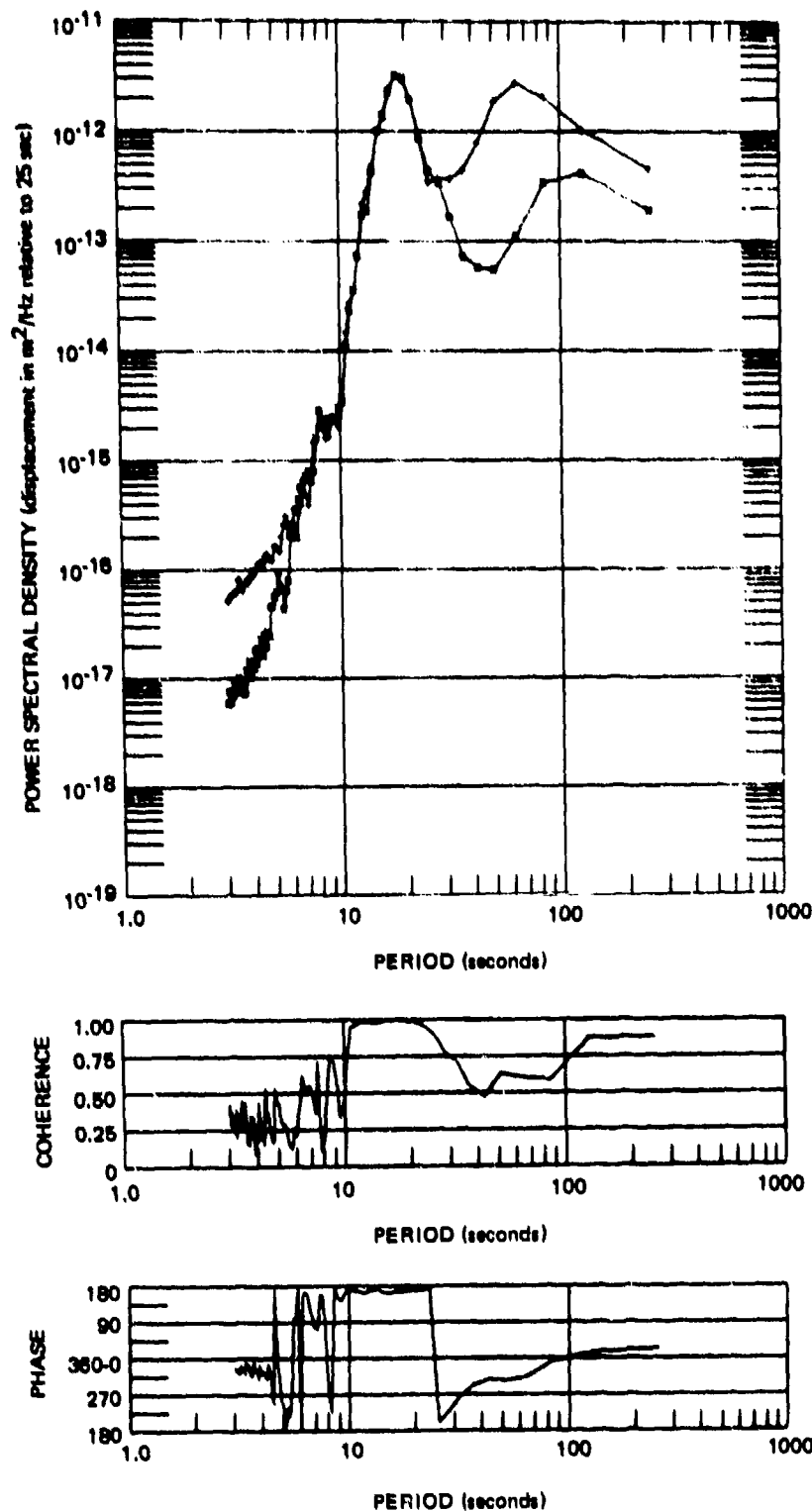
GULF OF ALASKA EARTHQUAKE MB 5.0

769 SAMPLES, 256 LINES, 2.08PS, HANNING SMOOTHING

UC-A2
03 OCTOBER 1970
0831/0838

* S325L
* P325L

3.3110E+09
1.0



a. Power spectral density

b. Coherence

c. Phase lead
P325L over
S325L

Figure 231. Power spectral density, coherence, and relative phase angle of P325L and S325L seismographs during Rayleigh wave of an $m_b = 5.0$ earthquake in the Gulf of Alaska

G 6768

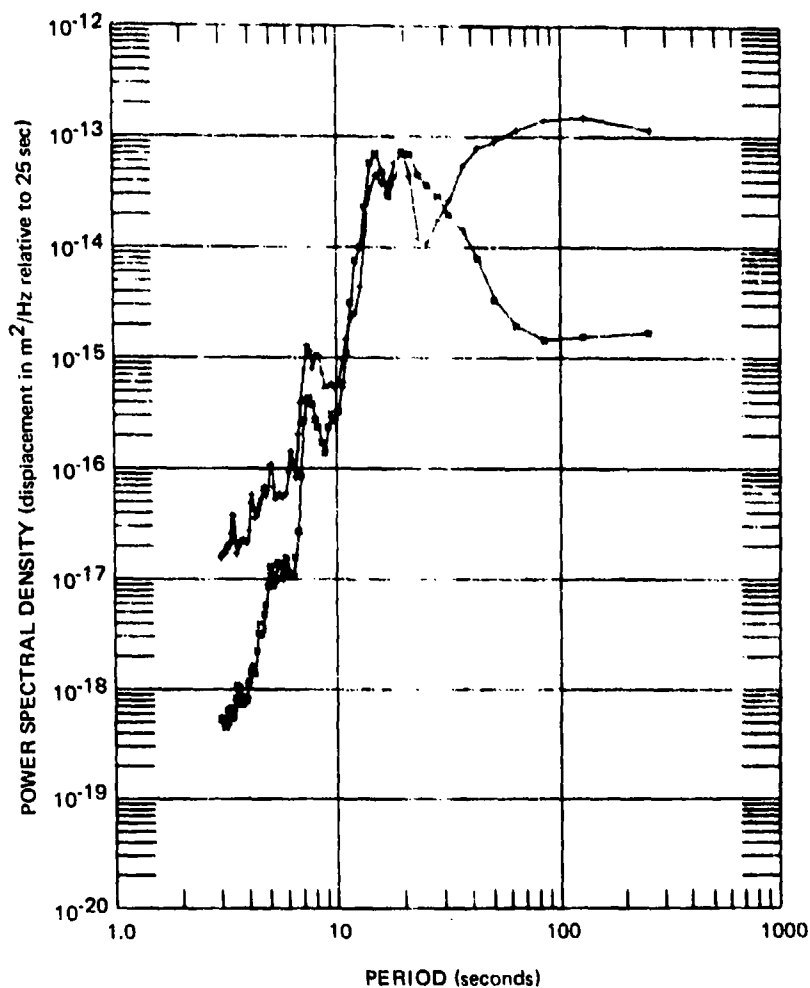
GULF OF ALASKA EARTHQUAKE $M_b = 5.0$

769 SAMPLES, 756 LAGS, 2 DSPS, HANNING SMOOTHING

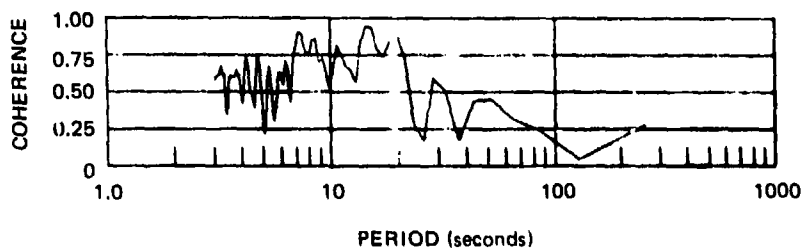
TA 02
03 OCTOBER 1970
0929/0835

• P55L
• S55L

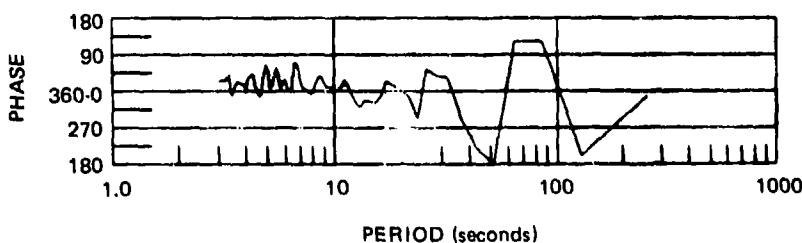
1.0
3.8800E+09



a. Power spectral density



b. Coherence

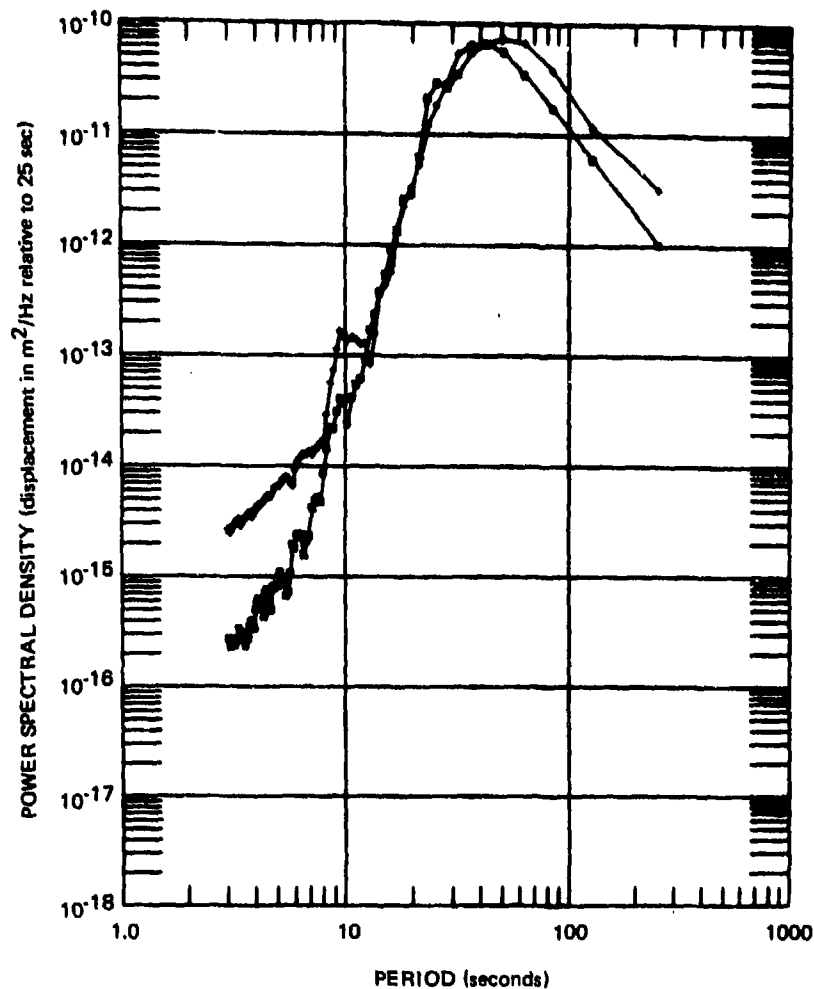


c. Phase lead
S55L over
P55L

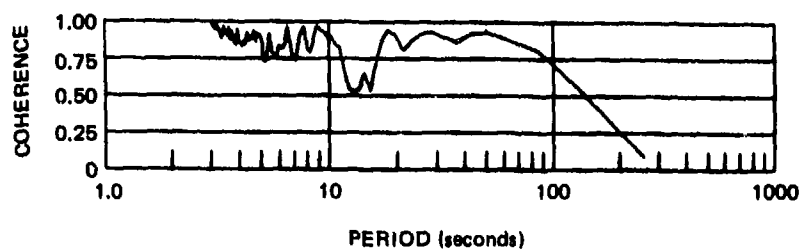
Figure 232. Power spectral density, coherence, and relative phase angle of P55L and S55L seismographs during Love wave of an $m_b = 5.0$ earthquake in the Gulf of Alaska

G 6769

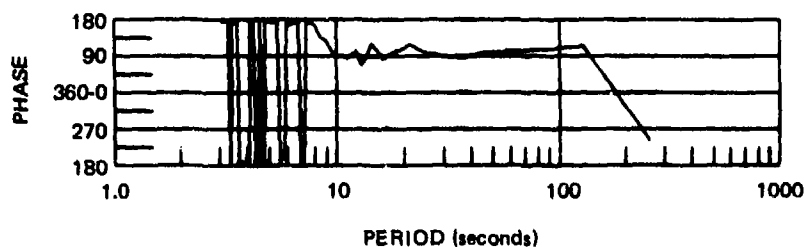
HONSHU EARTHQUAKE $M_b = 5.9$
 769 SAMPLES, 256 LAGS, 2.0SEPS, HANNING SMOOTHING
 DC-AS • PZLL 1.0
 16 OCTOBER 1970 • SZLL 3.3340E+11
 0601/0607



a. Power spectral density



b. Coherence

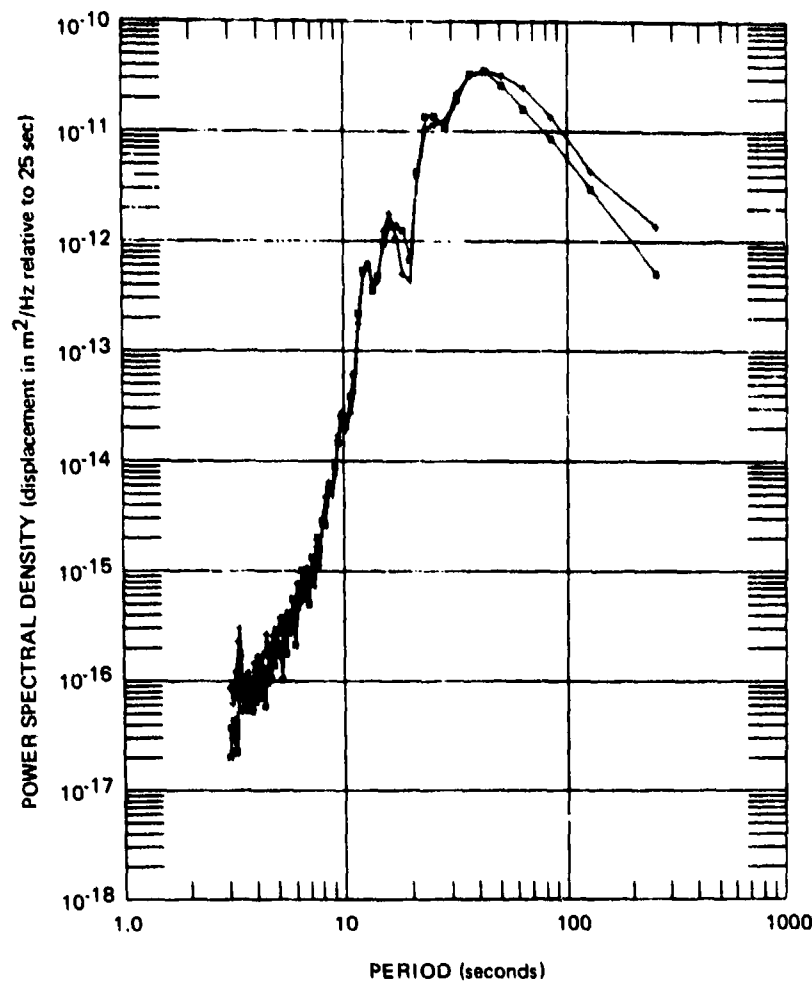


c. Phase lead SZLL over PZLL

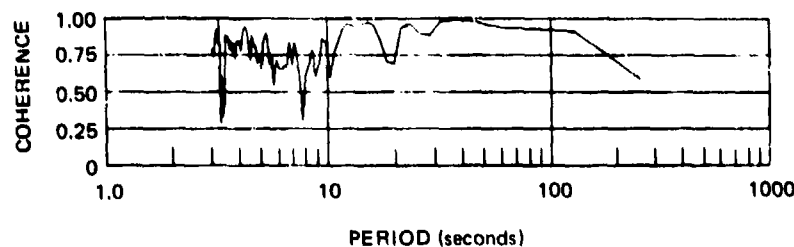
Figure 233. Power spectral density, coherence, and relative phase angle of PZLL and SZLL seismographs during Rayleigh wave of an $m_b = 5.9$ earthquake on Honshu, Japan

G 6770

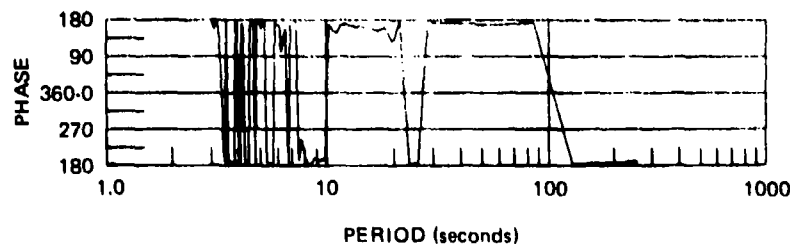
HONSHU EARTHQUAKE $M_B = 5.9$
 769 SAMPLES, 256 LAGS, 2 DSPS, HANNING SMOOTHING
 UC-AZ 16 OCTOBER 1970 0604/0610
 * S325LL * P325LL
 4 9090E+09 1 0



a. Power spectral density



b. Coherence

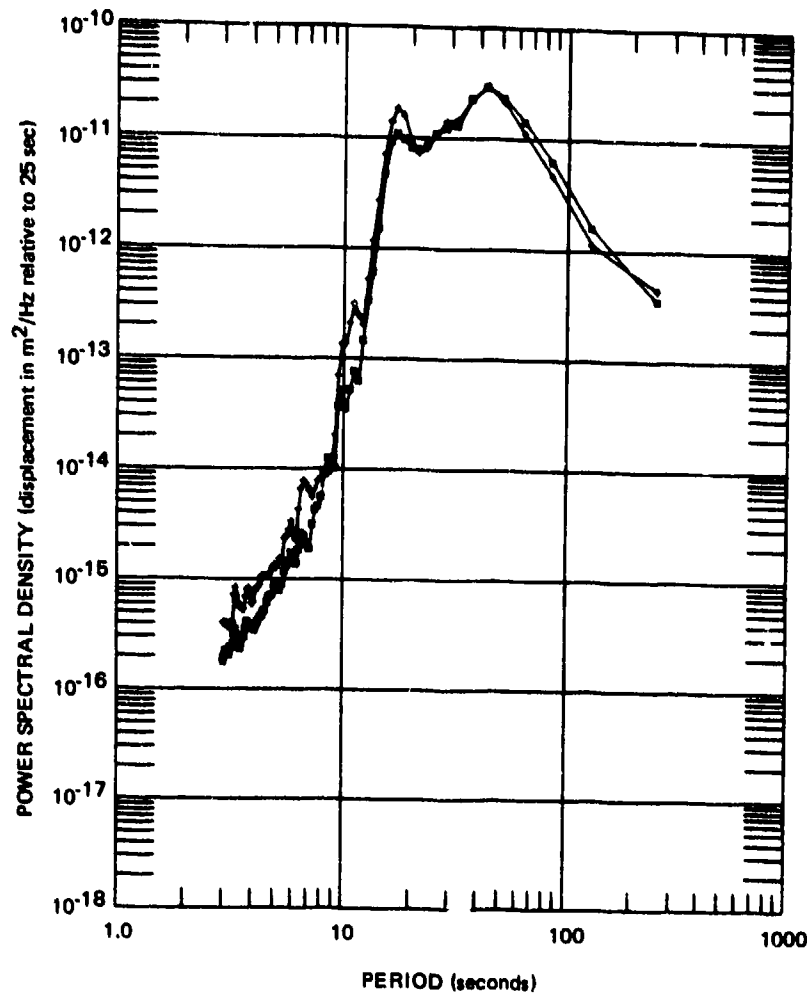


c. Phase lead
P325LL over
S325LL

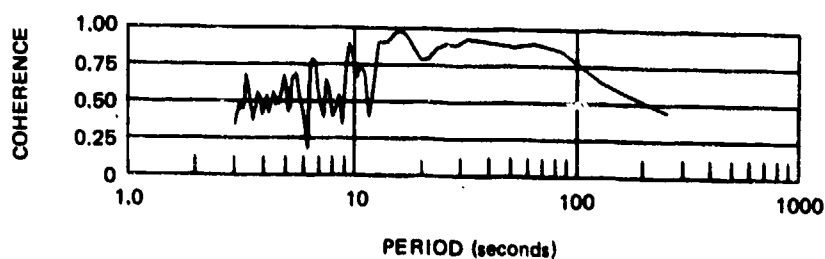
Figure 234. Power spectral density, coherence, and relative phase angle of P325LL and S325LL seismographs during Rayleigh wave of an $m_b = 5.9$ earthquake on Honshu, Japan

G 6771

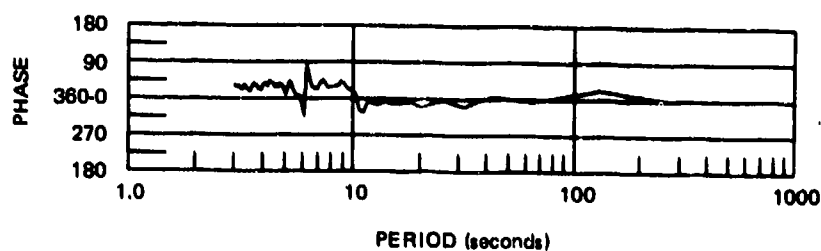
HONSHU EARTHQUAKE $M_B = 5.9$
 769 SAMPLES, 256 LAGS, 2.0SPS, HANNING SMOOTHING
 OC-A2 * S5LL 4.9070E+09
 16 OCTOBER 1970 * P5LL 1.0
 0604/0610



a. Power spectral density



b. Coherence



c. Phase Lead P5LL over S5LL

Figure 235. Power spectral density, coherence, and relative phase angle of P5LL and S5LL seismographs during Love wave of an $m_b = 5.9$ earthquake on Honshu, Japan

G 6772

Table 17. Epicenter data for recordings in figures 227 through 235

Figure No.	Date	Origin	Time	Latitude degrees	Longitude degrees	Depth km	Location	m _b	M _s	Distance degrees	Station to epicenter azimuth degrees
227	3 Oct 70	276	0016:25.9	55.2N	163.2E	31	Off East coast of Kamchatka	5.2	-	60.9	319.2
228											
229											
230	3 Oct 70	276	0812:20.8	58.4N	150.5W	25	Gulf of Alaska	5.0	4.7	36.2	326.0
231											
232											
233	16 Oct 70	289	0526:13.3	39.3N	140.7E	24	Honshu, Japan	5.9	5.8	81.6	311.6
234											
235											

SOLOMON ISLANDS EARTHQUAKE $M_B = 4.2$
 3841 SAMPLES, 256 LACS, 2.0 SPS, PAPER SMOOTHING
 QC-AE 2 OCTOBER 1970 1342/1415
 * SZL
 * PZL
 5.4400E-24
 1.0000E-14

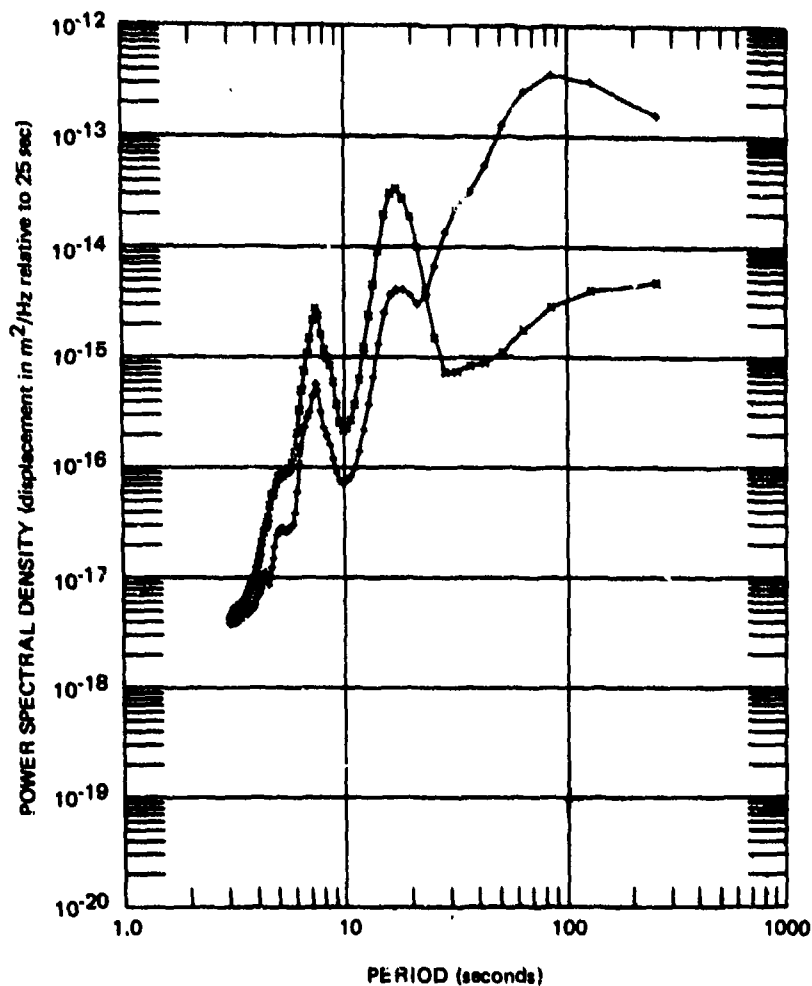


Figure 236. Power spectral density of PZL and SZL seismographs during Rayleigh wave of an $m_b = 4.2$ Solomon Islands earthquake, 2 October 1970

G 6773

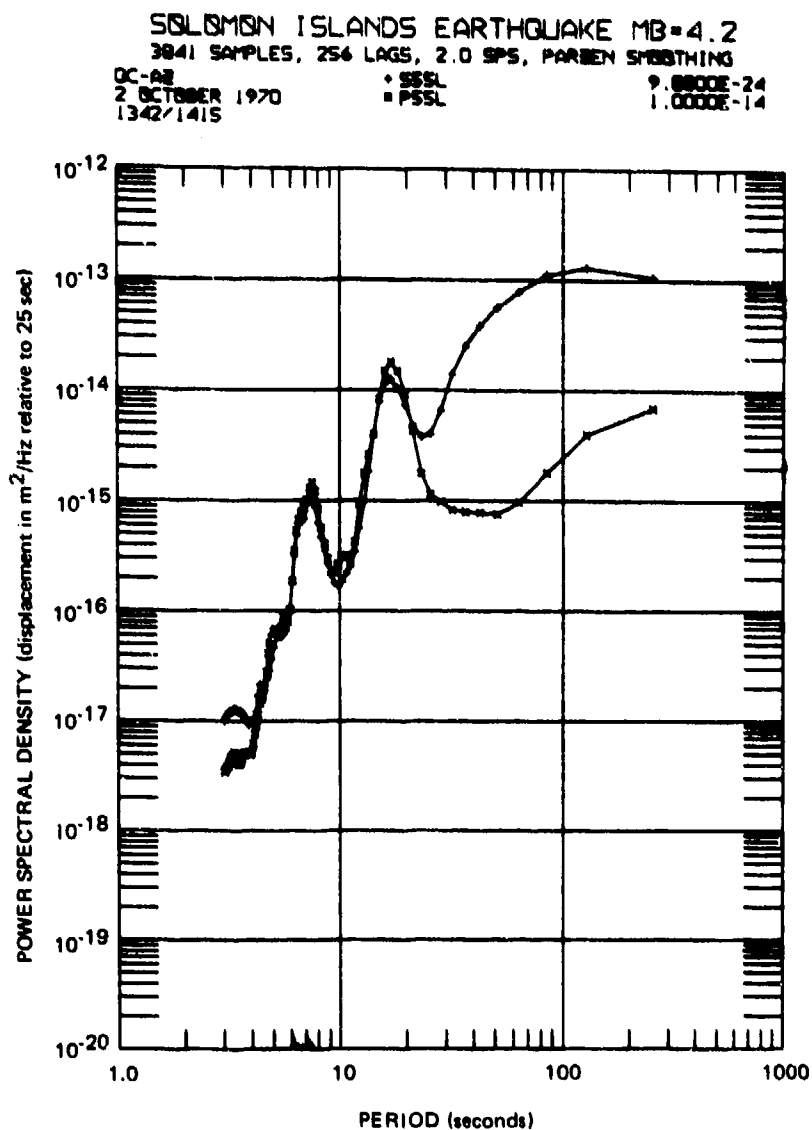


Figure 237. Power spectral density of P55L and S55L seismographs during Rayleigh wave of an $m_b = 4.2$ Solomon Islands earthquake, 2 October 1970

G 6774

SOLOMON ISLANDS EARTHQUAKE $M_b = 4.2$
 2640 SAMPLES, 256 LACS, 2.0 SPS, PAREN SMOOTHING
 QC-AE 3 OCTOBER 1970 5.4400E-24
 2018/2037 : SE 1.0000E-14
 : PE

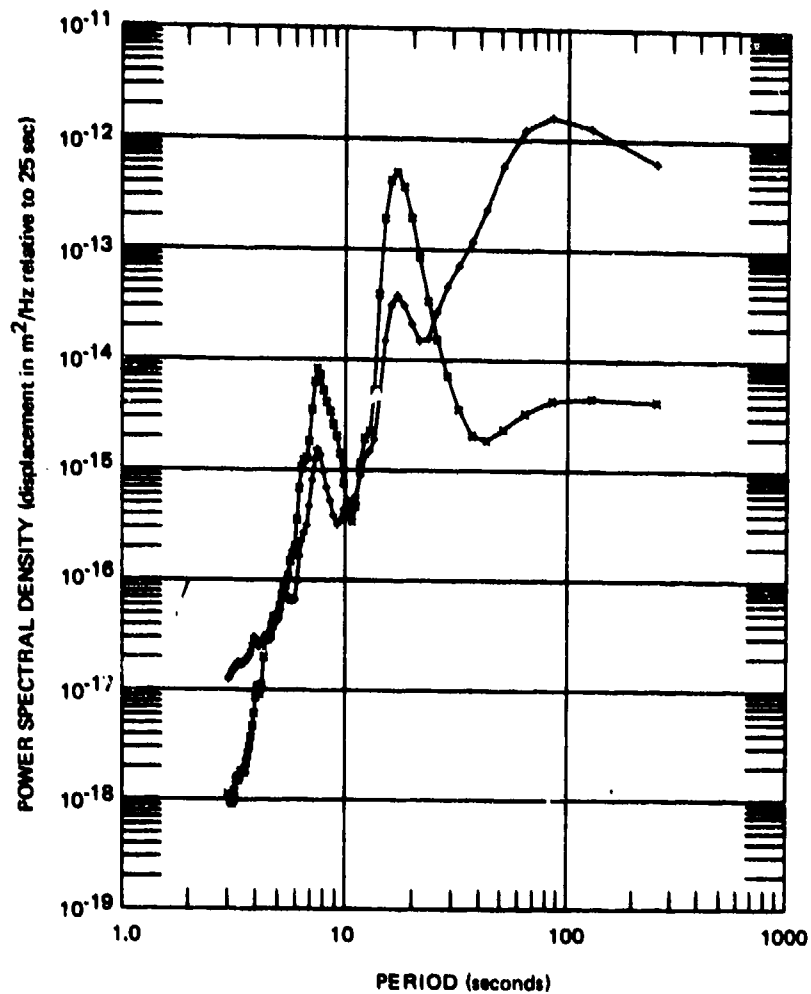


Figure 238. Power spectral density of PZL and SZL seismographs during Rayleigh wave of an $m_b = 4.2$ Solomon Islands earthquake, 3 October 1970

G 6778

SOLOMON ISLANDS EARTHQUAKE $M_B=4.2$

2640 SAMPLES, 256 LAGS, 2.0 SPS, PAREN SMOOTHING

DC-AE
3 OCTOBER 1970
2015/2037

• S55L
• P55L

9.800E-24
1.000E-14

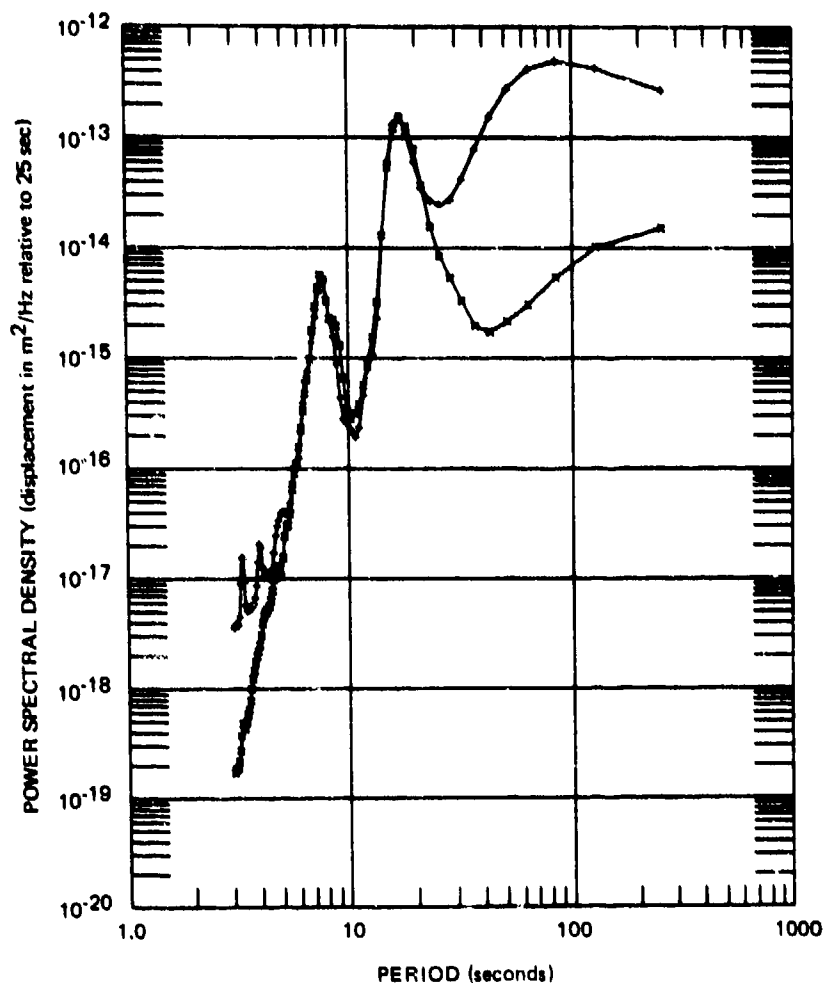


Figure 239. Power spectral density of P55L and S55L seismographs during Rayleigh wave of an $m_b = 4.2$ Solomon Islands earthquake, 3 October 1970

G 6776

from a mixture of wave types cannot be used to calculate the transfer function from displacement to strain. Perhaps if the signals were first separated, the transfer function and local phase velocity could be better estimated. The Lissajous pattern formed by strain and inertial seismograms can be used to separate waves with different wave numbers, to identify wave types, and to detect mixtures of wave types. The Lissajous patterns show hysteresis effects in the rock. In general, at periods of 50 sec and longer, the strain seismographs contain more noise than the inertial seismographs. The coherence between the inertial seismographs and the strain seismographs is often significant but less than 0.50 at periods of 50 sec and longer for medium to small signals.

13. EARTH TIDES

The tides of the solid earth are the subject of this section. They will be referred to as earth tides and are to be taken as the sum of all the effects on the earth from the gravitational attraction among the earth, the sun, and the moon. Of primary concern to this report is the use of the earth tide strains to investigate the performance of the three-component strain seismometers at the long periods of the tidal oscillations. The main objective of this section will be to use the earth tide signal to evaluate the coupling of the QC-AZ strainmeters to the earth. A microsketch of the theory of earth tides is given in section 13.1. A general overview of the literature on earth tides is presented in section 13.2. The earth tide strains observed at QC-AZ are compared to theoretically predicted strains in section 13.3. Pressure and temperature induced strains having tidal periods are discussed in section 13.4. One author's (JEF) comments on the results are given in section 13.5.

13.1 THEORY

This section presents only a microsketch of the theory of the earth tides. For a complete discussion, the reader should refer to Melchior (1966) who treats the entire subject of earth tides and cites 834 references from 1800 to 1964 in the bibliography.

The earth tide is derived in terms of a static theory for the perturbation of the gravity potential. The perturbing potential is written in terms of spherical harmonic functions, with the second-degree term commonly used to predict the theoretical tides.

The second-degree term can be written

$$W_2 = \frac{fm}{2} \frac{a^2}{r^3} (3 \cos^2 Z - 1) \quad (97)$$

where

- W_2 = second-degree term of the gravity potential perturbation
- f = universal gravitational constant
- m = mass of disturbing body
- r = radial variable
- a = value of r at surface of earth
- Z = zenith angle from point of observation to disturbing body, the term in parentheses is the Legendre polynomial of second degree.

From the trigonometric identity,

$$\cos Z = \sin \phi \sin \delta + \cos \phi \cos \delta \cos H \quad (98)$$

where

- ϕ = latitude of observation point
- λ = longitude of observation point
- H = hour angle of disturbing body
- δ = declination of disturbing body,

the potential can be written:

$$W_2 = G \left(\frac{c}{r} \right)^3 \left\{ \cos^2 \phi \cos^2 \delta \cos 2H + \sin 2\phi \sin 2\delta \cos H \right. \\ \left. + 3 \left(\sin^2 \phi - \frac{1}{3} \right) \left(\sin^2 \delta - \frac{1}{3} \right) \right\} \quad (99)$$

where G and c are combinations of gravitational and astronomical constants of the point of observation, the earth, and the disturbing body.

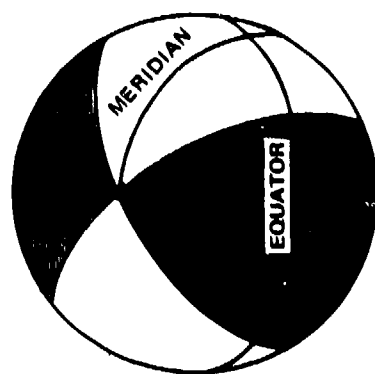
The three terms in the brackets in equation (99) have special significance to the earth tides. The first term is zero or has nodal lines where $\cos 2H$ is zero. If the disturbing body were over the equator at the zero meridian, the nodes would be at ± 45 deg and at ± 135 deg as shown in figure 240(a). This term is a sectorial function and the tides which correspond to it are semi-diurnal. The second term has nodal lines where $\sin 2\delta$ is zero and where $\cos H$ is zero. $\sin 2\delta$ is zero at the poles and the equator beneath the perturbing body, $\cos H$ is zero at ± 90 deg. The nodes for the second term are shown in figure 240(b). This term is a tesseral function and the tides that correspond to it are diurnal. The third term has nodal lines where $(\sin^2 \delta - \frac{1}{3})$ is zero, which are at parallels $\pm 35^\circ 16'$ from the equator beneath the perturbing body (figure 240(c)). This term is a zonal function and the lunar tides associated with it have a period of 14 days and the solar tides have a period of 6 months.

To derive the discrete periods of the tides, the term in brackets in equation (99) is broken down by various trigonometric identities into sums and differences of six astronomical angles. The principal tidal waves are listed in table 18. Periods are given in units of hours and seconds. Frequencies are given in units of deg/hr, Hz $\times 10^{-5}$, and cyc/hr. The ratio of the theoretical amplitude of the gravity tide component to the theoretical amplitude of the M_2 gravity tide is also listed.

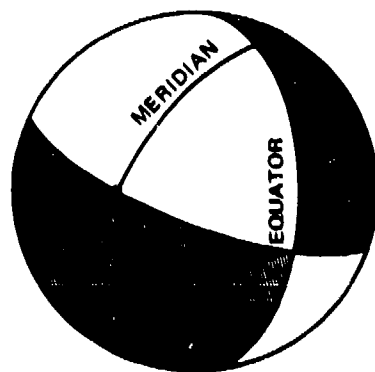
Love (1909, 1911) introduced two dimensionless numbers to relate various characteristics of the earth tide to the gravity potential perturbation. Shida (1912) has shown that a third number is necessary to completely represent all phenomena. These three numbers, and often combinations of them, are called Love numbers. The radial displacement u is related to the potential by

$$u = H(r) \frac{W_2}{g} \quad (100)$$

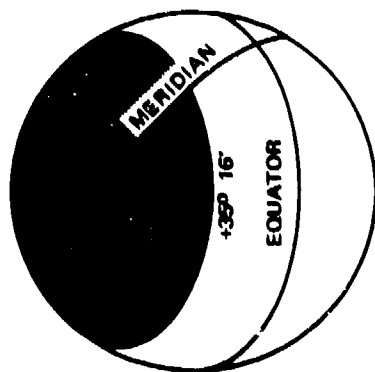
where g = acceleration of gravity.



a. Sectorial semi-diurnal tides



b. Tesserall diurnal tides



c. Zonal lunar 14 days
solar 6 months

Figure 240. Three types of tides from W_2 gravity potential

G 6777

Table 18. Principal tidal waves

Tide	Gravity amplitude relative to M ₂	Hourly displacement deg/hr	Period hr	Period sec	Frequency Hz X10 ⁻⁵	Frequency cyc/hr
M ₀	+ .354	0	0	0	*****	*****
S ₀	+ .258	0	0	0	*****	*****
S _a	+ .013	.041067	8766.162612	31558185.404	.0031687	.000114075
S _{sa}	+ .081	.082137	4382.921217	15778516.381	.0063377	.000228158
M _m	+ .091	.544375	661.308840	2380711.826	.0420042	.001512153
M _f	+ .172	1.098033	327.858999	1180292.396	.0847248	.003050092
Q ₁	+ .080	13.398661	26.868356	96726.083	1.0338473	.037218503
O ₁	+ .415	13.943036	25.819341	92949.627	1.0758515	.038730656
M ₁	- .033	14.496694	24.833248	89399.693	1.1185721	.040268594
Π ₁	+ .011	14.917865	24.132140	86875.702	1.1510698	.041438514
P ₁	+ .193	14.958931	24.065891	86637.207	1.1542385	.041552586
S ₁	- .005	15.000002	23.999997	86399.988	1.1574076	.041666672
M _{K1}	- .399	15.041069	23.934469	86164.088	1.1605763	.041780747
SK ₁	- .185	15.041069	23.934469	86164.088	1.1605763	.041780747
W ₁	- .005	15.082135	23.869300	85929.479	1.1637450	.041894819
Φ ₁	- .008	15.123206	23.804476	85696.115	1.1669140	.042008906
J ₁	- .033	15.585443	23.098477	83154.518	1.2025805	.043292897
OO ₁	- .018	16.139102	22.306074	80301.866	1.2453011	.044830839
2N ₂	+ .025	27.895355	12.905374	46459.348	2.1524194	.077487097
μ ₂	+ .031	27.968208	12.871758	46338.328	2.1580407	.077689467
N ₂	+ .191	28.439730	12.658348	45570.053	2.1944236	.078999250
ν ₂	+ .036	28.512583	12.626004	45453.616	2.2000450	.079201619
M ₂	+1.000	28.984104	12.420601	44714.165	2.2364278	.080511400
L ₂	- .007	29.455625	12.221774	43998.387	2.2728106	.081821181
T ₂	- .028	29.528479	12.191620	43889.833	2.2784320	.082023553
S ₂	+ .027	29.958933	12.016449	43259.218	2.3116461	.083219258
R ₂	+ .465	30.000000	12.000000	43200.000	2.3148148	.083333333
SK ₂	- .004	30.041067	11.983596	43140.944	2.3179836	.083447408
SK ₂	+ .087	30.082137	11.967235	43082.046	2.3211525	.083561492
M ₃	+ .040	30.082137	11.967235	43082.046	2.3211525	.083561492
	- .013	43.476156	8.280401	29809.443	3.3546417	.120767100

The cubic dilatation D is related to the potential by

$$D = F(r) \frac{W_2}{g} \quad (101)$$

The change in potential V resulting from the deformation itself, from the variation of density accompanying the cubic dilatation, and from the surface displacement is related to the original potential by

$$V = K(r) W_2 \quad (102)$$

The horizontal displacements are related to the potential by

$$v = \frac{L(r)}{g} \frac{\partial W_2}{\partial \theta} \quad \text{in the meridian} \quad (103)$$

$$w = \frac{L(r)}{g \sin \theta} \frac{\partial W_2}{\partial \lambda} \quad \text{in the prime vertical} \quad (104)$$

where θ = colatitude

λ = east longitude.

When evaluated at the surface of the earth $r = a$, the values of the above functions that relate the variables to the gravity potential are defined as Love numbers.

$$\begin{aligned} h &= H(a) \\ k &= K(a) \\ \ell &= L(a) \\ f &= F(a) \end{aligned} \quad (105)$$

Thus, h represents the ratio of the height of the earth tide to the height of the corresponding static ocean tide; k represents the ratio of the additional potential produced by this deformation to the deforming potential; and ℓ represents the ratio between the horizontal displacement of the solid earth and that of the corresponding static oceanic tide. The fourth Love number, f , represents the ratio between the cubic expansion and the height of the corresponding static tide.

The three strain components in the horizontal plane can be expressed in terms of the Love numbers and the disturbing potential as follows:

$$e_{\theta\theta} = \frac{\ell}{gr} \frac{\partial^2 W_2}{\partial \theta^2} + \frac{h}{gr} W_2 \quad (106)$$

$$e_{\lambda\lambda} = \frac{\ell}{gr \sin^2 \theta} \frac{\partial^2 W_2}{\partial \lambda^2} + \frac{\ell}{gr} \cdot \frac{\cos \theta}{\sin \theta} \frac{\partial W_2}{\partial \theta} + \frac{h}{gr} W_2 \quad (107)$$

$$\text{and } e_{\theta\lambda} = \frac{2\ell}{gr \sin \theta} \frac{\partial^2 W_2}{\partial \theta \partial \lambda} - \frac{2\ell}{gr \sin \theta} \cot \theta \frac{\partial W_2}{\partial \lambda} \quad (108)$$

The computer program used to predict the theoretical strain tides used in section 13.3 uses equations (106), (107), and (108) and the corresponding equations for the third and fourth degree gravity potentials W_3 and W_4 . This program was furnished by Dr. Stewart Smith, University of Washington. It was originally written by Berger and Farrell at the University of California, San Diego, and was modified by Smith for use on a CDC computer. The program was adapted to the CDC 1604 at the Seismic Data Laboratory by Lt. William E. Haynes, who provided the theoretical tide data for QC-AZ.

The computations follow the classic approach (Doodson, 1921, Schureman, 1940, Munk and Cartwright, 1966, and others) to calculate the gravity potential, but this program is the first (to the present author's knowledge) to use the Love numbers to calculate the strain tides from the gravity potentials. The Love numbers used in the computations were taken from Longman (1963). Longman (1962, 1963) developed a theory for the deformation of a gravitating elastic planet under static surface mass loads. His theory is an extension of the free oscillation theory of Pekeris and Jarosch (1958) and Alterman, Jarosch, and Pekeris (1959) applied to a frequency of zero and different boundary conditions. Longman used the Gutenberg-Bullen model of the earth from Takeuchi et al. (1962) to calculate the Love numbers h , k , and ℓ for degrees of 2 to 25. Alsop and Kuo (1964) have calculated Love numbers for the M_2 semi-diurnal tide for several earth models and for various assumed values for the rigidity of the core. Alsop and Kuo (1964) concluded that the excess load from the mass of ocean water had a more dominant effect on observed gravity tides than could be obtained with variations in the structure of the earth as represented by the models they investigated.

13.2 PREVIOUS INVESTIGATIONS OF EARTH TIDES

The majority of the observations reported in the literature on the earth tides have been of the gravity tide. The most complete references to the earth tides can be found in Melchior (1966) and in Tomascheck (1957). Both of these authors summarize the state-of-the-art of the theory, the sensing instruments, and the observations at the time their works were written. The gravity earth tide measurements made during the International Geophysical Year (IGY) are summarized by Harrison et al. (1963). Kuo et al. (1970), expanding on the work of Kuo and Ewing (1966), studied the effects on the gravity tide constituents M_2 and O_1 from regional geologic structure and from oceanic tidal

loading. They observed the gravity tides at nine stations across the U. S. around latitudes 39 to 41 deg N. By considering the effects of the oceanic tidal loading, they were able to fit the M_2 tidal observations with predicted amplitude and phase values. The fit of the theoretical values to the O_1 tidal observations was not as satisfactory. These authors concluded that the effects of regional geologic structure were masked by the larger effects of the oceanic tidal load and could not be discerned. Rigassi (1970) felt that the data of Kuo et al. (1970) did substantiate variations with regional geologic structure, but the original authors considered his interpretation of their data as optimistic.

Reports of measurements of strain earth tides are less numerous than of gravity tides. Melchior (1966) quotes amplitudes and phases for the M_2 tide from Ozawa (1961) at the Japanese stations of Osakayama, Kishu, and Suhara. These stations are 1 km, 65 km, and 15 km, respectively, from the ocean. Expressing the strain as

$$e_{ij} = A_{ij} \times 10^{-8} \cos (2t - \alpha_{ij}) \quad (109)$$

Ozawa observed the values of A_{ij} and α_{ij} given in table 19. The amplitudes and phases at each of these three stations are significantly different from each other and for each component at the three sites.

Table 19. Component M_2 obtained from the results of Japanese extensometers (from Melchior, 1966, after Ozawa, 1961)

Station	Osakayama		Kishu		Suhara	
Tangential components	A_{ij}	α_{ij}	A_{ij}	α_{ij}	A_{ij}	α_{ij}
$e_{\theta\theta}$	0.957	29.6°	1.691	5.2°	1.940	49.1°
$e_{\lambda\lambda}$	1.315	5.5°	0.244	256.2°	1.876	36.4°
$e_{\theta\lambda}$	1.650	74.8°	1.477	258.4°	2.092	96.0°
Radial components						
e_{rr}	0.642	193.6°				
Oblique components						
$e_{r\theta}$	0.463	226.4°				
$e_{r\lambda}$	0.539	183.3°				

Major et al. (1964) analyzed the earth tide strains at Ogdensburg, New Jersey, on two non-orthogonal horizontal strainmeters and on a vertical strainmeter. The observed strain amplitudes and phases at the period of M_2 were

$$e_{N29^{\circ}30'E} = 0.410 \times 10^{-8} \cos (2t - 19.5^{\circ})$$

$$e_{E42^{\circ}S} = 0.220 \times 10^{-8} \cos (2t + 78.5^{\circ})$$

$$e_z = 0.62 \times 10^{-8} \cos (2t + 180^{\circ})$$

These observations included the strains from the oceanic tidal load, which were estimated to be

$$e_{N29^{\circ}30'E} = 0.643 \times 10^{-8} \cos (2t + 178^{\circ})$$

$$e_{E42^{\circ}S} = 0.858 \times 10^{-8} \cos (2t + 178^{\circ})$$

The strain estimated from the oceanic tidal load is larger than the total observed strain and is significantly out-of-phase with the total horizontal observed strains. Kuo (1969), using three non-orthogonal horizontal strainmeters at Ogdensburg, New Jersey, compared observed and theoretical areal strains (the sum of any two orthogonal horizontal strain components) for the M_2 and O_1 tidal constituents. The areal strain is independent of the oceanic tidal load. The observed areal strains were

$$e_{M_2} = 1.662 \times 10^{-8} \cos (2t - 1.2^{\circ})$$

$$e_{O_1} = 1.150 \times 10^{-8} \cos (t - 5.7^{\circ})$$

The M_2 amplitude differed by 6 percent from the theoretical and the O_1 amplitude differed by 10 percent. Smith and Kind (1972) used earth tide data from the six single-component strain installations described by Shopland (1971) to establish the degree of coupling of the strainmeters to the earth. Fourier amplitudes of theoretical tides were graphically compared to Fourier amplitudes of the observed tides, but numerical comparisons were not presented for either amplitudes or phases. Shopland (1971), using different time samples from Smith and Kind (1972), compared observed strains at the six Nevada installations to theoretical tides calculated by the same computer program, as described in section 13.1. The predicted tides, observed tides, and the ratio between them are given in table 20 from Shopland (1971) for the strains at periods of 12.0 (S_2), 12.42 (M_2), 24.0 (S_1), and 25.8 (O_1) hr.

13.3 COMPARISON OF OBSERVED AND PREDICTED STRAINS

This section presents data on tidal period strains observed at QC-AZ during the 43-day interval from 7 April 1971 (day 97) through 17 May 1971 (day 139). The observed strains are compared to the theoretical strains in both the time domain and the frequency domain.

13.3.1 Preparation of Data

The broad-band strain seismographs (S_B) were hand digitized at 20 min intervals. Corrections were made for trace offsets introduced by instrument adjustments. A few corrections were made for temperature effects during short intervals when the lights were turned on in the mine. (This correction will be discussed in section 13.4). The data were calibrated using the calibration signals applied every 5 days. The raw data were then smoothed with a seven-point parabolic

Table 20. Apparent site coupling factors (column C) computed from the ratio of observed strain (column B) to the calculated earth tide (column A) for the S₂, M₂, S₁ and O₁ components of the earth tide corresponding to tidal periods of 12.0, 12.42, 24.0, and 25.8 hours, respectively (from Shopland, 1971)

Site	A Calculated Earth tide (x10 ⁻⁹)				B Observed Strain (x10 ⁻⁹)				C Apparent Coupling Factor, B/A			
	S ₂	M ₂	S ₁	O ₁	S ₂	M ₂	S ₁	O ₁	S ₂	M ₂	S ₁	O ₁
RH-NV	12	21	15	12	5.1	3.0	4.5	2.5	0.43	0.14	0.30	0.21
KP-NV	5.9	11	14	12	9.4	9.8	8.1	3.0	1.6	0.90	0.58	0.25
QM-NV	11	26	18	13	17	11	28	13	1.5	0.42	1.6	1.0
TI-NV	3.4	4.5	16	15	5.5	5.1	15	14	1.6	1.1	.94	.93
YM-NV	21	28	8.3	8.3	4.8	13	16	17	.23	.47	1.9	2.0
OB-NV	5.0	9.0	27	20	5.4	11	18	10	1.1	.12	.67	.50

least squares, smoothing (Lanczos, 1956). The mean and a linear trend were removed by least-squares. The observed data were then written on magnetic tape. The data were plotted from the magnetic tape for editing purposes to catch human errors of entering corrections with the incorrect sign. These data are plotted in figures 241, 242, and 243 for the SZB, S325B, and S55B seismographs, respectively. The vertical strain is plotted at 1/5 the sensitivity as the horizontal strains. The large offset in about the middle of the S325B is one of the human errors that was corrected in the final data set.

The tide recordings in these three figures are unfiltered. They can be seen to contain some long periods that are related to temperature and pressure variations, as will be discussed in section 13.4. For a closer comparison with the theoretical tides, the data were band-pass filtered for periods from 11.5 to 30 hr.

13.3.2 Secular Strains

The slope of the linear trend removed from the hand digitized data is a least-squares estimate of the secular strain rate over this 43-day interval. The secular strain rates obtained were:

<u>Component</u>	<u>Strain/Day</u>	<u>Strain/Mo</u>
SZB	2.90×10^{-8}	8.71×10^{-7}
S325B	6.73×10^{-9}	2.02×10^{-7}
S55B	2.39×10^{-9}	7.18×10^{-8}

The vertical secular strain rate is 3.2 times the sum of the horizontal secular strain rates. This large variance from the relationship for elastic strains at a point on a free surface suggests either that the rate of strain change with depth is a rapidly varying function or that the secular strain rates are not from elastic strains. The author expects that the first condition applies and that the large vertical strain rate is the differential displacement that results from seasonal temperature changes and the thermal expansion of the surface layers.

13.3.3 Time Domain Comparison

The observed strains are compared with the theoretically predicted strains by plots of the two time series. The band-pass filtered observed strains are plotted with dark lines and the predicted earth tide strains are plotted with light lines. In all cases, the amplitudes of the observed strains are smaller than the predicted strain. The horizontal strains in the 325 deg azimuth are plotted in figure 244. There is agreement in the general shape of the two traces, with many of the observed peaks occurring at the same time as the peaks in the predicted strains. However, a significant phase shift exists between the two. This phase shift can be recognized by comparing the relative times of the smaller peaks for each day.

The horizontal strains in the 55 deg azimuth are plotted in figure 245. The agreement between the observed and predicted strains is much better on this component. There is a detectable phase difference between the two time series.

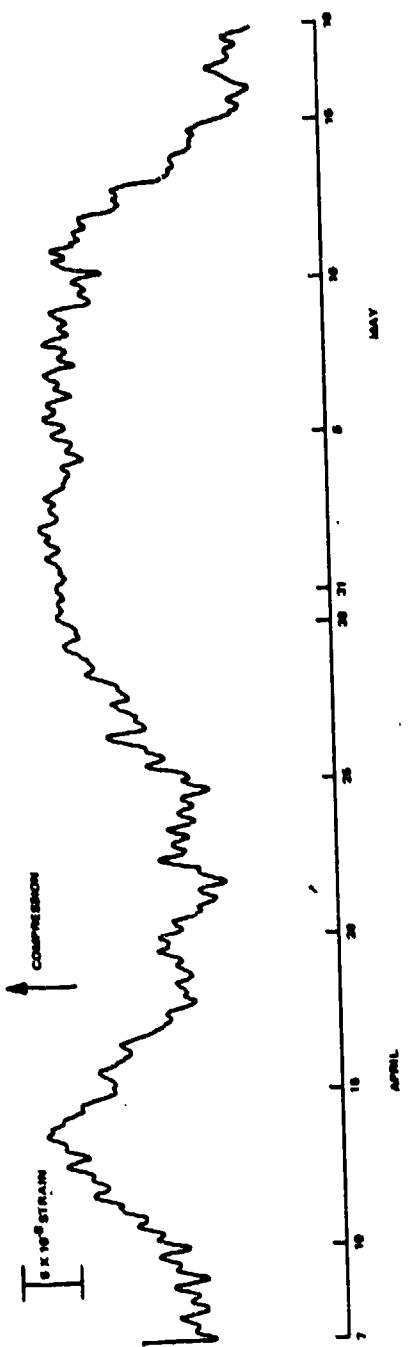
The observed vertical strains are plotted in figure 246 with the inverted (compression down) sum of the predicted strains in the 325 deg and in the 55 deg azimuths, the areal strain. The predicted areal strain should be larger than the vertical strain by the ratio $(\lambda + 2\mu)/\lambda$, which was found to be 2.17 in section 8.2.1. The agreement between the observed vertical strain and the predicted areal strain is better than the agreement in either of the horizontal directions. The two time series exhibit some small phase differences. The observed areal strain is plotted with the predicted areal strain in figure 247 with compression downward. The agreement between these two traces is the best of all pairs compared.

13.3.4 Frequency Domain Comparison

Frequency domain comparisons between the observed and the predicted earth tide strains are made with Fourier transform analysis and with power spectral density analysis. The Fourier transform analysis has the advantage of greater frequency resolution, which permits separation of several tidal components. The PSD analysis has the advantage of better spectral estimates in the presence of noise, a more stable phase estimate, and a coherence estimate.

A computer program was written by one of the authors (JEF) to calculate the Fourier transform of the tide strain data. Two algorithms were employed - the fast Fourier transform (FFT) and the Filon quadrature (Filon). The FFT requires data in powers of two. With hourly data samples for 43 days, there are 1032 samples. Eight were dropped and 1024 samples were used for the FFT with the predicted strain data and with the temperature and pressure data presented in section 13.4. For greater frequency resolution, the 3096 available samples of observed strain data were used with 1000 zeros added to reach the next larger power of two. The Filon algorithm can use any odd number of data samples and the Fourier transform can be evaluated at any desired period (frequency). The program was written to take the transform at a set of the exact tidal periods. Both algorithms give exact analytical answers for test cases with known complicated time series having known Fourier transforms. However, the author has more confidence in the FFT and only the results calculated with it are presented.

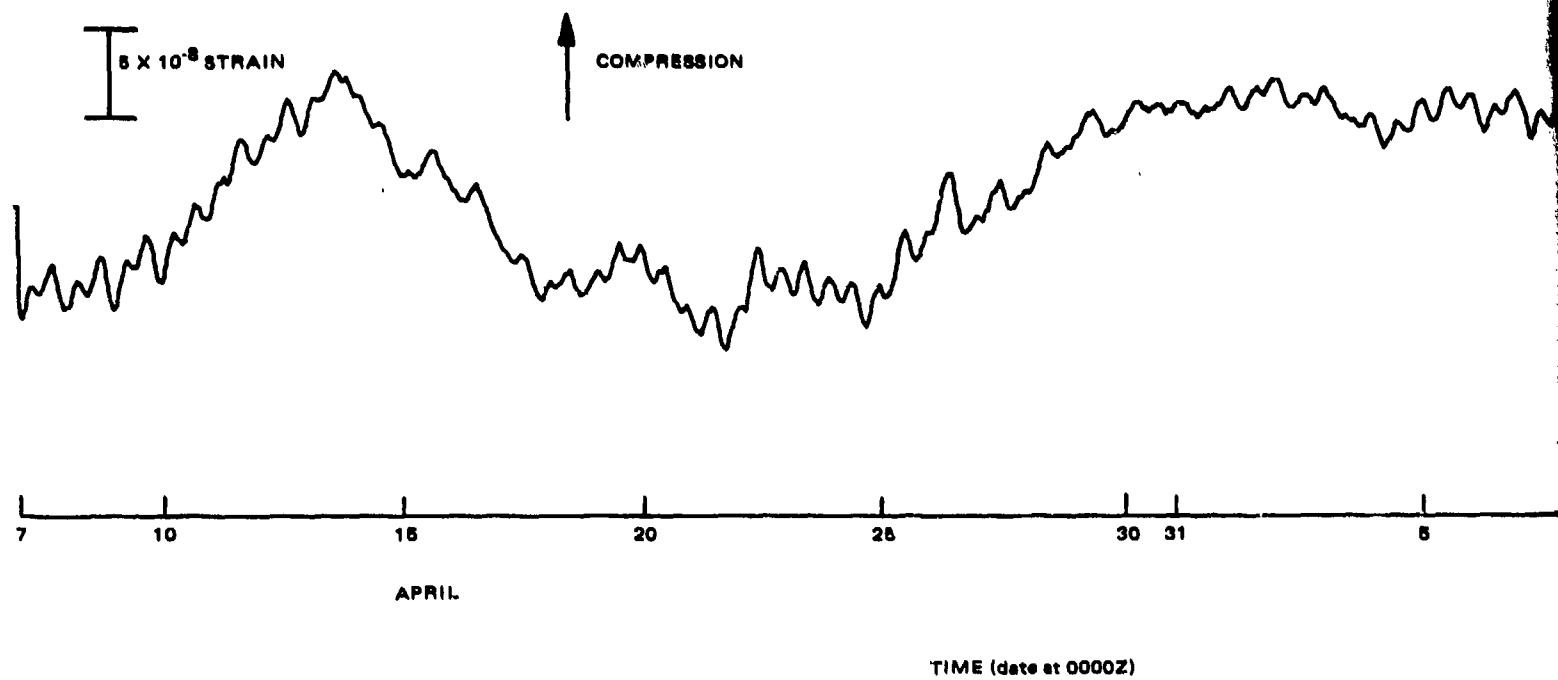
The results of the Fourier transform analysis will be presented first. The amplitude of the Fourier transforms of the strains in the 325 deg azimuth are plotted in figure 248. The spectra of the predicted strain tides are black and the spectra of the observed strains are light grey. The unfiltered data shown in figure 242 (corrected for the error) were used for the transformation. The effects of the M_2 tidal component at 327 hr and the M_3 tidal component at 8 hr can be seen in the spectra of the predicted tides. With the 1024 samples, the frequency resolution is sufficient to separate several other tidal components, which can be seen in figure 248 and the other figures. The semi-diurnal strains and the diurnal strains for the 325 deg azimuth are plotted on an expanded linear by linear scale in figure 249. The most important gravity tidal constituents are plotted in figure 250 as amplitudes relative to the M_2 component. By comparing figure 250 to the other figures on the same scale, the reader can visualize the degree of separation of the tidal components



Time (date at center)
 See the following pages
 for greater detail.

Figure 201. Vertical earth tide strains
 7 April to 18 May 1971
 ecm

-453/454-
 TR 72-3



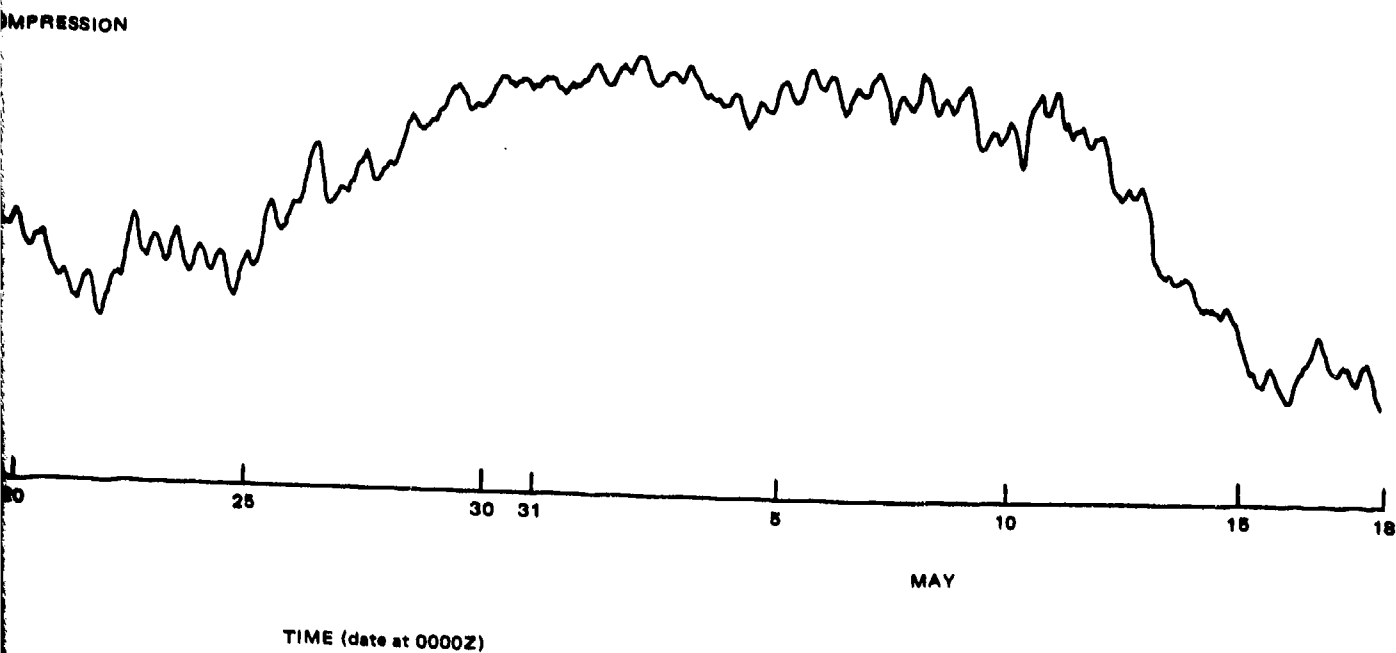


Figure 241. Vertical earth tide strains
7 April to 18 May 1971

G 6778

-453/454-

TR 72-3

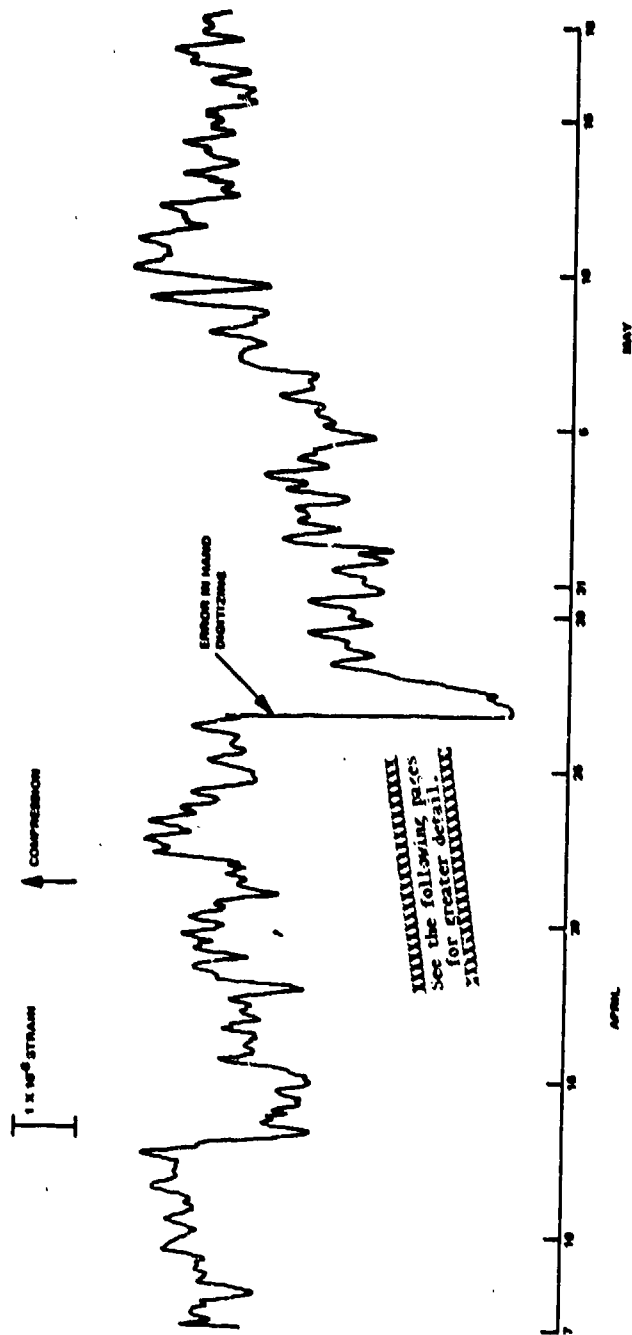


Figure 242. 325 deg azimuth earth tide strains 7 April to 18 May 1971

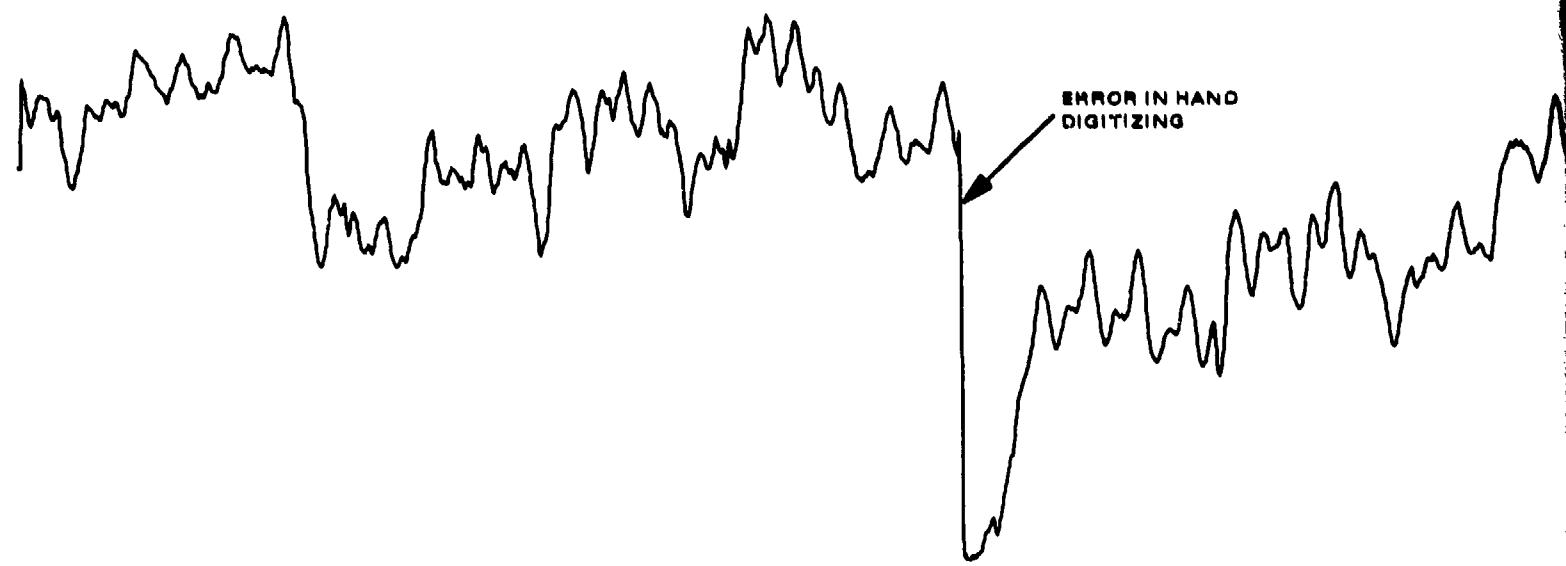
-655/456-

TR 77-

1 X 10⁻⁸ STRAIN

↑ COMPRESSION

ERROR IN HAND
DIGITIZING



7 10 15 20 25 30 31 5

APRIL

MA

TIME (date at 0000Z)

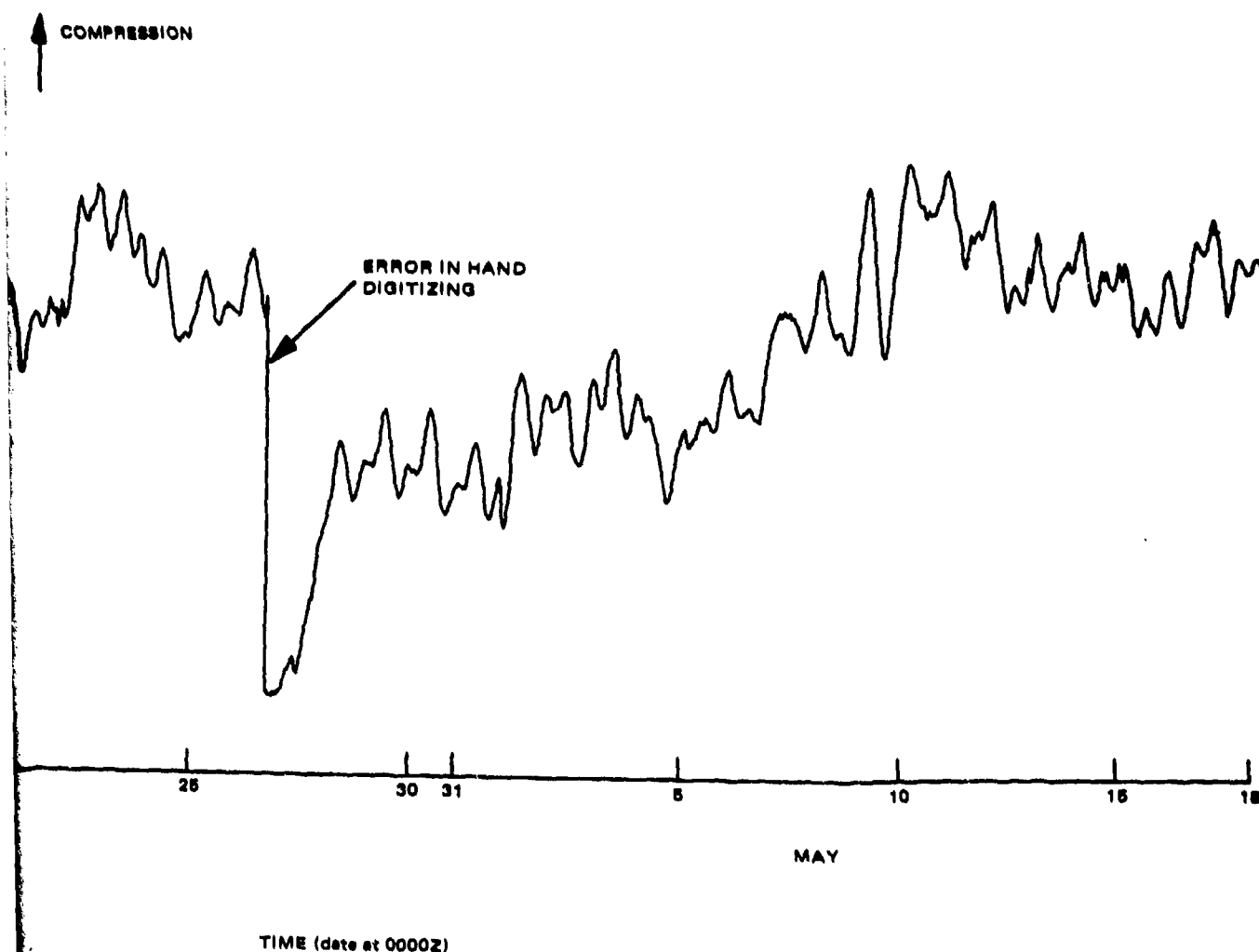
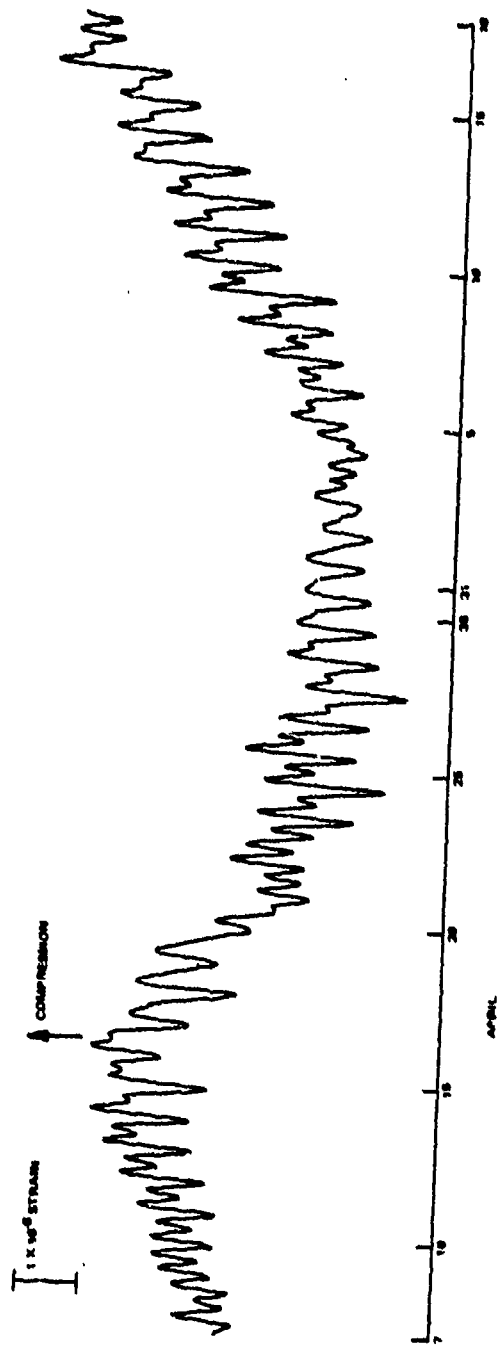


Figure 242. 325 deg azimuth earth tide strains 7 April to 18 May 1971

G 6770

-455/456-

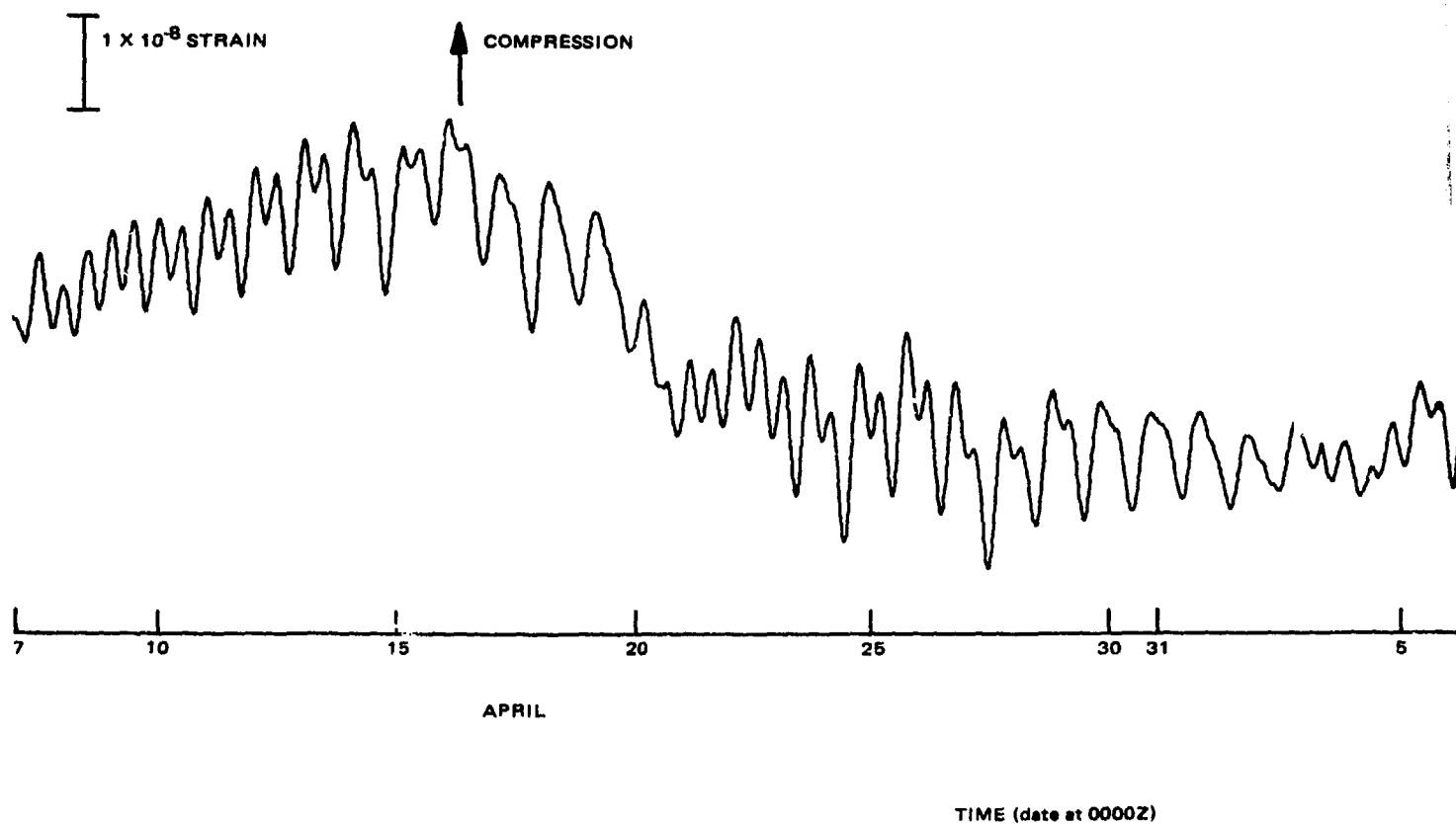
TR 72-3



XXXXXXXXXXXXXXXXXXXX
 See the following pages
 for further detail.
 XXXXXXXXXXXXXXXXXXXX

Figure 243. 55 deg azimuth earth tide strains 7 April to 18 May 1971

Case
 -457/458-
 TR 72-3



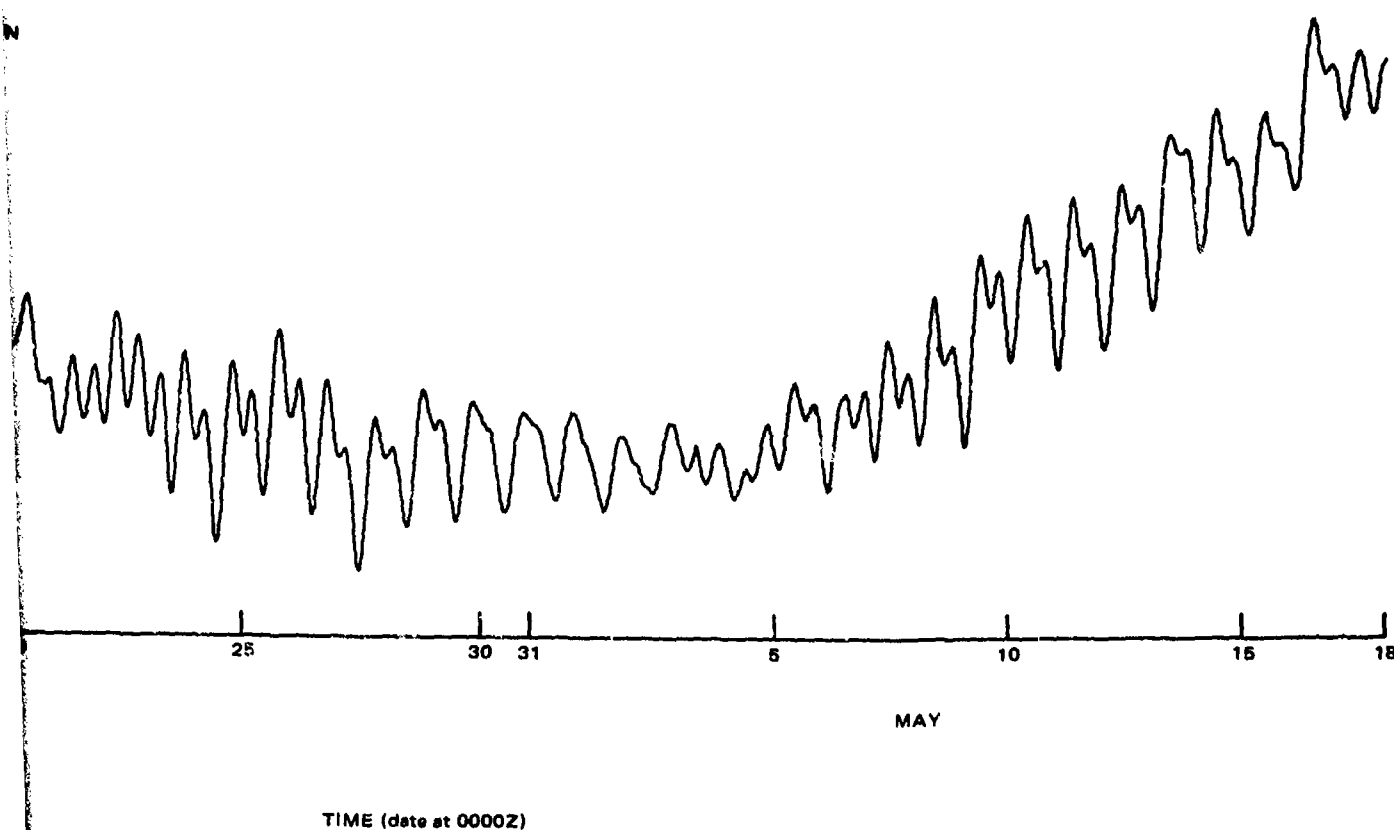


Figure 243. 55 deg azimuth earth tide strains 7 April to 18 May 1971

G 6780

-457/458-

TR 72-3

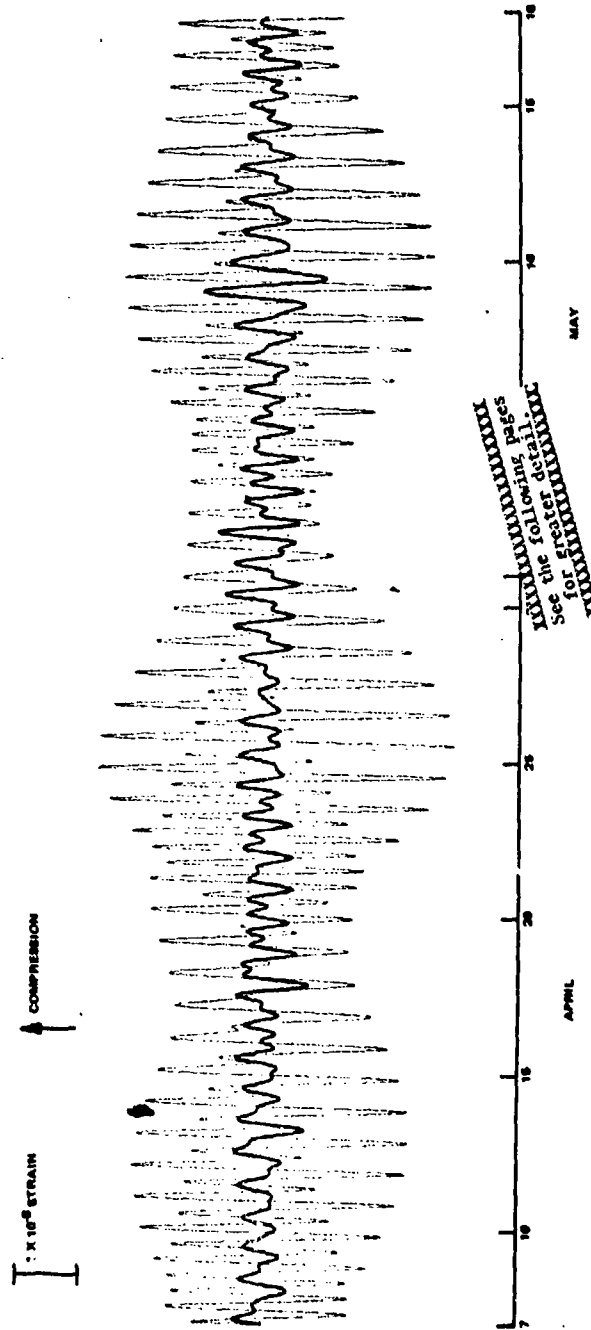
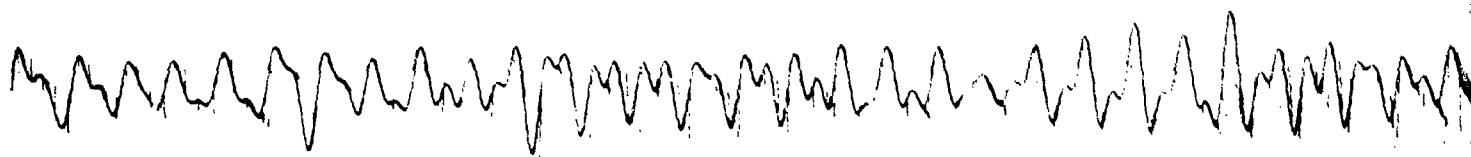


Figure 244. Observed (dark line) and predicted (light line) earth tide strain in 325 deg azimuth 7 April to 18 May 1971

TR 72-3

I
1 x 10⁻⁸ STRAIN

↑
COMPRESSION



L
10

L
15

L
20

L
25

L
30

L
31

L
32

APPROX

TIME (HRS) 10000.0

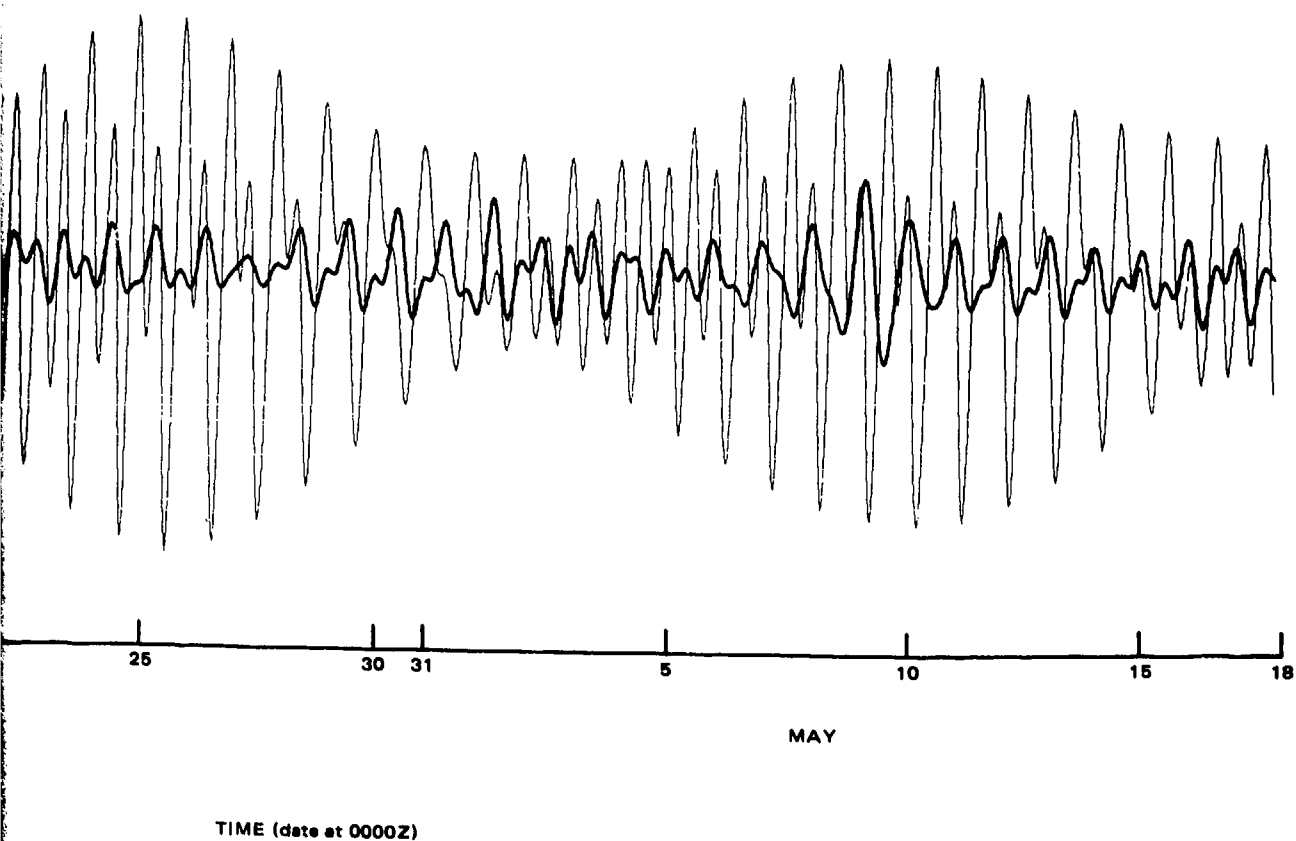
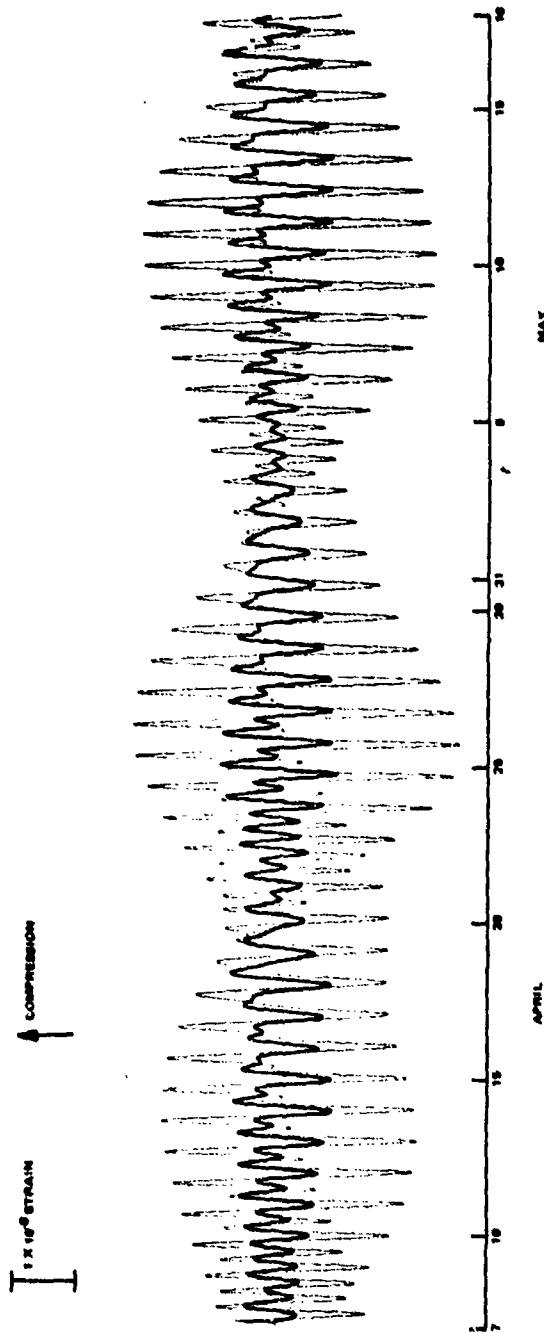


Figure 244. Observed (dark line) and predicted (light line) earth tide strain in 325 deg azimuth
7 April to 18 May 1971
-459/460-

G 6781



XXXXXXXXXXXXXXXXXXXX
See the following pages
for greater detail.
XXXXXXXXXXXXXXXXXXXX

TIME (GMT) at 0000Z

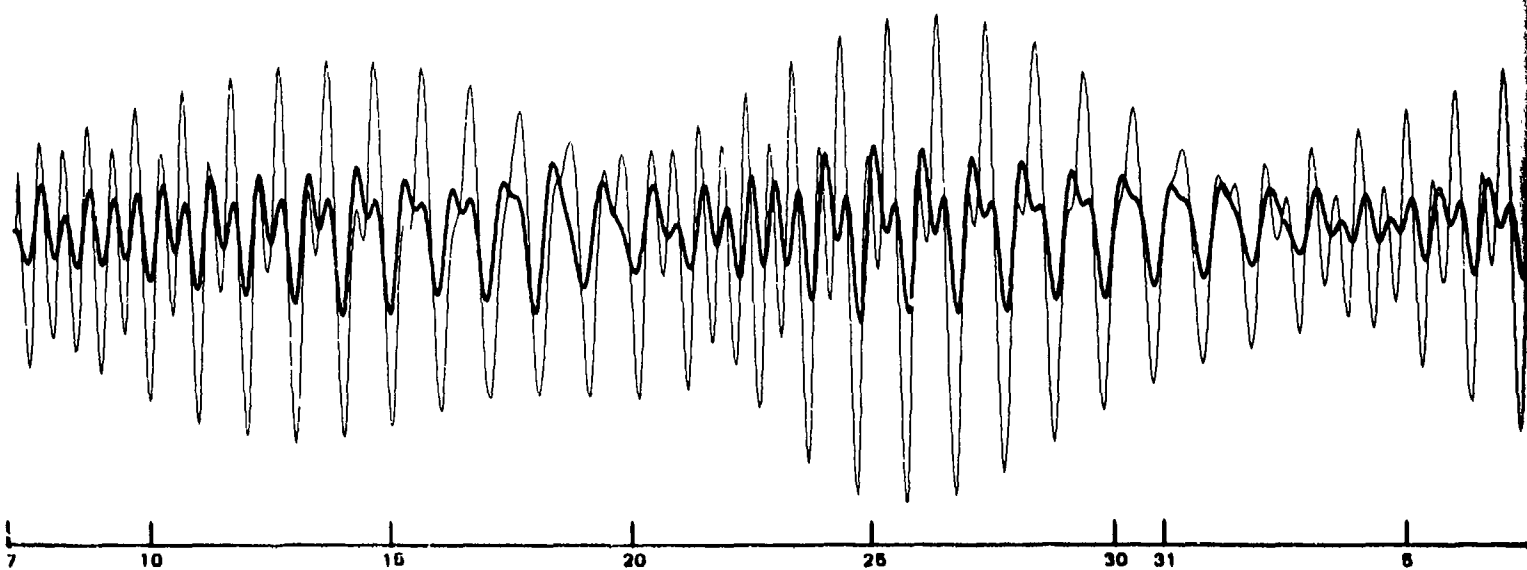
Figure 245. Observed (dark line) and predicted (light line) earth tide strain in 55 deg azimuth 7 April to 18 May 1971 GCMZ

-461/462-

TR 72-3

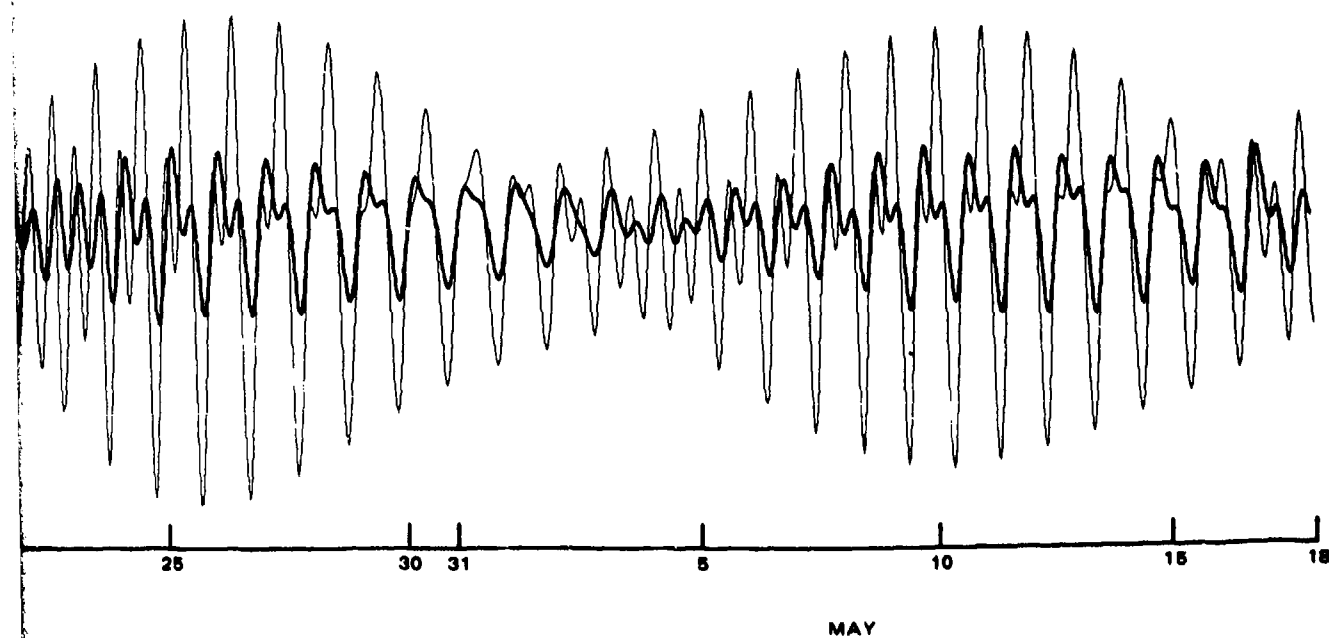
I 1×10^{-8} STRAIN

↑ COMPRESSION



APRIL

TIME (date at 0000Z)



TIME (date at 0000Z)

Figure 245. Observed (dark line) and predicted (light line) earth tide strain in 55 deg azimuth 7 April to 18 May 1971

G 6782

-461/462-

TR 72-3

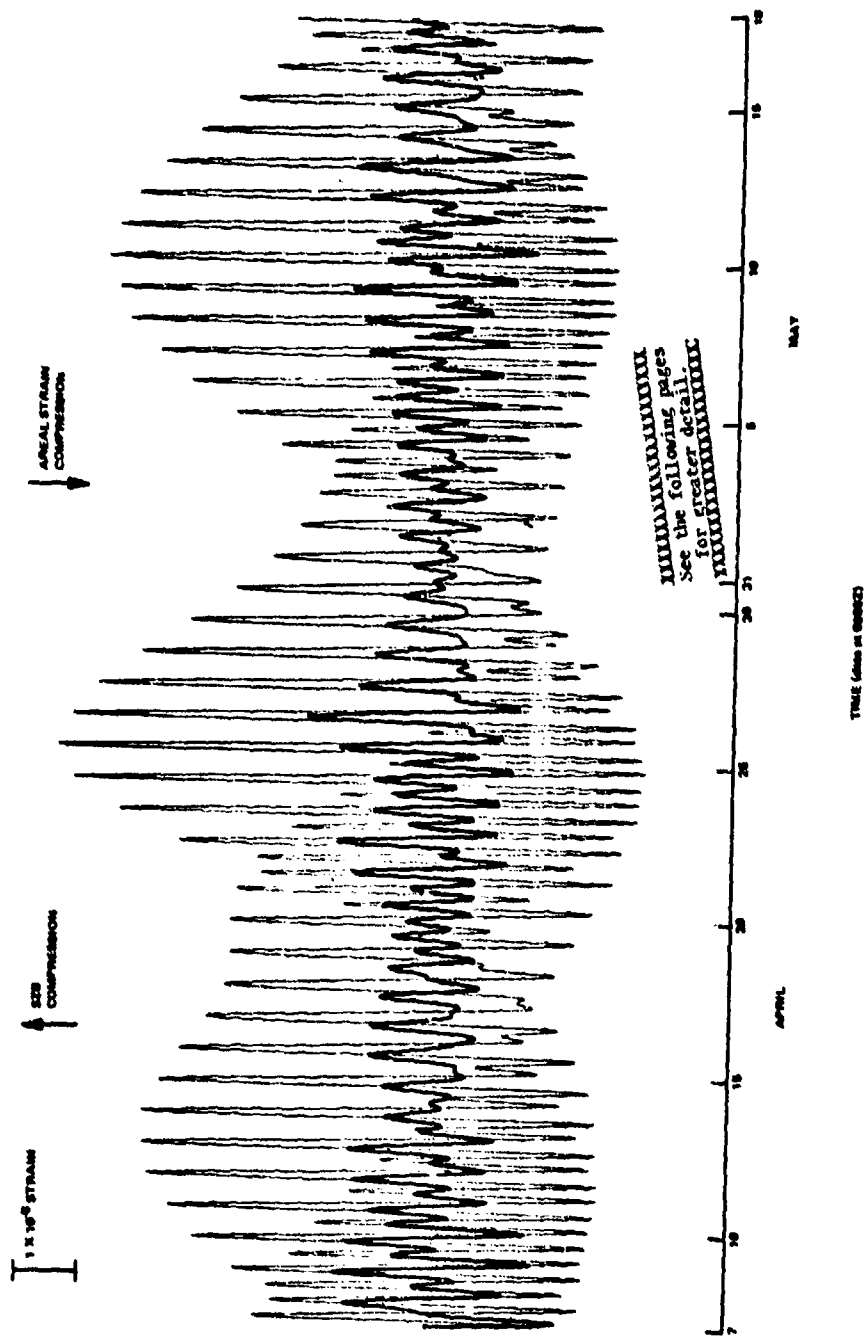


Figure 246. Observed vertical strain (dark line) and inverted predicted areal strain (light line) for earth tides 7 April to 18 May 1971

GONO

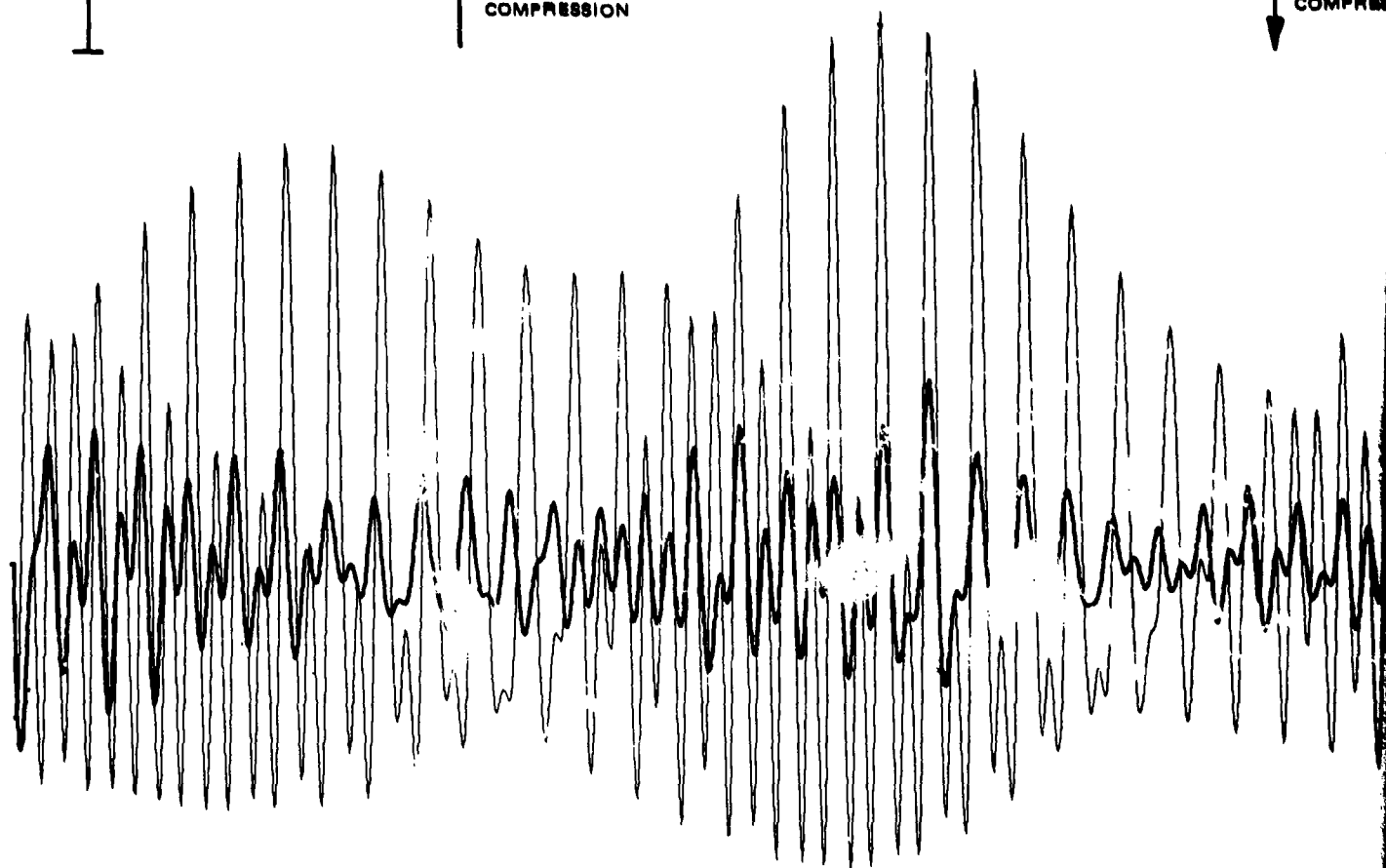
-463/464-

TR 72-3

1 X 10⁻⁸ STRAIN

↑ SZB
COMPRESSION

↓ AREAL
COMPRESSION



7 10 15 20 25 30 31

APRIL

TIME (date at 0000Z)

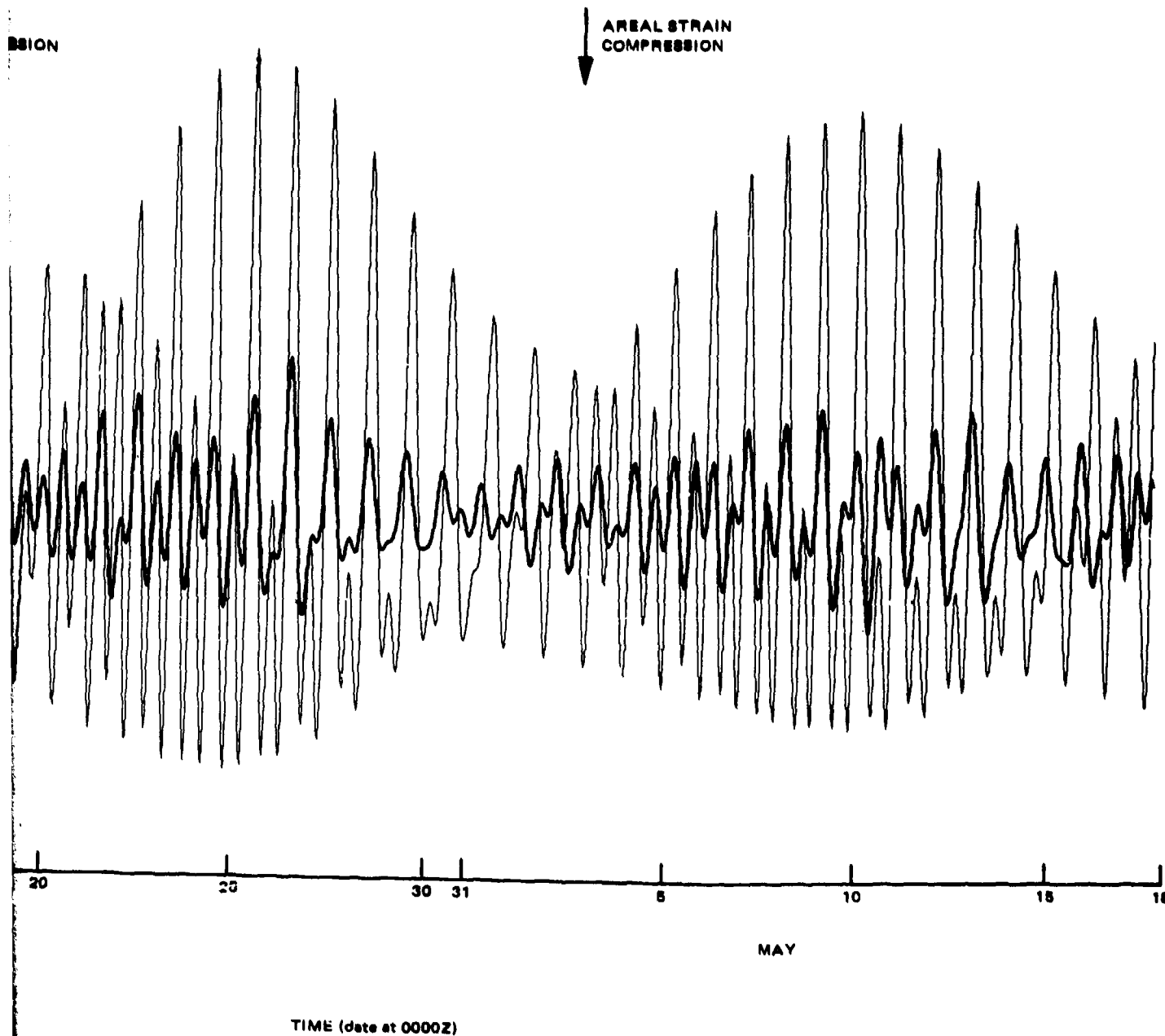


Figure 246. Observed vertical strain (dark line) and inverted predicted areal strain (light line) for earth tides 7 April to 18 May 1971

G 6783

-463/464-

TR 72-3

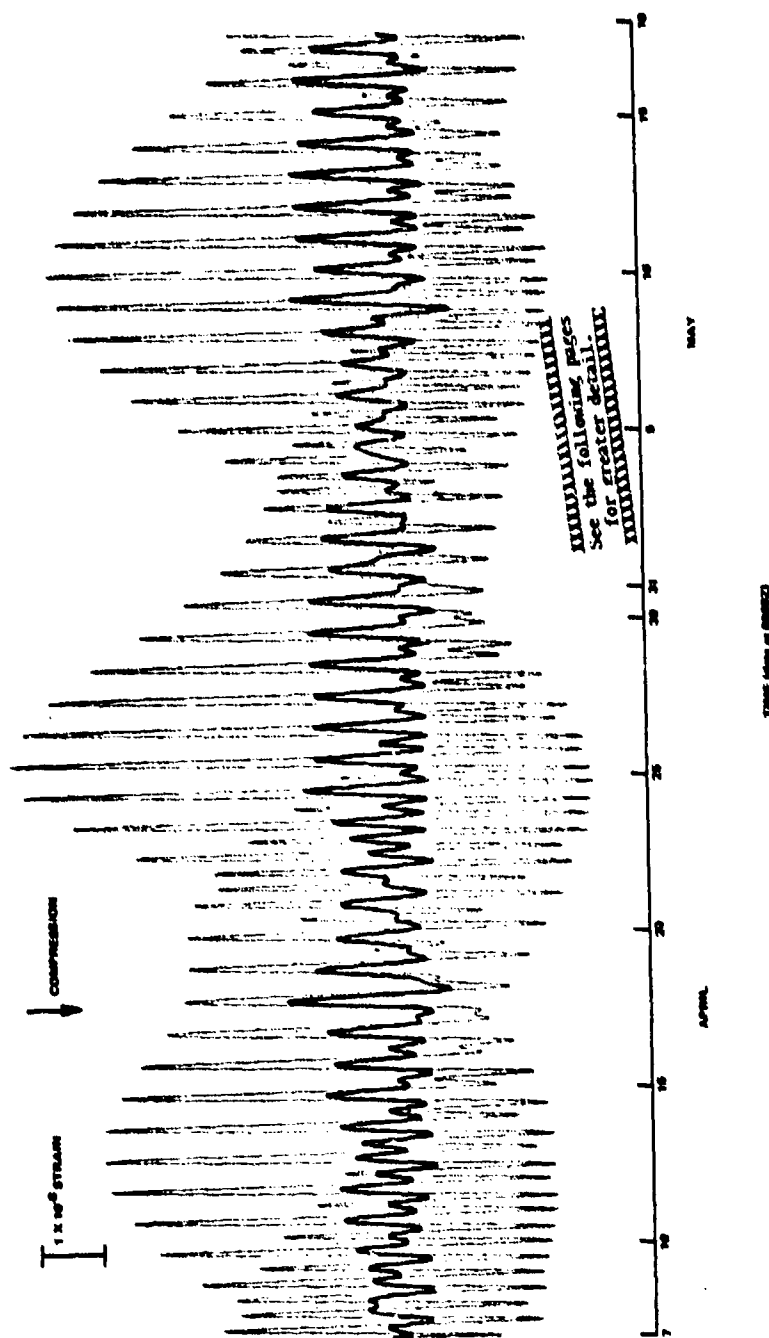
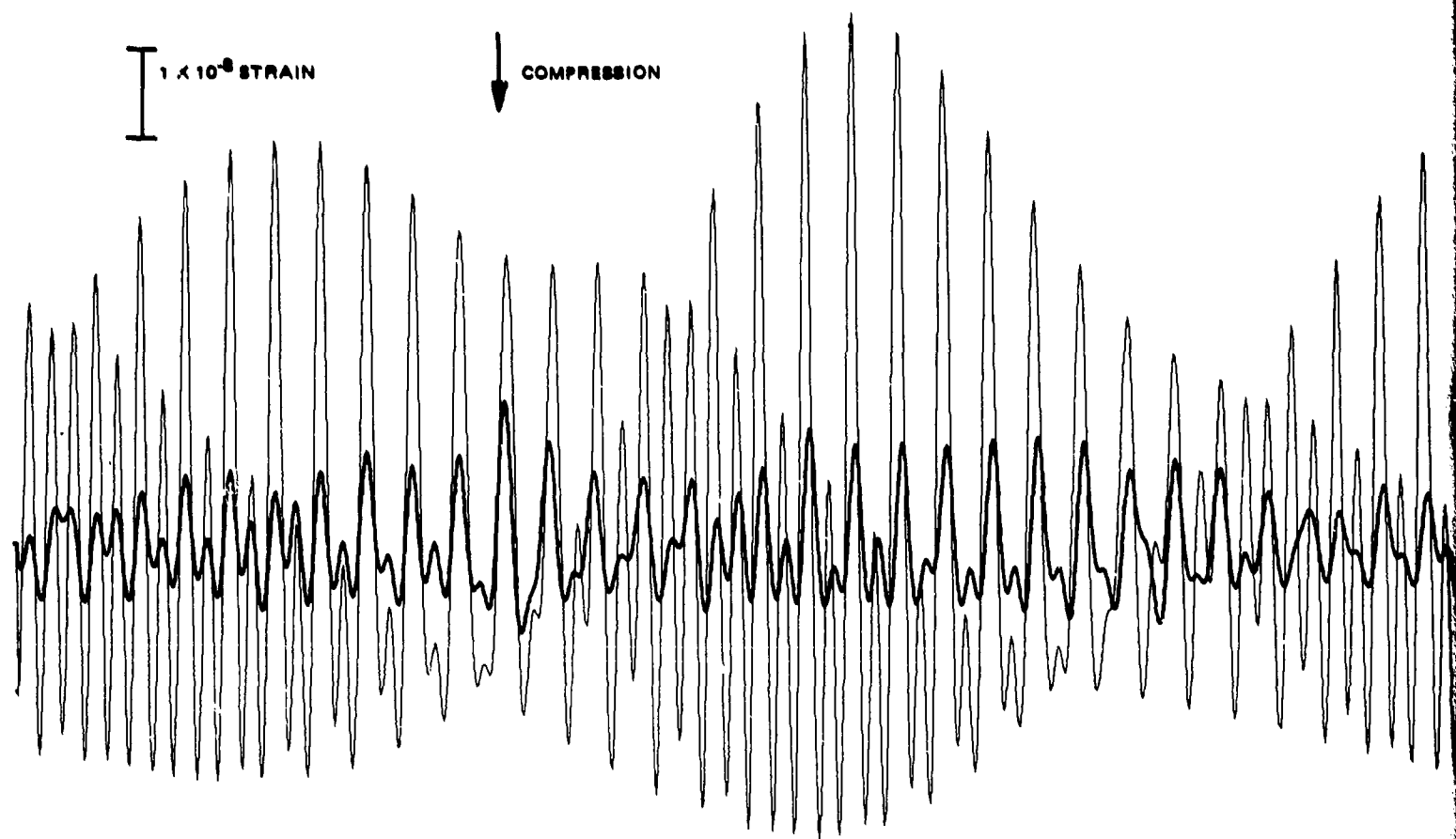


Figure 267. Observed (dark line) and predicted (light line) earth tide areal strain (reversed polarity) 7 April to 18 May 1971

-55/466-

TR 72-3



7 10 15 20 25 30 31 5

APRIL

TIME (date at 0000Z)

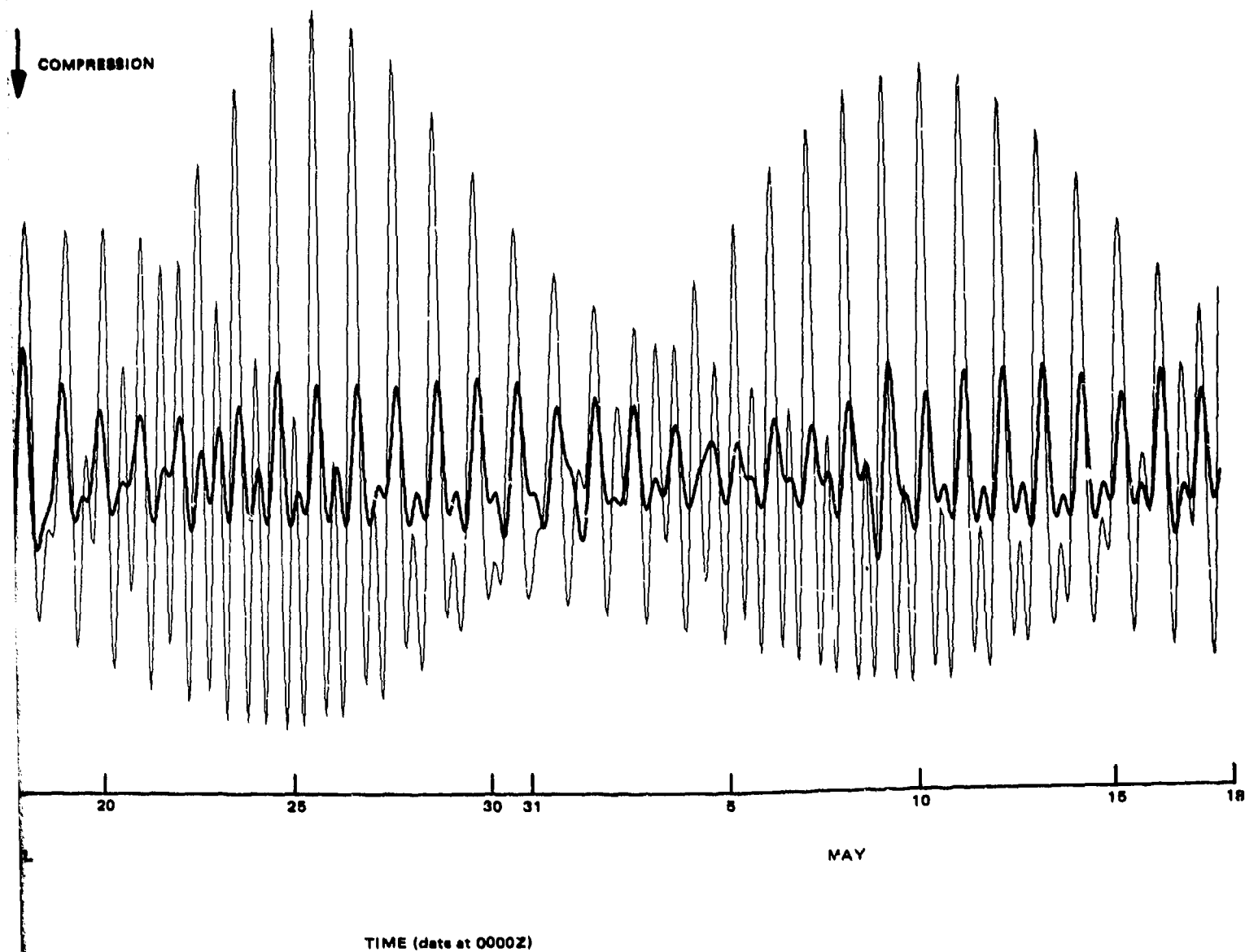


Figure 247. Observed (dark line) and predicted (light line) earth tide areal strain (reversed polarity) 7 April to 18 May 1971

G 6784

-465/466-

TR 72-3

EARTH TIDE FOURIER TRANSFORM

GC-AZ
7 APR-19 MAY 1971

+ GC325 THEORETCL
* S325B OBSERVED

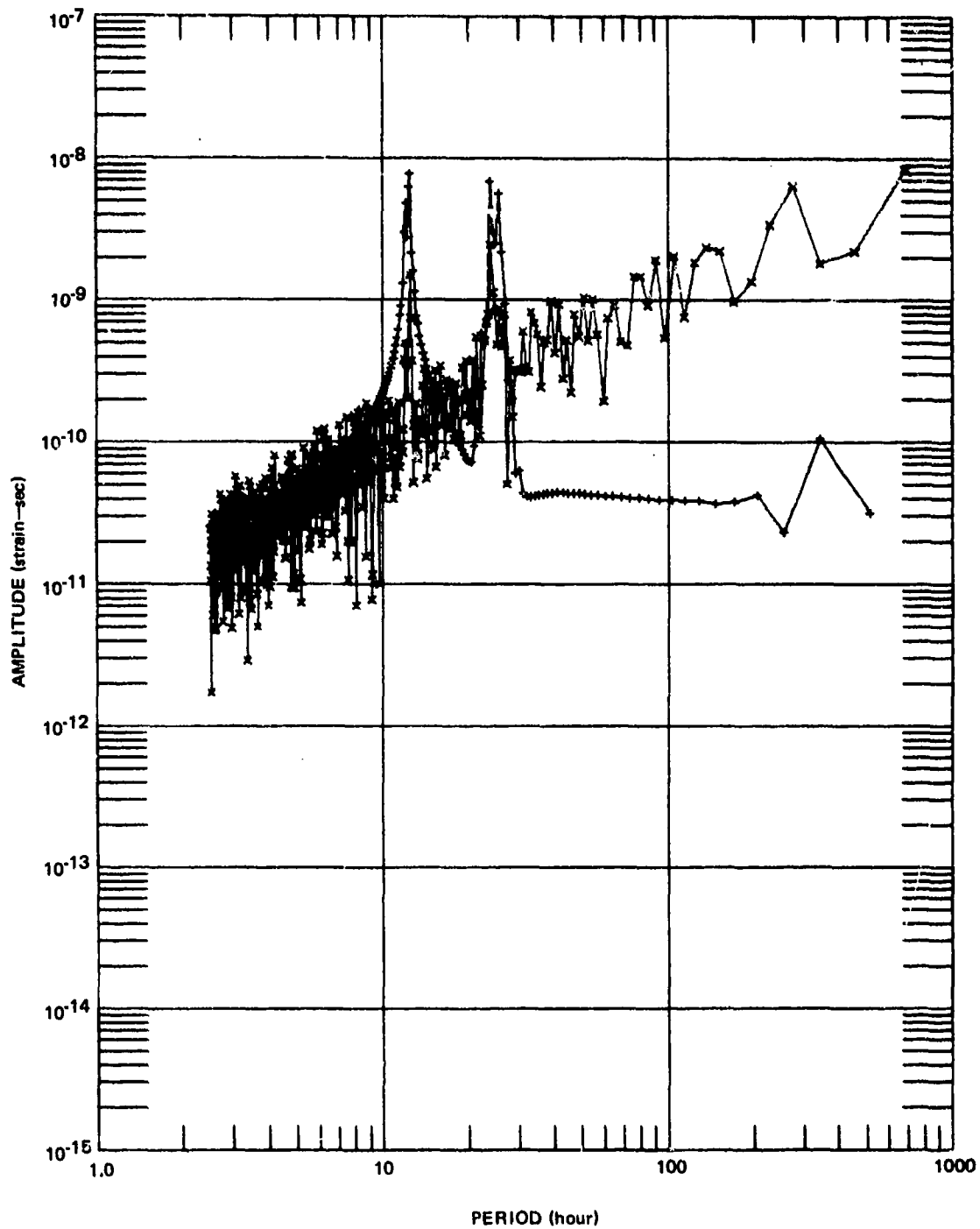


Figure 248. Fourier transform amplitude of observed and predicted earth tide strains in the 325 deg azimuth 7 April to 18 May 1971

G 6785

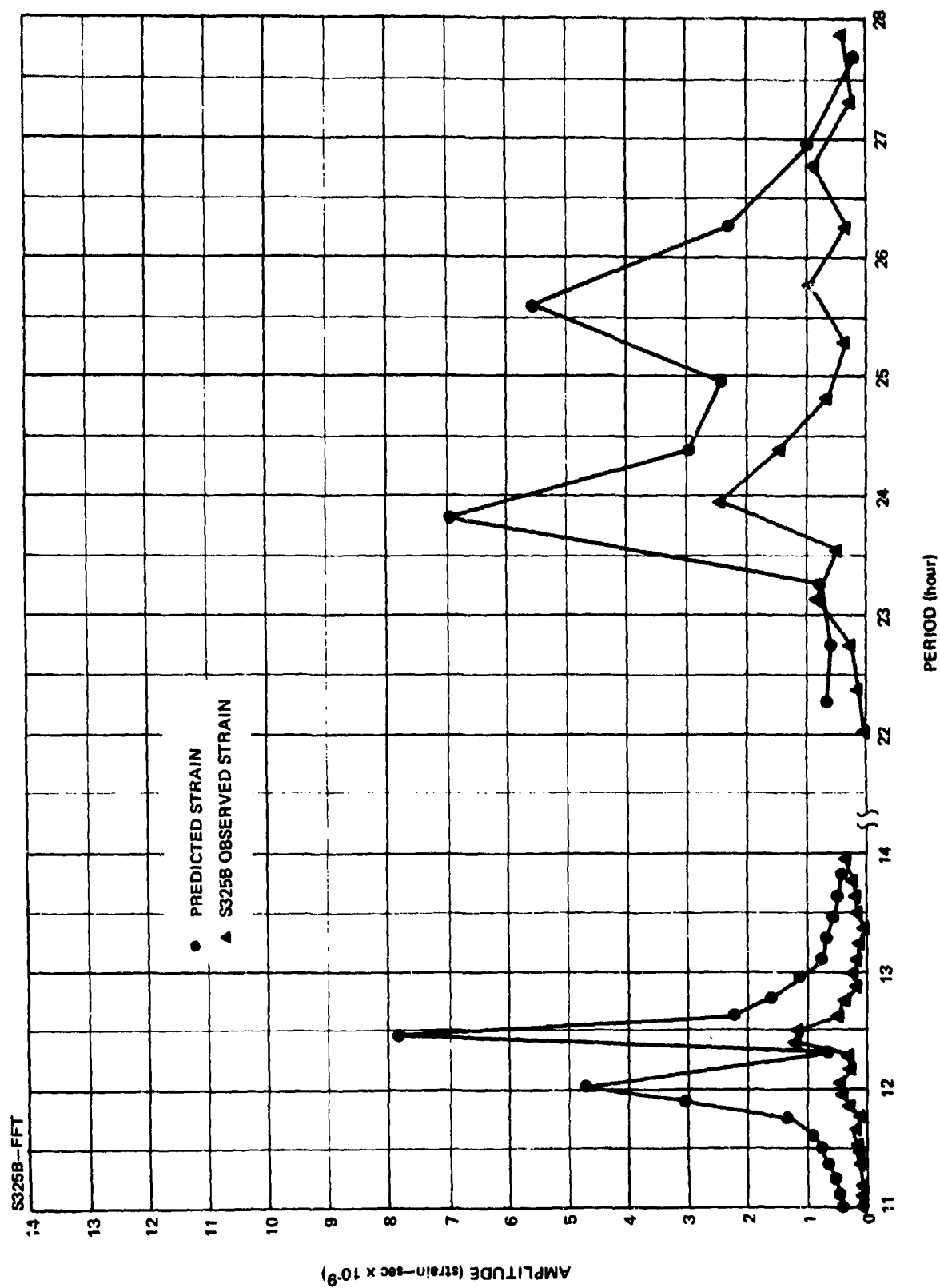


Figure 249. Fourier transform amplitude of observed and predicted earth tide strains in the 325 deg azimuth 7 April to 18 May 1971, expanded scale

G 6786

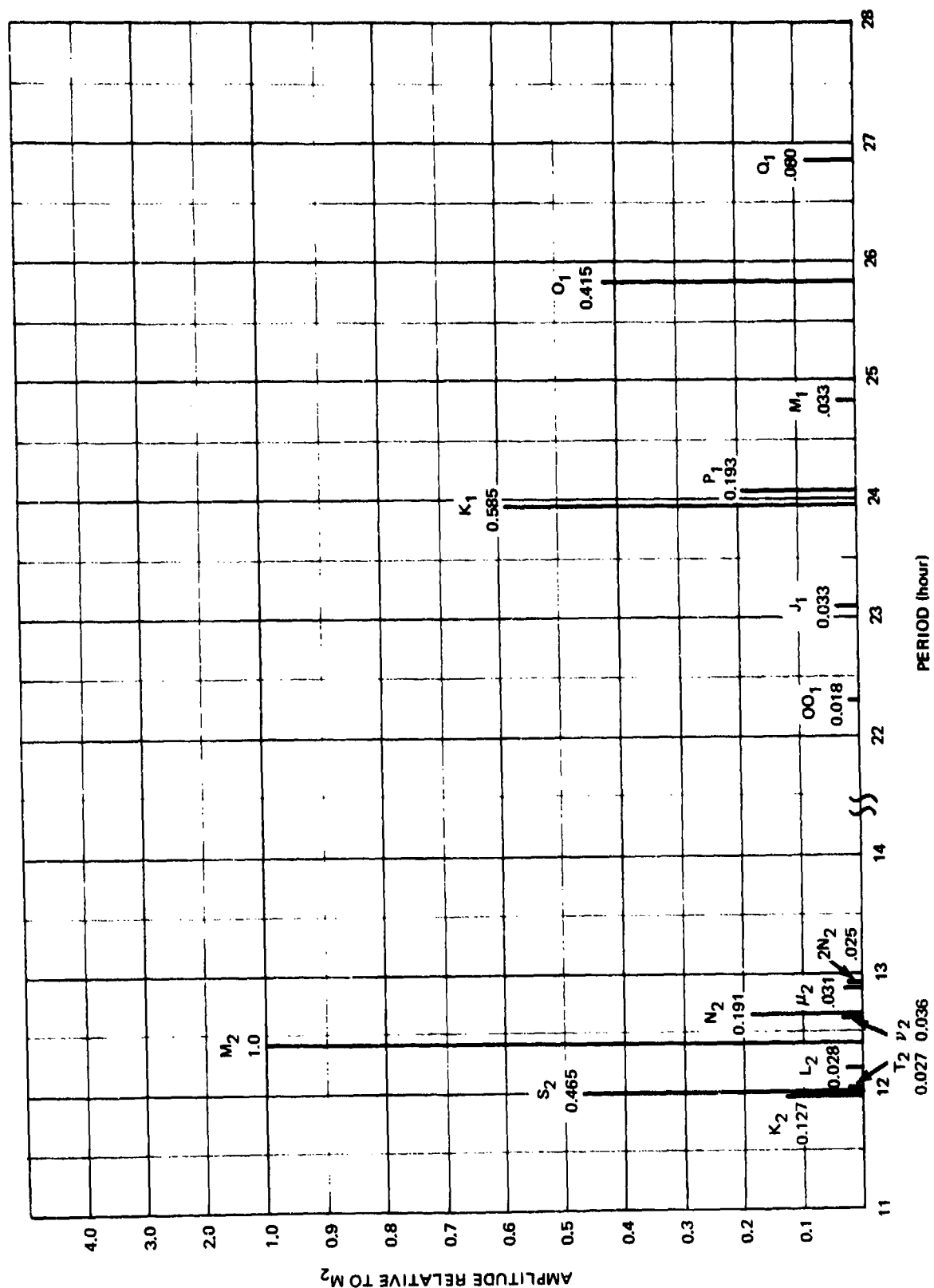


Figure 250. Gravity tide periods and amplitudes relative to M_2

G 6787

accomplished with the number of samples used in the analysis. The amplitudes of the Fourier transforms of the observed and predicted strains in the 55 deg azimuth are plotted in figure 251 and on an expanded linear scale in figure 252. The unfiltered observed strains illustrated in figure 243 were used to calculate the Fourier transform. The amplitudes of the Fourier transforms of the observed vertical strain (illustrated in figure 241) and the predicted areal strain are plotted in figure 253 and of the observed and predicted areal strains are plotted in figure 254. The amplitudes at the semi-diurnal and diurnal tide periods are plotted on an expanded linear scale in figure 255.

Table 21 summarizes the numerical results. The table gives the Fourier transform amplitudes of the observed strains, the ratio of the Fourier transform amplitudes of the predicted strains to the observed strains, and the relative Fourier transform phase angle of the observed strains to the predicted strains. The table summarizes the results at the principal tide periods for the three instrument components of observed strain relative to the predicted strain, for the observed areal strain relative to the predicted strain, and for the observed vertical strain relative to the observed areal strain. The Fourier transform phase angles vary rapidly with period, and the relative phase angles given in the table should be interpreted with caution.

Analysis and interpretation of earth tide spectra are difficult. Many of the periods of the tidal components are so close together (see figure 250) that they cannot be separated without having data for many years to increase the frequency resolution. Most tidal spectroscopy uses a time interval of 29 days. The 43 days of data used in this analysis have given sufficient frequency resolution to separate the two principal semi-diurnal components M_2 and S_2 and the principal diurnal component O_1 from the combined components K_1 and P_1 . The amplitudes in figures 249, 252, and 255 suggest that narrow band-pass filtering might yield information on the Q_1 , M_1 , J_1 , OO_1 , μ_2-2N_2 , ν_2-N_2 components.

The results in table 21 and in figures 249, 252, and 255 lead to several observations. The 55 deg azimuth strainmeter has smaller amplitude ratios relative to the predicted tides than the other two strainmeters and than the areal strain. This observation further substantiates its better coupling to the earth. Based on the amplitude ratios in the table, all components have more strain at a 24 hr period than at the other tidal periods. The vertical strainmeter is also anomalous at a 12 hr period. These excess strains are related to pressures and temperatures and will be discussed in section 13.4. In the narrow period intervals between the two semi-diurnal components and between the two diurnal components, the amplitude ratios of the strains vary significantly. Phase angles also vary significantly between the several tidal components. The areal strain is approximately equal to the vertical strain except at the 12 hr period where the vertical strain is anomalously high.

The power spectral density, coherence, and relative phase angles between the sets of observed and predicted earth tide strains are plotted in figures 256 through 260. Numerical values at the peaks of the spectra are given in table 22 for the semi-diurnal and the diurnal periods. The PSD analysis only has sufficient frequency resolution to separate the semi-diurnal components from the diurnal components.

EARTH TIDE FOURIER TRANSFORM

QC-AZ
7 APR-19 MAY 1971

* QC55 THEORETICAL
x S55B OBSERVED

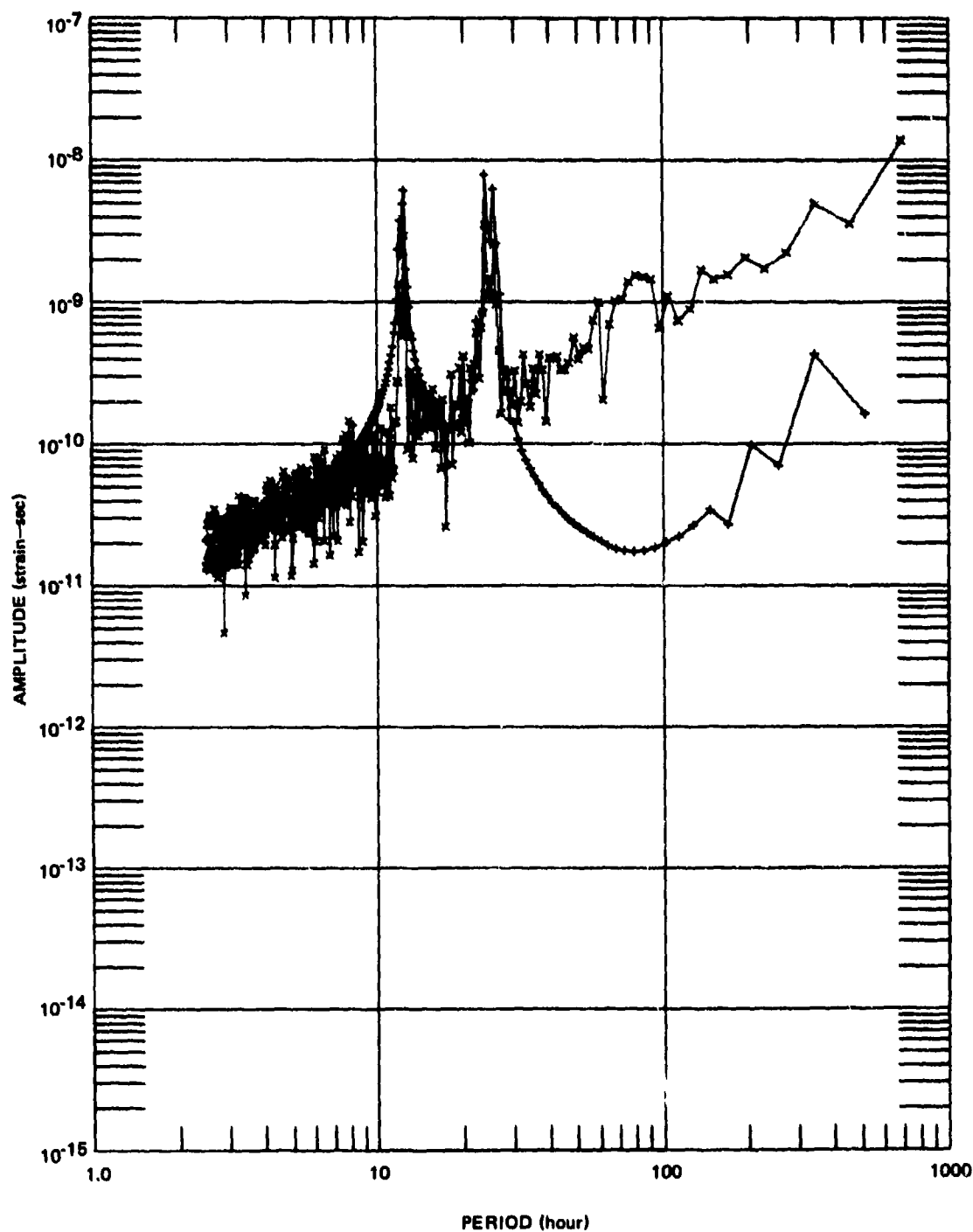


Figure 251. Fourier transform amplitude of observed and predicted earth tide strains in the 55 deg azimuth 7 April to 18 May 1971

G 6788

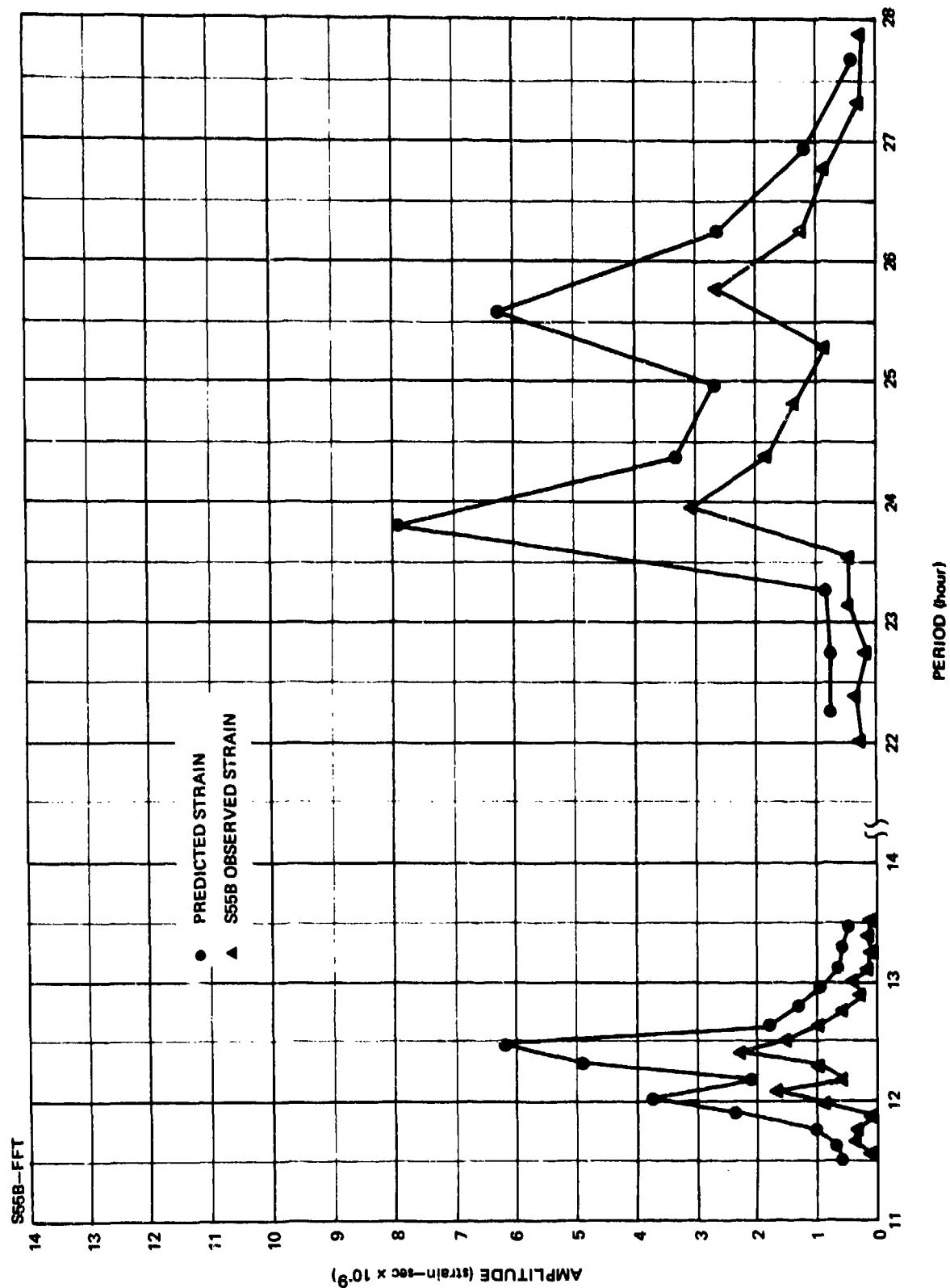


Figure 252. Fourier transform amplitude of observed and predicted earth tide strains in the 55 deg azimuth, 7 April to 18 May 1971, expanded scale

G 6789

EARTH TIDE FOURIER TRANSFORM

GC-AZ
7 APR-19 MAY 1971

+ GC55+GC325 THEB
* SZB OBSERVED

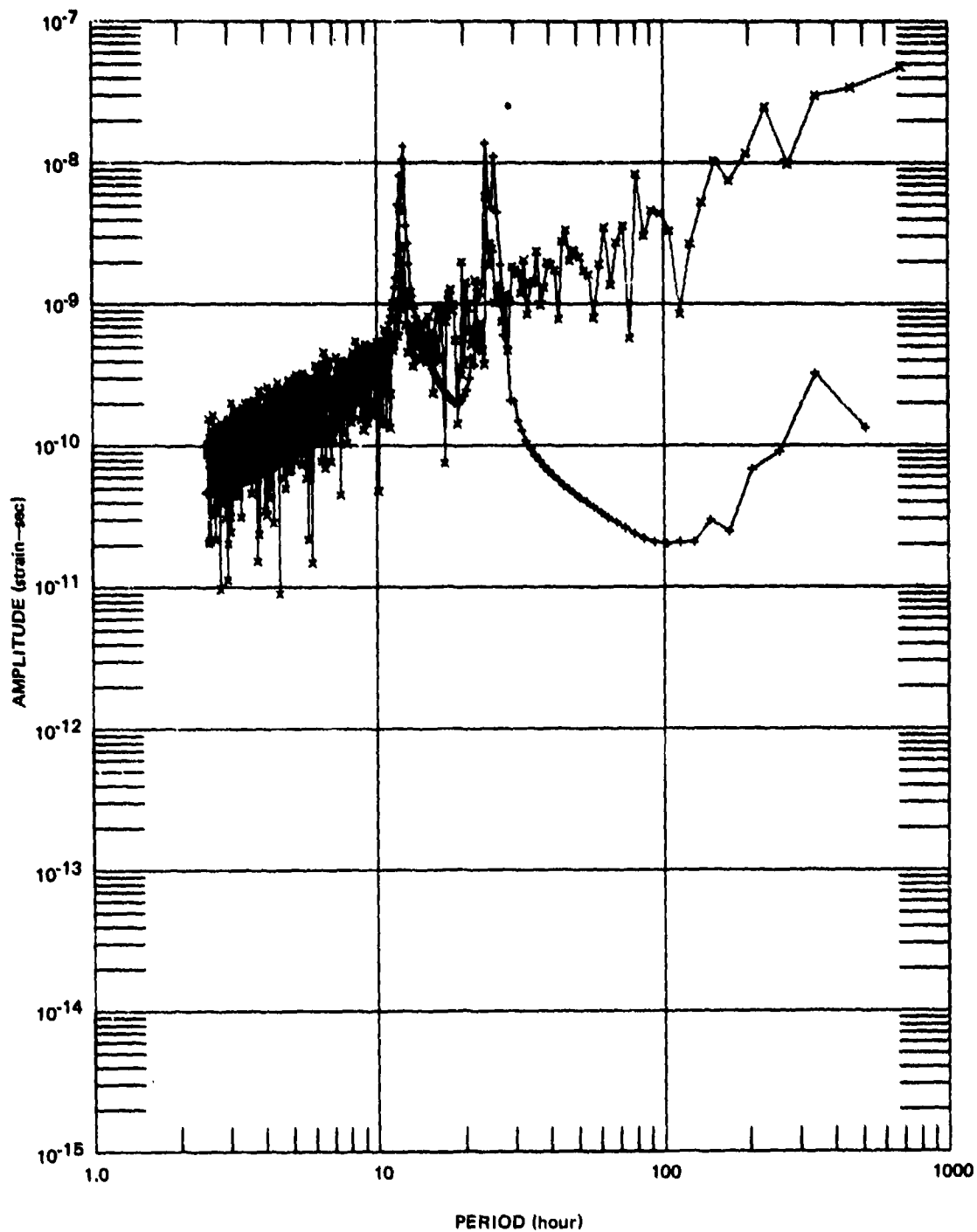


Figure 253. Fourier transform amplitude of observed vertical and predicted areal earth tide strains 7 April to 18 May 1971

G 6790

EARTH TIDE FOURIER TRANSFORM

QC-AZ
7 APR-19 MAY 1971

+ GC55+GC325 THEB
* S55B+S325B 085

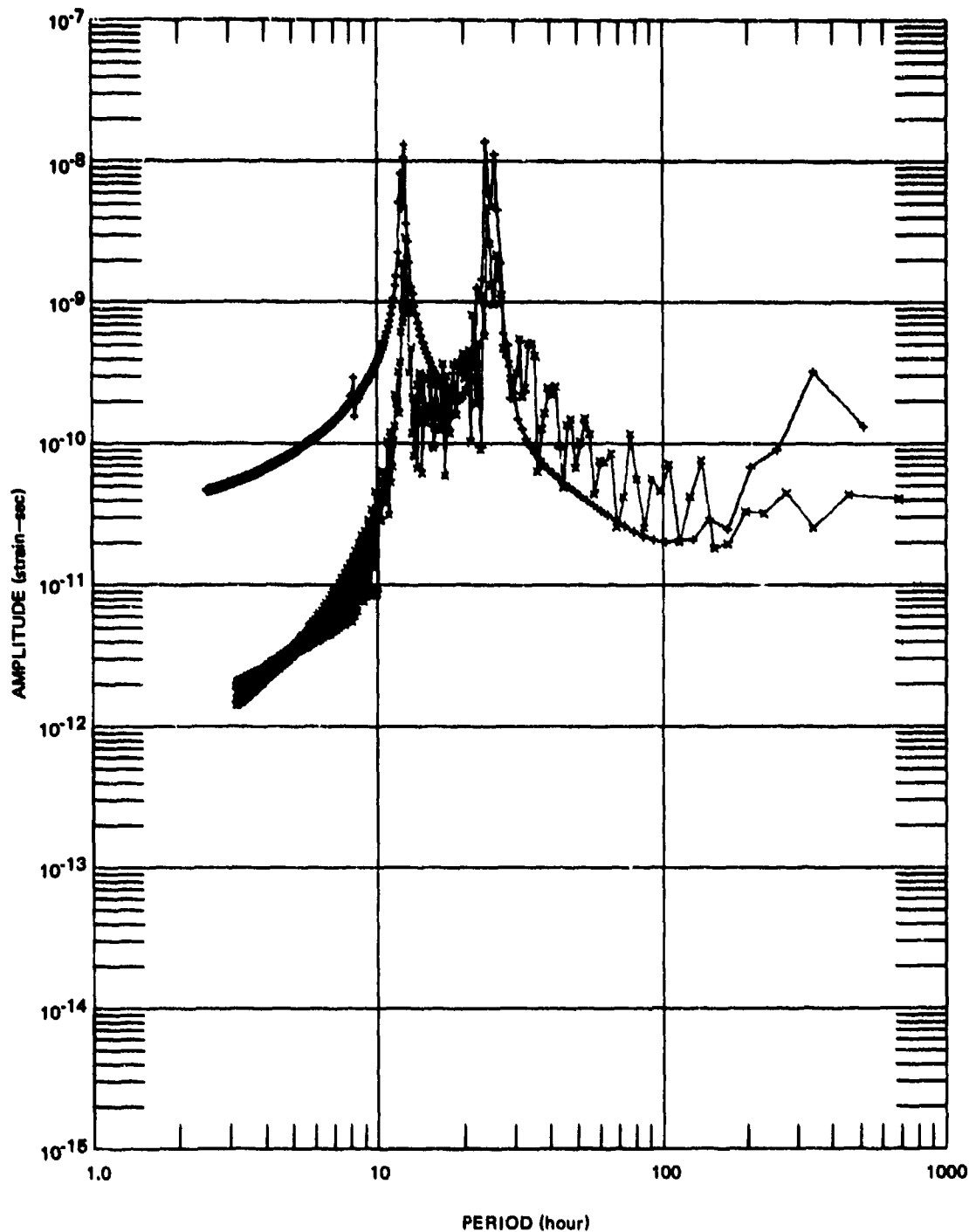


Figure 254. Fourier transform amplitude of observed and predicted areal earth tide strains 7 April to 18 May 1971

G 6791

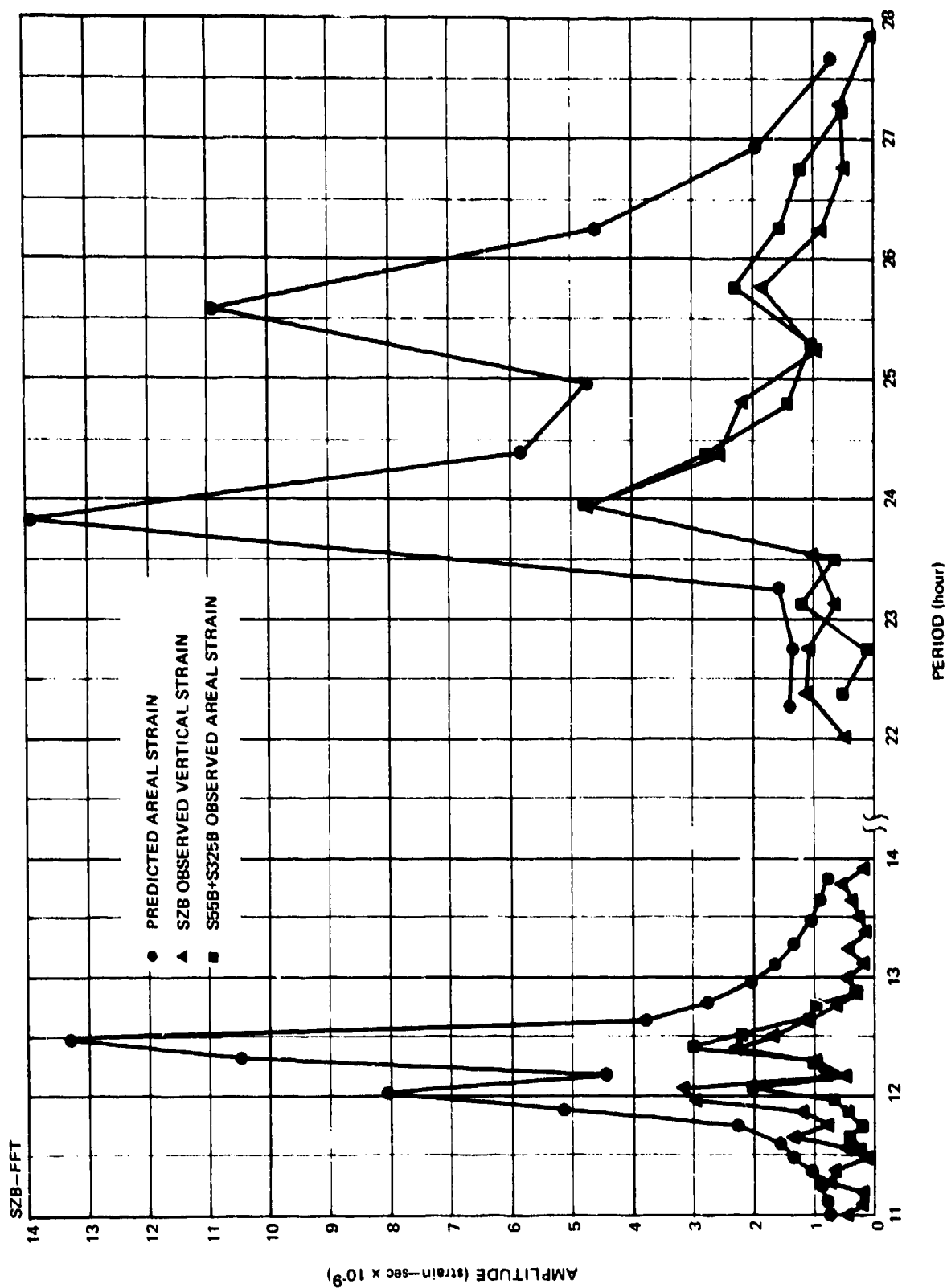


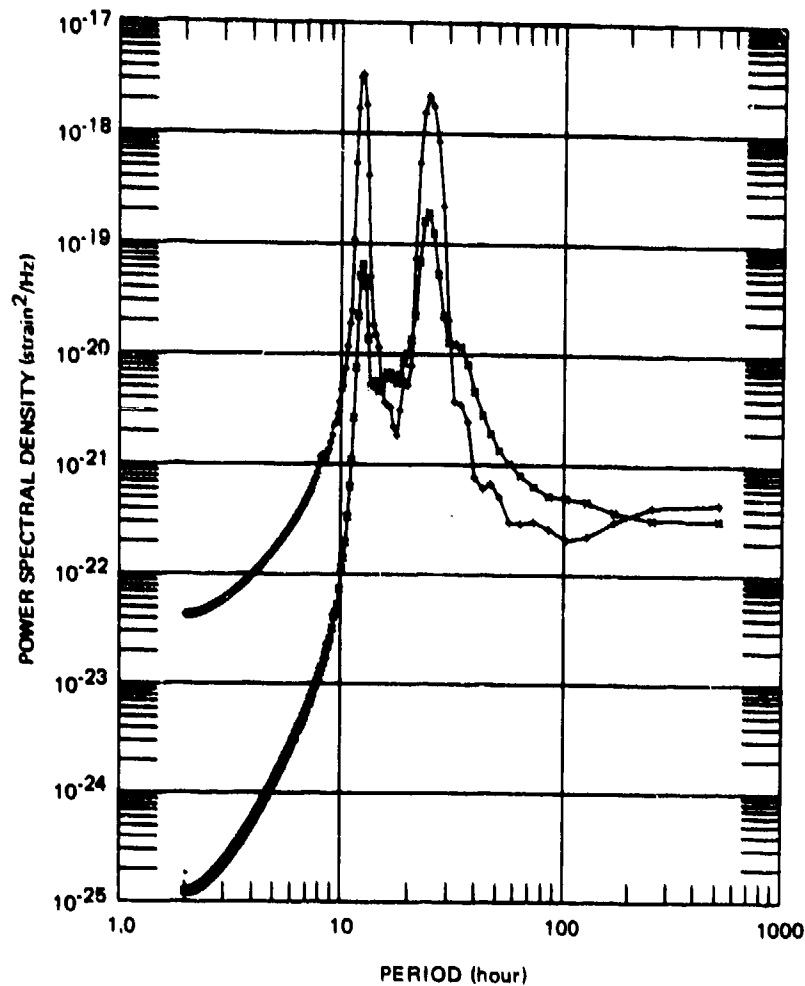
Figure 255. Fourier transform amplitude of observed vertical and observed areal earth tide strains and predicted areal earth tide strains 7 April to 18 May 1971, expanded scale

G 6792

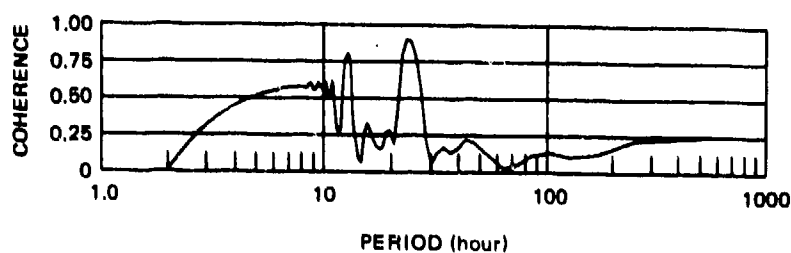
Table 21. Observed amplitude, amplitude ratio (theo/obs), and phase angle of observed relative to theoretical for earth tide strain components from the Fourier transform analysis

Component	Tide component and period	M ₂ 12.42 hr	S ₂ 12.00 hr K ₂ 11.97 hr	K ₁ 23.93 hr P ₁ 24.07 hr	O ₁ 25.82 hr
S325B	Observed amplitude Amplitude ratio Phase angle	1.53 x 10 ⁻⁹ 5.14 94° lag	0.512 x 10 ⁻⁹ 9.35 63° lead	2.51 x 10 ⁻⁹ 2.78 75° lag	0.89 x 10 ⁻⁹ 6.21 81° lag
S55B	Observed amplitude Amplitude ratio Phase angle	2.91 x 10 ⁻⁹ 2.13 12° lead	1.34 x 10 ⁻⁹ 2.79 150° lead	3.49 x 10 ⁻⁹ 2.27 33° lead	2.56 x 10 ⁻⁹ 2.44 62° lead
SZB	Observed amplitude Amplitude ratio Phase angle	2.52 x 10 ⁻⁹ 5.30 27° lead	4.48 x 10 ⁻⁹ 1.80 64° lead	5.48 x 10 ⁻⁹ 2.54 96° lag	2.64 x 10 ⁻⁹ 4.15 64° lead
S325B + S55B	Observed amplitude Amplitude ratio Phase angle	3.00 x 10 ⁻⁹ 4.45 176° lead	2.00 x 10 ⁻⁹ 4.04 117° lag	4.71 x 10 ⁻⁹ 2.96 30° lag	2.30 x 10 ⁻⁹ 4.75 109° lag
SZB (obs) S325B+S55B (obs)	Amplitude ratio Phase angle	1.19 149° lag	0.445 179° lag	0.858 66° lag	0.873 173° lead

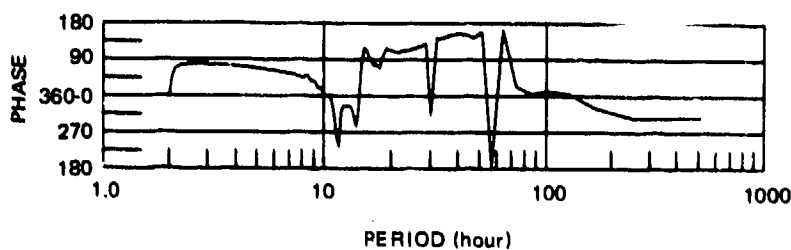
EARTH TIDE
 1024 SAMPLES, 255 LAGS, 1 SPH, PARZEN SMOOTHING
 OC-AE
 APR-MAY 1971
 • 325 THEORETICAL
 • 53258



a. Power spectral density



b. Coherence

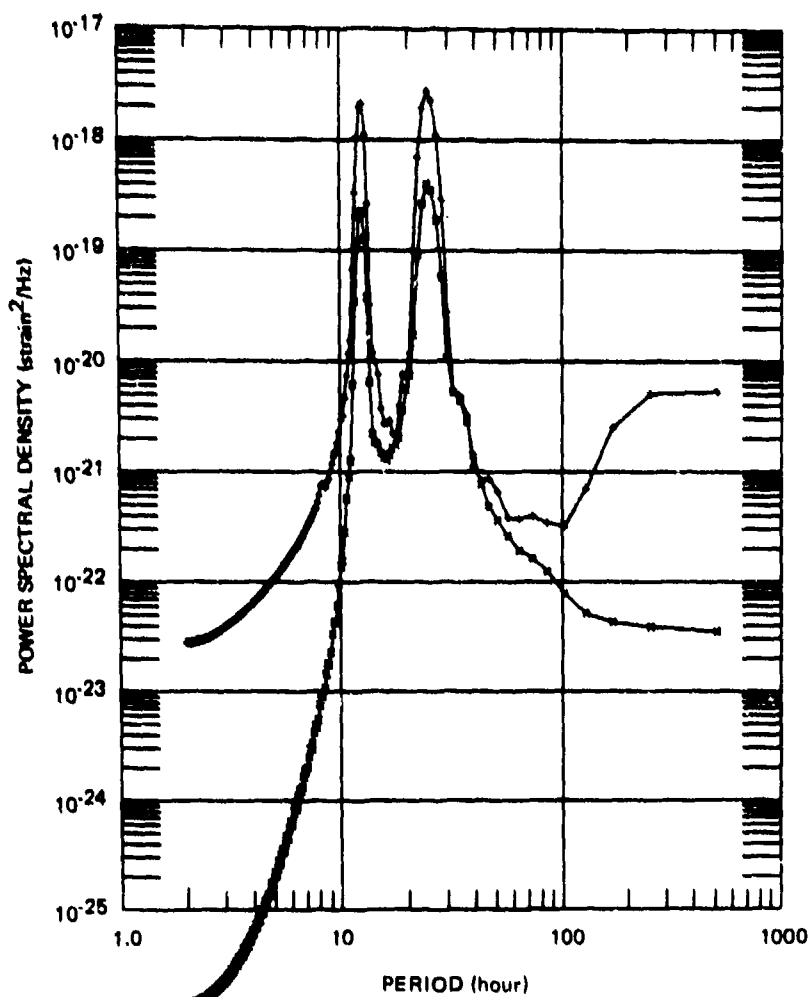


c. Phase lead observed over predicted

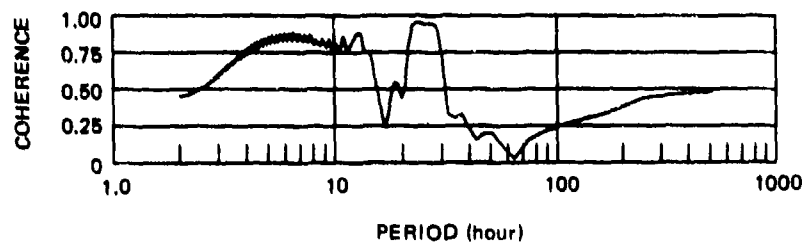
Figure 256. Power spectral density, coherence, and relative phase angle of observed and predicted earth tide strains in the 325 deg azimuth

G 6793

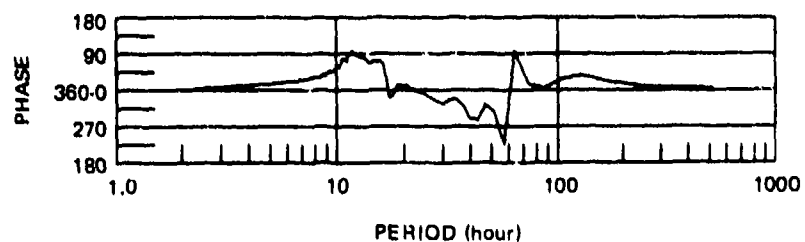
EARTH TIDE
 1024 SAMPLES, 255 LAGS, 1 SPH. PARZEN SMOOTHING
 DC-AR
 APR-MAY 1971
 • 55 THEORETICAL
 • 5550



a. Power spectral density



b. Coherence

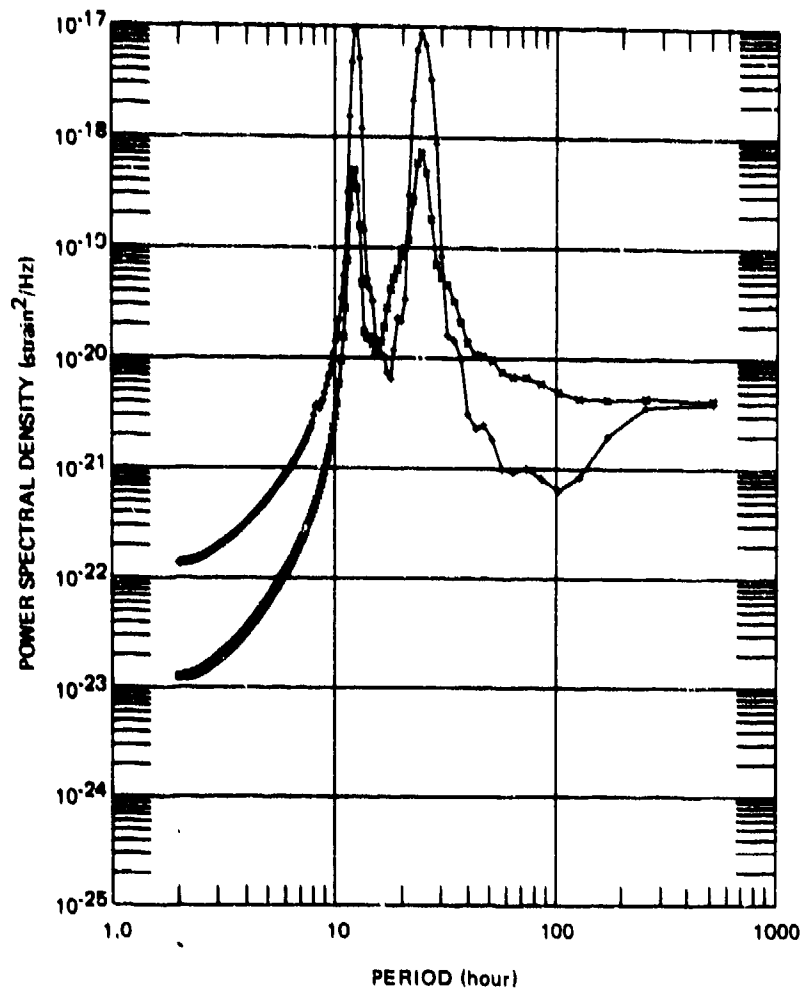


c. Phase lead observed over predicted

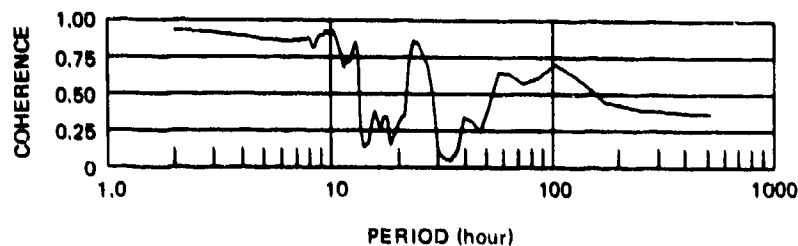
Figure 257. Power spectral density, coherence, and relative phase angle of observed and predicted earth tide strains in the 55 deg azimuth

G 6794

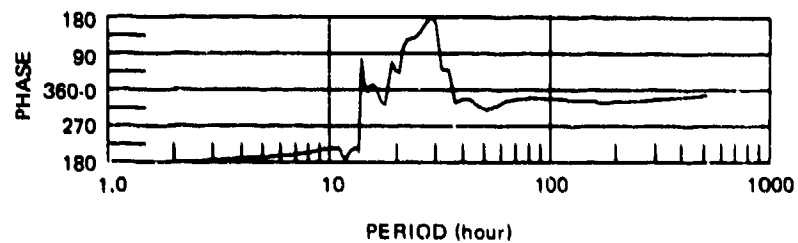
EARTH TIDE
 1024 SAMPLES, 255 LAGS, 1 SPH, PARZEN SMOOTHING
 DC-AR
 APR-MAY 1971
 • 2 THEORETICAL
 • 5PB



a. Power spectral density



b. Coherence



c. Phase lead observed over predicted

Figure 258. Power spectral density, coherence, and relative phase angle of observed vertical and predicted areal earth tide strains

G 6795

EARTH TIDE

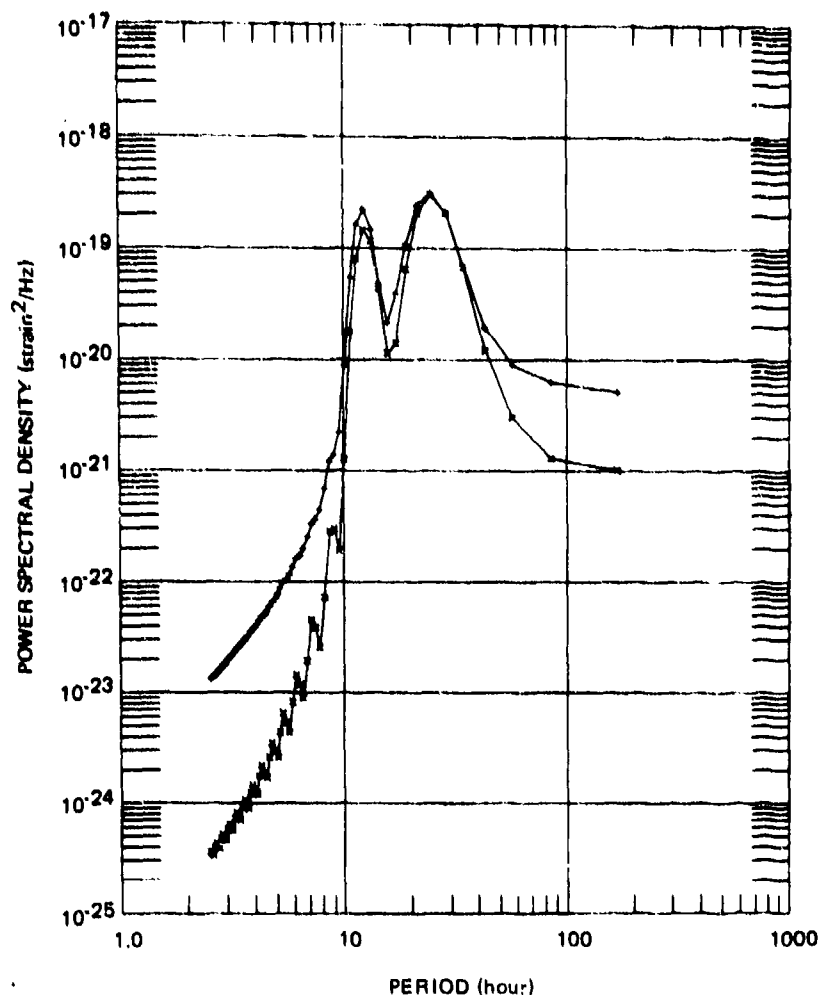
3072 SAMPLES, 256 LAGS, 3.0SPH, PARZEN SMOOTHING

QC-AZ

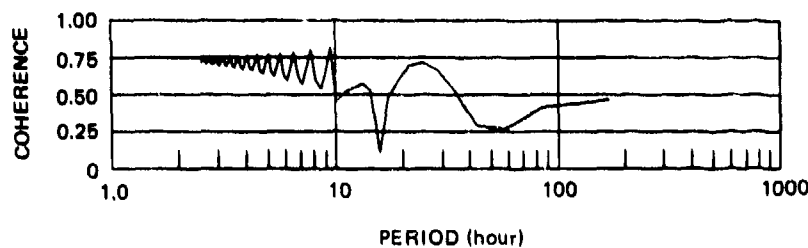
7 APR-19 MAY 1971

+ 520

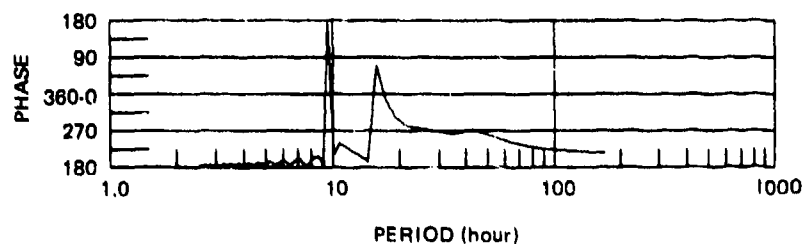
* 53250 + 5550



a. Power spectral density



b. Coherence

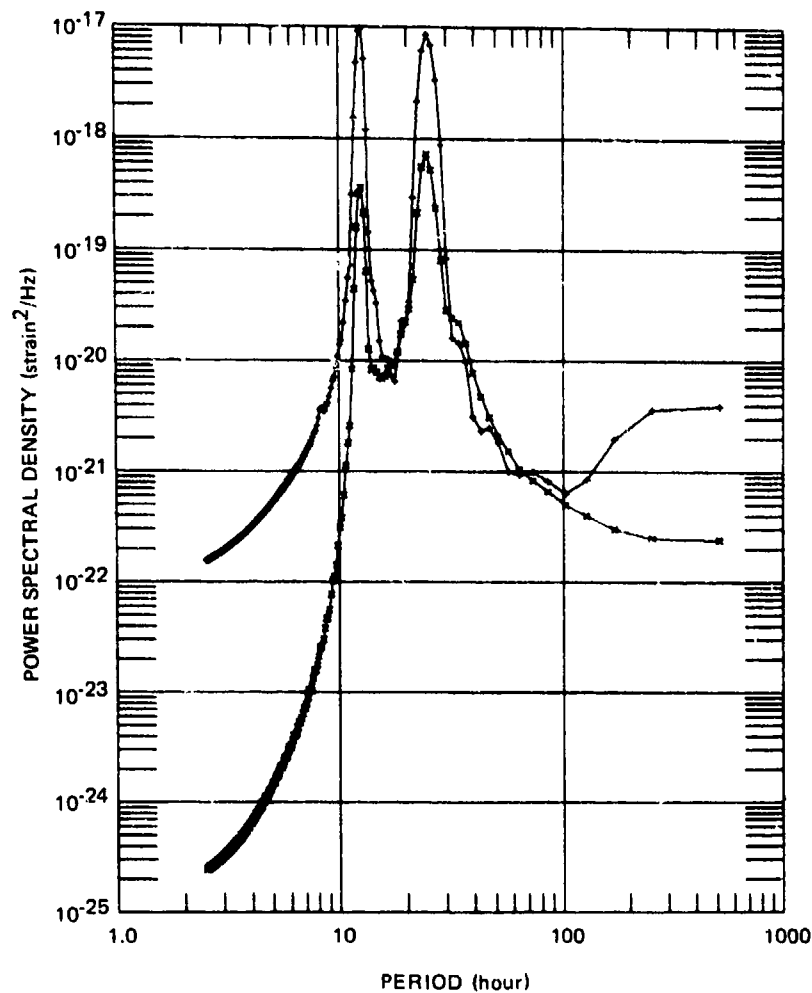


c. Phase lead
SZB over
S325B+S55B

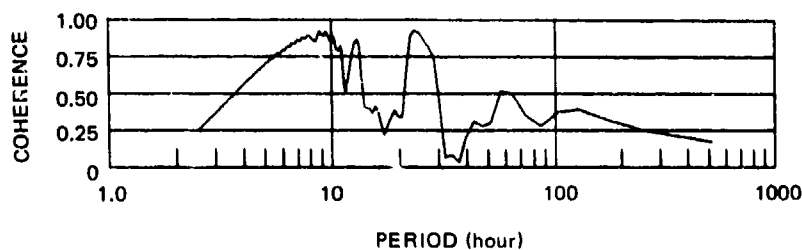
Figure 259. Power spectral density, coherence, and relative phase angle of observed vertical and observed areal earth tide strains

G 6796

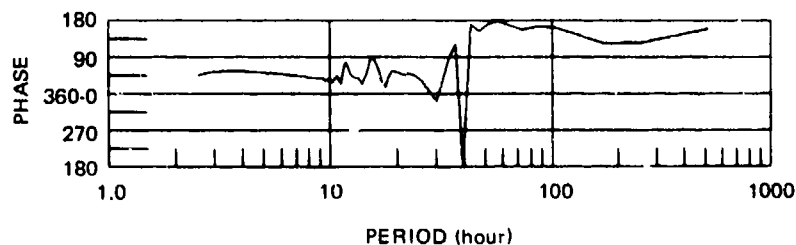
EARTH TIDE
 1024 SAMPLES, 256 LAGS, 1.05PH, PARZEN SMOOTHING
 QC-A2 * QC325+QC55 THEB
 7 APR-12 MAY 1971 * S3258+5558 885



a. Power spectral density



b. Coherence



c. Phase lead observed over predicted

Figure 260. Power spectral density, coherence, and relative phase angle of observed and predicted areal earth tide strains

G 6797

Table 22. Amplitude ratio (theo/obs), coherence, and phase angle of observed relative to theoretical for earth tide strain components from power spectral density analysis

Strain component	Tide component group	$\begin{Bmatrix} M_2 \\ S_2 \\ K_2 \end{Bmatrix}$	$\begin{Bmatrix} K_1 \\ P_1 \\ O_1 \end{Bmatrix}$
S55B	Amplitude ratio	2.97	2.59
	Coherence	0.99	0.97
	Phase angle	57° lead	24° lag
S325B	Amplitude ratio	7.05	3.35
	Coherence	0.87	0.91
	Phase angle	51° lead	97° lead
SZB	Amplitude ratio	5.27	3.41
	Coherence	0.80	0.85
	Phase angle	209° lead	133° lead
S325B + S55B	Amplitude ratio	5.14	3.42
	Coherence	0.84	0.91
	Phase angle	43° lead	42° lead
SZB (obs)	Amplitude ratio	1.25	1.02
S325B+S55B (obs)	Coherence	0.55	0.72
	Phase angle	221° (Z lags sum)	275° (Z lags sum)

The same observations can be made from the power spectral density analysis as from the Fourier transform analysis. The higher coherence indicates the 55 deg azimuth strainmeter is better coupled to the earth than the other two strain meters. The amplitude ratios indicate that there is more strain at the 24 hr period than at the 12 hr period. The vertical strain at a 12 hr period is anomalously high. In considering the phase angles, the reader should refer to figure 240 for the relative shape of the load forces on the surface of the earth from the W_2 gravity potential.

If the driving force for the strains in the three directions is the same, the outputs of the strainmeters might be expected to be in-phase. However, the driving forces are made up of the summation of a series of time-varying functions. Each of these time-varying functions has its own spatial and temporal transfer functions to the three strainmeters. The time-varying functions will combine in such a manner that the net phase angle of any strain component e_{ij} could have any value and the phase angles would not necessarily be the same for any two strain components. To evaluate what might be expected, a PSD analysis was performed on the two horizontal observed strain series and on the two horizontal predicted strain series. Numerical results are given in table 23 for the semi-diurnal and for the diurnal spectral peaks. Amplitude ratios and phase angles are different for the predicted strains and the coherence is 1.00.

Table 23. Comparison of horizontal Earth tide strains from power spectral density analysis

Strain	Tide component group	$\begin{Bmatrix} M_2 \\ S_2 \\ K_2 \end{Bmatrix}$	$\begin{Bmatrix} K_1 \\ P_1 \\ O_1 \end{Bmatrix}$
S55B (obs)	Amplitude ratio	1.90	1.44
S325B (obs)	Coherence	0.67	0.76
	Phase angle	65° lead	74° lag
55 (predicted)	Amplitude ratio	0.783	1.13
325 (predicted)	Coherence	1.00	1.00
	Phase angle	38° lag	43° lead

13.4 PRESSURE AND TEMPERATURE INDUCED STRAINS

The analysis of the earth tide strains in the previous section indicated that there were significant strains at periods of 12 hr and 24 hr that were not the direct result of the gravitational attraction among the earth, the moon, and the sun. These strains are related to pressure and temperature fluctuations.

The atmosphere responds to the gravitational attractions, and the spectra of air pressure have been found to have peaks at the tidal periods (Gossard, 1960, Tolstoy, 1968, Herron et al., 1969). Air temperature also fluctuates with the sun's radiation in a 24 hr period. Air temperature and air pressure are related by the gas laws so that for changes in either parameter some change is to be expected in the other. Thus, the gravitational attraction of the moon creates a direct strain tide; it changes air pressure, which changes the strain field related to pressure loads; and the pressure change results in a temperature change, which changes the thermal expansion strain field. The motion of the sun will have similar effects as the gravitational attraction of the moon plus the additional large effects from the rise and fall in temperature from the energy radiated by the sun. A rise in temperature will change the thermal expansion strain field; it will also change the air pressure, which will change the pressure induced strain field. The observed strain field is the resultant of the simultaneous variations in gravitational attraction from the moon, in gravitational attraction from the sun, in pressure loads on the surface, and in temperature variations.

Data from a recording barometer and a recording thermometer were hand digitized at 1 hr intervals for the 45 days from 4 April through 19 May 1971. The time series with the mean and linear trend removed are plotted in figures 261 (air pressure) and 262 (air temperature). The diurnal and semi-diurnal variations are clearly visible in both figures.

The time series were spectrally analyzed in the same manner as used with the strain signals in section 13.3. The amplitude of the Fourier transform of the

atmospheric pressure is given in figure 263 and the power spectral density is given in figure 264. Sharp peaks occur at the 12 hr and 24 hr tidal periods. Other major peaks occur at 78.8 and 256.0 hr (3.3 and 10.7 days, respectively) in both analyses. Less significant peaks at 41.0, 51.2, and 128 to 146 hr occur in the Fourier amplitudes. The periods of the major peaks can be seen in the time series in figure 261. The results of the temperature analyses are given in figure 265 (Fourier transform amplitude) and figure 266 (PSD). The major spectral peaks appear at similar periods as observed on the pressure spectra. These periods are 12.1, 23.8, 85.3, and 256 hr.

A power spectral density analysis was made to compare the pressure and the temperature with each of the three strain components. The PSD have been illustrated in previous figures. The coherences between the air pressure and the strains are plotted in figure 267 and the phase angles by which the strain components lead the pressure are plotted in figure 268. Coherences between air temperature and the strains are plotted in figure 269 and the relative phase angles are plotted in figure 270. Numerical values from the semi-diurnal and diurnal peaks are listed in table 24. The coherences are all greater than 0.8 except for the 325 deg azimuth at the 12 hr period for both the pressure and temperature effects.

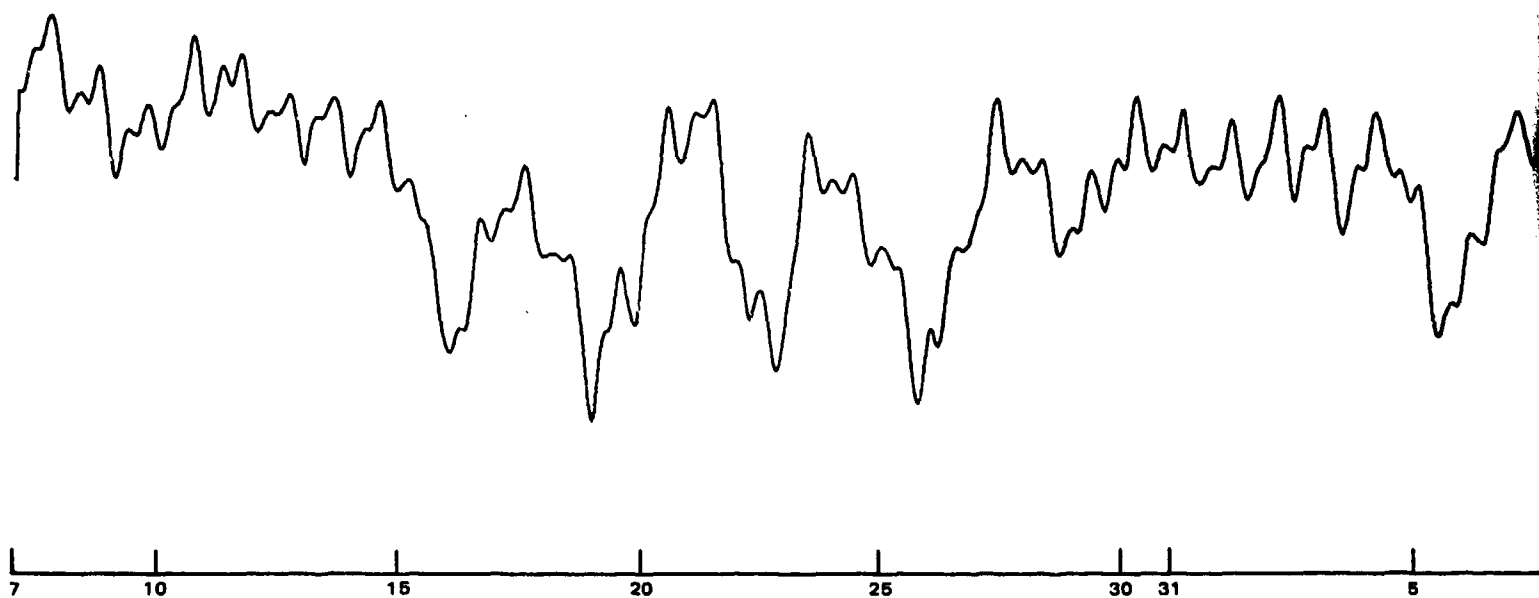
The high coherences between the observed strain field and each of the predicted tide strains, the air pressure, and the air temperature suggest that all are interacting as described above. The separation of the cause and effect between each of the phenomenon is beyond the scope of the present investigation.

The amplitude ratios between strain and pressure and between strain and temperature given in table 24 can be interpreted as transfer functions in the same manner as in section 7.6. The numerical values on the order of 10^{-12} strain/ μ bar are in agreement with the higher phase velocity and with the values determined from air pressure fluctuations of periods of 30 to 2560 sec. The numerical values on the order of 4×10^{-10} strain/deg F are much smaller than the 1×10^{-6} strain/deg F thermal expansion coefficient of quartz. (Goldmine Mountain is a quartz diorite.) The three-and-a-half orders of magnitude smaller transfer function is the result of the burial at approximately 1000 cm as implied by the X in the numerator of the second equality in equation (113) below. (This equation is usually applied in the cgs system of units.) No interpretation has been reached concerning the phase relationships.

A mathematical relation between surface temperature changes and observed thermal strain has been verified experimentally. On a few occasions, it was necessary to turn the lights on in the mine during the time interval used for the earth tide strain recordings. The heat from the lights raised the temperature in the seismometer chamber, causing thermal expansion of the rock and a strain signal output. Carslaw and Jaeger (1959) treat the case of heat flow in a semi-infinite solid whose initial temperature is V and whose surface is kept at zero temperature. The temperature v is a function of time t and depth in the solid X such that

$$v = V \operatorname{erf} \left\{ \frac{X}{2 \sqrt{kt}} \right\} \quad (110)$$

I
4 mbar



APRIL

TIME (date at 0000Z)

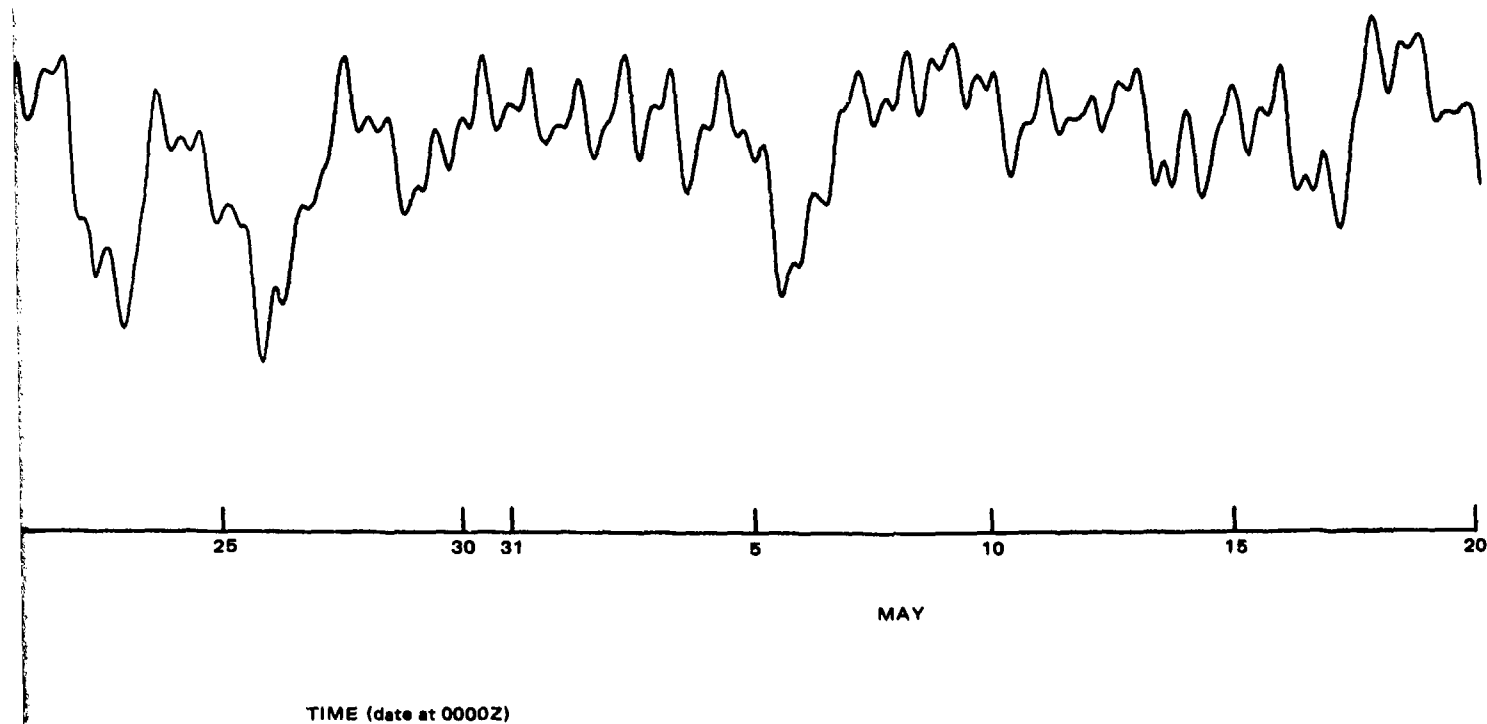


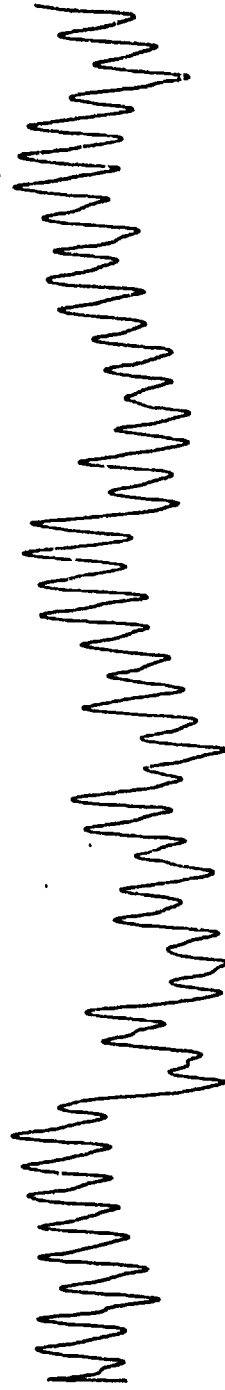
Figure 261. Air pressure fluctuations
7 April to 20 May 1971

G 6798

-485/486-

TR 72-3

20°F



TIME (hours at 0000Z)

XXXXXXXXXXXXXXXXXXXX
See the following pages
for greater detail.
XXXXXXXXXXXXXXXXXXXX

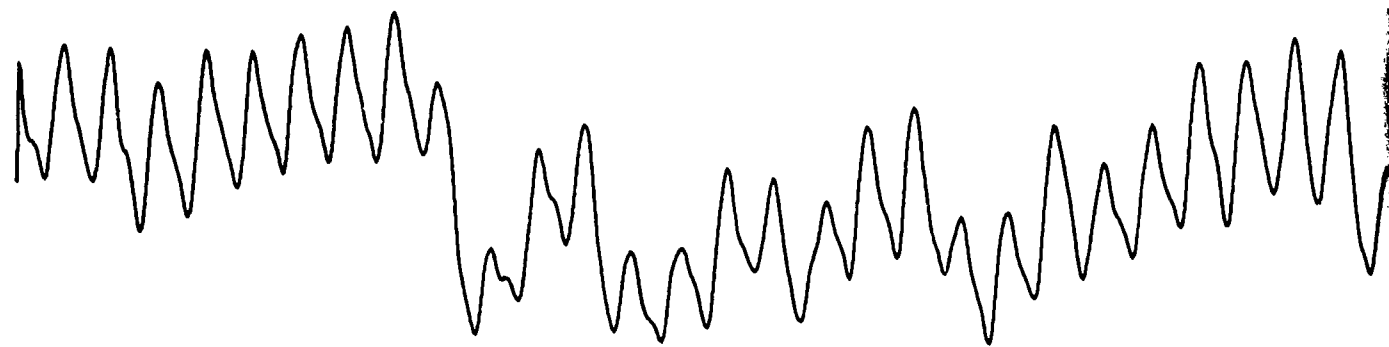
Figure 262. Air temperature fluctuations
7 April to 20 May 1971

64798

-487/488-

TR 72-3

25°F



7 10 15 20 25 30 31

APRIL

TIME (date at 0000Z)

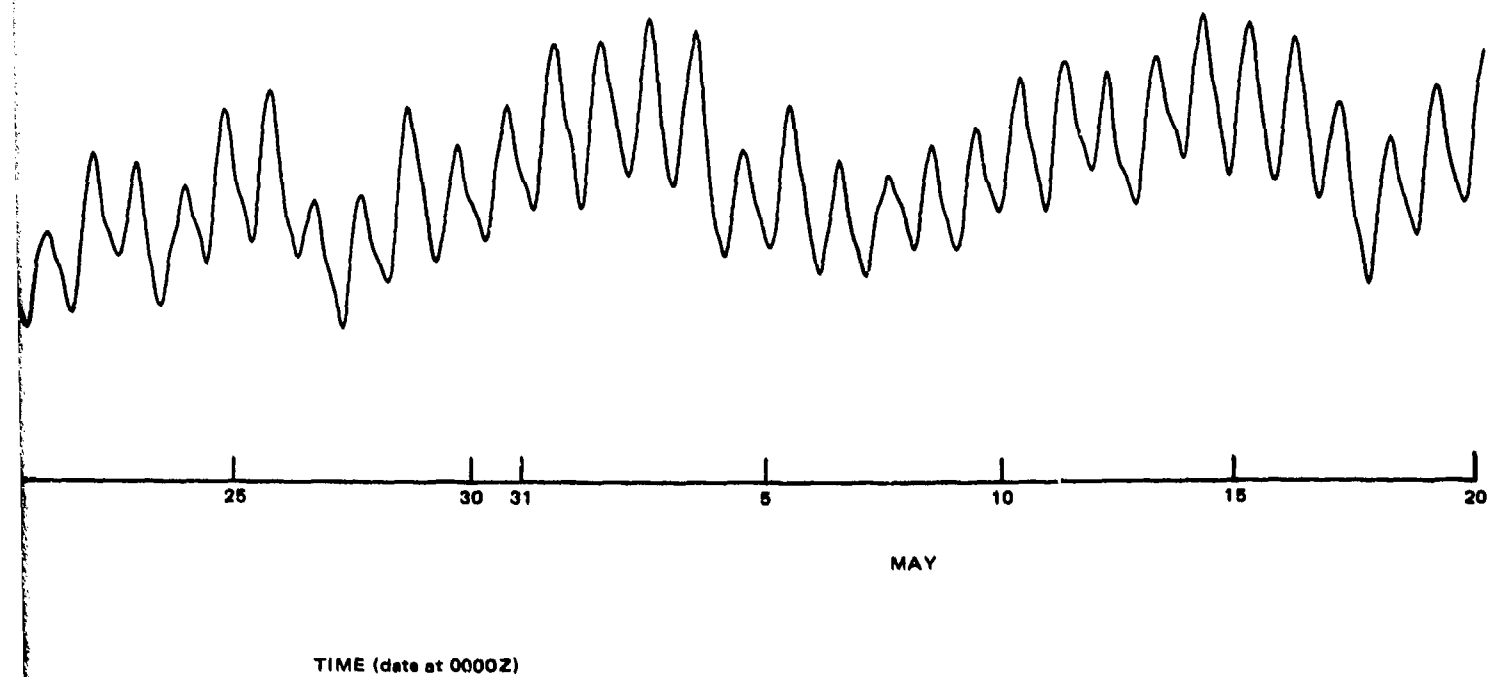


Figure 262. Air temperature fluctuations
7 April to 20 May 1971

G 6799

-487/488-

TR 72-3

ATMOSPHERIC PRESSURE

FOURIER TRANSFORM

GC-AZ

7 APR-19 MAY 1971

■ PRESSURE

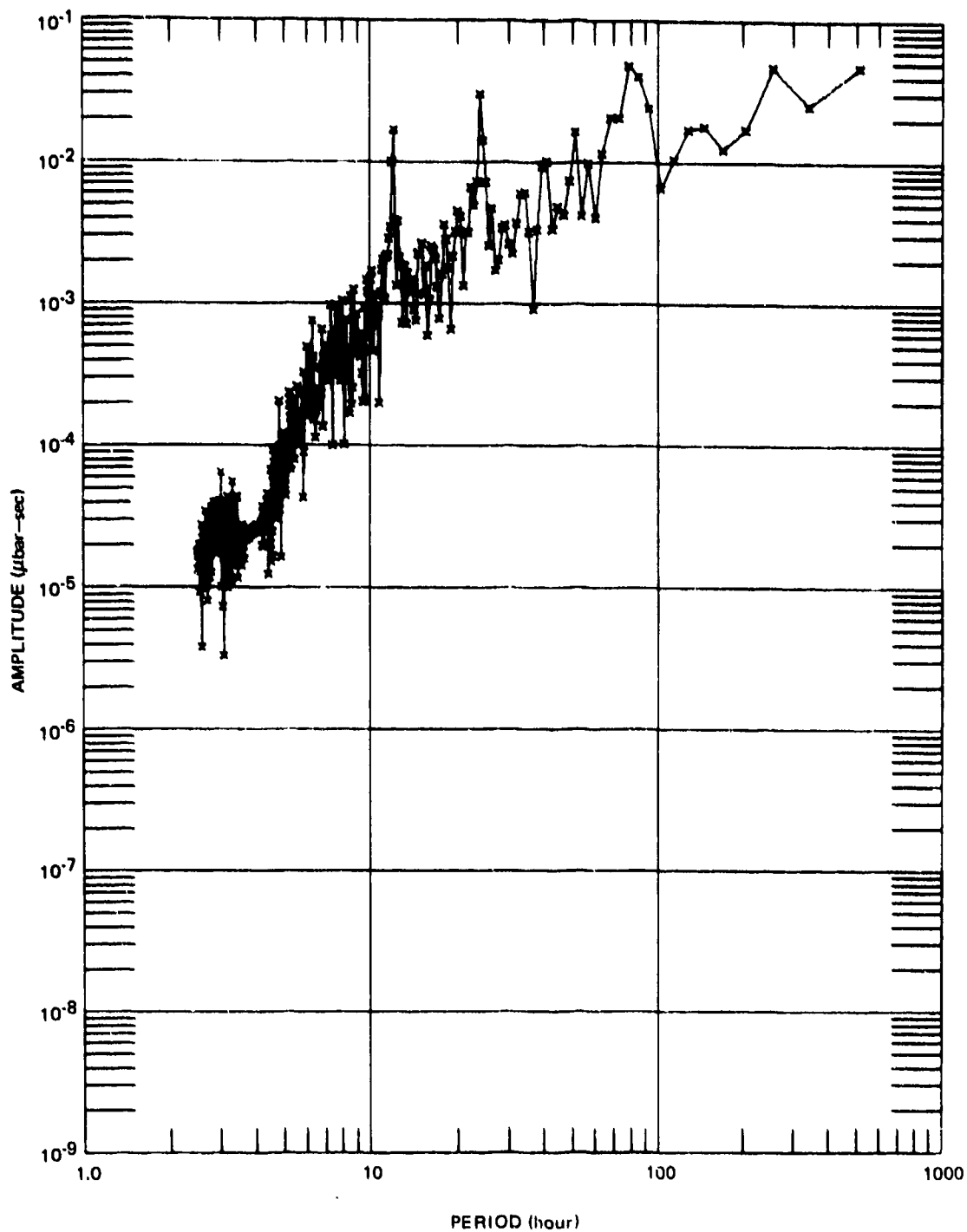


Figure 263. Fourier transform amplitude of observed air pressure
7 April to 19 May 1971

G 6800

ATMOSPHERIC PRESSURE 1074 SAMPLES, 255 LAGS, 1 SPM, PARZEN SMOOTHING

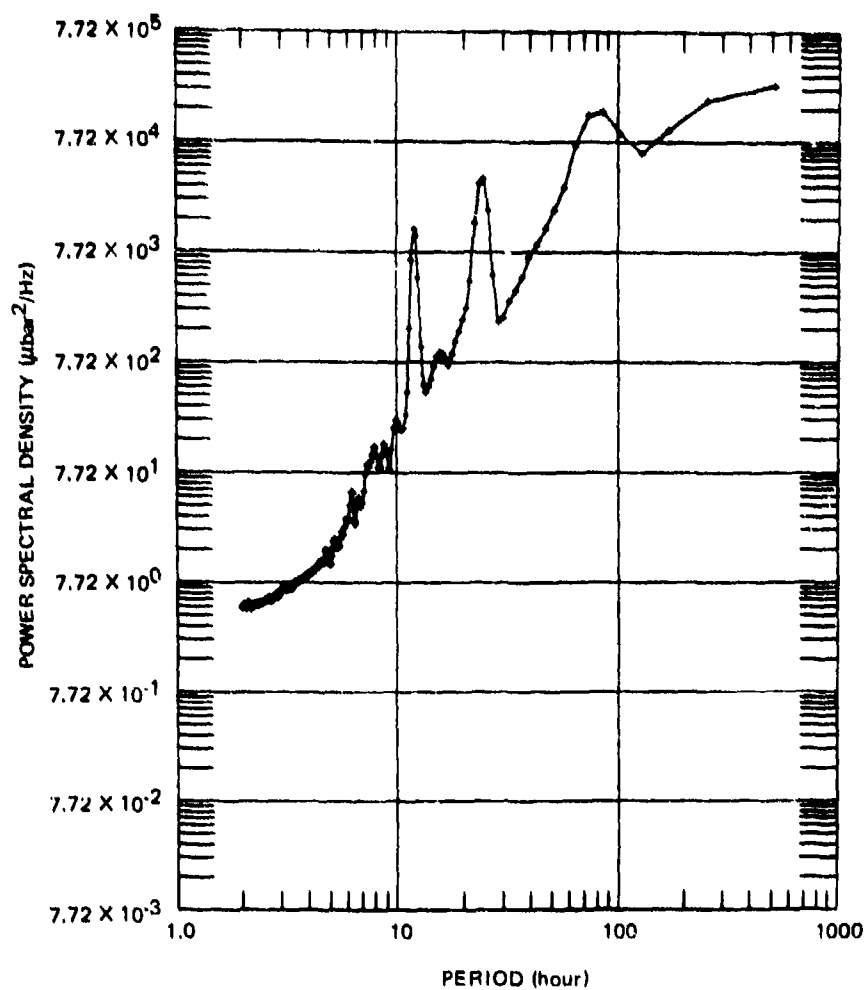


Figure 264. Power spectral density of observed air pressure
7 April to 19 May 1971

G 6801

TEMPERATURE
FOURIER TRANSFORM
* TEMPERATURE

GC-AZ
7 APR-19 MAY 1971

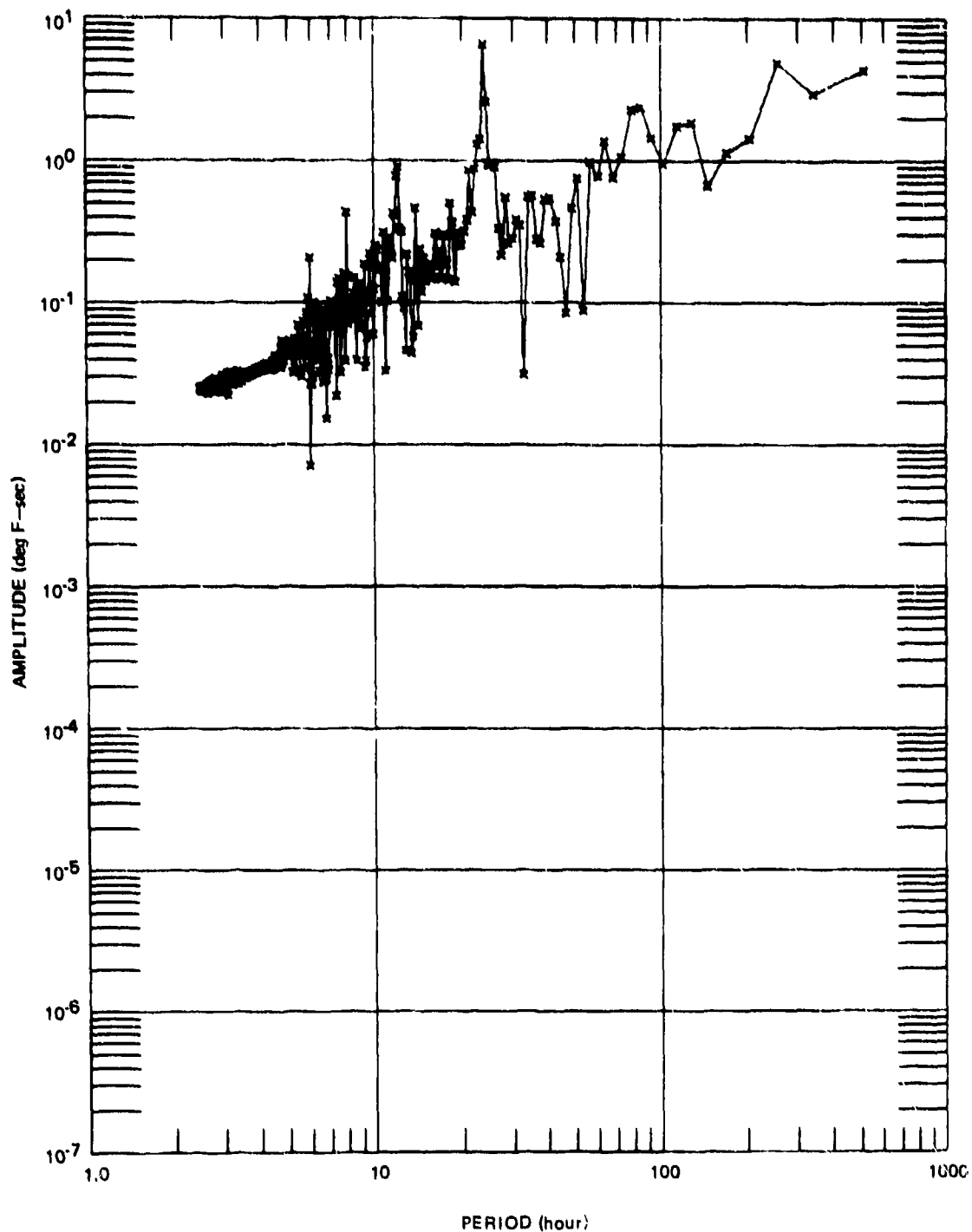


Figure 265. Fourier transform amplitude of observed air temperature
7 April to 19 May 1971

G 6802

TEMPERATURE
1024 SAMPLES, 255 LAGS, 1 SPH, PAREN SMOOTHING

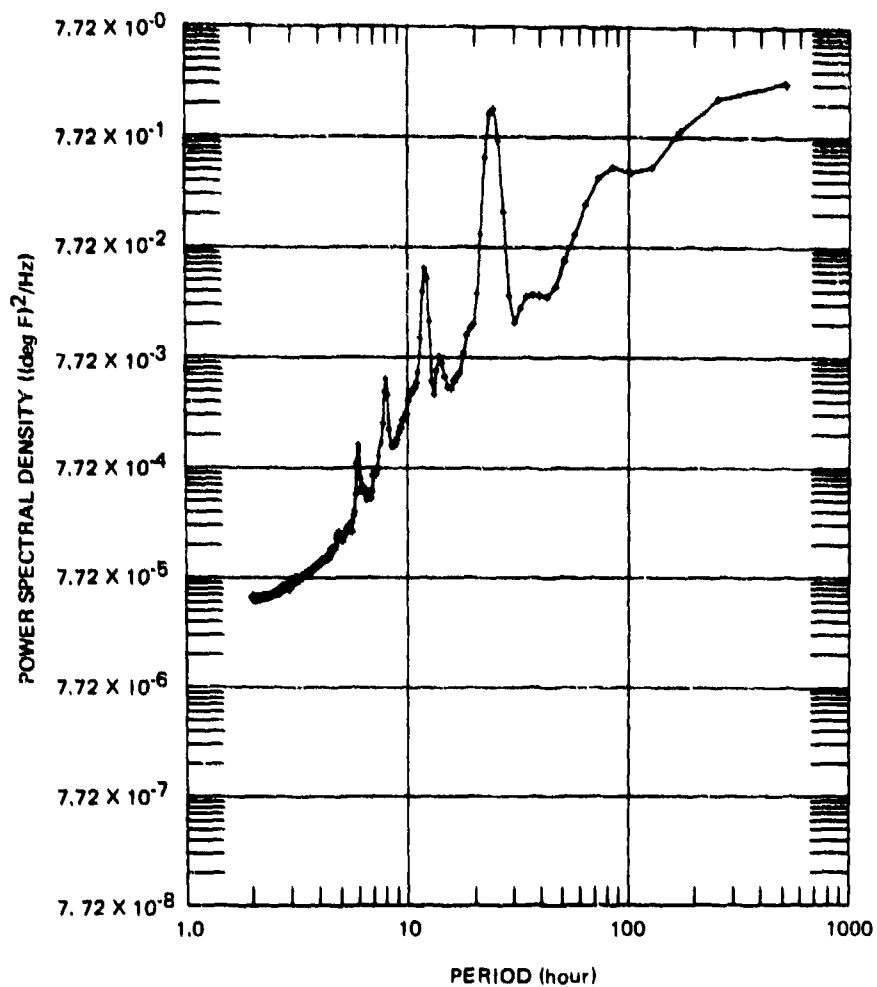
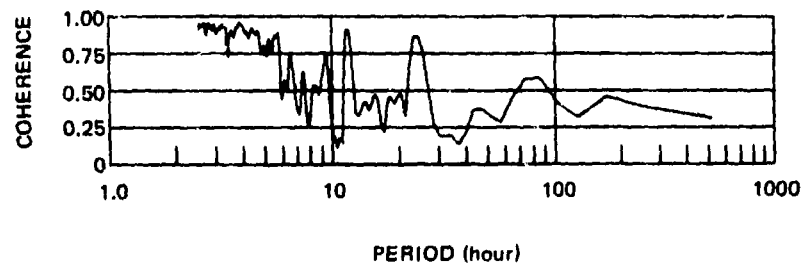


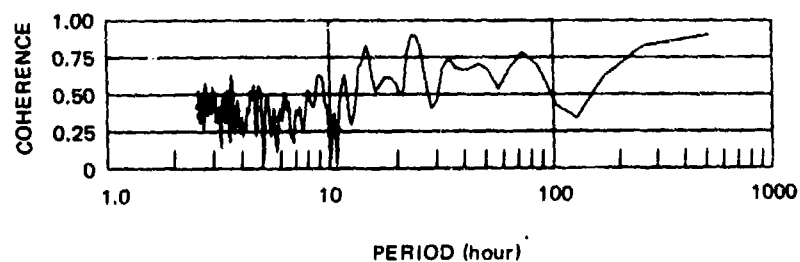
Figure 266. Power spectral density of observed air temperature
7 April to 19 May 1971

G 6803

EARTH TIDE
1024 SAMPLES, 256 LAGS, 1.0SPH, PARZEN SMOOTHING
QC-AZ PRESS X 528
7 APR-19 MAY 1971



EARTH TIDE
1024 SAMPLES, 256 LAGS, 1.0SPH, PARZEN SMOOTHING
QC-AZ PRESS X 53258
7 APR-19 MAY 1971



EARTH TIDE
1024 SAMPLES, 256 LAGS, 1.0SPH, PARZEN SMOOTHING
QC-AZ PRESS X 5558
7 APR-19 MAY 1971

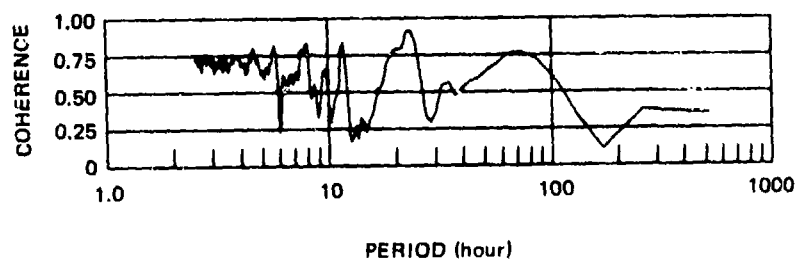


Figure 267. Coherence between air pressure and each strain component 7 April to 18 May 1971

G 6804

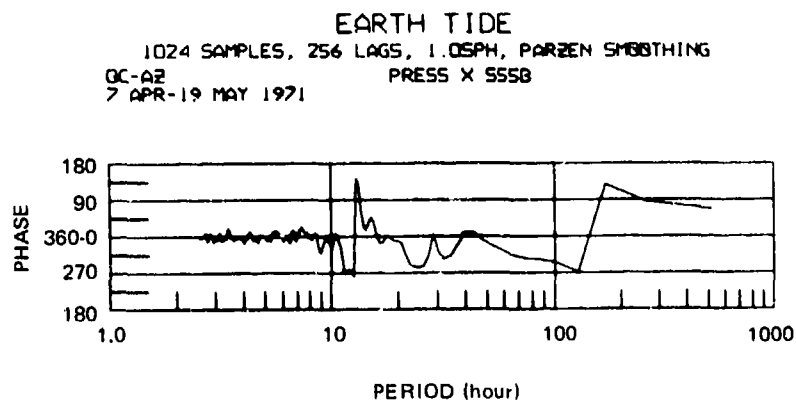
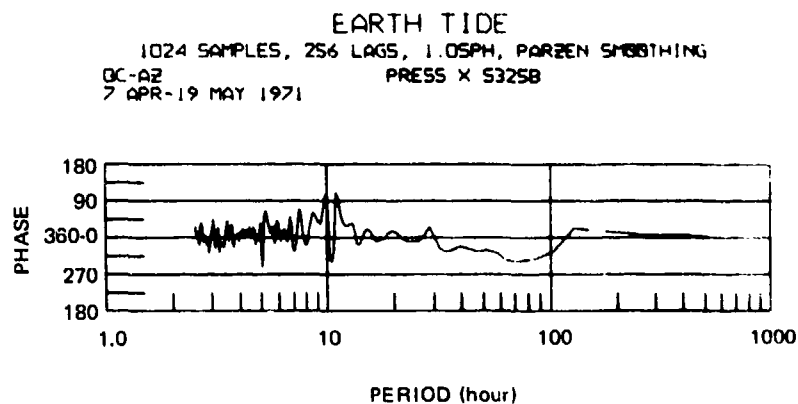
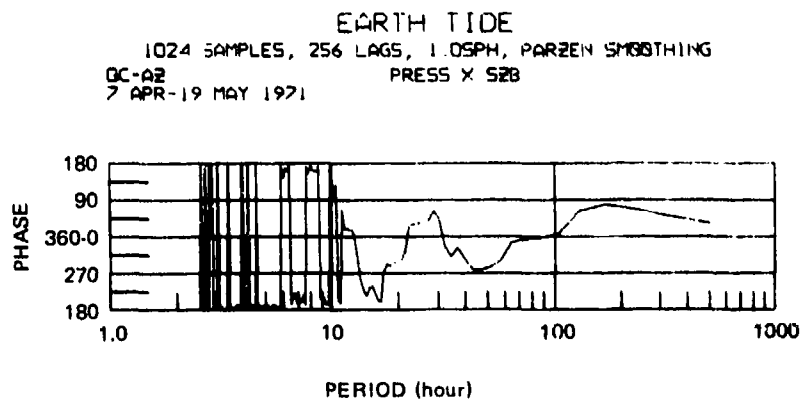
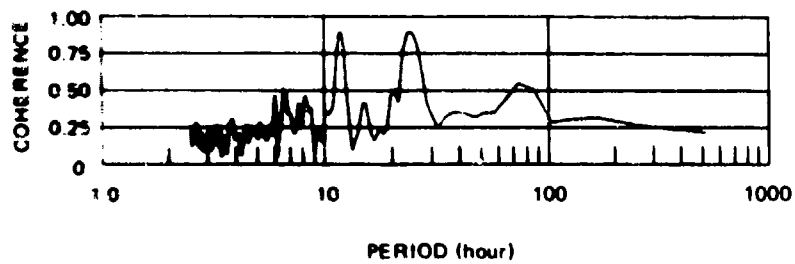


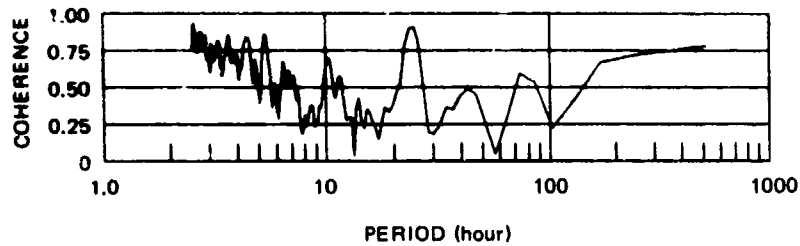
Figure 268. Phase angle that each strain component leads air pressure 7 April to 18 May 1971

G 6805

EARTH TIDE
1024 SAMPLES, 256 LAGS, 1.0SPH, PARZEN SMOOTHING
QC-A2 TEMP X 523
7 APR-19 MAY 1971



EARTH TIDE
1024 SAMPLES, 256 LAGS, 1.0SPH, PARZEN SMOOTHING
QC-A2 TEMP X 53258
7 APR-19 MAY 1971



EARTH TIDE
1024 SAMPLES, 256 LAGS, 1.0SPH, PARZEN SMOOTHING
QC-A2 TEMP X 5558
7 APR-19 MAY 1971

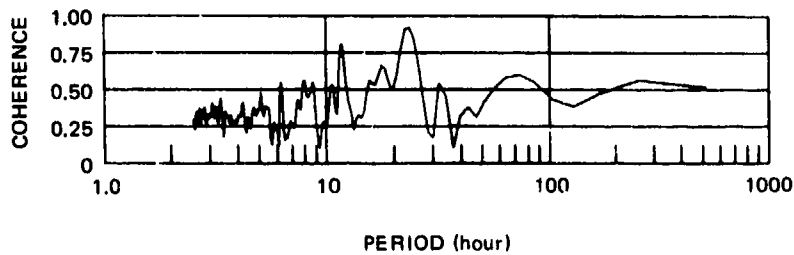


Figure 269. Coherence between air temperature and each strain component 7 April to 18 May 1971

G 6806

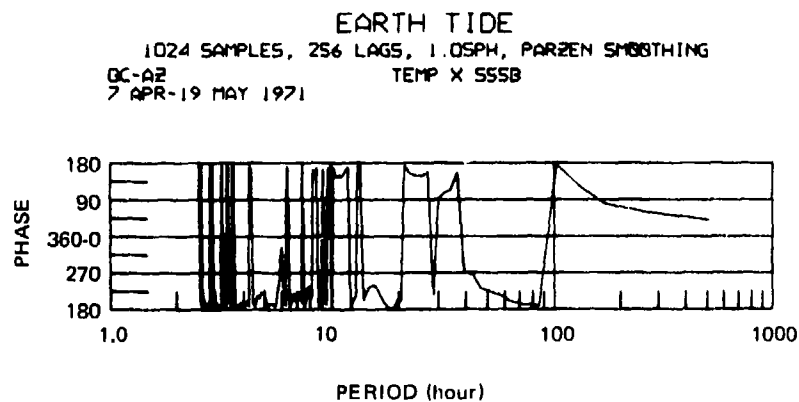
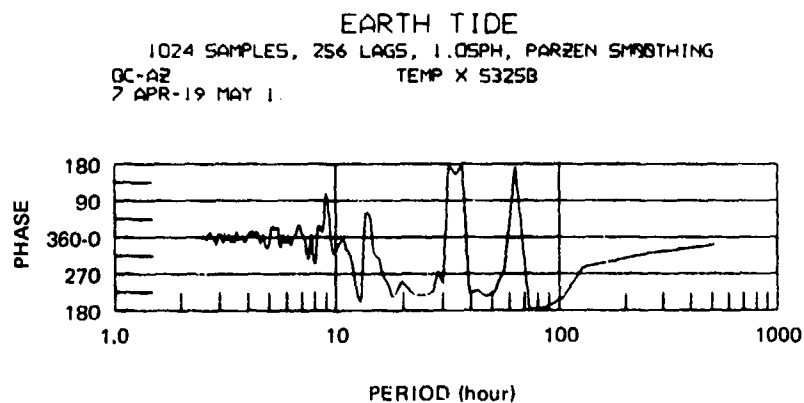
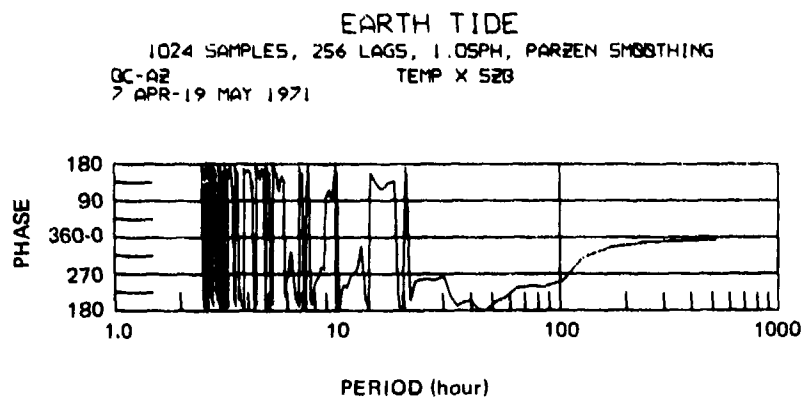


Figure 270. Phase angle that each strain component leads air temperature 7 April to 18 May 1971

G 6807

Table 24. Amplitude ratio, coherence, and phase angle of observed strain to pressure or temperature from power spectral density analysis

Strain component	Pressure		Temperature	
	Diurnal	Semi-diurnal	Diurnal	Semi-diurnal
SZB				
Amplitude ratio	$4.38 \times 10^{-12} \frac{\text{strain}}{\mu\text{bar}}$	$6.22 \times 10^{-12} \frac{\text{strain}}{\mu\text{bar}}$	$6.80 \times 10^{-10} \frac{\text{strain}}{\text{deg F}}$	$3.05 \times 10^{-10} \frac{\text{strain}}{\text{deg F}}$
Coherence	0.87	0.92	0.90	0.90
Phase angle	35° lead	20° lead	103° lag	88° lag
S325B				
Amplitude ratio	$2.02 \times 10^{-12} \frac{\text{strain}}{\mu\text{bar}}$	$0.74 \times 10^{-12} \frac{\text{strain}}{\mu\text{bar}}$	$3.31 \times 10^{-10} \frac{\text{strain}}{\text{deg F}}$	$3.09 \times 10^{-10} \frac{\text{strain}}{\text{deg F}}$
Coherence	0.90	0.64	0.91	0.59
Phase angle	9° lag	42° lead	142° lag	35° lag
S55B				
Amplitude ratio	$2.78 \times 10^{-12} \frac{\text{strain}}{\mu\text{bar}}$	$1.94 \times 10^{-12} \frac{\text{strain}}{\mu\text{bar}}$	$4.50 \times 10^{-10} \frac{\text{strain}}{\text{deg F}}$	$0.87 \times 10^{-10} \frac{\text{strain}}{\text{deg F}}$
Coherence	0.92	0.85	0.92	0.82
Phase angle	74° lag	86° lag	151° lead	163° lead

where $\text{erf}\{y\}$ is the error function of y and k is the diffusivity of the solid. The rate of cooling at any point is

$$-\frac{\partial v}{\partial t} = \frac{VX}{2\sqrt{\pi kt^3}} \exp\left(-\frac{X^2}{4kt}\right) \quad (111)$$

The temperature gradient at any point is

$$\frac{\partial v}{\partial x} = \frac{V}{\sqrt{\pi kt}} \exp\left(-\frac{X^2}{4kt}\right) \quad (112)$$

Equations (111) and (112) can be expressed in terms of the parameter $\frac{X}{2\sqrt{kt}}$ as

$$-\frac{t\sqrt{\pi}}{V} \frac{\partial v}{\partial t} = \frac{X\sqrt{\pi}}{2V} \frac{\partial v}{\partial X} = \frac{X}{2\sqrt{kt}} \exp\left(-\frac{X^2}{4kt}\right) \quad (113)$$

The right-hand equality of equation (113) is in the form of

$$y \exp(-y^2) \quad (114)$$

This is the mathematical relationship that was used to relate temperature change to observed strain. The maximum of expression (114) is 0.4288 and it occurs when $y = 1/\sqrt{2}$. The fit to the data was done by graphical trial and error. The maximum strain deflection was scaled to 0.4288. The time from the beginning of the disturbance to the maximum strain was used to scale the time axis. Generally, an acceptable fit was obtained on the third trial. The residual difference between the calculated and observed strain was then taken as the earth tide signal. On one occasion, the lights were left on for about 4 hr and it was necessary to convolve expression (114) with an assumed temperature time variation to match the observed strains. The fit of the experimental data to expression (114) implies that the observed thermal strain field is proportional to the temperature gradient in the rock. This implication is reasonable.

The earth tide strains can probably be corrected for thermal strains by convolving the air temperature with expression (114) and determining the amplitude of the transfer function by a least-squares estimate.

13.5 COMMENTS

The strain field at QC-AZ has been evaluated at the periods of the major tidal components. It has been determined that the strain field at the 100 m depth of the mine is linearly related to (coherent with) the gravitational forces from the moon and the sun, the air pressure, and the air temperature. The air pressure fluctuates with the gravitational forces. The air temperature

is affected by radiant energy from the sun. Air pressures and air temperatures interact with each other in accord with the gas laws.

The linear relationship between the gravitational forces, pressures, temperatures, and strains has prevented hard-number evaluation of the coupling of the QC-AZ strainmeters to the earth. The tidal analysis does substantiate the better coupling to the earth of the 55 deg azimuth strainmeter than the other two components. The ratio of about 2.3:1 between the predicted and the observed strains in the 55 deg azimuth is about the same as the ratio observed for Rayleigh waves. The ratio of observed to expected strains is larger at the 24 hr period on all three strain seismometers and on the vertical strainmeter at the 12 hr period. The ratio of predicted to observed strains is significantly different for the M_2 tides at 12.42 hr period than for the unseparated S_2 tide at 12.00 hr period and K_2 tide at 11.97 hr period. The ratio is also significantly different for the unseparated K_1 tide at 23.93 hr period and P_1 tide at 24.07 hr period than for the O_1 tide at 25.82 hr period.

Previous investigators have attributed discrepancies between observed tidal strains and predicted tidal strains to the effects of ocean loading only. The effects of pressure induced strains and of temperature induced strains have not been considered. The data presented in this section indicate that these disturbing forces must also be considered as well as the oceanic mass load.

14. ACOUSTIC SIGNALS ENHANCED BY STRAIN SEISMOGRAPHS

Strain seismographs respond to ground strains induced by air pressure loads on the surface. This section illustrates the recording and the enhancement of acoustic waves from two presumed acoustic sources. Section 14.1 is an application of the theory developed in section 7.6.2 and a review of the applicable literature on the propagation of acoustic waves in the atmosphere. Recordings of the acoustic wave induced strains and a time-varying spectral analysis of three acoustic wave trains are presented in section 14.2.

14.1 REVIEW OF THEORY AND LITERATURE

The strain seismographs respond to ground strain induced by air pressure loads on the surface. This response was discussed in section 7.6 as related to noise on the strain seismographs during intervals of large air pressure fluctuations that are accompanied by high winds. This section is concerned with the strain seismograph as a technique for detecting and enhancing acoustic waves.

The strain seismograph improves the signal-to-noise ratio of an acoustic wave to wind-related noise because of the depth attenuation factors. Repeating equation (6) from section 7.6.2, we have for the horizontal strain in the direction of propagation of a plane wave passing over a half-space

$$e_{11} = \frac{du_1}{dx_1} = \frac{P}{2\mu} \left(\frac{\mu}{\lambda + \mu} - \frac{|\omega_0| x_3}{c_0} \right) e^{-\frac{|\omega_0| x_3}{c_0}} e^{i\omega_0 \left(t - \frac{x_1}{c_0} \right)} \quad (6)$$

For a 50 sec acoustic wave, the wave length is about 15 km. Therefore, this model is a much better approximation for an acoustic wave than it is for air pressure (wind) noise, which has wave lengths of 100 to 700 m. There are two depth dependent (x_3) factors in equation (6). The amplitude coefficient in parentheses and the exponential depth attenuation factor $\exp(-|\omega_0| x_3 / c_0)$. As pointed out in section 7.6.2, the amplitude coefficient will become zero for some depth for each wave number $k_0 = \omega_0 / c_0$. To establish orders of magnitude, assume we have a plane acoustic wave of 50 sec period with a phase velocity of 300 m/sec and a plane pressure (wind noise) wave of the same period with a phase velocity of 30 m/sec (67 mi/hr).

If $\lambda = \mu$, with these parameters, we get

$\left(\frac{\mu}{\lambda + \mu} - k_0 x_3 \right) = 0$	acoustic wave at $x_3 = 1194$ m	wind noise at $x_3 = 119.4$ m
$\left(\frac{\mu}{\lambda + \mu} - k_0 x_3 \right)$ at 100 m =	0.458	0.080
$\exp(-k_0 x_3)$ at 100 m =	0.96	0.66

At the approximate 100 m depth of the QC-AZ mine, the strain from the assumed wind-related wave would be near the zero of the parentheses term and attenuated to 0.66 the strain at the surface from the exponential term. The strain from

the assumed acoustic wave would be almost the same as the strain at the surface. The ratio of the strains at depth to the strains at the surface are 0.88 for the acoustic wave and 0.11 for the wind-related wave, or an 8:1 S/N improvement.

The air pressure load creates tilts in the ground as well as strains. The tilt resulting from a plane pressure wave passing over a half-space is given in equation (9) of section 7.6.2. This equation is repeated here.

$$\text{tilt} = \frac{du_3}{dx_1} = \frac{iP}{2\mu} \left(\frac{\lambda+2\mu}{\lambda+\mu} + \frac{|\omega_0|x_3}{c_0} \right) e^{-\frac{|\omega_0|x_3}{c_0}} e^{i\omega_0 \left(t - \frac{x_1}{c_0} \right)} \quad (9)$$

The exponential depth attenuation factor is the same as for strain, but the amplitude coefficient is different and does not have a zero with depth. Using the assumed parameters above, at a 100 m depth, we get

$$\left(\frac{\lambda + 2\mu}{\lambda + \mu} + k_0 x_3 \right) = \begin{array}{cc} \text{acoustic wave} & \text{wind noise} \\ 1.54 & 1.92 \end{array}$$

The ratio of the tilts at the surface to tilts at depth are 1.48 for the acoustic wave and 1.27 for the wind-related wave, or a 1.2:1 S/N improvement. The tilt response of a horizontal inertial seismograph is equal to (g/ω^2) times the displacement response (see equation (14), section 7.7.1.) Therefore, the longer periods will be emphasized on the horizontal inertial seismograms. Since the XLP response (P_X seismograms) has a higher magnification at the long periods than the ALPS response (P_L seismograms), the tilt will be more evident on the XLP seismograms.

The propagation of acoustic-gravity waves in the atmosphere has been studied by several investigators. Press and Harkrider (1962) and Pfeffer and Zarichny (1962) represented the atmosphere with a model having many isothermal layers. The homogeneous problem of wave propagation was numerically evaluated for a number of models in terms of phase and group velocity dispersion curves for several modes of oscillation. Pfeffer and Zarichny (1963) improved and added to their earlier models by including two sound wave guides and a thicker atmosphere. They calculated theoretical dispersion curves and variations of kinetic energy with altitude for 11 normal modes and several model atmospheres. Comparison of the phase velocity and group velocity dispersion curves with the kinetic energy distribution with altitude led Pfeffer and Zarichny (1963) to the interpretation that there are two families of normal modes. The "quasi-horizontal modes" represent energy that propagates in the lower atmosphere and the "quasi-vertical modes" represent energy that propagates in the upper atmosphere. The "quasi-horizontal modes" are maxima in the group velocity curves; and since they propagate in the lower atmosphere, they are the modes recorded on barograms. Harkrider (1964) expanded the theory to include a source and presented amplitude spectra as well as dispersion curves for various source heights. He obtained a general fit to the observed dispersion curves of Donn and Ewing (1962a, 1962b). Harkrider (1964), from comparisons of theoretical and observed barograms from a large thermonuclear explosion, concluded that (1) the major features on the barogram can be explained by superposition of four modes; (2) different parts of the vertical temperature structure of the atmosphere control the relative excitation of these modes; (3) a scaled point source is sufficient to model thermonuclear explosions; (4) the observed shift in dominance of certain frequencies

with yield and altitude can be explained by means of empirical scaling laws; and (5) out to 50 deg from the source, the observed variation of amplitude with distance can be accounted for by geometrical spreading over a spherical surface. Pierce (1967) added a variable wind profile (west to east) to the variable temperature profile models employed by the previous investigators. In his model, Pierce (1967) found that the low frequencies (he considered periods of 1 to 10 min) travelled slightly faster and arrived earlier. Representative velocities in his solutions were

<u>Mode</u>	<u>Downwind</u>	<u>Upwind</u>
GR ₀	324.0 m/sec	296 m/sec
S ₀	323.6 m/sec	293 m/sec
S ₁	316 m/sec	285 m/sec

The dispersion curves for downwind and upwind propagation were similar in shape and the primary difference was only the net group velocity. Donn and Shaw (1967) presented 208 barograms made at 15 stations from 45 nuclear explosions together with the related data on source, times, and distances. Balachandran and Donn (1968) used normal mode theory to study the propagation of acoustic-gravity waves in a multi-layer model of the atmosphere with constant temperature and uniform wind in each layer. The envelope of their theoretical dispersion curves showed a good agreement with empirical dispersion curves from time-stepped Fourier transforms of actual barograms. They found that strong winds in the direction of propagation near 100 km altitude and opposing low altitude winds are favorable for inverse dispersion at long periods. Harkrider and Wells (1968) investigated the effect on dispersion curves of terminating the upper extreme of an atmospheric model with a free surface, rigid surface, and with a half-space beginning at 220, 310, and 490 km. All of their models showed a mode characterized by a long period velocity asymptote without a long period cutoff. This mode corresponds to the deep ocean surface wave mode with a long period limit of \sqrt{gH} where g is the acceleration of gravity and H is the thickness of the layer. Their kinetic energy density profiles showed that this early arriving wave travels in the upper atmosphere. Yamamoto (1968) has made the most complete study to date of propagation velocities over the northern hemisphere. He plotted isochrone maps of the short-arc wave arrival and the long-arc wave arrival from the Soviet nuclear explosion of 30 October 1961. The wind effects were excluded by taking the mean speed for the two paths. He found that the mean speed of propagation was in the range from 275 m/sec to 350 m/sec. Over the central Pacific, he found mean speeds higher than 350 m/sec; and over the Arctic region and off England, the mean speeds were lower than 275 m/sec. These high and low speeds could not be explained with the observed temperature structure up to the lower stratosphere. The difference of the propagation speed between the short-arc and long-arc waves gave a wind-induced increment of velocity which exceeded 50 m/sec over the Davis Strait and 20 m/sec north of the West Indies. A wind distribution that would give these velocity increments could not be found below the height of 25 km. Balachandran (1970) extended his previous study of the effects of winds on the dispersion of acoustic-gravity waves. He concluded that waves with periods less than about 400 sec were influenced mainly by winds close to the ground, whereas waves with periods longer than about 400 sec were influenced by high-altitude as well as low-altitude winds. Strong winds at altitudes near 100 km in the direction of propagation of the waves and winds near the ground in a direction opposite to

that of the waves were favorable for inverse dispersion in group velocities at long periods. Opposite wind conditions favored normal dispersion at all periods.

Ben-Menahem (1972) reports simultaneous recording on a mercury tiltmeter and on an infrasonic microbarograph of the first gravity mode (GR_0) and three acoustic modes (S_0 , S_1 , S_2) from the Chinese nuclear air blast of 14 October 1970. The recordings were made at Eilat, Israel, 5024.5 km from the NOS located epicenter. Observed group velocities were 293.0 to 280.0 km/sec in the period range from 400 to 48 sec. Ben-Menahem believes that the group velocities were decreased about 10 m/sec by westerly winds. He observed 300 μ bar pressure and 3×10^{-10} rdn tilt at 240 sec. These values give a transfer function of 10^{-12} rdn/ μ bar which Ben-Menahem states applies from 20 to 400 sec. Ben-Menahem (1972) derived expressions for pressure generated tilts and displacements. His expressions are similar to those of Sorrells (1969, Sorrells and Der, 1970, and Sorrells and Goforth, 1972) but are not as complete and are based on some assumptions that are not in accord with observations.

Tilt is part of the strain component e_{13} and is expected to be of the same order of magnitude as the strain per equations (6) and (9) above. Indeed, Ben-Menahem's transfer function of 10^{-12} rdn/ μ bar is identical to the 10^{-12} strain/ μ bar observed near 240 sec at QC-AZ for the wind related strain/pressure transfer function plotted in figures 100 through 103 and 105 through 107.

14.2 ACOUSTIC SIGNALS

This section presents the recording of an acoustic signal on the strain seismographs at QC-AZ and the group velocity dispersion curves of this signal for the short-arc wave path and for the long-arc wave path. Similar group velocity dispersion curves are also presented for another acoustic signal.

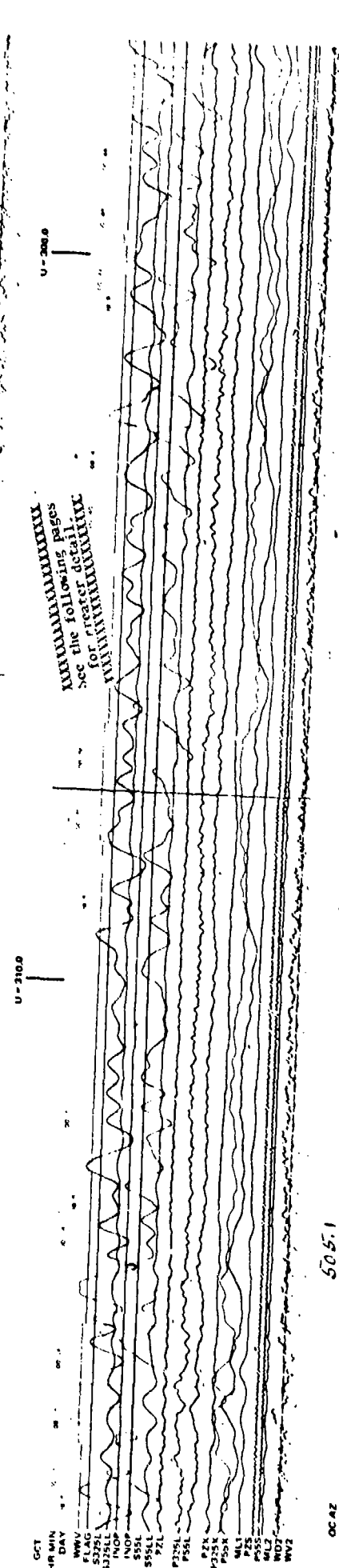
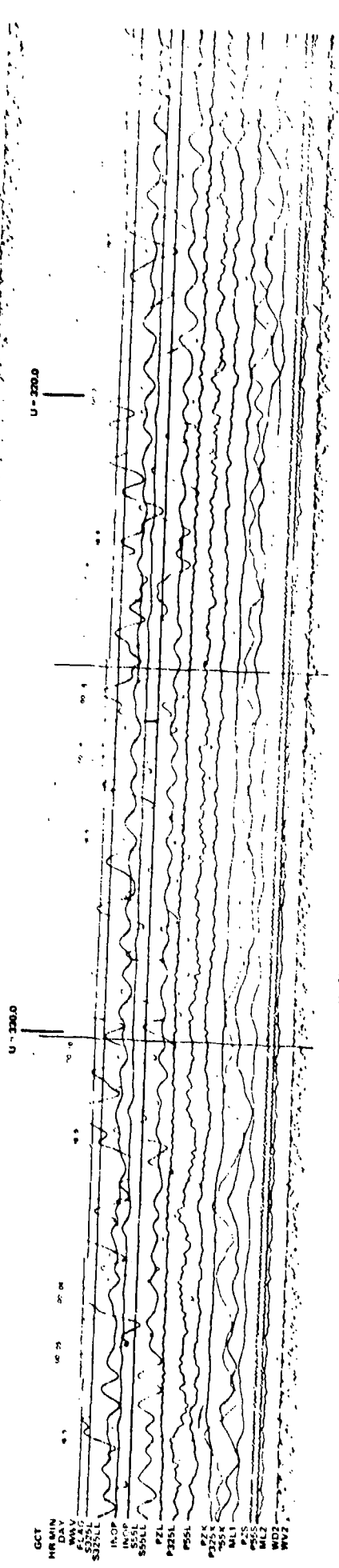
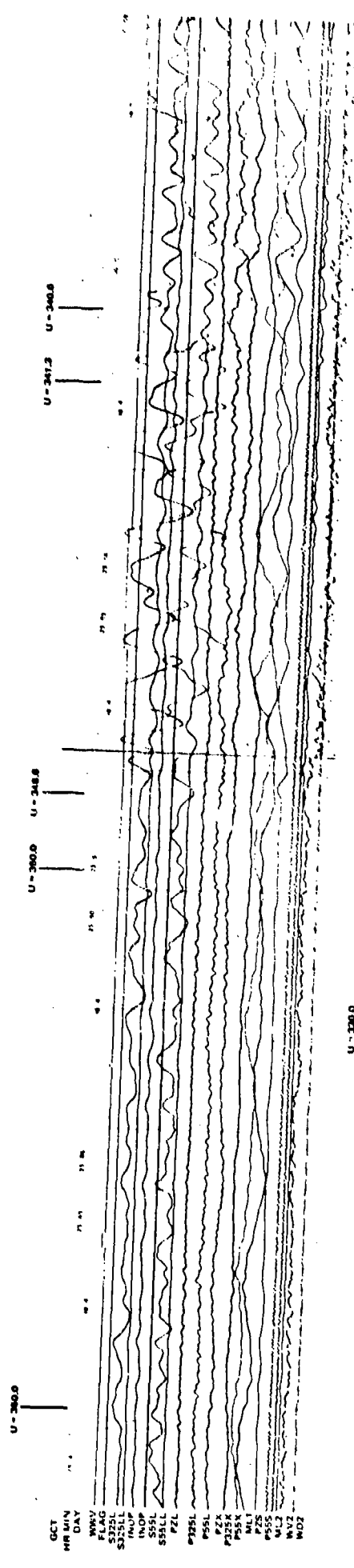
Signals from two presumed acoustic sources are presented. The NOS PDE data on the epicenters and the calculated epicentral distances and azimuths are given in table 25.

The seismograms recorded on camera 1 from the acoustic wave that travelled the short-arc from the 3 July 1970 presumed source are illustrated in figure 271(a) and (b). Group velocities U in m/sec are indicated in the figure. As predicted by the theory, the strain seismographs and the inertial seismographs respond to the acoustic wave. The largest response is by the two strain seismographs, with the P325X and P55X horizontal inertial seismographs responding to the tilts. The signal is also visible on the other four long period inertial seismographs. At the time this signal was recorded, the ML2 outside microbarograph and the ML1 inside microbarograph did not have their normal response. The air conditioner had failed in van No. 2 and tape recorders Nos. 2 and 3 could not be operated. When the microbarograph signals were turned off at the input to the tape recorders, a resistance to ground was put in parallel with a capacitor in the microbarograph electronics. These components formed a high-pass filter and attenuated the signal. The ML2 microbarograph did respond to the shorter period signals. (The ML2 microbarograph was operational during the 30 May 1970 signal and the group velocity dispersion curve from it will be shown later.)

The horizontal strain seismograms S325L and S55L are very similar in shape and opposite in polarity. If the longitudinal stress concentration factors are the

Table 25. Epicenter data

Date	Day	Origin time(GCT)	Lat. deg	Long. deg	Depth km	Location	Mb	Distance		Azimuth Sta. to Epi., deg
								deg	km	
30 May 70	150	1759:58.5	22.2S	138.8W	0	Tuamotu Archipelago region	4.7	60.9	6769	209.0
3 July 70	184	1829:59.1	21.8S	139.2W	0	Tuamotu Archipelago region	4.8	60.7	6747	209.6



See the following pages
for greater details

505.0

505.1

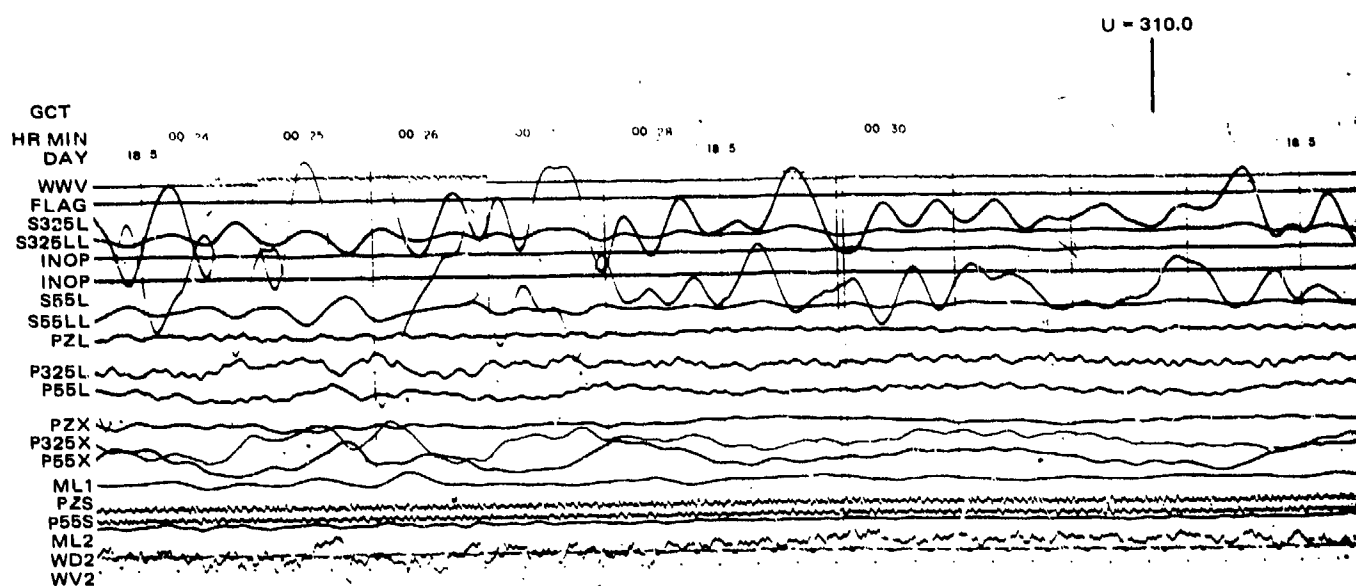
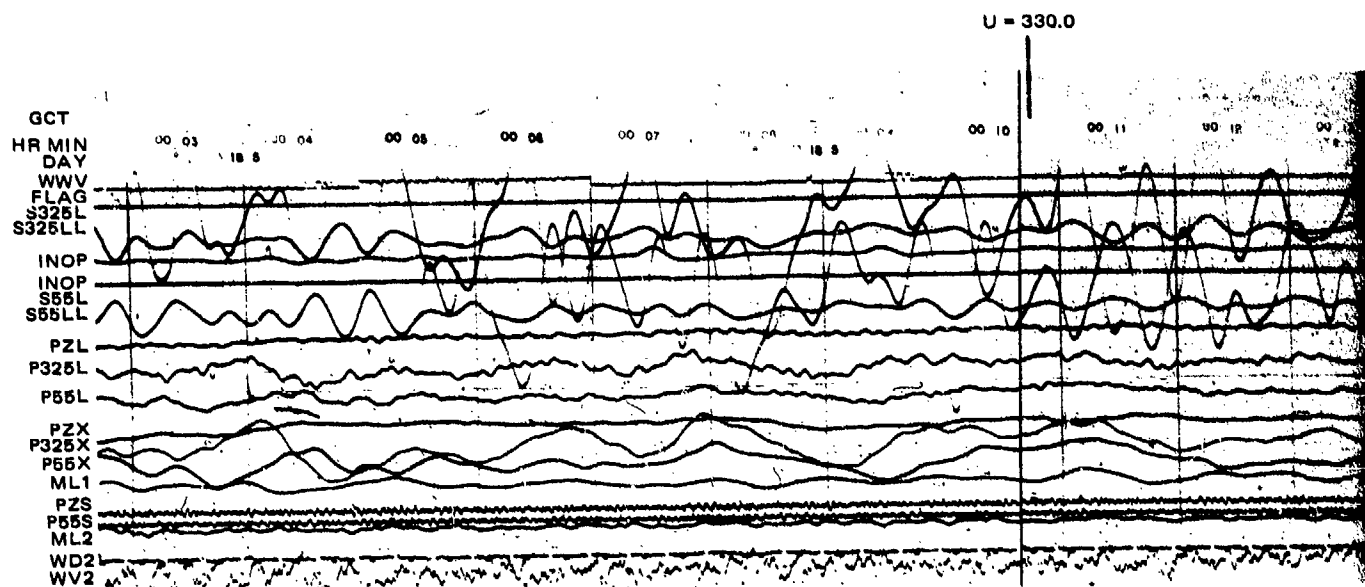
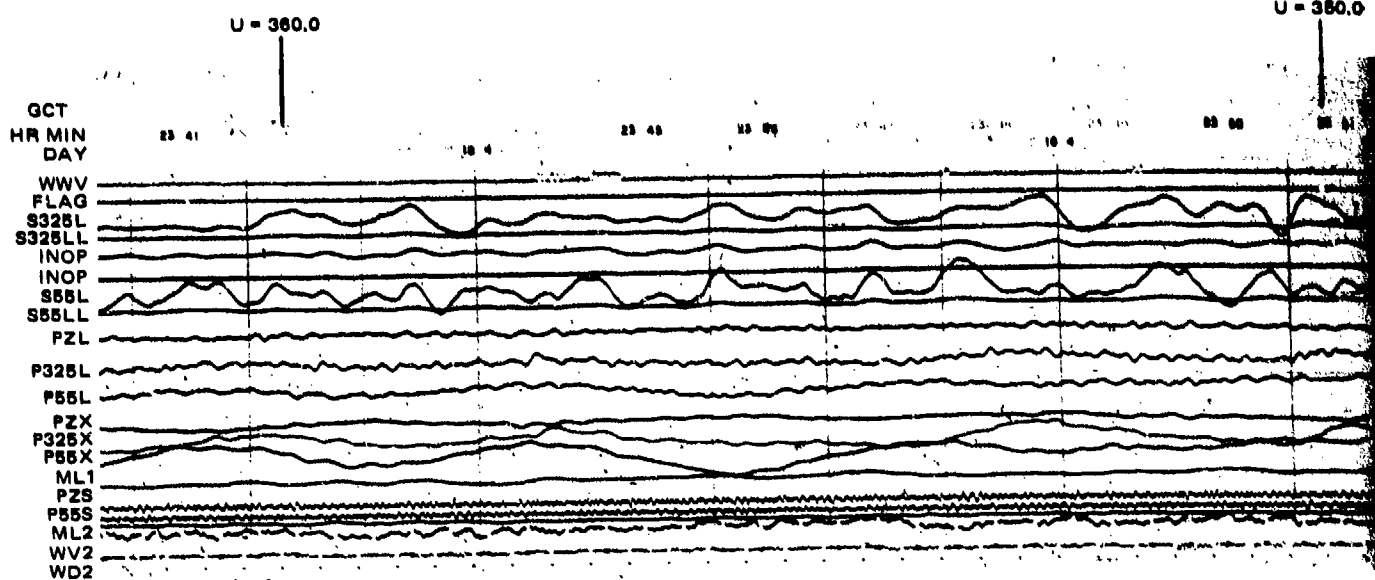
505.2

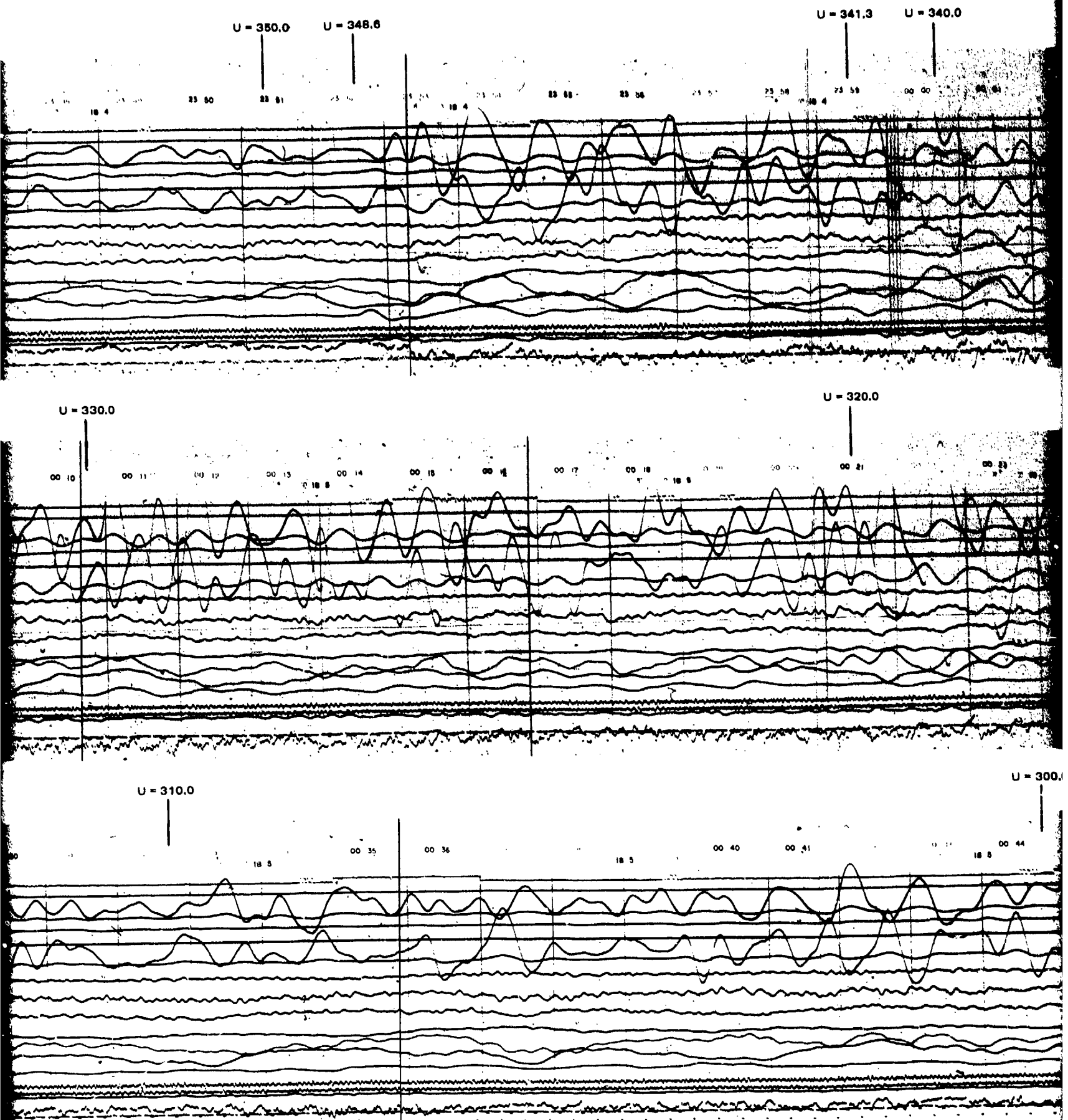
Figure 271a. Recordings of ground strain, ground tilt, ground vertical displacement, and air pressure variations from a presumed acoustic source in the Tuamotu Archipelago region, 3 July 1970

505.1

-505/506-

TR 72-3

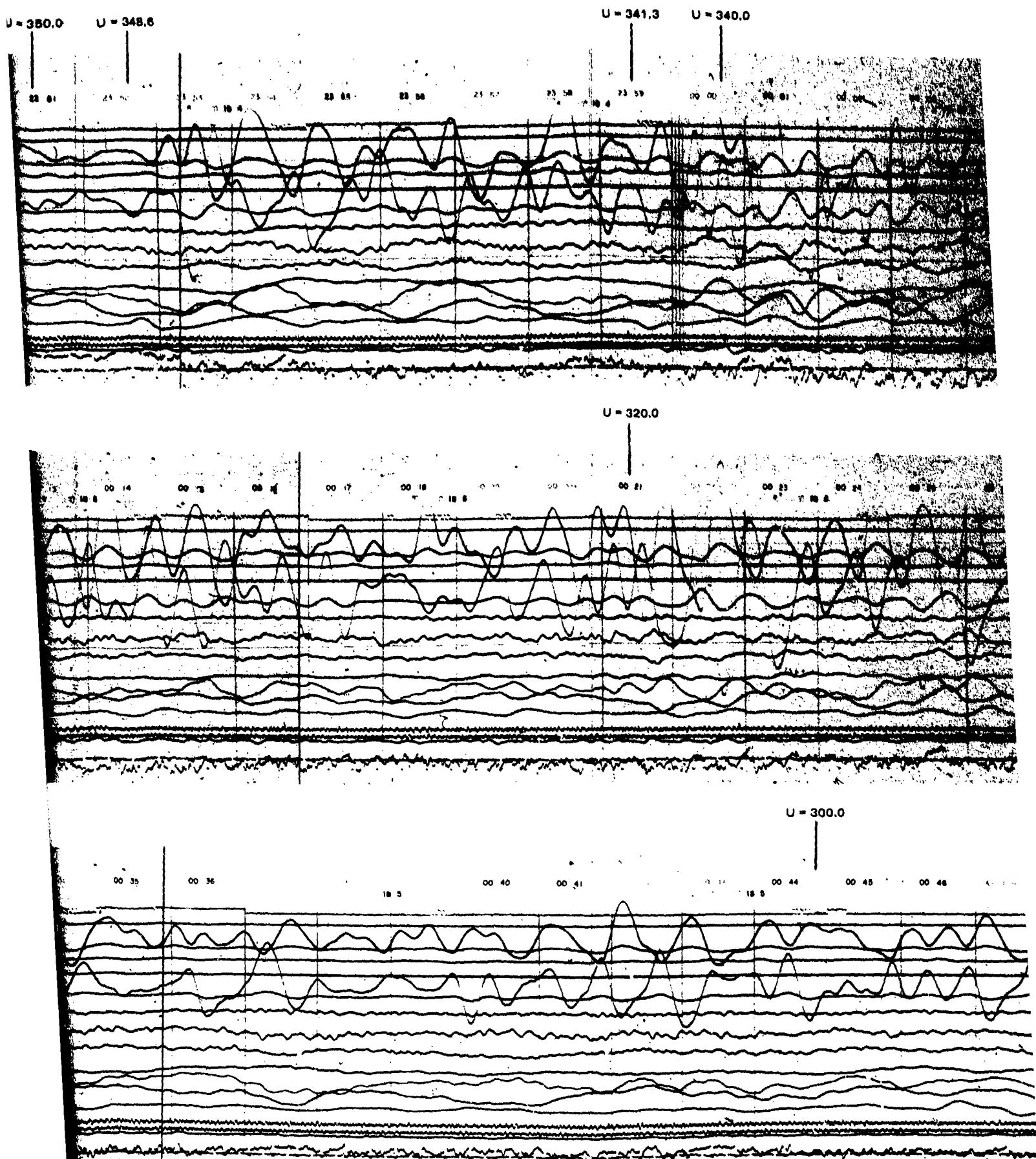




505.2

Figure 27la. Record of ground tilt, ground vertical displacement, and air pressure variations from an acoustic source in the Tuomotu Archipelago region, 3 July 1970

506.1

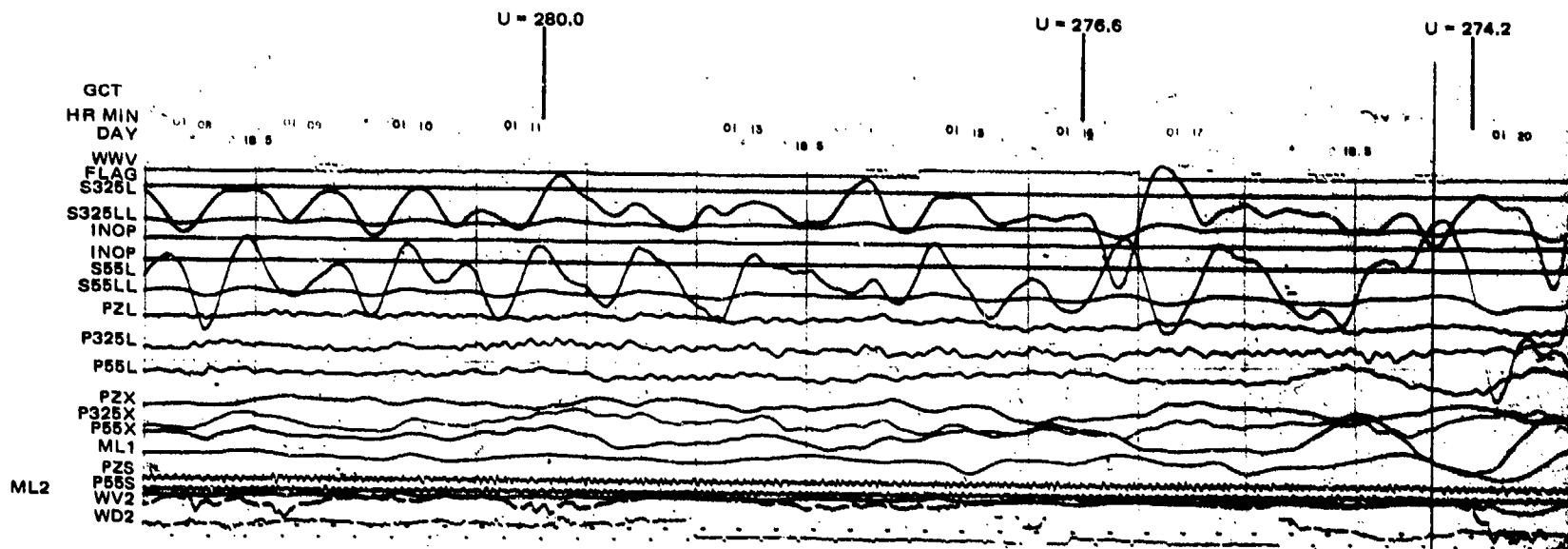
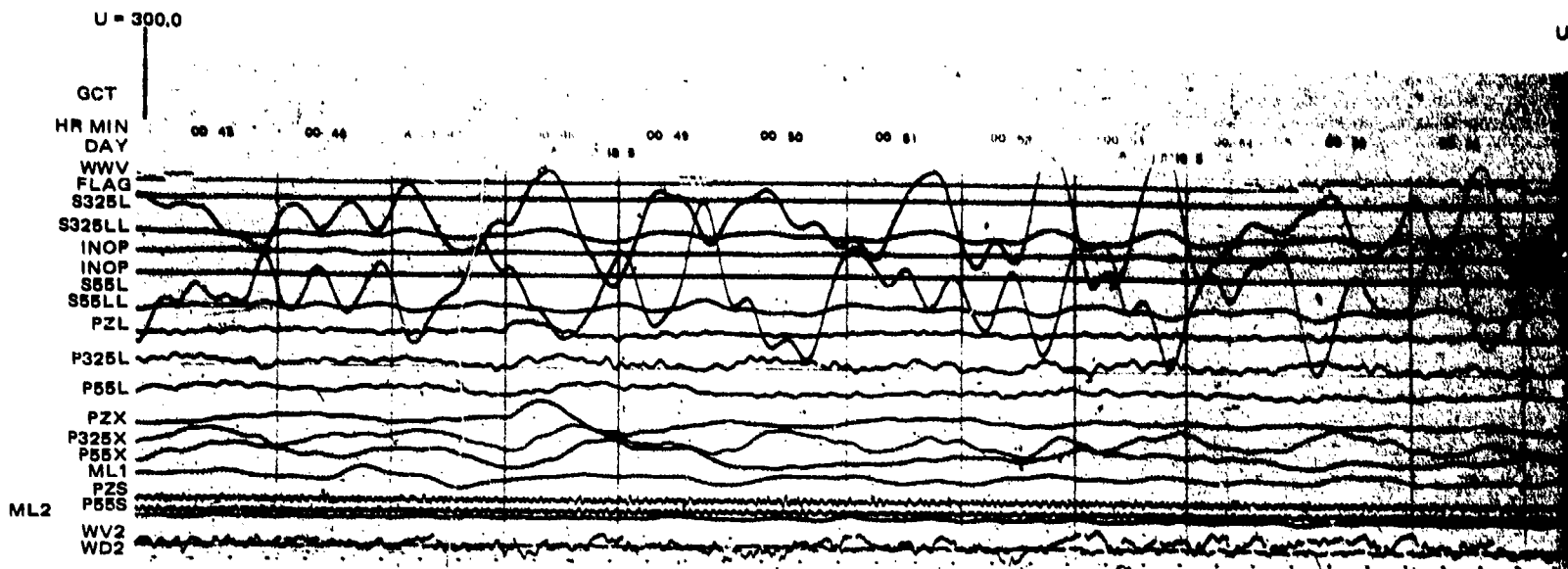


2 Figure 271a. Recordings of ground tilt, ground vertical displacement, and air pressure variations from a presumed acoustic source in the Tuomotu Archipelago region, 5 July 1970

50611

-505/506-

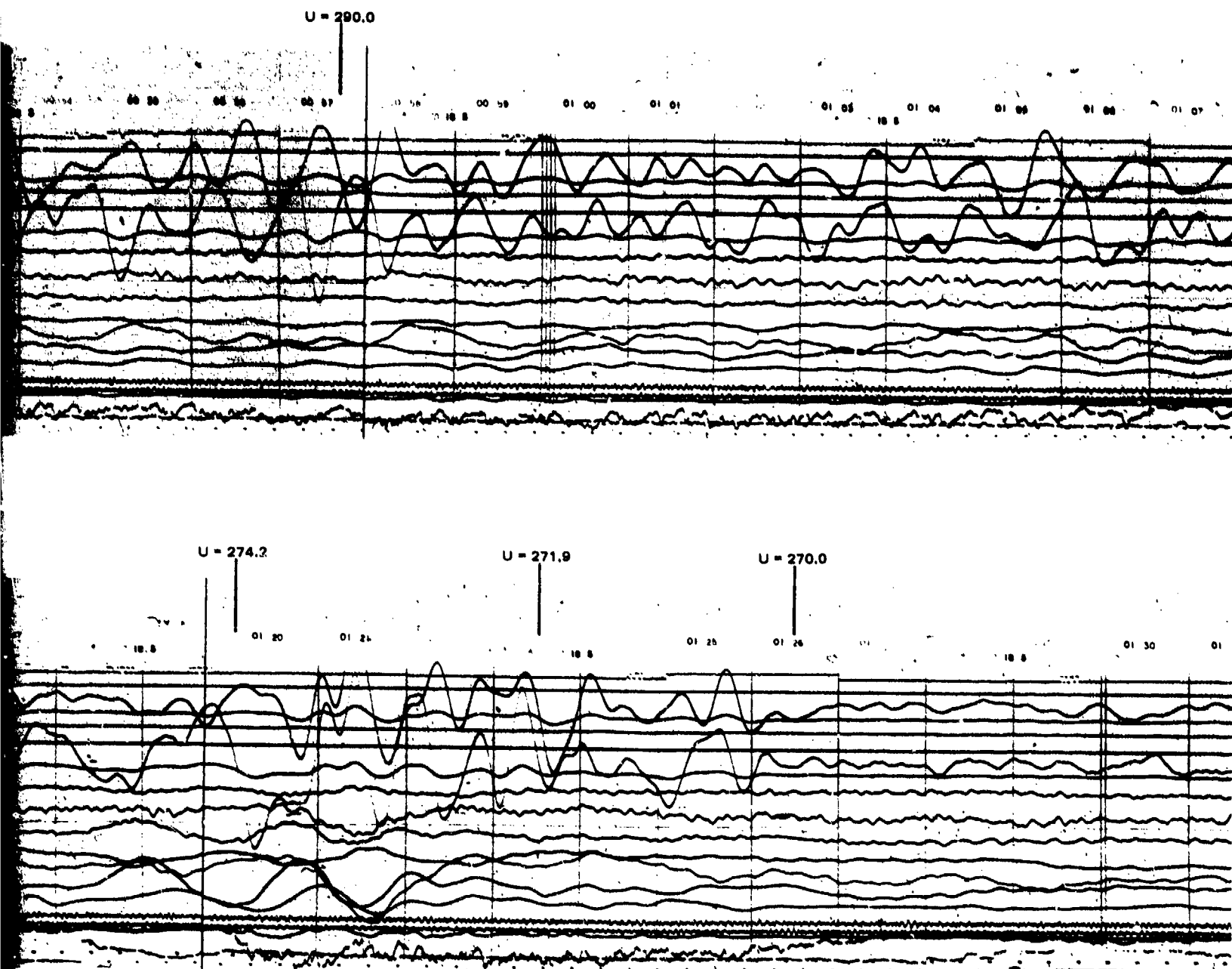
TR



QC-AZ
RUN 185
3 JULY 1970

509.1

509.2



509.2

508.1
Figure 271b. Recordings of ground strain, ground tilt, ground vertical displacement, and air pressure variations from a presumed acoustic source in the Tuomotu Archipelago region, 3 July 1970

G 6809

-507/508-

TR 72-3

same sign as the hoop stress concentration factors as found by Barjansky (1944) (see discussion in section 12.2), the opposite polarity is predicted for one strainmeter mounted on the wall and the other strainmeter mounted on the floor. The same opposite polarity is also observed for wind-related strains as illustrated in figure 78 in section 7.6.3 and in figure 132 in section 8.1.2. Four large energy bursts can be seen in the seismograms at 2352:35Z ($U = 349$ m/sec), at 2359:30Z ($U = 341$ m/sec), at 0021:22Z ($U = 320$ m/sec), and at 0120:04Z ($U = 274$ m/sec). The signal started abruptly at 2552:35Z ($U = 349$ m/sec) and stopped abruptly at 0127:00Z ($U = 270$ m/sec). The abrupt stop with a large burst of energy is predicted by the theoretical results in the literature. All the models give a group velocity-versus-period curve in which all modes flatten toward the same group velocity at the short periods. The flat group velocity curve produces the burst of energy. The abrupt stop occurs because this velocity is the slowest velocity of the "quasi-horizontal modes" and represents the velocity in the lower sound channel at about 85 km altitude.

Group velocity versus period has been calculated from the seismograms and the barogram for several of the acoustic signals with the computer program GROUP. The program takes samples of the time series (digitized seismogram) in groups of moving windows centered at the time corresponding to a selected group velocity. Each window is four times the selected period. The time series in each window is detrended and then smoothed with a cosine squared taper to minimize side lobes. The smoothed time series is Fourier transformed into the frequency domain and the amplitude modulus is stored as a decibel (or logarithmic) value in a table with a row for each group velocity and a column for each of 42 periods in a selected decade. Thus, the printed table serves as a plot of the logarithm of the Fourier amplitude on a logarithmic period scale versus a linear group velocity scale. In the figures that follow, no correction has been made for instrument response. Direct comparisons between amplitudes can be made at any given period; but to compare amplitudes at different periods, the seismograph response must be used. The group velocity corresponding to each period is the maximum Fourier amplitude at that period.

The dispersion curves for the several modes in these figures have been drawn with the horizontal portions and with the vertical portions in the period range of the corresponding horizontal and vertical portions of the theoretical group velocity dispersion curves of Pfeffer and Zarichny (1963). The modes have been identified with the nomenclature of Pfeffer and Zarichny (1963) rather than the nomenclature of Harkrider (1964). Figure 272 is a plot of the theoretical dispersion curves from figure 7 of Pfeffer and Zarichny (1963); the scale is the same as the observed curves that follow. These curves were calculated for a model atmosphere with a half-space beginning at an altitude of 300 km and with no winds. The horizontal portions of the dispersion curves are the quasi-horizontal modes that travel primarily in the lower atmosphere and that are expected to be recorded at the surface of the earth. The vertical portions of the dispersion curves are the quasi-vertical modes that travel primarily in the upper atmosphere.

The dispersion curves from the 3 July 1970 presumed source will be discussed first. The group velocity dispersion curves calculated from the S55L horizontal strain seismogram in figure 271 are plotted in figure 273. This acoustic wave travelled the 6747 km short-arc from the source. Dispersion curves are interpreted for the fundamental mode F, the first acoustic mode 1A, the second acoustic mode 2A, the third acoustic mode 3A, and the fourth acoustic mode 4A. Two complete sets of

dispersion curves for the five modes have been interpreted from the data for this signal. The energy arrivals in the first set were earlier than the theoretical group velocities predict, but their group velocity of 341 to 349 m/sec is identical with the 350 m/sec observed by Yamamoto (1968) over the central Pacific Ocean. The energy arrivals in the second set of dispersion curves arrived in the group velocity window from 330 to 270 m/sec in almost identical agreement with the theoretical dispersion curves as slightly speeded up by west to east winds.

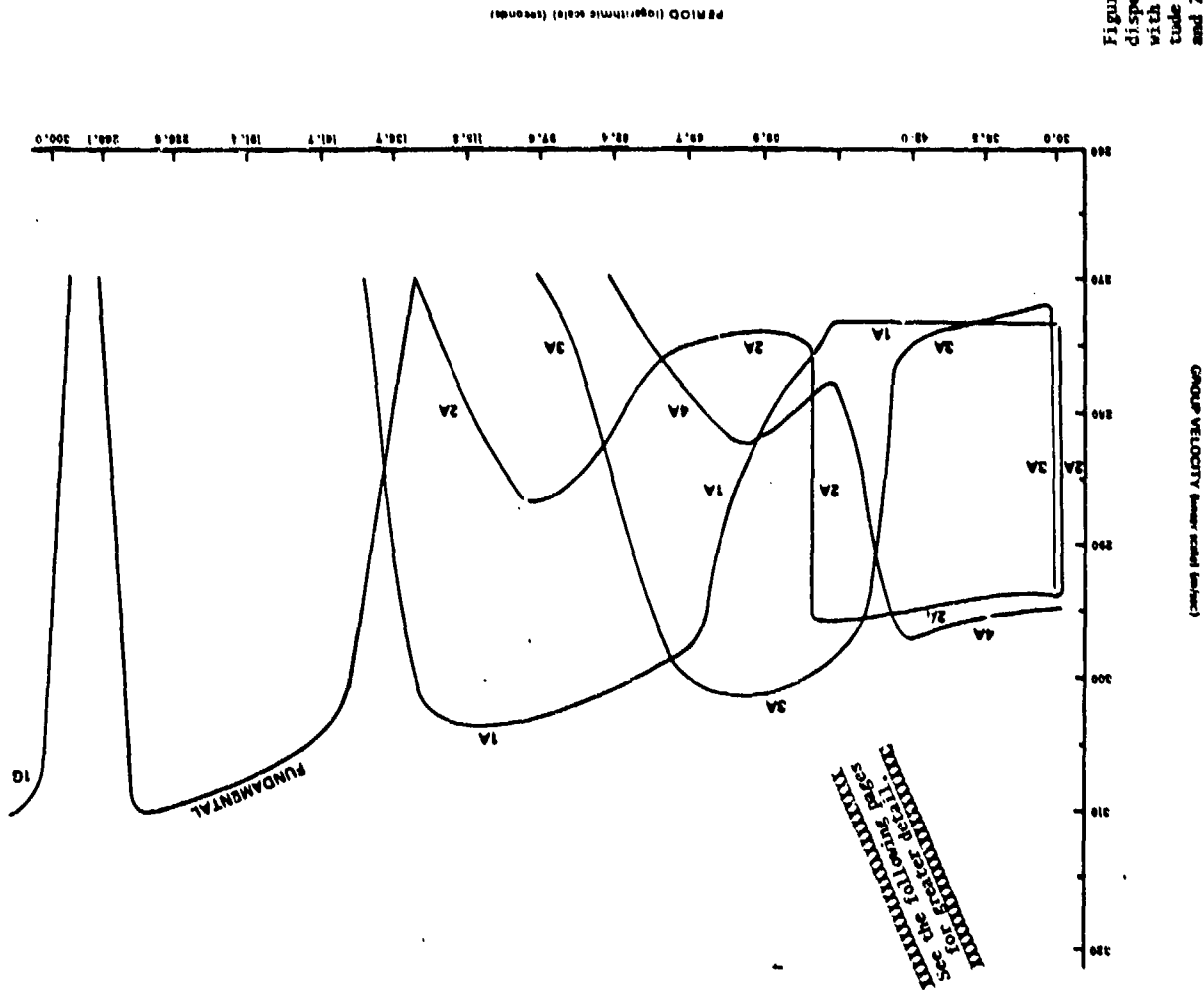
Sorrells et al. (1971b) illustrated the output of a correlation function from a three element, 5 km triangular microbarograph array at Grand Saline, Texas, for this same signal. The correlation function indicated an acoustic signal beginning at 0142Z, ending at about 0225Z, and having maximum energy at two times, 0147Z and 0202Z.

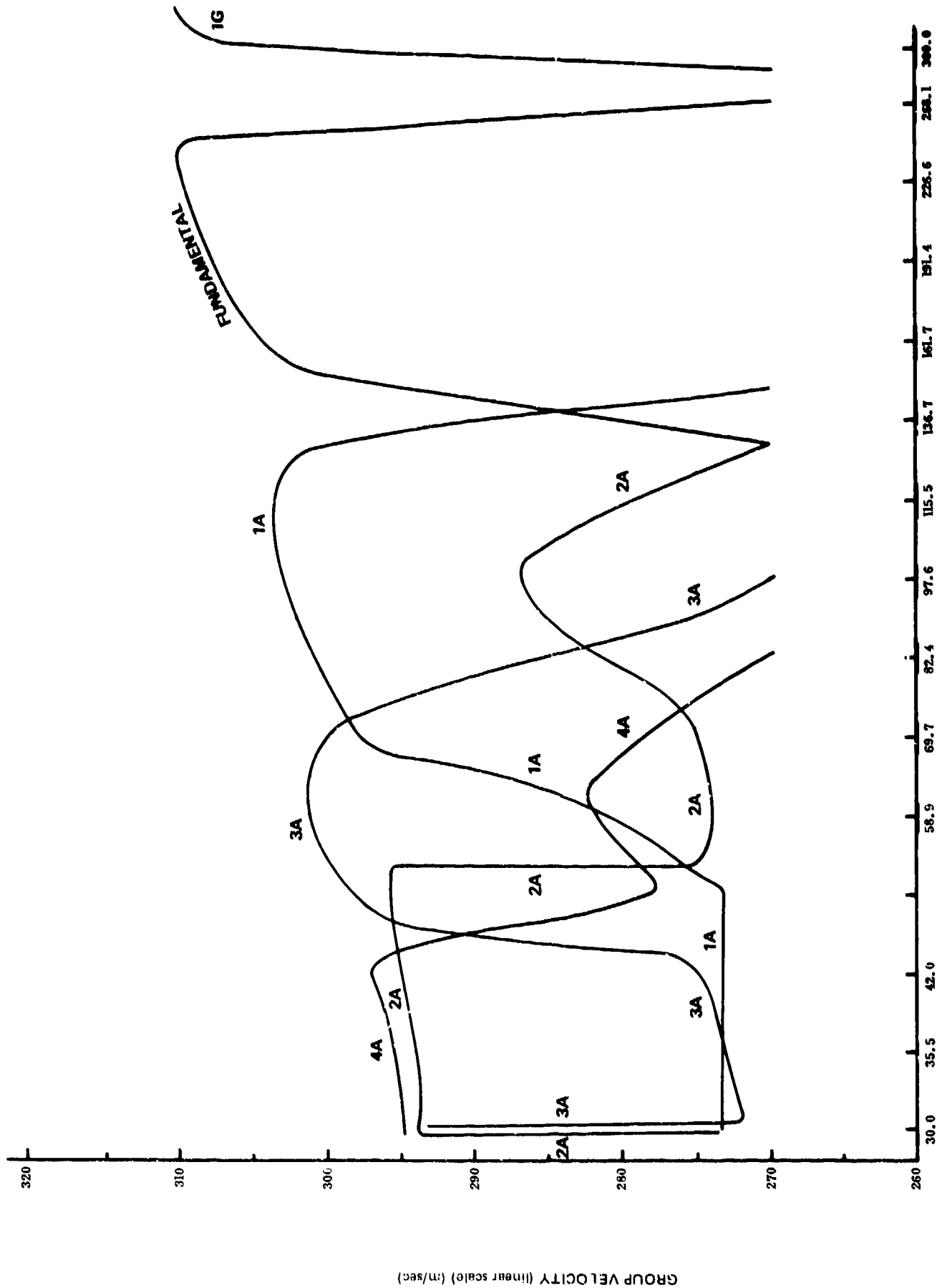
The present author (JEF) has not made any theoretical studies to explain these observations because that study is secondary to the objective of Project VT/8706. Two different mechanisms are postulated below. One is a dual path propagation with much higher velocity winds on one path, possibly a jet stream (Madden and Claerbout, 1968). The other mechanism is related to the vertical distribution of the energy. The early arrivals could be associated with energy that travelled most of the path in the upper sound channel where the velocities are higher, and the later arrivals could be associated with energy that travelled in a normal manner. The second postulated mechanism entails the problem that the energy would have to propagate at the higher velocities in the upper layers and then reform the several modes before reaching the station.

The burst of energy seen at 2359Z in figure 271 is associated with the quasi-horizontal modes of the 1A, 3A, and 4A acoustic modes. Note that the 92 dB and 91 dB peaks in figure 273 for both sets of arrivals of the 1A and 3A modes, respectively, are clearly separated in the frequency domain (figure 273) as predicted by the theory. The separation of the 3A and 4A modes in the first arrival and the 3A of the second arrival and 2A of the first arrival are separated but not as distinctly as the separation of the 1A and 3A modes. The higher modes travelled at slightly greater group velocities. In the first arrival set, 4A was slightly faster than 3A, 3A than 1A, and 1A than F. In the second arrival set, the same relationship held between 3A, 1A, and F, but 4A lagged.

The group velocity dispersion curves for the 33,283 km long-arc path from the 3 July 1970 presumed source are plotted in figure 274. This curve was calculated from the S325L strain seismogram. This path was in a direction in opposition to the general west-to-east winds, and slower group velocities are observed. Because of the greater distance the signal is weaker, but the dispersion curves for the same five modes can be seen in the data. Only one arrival set is identifiable.

The group velocity dispersion curves for the 6769 km short-arc path from the 30 May 1970 presumed source are plotted in figures 275 and 276. The dispersion curves in figure 275 were calculated from the S55L strain seismograph and the curves in figure 276 were calculated from the ML2 microbarograph. These two figures have identical dispersion curves. The group velocities are similar to the early arrival set in figure 273 and to the velocities found by Yamamoto (1968) for the central Pacific. There is a distinct difference in the relationship





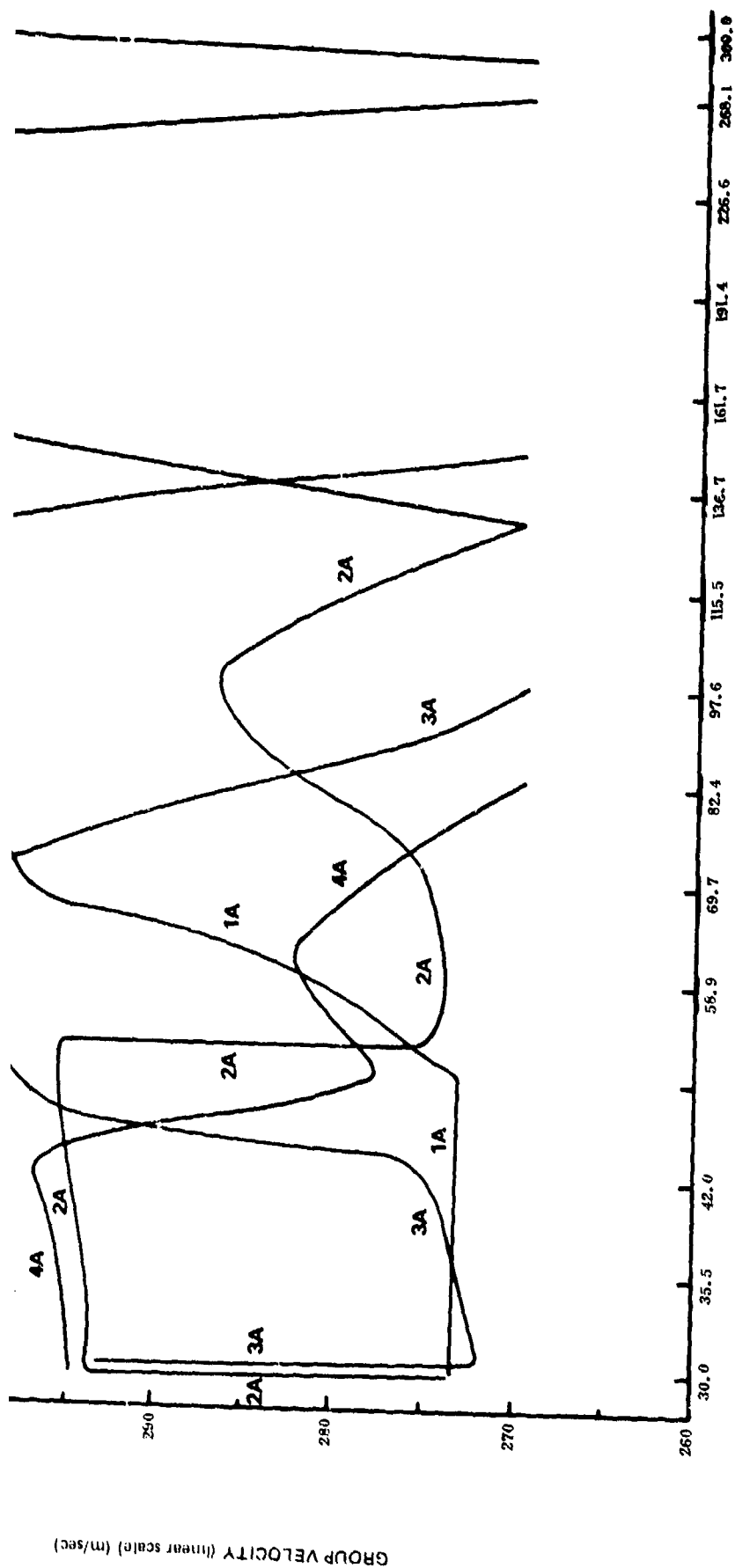


Figure 272. Theoretical group velocity dispersion curves for a model atmosphere with a half-space beginning at an altitude of 300 km (replotted from Pfeffer and Zarichny (1963))

06810

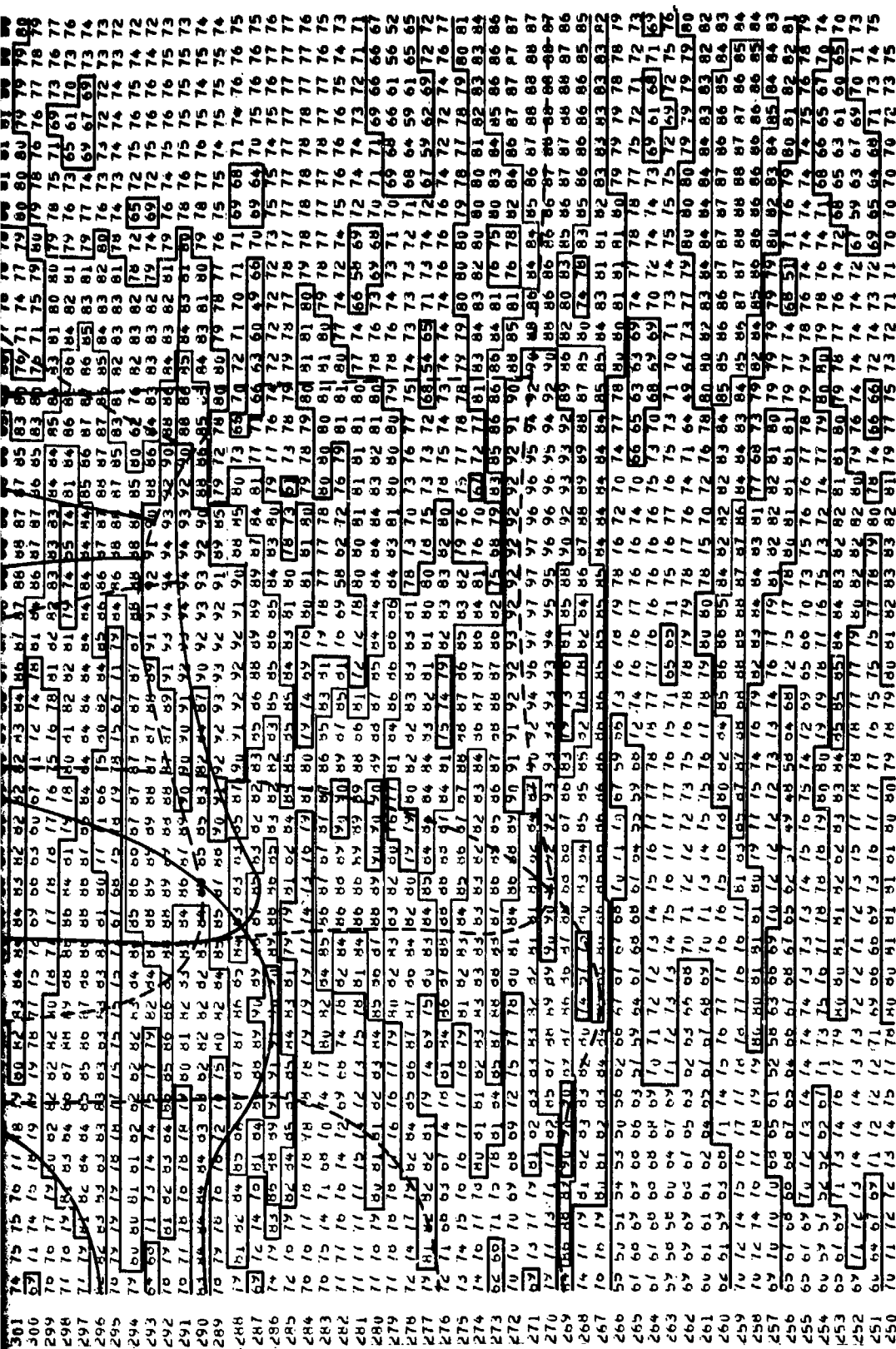
-511/512-

TR 72-3

IN 72-3



VEL 300.0 33.6 31.6 27.0 25.0 22.5 20.0 18.0 16.0 14.0 12.0 10.0 8.0 6.0 4.0 2.0 0.0
 31.0 35.5 39.7 44.4 49.1 53.8 58.5 63.2 67.9 72.6 77.3 82.0 86.7 91.4 96.1 100.8 105.5 110.2 114.9 119.6 124.3 129.0 133.7 138.4 143.1 147.8 152.5 157.2 161.9 166.6 171.3 176.0 180.7 185.4 190.1 194.8 199.5 204.2 208.9 213.6 218.3 223.0 227.7 232.4 237.1 241.8 246.5 251.2 255.9 260.6 265.3 270.0 274.7 279.4 284.1 288.8 293.5 298.2 302.9 307.6 312.3 317.0 321.7 326.4 331.1 335.8 340.5 345.2 349.9 354.6 359.3 364.0 368.7 373.4 378.1 382.8 387.5 392.2 396.9 401.6 406.3 411.0 415.7 420.4 425.1 429.8 434.5 439.2 443.9 448.6 453.3 458.0 462.7 467.4 472.1 476.8 481.5 486.2 490.9 495.6 500.3 505.0 509.7 514.4 519.1 523.8 528.5 533.2 537.9 542.6 547.3 552.0 556.7 561.4 566.1 570.8 575.5 580.2 584.9 589.6 594.3 599.0 603.7 608.4 613.1 617.8 622.5 627.2 631.9 636.6 641.3 646.0 650.7 655.4 660.1 664.8 669.5 674.2 678.9 683.6 688.3 693.0 697.7 702.4 707.1 711.8 716.5 721.2 725.9 730.6 735.3 740.0 744.7 749.4 754.1 758.8 763.5 768.2 772.9 777.6 782.3 787.0 791.7 796.4 801.1 805.8 810.5 815.2 820.0 824.7 829.4 834.1 838.8 843.5 848.2 852.9 857.6 862.3 867.0 871.7 876.4 881.1 885.8 890.5 895.2 900.0 904.7 909.4 914.1 918.8 923.5 928.2 932.9 937.6 942.3 947.0 951.7 956.4 961.1 965.8 970.5 975.2 979.9 984.6 989.3 994.0 998.7 1003.4 1008.1 1012.8 1017.5 1022.2 1026.9 1031.6 1036.3 1041.0 1045.7 1050.4 1055.1 1059.8 1064.5 1069.2 1073.9 1078.6 1083.3 1088.0 1092.7 1097.4 1102.1 1106.8 1111.5 1116.2 1120.9 1125.6 1130.3 1135.0 1139.7 1144.4 1149.1 1153.8 1158.5 1163.2 1167.9 1172.6 1177.3 1182.0 1186.7 1191.4 1196.1 1200.8 1205.5 1210.2 1214.9 1219.6 1224.3 1229.0 1233.7 1238.4 1243.1 1247.8 1252.5 1257.2 1261.9 1266.6 1271.3 1276.0 1280.7 1285.4 1290.1 1294.8 1299.5 1304.2 1308.9 1313.6 1318.3 1323.0 1327.7 1332.4 1337.1 1341.8 1346.5 1351.2 1355.9 1360.6 1365.3 1370.0 1374.7 1379.4 1384.1 1388.8 1393.5 1398.2 1402.9 1407.6 1412.3 1417.0 1421.7 1426.4 1431.1 1435.8 1440.5 1445.2 1449.9 1454.6 1459.3 1464.0 1468.7 1473.4 1478.1 1482.8 1487.5 1492.2 1496.9 1501.6 1506.3 1511.0 1515.7 1520.4 1525.1 1529.8 1534.5 1539.2 1543.9 1548.6 1553.3 1558.0 1562.7 1567.4 1572.1 1576.8 1581.5 1586.2 1590.9 1595.6 1600.3 1605.0 1609.7 1614.4 1619.1 1623.8 1628.5 1633.2 1637.9 1642.6 1647.3 1652.0 1656.7 1661.4 1666.1 1670.8 1675.5 1680.2 1684.9 1689.6 1694.3 1699.0 1703.7 1708.4 1713.1 1717.8 1722.5 1727.2 1731.9 1736.6 1741.3 1746.0 1750.7 1755.4 1760.1 1764.8 1769.5 1774.2 1778.9 1783.6 1788.3 1793.0 1797.7 1802.4 1807.1 1811.8 1816.5 1821.2 1825.9 1830.6 1835.3 1840.0 1844.7 1849.4 1854.1 1858.8 1863.5 1868.2 1872.9 1877.6 1882.3 1887.0 1891.7 1896.4 1901.1 1905.8 1910.5 1915.2 1919.9 1924.6 1929.3 1934.0 1938.7 1943.4 1948.1 1952.8 1957.5 1962.2 1966.9 1971.6 1976.3 1981.0 1985.7 1990.4 1995.1 1999.8 2004.5 2009.2 2013.9 2018.6 2023.3 2028.0 2032.7 2037.4 2042.1 2046.8 2051.5 2056.2 2060.9 2065.6 2070.3 2075.0 2079.7 2084.4 2089.1 2093.8 2098.5 2103.2 2107.9 2112.6 2117.3 2122.0 2126.7 2131.4 2136.1 2140.8 2145.5 2150.2 2154.9 2159.6 2164.3 2169.0 2173.7 2178.4 2183.1 2187.8 2192.5 2197.2 2201.9 2206.6 2211.3 2216.0 2220.7 2225.4 2230.1 2234.8 2239.5 2244.2 2248.9 2253.6 2258.3 2263.0 2267.7 2272.4 2277.1 2281.8 2286.5 2291.2 2295.9 2300.6 2305.3 2310.0 2314.7 2319.4 2324.1 2328.8 2333.5 2338.2 2342.9 2347.6 2352.3 2357.0 2361.7 2366.4 2371.1 2375.8 2380.5 2385.2 2389.9 2394.6 2399.3 2404.0 2408.7 2413.4 2418.1 2422.8 2427.5 2432.2 2436.9 2441.6 2446.3 2451.0 2455.7 2460.4 2465.1 2469.8 2474.5 2479.2 2483.9 2488.6 2493.3 2498.0 2502.7 2507.4 2512.1 2516.8 2521.5 2526.2 2530.9 2535.6 2540.3 2545.0 2549.7 2554.4 2559.1 2563.8 2568.5 2573.2 2577.9 2582.6 2587.3 2592.0 2596.7 2601.4 2606.1 2610.8 2615.5 2620.2 2624.9 2629.6 2634.3 2639.0 2643.7 2648.4 2653.1 2657.8 2662.5 2667.2 2671.9 2676.6 2681.3 2686.0 2690.7 2695.4 2700.1 2704.8 2709.5 2714.2 2718.9 2723.6 2728.3 2733.0 2737.7 2742.4 2747.1 2751.8 2756.5 2761.2 2765.9 2770.6 2775.3 2780.0 2784.7 2789.4 2794.1 2798.8 2803.5 2808.2 2812.9 2817.6 2822.3 2827.0 2831.7 2836.4 2841.1 2845.8 2850.5 2855.2 2859.9 2864.6 2869.3 2874.0 2878.7 2883.4 2888.1 2892.8 2897.5 2902.2 2906.9 2911.6 2916.3 2921.0 2925.7 2930.4 2935.1 2939.8 2944.5 2949.2 2953.9 2958.6 2963.3 2968.0 2972.7 2977.4 2982.1 2986.8 2991.5 2996.2 3000.9 3005.6 3010.3 3015.0 3019.7 3024.4 3029.1 3033.8 3038.5 3043.2 3047.9 3052.6 3057.3 3062.0 3066.7 3071.4 3076.1 3080.8 3085.5 3090.2 3094.9 3099.6 3104.3 3109.0 3113.7 3118.4 3123.1 3127.8 3132.5 3137.2 3141.9 3146.6 3151.3 3156.0 3160.7 3165.4 3170.1 3174.8 3179.5 3184.2 3188.9 3193.6 3198.3 3203.0 3207.7 3212.4 3217.1 3221.8 3226.5 3231.2 3235.9 3240.6 3245.3 3250.0 3254.7 3259.4 3264.1 3268.8 3273.5 3278.2 3282.9 3287.6 3292.3 3297.0 3301.7 3306.4 3311.1 3315.8 3320.5 3325.2 3329.9 3334.6 3339.3 3344.0 3348.7 3353.4 3358.1 3362.8 3367.5 3372.2 3376.9 3381.6 3386.3 3391.0 3395.7 3400.4 3405.1 3409.8 3414.5 3419.2 3423.9 3428.6 3433.3 3438.0 3442.7 3447.4 3452.1 3456.8 3461.5 3466.2 3470.9 3475.6 3480.3 3485.0 3489.7 3494.4 3499.1 3503.8 3508.5 3513.2 3517.9 3522.6 3527.3 3532.0 3536.7 3541.4 3546.1 3550.8 3555.5 3560.2 3564.9 3569.6 3574.3 3579.0 3583.7 3588.4 3593.1 3597.8 3602.5 3607.2 3611.9 3616.6 3621.3 3626.0 3630.7 3635.4 3640.1 3644.8 3649.5 3654.2 3658.9 3663.6 3668.3 3673.0 3677.7 3682.4 3687.1 3691.8 3696.5 3701.2 3705.9 3710.6 3715.3 3720.0 3724.7 3729.4 3734.1 3738.8 3743.5 3748.2 3752.9 3757.6 3762.3 3767.0 3771.7 3776.4 3781.1 3785.8 3790.5 3795.2 3800.0 3804.7 3809.4 3814.1 3818.8 3823.5 3828.2 3832.9 3837.6 3842.3 3847.0 3851.7 3856.4 3861.1 3865.8 3870.5 3875.2 3879.9 3884.6 3889.3 3894.0 3898.7 3903.4 3908.1 3912.8 3917.5 3922.2 3926.9 3931.6 3936.3 3941.0 3945.7 3950.4 3955.1 3959.8 3964.5 3969.2 3973.9 3978.6 3983.3 3988.0 3992.7 3997.4 4002.1 4006.8 4011.5 4016.2 4020.9 4025.6 4030.3 4035.0 4039.7 4044.4 4049.1 4053.8 4058.5 4063.2 4067.9 4072.6 4077.3 4082.0 4086.7 4091.4 4096.1 4100.8 4105.5 4110.2 4114.9 4119.6 4124.3 4129.0 4133.7 4138.4 4143.1 4147.8 4152.5 4157.2 4161.9 4166.6 4171.3 4176.0 4180.7 4185.4 4190.1 4194.8 4199.5 4204.2 4208.9 4213.6 4218.3 4223.0 4227.7 4232.4 4237.1 4241.8 4246.5 4251.2 4255.9 4260.6 4265.3 4270.0 4274.7 4279.4 4284.1 4288.8 4293.5 4298.2 4302.9 4307.6 4312.3 4317.0 4321.7 4326.4 4331.1 4335.8 4340.5 4345.2 4349.9 4354.6 4359.3 4364.0 4368.7 4373.4 4378.1 4382.8 4387.5 4392.2 4396.9 4401.6 4406.3 4411.0 4415.7 4420.4 4425.1 4429.8 4434.5 4439.2 4443.9 4448.6 4453.3 4458.0 4462.7 4467.4 4472.1 4476.8 4481.5 4486.2 4490.9 4495.6 4500.3 4505.0 4509.7 4514.4 4519.1 4523.8 4528.5 4533.2 4537.9 4542.6 4547.3 4552.0 4556.7 4561.4 4566.1 4570.8 4575.5 4580.2 4584.9 4589.6 4594.3 4599.0 4603.7 4608.4 4613.1 4617.8 4622.5 4627.2 4631.9 4636.6 4641.3 4646.0 4650.7 4655.4 4660.1 4664.8 4669.5 4674.2 4678.9 4683.6 4688.3 4693.0 4697.7 4702.4 4707.1 4711.8 4716.5 4721.2 4725.9 4730.6 4735.3 4740.0 4744.7 4749.4 4754.1 4758.8 4763.5 4768.2 4772.9 4777.6 4782.3 4787.0 4791.7 4796.4 4801.1 4805.8 4810.5 4815.2 4819.9 4824.6 4829.3 4834.0 4838.7 4843.4 4848.1 4852.8 4857.5 4862.2 4866.9 4871.6 4876.3 4881.0 4885.7 4890.4 4895.1 4899.8 4904.5 4909.2 4913.9 4918.6 4923.3 4928.0 4932.7 4937.4 4942.1 4946.8 4951.5 4956.2 4960.9 4965.6 4970.3 4975.0 4979.7 4984.4 4989.1 4993.8 4998.5 5003.2 5007.9 5012.6 5017.3 5022.0 5026.7 5031.4 5036.1 5040.8 5045.5 5050.2 5054.9 5059.6 5064.3 5069.0 5073.7 5078.4 5083.1 5087.8 5092.5 5097.2 5101.9 5106.6 5111.3 5116.0 5120.7 5125.4 5130.1 5134.8 5139.5 5144.2 5148.9 5153.6 5158.3 5163.0 5167.7 5172.4 5177.1 5181.8 5186.5 5191.2 5195.9 5200.6 5205.3 5210.0 5214.7 5219.4 5224.1 5228.8 5233.5 5238.2 5242.9 5247.6 5252.3 5257.0 5261.7 5266.4 5271.1 5275.8 5280.5 5285.2 5289.9 5294.6 5299.3 5304.0 5308.7 5313.4 5318.1 5322.8 5327.5 5332.2 5336.9 5341.6 5346.3 5351.0 5355.7 5360.4 5365.1 5369.8 5374.5 5379.2 5383.9 5388.6 5393.3 5398.0 5402.7 5407.4 5412.1 5416.8 5421.5 5426.2 5430.9 5435.6 5440.3 5445.0 5449.7 5454.4 5459.1 5463.8 5468.5 5473.2 5477.9 5482.6 5487.3 5492.0 5496.7 5501.4 5506.1 5510.8 5515.5 5520.2 5524.9 5529.6 5534.3 5539.0 5543.7 5548.4 5553.1 5557.8 5562.5 5567.2 5571.9 5576.6 5581.3 5586.0 5590.7 5595.4 5600.1 5604.8 5609.5 5614.2 5618.9 5623.6 5628.3 5633.0 5637.7 5642.4 5647.1 5651.8 5656.5 5661.2 5665.9 5670.6 5675.3 5680.0 5684.7 5689.4 5694.1 5698.8 5703.5 5708.2 5712.9 5717.6 5722.3 5727.0 5731.7 5736.4 5741.1 5745.8 5750.5 5755.2 5759.9 5764.6 5769.3 5774.0 5778.7 5783.4 5788.1 5792.8 5797.5 5802.2 5806.9 5811.6 5816.3 5821.0 5825.7 5830.4 5835.1 5839.8 5844.5 5849.2 5853.9 5858.6 5863.3 5868.0 5872.7 5877.4 5882.1 5886.8 5891.5 5896.2 5900.9 5905.6 5910.3 5915.0 5919.7 5924.4 5929.1 5933.8 5938.5 5943.2 5947.9 5952.6 5957.3 5962.0 5966.7 5971.4 5976.1 5980.8 5985.5 5990.2 5994.9 6000.0 6005.0 6010.0 6015.0 6020.0 6025.0 6030.0 6035.0 6040.0 6045.0 6050.0 6055.0 6060.0 6065.0 6070.0 6075.0 6080.0 6085.0 6090.0 6095.0 6100.0 6105.0 6110.0 6115.0 6120.0 6125.0 6130.0 6135.0 6140.0 6145.0 6150.0 6155.0 6160.0 6165.0 6170.0 6175.0 6180.0 6185.0 6190.0 6195.0 6200.0 6205.0 6210.0 6215.0 6220.0 6225.0 6230.0 6235.0 6240.0 6245.0 6250.0 6255.0 6260.0 6265.0 6270.0 6275.0 6280.0 6285.0 6290.0 6295.0 6300.0 6305.0 6310.0 6315.0 6320.0 6325.0 6330.0 6335.0 6340.0 6345.0 6350.0 6355.0 6360.0 6365.0 6370.0 6375.0 6380.0 6385.0 6390.0 6395.0 6400.0 6405.0 6410.0 6415.0 6420.0 6425.0 6430.0 6435.0 6440.0 6445.0 6450.0 6455.0 6460.0 6465.0 6470.0 6475.0 6480.0 6485.0 6490.0 6495.0 6500.0 6505.0 6510.0 6515.0 6520.0 6525.0 6530.0 6535.0 6540.0 6545.0 6550.0 6555.0 6560.0 6565.0 6570.0 6575.0 6580.0 6585.0 6590.0 6595.0 6600.0 6605.0 6610.0 6615.0 6620.0 6625.0 6630.0 6635.0 6640.0 6645.0 6650.0 6655.0 6660.0 6665.0 6670.0 6675.0 6680.0 6685.0 6690.0 6695.0 6700.0 6705.0 6710.0 6715.0 6720.0 6725.0 6730.0 6735.0 6740.0 6745.0 6750.0 6755.0 6760.0 6765.0 6770.0 6775.0 6780.0 6785.0 6790.0 6795.0 6800.0 6805.0 6810.0 6815.0 6820.0 6825.0 6830.0 6835.0 6840.0 6845.0 6850.0 6855.0 6860.0 6865.0 6870.0 6875.0 6880.0 6885.0 6890.0 6895.0 6900.0 6905.0 6910.0 6915.0 6920.0 6925.0 6930.0 6935.0 6940.0 6945.0 6950.0 6955.0 6960.0 6965.0 6970.0 6975.0 6980.0 6985.0 6990.0 6995.0 7000.0 7005.0 7010.0 7015.0 7020.0 7025.0 7030.0 7035.0 7040.0 7045.0 7050.0 7055.0 7060.0 7065.0 7070.0 7075.0 7080.0 7085.0 7090.0 7095.0 7100.0 7105.0 7110.0 7115.0 7120.0 7125.0 7130.0 7135.0 7140.0 7145.0 7150.0 7155.0 7160.0 7165.0 7170.0 7175.0 7180.0 7185.0 7190.0 7195.0 7200.0 7205.0 7210.0 7215.0 7220.0 7225.0 7230.0 7235.0 7240.0 7245.0 7250.0 7255.0 7260.0 7265.0 7270.0 7275.0 7280.0 7285.0 7290.0 7295.0 7300.0 7305.0 7310.0 7315.0 7320.0 7325.0 7330.0 7335.0 7340.0 7345.0 7350.0 7355.0 7360.0 7365.0 7370.0 7375.0 7380.0 7385.0 7390.0 7395.0 7400.0 7405.0 7410.0 7415.0 7420.0 7425.0 7430.0 7435.0 7440.0 7445.0 7450.0 7455.0 7460.0 7465.0 7470.0 7475.0 7480.0 7485.0 7490.0 7495.0 7500.0 7505.0 7510.0 7515.0 7520.0 7525.0 7530.0 7535.0 7540.0 7545.0 7550.0 7555.0 7560.0 7565.0 7570.0 7575.0 7580.0 7585.0 7590.0 7595.0 7600.0 7605.0 7610.0 7615.0 7620.0 7625.0 7630.0 7635.0 7640.0 7645.0 7650.0 7655.0 7660.0 7665.0 7670.0 7675.0 7680.0 7685.0 7690.0 7695.0 7700.0 7705.0 7710.0 7715.0 7720.0 7725.0 7730.0 7735.0 7740.0 7745.0 7750.0 7755.0 7760.0 7765.0 7770.0 7775.0 7780.0 7785.0 7790.0 7795.0 7800.0 7805.0 7810.0 7815.0 7820.0 7825.0 7830.0 7835.0 7840.0 7845.0 7850.0 7855.0 7860.0 7865.0 7870.0 7875.0 7880.0 7885.0 7890.0 7895.0 7900.0 7905.0 7910.0 7915.0 7920.0 7925.0 7930.0 7935.0 7940.0 7945.0 7950.0 7955.0 7960.0 7965.0 7970.0 7975.0 7980.0 7985.0 7990.0 7995.0 8000.0 8005.0 8010.0 8015.0 8020.0 8025.0 8030.0 8035.0 8040.0 8045.0 8050.0 8055.0 8060.0 8065.0 8070.0 8075.0 8080.0 8085.0 8090.0 8095.0 8100.0 8105.0 8110.0 8115.0 8120.0 8125.0 8130.0 8135.0 8140.0 8145.0 8150.0 8155.0 8160.0 8165.0 8170.0 8175.0 8180.0 8185.0 8190.0 8195.0 8200.0 8205.0 8210.0 8215.0 8220.0 8225.0 8230.0 8235.0 8240.0 8245.0 8250.0 8255.0 8260.0 8265.0 8270.0 8275.0 8280.0 8285.0 8290.0 8295.0 8300.0 8305.0 8310.0 8315.0 8320.0 8325.0 8330.0 8335.0 8340.0 8345.0 8350.0 8355.0 8360.0 8365.0 8370.0 8375.0 8380.0 8385.0 8390.0 8395.0 8400.0 8405.0 8410.0 8415.0 8420.0 8425.0 8430.0 8435.0 8440.0 8445.0 8450.0 8455.0 8460.0 8465.0 8470.0 8475.0 8480.0 8485.0 8490.0 8495.0 8500.0 8505.0 8510.0 8515.0 8520.0 8525.0 8530.0 8535.0 8540.0 8545.0 8550.0 8555.0 8560.0 8565.0 857

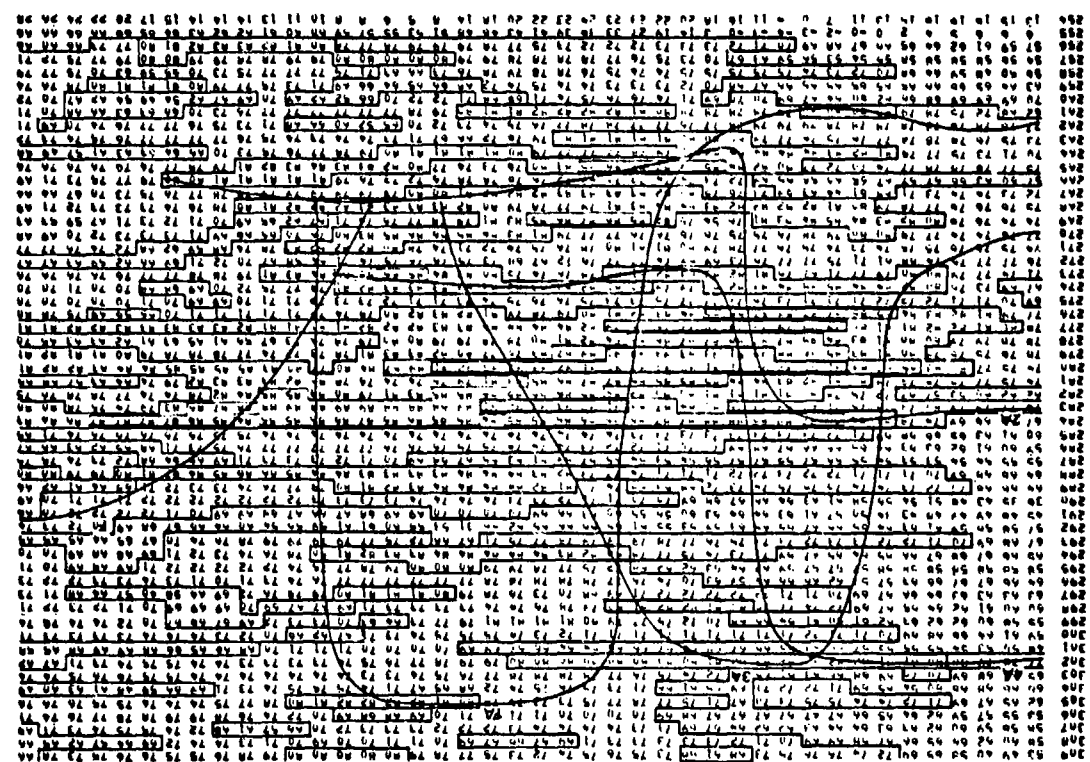


VEL 30.0 33.6 36.0 42.0 47.0 52.6 58.9 65.9 73.7 82.4 92.2 103.2 115.5 129.2 144.6 161.7 181.0 202.5 226.6 253.5 283.6
 31.7 35.5 39.1 44.4 49.1 55.6 62.3 69.1 76.9 85.7 95.6 106.6 118.9 132.7 148.1 165.1 183.6 203.6 225.2 248.6 274.1 300.0
 12285 * INKUL TAPE = S5 99 * S55L * 3 JULY 1970 * SHORT ARC

Figure 273. Group velocity dispersion curves calculated from S55L strain seismogram for 5 modes of acoustic-gravity waves that travelled the short-arc path from the presumed source on 3 July 1970

G 6811

31.7 35.5 37.5 42.0 47.0 52.0 55.0 57.0 59.0 60.0 62.0 64.0 66.0 68.0 70.0 72.0 74.0 76.0 78.0 80.0 82.0 84.0 86.0 88.0 90.0 92.0 94.0 96.0 98.0 100.0 102.0 104.0 106.0 108.0 110.0 112.0 114.0 116.0 118.0 120.0 122.0 124.0 126.0 128.0 130.0 132.0 134.0 136.0 138.0 140.0 142.0 144.0 146.0 148.0 150.0 152.0 154.0 156.0 158.0 160.0 162.0 164.0 166.0 168.0 170.0 172.0 174.0 176.0 178.0 180.0 182.0 184.0 186.0 188.0 190.0 192.0 194.0 196.0 198.0 200.0 202.0 204.0 206.0 208.0 210.0 212.0 214.0 216.0 218.0 220.0 222.0 224.0 226.0 228.0 230.0 232.0 234.0 236.0 238.0 240.0 242.0 244.0 246.0 248.0 250.0 252.0 254.0 256.0 258.0 260.0 262.0 264.0 266.0 268.0 270.0 272.0 274.0 276.0 278.0 280.0 282.0 284.0 286.0 288.0 290.0 292.0 294.0 296.0 298.0 300.0 302.0 304.0 306.0 308.0 310.0 312.0 314.0 316.0 318.0 320.0 322.0 324.0 326.0 328.0 330.0 332.0 334.0 336.0 338.0 340.0 342.0 344.0 346.0 348.0 350.0 352.0 354.0 356.0 358.0 360.0 362.0 364.0 366.0 368.0 370.0 372.0 374.0 376.0 378.0 380.0 382.0 384.0 386.0 388.0 390.0 392.0 394.0 396.0 398.0 400.0 402.0 404.0 406.0 408.0 410.0 412.0 414.0 416.0 418.0 420.0 422.0 424.0 426.0 428.0 430.0 432.0 434.0 436.0 438.0 440.0 442.0 444.0 446.0 448.0 450.0 452.0 454.0 456.0 458.0 460.0 462.0 464.0 466.0 468.0 470.0 472.0 474.0 476.0 478.0 480.0 482.0 484.0 486.0 488.0 490.0 492.0 494.0 496.0 498.0 500.0 502.0 504.0 506.0 508.0 510.0 512.0 514.0 516.0 518.0 520.0 522.0 524.0 526.0 528.0 530.0 532.0 534.0 536.0 538.0 540.0 542.0 544.0 546.0 548.0 550.0 552.0 554.0 556.0 558.0 560.0 562.0 564.0 566.0 568.0 570.0 572.0 574.0 576.0 578.0 580.0 582.0 584.0 586.0 588.0 590.0 592.0 594.0 596.0 598.0 600.0 602.0 604.0 606.0 608.0 610.0 612.0 614.0 616.0 618.0 620.0 622.0 624.0 626.0 628.0 630.0 632.0 634.0 636.0 638.0 640.0 642.0 644.0 646.0 648.0 650.0 652.0 654.0 656.0 658.0 660.0 662.0 664.0 666.0 668.0 670.0 672.0 674.0 676.0 678.0 680.0 682.0 684.0 686.0 688.0 690.0 692.0 694.0 696.0 698.0 700.0 702.0 704.0 706.0 708.0 710.0 712.0 714.0 716.0 718.0 720.0 722.0 724.0 726.0 728.0 730.0 732.0 734.0 736.0 738.0 740.0 742.0 744.0 746.0 748.0 750.0 752.0 754.0 756.0 758.0 760.0 762.0 764.0 766.0 768.0 770.0 772.0 774.0 776.0 778.0 780.0 782.0 784.0 786.0 788.0 790.0 792.0 794.0 796.0 798.0 800.0 802.0 804.0 806.0 808.0 810.0 812.0 814.0 816.0 818.0 820.0 822.0 824.0 826.0 828.0 830.0 832.0 834.0 836.0 838.0 840.0 842.0 844.0 846.0 848.0 850.0 852.0 854.0 856.0 858.0 860.0 862.0 864.0 866.0 868.0 870.0 872.0 874.0 876.0 878.0 880.0 882.0 884.0 886.0 888.0 890.0 892.0 894.0 896.0 898.0 900.0 902.0 904.0 906.0 908.0 910.0 912.0 914.0 916.0 918.0 920.0 922.0 924.0 926.0 928.0 930.0 932.0 934.0 936.0 938.0 940.0 942.0 944.0 946.0 948.0 950.0 952.0 954.0 956.0 958.0 960.0 962.0 964.0 966.0 968.0 970.0 972.0 974.0 976.0 978.0 980.0 982.0 984.0 986.0 988.0 990.0 992.0 994.0 996.0 998.0 1000.0



0.01 0.02 0.03 0.04 0.05 0.06 0.07 0.08 0.09 0.10 0.12 0.15 0.20 0.25 0.30 0.35 0.40 0.45 0.50 0.55 0.60 0.65 0.70 0.75 0.80 0.85 0.90 0.95 1.00 1.20 1.50 2.00 2.50 3.00 3.50 4.00 4.50 5.00 5.50 6.00 6.50 7.00 7.50 8.00 8.50 9.00 9.50 10.00

See the following for greater detail

Figure 274. Group velocity dispersion curve calculated from S325. strain seismogram for 5 modes of acoustic-gravity waves that travelled the long-arc path from the presumed source on 3 July 1970

GROUP VELOCITY (km/sec)

VEL 30.0 33.6 37.6 42.0 47.0 52.6 58.9 65.9 73.7 82.4 92.2 103.2 115.5 129.2 144.6 161.7 181.0 202.5 226.6 253.5 283.4
 31.7 35.5 39.7 44.4 49.7 55.6 62.3 69.7 77.9 87.2 97.6 109.2 122.1 136.7 152.9 171.1 191.4 214.2 239.6 268.1 300.0

309	53	49	40	50	65	69	72	74	76	76	74	73	68	61	58	73	75	76	75	74	72	73	75	77	78	79	80	80	80	80	80	79	78	76	75	75	76	76	75	73	78	46
308	58	60	62	64	65	66	67	68	69	69	70	71	72	73	73	73	73	73	73	71	69	67	66	67	69	70	71	71	70	69	70	71	73	74	74	72	69	65	57	62	45	48
307	58	59	60	62	63	64	64	64	64	63	62	61	60	59	58	57	74	74	74	74	74	74	72	72	73	73	73	73	72	70	66	57	61	68	72	74	75	74	73	71	69	
306	53	57	59	62	64	65	66	67	67	67	67	67	67	67	67	67	70	70	70	70	70	71	71	71	71	71	71	70	69	68	67	70	72	76	78	79	78	77	76	74	71	
305	62	65	67	69	71	72	74	75	75	73	70	67	71	75	77	78	77	75	73	72	71	70	69	68	67	66	65	64	63	62	61	60	59	58	57	56	55	54	53	52	51	
304	60	60	60	60	60	60	60	60	60	60	60	60	60	60	60	60	60	60	60	60	60	60	60	60	60	60	60	60	60	60	60	60	60	60	60	60	60	60	60	60		
303	65	68	69	70	71	72	73	74	75	76	77	78	79	80	81	82	83	84	85	86	87	88	89	90	91	92	93	94	95	96	97	98	99	100	101	102	103	104	105	106		
302	77	79	80	81	82	83	84	85	86	87	88	89	90	91	92	93	94	95	96	97	98	99	100	101	102	103	104	105	106	107	108	109	110	111	112	113	114	115	116	117		
301	88	89	90	91	92	93	94	95	96	97	98	99	100	101	102	103	104	105	106	107	108	109	110	111	112	113	114	115	116	117	118	119	120	121	122	123	124	125	126	127		
300	99	100	101	102	103	104	105	106	107	108	109	110	111	112	113	114	115	116	117	118	119	120	121	122	123	124	125	126	127	128	129	130	131	132	133	134	135	136	137	138		
299	55	58	60	62	64	66	68	70	72	74	76	78	80	82	84	86	88	90	92	94	96	98	100	102	104	106	108	110	112	114	116	118	120	122	124	126	128	130	132	134		
298	50	50	51	52	53	54	55	56	57	58	59	60	61	62	63	64	65	66	67	68	69	70	71	72	73	74	75	76	77	78	79	80	81	82	83	84	85	86	87	88		
297	63	63	63	64	64	64	64	64	64	64	64	64	64	64	64	64	64	64	64	64	64	64	64	64	64	64	64	64	64	64	64	64	64	64	64	64	64	64	64	64		
296	64	66	67	67	67	67	67	67	67	67	67	67	67	67	67	67	67	67	67	67	67	67	67	67	67	67	67	67	67	67	67	67	67	67	67	67	67	67	67	67		
295	58	58	58	58	58	58	58	58	58	58	58	58	58	58	58	58	58	58	58	58	58	58	58	58	58	58	58	58	58	58	58	58	58	58	58	58	58	58	58	58		
294	65	66	67	68	68	68	68	68	68	68	68	68	68	68	68	68	68	68	68	68	68	68	68	68	68	68	68	68	68	68	68	68	68	68	68	68	68	68	68	68		
293	67	68	69	70	71	72	73	74	75	76	77	78	79	80	81	82	83	84	85	86	87	88	89	90	91	92	93	94	95	96	97	98	99	100	101	102	103	104	105	106		
292	57	58	59	61	63	65	67	69	71	73	75	77	79	81	83	85	87	89	91	93	95	97	99	101	103	105	107	109	111	113	115	117	119	121	123	125	127	129	131	133		
291	45	48	49	49	48	47	46	45	44	43	42	41	40	39	38	37	36	35	34	33	32	31	30	29	28	27	26	25	24	23	22	21	20	19	18	17	16	15	14	13		
290	36	35	34	33	32	31	30	29	28	27	26	25	24	23	22	21	20	19	18	17	16	15	14	13	12	11	10	9	8	7	6	5	4	3	2	1	0	0	0	0		
289	64	66	68	70	72	74	76	78	80	82	84	86	88	90	92	94	96	98	100	102	104	106	108	110	112	114	116	118	120	122	124	126	128	130	132	134	136	138	140	142		
288	55	55	54	53	52	51	50	49	48	47	46	45	44	43	42	41	40	39	38	37	36	35	34	33	32	31	30	29	28	27	26	25	24	23	22	21	20	19	18	17		
287	55	55	54	53	52	51	50	49	48	47	46	45	44	43	42	41	40	39	38	37	36	35	34	33	32	31	30	29	28	27	26	25	24	23	22	21	20	19	18	17		
286	59	60	61	62	63	64	65	66	67	68	69	70	71	72	73	74	75	76	77	78	79	80	81	82	83	84	85	86	87	88	89	90	91	92	93	94	95	96	97			
285	60	61	63	65	68	71	74	77	80	83	86	89	92	95	98	101	104	107	110	113	116	119	122	125	128	131	134	137	140	143	146	149	152	155	158	161	164	167	170	173		
284	67	69	71	73	75	77	79	81	83	85	87	89	91	93	95	97	99	101	103	105	107	109	111	113	115	117	119	121	123	125	127	129	131	133	135	137	139	141	143	145		
283	77	79	81	83	85	87	89	91	93	95	97	99	101	103	105	107	109	111	113	115	117	119	121	123	125	127	129	131	133	135	137	139	141	143	145	147	149	151	153	155		
282	82	84	86	88	90	92	94	96	98	100	102	104	106	108	110	112	114	116	118	120	122	124	126	128	130	132	134	136	138	140	142	144	146	148	150	152	154	156	158	160	162	
281	74	75	77	79	81	83	85	87	89	91	93	95	97	99	101	103	105	107	109	111	113	115	117	119	121	123	125	127	129	131	133	135	137	139	141	143	145	147	149	151		
280	74	75	77	79	81	83	85	87	89	91	93	95	97	99	101	103	105	107	109	111	113	115	117	119	121	123	125	127	129	131	133	135	137	139	141	143	145	147	149	151		
279	76	78	80	82	84	86	88	90	92	94	96	98	100	102	104	106	108	110	112	114	116	118	120	122	124	126	128	130	132	134	136	138	140	142	144	146	148	150	152	154		
278	78	80	82	84	86	88	90	92	94	96	98	100	102	104	106	108	110	112	114	116	118	120	122	124	126	128	130	132	134	136	138	140	142	144	146	148	150	152	154	156		
277	78	80	82	84	86	88	90	92	94	96	98	100	102	104	106	108	110	112	114	116	118	120	122	124	126	128	130	132	134	136	138	140	142	144	146	148	150	152	154	156		
276	77	79	81	83	85	87	89	91	93	95	97	99	101	103	105	107	109	111	113	115	117	119	121	123	125	127	129	131	133	135	137	139	141	143	145	147	149	151	153			
275	69	70	71	72	73	74	75	76	77	78	79	80	81	82	83	84	85	86	87	88	89	90	91</																			

GROUP VELOCITY (linear scale) (m/sec)

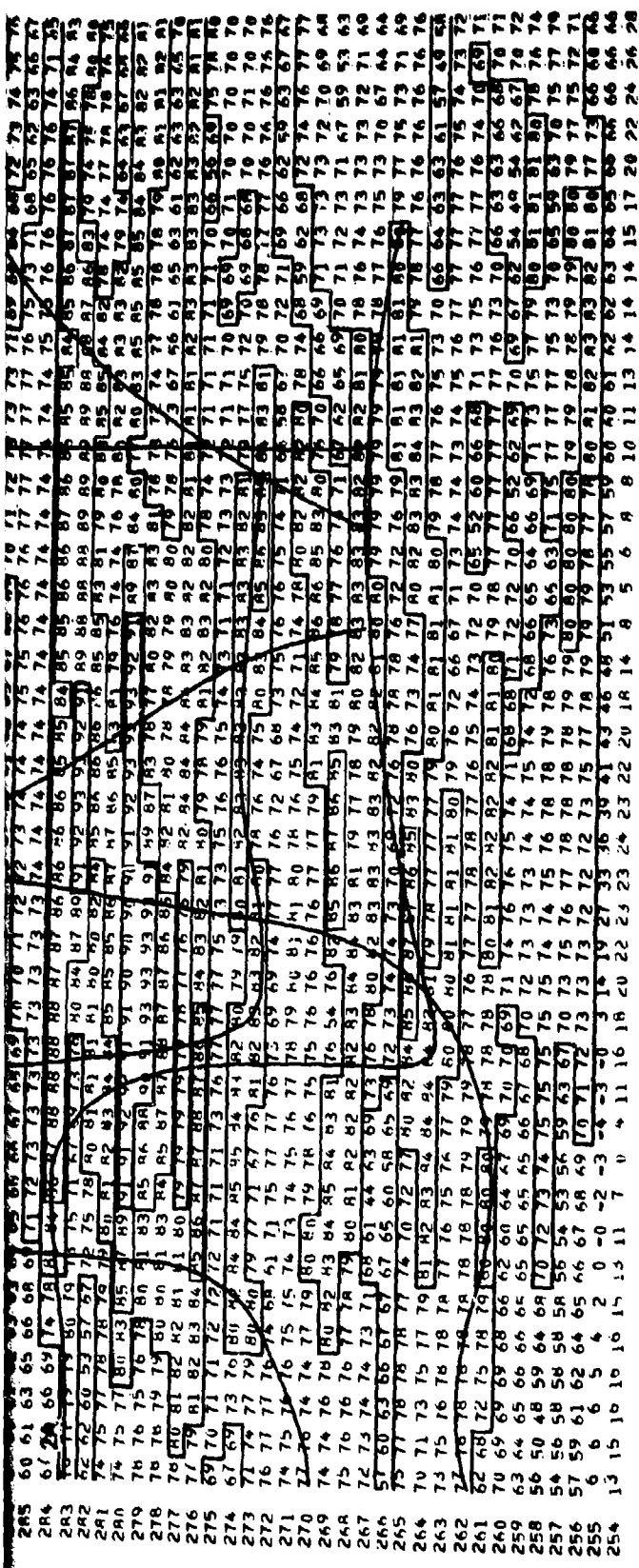
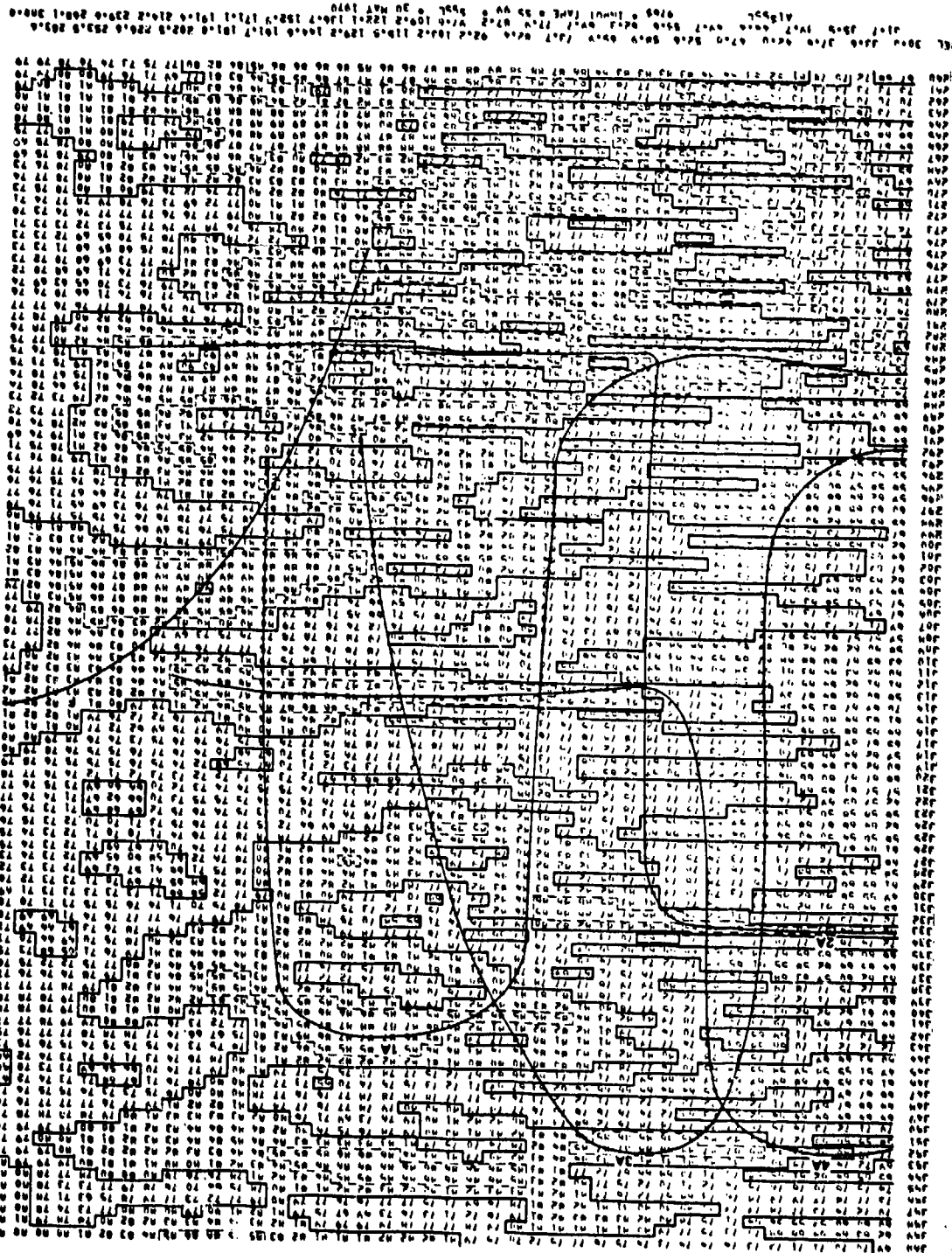


Figure 274. Group velocity dispersion curve calculated from S325L strain seismogram for 5 modes of acoustic-gravity waves that travelled the long-arc path from the presumed source on 3 July 1970

G 6812

-515/516-

TR 72-3



See the following for
the location of
the source

Figure 275. Group velocity dispersion curve calculated from SSSL strain seismogram for 5 modes of acoustic-gravity waves that travelled the short-arc path from the presumed source on 30 May 1970

G 0013

-517/518-

TR 72-3

518.1

517.2

(continued from previous page)

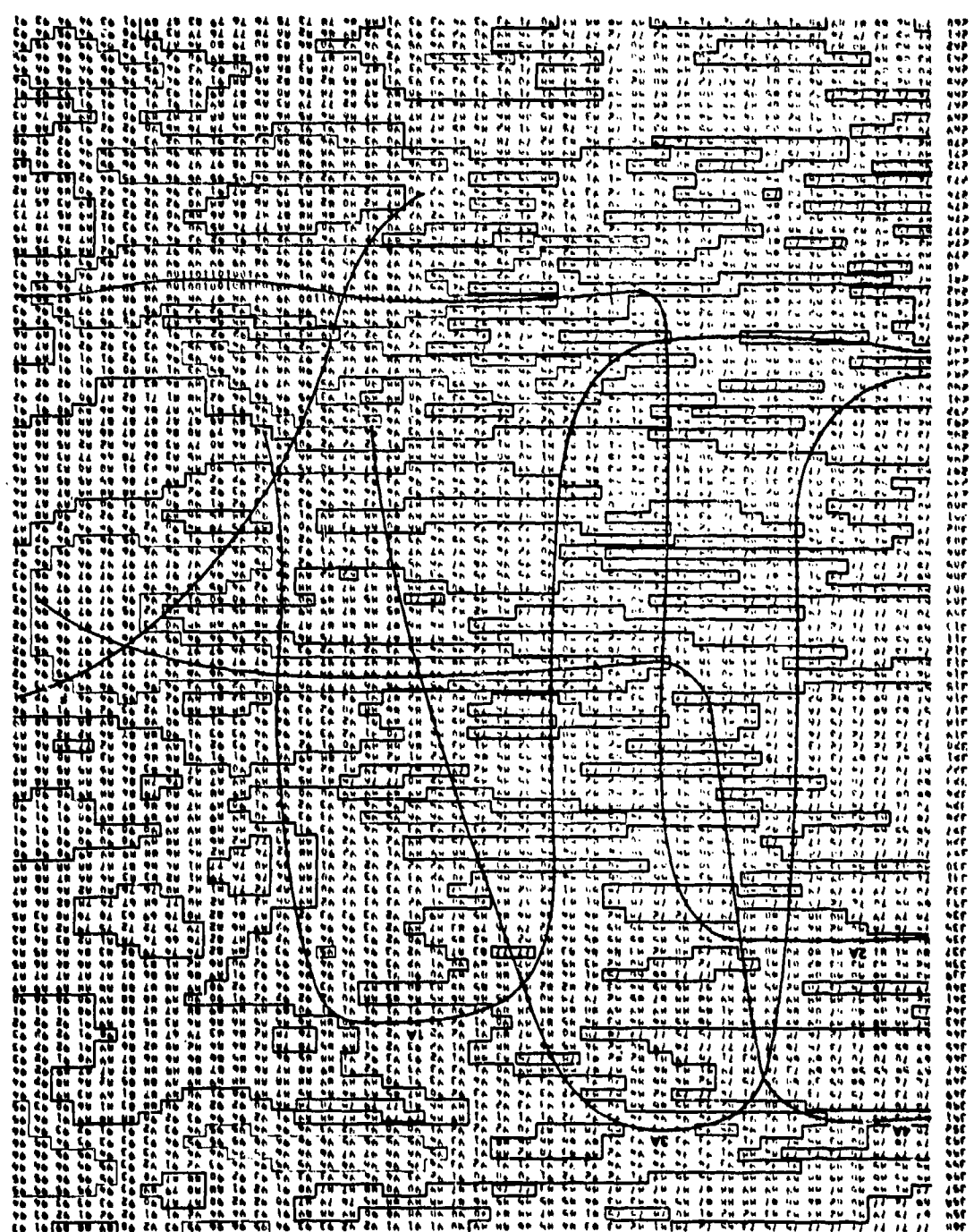
517.1



VEL 30.0 33.6 37.0 42.0 47.0 52.6 58.9 65.9 73.7 82.4 92.2 103.2 115.5 129.2 144.6 161.7 181.0 202.5 226.6 253.5 283.6
 31.7 35.5 39.7 44.4 49.7 55.6 62.3 69.7 77.9 87.2 97.6 109.2 122.1 136.7 152.9 171.1 191.4 216.2 239.6 268.1 300.0
 A1555L 9765 * INPU1 TAPE = 55 99 * 555L * 30 MAY 1970

Figure 275. Group velocity dispersion curve calculated from S55L strain seismogram for 5 modes of acoustic-gravity waves that travelled the short-arc path from the presumed source on 30 May 1970

10 MAY 1970 10:00 10:05 10:10 10:15 10:20 10:25 10:30 10:35 10:40 10:45 10:50 10:55 11:00 11:05 11:10 11:15 11:20 11:25 11:30 11:35 11:40 11:45 11:50 11:55 12:00 12:05 12:10 12:15 12:20 12:25 12:30 12:35 12:40 12:45 12:50 12:55 13:00 13:05 13:10 13:15 13:20 13:25 13:30 13:35 13:40 13:45 13:50 13:55 14:00 14:05 14:10 14:15 14:20 14:25 14:30 14:35 14:40 14:45 14:50 14:55 15:00 15:05 15:10 15:15 15:20 15:25 15:30 15:35 15:40 15:45 15:50 15:55 16:00 16:05 16:10 16:15 16:20 16:25 16:30 16:35 16:40 16:45 16:50 16:55 17:00 17:05 17:10 17:15 17:20 17:25 17:30 17:35 17:40 17:45 17:50 17:55 18:00 18:05 18:10 18:15 18:20 18:25 18:30 18:35 18:40 18:45 18:50 18:55 19:00 19:05 19:10 19:15 19:20 19:25 19:30 19:35 19:40 19:45 19:50 19:55 20:00 20:05 20:10 20:15 20:20 20:25 20:30 20:35 20:40 20:45 20:50 20:55 21:00 21:05 21:10 21:15 21:20 21:25 21:30 21:35 21:40 21:45 21:50 21:55 22:00 22:05 22:10 22:15 22:20 22:25 22:30 22:35 22:40 22:45 22:50 22:55 23:00 23:05 23:10 23:15 23:20 23:25 23:30 23:35 23:40 23:45 23:50 23:55 24:00



10 MAY 1970 10:00 10:05 10:10 10:15 10:20 10:25 10:30 10:35 10:40 10:45 10:50 10:55 11:00 11:05 11:10 11:15 11:20 11:25 11:30 11:35 11:40 11:45 11:50 11:55 12:00 12:05 12:10 12:15 12:20 12:25 12:30 12:35 12:40 12:45 12:50 12:55 13:00 13:05 13:10 13:15 13:20 13:25 13:30 13:35 13:40 13:45 13:50 13:55 14:00 14:05 14:10 14:15 14:20 14:25 14:30 14:35 14:40 14:45 14:50 14:55 15:00 15:05 15:10 15:15 15:20 15:25 15:30 15:35 15:40 15:45 15:50 15:55 16:00 16:05 16:10 16:15 16:20 16:25 16:30 16:35 16:40 16:45 16:50 16:55 17:00 17:05 17:10 17:15 17:20 17:25 17:30 17:35 17:40 17:45 17:50 17:55 18:00 18:05 18:10 18:15 18:20 18:25 18:30 18:35 18:40 18:45 18:50 18:55 19:00 19:05 19:10 19:15 19:20 19:25 19:30 19:35 19:40 19:45 19:50 19:55 20:00 20:05 20:10 20:15 20:20 20:25 20:30 20:35 20:40 20:45 20:50 20:55 21:00 21:05 21:10 21:15 21:20 21:25 21:30 21:35 21:40 21:45 21:50 21:55 22:00 22:05 22:10 22:15 22:20 22:25 22:30 22:35 22:40 22:45 22:50 22:55 23:00 23:05 23:10 23:15 23:20 23:25 23:30 23:35 23:40 23:45 23:50 23:55 24:00

See the following page for a more detailed description of the data.

Figure 276. Group velocity dispersion curve calculated from ML2 microbarogram for 5 modes of acoustic-gravity waves that travelled the short-arc path from the presumed source on 30 May 1970

519.1

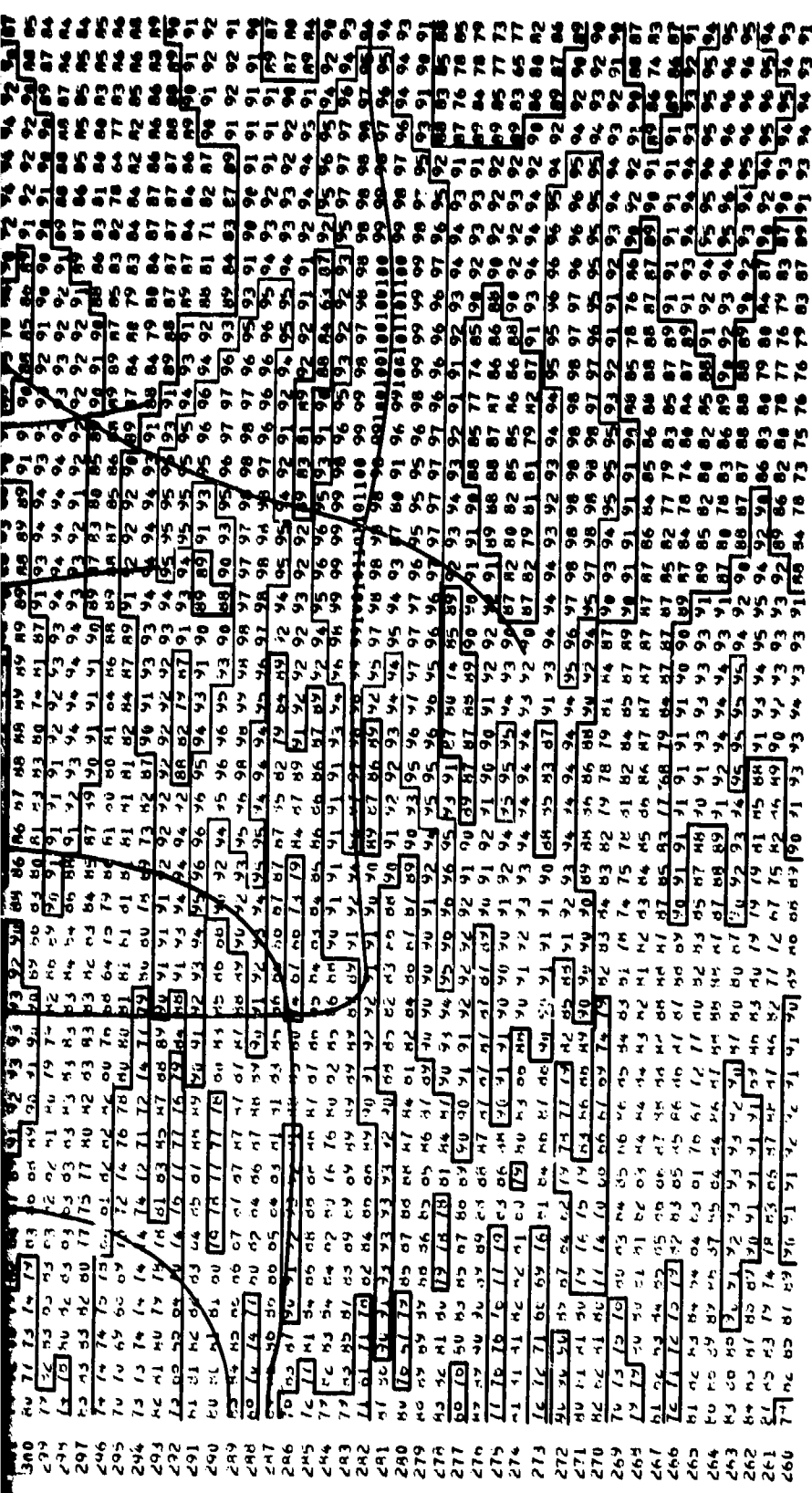
519.2

519.1

GROUP VELOCITY (km/sec)

[illegible]

519.1



VEL 30.0 33.5 36.0 42.0 47.0 52.0 58.0 63.0 68.0 73.0 78.0 83.0 88.0 93.0 98.0 103.0 108.0 113.0 118.0 123.0 128.0 133.0 138.0 143.0 148.0 153.0 158.0 163.0 168.0 173.0 178.0 183.0 188.0 193.0 198.0 203.0 208.0 213.0 218.0 223.0 228.0 233.0 238.0 243.0 248.0 253.0 258.0 260.0

0.1 0.2 0.3 0.4 0.5 0.6 0.7 0.8 0.9 1.0 1.2 1.5 2.0 2.5 3.0 4.0 5.0 6.0 7.0 8.0 9.0 10.0 12.0 15.0 20.0 25.0 30.0 40.0 50.0 60.0 70.0 80.0 90.0 100.0

ACMLC

Figure 276. Group velocity dispersion curve calculated from ML2 microbarogram for 5 modes of acoustic-gravity waves that travelled the short-arc path from the presumed source on 30 May 1970

of the 1A and F modes to the other three modes between the dispersion curves for the signals from the two dates. These differences are probably the combined result of the difference in the source and the difference in the wind structure along the propagation path during the two time intervals.

The other components of instrumentation all gave similar dispersion curves for the two signals. Only representative curves have been presented.

The similarity of the group velocity dispersion curves in figures 273 through 276 demonstrate that

- (1) Strain seismographs enhance strains generated by acoustic waves.
- (2) The strain seismographs have sufficient signal to detect energy from five modes of acoustic-gravity waves.
- (3) The strain seismographs have sufficient signal to produce repeatable group velocity dispersion curves for the five modes.

15. CONCLUSIONS

The primary conclusion of Project VT/8706 is that a three-component, high-sensitivity strain seismograph can be built to match a three-component, high-sensitivity inertial seismograph in magnification, in amplitude response, and in phase response. The strain seismographs can be combined with the inertial seismographs to provide on-line, real-time, signal enhancement and wave type discrimination. Rayleigh waves, Love waves, and body waves arriving as S phases are especially well enhanced. The 17 dB signal-to-noise ratio for a Rayleigh wave from an earthquake with an m_b of 4.2 at an epicentral distance of 100 deg indicates that the single station strain/inertial complex is a satisfactory concept for use in the problem of detecting and identifying earthquakes and explosions. This S/N ratio is comparable to the 11 dB microseismic noise reduction accomplished with the 63 element LASA LP array by Capon et al. (1969).

The directional array of sums and differences of strain and inertial seismographs is valuable as a real-time, beam-forming process. Comparison between a sum trace and a difference trace allowed many earthquakes to be detected with good estimates of azimuth and epicentral distance. Many of these detections were Rayleigh waves and often the associated Love wave could be identified. The worldwide long-period detection capability of QC-AZ is better than m_b of 4.35 at the 50 percent probability level.

After large earthquakes, the strain seismograph returns to its normal background earlier than the inertial seismograph, reducing the time that detection capability is degraded by the free oscillations.

The structure of the upper mantle under the Basin and Range Province significantly attenuates 45 to 60 sec Rayleigh waves. This energy dissipation materially affects the earthquake/explosion discriminants associated with the MS40 surface wave magnitude.

The design employed for the strainmeters was satisfactory. The velocity transducer provided ample signal and dynamic range so that the system was limited by ground motion and not by instrument noise. The method of attachment to the rock and of suspending the strain rod were satisfactory. Calibrations were of sufficient accuracy to maintain constant known magnifications.

Care must be exercised in selecting and preparing a strainmeter site. The seismometers should be installed in an underground chamber in solid rock at a depth of 100 m or more, preferably in flat terrain. The seismometer chamber must be sealed against air pressure variations. The strainmeter must be well insulated. Horizontal strainmeters should be installed on the wall where stress concentrations are compressive rather than on the floor or ceiling where stress concentrations are tensile.

Monitoring of environmental conditions with microbarographs, anemometers, recording barometers, and recording thermometers is needed to interpret the operating conditions of any long-period seismograph installation.

The directional array at QC-AZ would be improved by high-pass filtering with a 40 sec, 2 pole filter. The filter would reduce the longer period background signal from the strain seismographs. Because of the small 40 to 60 sec Rayleigh waves, signals would not be materially affected.

Strain created by large air pressure fluctuations degrades the capability of the strain seismographs and the horizontal inertial seismographs. Some outage of the directional array will result during times of high winds.

Steps-of-strain are related to the conditions in the vicinity of the station rather than being related to an earthquake source mechanism. Their time function at QC-AZ is exponential rather than a step.

The strain field at the earth tide periods is the result of interaction among gravitational attraction of the moon and the sun, pressure variations, and temperature variations.

The ability of strain seismographs to improve the acoustic signal-to-wind noise ratio allows the detection of acoustic signals. The strain recording is capable of being used to separate acoustic modes on a repeatable basis.

16. ADMINISTRATION

The Program Manager for Project VELA T/8706 is James E. Fix, Senior Research Geophysicist. He was assisted in the design and the supervision of the field operation by John R. Sherwin, Project Physicist. William H. Bohne, Engineer, designed the mechanical details of the strain seismometer. The Queen Creek, Arizona, Seismological Station was operated by Roy R. Parrett, research technician and team leader, Joe Morgan, research technician, and Don R. York, research technician. Data analysis and data processing techniques were developed by the program manager. Scientific programming and data processing were carried out by the program manager; Jerry Crowley, senior scientific programmer; and B. L. Fitch, systems analyst. Mrs. Betty Keeling, analyst, was analyst and data librarian. Preliminary site selection and supervision of the modifications to the mine were done by Lynn R. Mayer, TFO Station Geologist.

John R. Sherwin was author of sections 3, 4, and 5, and of section 6 except for section 6.1.4. James E. Fix was author of the balance of the report.

17. REFERENCES

- Alsop, Leonard E., and Kuo, John T., 1964, The characteristic numbers of semi-diurnal earth tidal components for various earth models: *Ann. de Geophys.*, v. 20, p. 286-300.
- Alterman, Z.; Jarosch, H.; and Pekeris, C. L., 1959, Oscillations of the Earth: *Proc. Roy. Soc. London, Series A*, v. 252, p. 80-95.
- Balachandran, Nambath K., 1970, Effects of winds on the dispersion of acoustic-gravity waves: *J. Acoustical Soc. of Am.*, v. 48, no. 1, pp. 211-220.
- Balachandran, N. K., and Donn, William L., 1968, Dispersion of acoustic-gravity waves in the atmosphere, in George, T. M., ed., *Proc. ESSA/ARPA symposium on acoustic-gravity waves in the atmosphere*, 15-17 July 1968: Washington, Supt. of Documents, U. S. Govt. Printing Office, 437 p.
- Barjansky, A., 1944, The distortion of the Boussinesq field due to a circular hole: *Quart. Appl. Math.*, v. 2, p. 16-30.
- Basham, P. W., 1969, Canadian magnitudes of earthquakes and nuclear explosions in south-western North America: *Geophys. J. Roy. Astr. Soc.*, v. 17, p. 1-13.
- Basham, P. W.; Weichert, D. H.; and Anglin, F. M., 1970, An analysis of the 'BENHAM' aftershocks sequence using Canadian recordings: *J. Geophys. Res.*, v. 75, p. 1545-1556.
- Ben-Menahem, Ari, 1972, Mercury tiltmeter as an infrasonic detector; theory, observations, and applications: *J. Geophys. Res.*, v. 77, no. 5, p. 818-825.
- Bendat, Julius S., and Piersol, Allan G., 1966, *Measurement and analysis of random data*: New York, John Wiley & Sons, Inc., 390 p.
- Benioff, Hugo, 1935, A linear strain seismograph: *Bull. Seism. Soc. Am.*, v. 25, no. 4, p. 283-309.
- Benioff, Hugo, 1955, Seismographs, in H. E. Landsberg, ed., *Advances in geophysics*, v. 2: New York, Academic Press.
- Benioff, Hugo, 1959, Fused-quartz extensometer for secular, tidal, and seismic strains: *Bull. Geol. Soc. of Am.*, v. 70, p. 1019-1032.
- Benioff, Hugo, 1960, Observations of geomagnetic fluctuations in the period range 0.3 to 120 second: *J. Geophys. Res.*, v. 65, no. 5, p. 1413-1422.
- Benioff, Hugo, 1962, The characteristics of strain and pendulum seismograph combinations in *Proceedings of the Colloquium on Detection of Underground Nuclear Explosions*, VESIAC Special Report 4410-36-X: Ann Arbor, Institute of Science and Technology, The University of Michigan.

- Benioff, Hugo and Gutenberg, B., 1952, The response of strain and pendulum seismographs to surface waves: Bull. Seism. Soc. Am., v. 42, p. 229-237.
- Benioff, H. et al., 1955, Progress report of the Seismological Laboratory: Trans. Am. Geophys. Union, v. 36, no. 4.
- Berg, Edward and Lutschak, William, 1971, Tilt field and tilt propagation velocity associated with earthquakes (abstract): EOS, Trans. Am. Geophys. Union, v. 52, no. 11, p. 864.
- Blackman, R. B., and Tukey, J. W., 1958, The measurement of power spectra: New York, Dover Publications, Inc., 190 p.
- Bolt, B. A. and O'Neill, M. E., 1965, Times and amplitudes of phases PK_1KP and $PKIIP$: Geophys. J. Roy. Astr. Soc., v. 9, p. 223-231.
- Bolt, Bruce A.; McEvilly, T. V.; and Filson, J. R., 1968, the San Andreas Geophysical Observatory: initial results (abstract): Trans. Am. Geophys. Union, v. 49, no. 1, p. 287.
- Boore, David M., 1970, Love waves in nonuniform wave guides; finite difference calculations: J. Geophys. Res., v. 75, no. 8, p. 1512-1527.
- Boucher, Gary, 1972, Directional variations of spectral shape for microearthquakes in west-central Nevada (abstract): EOS Trans. Am. Geophys. Union, v. 53, no. 4, p. 449.
- Boucher, Gary; Malone, Stephen D.; and Homuth, E. Fred, 1971, Strain effects of nuclear explosions in Nevada: Bull. Seism. Soc. Am., v. 61, no. 1, p. 55-64.
- Brahtz, J. H. A., 1940, Stress distribution around a tunnel, discussion: Proc. Am. Soc. C. E., v. 66, p. 323-331.
- Brune, James N. and Oliver, Jack, 1959, The seismic noise of the Earth's surface: Bull. Seism. Soc. Am., v. 49, p. 349-353.
- Bullen, K. E., 1963, An introduction to the theory of seismology, 3rd ed.: Cambridge, Cambridge University Press, 381 p.
- Burden, H. Owen, 1964, Operation and calibration of advanced long-period system, technical report no. 64-95: Garland, The Geotechnical Corporation, 30 p.
- Capon, J., 1970, Analysis of Rayleigh-wave multipath propagation at LASA: Bull. Seism. Soc. Am., v. 60, p. 1701-1731.
- Capon, J., 1971, Analysis of Rayleigh-wave multipath propagation at LASA: Working paper, presented at Wood's Hole Conference on Seismic Discrimination, 20-23 July 1970.

- Capon, J.; Greenfield, R. J.; and Lacoss, R. T., 1967, Long-period signal processing results for Large Aperture Seismic Array, Technical note 1967-50: Lexington, Lincoln Laboratory, Massachusetts Institute of Technology, 82 p.
- Capon, J.; Greenfield, R. J.; and Lacoss, R. T., 1969, Long-period signal processing results for the Large Aperture Seismic Array: Geophysics, v. 34, p. 305-329.
- Carslaw, H. S., and Jaeger, J. C., 1959 (2nd ed.), Conduction of heat in solids: Oxford, Clarendon Press, p. 58-62.
- Clark, Sydney P., Jr., Ed., 1966, Handbook of Physical Constants, Rev. Ed., Memoir 97: New York, The Geological Society of America, 587 p.
- Der, Zoltan, 1969, Long-period seismic noise and atmospheric pressure variations. Part 2. The response of a layered half space to atmospheric pressure changes, Technical note 4/69: Garland, Geotech, A Teledyne Company.
- Derr, John S., 1970, Discrimination of earthquakes and explosions by the Rayleigh-wave spectral ratio: Bull. Seism. Soc. Am., v. 60, no. 5, p. 1653-1668.
- Dickey, D. D., 1969, Strain associated with the BENHAM underground nuclear explosion: Bull. Seism. Soc. Am., v. 59, no. 6, p. 2221-2230.
- Dickey, D. D., 1971, Strain accompanying the JORUM underground nuclear explosion and its relation to geology: Bull. Seism. Soc. Am., v. 61, no. 6, p. 1571-1581.
- Donn, William L., and Ewing, Maurice, 1962a, Atmospheric waves from nuclear explosions: J. Geophys. Res., v. 67, no. 5, p. 1855-1866.
- Donn, William L., and Ewing, Maurice, 1962b, Atmospheric waves from nuclear explosions - Part II: the Soviet test of 30 October 1961: J. of the Atmospheric Sciences, v. 19, p. 264-273.
- Donn, William L. and Shaw, David M., 1967, Exploring the atmosphere with nuclear explosions: Rev. of Geophys., v. 5, no. 1, p. 53-82.
- Doodson, A. T., 1921, The harmonic development of the tide-generating potential: Proc. Roy. Soc. London, Series A, v. 100, p. 305-329.
- Dorman, James, 1969, Seismic surface-wave data on the upper mantle in Hart, Pembroke J., ed., The Earth's crust and upper mantle, geophysical monograph 13: Washington, Amer. Geophys. Union, p. 257-264.
- Engdahl, E. R.; Flinn, Edward A.; and Romney, Carl F., 1970, Seismic waves reflected from the Earth's inner core: Nature, v. 228, p. 852-853.
- Evernden, J. F., 1953, Direction of approach of Rayleigh waves and related problems, Part I: Bull. Seism. Soc. Am., v. 43, p. 335-374.

- Evernden, J. F., 1954, Direction of approach of Rayleigh waves and related problems, Part II: Bull. Seism. Soc. Am., v. 44, p. 159-184.
- Evernden, J. F., 1967, Magnitude determination at regional and near-regional distances in the United States: Bull. Seism. Soc. Am., v. 57, p. 581-639.
- Evernden, J. F., 1969, Identification of earthquakes and explosions by use of teleseismic data: J. Geophys. Res., v. 74, no. 15, p. 3828-3856.
- Evernden, J. F., 1971, Variation of Rayleigh-wave amplitude with distance: Bull. Seism. Soc. Am., v. 61, no. 2, p. 231-240.
- Fernando, P.C.B., and Kannargara, M.L.T., 1966, The frequency spectrum of P_c3 and P_c4 micropulsations observed at Colombo, a station near the geomagnetic equator: J. Geophys. Res., v. 71, no. 21, p. 5149-5155.
- Fix, James E., 1969, The western United States island arc structure: unpublished manuscript.
- Fix, James E., 1972, Volumetric strain - a tool for earthquake prediction: (in preparation).
- Fix, James E., and Sherwin, John R., 1970, A high-sensitivity strain/inertial seismograph installation: Bull. Seism. Soc. Am., v. 60, no. 6, p. 1803-1822.
- Frantti, G. E.; Willis, D. E.; and Wilson, James T., 1962, The spectrum of seismic noise: Bull. Seism. Soc. Am., v. 52, p. 113-121.
- The Geotechnical Corporation, 1960, Movement of rock salt surrounding experimental pit no. 2, Carey Salt mine, Hutchinson, Kansas, Progress report no. 1: Garland, The Geotechnical Corporation, 16 p.
- Grissom, David; Sherwin, John R.; and Shopland, R. C., 1968, Development of LP wave discrimination capability using LP strain instruments, quarterly report no. 1, Project VT/8706, technical report no. 68-44: Garland, Geotech, A Teledyne Co., 27 p.
- Gossard, Earl E., 1960, Spectra of atmospheric scalars: J. of Geophys. Res., v. 65, no. 10, p. 3339-3351.
- Gupta, J. C.; Stening, R. J.; and van Beek, G. Jansen, 1971, Micropulsations in P_c3 to P_c4 period range at four Canadian observatories: J. Geophys. Res., v. 76, no. 4, p. 933-946.
- Gutenberg, B., 1945, Amplitudes of surface waves and magnitudes of shallow earthquakes: Bull. Seism. Soc. Am., v. 35, p. 3-12.
- Gutenberg, B. and Richter, C. F., 1956, Magnitude and energy of earthquakes: Annali de Geofisica, v. 9, p. 1-15.

- Hamilton, Jack H., 1964, Summary of long-period seismograph work at Geotech, technical report no. 64-121: Garland, The Geotechnical Corp., 39 p.
- Harkrider, David G., 1964, Theoretical and observed acoustic-gravity waves from explosive sources in the atmosphere: J. Geophys. Res., v. 69, no. 24, p. 5295-5321.
- Harkrider, David G., and Wells, Frederick J., 1968, The excitation and dispersion of the atmosphere surface wave in Georges, T. M., ed., Proc. ESSA/ARPA Symposium on acoustic gravity waves in the atmosphere, 15-17 July 1968: Washington, Supt. of Documents, U. S. Govt. Printing Office, 437 p.
- Harrison, J. C., 1968, Preliminary results of tilt measurements in the Poorman Mine near Boulder (abstract): Trans. Am. Geophys. Union, v. 49, no. 4, p. 664.
- Harrison, J. C., 1969, More tilt measurements from the Poorman Mine near Boulder, Colorado (abstract): EOS, Trans. Am. Geophys. Union, v. 50, no. 11, p. 643.
- Harrison, J. C.; Ness, N. J.; Longman, I. M.; Forbes, R.T.S.; Kraut, E. A.; and Slichter, L. B., 1963, Earth-tide observations made during the International Geophysical Year: J. Geophys. Res., v. 68, no. 5, p. 1497-1516.
- Haubrich, Richard A., 1965, Earth noise, 5 to 500 millicycles per second 1. spectral stationarity, normality, and nonlinearity: J. Geophys. Res., v. 70, p. 1415-1427.
- Haubrich, Richard A. and MacKenzie, Glenn S., 1965, Earth noise, 5 to 500 millicycles per second 2. reaction of the Earth to oceans and atmosphere: J. Geophys. Res., v. 70, p. 1429-1440.
- Haubrich, Richard A. and McCamy, Keith, 1969, Microseisms: coastal and pelagic sources: Rev. Geophys., v. 7, p. 539-571.
- Herrin, Eugene, 1971, Chapter 9, A comparative study of upper mantle models: Canadian Shield and Basin and Range Provinces; in Robertson, E. C., Ed., Nature of the Solid Earth: New York, McGraw-Hill, p. 211-226.
- Herrin, Eugene T.; Sorrells, G. G.; McDonald, John A., 1970, A digital acquisition system for geophysical data and some preliminary results: Working paper presented at Wood's Hole Conference on Seismic Discrimination, 20-23 July 1970.
- Herron, T. J.; Tolstoy, I.; and Kraft, D. W., 1969, Atmospheric pressure background fluctuations in the mesoscale range: J. Geophys. Res., v. 74, no. 6, p. 1321-1329.
- James, David E., 1971, Anomalous Love wave phase velocities: J. Geophys. Res., v. 76, no. 8, p. 2077-2083.

- Japanese Network of Crustal Movement Observatories, 1970, Spatial distribution of strain-steps associated with the earthquake of the central part of Gifu Prefecture, September 9, 1969 (in Japanese): Bull. Earthq. Res. Inst., v. 48, p. 1217-1233.
- Jeffery, G. B., 1921, Plane stress and plain strain in bipolar coordinates: Phil. Trans. Roy. Soc., A, v. 221, p. 265-293.
- Jeffreys, Sir Harold, 1962, The Earth, 4th Ed.: Cambridge, Cambridge Univ. Press, 438 p.
- Khorosheva, V. V., 1958, Effect of the atmospheric pressure on the tilting of the Earth's surface: Izvestia, Geophys. Ser. 1958, p. 77-79.
- Kirkpatrick, B. M., 1968, Long-period triaxial seismograph development, Quarterly report no. 7, Project VT/6706, Technical report no. 68-20: Garland, Geotech, A Teledyne Company, 27 p.
- Kuo, John T., 1969, Areal strain of solid earth tides observed in Ogdensburg, New Jersey: J. Geophys. Res., v. 74, no. 6, p. 1635-1644.
- Kuo, John T. and Ewing, Maurice, 1966, Spatial variations of tidal gravity in Steinhart, John S., and Smith, T. Jefferson, The Earth beneath the continents, Geophys. Mono. 10: Washington, Amer. Geophys. Union, p. 595-610.
- Kuo, J. T.; Jachens, R. C.; Ewing, M.; and White, G., 1970, Transcontinental tidal gravity profile across the United States: Science, v. 168, p. 968-971.
- Kuo, John T., and Thompson, George A., 1963, Model studies on the effect of a sloping interface on Rayleigh waves: J. Geophys. Res., v. 68, no. 22, p. 6187-6197.
- Lanczos, Cornelius, 1956, Applied analysis: Englewood Cliffs, Prentice Hall, Inc., 539 p.
- Lewis, D., and Dally, J. W., 1970, Photoelastic analysis of Rayleigh wave propagation in wedges: J. Geophys. Res., v. 75, no. 17, p. 3387-3398.
- Liebermann, R. C., and Pomeroy, P. W., 1969, Relative excitation of surface waves by earthquakes and underground explosions: J. Geophys. Res., v. 74, p. 1575-1590.
- Longman, I. M., 1962, A Green's function for determining the deformation of the Earth under surface mass loads, 1. theory: J. Geophys. Res., v. 67, no. 2, p. 845-850.
- Longman, I. M., 1963, A Green's function for determining the deformation of the Earth under surface mass loads, 2. computations and numerical results: J. Geophys. Res., v. 68, no. 2, p. 485-496.
- Love, A. E. H., 1909, The yielding of the Earth to disturbing forces: Proc. Roy. Soc. London, Series A, v. 82, p. 73-88

- Love, A. E. H., 1911, General theory of Earth tides, Chap. IV in Some problems of geodynamics: New York, Dover Publications, Inc.
- Love, A. E. H., 1927, A treatise on the mathematical theory of elasticity: New York, Dover Publications, Inc.
- McGarr, Arthur, 1971a, Stable deformation of rock near deep-level tabular excavations: J. Geophys. Res., v. 76, no. 29, p. 7088-7106.
- McGarr, Arthur, 1971b, Violent deformation of rock near deep-level, tabular excavations-seismic events: Bull. Seism. Soc. Am., v. 61, no. 5, p. 1453-1466.
- McGinley, J. R., 1968, A comparison of observed permanent tilts and strains due to earthquakes with those calculated from displacement dislocations in elastic earth models: Ph.D. Thesis, Calif. Inst. of Tech. (University Microfilms No. 69-14,397).
- Madden, T. R., and Claerbout, J., 1968, Jet stream associated gravity waves and implications concerning jet stream stability, in Georges, T. M., ed., Proc. ESSA/ARPA symposium on acoustic-gravity waves in the atmosphere, 15-17 July 1968: Washington, Sup. of Documents, U. S. Govt. Printing Office, 437 p.
- Major, Maurice W.; Sutton, George H.; Oliver, Jack; and Metsger, Robert, 1964, On elastic strain of the Earth in the period range 5 seconds to 100 hours: Bull. Seism. Soc. Am., v. 54, no. 1, p. 295-346.
- Major, M. W.; Butler, David; and Tocher, Don, 1971, Episodic strain in the central Aleutians (abstract): EOS Trans. Am. Geophys. Union, v. 52, no. 11, p. 868.
- Maple, Elwood, 1959a, Geomagnetic oscillations of middle latitudes, Part I. the observational data: J. Geophys. Res., v. 64, no. 10, p. 1395-1404.
- Maple, Elwood, 1959b, Geomagnetic oscillations at middle latitudes, Part II. sources of the oscillations: J. Geophys. Res., v. 64, no. 10, p. 1405-1409.
- Martin, Randolph J., III, 1972, Static fatigue and creep of quartzite (abstract): EOS Trans. Amer. Geophys. Union, v. 53, no. 4, p. 515.
- Melchior, Paul, 1966, The Earth tides: New York, Pergamon Press, 458 p.
- Milam, W. C., 1965, Final report on study of the operation of the Advanced Long-Period System, Technical report no. 65-93: Garland, Teledyne Industries, Geotech Div., 78 p., 6 app.
- Mindlin, Raymond D., 1939, Stress distribution around a tunnel: Proc. Am. Soc. C. E., v. 65, p. 619-642.
- Mindlin, Raymond D., 1940, Stress distribution around a tunnel, discussion: Proc. Am. Soc. C. E., v. 66, p. 1063-1064.

- Mindlin, Raymond D. and Cheng, David H., 1950, Nuclei of strain in a semi-infinite solid: J. Appl. Phys., v. 21, p. 926-930.
- Mitchell, B. J. and Landisman, M., 1969, Electromagnetic seismograph constants by least-squares inversion: Bull. Seism. Soc. Am., v. 59, no. 3, p. 1335-1348.
- Mogi, K., 1968a, Migration of seismic activity: Bull. Earthquake Res. Inst., v. 46, p. 53-74.
- Mogi, Kiyoo, 1968b, Sequential occurrences of recent great earthquakes: J. Phys. Earth, v. 16, no. 1, p. 30-36.
- Mogi, Kiyoo, 1968c, Development of aftershock areas of great earthquakes: Bull. Earthquake Res. Inst., v. 46, p. 175-203.
- Mogi, Kiyoo, 1969a, Some features of recent seismic activity in and near Japan (2) activity before and after great earthquakes: Bull. Earthquake Res. Inst., v. 47, p. 395-417.
- Mogi, Kiyoo, 1969b, Monthly distribution of large earthquakes in Japan: Bull. Earthquake Res. Inst., v. 47, p. 419-427.
- Mogi, Kiyoo, 1969c, Relationship between the occurrence of great earthquakes and tectonic structures: Bull. Earthquake Res. Inst., v. 47, p. 429-451.
- Morse, Philip M., and Feshbach, Hermann, 1953, Methods of theoretical physics: New York, McGraw-Hill Book Company, Inc.
- Molnar, Peter; Savino, John; Sykes, Lynn R.; Liebermann, Robert C.; Hade, George; and Pomeroy, Paul W., 1969, Small earthquakes and explosions in western North America recorded by new high-gain, long-period seismographs: Nature v. 224, p. 1268-1273.
- Munk, W. H. and Cartwright, D. E., 1966, Tidal spectroscopy and prediction: Phil. Trans. R. Soc. London, Series A, v. 259, p. 533-581.
- Nason, R. D., 1969, Preliminary instrumental measurements of fault-creep slippage on the San Andreas fault, California: Earthquake Notes, v. 40, p. 7-10.
- Olsen, C. W., 1967, Time history of the cavity pressure and temperature following a nuclear detonation in alluvium: J. Geophys. Res., v. 72, p. 5037-5041.
- Olsen, C. W., 1970, Soil strain near a nuclear detonation: Bull. Seism. Soc. Am., v. 60, no. 6, p. 1999-2014.
- Ozawa, I., 1961, On the observations of the earth tide by means of extensometers in horizontal components: Dis. Prev. Res. Inst., Kyoto Univ. Bull., no. 46, p. 1-15.

- Pekeris, C. L. and Jarosch, H., 1958, The free oscillations of the Earth in Benioff, H.; Ewing, M.; Howell, Jr., B. F.; and Press, Frank, Contributions in geophysics in honor of Beno Gutenberg: New York, Pergamon Press, p. 171-192.
- Peterson, Donald L., 1968, Bouguer gravity map of parts of Maricopa, Pima, Pinal, and Yuma Counties, Arizona, Geophysical Investigations Map GP-615: Washington, U. S. Geological Survey.
- Pfeffer, Richard L. and Zarichny, James, 1962, Acoustic-gravity wave propagation from nuclear explosions in the Earth's atmosphere: J. of the Atmospheric Sciences, v. 19, p. 256-263.
- Pfeffer, Richard L. and Zarichny, James, 1963, Acoustic-gravity wave propagation in an atmosphere with two sound channels: Geofisica Pura E Applicata - Milano, v. 55, p. 175-199.
- Pierce, Allan D., 1967, Guided infrasonic modes in a temperature- and wind-stratified atmosphere: J. Acoustical Soc. Am., v. 41, no. 3, p. 597-611.
- Pilant, W. L. 1967, Tectonic features of the Earth's crust and upper mantle, final technical report: Pittsburgh, University of Pittsburgh, (Clearinghouse for Fed. Sci. and Tech. Info. No. AD 658053).
- Pilant, W. L. and Knopoff, L., 1964, Observations of multiple seismic events: Bull. Seism. Soc. Am., v. 54, no. 1, p. 1939.
- Pomeroy, Paul W.; Hade, George; Savino, John; and Chander, Ramesh, 1969, Preliminary results from high-gain wide-band long-period electromagnetic seismograph systems: J. Geophys. Res., v. 74, no. 12, p. 3295-3298.
- Press, Frank, 1965, Displacements, strains, and tilts at teleseismic distances: J. Geophys. Res., v. 70, no. 10, p. 2395-2412.
- Press, Frank and Harkrider, David, 1962, Propagation of acoustic-gravity waves in the atmosphere: J. Geophys. Res., v. 67, no. 10, p. 3889-3908.
- Rector, Robert E., 1965, Shallow-hole test of long-period horizontal seismometer, Technical report no. 65-30: Garland, The Geotechnical Corp., 22 p.
- Richmond, W. O., and Feld, Jacob, 1939, Stress distribution around a tunnel, discussion: Proc. Am. Soc. C. E., v. 65, p. 1465-1468.
- Rigassi, Danilo A., 1970, Tidal anomalies and regional geological structure: Science, v. 170, p. 1002-1003.
- Rodgers, P. W., 1968, The response of the horizontal pendulum seismometer to Rayleigh and Love waves, tilt, and free oscillations of the Earth: Bull. Seism. Soc. Am., v. 58, no. 5, p. 1384-1406.
- Romig, P. R.; Major, M. W.; Wideman, C. J.; and Tocher, Don, 1969, Residual strains associated with a nuclear explosion: Bull. Seism. Soc. Am., v. 59, no. 6, p. 2167-2176.

- Romney, Carl, 1964, Combinations of strain and pendulum seismographs for increasing the detectability of P: *Bull. Seism. Soc. Am.*, v. 54, no. 6B, p. 2165-2174.
- Satô, Yasuo, 1958, Attenuation, dispersion and the wave guide of the G wave: *Bull. Seism. Soc. Am.*, v. 48, p. 231-251.
- Savage, J. C., 1971, A theory of creep waves propagating along a transform fault: *J. Geophys. Res.*, v. 76, no. 8, p. 1954-1966.
- Savino, John, 1970, Long-period earth noise and the detection of and discrimination between earthquakes and underground explosions: Working paper, presented at Wood's Hole Conference on Seismic Discrimination, 20-23 July 1970.
- Savino, John, and Hade, George, 1970, Long-period (15-150 sec) seismic noise observations at the Ogdensburg Mine Observatory (abstract): *Trans. Amer. Geophys. Union*, v. 51, no. 4, p. 363.
- Savino, John; McCamy, Keith; and Hade, George, 1972, Structures in Earth noise beyond 20 sec: a window for earthquakes: *Bull. Seism. Soc. Am.*, v. 62, no. 1, p. 141-176.
- Savino, J.; Sykes, L. R.; Liebermann, R. C.; and Molnar, P., 1971, Excitation of seismic surface waves with periods of 15 to 70 seconds from earthquakes and explosions: *J. Geophys. Res.*, v. 76, no. 32, p. 8003-8020.
- Schureman, P., 1940 (rev. ed.), A manual of the harmonic analysis and prediction of tides, U. S. Coast and Geodetic Survey Spec. Publ. 98: Washington, Supt. of Doc. (reprinted 1958 with corrections).
- Sen, Amiya K., 1971, Propagation of extra low frequency waves in the magnetosphere: *Geophys. J. R. Astr. Soc.*, v. 23, no. 2, p. 161-172.
- Shames, Irving, H., 1964, Mechanics of deformable solids: Englewood Cliffs, Prentice-Hall, Inc., 475 p.
- Shichi, Ryuichi; Iida, Kumizi; and Yamauchi, Tsuneo, 1970, Some considerations on the strain-step associated with the earthquake of the central part of Gifu Prefecture, September 9, 1969 (in Japanese): *Bull. Earthq. Res. Inst.*, v. 48, p. 1241-1249.
- Shida, T. and Matsuyoma, M., 1912, Note on Hecker's observations of horizontal pendulums: *Memoirs of Coll. of Sci. and Engr.*, Kyoto Imperial Univ., v. 4, p. 187-224.
- Shopland, Robert C., 1966, Shallow strain seismograph installation at the Wichita Mountains Seismological Observatory: *Bull. Seism. Soc. Am.*, vol. 56, no. 2, p. 337-360.
- Shopland, Robert C., 1968, Final Report, Project VT/5081, Multicomponent strain seismograph, 1 July 1965 to 31 December 1967, Technical report no. 68-3: Garland, Geotech, A Teledyne Company, 156 p., 2 app.

- Shopland, Robert C., 1970, Design of portable strainmeter system, Technical report no. 70-6: Garland, Teledyne Geotech, 55 p.
- Shopland, Robert C., 1971, Analysis of data from six portable strainmeters in southern Nevada, Special Report, VT/0703, Technical report no. 71-20: Garland, Teledyne Geotech, 89 p.
- Shopland, Robert C. and Kirklin, Richard H., 1969, Application of strain seismographs to the discrimination of seismic waves: Bull. Seism. Soc. Am., v. 59, p. 673-689.
- Shopland, Robert C. and Kirklin, Richard H., 1970, Application of a vertical strain seismograph to the enhancement of P waves: Bull. Seism. Soc. Am., v. 60, p. 105-124.
- Simons, R. S., 1968, Operation of long-period seismographs in deactivated missile silos, Technical report no. 68-4: Garland, Geotech, A Teledyne Company, 45 p.
- Simon, Ruth B., 1968, Earthquake interpretations: Golden, Colorado School of Mines, plate 18.
- Smith, Stewart W.; Archambeau, Charles B.; and Gile, William, 1969, Transient and residual strains from large underground explosions: Bull. Seism. Soc. Am., v. 59, no. 6, p. 2185-2196.
- Smith, Stewart W. and Kasahara, Keichi, 1969, Wave and mode separation with strain seismographs: Bull. Earthq. Res. Inst., v. 47, p. 831-848.
- Smith, Stewart W. and Kind, Ranier, 1972, Regional secular strain fields in southern Nevada: unpublished manuscript.
- Sorrells, G. G., 1969, Long-period seismic noise and atmospheric pressure variations. Part I. The response of an isotropic half space to a plane pressure wave, Technical note 3/69: Garland, Geotech, A Teledyne Company, 20 p.
- Sorrells, G. G., and Der, Zoltan, 1970, Long-period seismic noise and atmospheric pressure variations, Technical report no. 70-12: Garland, Teledyne Geotech, 76 p.
- Sorrells, G. G., and Goforth, T. M., 1972, The Earth's response to a wind generated pressure field: (in preparation).
- Sorrells, G. G.; McDonald, John A.; Der, Z. A.; Herrin, Eugene, 1971a, Earth motion caused by local atmospheric pressure changes: Garland, Texas, Teledyne-Geotech, 38 p.
- Sorrells, G. G.,; McDonald, John A.; and Herrin, Eugene T., 1971b, Ground motion associated with acoustic waves: Nature Physical Science, v. 229, no. 1, p. 14-16.

- Stacey, F. D. and Rynn, J. M. W., 1970, Spurious local effects associated with teleseismic tilts and strains, in Mansinha, L.; Smylie, D. E.; and Beck, A. E., eds, Earthquake Displacement Fields and the Rotation of the Earth: New York, Springer-Verlag New York Inc., p. 230-233.
- Stening, Robert J., and Gupta, Jagdish C., 1971, Amplitudes and periods of geomagnetic micropulsations in the $F_{C3, 4}$ range at Canadian observatories: Geophys. J. R. Astr. Soc., v. 23, no. 4, p. 379-386.
- Takemoto, Shuzo, 1970, Strain steps and the dislocation fault model: Bull. Dias. Prev. Res. Inst., Kyoto Univ., v. 20, part 1, no. 168, p. 1-15.
- Takeuchi, H.; Saito, M.; and Kobayashi, N., 1962, Statical deformations and free oscillations of a model Earth: J. Geophys. Res., v. 67, no. 3, p. 1141-1154.
- Teisseyre, Roman, 1966, Density field of dislocations and fold deformation problem: Bull. Earthquake Res. Inst., v. 44, p. 153-165.
- Teisseyre, Roman, 1967, Dislocation flow through a layered earth structure: Bull. Earthquake Res. Inst., v. 45, p. 359-374.
- Teisseyre, R., 1970, Crack formation and energy release caused by the concentration of dislocations along fault planes: Tectonophysics, v. 9, p. 547-557.
- Teledyne Industries, Geotech Division, 1966, Operation of two observatories, final report, Project VT/5054, 1 May 1965 through 30 April 1966, Technical report no. 66-54: Garland, Teledyne Industries, Geotech Division, 100 p., 3 app.
- Thirlaway, H. I. S., and Carpenter, E. W., 1966, Proc. VESIAC Special Study Conf. on Seismic Signal Anomalies, Travel Times, Amplitudes and Pulse Shapes, Beaugency, France, October 1964, VESIAC Rept 4410-99-X: Ann Arbor, VESIAC, University of Michigan.
- Tolstoy, Ivan, 1968, Mesoscale pressure fluctuations in the atmosphere in Georges, T. M., ed., Proc. ESSA/ARPA symposium on acoustic-gravity waves in the atmosphere, 15-17 July 1968: Washington, Supt. of Documents, U. S. Govt. Printing Office, 437 p.
- Tomascheck, R., 1937, Schwerkraftmessungen (in German): Die Naturwissenschaften, v. 12, p. 177-185.
- Tomascheck, R., 1953, Non-elastic tilt of the Earth's crust due to meteorological pressure distributions: Geofisica Pura e Applicata, v. 25, p. 17-25.
- Tomascheck, Rudolf, 1957, Tides of the solid Earth, in Encyclopedia of Physics, v. 47, Geophysics 2: Berlin, Springer-Verlag, p. 775-845.
- Trott, Wayne, 1965, Investigation of noise in long-period seismographs, technical report no. 65-91: Garland, Teledyne Industries, Geotech Div., 54 p., 2 app.

- Trott, Wayne, 1966, Experimental investigation of thermal noise, technical report no. 66-90: Garland, Geotech, A Teledyne Company, 39 p., 2 app.
- Vali, V.; Krogstad, R. J.; and Moss, R. W., 1965, Laser interferometer for earth strain measurements: Rev. Scient. Inst., v. 36, no. 9, p. 1352-1355.
- Ward, Peter L. and Hade, George, 1970, Design and deployment of five high-gain, broad-band, long-period seismograph stations, technical report: Palisades, Lamont-Doherty Geological Observatory of Columbia University, 13 p.
- Warren, N. M., 1966, Long-period seismograph installation, La Paz, Bolivia, Technical report no. 66-60: Garland, Teledyne Industries, Geotech Division, 16 p.
- West, Robert E. and Sumner, John S., 1972, Regional Bouguer gravity anomaly map of Arizona (abstract): EOS, Trans. Am. Geophys. Union, v. 53, no. 4, p. 343.
- Whalen, Joseph M., 1963, Instrumentation noise of long-period seismographs, paper presented at 13th IUGG General Assembly, Berkeley, California; also Technical report no. 63-81: Garland, The Geotechnical Corp., 26 p.
- Wideman, C. J. and Major, M. W., 1967, Strain steps associated with earthquakes: Bull. Seism. Soc. Am., v. 57, no. 6, p. 1429-1444.
- Wilson, Eldred D.; Moore, Richard T.; and Cooper, John R., 1969, Geologic map of Arizona, Map G61063: Washington, U. S. Geological Survey.
- Yamamoto, Ryoaburo, 1968, Propagation velocity of acoustic gravity wave due to large nuclear explosion in Georges, T. M., ed., Proc. ESSA/ARPA symposium on acoustic-gravity waves in the atmosphere, 15-17 July 1968: Washington, Supt. of Documents, U. S. Govt. Printing Office, 437 p.

APPENDIX 1 to TECHNICAL REPORT NO. 72-3

BIBLIOGRAPHY OF REPORTS SUBMITTED
ON PROJECT VT/8706

BIBLIOGRAPHY OF REPORTS SUBMITTED ON PROJECT VT/8706

The following is a bibliography in chronological order of the quarterly reports and special reports submitted under Project VELA T/8706.

- Grissom, David; Sherwin, John R.; and Shopland, R.C., 1968, Development of LP wave discrimination capability using LP strain instruments, quarterly report no. 1, Project VT/8706, technical report no. 68-44: Garland, Geotech, A Teledyne Company, 27 p.
- Fix, James E., 1969, Development of LP wave discrimination capability using LP strain instruments, quarterly report no. 2, Project VT/8706, technical report no. 69-6: Garland, Geotech, A Teledyne Company, 43 p.
- Fix, James E., 1969, Measurement of the total strain tensor, technical report no. 69-13: Garland, Geotech, A Teledyne Company, 16 p.
- Fix, James E. and Sherwin, John R., 1969, Development of LP wave discrimination capability using LP strain instruments, quarterly report, no. 3, Project VT/8706, technical report no. 69-18: Garland, Geotech, A Teledyne Company, 17 p.
- Fix, James E. and Sherwin, John R., 1969, Development of LP wave discrimination capability using LP strain instruments, quarterly report no. 4, Project VT/8706, technical report no. 69-45: Garland, Geotech, A Teledyne Company, 21 p., 1 app.
- Fix, James E., 1969, Development of LP wave discrimination capability using LP strain instruments, quarterly report no. 5, Project VT/8706, technical report no. 69-50: Garland, Geotech, A Teledyne Company, 7 p.
- Fix, James E. and Sherwin, John R., 1970, A high-sensitivity strain/inertial seismograph installation, technical report no. 70-3: Garland, Teledyne Geotech, 44 p.
- Fix, James E. and Sherwin, John R., 1970, Development of LP wave discrimination capability using LP strain instruments, quarterly report no. 6, Project VT/8706, technical report no. 70-5: Garland, Teledyne Geotech, 38 p., 1 app.
- Fix, James E., 1970, Development of LP wave discrimination capability using LP strain instruments, quarterly report no. 7, Project VT/8706, technical report no. 70-17: Garland, Teledyne Geotech, 27 p.
- Fix, James E. and Sherwin, John R., 1970, Development of LP wave discrimination capability using LP strain instruments, quarterly report no. 8, Project VT/8706, technical report no. 70-29: Garland, Teledyne Geotech, 99 p., 1 app.

- Fix, James E. and Sherwin, John R., 1970, Development of LP wave discrimination capability using LP strain instruments, quarterly report no. 9, Project VT/8706, technical report no. 70-31: Garland, Teledyne Geotech, 71 p., 1 app.
- Fix, James E. and Sherwin, John R., 1971, Development of LP wave discrimination capability using LP strain instruments, quarterly report no. 10, Project VT/8706, technical report no. 71-3: Garland, Teledyne Geotech, 47 p., 2 app.
- Fix, James E. and Sherwin, John R., 1971, Development of LP wave discrimination capability using LP strain instruments, quarterly report no. 11, Project VT/8706, technical report no. 71-6: Garland, Teledyne Geotech, 11 p.
- Fix, James E. and Sherwin, John R., 1972, Final Report, Project VT/8706, Development of LP wave discrimination capability using LP strain instruments, technical report no. 72-3: Garland, Teledyne Geotech, 537 p, 6 app.

APPENDIX 2 to TECHNICAL REPORT NO. 72-3

SENSITIVITY REQUIRED FOR LONG-PERIOD STRAIN
TO BE EQUIVALENT TO ADVANCED LONG-PERIOD
INERTIAL SYSTEM

SENSITIVITY REQUIRED FOR LONG-PERIOD STRAIN
TO BE EQUIVALENT TO ADVANCED LONG-PERIOD
INERTIAL SYSTEM

METHOD

1. Define resolution as $1 \text{ mm} = 1 \times 10^{-3} \text{ m}$ peak-to-peak at X10 view.
2. From response curve of high-gain advanced long-period channel, determine ground displacement resolution.
3. Using Benioff's horizontal strain equation and available Rayleigh wave phase velocities calculate strain and differential displacement required to equal sensitivity of inertial system.
4. Using Romney's relation between summed horizontals and vertical strain seismographs and $\frac{\lambda+2\mu}{\lambda} = 2.75$ estimate vertical strain.

SAMPLE CALCULATIONS

At 25 sec period maximum magnification of inertial system is 100,000

1. Displacement resolution defined as $\frac{1 \times 10^{-3} \text{ m}}{10^5} = 1 \times 10^{-8} \text{ m} = 10 \text{ nm}$ (1)
2. Benioff (1935, BSSA) equation (8) p 290 for longitudinal apparent waves

$$y = - \frac{L}{c} \cos^2 \beta \frac{du}{dt} \quad (2)$$

where:

y = total relative displacement of piers parallel to the line joining them

L = distance between piers

β = angle between direction of u and direction between piers

u = horizontal displacement of the ground in direction of wave travel

t = time

c = phase velocity

We are interested in y as differential displacement and y/L as strain.

Let us consider the case where $\beta = 0$ and $\cos^2 \beta = 1$. Also write du/dt as $i\omega u$ and substitute $2\pi/T$ for ω . (ω = angular frequency and T = period.) Equation (2) then becomes

$$y = \frac{iL2\pi u}{cT} \quad (3)$$

or

$$\frac{y}{L} = - \frac{i2\pi u}{cT} \quad (4)$$

For numerical values, we will neglect the phase shift indicated by $-i$.

3. For $T = 25$ sec, $L = 20$ m, $c = 4.0 \times 10^3$ m/sec

$$y = \frac{(20 \text{ m})(2\pi)(1 \times 10^{-8} \text{ m})}{(4.0 \times 10^3 \text{ m/sec})(25 \text{ sec})}$$

$$= 1.26 \times 10^{-11} \text{ m} = \text{horizontal differential displacement}$$

$$\frac{y}{L} = 6.28 \times 10^{-13} \frac{\text{m}}{\text{m}} = \text{horizontal strain}$$

4. Vertical strain

$$\frac{z}{L} = \frac{6.28 \times 10^{-13} \frac{\text{m}}{\text{m}}}{2.75}$$

$$= 2.28 \times 10^{-13} \frac{\text{m}}{\text{m}} \text{ vertical strain}$$

TABULATED CALCULATIONS

T	Period (sec)	Advanced long-period inertial sensitivity (high-gain channel)	magnification	displacement u	Phase velocity c	$\frac{y}{L} = \frac{2\pi}{cT}$	Strain m/m per meter displacement at surfaces	Horizontal strain equivalent to inertial sensitivity	Z/L	Vertical strain equivalent to inertial sensi- tivity	Differential displacement, L = 20
3			1.5x10 ²	6.6x10 ⁻⁶	3.20 ^a	6.55x10 ⁻⁴	4.32x10 ⁻⁹	1.57x10 ⁻⁹	1.79x10 ⁻¹¹	8.64x10 ⁻⁸	
6			1.0x10 ²	1x10 ⁻⁵	3.25 ^a	3.22x10 ⁻⁴	3.22x10 ⁻⁹	1.17x10 ⁻⁹	1.26x10 ⁻¹¹	6.44x10 ⁻⁸	
8			2.0x10 ³	5x10 ⁻⁷	3.35 ^a	2.35x10 ⁻⁴	1.18x10 ⁻¹⁰	4.3x10 ⁻¹¹	1.05x10 ⁻¹¹	2.36x10 ⁻¹⁰	
10			8.0x10 ³	1.25x10 ⁻⁷	3.40 ^a	1.85x10 ⁻⁴	2.31x10 ⁻¹¹	8.4x10 ⁻¹²	1.12x10 ⁻¹¹	4.62x10 ⁻¹⁰	
15			4.5x10 ⁴	2.22x10 ⁻⁸	3.75 ^b	1.12x10 ⁻⁴	2.48x10 ⁻¹²	9.0x10 ⁻¹³	1.63x10 ⁻¹¹	4.96x10 ⁻¹¹	
20			9.0x10 ⁴	1.11x10 ⁻⁸	3.90 ^c	8.05x10 ⁻⁵	8.95x10 ⁻¹³	3.25x10 ⁻¹³	1.79x10 ⁻¹¹	1.79x10 ⁻¹¹	
25			1.0x10 ⁵	1.0x10 ⁻⁸	4.00 ^c	6.28x10 ⁻⁵	6.28x10 ⁻¹³	2.28x10 ⁻¹³	1.26x10 ⁻¹¹	1.26x10 ⁻¹¹	
30			1.0x10 ⁵	1.0x10 ⁻⁸	4.00 ^c	5.24x10 ⁻⁵	5.24x10 ⁻¹³	1.90x10 ⁻¹³	1.05x10 ⁻¹¹	1.05x10 ⁻¹¹	
40			7x10 ⁴	1.43x10 ⁻⁸	4.00 ^c	3.93x10 ⁻⁵	5.61x10 ⁻¹³	2.04x10 ⁻¹³	1.12x10 ⁻¹¹	1.12x10 ⁻¹¹	
60			3.2x10 ⁴	3.12x10 ⁻⁸	4.00 ^c	2.62x10 ⁻⁵	8.16x10 ⁻¹³	2.95x10 ⁻¹³	1.63x10 ⁻¹¹	1.63x10 ⁻¹¹	
100			1.0x10 ⁴	1.0x10 ⁻⁷	4.20 ^c	1.49x10 ⁻⁵	1.49x10 ⁻¹²	5.42x10 ⁻¹³	2.98x10 ⁻¹¹	2.98x10 ⁻¹¹	
200			1.4x10 ³	7.15x10 ⁻⁷	4.55 ^d	6.90x10 ⁻⁶	4.95x10 ⁻¹²	1.80x10 ⁻¹²	9.90x10 ⁻¹¹	9.90x10 ⁻¹¹	
400			1.8x10 ²	5.55x10 ⁻⁶	6.00 ^d	2.62x10 ⁻⁶	1.45x10 ⁻¹¹	5.27x10 ⁻¹²	2.90x10 ⁻¹⁰	2.90x10 ⁻¹⁰	
600			5.8x10 ¹	1.72x10 ⁻⁵	6.65 ^d	1.57x10 ⁻⁶	2.70x10 ⁻¹¹	9.80x10 ⁻¹²	5.40x10 ⁻¹⁰	5.40x10 ⁻¹⁰	
1000			15.0	6.67x10 ⁻⁵	6.40 ^d	9.80x10 ⁻⁷	6.65x10 ⁻¹¹	2.42x10 ⁻¹¹	1.33x10 ⁻⁹	1.33x10 ⁻⁹	

a WMSO model

b interpolated

c. Kuo, Brune, and Major, 1962, BSSA

Brune, Benioff, and Ewing, 1961, BSSA

APPENDIX 3 to TECHNICAL REPORT NO. 72-3

INSTRUMENT NOMENCLATURE, RECORDER
CHANNEL ALLOCATION, AND POLARITY

INSTRUMENT NOMENCLATURE, RECORDER CHANNEL ALLOCATION, AND POLARITY

This appendix lists the instrument nomenclature, the normal recorder channel assignments, and the polarity convention for the Queen Creek Seismological Station (QC-AZ).

1. NOMENCLATURE

The nomenclature used for the instrument system identifiers is:

<u>Category of data</u>	<u>Identifier</u>
Time:	BCD = binary coded decimal station time WWV = WWV time
Compensation:	Comp = playback compensation channel
Data:	first symbol: S = strain P = pendulum M = microbarograph* W = wind second symbol*: Z = vertical 325 = 325 degree azimuth 55 = 55 degree azimuth V = (wind) velocity D = (wind) direction third symbol: L = Advanced Long-Period System (ALPS) response U = Ultra-Long-Period (ULP) response V = Extended-Long-Period response B = Broad-Band (BB) response

S = Short-Period (SP) response

fourth symbol: L = Low gain

1,2,3 = numbers assigned to similar instruments

*Microbarograph channel identifiers do not have a symbol in the second symbol category.

Flag: flag = identifier for clipping at Ithaco amplifier output

2. RECORDER CHANNELS

2.1 TAPE RECORDERS

<u>Channel No.</u>	<u>Recorder</u>		
	<u>No. 1</u>	<u>No. 2</u>	<u>No. 3</u>
1	BCD	BCD	BCD
2	SZLL	WV2	MU
3	P325LL	SZB	SZUL
4	P55L	P55S	P55X
5	S325L'	S55B	S325UL
6	S55L	S55S	S55U
7	Comp	Comp	Comp
8	S325L	S325S	S325U
9	SZL	SZS	SZU
10	P325L	P325S	P325X
11	PZL	PZS	PZX
12	S55LL	WD2	S55UL
13	PZLL	S325B	ML1
14	P55LL	WWV	ML2

2.2 16 mm FILM RECORDERS

<u>Channel No.</u>	<u>No. 1</u>	Recorder	<u>No. 2</u>
1	FLAG		WV
2	WV		S325L-S55L
3	SZL		SZL+S325L+S55L
4	SZLL		S325L+S55L
5	S325L		SZL
6	S325LL		PZL
7	S55L		S325L+P325L
8	S55LL		S325L+P325L
9	PZL		S55L+P55L
10	P325L		S55L-P55L
11	P55L		ML1
12	PZX		off
13	P325X		off
14	P55X		off
15	ML1		off
16	PZS		off
17	ML2		only
18	WV		16
19	WD		channels

2.3 35 mm FILM RECORDER

<u>Channel No.</u>	
1	SZU
2	S55U
3	S325U
4	MU

2.4 PAPER CHART RECORDERS

	<u>Recorder</u>
SZB	No. 1
S325B	No. 2
S55B	No. 3

3. POLARITY

The polarity convention used on QC-AZ recorders is as follows:

Strain:	Compression is up on film recorders and positive voltage into the magnetic-tape recorders.
Inertial:	Displacement toward up, toward 325 deg azimuth, and toward 55 deg azimuth are up on film recorders and positive voltage into the magnetic-tape recorders.
Electromagnetic calibration coils:	Connected so that a dc current turned on produces a positive output.

APPENDIX 4 to TECHNICAL REPORT NO. 72-3

ROUTINE OPERATING INSTRUCTIONS FOR QC-AZ

ROUTINE OPERATING INSTRUCTIONS FOR QC-AZ

OPERATIONS

1. General

- 1.1 Logs - Logs must be able to stand alone. For example, if a seismic channel is off the air, an entry should be made in the log of every recorder affected for every day the condition continues. Similarly, non-routine special tests, high level recordings, and the like should be noted on every affected log for as long as the test is in progress. This means that considerable writing and duplication will be required, but it is necessary. Remember that there is no such thing as an over-documented log.
- 1.2 Dc Offsets - Check dc offsets daily, and adjust as necessary. This is especially important for SP and ULP channels not recorded on a Develocorder.
- 1.3 General Maintenance - At least once per month, perform general maintenance and cleaning on all equipment in the vans. Don't forget such items as battery electrolyte level and voltage, air conditioner filters, microbarograph power supply operation, etc. A few hours loss of data due to regular preventative maintenance is far more acceptable than the unexpected loss of overnight recording, which usually occurs at precisely the wrong time.
- 1.4 Weekly Log - A general log of any extraordinary item affecting any channel should be kept on a daily basis and sent to Garland with film shipments every week. Items to include are (1) special tests, (2) major maintenance, (3) calibration constant changes, (4) filter changes, etc. Comments need only refer briefly to the item in question so that Garland personnel may refer to the daily logs for details.
- 1.5 Recording - Recordings are to be maintained on as continuous a basis as possible. Do not enter the mine unless maintenance on a channel is absolutely necessary. If at all possible, do not turn on mine lights which cause long-lasting temperature effects. Keep personnel time in the mine to a minimum.

When necessary to enter the mine for work on any instrument, all data channels (film and tape), with the exception of the channels worked on, are to be left turned on. This will allow analysts to determine, for example, what effects personnel in the mine have on temperature changes or the like.

2. Develocorder #1

- 2.1 High gain strains, ALPS, and Extended Range LP's should be maintained at 50K @ 25 sec, \pm 10%.
- 2.2 Low gain strains should be maintained at about 5K (equiv).

- 2.3 Short-period inertials should be operated at 500K @ 1 Hz, $\pm 10\%$.
- 2.4 Trace overlining due to long-term drift should be avoided.
- 2.5 Adjust radio reception to obtain readable WWV recording for the greatest possible time.

3. Develocorder #2

- 3.1 Maintain all seismic channels at a gain of 25K $\pm 10\%$.
- 3.2 Maintain gain of channels incorporated in algebraic sums within $\pm 5\%$.

4. Tape Recorders

- 4.1 Routine background level for all high gain channels is 100 mV p-p.
- 4.2 Routine calibration levels for all high gain channels is 2 to 2.5 V, p-p.
- 4.3 Tape channel alignment and playback noise level should be performed at least once every 3 days for each recorder. Scheduling is optional, but some routine should be established.
- 4.4 Monitor connecting chassis power supply noise and ripple once every 2 weeks. Noise should not exceed 100 mV.
- 4.5 General preventative maintenance - oiling, cleaning, bearing checks, etc. - should be performed on a regular 3 month basis.
- 4.6 DAILY - Mark tape near leader with following information: QC-AZ, date, TR # _____. Make leader of approximately 15 turns on take-up reel. Mark record start across tape.

5. ULPS Recorder

- 5.1 Change every 5 days.
- 5.2 Position drums so that 0000Z is first hour mark appearing on the film.
- 5.3 Read starting and ending calibrations and record results on logs.
- 5.4 Background levels should be set so that no trace goes off film except for large events. Nominal background should not exceed 15 to 20 mm at X10 view.

6. Critical Run Procedure

- 6.1 Stop all except emergency maintenance by 1800Z on day prior to critical day.
- 6.2 Attenuate as required and carefully check all recorders for proper operation, dc offsets, etc.

Short-period channel gains are calculated for the expected amplitude of the Lg phase. Since the recorded LR phase is about six times

greater in amplitude on the LP channels, LP's should be operated at one-sixth of the SP gain or at operate, whichever is smaller.

Attenuate the strain channels as follows:

<u>Req'd attenuation</u>	<u>Input attenuation</u>	<u>Gain</u>
0 to 20 dB	20 dB	0 to 18 dB max
20 to 30 dB	30 dB	0 to 12 dB max
30 to 40 dB	40 dB	0 to 12 dB max

- 6.3 Calibrate S-S, P-S, S-L, P-L channels after changing tapes and prior to the end of the work day.
 - 6.4 Do not disturb any instrument on critical day unless notified otherwise.
 - 6.5 Calibrate S-S, P-S, S-L, P-L channels before tape change if critical period is past.
 - 6.6 Return to routine operation -- Check all channels for proper operation.
7. Broad-Band Recorders
- 7.1 Record at highest sensitivity practical, ultimately limited by earth tides at about 1 μ m p-p relative pier displacement.
 - 7.2 Set chart clipping to ± 1.4 V as a monitor for tape clipping.
 - 7.3 Check dc balance at least twice per day and adjust as necessary. Balancing circuits are useful for up to ± 9 volts offset from the transducer itself. When offsets exceed ± 9 volts, reset mechanical zero (micrometer) to produce zero volts transducer output. Record and graph required mechanical adjustments for long-term secular strain studies.
 - 7.4 Chart records should be sent to Garland on a weekly basis.

CALIBRATIONS

1. ULPS System

- 1.1 Calibrate at 100 seconds for 10 minutes, minimum.
- 1.2 Set calibration current to produce a signal-to-noise ratio of 5:1, minimum. Separate calibrations may be necessary to satisfy both tape and film requirements.
- 1.3 Calibrate start and end of every film record.
- 1.4 Read calibrations, compute gains for both calibrations, and record on log.

1.5 Calibrate MUI once per record, if possible.

2. ALPS System (Strain and Pendulum)

2.1 Calibrate at 25 seconds for 3 minutes, minimum.

2.2 Set calibration current to produce a signal-to-noise ratio of 5:1, minimum. Separate calibrations may be necessary to satisfy both tape and film requirements.

2.3 Calibrate every channel in operation at the beginning of every work day.

2.4 As soon as practical (e.g., just before lunch), read cals and compute gains - enter on logs. Any channel not meeting gain tolerances should be adjusted and re-calibrated immediately.

2.5 Record pendulum seismometer free periods weekly. Adjust as necessary to maintain a tolerance of 17.1 to 17.4 seconds.

3. SP System (Strain and Pendulum)

3.1 Calibrate daily at 1 Hz for 15 seconds, minimum.

3.2 Read calibrations, compute gains and record results on logs.

4. Broad-Band System

4.1 Calibrate with a dc pulse of at least 10 minutes duration once every 5 days and after any gain changes.

4.2 Read calibration amplitude and compute peak-to-peak sensitivity of chart record. Record results on each chart.

APPENDIX 5 to TECHNICAL REPORT NO. 72-3

OPERATING HISTORY OF QC-AZ

OPERATING HISTORY OF QC-AZ

The following is a chronological listing of the major events during the operations at QC-AZ. Many of these entries will be useful to those desiring to use the QC-AZ data.

<u>Run No.</u>	<u>Date</u>	<u>Event</u>
233-69	21 August 1969	Recording vans arrive and are set up on-site. Mine modification in progress.
275-69	02 October 1969	SP inertial instruments set up temporarily at mine adit; gain to 500K at night.
308-69	04 November 1969	All major parts of strain seismometer, except main magnets, arrive at site.
330-69	26 November 1969	Temporary operation and testing begun on un-insulated strain seismometer - S55.
358-69	24 December 1969	Inertial LP seismographs placed in temporary operation for tests; gain to about 20K.
002-70	02 January 1970	6 sec notched filters (Geotech Model 6824-15) placed in P_L channels.
033-70	02 February 1970	Mine modification work terminated. All mining equipment removed.
019-056-70	19 Jan-25 Feb 70	Major installation - SP and LP inertials permanently installed; side-by-side 325 degree azimuth strain seismometers installed; strain seismometers insulated; three ship's doors installed in mine.
057-70	26 February 1970	All equipment placed in operation; P_L's and S_L's have notched filters (6824-15).
099-70	09 April 1970	ULP response reduced for long-period noise; replaced 1000 sec low pass filter with similar 283 sec unit.
117-70	27 April 1970	"Flag" trace added to Develocorder film; large pulses on S_L channels traced to saturation of Ithaco amplifiers on SP signals.
119-70	29 April 1970	P_L Junction Assemblies improperly wired - seismometers overdamped since being placed in operation.

<u>Run No.</u>	<u>Date</u>	<u>Event</u>
125 to 127-70	5-7 May 1970	Work on P_L's; tests showed that instruments could not be matched to design parameters with more efficient transducers on GFE seismometers
131-70	11 May 1970	Temporary capacitors placed across S55 and S325-1 data coils to form approximate 0.8 Hz low pass filters. "Flag" indications on film cease except for very large events.
160-70	09 June 1970	Unnotched filters (Model 6824-14) installed in P_L and S_L seismographs.
167 to 170-70	16-19 June 1970	Final parameter adjustments on P_L seismometer after installing old design coils and magnets.
181-70	30 June 1970	Operations terminated on S325-2.
191-70	10 July 1970	Vertical Strain (SZ) on the air.
194 to 196-70	13-15 July 1970	Cemented S325 anchor to prevent creep.
202-70	21 July 1970	Reworked lightning protection cricuits for Ithaco amplifier - no further failures experienced.
205-70	24 July 1970	S325B transducer on the air.
216-70	04 August 1970	Routine operating instructions put into effect.
225-70	13 August 1970	Capacitors installed across 3 strain data coils to form 0.80 Hz filters.
226-70	14 August 1970	S55B and SZB placed in operation.
231-70	19 August 1970	Modifications to redamp P_S and S_S circuits complete; necessary due to addition of capacitors at input to strain Ithaco amplifiers.
265 to 268-70	22-25 September 1970	Step-of-strain tests.
278 to 282-70	5-9 October 1970	Step-of-strain tests.
307-70	3 November 1970	0.8 Hz low pass filter added to all P_L channels to improve phase match at shorter periods (15 to 10 sec)
323-70	19 November 1970	Time constant of instrument room behind sealed door (#3 only) - 39 minutes.

342-70	08 December 1970	Notched filters (Geotech 6824-15) installed in P_L and S_L channels.
046 to 048-71	15-17 February 1971	Timbering and ventilation of mine.
049-71	18 February 1971	40-sec high pass filter added to summed channels on Develocorder #2 only.
069-71	10 March 1971	Following equipment turned off: 35 mm film recorder, tape recorder #3, P_X seismographs, S_U seismographs, inside microbarograph (ML1).
125-71	5 May 1971	Placed 40-sec high pass filters on all S_L and P_L horizontal traces.
132-71	12 May 1971	40-sec filters on all PZL and SZL channels.
152-71	01 June 1971	QC-AZ shut down 1700Z.

APPENDIX 6 to TECHNICAL REPORT NO. 72-3

SELECTED BIBLIOGRAPHY

of

DISLOCATION THEORY AND OBSERVATIONS OF RESIDUAL STRAINS

SELECTED BIBLIOGRAPHY
of
DISLOCATION THEORY AND OBSERVATIONS OF RESIDUAL STRAINS

- Aki, Keiiti, 1968, Seismic displacements near a fault: J. Geophys. Res., v. 73, no. 16, p. 5359-5376.
- Banaugh, Robert P., 1964, Application of integral representations of displacement potentials in elasto-dynamics: Bull. Seism. Soc. Am., v. 54, no. 4, p. 1073-1086.
- Ben-Menahem, Ari and Gillon, Allon, 1970, Crustal deformation by earthquakes and explosions: Bull. Seism. Soc. Am., v. 60, no. 1, p. 193-215.
- Ben-Menahem, Ari and Israel, Moshe, 1970, Effects of major seismic events on the rotation of the Earth: Geophys. J. R. Astr. Soc., v. 19, p. 367-393.
- Ben-Menahem, Ari and Singh, Sarva Jit, 1968, Eigenvector expansions of Green's dyads with applications to geophysical theory: Geophys. J. R. Astr. Soc., v. 16, p. 417-452.
- Ben-Menahem, A. and Singh, S. J., 1970, Deformation of a spherical earth model by finite dislocations in Mansinha, L; Smylie, D. E., eds., Earthquake Displacement Fields and the Rotation of the Earth: New York, Springer-Verlag New York, Inc., p. 30-45.
- Ben-Menahem, Ari; Singh, Sarva Jit; and Solomon, Faiza, 1969, Static deformation of a spherical earth model by internal dislocations: Bull. Seism. Soc. Am., v. 59, no. 2, p. 813-953.
- Blackford, M. E.; Major, M. W.; and Butler, D. L., 1969, Strain steps from the nuclear explosion MILROW (postdeadline abstract): Presented at the Fall meeting AGU, Dec. 1969.
- Bonchkovsky, V. F., 1958, Deformation of the Earth's surface, preceding and accompanying a catastrophic earthquake: Izv., Geophys. Ser., p. 1111-1113.
- Bonchkovsky, V. F., 1962, Deformations of the Earth's surface accompanying certain disastrous distant earthquakes: Izv., Geophys. Ser., p. 190-193.
- Boore, David M.; Aki, Keiiti; and Todd, Terry, 1971, A two-dimensional moving dislocation model for a strike-slip fault: Bull. Seism. Soc. Am., v. 61, no. 1, p. 177-194.
- Boucher, Gary W.; Ryall, Alan; Homuth, E. F.; and Savage, W. U., 1969, Strain and field-seismic observations of effects due to the Nevada underground nuclear test JORUM (postdeadline abstract): Presented at the Fall Meeting AGU, Dec., 1969.
- Chinnery, M. A., 1961, The deformation of the ground around surface faults: Bull. Seism. Soc. Am., v. 51, no. 3, p. 355-372.

- Chinnery, M. A., 1963, The stress changes that accompany strike-slip faulting: Bull. Seism. Soc. Am., v. 53, no. 5, p. 921-932.
- Chinnery, M. A., 1965, The vertical displacements associated with trans-current faulting: J. Geophys. Res., v. 70, no. 18, p. 4627-4632.
- Chinnery, M. A., 1966a, Secondary faulting I. Theoretical aspects: Canadian Journal of Earth Sciences, v. 3, p. 163-174.
- Chinnery, M. A., 1966b, Secondary faulting II. Geological aspects: Canadian Journal of Earth Sciences, v. 3, p. 175-190.
- Chinnery, M. A., 1970, Earthquake displacement fields in Mansinha, L.; Smylie, D. E.; and Beck, A. E., eds. Earthquake Displacement Fields and the Rotation of the Earth: New York, Springer-Verlag New York, Inc., p. 17-38.
- Chinnery, Michael A. and Petrak, John A., 1967, The dislocation fault model with a variable discontinuity: Tectonophysics, v. 5, no. 6, p. 513-529.
- Commerce Today, 1971, Puzzling creeps detected along quake-prone San Andreas fault; Science & Technology Report
- Dickey, D. D., 1971, Strain accompanying the JORUM underground nuclear explosion and its relation to geology: Bull. Seism. Soc. Am., v. 61, no. 6, p. 1571-1581.
- Droste, Sophia and Teisseyre, Roman, 1960, The theory of the dislocation processes and its application to the Pacific region: Bull. Seism. Soc. Am., v. 50, no. 1, p. 57-70.
- Duval, Wilbur I., 1953, Strain-wave shapes in rock near explosions: Geophysics, v. 18, p. 310-323.
- Engdahl, Eric R.; Brockman, Stanley R.; and King, Kenneth W., 1969, MILROW seismic effects (postdeadline abstract): Presented at the Fall meeting AGU, Dec. 1969.
- Ewing, Maurice and Donn, William L., 1963, Polar wandering and climate in Polar wandering and continental drift: Society of Economic Paleontologists and Mineralogists.
- Frank, F. C., 1951, Crystal dislocations. - Elementary concepts and definitions: Philosophical Magazine, ser. 7, v. 42, p. 809-819.
- Hamilton, R. M. and Healy, J. H., 1969, Aftershocks of the JORUM underground nuclear explosion (postdeadline abstract): Presented at the Fall meeting AGU, Dec., 1969.
- Haskell, N. A., 1969, Elastic displacements in the near-field of a propagating fault: Bull. Seism. Soc. Am., v. 59, no. 2, p. 865-908.

- Hastie, L. M. and Savage, J. C., 1970, A dislocation model for the 1964 Alaska earthquake: Bull. Seism. Soc. Am., v. 60, no. 4, p. 1389-1392.
- Healy, J. H.; Rubey, W. W.; Griggs, D. T.; and Raleigh, C. B., 1968, The Denver earthquakes: Science, v. 161, no. 3848, p. 1301-1310.
- Herrera, I., 1964, On a method to obtain a Green's function for a multi-layered half space: Bull. Seism. Soc. Am., v. 54, no. 4, p. 1087-1096.
- Honda, H. and Miura, T., 1935, On the strain produced in a semi-infinite elastic solid by statical surface force, with some applications to seismology: Geophys. Magazine, v. 9, p. 61-81.
- Kabuzenko, S. N., 1959, The theory of thermal deformations of the Earth's surface: Izv., Geophys. Ser., Bull. Acad. Sci. USSR, p. 445-449.
- Kasahara, Keichi, 1957, The nature of seismic origins as inferred from seismological and geodetic observations (1): Bull. of the Earthquake Res. Inst., v. 35, p. 474-530.
- Kasahara, Keichi, 1958, The nature of seismic origins as inferred from seismological and geodetic observations (2): Bull. of the Earthquake Res. Inst., v. 36, p. 21-53.
- Kasahara, Keichi, 1959, Physical conditions of earthquake faults II. (A model of strike-slip faults with various dip angles): Bull. of the Earthquake Res. Inst., v. 37, p. 39-51.
- Kasahara, Keichi, 1964, A strike-slip fault buried in a layered medium: Bull. of the Earthquake Res. Inst., v. 42, p. 609-619.
- Kostrov, B. V. and Nikitin, L. V., 1968, Emission of elastic waves during a break in the continuity of an elastic medium plane problem: Izv., Earth Physics, no. 7, p. 413-417.
- Major, M. W. and Butler, D. L., 1969, New earth-strain observatories in the Aleutian Islands (postdeadline abstract): Presented at the Fall meeting AGU, Dec. 1969.
- Mansinha, L. and Smylie, D. E., 1967, Effect of earthquakes on the Chandler Wobble and the secular polar shift: J. Geophys. Res., v. 72, no. 18, p. 4731 f.
- Mansinha, L. and Smylie, D. E., 1968, Earthquakes and the Earth's wobble: Science, v. 161, p. 1127-1129.
- Mansinha, L. and Smylie, D. E., 1971, The displacement fields of inclined faults: Bull. Seism. Soc. Am., v. 61, no. 5, p. 1433-1440.
- Marshall, G. E. and Stephens, J. R., 1968, Observations of earth-tilt and earthquake correlation, Denver area, Colorado: Earthquake Notes, v. 39, p. 23-36.

- Maruyama, Takuo, 1963, On the force equivalents of dynamical elastic dislocations with reference to the earthquake mechanism: Bull. of the Earthquake Res. Inst., v. 41, p. 467-486.
- Maruyama, Takuo, 1964, Statical elastic dislocations in an infinite and semi-infinite medium: Bull. of the Earthquake Res. Inst., v. 42, p. 289-368.
- Maruyama, Takuo, 1966, On two-dimensional elastic dislocations in an infinite and semi-infinite medium: Bull. of the Earthquake Res. Inst., v. 44, p. 811-871.
- Maruyama, Takuo, 1969, Stress fields in the neighborhood of a crack: Bull. of the Earthquake Res. Inst., v. 47, p. 1-29.
- McKeown, F. A.; Dickey, D. C.; and Bucknam, R. C., 1969, Preliminary analysis of geologic and geodetic data from the JORUM and MILROW nuclear events (postdeadline abstract): Presented at the Fall meeting AGU, Dec., 1969.
- Merritt, M. L. and Perret, W. R., 1969, Ground shock and water pressures from MILROW (postdeadline abstract): Presented at the Fall meeting AGU, Dec., 1969.
- Mindlin, Raymond D., and Cheng, David H., 1950, Nuclei of strain in the semi-infinite solid: J. of Applied Physics, v. 21, p. 926-930.
- Mogi, Kiyoo, 1963a, The fracture of a semi-infinite body caused by an inner stress origin and its relation to the earthquake phenomena (second paper): Bull. of the Earthquake Res. Inst., v. 41, p. 595-614.
- Mogi, Kiyoo, 1963b, Some discussions on aftershocks, foreshocks and earthquake swarms - the fracture of a semi-infinite body caused by an inner stress origin and its relation to the earthquake phenomena (third paper): Bull. of the Earthquake Res. Inst., v. 41, p. 615-658.
- Moskvina, A. G., 1969, Study of the displacement field of elastic waves in dependence of the characteristics of earthquake foci: Izv., Earth Physics, v. 9, p. 545-552.
- Nabarro, F.R.N., 1951, The synthesis of elastic dislocation fields: Philosophical Magazine, series 7, v. 42, p. 1224-1231.
- Nason, R. D. and Tocher, D., 1970, Measurement of movement on the San Andreas Fault in Mansinha, L; Smylie, D. E.; and Beck, A. E., eds., Earthquake Displacement Fields and the Rotation of the Earth: New York, Springer-Verlag New York, Inc., p. 246-255.
- Otsuka, Michio, 1964, Earthquake magnitude and surface fault formation: J. of Phys. of Earth, v. 12, no. 1, p. 19-24.
- Press, Frank, 1965, Displacements, strains, and tilts at teleseismic distances: J. of Geophys. Res., v. 70, no. 10, p. 2395-2412.

Raleigh, C. B.; Hoskins, E. L.; and Kirby, S. H., 1969, Deep-hole determinations of strain and in-situ stress related to the JORUM event (postdeadline abstract): Presented at the Fall meeting AGU, Dec., 1969.

Rexin, Elmer E.; Oliver, Jack; and Prantiss, David, 1962, Seismically-induced fluctuations of the water level in the Nunn-Bush well in Milwaukee: Bull. Seism. Soc. Am., v. 52, no. 1, p. 17-25.

Rikitake, Tsuneji and Yamazaki, Yoshio, 1969, Electrical conductivity of strained rocks, the fifth paper. Residual strains associated with large earthquakes as observed by a resistivity variometer: Bull. Earthquake Res. Inst., v. 47, p. 99-105.

Rochester, M. G., 1956, The application of dislocation theory to fracture of the Earth's crust: M. S. thesis, Univ. of Toronto.

Rochester, M. G., 1970, Polar wobble and drift: a brief history in Mansinha, L.; Smylie, D. E.; and Beck, A. E., eds., Earthquake Displacement Fields and the Rotation of the Earth: New York, Springer-Verlag New York, Inc., p. 3-16.

Romig, Phillip R.; Widaman, C. J.; VanWormer, J. D.; and Tocher, Don, 1969, Strain steps from the nuclear explosion JORUM (postdeadline abstract): Presented at the Fall meeting AGU, Dec., 1969.

Rybicki, Kacper, 1971, The elastic residual field of a very long strike-slip fault in the presence of a discontinuity: Bull. Seism. Soc. Am., v. 61, no. 1, p. 79-92.

Savage, J. C., 1969, Steketee's paradox: Bull. Seism. Soc. Amer., v. 59, no. 1, p. 381-384.

Savage, J. C. and Hastie, L. M., 1966, Surface deformation associated with dip-slip faulting: J. Geophys. Res., v. 71, p. 4897-4904.

Savage, J. C. and Hastie, L. M., 1969, A dislocation model for the Fairview Peak, Nevada, earthquake: Bull. Seism. Soc. Am., v. 59, p. 1937-1948.

Savage, J. C. and Kinoshita, W. T., 1971, Absence of observable geodetic strain accompanying Danville, California, earthquake sequence: Bull. Seism. Soc. Am., v. 61, no. 6, p. 1795-1799.

Savino, John; Sykes, Lynn R.; Liebermann, Robert C.; Murphy, Andrew; and Kelleher, John, 1969, Tectonic strain release by the underground explosions JORUM and MILROW (postdeadline abstract): Presented at the Fall meeting AGU, Dec., 1969.

Shamsi, Sabiha and Stacey, Frank D., 1969, Dislocation models and seismo-magnetic calculations for California 1906 and Alaska 1964 earthquakes: Bull. Seism. Soc. Am., v. 59, no. 4, p. 1435-1448.

Singh, Sarva Jit, 1971, Deformation of a multilayered half-space by stress dislocations and concentrated forces: Bull. Seism. Soc. Am., v. 61, no. 6, p. 1625-1637.

- Singh, Sarva Jit and Ben-Menahem, Ari, 1968, Eigenvibrations of the earth excited by finite dislocations II spheroidal oscillations: *Geophys. J. R. Astr. Soc.*, v. 17, p. 333-350.
- Singh, Sarva Jit and Ben-Menahem, Ari, 1969a, Eigenvibrations of the earth excited by finite dislocations - toroidal oscillations: *Geophys. J. R. Astr. Soc.*, v. 17, p. 151-177.
- Singh, Sarva Jit and Ben-Menahem, Ari, 1969b, Displacement and strain fields due to faulting in a sphere: *Phys. Earth Planet. Interiors*, v. 2, p. 77-78.
- Smith, Stewart W., 1969, Tectonic strain readjustments as a result of a large underground explosion (postdeadline abstract): Presented at the Fall meeting AGU, Dec., 1969.
- Smith, Stewart W.; Archambeau, Charles B.; and Gile, William, 1969, Transient and residual strains from large underground explosions: *Bull. Seism. Soc. Am.*, v. 59, no. 6, p. 2185-2196.
- Smith, Stewart W. and Van de Lindt, William, 1969, Strain adjustments associated with earthquakes in southern California: *Bull. Seism. Soc. Am.*, v. 59, no. 4, p. 1569-1589.
- Smylie, D. E. and Mansinha, L., 1967, Effect of earthquakes on the Chandler Wobble and the secular polar shift: *J. Geophys. Res.*, v. 72, no. 18, p. 4731-4732.
- Sneddon, I. N., 1946, The distribution of stress in the neighbourhood of a crack in an elastic solid: *Proc. of the Royal Soc. of London*, ser. 2, v. 187, p. 229-260.
- Stacey, F. D. and Rynn, J. M. W., 1970, Spurious local effects associated with teleseismic tilts and strains in Mansinha, L.; Smylie, D. E.; and Beck, A. E., eds., *Earthquake Displacement Fields and the Rotation of the Earth*: New York, Springer-Verlag New York, Inc., p. 230-233.
- Steketee, J. A., 1958a, On Volterra's dislocations in a semi-infinite elastic medium: *Can. J. Phys.*, v. 36, p. 192-205.
- Steketee, J. A., 1958b, Some geophysical applications of the elasticity theory of dislocations: *Can. J. Phys.*, v. 36, p. 1168-1198.
- Takemoto, Shuzo, 1970, Strain steps and the dislocation fault model: *Bull. Disaster Prev. Res. Inst., Tokyo Univ.*, v. 20, Part 1, no. 168, p. 1-15.
- Teisseyre, Roman, 1966, Density field of dislocations and fold deformation problem: *Bull. of the Earthquake Res. Inst.*, v. 44, p. 153-165.
- Vvedenskaya, A. V., 1958, Displacements in the surface of a fracture, accompanied by slip: *Bull. of the Academy of Sciences of the USSR, Geophysics, Series 1958*, p. 102-105.

- Vvedenskaya, A. V., 1959, The displacement field associated with discontinuities in an elastic medium: Izv., Geophys. Ser., Bull. Acad. Sci. USSR, Ser. 1959, p. 516-526.
- Weertman, J., 1965, Relationship between displacements on a free surface and the stress on a fault: Bull. Seism. Soc. Am., v. 55, no. 6, p. 945-953.
- Whipple, F.J.W., 1936, On the theory of the strains in an elastic solid bounded by a plane when there is a nucleus of strain at an internal point, and on the relation of the theory to seismology: Mon. Not. Roy. Astr. Soc., Geophys. Sup., v. 3, p. 380-388.
- Wideman, C. J. and Major, M. W., 1967a, Strain steps associated with earthquakes: AIAA Paper, no. 67-539, p. 1-6.
- Wideman, C. J. and Major, M. W., 1967b, Strain steps associated with earthquakes: Bull. Seism. Soc. Am., v. 57, no. 6, p. 1429-1444.
- Wood, M. D. and Allen, R. V., 1971, Anomalous microtilt preceding a local earthquake: Bull. Seism. Soc. Am., v. 61, no. 6, p. 1801-1809.
- Yoffe, Elizabeth H., 1961, A dislocation at a free surface: Philosophical Magazine, v. 6, no. 69, p. 1147-1155.
- Zienkiewicz, O. C. and Gerstner, R. W., 1961, The method of interface stress adjustment and its uses in the solution of some plane elasticity problems: Int. J. Mech. Sci., Pergamon Press Ltd, v. 2, p. 267-276.